frontiers | Research Topics

Neuroimaging in parkinson's disease and parkinsonism

Edited by
Yu Zhang, Maria Carmela Tartaglia, Wang Zhan and Edward Ofori

Published in
Frontiers in Neurology



FRONTIERS EBOOK COPYRIGHT STATEMENT

The copyright in the text of individual articles in this ebook is the property of their respective authors or their respective institutions or funders. The copyright in graphics and images within each article may be subject to copyright of other parties. In both cases this is subject to a license granted to Frontiers.

The compilation of articles constituting this ebook is the property of Frontiers.

Each article within this ebook, and the ebook itself, are published under the most recent version of the Creative Commons CC-BY licence. The version current at the date of publication of this ebook is CC-BY 4.0. If the CC-BY licence is updated, the licence granted by Frontiers is automatically updated to the new version.

When exercising any right under the CC-BY licence, Frontiers must be attributed as the original publisher of the article or ebook, as applicable.

Authors have the responsibility of ensuring that any graphics or other materials which are the property of others may be included in the CC-BY licence, but this should be checked before relying on the CC-BY licence to reproduce those materials. Any copyright notices relating to those materials must be complied with.

Copyright and source acknowledgement notices may not be removed and must be displayed in any copy, derivative work or partial copy which includes the elements in question.

All copyright, and all rights therein, are protected by national and international copyright laws. The above represents a summary only. For further information please read Frontiers' Conditions for Website Use and Copyright Statement, and the applicable CC-BY licence.

ISSN 1664-8714
ISBN 978-2-83251-851-9
DOI 10.3389/978-2-83251-851-9

About Frontiers

Frontiers is more than just an open access publisher of scholarly articles: it is a pioneering approach to the world of academia, radically improving the way scholarly research is managed. The grand vision of Frontiers is a world where all people have an equal opportunity to seek, share and generate knowledge. Frontiers provides immediate and permanent online open access to all its publications, but this alone is not enough to realize our grand goals.

Frontiers journal series

The Frontiers journal series is a multi-tier and interdisciplinary set of open-access, online journals, promising a paradigm shift from the current review, selection and dissemination processes in academic publishing. All Frontiers journals are driven by researchers for researchers; therefore, they constitute a service to the scholarly community. At the same time, the *Frontiers journal series* operates on a revolutionary invention, the tiered publishing system, initially addressing specific communities of scholars, and gradually climbing up to broader public understanding, thus serving the interests of the lay society, too.

Dedication to quality

Each Frontiers article is a landmark of the highest quality, thanks to genuinely collaborative interactions between authors and review editors, who include some of the world's best academicians. Research must be certified by peers before entering a stream of knowledge that may eventually reach the public - and shape society; therefore, Frontiers only applies the most rigorous and unbiased reviews. Frontiers revolutionizes research publishing by freely delivering the most outstanding research, evaluated with no bias from both the academic and social point of view. By applying the most advanced information technologies, Frontiers is catapulting scholarly publishing into a new generation.

What are Frontiers Research Topics?

Frontiers Research Topics are very popular trademarks of the *Frontiers journals series*: they are collections of at least ten articles, all centered on a particular subject. With their unique mix of varied contributions from Original Research to Review Articles, Frontiers Research Topics unify the most influential researchers, the latest key findings and historical advances in a hot research area.

Find out more on how to host your own Frontiers Research Topic or contribute to one as an author by contacting the Frontiers editorial office: frontiersin.org/about/contact

Neuroimaging in parkinson's disease and parkinsonism

Topic editors

Yu Zhang — VA Palo Alto Health Care System, Veterans Health Administration, United States Department of Veterans Affairs, United States
Maria Carmela Tartaglia — University of Toronto, Canada
Wang Zhan — University of Maryland, College Park, United States
Edward Ofori — Arizona State University, United States

Citation

Zhang, Y., Tartaglia, M. C., Zhan, W., Ofori, E., eds. (2023). *Neuroimaging in parkinson's disease and parkinsonism*. Lausanne: Frontiers Media SA.
doi: 10.3389/978-2-83251-851-9

Table of contents

06 Editorial: Neuroimaging in Parkinson's disease and Parkinsonism
Yu Zhang, Maria Carmela Tartaglia, Wang Zhan and Edward Ofori

10 Low Pulvinar Intensity in Susceptibility-Weighted Imaging May Suggest Cognitive Worsening After Deep Brain Stimulation Therapy in Patients With Parkinson's Disease
Keita Matsuura, Masayuki Maeda, Masayuki Satoh, Ken-ichi Tabei, Tomohiro Araki, Maki Umino, Hiroyuki Kajikawa, Naoko Nakamura and Hidekazu Tomimoto

18 Blood Flow and Glucose Metabolism Dissociation in the Putamen Is Predictive of Levodopa Induced Dyskinesia in Parkinson's Disease Patients
Maram Aljuaid, Samuel Booth, Douglas E. Hobson, Andrew Borys, Kelly Williams, Audrey Katako, Lawrence Ryner, Andrew L. Goertzen and Ji Hyun Ko

28 Diffusion Kurtosis Imaging for Detection of Early Brain Changes in Parkinson's Disease
Jitian Guan, Xilun Ma, Yiqun Geng, Dan Qi, Yuanyu Shen, Zhiwei Shen, Yanzi Chen, Erxi Wu and Renhua Wu

34 Brain MRI Reveals Ascending Atrophy in Parkinson's Disease Across Severity
Jamie C. Blair, Matthew J. Barrett, James Patrie, Joseph L. Flanigan, Scott A. Sperling, W. Jeffrey Elias and T. Jason Druzgal

49 Imaging Mild Cognitive Impairment and Dementia in Parkinson's Disease
Sanskriti Sasikumar and Antonio P. Strafella

57 Changed Resting-State Brain Signal in Parkinson's Patients With Mild Depression
Min Wang, Haiyan Liao, Qin Shen, Sainan Cai, Hongchun Zhang, Yijuan Xiang, Siyu Liu, Tianyu Wang, Yuheng Zi, Zhenni Mao and Changlian Tan

63 Diffusion Kurtosis Imaging of Microstructural Changes in Gray Matter Nucleus in Parkinson Disease
Gao Bingbing, Zhou Yujing, Miao Yanwei, Dong Chunbo, Wang Weiwei, Tian Shiyun, Liu Yangyingqiu, Shang Jin, Song Qingwei, Liu Ailian and Xie Lizhi

70 Dopamine Buffering Capacity Imaging: A Pharmacodynamic fMRI Method for Staging Parkinson Disease
Kevin J. Black, Haley K. Acevedo and Jonathan M. Koller

79 Assessing White Matter Pathology in Early-Stage Parkinson Disease Using Diffusion MRI: A Systematic Review
Maurizio Bergamino, Elizabeth G. Keeling, Virendra R. Mishra, Ashley M. Stokes and Ryan R. Walsh

100 Iron Imaging as a Diagnostic Tool for Parkinson's Disease: A Systematic Review and Meta-Analysis
Nadya Pyatigorskaya, Clara B. Sanz-Morère, Rahul Gaurav, Emma Biondetti, Romain Valabregue, Mathieu Santin, Lydia Yahia-Cherif and Stéphane Lehéricy

116 PET Tau Imaging and Motor Impairments Differ Between Corticobasal Syndrome and Progressive Supranuclear Palsy With and Without Alzheimer's Disease Biomarkers
Anna Vasilevskaya, Foad Taghdiri, Namita Multani, Cassandra Anor, Karen Misquitta, Sylvain Houle, Charles Burke, David Tang-Wai, Anthony E. Lang, Susan Fox, Elizabeth Slow, Pablo Rusjan and Maria C. Tartaglia

130 The Role of Magnetic Resonance Imaging for the Diagnosis of Atypical Parkinsonism
Lydia Chougar, Nadya Pyatigorskaya, Bertrand Degos, David Grabli and Stéphane Lehéricy

147 Abnormal Spontaneous Brain Activity in Left-Onset Parkinson Disease: A Resting-State Functional MRI Study
Kai Li, Wen Su, Min Chen, Chun-Mei Li, Xin-Xin Ma, Rui Wang, Bao-Hui Lou, Hong Zhao, Hai-Bo Chen and Chuan-Zhu Yan

155 Modern Brainstem MRI Techniques for the Diagnosis of Parkinson's Disease and Parkinsonisms
Germain Arribarat, Amaury De Barros and Patrice Péran

162 Usefulness of PET With [^{18}F]LBT-999 for the Evaluation of Presynaptic Dopaminergic Neuronal Loss in a Clinical Environment
Maria-Joao Ribeiro, Johnny Vercouillie, Nicolas Arlicot, Clovis Tauber, Valérie Gissot, Karl Mondon, Laurent Barantin, Jean-Philippe Cottier, Serge Maia, Jean-Bernard Deloye, Patrick Emond and Denis Guilloteau

169 Efficacy of Olfactory and Pareidolia Tests Compared With That of Indicative Biomarkers in Diagnosis of Dementia With Lewy Bodies
Yuta Inagawa, Hidekazu Kanetaka, Akito Tsugawa, Shu Sakurai, Shuntaro Serisawa, Soichiro Shimizu, Hirofumi Sakurai and Haruo Hanyu

175 Diffusion Tensor Imaging in Parkinson's Disease and Parkinsonian Syndrome: A Systematic Review
Yu Zhang and Marc A. Burock

200 Corrigendum: Diffusion Tensor Imaging in Parkinson's Disease and Parkinsonian Syndrome: A Systematic Review
Yu Zhang and Marc A. Burock

201 Neuroimaging Advances in Parkinson's Disease and Atypical Parkinsonian Syndromes
Usman Saeed, Anthony E. Lang and Mario Masellis

235 Association of MRI Measures With Disease Severity and Progression in Progressive Supranuclear Palsy
Marina Picillo, Filomena Abate, Sara Ponticorvo, Maria Francesca Tepedino, Roberto Erro, Daniela Frosini, Eleonora Del Prete, Paolo Cecchi, Mirco Cosottini, Roberto Ceravolo, Gianfranco Di Salle, Francesco Di Salle, Fabrizio Esposito, Maria Teresa Pellecchia, Renzo Manara and Paolo Barone

244 Differentiating Mild Cognitive Impairment, Alzheimer's Disease, and Dementia With Lewy Bodies Using Cingulate Island Sign on Perfusion IMP-SPECT
Hidekazu Kanetaka, Soichiro Shimizu, Yuta Inagawa, Daisuke Hirose, Naoto Takenoshita, Hirofumi Sakurai and Haruo Hanyu

250 Changes in Prefrontal Cortical Activity During Walking and Cognitive Functions Among Patients With Parkinson's Disease
Maud Ranchet, Isabelle Hoang, Maxime Cheminon, Romain Derollepot, Hannes Devos, Stephane Perrey, Jacques Luauté, Teodor Danaila and Laurence Paire-Ficout

263 Utility of Multi-Modal MRI for Differentiating of Parkinson's Disease and Progressive Supranuclear Palsy Using Machine Learning
Aron S. Talai, Jan Sedlacik, Kai Boelmans and Nils D. Forkert

274 Integrating Structural and Functional Interhemispheric Brain Connectivity of Gait Freezing in Parkinson's Disease
Chaoyang Jin, Shouliang Qi, Yueyang Teng, Chen Li, Yudong Yao, Xiuhang Ruan and Xinhua Wei

287 A Multimodal Imaging Approach Demonstrates Reduced Midbrain Functional Network Connectivity Is Associated With Freezing of Gait in Parkinson's Disease
Amgad Droby, Elisa Pelosin, Martina Putzolu, Giulia Bommarito, Roberta Marchese, Luca Mazzella, Laura Avanzino and Matilde Inglese

296 Proton Magnetic Resonance Spectroscopy for Diagnosis of Non-Motor Symptoms in Parkinson's Disease
Ji-tian Guan, Xin Zheng, Lingfeng Lai, Shuyi Sun, Yiqun Geng, Xiaolei Zhang, Teng Zhou, Huan-ze Wu, Jia-qing Chen, Zhong-xian Yang, Xiao-hong zheng, Jia-xu Wang, Wei Chen and You-qiao Zhang

frontiers | Frontiers in Neurology

TYPE Editorial
PUBLISHED 22 February 2023
DOI 10.3389/fneur.2023.1153682

Check for updates

OPEN ACCESS

EDITED AND REVIEWED BY
Alberto Albanese,
Catholic University of the Sacred Heart, Italy

*CORRESPONDENCE
Yu Zhang
✉ yuzhangucsfedu@gmail.com

SPECIALTY SECTION
This article was submitted to Movement Disorders, a section of the journal Frontiers in Neurology

RECEIVED 29 January 2023
ACCEPTED 08 February 2023
PUBLISHED 22 February 2023

CITATION
Zhang Y, Tartaglia MC, Zhan W and Ofori E (2023) Editorial: Neuroimaging in Parkinson's disease and Parkinsonism.
Front. Neurol. 14:1153682.
doi: 10.3389/fneur.2023.1153682

COPYRIGHT
© 2023 Zhang, Tartaglia, Zhan and Ofori. This is an open-access article distributed under the terms of the Creative Commons Attribution License (CC BY). The use, distribution or reproduction in other forums is permitted, provided the original author(s) and the copyright owner(s) are credited and that the original publication in this journal is cited, in accordance with accepted academic practice. No use, distribution or reproduction is permitted which does not comply with these terms.

Editorial: Neuroimaging in Parkinson's disease and Parkinsonism

Yu Zhang[1]*, Maria Carmela Tartaglia[2], Wang Zhan[3] and Edward Ofori[4]

[1]War Related Illness and Injury Study Center, VA Palo Alto Health Care System, Palo Alto, CA, United States, [2]Tanz Centre for Research in Neurodegenerative Diseases, University of Toronto, Toronto, ON, Canada, [3]Maryland Neuroimaging Center, University of Maryland, College Park, MD, United States, [4]Pathomechanics & Neuroimaging Laboratory, College of Health Solutions, Arizona State University, Phoenix, AZ, United States

KEYWORDS

Parkinson's disease, Parkinsonism, neuroimaging, movement disorder, dopamine

Editorial on the Research Topic
Neuroimaging in Parkinson's disease and Parkinsonism

As new pharmacological and surgical treatments developed, neuroimaging became one of the most promising biomarkers for diagnosis of Parkinson's Disease (PD) and Parkinsonism and monitoring disease progression and treatment. This Research Topic collected 25 articles (seven reviews, 15 original research articles, two brief research articles, and one hypothesis theory) that applied neuroimaging in PD and Parkinsonism. Imaging types included diffusion-MRI, proton-MRI, susceptibility-weighted imaging (SWI), structural and functional MRI (fMRI), glucose- and tau- positron emission tomography (PET), single photon emission computed tomography (SPECT), dopamine buffering capacity imaging, and as well as combinations of these approaches. We classified these articles into the following categories.

1. Meta-analysis and review articles addressing neuroimaging advantages in PD and Parkinsonism

These review articles have indicated that neuroimaging techniques are useful markers in detecting early changes in PD and parkinsonian syndromes. The brainstem and substantia nigra (SN) have been identified as vulnerable structures in PD and Parkinsonism, and neuromelanin-sensitive imaging has been shown to detect dorsolateral nigral hyperintensity, which implies SN neurodegeneration in Parkinsonism. Additionally, cognitive dysfunction is a significant non-motor feature of PD, and functional and anatomical imaging characteristics have been identified as potential predictors of cognitive impairment in PD. However, further research is required to fully understand the underlying mechanisms of cognitive impairment in PD and to develop more effective diagnostic and treatment options.

In a meta-analysis of 46 SN iron imaging studies in PD, Pyatigorskaya et al. found a notable size effect in the SN in PD for R2* increase (effect size = 0.84), for SWI measurements (effect size = 1.14), and for quantitative susceptibility mapping (QSM) increase (effect size = 1.13). Correlations between imaging measurements and motor

severity were mostly observed for QSM. These studies yielded consistently increased iron content in PD using R2, SWI, or QSM techniques, suggesting that these MRI measurements provide reliable markers of iron deposition in PD. Further, QSM appeared more robust and reproducible than R2* and more suitable to multicenter samples.

Bergamino et al. reviewed diffusion MRI studies in early-stage PD, with a focus on recent advances in the diffusion tensor imaging (DTI) methodology, such as the advantages and disadvantages of different diffusion MRI techniques, analysis methods, and software employed. These advanced methods have been shown to detect diffuse white matter changes in early-stage PD.

Arribarat et al. proposed that the brainstem is the earliest vulnerable structure in multiple system atrophy (MSA) or PD. In a brief overview on recent advances in brainstem-related MRI markers in PD and Parkinsonism, the authors summarized the ability of brainstem imaging, including iron-sensitive MRI, nigrosome imaging, neuromelanin-sensitive MRI, DTI, and advanced diffusion imaging, to discriminate patients with PD from controls or to discriminate patients with PD from patients with atypical parkinsonism. A standardized multimodal brainstem-dedicated MRI approach is promising for detecting early changes in PD and parkinsonian syndromes.

Based on predominant protein aggregates observed within the brain, Parkinsonian disorders are categorized as a-synucleinopathies and tauopathies. Saeed et al. reviewed studies that use neuroimaging biomarkers, including structural MRI, diffusion MRI, functional MRI, proton magnetic resonance spectroscopy, and transcranial B-mode sonography, for measuring SN and lentiform nucleus echogenicity, as well as SPECT and PET that are used to improve diagnostic certainty and ensure more informed diagnostic decisions.

By reviewing multimodal MRI in Parkinsonian syndromes, Chougar et al. reported the development of several imaging signs/measurements, some of which have shown individual-level diagnostic utility. Specifically, neuromelanin-sensitive imaging detecting dorsolateral nigral hyperintensity implies SNc neurodegeneration in Parkinsonism; neuromelanin signal loss in coeruleus is associated with rapid eye movement sleep behavior disorder (RBD), and is an early sign of PD and MSA. The midbrain to pons ratio and the MR Parkinsonism Index (MRPI) are robust clinical biomarkers of progressive supranuclear palsy (PSP), while abnormalities in the putamen, pons, and cerebellum strongly support the diagnosis of MSA.

Cognitive dysfunction is a significant non-motor feature of PD; however, the pathophysiology of cognitive impairment in PD cannot be explained by dopaminergic loss alone. A review article by Sasikumar and Strafella identified functional and anatomical imaging characteristics that predict cognitive impairment in PD, the limitations that challenge this process, and the avenues of potential research.

2. Neuroimaging in early diagnosis of PD

Neuroimaging techniques, such as DTI, diffusion kurtosis imaging (DKI), and functional near infrared spectroscopy (fNIRS), have been found to be useful in the early diagnosis and tracking of PD. The use of DTI and DKI in particular has shown promise in identifying changes in the brain's microstructure, which may aid in diagnosing early-stage PD. Additionally, the use of fNIRS has been found to be useful in assessing changes in cortical activity during tasks such as walking, which may be indicative of compensation for executive deficits in patients with PD. Furthermore, the new assessment of dopamine transporter (DAT) using [18F]LBT-999 and short PET acquisition can be an alternative to assess dopaminergic presynaptic injury in PD using a single 10 min acquisition. These findings suggest that neuroimaging may be an important tool in the early diagnosis of PD.

Zhang and Burock reviewed DTI analyses of PD, focusing on the utility of DTI as a marker of diagnosing early PD, correlating motor symptoms, tracking disease progression, and treatment effects. This review article highlighted a complex pattern of fractional anisotropic (FA) changes in the first few years of PD, in which, FA shows compensatory responses to motor deficits in some motor areas, and these increased anisotropic findings can be observed in young-onset and early-stage PD.

Guan J. et al. evaluated mean kurtosis (MK) values in the bilateral red nucleus and SN using DKI in 26 (14 early-stage and 12 advanced-stage) patients with PD and 15 healthy controls. The authors found that MK values in the bilateral SN were significantly lower in all patients than in controls. Advanced-stage PD had a lower MK in the left SN than that of early-stage PD. While no significant differences in FA or mean diffusivity (MD) were detected between groups, the findings suggested that DKI measurements of the SN may aid the diagnoses of early PD and PD stages.

Bbingbing et al. also examined DKI and DTI in the basal ganglia nuclei and found that MD in the globus pallidus provides the largest area under the Receiver Operating Characteristic curve for distinguishing PD from healthy controls. Furthermore, all DKI parameters correlated to the Mini-Mental State Examination, and these can be a useful indicator of microstructures in extrapyramidal nuclei in PD.

Similar to the imaging of functional activity using task-based fMRI, Ranchet et al. measured cortical activity in the dorsolateral prefrontal cortex (DLPFC) by analyzing oxy-hemoglobin (1HbO2) and deoxy-hemoglobin (1HbR) using a functional near infrared spectroscopy (fNIRS) device, to asses DLPFC activation during usual walking and dual-task walking conditions in patients with PD. The authors suggested that the increased DLPFC activity in patients during usual walking suggests a potential compensation for executive deficits.

Ribeiro et al. proposed a novel assessment of DAT using [18F]LBT-999 and a short PET acquisition. The authors reported that the striatal uptake of DAT was lower than in controls, which was confirmed by binding potential, distribution volume ratios, and ratios calculated for both the striatal nuclei and SN, which were significantly lower in patients with PD compared with controls. The study demonstrated that [18F]LBT-999 PET could be an alternative to assess dopaminergic presynaptic injury in PD using a single 10 min acquisition.

3. Neuroimaging in monitoring PD progression and treatment-induced syndromes

Neuroimaging has played a vital role in understanding the progression and treatment-induced syndromes of PD. Studies have shown that MRI-based gray matter density can detect an organized pattern of atrophy across disease progression and that a novel pharmacological fMRI (phMRI) method can objectively quantify disease severity in PD. Additionally, pulvinar thalamic hypointensity and the putamen-to-thalamus Hyper-Perfusion/Hypo-Metabolism Index (PHI) have been proposed as potential biomarkers for cognitive worsening and Levodopa-induced dyskinesia (LID), respectively.

Blair et al. retrospectively used MRI-based gray matter density in regions of interest (ROIs) in PD studies of 228 patients with early PD, 136 patients with advanced PD, and 103 control subjects to assess the caudal-rostral pattern of the progression of Lewy body pathology in PD. The study found that patients with advanced PD had a lower gray matter density in the basal forebrain, amygdala, and entorhinal cortex than patients with early PD and controls. Across all patients with PD, the gray matter density in nearly all subcortical regions significantly decreased with disease duration. These findings suggest an organized pattern of atrophy across disease progression.

Black et al. proposed a novel phMRI method for objectively quantifying disease severity in PD. Specifically, the authors proposed a method to measure the effect site rate constant and the predicted time using phMRI, based on the timing of the known response of several brain regions to exogenous levodopa. This new method will enable measurement of the severity of dopamine denervation objectively and will simultaneously provide a robust imaging response to exogenous levodopa.

Matsuura et al. examined pulvinar thalamic hypointensity in 21 patients with PD who underwent deep brain stimulation (DBS) at baseline and 1 year after using SWI. Pulvinar hypointensity was identified in 11 of the 21 patients at baseline. One year after DBS, pulvinar hypointensity was found in five of the six patients who had worsened cognitive performance, and in all six patients who had hallucinations. These findings, i.e., pulvinar hypointensity in patients after DBS, are helpful for detecting cognitive worsening and the emergence of hallucinations.

Patients with PD and LID often present increased cerebral blood flow and decreased putaminal metabolism. Aljuaid et al. studied the effects of anti-parkinsonian medications in 10 patients with PD (5 with LID and 5 without LID), using FDG-PET and perfusion MRI in their ON and OFF states. The study found a significant interactive effect in putamen, in which glucose metabolism was consistently decreased by anti-parkinsonian medication, while mixed effects were observed in CBF perfusion. Furthermore, the putamen-to-thalamus PHI may be a potential biomarker for LID.

4. Neuroimaging in PD-associated motor and non-motor symptoms

Neuroimaging studies have provided new insights into the distinct characteristics of brain activity, midbrain atrophy, dysconnectivity, and metabolic alterations associated with PD. These studies have highlighted the potential of neuroimaging in detecting PD-associated motor and non-motor symptoms such as freezing of gait (FOG), depression, and cognitive dysfunction.

Li et al. evaluated motor asymmetry in PD using amplitude of low-frequency fluctuation (ALFF), assessed with resting state fMRI (rs-fMRI). The study found altered ALFF in patients with left-onset PD (LPD) compared with a control group. ALFF of the left inferior temporal gyrus correlated with motor function, and ALFF of the thalamus correlated with cognition. These findings provide new insights into the distinct characteristics of spontaneous brain activity in LPD.

Using multi-modal analyses with voxel-based morphometry and functional connectivity (FC), Droby et al. reported midbrain atrophy in patients with PD and FOG compared with those without FOG. Furthermore, decreased midbrain-cortical FC was found to be associated with FOG occurrence and the severity scores of patients with PD.

To reveal the dysconnectivity mechanism underlying PD with and without freezing of gait, Jin et al. analyzed structural and functional connectivity using FA and MD measurements from DTI and voxel-mirrored homotopic connectivity (VMHC), calculated from rs-fMRI images of 24 patients with PD and FOG+, 37 patients with PD and FOG–, and 24 healthy controls. Patients with PD and FOG+ had impaired interhemispheric brain connectivity, measured by FA, MD, and VMHC, which was related to clinical FOG severity. These results demonstrate that integrating structural and functional MRI analyses can provide information on the pathophysiological mechanisms of FOG in PD.

Wang et al. studied brain blood-oxygen-level-dependent (BOLD) activities using Regional Homogeneity (ReHo), calculated from rs-fMRI. The authors reported that mildly-moderately depressed PD had a lower ReHo in the anterior cingulate cortex than that for non-depressed PD. Severely depressed PD had a higher ReHo in the frontal area than that for mildly-moderately depressed PD. Severely depressed PD had a higher ReHo in the supplementary motor area than that for non-depressed PD. ReHo measurement may provide evidence for the prediction of PD with subclinical depression.

Guan J-t. et al. used 1H-MRS to investigate the alteration of metabolites in patients with PD at different stages of the disease. The results revealed that altered metabolites are associated with non-motor symptoms, including sleep and gastrointestinal and cognitive dysfunction in patients with PD at late stages, suggesting that these metabolic markers may be able to track disease progression in PD.

5. Neuroimaging in differentiating among atypical Parkinsonism

Atypical Parkinsonism shares typical motor symptoms with sporadic PD, and misdiagnosis is frequent. Measuring neuromelanin-sensitive signals as well as structural indices of the brainstem, cerebellum, midbrain, and basal ganglia nuclei help differentiate corticobasal syndrome (CBS), PSP, and MSA from PD. Tau-PET and DAT imaging have shown strong effects in differentiating dementia with Lewy bodies (DLB) from Alzheimer's disease (AD).

Picillo et al. performed midbrain-based MRI morphometric assessments in 67 patients with PSP. The study reported that reduced midbrain size is significantly associated with greater ocular motor dysfunction at baseline MRI as well as more rapid disease progression upon follow up.

Vasilevskaya et al. compared parkinsonian syndromes (CBS/PSP) without AD biomarkers (CBS/PSP-non-AD, $n = 17$) to parkinsonian syndromes with AD biomarkers (CBS/PSP-AD, $n = 7$), using MRI and PET imaging with a tau ligand [18F]-AV1451 tracer. The AD biomarker–positive group had increased Tau-uptake and lower volumes in AD-specific areas. These results suggested that CBS and PSP syndromes are strongly affected by the presence of AD biomarkers.

Talai et al. compared the accuracy of using multi-modal MRI datasets for automatic differentiation of patients with PD, patients with progressive supranuclear palsy Richardson's syndrome (PSP-RS), and healthy controls. Machine learning models showed that regional DTI metrics performed excellently, with a 95.1% classifying accuracy, similar to the optimal multi-modal machine learning model. These uni-modal DTI and multi-modal (morphometric T1WI, iron-sensitive T2WI, and DTI) datasets may provide useful markers in differentiating PD and PSP-RS.

The cingulate island sign (CIS), which is a preserved pattern in the posterior cingulate gyrus on FDG-PET, is an important sign to distinguish DLB from AD. Kanetaka et al. studied CIS using IMP-SPECT in patients with mild cognitive impairment (MCI), AD, or DLB. The CIS score in the AD group was significantly higher than that in the DLB or MCI groups. The results suggest that the diagnostic power of IMP-SPECT is not inferior to that of ECD-SPECT in differentiating DLB from AD.

Inagawa et al. investigated the efficacy of olfactory and hallucination tests in differentiating AD from DLB, in comparison with the known biomarkers for DLB, including DAT-SPECT and meta-iodobenzylguanidine (MIBG) in myocardial scintigraphy. Their results suggest that the hallucination and olfactory tests may be considered before resorting to nuclear neuroimaging in the diagnosis of DLB.

In conclusion, this Research Topic provided articles on well-established and emerging neuroimaging biomarkers to improve diagnostic certainty and to ensure more precise treatment strategies. A remarkable advantage is the integrative multimodal neuroimaging approach, which proved superior to single modality-based methods. We hope that readers will find this Research Topic a useful reference for state-of-the-art neuroimaging developments and applications in Parkinson's Disease and Parkinsonism.

Author contributions

All authors listed have made a substantial, direct, and intellectual contribution to the work and approved it for publication.

Conflict of interest

The authors declare that the research was conducted in the absence of any commercial or financial relationships that could be construed as a potential conflict of interest.

Publisher's note

All claims expressed in this article are solely those of the authors and do not necessarily represent those of their affiliated organizations, or those of the publisher, the editors and the reviewers. Any product that may be evaluated in this article, or claim that may be made by its manufacturer, is not guaranteed or endorsed by the publisher.

frontiers in Neurology

ORIGINAL RESEARCH
published: 31 October 2019
doi: 10.3389/fneur.2019.01158

Low Pulvinar Intensity in Susceptibility-Weighted Imaging May Suggest Cognitive Worsening After Deep Brain Stimulation Therapy in Patients With Parkinson's Disease

Keita Matsuura[1,2], Masayuki Maeda[3], Masayuki Satoh[4], Ken-ichi Tabei[4], Tomohiro Araki[5], Maki Umino[6], Hiroyuki Kajikawa[2], Naoko Nakamura[2] and Hidekazu Tomimoto[1]*

[1] Department of Neurology, Graduate School of Medicine, Mie University, Tsu, Japan, [2] Department of Neurology, Suzuka Kaisei Hospital, Suzuka, Japan, [3] Department of Advanced Diagnostic Imaging, Graduate School of Medicine, Mie University, Tsu, Japan, [4] Dementia Prevention and Therapeutics, Mie University, Tsu, Japan, [5] Department of Neurosurgery, Suzuka Kaisei Hospital, Suzuka, Japan, [6] Department of Radiology, Graduate School of Medicine, Mie University, Tsu, Japan

Purpose: Deep brain stimulation (DBS) is an established therapy for Parkinson's disease (PD). However, deteriorating cognitive function after DBS is a considerable problem for affected patients. This study was undertaken to assess whether pulvinar findings in susceptibility-weighted imaging (SWI) can suggest cognitive worsening.

Methods: We examined 21 patients with PD who underwent DBS along with SWI and neuromelanin-sensitive MR imaging (NMI). We further assessed pulvinar hypointensity based on the SWI findings and also the area of the substantia nigra (SN) pars compacta in NMI. We then examined associations among cognitive changes, pulvinar hypointensity, and SN area. The cognitive function of the patient immediately before surgery was compared with function at 1 year postoperatively.

Results: Pulvinar hypointensity in SWI was found in 11 of 21 patients with PD at baseline. One year postoperatively, six of the 21 patients demonstrated a Mini-Mental State Examination score that was ≥3 points lower than the baseline score. We observed pulvinar hypointensity in SWI before DBS surgery in five of these six patients ($p = 0.072$). During the first postoperative year, six of 21 patients reported both transient or permanent hallucinations; we observed pulvinar hypointensity in these six patients, while 10 patients without pulvinar hypointensity had no hallucinations.

Conclusion: Pulvinar hypointensity in SWI in patients with PD may provide information that is useful for suggesting cognitive deterioration after DBS treatment.

Keywords: pulvinar nuclei, susceptibility-weighted imaging, diffusion-weighted imaging, Parkinson's disease, deep brain stimulation, cognitive function

OPEN ACCESS

Edited by:
Edward Ofori, Arizona State University, United States

Reviewed by:
Chon-Haw Tsai, China Medical University Hospital, Taiwan
Marian L. Dale, Oregon Health & Science University, United States

****Correspondence:***
Keita Matsuura
matsuura@kaiseihp.com

Specialty section:
This article was submitted to Movement Disorders, a section of the journal Frontiers in Neurology

Received: *26 July 2019*
Accepted: *15 October 2019*
Published: *31 October 2019*

Citation:
Matsuura K, Maeda M, Satoh M, Tabei K, Araki T, Umino M, Kajikawa H, Nakamura N and Tomimoto H (2019) Low Pulvinar Intensity in Susceptibility-Weighted Imaging May Suggest Cognitive Worsening After Deep Brain Stimulation Therapy in Patients With Parkinson's Disease. Front. Neurol. 10:1158. doi: 10.3389/fneur.2019.01158

INTRODUCTION

Deep brain stimulation (DBS) is an established therapy for Parkinson's disease (PD) (1). However, patients who undergo DBS may experience side effects such as headaches, seizures, recall difficulty, and postoperative deterioration of cognitive function (2). Frontal 18-fluorodeoxyglucose positron emission tomography (PET) activity is reportedly related to cognitive outcome after DBS of the

subthalamic nucleus (STN) in patients with advanced PD disease (3). In daily practice, however, it is difficult to use PET scans.

Recently, hypointensity of the pulvinar nucleus on fluid-attenuated inversion recovery (FLAIR) images has been found in patients with Alzheimer's disease; this is suspected to represent abnormal iron accumulation (4). We have shown that a low signal from the pulvinar nucleus on diffusion-weighted imaging (DWI) is associated with hallucinations in dementia patients (5). Furthermore, some reports have indicated a relationship between pulvinar change and Lewy body dementia (DLB) (6–8). In particular, Erskine et al. reported that α-synuclein was present throughout the pulvinar in DLB (6). Notably, α-synuclein can bind Fe(II) and Fe(III) (9–12), and susceptibility-weighted imaging (SWI) exploits the tissues' magnetic properties, such as blood or iron content (13). Hence, we hypothesized that hypointensity of the pulvinar nucleus in SWI will suggest cognitive worsening after DBS during prodromal cognitive impairment in patients with PD because it may represent α-synuclein pathology.

Furthermore, neuromelanin-sensitive MR imaging (NMI) is a useful tool for the diagnosis and follow-up of patients with PD (14–19). Hatano et al. reported that patients with PD with motor complications (MC) had markedly smaller substantia nigra (SN) pars compacta areas in NMI compared with patients with PD without MC (20). Several papers have reported a correlation between motor symptom severity and NMI signal changes in patients with PD (16–19). However, there have been no reports of correlations between cognitive function and NMI signal changes in patients with PD. In this study, we aimed to evaluate the relationships between cognitive worsening in patients with PD after DBS, the hypointensity of the pulvinar nucleus in SWI, and the SN area in NMI.

MATERIALS AND METHODS

This study was conducted retrospectively. Inclusion criteria were as follows: patients with PD who fulfilled the United Kingdom Brain Bank criteria (21) and underwent DBS therapy at our institution between November 2010 and April 2016. Twenty-one patients (16 women, five men; mean age: 62.1 years) matched these criteria. This study was approved by the Institutional Review Boards of our institutions, and informed consent was provided by all patients before enrollment in the study.

All patients underwent MRI at a 3T MRI unit (Verio; Siemens AG, Erlangen, Germany) with a 32-channel head coil. MR sequences consisted of SWI, DWI, three-dimensional (3D)-FLAIR, NMI, and 3D-T1-weighted imaging. The SWI parameters were as follows: repetition time (TR), 25 ms; echo time (TE), 20 ms; flip angle, 16°; field of view (FOV), 210 mm; matrix size, 510 × 512; section thickness, 1.2 mm; acquisition time, 3 min 42 s. The DWI parameters were as follows: TR, 5,900 ms; TE, 85 ms; FOV, 230 × 230 mm; matrix size, 114 × 114; slice thickness, 3.0 mm; acquisition time, 1 min 17 s. The 3D-FLAIR parameters were as follows: TR, 10,000 ms; TE, 617 ms; flip angle, T2 var; FOV, 267 × 267 mm; matrix size, 256 × 256; slice thickness, 1.1 mm; acquisition time, 6 min 20 s. The pulse sequence used for NMI was a T1-weighted fast spin-echo technique; TR, 550 ms; TE, 11 ms; echo train length, 4; FOV, 200 mm; matrix size, 448 × 311 (pixel size: 0.45 × 0.64 mm); slice thickness, 2.5 mm (gapless, 6-averaged, 12 slices); acquisition time, 9 min (14, 16, 18). For voxel-based morphometry (VBM), the parameters used for 3D-T1-weighted imaging were as follows: TR, shortest; TE, 15 ms; flip angle, 90°; FOV, 230 × 230 mm; matrix size, 256 × 256; slice thickness, 1.1 mm; acquisition time, 6 min 20 s.

All patients underwent bilateral electrode placement for STN (17 patients) or pallidal (four patients) DBS. Electrodes (Medtronic DBS lead models 3389 and 3387, Medtronic, Minneapolis, MN, USA; and the Vercise® DBS lead, Boston Scientific, Natick, MA, USA) were implanted under local anesthesia using a Leksell stereotactic frame (Elekta Instruments AB, Stockholm, Sweden) and anatomical (MRI and computed tomography) and physiological targeting. Based on microelectrode recordings, electrodes were considered correctly located in the target region. Impulse generators (Activa SC/RC, Medtronic; Vercise® system, Boston Scientific) were implanted and connected during a second surgical procedure on the same day.

The levodopa equivalent daily dose (LEDD) for each patient was calculated as follows: 100 mg L-dopa/decarboxylase inhibitor = 1 mg pramipexole = 5 mg ropinirole = 3.3 mg/day rotigotine = 4 mg cabergoline = 70 mg L-dopa/decarboxylase inhibitor with entacapone (22–24).

By performing SWI, FLAIR, and DWI at the level of 2 mm above the anterior to posterior commissure (AC–PC) line, signal intensities for the pulvinar nucleus were evaluated for normal intensity or hypointensity by two reviewers in a blinded manner (**Figure 1**). The SN area was measured at the section through the inferior edge of the inferior colliculus using ImageJ (National Institutes of Health, Bethesda, MD, USA). Briefly, image files containing neuromelanin-related contrast (NRC) at the section through the inferior edge of the inferior colliculus were imported to ImageJ, converted into 8-bit files, and smoothed. Next, the SN threshold was adjusted to a level that eliminated noise contrast, leaving NRC in the SN and additional contrast in two small areas lateral to the aqueduct. The areas filled with white were originally shown in red on the computer color display. The number of pixels in each area was calculated automatically (16, 18, 19).

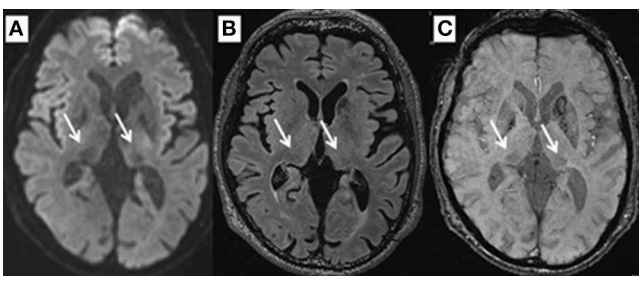


FIGURE 1 | Pulvinar hypointensity MRI of a 61-year-old man in DWI **(A)**, FLAIR **(B)**, and SWI **(C)**.

We also performed N-isopropyl-p-[123I]-iodoamphetamine ([123I]-IMP) single-photon emission computerized tomography (SPECT) scans for all patients. All subjects were injected with 167 MBq of [123I]-IMP while in a supine resting state with their eyes closed. After 5 min, brain SPECT scanning was performed for 25–30 min using an E.CAM system, an LMEGP collimator, and a GMS-5000 WorkStation (Toshiba, Tokyo, Japan). Axial images were obtained by filtered back-projection methods. Cerebral blood flow (CBF) was measured by Graph Plot Analysis (25).

MRI data for VBM were analyzed using SPM12 (Wellcome Institute of Neurology, University College London, London, UK) running on MATLAB R2012a (MathWorks, Natick, MA, USA). In the pre-processing phase, images were set to match the AC-PC line using an automated MATLAB script. The images were then visually inspected to detect possible scan issues such as field distortion and movement artifacts. Reoriented images were corrected for intensity inhomogeneity and segmented into gray matter (GM), white matter (WM), cerebrospinal fluid, and other tissues outside of the brain by SPM12 tissue probability maps. The images were registered with the East Asian Brains International Consortium for Brain Mapping space template through affine regularization. We created a population-specific template using the SPM12 DARTEL template procedure to compare groups directly, with or without pulvinar hypointensity in SWI, cognitive worsening, and hallucination; thus, we investigated whole-brain GM differences between groups. GM and WM segments were inputted into high-dimensional DARTEL to create non-linear, modulated-normalized, GM images that were smoothed using a Gaussian kernel of 8 mm full width at half maximum. No participants were excluded from analysis after these steps.

For the region of interest of pulvinar nucleus analyses, we assessed the statistical significance at a voxel threshold of $p < 0.005$ (uncorrected); contiguous clusters of at least 10 voxels were reported. We obtained both Montreal Neurological Institute (MNI) and Talairach coordinates to detect the anatomical regions of the clusters. We used a transformation from Matthew Brett (http://imaging.mrc-cbu.cam.ac.uk/imaging/MniTalairach) to convert MNI coordinates to Talairach coordinates, and Talairach Client 2.4.3 was used to identify the anatomical regions corresponding to Talairach coordinates (26). We performed assessments including the Unified Parkinson's Disease Rating Scale (UPDRS), LEDD, Mini-Mental State Examination (MMSE), Frontal Assessment Battery (FAB), the Trail Making Test (TMT), and the Center for Epidemiologic Studies Depression Scale (CES-D) for all patients before DBS (i.e., baseline) and at 1 year postoperatively (27–31). We also checked for the presence or absence of hallucinations based on medical records.

All statistical analyses were performed using SPSS software (version 23, IBM Corp., Armonk, NY, USA). To compare the Hoehn-Yahr stage, UPDRS, use of dopamine agonist, entacapone, selegiline and zonisamide, MMSE, FAB, and CES-D between baseline and 1 year postoperatively, we used Wilcoxon signed-rank tests. To compare the LEDD, L-dopa dosage, and TMT-A between baseline and 1 year postoperatively, we used paired *t*-tests. To compare the MMSE score change, MMSE score at baseline, and Hoehn-Yahr stage between the groups with a worsened and with a stationary or better MMSE score, we used Mann–Whitney's *U*-test. To compare age, disease duration, and LEDD between the groups with a worsened and with a stationary or better MMSE score, we used unpaired *t*-tests. To compare the change in TMT-A and FAB scores between the groups with pulvinar isointensity and pulvinar hypointensity in SWI, we used Mann-Whitney's *U*-test. Fisher's exact test was used to analyze pulvinar hypointensity or isointensity in the SWI, DWI, and FLAIR groups and to compare between groups with SN areas $\geq$12 and $<$12 for changes in MMSE scores. Correlations between changes in the MMSE score and SN area, as well as between UPDRS and SN area, were analyzed using Spearman's rank correlation coefficient. We used a Student's *t*-test to compare CBF between groups. An α level of 0.05 was considered statistically significant.

TABLE 1 | Patient profile.

	Pre-operation	After 1 year
Age	62.1 ± 8.6	
Sex (M:F)	5:16	
Disease duration (years)	11.3 ± 6.3	
DBS target	STN17 GPi4	
Hoehn-Yahr stage (on state)	2.4 ± 0.8	2.1 ± 0.9*
Hoehn-Yahr stage (off state)	3.7 ± 0.8	2.7 ± 0.8**
UPDRS Part I	3.0 ± 2.6	0.95 ± 1.28**
UPDRS Part II	9.5 ± 6.2	8.0 ± 5.9
UPDRS Part III	18.3 ± 12.3	11.4 ± 8.5**
UPDRS Part IV	7.4 ± 2.9	3.3 ± 2.7**
LEDD (mg)	694 ± 294	427 ± 219**
L-Dopa (mg)	376 ± 161	208 ± 121**
DA (use rate; %)	86%	81%
Entacapone (use rate; %)	71%	52%
Selegiline (use rate; %)	24%	24%
Zonisamide (use rate; %)	33%	38%
MMSE	26.24 ± 3.38	25.86 ± 5.14
FAB	13.76 ± 3.08	14.75 ± 2.40
TMT-A (s)	200 ± 149	153 ± 81
CES-D	16.4 ± 13.0	13.2 ± 13.3

*$p < 0.05$, **$p < 0.01$. DBS, deep brain stimulation; STN, subthalamic nucleus; GPi, internal segment of globus pallidus; UPDRS, the Unified Parkinson's disease rating scale; LEDD, levodopa equivalent daily dose; DA, dopamine agonist; MMSE, Mini-Mental State Examination; FAB, Frontal Assessment Battery; TMT, Trail Making Test; CES-D, the Center for Epidemiologic Studies Depression Scale.*

RESULTS

At the time of the DBS operation, the patients' average age (mean ± standard deviation) was 62.1 ± 8.6 years. Immediately after DBS, the average motor performance (Hoehn-Yahr stage, UPDRS) significantly improved, and LEDD and L-dopa dosage significantly decreased (**Table 1**). Cognitive performance

TABLE 2 | Relationship between cognitive function and pulvinar hypointensity in SWI.

	MMSE score 1 year after DBS operation		MMSE score worsened over 3 points from baseline		Hallucination occurred during follow-up period	
Pulvinar in SWI	**Normal**	**Under 24**	**Stationary or better**	**Worsened**	**Nothing**	**Occurred**
Hypointensity	5	6	6	5	5	6
Isointensity	10	0	9	1	10	0
	$p = 0.0057$		$p = 0.072$		$p = 0.0057$	

(MMSE, FAB, and TMT-A) and the depression scale remained unchanged (**Table 1**). One year postoperatively, the average Hoehn-Yahr stages in on and off states, respectively, improved compared with baseline ($p = 0.031$ and $p < 0.001$, respectively) (**Table 1**). All patients had no hallucinations at the baseline.

In this series, pulvinar hypointensity, as assessed by visual inspection by performing SWI, DWI, and FLAIR, was present in 11, 9, and 7 patients, respectively (**Figure 1**). One year postoperatively, six of 21 patients had MMSE scores < 24. Four of these six cases showed a reduction of ≥3 points in the MMSE score from baseline, and five of the six cases experienced transient or permanent hallucinations. The type of hallucination was both visual and auditory in three cases and only visual in three cases. We observed pulvinar hypointensity in SWI in all six patients (**Table 2**, $p = 0.0057$). Six of 21 patients showed a reduction of ≥3 points in the MMSE score from baseline; five of these six patients showed pulvinar hypointensity in SWI (**Table 2**, $p = 0.072$). During the observation period, six of 21 patients reported both transient and permanent hallucinations; all six patients showed hypointensity in SWI. In contrast, 10 patients without pulvinar nucleus hypointensity in SWI reported no hallucinations (**Table 2**, $p = 0.0057$). We compared age, disease duration, LEDD, and MMSE score at baseline between the groups with a worsened and with a stationary or better MMSE score 1 year postoperatively. A difference was observed between age at the operation and pulvinar hypointensity in SWI ($p = 0.100$ and 0.072, respectively; **Table 3**). Nine cases showed pulvinar hypointensity in DWI and no association with the MMSE score, deterioration of cognitive function, or occurrence of hallucinations 1 year postoperatively ($p = 0.48$, 0.93, and 0.79, respectively). Seven cases showed pulvinar hypointensity by FLAIR and no association with the MMSE score, deterioration of cognitive function, or occurrence of hallucinations 1 year postoperatively ($p = 0.15$, 0.66, and 0.30, respectively). No significant differences were observed in the change in TMT A time between the groups with pulvinar isointensity (−42.8 ± 41.3) and hypointensity (2.2 ± 114.7, $p = 0.0642$) in SWI. There was no significant difference in the change in FAB score between the groups with pulvinar isointensity (0.3 ± 1.8) and hypointensity (1.1 ± 3.1, $p = 0.133$) in SWI (**Figure 2**). The group with pulvinar hypointensity in SWI was divided into two. One was a group with an MMSE score reduction of ≥3 points, and the other was a group with an MMSE score reduction of <3 points. Age, disease duration, LEDD, and severity (Hoehn-Yahr stage) at the baseline were not significantly different between the two groups. The intraclass correlation coefficient of visual inspection of the iso- or hypointensity of the pulvinar nucleus in SWI was 0.931, indicating excellent correlation.

TABLE 3 | Comparison between the worsened and stationary or better MMSE score groups.

	MMSE score worsened over 3 points from baseline		
	Worsened (6 cases)	**Stationary or better (15 cases)**	***p*-value**
MMSE score pre-operation	26.3 ± 2.4	26.2 ± 3.8	0.937
Change in MMSE score	−6.0 ± 3.9	1.9 ± 2.3	0.00110
Age (years)	67.0 ± 6.5	60.1 ± 8.8	0.100
Disease duration (years)	10.3 ± 6.3	11.7 ± 6.7	0.666
LEDD (mg)	631 ± 410	719 ± 258	0.559
Hoehn-Yahr stage (On/Off)	3.0 ± 0.6/3.7 ± 0.8	2.2 ± 0.8/3.7 ± 0.9	0.075/0.577
Pulvinar hypointensity in SWI	83% (5/6)	40% (6/15)	0.072

MMSE, Mini-Mental State Examination; LEDD, levodopa equivalent daily dose; SWI, susceptibility-weighted imaging.

No correlation was found between the SN area calculated by NMI and the MMSE score change (rs = −0.22, $p = 0.32$) (**Figure 3A**). However, in the group with ≥12 pixels of the SN area (13 patients), only one patient showed an MMSE score reduction of 3 points between baseline and 1 year postoperatively ($p = 0.0046$) (**Table 4**). Moreover, the SN area in 21 patients with PD by NMI was correlated with UPDRS parts II and III, when assessed in the on state 1 year postoperatively (rs = −0.46 and −0.48, $p = 0.042$ and 0.031) (**Figure 3B**).

In the baseline SPECT evaluation, the average occipital CBF in the group with hallucinations (30.66 ± 3.27 ml/100 g/min) was significantly lower than that of the group without hallucinations (38.90 ± 6.30 ml/100 g/min, $p = 0.0036$). In the VBM analysis, the volume of the left pulvinar nucleus with isointensity in SWI was greater than that of the pulvinar nucleus with hypointensity in SWI (**Figure 4**). On the other hand, there

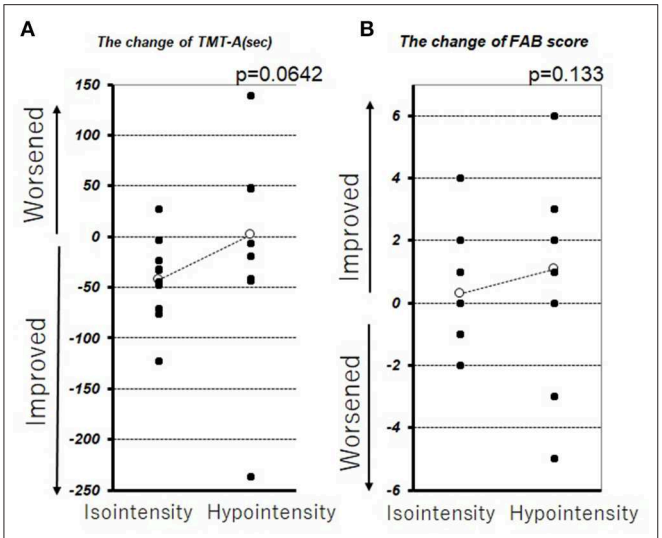


FIGURE 2 | Change in TMT-A **(A)** and FAB **(B)** before DBS therapy and 1 year after DBS therapy. The white circle represents the average.

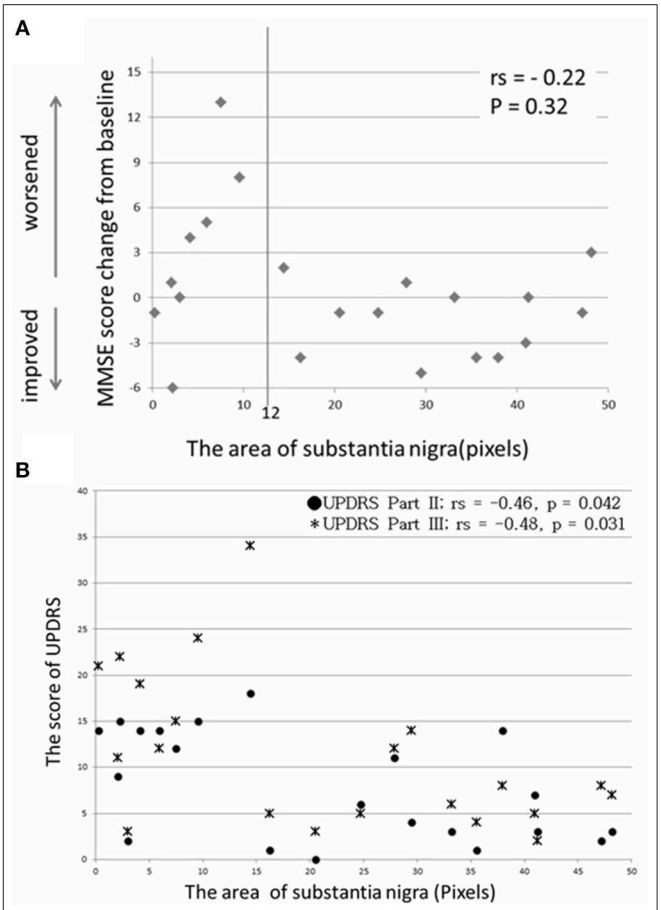


FIGURE 3 | No significant correlation was found between SN area and MMSE score change **(A)**, and a moderate correlation was found between SN area and UPDRS score 1 year postoperatively **(B)**.

was no difference between these two groups in other areas, including the caudate nucleus, periventricular white matter area, and centrum semiovale white matter area.

DISCUSSION

In the present study, we found that pulvinar hypointensity in SWI helps suggest cognitive worsening and the emergence of hallucinations. The SN area seen on NMI suggests the score of UPDRS part II and III 1 year after DBS surgery. In general, the cognitive impairment of patients with PD is strongly related to their quality of life (32). Therefore, patients with PD need to avoid deterioration of cognitive function and hallucinations induced by DBS surgery. STN-DBS therapy is beneficial for some elderly patients with PD aged ≥70 years; however, their clinical benefits are inferior to those of younger patients (33). Indeed, elderly patients with PD aged ≥70 years are frequently excluded from DBS therapy worldwide (34, 35). This study also suggested MMSE deterioration with age.

The present study suggested a correlation between pulvinar hypointensity in SWI and MMSE score change after DBS. Recently, it was reported that the pulvinar nucleus is involved in visual attention and modulation of behavioral responses through indirect cortico-cortical connections (36). A neuroimaging study demonstrated modulation of responses in the pulvinar nucleus with the usage of selective attention tasks that direct attention to a particular spatial location, shift attention across the visual fields, or exclude unwanted information (36). We previously reported a correlation between pulvinar hypointensity in DWI and hallucination in dementia patients (5), which is probably due to functional changes in lateral and inferior pulvinar subnuclei related to their strong connections with the visual cortex (36, 37). Moon et al. reported that the pulvinar nucleus exhibited a low signal on FLAIR images in Alzheimer's disease, describing potential iron accumulation on T2-weighted images (4). Based on these reports, pulvinar hypointensity in SWI may reflect iron deposition in the pulvinar nucleus. However, we did not observe significant correlations between pulvinar hypointensity on DWI or FLAIR and the MMSE score. Pulvinar hypointensity was detected by FLAIR, DWI, and SWI in 7, 9, and 11 cases, respectively. One possible explanation of the lack of correlation with MMSE score in DWI and FLAIR is that the detectability for pulvinar hypointensity was lower in these methods than in SWI. In this regard, further studies including a larger number of cases will be needed. There was no significant difference in age, disease duration, LEDD, and severity between the worsened-cognition group and the stationary or better group. We do not know why these differences occur, and further investigations are needed.

Recently, a relationship was reported between changes in the pulvinar nucleus and the presence of DLB, supported by MRI and pathological findings (8, 9). Accumulation of α-synuclein in the pulvinar nucleus has been demonstrated in pathological analysis of DLB patients (8). Furthermore, cultured neurons over-expressing α-synuclein exhibited iron accumulation when

TABLE 4 | Relationship between cognitive function and the SN area in NMI.

SN area (pixels)	MMSE score	
	Stationary or better	Worsened
≥12	12	1
<12	4	4

$p = 0.0018$

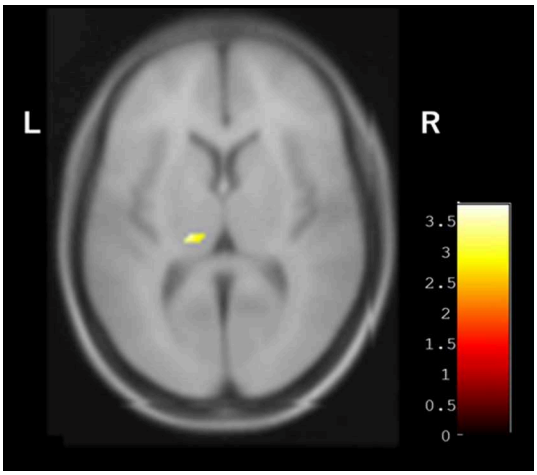


FIGURE 4 | VBM analysis showing the difference between groups with and without pulvinar hypointensity in SWI. Left pulvinar volumes of the group with pulvinar hypointensity in SWI were smaller than those of the group without pulvinar hypointensity in SWI.

exposed to excess iron (38). Based on these findings, the low signal in SWI may reflect the spread of α-synuclein, leading to cognitive impairment and hallucination. In prior findings and the present results, pulvinar hypointensity in SWI may be compatible with stages 5 and 6 of the Braak hypothesis of Lewy body pathology in patients with PD (39). The smaller left pulvinar nucleus in the group with pulvinar hypointensity observed during VBM analysis may reflect the change in pulvinar nuclei and support this hypothesis (**Figure 4**). Moreover, Watson et al. reported that the region of the left pulvinar and ventral lateral nucleus was associated with impaired attentional function in DLB (7). In a comparison between pulvinar hypointensity and isointensity in SWI, the TMT A of isointensity group showed improvement after surgery, whereas no change was observed in the hypointensity group. The result of TMT-A did not reach a significant level because of an outlier in the hypointensity group, which showed remarkable improvement (**Figure 2**). Therefore, TMT-A might improve after surgery in the pulvinar isointensity group and worsen in the hypointensity group. The fact that there was atrophy of the left pulvinar nuclei of the hypointensity group in the significant hemisphere is congruent with the fact that pulvinar nuclei are related to visual attention (36, 37). It was suggested that, because of visual attention deficit, the result of TMT-A in the hypointensity group tended to worsen after surgery. Regarding the result of FAB, there was also no difference between the pulvinar isointensity and hypointensity groups. Though FAB is regarded as one of the tests for frontal function, it includes various tasks such as similarities, motor series, and Go–No Go, not necessarily just attention (29). It can reasonably be concluded that diversity of FAB can occur with no tendency in the hypointensity group.

Conversely, there was no direct association between the SN area in NMI and the MMSE score, and only one patient showed considerable deterioration (≥12 pixels). Moreover, 1 year postoperatively, there was a correlation between the SN area in NMI and UPDRS parts II and III. Thus, a larger SN area in NMI indicated possible motor function improvement. Cognitive function is suggested not to worsen when the SN area maintains a specific level of positive pixels. However, a direct association between the SN area and cognitive function remains unclear. Therefore, this should be examined in a prospective study with a larger number of patients.

The present study had several limitations. First, pulvinar hypointensity was assessed based on visual inspection. Future studies should confirm and extend our findings using a quantitative method, such as quantitative susceptibility mapping (QSM). We are currently conducting the study using QSM. Second, in this study, we could not distinguish and analyze changes in specific pulvinar subnuclei. The pulvinar nucleus has several connections, and there are differences among subnuclei. If pulvinar subnucleus changes can be elucidated, such information may be more useful for clarifying the pathophysiological significance of this phenomenon.

Pulvinar hypointensity observed in SWI in patients with PD before DBS treatment reflects the cognitive function after DBS, and the SN area on NMI reflects the UPDRS parts II and III at 1 year after DBS, which may provide useful information regarding the prognosis of cognitive and motor functions after DBS.

DATA AVAILABILITY STATEMENT

The data are not available for public access because of patient privacy concerns but are available from the corresponding author on reasonable request.

ETHICS STATEMENT

The studies involving human participants were reviewed and approved by Mie University Hospital ethics committee and Suzuka Kaisei Hospital ethics committee. Written informed consent for participation was not required for this study in accordance with the national legislation and the institutional requirements.

AUTHOR CONTRIBUTIONS

KM, TA, MM, and HT planned the study. KM, HK, and NN assessed patients. KT, MU, and KM analyzed the data. KM, MM, MS, KT, and HT wrote and corrected the manuscript.

FUNDING

This research received no specific grant from any funding agency in the public, commercial, or not-for-profit sectors.

ACKNOWLEDGMENTS

We would like to thank Enago (www.enago.jp) for the English language review.

REFERENCES

1. Krack P, Batir A, Van Blercom N, Chabardes S, Fraix V, Ardouin C, et al. Five-year follow-up of bilateral stimulation of the subthalamic nucleus in advanced Parkinson's disease. *N Engl J Med*. (2003) 349:1925–34. doi: 10.1056/NEJMoa035275
2. Heo J, Lee K-M, Paek SH, Kim M-J, Lee J, Kim J-Y, et al. The effects of bilateral Subthalamic Nucleus Deep Brain Stimulation (STN DBS) on cognition in Parkinson disease. *J Neurol Sci*. (2008) 273:19–24. doi: 10.1016/j.jns.2008.06.010
3. Kalbe E, Voges J, Weber T, Haarer M, Baudrexel S, Klein JC, et al. Frontal FDG-PET activity correlates with cognitive outcome after STN-DBS in Parkinson disease. *Neurology*. (2009) 72:42–9. doi: 10.1212/01.wnl.0000338536.31388.f0
4. Moon WJ, Kim HJ, Roh HG, Choi JW, Han SH. Fluid-attenuated inversion recovery hypointensity of the pulvinar nucleus of patients with Alzheimer disease: its possible association with iron accumulation as evidenced by the T2* map. *Korean J Radiol*. (2012) 13:674–83. doi: 10.3348/kjr.2012.13.6.674
5. Sugiura M, Satoh M, Tabei K, Saito T, Mori M, Abe M, et al. Detection of low-signal pulvinar areas using diffusion-weighted imaging in patients with dementia experiencing visual hallucinations. *Dement Geriatr Cogn Dis Extra*. (2016) 6:458–64. doi: 10.1159/000449409
6. Erskine D, Thomas AJ, Attems J, Taylor J-P, McKeith IG, Morris CM, et al. Specific patterns of neuronal loss in the pulvinar nucleus in dementia with lewy bodies. *Mov Disord*. (2017) 32:414–22. doi: 10.1002/mds.26887
7. Watson R, Colloby SJ, Blamire AM, Wesnes KA, Wood J, O'Brien JT. Does attentional dysfunction and thalamic atrophy predict decline in dementia with Lewy bodies? *Parkinsonism Relat Disord*. (2017) 45:69–74. doi: 10.1016/j.parkreldis.2017.10.006
8. Yamamoto R, Iseki E, Murayama N, Minegishi M, Marui W, Togo T, et al. Investigation of Lewy pathology in the visual pathway of brains of dementia with Lewy bodies. *J Neurol Sci*. (2006) 246:95–101. doi: 10.1016/j.jns.2006.02.016
9. Golts N, Snyder H, Frasier M, Theisler C, Choi P, Wolozin B. Magnesium inhibits spontaneous and iron-induced aggregation of α-synuclein. *J Biol Chem*. (2002) 277:16116–23. doi: 10.1074/jbc.M107866200
10. Binolfi A, Rasia RM, Bertoncini CW, Ceolin M, Zweckstetter M, Griesinger C, et al. Interaction of alpha-synuclein with divalent metal ions reveals key differences: a link between structure, binding specificity and fibrillation enhancement. *J Am Chem Soc*. (2006) 128:9893–901. doi: 10.1021/ja0618649
11. Bharathi, Rao KSJ. Thermodynamics imprinting reveals differential binding of metals to α-synuclein: Relevance to parkinson's disease. *Biochem Biophys Res Commun*. (2007) 359:115–20. doi: 10.1016/j.bbrc.2007.05.060
12. Davies P, Moualla D, Brown DR. Alpha-synuclein is a cellular ferrireductase. *PLoS ONE*. (2011) 6:e15814. doi: 10.1371/journal.pone.0015814
13. Sehgal V, Delproposto Z, Haacke EM, Tong KA, Wycliffe N, Kido DK, et al. Clinical applications of neuroimaging with susceptibility-weighted imaging. *J Magn Reson Imaging*. (2005) 22:439–50. doi: 10.1002/jmri.20404
14. Sasaki M, Shibata E, Tohyama K, Takahashi J, Otsuka K, Tsuchiya K, et al. Neuromelanin magnetic resonance imaging of locus ceruleus and substantia nigra in Parkinson's disease. *Neuroreport*. (2006) 17:1215–8. doi: 10.1097/01.wnr.0000227984.84927.a7
15. Kashihara K, Shinya T, Higaki F. Neuromelanin magnetic resonance imaging of nigral volume loss in patients with Parkinson's disease. *J Clin Neurosci*. (2011) 18:1093–6. doi: 10.1016/j.jocn.2010.08.043
16. Matsuura K, Maeda M, Yata K, Ichiba Y, Yamaguchi T, Kanamaru K, et al. Neuromelanin magnetic resonance imaging in Parkinson's disease and multiple system atrophy. *Eur Neurol*. (2013) 70:70–7. doi: 10.1159/000350291
17. Ohtsuka C, Sasaki M, Konno K, Koide M, Kato K, Takahashi J, et al. Changes in substantia nigra and locus coeruleus in patients with early-stage Parkinson's disease using neuromelanin-sensitive MR imaging. *Neurosci Lett*. (2013) 541:93–8. doi: 10.1016/j.neulet.2013.02.012
18. Matsuura K, Maeda M, Tabei K, Umino M, Kajikawa H, Satoh M, et al. A longitudinal study of neuromelanin-sensitive magnetic resonance imaging in Parkinson's disease. *Neurosci Lett*. (2016) 633:112–7. doi: 10.1016/j.neulet.2016.09.011
19. Tanaka M, Aihara Y, Ikeda S, Aihara Y. Neuromelanin-related contrast in the substantia nigra semiquantitatively evaluated by magnetic resonance imaging at 3T: comparison between normal aging and Parkinson disease. *Clin Neurol*. (2011) 51:14–20. doi: 10.5692/clinicalneurol.51.14
20. Hatano T, Okuzumi A, Kamagata K, Daida K, Taniguchi D, Hori M, et al. Neuromelanin MRI is useful for monitoring motor complications in Parkinson's and PARK2 disease. *J Neural Transm*. (2017) 124:407–15. doi: 10.1007/s00702-017-1688-9
21. Hughes AJ, Daniel SE, Kilford L, Lees AJ. Accuracy of clinical diagnosis of idiopathic Parkinson's disease: a clinico-pathological study of 100 cases. *J Neurol Neurosurg Psychiatry*. (1992) 55:181–4. doi: 10.1136/jnnp.55.3.181
22. Maschke M, Gomez CM, Tuite PJ, Konczak J. Dysfunction of the basal ganglia, but not the cerebellum, impairs kinaesthesia. *Brain*. (2003) 126:2312–22. doi: 10.1093/brain/awg230
23. Parkin SG, Gregory RP, Scott R, Bain P, Silburn P, Hall B, et al. Unilateral and bilateral pallidotomy for idiopathic Parkinson's disease: a case series of 115 patients. *Mov Disord*. (2002) 17:682–92. doi: 10.1002/mds.10186
24. Rabinak CA, Nirenberg MJ. Dopamine agonist withdrawal syndrome in Parkinson disease. *Arch Neurol*. (2010) 67:58–63. doi: 10.1001/archneurol.2009.294
25. Okamoto K, Ushijima Y, Okuyama C, Nakamura T, Nishimura T. Measurement of cerebral blood flow using graph plot analysis and I-123 iodoamphetamine. *Clin Nucl Med*. (2002) 27:191–6. doi: 10.1097/00003072-200203000-00009
26. Lancaster JL, Woldorff MG, Parsons LM, Liotti M, Freitas CS, Rainey L, et al. Automated Talairach atlas labels for functional brain mapping. *Hum Brain Mapp*. (2000) 10:120–31. doi: 10.1002/1097-0193(200007)10:3%3C120::aid-hbm30%3E3.0.co;2-8
27. Fahn S, Elton RL. Unified Parkinson's disease rating scale. In: Fahn S, Marsden CD, Calne D, Goldstein M, editors. *Recent Developments in Parkinson's Disease*. Florham Park, NJ: Macmillan Health Care Information (1987). p. 153–63.
28. Folstein MF, Folstein SE, McHugh PR. "Mini-mental state." A practical method for grading the cognitive state of patients for the clinician. *J Psychiatr Res*. (1975) 12:189–98.
29. Dubois B, Slachevsky A, Litvan I, Pillon B. The FAB: a Frontal Assessment Battery at bedside. *Neurology*. (2002) 551621–6. doi: 10.1212/wnl.55.11.1621
30. Partington JE, Leiter RG. Partington's pathway test. *Psychol Serv Center J*. (1949) 1:11–20.
31. Lewinsohn PM, Seeley JR, Roberts RE, Allen NB. Center for Epidemiologic Studies Depression Scale (CES-D) as a screening instrument for depression among community-residing older adults. *Psychol Aging*. (1997) 12:277–87. doi: 10.1037//0882-7974.12.2.277
32. Lawson RA, Yarnall AJ, Johnston F, Duncan GW, Khoo TK, Collerton D, et al. Cognitive impairment in Parkinson's disease: impact on quality of life of carers. *Int J Geriatr Psychiatry*. (2017) 32:1362–70. doi: 10.1002/gps.4623
33. Chiou S-M. Benefits of subthalamic stimulation for elderly Parkinsonian patients aged 70 years or older. *Clin Neurol Neurosurg*. (2016) 149:81–6. doi: 10.1016/j.clineuro.2016.07.028
34. Lang AE, Houeto J-L, Krack P, Kubu C, Lyons KE, Moro E, et al. Deep brain stimulation: preoperative issues. *Mov Disord*. (2006) 21(Suppl. 14):S171–96. doi: 10.1002/mds.20955

35. Moro E, Allert N, Eleopra R, Houeto J-L, Phan T-M, Stoevelaar H, et al. A decision tool to support appropriate referral for deep brain stimulation in Parkinson's disease. *J Neurol*. (2009) 56:83–8. doi: 10.1007/s00415-009-0069-1
36. Benarroch EE. Pulvinar: associative role in cortical function and clinical correlations. *Neurology*. (2015) 84:738–47. doi: 10.1212/WNL.0000000000001276
37. Bridge H, Leopold DA, Bourne JA. Adaptive pulvinar circuitry supports visual cognition. *Trends Cogn Sci*. (2016) 20:146–57. doi: 10.1016/j.tics.2015.10.003
38. Ortega R, Carmona A, Roudeau S, Perrin L, Dučić T, Carboni E, et al. α-synuclein over-expression induces increased iron accumulation and redistribution in iron-exposed neurons. *Mol Neurobiol*. (2016) 53:1925–34. doi: 10.1007/s12035-015-9146-x
39. Braak H, Rüb U, Gai WP, Del Tredici K. Idiopathic Parkinson's disease: possible routes by which vulnerable neuronal types may be subject to neuroinvasion by an unknown pathogen. *J Neural Transm*. (2003) 110:517–36. doi: 10.1007/s00702-002-0808-2

Conflict of Interest: The authors declare that the research was conducted in the absence of any commercial or financial relationships that could be construed as a potential conflict of interest.

Copyright © 2019 Matsuura, Maeda, Satoh, Tabei, Araki, Umino, Kajikawa, Nakamura and Tomimoto. This is an open-access article distributed under the terms of the Creative Commons Attribution License (CC BY). The use, distribution or reproduction in other forums is permitted, provided the original author(s) and the copyright owner(s) are credited and that the original publication in this journal is cited, in accordance with accepted academic practice. No use, distribution or reproduction is permitted which does not comply with these terms.

frontiers in Neurology

ORIGINAL RESEARCH
published: 21 November 2019
doi: 10.3389/fneur.2019.01217

Blood Flow and Glucose Metabolism Dissociation in the Putamen Is Predictive of Levodopa Induced Dyskinesia in Parkinson's Disease Patients

*Maram Aljuaid[1,2], Samuel Booth[1,2], Douglas E. Hobson[3], Andrew Borys[3], Kelly Williams[3], Audrey Katako[1,2], Lawrence Ryner[4], Andrew L. Goertzen[4] and Ji Hyun Ko[1,2]**

[1] Department of Human Anatomy and Cell Science, Rady Faculty of Health Sciences, Max Rady College of Medicine, University of Manitoba, Winnipeg, MB, Canada, [2] Neuroscience Research Program, Kleysen Institute for Advanced Medicine, Health Sciences Centre, Winnipeg, MB, Canada, [3] Section of Neurology, Department of Internal Medicine, Rady Faculty of Health Sciences, Max Rady College of Medicine, University of Manitoba, Winnipeg, MB, Canada, [4] Department of Radiology, Rady Faculty of Health Sciences, Max Rady College of Medicine, University of Manitoba, Winnipeg, MB, Canada

OPEN ACCESS

Edited by:
Maria Carmela Tartaglia,
University of Toronto, Canada

Reviewed by:
Paolo Calabresi,
University of Perugia, Italy
João Laranjinha,
University of Coimbra, Portugal

***Correspondence:**
Ji Hyun Ko
ji.ko@umanitoba.ca

Specialty section:
This article was submitted to Movement Disorders, a section of the journal Frontiers in Neurology

Received: 01 August 2019
Accepted: 01 November 2019
Published: 21 November 2019

Citation:
Aljuaid M, Booth S, Hobson DE, Borys A, Williams K, Katako A, Ryner L, Goertzen AL and Ko JH (2019) Blood Flow and Glucose Metabolism Dissociation in the Putamen Is Predictive of Levodopa Induced Dyskinesia in Parkinson's Disease Patients. Front. Neurol. 10:1217. doi: 10.3389/fneur.2019.01217

Background: The forefront treatment of Parkinson's disease (PD) is Levodopa. When patients are treated with Levodopa cerebral blood flow is increased while cerebral metabolic rate is decreased in key subcortical regions including the putamen. This phenomenon is especially pronounced in patients with Levodopa-induced dyskinesia (LID).

Method: To study the effect of clinically-determined anti-parkinsonian medications, 10 PD patients (5 with LID and 5 without LID) have been scanned with FDG-PET (a probe for glucose metabolism) and perfusion MRI (a probe for cerebral blood flow) both when they are ON and OFF medications. Patients additionally underwent resting state fMRI to detect changes in dopamine-mediated cortico-striatal connectivity. The degree of blood flow-glucose metabolism dissociation was quantified by comparing the FDG-PET and perfusion MRI data.

Results: A significant interaction effect (imaging modality × medication; blood flow-glucose metabolism dissociation) has been found in the putamen ($p = 0.023$). *Post-hoc* analysis revealed that anti-parkinsonian medication consistently normalized the pathologically hyper-metabolic state of the putamen while mixed effects were observed in cerebral blood flow changes. This dissociation was especially predominant in patients with LID compared to those without. Unlike the prior study, this differentiation was not observed when cortico-striatal functional connectivity was assessed.

Conclusion: We confirmed striatal neurovascular dissociation between FDG-PET and perfusion MRI in response to clinically determined anti-parkinsonian medication. We further proposed a novel analytical method to quantify the degree of dissociation

in the putamen using only the ON condition scans, Putamen-to-thalamus Hyper-perfusion/hypo-metabolism Index (PHI), which may have the potential to be used as a biomarker for LID (correctly classifying 8 out 10 patients). For wider use of PHI, a larger validation study is warranted.

Keywords: cerebral blood flow, glucose metabolism, magnetic resonance imaging, neurovascular coupling hypothesis, positron emission tomography

BACKGROUND

Levodopa (LD) has been the first line of treatment of Parkinson's disease (PD) since its introduction. More than 50% of patients develop Levodopa induced dyskinesia (LID) after 5–10 years of treatment (1). While the exact cause of LID is still unknown, epidemiological studies suggest disease duration, symptom severity, young age at the time of onset, duration of Levodopa treatment and overall dose are the major risk factors of these side effects (2). LID can be a very disabling and hard to treat side effect once it is established. It not only interferes with the patient's quality of life but also places a significant burden on the health care system. Knowledge of how to prevent the onset of dyskinesia and the optimum way of managing it once it occurs is an unmet need. Amantadine is, to date, the only US Food and Drug Administration approved anti-dyskinetic medication that does not compromise antiparkinsonian medication's benefit (1), but it typically loses its efficacy in an average of 8 months (3).

The degree of LID fluctuates throughout the day, so its documentation is often highly dependent on subjective opinions of patients, which makes it difficult to conduct a clinical trial targeting LID. An objective and quantifiable biomarker for LID is highly desired to monitor the effects of treatment as well as to identify those individuals at higher risk of developing LID.

In vivo functional brain imaging techniques such as PET and fMRI have great clinical utility in monitoring disease progression and response to treatment in patients. Previously, functional imaging has shown that therapeutic levels of levodopa normalizes aberrant regional brain metabolism in Parkinson's disease patients, in a manner which correlates with clinical improvement of motor symptoms (4, 5). Radiological studies in LID patients have revealed that LID is acutely triggered by large, transient increases in striatal dopamine release following Levodopa administration (6). Patients who do not have motor complications show stable levels of synaptic dopamine concentration after Levodopa administration (7–9). In comparison, at 4 h post Levodopa administration PD patients with motor complications have significant synaptic dopamine level reduction in the putamen, whereas in the stable group synaptic dopamine level remains constant (8, 9). These findings suggest that rapid swing and turnover of Levodopa levels at striatal synapses may contribute to the development of Levodopa—induced motor complications (9).

This acute overshoot of dopaminergic input after Levodopa administration can be partly explained by both the serotonergic reserve hypothesis and the neurovascular de-coupling hypothesis (10). The former suggests that Levodopa is converted to dopamine by reserved serotonergic neurons in the putamen then released in an uncontrolled manner due to lack of auto-receptors feedback mechanisms (11). The latter suggests that sustained D1 receptor stimulation resulting from the down-regulated reuptake (as part of a compensatory mechanism) may induce angiogenesis in the putamen (12–14). As dopamine also acts as a vasodilator (15), acute Levodopa challenge can increase cerebral blood flow while it normalizes pathologically high neuronal activity in the putamen, resulting in excessive levodopa delivery and dopamine release (16). This dissociation is a violation of the neurovascular coupling hypothesis, which is attributed to the potent vasoactive effects of levodopa on cerebral microvasculature through D1-like receptors on astrocytes and vascular smooth muscle (17–20). The neurovascular coupling hypothesis suggests that an increase neuronal activity is followed by increased cerebral metabolic rate (CMR) and cerebral blood flow (CBF) (21). The neurovascular "de-coupling" phenomenon is especially predominant in PD patients with LID (22, 23), suggesting that chronic Levodopa exposure induces angiogenesis and that it may be involved with LID (16). A previous study investigated the effect of constant Levodopa infusion (intravenous Levodopa infusion titrated to achieve maximal improvement in PD motor symptoms without inducing dyskinesia) and its related motor complications in PD (22). They used [^{15}-O]-H_2O PET to measure CBF and fluorodeoxyglucose (FDG)-PET to measure CMR, finding that CBF was increased while CMR was decreased by Levodopa in the putamen, thalamus, pons, and subthalamic nucleus (STN). Based on the hypothesis that the changes in FDG PET signal represents synaptic activity (24), the dissociation between CMR and CBF violates the neurovascular coupling hypothesis. This dissociation was especially predominant in PD patients with LID compared to those without.

Previous fMRI studies have indicated that cortical regions such as the supplementary motor area (SMA), primary motor cortex (M1), and right inferior frontal gyrus (rIFG) also play a key role in the development and severity of LID in PD patients (25–28). Dopaminergic modulation of cortico-striatal networks could therefore be used to classify LID

Abbreviations: AIMs, abnormal involuntary movement scale; BDI-II, beck depression inventory; BBB, blood-brain-barrier; CBF, cerebral blood flow; CMR, cerebral metabolic rate; FDG, fluorodeoxyglucose; fMRI, functional magnetic resonance imaging; LID, levodopa induced dyskinesia; MoCA, montreal cognitive assessment; MDS-UPDRS, movement disorder society—unified Parkinson's disease rating scale; PD, Parkinson's disease; pMRI, perfusion MRI; PET, positron emission tomography; M1, primary motor cortex; pCASL, pseudo-continuous arterial spin labeling; PHI, putamen hyper-perfusion/hypo-metabolism index; ROI, regions of interest; rIFG, right inferior frontal gyrus; STN, subthalamic nucleus; SMA, supplementary motor area; VEGF, vascular endothelial growth factor; LD, Levodopa.

and non-LID patients. A recent analysis using 6 LID and 6 non-LID subjects found that levodopa-induced reduction in resting state functional connectivity between the putamen and M1 predicted LID with 91% sensitivity and 100% specificity (29). Additionally, dopaminergic modulation of putamen-SMA connectivity was shown to negatively correlate with dyskinesia severity (30).

In the current study, we investigate if clinically determined anti-parkinsonian medications also dissociate the CBF and glucose metabolic activity using perfusion MRI (pMRI) and FDG-PET, respectively. Additionally, we investigate the proposed effect of anti-parkinsonian medications on cortico-striatal functional connectivity in LID and non-LID patients. We further propose an analytic method to quantify the degree of dissociation in the putamen which may have the potential to be used as a biomarker for LID.

MATERIALS AND METHODS

Subjects

In order to investigate the potential effects of anti-parkinsonian medications, 10 PD patients (age: 67 ± 7.71, 8 males, 5 with LID, disease duration: 9.22 ± 4.54 years) have been recruited from a local movement disorder clinic in Winnipeg, Manitoba, Canada. All patients were on clinically determined anti-parkinsonian medications. Only patients who had been taking Levodopa for the last 3 months without any changes in dosage were recruited. Each patient was scanned by FDG-PET and functional MRI when she/he was on anti-parkinsonian medications (ON) vs. while all anti-parkinsonian medications were withdrawn for >12 h (OFF). For PET scans in the ON condition, patients took their regular morning dose of anti-parkinsonian medications before FDG injection, which was followed by PET scans 30–45 min later. For MRI, patients took their medications 30–45 min before the scan. The severity of clinical symptoms was evaluated immediately after the FDG-PET scans by the Movement Disorder Society—Unified Parkinson's Disease Rating Scale (MDS-UPDRS) (31) and LID severity was evaluated with the Abnormal Involuntary Movement Scale (AIMs) (32). Patients were also assessed using the Beck Depression Inventory (BDI-II) (33) and Montreal Cognitive Assessment (MoCA) (34). The study was approved by the Biomedical Research Ethics Board at the University of Manitoba, and written informed consent was obtained from each subject. Summary of demographic information of the study group is presented in **Table 1.**

Image Acquisition

Magnetic Resonance Imaging

All patients underwent MRI using a 3T Siemens/IMRIS MR System equipped with an 18 channel head coil located at the Kleysen Institute for Advanced Medicine at the Bannatyne campus of the University of Manitoba. The structural T1-weighted image utilized the MP-RAGE pulse sequence with an acquisition time of 8 min. The CBF acquisition utilized the pseudo-continuous arterial spin labeling (pCASL) pulse sequence with an acquisition time of 5 min (35). Acquisition parameters were TR = 4.0 s, TE = 12 ms, FOV = 240 × 240 mm^2, matrix = 64 × 64 × 20, slice thickness = 5 mm, inter-slice space = 1 mm, labeling time = 2 s, post label delay time = 1.2 s, bandwidth = 3 kHz/pixel, flip angle = 90°. Forty five label/control image pairs were acquired for each subject.

Each fMRI session was comprised of 300 T2* weighted echo planar images (FOV 220 mm, slice thickness 4.0 mm, TR 2,000 ms, TE 28 ms, Flip Angle 77°, with 37 total slices covering the whole brain volume). All subjects underwent metabolic imaging with FDG PET after fasting for at least 6 h before scanning. Patients were injected i.v. with 185 MBq of FDG and a 15 min static image was acquired starting 40 min post-injection. A head CT scan was acquired for attenuation correction purposes. All PET imaging data for this project were acquired

TABLE 1 | Summary of PD patients' demographic information in the current study.

Group	ID	Age	Sex	PD duration (years)	MoCA	LID duration (years)	BDI	MDS-UPDRS-III		AIMS	Anti-PD medications
								OFF	ON		
LID	PD02	76	M	6	22	2.5	12	31	19	2	LD. Amantadine
	PD03	66	M	11	23	1.25	6	20	10	1	LD. DA
	PD05	73	M	18	21	6	9	52	43	3	LD. Amantadine
	PD09	55	M	5	24	1.5	6	37	30	2	LD.
	PD10	65	F	14	29	8	10	37	21	3	LD. Amantadine
Non-LID	PD01	55	M	5	30		0	19	9	0	LD. Amantadine
	PD04	71	M	7	29		4	31	30	0	LD. DA.MOA-B.
	PD06	64	M	4	23		5	53	14	0	LD.
	PD07	68	M	8	27		8	22	16	0	LD.
	PD08	77	F	10	29		4	24	23	0	LD.MOA-B
P-value		1.0		0.22	0.07		0.13	0.32	0.49	0.004	

PD, Parkinson's disease; MoCA, Montreal cognitive assessment test; MDS-UPDRS, movement disorder society—unified Parkinson's disease rating scale; AIMS, abnormal involuntary movement scale; LD, Levodopa; DA, dopamine agonist; MOA-B, Monoamine oxidase B inhibitors; M, male; F, female.

on a Siemens Biograph 16 HiRez PET/CT (Siemens Medical Solutions, Knoxville, TN) scanner located in the John Buhler Research Centre at the Bannatyne campus of the University of Manitoba.

Image Pre-processing

Resting-state fMRI images were realigned to the first image in the set and head movement parameters were extracted and used as regressors of no interest in first level analysis. CBF images were derived from the pCASL images using the Arterial Spin Labeled Perfusion MRI data processing toolbox (35), then pre-processed using SPM12 (http://www.fil.ion.ucl.ac.uk/spm/software/spm12/). For both resting-state fMRI and CBF, the standard procedures, i.e., co-registration with structural T1-MRI, normalization to ICBM template, segmentation, and smoothing with 8 × 8 × 8 mm Gaussian kernel were performed with the default parameters. The same SPM pre-processing steps were performed on all FDG PET images with their corresponding structural T1-MRI using SPM12. Voxel values were divided by the mean value of white matter to account for non-specific inter-individual differences (36, 37).

Neurovascular Uncoupling Analysis

Based on the previous study that demonstrated dissociation between CBF and CMR (22), multiple key subcortical brain regions of interest (ROI) were defined including: putamen, caudate, thalamus, M1, and STN as delineated in automated anatomical labeling (38). The mean CBF and FDG uptake values were extracted for each region under different conditions (ON and OFF scans).

Putamen Hyper-Perfusion/Hypo-Metabolism Index (PHI)

While the medication-induced flow-metabolism dissociation can be readily estimated by comparing the two conditions (ON vs. OFF), it may not be a practically desirable method that can be easily implemented in clinical or research trial settings. We developed a novel brain imaging-based method that quantifies the spatial extent of putamen hyper-perfusion/hypo-metabolism in which only the ON condition scans are used. The thalamus was selected as a reference region for following the reasons: (1) the neurovascular coupling hypothesis is not violated in the thalamus when estimated with FDG PET and pCASL MRI (**Figure 2B**);

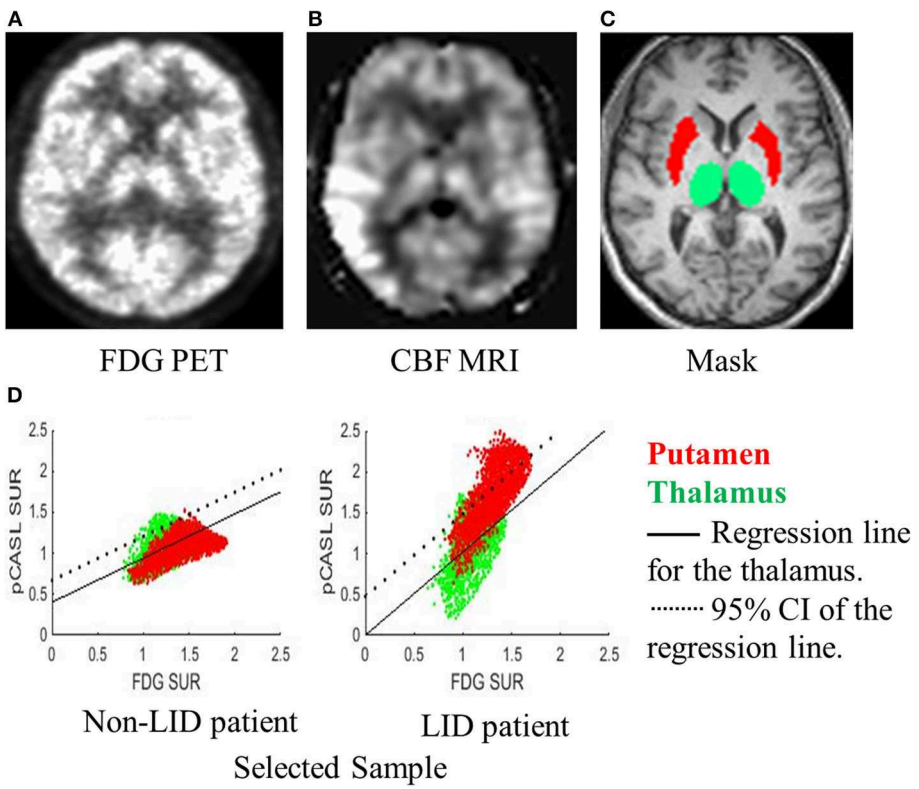


FIGURE 1 | A novel method for quantifying dissociation of metabolic-blood flow with only ON-scans. A representative subject's **(A)** FDG-PET, **(B)** CBF-MRI, and **(C)** mask labeling are displayed. **(D)** Regression between FDG-PET and CBF-MRI was performed for the voxels in the thalamus (green dots). A voxel-to-voxel plot of FDG-PET (x-axis) and CBF-MRI (y-axis) and regression line (black solid line) and 95% confidence interval (CI; dotted line) for the thalamus are displayed for a sample patient without LID (left) and a patient with LID (right). The proportion of voxels in the putamen (red dots) falling above the 95% CI estimated from the thalamus was quantified and named the Putamen Hyper-perfusion/hypo-metabolism Index (PHI). The PHI score represents the spatial extent of voxels that are hyper-perfused compared to the thalamus.

(2) the D1 receptor, i.e., the main pathway of Levodopa-induced vasodilation, is reported to be the least available in the thalamus (39), and (3) it is located in close proximity and has a similar size to the putamen, thus the image quality and spatial resolution is similar for the thalamus and the putamen. The Putamen Hyper-perfusion/Hypo-metabolism Index (PHI) was defined as the proportion of voxels in the putamen that lie above 95% CI of the regression line of the thalamus between FDG uptake vs. pCASL perfusion (**Figure 1**). Therefore, the null hypothesis is that the relationship between perfusion and glucose metabolism is linear and it should be identical between the putamen and the thalamus in the "normal" condition. If the degree of relative hyper-perfusion and hypo-metabolism in the putamen is beyond the 95% CI of the thalamus, it may be pathological. Thus, the PHI score represents the spatial extent of abnormally hyper-perfused and/or hypo-metabolic voxels in the putamen.

Functional Connectivity Analysis

The first eigenvariate of all voxels for the left and right putamen for the timeseries of each subject was extracted and used as a regressor for a general linear model for each subject. This produced a statistical parametric map for each subject in which the beta weights represent the coefficient of covariance between that particular voxel and the putamen in that subject, representing a measure of functional connectivity. The regional coefficient of covariance was extracted from each ROI using the unthresholded first eigenvariate of that anatomical region. From this we generated the coefficient of connectivity between the seed region (bilateral putamen) and each ROI in our analysis in both the OFF state and ON state from each patient. The measures for each region were converted to z-scores by subtracting each connectivity coefficient from the group mean (including both LID and non-LID patients in the OFF state) and dividing by

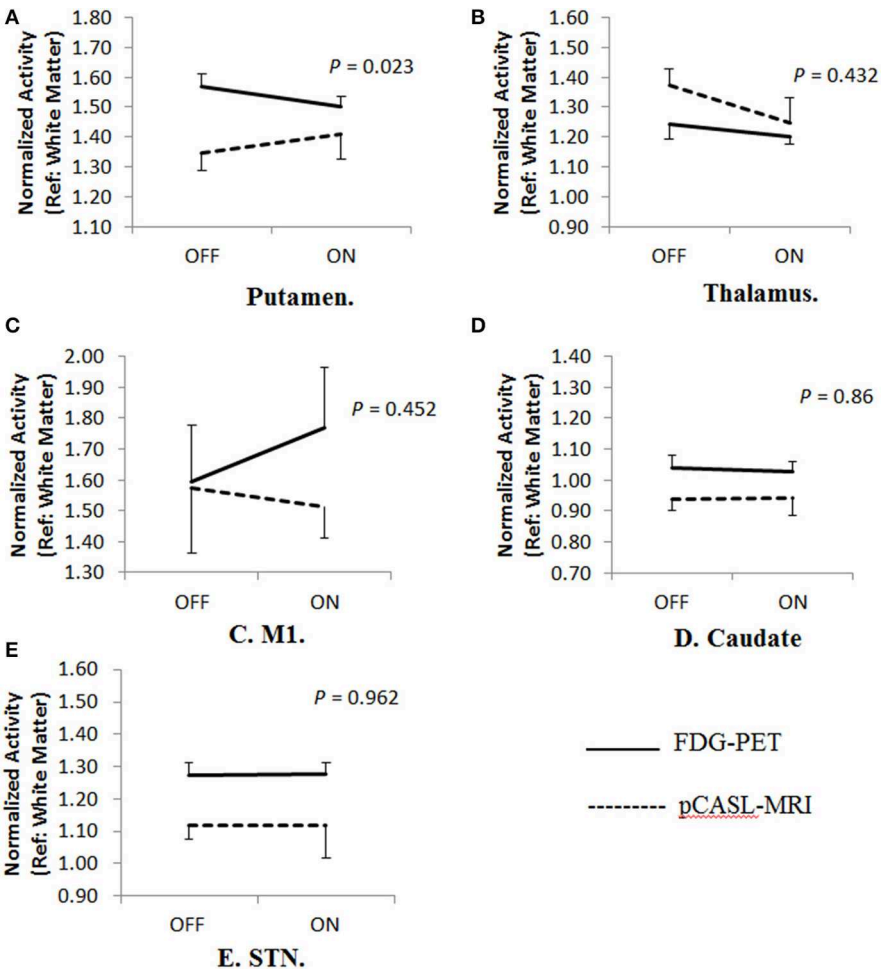


FIGURE 2 | Cerebral blood flow-metabolism dissociation in different brain regions. **(A)** A significant Cerebral Blood Flow-Metabolism dissociation in the putamen using FDG-PET and pCASL-MRI [Interaction effects, $F_{(1,8)} = 7.491$, $p = 0.023$]. In the putamen, the FDG uptake was consistently decreased by anti-parkinsonian medication ($p = 0.001$, *post-hoc* Bonferroni) while mixed effects were observed in CBF changes ($p = 0.214$, *post-hoc* Bonferroni). When different groups are separately analyzed, trend-level of interaction effects were only observed in LID group [medication × modality: $F_{(1,4)} = 5.648$, $p = 0.076$] but not in non-LID group [medication × modality: $F_{(1,4)} = 2.334$, $p = 0.201$]. However, no significant dissociation was observed in other regions including **(B)** thalamus [$F_{(1,8)} = 0.678$, $p = 0.432$], **(C)** primary motor area (M1) [$F_{(1,8)} = 0.618$, $p = 0.452$], **(D)** caudate [$F_{(1,8)} = 0.033$, $p = 0.86$], and **(E)** subthalamic nucleus (STN) [$F_{(1,8)} = 0.002$, $p = 0.962$].

the standard deviation. Dopaminergic modulation of resting state connectivity was calculated as the difference in z-scores between the OFF and ON state for each patient.

Statistical Analysis

The Student *t*-test was performed to investigate group differences in age, disease duration, PD motor symptoms severity, cognition impairment, and depression between LID vs. non-LID subjects. The neurovascular uncoupling results were analyzed by the 2 × 2 repeated measures ANOVA to investigate the main effect of imaging modality (PET vs. MRI) and medication (ON vs. OFF) and their interaction effects. When applicable, a *post-hoc* Bonferroni test was performed. The functional connectivity results (comparing LID vs. non-LID) were assessed via *t*-test. The applicability of PHI (ON) score for differentiating LID vs. non-LID was examined by observing how many patients were above the "normal" level of PHI score determined in the OFF condition (mean + 2SD).

RESULTS

Clinical Effects of Anti-parkinsonian Treatment

Patients were not significantly different between the groups (LID vs. non-LID) in overall motor symptoms [MDS-UPDRS-III: (ON) $t_{(8)} = 0.755$, $p = 0.492$, (OFF) $t_{(8)} = 1.116$, $p = 0.327$], age [$t_{(8)} = 0$, $p = 1.0$], cognitive symptom severity [MoCA: $t_{(8)} = 2.031$, $p = 0.077$], depression level [BDI-II: $t_{(8)} = 1.901$, $p = 0.130$], and disease duration since the first diagnosis [$t_{(8)} = 1.423$, $p = 0.228$]. In 2 × 2 repeated measures ANOVA, all patient's motor symptoms were ameliorated by anti-parkinsonian medication [Effect of medication: $F_{(1,8)} = 9.334$, $p = 0.016$] and no significant group difference was noted in changes in MDS-UPDRS-III (interaction effect of medication × group: $F_{(1,8)} = 0.007$, $p = 0.936$]. As expected, non-LID patients do not show any signs of dyskinesia when assessed by AIMs. In LID patients, the severity of dyskinesia varied across patients (**Table 1**).

Cerebral Blood Flow—FDG Uptake Dissociation Response to Anti-parkinsonian Treatment in Parkinson Patients

In the 2 × 2 repeated measures ANOVA, there were no significant main effects of different imaging modality (FDG-PET vs. pCASL-MRI: $p > 0.075$) or anti-parkinsonian medications (OFF vs. ON: $p > 0.099$) in any regions investigated. Significant interaction effect (medication × modality) has been only found in the putamen [$F_{(1, 8)} = 7.491$, $p = 0.023$], but not in the thalamus [$F_{(1, 8)} = 0.678$, $p = 0.432$], caudate [$F_{(1, 8)} = 0.033$, $p = 0.860$], STN [$F_{(1,8)} = 0.002$, $p = 0.962$], nor M1 [$F_{(1, 8)} = 0.618$, $p = 0.452$] (**Figure 2**). In the putamen, the FDG uptake was consistently decreased by anti-parkinsonian medication ($p = 0.001$, *post-hoc* Bonferroni) while mixed effects were observed in CBF changes ($p = 0.214$, *post-hoc* Bonferroni). Interestingly, when different groups are separately analyzed, a trend-level of interaction effect was observed in the LID group [medication × modality: $F_{(1, 4)} = 5.648$, $p = 0.076$] but not in the non-LID group [medication × modality: $F_{(1, 4)} = 2.334$, $p = 0.201$].

Dopaminergic Modulation of Resting State Connectivity

No significant interaction effects of resting-state connectivity (group vs. medication) were noted in any of the ROIs examined, including between the bilateral putamen and M1 ($p = 0.2831$) or between bilateral putamen and SMA ($p = 0.8210$; **Figure 3**). Importantly, these results did not change when using ROIs from only the most affected hemisphere (ipsilateral to the side with greatest symptoms measured with UPRDS-III).

Putamen-to-Thalamus Hyper-Perfusion/Hypo-Metabolism Index (PHI)

The PHI was introduced to estimate the spatial extent of relative hyper-perfusion and hypo-metabolism of the putamen compared to the thalamus, which has similar features (see section

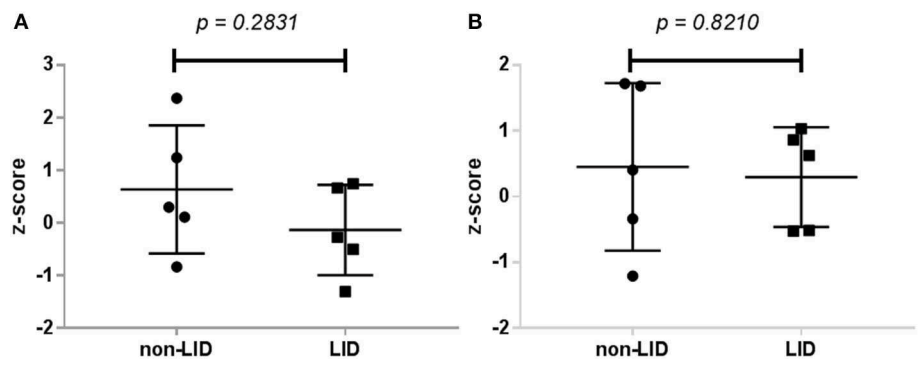


FIGURE 3 | Dopaminergic modulation of resting-state connectivity in LID and non-LID patients. **(A)** Change in connectivity between bilateral putamen and M1. **(B)** Change in connectivity coefficient between putamen and SMA. Dopaminergic modulation was calculated as the difference in z-transformed connectivity coefficients between all voxels in the seed region (putamen) with the region of interest from the OFF condition to the ON condition.

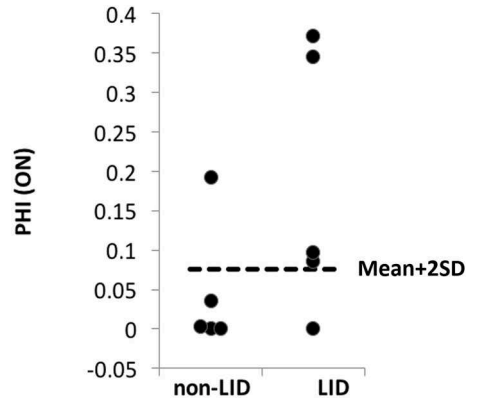


FIGURE 4 | PHI comparison between LID and non-LID. The "normal" level of PHI was determined based on the scores of all patients ($n = 10$) estimated at the OFF condition assuming that no dissociation occurs in the OFF condition. Any PHI scores above mean + 2 × SD (dashed lines) were considered "abnormal." In the ON condition, 4 out of 5 LID patients' PHI scores were abnormally high, while only 1 out of 5 non-LID patients' PHI score was higher than the normal range.

Materials and Methods). Anti-parkinsonian treatment increased PHI above the mean + 2SD (determined in the OFF condition) in 4 of 5 LID patients and 1 of 5 non-LID patients (Sensitivity = 0.8, Specificity = 0.8; **Figure 4**).

DISCUSSION

As expected based on prior studies (22, 23), putamen FDG uptake was reduced by clinically-determined anti-parkinsonian medications in all patients, suggesting that the therapy normalized the pathologically hyper-metabolic state of the putamen (16). However, its effect on CBF was not uniform, resulting in significant dissociation between CBF and FDG uptake. The separate group analysis suggests that the significant dissociation mainly originated from LID patients rather than non-LID patients, which is in line with the previous studies (22, 23).

Unlike in previous studies, dissociation in other brain regions (i.e., thalamus, STN, caudate, and M1) was not observed (22, 23). This discrepancy may have originated from the previous studies only investigating the effects of Levodopa while other anti-parkinsonian medications (e.g., dopamine agonist, monoamine oxidase B inhibitor) were also withheld for the OFF condition in our study. In addition, four patients were on amantadine [half-life: 9.7–14.5 h (40)] which has been shown to have anti-dyskinetic and vasoconstrictive effects (41). It should be noted that the LID patients' dyskinesia was not completely controlled by their current anti-parkinsonian/anti-dyskinetic treatment while in contrast, the previous studies used Levodopa infusion with dose titrated not to induce dyskinesia during scanning (22, 23). This signifies the relevance of the putamen's dissociation with LID over other brain regions that have been tested, which was most prominent among the regions that previously showed dissociation (23).

Different hypotheses lie behind CBF and FDG uptake dissociation. Experiments with 6-OHDA-lesioned rats have demonstrated Levodopa-mediated blood flow-metabolism dissociation in the striatum after both acute and chronic injection of Levodopa (42, 43). The acute rise in CBF is mediated by increases in the blood-brain-barrier (BBB) permeability as well as vasodilation controlled by smooth muscle cells and endothelium changes in the striatum (16). This dissociation is specific to the regions of dopaminergic degeneration and was not reported in the contralateral intact hemisphere of the 6-OHDA lesioned PD animals (12). Chronic exposure to Levodopa induced significant growth of immature endothelial cells, stimulated micro-vessel proliferation and increased synthesis and expression of vascular endothelial growth factor (VEGF) in the basal ganglia (14). The degree of VEGF expression was positively correlated with the total dose of Levodopa (14). A post-mortem study with PD patients also revealed significant VEGF transcriptions and subsequent expression of VEGF mRNA and an increase in nestin stain (a marker of immature endothelial cells) (43). Interestingly, in rat models following chronic exposure with Levodopa, VEGF expression, angiogenesis, and proliferating micro vessels stained by nestin were more prominent in animals with dyskinesia (14). These findings were reversed by a VEGF signaling inhibitor, which reduced dyskinesia in PD-LID model animals (43).

At therapeutic doses of Levodopa, dopamine has a vasodilation effect and increases regional CBF, which facilitates the transport of the drug across the BBB (15). The increased microvasculature discussed above may prime the regional neurovascular unit to have an exaggerated response to Levodopa-supplied dopamine transmission and further stimulate angiogenesis, forming a vicious cycle to further increase dopamine transmission beyond the optimal level (16).

As an alternative brain-imaging biomarker for LID, we investigated dopaminergic modulation of resting-state connectivity in the cortico-striatal axis using M1 and SMA as our primary ROI. This is based on the theory that abnormal dopaminergic modulation of the cortico-basal ganglia motor loops preconfigure the emergence of LID (44). We have not found a significant difference in dopaminergic modulation of resting state connectivity between LID and non-LID patients in either of these ROIs either bilaterally or using the most affected hemisphere. In a previously reported study dopamine treatment was shown to significantly decrease connectivity between putamen and M1 in LID patients compared to non-LID patients with a very high sensitivity (91%) and specificity (100%) (30). It is important to note that low sample size or differences in scanning protocol may have reduced the sensitivity of this technique in our subjects.

The Use of PET+MRI as a LID Biomarker

Dopamine has a vasodilating effect in the putamen through stimulation of D1 receptors (17). It has been reported previously that D1 receptors are found with high density in the striatum, nucleus accumbens, and substantia nigra pars reticulata (18). However, the D1 receptor, i.e., the main pathway of Levodopa-induced vasodilation and angiogenesis (43), is reported to be the

least available in the thalamus (39). This makes the thalamus the optimal reference region to estimate the CBF-FDG uptake dissociation (see section Materials and Methods).

We found that in 4 out of 5 LID patients the PHI score in the ON condition is above the normal level (mean + 2SD of the OFF condition), suggesting that it may be used as a sensitive biomarker for LID (80% sensitivity, albeit with a small sample size). Patient PD010 is the only LID patient whose PHI is below the abnormality threshold. It should be noted that multiple hypotheses exist surrounding the pathophysiology of LID (10, 45). Indeed, this patient's LID may not be related to Levodopa-induced angiogenesis/vasodilation but may exclusively involve other pathways such as serotonergic reserve (46, 47). This finding can be interpreted as suggesting that those patients who have low PHI score may not benefit from anti-angiogenic treatment, a potential preventive medicine against LID (48). Also, this type of patient (who shows low PHI score) may need to be precluded from future clinical trials and subsequent clinical practice targeting angiogenesis.

Interestingly, patient PD010 is also the only patient in the LID group who had depression and is treated with an atypical antidepressant, Bupropion, which is a dopamine norepinephrine reuptake inhibitor. This could interfere with neurotransmitter balance and inhibit regional CBF. Norepinephrine acts on alpha 1 and alpha 2 receptors in most systemic arteries and veins and induces vasoconstriction, which eventually raises the systemic vascular resistance and reduces blood flow (49, 50).

Among non-LID patients, only one patient (PD004) out of five lies above the abnormality threshold (mean + 2SD of the OFF condition). The adjusted R^2 of the thalamic linear regression model of FDG uptake vs. CBF can serve as an indicator for nonspecific noise (e.g., motion artifacts and mis-registration) and it was the lowest in the PD004 (Adj. $R^2 = 0.0062$; other image pairs' Adj. $R^2 > 0.14$), suggesting a possibility of false positive due to technical issues rather than a physiological outlier. Potential implications for future research trials include that the patients in which the brain imaging pairs' Adj. R^2 yields <0.1 may need to be re-scanned.

Limitations

The power of statistical analysis is mainly defined by the sample size and noise level of the data. In this regard, the low sample size is the main limiting factor for this present study, which warrants a larger-scale longitudinal study to confirm the usability of the proposed method. Nevertheless, by utilizing the expected "normal" level of neurovascular coupling from the thalamus within each patient, the threshold for "abnormality" could be reliably estimated from the OFF condition, which reduced the non-specific noise associated with the image quality. PD is a movement disorder that affects non-medicated patients with tremor and medicated ones with potential dyskinesia, therefore it is typically very troublesome to ensure high quality imaging studies. Since the thalamus is located in a close proximity and has similar volume and spatial resolution as the putamen, it receives the same level of non-specific noise effects as the putamen, e.g., motion artifacts. The thalamic confidence level of the PET-MRI correspondence serves as an optimal indicator for defining "abnormality" in the putamen in the given imaging quality, which enhanced the statistical power of the proposed method.

The most interesting potential implication is whether the proposed PHI method can predict future emergence of LID from non-LID state, which can be only addressed with a longitudinal dataset. Our current study identified a non-LID patient (PD004) with a high PHI score, which warrants an on-going follow-up on dyskinesia state of this patient. Anecdotally, this patient has not developed LID in the 1 year since the PET+MRI scans. Moreover, we postulated that the high PHI score of this patient is likely due to a technical origin (Adj. $R^2 < 0.1$), rather than a pathological origin.

CONCLUSION

The exact pathology of LID in PD is not known. Using the flow-metabolism dissociation that is specific to LID, we proposed a novel PET+MRI-based biomarker for LID (i.e., PHI). Conditional on a larger-scale longitudinal study confirmation, the proposed method may be useful in identifying patients who are at risk of developing LID and who will most likely benefit from anti-angiogenic treatment, and in determining the outcome responses of a preventive medicine trial for LID.

DATA AVAILABILITY STATEMENT

The de-identified relevant data produced in the current study can be accessed via http://www.kolabneuro.com/. The raw data are not publicly available as they contain patient medical data which can only be accessed under the Personal Health Information Act (PHIA), information regarding which can be found at http://www.gov.mb.ca/health/phia/.

ETHICS STATEMENT

The studies involving human participants were reviewed and approved by Biomedical Research Ethics Board, University of Manitoba. The patients/participants provided their written informed consent to participate in this study.

CONSENT FOR PUBLICATION

All participating individuals gave an informed consent for us to publish the de-identified data that were collected from this study.

AUTHOR CONTRIBUTIONS

DH, LR, AG, and JK conceived the study. MA, DH, AB, KW, AK, LR, and AG contributed to the data collection including interviews, clinical tests, and imaging. MA, SB, and JK analyzed the data. MA and SB drafted the manuscript. All authors contributed to the revision of the manuscript.

FUNDING

This work was supported by Manitoba Medical Service Foundation (8-2015-04), Natural Science and Engineering

Council of Canada (RGPIN-2016-05964), Brain Canada, University of Manitoba, King Saud University, Riyadh, Saudi Arabia, and Saudi Arabian Culture Bureau in Canada.

ACKNOWLEDGMENTS

We thank the staff members of PET and MRI centers at Health Science Centre for data acquisition.

REFERENCES

1. Zesiewicz TA. Levodopa-induced Dyskinesia in Parkinson's disease: epidemiology, etiology, and treatment. *Curr Neurol Neurosci Rep.* (2007) 7:302. doi: 10.1007/s11910-007-0046-y
2. Aquino CC, Fox SH. Clinical spectrum of levodopa-induced complications. *Mov Disord.* (2015) 30:80–89. doi: 10.1002/mds.26125
3. Thomas A, Iacono D, Luciano AL, Armellino K, Di Iorio A, Onofrj M. Duration of amantadine benefit on dyskinesia of severe Parkinson's disease. *J Neurol Neurosurg Psychiatry.* (2004) 75:141–3.
4. Asanuma K, Tang C, Ma Y, Dhawan V, Mattis P, Edwards C, et al. Network modulation in the treatment of Parkinson's disease. *Brain.* (2006) 129:2667–78. doi: 10.1093/brain/awl162
5. Feigin A, Fukuda M, Dhawan V, Przedborski S, Jackson–Lewis V, Mentis MJ, et al. Metabolic correlates of levodopa response in Parkinson's disease. *Neurology.* (2001) 57:2083–8. doi: 10.1212/WNL.57.11.2083
6. Pavese N, Evans AH, Tai YF, Hotton G, Brooks DJ, Lees AJ, et al. Clinical correlates of levodopa-induced dopamine release in Parkinson disease: a PET study. *Neurology.* (2006) 67:1612–7. doi: 10.1212/01.wnl.0000242888.30755.5d
7. De La Fuente-Fernández R, Schulzer M, Mak E, Calne DB, Stoessl AJ. Presynaptic mechanisms of motor fluctuations in Parkinson's disease: a probabilistic model. *Brain.* (2004) 127:888–99. doi: 10.1093/brain/awh102
8. De La Fuente-Fernández R, Sossi V, Huang Z, Furtado S, Lu JQ, Calne DB, et al. Levodopa-induced changes in synaptic dopamine levels increase with progression of Parkinson's disease: implications for dyskinesias. *Brain.* (2004) 127:2747–54. doi: 10.1093/brain/awh290
9. Niccolini F, Loane C, Politis M. Dyskinesias in Parkinson's disease: views from positron emission tomography studies. *Eur J Neurol.* (2014) 21:694-e43. doi: 10.1111/ene.12362
10. Angela Cenci M. Presynaptic mechanisms of L-DOPA-induced dyskinesia: the findings, the debate, the therapeutic implications. *Front Neurol.* (2014) 5:242. doi: 10.3389/fneur.2014.00242
11. Politis M, Wu K, Loane C, Brooks DJ, Kiferle L, Turkheimer FE, et al. Serotonergic mechanisms responsible for levodopa-induced dyskinesias in Parkinson's disease patients. *J Clin Invest.* (2014) 124:1340–9. doi: 10.1172/JCI71640
12. Lerner RP, Bimpisidis Z, Agorastos S, Scherrer S, Dewey SL, Cenci MA, et al. Dissociation of metabolic and hemodynamic levodopa responses in the 6-hydroxydopamine rat model. *Neurobiol Dis.* (2016) 96:31–7. doi: 10.1016/j.nbd.2016.08.010
13. Troiano AR, De La Fuente-Fernandez RJ, Sossi VJ, Schulzer MJ, Mak EJ, Ruth TJ, et al. PET demonstrates reduced dopamine transporter expression in PD with dyskinesias. *Neurology.* (2009) 72:1211–6. doi: 10.1212/01.wnl.0000338631.73211.56
14. Westin JE, Lindgren HS, Gardi J, Nyengaard JR, Brundin P, Mohapel P, et al. Endothelial proliferation and increased blood – brain barrier permeability in the basal ganglia in a rat model of 3, 4-dihydroxyphenyl- L -alanine-induced dyskinesia. *J Neurosci.* (2006) 26:9448–61. doi: 10.1523/JNEUROSCI.0944-06.2006
15. Iadecola C. Neurogenic control of the cerebral microcirculation: is dopamine minding the store? *Nat Neurosci.* (1998) 1:263–5. doi: 10.1038/1074
16. Ko JH, Lerner RP, Eidelberg D. Effects of levodopa on regional cerebral metabolism and blood flow. *Mov Disord.* (2015) 30:54–63. doi: 10.1002/mds.26041
17. Choi J-K, Chen YI, Hamel E, Jenkins BG. Brain hemodynamic changes mediated by dopamine receptors: Role of the cerebral microvasculature in dopamine-mediated neurovascular coupling. *Neuroimage.* (2006) 30:700–12. doi: 10.1016/j.neuroimage.2005.10.029
18. Chen YC, Galpern WR, Brownell AL, Matthews RT, Bogdanov M, Isacson O, et al. Detection of dopaminergic neurotransmitter activity using pharmacologic MRI: correlation with PET, microdialysis, and behavioral data. *Magn Reson Med.* (1997) 38:389–98. doi: 10.1002/mrm.1910380306
19. Chen Q, Andersen AH, Zhang Z, Ovadia A, Gash DM, Avison MJ. Mapping drug-induced changes in cerebral R2* by Multiple Gradient Recalled Echo functional MRI. *Magn Reson Imaging.* (1996) 14:469–76. doi: 10.1016/0730-725X(95)02100-8
20. Sirohi D, Chen Z, Sun L, Klose T, Pierson TC, Rossmann MG, et al. The 3.8 Å resolution cryo-EM structure of Zika virus. *Science.* (2016) 352:467–70. doi: 10.1126/science.aaf5316
21. Attwell D, Buchan AM, Charpak S, Lauritzen M, MacVicar BA, Newman EA. Glial and neuronal control of brain blood flow. *Nature.* (2010) 468:232–43. doi: 10.1038/nature09613
22. Hirano S, Asanuma K, Ma Y, Tang C, Feigin A, Dhawan V, et al. Dissociation of metabolic and neurovascular responses to levodopa in the treatment of Parkinson's disease. *J Neurosci.* (2008) 28:4201–9. doi: 10.1523/JNEUROSCI.0582-08.2008
23. Jourdain VA, Tang CC, Holtbernd F, Dresel C, Choi YY, Ma Y, et al. Flow-metabolism dissociation in the pathogenesis of levodopa-induced dyskinesia. *JCI Insight.* (2016) 1:1–18. doi: 10.1172/jci.insight.86615
24. Stoessl AJ. Glucose utilization: still in the synapse. *Nat Neurosci.* (2017) 20:382–4. doi: 10.1038/nn.4513
25. Cerasa A, Koch G, Donzuso G, Mangone G, Morelli M, Brusa L, et al. A network centred on the inferior frontal cortex is critically involved in levodopa-induced dyskinesias. *Brain.* (2015) 138:414–27. doi: 10.1093/brain/awu329
26. Cerasa A, Morelli M, Augimeri A, Salsone M, Novellino F, Gioia MC, et al. Prefrontal thickening in PD with levodopa-induced dyskinesias: New evidence from cortical thickness measurement. *Park Relat Disord.* (2013) 19:123–5. doi: 10.1016/j.parkreldis.2012.06.003
27. Cerasa A, Pugliese P, Messina D, Morelli M, Cecilia Gioia M, Salsone M, et al. Prefrontal alterations in Parkinson's disease with levodopa-induced dyskinesia during fMRI motor task. *Mov Disord.* (2012) 27:364–71. doi: 10.1002/mds.24017
28. Herz DM, Haagensen BN, Christensen MS, Madsen KH, Rowe JB, L??kkegaard A, Siebner HR. The acute brain response to levodopa heralds dyskinesias in Parkinson disease. *Ann Neurol.* (2014) 75:829–836. doi: 10.1002/ana.24138
29. Herz DM, Haagensen BN, Christensen MS, Madsen KH, Rowe JB, Løkkegaard A, et al. Abnormal dopaminergic modulation of striato-cortical networks underlies levodopa-induced dyskinesias in humans. *Brain.* (2015) 138:1658–66. doi: 10.1093/brain/awv096
30. Herz DM, Haagensen BN, Nielsen SH, Madsen KH, Løkkegaard A, Siebner HR. Resting-state connectivity predicts levodopa-induced dyskinesias in Parkinson's disease. *Mov Disord.* (2016) 31:521–9. doi: 10.1002/mds.26540
31. Ramaker C, Marinus J, Stiggelbout AM, Van Hilten BJ. Systematic evaluation of rating scales for impairment and disability in Parkinson's disease. *Mov Disord.* (2002) 17:867–76. doi: 10.1002/mds.10248
32. Gharabawi GM, Bossie CA, Lasser RA, Turkoz I, Rodriguez S, Chouinard G. Abnormal Involuntary Movement Scale (AIMS) and Extrapyramidal Symptom Rating Scale (ESRS): cross-scale comparison in assessing tardive dyskinesia. *Schizophr Res.* (2005) 77:119–28. doi: 10.1016/j.schres.2005.03.008
33. Beck AT, Steer RA, Ball R, Ranieri W. Comparison of beck depression inventories -IA and -II in psychiatric outpatients. *J Pers Assess.* (1996) 67:588–97.
34. Nasreddine ZS, Phillips NA, Bédirian V, Charbonneau S, Whitehead V, Collin I, et al. The montreal cognitive assessment, MoCA: a brief screening

tool for mild cognitive impairment. *J Am Geriatr Soc.* (2005) 53:695–9. doi: 10.1111/j.1532-5415.2005.53221.x
35. Wang Z, Aguirre GK, Rao H, Wang J, Fernández-Seara MA, Childress AR, et al. Empirical optimization of ASL data analysis using an ASL data processing toolbox: ASLtbx. *Magn Reson Imaging.* (2008) 26:261–9. doi: 10.1016/j.mri.2007.07.003
36. Borghammer P, Jonsdottir KY, Cumming P, Ostergaard K, Vang K, Ashkanian M, et al. Normalization in PET group comparison studies—The importance of a valid reference region. *Neuroimage.* (2008) 40:529–40. doi: 10.1016/j.neuroimage.2007.12.057
37. Spence JS, Carmack PS, Gunst RF, Schucany WR, Woodward WA, Haley RW. Using a white matter reference to remove the dependency of global signal on experimental conditions in SPECT analyses. *Neuroimage.* (2006) 32:49–53. doi: 10.1016/j.neuroimage.2006.03.025
38. Tzourio-Mazoyer N, Landeau B, Papathanassiou D, Crivello F, Etard O, Delcroix N, et al. Automated anatomical labeling of activations in SPM using a macroscopic anatomical parcellation of the MNI MRI single-subject brain. *Neuroimage.* (2002) 15:273–89. doi: 10.1006/nimg.2001.0978
39. Abi-Dargham A, Moore H. Prefrontal DA transmission at D1 receptors and the pathology of schizophrenia. *Neuroscience.* (2003) 9:404–16. doi: 10.1177/1073858403252674
40. Horadam VW, Sharp JG, Smilack JD, McAnalley BH, Garriott JC, Stephens MK, et al. Pharmacokinetics of amantadine hydrochloride in subjects with normal and impaired renal function. *Ann Intern Med.* (1981) 94:454. doi: 10.7326/0003-4819-94-4-454
41. Demaagd G, Philip A. Parkinson's disease and its management: part 3: nondopaminergic and nonpharmacological treatment options. *P T.* (2015) 40:668–9.
42. Aron AR, Robbins TW, Poldrack RA. Inhibition and the right inferior frontal cortex: one decade on. *Trends Cogn Sci.* (2014) 18:177–85. doi: 10.1016/j.tics.2013.12.003
43. Ohlin KE, Sebastianutto I, Adkins CE, Lundblad C, Lockman PR, Cenci MA. Impact of L-DOPA treatment on regional cerebral blood flow and metabolism in the basal ganglia in a rat model of Parkinson's disease. *Neuroimage.* (2012) 61:228–39. doi: 10.1016/j.neuroimage.2012.02.066
44. Calabresi P, Picconi B, Tozzi A, Di Filippo M. Dopamine-mediated regulation of corticostriatal synaptic plasticity. *Trends Neurosci.* (2007) 30:211–9. doi: 10.1016/j.tins.2007.03.001
45. Iravani M, Jenner P. Mechanisms underlying the onset and expression of levodopa-induced dyskinesia and their pharmacological manipulation. *J Neural Transm.* (2011) 118:1661–90. doi: 10.1007/s00702-011-0698-2
46. Hong JY, Oh JS, Lee I, Sunwoo MK, Ham JH, Lee JE, et al. Presynaptic dopamine depletion predicts levodopa-induced dyskinesia in de novo Parkinson disease. *Neurology.* (2014) 82:1597–604. doi: 10.1212/WNL.0000000000000385
47. Roussakis A-A, Politis M, Towey D, Piccini P. Serotonin-to-dopamine transporter ratios in Parkinson disease: relevance for dyskinesias. *Neurology.* (2016) 86:1152–8. doi: 10.1212/WNL.0000000000002494
48. Ohlin KE, Francardo V, Lindgren HS, Sillivan SE, O'Sullivan SS, Luksik AS, et al. Vascular endothelial growth factor is upregulated by l-dopa in the parkinsonian brain: implications for the development of dyskinesia. *Brain.* (2011) 134:2339–57. doi: 10.1093/brain/awr165
49. Hjemdahl P, Belfrage E, Daleskog M. Vascular and metabolic effects of circulating epinephrine and norepinephrine. Concentration-effect study in dogs. *J Clin Invest.* (1979) 64:1221–8. doi: 10.1172/JCI109576
50. Quisth V, Enoksson S, Blaak E, Hagström-Toft E, Arner P, Bolinder J. Major differences in noradrenaline action on lipolysis and blood flow rates in skeletal muscle and adipose tissue *in vivo. Diabetologia.* (2005) 48:946–53. doi: 10.1007/s00125-005-1708-4

Conflict of Interest: The authors declare that the research was conducted in the absence of any commercial or financial relationships that could be construed as a potential conflict of interest.

Copyright © 2019 Aljuaid, Booth, Hobson, Borys, Williams, Katako, Ryner, Goertzen and Ko. This is an open-access article distributed under the terms of the Creative Commons Attribution License (CC BY). The use, distribution or reproduction in other forums is permitted, provided the original author(s) and the copyright owner(s) are credited and that the original publication in this journal is cited, in accordance with accepted academic practice. No use, distribution or reproduction is permitted which does not comply with these terms.

frontiers in Neurology

ORIGINAL RESEARCH
published: 10 December 2019
doi: 10.3389/fneur.2019.01285

Diffusion Kurtosis Imaging for Detection of Early Brain Changes in Parkinson's Disease

Jitian Guan[1,2,3†], Xilun Ma[4†], Yiqun Geng[2,3,5], Dan Qi[2,3], Yuanyu Shen[1], Zhiwei Shen[1], Yanzi Chen[1], Erxi Wu[2,3,6,7,8] and Renhua Wu[1]*

[1] Department of Radiology, The Second Affiliated Hospital of Shantou University Medical College, Shantou, China, [2] Department of Neurosurgery, Baylor Scott & White Health, Temple, TX, United States, [3] Neuroscience Institute, Baylor Scott & White Health, Temple, TX, United States, [4] Department of Radiology, The First Affiliated Hospital of Shantou University Medical College, Shantou, China, [5] Laboratory of Molecular Pathology, Shantou University Medical College, Shantou, China, [6] Department of Surgery, Texas A&M University Health Science Center College of Medicine, Temple, TX, United States, [7] Department of Pharmaceutical Sciences, College of Pharmacy, Texas A&M University Health Science Center, College Station, TX, United States, [8] Dell Medical School, LIVESTRONG Cancer Institute, The University of Texas at Austin, Austin, TX, United States

We aimed to evaluate microscale changes in the bilateral red nucleus and substantia nigra of patients with Parkinson's disease (PD) using diffusion kurtosis imaging (DKI). Twenty-six patients with PD [mean age, 62.5 ± 8.7 years; Hoehn-Yahr stage, 0–4.0; Unified Parkinson's Disease Rating Scale (UPDRS) scores, 8–43] and 15 healthy controls (mean age, 59.5 ± 9.4 years) underwent DKI of the substantia nigra and red nucleus. Imaging was performed using a General Electric (GE) Signa 3.0-T MRI system. Patients with PD were divided into two groups consisting of 12 patients with UPDRS scores ≥ 30 and 14 patients with UPDRS scores < 30. All DKI data processing operations were performed with commercial workstations (GE, ADW 4.6) using Functool software to generate color-coded and parametric maps of mean kurtosis (MK), fractional anisotropy (FA), and mean diffusivity (MD). MK values in the bilateral substantia nigra were significantly lower in patients with early- and advanced-stage PD than in controls. Moreover, MK values in the left substantia nigra were significantly lower in patients with advanced-stage PD than in those with early-stage PD. Patients with advanced-stage PD also exhibited significant decreases in MK values in the bilateral red nucleus relative to controls. No significant differences in FA or MD values were observed between the PD and control groups. There were no significant correlations between MK, FA, or MD values and UPDRS scores. Our findings suggest that decreased MK values in the substantia nigra may aid in determining the severity of PD and help provide early diagnoses.

Keywords: diffusion kurtosis imaging, magnetic resonance imaging, Parkinson's disease, red nucleus, substantia nigra

OPEN ACCESS

Edited by:
Edward Ofori, Arizona State University, United States

Reviewed by:
Mohamed Mosaad Salama, Mansoura University, Egypt
Pedro Ribeiro, Federal University of Rio de Janeiro, Brazil

***Correspondence:**
Renhua Wu
cjr.wurenhua@vip.163.com

[†] These authors share first authorship

Specialty section:
This article was submitted to Movement Disorders, a section of the journal Frontiers in Neurology

Received: *01 August 2019*
Accepted: *20 November 2019*
Published: *10 December 2019*

Citation:
Guan J, Ma X, Geng Y, Qi D, Shen Y, Shen Z, Chen Y, Wu E and Wu R (2019) Diffusion Kurtosis Imaging for Detection of Early Brain Changes in Parkinson's Disease. Front. Neurol. 10:1285. doi: 10.3389/fneur.2019.01285

INTRODUCTION

Parkinson's disease (PD) is a progressive neurodegenerative disease caused by the degeneration of nigrostriatal dopaminergic neurons. The main pathological changes associated with PD include the loss of dopaminergic neurons in the substantia nigra/striatum and the presence of Lewy neuritis, which result in movement disorders. However, the initial diagnosis of PD is based on cardinal signs

such as bradykinesia, resting tremor, postural instability, gait disorder, and muscular rigidity, all of which become evident only after an 80% loss of dopaminergic neurons in the striatum (1, 2). In the recent years, many laboratory tests (e.g., cerebrospinal fluid analysis, blood tests) have been used to provide excellent support for the early prediction of PD. However, use of these biomarkers alone is not sufficient for diagnosis, as PD is not a disease with a single characteristic; specific biomarkers for motor and non-motor dysfunction would lead to more precise and individualized treatment for patients with PD. Combining findings from different fields may assist in identifying them. More sensitive diagnostic methods are therefore required to ensure timely and appropriate treatment.

Diffusion tensor imaging (DTI), a non-invasive MRI technique based on diffusion-weight imaging (DWI), has been used for *in vivo* assessments of white matter integrity. To date, both DTI and DWI have been applied for the diagnosis of various diseases (3, 4). Previous studies have allowed for the evaluation of conventional diffusion tensor metrics such as mean diffusivity (MD) and fractional anisotropy (FA). Several studies using DTI revealed microstructural alterations in the white matter in PD patients with motor impairment (5–7). DTI is also used to examine gray matter areas. Several studies measuring DTI parameters such as FA have shown that FA in the substantia nigra is reduced in patients with PD compared to healthy controls, which indicates that FA may be a diagnostic biomarker of PD (8–10). However, the results using FA are not always consistent. Authors of another study observed that the FA in the substantia nigra of PD patients did not differ significantly from that of controls (11). While measuring MD targeting the substantia nigra, one study showed that increased MD in this region helped distinguish patients with PD from those with multiple system atrophy (12). In contrast, other studies found that nigral MD changes had no significant effect on the disease (13, 14). Diffusion kurtosis imaging (DKI) can provide other metrics related to non-Gaussian water diffusion such as mean kurtosis (MK) (15). In general, MK is related to the complexity of the microstructure. A previous study demonstrated that MK was significantly increased in the substantia nigra of PD patients; MK in the substantia nigra was thought to be a sensitive metric for early diagnosis of PD (16).

In the present study, we utilized DKI to evaluate microscale changes in the substantia nigra and red nucleus of patients with PD and to determine how these regions are altered at different stages of PD.

RESULTS

General Characteristics of Study Participants

There were no significant differences in age ($F = 0.224$, $p = 0.303$) or gender ($X^2 = 0.383$, $p = 0.536$) between the PD and control (CTL) groups. Furthermore, there were no significant differences in age ($F = 0.949$, $p = 0.625$) or gender ($X^2 = 2.872$, $p = 0.238$) among the early-stage PD, advanced-stage PD, and CTL groups.

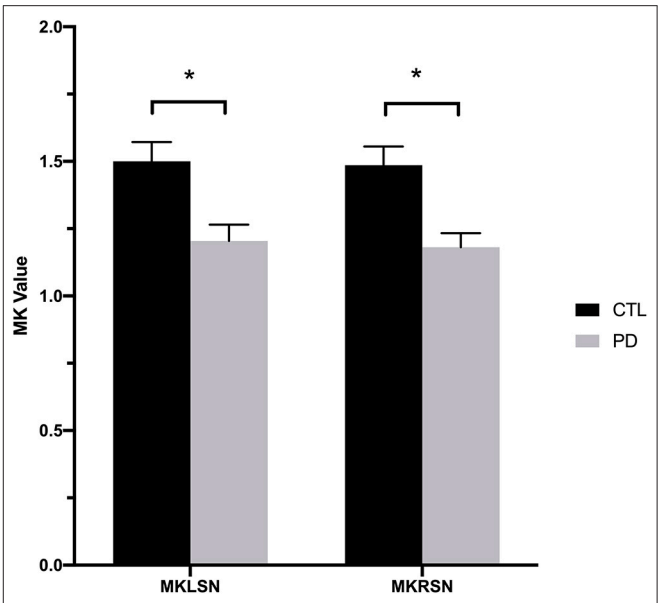


FIGURE 1 | Mean kurtosis values for the bilateral substantia nigra in the Parkinson's disease and control groups. CTL, control; MKLSN, mean kurtosis of the left substantia nigra; MKRSN, mean kurtosis of the right substantia nigra; PD, Parkinson's disease. *$p < 0.05$.

Comparison of MK, FA, and MD Values in the Substantia Nigra and Red Nucleus

MK values in the substantia nigra were significantly lower in patients with early- and advanced-stage PD than in controls (**Figure 1**, **Table 1**). In addition, MK values in the left substantia nigra were significantly lower in patients with advanced-stage PD than in patients with early-stage PD (**Figure 2**, **Table 2**). MK values in the bilateral red nucleus were significantly lower in patients with advanced-stage PD than in controls (**Figure 3**, **Table 2**). No significant differences in FA or MD values were observed between the PD and CTL groups (**Figures 2**, **3**, **Table 2**).

Correlation Between FA, MD, or MK Values in the Substantia Nigra and Unified Parkinson's Disease Rating Scale Scores

There were no significant correlations between MK, FA, or MD values and Unified Parkinson's Disease Rating Scale (UPDRS III) scores.

DISCUSSION

Early diagnosis of PD using conventional MRI is challenging; more sensitive brain imaging techniques are needed to facilitate early diagnosis and assessment of disease severity. In this study, we used DKI to investigate brain changes in patients with PD. Importantly, these studies revealed that MK values in the bilateral

Abbreviations: CTL, control; DKI, diffusion kurtosis imaging; DTI, diffusion tensor imaging; DWI, diffusion-weight imaging; FA, fractional anisotropy; FOV, field of view; MD, mean diffusivity; MK, mean kurtosis; PD, Parkinson's disease; TE, echo time; TR, repetition time; UPDRS, Unified Parkinson's Disease Rating Scale.

TABLE 1 | Diffusion kurtosis imaging values in the bilateral red nucleus and substantia nigra in the Parkinson's disease and control groups.

DKI values	PD ($N = 26$)	CTL ($N = 15$)	*p* value
	Mean ± SD	Mean ± SD	
Left SN			
MK	1.204 ± 0.061	1.500 ± 0.072	0.022*
MD	0.547 ± 0.125	0.551 ± 0.119	0.934
FA	0.454 ± 0.134	0.497 ± 0.109	0.296
Right SN			
MK	1.181 ± 0.052	1.486 ± 0.069	0.023*
MD	0.520 ± 0.116	0.538 ± 0.110	0.617
FA	0.477 ± 0.087	0.464 ± 0.144	0.728
Left RN			
MK	1.336 ± 0.247	1.451 ± 0.184	0.127
MD	0.517 ± 0.114	0.551 ± 0.159	0.440
FA	0.447 ± 0.112	0.511 ± 0.145	0.125
Right RN			
MK	1.407 ± 0.251	1.525 ± 0.188	0.119
MD	0.500 ± 0.137	0.521 ± 0.121	0.622
FA	0.450 ± 0.112	0.501 ± 0.159	0.241

*CTL, control; DKI, diffusion kurtosis imaging; FA, fractional anisotropy; MD, mean diffusivity; MK, mean kurtosis; PD, Parkinson's disease; RN, red nuclei; SN, substantia nigra; SD, standard deviation. *p < 0.05, PD vs. CTL.*

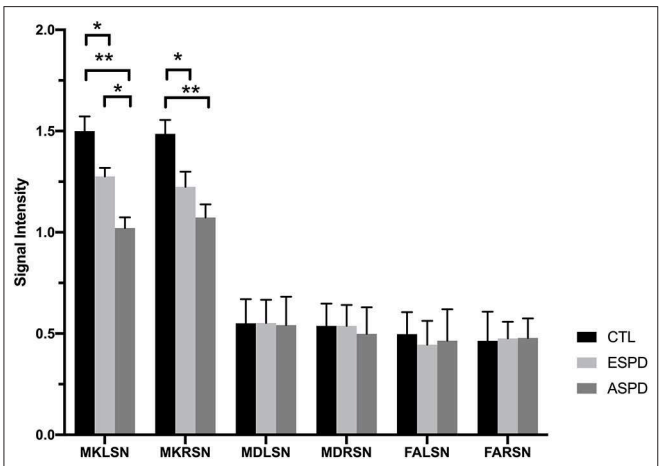


FIGURE 2 | Diffusion kurtosis imaging values in the substantia nigra for the control, early-stage Parkinson's disease, and advanced-stage Parkinson's disease groups. ASPD, advanced-stage Parkinson's disease; CTL, control; ESPD, early-stage Parkinson's disease; FALSN, fractional anisotropy of the left substantia nigra; FARSN, fractional anisotropy of the right substantia nigra; MDLSN, mean diffusivity of the left substantia nigra; MDRSN, mean diffusivity of the right substantia nigra; MKLSN, mean kurtosis of the left substantia nigra; MKRSN, mean kurtosis of the right substantia nigra. **$p < 0.01$, ASPD vs. CTL; *$p < 0.05$, early-stage PD vs. CTL or advanced-stage PD vs. CTL or advanced-stage PD vs. early-stage PD.

substantia nigra were significantly lower in patients with early- and advanced-stage PD than in controls. Moreover, MK values in the left substantia nigra were significantly lower in patients with advanced-stage PD than in those with early-stage PD. Patients with advanced-stage PD also exhibited significantly decreased

TABLE 2 | Diffusion kurtosis imaging values in the bilateral red nucleus and substantia nigra in the control, early-stage Parkinson's disease, and advanced-stage Parkinson's disease groups.

DKI values	CTL ($N = 15$)	Early-stage PD ($N = 14$)	Advanced-stage PD ($N = 12$)
	Mean ± SD	Mean ± SD	Mean ± SD
Left SN			
MK	1.500 ± 0.072	1.276 ± 0.042*	1.021 ± 0.053**
MD	0.551 ± 0.119	0.552 ± 0.115	0.542 ± 0.140
FA	0.497 ± 0.109	0.445 ± 0.118	0.465 ± 0.155
Right SN			
MK	1.486 ± 0.069	1.225 ± 0.074*	1.073 ± 0.065**
MD	0.538 ± 0.110	0.538 ± 0.103	0.499 ± 0.131
FA	0.464 ± 0.144	0.476 ± 0.082	0.478 ± 0.097
Left RN			
MK	1.511 ± 0.084	1.391 ± 0.075	1.232 ± 0.096*
MD	0.551 ± 0.159	0.448 ± 0.112	0.453 ± 0.117
FA	0.511 ± 0.145	0.434 ± 0.101	0.463 ± 0.127
Right RN			
MK	1.525 ± 0.096	1.419 ± 0.093	1.271 ± 0.085*
MD	0.521 ± 0.121	0.512 ± 0.145	0.485 ± 0.133
FA	0.501 ± 0.159	0.448 ± 0.112	0.453 ± 0.117

*CTL, control; DKI, diffusion kurtosis imaging; FA, fractional anisotropy; MD, mean diffusivity; MK, mean kurtosis; PD, Parkinson's disease; RN, red nuclei; SN, substantia nigra; SD, standard deviation. *p < 0.05, early-stage PD vs. CTL or advanced-stage PD vs. CT or advanced-stage PD vs. early-stage PD. **p < 0.01, advanced-stage PD vs. CTL.*

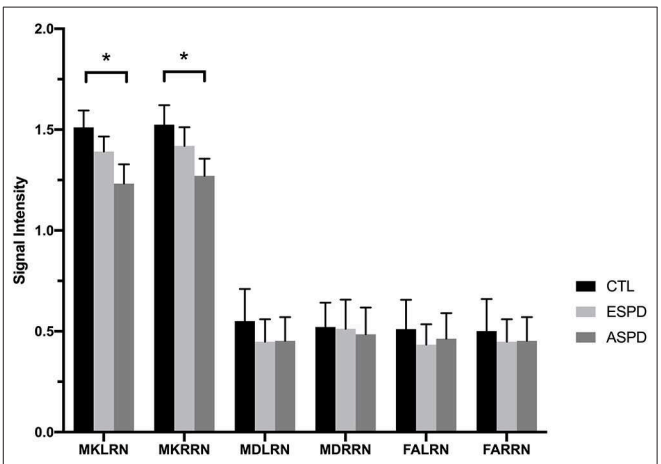


FIGURE 3 | Diffusion kurtosis imaging values in the red nucleus for the control, early-stage Parkinson's disease, and advanced-stage Parkinson's disease groups. ASPD, advanced-stage Parkinson's disease; CTL, control; ESPD, early-stage Parkinson's disease; MDLRN, mean diffusivity of the left red nucleus; FALRN, fractional anisotropy of the left red nucleus; FARRN, fractional anisotropy of the right red nucleus; MDRRN, mean diffusivity of the right red nucleus; MKLRN, mean kurtosis of the left red nucleus; MKRRN, mean kurtosis of the right red nucleus. *$p < 0.05$, ESPD vs. CTL or ASPD vs. CTL or ASPD vs. ESPD.

MK values in the bilateral red nucleus relative to controls. Hence, DKI may be a useful imaging technique for the diagnosis of PD and assessment of disease severity.

The cardinal motor symptoms of PD include bradykinesia, resting tremor, rigidity, and postural instability, which predominantly result from dysfunction of the substantia nigra pars reticulata and other brain structures (9). The levels of oxidative stress markers in the substantia nigra are greatly increased in patients with PD, which may explain damage to dopaminergic neurons (10). In addition, iron ions, which are abundant in many brain structures, including the substantia nigra and red nucleus (11–13), may play an important role in oxidative stress (14). Thus, pathophysiological changes in the substantia nigra and red nucleus may influence the development and progression of PD.

In our study, we divided patients with PD into early- and advanced-stage PD groups based on UPDRS scores. Our findings indicate that early- and advanced-stage PD were associated with significant decreases in MK values in the bilateral substantia nigra. DKI is a quantitative technique used to reflect non-Gaussian water diffusion in living tissue (5, 17). MK, which is related to structural complexity, is the most commonly used kurtosis index. Thus, as reduced MK values reflect decreases in structural complexity, our findings may be related to neuronal loss and gliosis in the bilateral substantia nigra. Alternatively, iron deposits in the substantia nigra, which aggravate oxidative stress, may also explain the observed decreases in kurtosis. We also observed significant decreases in MK values in the left substantia nigra in patients with advanced-stage PD when compared to those with early-stage PD. These findings indicate that, while the initial onset of motor symptoms occurred on the right side in most patients, the initial lesions occurred in the left substantia nigra. Therefore, our results suggest that MK values can be used to evaluate PD progression.

DKI is a relatively new technique, and previous studies have primarily focused on comparing changes in DKI indices in different brain regions of patients with PD and controls. Few DKI studies have compared these indices among different PD groups. In a study involving 30 PD patients and 30 controls, MK values were increased in the caudate nucleus, putamen, globus pallidus, and substantia nigra in patients with PD (18). More recently, Zhang et al. (19) conducted a large study involving 72 patients with early-stage PD and 72 healthy volunteers. They also observed increased MK values in the substantia nigra of patients with PD relative to those observed in healthy volunteers. In contrast, some studies have reported that MK values are reduced in the white matter of multiple encephalic regions in patients with PD (16, 20). Although, the decreases in MK values observed in the present study differ from those reported in some prior DKI studies, our results may better explain the damage to the substantia nigra in patients with PD. Discrepancies in the levels of MK among these studies may reflect differences in the severity of PD, as MK in the substantia nigra correlates with the severity of motor dysfunction in PD patients (19). For example, Zhang et al. (19) included patients with Hoehn-Yahr stages 1 and 2, while we included patients with Hoehn-Yahr stages 1–4. Differences in methodology may also underlie the lack of agreement between the results of these studies. For example, all image processing operations in a study by Wang et al. (18) were performed using MATLAB 7.8, whereas we utilized Functool software for postprocessing of the DKI data. We speculate that differences in scanning protocols may have contributed to the inconsistencies in MK values between these studies.

MK values in the red nucleus were significantly lower in patients with advanced-stage PD compared to those of patients in the CTL group. However, no such differences were observed between patients with early-stage PD and those in the CTL group or with advanced-stage PD, suggesting that the degeneration of red nucleus neurons arises later during the progression of PD. The degeneration of dopamine neurons is reported to occur not only in the substantia nigra but also in other brain regions ranging from the lower brain stem to the basal ganglia (21). In addition, the red nucleus exhibits a close relationship with the cardinal motor symptoms of PD (22). In accordance with these previous findings, MK values in the red nucleus decreased as symptom severity increased in our patients with PD. This suggests a close relationship between pathophysiological changes in the red nucleus and the cardinal motor symptoms of PD.

As noted in previous studies, we observed no significant differences in FA or MD values among the PD and control groups (23, 24). However, in one previous study, the measurement of diffusion indices in 73 patients with a clinical diagnosis of idiopathic PD and 78 controls using DTI revealed significant decreases in FA values in the substantia nigra in patients with PD (25). Other studies have reported similar results (26–28). Although we observed no changes in FA or MD values, the observed reductions in MK values may indicate that DKI is more sensitive than DTI for the diagnosis of PD.

Consistent with previous findings (18), we observed no correlation between diffusion indices and UPDRS scores. Others, however, have reported a positive association between MK values and UPDRS scores (19). Such discrepancies may be due to the subjectivity of UPDRS scoring and the inability of older PD patients to express their symptoms.

Our study had several limitations. First, although loss of dopamine neurons mainly occurs in the substantia nigra pars compacta, our region of interest included the whole substantia nigra, for which the mean diffusion indices were calculated. In addition, iron deposition may have influenced the measurement of diffusion indices. Future studies should utilize DKI in conjunction with other methods to determine the precise relationship between iron deposition and MK values.

CONCLUSION

MK values may aid clinicians in diagnosing PD early, monitoring disease severity, and assessing changes in the bilateral substantia nigra. Changes in the red nucleus are mainly observed in patients with advanced-stage PD. Therefore, MK in the substantia nigra is a potential biomarker of PD in imaging studies and may readily identify patients with Parkinsonism.

MATERIALS AND METHODS

Participants

The present study included 26 patients with PD (mean age, 62.5 ± 8.7 years; Hoehn-Yahr stage, 0–4.0; UPDRS scores, 8–43) and 15 controls (mean age, 59.5 ± 9.4 years). Twenty-four patients with PD exhibited right-sided onset of motor

symptoms, while two patients exhibited left-sided onset. Patients with PD were recruited from the Department of Neurology at our hospital, and all CTL participants were recruited from the Medical Examination Center at our hospital. All participants underwent DKI, which was performed using a General Electric (GE) Signa 3.0 T MR Imaging System. PD severity was assessed using the Hoehn-Yahr scale and the UPDRS III. Fifteen patients had a history of medication use, but no adverse reactions were observed among these patients. The PD group was further divided into an advanced-stage PD group (UPDRS $\geq$ 30; 8 men, 4 women; mean age, 60.1 $\pm$ 8.8 years) and an early-stage PD group (UPDRS $<$ 30; 5 men, 9 women; mean age, 64.6 $\pm$ 8.290 years).

The present study was approved by the Ethics Committee of the Medical College of Shantou University (protocol ID: 2016-05), and all participants provided written informed consent in accordance with the Declaration of Helsinki. Exclusion criteria were as follows: (1) other neurological conditions, including cerebral infarction, cerebral hemorrhage, brain tumor, brain trauma, carbon monoxide poisoning, demyelization, degeneration injury, and vascular dementia; (2) alcohol dependence or a history of taking other psychoactive substances (e.g., antipsychotics or benzodiazepines); (3) history of diabetes or coma due to diabetic ketoacidosis; (4) history of serious medical disease (e.g., heart or respiratory failure, significant liver or kidney dysfunction, anemia, chronic electrolyte disturbance, or heavy metal poisoning); (5) mental illness; and (6) metabolic syndrome lasting longer than 5 years.

Image Acquisition and Postprocessing

MRI scans were performed using a 3.0-T GE scanner (Signa; General Electric Medical Systems) equipped with a standard eight-channel head coil. We used sponge padding and cotton balls to limit head motion and reduce scanner noise. Initial routine MRI and T2-weighted images [repetition time (TR) = 4,420.0 ms; echo time (TE) = 112.1 ms; 5.0 mm thickness; 1.0 mm septation; matrix 512 $\times$ 512; field of view (FOV) = 160 $\times$ 160 mm] were obtained for all participants. Two experienced neuroradiologists assisted in the diagnostic process for every view obtained.

An echo-planar imaging sequence was used to obtain DKI images with the following scanning parameters: TR, 4,500 ms; TE, 84.1 ms; diffusion gradient pulse duration (δ), 32.2 ms; diffusion gradient separation (Δ), 38.776 ms; FOV, 240 $\times$ 240 mm; matrix, 128 $\times$ 128; number of excitations, 1; 5.0 mm thickness with no interslice gap; number of slices, 20. Total scan time was 3 min 5 s. Diffusion encoding was applied in 15 directions with three b values (0, 1,000, and 2,000 s/mm^2). All images were postprocessed on commercial workstations (GE, ADW 4.6) equipped with Functool software to generate color-coded and parametric maps of MK, MD, and FA. Volumes of interest in the bilateral substantia nigra and red nucleus were independently drawn three times, with a fixed-in-size (8 mm^2) ellipse (see **Figure 4**).

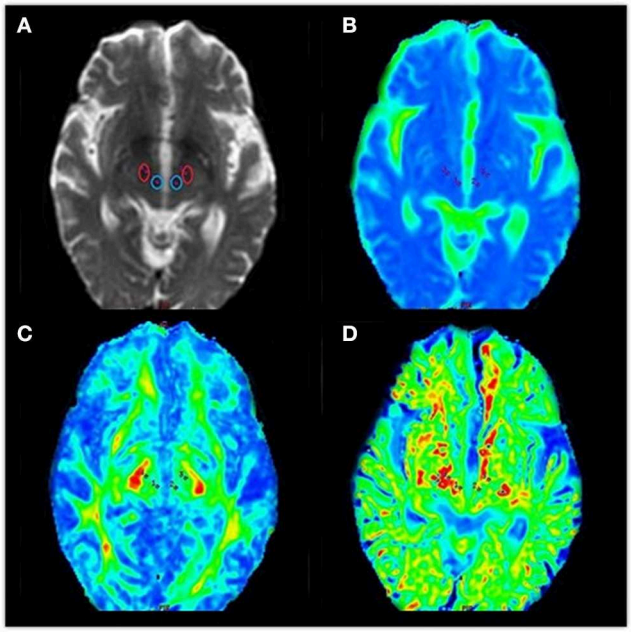


FIGURE 4 | Diffusional kurtosis images of volumes of interest in the bilateral red nucleus and substantia nigra **(A–D)**. **(A)** Volumes of interest in the bilateral red nucleus and substantia nigra. We obtained data from maps of the **(B)** mean diffusivity, **(C)** fractional anisotropy, and **(D)** mean kurtosis.

Statistical Analyses

All data were analyzed using SPSS 20.0 statistical software (SPSS, Inc., Chicago, IL, USA). A one-way analyses of variance test and least significant difference tests were used to evaluate differences in MK, FA, and MD among early-stage PD, advanced-stage PD, and CTL groups. Independent samples t-tests were used to compare age and diffusion indices between the PD and CTL groups. Associations between diffusion indices and UPDRS scores were assessed using Spearman's rank correlation coefficient. Chi-square tests were used to evaluate gender differences among the groups. A $p < 0.05$ was considered statistically significant.

ETHICS STATEMENT

The studies involving human participants were reviewed and approved by the Ethics Committee of the Medical College of Shantou University. The patients/participants provided their written informed consent to participate in this study.

AUTHOR CONTRIBUTIONS

JG and XM designed and performed the experiments and contributed to the manuscript design and preparation. XM and YG analyzed the results. YG and DQ contributed to the statistical analysis. DQ, EW, YC, ZS, and YS contributed to the editing of the manuscript. JG and RW conceived the research project and helped design the study.

FUNDING

This work was supported by the National Natural Science Foundation of China (Grant No. 81471730), the National High Technology Research and Development Program (863 Program) of China (Program No. 2014AA021101), the Department of Education, Guangdong Government, under the Top-tier University Development Scheme for Research and Control of Infectious Diseases (Grant No. 2015034), and the Natural Science Foundation of Guangdong Province, China (Grant No. 2015A030313444).

REFERENCES

1. Obeso JA, Rodríguez-Oroz MC, Rodríguez M, Lanciego JL, Artieda J, Gonzalo N, et al. Pathophysiology of the basal ganglia in Parkinson's disease. *Trends Neurosci.* (2000) 23:S8–19. doi: 10.1016/S1471-1931(00)00028-8
2. Gazewood JD, Richards DR, Clebak K. Parkinson disease: an update. *Am Fam Physician.* (2013) 87:267–73. Available online at: https://www.aafp.org/afp/2013/0215/p267.html
3. Cauter SV, Veraart J, Sijbers J, Peeters RR, Himmelreich U, Keyzer FD, et al. Gliomas: diffusion kurtosis MR imaging in grading. *Radiology.* (2012) 263:492–501. doi: 10.1148/radiol.12110927
4. Yan G, Dai Z, Xuan Y, Wu R. Early metabolic changes following ischemia onset in rats: an *in vivo* diffusion-weighted imaging and 1H-magnetic resonance spectroscopy study at 7.0 T. *Mol Med Rep.* (2015) 11:4109–14. doi: 10.3892/mmr.2015.3283
5. Jensen JH, Helpern JA, Lu H, Kaczynski K. Diffusional kurtosis imaging: the quantification of non-gaussian water diffusion by means of magnetic resonance imaging. *Magn Reson Med.* (2005) 53:1432–40. doi: 10.1002/mrm.20508
6. Zhang Z, Wang Y, Shen Z, Yang Z, Li L, Chen D, et al. The neurochemical and microstructural changes in the brain of systemic lupus erythematosus patients: a multimodal MRI study. *Sci Rep.* (2016) 6:19026. doi: 10.1038/srep19026
7. Sui YV, Donaldson J, Miles L, Babb JS, Castellanos FX, Lazar M. Diffusional kurtosis imaging of the corpus callosum in autism. *Mol Autism.* (2018) 9:62. doi: 10.1186/s13229-018-0245-1
8. Hori M, Fukunaga I, Masutani Y, Nakanishi A, Shimoji K, Kamagata K, et al. New diffusion metrics for spondylotic myelopathy at an early clinical stage. *Eur Radiol.* (2012) 22:1797–802. doi: 10.1007/s00330-012-2410-9
9. Albin RL, Young AB, Penney JB. The functional anatomy of disorders of the basal ganglia. *Annu Rev Neurosci.* (1995) 18:63–4. doi: 10.1016/0166-2236(95)80020-3
10. Sanchezguajardo V, Barnum CJ, Tansey MG, Romeroramos M. Neuroimmunological processes in Parkinson's disease and their relation to α-synuclein: microglia as the referee between neuronal processes and peripheral immunity. *Asn Neuro.* (2013) 5:113–39. doi: 10.1042/AN20120066
11. Yoon RG, Kim SJ, Kim HS, Choi CG, Kim JS, Oh J, et al. The utility of susceptibility-weighted imaging for differentiating Parkinsonism-predominant multiple system atrophy from Parkinson's disease: correlation with 18F-flurodeoxyglucose positron-emission tomography. *Neurosci Lett.* (2015) 584:296–301. doi: 10.1016/j.neulet.2014.10.046
12. Martin WRW, Wieler M, Gee M. Midbrain iron content in early Parkinson disease. *Neurology.* (2008) 70(16 Pt 2):1411–7. doi: 10.1212/01.wnl.0000286384.31050.b5
13. Lotfipour AK, Wharton S, Schwarz ST, Gontu V, Schäfer A, Peters AM, et al. High resolution magnetic susceptibility mapping of the substantia nigra in Parkinson's disease. *J Magn Reson Imaging.* (2012) 35:48–55. doi: 10.1002/jmri.22752
14. Double KL, Halliday GM. New face of neuromelanin. *J Neural Trans Supplem.* (2006) 70:119–23. doi: 10.1007/978-3-211-45295-0_19
15. Paydar A, Fieremans E, Nwankwo JI, Lazar M, Sheth HD, Adisetiyo V, et al. Diffusional kurtosis imaging of the developing brain. *Am J Neuroradiol.* (2014) 35:255–74. doi: 10.3174/ajnr.A3764
16. Ito K, Ohtsuka C, Yoshioka K, Kameda H, Yokosawa S, Sato R, et al. Differential diagnosis of parkinsonism by a combined use of diffusion kurtosis imaging and quantitative susceptibility mapping. *Neuroradiology.* (2017) 59:759–69. doi: 10.1007/s00234-017-1870-7
17. Lu H, Jensen JH, Ramani A, Helpern JA. Three-dimensional characterization of non-gaussian water diffusion in humans using diffusion kurtosis imaging. *NMR Biomed.* (2006) 19:236–47. doi: 10.1002/nbm.1020
18. Wang JJ, Lin WY, Lu CS, Weng YH, Ng SH, Wang CH, et al. Parkinson disease: diagnostic utility of diffusion kurtosis imaging. *Radiology.* (2011) 261:210–7. doi: 10.1148/radiol.11102277
19. Zhang G, Zhang Y, Zhang C, Wang Y, Ma G, Nie K, et al. Diffusion kurtosis imaging of substantia nigra is a sensitive method for early diagnosis and disease evaluation in Parkinson's disease. *Parkinsons Dis.* (2015) 2015:207624. doi: 10.1155/2015/207624
20. Kamagata K, Tomiyama H, Hatano T, Motoi Y, Abe O, Shimoji K, et al. A preliminary diffusional kurtosis imaging study of Parkinson disease: comparison with conventional diffusion tensor imaging. *Neuroradiology.* (2014) 56:251–8. doi: 10.1007/s00234-014-1327-1
21. Braak H, Tredici KD, Rüb U, Vos RAID, Steur ENHJ, Braak E. Staging of brain pathology related to sporadic Parkinson's disease. *Neurobiol Aging.* (2003) 24:197–211. doi: 10.1016/S0197-4580(02)00065-9
22. Rodriguez-Oroz MC, Manolo R, Carlos L, Miguel RP, Juan N, David GG, et al. Neuronal activity of the red nucleus in Parkinson's disease. *Mov Disord.* (2008) 23:908–11. doi: 10.1002/mds.22000
23. Menke RA, Jbabdi S, Miller KL, Matthews PM, Zarei M. Connectivity-based segmentation of the substantia nigra in human and its implications in Parkinson's disease. *Neuroimage.* (2010) 52:1175–80. doi: 10.1016/j.neuroimage.2010.05.086
24. Focke NK, Helms G, Pantel PM, Scheewe S, Knauth M, Bachmann CG, et al. Differentiation of typical and atypical Parkinson syndromes by quantitative MR imaging. *Am J Neuroradiol.* (2011) 32:2087–92. doi: 10.3174/ajnr.A2865
25. Chan LL, Rumpel H, Yap K, Lee E, Loo HV, Ho GL, et al. Case control study of diffusion tensor imaging in Parkinson's disease. *J Neurol Neurosurg Psychiatry.* (2008) 78:1383–6. doi: 10.1136/jnnp.2007.121525
26. Vaillancourt DE, Spraker MB, Prodoehl J, Abraham I, Corcos DM, Zhou XJ, et al. High-resolution diffusion tensor imaging in the substantia nigra of *de novo* Parkinson disease. *Neurology.* (2009) 72:1378. doi: 10.1212/01.wnl.0000340982.01727.6e
27. Rolheiser TM, Fulton HG, Good KP, Fisk JD, Mckelvey JR, Scherfler C, et al. Diffusion tensor imaging and olfactory identification testing in early-stage Parkinson's disease. *J Neurol.* (2011) 258:1254. doi: 10.1007/s00415-011-5915-2
28. Skorpil M, Söderlund V, Sundin A, Svenningsson P. MRI diffusion in Parkinson's disease: using the technique's inherent directional information to study the olfactory bulb and substantia nigra. *J Parkinsons Dis.* (2012) 2:171–80. doi: 10.3233/JPD-2012-12091

Conflict of Interest: The authors declare that the research was conducted in the absence of any commercial or financial relationships that could be construed as a potential conflict of interest.

Copyright © 2019 Guan, Ma, Geng, Qi, Shen, Shen, Chen, Wu and Wu. This is an open-access article distributed under the terms of the Creative Commons Attribution License (CC BY). The use, distribution or reproduction in other forums is permitted, provided the original author(s) and the copyright owner(s) are credited and that the original publication in this journal is cited, in accordance with accepted academic practice. No use, distribution or reproduction is permitted which does not comply with these terms.

frontiers in Neurology

ORIGINAL RESEARCH
published: 18 December 2019
doi: 10.3389/fneur.2019.01329

Brain MRI Reveals Ascending Atrophy in Parkinson's Disease Across Severity

Jamie C. Blair[1], *Matthew J. Barrett*[2], *James Patrie*[3], *Joseph L. Flanigan*[2], *Scott A. Sperling*[2], *W. Jeffrey Elias*[4,5] *and T. Jason Druzgal*[1,4]*

[1] Department of Radiology and Medical Imaging, University of Virginia Health System, Charlottesville, VA, United States, [2] Department of Neurology, University of Virginia Health System, Charlottesville, VA, United States, [3] Department of Public Health Sciences, University of Virginia Health System, Charlottesville, VA, United States, [4] Brain Institute, University of Virginia, Charlottesville, VA, United States, [5] Department of Neurosurgery, University of Virginia Health System, Charlottesville, VA, United States

Models which assess the progression of Lewy pathology in Parkinson's disease have proposed ascending spread in a caudal-rostral pattern. *In-vivo* human evidence for this theory is limited, in part because there are no biomarkers that allow for direct assessment of Lewy pathology. Here, we measured neurodegeneration via MRI, an outcome which may serve as a proxy for a more direct assessment of ascending models using a combination of (1) MRI-based measures of gray matter density and (2) regions of interest (ROIs) corresponding to cortical and subcortical loci implicated in past MRI and stereological studies of Parkinson's disease. Gray matter density was measured using brain MRI voxel-based morphometry from three cohorts: (1) early Parkinson's disease, (2) more advanced Parkinson's disease and (3) healthy controls. Early Parkinson's disease patients ($N = 228$, mean age = 61.9 years, mean disease duration = 0.6 years) were newly diagnosed by the Parkinson's Progression Markers Initiative (PPMI). Advanced Parkinson's disease patients ($N = 136$, mean age = 63.5 years, mean disease duration = 8.0 years) were collected retrospectively from a local cohort undergoing evaluation for functional neurosurgery. Control subjects ($N = 103$, mean age = 60.2 years) were from PPMI. Comparative analyses focused on gray matter regions ranging from deep gray subcortical structures to the neocortex. ROIs were defined with existing probabilistic cytoarchitectonic brain maps. For subcortical regions of the basal forebrain, amygdala, and entorhinal cortex, advanced Parkinson's disease patients had significantly lower gray matter density when compared to both early Parkinson's disease and healthy controls. No differences were seen in neocortical regions that are "higher" in any proposed ascending pattern. Across early and advanced Parkinson's disease, gray matter density from nearly all subcortical regions significantly decreased with disease duration; no neocortical regions showed this effect. These results demonstrate that atrophy in advanced Parkinson's patients compared to early patients and healthy controls is largely confined to subcortical gray matter structures. The degree of atrophy in subcortical brain regions was linked to overall disease duration, suggesting an organized pattern of atrophy across severity.

Keywords: Parkinson's disease, magnetic resonance imaging, gray matter, atrophy, voxel-based morphometry, braak hypothesis

OPEN ACCESS

Edited by:
Edward Ofori,
Arizona State University, United States

Reviewed by:
David Vaillancourt,
University of Florida, United States
Pramod Kumar Pal,
National Institute of Mental Health and Neurosciences, India

***Correspondence:**
T. Jason Druzgal
jasondruzgal@gmail.com

Specialty section:
This article was submitted to Movement Disorders, a section of the journal Frontiers in Neurology

Received: *06 July 2019*
Accepted: *02 December 2019*
Published: *18 December 2019*

Citation:
Blair JC, Barrett MJ, Patrie J, Flanigan JL, Sperling SA, Elias WJ and Druzgal TJ (2019) Brain MRI Reveals Ascending Atrophy in Parkinson's Disease Across Severity. Front. Neurol. 10:1329. doi: 10.3389/fneur.2019.01329

INTRODUCTION

Parkinson's disease, a progressive neurodegenerative disorder, is characterized by cell death within the substantia nigra and presence of misfolded α-synuclein aggregates known as Lewy Bodies throughout the brain parenchyma (1–3). Braak and colleagues first described the pathological progression of α-synuclein aggregates in PD as occurring in an organized and ascending manner, beginning in subcortical brain structures and ending in the neocortex (4). Braak's model and others which propose ascending spread are underpinned by the "prion hypothesis," which posits that α-synuclein aggregates are taken up by neurons, undergo axonal transport, and are transferred to other neurons as part of a prion-like process (5). Recently, this model has been challenged (6), and other theories have emerged which attempt to explain why large subsets of PD patients do not follow proposed ascending patterns (7).

Important elements of hypotheses proposing ascending spread in PD enjoy support from *ex-vivo* (8–10), *in-vitro* (11–13) and *in-vivo* animal (2, 14, 15) studies of Parkinson's disease. However, because there is currently no method for the detection of α-synuclein aggregates in living human patients (16), there is a general lack of human *in-vivo* support for ascending spread models. As a proxy for Lewy pathology, many studies have utilized MRI methods to study neurodegeneration in PD. Though it is important to note that evidence connecting Lewy pathology and neuronal death is limited and neurodegeneration is an imperfect proxy for Lewy pathology (16, 17), neurodegeneration may nevertheless follow an ascending pattern in PD that is measurable via MRI techniques.

Qualitative evaluation of T1- and T2-weighted "conventional" structural MRI is generally considered normal in early PD patients (18, 19). More advanced techniques, which allow for quantitative evaluation of changes to tissue structure, provide an opportunity to study neurodegeneration in PD (20). The literature employing MRI to measure PD neurodegeneration has utilized techniques such as such as voxel and deformation-based morphometry (21–24), cortical thickness (25, 26), functional MRI (27–29), and free-water diffusion (30, 31) amongst numerous other methods. However, the MRI literature as a whole has reported inconsistent findings with respect to neurodegeneration (32, 33), perhaps due to methodological issues related to the lack of a standardized protocol for measuring atrophy in brain regions. With respect to PD progression, few MRI studies have attempted to study the disease process as a whole, tending instead to focus on individual ROIs or small subsets of ROIs. Studies in notable exception to the previous statement have introduced evidence both for and against ascending spread of neurodegeneration (23, 25), underscoring the need for further investigation.

A difficulty inherent to any study of progressive PD neurodegeneration is the disparate methods required to properly measure the brain regions known to degenerate in PD. For example, the substantia nigra is difficult to quantify with conventional MRI sequences due to the disparate magnetic properties of gray matter and neuromelanin (34). Successful quantification of substantia nigra degenereation has generally relied on combinations of T1-, T2, and T2*-weighted imaging (35) or attempts to image neuromelanin directly (36, 37). The small size and complexity of brainstem regions such as the locus coeruleus require the use of ultrahigh-field MRI scanners for proper resolution (38). Due to these challenges, no single MRI method is currently appropriate for measuring the earliest regions involved in the proposed ascending pattern of neurodegeneration in PD. However, voxel-based morphometry (VBM), a technique known to agree with findings from autopsy studies and other imaging modalities (39–41), allows for the measurement of many gray matter structures implicated in PD ranging from basal forebrain to the neocortex. Past VBM studies of PD have identified neurodegeneration in the basal forebrain (21, 22), amygdala (24, 42), hippocampus (43, 44), and neocortex (42, 45).

Here, we aimed to evaluate neurodegeneration in PD patients through measurements of gray matter density (GMD) obtained through VBM processing of T1-weighted MRI. This study focused on a specific subset of gray matter ROIs which were: (1) implicated by ascending models for PD, (2) demonstrated consistent findings between past MRI and stereological PD studies, and (3) could be measured by a combination of VBM and existing brain maps. Sub-regions of the basal forebrain (22, 46–48), amygdala (24, 42, 49), hippocampus (44, 50–52), and neocortex (23, 26, 53) all met the aforementioned criteria. Whole-brain GMD was obtained from three cohorts delineated by their disease duration: (1) early Parkinson's disease patients, (2) more advanced Parkinson's disease patients, and (3) healthy control subjects. Regional GMD was extracted according to existing MRI maps and compared between the groups to test the general hypothesis that patients with more advanced Parkinson's disease would show decreases in GMD in subcortical regions with relative sparing of cortical regions.

MATERIALS AND METHODS

Subjects

Healthy Controls

One hundred and three healthy control subjects (males = 67, females = 36, mean age = 60.2 years) were obtained from the PPMI database. The PPMI study is well-described at ppmi-info.org. Briefly, PPMI is a comprehensive multi-center study designed to identify biomarkers of PD with the goal of improving evaluation of disease modifying therapeutics (54). Healthy control subjects included in PPMI were above 30 years of age, had never been diagnosed with any major neurological disorder, had no first-degree relatives with idiopathic PD, and were not cognitively impaired based on a score of 26 or above on the Montreal Cognitive Assessment. Healthy controls included in this study had a 3D Magnetization Prepared Rapid Acquisition Gradient Echo (MP-RAGE) MRI sequence acquired on a Siemens MRI scanner at baseline event. Control subjects were excluded from analysis in this study if a non-MPRAGE sequence such as Spoiled Gradient Echo (SPGR) was acquired, or if a non-Siemens MRI scanner was used. Subjects were also excluded if images did not meet quality control standards described below.

Early Parkinson's Disease

Two hundred and twenty-eight early Parkinson's disease subjects (males = 141, females = 87, mean age = 61.9 years) were obtained from the baseline time point of the longitudinal PPMI database. The PPMI study is well-described at ppmi-info.org. Parkinson's Disease subjects included in PPMI were above 30 years of age, had received a clinical diagnosis of PD within 2 years of screening, had not taken nor were expected to take PD medication within 6 months of enrollment, had not received a clinical diagnosis of dementia, and had their PD diagnosis confirmed by DaTscan, a measurement of dopamine transporter which is known to have a high degree of specificity for PD (55). Early PD subjects included in this study had a 3D Magnetization Prepared Rapid Acquisition Gradient Echo (MP-RAGE) MRI sequence acquired on a Siemens MRI scanner at the baseline event. Early PD subjects were excluded from analysis in this study if a non-MPRAGE sequence such as Spoiled Gradient Echo (SPGR) was acquired, or if a non-Siemens MRI scanner was used. Subjects were also excluded if images did not meet quality control standards described below.

Advanced Parkinson's Disease

One hundred and thirty-six advanced PD subjects (males = 101, females = 35, mean age = 63.5 years) were obtained from a cohort of patients who underwent a first neurosurgical procedure to treat motor symptoms between January 1, 2010 and July 1, 2016 at the University of Virginia. Patients presenting for these procedures have generally carried the PD diagnosis for multiple years and have a motor symptom that is not (or inconsistently) responsive to oral medication. The procedures included deep brain stimulation, radiofrequency ablation, and focused ultrasound. The diagnosis of Parkinson's disease was confirmed by a movement disorders neurologist as part of the pre-surgical evaluation. Subjects with a 3D MP-RAGE MRI which met quality control standards were included for analysis in this study. Subjects were excluded if a non-MPRAGE sequence was acquired, or if imaging data was not acquired as part of the presurgical procedure. No post-surgically acquired MRI was included for analysis in this study. The University of Virginia Institutional Review Board for Health Sciences Research approved the retrospective collection of MRI images and medical information from patients for use in this study. On the basis of having carried the diagnosis longer than the early PD group, we refer to these patients as "Advanced" throughout the remainder of the manuscript.

MRI Acquisition and Quality Control

Healthy control and early PD MRI images were acquired with the MP-RAGE T1 weighted MRI sequence on Siemens MRI scanners. MRI sequence information can be found in the MRI technical operations manual (http://www.ppmi-info.org/wp-content/uploads/2017/06/PPMI-MRI-Operations-Manual-V7.pdf). PPMI image acquisition guidelines required slice thickness of 1.5 mm or less and no interslice gap, with repetition (TR) and echo (TE) time varying according to suggested settings at each site. PPMI images were obtained from the PPMI imaging database on 1/04/2017. Advanced PD images were also acquired with an MP-RAGE T1 sequence on Siemens MRI scanners. MRIs for the advanced PD cohort were obtained as part of routine clinical care on multiple MRI scanners, resulting in less standardization of MP-RAGE sequence parameters than found in PPMI. Voxel size in healthy control and early PD images measured either $1 \times 1 \times 1$ mm or $1 \times 1 \times 1.2$ mm while advanced PD voxel size varied but did not exceed $1 \times 1 \times 1.2$.

All images analyzed in this study were processed through the automated quality control function contained within the CAT12 toolbox (http://dbm.neuro.uni-jena.de/cat/) in MATLAB. This tool considers noise, inhomogeneities, and image resolution to create a composite score on a scale of A to E. Only images receiving a composite score of B- or higher, corresponding to "good" image quality, were included for final analysis in this study.

Voxel Based Morphometry Processing

Regional gray matter density was calculated from all images according to previously published methods (56). Processing took place in two main steps: (1) preprocessing via voxel-based morphometry and (2) application of cytoarchitectonic probabilities to processed gray matter density volumes. Voxel-based morphometry (57, 58) was applied to all images from the MIRIAD database using the CAT12 toolbox (http://www.neuro.uni-jena.de/cat/) within SPM12 (Wellcome Department of Imaging Neuroscience Group, London, UK; http://www.fil.ion.ucl.ac.uk/spm). The VBM analysis pipeline has been described at length previously (59, 60). Briefly, before processing, the origin of each image was manually reoriented to the anterior commissure in SPM12. Within the CAT12 toolbox, images were denoised according to spatial-adaptive Non-Local Means (SANLM) denoising (61) and Markov Random Field (62) approaches. Images were bias-corrected, spatially normalized to standard stereotactic space with an affine registration, and a local intensity transformation was performed. Normalized images were segmented into gray matter, white matter, and cerebrospinal fluid according to the Adaptive Maximum A Posterior (AMAP) technique (62). Lorio et al.'s (63) tissue priors were used for spatial normalization, skull-stripping, and initial segmentation estimate within the AMAP segmentation. Partial Volume Estimation (64) estimated partial volume fractions to account for voxels which may contain more than one tissue type. The Diffeomorphic Anatomic Registration Through Exponentiated Lie [DARTEL; (65)] algorithm as well as Geodesic Shooting (66) were used to register segmented images into standard MNI space. Finally, segmented images were modulated by the amount of volume changes from the spatial registration to preserve the total amount of gray matter.

Regions of Interest

Region specific GMD was measured according to cytoarchitectonic probabilistic maps for the reference MNI single subject brain that were derived from 3D reconstruction of histological sections from post mortem brains. Regional GMD was calculated using a custom MATLAB script, which multiplied the GMD value for each voxel by the weighting contained within the probabilistic map. Weighted GMD values were summed

bilaterally, and then standardized by dividing each image by the sum of the weighting contained within each probabilistic mask. All probabilistic tissue maps were obtained from the Anatomy Toolbox, contained within SPM12, and moved from the anatomical space of the single subject MNI template into standard MNI template space by an affine translation along the y and z axes of 4 and 5 mm (67).

From the Anatomy Toolbox Version 2.2b, 13 subcortical cytoarchitechtonically-defined regions of interest were selected: Ch4 of the basal forebrain [abbr: Ch4; (68)], Ch1-3 of the basal forebrain [abbr: Ch1-3; (68)], centromedial amygdala [abbr: CM; (69)], laterobasal amygdala [abbr: LB; (69)] superficial amygdala [abbr: SF; (69)], hippocampal-amygdala transition area [abbr: HATA; (69)], amygdala-striatal transition area [abbr: ASTR; (69)], entorhinal cortex [abbr: EC; (69)], CA1 of the hippocampus [abbr: CA1, (69)], CA2 of the hippocampus [abbr: CA2; (69)], CA3 of the hippocampus [abbr: CA3; (69)], subiculum [abbr: SUBC; (69)], and dentate gyrus [abbr: DG; (69)]. The Anatomy Toolbox contains a list of more than 50 possible cytoarchitectonically-defined neocortical regions to consider. To survey a similar number of cortical regions while limiting the number of statistical comparisons, we chose a group of 14 neocortical regions: primary motor cortex area 4a [abbr: PMC 4a; (70)], primary motor cortex area 4p [abbr: PMC 4p; (70)], primary auditory cortex are TE 1.0 [abbr: TE 1.0; (71)], primary auditory cortex are TE 1.1 [abbr: TE 1.1; (71)], primary auditory cortex are TE 1.2 [abbr: TE 1.2; (71)], secondary auditory cortex are TE 3 [abbr: TE 3; (71)], primary somatosensory cortex area 1 [abbr: PSC 1; (72)], primary somatosensory cortex area 2 [abbr: PSC 2; (72)], primary somatosensory cortex area 3a [abbr: PSC 3a; (72)], primary somatosensory cortex area 3b [abbr: PSC 3b; (72)], Broca's area 44 [abbr: BA 44; (73)], Broca's area 45 [abbr: BA 45; (73)], occipital cortex area V1 [abbr: V1; (74)], and occipital cortex area V2 [abbr: V2; (74)]. **Table 1** lists each of the brain regions measured in this study and the reference for how that region was defined.

TABLE 1 | Complete list of brain regions included for analysis.

Region of interest	References
Ch4 Basal Forebrain	(68)
Ch 1-3 Basal Forebrain	(68)
Centromedial Amygdala	(69)
Laterobasal Amygdala	(69)
Superficial Amygdala	(69)
Amygdala-Striatal Transition Area	(69)
Hippocampal-Amygdala Transition Area	(69)
Entorhinal Cortex	(69)
CA1 Hippocampus	(69)
CA2 Hippocampus	(69)
CA3 Hippocampus	(69)
Subiculum	(69)
Dentate Gyrus	(69)
4a Primary Motor Cortex	(70)
4p Primary Motor Cortex	(70)
TE 1.0 Primary Auditory Cortex	(71)
TE 1.1 Primary Auditory Cortex	(71)
TE 1.2 Primary Auditory Cortex	(71)
TE3 Secondary Auditory Cortex	(75)
1 Primary Somatosensory Cortex	(72)
2 Primary Somatosensory Cortex	(72)
3a Primary Somatosensory Cortex	(72)
3b Primary Somatosensory Cortex	(72)
V1 Occipital Cortex	(74)
V2 Occipital Cortex	(74)
44 Broca's Area	(73)
45 Broca's Area	(73)

Statistical Methods

Participant Characteristics

For the early PD, advanced PD, and healthy control groups, sex distributions were summarized as frequencies and percentages and ages were summarized as mean, standard deviation (SD), and range of the empirical distribution. Sex frequencies were compared using Fisher's exact-test and ages were compared using the two-sample *Student's* t-test.

Gray Matter Density and Age Associations

Among all Parkinson's disease cases, ordinary least-squares (OLS) linear regression was utilized to examine, for each test-region of the brain, the association between GMD and chronological age. With regard to the OLS linear regression model specification, GMD functioned as the dependent variable and chronological age (yrs.) functioned as the independent variable. The focus of hypothesis testing was on testing if the OLS linear regression slope parameter is equal to zero with the restriction that the hypothesis testing procedure is carried out in a way in which among all 27 test-regions of the brain, no more than 5% of rejected null hypotheses will be in error. With this focus in mind, for each of the 27 test-regions of the brain, a *p*-value was calculated based on the regression slope coefficient F-statistic and the corresponding F-distribution of the F-statistic that reflected the chance of observing a F-statistic as large or larger when the null hypothesis is true: i.e., the underlying slope of the relationship between GMD and chronological age is equal to 0. The complete set of 27 *p*-values were sorted in ascending order and compared to the corresponding Benjamini & Hochberg (BH) false positive discovery error rate rejection threshold (76), which was computed under the restriction that among all null hypotheses rejected, no more than 5% of the rejected null hypotheses will be in error. For test-regions of the brain in which the *p*-value was less than the BH false positive discovery error rate threshold, the null hypothesis that the true value of the regression slope parameter is equal to zero was rejected.

Between-Group Differences in Gray Matter Density

Per test-region of the brain, the distributions of GMD were compared between the early PD patients, advanced PD patients, and healthy controls by way of analysis of covariance (ANCOVA). Three sets of ANCOVAs were conducted. One set

of ANCOVAs was focused on comparing the GMD of the early PD patients and the advanced PD patients, while a second set of ANCOVAs was focused on comparing the GMD of the advanced PD patients and the healthy controls, and the third set of ANCOVAs was focused on comparing the GMD of early PD patients and healthy controls. All three sets of ANCOVAs were conducted using the same model specification. The dependent variable was the test-region $\log_e$(GMD) and the independent factor of interest was a categorical variable that distinguished the members of one study-group (e.g., advanced PD patients) from members of the other study-group (e.g., early PD patients). Chronological age and sex served as covariate adjustments in the ANCOVA model. Variables which were completely confounded between the early PD and advanced PD groups (e.g., medication status) were not included in the model. Per ANCOVA, a chronological age and sex adjusted linear contrast of least-squared means was used to test the null hypothesis that the covariate adjusted mean $\log_e$(GMD) is the same irrespective of the study-group. Since each set of between-group comparisons required testing a total of 27 null hypotheses (i.e., one per test-region of the brain), the BH false discovery error rate control procedure (see above) was used so that no more than 5% of rejected null hypotheses will be in error.

Gray Matter Density Disease Duration Association

Among all PD cases, OLS linear regression was utilized to examine, for each test-region of the brain, the association between GMD and disease duration (yrs.). The analytical methods and hypothesis testing strategy that were used to examine the associations between GMD and disease duration were identical to the analytical methods and hypothesis testing strategy that were used to examine the associations between GMD and chronological age.

Differences in GMD Slope Directionality

For each test-region of the brain, the distributions of OLS linear regression slope directionality were compared between cortical and subcortical brain regions (as delineated in the experimental methods) separately for early PD and advanced PD patients by Fischer's exact test. Slope directionality was based on sign of expression and not dependent on the statistical significance.

RESULTS

GMD measurements from, 228 early PD, 136 advanced PD, and 103 control subjects were included for analysis in this study (**Table 2**). With respect to sex distribution, males represented the majority of the subjects of each group. 61.8% of the early PD were male, 74.3% of the advanced PD were male, and 65.0% of the healthy controls were male, with males more highly represented in the advanced PD group than in the early PD group ($p = 0.016$). The advanced PD group was older (mean = 63.5 yrs., SD = 8.7 yrs., range = [38.8, 91.1 yrs.]) than the healthy control group (mean = 60.2 yrs., SD = 11.2 yrs., range = [31.1, 82.1 yrs.]) ($p = 0.01$), and trended older than the early PD group (mean = 61.9 yrs., SD = 9.5 yrs., range = [33.7, 82.9 yrs.]) ($p = 0.10$). The advanced PD group had longer disease duration (mean = 8.0 yrs., SD = 4.8 yrs., range = [<0.5, 27.6 yrs.]) than the early PD group (mean = 0.6 yrs., SD = 0.6 yrs., range=[<0.5, 3.0 yrs]) ($p < 0.001$). The advanced PD group had higher mean UPDRS III score (mean = 35.1, SD = 11.2 yrs, range = [9, 64]) than the early PD group (mean = 20.7, SD = 8.7, range = [4, 47]) ($p < 0.001$). The advanced PD group had lower mean Montreal Cognitive Assessment (MoCA) score (mean = 24.9, SD = 11.2, range = [11, 30]) than the early PD group (mean = 27.1, SD = 2.4, range = [17, 30]) or the healthy control group (mean = 28.3, SD = 1.2, range = [26. 30]) ($p < 0.001$).

TABLE 2 | Descriptive statistics for subjects included in the present study.

	Early PD	Advanced PD	Controls
Demographics			
n	228	136	103
Female	87	35	36
Male	141	101	67
Age at MRI (years)	61.9 ± 9.5	63.5 ± 8.7	60.2 ± 11.2
Disease duration (years)	0.6 ± 0.6	8.0 ± 4.8	0
UPDRS III total	20.7 ± 8.7	35.1 ± 11.2	0.7 ± 1.3
MoCA	27.1 ± 2.4	24.9 ± 11.2	28.3 ± 1.2

Gray Matter Density and Age Associations

Among PD patients as a whole (i.e., non-differentiated by disease stage), GMD was negatively associated with age for 22 of the 27 test-regions of interest (**Supplementary Table 1**). Regions in which GMD was not associated with age were primarily located in the hippocampus (CA2, HATA, subiculum, entorhinal cortex). Additionally, laterobasal amygdala GMD was not associated with age.

Between-Group Differences in GM Density

For subcortical regions, Ch4 GMD was 4.0% less (95% CI: [1.8, 6.1%]) for the advanced PD patients when compared to early PD patients ($p < 0.001$) and 4.3% less (95% CI: [2.0, 6.5%]) when compared to healthy controls ($p < 0.001$); while Ch4 GMD was comparable for the early PD patients and the healthy controls. Ch123 GMD was 3.7% less (95% CI: [1.4, 6.0%]) for advanced PD patients when compared to early PD patients ($p = 0.002$), but was comparable to the GM of the healthy controls. Early PD patients and healthy controls also had comparable Ch123 GMD (**Figure 1**, **Supplementary Tables 2–4**).

Centromedial-amygdala GMD was 15.9% less (95% CI: [13.1, 18.6%]) for the advanced PD patients when compared to the early PD patients ($p < 0.001$) and 16.5% less (95% CI: [12.3, 20.5%] when compared to the healthy controls ($p < 0.001$), while centromedial-amygdala GMD was not significantly different between the early PD patients and the healthy controls. Superficial-amygdala GMD was 19.5% less (95% CI: [14.5, 24.2%]) for the advanced PD patients when compared to early PD patients ($p < 0.001$), and 20.0% less (95% CI: [14.9, 24.7%]) when compared to the heathy controls ($p < 0.001$); while superficial-amygdala GMD was comparable for the early PD patients and healthy controls. Laterobasal-amygdala GMD was 12.6% less

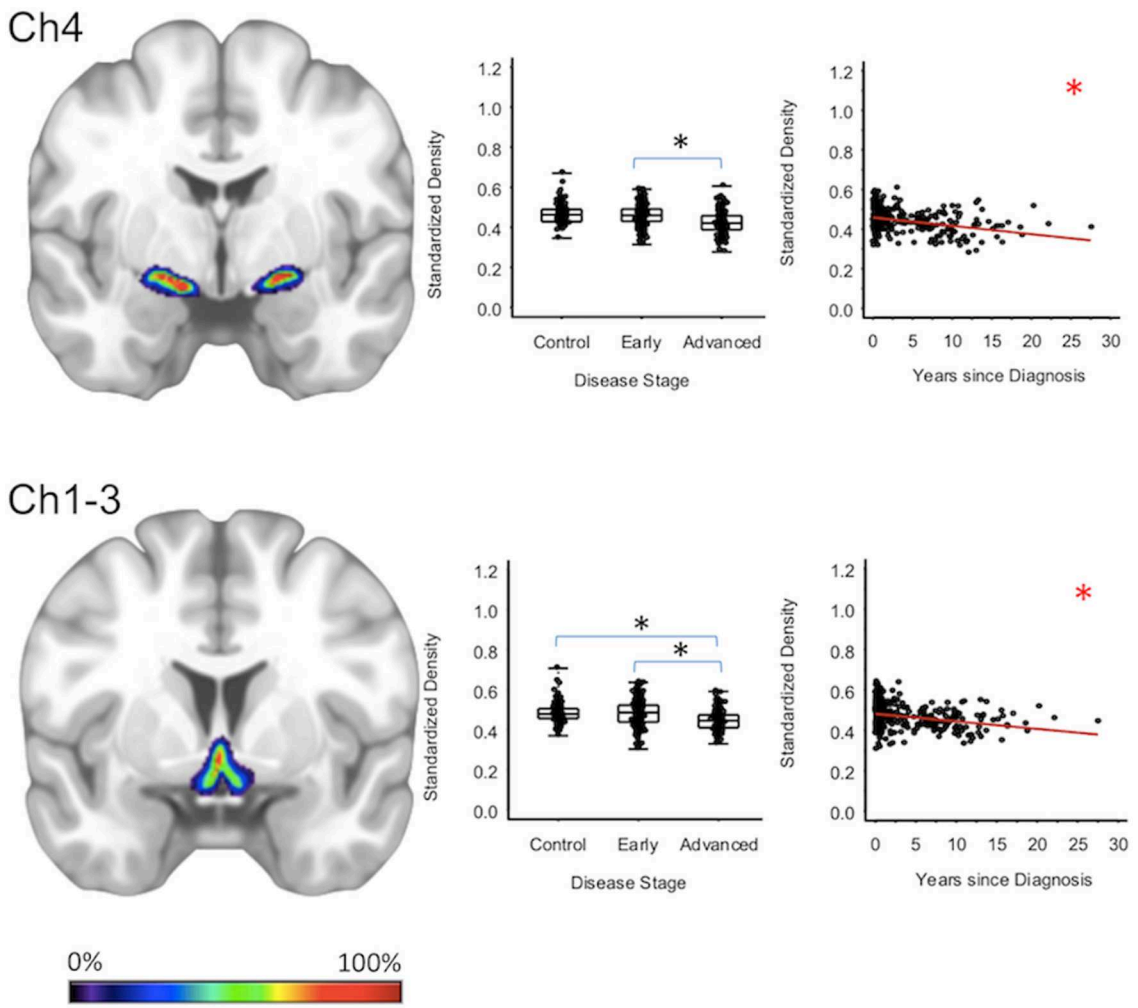


FIGURE 1 | Cholinergic Basal Forebrain Regions. Group level gray matter density differences and relationship between disease duration and gray matter density. (Ch4) Ch4 nucleus of the basal forebrain. (Ch1-3) Ch1-3 nuclei of the basal forebrain. Color legend indicates probabilities contained within the mask from 0% (blue) to 100% (red). *Significant at $p < 0.05$, FDR corrected for multiple comparisons.

(95% CI: [9.1, 16.0%]) for the advanced PD patients when compared to the early PD patients ($p < 0.001$) and 13.2% less (95% CI: [9.3, 16.9%] when compared to healthy controls ($p < 0.001$); while laterobasal-amygdala GMD was comparable for the early PD patients and healthy controls. GMD of the amygdala-striatal transition area of the advanced PD patients was 6.4% less (95% CI: [3.5, 9.3%]) than the GMD of the early PD patients ($p < 0.001$) and 6.2% less (95% CI: [3.1, 9.2%]) than the GMD of healthy controls ($p < 0.001$); while amygdala-striatal transition area GMD was comparable for the early PD patients and healthy controls. HATA GMD was 7.0% less (95% CI: [3.0, 10.8%]) for the advanced PD patients when compared to the early PD patients ($p < 0.001$), and 6.9% less (95% CI: [0.80, 12.7%]) when compared to the healthy controls—which after false positive discovery adjustment was not deemed significant—while HATA GMD was comparable for the early PD patients and the healthy controls (**Figure 2**, **Supplementary Tables 2–4**).

Entorhinal cortex GMD was 10.1% less (95% CI: [6.0, 14.0%]) for the advanced PD patients when compared to the early PD patients ($p < 0.001$), and 10.2% less (95% CI: [5.9, 14.4%]) when compared to the healthy controls ($p < 0.001$); while entorhinal cortex GMD was comparable for the early PD patients and healthy controls. GMD of the CA3 of the hippocampus of advanced PD patients was 4.3% less (95% CI: [0.70, 7.7%]) than the GMD of the early PD patients ($p = 0.018$). The GMD of the CA3 of the hippocampus was comparable for the advanced PD patients and the healthy controls and comparable for the early PD patients and healthy controls (**Figure 3**, **Supplementary Tables 2–4**).

For cortical regions, the secondary auditory area TE3 GMD was 3.5% less (95% CI: [1.8, 5.3%]) for the advanced PD patients when compared to the early PD patients ($p < 0.001$), and 3.2% less (95% CI: [1.4, 4.9%]) when compared to the healthy controls ($p = 0.001$). The secondary auditory area TE3 GMD was

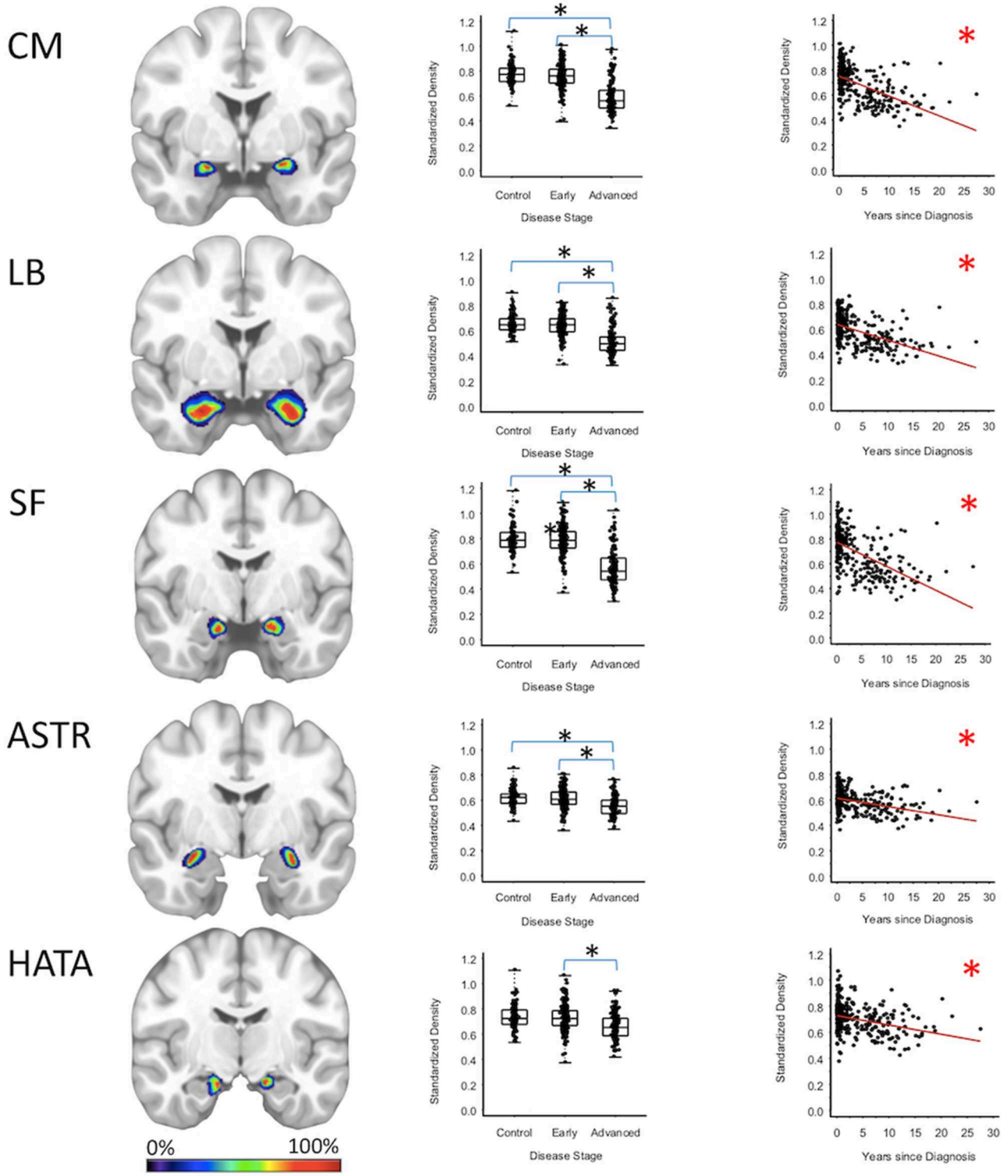


FIGURE 2 | Amygdala Regions. Group level gray matter density differences and relationship between disease duration and gray matter density. (CM) Centromedial amygdala, (LB) Laterobasal amygdala, (SF) Superficial amygdala, (ASTR) Amygdala-Striatal Transition Area, (HATA) Hippocampal-Amygdala Transition Area. Color legend indicates probabilities contained within the mask from 0% (blue) to 100% (red). *Significant at $p < 0.05$, FDR corrected for multiple comparisons.

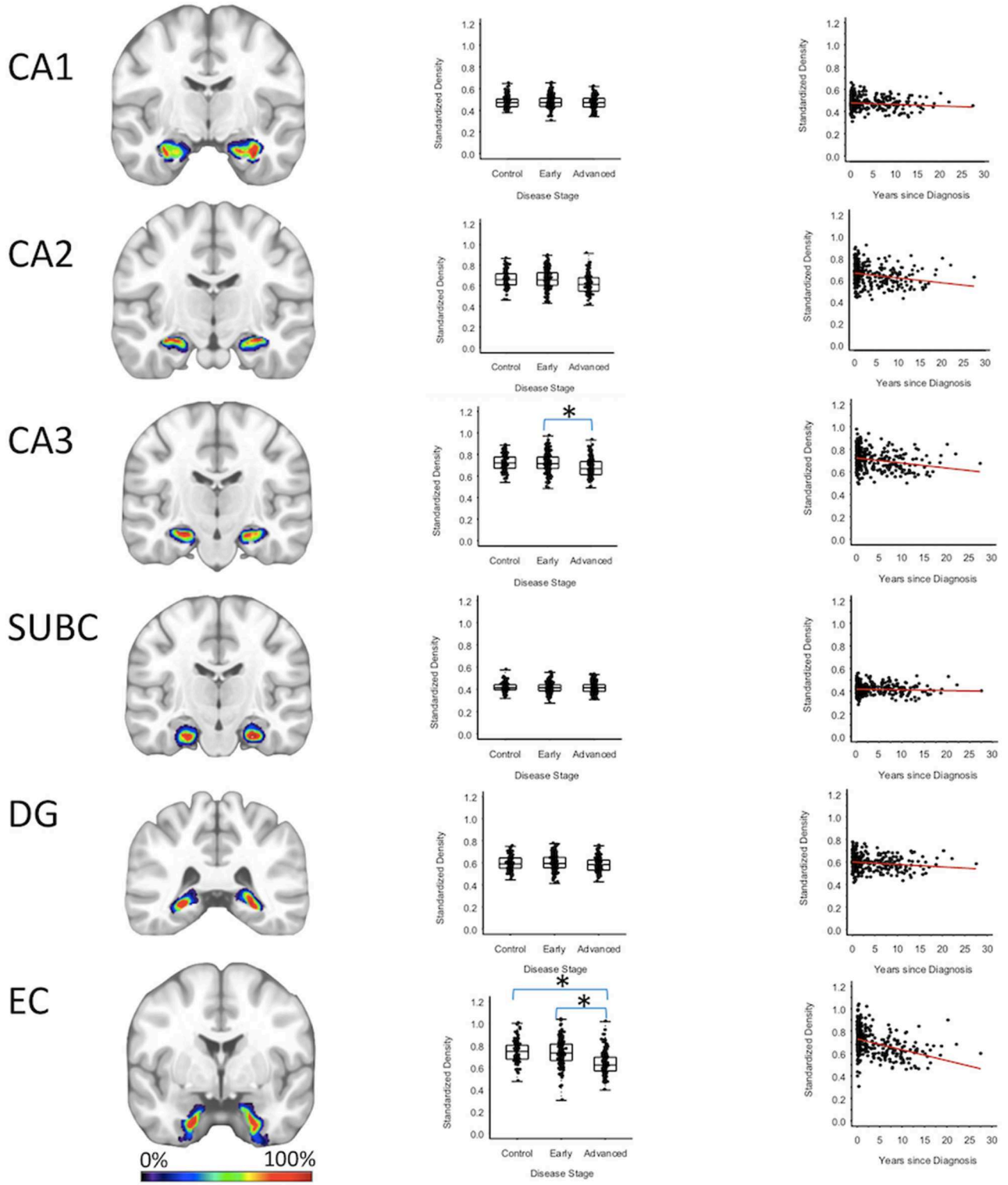


FIGURE 3 | Hippocampus Regions. Group level gray matter density differences and relationship between disease duration and gray matter density. (CA1) CA1 of hippocampus, (CA2) CA2 of hippocampus, (CA3) CA3 of hippocampus, (SUBC) Subiculum, (DG) Dentate Gyrus, (EC) Entorhinal Cortex. Color legend indicates probabilities contained within the mask from 0% (blue) to 100% (red). *Significant at $p < 0.05$, FDR corrected for multiple comparisons.

comparable between early PD patients and the healthy controls. Between-group comparisons of the GMDs of remaining stage six regions (i.e., the primary motor cortex, primary somatosensory cortex, occipital cortex, primary auditory cortex, and Broca's area) showed the GMD of the early PD, advanced PD, and healthy control groups to be not significantly different after false positive discovery adjustment (**Figure 4**, **Supplementary Figures 1**, **2**, **Supplementary Tables 2**–**4**).

Gray Matter Density and Disease Duration Associations

To confirm that group level differences in regional GMD were related to disease duration, a set of regression analyses that examined the relationship between GMD and disease duration controlling for chronological age and sex was performed. The individual regression analyses were conducted using the data of both early and advanced PD patients to increase the range of disease duration present in the sample. For subcortical regions, Ch4 GMD declined with disease duration (slope = −0.010 units/yr; 95% CI: [−0.015,−0.005], $p < 0.001$) and Ch123 GMD declined with disease duration (slope = −0.008 units/yr; 95% CI: [−0.013,−0.002], $p = 0.009$) (**Figure 1**, **Supplementary Table 5**). The centromedial amygdala GMD declined with disease duration (slope = −0.025 units/yr; 95% CI: [−0.033,−0.017], $p < 0.001$), superficial amygdala GMD declined with disease duration (slope = −0.031 units/yr; 95% CI: [−0.040,−0.021], $p < 0.001$), laterobasal amygdala GMD declined with disease duration (slope = −0.023 units/yr; 95% CI: [−0.040,−0.005], $p = 0.013$), amygdala-striatal transition area GMD declined with disease duration (slope = −0.012 units/yr; 95% CI: [−0.017,−0.006], $p < 0.001$), and HATA GMD declined with disease duration (slope = −0.011 units/yr; 95% CI: [−0.017,−0.004], $p = 0.001$) (**Figure 2**). Entorhinal cortex GMD declined with disease duration (slope = −0.014 units/yr; 95% CI: [−0.022,−0.007], $p < 0.001$) (**Figure 3**). For cortical regions, only the GMD of the secondary auditory association area TE3 declined with disease duration (slope = −0.011 units/yr; 95% CI: [−0.017, −0.005], $p < 0.001$) (**Figure 4**, **Supplementary Table 5**).

Regional Differences in GMD Slope Directionality

To further test differences in disease progression between early and PD groups, a comparison of the directionality of the early and PD slope parameters for the age and sex adjusted relationships between duration of disease and GMD was performed. For subcortical regions in early PD, one region (7.7%) had a positive slope, compared to 12 regions (92.3%) which had a negative slope. For subcortical regions in advanced PD patients, all 13 regions (100%) had a negative slope. For cortical regions in early PD, 13 regions (92.9%) had a positive slope, compared to one region (7.1%) which had a negative slope. For cortical regions in advanced PD patients, all 14 regions (100%) had a negative slope. The difference in the distribution of positive and negative slopes for subcortical and cortical regions in early PD is significant ($p < 0.001$). Additionally, the difference in the distribution of positive and negative slopes for cortical regions between early PD and advanced PD is significant ($p < 0.001$).

DISCUSSION

Loss of gray matter in Parkinson's disease is pathological, and additive to the normal aging process (45, 77, 78). This study found pathological gray matter degeneration in subcortical regions of the cholinergic basal forebrain and amygdala, but found general sparing of hippocampal and neo-cortical regions in a population of advanced Parkinson's disease patients. These findings suggest a pattern that could be described roughly as "ascending" when comparing groups differentiated by disease duration.

MRI study of Parkinson's disease is extensive, but results have not demonstrated a consistent pattern of disease related atrophy (33). Previous studies have identified gray matter atrophy in early non-demented Parkinson's disease subjects (79, 80), while others have found no differences when compared to healthy controls (81–83). In advanced Parkinson's disease subjects, studies have found gray matter atrophy in the hippocampus (44, 52), amygdala (44, 84), and caudate (85). The advanced Parkinson's disease group evaluated in this study showed extensive degeneration of the basal forebrain and amygdala when compared to healthy control and early Parkinson's disease groups, but showed limited degeneration in the hippocampus and neocortex. When compared to previous neuroimaging studies, results from this study place the advanced Parkinson's disease group at the threshold of advanced disease, where degeneration in meso- or neo-cortical areas has either not occurred, or not yet resulted in measurable loss of GMD.

This study did not identify regional differences in GMD between early Parkinson's disease and healthy control groups. These findings fit within a literature that has failed to consistently detect atrophy in MRI studies of early Parkinson's disease (86, 87). A notable exception to past negative findings are deformation based morphometry studies of PPMI Parkinson's disease subjects at baseline which identified atrophy in subcortical regions such as the basal ganglia, basal forebrain, and hippocampus and predicted pathological spread of PD to subcortical regions ahead of cortical regions (23, 25). However, Zeighami et al. also identified extensive cortical atrophy, a finding not expected from a sample acquired at baseline of motor diagnosis by PPMI (23). To address the discrepancy between these studies, we compared the directionality of the early and advanced Parkinson's disease slope parameters for relationships between disease duration and regional GMD. For early Parkinson's disease subjects, 92.3% of subcortical regions displayed the expected negative slope, compared to only 7.1% of cortical regions. For advanced Parkinson's disease patients, 100% of cortical and subcortical regions displayed a negative slope. This ascending pattern of isolated subcortical atrophy in early PD patients which did not reach the level of traditional statistical significance may result from the nature of gray matter density as a downstream proxy for potential mechanisms of neurodegeneration in Parkinson's disease. Perhaps a lag

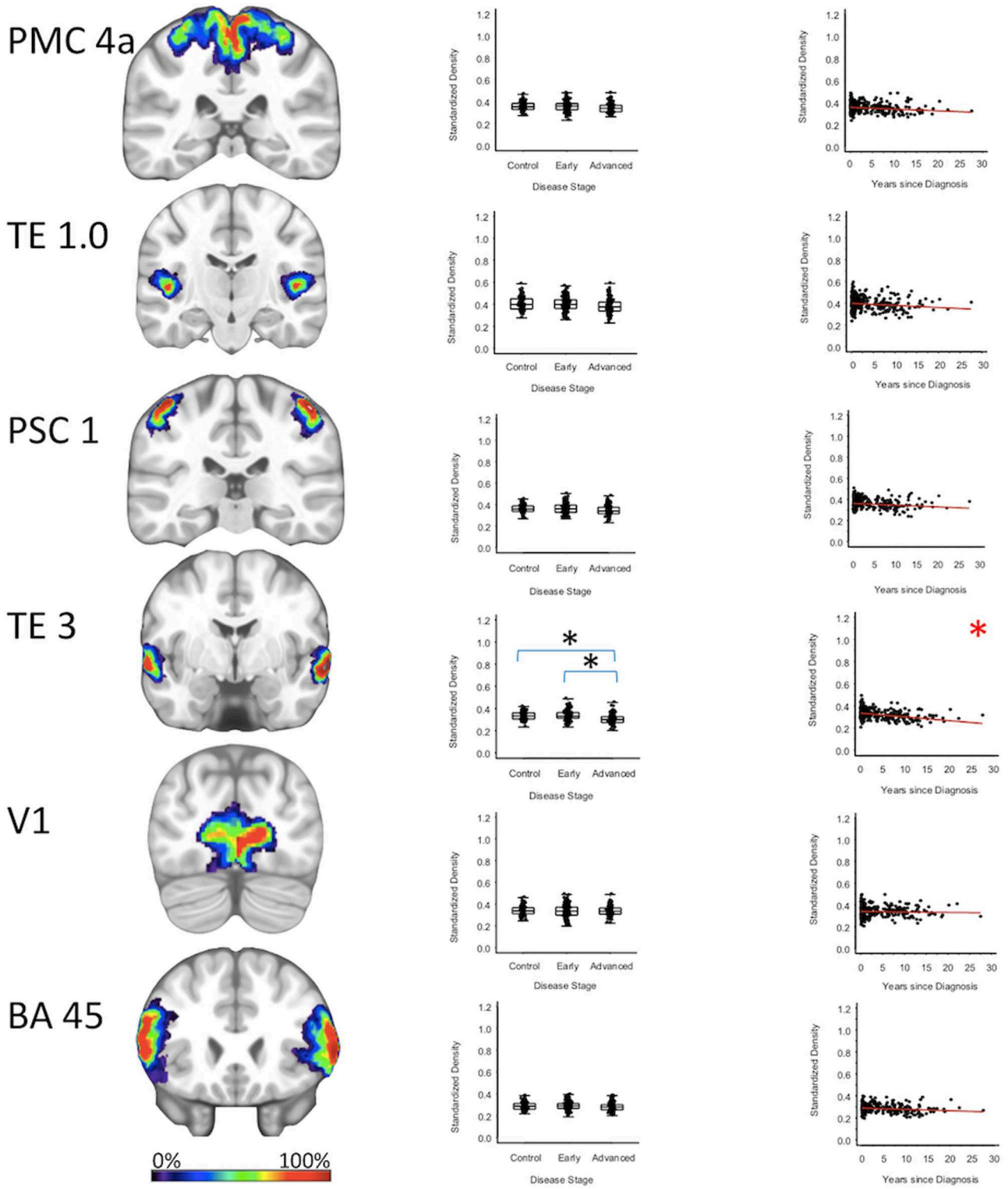


FIGURE 4 | Neocortical Regions. Group level gray matter density differences and relationship between disease duration and gray matter density. (PMC4a) Primary motor cortex area 4a (TE1.0) Primary auditory area TE1.0 (PSC1) Primary somatosensory cortex area 1 (TE3) Secondary auditory area (TE3 V1) Area V1 of the occipital cortex (BA45) Broca's area defined by Brodmann area 45. Color legend indicates probabilities contained within the mask from 0% (blue) to 100% (red). *Significant at $p < 0.05$, FDR corrected for multiple comparisons.

exists between still unknown neurodegenerative mechanisms and ability to detect loss of gray matter density via VBM. MRI methods capable of measuring tissue microstructure (e.g., diffusion MRI) or physiology (e.g., functional MRI) may be better equipped to detect differences which precede those detectable by VBM.

A novel finding of this study is the consistency with which each region of the amygdala was shown to have degenerated in the advanced Parkinson's disease group. The amygdala, which is extensively connected to the cortex, diencephalon, basal ganglia, and olfactory bulb is associated with a number of functions in humans including learning and memory, emotion regulation, and motivation (69, 88). Degeneration of the amygdala in Parkinson's disease and other neurodegenerative diseases such as AD and dementia with Lewy bodies may result in common behavioral and cognitive deficits (88). Specifically in Parkinson's disease, the amygdala is known to undergo severe pathological change over time (89). Pathological study of the amygdala in advanced Parkinson's disease subjects has identified a selective pattern of degeneration localized to the corticomedial and basolateral formation and an association between pathological load in the laterobasal amygdala and visual hallucinations (49). MRI studies of the amygdala in Parkinson's disease have contributed mixed findings to date; reporting no difference between Parkinson's disease and control subjects (90) or slightly reduced volume of the right amygdala in Parkinson's disease relative to healthy controls (91, 92). The current study reports significant atrophy in advanced Parkinson's disease relative to early Parkinson's disease and healthy control subjects, a finding which has not previously been reported using MRI methodology. Evidence from the current study most strongly supports prior histological evaluation that showed significant regional amygdala pathology (49), perhaps due to our use of histologically defined brain maps.

Prior MRI studies of Parkinson's disease, which have not consistently identified the amygdala as an area of degeneration in Parkinson's disease, differ from the current study through application of deterministic mapping, which allows each voxel in a brain region to contribute equally to an output measure (93, 94). This study utilized probabilistic mapping, which allows voxels to differentially contribute to an output measure and account for the likelihood that they accurately reflect anatomical boundaries in an individual (69, 95). The use of histologically defined probabilistic maps is particularly indicated in the case of brain regions, such as the amygdala, which can only be properly delineated by cytoarchitecture, and may have poor or limited contrast in structural MRI (69). The consistent degeneration identified in the amygdala in this study possibly reflects this methodological difference with prior studies. These findings implicate the amygdala as an area of future MRI investigation in Parkinson's disease.

Voxel based morphometry is sensitive to effects of age (96), which manifest as wide-ranging reductions in cortical and subcortical gray matter over time (97, 98). This study attempted to control for these effects by selecting cohorts with similar mean age, but which differed by PD disease duration. Though considered a strength of this study, this design choice may limit our ability to make inferences about the "typical" pattern of atrophy in advanced PD. Recent study of outcomes in PD identified age at PD diagnosis as a strong predictor of progression to disease milestones and death (99). Older age at PD onset is associated with more severe motor and non-motor phenotypes and greater dopaminergic impairment (100). Because the advanced PD group in this study was diagnosed on average 5.8 years earlier than the early PD group, it is possible that they belong to a PD subtype which progressed to reductions in subcortical GMD at a different rate than the early PD group, and that these groups may have different relationships between GMD and duration of disease.

The major limitation of this study design stems from retrospective collection of data in the advanced Parkinson's disease group. The acquisition of the neuroimaging and neuropsychological data from the advanced PD patients took place as part of routine clinical care, and not as part of a standardized protocol. As a result, MRI images from advanced PD patients had more variable acquisition parameters and were acquired on multiple different Siemens MRI scanners. Conversely, PPMI images were acquired with relatively standardized acquisition parameters on fewer MRI scanners from different vendors. Unfortunately, there are no consensus methods for retrospective data harmonization of brain MRI structural data, a problem that was noted in a recent survey of the neuroimaging community (101, 102). Due to a noted vulnerability of datasets to cross-vendor harmonization issues (101, 102), we also chose to exclude all PPMI data not acquired Siemens scanners with an MP-RAGE protocol. Several elements of our data processing methods attempted to improve consistency between the groups (e.g., inspection for missing data, a robust, automated quality control protocol, consistent application of image registration techniques, and normalization steps intrinsic to the VBM method). Despite these steps, the possibility of confounds related to difference in MRI must be acknowledged; however, two important control findings provide a measure of confidence in the major findings of this study. First, negative findings between the advanced Parkinson's disease group and both PPMI groups for the majority of hippocampal and neocortical regions suggest that any potential confounds attributable to differences in MRI acquisition would need to be confined to specific *subcortical* regions. Second, the analysis examining early vs. advanced differences in regional slope directionality related to duration of Parkinson's disease showed change of slope direction in nearly all of the cortical regions; here, any potential confounds would need to be confined to a different set of *neocortical* regions. So, while it is possible that MRI acquisition differences alone could account for the specific, ascending pattern of regional atrophy identified in this study, such a finding would be highly improbable.

The current study provided *in-vivo* human evidence suggesting a pattern of neurodegeneration in Parkinson's disease in subcortical regions ahead of cortical regions. Widespread subcortical degeneration in the basal forebrain and amygdala of the advanced Parkinson's disease group compared to early Parkinson's disease or healthy controls suggests an organized degenerative process which effects subcortical structures in

advance of cortical structures. Ongoing research efforts will utilize new MRI techniques and longitudinal data to further evaluate the progression of pathology during the course of Parkinson's disease.

DATA AVAILABILITY STATEMENT

All code used in calculation of GMD is available at https://github.com/DruzgalLabUVA/Ascending_Spread_MRI. MRI images and demographic information from PPMI are available to qualifying researchers following an application process. Collection of the advanced Parkinson's disease data was retrospective and release of individual MRI and demographic data is precluded by HIPAA.

ETHICS STATEMENT

The University of Virginia Institutional Review Board for Health Sciences Research approved this study.

AUTHOR CONTRIBUTIONS

JB, MB, SS, WE, and TD contributed to study concept and design. JB, JF, and MB contributed to acquisition of data. JP conducted statistical analysis. JB, MB, JP, and TD contributed to analysis and interpretation of data. JB, JP, and TD drafted the manuscript. MB, JF, SS, and WE contributed to critical revision of manuscript for intellectual content.

ACKNOWLEDGMENTS

Data used in the preparation of this article were obtained from the Parkinson's Progression Markers Initiative (PPMI) database (www.ppmi-info.org/data). For up-to-date information on the study, visit www.ppmi-info.org. PPMI, a public-private partnership, was funded by the Michael J. Fox Foundation (MJFF) for Parkinson's Research and funding partners, including Abbvie, Avid Radiopharmaceuticals, Biogen, Britsol-Myers Squibb, Covance, GE Healthcare, Genetech, GlaxoSmithKline, Lilly, Lundbeck, Merck, Meso Scale Discovery, Pfizer, Piramal, Roche, Servier, and UCB. Neither the funding agency nor any of the sponsors of the PPMI were involved in the design and conduct of the study; collection, management, analysis, and interpretation of the data; preparation, review, or approval of the manuscript; and decision to submit the manuscript for publication.

The authors wish to acknowledge the following sources of support: JB: grant from Department of Defense and Commonwealth of Virginia's Alzheimer's and Related Diseases Research Award Fund; fellowship from University of Virginia. MB: grant from Department of Defense, Commonwealth of Virginia's Alzheimer's and Related Diseases Research Award Fund, and NIH; site PI for clinical trials funded by NIH, Azevan, Eisai, Biogen, Axovant, and Merck. JP: grant from Commonwealth of Virginia's Alzheimer's and Related Diseases Research Award Fund and University of Virginia. JF: grant from Department of Defense and Commonwealth of Virginia's Alzheimer's and Related Diseases Research Award Fund; salary support from Acadia Pharmaceuticals. SS: grant from Department of Defense and Commonwealth of Virginia's Alzheimer's and Related Diseases Research Award Fund. WE: grant from Insightec, Commonwealth of Virginia, and University of Virginia. JD: grant from Department of Defense, Commonwealth of Virginia's Alzheimer's and Related Diseases Research Award Fund, and University of Virginia.

SUPPLEMENTARY MATERIAL

The Supplementary Material for this article can be found online at: https://www.frontiersin.org/articles/10.3389/fneur.2019.01329/full#supplementary-material

REFERENCES

1. Chartier S, Duyckaerts C. Is Lewy pathology in the human nervous system chiefly an indicator of neuronal protection or of toxicity? *Cell Tissue Res.* (2018) 373:149–60. doi: 10.1007/s00441-018-2854-6
2. Recasens A, Ulusoy A, Kahle PJ, Di Monte DA, Dehay B. *In vivo* models of alpha-synuclein transmission and propagation. *Cell Tissue Res.* (2018) 373:183–93. doi: 10.1007/s00441-017-2730-9
3. Kalia LV, Lang AE. Parkinson's disease. *Lancet.* (2015) 386:896–912. doi: 10.1016/S0140-6736(14)61393-3
4. Braak H, Del Tredici K, Rüb U, de Vos RAI, Jansen Steur EN, Braak E. Staging of brain pathology related to sporadic Parkinson's disease. *Neurobiol Aging.* (2003) 24:197–211. doi: 10.1016/S0197-4580(02)00065-9
5. Brundin P, Melki R. Prying into the Prion Hypothesis for Parkinson's Disease. *J Neurosci.* (2017) 37:9808–18. doi: 10.1523/JNEUROSCI.1788-16.2017
6. Visanji NP, Brooks PL, Hazrati L-N, Lang AE. The prion hypothesis in Parkinson's disease: Braak to the future. *Acta Neuropathol Commun.* (2013) 1:2. doi: 10.1186/2051-5960-1-2
7. Engelender S, Isacson O. The threshold theory for Parkinson's Disease. *Trends Neurosci.* (2017) 40:4–14. doi: 10.1016/j.tins.2016.10.008
8. Kordower JH, Chu Y, Hauser RA, Freeman TB, Olanow CW. Lewy body-like pathology in long-term embryonic nigral transplants in Parkinson's disease. *Nat Med.* (2008) 14:504–06. doi: 10.1038/nm1747
9. Kordower JH, Chu Y, Hauser RA, Olanow CW, Freeman TB. Transplanted dopaminergic neurons develop PD pathologic changes: a second case report. *Mov Disord.* (2008) 23:2303–06. doi: 10.1002/mds.22369
10. Li J-Y, Englund E, Holton JL, Soulet D, Hagell P, Lees AJ, et al. Lewy bodies in grafted neurons in subjects with Parkinson's disease suggest host-to-graft disease propagation. *Nat Med.* (2008) 14:501–03. doi: 10.1038/nm1746
11. Brahic M, Bousset L, Bieri G, Melki R, Gitler AD. Axonal transport and secretion of fibrillar forms of α-synuclein, Aβ42 peptide and HTTExon 1. *Acta Neuropathol.* (2016) 131:539–48. doi: 10.1007/s00401-016-1538-0
12. Hansen C, Angot E, Bergström A-L, Steiner JA, Pieri L, Paul G, et al. α-Synuclein propagates from mouse brain to grafted dopaminergic neurons and seeds aggregation in cultured human cells. *J Clin Invest.* (2011) 121:715–25. doi: 10.1172/JCI43366
13. Desplats P, Lee H-J, Bae E-J, Patrick C, Rockenstein E, Crews L, et al. Inclusion formation and neuronal cell death through neuron-to-neuron transmission of alpha-synuclein. *Proc Natl Acad Sci USA.* (2009) 106:13010–15. doi: 10.1073/pnas.0903691106
14. Peelaerts W, Bousset L, Van der Perren A, Moskalyuk A, Pulizzi R, Giugliano M, et al. α-Synuclein strains cause distinct synucleinopathies

after local and systemic administration. *Nature*. (2015) 522:340–4. doi: 10.1038/nature14547
15. Recasens A, Dehay B, Bové J, Carballo-Carbajal I, Dovero S, Pérez-Villalba A, et al. Lewy body extracts from Parkinson disease brains trigger α-synuclein pathology and neurodegeneration in mice and monkeys: LB-induced pathology. *Ann Neurol.* (2014) 75:351–62. doi: 10.1002/ana.24066
16. Surmeier DJ, Obeso JA, Halliday GM. Selective neuronal vulnerability in Parkinson disease. *Nat Rev Neurosci.* (2017) 18:101–13. doi: 10.1038/nrn.2016.178
17. Giguère N, Burke Nanni S, Trudeau L-E. On cell loss and selective vulnerability of neuronal populations in Parkinson's disease. *Front Neurol.* (2018) 9:455. doi: 10.3389/fneur.2018.00455
18. Heim B, Krismer F, De Marzi R, Seppi K. Magnetic resonance imaging for the diagnosis of Parkinson's disease. *J Neural Transm.* (2017) 124:915–64. doi: 10.1007/s00702-017-1717-8
19. Broski SM, Hunt CH, Johnson GB, Morreale RF, Lowe VJ, Peller PJ. Structural and functional imaging in parkinsonian syndromes. *Radiographics.* (2014) 34:1273–92. doi: 10.1148/rg.345140009
20. Rizzo G, Zanigni S, De Blasi R, Grasso D, Martino D, Savica R, et al. Brain MR contribution to the differential diagnosis of parkinsonian syndromes: an update. *Parkinsons Dis.* (2016) 2016:2983638. doi: 10.1155/2016/2983638
21. Barrett MJ, Blair JC, Sperling SA, Smolkin ME, Druzgal TJ. Baseline symptoms and basal forebrain volume predict future psychosis in early Parkinson disease. *Neurology.* (2018) 90:e1618–26. doi: 10.1212/WNL.0000000000005421
22. Ray NJ, Bradburn S, Murgatroyd C, Toseeb U, Mir P, Kountouriotis GK, et al. *In vivo* cholinergic basal forebrain atrophy predicts cognitive decline in *de novo* Parkinson's disease. *Brain.* (2018) 141:165–76. doi: 10.1093/brain/awx310
23. Zeighami Y, Ulla M, Iturria-Medina Y, Dadar M, Zhang Y, Larcher KM-H, et al. Network structure of brain atrophy in *de novo* Parkinson's disease. *Elife.* (2015) 4:e08440. doi: 10.7554/eLife.08440
24. Ibarretxe-Bilbao N, Tolosa E, Junque C, Marti MJ. MRI and cognitive impairment in Parkinson's disease. *Mov Disord.* (2009) 24(Suppl. 2):S748–53. doi: 10.1002/mds.22670
25. Pandya S, Zeighami Y, Freeze B, Dadar M, Collins DL, Dagher A, et al. Predictive model of spread of Parkinson's pathology using network diffusion. *NeuroImage.* (2019) 192:178–94. doi: 10.1016/j.neuroimage.2019.03.001
26. Uribe C, Segura B, Baggio HC, Abos A, Garcia-Diaz AI, Campabadal A, et al. Cortical atrophy patterns in early Parkinson's disease patients using hierarchical cluster analysis. *Parkinsonism Relat Disord.* (2018) 50:3–9. doi: 10.1016/j.parkreldis.2018.02.006
27. de Schipper LJ, Hafkemeijer A, van der Grond J, Marinus J, Henselmans JML, van Hilten JJ. Altered whole-brain and network-based functional connectivity in parkinson's disease. *Front Neurol.* (2018) 9:419. doi: 10.3389/fneur.2018.00419
28. Baggio HC, Segura B, Junque C. Resting-state functional brain networks in Parkinson's disease CNS. *Neurosci Ther.* (2015) 21:793–801. doi: 10.1111/cns.12417
29. Göttlich M, Münte TF, Heldmann M, Kasten M, Hagenah J, Krämer UM. Altered resting state brain networks in Parkinson's disease. *PLoS ONE.* (2013) 8:e77336. doi: 10.1371/journal.pone.0077336
30. Ofori E, Pasternak O, Planetta PJ, Burciu R, Snyder A, Febo M, et al. Increased free water in the substantia nigra of Parkinson's disease: a single-site and multi-site study. *Neurobiol Aging.* (2015) 36:1097–104. doi: 10.1016/j.neurobiolaging.2014.10.029
31. Ofori E, Pasternak O, Planetta PJ, Li H, Burciu RG, Snyder AF, et al. Longitudinal changes in free-water within the substantia nigra of Parkinson's disease. *Brain.* (2015) 138:2322–31. doi: 10.1093/brain/awv136
32. Sterling NW, Lewis MM, Du G, Huang X. Structural Imaging and Parkinson's disease: moving toward quantitative markers of disease progression. *JPD.* (2016) 6:557–67. doi: 10.3233/JPD-160824
33. Duncan GW, Firbank MJ, OBrien JT, Burn DJ. Magnetic resonance imaging: a biomarker for cognitive impairment in Parkinson's disease? *Mov Disord.* (2013) 28:425–38. doi: 10.1002/mds.25352
34. De Micco R, Russo A, Tessitore A. Structural MRI in Idiopathic Parkinson's Disease. In: Politis M, editor. *International Review of Neurobiology*. New York, NY: Elsevier (2018). p. 405−38. doi: 10.1016/bs.irn.2018.08.011
35. Ziegler DA, Wonderlick JS, Ashourian P, Hansen LA, Young JC, Murphy AJ, et al. Substantia Nigra volume loss before basal forebrain degeneration in early Parkinson disease. *JAMA Neurol.* (2013) 70:241–7. doi: 10.1001/jamaneurol.2013.597
36. Reimão S, Pita Lobo P, Neutel D, Correia Guedes L, Coelho M, Rosa MM, et al. Substantia nigra neuromelanin magnetic resonance imaging in *de novo* Parkinson's disease patients. *Eur J Neurol.* (2015) 22:540–46. doi: 10.1111/ene.12613
37. Nakamura K, Sugaya K. Neuromelanin-sensitive magnetic resonance imaging: a promising technique for depicting tissue characteristics containing neuromelanin. *Neural Regen Res.* (2014) 9:759–60. doi: 10.4103/1673-5374.131583
38. Sclocco R, Beissner F, Bianciardi M, Polimeni JR, Napadow V. Challenges and opportunities for brainstem neuroimaging with ultrahigh field MRI. *Neuroimage.* (2018) 168:412–26. doi: 10.1016/j.neuroimage.2017.02.052
39. Ewers M, Teipel SJ, Dietrich O, Schönberg SO, Jessen F, Heun R, et al. Multicenter assessment of reliability of cranial MRI. *Neurobiol Aging.* (2006) 27:1051–59. doi: 10.1016/j.neurobiolaging.2005.05.032
40. Whitwell JL, Josephs KA, Murray ME, Kantarci K, Przybelski SA, Weigand SD, et al. MRI correlates of neurofibrillary tangle pathology at autopsy: a voxel-based morphometry study. *Neurology.* (2008) 71:743–49. doi: 10.1212/01.wnl.0000324924.91351.7d
41. Teipel SJ, Grothe M, Lista S, Toschi N, Garaci FG, Hampel H. Relevance of magnetic resonance imaging for early detection and diagnosis of Alzheimer disease. *Med Clin North Am.* (2013) 97:399–424. doi: 10.1016/j.mcna.2012.12.013
42. Ibarretxe-Bilbao N, Junque C, Segura B, Baggio HC, Marti MJ, Valldeoriola F, et al. Progression of cortical thinning in early Parkinson's disease. *Mov Disord.* (2012) 27:1746–53. doi: 10.1002/mds.25240
43. Noh SW, Han YH, Mun CW, Chung EJ, Kim EG, Ji KH, et al. Analysis among cognitive profiles and gray matter volume in newly diagnosed Parkinson's disease with mild cognitive impairment. *J Neurol Sci.* (2014) 347:210–13. doi: 10.1016/j.jns.2014.09.049
44. Ibarretxe-Bilbao N, Ramírez-Ruiz B, Tolosa E, Mart,í MJ, Valldeoriola F, Bargalló N, et al. Hippocampal head atrophy predominance in Parkinson's disease with hallucinations and with dementia. *J Neurol.* (2008) 255:1324–31. doi: 10.1007/s00415-008-0885-8
45. Fioravanti V, Benuzzi F, Codeluppi L, Contardi S, Cavallieri F, Nichelli P, et al. MRI correlates of parkinson's disease progression: a voxel based morphometry study. *Parkinson's Dis.* (2015) 2015:1–8. doi: 10.1155/2015/378032
46. Schulz J, Pagano G, Fernández Bonfante JA, Wilson H, Politis M. Nucleus basalis of Meynert degeneration precedes and predicts cognitive impairment in Parkinson's disease. *Brain.* (2018) 141:1501–516. doi: 10.1093/brain/awy072
47. Arendt T, Bigl V, Arendt A, Tennstedt A. Loss of neurons in the nucleus basalis of Meynert in Alzheimer's disease, paralysis agitans and Korsakoff's Disease. *Acta Neuropathol.* (1983) 61:101–8. doi: 10.1007/BF00697388
48. Candy JM, Perry RH, Perry EK, Irving D, Blessed G, Fairbairn AF, et al. Pathological changes in the nucleus of meynert in Alzheimer's and Parkinson's diseases. *J Neurol Sci.* (1983) 59:277–89. doi: 10.1016/0022-510X(83)90045-X
49. Harding AJ, Stimson E, Henderson JM, Halliday GM. Clinical correlates of selective pathology in the amygdala of patients with Parkinson's disease. *Brain.* (2002) 125:2431–45. doi: 10.1093/brain/awf251
50. Goldman JG, Stebbins GT, Bernard B, Stoub TR, Goetz CG, deToledo-Morrell L. Entorhinal cortex atrophy differentiates Parkinson's disease patients with and without dementia. *Mov Disord.* (2012) 27:727–34. doi: 10.1002/mds.24938
51. Joelving FC, Billeskov R, Christensen JR, West M, Pakkenberg B. Hippocampal neuron and glial cell numbers in Parkinson's disease–a stereological study. *Hippocampus.* (2006) 16:826–33. doi: 10.1002/hipo.20212
52. Camicioli R, Moore MM, Kinney A, Corbridge E, Glassberg K, Kaye JA. Parkinson's disease is associated with hippocampal atrophy. *Mov Disord.* (2003) 18:784–90. doi: 10.1002/mds.10444

53. MacDonald V, Halliday GM. Selective loss of pyramidal neurons in the pre-supplementary motor cortex in Parkinson's disease. *Mov Disord.* (2002) 17:1166–73. doi: 10.1002/mds.10258
54. Parkinson Progression Marker Initiative. The Parkinson progression marker initiative (PPMI). *Prog Neurobiol.* (2011) 95:629–35. doi: 10.1016/j.pneurobio.2011.09.005
55. Benamer TS, Patterson J, Grosset DG, Booij J, de Bruin K, van Royen E, et al. Accurate differentiation of parkinsonism and essential tremor using visual assessment of [123I]-FP-CIT SPECT imaging: the [123I]-FP-CIT study group. *Mov Disord.* (2000) 15:503–10. doi: 10.1002/1531-8257(200005)15:3<503::AID-MDS1013>3.0.CO;2-V
56. Kurth F, Jancke L, Luders E. Integrating cytoarchitectonic probabilities with MRI-based signal intensities to calculate regional volumes of interest. In: Spalletta G, Piras F, Gili T, editors. *Brain Morphometry*. New York, NY: Springer New York (2018). p. 121–9. doi: 10.1007/978-1-4939-7647-8_8
57. Ashburner J, Friston KJ. Unified segmentation. *Neuroimage.* (2005) 26:839–51. doi: 10.1016/j.neuroimage.2005.02.018
58. Ashburner J, Friston KJ. Voxel-based morphometry–the methods. *Neuroimage.* (2000) 11:805–21. doi: 10.1006/nimg.2000.0582
59. Farokhian F, Beheshti I, Sone D, Matsuda H. Comparing CAT12 and VBM8 for detecting brain morphological abnormalities in temporal lobe epilepsy. *Front Neurol.* (2017) 8:428. doi: 10.3389/fneur.2017.00428
60. Kurth F, Gaser C, Luders E. A 12-step user guide for analyzing voxel-wise gray matter asymmetries in statistical parametric mapping (SPM). *Nat Protoc.* (2015) 10:293–304. doi: 10.1038/nprot.2015.014
61. Manjón JV, Coupé P, Martí-Bonmatí L, Collins DL, Robles M. Adaptive non-local means denoising of MR images with spatially varying noise levels. *J Magn Reson Imaging.* (2010) 31:192–203. doi: 10.1002/jmri.22003
62. Rajapakse JC, Giedd JN, Rapoport JL. Statistical approach to segmentation of single-channel cerebral MR images. *IEEE Trans Med Imaging.* (1997) 16:176–86. doi: 10.1109/42.563663
63. Lorio S, Fresard S, Adaszewski S, Kherif F, Chowdhury R, Frackowiak RS, et al. New tissue priors for improved automated classification of subcortical brain structures on MRI. *Neuroimage.* (2016) 130:157–66. doi: 10.1016/j.neuroimage.2016.01.062
64. Tohka J, Zijdenbos A, Evans A. Fast and robust parameter estimation for statistical partial volume models in brain MRI. *Neuroimage.* (2004) 23:84–97. doi: 10.1016/j.neuroimage.2004.05.007
65. Ashburner J. A fast diffeomorphic image registration algorithm. *Neuroimage.* (2007) 38:95–113. doi: 10.1016/j.neuroimage.2007.07.007
66. Ashburner J, Friston KJ. Diffeomorphic registration using geodesic shooting and Gauss–Newton optimisation. *NeuroImage.* (2011) 55:954–67. doi: 10.1016/j.neuroimage.2010.12.049
67. Eickhoff SB, Stephan KE, Mohlberg H, Grefkes C, Fink GR, Amunts K, et al. A new SPM toolbox for combining probabilistic cytoarchitectonic maps and functional imaging data. *Neuroimage.* (2005) 25:1325–35. doi: 10.1016/j.neuroimage.2004.12.034
68. Zaborszky L, Hoemke L, Mohlberg H, Schleicher A, Amunts K, Zilles K. Stereotaxic probabilistic maps of the magnocellular cell groups in human basal forebrain. *Neuroimage.* (2008) 42:1127–41. doi: 10.1016/j.neuroimage.2008.05.055
69. Amunts K, Kedo O, Kindler M, Pieperhoff P, Mohlberg H, Shah NJ. Cytoarchitectonic mapping of the human amygdala, hippocampal region and entorhinal cortex: intersubject variability and probability maps. *Anat Embryol.* (2005) 210:343–52. doi: 10.1007/s00429-005-0025-5
70. Geyer S, Ledberg A, Schleicher A, Kinomura S, Schormann T, Bürgel U, et al. Two different areas within the primary motor cortex of man. *Nature.* (1996) 382:805–7. doi: 10.1038/382805a0
71. Morosan P, Rademacher J, Schleicher A, Amunts K, Schormann T, Zilles K. Human primary auditory cortex: cytoarchitectonic subdivisions and mapping into a spatial reference system. *Neuroimage.* (2001) 13:684–701. doi: 10.1006/nimg.2000.0715
72. Geyer S, Schormann T, Mohlberg H, Zilles K. Areas 3a, 3b, and 1 of human primary somatosensory cortex. Part 2. Spatial normalization to standard anatomical space. *Neuroimage.* (2000) 11:684–96. doi: 10.1006/nimg.2000.0548
73. Amunts K, Weiss PH, Mohlberg H, Pieperhoff P, Eickhoff S, Gurd JM, et al. Analysis of neural mechanisms underlying verbal fluency in cytoarchitectonically defined stereotaxic space–the roles of Brodmann areas 44 and 45. *Neuroimage.* (2004) 22:42–56. doi: 10.1016/j.neuroimage.2003.12.031
74. Amunts K, Malikovic A, Mohlberg H, Schormann T, Zilles K. Brodmann's areas 17 and 18 brought into stereotaxic space-where and how variable? *Neuroimage.* (2000) 11:66–84. doi: 10.1006/nimg.1999.0516
75. Morosan P, Schleicher A, Amunts K, Zilles K. Multimodal architectonic mapping of human superior temporal gyrus. *Anat Embryol.* (2005) 210:401–06. doi: 10.1007/s00429-005-0029-1
76. Glickman ME, Rao SR, Schultz MR. False discovery rate control is a recommended alternative to Bonferroni-type adjustments in health studies. *J Clin Epidemiol.* (2014) 67:850–57. doi: 10.1016/j.jclinepi.2014.03.012
77. Lewis MM, Du G, Lee E-Y, Nasralah Z, Sterling NW, Zhang L, et al. The pattern of gray matter atrophy in Parkinson's disease differs in cortical and subcortical regions. *J Neurol.* (2016) 263:68–75. doi: 10.1007/s00415-015-7929-7
78. Mak E, Bergsland N, Dwyer MG, Zivadinov R, Kandiah N. Subcortical atrophy is associated with cognitive impairment in mild Parkinson disease: a combined investigation of volumetric changes, cortical thickness, and vertex-based shape analysis. *AJNR Am J Neuroradiol.* (2014) 35:2257–64. doi: 10.3174/ajnr.A4055
79. Lee E-Y, Sen S, Eslinger PJ, Wagner D, Shaffer ML, Kong L, et al. Early cortical gray matter loss and cognitive correlates in non-demented Parkinson's patients. *Parkinsonism Relat Disord.* (2013) 19:1088–93. doi: 10.1016/j.parkreldis.2013.07.018
80. Brück A, Kurki T, Kaasinen V, Vahlberg T, Rinne JO. Hippocampal and prefrontal atrophy in patients with early non-demented Parkinson's disease is related to cognitive impairment. *J Neurol Neurosurg Psychiatry.* (2004) 75:1467–9. doi: 10.1136/jnnp.2003.031237
81. Kunst J, Marecek R, Klobusiakova P, Balazova Z, Anderkova L, Nemcova-Elfmarkova N, et al. Patterns of Grey Matter Atrophy at different stages of Parkinson's and Alzheimer's diseases and relation to cognition. *Brain Topogr.* (2019) 32:142–60. doi: 10.1007/s10548-018-0675-2
82. Agosta F, Canu E, Stojković T, Pievani M, Tomić A, Sarro L, et al. The topography of brain damage at different stages of Parkinson's disease. *Hum Brain Mapp.* (2013) 34:2798–807. doi: 10.1002/hbm.22101
83. Dalaker TO, Zivadinov R, Larsen JP, Beyer MK, Cox JL, Alves G, et al. Gray matter correlations of cognition in incident Parkinson's disease. *Mov Disord.* (2010) 25:629–33. doi: 10.1002/mds.22867
84. Junqué C, Ramírez-Ruiz B, Tolosa E, Summerfield C, Martí MJ, Pastor P, et al. Amygdalar and hippocampal MRI volumetric reductions in Parkinson's disease with dementia. *Mov Disord.* (2005) 20:540–4. doi: 10.1002/mds.20371
85. Apostolova LG, Beyer M, Green AE, Hwang KS, Morra JH, Chou Y-Y, et al. Hippocampal, caudate, and ventricular changes in Parkinson's disease with and without dementia. *Mov Disord.* (2010) 25:687–95. doi: 10.1002/mds.22799
86. Pyatigorskaya N, Gallea C, Garcia-Lorenzo D, Vidailhet M, Lehericy S. A review of the use of magnetic resonance imaging in Parkinson's disease. *Ther Adv Neurol Disord.* (2014) 7:206–20. doi: 10.1177/1756285613511507
87. Longoni G, Agosta F, Kostić V. S., Stojkovi,ć T, Pagani E, Stošić-Opinćal T, et al. MRI measurements of brainstem structures in patients with Richardson's syndrome, progressive supranuclear palsy-parkinsonism, and Parkinson's disease. *Mov Disord.* (2011) 26:247–55. doi: 10.1002/mds.23293
88. Benarroch EE. The amygdala: functional organization and involvement in neurologic disorders. *Neurology.* (2015) 84:313–24. doi: 10.1212/WNL.0000000000001171
89. Braak H, Braak E, Yilmazer D, de Vos RA, Jansen EN, Bohl J, et al. Amygdala pathology in Parkinson's disease. *Acta Neuropathol.* (1994) 88:493–500. doi: 10.1007/BF00296485
90. Tanner JJ, McFarland NR, Price CC. Striatal and hippocampal atrophy in idiopathic Parkinson's Disease Patients without dementia: a morphometric analysis. *Front Neurol.* (2017) 8:139. doi: 10.3389/fneur.2017.00139
91. Li X, Xing Y, Schwarz ST, Auer DP. Limbic grey matter changes in early Parkinson's disease. *Hum Brain Mapp.* (2017) 38:3566–78. doi: 10.1002/hbm.23610

92. Bouchard TP, Malykhin N, Martin WRW, Hanstock CC, Emery DJ, Fisher NJ, et al. Age and dementia-associated atrophy predominates in the hippocampal head and amygdala in Parkinson's disease. *Neurobiol Aging.* (2008) 29:1027–39. doi: 10.1016/j.neurobiolaging.2007.02.002
93. Mazziotta J, Toga A, Evans A, Fox P, Lancaster J, Zilles K, et al. A probabilistic atlas and reference system for the human brain: international consortium for brain mapping (ICBM). *Philos Trans R Soc Lond B Biol Sci.* (2001) 356:1293–322. doi: 10.1098/rstb.2001.0915
94. Mazziotta JC, Toga AW, Evans A, Fox P, Lancaster J. A probabilistic atlas of the human brain: theory and rationale for its development. The International Consortium for Brain Mapping (ICBM). *Neuroimage.* (1995) 2:89–101. doi: 10.1006/nimg.1995.1012
95. Amunts K, Zilles K. Advances in cytoarchitectonic mapping of the human cerebral cortex. *Neuroimaging Clin N Am.* (2001) 11:151–69.
96. Lehmbeck JT, Brassen S, Weber-Fahr W, Braus DF. Combining voxel-based morphometry and diffusion tensor imaging to detect age-related brain changes. *Neuroreport.* (2006) 17:467–70. doi: 10.1097/01.wnr.0000209012.24341.7f
97. Giorgio A, Santelli L, Tomassini V, Bosnell R, Smith S, De Stefano N, et al. Age-related changes in grey and white matter structure throughout adulthood. *Neuroimage.* (2010) 51:943–51. doi: 10.1016/j.neuroimage.2010.03.004
98. Walhovd KB, Fjell AM, Reinvang I, Lundervold A, Dale AM, Eilertsen DE, et al. Effects of age on volumes of cortex, white matter and subcortical structures. *Neurobiol Aging.* (2005) 26:1261–70; discussion 1275–78. doi: 10.1016/j.neurobiolaging.2005.05.020
99. De Pablo-Fernández E, Lees AJ, Holton JL, Warner TT. Prognosis and neuropathologic correlation of clinical subtypes of parkinson disease. *JAMA Neurol.* (2019) 76:470–9. doi: 10.1001/jamaneurol.2018.4377
100. Pagano G, Ferrara N, Brooks DJ, Pavese N. Age at onset and Parkinson disease phenotype. *Neurology.* (2016) 86:1400–07. doi: 10.1212/WNL.0000000000002461
101. Jovicich J, Barkhof F, Babiloni C, Herholz K, Mulert C, van Berckel BNM, et al. Harmonization of neuroimaging biomarkers for neurodegenerative diseases: a survey in the imaging community of perceived barriers and suggested actions. *Alzheimer's Dementia.* (2019) 11:69–73. doi: 10.1016/j.dadm.2018.11.005
102. Jovicich J, Barkhof F, Babiloni C, Herholz K, Mulert C, van Brckel BNM, et al. Harmonization of neuroimaging biormarkers for neurode generative diseases: a survey for best practice guidelines. In: *Alzheimer's Association International Conference*. London (2017).

Conflict of Interest: The authors declare that the research was conducted in the absence of any commercial or financial relationships that could be construed as a potential conflict of interest.

Copyright © 2019 Blair, Barrett, Patrie, Flanigan, Sperling, Elias and Druzgal. This is an open-access article distributed under the terms of the Creative Commons Attribution License (CC BY). The use, distribution or reproduction in other forums is permitted, provided the original author(s) and the copyright owner(s) are credited and that the original publication in this journal is cited, in accordance with accepted academic practice. No use, distribution or reproduction is permitted which does not comply with these terms.

frontiers in Neurology

REVIEW
published: 31 January 2020
doi: 10.3389/fneur.2020.00047

Imaging Mild Cognitive Impairment and Dementia in Parkinson's Disease

Sanskriti Sasikumar[1] *and Antonio P. Strafella*[1,2,3,4]*

[1] Division of Neurology, University of Toronto, Toronto, ON, Canada, [2] Morton and Gloria Shulman Movement Disorder Unit & E. J. Safra Parkinson Disease Program, Neurology Division, Department of Medicine, Toronto Western Hospital, UHN, University of Toronto, Toronto, ON, Canada, [3] Research Imaging Centre, Centre for Addiction and Mental Health, Campbell Family Mental Health Research Institute, University of Toronto, Toronto, ON, Canada, [4] Division of Brain, Imaging and Behaviour – Systems Neuroscience, Krembil Research Institute, UHN, University of Toronto, Toronto, ON, Canada

Cognitive dysfunction is a significant non-motor feature of Parkinson's disease, with the risk of dementia increasing with prolonged disease duration. Multiple cognitive domains are affected, and the pathophysiology cannot be explained by dopaminergic loss alone. Sophisticated neuroimaging techniques can detect the nature and extent of extra-nigral involvement by targeting neurotransmitters, abnormal protein aggregates and tissue metabolism. This review identifies the functional and anatomical imaging characteristics that predict cognitive impairment in PD, the limitations that challenge this process, and the avenues of potential research.

Keywords: mild cognitive impairment, dementia, Parkinson's disease, biomarker, imaging

OPEN ACCESS

Edited by:
Yu Zhang,
VA Palo Alto Health Care System,
United States

Reviewed by:
Lin Tan,
Qingdao Municipal Hospital, China
Soichiro Shimizu,
Tokyo Medical University, Japan

***Correspondence:**
Antonio P. Strafella
antonio.strafella@uhn.ca

Specialty section:
This article was submitted to Movement Disorders, a section of the journal Frontiers in Neurology

Received: *11 November 2019*
Accepted: *14 January 2020*
Published: *31 January 2020*

Citation:
Sasikumar S and Strafella AP (2020) Imaging Mild Cognitive Impairment and Dementia in Parkinson's Disease. Front. Neurol. 11:47. doi: 10.3389/fneur.2020.00047

INTRODUCTION

Parkinson's Disease (PD) is a neurodegenerative disorder that is often characterized by motor symptoms such as resting tremor, rigidity, bradykinesia, and postural instability. However, non-motor features such as cognitive impairment play a significant role in this progressive, multisystem condition, and often precede the onset of motor symptoms. In fact, mild cognitive impairment (MCI) is present in 42.5% of patients at the time of diagnosis, and progresses to dementia (PDD) in 70–80% of cases within 15–20 years (1, 2). The prevalence of dementia in PD is 3 times higher than the general population (3, 4), and leads to caregiver burden, early institutionalization and death (5).

The clinical syndrome in PD reflects the progressive degeneration of nigrostriatal dopamine neurons and accumulation of intranuclear misfolded alpha-synuclein, referred to as Lewy bodies. Executive dysfunction, that is a prominent feature of the cognitive dysfunction in PD, can be attributed to dopaminergic fronto-striatal impairment. However, other symptoms like alertness and visuo-perceptual dysfunction, cannot fully be explained by dopaminergic loss, and is suspected to involve several other neurotransmitter systems such as serotonergic, noradrenergic and cholinergic circuits. However, the role of extra-dopaminergic pathways in the cognitive symptoms in PD has not been fully elucidated and remains poorly understood.

The advent of sophisticated neuroimaging techniques has facilitated the detection of disease beyond the limitations of the clinical examination. Imaging biomarkers can be used as a potential tool to detect these extra-dopaminergic pathways, by specifically targeting neurotransmitters, abnormal protein aggregates and tissue metabolism (**Table 1**). They can also clarify the pathological burden that results in cognitive impairment, and can prognosticate the risk factors that determine the progression to dementia. This review highlights the imaging modalities that facilitate the detection of cognitive impairment and dementia in PD, and identify prognostic factors and molecular mechanisms that result in its pathology.

TABLE 1 | Summary of imaging biomarkers in cognitive impairment and dementia in Parkinson's Disease, with their respective grades of evidence.

Imaging modality	Functional and anatomical biomarkers	Summary of evidence	Level of evidence
MRI	White matter hyperintensities	Compared to age-matched controls, white matter hyperintensities are not predictive of cognitive impairment in PD	Level 2
	Cortical thickness	Cortical thinning predicts the risk of dementia in PD-MCI	Level 2
	DTI	– In PD, there is increased mean diffusivity and decreased functional anisotropy in the hippocampus and bilateral frontal and temporal lobes – This further corresponds to impaired performance in verbal and visuospatial memory, semantic fluency and executive function	Level 3
	Resting state fMRI	– PD-MCI and PDD subjects demonstrate progressive loss of resting state nuclei in multiple brain regions – Visuospatial deficits in PD-MCI correlates with impaired functional connectivity in the parieto-temporal region, and is predictive of cognitive impairment	Level 2
	Task-specific fMRI	Impaired nigrostriatal and mesocortical dopaminergic pathways correspond to cognitive deficits in PD	Level 3
PET	11C-raclopride: dopamine D2-receptor marker 11C-dihydrotetrabenazine: D2-receptor and vesicular monoamine transporter (VMAT2) ligand marker	– Cognitive dysfunction in PD arises from nigrostriatal dopamine dysfunction and subsequent impairment of cortico-basal ganglia circuit – Reduction in D2 receptors in the insular cortex, anterior cingulate gyrus, and parahippocampal gyrus is seen in PD-MCI, with larger reduction seen in amnestic MCI subjects	Level 3
	Glucose (FDG-PET)	– PD cognition-related pattern (metabolic reduction in medial prefrontal, premotor and parietal association areas) identifies individuals with PD-MCI whose executive function will improve with levodopa – Individuals with PDD have more pronounced impairment of glucose metabolism in the primary visual cortex, with relative preservation of the medial temporal region	– Level 2 – Level 3
	^{11}C-MP4A : acetylcholinesterase activity	– Cortical cholinergic activity is reduced by 30% in PDD and 11% in PD, and is associated with worse attention, memory and executive dysfunction	Level 3
	^{11}C-PIB & 18F-FBB: bind to amyloid beta	– No difference in amyloid plaque burden between PD-MCI and healthy age-matched controls Predicts cognitive decline rather than reflecting cognitive impairment	Level 3
	[^{18}F] AV-1451: binds to tau	– Conflicting reports about whether tau accumulation varies in PD-MCI compared to cognitive normal PD and age-matched controls – Presence of tau reflects more severe cognitive impairment, and usually accompanies the presence of amyloid beta	Level 3
	^{11}C-PK11195: traces TSPO, expressed by activated microglia)	Inconsistent binding to midbrain, frontal and temporal cortices	Level 3
SPECT	^{123}I-FP-CIT & [123I] ioflupane: *in vivo* marker of dopamine transporter binding	– Reduced uptake in striatum in DLB and PDD, and corresponds to low MMSE scores in PDD – Executive dysfunction could also be explained by impaired nigrostriatal function	Level 3
	^{123}I-BVM: acetylcholine vesicle transport marker	Cholinergic activity is reduced in the parietal and occipital cortex in PD, with more extensive cortical reduction in PDD	Level 3
	(99m)Tc-ethyl cysteinate dimer (ECD): lipophilic agent used for SPECT perfusion imaging	– Global cortical hypoperfusion, most prominent in the temporo-parietal regions in PDD compared to healthy controls – Hypoperfusion in the posterior parieto-occipital regions in PD-MCI, with the most difference appreciated when compared to healthy controls and amnestic MCI than cognitively intact PD	Level 3

SEARCH STRATEGIES AND SELECTION CRITERIA

A search strategy was conducted using the PubMed database (www.ncbi.nlm.nih.gov/pubmed). The search criteria consisted of all English language articles published until September 23rd 2019, that contained combinations of "Parkinson," "cognitive impairment," "dementia," "imaging," "amyloid," "tau," "microglia," "MRI," and "PET." The abstracts were screened for relevance, and read in their entirety if they were suitable.

MAGNETIC RESONANCE IMAGING (MRI)

White Matter Hyperintensities

White matter hyperintensities (WMH) can be best visualized on the T2-weighted, fluid-attenuated inversion recovery (FLAIR) and proton density-weighted sequences, and their presence has been associated with worse cognition and postural stability in PD (6). However, previous studies have been inconsistent with the association of cognitive impairment and WMH.

White matter hyperintensities arise due to ischemic injury from either hemodynamic compromise, lipohyalinosis, or arteriosclerosis (7, 8). They are increasingly present with age, and are distributed in the deep subcortical white matter and periventricular regions (9, 10). Risk factors for their formation include hypertension, fluctuations in blood pressure and loss of cerebral vascular autoregulation (11). Because of their prevalence, it can be challenging to attribute pathology to their presence. A recent study by Pozorski et al. used an automated lesion segmentation tool to compare the WMH burden in PD to age matched controls over an 18-month period. Their findings reveal that PD patients do not experience more WMH than the average population, but the concurrent presence of WMH can exacerbate the cognitive and motor symptoms in the condition (12).

Volumetric Assessment of Cortical Thickness

Atrophy in PD with mild cognitive impairment (PD-MCI) occurs predominantly over the frontal, temporal and parietal regions, as well as the basal forebrain, and it becomes more pronounced with progression to dementia (13). MRI analysis of cortical thickness can also be a means of prognosticating conversion to dementia. In a study that followed subjects with PD-MCI and healthy controls, cortical thinning in the frontal, left medial temporal and insular regions was associated with increased likelihood for MCI subjects converting to dementia (14). Loss of tissue volume in these regions is associated with impaired decision-making, executive function, recognition of facial expressions and visual memory (14). Voxel-based assessment of gray matter volume (GMV) corroborates this loss in the frontal-limbic and temporal regions, and suggests that unilateral-to-bilateral loss of GMV is a quantitative predictor for the progression from PD-MCI to PDD (15).

The cortex of PD-MCI converters is thinner than non-converters, despite the degree of cognitive impairment being comparable between the two groups (16). More cortical thinning poses an increased risk of developing dementia (16). Retrospective analysis of structural MRI imaging in cognitively intact individuals with PD demonstrated that cognitive impairment can be predicted based on the region of atrophy. PD-MCI occurred within 6 months of hippocampal atrophy (17), 18 months of temporal cortex atrophy (18), and 2 years of prefrontal cortex, insular and caudate atrophy (19, 20).

Diffusion Tensor Imaging (DTI)

DTI is an MRI-based imaging technique that measures the magnitude (mean diffusivity) and direction (fractional anisotropy) of water molecule flow along the white matter tracts. In PD, there is increased mean diffusivity and decreased fractional anisotropy predominantly in the bilateral frontal and temporal regions and hippocampus, suggesting damage to the white matter tracts in these regions (21–25). These manifest clinically with impaired performance in verbal and visuospatial memory, semantic fluency and executive function (22).

Resting State Functional MRI (fMRI)

Functional MRI measures the blood-oxygen-level dependent (BOLD) signal to reflect the functional connectivity (FC) in the brain. This provides information about the interaction between different cortical regions that make up resting-state networks (RSN). These fMRI images are obtained in the absence of prompted task, and demonstrate the resting connectivity in the brain.

PD subjects demonstrate a progressive loss of RSN in multiple brain regions over the course of a 3-year follow-up (26). Despite controlling for dopaminergic medications, subjects with PD-MCI and PDD demonstrate impaired FC in the fronto-parietal network and its associated RSNs (27, 28). In PD-MCI with visuo-spatial impairment, the FC changes involve the parieto-temporal regions as well, and is predictive of evolution to dementia (26, 29). These findings suggest a dual signature of cognitive impairment: the dopaminergic fronto-striatal pathway and the parieto-temporal pathway (30, 31).

Task-Based fMRI

In individuals with PD, task-based MRI performed during attentional set-shifting tasks show reduced fronto-striatal activity (32–34). PD-MCI off dopaminergic medication further show diminished activation between the prefrontal cortex and caudate nucleus when performing set-shifting tasks (34). Some studies indicate that the medial temporal lobe compensates for this diminished functioning, and attempts to preserve cognitive function in PD (34–36). Task-based MRI studies demonstrate that the nigrostriatal and mesocortical dopaminergic pathways are involved in the cognitive deficits seen in PD (14).

POSITRON EMISSION TOMOGRAPHY (PET)

Dopamine

Dopaminergic molecular imaging has been useful in identifying the subcortical regions of dopamine hypoactivity that contributes to cognitive impairment in PD. By using a marker for dopamine

D2-receptor availability and synaptic dopamine function (11C-raclopride, or RAC), Sawamoto et al. studied subjects with early symptomatic PD and age-matched controls during a spatial working memory task and visuomotor task to determine whether the cognitive impairment in PD results from frontal lobe or striatal dopaminergic dysfunction (37). They found that dopamine release in the dorsal caudate was significantly reduced in PD, but preserved in the medial prefrontal cortex, suggesting that cognitive deficits in early patients with PD arises from nigrostriatal dopamine dysfunction and subsequent impairment of the cortico-basal ganglia circuit (37).

Contrary to prior studies that implicated frontal dopamine depletion in cognitive impairment, there was relative preservation of mesocortical dopamine transmission (37). However, the studies that demonstrated diminished activity in the mesolimbic and mesocortical regions (38, 39), were done in PDD instead of early PD with MCI. So, it is possible that with disease progression, the cortical dopaminergic activity becomes more impaired.

By using a D2-receptor and vesicular monoamine transporter (VMAT2) ligands as a marker for dopamine receptor integrity in the cortex and striatum respectively, Christopher et al. demonstrated that cognitive impairment in PD is associated with D2 receptor reduction in the insular cortex, anterior cingulate gyrus and parahippocampal gyrus compared to cognitively intact PD controls. This reduction was also larger in amnestic compared to non-amnestic MCI subjects. This suggests that the medial temporal lobe contributes to the memory impairment and executive dysfunction in PD (40).

Glucose

FDG-PET findings in PDD manifest in a similar pattern to Alzheimer's Disease, where the regional glucose cerebral metabolism affects the posterior cingulate gyrus first, then progresses to the temporal and parietal association cortex, and finally affects the prefrontal cortex (41, 42). Studies on PD-MCI also reveal diminished glucose metabolism in the parietal, temporal, cingulate, and frontal cortices (43, 44).

Despite similar findings in AD and PDD, the degree of regional cerebral hypometabolism can distinguish between the two conditions when matched for age, sex, and dementia severity. Individuals with PDD have pronounced impairment of glucose metabolism in the primary visual cortex, with relative preservation of the medial temporal region (45). However, in AD, there is only mild reduction in glucose metabolism in these regions (45).

Dementia with Lewy Bodies (DLB) is another neurodegenerative condition that shares similar PET imaging features with PDD. Compared to PD, PDD and DLB demonstrate relatively reduced metabolism in the bilateral inferior and medial frontal lobes, as well as the right parietal lobe (46). The only distinguishing feature is that glucose metabolism is more diminished in the anterior cingulate gyrus in DLB compared to PDD (46).

Spatial covariance analysis of FDG-PET images in PD reveals metabolic reductions in the medial prefrontal, premotor and parietal association areas in a pattern that is referred to as PD cognition-related pattern (PDCP). PDCP is associated with severe cognitive impairment, and can identify the population of patients with MCI whose executive function will improve with levodopa; those who do not demonstrate this pattern, do not respond to therapy (47).

Acetylcholinesterase Activity

Cortical cholinergic deficiency plays a critical role in the cognitive decline seen in PD. Cholinergic denervation occurs early in PD, and is more pronounced in individuals with cognitive impairment and dementia (48–50). Lower cortical cholinergic activity is associated with worse cognitive performance scores for attention, memory, and executive function, and is sensitive enough to detect subclinical MCI (51). This justifies the use of cholinergic inhibitors for the symptomatic treatment of cognitive impairment in PDD (51).

While cortical cholinergic deficiency does not correlate with motor symptoms in PD, it appears to be the primary etiology associated with significant cognitive decline (48–50). Cortical binding of ^{11}C-MP4A, a marker of acetylcholinesterase activity, is globally reduced by 30% in PDD, compared to 11% in PD (42). This pattern of cortical hypometabolism is also seen in DLB and AD, with AD demonstrating additional involvement of the thalamus (49, 51). Cholinergic PET also correlates with loss of forebrain cholinergic neurons seen on post-mortem pathology (48–50). ^{18}F-dopa studies indicate that diminished dopaminergic uptake in the frontal and temporo-parietal regions correlates with cholinergic deficiency, suggesting that both systems reduce in conjunction in PD and PDD (48).

Amyloid Beta

The role of amyloid beta in the development of cognitive impairment in PD is debated. Using the ^{11}C-PIB marker, amyloid beta plaques can be identified in the cortex (52–54), but the degree is significantly less in PD compared to cognitively normal elderly people (55, 56). However, there is a higher plaque burden observed in the cortex and striatum of individuals with PDD (15–20%) and DLB (52, 57).

The presence of amyloid beta plaques is not presumed to be a major player in the pathogenesis of cognitive impairment in PD. There was no difference in amyloid beta burden between PD-MCI and healthy age-matched controls, but long-term follow up indicates that both groups experience cognitive decline at 2.5 years (58). This suggests that the presence of plaques might predict cognitive decline rather than reflect the severity of cognitive impairment (58). Additionally, the presence of amyloid plaque in the striatum is associated with worse cognitive decline compared to its presence in the cortex alone (59).

The *in vivo* amyloid beta PET imaging studies have several limitations; particularly, low sample size, low power, lack of cognitive characterization and no standardization for age (60). A recently published cross-sectional study by Melzer et al. (60) looked at 115 subjects divided into PD-CN, PD-MCI and PDD. Using 18F-Florbetaben (FBB) amyloid PET and structural MRI, the study determined that while FBB binding was higher in PDD population, it was not significant when adjusted to findings in

age-matched controls, and is much lower than the deposition seen in AD (54, 61–63). This further suggests that amyloid beta is not the primary pathology that constitutes the cognitive impairment seen in PD.

Tau

Tau deposits using tracer [^{18}F] AV-1451 show increased binding in precuneus and inferior temporal gyrus in PDD and DLB, compared to age-matched controls (64, 65). However, in a recent cross-sectional study by Winer et al., tau accumulation did not differ between PD-CN and PD-MCI compared to age-matched controls (66). This suggests that cortical tau aggregates are present with more progressive disease only. While it is uncertain whether they contribute to cognitive dysfunction in PD, their presence certainly reflects more advanced cognitive impairment (51). Additionally, tau accumulation increases with amyloid beta, regardless of cognitive status and age (66).

Microglia

Microglia are resident macrophages of the central nervous system that are activated during neuronal injury. They have been implicated in the pathogenesis of PD because post-mortem studies demonstrate increased microglia in the substantia nigra, putamen, hippocampus, cingulate and temporal cortex (67). As such, identifying microglial activity could serve as a biomarker of inflammation and potentially, PD.

Upon activation, microglia express TSPO (18 kDA translocator protein) in the outer mitochondrial membrane (68). However, PET studies using the ^{11}C-PK11195 tracer show inconsistent binding to TSPO in the midbrain (69), frontal and temporal cortices (70). This variability might be explained by the limitations of the tracer itself, as ^{11}C-PK11195 has non-specific binding, low blood-brain barrier penetration, and high plasma protein binding. It is also challenging to prepare, and these demonstrate different affinities because of polymorphisms in TPSO (71, 72).

Increased cortical microglial activation is associated with glucose hypometabolism in the posterior cingulate, frontal, temporal, parietal, and occipital regions in PD-MCI and PDD, suggesting that neuronal disconnections occur both locally and remotely (73). The degree of microglial activation also correlates with the cortical load of amyloid beta, so neuroinflammation may be an early event in dementia and likely initiates neuronal dysfunction (73).

SINGLE-PROTON EMISSION COMPUTED TOMOGRAPHY (SPECT)

Dopamine

Similar to PET imaging, SPECT employs radiotracers to study the basal ganglia and its synaptic projections. ^{123}I-FP-CIT SPECT, which is an *in vivo* marker of dopamine transporter (DAT) binding, shows reduced striatal uptake in individuals with DLB and PDD (74). In comparison, cognitively intact individuals with PD demonstrate more selective DAT binding to the putamen (75). Moreover, ^{123}I-FP-CIT SPECT binding corresponds to MMSE scores in PDD patients, suggesting that striatal dopaminergic loss contributes to cognitive impairment in PD (74). SPECT studies using [123I] ioflupane suggest that executive dysfunction in PD could also be explained by impaired nigrostriatal function (76, 77).

Acetylcholine

^{123}I-BVM is a marker of acetylcholine vesicle transport, and reflects cholinergic deficiency in PD. Cognitively intact individuals with PD have reduced ^{123}I-BVM binding in the parietal and occipital cortex, whereas those with PDD show extensive reduction in cortical binding (78).

Perfusion

There is limited data on the role of SPECT perfusion imaging in PD-related cognitive impairment, but the reported literature suggests its potential in reflecting the severity of underlying cognitive impairment. A study of 22 patients with PDD using the SPECT radiotracer (99m)Tc-ethyl cysteinate dimer (ECD) reveals global cortical hypoperfusion, most prominent in the temporo-parietal regions, compared to healthy, age-matched controls (79). In individuals with PD-MCI, the hypoperfusion pattern is limited to the posterior parieto-occipital regions, with the most difference seen in comparison to healthy controls and amnestic MCI than to those with cognitively intact PD (80).

ALPHA SYNUCLEIN

The pathology of alpha-synuclein's invasion into the nervous system is unknown. It is theorized to originate in the enteric or peripheral nervous system, and enter the central nervous system through retrograde vagal nerve transport. However, not all PD subjects demonstrate pathology in the dorsal motor nucleus of the vagus to support this theory (81). Borghammer et al. hypothesize that there are two types of disease processes: (i) peripheral nervous system first, which manifests clinically with REM sleep behavioral disorder (RSBD) and (ii) central nervous system first, with nigrostriatal dopamine involvement prior to autonomic symptoms (81).

They support this theory using *in vivo* imaging of RSBD positive (idiopathic RSBD, who eventually develop PD or DLB) and RSBD negative (*de novo* H&Y Stage I PD patients) subjects. This revealed that RSBD positive subjects demonstrate severely reduced sympathetic cardiac innervation (using 123 I -MIBG scintigraphy) but normal striatal dopamine storage capacity (using 18 F-DOPA PET). RSBD negative subjects, who represent *de novo* PD, show normal cardiac innervation and reduced striatal dopamine capacity. These findings suggest that distinguishing RSBD reflects the initial location of the alpha synuclein pathology (81). Whether the disease starts in the enteric and peripheral nervous system vs. brainstem and limbic system might be determined by different patterns of cellular vulnerability (81). Unfortunately, there is no nucleotide tracer for alpha-synuclein, so much of its role in PD remains theoretical, as does its role in the progression of PD-MCI to PDD.

DISCUSSION

Emerging imaging techniques have facilitated a broader understanding of cognitive impairment, where extra-nigral pathways have been identified to play a key role in the pathogenesis of neurodegeneration in PD. Several mechanisms have been identified, including location of cortical atrophy as means of predicting risk of progression to dementia (17–20), meso-cortical dopaminergic dysfunction in advanced dementia, glucose hypometabolism in the posterior cingulate gyrus and temporo-parietal association cortices, and diffusely diminished cholinergic activity. Certain features like cortical deposition of amyloid beta and tau, as well as white matter burden, are associated with advanced cognitive impairment but do not participate in the primary pathology of cognitive impairment in PD. These processes act synergistically, and have poor prognostic implications for individuals with the disease (58, 82).

Cognitive impairment in PD starts in the temporo-parietal cortices before involving the remainder of the cortex and subcortical gray matter, and predicts the progression to PDD. There is diminished cholinergic activity in this region, as well as in the basal nucleus and occipital cortex, which justifies the use of cholinergic inhibitors for symptomatic treatment of attention and visuospatial disorientation in PD.

There are several limitations to the value of imaging to detect cognitive impairment in PD. Co-pathology of synucleinopathy (Lewy Body inclusions) and proteinopathy (amyloid beta and tau) is a feature shared with other dementing conditions like DLB and AD, which makes it challenging to distinguish PD-related cognitive impairment from these co-pathologies (83). It also remains unclear whether amyloid beta and tau influence the onset of cognitive impairment in PD, enhance existing symptoms or are predictive of its rate of progression. Studies are further limited by design and sample size, which challenges the ability to draw conclusions from their results. The average age of the patient population in the reported studies is over 55 years, with a disease duration between 8 and 10 years, so the relevance of these biomarkers to early-onset PD cannot be determined. There is also a need for new ligands with high affinity and better selectivity, that not only assess neurotransmission but also neuroinflammation (84). This will shed light on the series of events that take place in cognitive impairment, and determine the risk factors that drive this process. Identifying anatomical and functional predictors of cognitive impairment can facilitate early detection and target appropriate interventions to optimize patient care.

AUTHOR CONTRIBUTIONS

SS: execution and write-up of first draft of the manuscript. AS: conception of research subject and reviewing the manuscript.

FUNDING

This work was supported by Canadian Institutes of Health Research (MOP-136778) to AS. AS was supported by Canada Research Chair Program.

REFERENCES

1. Aarsland D, Bronnick K, Williams-Gray C, Weintraub D, Marder K, Kulisevsky J, et al. Mild cognitive impairment in Parkinson disease: a multicenter pooled analysis. *Neurology*. (2010) 75:1062–9. doi: 10.1212/WNL.0b013e3181f39d0e
2. Palavra NC, Naismith SL, Lewis SJ. Mild cognitive impairment in Parkinson's disease: a review of current concepts. *Neurol Res Int*. (2013) 2013:576091. doi: 10.1155/2013/576091
3. Aarsland D, Andersen K, Larsen JP, Lolk A. Prevalence and characteristics of dementia in Parkinson disease: an 8-year prospective study. *Arch Neurol*. (2003) 60:387–92. doi: 10.1001/archneur.60.3.387
4. Svenningsson P, Westman E, Ballard C, Aarsland D. Cognitive impairment in patients with Parkinson's disease: diagnosis, biomarkers, and treatment. *Lancet Neurol*. (2012) 11:697–707. doi: 10.1016/S1474-4422(12)70152-7
5. Jones AJ, Kuijer RG, Livingston L, Myall D, Horne K, MacAskill M, et al. Caregiver burden is increased in Parkinson's disease with mild cognitive impairment (PD-MCI). *Transl Neurodegeneration*. (2017) 6:17. doi: 10.1186/s40035-017-0085-5
6. Duncan GW, Firbank MJ, O'Brien JT, Burn DJ. Magnetic resonance imaging: a biomarker for cognitive impairment in Parkinson's disease? *Mov Disord*. (2013) 28:425–38. doi: 10.1002/mds.25352
7. Kim KW, MacFall JR, Payne ME. Classification of white matter lesions on magnetic resonance imaging in elderly persons. *Biol Psychiatr*. (2008) 64:273–80. doi: 10.1016/j.biopsych.2008.03.024
8. Xiong YY, Mok V. Age-related white matter changes. *J Aging Res*. (2011) 2011:617927. doi: 10.4061/2011/617927
9. Murray ME, Senjem ML, Petersen RC, Hollman JH, Preboske GM, Weigand SD, et al. Functional impact of white matter hyperintensities in cognitively normal elderly subjects. *Arch Neurol*. (2010) 67:1379–85. doi: 10.1001/archneurol.2010.280
10. Yamawaki M, Wada-Isoe K, Yamamoto M, Nakashita S, Uemura Y, Takahashi Y, et al. Association of cerebral white matter lesions with cognitive function and mood in Japanese elderly people: a population-based study. *Brain Behav*. (2015) 5:e00315. doi: 10.1002/brb3.315
11. Mok V, Kim JS. Prevention and management of cerebral small vessel disease. *J Stroke*. (2015) 17:111. doi: 10.5853/jos.2015.17.2.111
12. Pozorski V, Oh JM, Okonkwo O, Krislov S, Barzgari A, Theisen F, et al. Cross-sectional and longitudinal associations between total and regional white matter hyperintensity volume and cognitive and motor function in Parkinson's disease. *NeuroImage Clin*. (2019) 23:101870. doi: 10.1016/j.nicl.2019.101870
13. Delgado-Alvarado M, Gago B, Navalpotro-Gomez I, Jiménez-Urbieta H, Rodriguez-Oroz MC. Biomarkers for dementia and mild cognitive impairment in Parkinson's disease. *Mov Disord*. (2016) 31:861–81. doi: 10.1002/mds.26662
14. Lehericy S, Vaillancourt DE, Seppi K, Monchi O, Rektorova I, Antonini A, et al. The role of high-field magnetic resonance imaging in parkinsonian disorders: pushing the boundaries forward. *Mov Disord*. (2017) 32:510–25. doi: 10.1002/mds.26968
15. Xu Y, Yang J, Hu X, Shang H. Voxel-based meta-analysis of gray matter volume reductions associated with cognitive impairment in Parkinson's disease. *J Neurol*. (2016) 263:1178–87. doi: 10.1007/s00415-016-8122-3
16. Gasca-Salas C, García-Lorenzo D, Garcia-Garcia D, Clavero P, Obeso JA, Lehericy S, et al. Parkinson's disease with mild cognitive impairment: severe cortical thinning antedates dementia. *Brain Imaging Behav*. (2019) 13:180–8. doi: 10.1007/s11682-017-9751-6
17. Kandiah N, Zainal NH, Narasimhalu K, Chander RJ, Ng A, Mak E, et al. Hippocampal volume and white matter disease in the prediction of

dementia in Parkinson's disease. *Parkinsonism Relat Disord*. (2014) 20:1203–8. doi: 10.1016/j.parkreldis.2014.08.024
18. Mak E, Su L, Williams GB, Firbank MJ, Lawson RA, Yarnall AJ, et al. Baseline and longitudinal grey matter changes in newly diagnosed Parkinson's disease: ICICLE-PD study. *Brain*. (2015) 138:2974–86. doi: 10.1093/brain/awv211
19. Lee JE, Cho KH, Song SK, Kim HJ, Lee HS, Sohn YH, et al. Exploratory analysis of neuropsychological and neuroanatomical correlates of progressive mild cognitive impairment in Parkinson's disease. *J Neurol Neurosurg Psychiatr*. (2014) 85:7–16. doi: 10.1136/jnnp-2013-305062
20. Aarsland D, Creese B, Politis M, Chaudhuri KR, Weintraub D, Ballard C. Cognitive decline in Parkinson disease. *Nat Rev Neurol*. (2017) 13:217. doi: 10.1038/nrneurol.2017.27
21. Koshimori Y, Segura B, Christopher L, Lobaugh N, Duff-Canning S, Mizrahi R, et al. Imaging changes associated with cognitive abnormalities in Parkinson's disease. *Brain Struct Funct*. (2015) 220:2249–61. doi: 10.1007/s00429-014-0785-x
22. Duncan GW, Firbank MJ, Yarnall AJ, Khoo TK, Brooks DJ, Barker RA, et al. Gray and white matter imaging: a biomarker for cognitive impairment in early P arkinson's disease? *Mov Disord*. (2016) 31:103–10. doi: 10.1002/mds.26312
23. Carlesimo GA, Piras F, Assogna F, Pontieri FE, Caltagirone C, Spalletta G. Hippocampal abnormalities and memory deficits in Parkinson disease: a multimodal imaging study. *Neurology*. (2012) 78:1939–45. doi: 10.1212/WNL.0b013e318259e1c5
24. Agosta F, Canu E, Stefanova E, Sarro L, Tomić A, Špica V, et al. Mild cognitive impairment in Parkinson's disease is associated with a distributed pattern of brain white matter damage. *Human Brain Mapp*. (2014) 35:1921–9. doi: 10.1002/hbm.22302
25. Chen B, Fan GG, Liu H, Wang S. Changes in anatomical and functional connectivity of Parkinson's disease patients according to cognitive status. *Eur J Radiol*. (2015) 84:1318–24. doi: 10.1016/j.ejrad.2015.04.014
26. Dubbelink KT, Schoonheim MM, Deijen JB, Twisk JW, Barkhof F, Berendse HW. Functional connectivity and cognitive decline over 3 years in Parkinson disease. *Neurology*. (2014) 83:2046–53. doi: 10.1212/WNL.0000000000001020
27. Rektorova I, Krajcovicova L, Marecek R, Mikl M. Default mode network and extrastriate visual resting state network in patients with Parkinson's disease dementia. *Neurodegenerative Dis*. (2012) 10:232–7. doi: 10.1159/000334765
28. Borroni B, Premi E, Formenti A, Turrone R, Alberici A, Cottini E, et al. Structural and functional imaging study in dementia with Lewy bodies and Parkinson's disease dementia. *Parkinsonism Relat Disord*. (2015) 21:1049–55. doi: 10.1016/j.parkreldis.2015.06.013
29. Baggio HC, Segura B, Sala-Llonch R, Marti MJ, Valldeoriola F, Compta Y, et al. Cognitive impairment and resting-state network connectivity in P arkinson's disease. *Human Brain Mapp*. (2015) 36:199–212. doi: 10.1002/hbm.22622
30. Kehagia AA, Barker RA, Robbins TW. Neuropsychological and clinical heterogeneity of cognitive impairment and dementia in patients with Parkinson's disease. *Lancet Neurol*. (2010) 9:1200–13. doi: 10.1016/S1474-4422(10)70212-X
31. Williams-Gray CH, Evans JR, Goris A, Foltynie T, Ban M, Robbins TW, et al. The distinct cognitive syndromes of Parkinson's disease: 5 year follow-up of the CamPaIGN cohort. *Brain*. (2009) 132:2958–69. doi: 10.1093/brain/awp245
32. Lewis SJ, Dove A, Robbins TW, Barker RA, Owen AM. Cognitive impairments in early Parkinson's disease are accompanied by reductions in activity in frontostriatal neural circuitry. *J Neurosci*. (2003) 23:6351–6. doi: 10.1523/JNEUROSCI.23-15-06351.2003
33. Monchi O, Petrides M, Doyon J, Postuma RB, Worsley K, Dagher A. Neural bases of set-shifting deficits in Parkinson's disease. *J Neurosci*. (2004) 24:702–10. doi: 10.1523/JNEUROSCI.4860-03.2004
34. Nagano-Saito A, Habak C, Mejía-Constaín B, Degroot C, Monetta L, Jubault T, et al. Effect of mild cognitive impairment on the patterns of neural activity in early Parkinson's disease. *Neurobiol Aging*. (2014) 35:223–31. doi: 10.1016/j.neurobiolaging.2013.06.025
35. Carbon M, Reetz K, Ghilardi MF, Dhawan V, Eidelberg D. Early Parkinson's disease: longitudinal changes in brain activity during sequence learning. *Neurobiol Dis*. (2010) 37:455–60. doi: 10.1016/j.nbd.2009.10.025
36. Dagher A, Owen AM, Boecker H, Brooks DJ. The role of the striatum and hippocampus in planning: a PET activation study in Parkinson's disease. *Brain*. (2001) 124:1020–32. doi: 10.1093/brain/124.5.1020
37. Sawamoto N, Piccini P, Hotton G, Pavese N, Thielemans K, Brooks DJ. Cognitive deficits and striato-frontal dopamine release in Parkinson's disease. *Brain*. (2008) 131:1294–302. doi: 10.1093/brain/awn054
38. Ito K, Nagano-Saito A, Kato T, Arahata Y, Nakamura A, Kawasumi Y, et al. Striatal and extrastriatal dysfunction in Parkinson's disease with dementia: a 6-[18F] fluoro-l-dopa PET study. *Brain*. (2002) 125:1358–65. doi: 10.1093/brain/awf134
39. Nagano-Saito A, Kato T, Arahata Y, Washimi Y, Nakamura A, Abe Y, et al. Cognitive-and motor-related regions in Parkinson's disease: FDOPA and FDG PET studies. *Neuroimage*. (2004) 22:553–61. doi: 10.1016/j.neuroimage.2004.01.030
40. Christopher L, Duff-Canning S, Koshimori Y, Segura B, Boileau I, Chen R, et al. Salience network and parahippocampal dopamine dysfunction in memory-impaired Parkinson disease. *Ann Neurol*. (2015) 77:269–80. doi: 10.1002/ana.24323
41. Hoffman JM, Welsh-Bohmer KA, Hanson M, Crain B, Hulette C, Earl N, et al. FDG PET imaging in patients with pathologically verified dementia. *J Nucl Med*. (2000) 41:1920–8.
42. Brooks DJ, Pavese N. Imaging non-motor aspects of Parkinson's disease. *Prog Brain Res*. (2010) 184:205–18. doi: 10.1016/S0079-6123(10)84011-7
43. Gonzalez-Redondo R, García-García D, Clavero P, Gasca-Salas C, García-Eulate R, Zubieta JL, et al. Grey matter hypometabolism and atrophy in Parkinson's disease with cognitive impairment: a two-step process. *Brain*. (2014) 137:2356–67. doi: 10.1093/brain/awu159
44. Pappatá S, Santangelo G, Aarsland D, Vicidomini C, Longo K, Bronnick K, et al. Mild cognitive impairment in drug-naive patients with PD is associated with cerebral hypometabolism. *Neurology*. (2011) 77:1357–62. doi: 10.1212/WNL.0b013e3182315259
45. Vander Borght T, Minoshima S, Giordani B, Foster NL, Frey KA, Berent S, et al. Cerebral metabolic differences in Parkinson's and Alzheimer's Diseases matched for dementia severity. *J Nucl Med*. (1997) 38:797–802.
46. Yong SW, Yoon JK, An YS, Lee PH. A comparison of cerebral glucose metabolism in Parkinson's disease, Parkinson's disease dementia and dementia with Lewy bodies. *Eur J Neurol*. (2007) 14:1357–62. doi: 10.1111/j.1468-1331.2007.01977.x
47. Hirano S, Shinotoh H, Eidelberg D. Functional brain imaging of cognitive dysfunction in Parkinson's disease. *J Neurol Neurosurg Psychiatr*. (2012) 83:963–9. doi: 10.1136/jnnp-2011-301818
48. Hilker R, Thomas AV, Klein JC, Weisenbach S, Kalbe E, Burghaus L, et al. Dementia in Parkinson disease: functional imaging of cholinergic and dopaminergic pathways. *Neurology*. (2005) 65:1716–22. doi: 10.1212/01.wnl.0000191154.78131.f6
49. Bohnen NI, Kaufer DI, Ivanco LS, Lopresti B, Koeppe RA, Davis JG, et al. Cortical cholinergic function is more severely affected in parkinsonian dementia than in Alzheimer disease: an *in vivo* positron emission tomographic study. *Arch Neurol*. (2003) 60:1745–8. doi: 10.1001/archneur.60.12.1745
50. Shimada H, Hirano S, Shinotoh H, Aotsuka A, Sato K, Tanaka N, et al. Mapping of brain acetylcholinesterase alterations in Lewy body disease by PET. *Neurology*. (2009) 73:273–8. doi: 10.1212/WNL.0b013e3181ab2b58
51. Kotagal V, Müller ML, Kaufer DI, Koeppe RA, Bohnen NI. Thalamic cholinergic innervation is spared in Alzheimer disease compared to parkinsonian disorders. *Neurosci Lett*. (2012) 514:169–72. doi: 10.1016/j.neulet.2012.02.083
52. Edison P, Archer HA, Gerhard A, Hinz R, Pavese N, Turkheimer FE, et al. Microglia, amyloid, and cognition in Alzheimer's disease: An [11C](R) PK11195-PET and [11C] PIB-PET study. *Neurobiol Dis*. (2008) 32:412–9. doi: 10.1016/j.nbd.2008.08.001
53. Rowe CC, Ng S, Ackermann U, Gong SJ, Pike K, Savage G, et al. Imaging β-amyloid burden in aging and dementia. *Neurology*. (2007) 68:1718–25. doi: 10.1212/01.wnl.0000261919.22630.ea
54. Gomperts SN, Rentz DM, Moran E, Becker JA, Locascio JJ, Klunk WE, et al. Imaging amyloid deposition in Lewy body diseases. *Neurology*. (2008) 71:903–10. doi: 10.1212/01.wnl.0000326146.60732.d6
55. Mielke MM, Wiste HJ, Weigand SD, Knopman DS, Lowe VJ, Roberts RO, et al. Indicators of amyloid burden in a population-based study of cognitively normal elderly. *Neurology*. (2012) 79:1570–7. doi: 10.1212/WNL.0b013e31826e2696

56. Ghadery C, Koshimori Y, Christopher L, Kim J, Rusjan P, Lang AE, et al. The interaction between neuroinflammation and β-amyloid in cognitive decline in Parkinson's Disease. *Mol Neurobiol*. (2019) 57:492–501. doi: 10.1007/s12035-019-01714-6
57. Maetzler W, Reimold M, Liepelt I, Solbach C, Leyhe T, Schweitzer K, et al. [11C] PIB binding in Parkinson's disease dementia. *Neuroimage*. (2008) 39:1027–33. doi: 10.1016/j.neuroimage.2007.09.072
58. Gomperts SN, Locascio JJ, Rentz D, Santarlasci A, Marquie M, Johnson KA, et al. Amyloid is linked to cognitive decline in patients with Parkinson disease without dementia. *Neurology*. (2013) 80:85–91. doi: 10.1212/WNL.0b013e31827b1a07
59. Shah N, Frey KA, Müller ML, Petrou M, Kotagal V, Koeppe RA, et al. Striatal and cortical β-amyloidopathy and cognition in Parkinson's Disease. *Mov Disord*. (2016) 31:111–7. doi: 10.1002/mds.26369
60. Melzer TR, Stark MR, Keenan RJ, Myall DJ, MacAskill MR, Pitcher TL, et al. Beta amyloid deposition is not associated with cognitive impairment in Parkinson's disease. *Front Neurol*. (2019) 10:391. doi: 10.3389/fneur.2019.00391
61. Petrou M, Bohnen NI, Müller ML, Koeppe RA, Albin RL, Frey KA. Aβ-amyloid deposition in patients with Parkinson disease at risk for development of dementia. *Neurology*. (2012) 79:1161–7. doi: 10.1212/WNL.0b013e3182698d4a
62. Lee SH, Cho H, Choi JY, Lee JH, Ryu YH, Lee MS, et al. Distinct patterns of amyloid-dependent tau accumulation in Lewy body diseases. *Mov Disord*. (2018) 33:262–72. doi: 10.1002/mds.27252
63. Donaghy PC, Firbank MJ, Thomas AJ, Lloyd J, Petrides G, Barnett N, et al. Clinical and imaging correlates of amyloid deposition in dementia with Lewy bodies. *Mov Disord*. (2018) 33:1130–8. doi: 10.1002/mds.27403
64. Gomperts SN, Locascio JJ, Makaretz SJ, Schultz A, Caso C, Vasdev N, et al. Tau positron emission tomographic imaging in the Lewy body diseases. *JAMA Neurol*. (2016) 73:1334–41. doi: 10.1001/jamaneurol.2016.3338
65. Kantarci K, Lowe VJ, Boeve BF, Senjem ML, Tosakulwong N, Lesnick TG, et al. AV-1451 tau and β-amyloid positron emission tomography imaging in dementia with Lewy bodies. *Ann Neurol*. (2017) 81:58–67. doi: 10.1002/ana.24825
66. Winer JR, Maass A, Pressman P, Stiver J, Schonhaut DR, Baker SL, et al. Associations between tau, β-amyloid, and cognition in parkinson disease. *JAMA Neurol*. (2018) 75:227–35. doi: 10.1001/jamaneurol.2017.3713
67. Best L, Ghadery C, Pavese N, Tai YF, Strafella AP. New and old TSPO PET radioligands for imaging brain microglial activation in neurodegenerative disease. *Curr Neurol Neurosci Rep*. (2019) 19:24. doi: 10.1007/s11910-019-0934-y
68. Stoessl AJ, Lehericy S, Strafella AP. Imaging insights into basal ganglia function, Parkinson's disease, and dystonia. *Lancet*. (2014) 384:532–44. doi: 10.1016/S0140-6736(14)60041-6
69. Ouchi Y, Yoshikawa E, Sekine Y, Futatsubashi M, Kanno T, Ogusu T, et al. Microglial activation and dopamine terminal loss in early Parkinson's disease. *Ann Neurol*. (2005) 57:168–75. doi: 10.1002/ana.20338
70. Gerhard A, Pavese N, Hotton G, Turkheimer F, Es M, Hammers A, et al. *In vivo* imaging of microglial activation with [11C](R)-PK11195 PET in idiopathic Parkinson's disease. *Neurobiol Dis*. (2006) 21:404–12. doi: 10.1016/j.nbd.2005.08.002
71. Gerhard A, Banati RB, Goerres GB, Cagnin A, Myers R, Gunn RN, et al. [11C](R)-PK11195 PET imaging of microglial activation in multiple system atrophy. *Neurology*. (2003) 61:686–9. doi: 10.1212/01.WNL.0000078192.95645.E6
72. Owen DR, Yeo AJ, Gunn RN, Song K, Wadsworth G, Lewis A, et al. An 18-kDa translocator protein (TSPO) polymorphism explains differences in binding affinity of the PET radioligand PBR28. *J Cereb Blood Flow Metab*. (2012) 32:1–5. doi: 10.1038/jcbfm.2011.147
73. Fan Z, Aman Y, Ahmed I, Chetelat G, Landeau B, Chaudhuri KR, et al. Influence of microglial activation on neuronal function in Alzheimer's and Parkinson's disease dementia. *Alzheimer's Demen*. (2015) 11:608–21. doi: 10.1016/j.jalz.2014.06.016
74. O'Brien JT, McKeith IG, Walker Z, Tatsch K, Booij J, Darcourt J, et al. Diagnostic accuracy of 123 I-FP-CIT SPECT in possible dementia with Lewy bodies. *Br J Psychiatr*. (2009) 194:34–9. doi: 10.1192/bjp.bp.108.052050
75. Walker Z, Costa DC, Walker RW, Shaw K, Gacinovic S, Stevens T, et al. Differentiation of dementia with Lewy bodies from Alzheimer's disease using a dopaminergic presynaptic ligand. *J Neurol Neurosurg Psychiatr*. (2002) 73:134–40. doi: 10.1136/jnnp.73.2.134
76. Nobili F, Campus C, Arnaldi D, De Carli F, Cabassi G, Brugnolo A, et al. Cognitive-nigrostriatal relationships in *de novo*, drug-naïve Parkinson's disease patients: a [I-123] FP-CIT SPECT study. *Mov Disord*. (2010) 25:35–43. doi: 10.1002/mds.22899
77. Antonelli F, Ray N, Strafella AP. Imaging cognitive and behavioral symptoms in Parkinson's disease. *Exp Rev Neurother*. (2010) 10:1827–38. doi: 10.1586/ern.10.173
78. Kuhl DE, Minoshima S, Fessler JA, Ficaro EP, Wieland DM, Koeppe RA, et al. *In vivo* mapping of cholinergic terminals in normal aging, Alzheimer's disease, and Parkinson's disease. *Ann Neurol*. (1996) 40:399–410. doi: 10.1002/ana.410400309
79. Antonini A, De Notaris R, Benti R, De Gaspari D, Pezzoli G. Perfusion ECD/SPECT in the characterization of cognitive deficits in Parkinson's disease. *Neurol Sci*. (2001) 22:45–6. doi: 10.1007/s100720170039
80. Nobili F, Abbruzzese G, Morbelli S, Marchese R, Girtler N, Dessi B, et al. Amnestic mild cognitive impairment in Parkinson's disease: a brain perfusion SPECT study. *Mov Disord*. (2009) 24:414–21. doi: 10.1002/mds.22381
81. Borghammer P, Van Den Berge N. Brain-first versus gut-first Parkinson's Disease: A hypothesis. *J Parkinson's Dis*. (2019) 9:S281–95. doi: 10.3233/JPD-191721.
82. Braak H, Del Tredici K, Rüb U, De Vos RA, Steur EN, Braak E. Staging of brain pathology related to sporadic Parkinson's disease. *Neurobiol Aging*. (2003) 24:197–211. doi: 10.1016/S0197-4580(02)00065-9
83. Shi M, Huber BR, Zhang J. Biomarkers for cognitive impairment in Parkinson disease. *Brain Pathol*. (2010) 20:660–71. doi: 10.1111/j.1750-3639.2009.00370.x
84. Hanna-Pladdy B, Gullapalli R, Chen H. Functional magnetic resonance imaging biomarkers predicting cognitive progression in Parkinson Disease: protocol for a Prospective Longitudinal Cohort Study. *JMIR Res Protoc*. (2019) 8:e12870. doi: 10.2196/12870

Conflict of Interest: The authors declare that the study was performed in the absence of commercial or financial relationships that could be construed as a potential conflict of interest.

Copyright © 2020 Sasikumar and Strafella. This is an open-access article distributed under the terms of the Creative Commons Attribution License (CC BY). The use, distribution or reproduction in other forums is permitted, provided the original author(s) and the copyright owner(s) are credited and that the original publication in this journal is cited, in accordance with accepted academic practice. No use, distribution or reproduction is permitted which does not comply with these terms.

frontiers in Neurology

ORIGINAL RESEARCH
published: 31 January 2020
doi: 10.3389/fneur.2020.00028

Changed Resting-State Brain Signal in Parkinson's Patients With Mild Depression

*Min Wang[1], Haiyan Liao[1], Qin Shen[1], Sainan Cai[1], Hongchun Zhang[2], Yijuan Xiang[1], Siyu Liu[1], Tianyu Wang[1], Yuheng Zi[1], Zhenni Mao[1] and Changlian Tan[1]**

[1] Department of Radiology, The Second Xiangya Hospital, Central South University, Changsha, China, [2] Department of Radiology, The First Affiliated Hospital, University of Science and Technology of China, Changsha, China

Background: Depression is reported to occur 5–10 years early than the onset of motor symptoms in Parkinson (PD) patients. However, markers for early diagnosis of PD in individuals with sub-clinical depression still remain to be identified.

Purpose: This study utilized Regional Homogeneity (ReHo) to investigate the alterations in resting state brain activities in Parkinson (PD) patients with different degrees of depression.

Methods: Twenty non-depressed PD patients, twenty mild to moderately depressed PD patients, and thirteen severely depressed PD patients were recruited. Hamilton Depression Scale (HDS) and the Beck Depression Inventory (BDI) were assessed depression. Resting-state functional magnetic resonance imaging (rs-MRI) was analyzed with ReHo.

Results: PD patients with mild to moderate depression had decreased ReHo in the left dorsal anterior cingulate cortex when compared with PD patients without depression. PD patients with severe depression exhibited increased ReHo in the left inferior prefrontal gyrus and right orbitofrontal area when compared with PD patients with mild to moderate depression. ReHo values in the bilateral supplementary motor area (SMA) in PD patients with severe depression was also increased when compared with PD patients without depression.

Conclusions: This study suggests that rs-MRI with ReHo analysis can detect early changes in brain function that associate with depression in PD patients, which could be biomarkers for early diagnosis and treatment of PD related depression.

Keywords: parkinson's diseases, mild depression, early treatment, regional homogeneity, resting-states, functional MRI

OPEN ACCESS

Edited by:
Yu Zhang,
VA Palo Alto Health Care System, United States

Reviewed by:
Xiangyu Long,
University of Calgary, Canada
Chien-Han Lai,
National Yang-Ming University, Taiwan

***Correspondence:**
Changlian Tan
tanchanglian@csu.edu.cn

Specialty section:
This article was submitted to Applied Neuroimaging, a section of the journal Frontiers in Neurology

Received: *06 September 2019*
Accepted: *09 January 2020*
Published: *31 January 2020*

Citation:
Wang M, Liao H, Shen Q, Cai S, Zhang H, Xiang Y, Liu S, Wang T, Zi Y, Mao Z and Tan C (2020) Changed Resting-State Brain Signal in Parkinson's Patients With Mild Depression. Front. Neurol. 11:28. doi: 10.3389/fneur.2020.00028

INTRODUCTION

Parkinson's disease (PD) is a common degenerative disease of the central nervous system with an incidence only secondary to Alzheimer's disease (1). Approximately 2% of people over 65 years old and 3% of people over 80 years old suffer from PD (2). It is predicted that the incidence and prevalence of PD will be twice as high as now by 2030 (3). Clinical symptoms of PD include motor symptoms and non-motor symptoms, but its treatments mainly focus on the motor symptoms.

However, more and more studies found that non-motor symptoms often appeared several years or even decades before motor symptoms in PD patients (4), suggesting that these non-motor symptoms may be possible the signs for predicting PD occurrence. Among those non-motor symptoms, depression is the most common symptoms with a rate of 30–40% (5). A retrospective study in 32,415 Netherlanders demonstrated that depressive symptoms occurred 10 years in average before the motor symptoms in PD (6). A study in Americans revealed that depression was diagnosed about 5 years before motor symptoms in PD (7). In addition, tricyclic antidepressants can effectively treat PD-related depression, which can also subsequently delay the progression of PD disease (8). Reichmann's review proposed that it is not the depression to cause PD, but rather that a common pathology, such as the impairment and malfunction of dopaminergic, noradrenergic, and serotonergic systems, leads to depression, and motor symptoms sequentially (9). A previous study found that PD patients with mild depressive symptoms were six times more at risk to develop moderate to severe depressive symptoms than PD patients without depressive symptoms (10, 11). We therefore, hypothesize that a comparative study in PD patients with different degrees of depression may identify markers for the early detection of PD.

PD is thought to cause depletion of dopamine in the frontal and limbic systems. However, selective abnormalities in dopamine and other neurotransmitters in the limbic system were observed in PD patients with depression relative to PD patients without depression (12). Abnormalities in functional connectivity in the prefronto-limbic system (13) and structures in the prefrontal lobe, limbic system, and temporal lobe (14) were reported to be associated with depression in PD patients. Therefore, detecting the brain structural alterations in PD patients with depression may find markers for early diagnosis of PD. Functional magnetic resonance imaging (functional MRI, fMRI) is a non-invasive functional imaging technique that can detect changes in blood-oxygen-level-dependent (BOLD) signals. The fMRI includes a task state and a resting state for data acquisition and analysis. Resting-state functional MRI (R-fMRI) reflects the spontaneous neuronal activity. The data collected in the resting state is relatively stable, easy to obtain, and is therefore widely used in the study of brain function. Regional homogeneity (ReHo) refers to the similarity of BOLD signal changes of adjacent voxels in the same time series (15). The increase in ReHo indicates an increase in the consistency of neuronal activity in the local brain region (16). Previous studies with ReHo demonstrated that neural activity in the resting state is changed in multiple brain regions of PD patients (17–20). A study compared ReHo between PD patients with depression and PD patients without depression and found that PD patients with depression exhibited significant increases of ReHo in the left middle frontal gyrus and right inferior frontal gyrus, and decreases of ReHo in the left amygdala and bilateral lingual gyrus (21). Thus, a specific alteration in rs-MRI with ReHo analysis in PD patients with mild depression may be used as a marker for early diagnosis or prediction of PD.

This study investigated the alterations in resting state brain activities using ReHo in PD patients with different degrees of depression and non-depression.

MATERIALS AND METHODS

Subjects

The patients with Parkinson's disease were recruited from the Department of Neurology, the Second Xiangya Hospital of Central South University from December 2015 to October 2018. Patients were diagnosed according to the British Brain Bank PD diagnostic criteria. PD patients were divided into PD without depression (ndPD, $n = 20$, 9 females), PD with mild to moderate depression (mdPD, $n = 20$, 8 females), and PD with severe depression (sdPD, $n = 13$, 7 females) according to the Hamilton Depression Scale (version 17) and the Beck Depression Inventory (BDI). In the ndPD group, the Hamilton score was <7 while BDI was <10; in the mdPD group, the Hamilton score was between 17 and 24 points while the BDI was between 10 and 25; and in the sdPD group, the Hamilton score was more than 24 while the BDI was more than 25. The demographic and clinical data of all participants are shown in **Table 1**.

This study was approved by the Medical Ethics Committee of the Second Xiangya Hospital, Central South University. All subjects enrolled in the study were voluntarily involved in the study after fully understanding the risks, research purposes, etc. The signed informed consents were obtained from the subjects or their guardians.

Inclusion Criteria

Patients were included in the study if (1) they complied with the diagnosis of PD in the British Brain Bank PD diagnostic criteria; (2) were right handed; (3) had no dementia; and (4) their clinical data were available and they can finish MRI examination.

Exclusion Criteria

Patients were excluded from the study if (1) they had unsuitable or contraindicated MRI examinations; (2) they had claustrophobia; (3) they felt discomfort during MRI examination, and cannot continue to complete the examination; (4) they had a history of long-term alcohol abuse or other histories of drug abuse; (5) they had a definite cause for depression, and (6) they were left handed.

Two experienced neurological physicians collected all subjects' age, gender, medical history, and course of the disease with exact consistency. They also recorded the patient's Hoehn-Yahr grading according to the nervous system. A two-way random model was then used to calculate the intraclass correlation coefficient of Hoehn-Yahr grading. It was 0.961 ($P < 0.001$), suggesting an absolute consistency between two physicians. All patients completed the Parkinson's disease rating scale (UPDRS), the BDI, the Hamilton Depression Scale, and the Mini-mental state examination (MMSE) survey.

Scanning Parameters

The scanning session was performed at the Radiology Department of Second Xiangya Hospital, Central South

TABLE 1 | Demographics and clinical details (mean ± SD).

	ndPD	mdPD	sdPD	*P* value		
				mdPD vs.ndPD	sdPD vs.mdPD	sdPD vs.ndPD
Gender(male/female)	11/9	12/8	6/7			
Age (year)	58.40 ± 6.96	60.55 ± 7.21	63.92 ± 10.57	0.403	0.246	0.060
Duration of disease(month)	28.35 ± 18.98	34.50 ± 33.07	29.00 ± 22.24	0.456	0.554	0.994
UPDRS	43.10 ± 4.94	42.42 ± 7.1	50.46 ± 8.40	0.889	0.002	0.004
H-Y	1.62 ± 0.64	1.62 ± 0.80	1.88 ± 0.68	1.000	0.317	0.317
HAMD	3.15 ± 1.69	18.70 ± 1.45	29.84 ± 3.46	< 0.001	< 0.001	< 0.001
BDI	6.40 ± 2.28	16.95 ± 5.09	33.00 ± 5.88	< 0.001	< 0.001	< 0.001
MMSE	27.30 ± 2.65	25.70 ± 3.93	22.15 ± 4.54	0.175	0.009	< 0.001

PD, Parkinson's disease; ndPD, PD without depression; mdPD, PD with mild and moderate depression; sdPD, nPD with severe depression; UPDRS, Unified Parkinson's Disease Rating Scale; HAMD, the Hamilton Depression Scale; BDI, the Beck Depression Inventory; MMSE, Minimum Mental State Examination; H-Y, Hoehn & Yahr stage.

University, on a SIEMENS 3.0 T scanner. A total of 580 T2- weighted EPI scans were acquired during the entire functional run (TR = 2,500 ms, TE = 25 ms, FA = 90°, FOV = 240 × 240 mm, 39 axial slices, slice thickness 3.50 mm, no gap). Two more dummy scans were acquired before each run to allow the fMRI signal to reach a steady state. Before the functional run, an anatomical volume consisting of T2-weighted MPRAGE scans with the high spatial resolution was also acquired.

MRI and Data Analysis

RS-fMRI images were preprocessed using the toolboxes data processing assistant for resting-state functional MR imaging (DPARSF; http://www.restfmri.net/forum/DPARSF) through an RS-fMRI data analysis toolkit (REST1.8; http://www.restfmri.net) running on MATLAB R2010a (Mathworks). The first ten volumes of the functional images were discarded.

The imaging data were preprocessed by slice timing, realignment, co-registration to individual structural T1 scan, segmentation into gray matter (GM), white matter (WM), and cerebrospinal fluid (CSF), as well as spatial normalization to Montreal Neurological Institute coordinates (MNI) space using the normalization parameters estimated in DARTEL, with a resampling voxel size of 3 mm × 3 mm × 3 mm. A temporal filter (0.01–0.08 Hz) was used to decrease the effect of low-frequency drifts and physiological high-frequency noise. The linear trends were then removed. Finally, the generated images were spatially smoothed with a 6 mm full-width at half- maximum (FWHM) Gaussian kernel after ReHo analysis.

ReHo analysis was performed in DPARSF software. ReHo maps of each subject were obtained on a voxel-wise basis by calculating Kendall's coefficient of concordance (KCC) between the time series of a given voxel and those of its nearest neighboring 26 voxels (15). The greater ReHo value of a given voxel means the higher degree of localized temporal synchronization within a neighboring cluster. Then, the voxel ReHo was divided by the average ReHo value of the entire brain in each subject for the purpose of standardization.

Statistical Analysis

Statistical analyses were conducted with SPSS 20.0 statistical analysis software (SPSS Inc. Chicago, IL, USA). The significant threshold was set to $p = 0.05$. The one-way analysis of covariance (ANCOVA) was used to compare the differences between ReHo values and other demographic data among the three groups. The significant differences were set at $p < 0.05$ (with a combined threshold of $p < 0.05$ and a minimum cluster size of 26 voxels), corrected by the AlphaSim program in the REST Software. A two-sample post hoc *t*-test was performed between each pair of the three groups.

RESULTS

There were no significant differences in gender, age, and duration of disease between the three groups. Additionally, head motion caused no significant differences between those patients ($p > 0.05$). There were significant differences in Unified Parkinson's Disease Rating Scale and Minimum Mental State Examination between sdPD and mdPD groups as well as between sdPD and ndPD groups. There were significant differences in the Hamilton Depression scores and BDI scores between any two groups among the three groups (**Table 1**).

mdPD patients showed decreased ReHo values in the left dorsal anterior cingulate cortex when compared with ndPD patients (**Figure 1**). sdPD patients showed significant increased ReHo values in the inferior prefrontal gyrus and right orbitofrontal area when compared to mdPD patients (**Figure 2**). sdPD patients showed increased ReHo in the bilateral supplementary motor area (SMA) when compared with ndPD patients (**Figure 3** and **Table 2**).

DISCUSSIONS

Depression is thought not only a non-motor symptom of PD, but also a predictive marker for the occurrence of PD in its early stage. This study found that PD patients with mild to moderate depression had a reduced ReHo value in the dorsal anterior cingulate gyrus of the left cerebral hemisphere compared with PD patients without depression. Also, PD patients with severe

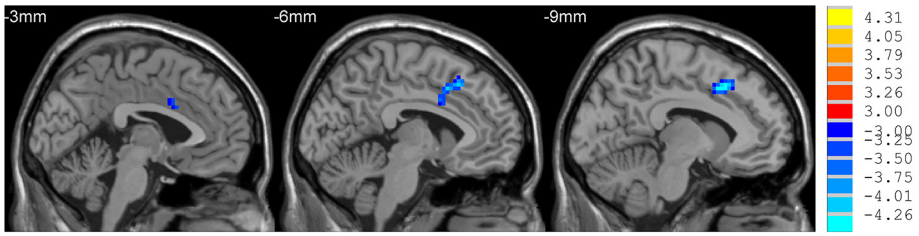


FIGURE 1 | Comparison of ReHo between mdPD and ndPD group. There was a decrease in ReHo value in the left dorsal anterior cingulate cortex in PD patients with mild to moderate depression ($P < 0.05$).

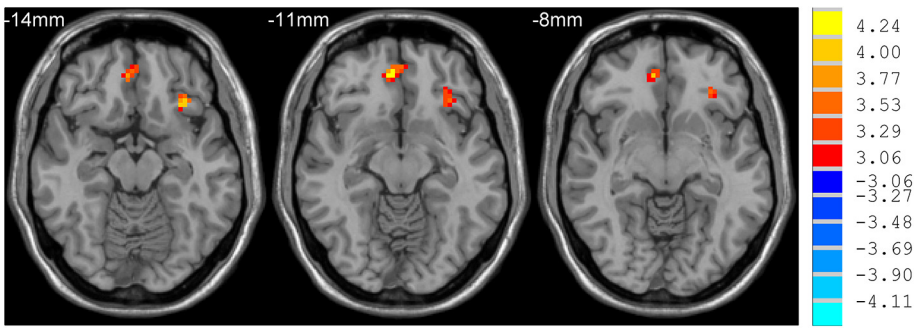


FIGURE 2 | Comparison of ReHo between sdPD and mdPD group. There was an increase of ReHo value in the left inferior prefrontal gyrus and right orbitofrontal area in PD patients with severe depression ($P < 0.05$).

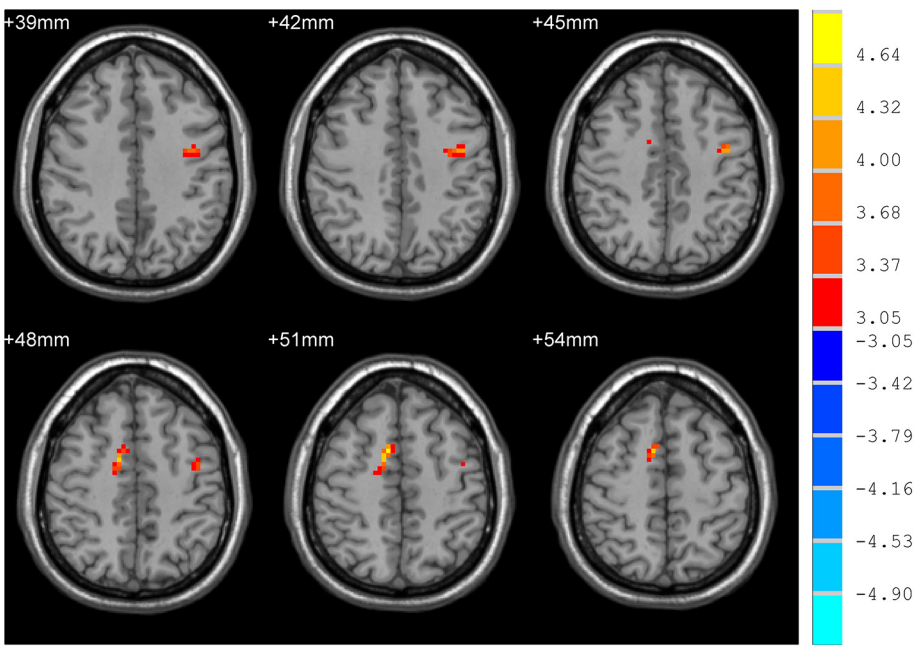


FIGURE 3 | Comparison of ReHo between sdPD and ndPD group. There was an increase of ReHo values in the bilateral supplementary motor area in PD patients with severe depression ($P < 0.05$).

depression had an increased ReHo value in the left inferior frontal gyrus (Brodmann 47) and right temporal gyrus (Brodmann 11) compared with PD patients with mild to moderate depression, as well as an increased ReHo value in the bilateral assisted motor zone (SMA) compared with PD patients without depression. Thus, this study suggests that rs-MRI with ReHo analysis may provide imaging marker for early diagnosis and prediction of PD in patients with sub-clinical depression.

TABLE 2 | Brain regions showing ReHo differences among groups.

Brodmann Area	Brain regions	Cluster size (voxles)	Peak T values	Peak Coordinates in MNI		
				X	Y	Z
mdPD-ndPD						
32	DPFC-L	41	−4.5075	−9	15	42
sdPD-mdPD						
47	IPG-L	39	4.1459	−33	27	15
11	OFA-R	28	4.4753	9	45	−12
sdPD-ndPD						
6	SMA-R	38	4.9573	9	6	51
6	SMA-L	30	4.2223	−39	−6	42

PD, Parkinson's disease; ndPD, PD without depression; mdPD, PD with mild and moderate depression; sdPD, PD with severe depression; DPFC-L, left dorsolateral prefrontal cortex; IPG-L, left inferior prefrontal gyrus; OFA-R, right orbitofrontal area, SMA-R, right supplementary motor area, SMA-L, left supplementary motor area.

The cingulate cortex is not only a vital hub in the default network, but also a critical hub in the limbic system. A previous study using resting-state fMRI and seed-based functional connectivity analysis revealed an increased functional connectivity between the ventral tegmental area and anterior cingulate cortex in depressed PD patients relative to healthy controls and non-depressed PD patients. Also, this aberrant connectivity correlated with the severity of depression in PD patients (16). Wang et al. study also observed degree centrality abnormalities in the anterior cingulate cortices in depressed PD patients compared to non-depressed PD patients (17). Skidmore et al. reported that the severity of depression in PD patients was positively correlated with the ALFF signal of the cingulate gyrus (22). In this study, we found a decreased ReHo value in the left dorsal anterior cingulate cortex of Parkinson patients with mild to moderate depression when compared with non-depressed PD patients. Thus, our study confirmed the involvement of the cingulate cortex in the depression of PD patients.

The prefrontal cortex includes the Brodmann Area 47 and 11. A meta-analysis revealed that repetitive transcranial magnetic stimulation over the prefrontal cortex exhibited a significant anti-depressive effect in PD patients (23). A SPECT study showed that the perfusion in the right medial orbitofrontal cortex was reduced in the depressed PD patients as compared with non-depressed PD patients (24). Sheng et al. study with ReHo and FC methods found that PD patients with depression had increased regional activity in the left frontal and medial frontal gyrus when compared with non-depressed PD patients. Brain network connectivity analysis demonstrated that the function of the prefrontal-limbic system was significantly weakened in depressed PD patients (21). Hu et al. study found that the connection of the left cingulate band back to the posterior cingulate gyrus, the anterior frontal lobes, the prefrontal lobes, and the inferior frontal gyrus was significantly enhanced in depressed PD patients compared to non-depressed PD patients (25). Our study also found that PD patients with severe depression had increased ReHo values in the left inferior prefrontal gyrus and right orbitofrontal area compared with patients with mild to moderate depression.

The supplementary motor area (SMA), the posterior third of the medial aspect of superior frontal gyrus, is involved in self-initiated motor movements, planning, and sequencing the motor action, response inhibition, and bimanual movements. A randomized, double-blind, sham-controlled, multi-center study revealed that the 1-Hz repetitive transcranial magnetic stimulation over the SMA was effective for improving the motor symptoms in PD (26). However, whether the SMA is associated with PD related depression remains to be further studied. In this study, we found that PD patients with severe depression had increased ReHo values in the bilateral SMA compared to PD without depression.

In our study, depressed PD patients had abnormal ReHo values both in the cingulate cortex and the orbitofrontal area. Luo et al. study with a resting-state functional MRI demonstrated that PD with depression showed significantly higher ALFF value in the left orbitofrontal area, which positively correlates with the scores of Hamilton Depression Rating Scale (27). However, Skidmore et al. study explored the relationships between depression and ALFF in patients with PD, and found that the severity of depression positively correlates with ALFF value in the right cingulate cortex (23). Our study suggests that it may also be associated with abnormal brain regions at different stages of depression in PD patients.

We acknowledge several limitations of the current study. First, the sample size in this study is relatively small and further studies from multiple centers with large sample size may provide more reliable conclusions. Second, although there was no statistical difference in the ages between three groups of PD patients, there was subtle difference. This may implicate that the effects of age were not completely ruled out. Third, this study used a combination of two scales to determine the degree of depression in Parkinson's patients. Patients with inconsistent grading of the two scales were not included in the study. This may have a bias.

In conclusion, PD patients with and without depression have different abnormal brain areas; PD patients with different degrees of depression have different abnormal brain regions; and rs-MRI with ReHo analysis may provide imaging evidence as markers for early diagnosis and prediction of PD in patients with sub-clinical depression.

DATA AVAILABILITY STATEMENT

The raw data supporting the conclusions of this article will be made available by the authors, without undue reservation, to any qualified researcher.

ETHICS STATEMENT

The studies involving human participants were reviewed and approved by the Medical Ethics Committee of the Second Xiangya Hospital, Central South University. The

patients/participants provided their written informed consent to participate in this study.

AUTHOR CONTRIBUTIONS

MW, HL, QS, YZ, and ZM: data collection. MW, HL, QS, SC, HZ, YX, SL, TW, YZ, and ZM: data collection and data analysis. MW and HL: manuscript writing. CT: project development and manuscript revising. All authors: read and approved the final manuscript.

FUNDING

This study was supported by the National Natural Science Foundation of China (No. 81471646).

ACKNOWLEDGMENTS

We would like to thank the patients as volunteers for participating in this study.

REFERENCES

1. Aaseth J, Dusek P, Roos PM. Prevention of progression in Parkinson's disease. *Biometals*. (2018) 31:737–47. doi: 10.1007/s10534-018-0131-5
2. Tysnes OB, Storstein A. Epidemiology of Parkinson's disease. *J Neural Trans*. (2017) 124:901–5. doi: 10.1007/s00702-017-1686-y
3. Lee A, Gilbert RM. Epidemiology of Parkinson disease. *Neurol clin*. (2016) 34:955–65. doi: 10.1016/j.ncl.2016.06.012
4. Haehner A, Hummel T, Hummel C, Sommer U, Junghanns S, Reichmann H. Olfactory loss may be a first sign of idiopathic Parkinson's disease. *Mov Disord*. (2007) 22:839–42. doi: 10.1002/mds.21413
5. Aarsland D, Pahlhagen S, Ballard CG, Ehrt U, Svenningsson P. Depression in Parkinson disease–epidemiology, mechanisms and management. *Nat Rev Neurol*. (2011) 8:35–47. doi: 10.1038/nrneurol.2011.189
6. Leentjens AF, Van den Akker M, Metsemakers JF, Lousberg R, Verhey FR. Higher incidence of depression preceding the onset of Parkinson's disease: a register study. *Mov Disord*. (2003) 18:414–18. doi: 10.1002/mds.10387
7. Jacob EI, Gatto NM, Thompson A, Bordelon Y, Ritz B. Occurrence of depression and anxietyy prior to Parkinson's disease. *Park Relat Disord*. (2010) 16:576–81. doi: 10.1016/j.parkreldis.2010.06.014
8. Paumier KL, Siderowf AD, Auinger P, Oakes D, Madhavan L, Espay AJ, et al. Tricyclic antidepressants delay the need for dopaminergic therapy in early Parkinson's disease. *Mov Disord*. (2012) 27:880–77. doi: 10.1002/mds.24978
9. Reichmann H. Premotor diagnosis of Parkinson's disease. *Neurosci Bull*. (2017) 33:526–34. doi: 10.1007/s12264-017-0159-5
10. Ravina B, Elm J, Camicioli R, Como PG, Marsh L, Jankovic J, et al. The course of depressive symptoms in early Parkinson's disease. *Mov Disord*. (2009) 24:1306–11. doi: 10.1002/mds.22572
11. Iranzo A, Serradell M, Vilaseca I, Valldeoriola F, Salamero M, Molina C, et al. Longitudinal assessment of olfactory function in idiopathic REM sleep behavior disorder. *Parkinsonism Relat Disord*. (2013) 19:600–4. doi: 10.1016/j.parkreldis.2013.02.009
12. Remy P, Doder M, Lees A, Turjanski N, Brooks D. Depression in Parkinson's disease: loss of dopamine and noradrenaline innervation in the limbic system. *Brain*. (2005) 128:1314–22. doi: 10.1093/brain/awh445
13. Wu JY, Zhang Y, Wu WB, Hu G, Xu Y. Impaired long contact white matter fibers integrity is related to depression in Parkinson's disease. *CNS Neurosci Ther*. (2018) 24:108–14. doi: 10.1111/cns.12778
14. Chagas MH, Linares IM, Garcia GJ, Hallak JE, Tumas V, Crippa JA. Neuroimaging of depression in Parkinson's disease: a review. *Int sychogeriatr*. (2013) 25:1953–61. doi: 10.1017/S1041610213001427
15. Zang Y, Jiang T, Lu Y, He Y, Tian L. Regional homogeneity approach to fMRI data analysis. *Neuroimage*. (2004) 22:394–400. doi: 10.1016/j.neuroimage.2003.12.030
16. Zhu Y, Gao H, Tong L, Li Z, Wang L, Zhang C, Yang Q, Yan B. Emotion regulation of hippocampus using real-time fMRI neurofeedback in healthy human. *Front Hum Neurosci*. (2019) 13:242. doi: 10.3389/fnhum.2019.00242
17. Wu T, Long X, Zang Y, Wang L, Hallett M, Li K, Chan P. Regional homogeneity changes in patients with Parkinson's disease. *Hum Brain Mapp*. (2009) 30:1502–10. doi: 10.1002/hbm.20622
18. Yang H, Zhou XJ, Zhang MM, Zheng XN, Zhao YL, Wang J. Changes in spontaneous brain activity in early Parkinson's disease. *Neurosci Lett*. (2013) 549:24–8. doi: 10.1016/j.neulet.2013.05.080
19. Choe IH, Yeo S, Chung KC, Kim SH, Lim S. Decreased and increased cerebral regional homogeneity in early Parkinson's disease. *Brain Res*. (2013) 1527:230–7. doi: 10.1016/j.brainres.2013.06.027
20. Li Y, Liang P, Jia X, Li K. Abnormal regional homogeneity in Parkinson's disease: a resting state fMRI study. *Clin Radiol*. (2016) 71:e28-34. doi: 10.1016/j.crad.2015.10.006
21. Sheng K, Fang W, Su M, Li R, Zou D, Han Y, Wang X, Cheng O. Altered spontaneous brain activity in patients with Parkinson's disease accompanied by depressive symptoms, as revealed by regional homogeneity and functional connectivity in the prefrontal-limbic system. *PLoS ONE*. (2014) 9:e84705. doi: 10.1371/journal.pone.0084705
22. Skidmore FM, Yang M, Baxter L, von Deneen K, Collingwood J, He G, et al. Apathy, depression, and motor symptoms have distinct and separable resting activity patterns in idiopathic Parkinson disease. *Neuroimage*. (2013) 81:484–95. doi: 10.1016/j.neuroimage.2011.07.012
23. Zhou L, Guo Z, Xing G, Peng H, Cai M, Chen H, et al. Antidepressant effects of repetitive transcranial magnetic stimulation over prefrontal cortex of parkinson's disease patients with depression: a meta-analysis. *Front Psychiatr*. (2018) 9:769. doi: 10.3389/fpsyt.2018.00769
24. Kim YD, Jeong HS, Song IU, Chung YA, Namgung E, Kim YD. Brain perfusion alterations in depressed patients with Parkinson's disease. *Annal Nucl Med*. (2016) 30:731–7. doi: 10.1007/s12149-016-1119-2
25. Hu X, Song X, Li E, Liu J, Yuan Y, Liu W, et al. Altered resting-state brain activity and connectivity in depressed Parkinson's disease. *PLoS ONE*. (2015) 10:e0131133. doi: 10.1371/journal.pone.0131133
26. Shirota Y, Ohtsu H, Hamada M, Enomoto H, Ugawa Y. Supplementary motor area stimulation for Parkinson disease: a randomized controlled study. *Neurology*. (2013) 80:1400–5. doi: 10.1212/WNL.0b013e31828c2f66
27. Luo C, Chen Q, Song W, Chen K, Guo X, Yang J, et al. Resting-state fMRI study on drug-naive patients with Parkinson's disease and with depression. *J Neurol Neurosurg Psychiatry*. (2014) 85:675–83. doi: 10.1136/jnnp-2013-306237

Conflict of Interest: The authors declare that the research was conducted in the absence of any commercial or financial relationships that could be construed as a potential conflict of interest.

Copyright © 2020 Wang, Liao, Shen, Cai, Zhang, Xiang, Liu, Wang, Zi, Mao and Tan. This is an open-access article distributed under the terms of the Creative Commons Attribution License (CC BY). The use, distribution or reproduction in other forums is permitted, provided the original author(s) and the copyright owner(s) are credited and that the original publication in this journal is cited, in accordance with accepted academic practice. No use, distribution or reproduction is permitted which does not comply with these terms.

frontiers in Neurology

ORIGINAL RESEARCH
published: 17 April 2020
doi: 10.3389/fneur.2020.00252

Diffusion Kurtosis Imaging of Microstructural Changes in Gray Matter Nucleus in Parkinson Disease

Gao Bingbing[1†], Zhou Yujing[1†], Miao Yanwei[1], Dong Chunbo[1*], Wang Weiwei[1], Tian Shiyun[1], Liu Yangyingqiu[1], Shang Jin[1], Song Qingwei[1], Liu Ailian[1] and Xie Lizhi[2]*

[1] Department of Radiology, First Affiliated Hospital of Dalian Medical University, Dalian, China, [2] GE Healthcare, MR Research, Beijing, China

Objective: To explore the microstructural damage of extrapyramidal system gray matter nuclei in Parkinson disease (PD) using diffusion kurtosis imaging (DKI).

Materials and Methods: We enrolled 35 clinically confirmed PD patients and 23 healthy volunteers. All patients underwent MR examination with conventional MRI scan sequences and an additional DKI sequence. We subsequently reconstructed the DKI raw images and analyzed the data. A radiologist in our hospital collected the Mini-Mental State Examination (MMSE) score of all subjects.

Results: In the PD group, the mean kurtosis and axial kurtosis level decreased in the red nucleus (RN) and thalamus; the radial kurtosis increased in the substantia nigra (SN) and globus pallidus (GP). Fractional anisotropy decreased in the putamen. The largest area under the ROC curve of mean diffusion in GP was 0.811. Most kurtosis parameters demonstrated a positive correlation with the MMSE score, while several diffusion parameters showed a negative correlation with the same.

Conclusion: DKI can qualitatively distinguish PD from healthy controls; furthermore, DKI-derived parameters can quantitatively evaluate the modifications of microstructures in extrapyramidal system gray matter nucleus in PD.

Keywords: parkinson disease, diffusion magnetic resonance imaging, gray matter, extrapyramidal tracts, neurodegenerative diseases

OPEN ACCESS

Edited by:
Yu Zhang,
VA Palo Alto Health Care System, United States

Reviewed by:
Masaaki Hori,
Toho University, Japan
Brian Hansen,
Aarhus University, Denmark

****Correspondence:***
Miao Yanwei
ywmiao716@163.com
Dong Chunbo
dcb101@sina.com

† These authors have contributed equally to this work

Specialty section:
This article was submitted to Applied Neuroimaging, a section of the journal Frontiers in Neurology

Received: *07 November 2019*
Accepted: *17 March 2020*
Published: *17 April 2020*

Citation:
Bingbing G, Yujing Z, Yanwei M, Chunbo D, Weiwei W, Shiyun T, Yangyingqiu L, Jin S, Qingwei S, Ailian L and Lizhi X (2020) Diffusion Kurtosis Imaging of Microstructural Changes in Gray Matter Nucleus in Parkinson Disease. Front. Neurol. 11:252. doi: 10.3389/fneur.2020.00252

INTRODUCTION

Parkinson disease (PD) is the second most common neurodegenerative disease. Clinical diagnosis of PD is based on motor symptoms and signs including rest tremor, bradykinesia, rigidity and postural instability, and several variations of clinical scales. However, these symptoms are not particularly exclusive to PD, considering the fact that a number of other diseases have similar symptoms or atypical parkinsonian disorders. Due to this, the early diagnosis of PD is particularly difficult in clinical settings. This issue can be addressed by radiologists, by exploring the structural and functional changes in the brain of PD patients via various MR protocols. A previous study reported that neurons projecting from lateral nigra to posterior dorsal putamen were most severely affected by Lewy body pathology in PD (1). Volumetric analysis of basal ganglia nuclei and SN in patients with PD revealed tissue atrophy at the cortical, basal ganglia, and brainstem (particularly the SN and red nucleus, RN) levels (2); furthermore, the motor nerve conduction

among these were divided into the pyramidal and extrapyramidal systems. Pathophysiology and pathology of PD demonstrated that the diminution of the brainstem is attributed to the neurotic breakdown and necrosis in SN, which indicated the existence of microstructural changes inside the nucleus. Pathological studies also reported the presence of neurotic changes at levels of the cortex and basal ganglia (2). We hypothesized that there must be a connection inside the nuclei of the extrapyramidal system. Diffusion kurtosis imaging (DKI) offers improved sensitivity to tissue microstructure (3), which may be considered as an advantage over diffusion tensor imaging (DTI) (4). The basal ganglia and brainstem can be visualized in the DKI images (5). We aimed to investigate microstructural changes of extrapyramidal system nuclei in PD patients and its association with the disease progression, and to explore the connection of nuclei exchange between the levels of the basal ganglia and brainstem.

MATERIALS AND METHODS

Subjects

The prospective study was approved by local ethics committee, and each participant provided written consent. We enrolled 35 clinical diagnosed PD patients hospitalized in our hospital, along with 23 sex- and age-matched healthy controls (HC). PD was diagnosed based on the criteria provided by UK Parkinson Disease Society Brain Bank. The criteria also included the absolute exclusion criteria of PD, resulting in the exclusion of patients with hypertension and diabetes. The exclusion criteria for those in the HC group were history of surgery, cardiovascular disease, hypertension, diabetes, and other chronic diseases. The demographic and clinical data of the two groups are presented in **Table 1**. All patients and HC were right-handed. We assessed the Mini-Mental State Examination (MMSE) of all subjects; the MMSE score of all HC was above 27. Moreover, subjects with none or mild T2WI or T2 FLAIR high signal (Fazekas, grade 1) were considered normal. All subjects had no trauma, tumor, or a history of surgeries involving the central nervous system.

Images

Each subject underwent a GE Revolution CT scan of whole brain to exclude physiological or pathological calcification. All subjects underwent MR examination on a GE Signa HDxT 3.0 T MR scanner with a dedicated eight-channel head coil. The protocols included routine axial T1-, T2-, and diffusion kurtosis weighted images. DKI was obtained using an echo-planar imaging technique with b values of 0, 1,000, and 2,000 s/mm^2 in 15 directions. Parameters of each protocol are described in **Table 2**. Scan baseline was parallel to the line running through the anterior commissure and the posterior commissure. Scan area ranged from the foramen magnum to the cranial vault.

DKI Interpretation

Quantitative Assessment

Initial DKI images of all subjects were reconstructed on ADW4.4 workstation with Functool 2 software using all b values. The reconstructive images included mean kurtosis image (MK), axial kurtosis image (Ka), radial kurtosis image (Kr), mean diffusivity image (MD), axial diffusivity image (Da), radial diffusivity image (Dr), and fractional anisotropy image (FA), and the parameters were recorded as MK, Ka, Kr, MD, Da, Dr, and FA, respectively (**Supplementary Table 2**). Small round region of interest (ROI) was drawn with a diameter of 3 mm at the center of the maximum level of target nucleus (**Supplementary Figure 1**), which included RN, SN, thalamus (T), putamen (P), globus pallidus (GP), and the head of caudate nuclei (HCN). The ROIs were manually drawn by two neuroradiologists in the same manner. To improve intra-observer reliability, the neuroradiologists performed the same measurements for all subjects three times and average the results. To evaluate interobserver reliability, the intraclass correlation coefficients (ICCs) were calculated.

Statistical Analysis

Demographic variables and MMSE scores were compared using two-tailed t tests and chi-squared tests. ICC test was calculated to evaluate interobserver reliability prior to data analysis. The consequent analysis would be performed if ICC test returned a consistent result (i.e., ICC $\geq$ 0.75). The diffusion and kurtosis parameters of right and left deep gray matter structures were compared using two-sided Satterthwaite T test. Two independent-samples T tests or two-sample Mann–Whitney U tests were used to compare the parameters of six nuclei between two groups. We performed the receiver operating characteristic (ROC) test to assess the ability of distinguishing two groups for each DKI parameter of every nucleus. The correlations between DKI parameters and MMSE score were tested using Spearman's correlation test. All measurement data were presented as mean value and standard deviation. $P < 0.05$ was set to be statistically significant.

TABLE 1 | Clinical data of PD and HC groups.

	PD	HC
n	35	23
Age (years), mean ± SD	67.00 ± 8.76	66.48 ± 5.20
Sex (M/F)	18/17	12/11
MMSE (score), mean ± SD	22.91 ± 4.27	29.91 ± 0.42
Course (years)	3–10	—

All patients had been treated with dopamine agonists.

TABLE 2 | MRI protocol parameters.

Protocol	TR (ms)	TE (ms)	TI (ms)	Thick slices (mm)	Intersection (mm)	FOV (cm × cm)	Matrix size
T1WI	2,500	25	/	6	1	22.0 × 19.8	320 × 256
T2WI	5,000	118	/	6	1	22.0 × 19.8	320 × 256
T2 Flair	9,000	172	2250	6	1	22.0 × 22.0	256 × 192
DKI	10,000	107	/	4	0	24.0 × 24.0	128 × 128

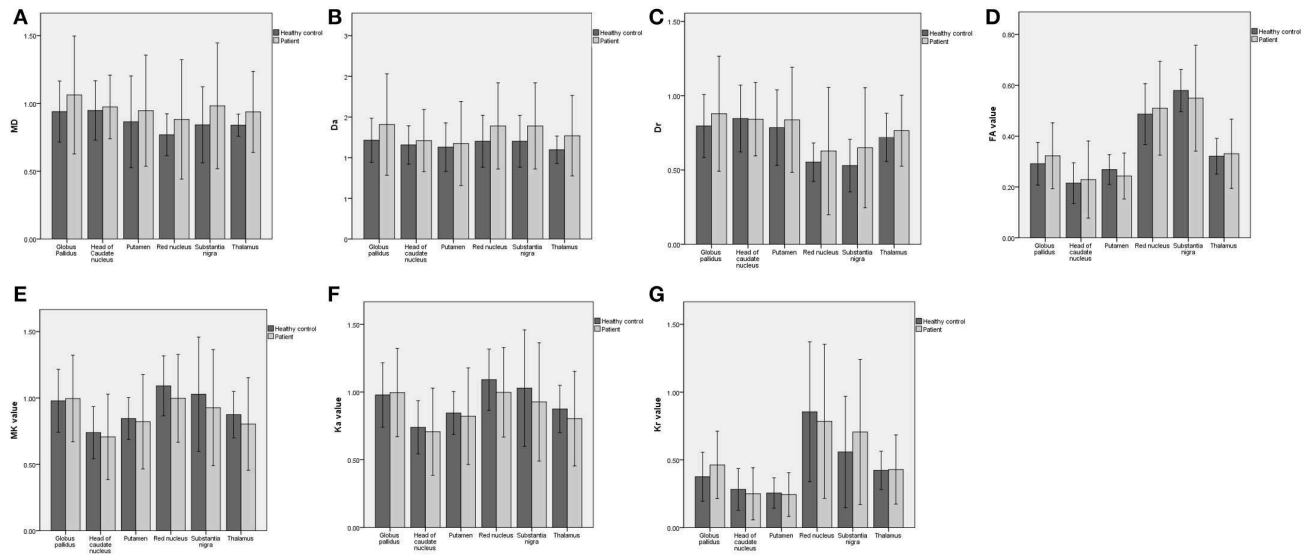


FIGURE 1 | Comparison of DKI parameters between PD and HC groups.

TABLE 3 | ROI analysis of DKI parameters of nuclei.

Nucleus	Parameter	Accuracy	Cutoff	Sensitivity	Specificity
GP	**MD**	**0.811**	**0.979**	**0.657**	**0.870**
RN	Da	0.796	1.285	0.686	0.783
SN	MD	0.775	0.900	0.714	0.826
GP	Da	0.763	1.450	0.457	**1.000**
SN	Da	0.742	1.560	0.714	0.826
SN	Dr	0.724	0.576	0.600	0.913
Putamen	MD	0.701	0.890	0.571	0.783

The bold values are statistically significant results.

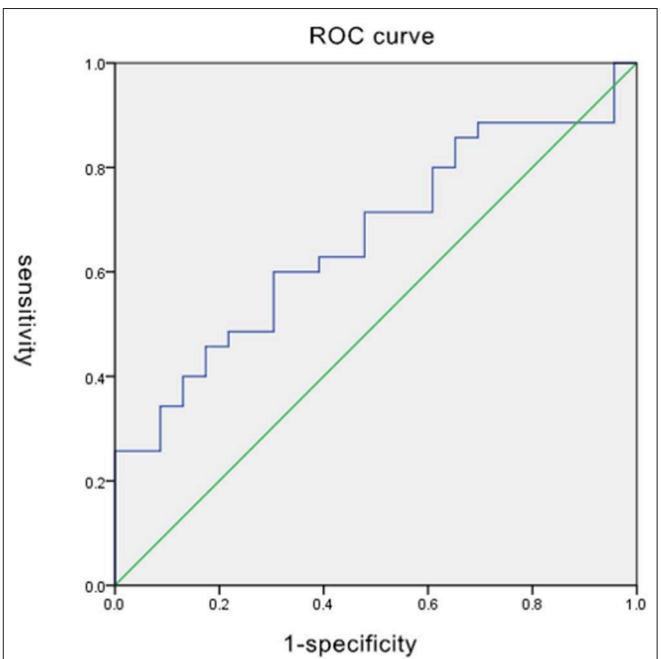


FIGURE 2 | Sensitivity and specificity of MD of GP.

RESULTS

Clinical Data

There were no observed significant differences between patient's age ($t = 0.284$, $P = 0.777$) and sex ($\chi^2 = 0.069$, $P = 0.793$) between the two groups. However, there was a significant intergroup difference in the MMSE score ($t = 7.807$, $P = 0.000$).

DKI Data

The ICC values of all ROIs were >0.75 (shown in **Supplementary Table 1**). The results did not show any lateral difference in any of MK, Ka, Kr, MD, Da, Dr, and FA of each nucleus for all subjects ($P > 0.05$). Comparison of all the derived parameters between groups is presented in **Figure 1**.

ROC Analysis

The largest area under ROC curve (AUC) value of 0.811 was observed for MD in GP. MD of GP had a sensitivity, specificity, and accuracy of 65.7% (23 out of 35), 87% (30 out of 35), and 81.1% (28 out of 35) when using a cutoff of 0.979 (shown in **Table 3** and **Figure 2**).

MMSE Score

The majority of the diffusion kurtosis parameters (MK, Ka, and Kr) demonstrated positive correlations with MMSE scores while the diffusion parameters exhibited several negative correlations (shown in **Tables 4**, **5** and **Figure 3**).

TABLE 4 | The positive correlation of kurtosis parameters and MMSE scores.

Score	Nucleus		MK value	Ka value	Kr value
MMSE	Substantia nigra	*r*	0.284	**0.389**	0.130
		P	0.098	**0.021**	0.456
	Globus pallidus	*r*	**0.428**	**0.458**	**0.340**
		P	**0.010**	**0.006**	**0.046**
	Red nucleus	*r*	**0.353**	**0.337**	0.210
		P	**0.038**	**0.048**	0.226

r refers to the correlation coefficient, P is 95% confidence (two-tailed).
The bold values are statistically significant results.

TABLE 5 | The negative correlation of diffusion parameters and MMSE scores.

Scores	Nucleus		MD value	Da value	Dr value
MMSE	Thalamus	*r*	**−0.408**	**−0.384**	−0.241
		P	**0.015**	**0.023**	0.163
	Head of caudate nucleus	*r*	**−0.369**	−0.280	**−0.340**
		P	**0.029**	0.104	**0.045**
	Red nucleus	*r*	−0.091	**−0.354**	−0.043
		P	0.602	**0.037**	0.805

r refers to the correlation coefficient, P is 95% confidence (two-tailed).
The bold values are statistically significant results.

DISCUSSION

DKI parameters provide a quantitative analysis of PD, and certain derived parameters offer novel diagnostic perspectives. A previous report revealed that DKI was highly sensitive to microstructural changes in tissue, which is not typically highlighted by the diffusion coefficient value (6). We observed statistical differences of DKI parameters between PD patients and HC, among which MD of GP was the best biomarker for diagnosis. It is well-recognized that DKI is sensitive to capture the "complexity" of tissue microstructure; thus, it has already been extensively used to probe microstructural changes in normal aging. The FA and MK of frontal lobe, temporal lobe, corpus callosum (knee and splenium), thalamus, posterior limb of internal capsule, and head of the caudate nucleus decreased with aging; however, there was an increase in the MD levels (7, 8). Another study by Latt, which focused on healthy adults across different age groups, observed that MK of thalamus, white matter of frontal lobe, knee of corpus callosum, and centrum semiovale were negatively linearly correlated with aging (9). Overall, a pattern of increased MD and radial and axial diffusivity, together with decreased FA, MK, and radial and axial kurtosis in GM, was found in normal aging (9–12). These age-related alterations may possibly be driven by mixed effects of axonal disintegration, cell loss, and iron accumulation. In our research, MD, Da, and Dr in some deep GM of PD group appeared to be higher than that of the HC group. However, a specific pattern of increased Kr in SN and GP was found in PD, which has the highest iron concentration in the brain in PD (13). Therefore, one probable interpretation of our result is excessive deposition of iron, neuronal degeneration, and apoptosis in SN and GP in PD patients, especially along the "radial" direction. We speculate that the alterations in diffusion metrics in PD may reflect both iron-related and age-related microstructure changes, with a leading factor by the former. This idea is supported by earlier research about effect of cocaine addiction and age on the microstructure of striatum and thalamus using DKI (14). Pathological studies of PD patients suggested that microstructural changes occur from brainstem at an early stage and subsequently spread to the limbic system and the cortices (15, 16). Therefore, the goal of this present study was to assess the microstructural changes in extrapyramidal system and to elucidate its associations.

Diffusion and Kurtosis Parameters

Here, three diffusion parameters of the PD group appeared to be higher than that of the HC group. Studies have reported the presence of heterogeneous pathological encephalatrophy of brain in PD patients; additionally, the earliest onset was demonstrated in the SN and was considered as the most vulnerable structure (16). It was proposed that the dilated intercellular space caused by neuronal degeneration and apoptosis could enhance water molecule movement. Furthermore, the remaining areas of gray matter in PD patients may also experience a similar degree of modification. Damage in the neurons of the brainstem will lead to an accumulation of the materials in synapses of the nerve fibers transporting nutrients from cerebrum downward to the brainstem, resulting in the deficiency of nutritious materials in fibers from the brainstem downward to the spine. Both consequences will lead to secondary damage to adjacent structures and increase membrane permeability to facilitate the diffusion of water molecules.

Diffusion kurtosis parameters were associated with the complexity of structures, which varied across the diverse brain structures in healthy adults. The observed decline in the diffusion kurtosis parameters and FA may be due to neuronal degeneration and apoptosis combined with secondary damage of adjacent structures. Microglial cells are the most significant immune cells of brain. They distribute heterogeneously in brain, with their highest intensity being in the SN. In the resting (physiological) state, microglial cells provide a certain extent of protection to the central nervous system. While in the activated (pathological) state, they may cause damage to central nervous system by secreting varieties of interleukins and cytokines that are closely related to inflammatory reactions and neuronal repair (17, 18). The pathological examination of PD demonstrated a large number of activated microglial cells in the SN, with an even higher intensity in the areas of neuronal degeneration (19, 20). In addition to neuronal damage in the brain of PD patients, the formation of Lewy body, accumulation of microglial cells, and repair of neurons enhanced the complexity of tissue structures and resulted in the increase of diffusion kurtosis parameters. Here, PD patients were not categorized into subtypes according to an early or late clinical period or in consideration of shorter or longer disease duration. The decrease observed in MK, Ka, and FA of deep GM may be attributed to neuronal damage. The

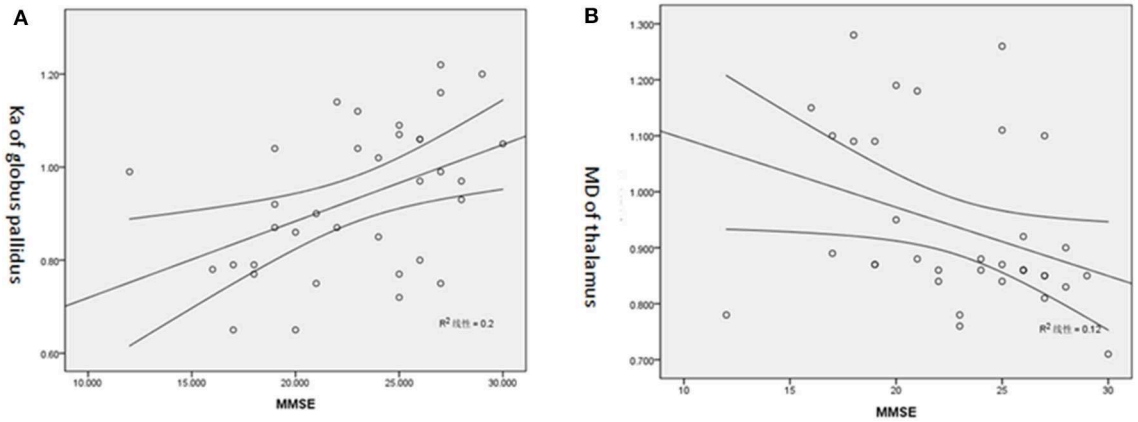


FIGURE 3 | (A) Positive correlation of Ka of GP and MMSE score. **(B)** Negative correlation of MD of T and MMSE score.

increase of Kr in SN and GP may be due to the dominating effect of neuronal repair in the region.

DKI is an extension of DTI, which could reflect microstructural complexity, particularly in isotropic tissues such as gray matter (10). Some research focused on gray matter seemed more concerned with the overall diffusional metrics of MK, FA, and MD, rather than directional metrics such as axial diffusivity and radial kurtosis. This is because the GM microstructure lacks evident directionality that the radial and axial directions will be random and highly influenced by noise (21). However, a variety of changed Kr, Dr, Ka, and Kr in GM continue to be reported in normal aging (9–12, 22), in Moyamoya Disease (23), in Bipolar Disorders (24), and in various neurodegenerative processes including Alzheimer's disease (25, 26) and Parkinson's disease (27, 28). In fact, some of the deep GMs are composed of both gray matter and white matter (10, 29). The caudate nucleus includes the associative fibers projecting to the prefrontal cortex. The putamen contains projecting fibers from the primary motor and premotor cortices. Different from the caudate nucleus and putamen, the globus pallidus is rich in long, smooth, and sparsely branched neuronal dendrites that are well-protected by myelin. The red nucleus consists of densely packed cells and small myelinated axons (12, 30). These findings may suggest that varying proportion of white matter in the deep GM make motion of water restricted and directional. Actually, anisotropic water diffusion depends on oriented barriers. The deep GM is composed primarily of neurons and glia, which also have the highest iron deposits in the brain (12, 31). The myelinated axons, large cells, and ferritin protein constitute a complex microstructure that imposed extensive hindrance to free diffusion of water molecules. Thus, diffusion metrics in the deep GM appears to be different and more complicated than that in white matter. The degeneration of nigrostriatal dopaminergic neurons in the substantia nigra (SN) is the neuropathologic hallmark of PD (28). One previous study using the PD mouse model indicates that Dr in the SN is related with the numbers of SN dopaminergic neurons (32). As interesting findings in directional diffusion metrics were observed in deep GM, we speculate that they are of potential significance in deep GM. However, their underlying pathophysiological meaning should be examined in further studies. In our study, all diffusion parameters including the directional ones were presented to provide a comprehensive view with potentially intriguing findings.

Diagnostic Efficiency of DKI Parameters

In our study, ROC analysis revealed that the MD for the globus pallidus had the best diagnostic performance. It is worth noting that, although the loss of dopaminergic neurons in the SN is the neuropathological hallmark in PD, the diffusion metric for the globus pallidus is the best biomarker to differentiate PD patients from HC. Globus pallidus is the most important relayed nucleus between striatum and subthalamic nuclei (STN) and plays an important role in the integration between inhibition from striatum and excitation from neocortex, thalamus, and STN (33). Changes in activity of neurotransmitters and related receptors along with abnormal synchronized oscillatory activity in the globus pallidus are associated with PD symptoms, such as bradykinesia, rigidity, and tremor, which reflects that globus pallidus plays an important role in the process of PD (34, 35). DBS researches have confirmed that stimulation of the globus pallidus is effective in reducing parkinsonian motor signs (36, 37). Among all the deep gray matter structures, globus pallidus has the relatively complex microstructural compositions and has the highest iron concentration in the brain (31). In summary, these results suggested that changed MD for the globus pallidus may reflect distinct pathological changes in PD. Future studies are needed to shed more light on the mechanisms underlying the changes in globus pallidus of patients with PD. Diffusivity parameters of RN and SN were useful; however, their sensitivity was not sufficiently high for clinical purposes. Alternatively, the diagnostic confidence was promoted with an accurate final diagnosis, considering that it is possible to employ these diagnostic parameters and that they may be applied in the form of assisted methods.

MMSE Score

The correlation between DKI parameters and MMSE in our subjects suggested that the changes in the microstructure detected by DKI corresponded to the psycho-neural state; therefore, further investigation of DKI may benefit PD patients with dementia. As discussed previously, when the neuron repair dominated a particular region, the damage to the central neural system was restrained. This indicated that the psycho-neural state would be better in cases with a higher MMSE score. Diffusivity parameters represent the severity of damage that occurs to the brain, with higher levels indicating greater damage and a lower MMSE score. Therefore, both diffusivity and kurtosis parameters work as independent biomarkers to assess the psycho-neural state of PD patients. It was of great importance to note that the kurtosis parameters correlating with MMSE was focused on GP, RN, and SN, which had the most complicated microstructural compositions (12). We speculate that microstructural "complexity" in GP, RN, and SN may be the basis of psycho-neural state in PD. Meanwhile, negative correlations with MMSE score were observed for axial, radial, and mean diffusivity of the thalamus and HCN in our study. The caudate nucleus and thalamus had a relatively simple microstructure, which were mostly constituted by neurons and glia (12). The diffusion parameters of these regions likely reflect the distribution of neuron cell bodies, synapses, and dendrites. This may suggest that the integrity of thalamus and HCN had potential correlation with the psycho-neural state in PD.

CONCLUSION

DKI can qualitatively distinguish PD from HC; furthermore, DKI-derived parameters can quantitatively evaluate the modifications of microstructures in extrapyramidal system gray matter nucleus in PD.

LIMITATIONS

One limitation of our study is that the spatial resolution is $1.875 \times 1.875 \times 4$ mm^3. This may yield imperfect reference values and is thus biased. Another limitation is that treatment medication is not taken into account, the impact of which may lead to distorted brain structure. This needs to be explored in a future study.

DATA AVAILABILITY STATEMENT

The raw data supporting the conclusions of this article will be made available by the authors, without undue reservation, to any qualified researcher.

ETHICS STATEMENT

The studies involving human participants were reviewed and approved by Ethics Committee of First Affiliated Hospital of Dalian Medical University. The patients/participants provided their written informed consent to participate in this study.

AUTHOR CONTRIBUTIONS

GB, MY, and LA conceived the study and participated in its design, data collection. TS, LY, and WW participated in statistical analysis, sketching ROI and drafting of the manuscript. SJ, SQ, and XL participated in image reconstruction and data analysis. ZY and DC participated in the manuscript revise, including statistical analysis. The authors read and approved the final manuscript.

FUNDING

This study was supported by the National Natural Science Foundation of China (81671646, 81801657).

ACKNOWLEDGMENTS

The authors are grateful to the Department of Radiology, First Affiliated Hospital of Dalian Medical University, for supporting this study. The authors thank all patients and healthy control volunteers who participated in this study.

SUPPLEMENTARY MATERIAL

The Supplementary Material for this article can be found online at: https://www.frontiersin.org/articles/10.3389/fneur.2020.00252/full#supplementary-material

REFERENCES

1. Hughes AJ, Ben-Shlomo Y, Daniel SE, Lees AJ. What features improve the accuracy of clinical diagnosis in Parkinson's disease: a clinicopathologic study. *Neurology*. (1992) (2001) 57:S34–8.
2. Geng DY, Li YX, Zee CS. Magnetic resonance imaging-based volumetric analysis of basal ganglia nuclei and substantia nigra in patients with Parkinson's disease. *Neurosurgery*. (2006) 58:256-62; discussion 256–62. doi: 10.1227/01.NEU.0000194845.19462.7B
3. Hansen B, Jespersen SN. Recent developments in fast kurtosis imaging. *Front Phys*. (2017) 5:40. doi: 10.3389/fphy.2017.00040
4. Kamagata K, Tomiyama H, Motoi Y, Kano M, Abe O, Ito K, et al. Diffusional kurtosis imaging of cingulate fibers in Parkinson disease: comparison with conventional diffusion tensor imaging. *Magnet Resonance Imaging*. (2013) 31:1501–6. doi: 10.1016/j.mri.2013.06.009
5. Kamagata K, Tomiyama K, Hatano T, Motoi Y, Abe O, Shimoji K, et al. A preliminary diffusional kurtosis imaging study of Parkinson disease: comparison with conventional diffusion tensor imaging. *Neuroradiology*. (2014) 56:251–8. doi: 10.1007/s00234-014-1327-1
6. Gloria C, Nie SD. Diffusion kurtosis imaging for diagnosis of Parkinson's disease: a novel software tool proposal. *J Xray Sci Technol*. (2017) 25:561–71.
7. Coutu JP, Chen JJ, Rosas HD, Salat DH. Non-Gaussian water diffusion in aging white matter. *Neurobiol Aging*. (2014) 35:1412–21. doi: 10.1016/j.neurobiolaging.2013.12.001

8. Billiet T, Vandenbulcke M, Mädler B, Peeters R, Dhollander T, Zhang H, et al. Age-related microstructural differences quantified using myelin water imaging and advanced diffusion MRI. *Neurobiol Aging.* (2015) 36:2107–21. doi: 10.1016/j.neurobiolaging.2015.02.029
9. Lätt J, Nilsson M, Wirestam R, Ståhlberg F, Karlsson N, Johansson M, et al. Regional values of diffusional kurtosis estimates in the healthy brain. *J Magnet Resonan Imaging.* (2013) 37:610–8. doi: 10.1002/jmri.23857
10. Wang Q, Xu X, Zhang M. Normal aging in the basal ganglia evaluated by eigenvalues of diffusion tensor imaging. *AJNR.* (2010) 31:516–20. doi: 10.3174/ajnr.A1862
11. Vaillancourt DE, Spraker MB, Prodoehl J, Zhou XJ, Little DM. Effects of aging on the ventral and dorsal substantia nigra using diffusion tensor imaging. *Neurobiol Aging.* (2012) 33:35–42. doi: 10.1016/j.neurobiolaging.2010.02.006
12. Gong NJ, Wong CS, Chan CC, Leung LM, Chu YC. Aging in deep gray matter and white matter revealed by diffusional kurtosis imaging. *Neurobiol Aging.* (2014) 35:2203–16. doi: 10.1016/j.neurobiolaging.2014.03.011
13. McDonald C, Gordon G, Hand A, Walker RW, Fisher JM. 200 years of parkinson's disease: what have we learnt from James Parkinson? *Age Ageing.* (2018) 47:209–14. doi: 10.1093/ageing/afx196
14. Garza-Villarreal EA, Chakravarty MM, Hansen B, Eskildsen SF, Devenyi GA, Castillo-Padilla D, et al. The effect of crack cocaine addiction and age on the microstructure and morphology of the human striatum and thalamus using shape analysis and fast diffusion kurtosis imaging. *Transl Psychiatr.* (2017) 7:e1122. doi: 10.1038/tp.2017.92
15. Hughes AJ, Daniel SE, Kilford L, Lees AJ. Accuracy of clinical diagnosis of idiopathic Parkinson's disease: a clinico-pathological study of 100 cases. *J Neurol Neurosurg Psychiatr.* (1992) 55:181–4. doi: 10.1136/jnnp.55.3.181
16. Goedert M, Spillantini MG, Del Tredici K, Braak H. 100 years of lewy pathology. *Nat Rev Neurol.* (2013) 9:13–24. doi: 10.1038/nrneurol.2012.242
17. Shimura H, Hattori N, Kubo Si, Mizuno Y, Asakawa S, Minoshima S, et al. Familial parkinson disease gene product, parkin, is a ubiquitin-protein ligase. *Nat Genet.* (2000) 25:302–5. doi: 10.1038/77060
18. Gorell JM, Ordidge RJ, Brown GG, Deniau JC, Buderer NM, Helpern JA. Increased iron-related MRI contrast in the substantia nigra in Parkinson's disease. *Neurology.* (1995) 45:1138–43. doi: 10.1212/WNL.45.6.1138
19. Koshimori Y, Ko JH, Mizrahi R, Rusjan P, Mabrouk R, Jacobs MF, et al. Imaging striatal microglial activation in patients with parkinson's disease. *PLoS ONE.* (2015) 10:e0138721. doi: 10.1371/journal.pone.0138721
20. Fan Z, Aman Y, Ahmed I, Chetelat G, Landeau B, Ray Chaudhuri K, et al. Influence of microglial activation on neuronal function in Alzheimer's and Parkinson's disease dementia. *Alzheim Dement.* (2015) 11:608–21.e7. doi: 10.1016/j.jalz.2014.06.016
21. Hansen B, Shemesh N, Jespersen SN. Fast imaging of mean, axial and radial diffusion kurtosis. *Neuroimage.* (2016) 142:381–93. doi: 10.1016/j.neuroimage.2016.08.022
22. Das SK, Wang JL, Bing L, Bhetuwal A, Yang HF. Regional values of diffusional kurtosis estimates in the healthy brain during normal aging. *Clin Neuroradiol.* (2017) 27:283–98. doi: 10.1007/s00062-015-0490-z
23. Qiao PG, Cheng X, Li GJ, Song P, Han C, Yang ZH. MR Diffusional kurtosis imaging-based assessment of brain microstructural changes in patients with moyamoya disease before and after revascularization. *AJNR.* (2020) 41:246–54. doi: 10.3174/ajnr.A6392
24. Zhao L, Wang Y, Jia Y, Zhong S, Sun Y, Zhou Z, et al. Microstructural abnormalities of basal ganglia and thalamus in bipolar and unipolar disorders: a diffusion kurtosis and perfusion imaging study. *Psychiatr Invest.* (2017) 14:471–82. doi: 10.4306/pi.2017.14.4.471
25. Falangola MF, Jensen JH, Tabesh A, Hu C, Deardorff RL, Babb JS, et al. Non-gaussian diffusion MRI assessment of brain microstructure in mild cognitive impairment and Alzheimer's disease. *Magnet Resonan Imag.* (2013) 31:840–6. doi: 10.1016/j.mri.2013.02.008
26. Gong NJ, Wong CS, Chan CC, Leung LM, Chu YC. Correlations between microstructural alterations and severity of cognitive deficiency in Alzheimer's disease and mild cognitive impairment: a diffusional kurtosis imaging study. *Magnet Resonan Imaging.* (2013) 31:688–94. doi: 10.1016/j.mri.2012.10.027
27. Nagae LM, Honce JM, Tanabe J, Shelton E, Sillau SH, Berman BD. Microstructural changes within the basal ganglia differ between parkinson disease subtypes. *Front Neuroanat.* (2016) 17:10. doi: 10.3389/fnana.2016.00017
28. Kamagata K, Zalesky A, Hatano T, Ueda R, Di Biase MA, Okuzumi A, et al. Gray matter abnormalities in idiopathic parkinson's disease: evaluation by diffusional kurtosis imaging and neurite orientation dispersion and density imaging. *Human Brain Mapp.* (2017) 38:3704–22. doi: 10.1002/hbm.23628
29. Si J, Chang L, Wang J, Zhang S, Yao Y, Zhang S, et al. Initial application of diffusional kurtosis imaging in evaluating brain development of healthy preterm infants. *PLoS ONE.* (2016) 11:e0154146. doi: 10.1371/journal.pone.0154146
30. Onodera S, Hicks TP. A comparative neuroanatomical study of the red nucleus of the cat, macaque and human. *PLoS ONE.* (2009) 4:e6623. doi: 10.1371/journal.pone.0006623
31. Haacke EM, Cheng NY, House MJ, Liu Q, Neelavalli J, Ogg RJ, et al. Imaging iron stores in the brain using magnetic resonance imaging. *Magnet Resonance Imaging.* (2005) 23:1–25. doi: 10.1016/j.mri.2004.10.001
32. Boska MD, Hasan KM, Kibuule D, Banerjee R, McIntyre E, Nelson JA, et al. Quantitative diffusion tensor imaging detects dopaminergic neuronal degeneration in a murine model of Parkinson's disease. *Neurobiol Dis.* (2007) 26:590–6. doi: 10.1016/j.nbd.2007.02.010
33. Langenecker SA, Briceno EM, Hamid NM, Nielson KA. An evaluation of distinct volumetric and functional MRI contributions toward understanding age and task performance: a study in the basal ganglia. *Brain Res.* (2007) 1135:58–68. doi: 10.1016/j.brainres.2006.11.068
34. Eusebio A, Brown P. Oscillatory activity in the basal ganglia. *Parkinson Related Disord.* (2007) S434–6. doi: 10.1016/S1353-8020(08)70044-0
35. Milosevic L, Gramer R, Kim TH, Algarni M, Fasano A, Kalia SK, et al. Modulation of inhibitory plasticity in basal ganglia output nuclei of patients with Parkinson's disease. *Neurobiol Dis.* (2019) 124:46–56. doi: 10.1016/j.nbd.2018.10.020
36. Follett KA, Weaver FM, Stern M, Hur K, Harris CL, Luo PM, et al. Pallidal versus subthalamic deep-brain stimulation for Parkinson's disease. *N Engl J Med.* (2010) 362:2077–91. doi: 10.1056/NEJMoa0907083
37. Fan SY, Wang KL, Hu W, Eisinger RS, Han A, Han CL, et al. Pallidal versus subthalamic nucleus deep brain stimulation for levodopa-induced dyskinesia. *Annals Clin Transl Neurol.* (2020) 7:59–68. doi: 10.1002/acn3.50961

Conflict of Interest: The authors declare that the research was conducted in the absence of any commercial or financial relationships that could be construed as a potential conflict of interest.

Copyright © 2020 Bingbing, Yujing, Yanwei, Chunbo, Weiwei, Shiyun, Yangyingqiu, Jin, Qingwei, Ailian and Lizhi. This is an open-access article distributed under the terms of the Creative Commons Attribution License (CC BY). The use, distribution or reproduction in other forums is permitted, provided the original author(s) and the copyright owner(s) are credited and that the original publication in this journal is cited, in accordance with accepted academic practice. No use, distribution or reproduction is permitted which does not comply with these terms.

frontiers in Neurology

HYPOTHESIS AND THEORY
published: 06 May 2020
doi: 10.3389/fneur.2020.00370

Dopamine Buffering Capacity Imaging: A Pharmacodynamic fMRI Method for Staging Parkinson Disease

Kevin J. Black[1,2]*, *Haley K. Acevedo*[1] *and Jonathan M. Koller*[1]

[1] Department of Psychiatry, Washington University in St. Louis, St. Louis, MO, United States, [2] Departments of Neurology, Radiology and Neuroscience, Washington University in St. Louis, St. Louis, MO, United States

We propose a novel pharmacological fMRI (phMRI) method for objectively quantifying disease severity in Parkinson disease (PD). It is based on the clinical observation that the benefit from a dose of levodopa wears off more quickly as PD progresses. Biologically this has been thought to represent decreased buffering capacity for dopamine as nigrostriatal cells die. Buffering capacity has been modeled based on clinical effects, but clinical measurements are influenced by confounding factors. The new method proposes to measure the effect objectively based on the timing of the known response of several brain regions to exogenous levodopa. Such responses are robust and can be quantified using perfusion MRI. Here we present simulation studies based on published clinical dose-response data and an intravenous levodopa infusion. Standard pharmacokinetic-pharmacodynamic methods were used to model the response. Then the effect site rate constant k_e was estimated from simulated response data plus Gaussian noise. Predicted time – effect curves sampled at times consistent with phMRI differ substantially based on clinical severity. Estimated k_e from noisy input data was recovered with good accuracy. These simulation results support the feasibility of levodopa phMRI hysteresis mapping to measure the severity of dopamine denervation objectively and simultaneously in all brain regions with a robust imaging response to exogenous levodopa.

Keywords: phMRI, drug discovery and development, pharmacological biomarkers, levodopa, pharmacodynamics, hysteresis, pharmacokinetic-pharmacodynamic modeling, ASL

OPEN ACCESS

Edited by:
Edward Ofori,
Arizona State University, United States

Reviewed by:
Konstantinos Kalafatakis,
University of Ioannina, Greece
Bo Gao,
Affiliated Hospital of Guizhou Medical University, China

***Correspondence:**
Kevin J. Black
kevin@wustl.edu

Specialty section:
This article was submitted to Applied Neuroimaging, a section of the journal Frontiers in Neurology

Received: *18 February 2020*
Accepted: *14 April 2020*
Published: *06 May 2020*

Citation:
Black KJ, Acevedo HK and Koller JM (2020) Dopamine Buffering Capacity Imaging: A Pharmacodynamic fMRI Method for Staging Parkinson Disease. Front. Neurol. 11:370. doi: 10.3389/fneur.2020.00370

INTRODUCTION

> *The intensity and duration of the effect after injection appear to correlate with the degree of akinesia, the action of* L-DOPA *lasting longer the less pronounced the akinesia.*
> —Hirschmann and Mayer (translated) (1).

Parkinson disease (PD) is characterized by progressive death of cells projecting from the substantia nigra to the striatum. One of the most important unmet needs in PD is to find objective, quantitative *in vivo* biomarkers of disease severity. Biomarkers of nigrostriatal denervation are sought for several important reasons, including as surrogate markers of disease progression in treatment trials (2, 3). Putative imaging biomarkers of disease progression include striatal

[^{18}F]fluorodopa PET or [^{123}I]ioflupane SPECT. Unfortunately, these techniques do not accurately quantify nigrostriatal cell loss (4). Presynaptic dopaminergic imaging of the midbrain does (5); nevertheless, alternative methods would be welcome.

Here we describe a novel potential biomarker, based on the common clinical observation that the benefit from a dose of levodopa wears off more quickly as PD progresses. Early in the course of disease, a small dose of levodopa provides benefit long after the plasma levodopa concentration has declined substantially from its peak. The body responds as if the levodopa in the plasma filled a reservoir and then slowly leaked out to produce benefit. With disease progression, even though the same amount of levodopa circulates in the blood, the benefit wears off much faster, as if the reservoir had become leakier. Biologically, the reservoir may represent the diminishing buffering capacity of ascending dopaminergic axons as midbrain dopamine neurons die off (6). This wearing off of benefit has been quantified by a mathematical model that postulates a central effect compartment (reservoir) whose concentration of levodopa directly determines the clinical benefit. The buffering capacity in this model can be characterized by a single number, the effect site rate constant k_e, which can be computed from serial measurements of both plasma concentration and clinical status (7). On average, patients with more severe PD and longer disease duration have a larger ("leakier") k_e when modeled this way (**Figure 1**) (8–13). In fact, k_e can be the strongest predictor of the kinetics of response to levodopa in PD (9, 12). Dopamine buffering capacity as measured by k_e also correlates significantly with nigrostriatal denervation as measured by DOPA uptake (14) or dopamine transporter imaging (15). Unfortunately, the clinical measurements used to determine k_e are influenced by confounding factors such as patient fatigue and motivation, which likely add variance to the measurement. A direct, objective brain measure of response to levodopa may reduce this added variance.

The effect of levodopa on the brain can be seen by measuring movement, but also by measuring regional cerebral blood flow (rCBF), reflecting regional brain activity (16–19). Crucially, using quantitative techniques, levodopa has no direct vascular effects after adequate carbidopa pretreatment (16–18). Levodopa's regional CBF effects reflect its regional effects on glucose metabolism and are prominent in pons and midbrain, thalamus, middle frontal gyrus, insula, putamen and cingulate cortex (17, 19). Drug effects on rCBF in PD can be quantified without ionizing radiation using arterial spin labeling (ASL) perfusion MRI (20–22). The midbrain rCBF response to levodopa is robust whether measured with [^{15}O]water PET (16–19) or with perfusion MRI (22).

Here we show, using simulated data based on published results in human PD patients, that quantifying dopamine buffering capacity k_e is likely to be feasible with existing technology.

METHODS

Pharmacokinetics

Measuring k_e with levodopa phMRI would be infeasible if one had to repeatedly image a subject until a dose of levodopa wore off completely, perhaps for several hours in early PD. Fortunately, with faster wearing-off as PD progresses, there is also faster "wearing-on" or onset of drug effect (10, 23–25). In fact, with a completely unrelated drug that also shows equilibration delay, giving the drug as a rapid intravenous (i.v.) infusion followed by a slow maintenance infusion allowed estimating the k_e just as precisely from the first 20 min of data as from 3½ h of data (7). Fortunately we have used exactly this approach to dose levodopa in PD: a fast i.v. loading dose followed by a slow maintenance infusion (26) (**Figure 2**). This infusion method allows us to transiently achieve plasma levodopa concentrations of 1,500–3,500 ng/mL, so we can measure k_e from both the rapid rise and fall of plasma levels.

For present purposes, likely time – concentration curves $C_p(t)$ in people with PD were taken from this infusion protocol, which aims to produce a steady-state levodopa concentration of 600 ng/ml, and consists of a 10-min loading dose at 0.6426

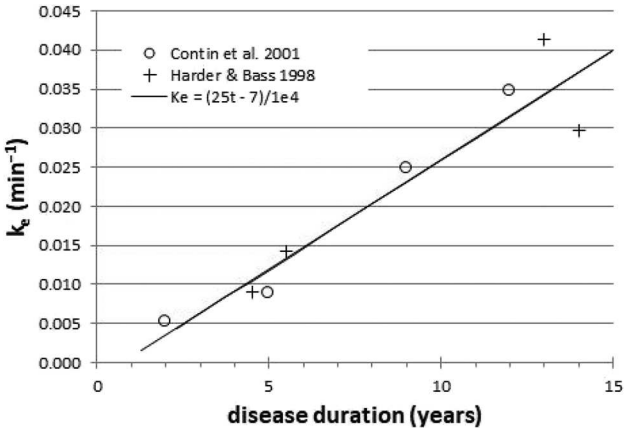


FIGURE 1 | Across groups of PD patients, k_e is a surrogate for disease duration ($r = 0.95$). Data redrawn from Harder and Baas (8) and Contin et al. (9).

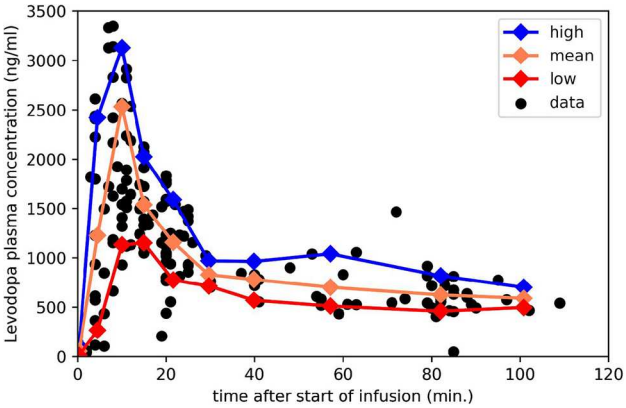


FIGURE 2 | Plasma levodopa concentrations in PD patients following the "final dose" intravenous infusion method in Black et al. (26). The 3 lines mark the mean, 90th and 10th percentile for samples collected in the corresponding intervals. Redrawn from data reported in Black et al. (26).

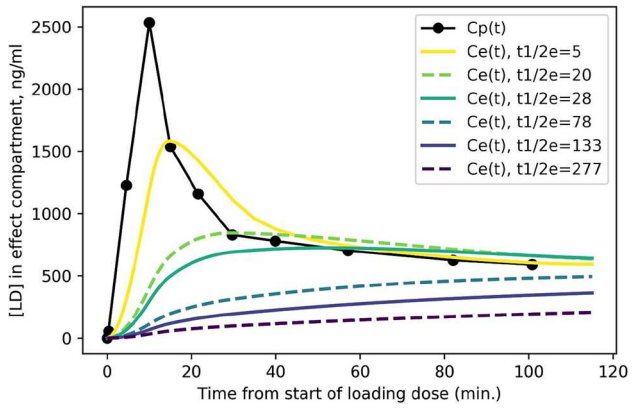


FIGURE 3 | Predicted levodopa concentration in the effect compartment at various disease severity levels. Curves are labeled by $t_{½e} = ln\ 2/k_e$ from more severe PD ($t_{½e}$ = 5 min.) to milder PD ($t_{½e}$ = 277 min.).

mg/kg followed by a maintenance infusion at 2.882×10^{-5} mg/kg/min × (140 yr–age)/yr (26). For a 65-year-old 70-kg person that means 45 mg over 10 min followed by 0.15 mg/min, for a total dose over 150 min of 66 mg. That i.v. dose is bioequivalent to 78 mg oral levodopa (27), though of course i.v. dosing leads to much higher transient peak plasma concentrations.

Using those data, we aggregated individual data points by time bins and plotted the mean, to estimate the most likely $C_p(t)$, and the 10th and 90th percentile, to deal with a range of metabolic rates in patients (**Figure 2**); see mpdp1.ipynb at https://bitbucket.org/kbmd/hysteresis). The NumPy and matplotlib libraries in Python were used for simulations and data visualization (Python Programming Language, RRID:SCR_008394; NumPy, RRID:SCR_008633; MatPlotLib, RRID:SCR_008624) (28, 29).

Modeling the Effect Compartment

Holford and Sheiner describe the theoretical background for the effect compartment model (30). A later paper by Sheiner's group simplifies the modeling with the assumption that $C_e = C_p$ at steady state, leading to the definition of the effect compartment concentration curve by the simpler differential equation $C_e' = k_e(C_p - C_e)$ (31).

If we use piecewise linear interpolation to estimate $C_p(t)$ between blood samples [as did Unadkat et al. (31)], C_e can be computed in closed form. We can write C_p as $C_p(t-t_i) = C_p(t_i) + m_i(t-t_i)$ on the interval $[t_i, t_{i+1}]$, where $m_i = [C_p(t_{i+1}) - C_p(t_i)]/[t_{i+1} - t_i]$. We need a value for the effect site concentration before the infusion starts, $C_e(t_0)$. For the purposes of this report, we can reasonably assume $C_e(t_0) = C_p(t_0)$, which will be approximately true if at the time of the first blood draw patients have refrained from taking oral levodopa for 8–10 h, since $t_{½e}$ is <5 h, and usually <2.5 h [see Table 4 in Contin et al. (9)].

The solution to this initial value problem is

$$C_e(t) = \left(C_p(t_i) - \frac{m_i}{k_e}\right) + m_i(t - t_i) + \left(C_e(t_i) - C_p(t_i) + \frac{m_i}{k_e}\right) e^{-k(t-t_i)}$$

defined on the interval $(t_i, t_{i+1}]$ (32).

Predicting Effect From Levodopa Concentrations in PD

To test this method, one needs to estimate a reasonable variety of time: effect curves in PD. Not only k_e but also the concentration–effect curve changes with disease severity. Contin et al. showed that a sigmoid E_{max} model reasonably fit the data from a wide range of PD severity (9). We adopt their measurements of EC_{50}, n (the Hill coefficient) and k_e for a variety of disease severity groups; namely, means for Hoehn and Yahr (33) stages I through IV in addition to the mildest and most severely affected individual subjects in the Contin et al. report (their Table 4). These parameters and the sigmoid E_{max} model are combined to create time–effect curves that we could expect from a brain region whose activity changes reliably with increased dopamine release in the brain with administration of exogenous levodopa. Note that the dopamine receptor may be "upstream" (e.g., posterior putamen) to the dopa-responsive region (e.g., motor cortex); dopamine receptors are not needed in the dopa-responsive region itself. The simulated data use a baseline CBF of 50 ml/hg/min and maximal effect was set at 35 ml/hg/min, consistent with a ∼70% rCBF increase in midbrain after a relatively large levodopa-carbidopa dose (22).

Adding Noise

The brain imaging time–effect curves assessed by any real brain imaging method will not be perfect, noise-free estimates, but will be contaminated by variability from biological or instrumentation issues. To test how well we can expect to recover k_e (and the other pharmacodynamic parameters) from a real experiment, we add noise to the simulated data described in the previous paragraph. We added Gaussian noise with a coefficient of variation (CoV) of 12.9%; this value was chosen based on the CoV in a cortical gray matter region across sixteen 34-s CBF images in 11 adults with PD scanned with a pCASL sequence while fixating a crosshair (unpublished data, K. J. Black and colleagues) (34, 35). For this study, all methods were carried out in accordance with relevant guidelines. The experimental protocol was approved by the Washington University Human Research Protection Office (ID # 201703122). All participants provided informed consent.

Parameter Estimation

We simultaneously estimated k_e, EC_{50}, and n from the data, given the model, using the lmfit package in Python (ampgo followed by emcee modules) (36).

Accuracy

The accuracy of the method was tested by comparing the estimated k_e to the input k_e. Secondary similar analyses were done for EC_{50} and n.

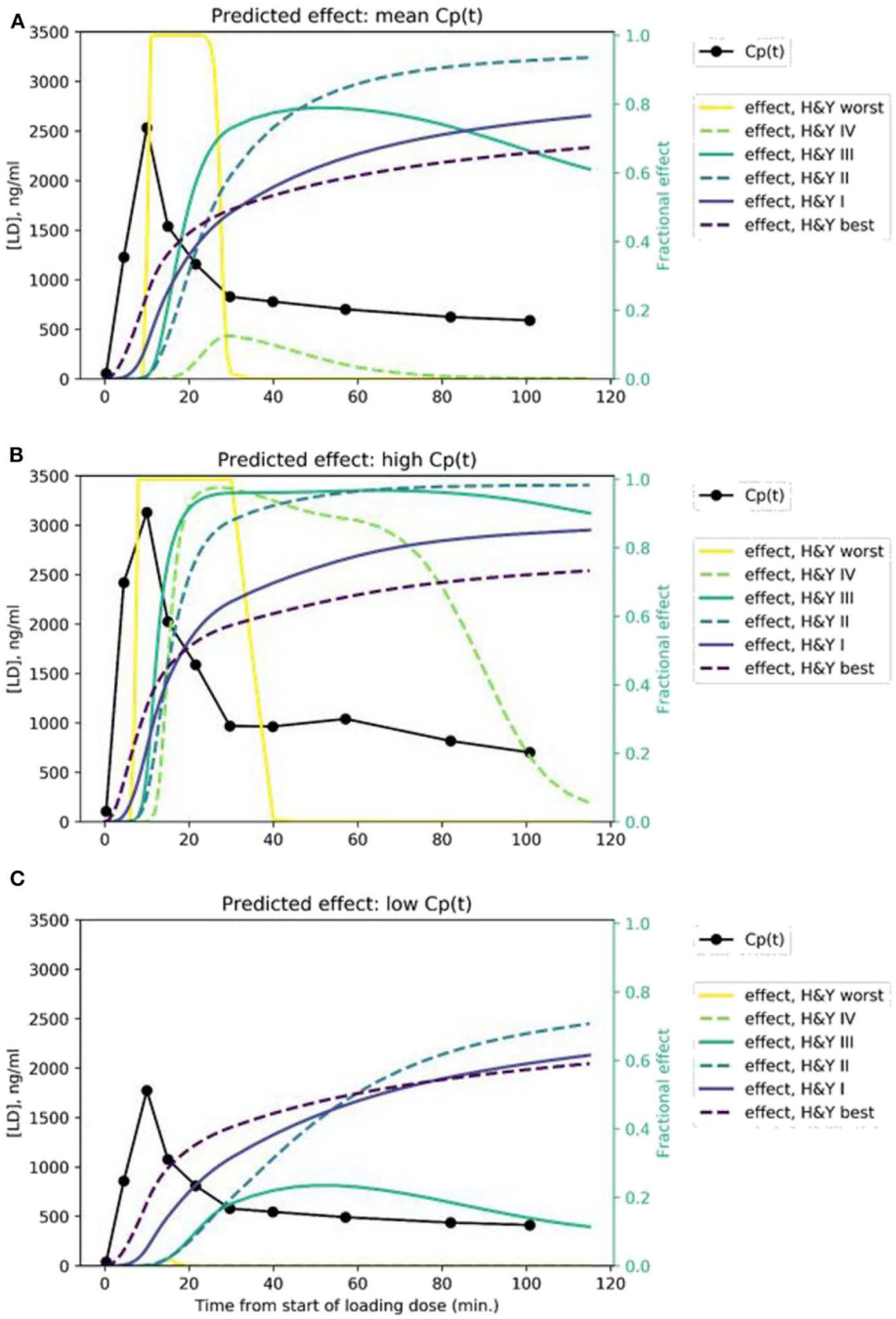


FIGURE 4 | Predicted time:effect curves at various disease severity levels assuming **(A)** mean, **(B)** high, and **(C)** low $C_p(t)$ in response to the levodopa infusion.

RESULTS

Predicted Levodopa Time: Concentration Curves in Effect Compartment

Figure 3 shows the expected concentration over time in the effect compartment, depending on the severity of PD. One can easily appreciate the faster exchange between plasma and the effect compartment when k_e is high (i.e., when the equilibration half-life $t_{½e}$ is short).

Time: Effect Curves by Disease Severity

We modeled the expected rCBF response in midbrain to the rapid i.v. infusion, based on published levodopa pharmacokinetics in PD (26) and published mean pharmacodynamic parameters for

Hoehn & Yahr stages I, II, III, and IV (8, 9). The predicted signals are quite distinct, assuming a typical $C_p(t)$ time:plasma curve (**Figure 4A**). If a given subject's pharmacokinetics produce higher plasma levels, the distinctions are still fairly clear (**Figure 4B**). Of course, if an individual's plasma levels are low, an effect may not be evident, especially in more severe PD (**Figure 4C**).

Accuracy

k_e estimated from time: effect curves in the presence of noise was generally accurate (**Figure 5**; see also **Supplementary Table 1**). More advanced disease led to more distinct predicted time–activity curves (see **Figure 4A**), reflected in more accurate results (**Figures 5A–C**).

Results were more accurate if the noise was reduced from a CoV of 12.9 to 5% (**Figures 5D–F**; see also **Supplementary Table 2**). Similar plots for EC_{50} and n are provided as **Supplementary Figures 1-2**.

In an attempt to improve further the accuracy, we examined the effect of spreading the levodopa infusion over twice the time. We hypothesized that the limited temporal resolution of the perfusion MR method, combined with the relatively small timing difference in onset of action in mild vs. very mild PD, limited discrimination at the milder end of the severity range. Results are shown in **Figure 6**. Similar plots for EC_{50} and n are provided as **Supplementary Figures 3, 4**.

DISCUSSION

We present a novel brain imaging method for objectively quantifying disease severity in Parkinson disease (PD), which we refer to as dopamine buffering capacity imaging, or more precisely, levodopa phMRI hysteresis mapping. The temporally distinct time: effect curves predicted in **Figure 4** suggest that even with some imperfection in the rCBF signal, we can expect to derive a reasonably accurate k_e for a brain region that responds to exogenous levodopa with a clear dose-response curve.

Demonstrating efficacy for potential disease-modifying therapies in PD has been difficult. Delayed start designs and similar approaches that rely on change in clinical severity over time require years to complete, large patient groups, and even then have not yet been successful (37). A validated biomarker would be of great value in improving this situation (2). The Michael J. Fox Foundation for Parkinson's Research designates "the identification, development and use of biomarkers to diagnose and track Parkinson's disease" as a priority area, noting that a successful biomarker "would mean better disease management for patients" and "improve and speed clinical development of disease-modifying therapies" (38). In simulated data based on published results and reasonable assumptions, levodopa phMRI hysteresis mapping appears likely to fill that need.

Of course one does not need an MRI machine to tell if a drug is improving movement in PD, and the present proposal draws on previous studies using pharmacokinetic-pharmacodynamic (PK-PD) modeling of tapping speed or UPDRS score response to levodopa challenge. However, the assessment of drug response using brain imaging is novel, and provides several potential advantages. The rCBF response is objective, rater-independent, and does not require subject movement. Furthermore, buffering capacity is measured simultaneously in all levodopa-responsive brain regions rather than just the motor system, potentially informing pathophysiological research on the increasingly

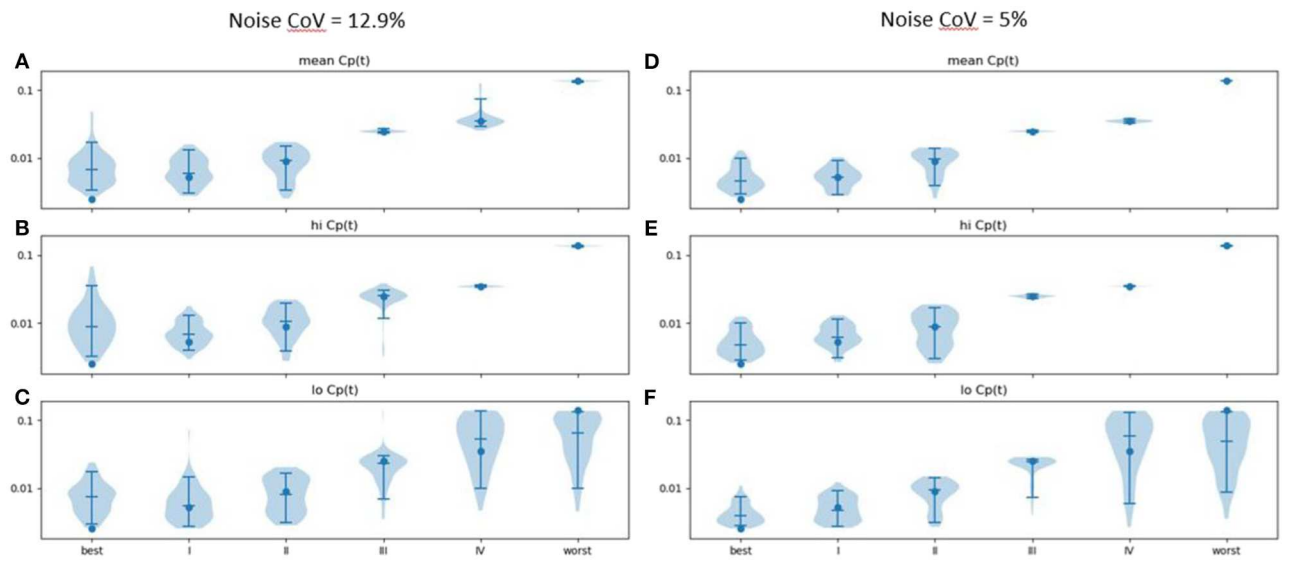


FIGURE 5 | Estimated k_e (vertical axis) across 100 sets of noise added to the time: effect curve computed for the k_e, EC_{50}, and n for various severities of PD as reported in Contin et al. (9) (horizontal axis), assuming **(A)** mean, **(B)** high and **(C)** low $C_p(t)$ in response to the levodopa infusion. Noise CoV = 12.9%. Width of plot is proportional to frequency of output of the given magnitude. Filled circle: input n. Horizontal lines note the 5, 50, and 95th percentiles. At right, similar results are shown for noise CoV = 5% for **(D)** mean, **(E)** high, and **(F)** low $C_p(t)$ responses to the LD infusion.

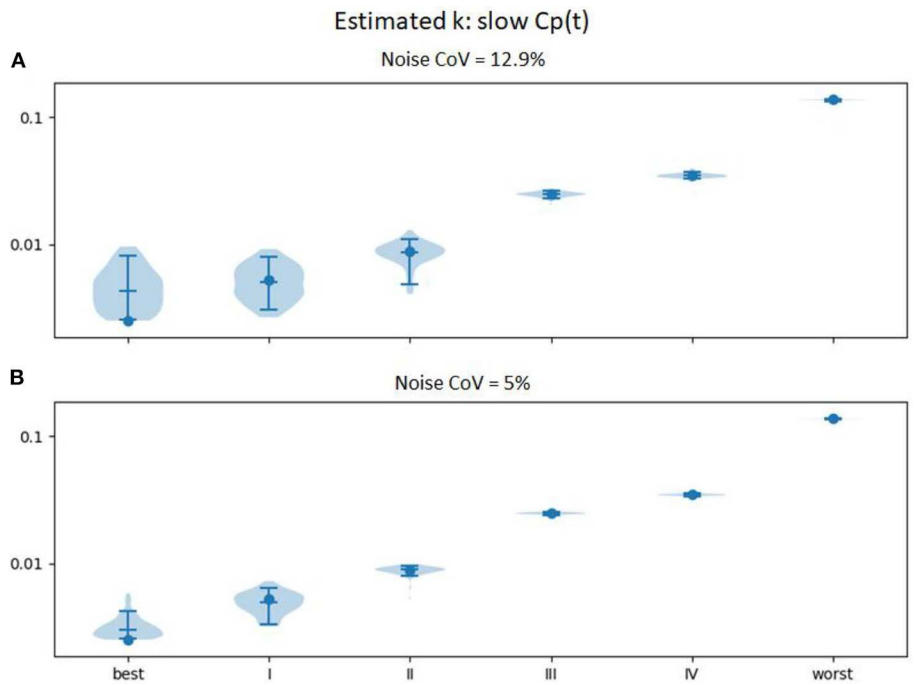


FIGURE 6 | Estimated k_e (vertical axis) across 100 sets of noise added to the time:effect curve computed for the k_e, EC_{50}, and n for various severities of PD as reported in Contin et al. (9) (horizontal axis), with $C_p(t)$ estimated for an levodopa infusion twice as long (at half the rate, so that the total infused dose is equivalent). **(A)** noise CoV = 12.9%; **(B)** noise CoV = 5%.

recognized non-motor symptoms of PD (39). The only assumption is that regional brain activity somewhere in the brain corresponds temporally to clinical severity.

Chan, Nutt, and Holford have subsequently extended the PK-PD model with the aim of better modeling long-term changes with disease progression in PD (40, 41). Their revised model includes factors intended to account for clinical observations like morning benefit and the long-duration response, and in their data k_e (reported as $T_{eqf} = ln\ 2/k_e$) did not change significantly over time. However, as they note, other factors could explain the difference in results, and their more complicated model was made possible by a very large set of longitudinal data. While the extended model may be ideal for optimal understanding of physiology from clinical PK-PD data, it is not essential for the present purpose of identifying a biomarker of nigrostriatal denervation in PD. In other words, if k_e as derived from the model we use correlates highly with disease severity, it will serve its intended purpose just fine.

Every step of this method has been proven individually: i.v. levodopa has been used safely for over 50 years (42); the infusion method described for the simulated data has been used in over 100 subjects [(20, 26) and Black et al. unpublished data]; levodopa concentration can be quantified accurately in plasma (43); the response to levodopa can be measured by ASL fMRI (20–22); midbrain has a robust rCBF response to single, clinically sensible doses of levodopa (16–19, 22), and software exists for estimating PK-PD parameters from fMRI data on a voxel-by-voxel or regional level (36, 44). In other words, every part of the method described here is well proven; it is their combination and interpretation as a disease severity measure that is novel.

Foreseeable Obstacles and Possible Solutions

Some potential difficulties in implementing dopamine buffering capacity imaging are foreseeable, but can be mitigated. These include a need for high temporal resolution, uncertain optimal dosing, head movement during MRI, and variable attention and alertness during the scans.

Temporal Resolution

Prior data showing robust rCBF responses to levodopa averaged data across a group and over several scans in the pre- and on-drug conditions, i.e., with a time resolution of about 30 min. Measuring dopamine buffering capacity in individual subjects pushes the envelope, requiring measuring response to levodopa in single subjects and at a time resolution of 1–2 min or better. Fortunately, current pCASL methods allow an unbiased whole-brain measure of blood flow in about 5–35 s. However, these images are statistically noisy. If estimated k_e proves less accurate with individual subject data than these simulations predict, additional information contained in the data may strengthen prediction of disease severity. Specifically, from the plasma levodopa concentration curve and the MRI response data one computes not only k_e but also EC_{50} and n, which also change with disease severity (9). Possibly combining all three parameter estimates may more accurately measure disease severity.

Optimal Dosing

Subjects with more advanced disease will show little response if they also happen to have low plasma levodopa levels. Solutions could include higher dosing for more severely affected individuals, though this choice could increase the risk of dyskinesias in the scanner that could affect comfort or head movement. Alternatively, if needed, one could estimate the optimal dose for each subject with, say, a single small test dose of i.v. levodopa with a pre- and post-drug blood sample, on a day prior to the scan day.

Head Movement

In our experience, most PD patients do well holding the head still during an MRI session. However, acquiring a single CBF image can take 6–34 s (34), an interval long enough that head movement on the scale of mm may be non-trivial. Participants with levodopa-induced dyskinesias may have additional head movement. Within-frame head movement adds to variance and may bias quantitative estimates. Solutions may include more rigid head fixation, shorter repetition times (TRs), prospective motion correction, or removing or underweighting CBF images compromised by movement (45).

Attention/Alertness

In initial pilot studies, we find that several factors combine to make continued alertness throughout the scan period difficult: PD patients often have insomnia, the scans are long and repetitive, and levodopa contributes to sleepiness. Solutions may include adding an attention task (though that will change resting brain activity), study staff repeatedly awakening the participant, or monitoring for alertness and removing or accounting statistically for frames during which the participant appears asleep.

Next Steps

The simplest first step to validating this method is correlative in nature. Specifically, one would enroll people with a wide variety of PD severity and compare regional k_e values, most likely in midbrain or posterior putamen, to clinical measures of disease severity such as off-period UPDRS scores (46). More definitive validation of dopamine buffering imaging may include longer-term or autopsy studies in patients, necropsy studies in animals with graded nigrostriatal lesions, or comparison to the recently validated midbrain [^{11}C]DTBZ PET approach (5). If these studies are successful, the dopamine buffering capacity imaging method will beg for further application as a surrogate marker of disease severity in PD.

DATA AVAILABILITY STATEMENT

The data generated for this study can be found with the code used to generate it, at [https://bitbucket.org/kbmd/hysteresis/].

ETHICS STATEMENT

The studies involving human participants were reviewed and approved by Washington University Human Research Protection Office. The patients/participants provided their written informed consent to participate in this study.

AUTHOR CONTRIBUTIONS

KB designed the study, generated the test data, and wrote the initial draft. HA and JK performed simulation testing and revised the text. All authors gave final approval for publication.

FUNDING

Supported in part by the National Institutes of Health (R01NS044598). Resting pCASL data acquisition was funded by the Michael J. Fox Foundation for Parkinson's Research and carried out in the East Building MIR Facility of the Washington University Medical Center. The funders had no role in study design, analysis, decision to publish, or preparation of the manuscript.

ACKNOWLEDGMENTS

Resting pCASL data acquisition used a sequence kindly supplied by Dr. Danny J. J. Wang. This manuscript has been released as a preprint at bioRxiv (47).

SUPPLEMENTARY MATERIAL

The Supplementary Material for this article can be found online at: https://www.frontiersin.org/articles/10.3389/fneur.2020.00370/full#supplementary-material

REFERENCES

1. Hirschmann J, Mayer K. Zur beeinflussung der akinese und anderer extrapyramidal-motorischer störungen mit L-dopa (L-dihydroxyphenylalanin) [on the control of akinesia and other extrapyramidal motor disorders with L-dopa (L-dihydroxyphenylalanine)]. *Dtsch Med Wochenschr.* (1964) 89:1877–80. doi: 10.1055/s-0028-1113210
2. Gwinn K, David KK, Swanson-Fischer C, Albin R, Hillaire-Clarke CS, Sieber B-A, et al. Parkinson's disease biomarkers: perspective from the NINDS Parkinson's disease biomarkers program. *Biomark Med.* (2017) 11:451–73. doi: 10.2217/bmm-2016-0370
3. Ryman SG, Poston KL. MRI biomarkers of motor and non-motor symptoms in Parkinson's disease. *Parkinson Relat Disord.* (2019) S1353-8020:30429–8. doi: 10.1016/j.parkreldis.2019.10.002
4. Karimi M, Tian L, Brown CA, Flores HP, Loftin SK, Videen TO, et al. Validation of nigrostriatal positron emission tomography measures: critical limits. *Ann Neurol.* (2013) 73:390–6. doi: 10.1002/ana.23798
5. Brown CA, Karimi MK, Tian L, Flores H, Su Y, Tabbal SD, et al. Validation of midbrain positron emission tomography measures for nigrostriatal neurons in macaques. *Ann Neurol.* (2013) 74:602–10. doi: 10.1002/ana.23939
6. Marsden CD, Parkes JD. "On-off" effects in patients with Parkinson's disease on chronic levodopa therapy. *Lancet.* (1976) 1:292–6. doi: 10.1016/S0140-6736(76)91416-1

7. Sheiner LB, Stanski DR, Vozeh S, Miller RD, Ham J. Simultaneous modeling of pharmacokinetics and pharmacodynamics: application to d-tubocurarine. *Clin Pharmacol Ther.* (1979) 25:358–71. doi: 10.1002/cpt197953358
8. Harder S, Baas H. Concentration-response relationship of levodopa in patients at different stages of Parkinson's disease. *Clin Pharmacol Ther.* (1998) 64:183–91. doi: 10.1016/S0009-9236(98)90152-7
9. Contin M, Riva R, Martinelli P, Albani F, Avoni P, Baruzzi A. Levodopa therapy monitoring in patients with Parkinson disease: a kinetic-dynamic approach. *Ther Drug Monit.* (2001) 23:621–29. doi: 10.1097/00007691-200112000-00005
10. Nutt JG, Woodward WR, Carter JH, Gancher ST. Effect of long-term therapy on the pharmacodynamics of levodopa. Relation to on-off phenomenon. *Arch Neurol.* (1992) 49:1123–30. doi: 10.1001/archneur.1992.00530350037016
11. Contin M, Riva R, Martinelli P, Cortelli P, Albani F, Baruzzi A. Longitudinal monitoring of the levodopa concentration-effect relationship in Parkinson's disease. *Neurology.* (1994) 44:1287–92. doi: 10.1212/WNL.44.7.1287
12. Nutt JG, Holford NH. The response to levodopa in Parkinson's disease: imposing pharmacological law and order. *Ann Neurol.* (1996) 39:561–73. doi: 10.1002/ana.410390504
13. Triggs EJ, Charles BG, Contin M, Martinelli P, Cortelli P, Riva R, et al. Population pharmacokinetics and pharmacodynamics of oral levodopa in Parkinsonian patients. *Eur J Clin Pharmacol.* (1996) 51:59–67. doi: 10.1007/s002280050161
14. Dietz M, Harder S, Graff J, Künig G, Vontobel P, Leenders KL, et al. Levodopa pharmacokinetic-pharmacodynamic modeling and 6-[^{18}F]levodopa positron emission tomography in patients with Parkinson's disease. *Clin Pharmacol Ther.* (2001) 70:33–41. doi: 10.1067/mcp.2001.116328
15. Contin M, Martinelli P, Riva R, Dondi M, Fanti S, Pettinato C, et al. Assessing dopaminergic function in Parkinson's disease: levodopa kinetic-dynamic modeling and SPECT. *J Neurol.* (2003) 250:1475–81. doi: 10.1007/s00415-003-0257-3
16. Hershey T, Black KJ, Stambuk MK, Carl JL, McGee-Minnich LA, Perlmutter JS. Altered thalamic response to levodopa in Parkinson's patients with dopa-induced dyskinesias. *Proc Natl Acad Sci USA.* (1998) 95:12016–21. doi: 10.1073/pnas.95.20.12016
17. Hershey T, Black KJ, Carl JL, Perlmutter JS. Dopa-induced blood flow responses in nonhuman primates. *Exp Neurol.* (2000) 166:342–9. doi: 10.1006/exnr.2000.7522
18. Hershey T, Black KJ, Carl JL, McGee-Minnich L, Snyder AZ, Perlmutter JS. Long term treatment and disease severity change brain responses to levodopa in Parkinson's disease. *J Neurol Neurosurg Psychiatry.* (2003) 74:844–51. doi: 10.1136/jnnp.74.7.844
19. Black KJ, Hershey T, Hartlein JM, Carl JL, Perlmutter JS. Levodopa challenge neuroimaging of levodopa-related mood fluctuations in Parkinson's disease. *Neuropsychopharmacology.* (2005) 30:590–601. doi: 10.1038/sj.npp.1300632
20. Black KJ, Koller JM, Campbell MC, Gusnard DA, Bandak SI. Quantification of indirect pathway inhibition by the adenosine A2a antagonist SYN115 in Parkinson disease. *J Neurosci.* (2010) 30:16284–92. doi: 10.1523/JNEUROSCI.2590-10.2010
21. Stewart SB, Koller JM, Campbell MC, Black KJ. Arterial spin labeling versus BOLD in direct challenge and drug-task interaction pharmacological fMRI. *PeerJ.* (2014) 2:e687. doi: 10.7717/peerj.687
22. Chen Y, Pressman P, Simuni T, Parrish TB, Gitelman DR. Effects of acute levodopa challenge on resting cerebral blood flow in Parkinson's disease patients assessed using pseudo-continuous arterial spin labeling. *PeerJ.* (2015) 3:e1381. doi: 10.7717/peerj.1381
23. Contin M, Riva R, Martinelli P, Procaccianti G, Cortelli P, Avoni P, et al. Response to a standard oral levodopa test in Parkinsonian patients with and without motor fluctuations. *Clin Neuropharmacol.* (1990) 13:19–28. doi: 10.1097/00002826-199002000-00002
24. Sohn YH, Metman LV, Bravi D, Linfante I, Aotsuka A, Mouradian MM, et al. Levodopa peak response time reflects severity of dopamine neuron loss in Parkinson's disease. *Neurology.* (1994) 44:755–7. doi: 10.1212/WNL.44.4.755
25. Nutt JG, Carter JH, Lea ES, Sexton GJ. Evolution of the response to levodopa during the first 4 years of therapy. *Ann Neurol.* (2002) 51:686–93. doi: 10.1002/ana.10189
26. Black KJ, Carl JL, Hartlein JM, Warren SL, Hershey T, Perlmutter JS. Rapid intravenous loading of levodopa for human research: clinical results. *J Neurosci Methods.* (2003) 127:19–29. doi: 10.1016/S0165-0270(03)00096-7
27. Robertson DR, Wood ND, Everest H, Monks K, Waller DG, Renwick AG, et al. The effect of age on the pharmacokinetics of levodopa administered alone and in the presence of carbidopa. *Br J Clin Pharmacol.* (1989) 28:61–9. doi: 10.1111/j.1365-2125.1989.tb03506.x
28. Oliphant TE. *Guide to NumPy.* 2nd edn. Austin, TX: Continuum Press (2015). Available online at: https://www.amazon.com/Guide-NumPy-Travis-Oliphant-PhD/dp/151730007X/
29. Hunter JD. Matplotlib: a 2D graphics environment. *Comput Sci Eng.* (2007) 9:90–5. doi: 10.1109/MCSE.2007.55
30. Holford NH, Sheiner LB. Understanding the dose-effect relationship: clinical application of pharmacokinetic-pharmacodynamic models. *Clin Pharmacokinet.* (1981) 6:429–53. doi: 10.2165/00003088-198106060-00002
31. Unadkat JD, Bartha F, Sheiner LB. Simultaneous modeling of pharmacokinetics and pharmacodynamics with nonparametric kinetic and dynamic models. *Clin Pharmacol Ther.* (1986) 40:86–93. doi: 10.1038/clpt.1986.143
32. Maxima. *wxMaxima, a Computer Algebra System.* (2014). Available online at: https://wxmaxima-developers.github.io/wxmaxima/help.html (accessed May 31, 2019).
33. Hoehn MM, Yahr MD. Parkinsonism: onset, progression and mortality. *Neurology.* (1967) 17:427–42. doi: 10.1212/WNL.17.5.427
34. Wang DJJ, Alger JR, Qiao JX, Hao Q, Hou S, Fiaz R, et al. The value of arterial spin-labeled perfusion imaging in acute ischemic stroke: comparison with dynamic susceptibility contrast-enhanced MRI. *Stroke.* (2012) 43:1018–24. doi: 10.1161/STROKEAHA.111.631929
35. Kilroy E, Apostolova L, Liu C, Yan L, Ringman J, Wang DJJ. Reliability of two-dimensional and three-dimensional pseudo-continuous arterial spin labeling perfusion MRI in elderly populations: comparison with ^{15}O-water positron emission tomography. *J Magn Reson Imaging.* (2014) 39:931–9. doi: 10.1002/jmri.24246
36. Newville M, Otten R, Nelson A, Ingargiola A, Stensitzki T, Allan DB, et al. *LMFIT: Non-Linear Least-Square Minimization and Curve-Fitting for Python.* (2019). Available online at: https://zenodo.org/record/2620617 (accessed May 31, 2019).
37. Hurley D. FDA committee: rasagiline rejected as "disease modifying" for Parkinson disease. *Neurology Today.* (2011) 11:1. doi: 10.1097/01.NT.0000407898.33659.0c
38. The Michael J. *Fox Foundation For Parkinson's Research. Biomarkers Priority Area.* (2018). Availble online at: http://www.webcitation.org/74c3hP06K (accessed December 11, 2018).
39. Kehagia AA. Neuropsychiatric symptoms in Parkinson's disease: beyond complications. *Front Psychiatry.* (2016) 7:110. doi: 10.3389/fpsyt.2016.00110
40. Chan PLS, Nutt JG, Holford NHG. Pharmacokinetic and pharmacodynamic changes during the first four years of levodopa treatment in Parkinson's disease. *J Pharmacokinet Pharmacodyn.* (2005) 32:459–84. doi: 10.1007/s10928-005-0055-x
41. Holford NHG, Chan PLS, Nutt JG, Kieburtz K, Shoulson I, Parkinson Study Group. Disease progression and pharmacodynamics in Parkinson disease - evidence for functional protection with levodopa and other treatments. *J Pharmacokinet Pharmacodyn.* (2006) 33:281–311. doi: 10.1007/s10928-006-9012-6
42. Siddiqi SH, Abraham NK, Geiger CL, Karimi M, Perlmutter JS, Black KJ. The human experience with intravenous levodopa. *Front Pharmacol.* (2015) 6:307. doi: 10.3389/fphar.2015.00307
43. Karimi M, Carl JL, Loftin S, Perlmutter JS. Modified high-performance liquid chromatography with electrochemical detection method for plasma measurement of levodopa, 3-O-methyldopa, dopamine, carbidopa and 3,4-dihydroxyphenyl acetic acid. *J Chromatogr B Analyt Technol Biomed Life Sci.* (2006) 836:120–23. doi: 10.1016/j.jchromb.2006.03.027

44. Koller JM, Vachon MJ, Bretthorst GL, Black KJ. Rapid quantitative pharmacodynamic imaging with Bayesian estimation. *Front Neurosci.* (2016) 10:144. doi: 10.3389/fnins.2016.00144
45. Tanenbaum AB, Snyder AZ, Brier MR, Ances BM. A method for reducing the effects of motion contamination in arterial spin labeling magnetic resonance imaging. *J Cereb Blood Flow Metab.* (2015) 35:1697–702. doi: 10.1038/jcbfm.2015.124
46. Fahn S, Elton R, UPDRS program members. Unified Parkinson's disease rating scale. In: Fahn S, Marsden CD, Goldstein M, Calne DB, editors. *Recent Developments in Parkinson's Disease,* Vol. 2. Florham Park, NJ: Macmillan Healthcare Information (1987). p. 153–63, 293–304.
47. Black KJ, Acevedo HK, Koller JM. Dopamine buffering capacity imaging: a pharmacodynamic fMRI method for staging Parkinson disease. *bioRxiv*. (2019) 817106. doi: 10.1101/817106

Conflict of Interest: KB and JK have intellectual property rights in the method described herein (U.S. patent 11,583,896 and application US2018/0286498A1).

The remaining author declares that the research was conducted in the absence of any commercial or financial relationships that could be construed as a potential conflict of interest.

Copyright © 2020 Black, Acevedo and Koller. This is an open-access article distributed under the terms of the Creative Commons Attribution License (CC BY). The use, distribution or reproduction in other forums is permitted, provided the original author(s) and the copyright owner(s) are credited and that the original publication in this journal is cited, in accordance with accepted academic practice. No use, distribution or reproduction is permitted which does not comply with these terms.

frontiers in Neurology

SYSTEMATIC REVIEW
published: 14 May 2020
doi: 10.3389/fneur.2020.00314

Assessing White Matter Pathology in Early-Stage Parkinson Disease Using Diffusion MRI: A Systematic Review

Maurizio Bergamino[1], Elizabeth G. Keeling[1,2], Virendra R. Mishra[3], Ashley M. Stokes[1] and Ryan R. Walsh[4]*

[1] Division of Neuroimaging Research, Barrow Neurological Institute, Phoenix, AZ, United States, [2] School of Life Sciences, Arizona State University, Tempe, AZ, United States, [3] Imaging Research, Cleveland Clinic Lou Ruvo Center for Brain Health, Las Vegas, NV, United States, [4] Muhammad Ali Parkinson Center, Barrow Neurological Institute, Phoenix, AZ, United States

Structural brain white matter (WM) changes such as axonal caliber, density, myelination, and orientation, along with WM-dependent structural connectivity, may be impacted early in Parkinson disease (PD). Diffusion magnetic resonance imaging (dMRI) has been used extensively to understand such pathological WM changes, and the focus of this systematic review is to understand both the methods utilized and their corresponding results in the context of early-stage PD. Diffusion tensor imaging (DTI) is the most commonly utilized method to probe WM pathological changes. Previous studies have suggested that DTI metrics are sensitive in capturing early disease-associated WM changes in preclinical symptomatic regions such as olfactory regions and the substantia nigra, which is considered to be a hallmark of PD pathology and progression. Postprocessing analytic approaches include region of interest–based analysis, voxel-based analysis, skeletonized approaches, and connectome analysis, each with unique advantages and challenges. While DTI has been used extensively to study WM disorganization in early-stage PD, it has several limitations, including an inability to resolve multiple fiber orientations within each voxel and sensitivity to partial volume effects. Given the subtle changes associated with early-stage PD, these limitations result in inaccuracies that severely impact the reliability of DTI-based metrics as potential biomarkers. To overcome these limitations, advanced dMRI acquisition and analysis methods have been employed, including diffusion kurtosis imaging and q-space diffeomorphic reconstruction. The combination of improved acquisition and analysis in DTI may yield novel and accurate information related to WM-associated changes in early-stage PD. In the current article, we present a systematic and critical review of dMRI studies in early-stage PD, with a focus on recent advances in DTI methodology. Yielding novel metrics, these advanced methods have been shown to detect diffuse WM changes in early-stage PD. These findings support the notion of early axonal damage in PD and suggest that WM pathology may go unrecognized until symptoms appear. Finally, the advantages and disadvantages of different dMRI techniques, analysis methods, and software employed are discussed in the context of PD-related pathology.

Keywords: MRI diffusion, early-stage Parkinson disease, diffusion tensor imaging, diffusion kurtosis imaging, q-space diffeomorphic reconstruction, fractional anisotropy, substantia nigra

OPEN ACCESS

Edited by:
Yu Zhang,
VA Palo Alto Health Care System, United States

Reviewed by:
Guangwei Du,
Penn State Milton S. Hershey Medical Center, United States
Niklas Lenfeldt,
Umeå University, Sweden
Masaaki Hori,
Toho University, Japan
Maria Eugenia Caligiuri,
University of Magna Graecia, Italy

****Correspondence:***
Maurizio Bergamino
maurizio.bergamino@barrowneuro.org

Specialty section:
This article was submitted to Applied Neuroimaging, a section of the journal Frontiers in Neurology

Received: *23 December 2019*
Accepted: *31 March 2020*
Published: *14 May 2020*

Citation:
Bergamino M, Keeling EG, Mishra VR, Stokes AM and Walsh RR (2020) Assessing White Matter Pathology in Early-Stage Parkinson Disease Using Diffusion MRI: A Systematic Review. Front. Neurol. 11:314. doi: 10.3389/fneur.2020.00314

INTRODUCTION

Parkinson disease (PD) is a chronic progressive neurodegenerative disease that affects more than 10 million people worldwide (1–3). Parkinson disease pathology is characterized by Lewy body aggregates and neurites (4, 5), which play a causative role in degeneration of dopaminergic neurons in the substantia nigra (SN); motor symptoms associated with PD have been primarily attributed to this process (6). By the time PD becomes symptomatic, an estimated 60% of dopaminergic neurons have degenerated, representing a moderate to severe state of disease (7). Biomarkers, including fluid and imaging based, may play a critical role in understanding the natural history of progression of PD and enable appropriate therapeutic intervention, thereby optimizing preservation of neural health (8). However, to date, no definitive biomarker exists for this purpose, despite the clear need for one.

Imaging-based biomarkers for PD can yield insight into atrophy, microstructural changes, neuronal activity, and vascular hemodynamics. Magnetic resonance imaging (MRI) biomarkers, both structural and functional, are increasingly used in PD for more comprehensive evaluation of neuropathology. Subtle brain atrophy has been demonstrated in PD using voxel-based morphometry (VBM), which is an automated analysis approach to characterize volumetric brain changes from three-dimensional structural imaging (9–11). Altered patterns of neuronal activation, measured via functional MRI (fMRI), have been observed in multiple regions of the cortex in PD using a range of motoric tasks (12–14). Resting-state fMRI is measured in the absence of tasks and can identify abnormalities in spontaneous neuronal activity (15). In particular, this approach has revealed changes in the corticosubcortical functional connectivity in PD compared with healthy controls (HCs) (16).

Diffusion MRI (dMRI) comprises a set of complementary techniques to non-invasively probe microstructural characteristics via diffusivity of water molecules in the brain. As water predominantly diffuses along axons, dMRI can be used to probe white matter (WM) changes such as axonal caliber, density, myelination, and orientation. Diffusion tensor imaging (DTI), the most common dMRI model, can provide measures such as fractional anisotropy (FA), mean diffusivity (MD), axial diffusivity (AxD), and radial diffusivity (RD) (17) that are sensitive to subtle WM microstructural organization. Since the inception of DTI in the mid-1990s (18), significant improvements have been made in both acquisition and analysis methods. These advances include the implementation of multishell and high-angular-resolution dMRI data, such as those with more diffusion-encoding gradient directions, resulting in the development of advanced algorithms to improve dMRI postprocessing and overcome some of the known limitations of DTI. The availability of standard software has further enabled quantitative analysis of DTI and DTI-related metrics including advanced dMRI models. At present, DTI represents one of the most widely used neuroimaging methods, in both preclinical animal and human studies, for its versatility and specificity to WM microstructure (19). We encourage interested readers to refer to References (9, 20–23) for a more in-depth understanding of DTI.

White matter changes in PD vs. controls (healthy subjects; HCs) have previously been evaluated by DTI using various metrics, acquisitions, analyses, and software tools (24). More specifically, a recent meta-analysis encompassing wide disease duration DTI studies in PD found that both FA and MD were able to distinguish between PD and HC, with regional DTI changes observed in the SN, corpus callosum, cingulate, and temporal cortices. Considering the growing interest in defining the early phases of PD through the use of neuroimaging biomarkers, the focus of this systematic review is the current state of dMRI-based biomarkers for understanding early-stage PD, with an emphasis on the technical methodologies employed for dMRI. More specifically, the basic theoretical background for standard DTI will be provided, along with three more advanced methods that go beyond standard DTI methods [diffusion kurtosis imaging (DKI), neurite orientation dispersion and density imaging (NODDI), and Q-space diffeomorphic reconstruction (QSDR)]. The relevant results in early-stage PD will be discussed for each of these methods. Additionally, the advantages and disadvantages of different dMRI acquisition techniques, analysis methods, and software employed will be discussed in the context of early-stage PD-related pathology. The commonalities and incongruences in findings in early-stage PD will be contextualized between the various dMRI methods. Finally, given the current state of understanding of early-stage PD and known capabilities of dMRI approaches, the outlook for future opportunities in dMRI to improve pathophysiological characterization of early-stage PD will be discussed.

Abbreviations: dMRI, Diffusion MRI; PD, Parkinson disease; SN, substantia nigra; MRI, Magnetic resonance imaging; VBM, voxel-based morphometry; fMRI, functional MRI; rs-fMRI, Resting-state-fMRI; HC, healthy controls; DTI, Diffusion tensor imaging; WM, white matter; FA, fractional anisotropy; MD, mean diffusivity; AxD, axial diffusivity; RD, radial diffusivity; DKI, diffusion kurtosis imaging; H&Y, Hoehn & Yahr; PPMI, Parkinson's Progression Markers Initiative; NODDI, neurite orientation dispersion and density imaging; QSDR, Q-space diffeomorphic reconstruction; ROI, region of interest; VBA, voxel-based analysis; TBSS, Tract-Based Spatial Statistics; CSF, cerebrospinal fluid; ASL, arterial spin labeling; CBF, cerebral blood flow; GM, gray matter; AP, atypical parkinsonism; MK, mean kurtosis; RK, radial kurtosis; AK, axial kurtosis; UPDRS-III, Unified Parkinson's Disease Rating Scale; ODF, orientation distribution function; HARDI, high angular resolution diffusion imaging; DSI, diffusion spectrum imaging; SDF, spin distribution function; GQI, generalized Q-sampling imaging; QA, quantitative anisotropy; PIGD, postural instability and gait difficulty; NBS, network-based statistics; LLS, linear least squares; WLLS, weighted linear least squares; RESTORE, robust estimation of tensors involving the outlier rejection; TORTOISE, tolerably obsessive registration and tensor optimization indolent software ensemble; AFNI, Analysis of Functional NeuroImages; Tracula, TRActs Constrained by UnderLying Anatomy; BCT, Brain Connectivity Toolbox.

METHODS

Following Preferred Reporting Items for Systematic Reviews and Meta-Analyses (PRISMA) guidelines (25), we searched three databases (**Figure 1**) for works that included at least one group of early PD [defined as subjects with Hoehn & Yahr (H&Y) stage $\leq$2 and/or disease duration <5 years] and where one or more dMRI methods were used (see PRISMA diagram in

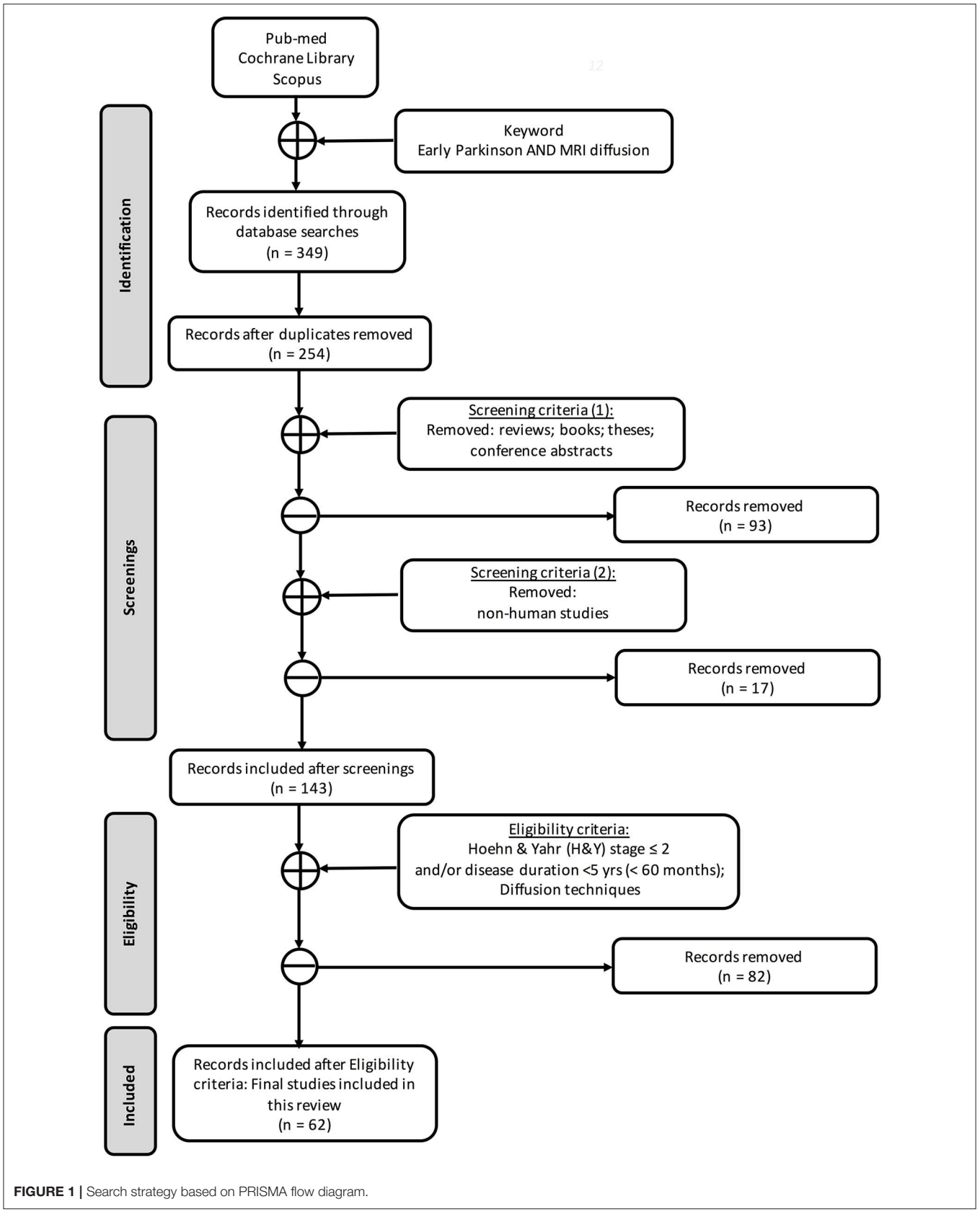


FIGURE 1 | Search strategy based on PRISMA flow diagram.

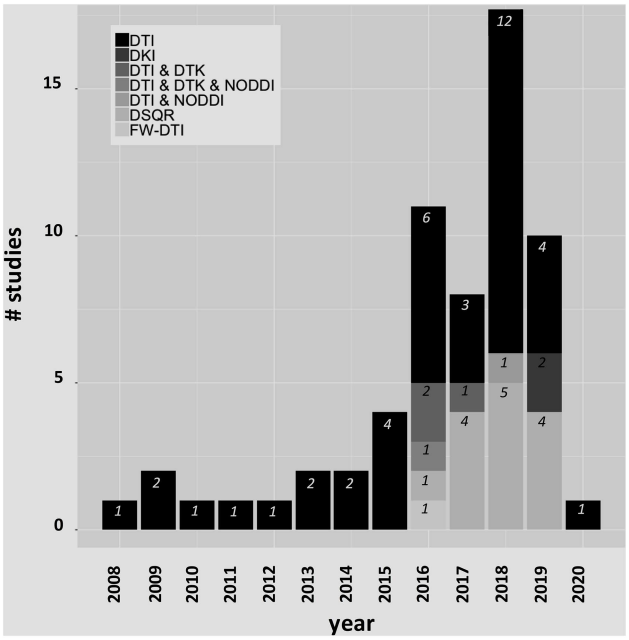


FIGURE 2 | Histograms for the publication years and dMRI techniques included in this review.

Figure 1). To identify the articles for this systematic review, we searched for publications on PubMed, Cochrane Library, and Scopus databases by using the keywords "early Parkinson," "MRI diffusion," and "DTI" without any temporal restriction. In total, we found 349 records. After excluding duplicates ($n = 254$), screening and eligibility further reduced the number to 62 articles retained for this review.

While most studies used site-specific data, several studies leveraged the open-access availability of data from the Parkinson's Progression Markers Initiative (PPMI) (http://www.ppmi-info.org). Parkinson's Progression Markers Initiative is a multicenter international database of *de novo* individuals with early idiopathic PD that includes clinical, imaging, and biological data. Studies using PPMI and other shared datasets will be denoted in the text. Histograms are shown in **Figure 2** for the publication years and dMRI techniques used in each article included in this review. The complete list of the PD studies that are included in this review is reported in **Table 1**.

THEORY AND RESULTS

Diffusion Tensor Imaging: Theory, Acquisition, and Analysis

Diffusion tensor imaging relies on motion-sensitizing gradients to probe the displacement of water molecules, which is often simplified using a Gaussian distribution model. The diffusion-weighted signal intensity for this distribution can be described by the following equation:

$$S = S_0 exp\left[-bD\right] \tag{1}$$

where S_0 is the signal intensity without the diffusion gradient, D is the diffusion coefficient, and b is the diffusion-weighting factor, where the b factor is largely dependent on the gradient waveform. The diffusion can thus be represented by the following equation:

$$ln\left[\frac{S}{S_0}\right] = -b\overline{g}^T\overline{D}\,\overline{g} \tag{2}$$

where $\overline{g}$ is a three-element column vector representing a gradient direction, $\overline{g}^T$ is the transpose of $\overline{g}$, and $\overline{D}$ is the apparent diffusion tensor (3×3 symmetric matrix).

Diffusion tensor imaging provides a direct relationship between the chosen experimental parameters, such as b and $\overline{g}$, the MR measurements (S and S_0), and the parameters of the diffusion tensor model $\overline{D}$.

Eigendecomposition of the diffusion matrix yields a symmetric diffusion tensor:

$$\overline{D} = \left[\epsilon_1\ \epsilon_2\ \epsilon_3\right] \cdot \begin{bmatrix} \lambda_1\ 0\ 0 \\ 0\ \lambda_2\ 0 \\ 0\ 0\ \lambda_3 \end{bmatrix} \cdot \begin{bmatrix} \epsilon_1 \\ \epsilon_2 \\ \epsilon_3 \end{bmatrix} \tag{3}$$

where λ_1, λ_2, and λ_3 are the eigenvalues (with $\lambda_1 \geq \lambda_2 \geq \lambda_3$) and ϵ_1, ϵ_2, and ϵ_3 are the eigenvectors of $\overline{D}$. The diffusion tensor is completely characterized by these eigenvalues, which describe the length of the three axes of the diffusion ellipsoid, and their corresponding eigenvectors, which describe the orientation of these axes in space. As the eigenvectors provide information about the direction of water diffusion within a voxel, they form the basis of brain fiber tracking (88, 89). The geometric shape associated with the diffusion tensor is assumed to be a three-dimensional ellipsoid with the length of the three orthogonal principal axes proportional to the ordered tensor eigenvalues.

The first eigenvalue (λ_1) represents water diffusivity along the principal axis and is termed axial (or longitudinal or parallel) diffusivity ($\lambda_\parallel$ or AxD). The radial (or transverse or perpendicular) diffusivity ($\lambda_\perp$ or RD) represents water diffusion perpendicular to the principal direction and is given by the average of the remaining eigenvalues ($(\lambda_2 + \lambda_3)/2$). Axial diffusivity has been associated with axonal damage, whereas RD may be associated with myelin integrity, axonal diameter and density, and fiber coherence (90, 91). Mean diffusivity is a rotationally invariant metric, obtained from a simple average of the diffusion eigenvectors ($(\lambda_1 + \lambda_2 + \lambda_3)/3$), which describes the overall size of the tensor.

Fractional anisotropy quantifies the degree of anisotropy of the diffusion tensor and is the most common DTI-related index. Fractional anisotropy ranges from 0 to 1, where 0 represents isotropic diffusion and 1 represents completely anisotropic diffusion. Fractional anisotropy can be calculated in each voxel using the following equation:

$$FA = \sqrt{\frac{1}{2}}\frac{\sqrt{(\lambda_1-\lambda_2)^2+(\lambda_2-\lambda_3)^2+(\lambda_3-\lambda_1)^2}}{\sqrt{\lambda_1^2+\lambda_2^2+\lambda_3^2}} \tag{4}$$

While this index has often been interpreted as a quantitative biomarker of WM disorganization, equating FA with WM

TABLE 1 | Summary of diffusion studies in early-stage PD.

References	Diffusion method	Analysis method (for diffusion)	Software	PD subjects	# Diffusion directions/# *b* value(s)
Vriend et al. (26)	DTI	Connectivity	FSL, BCT	23 early-stage PD (H&Y 1–3)	30/2
Arrigo et al. (27)	DTI	Connectivity	SPM8, FSL, MRtrix, Camino	20 newly diagnosed PD (H&Y = 1)	61/2
Tinaz et al. (28)	DTI	Connectivity	BCT, FATCAT, 3dTrackID, TORTOISE, AFNI	20 non-demented PD patients (H&Y = 2; disease duration (year) = 7.1)	70/—
Peña-Nogales et al. (29)	DTI	Connectivity	FSL–MRtrix	PPMI subjects	64/2
Nigro et al. (30)	DTI	Connectivity	PANDA (Matlab) –BCT–FSL	H&Y = 1.5 and disease duration = 19.28 months	27/2
Tessa et al. (31)	DTI	Histogram	FSL	27 patients with *de novo* drug-naive PD [tremor-dominant type (n = 13), akinetic-rigid type (n = 11), and mixed type (n = 3)]–H&Y = 1.2 and 1	6/2
Knossalla et al. (32)	DTI	ROI	—	10 early-stage PD (H&Y = 1–2)	20/2
Joshi et al. (33)	DTI	ROI	FSL	24 early-stage PD (disease duration average 2.94 years, SD 2.93 years; nine HY1 patients, 13 HY2, two unknown)	55/—
Wang et al. (34)	DTI	ROI	Siemens Syngo MR Neuro 3D, SPM8, FSL	27 early-stage PD (H&Y = 1–2; duration of disease = 1.7 Y)	60/2
Aquino et al. (35)	DTI	ROI	FSL	22 early-stage PD (Duration of disease = 4.0 years) and 20 late PD	64/—
Vaillancourt et al. (36)	DTI	ROI	AFNI	14 with early stage PD (H&Y = 1–2; duration of disease = <34 months)	27/2
Gattellaro et al. (37)	DTI	ROI	ImageJ (for ROI)	10 PD without dementia (H&Y = 1–2)	12/2
Du et al. (38)	DTI	ROI	DTIPrep, Matlab	15 early-stage PD (disease duration ≤1 years), 14 midstage PD (duration 2–5 years), and 11 late-stage (duration >5 years)	42/2
Loane et al. (39)	DTI	ROI	ExploreDTI	18 early stage PD (treated) [avg (SD) disease duration (years): 3.9 (2.2); no H&Y provided]	64/2
Schuff et al. (40)	DTI	ROI	Processed from PPMI	PPMI subjects	64/2
Pelizzari et al. (41)	DTI	ROI	FSL, ANTs	26 PD (H&Y = 1–1.6; duration of disease = 3.0 years)	64/2
Guan et al. (42)	DKI	ROI	GE adw 4.6	The PD divided into an advanced-stage PD group and an early-stage PD group	15/3
Liu et al. (43)	DTI	ROI	Probably Scanner software	early diagnosis of Parkinson disease	25/2
Mangia et al. (44)	DTI	ROI	FSL	Nine early-diagnosed PD	93/2
Klein et al. (45)	DTI	ROI	—	20 early-stage PD patients (disease duration 1.9 ± 0.97 years, H&Y 1–2)	60/2
Planetta et al. (46)	DTI	ROI, tractography	DTI Studio, AFNI,	20 with early stage PD (Duration of disease = 12 months)	27/2
Wei et al. (47)	DTI	ROI, tractography	GE adw 4.5	21 early (H&Y <2) and 22 mid–late PD (H&Y ≥2)	25/2
Li et al. (48)	DTI	TBSS	FSL	31 early-stage PD (H&Y = 1–2)	32/2
Rolheiser et al. (49)	DTI	TBSS	FSL	14 early stage PD (H&Y = 1–2; duration of disease <72 months)	31/2
Ibarretxe-Bilbao et al. (50)	DTI	TBSS	FSL	24 early-stage PD (H&Y = 1–2)	30/2
Minett et al. (51)	DTI	TBSS	FSL	120 early stage PD [27 with mild cognitive impairment (H&Y = 2.3) and 93 with normal cognition (H&Y = 1.9)]; duration of disease 5.6–6.4 months (longitudinal study)	64/2

(Continued)

TABLE 1 | Continued

References	Diffusion method	Analysis method (for diffusion)	Software	PD subjects	# Diffusion directions/# *b* value(s)
Duncan et al. (52)	DTI	TBSS	FSL	125 non-demented PD (H&Y = 2.0; average duration of disease = 6.15)	64/2
Lacey et al. (53)	DTI	TBSS	FSL	PPMI subjects	64/2
Pozorski et al. (54)	DTI	TBSS	FSL–DTIprep–DTI_TK	H&Y stage at baseline 16 subjects with <2 and 13 subjects (≥2); mean disease duration (years) 3.7 (3.2)	40/2
Rektor et al. (55)	DTI	TBSS	FSL	H&Y stage 1–1.5 and disease duration up to 5 years	60/2
Pelizzari et al. (56)	DTI	TBSS	FSL	12 PD [median H&Y (IQR) = 1.5 (1.1–2)]	64/2
Chen et al. (57)	DTI	TBSS (only for normalization procedure), ROI	FSL	30 early stage PD (H&Y = 1.74; average duration of disease = 62)	25/2
Mishra et al. (58)	DTI	TBSS (skeleton), ROI, VBA	FSL, DTI-TK	PPMI subjects	64/2
Gou et al. (59)	DTI	TBSS, Connectivity	FSL, SPM12, PANDA, FACT	PPMI subjects	64/2
Meijer et al. (60)	DTI	TBSS, ROI	FSL	49 early stage PD [19 atypical parkinsonism (H&Y = 2.4) and 30 PD (H&Y = 1.7)], disease = 21.6–28.4 months. Longitudinal study	30/2
Guimarães et al. (61)	DTI	TBSS, ROI, tractography	FSL, Explore DTI, SPM8	early-stage PD, moderate PD, and severe PD	32/2
Prange et al. (62)	DTI	TBSS, VBM	FSL	14 apathetic and 13 non-apathetic patients with *de novo* PD	24/2
Ford et al. (63)	DTI	TBSS, VBM	FSL, SPM8 (for VBM)	124 early-stage PD	64/2
Zhang et al. (64)	DTI	Tractography	SPM8, TrackVis	PPMI subjects	64/2
Lorio et al. (65)	DTI	VBA	SPM12, FSL	PPMI subjects	64/2
Taylor et al. (66)	DTI	VBA	TEEM tool (from PPMI)	PPMI subjects	64/2
Planetta et al. (67)	DTI (free water)	ROI	FSL–Matlab for free water	34 patients with early stage PD	64/2
Rahmani et al. (68)	QSDR	Connectivity	Explore DTI–DSI Studio	PPMI subjects	64/2
Ghazi Sherbaf et al. (69)	QSDR	Connectivity	Explore DTI–DSI Studio	PPMI subjects	64/2
Ansari et al. (70)	QSDR	Connectivity	Explore DTI–DSI Studio	PPMI subjects	64/2
Ansari et al. (71)	QSDR	Connectivity	DSI Studio	PPMI subjects	64/2
Ghazi Sherbaf et al. (72)	QSDR	Connectivity	DSI Studio–Explore DTI	PPMI subjects	64/2
Wen et al. (73)	QSDR	Connectivity	FSL, DSI Studio	20 prodromal phase of PD; 106 PD;	64/2
Haghshomar et al. (74)	QSDR	Connectivity	ExploreDTI, DSI-Studio	PPMI subjects	64/2
Ashraf-Ganjouei et al. (75)	QSDR	Connectivity	DSI Studio	PPMI subjects	64/2
Sanjari Moghaddam et al. (76)	QSDR	Connectivity	DSI Studio–Explore DTI	PPMI subjects	64/2
Sobhani et al. (77)	QSDR	Connectivity	DSI Studio	PPMI subjects	64/2
Ghazi Sherbaf et al. (78)	QSDR	ROI	DSI Studio, ExploreDTI	PPMI subjects	64/2
Wen et al. (79)	QSDR	TBSS–Connectivity	DSI Studio–FSL	PPMI subjects	64/2
Wen et al. (80)	QSDR	TBSS, Connectivity	FSL, DSI Studio, BCT,	PPMI subjects	64/2
Wen et al. (81)	QSDR	TBSS, Connectivity	FSL, DSI Studio, BCT	PPMI subjects	64/2
Zhang et al. (82)	DKI	ROI	GE adw 4.5	Initial H&Y staging 1.58 and 1.65; H&Y staging after 2 years 2.08 and 1.84	25/3
Zhang et al. (83)	DKI	ROI	GE adw 4.5	72 early-stage PD (H&Y = 1.67; duration of disease = 13.50 months)	25/2

(Continued)

TABLE 1 | Continued

References	Diffusion method	Analysis method (for diffusion)	Software	PD subjects	# Diffusion directions/# *b* value(s)
Zhang et al. (84)	DKI	ROI	GE adw 4.5	28 PD with Striatal silent lacunar infarction PD (H&Y = 1.68 -> 2.39(FU); duration of disease = 14.21 months); 32 PD et al. [H&Y = 1.63 to >1.91 (FU); duration of disease = 14.68 months]	25/2
Zhang et al. (85)	DKI	ROI	GE adw 4.5	72 with early stage PD divided in control and striatal silent lacunar infarction (H&Y = 1.63 and 1.71; duration of disease <14 months)	25/2
Surova et al. (86)	DTI–DKI–NODDI	ROI, tractography	FSL, in-house developed software (for DKI)	105 patients with PD et al. [H&Y = 2; disease duration (years) = 5]	94/4
Andica et al. (87)	DTI–NODDI	Tractography	NODDI Matlab Toolbox5, FSL, AMICO, TrackVis	29 PD (H&Y = 1.97; average duration of disease = 6.24 years)	32/2

—, no information available. In the last column, the B0 image acquisition is included in the number of b values.

disorganization is not strictly accurate, given that FA cannot disentangle the individual microscopic contributions, such as different WM fiber populations and/or cerebrospinal fluid (CSF) contamination (92, 93). Fractional anisotropy has also been equated as a marker of demyelination (94), which is also not accurate because the regional anisotropy may also reflect altered axonal diameter, packing density, or membrane permeability (95). Despite these limitations, DTI-based FA has often been utilized as a neuroimaging biomarker because of its robustness to noise (96, 97). Example maps for FA (gray-scale and colorized), MD, AxD, and RD are shown in **Figure 3** in an HC.

Tractography goes beyond the conventional quantitative voxel-wise metrics to generate a three-dimensional representation of WM fiber bundles. **Figure 4** shows an example tractography (B), with FA shown in (A), in an HC. Tractography consists of a multistep procedure to reconstruct WM fiber bundles inside the brain, namely, seeding, propagation, and termination. Many options, and best practices, for each of these steps can be found in the literature (23, 98), and software exists to perform these functions at varying levels. Some of the known limitations of tractography are related to acquisition (minimum number of DTI directions) and WM architecture (crossing, kissing, and diverging fibers). Other limitations include possible inaccuracies of tractography due to the presence of neuropathological changes (99).

Upon generation of DTI-based metrics, subsequent quantitative analyses can be performed using histogram analysis, region of interest (ROI) analysis, voxel-based analysis (VBA), or skeletonized analysis [also called tract-based spatial statistics (TBSS)]. Additionally, DTI enables measurement of the macroscopic orientation of WM tissue and analysis of structural connectivity through tractography algorithms. These different analysis methods are demonstrated in **Figure 5** and are discussed in greater detail below.

One of the simplest analyses is whole-brain histogram analysis (**Figure 5A**). Beyond mean and median, histograms permit extraction of parameters such as histogram peak height and location that can be compared across subjects or correlated with other variables. A major advantage of whole-brain histogram analysis is that no *a priori* choice of region is required; however, one ensuing drawback is that the results may be affected by CSF contamination (92). Region-of-interest analysis (**Figure 5B**) is a commonly used method to analyze DTI-derived indices, where ROIs can be obtained from automated segmentation (e.g., FreeSurfer; https://surfer.nmr.mgh.harvard.edu/) or by manual delineation. Although ROIs can be drawn directly on the DTI-derived indices, their placement may be difficult due to low-resolution images and the intensity of DTI-derived maps (e.g., FA) may spuriously influence the ROI boundaries, thereby introducing bias into the analysis. Alternatively, ROIs may be drawn on anatomical T1- or T2-weighted images, which necessitates reliable co-registration with dMRI data. One drawback to ROI analysis is that it requires either an *a priori* hypothesis regarding where WM differences are expected to be present in a pathology or normal development as the inclusion of many ROIs increases the number of statistical tests and requires correction for multiple comparisons.

Moving beyond ROI analysis, VBA is a fully automated approach that allows for the investigation of microstructural organization in each voxel inside the whole brain (**Figure 5C**). It involves the spatial normalization of high- and low-resolution images from the subjects' native space to stereotactic space, and thus, reliable co-registration is crucial. Additionally, smoothing of the data during analysis can increase the impact of partial volume effects (PVE), as the voxels may combine both WM and gray matter (GM) in such a way that the results are less robust and less specific to a specific component. As statistical analysis is performed in each voxel, there is also an increased risk of false-positive findings, such that multiple comparison corrections are compulsory. Finally, pathologies and lesions can strongly affect VBA results. Alternatively, TBSS (or skeletonized analysis, **Figure 5D**) can alleviate the alignment and smoothing challenges associated with VBA (100). Tract-based spatial statistics is a popular pipeline used to coregister sets of DTI maps for performing voxel-wise comparisons on skeletonized WM tracts. As a result, it precludes the study of whole-brain WM tracts, focusing instead on the components of WM tracts common across all subjects (hence the name skeletonized). In recent years,

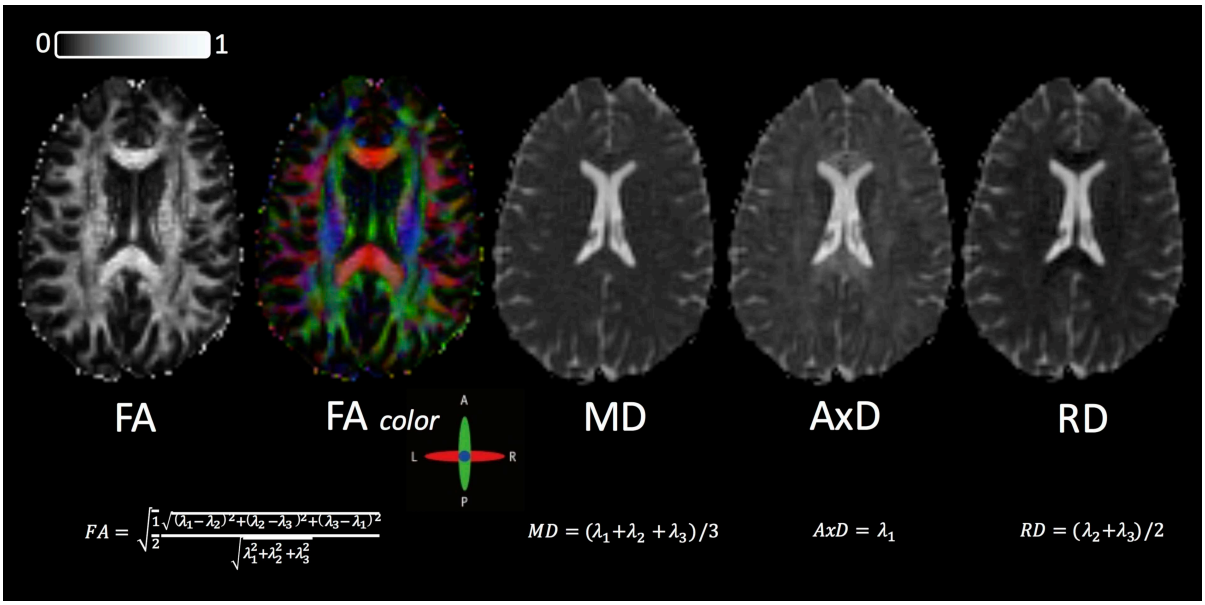


FIGURE 3 | Standard DTI maps, from a healthy volunteer, created by DSI Studio with a DTI diffusion scheme with a total of 67 diffusion sampling directions. The *b* value was 1,000 s/mm^2. The in-plane resolution was 2 mm, and the slice thickness was 2 mm. FA, fractional anisotropy; MD, mean diffusivity; AxD, axial diffusivity; RD, radial diffusivity. The range of FA in between 0 (isotropic diffusion) and 1 (anisotropic diffusion).

several studies have questioned the reliability and interpretability of TBSS (101), and improvements over the original TBSS pipeline have been suggested (102).

The final analysis method covered to this review is the connectome analysis (**Figure 5E**), which pertains to whether there are global changes in structural connectivity patterns at the end of WM pathways (103). Advantages of this method include that it is automated and identifies the global shift in WM connectivity pattern between the groups. Network-based measures derived through this connectome analysis can then be utilized to not only understand whether there is a global shift in WM-derived structural connectivity due to pathology but also to understand its correlations with clinical and pathological presentations.

DTI in Early-Stage PD

Given the known spatiotemporal progression of changes associated with PD, ROI analysis has been used widely in early-stage PD. Moreover, given the recognized involvement of the SN early in pathophysiological progression of PD, many DTI studies have focused on ROI analysis of the SN. For example, reduced FA of SN in subjects with early-stage PD compared with controls was observed by Vaillancourt et al. (36), whereas Liu et al. (43) similarly found that FAs in the rostral, middle, and caudal areas of the SN were decreased significantly in subjects with early-stage PD compared with controls. Mangia et al. (44) explored the SN and other brain locations from a multimodal MRI approach and reported neuronal degeneration of the SN in the early-PD group. However, not all studies have reported similar results. For instance, Pellizari et al. (41) observed no differences in FA in the SN between early-stage PD and HC, although differences in AxD were reported. Similarly, Joshi et al. (33) compared all DTI-derived metrics in 24 early-stage PD subjects and found increased MD in the SN. Finally, in a longitudinal study over almost 2 years, Loane et al. (39) found no significant differences in DTI metrics at baseline, but significant differences in nigral FA (decrease in PD) and MD (increase in PD) metrics were observed at the follow-up time point. As a result, the authors hypothesized that diffusion metrics in the SN may be sensitive measures of disease progression.

Parkinson disease is often associated with olfactory dysfunction, and impaired sense of smell is one of the earliest clinical symptoms of PD, preceding even the classic motor signs (104). Using ROI analysis, significant group differences in FA and MD have been observed in the anterior olfactory structures (33). These results were confirmed by Rolheiser et al. (49), who leveraged TBSS to reveal significant group differences between PD and controls in the anterior olfactory region, as well as the SN. Furthermore, reduced FA in WM associated with the central olfactory system was observed using TBSS in early-stage PD patients and was associated with a reduced ability to smell (50).

Parkinson disease–associated pathological changes are not isolated to the SN and olfactory regions. In fact, alterations have been observed in other WM areas, including the genu of the corpus callosum, superior longitudinal fasciculus, putamen, external capsule, midbrain, superior cerebellum, and superior cerebellar peduncles (37, 60). Using both ROI and tractography methods, Planetta et al. (46) found that FA values were significantly reduced in PD in fibers projecting from the anterior nucleus, ventral anterior nucleus, and dorsomedial nucleus. In addition, reduced FA values approached significance in the ventral lateral nucleus of patients with PD. Similarly, regions

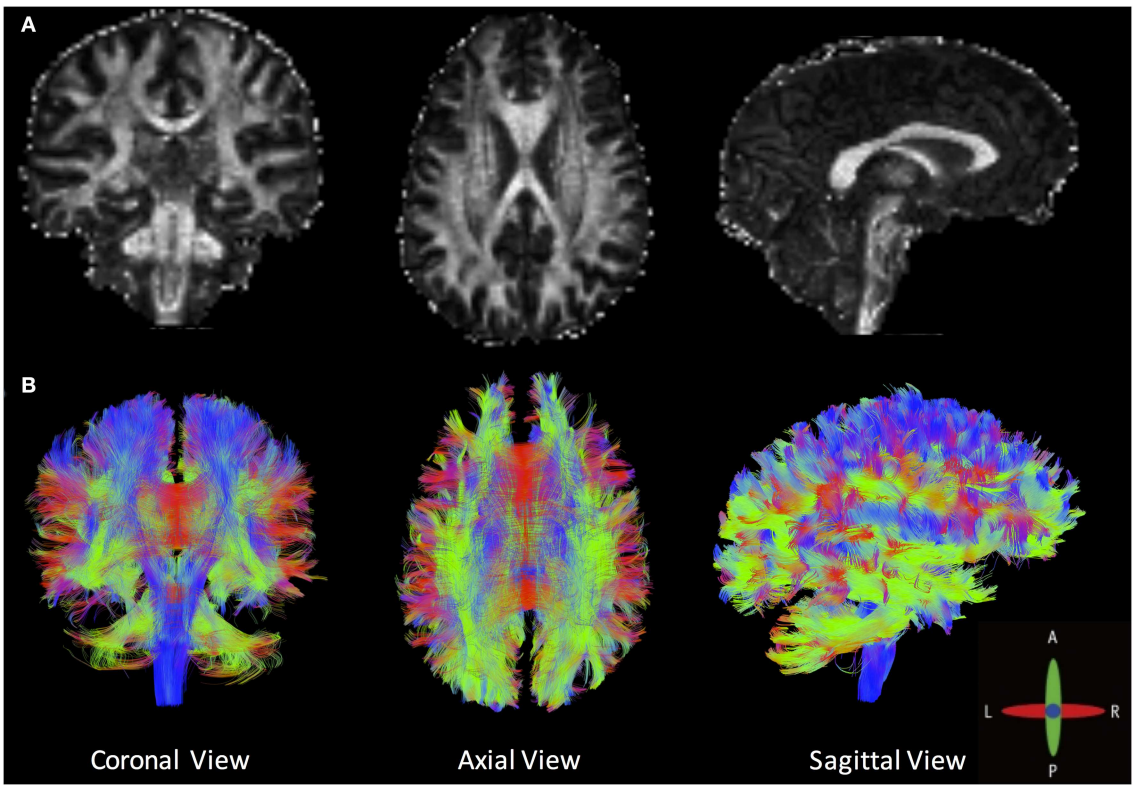


FIGURE 4 | (A) Fractional anisotropy maps and **(B)** an example of whole-brain deterministic tractography created by DSI Studio in a healthy volunteer (angular threshold: 60 degrees; step size: 1 mm; anisotropy threshold: 0.20. Tracks with length shorter than 50 or longer than 300 mm were discarded. A total of 500,000 seeds were placed inside the whole brain).

that have shown reduced FA using TBSS include the bilateral anterior corona radiata, upper corona radiata, posterior thalamic radiation, optic radiation, fornix, and corpus callosum, among others (48, 56). In a study of 125 early-stage PD and 50 HC individuals, increased MD in PD subjects was observed in several WM locations, suggesting early axonal damage (52). On the other hand, some studies have reported no significant differences between early-stage PD and controls (35, 39), whereas higher FA values in several WM locations have also been reported (57).

Given the evidence of widespread WM changes, whole-brain metrics may be of interest. Tessa et al. (31) previously used whole-brain histogram analysis to compare FA metrics between controls and *de novo* drug-naive PD ($n = 27$), the latter of which was divided in tremor-dominant, akinetic-rigid, and mixed types. Increased FA was observed in patients with PD, which was more pronounced in patients with the akinetic-rigid subtype. Considering the use of whole-brain analysis, these results support the hypothesis that widespread neuropathology exists at the time of clinical onset, possibly driven by the inclusion of GM in whole-brain analysis. Connectome analysis has also shown significant differences in the WM-derived structural connectome associated with PD (29, 30, 105). More specifically, lower global efficiency and global clustering coefficient have been observed in PD compared with HCs (26). Arrigo et al. (27) found significant alterations in optic radiation connectivity distribution, a significant increase in optic radiation MD, and a significant reduction in WM concentration in early-stage PD. Finally, Tinaz et al. (28) investigated the structural and functional organization in PD subjects, finding reduced WM connectivity in frontoparietal–striatal nodes compared to controls, but no change in modular organization of the WM tracts. A recent study by Mishra et al. (105) reported that there is an early-stage PD-specific WM-derived connectome comprising pathophysiologically relevant regions and that the overall connectivity in early-stage PD in these regions is significantly higher than that compared to HC. Additionally, PD groups have shown reduction in functional local network metrics in many nodes distributed across the connectome (28).

Several studies have sought to correlate DTI findings with clinical metrics, including functional and cognitive measures, both cross-sectionally and longitudinally. The cross-sectional results have been mixed with both ROI analysis and TBSS, with some studies showing no correlations between DTI-derived metrics and clinical measures (38, 48) and other studies reporting significant correlations, particularly in the caudate nucleus (34, 41). Minett et al. (51) found that at baseline patients with early-stage PD had significantly higher MD relative to HC, and in patients with PD and mild cognitive impairment,

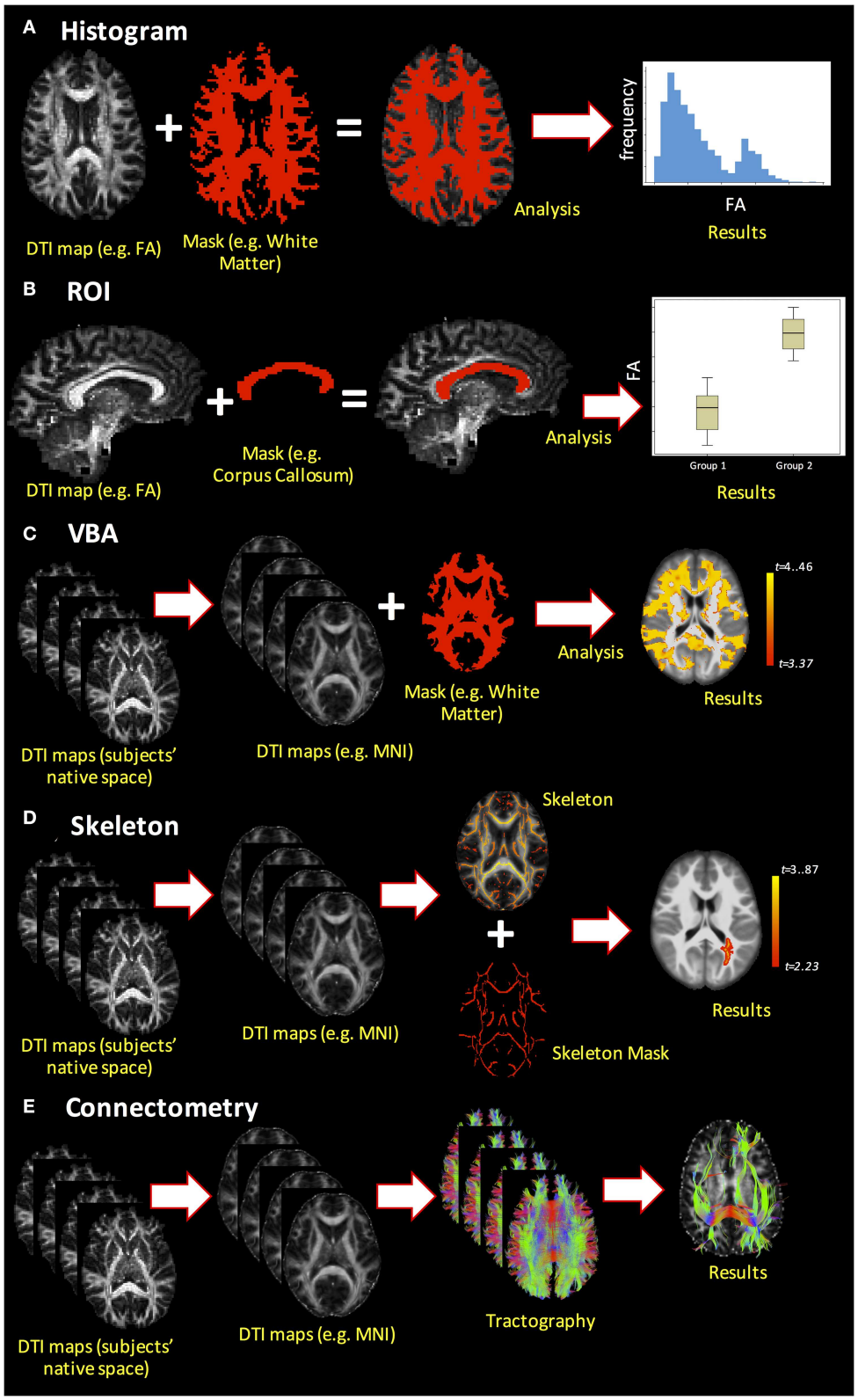


FIGURE 5 | Example of the different dMRI analysis methods. **(A)** Histogram analysis; **(B)** ROI analysis; **(C)** voxel-based analysis (VBA); **(D)** skeletonized analysis (e.g., TBSS pipeline); **(E)** connectome analysis.

higher MD was significantly correlated with lower attention and executive function scores. In this longitudinal study, DTI-derived WM microstructural changes were assessed as potential prognostic biomarkers of worsening motor features or cognitive decline in patients with PD. At follow-up, frontal MD increased significantly when comparing patients with PD and mild cognitive impairment with HC. In another longitudinal study over 18 months, patients with early-stage PD with unilateral disease were shown to have higher rates of microstructural changes compared to patients with later-stage PD with bilateral disease, suggesting that substantial microstructural changes occur during the early stages of disease (54). Gray matter changes have also been implicated in PD-associated cognitive impairment, where reduced cortical microstructural integrity was associated with reduced cognitive performance in early-stage PD patients (45).

While many of the aforementioned studies have used subject sample sizes on the order of 20 to 30, several studies have leveraged the PPMI database that features larger patient enrollment and longitudinal data, along with clinical metrics. Using ROI analysis, Schuff et al. (40) analyzed WM abnormalities in 153 early-stage drug-naive *de novo* PD and compared these measures with 67 HC from the PPMI database, finding a marginally non-significant interaction between nigral FA and disease status. However, significant interactions between WM regions and disease status have been found in several other non-PPMI studies (32, 38, 106). Analyzing longitudinal PPMI data using VBA, Taylor et al. (66) found significantly increased FA in brainstem, cerebellar, anterior corpus callosal, inferior frontal, and inferior fronto-occipital WM and increased MD in primary sensorimotor and supplementary motor regions. After 1 year, PD patients showed a significantly stronger decline in FA compared to HC in the optic radiation and corpus callosum, as well as parietal, occipital, posterior temporal, posterior thalamic, and vermis GM. The authors postulate that these findings are in line with spatiotemporal patterns of α-synuclein, in both WM and cortical GM. Diffusion tensor imaging–derived metrics of the nigrostriatal tract were shown to have a systematic abnormalities in 50 PD patients from PPMI using tractography; in addition, variations in FA and RD of the nigrostriatal tract were associated with the degree of motor deficits in PD patients (64).

Given the numerous permutations of DTI analysis methods, Mishra et al. (58) performed a systematic comparison of various postprocessing approaches used for identifying WM differences using DTI data from PPMI database. Region-of-interest–based analysis, VBA with varying spatial smoothing, and two widely used skeletonized approaches (TBSS and tensor-based registration with DTI-TK) were compared in a group of 81 early-stage PD and 44 HCs from PPMI. Both skeletonized approaches revealed significant negative correlations for FA with disease duration, although DTI-TK was found to be more accurate for assessing disease progression. However, no analytic techniques showed any group difference in any region between early-stage PD and HC. These types of comparisons provide context for studies that have shown conflicting findings with different analysis pipelines and highlight the importance of standardization of DTI analysis.

To provide a more comprehensive view of early-stage PD-related neuropathological changes, several studies have combined imaging metrics with different underlying pathophysiological correlates. Wei et al. (47) and Pelizzari et al. (41) combined microstructural DTI-derived metrics with perfusion using arterial spin labeling to increase diagnostic accuracy for early-stage PD. In those studies, both FA and cerebral blood flow in the hippocampus, prefrontal cortex, and parietal WM regions were decreased in early-stage PD and mid-late PD compared with HC. In addition, FA was decreased in the SN, while hypoperfusion was observed in the frontal/occipital WM regions. Several authors have also used DTI together with VBM, which can detect subtle brain volumetric changes using structural images, to investigate the relationship between WM tracts, GM volume and PD. These studies found reduced WM microstructural integrity and reduction of GM volume in PD subjects in several regions, such as cingulum, superior longitudinal fasciculus, inferior longitudinal fasciculus, inferior fronto-occipital fasciculus, striatum, and the frontal, temporal, limbic, and paralimbic areas (27, 45, 52, 55, 62, 65, 107).

Sleep disorders, such as rapid eye movement sleep behavior disorder, may coincide with early-stage PD, and the combination of sleep disorders and early-stage PD has been associated with more advanced disease status, despite similar clinical characteristics and cognitive performance (63). Parkinson disease patients with sleep disorders have shown regions of reduced cortical GM volume, as assessed by VBM, and WM changes, most notably reduced FA using TBSS, compared with those who did not have sleep disorders, though not significant when adjusted for multiple comparisons. In a separate study, cortical and subcortical alterations in *de novo* PD patients were observed using VBA-DTI (65); notably, many of these changes occurred in the brainstem, specifically the pontine tegmentum, which has been implicated in the regulation of sleep cycles (108).

Mood disorders, including depression, apathy, and anxiety, have been associated with more advanced PD stages and may be related to dopaminergic depletion (109); however, these neuropsychiatric conditions have also been implicated in early-stage disease and may have a different underlying etiology (62). Gou et al. found no significant WM microstructural differences between depressed and non-depressed PD groups using TBSS (59), a finding that was replicated by Lacey et al. using data from PPMI (53). However, connectivity analysis revealed significant network changes associated with PD patients with depression (59). Parkinson disease with apathy has also been associated with bilateral microstructural alterations in the medial corticostriatal limbic system; more specifically, decreased FA and increased MD were observed in the anterior striatum and pregenual anterior cingulate cortex, along with concomitant serotonergic dysfunction (62).

While most studies have sought to differentiate between PD and HC groups, some studies have assessed the potential of DTI biomarkers to differentiate PD subgroups. In one study, decreased FA was observed in the SN using ROI analysis in early and mid–late PD patients compared with healthy subjects, but there were no significant differences in the same metrics between early-stage PD and mid–late PD

groups (47). These results suggest that SN changes occur early in the pathology of PD and rapidly reach a plateau, such that longer disease duration is not indicative of increased nigral microstructural changes. Comparing early-stage PD and neurodegenerative atypical parkinsonism (AP), higher MD in the centrum semiovale, body of the corpus callosum, putamen, external capsule, midbrain, superior cerebellum, and superior cerebellar peduncles has been observed in AP (60). Another study using ROI analysis across PD subgroups found that widespread microstructural changes were present only in late-stage PD groups and not in early and moderate PD groups (61). The authors further suggest that standard DTI methods may not be sensitive to early PD pathology, which may indicate a role for more advanced methods.

Free-Water Algorithms for DTI Correction

The complex organization of brain tissue, in combination with the relatively large voxel size in dMRI acquisition, results in PVE in diffusion tensor measurements. Consequently, DTI-derived metrics are influenced by the combined contributions of different brain tissue compartments, including CSF and/or extracellular free water (110). Free-water is defined as water molecules that neither experience flow nor are restricted by their surroundings. In the human brain, free water is found in CSF within the ventricles and around the brain parenchyma. For instance, CSF has a relatively large diffusion coefficient compared with that of the brain parenchyma, such that PVE in the periventricular regions and the sulci may overestimate the ADC values by 15–30% (111). Several methods can be employed to remove free-water contributions, such as fluid-attenuated inversion recovery diffusion-weighted imaging (FLAIR-DWI) (112) or the free-water correction algorithm developed by Pasternak et al. (113) for single-shell acquisitions and later extended to multishell acquisitions (114). Planetta et al. (67) used a free-water DTI algorithm in the context of early-stage PD patients taking rasagiline, a monoamine oxidase inhibitor used to treat PD, and found that the +rasagiline group had less free water in the posterior SN and better performance on a coordination task than the –rasagiline group. However, interpretation of changes in free-water measures from single-shell dMRI acquisitions must be interpreted cautiously, as the measures are biased at crossing-fiber regions (115), which make up approximately 90% of WM voxels (116).

Beyond DTI: Diffusion Kurtosis Imaging

Although DTI is widely used to study WM organization, its inherent assumption of a Gaussian distribution results in an inability to resolve tracts in voxels with complex fiber arrangements (99). To overcome this issue, other techniques such as DKI have been developed. Kurtosis is a statistical measure of the deviation from a Gaussian distribution (which is the assumed distribution for DTI), and thus, DKI-based methods can quantify non-Gaussian diffusion (117). This technique is largely based on the same type of pulse sequences employed for DTI, but DKI requires multishell dMRI at higher b values than those conventionally utilized for DTI analysis.

For DKI, the natural logarithm of the diffusion-weighted signal can be approximated by an expansion in terms of the b values:

$$ln\left[S(b)\right] = ln\left[S(0)\right] - bD_{app} + \frac{1}{6}b^2D_{app}^2K_{app} + O(b^3) \quad (5)$$

where $S(b)$ is the signal intensity, D_{app} is the apparent diffusion coefficient, and K_{app} is the apparent diffusional kurtosis, and the term $O(b^3)$ is the Taylor expansion for power of $b > 2$. In the case of Gaussian diffusion, K_{app} is zero, and Equation (5) reduces to the standard DTI equation. Analogous to DTI, this equation is solvable to yield the diffusion kurtosis tensor $\overline{W}$.

Diffusion kurtosis imaging processing is only slightly more complex than DTI processing, although DKI provides a significantly more complete characterization of water diffusion and tissue structure.

Diffusion kurtosis imaging provides the same set of diffusion parameters as DTI (DKI-FA, DKI-RD, DKI-AD, and DKI-MD), in addition to mean kurtosis (MK), radial kurtosis (RK), and axial kurtosis (AK), which are the most commonly used kurtosis metrics. Similar to DTI, AK is the primary eigenvalue of the apparent kurtosis tensor along the main diffusion direction, whereas RK is the average of the kurtosis coefficients on the equatorial plane. Kurtosis anisotropy is the DKI analog to FA (118).

Even though DKI is more complete than DTI and is able to quantify non-Gaussian diffusion in the brain, DKI-derived diffusion parameters (e.g., DKI-FA) are limited in their sensitivity to detect abnormalities in WM regions with complex fiber arrangements (119). Therefore, the kurtosis indices, such as MK, may be more accurate metrics for WM structural analysis using DKI.

DKI in Early-Stage PD

Diffusion kurtosis imaging has been used in several studies to assess the early stages of PD. Zhang et al. (82–85) published several studies with DKI in early-stage PD with both cross-sectional and longitudinal designs. In these studies, MK in the SN was significantly increased in PD compared with HCs. Additionally, MK in the SN was positively correlated with the H&Y score staging and part III of the Unified Parkinson's Disease Rating Scale (UPDRS-III). In another study, Surova et al. (86) used DKI to study 105 patients with early-stage PD. They found differences in DTI and DKI metrics between PD subjects and HC in the putamen, thalamus, and superior longitudinal fasciculus, which were also associated with increased disease severity. Guan et al. (42) used ROI analysis of DKI metrics to study advanced and early-stage PD, and MK was found to be significantly lower in bilateral SN in patients with both early-stage and advanced PD than in controls. In addition, MK in the left SN was significantly lower in patients with advanced PD than in those with early-stage PD. However, no differences in FA or MD values were observed between the PD and control groups in that study, and no significant correlations between MK, FA, or MD values and the UPDRS scores were observed.

Beyond DTI: Neurite Orientation Dispersion and Density Imaging

Neurite orientation dispersion and density imaging is a practical dMRI technique for estimating the microstructural complexity of dendrites and axons *in vivo* (120). Neurite orientation dispersion and density imaging distinguishes between three microstructural environments: intracellular, extracellular, and CSF compartments. Each compartment affects water diffusion in a unique way (121) and gives rise to a separate normalized MR signal. The full normalized signal, $S(A)$, which includes all environments, is written as follows:

$$S(A) = (1 - v_{iso}) \cdot (v_{ic}A_{ic} + (1 - v_{ic})\, A_{ec}) + v_{iso}A_{iso} \quad (6)$$

where A_{ic} and v_{ic} are the normalized signal and volume fraction of the intracellular compartment, respectively; A_{ec} is the normalized signal of the extracellular compartment; and A_{iso} and v_{ec} are the normalized signal and volume fraction of the CSF compartment, respectively (120). By fitting Equation (6), it is possible to obtain v_{ic}, v_{iso}, and the concentration parameter of the Watson distribution (k), which is a parameter related to A_{ic}. Using k, the orientation dispersion (OD) index can be defined as follows:

$$OD = \frac{2}{\pi} arctan\left(\frac{1}{k}\right) \quad (7)$$

Neurite orientation dispersion and density imaging–derived indices have been suggested as imaging biomarkers in early-stage PD, as discussed below. Moreover, NODDI-derived metrics are less sensitive to partial volume effects than DTI (122), which are known to reduce the accuracy of DTI-derived metrics.

NODDI in Early-Stage PD

Neurite orientation dispersion and density imaging has been used in only two studies in early-stage PD. Andica et al. (87) used both NODDI and tractography to compare v_{ic}, OD, and v_{iso} between groups of PD and HCs. They found that the contralateral distal v_{ic} of the nigrostriatal pathway was significantly lower in PD patients than in HCs. However, no correlations were detected between different NODDI indices and disease duration or motor symptom severity. Surova et al. (86) used NODDI, in addition to DKI as discussed above, and ROI analysis in 105 patients with PD, finding increased v_{iso} in the superior longitudinal fasciculus and decreased v_{iso} in the corticospinal tract.

Beyond DTI: Q-Space Diffeomorphic Reconstruction

In addition to limitations of DTI related to non-Gaussian diffusion, other known limitations such as its inability to independently resolve crossing fibers (123) and sensitivity to PVE, result in DTI-derived metrics that reflect a weighted average of multiple diffusion components within a voxel. These limitations reduce the accuracy of DTI-derived metrics and also of WM tractography. For instance, in voxels with multiple tract orientations, a decrease in FA for one of these fiber populations may result in a contradictory increase in the overall FA (124). To partially overcome this issue, dMRI techniques such as QSDR have been developed.

The orientation distribution function (ODF) can be used to characterize the diffusion distribution of fiber populations, thus overcoming crossing fiber limitations. To calculate the ODF, diffusion data can be acquired using a single-shell diffusion sampling scheme, also known as high angular resolution diffusion imaging (HARDI) (123), or a grid sampling scheme, which is known as diffusion spectrum imaging (DSI) acquisition (125). However, studies using ODF to characterize the diffusion distribution may also suffer from partial volume effects. To overcome these effects, the spin distribution function (SDF) can be obtained from generalized Q-sampling imaging (GQI) (126), where SDF represents the proportion of spins undergoing diffusion in different orientations. Q-space diffeomorphic reconstruction is an advanced method to calculate transformed SDFs in any given deformation field that satisfies diffeomorphism (127). Therefore, QSDR can resolve crossing fibers with substantially smaller impact of partial volume effects.

The quantitative anisotropy (QA), which is defined as the proportion of spins that undergo diffusion along a given fiber orientation, can characterize the diffusion behavior of a fiber population. Quantitative anisotropy is calculated from the peak orientations on an SDF. Each peak orientation defines a QA value:

$$QA\left(\hat{a}\right) = Z_0\left(\psi_Q\left(\hat{a}\right) - I\left(\psi_Q\right)\right) \quad (8)$$

where ψ_Q is the SDF, Z_0 is the SDF scaling constant, $\hat{a}$ is the orientation of the fiber defined by the local maximum of the SDF, and $I\left(\psi_Q\right)$ is the background isotropic component, which can

be approximated by the minimum value of the SDF. With QSDR and the QA index, it is possible to run subsequent analysis, such as VBA (through the normalized QA; nQA = QA/[max QA value]), tractography, and connectome analyses (**Figure 6**).

QSDR in Early-Stage PD

All QSDR studies in early-stage PD used patients from the PPMI database. Ghazi Sherbaf et al. (69) published several studies by using this technique utilizing PPMI database. They studied PD subjects with depression and sleep behavior disorder (70–72). Additionally, they found that PD patients exhibited negative correlations between QA and insulinlike growth factor 1 level in several WM locations, including the middle cerebellar peduncle, left and right cingulum, and genu and splenium of the corpus callosum (72); additionally, they demonstrated that the blood marker apolipoprotein A-1 can predict microstructural changes in WM regions in early-stage PD patients with undisturbed cognition and mild motor disability (68). Utilizing QA in a connectome analyses, Haghshomar et al. (74) previously studied the structural correlation of various WM tracts in 81 early-stage PD patients with the whole-blood neutrophil-to-lymphocyte ratio and identified that the QA index correlated with this ratio in the bilateral cingulum, body and left crus of fornix, bilateral corticospinal tract, body and splenium of corpus callosum, and superior cerebellar peduncle. In another study of 85 subjects with PD, connectome analysis of QA revealed a positive association

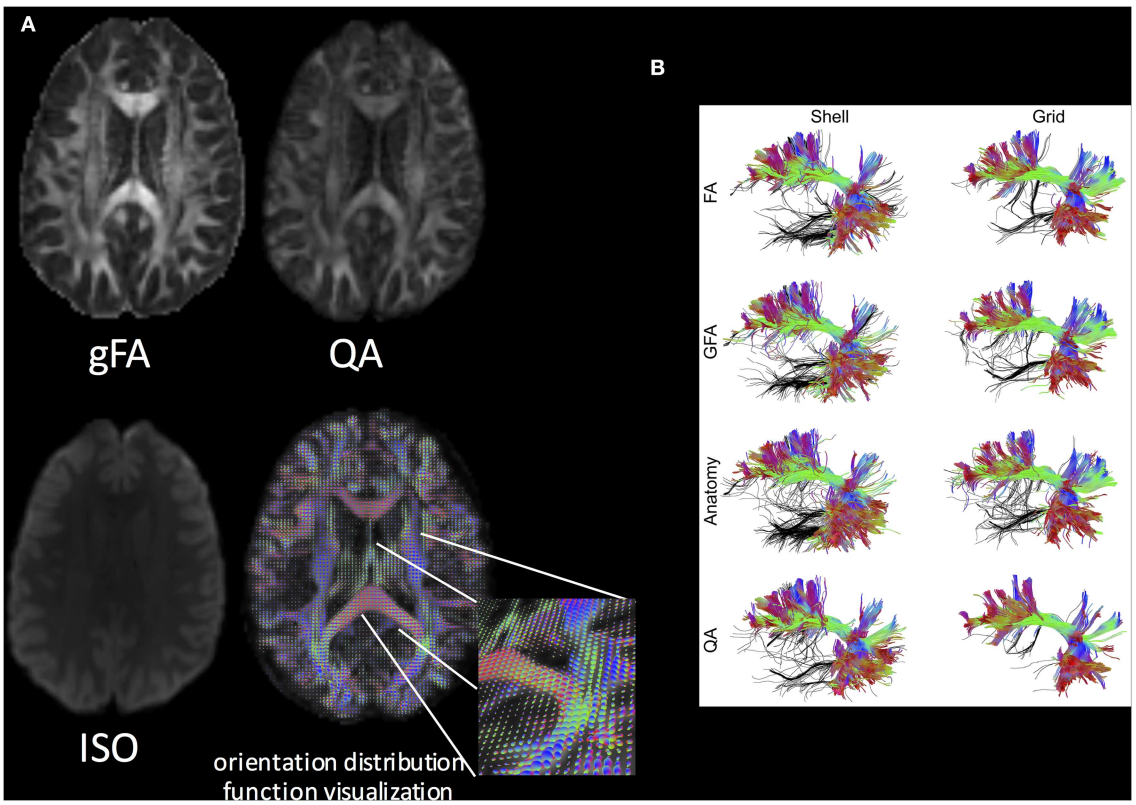


FIGURE 6 | (A) Q-space diffeomorphic reconstruction using DSI Studio. gFA, QA, ISO (represents background isotropic diffusion contributed from CSF), and the ODF visualization are shown. **(B)** The performance of the FA-aided, GFA-aided, anatomy-aided, and QA-aided tractographies showing arcuate fasciculus using shell and grid sampling data. The false tracks are colored in black, whereas accurate trajectories are coded by directional color. The tractographies using FA, GFA, and anatomical information show substantially more false tracks than do those using QA. The best performance can be observed in the tractography using QA and the grid dataset. Reproduced with permission from Yeh et al. (128).

with WM density in bilateral corticospinal tract in the H&Y stage 1 patients, whereas a negative association was observed in the genu of the corpus callosum and bilateral cingulum in H&Y stages 1 and 2 groups (75). In addition, associations between autonomic functional scores and structural brain connectivity in PD were found. Wen et al. (80) used TBSS with graph-theoretical and network-based analyses with QSDR reconstruction to compare WM regional and network features between early-stage PD [tremor-dominant and postural instability and gait difficulty (PIGD) subtypes] and HC groups. Using TBSS and QSDR, tremor-dominant patients showed increased FA and decreased RD and AxD in several areas. Additionally, motor severity had mild to moderate correlations with FA and RD in the genu of the corpus callosum in tremor-dominant subjects, whereas motor severity had strong correlations with FA and RD of multiple association tracts in PIGD subjects. On the other hand, network-based statistical analysis did not reveal any subnetworks with connectivity differences between groups.

Structural network alterations have also been investigated from healthy aging to the prodromal phase of PD to early-stage PD (73). Compared with HCs and *de novo* PD patients, prodromal PD patients showed significantly increased small-world-ness, higher clustering coefficient, and greater local connectivity between regions relating to motor, olfactory, and sleep functions. Parkinson disease patients without hyposmia have shown a significant decrease in global efficiency compared to controls using TBSS with graph-theoretical methods and network-based statistics (81). Additionally, PD patients with hyposmia were shown to exhibit significantly reduced global and local efficiency, as well as a disrupted connection between the right medial orbitofrontal cortex and left rectus, with poorer frontal-related cognitive functioning. Utilizing connectome analysis in 18 early-stage PD and 17 prodromal PD patients, Sanjari Moghaddam et al. (76) investigated the microstructural association of olfaction in prodromal PD as compared to early-stage drug-naive PD patients. Their studies suggested that individuals with prodromal PD have a significantly higher QA as compared to PD patients in bilateral middle cerebellar peduncles and right arcuate fasciculus.

Wen et al. (79) analyzed two different groups of early-stage PD (H&Y stages 1 and 2) using TBSS and QSDR connectome analysis. They found that the earlier stage PD (H&Y stage 1) was associated with higher FA and lower MD and RD in callosal, projection, and association fibers than both HCs and higher-stage PD (H&Y stage 2). The timeline of these alterations between

HC and H&Y stage 2 PD was hypothesized to be indicative of compensatory mechanisms arising from early dopaminergic dysfunction in the SN, although further studies are needed to confirm the presence of these neural compensation mechanisms. In addition, motor severity was inversely correlated with FA and positively correlated with MD and RD in PD patients. Moreover, connectome analysis also revealed increased WM density in the aforementioned tracts in PD patients, compared with HCs.

Finally, olfactory dysfunction has been investigated in relation to QSDR findings. Multiple regression analysis in prodromal PD demonstrated positive association between the University of Pennsylvania Smell Identification Test (UPSIT) score and connectivity in left and right subgenual cingulum, right inferior fronto-occipital fasciculus, left corticospinal tract, left parietopontine, left corticothalamic tract, and the body and the splenium of corpus callosum. Sobhani et al. (77) studied olfactory dysfunction in PD, confirming a discriminative role for UPSIT score in identifying WM microstructure changes in early-PD subjects.

Software for DTI Analysis

Different software packages have been used for diffusion analysis in early-stage PD (**Table 2**). Most of the available software provides both preprocessing and processing steps within the same pipeline. A standalone preprocessing method, DTIprep, may also be used, which performs an automatic study-specific protocol for DWI/DTI quality control and preparation. After preprocessing, multiple software packages are available to generate DTI-derived metrics. FSL is one of the most widely used software packages for DTI analysis. FDT-FSL employs both linear least squares (LLS) and weighted linear least squares (WLLS) fitting procedures. CAMINO is another open-source software toolkit for dMRI processing. It employs LLS, WLLS, unconstrained non-linear optimization, and the robust estimation of tensors involving the outlier rejection (RESTORE) fitting algorithms. Robust fitting methods (RESTORE and iRESTORE), together with LLS fitting, can also be found in the tolerably obsessive registration and tensor optimization indolent software ensemble (TORTOISE) software. Analysis of Functional NeuroImages (AFNI) is frequently used for fMRI analysis, but it can also be employed for DTI fitting (LLS and non-LLS). Diffusion spectrum imaging Studio is a tractography software tool that maps brain connections and correlates findings with neuropsychological disorders. It works with several dMRI methods, including DTI, GQI, QSDR, dMRI connectome analysis, and generalized deterministic fiber tracking. DTI Studio and Explore DTI are other reliable software packages for DTI fitting and dMRI analysis. FSL's probtrackx (within FDT) and the TRActs Constrained by UnderLying Anatomy (Tracula, within FreeSurfer) are both used for probabilistic tractography; DSI Studio and TrackVis are appropriate for deterministic tractography, whereas MRtrix contains both probabilistic and deterministic algorithms. Matlab toolboxes include the Brain Connectivity Toolbox (BCT) for dMRI-derived structural connectivity analysis, DTI and Fiber Tracking toolbox for DTI fitting and tractography, and NODDI toolbox for NODDI analysis. In several studies, authors used in-house software or MRI workstation software for DTI and DKI analysis.

DISCUSSION

Current State of dMRI in Early-Stage PD

Overall, dMRI has been widely used in research settings to investigate WM changes in early-stage PD. In general, DTI acquisition (and similarly DKI) is fairly standardized across vendors and sites, leading to high consistency for data acquisition. The vast majority (56 of 62) of studies included in this systematic review used two b values (typically $b =$ 1,000 s/mm^2 and $b = 0$), although three studies used more b values (up to four b values), and three did not provide this information. More variability is observed in terms of the number of diffusion directions across studies, although the majority used more than 60 directions (37 of 62 studies). Several studies used 30 to 39 directions (seven studies) or 20 to 29 directions (12 studies). Only three studies used fewer than 20 directions. As stated above, more advanced methods require high angular resolution dMRI data, whereas even standard DTI may benefit from improved data acquisition. In general, more than 30 directions can be recommended, and multiple shells may enable improved quantification of dMRI metrics. Despite the similarity in acquisitions, analysis methods can vary widely across studies and are less standardized.

Additionally, the various preprocessing steps for diffusion data can lead to different findings. Echo-planar imaging (EPI) acquisitions suffer from geometric and intensity distortions caused by static magnetic field inhomogeneity, which is worse at higher field strengths; additionally, DTI images are susceptible to the distortions caused by eddy currents induced by large diffusion gradients. There are several methods to correct these issues as part of the preprocessing pipeline. For example, the FSL toolbox includes several tools, including eddy and top-up, which can be used alone or in concert to correct dMRI images. Moreover, the effects of the signal-to-noise ratio can have effect on the accuracy and reproducibility of DTI-derived metrics (129), highlighting the importance of both acquisition and preprocessing steps.

Another important point to consider in light of the dMRI findings in early-stage PD is the effects of the different statistical methods used. Correction of p-values can be achieved in multiple ways and may vary across studies. For instance, the threshold-free cluster enhancement is a method for finding significant clusters without having to define binary clusters, whereas cluster-based thresholding methods are used to correct data for multiple comparisons. Often, the data are reported as family-wise error (FWE)-corrected, which means that the family-wise error rate is controlled. It is important to note that correction for multiple comparisons (e.g., Bonferroni or false discovery rate) is compulsory when analysis includes more than two groups (e.g., analysis of variance *post hoc* analysis) and/or when using multiple ROI analysis.

TABLE 2 | List of the main software for dMRI data processing and analysis available.

Software	Diffusion method	Link	Capabilities
FMRIB's Diffusion Toolbox (FDT) in FMRIB Software Library (FSL)	DTI	https://fsl.fmrib.ox.ac.uk/fsl/fslwiki	Preprocessing, fitting, and tractography
Tract-Based Spatial Statistics (TBSS) in FSL	DTI	https://fsl.fmrib.ox.ac.uk/fsl/fslwiki	Skeletonized analysis
Camino	DTI, tractography, multifiber and HARDI reconstruction techniques	http://camino.cs.ucl.ac.uk/index.php?n=Main.HomePage	Preanalysis and postanalysis
Tolerably obsessive registration and tensor optimization indolent software ensemble (TORTOISE)	DTI	https://tortoise.nibib.nih.gov/	Prefitting and fitting
Analysis of Functional NeuroImages (AFNI)	DTI	https://afni.nimh.nih.gov/	Fitting
DSI Studio	DTI, GQI, QSDR, DSI, connectometry, tractography	http://dsi-studio.labsolver.org/	Preprocessing and data analysis
DTI Studio	DTI	http://lbam.med.jhmi.edu/	Fitting
Explore DTI	DTI, tractography	http://www.exploredti.com/	DTI MRI and fiber tractography
MRtrix	Tractography	https://www.mrtrix.org/	Fiber tractography analysis
TrackVis	Tractography for DTI/DSI/HARDI/Q-Ball	http://www.trackvis.org/	Fiber tractography analysis
Brain Connectivity Toolbox (BCT)—(MATLAB)	Connectivity	https://sites.google.com/site/bctnet/	Connectivity analysis
DTI and Fiber Tracking (MATLAB)	DTI, tractography	https://www.mathworks.com/matlabcentral/fileexchange/21130-dti-and-fiber-tracking	Fitting and fiber tracking
DTIprep	DWI/DTI quality control and preparation	https://www.nitrc.org/projects/dtiprep	Preprocessing

Despite the lack of standardized methods, dMRI methods are increasingly used to understand whether dMRI-derived metrics suggesting WM disorganization are related to clinical presentation. Early-stage PD patients with non-motor symptoms, such as those with olfactory dysfunction or those with substantial SN dopaminergic neuron loss, have been analyzed with various dMRI techniques. Conventional single-tensor DTI models, as well as more sophisticated dMRI models such as DKI and NODDI, have independently suggested diffuse WM changes in early-stage PD, supporting the notion of early axonal damage in PD while simultaneously suggesting that PD pathology may go unrecognized until symptoms appear. Moreover, conventional DTI metrics such as FA and MD have displayed sensitivity to potentially identify earlier symptomatic regions, such as olfactory structures, using correlations with clinical presentations in predetermined ROI analysis. In addition, several studies have considered dMRI changes in GM (10, 45, 65, 66, 86, 107, 122), which may also be implicated in PD pathology. However, as GM lacks the microstructural organization of WM, interpretation of GM-DTI must be approached with caution. In contrast, NODDI has previously been shown to reflect the neurobiology of cortical microstructures (122), suggesting that more advanced dMRI models may enable robust GM characterization in early-stage PD.

However, studies have often displayed heterogeneous results, which may be at least partially attributable to the varying preprocessing and postprocessing steps and statistical approaches utilized. Early-stage PD patients are also heterogeneous in their clinical presentations, and this may further contribute to such varied findings. Although the combination of different dMRI acquisitions and analyses may yield new and more accurate information related to dMRI-derived WM structural disorganization and global connectivity changes in early-stage PD, dMRI has the capability to be developed as a useful neuroimaging tool for diagnosis and prognosis of early-stage PD by rigorously developing and enforcing a set of standardized acquisition and postprocessing tools. This will ultimately provide more reliable dMRI-derived neuroimaging biomarkers that are not only significantly different when compared to HC in early-stage PD, but also attempt to explain their correlations with clinical presentation. Altogether, these will in turn help to understand the neuropathological underpinnings of the progression of PD. Utilizing advanced dMRI methods that overcome some of the known limitations of DTI is also imperative, as measures derived through these advanced dMRI methods may help to understand tract-specific deterioration of WM organization in the progression of PD. Ultimately, ensuring standardization of patient recruitment, data acquisition,

postprocessing analytical tools, and statistical approaches could move dMRI toward clinical implementation for identifying dMRI-derived neuroimaging biomarkers.

Challenges of dMRI in Early-Stage PD

As previously mentioned, conflicting results are often reported in dMRI studies on PD subjects. The small sample size of participants, heterogeneous clinical presentation, and sex imbalance may be responsible for such non-reproducible results reported in the literature. Moreover, the heterogeneity of findings may also be related to the dMRI data acquisition. It is important to emphasize that dMRI acquisitions with fewer than 30 directions may not correctly estimate DTI metrics. For robust estimation of anisotropy, at least 20 unique sampling orientations are necessary, whereas at least 30 unique sampling orientations are required for robust estimation of both tensor orientation and MD. Diffusion schemes with a lower number of sampling orientations may introduce bias and spurious correlations between tensor orientation and apparent diffusion characteristics (130). Hence, acquiring data with at least 45 to 60 diffusion-encoding directions might help to better resolve crossing fibers, may aid in connectome analyses, and can be generally recommended for dMRI data acquisition.

The trend to acquire multishell dMRI data with multiple *b* values is increasing and is also widely recommended. With the advent of simultaneous multislice techniques, it is now clinically feasible to acquire high angular resolution data with multiple shells in clinically acceptable time of approximately 20 min. Acquiring such high angular resolution data with multiple shells permits estimation of advanced dMRI-derived metrics, such as free-water corrected DTI metrics, DKI-derived metrics, and NODDI-metrics. In the future, the sensitivity and specificity of each of these measures should be compared with disease progression to identify the most reproducible, sensitive, and specific dMRI-derived neuroimaging biomarkers for understanding neuropathological underpinnings of PD.

Another possible source of different results lies in the different postprocessing software and statistical approaches used. The algorithms used for tensor fitting of diffusion-weighted data can have substantial effects on the results, not only for PD, but also for other diseases (131, 132). For instance, although LLS fitting model is fast, it incorrectly assumes that data outliers are homogeneously distributed, and therefore it fails to appropriately deweight their contributions. On the other hand, WLLS is slower than the LLS but assigns a weight according to how much the original noise variation is affected by logarithmic transform of the data. While more robust fitting algorithms are available, such as RESTORE and iRESTORE, these are not frequently used because of more complicated pipelines. Identifying the most reproducible statistical approach and the best preprocessing and postprocessing tools are important unmet needs in analysis of dMRI data.

New Avenues for dMRI in Early-Stage PD

We previously discussed that DTI has several limitations related to an assumption of Gaussian diffusion, presence of crossing fibers, and partial volume effects. Each of the methods presented above that move beyond standard DTI has some aspect that overcomes these limitations, such as DKI to characterize deviations from Gaussian diffusion, NODDI to characterize and minimize partial volume effects, and QSDR to characterize both intravoxel fiber orientation heterogeneity and partial volume effects. Network-based approaches that do not assume the caliber or density of axons in WM, but rather only the orientation of axons, have seen a surge in recent years since PD has been postulated as a network disorder. In several early-stage PD studies, these advanced approaches have been used to overcome DTI-related limitations, although other options are available and have not been investigated. For example, DSI (133) is a technique that can resolve the fiber crossing limitation; however, DSI requires both more time for acquisition than standard DTI and larger pulsed field gradients.

While each of these methods may overcome a fundamental limitation for DTI, these methods may have different limitations themselves (113). For instance, DKI and NODDI suffer from their inherent mathematical assumptions that require data collection methods and analysis that may not be practical or feasible. Interpreting the free-water contribution as applied to DTI is also challenging. Studying network topology through WM-derived structural connectivity may be limited because there is no consensus on the choice of tracking algorithm or edge weights. However, high angular resolution dMRI data acquisition at multiple shells in a clinically acceptable time lends hope in applying and standardizing these advanced dMRI techniques, while simultaneously permitting the incorporation of metrics from these advanced dMRI techniques into network-based analysis.

Outlook for Future of dMRI in Early-Stage PD

The clinical management of PD faces a significant challenge because moderate to severe neurodegeneration has been shown to be present before the diagnosis is rendered. In addition, the classic presentation of motor disability in PD is shown to co-occur with non-motor symptoms such as changes in mood and behavior, cognitive impairment, sleep disorders, and olfactory dysfunction. The need for neuroimaging biomarkers to detect initial neuropathological changes is crucial to optimize patient care via correct diagnosis and treatment.

Diffusion tensor imaging–based metrics have shown significant but subtle changes in early-stage PD in many areas, such as the motor, premotor, and supplementary motor cortices, corpus callosum, and SN (37, 134, 135). Moreover, non-motor features common to PD, including olfactory dysfunction, REM sleep behavior disorder, cognitive impairment, excessive daytime sleepiness, and depression, can appear in the early stages of PD, providing rationale for screening for PD-like pathology (136). While all of these symptoms have been studied with DTI, the results have been limited or heterogeneous (137, 138). Although hallmark regions such as the SN have been extensively studied using DTI, other regions, along

with corresponding hallmarks of PD pathology, should be examined more extensively via advanced dMRI techniques. Additionally, further studies and the inclusion of advanced dMRI methods may aid in establishing more coherent knowledge of WM changes in PD-associated non-motoric symptoms, possibly providing neuroimaging-based biomarkers and thus creating an avenue for advancement of patient care and treatment.

DATA AVAILABILITY STATEMENT

All datasets generated for this study are included in the article/supplementary material.

AUTHOR CONTRIBUTIONS

RW conceived of the presented idea. MB and EK performed the literature search and method review. MB created all figures and tables. MB, EK, VM, and AS wrote the manuscript. All authors edited and approved the manuscript. AS and RW share senior authorship.

FUNDING

This work was supported by the Barrow Neurological Foundation, Sam & Peggy Grossman Family Foundation, and Samuel P. Mandell Foundation.

REFERENCES

1. Marras C, Beck JC, Bower JH, Roberts E, Ritz B, Ross GW, et al. Prevalence of Parkinson's disease across North America. *NPJ Parkinsons Dis*. (2018) 4:21. doi: 10.1038/s41531-018-0058-0
2. Parashos SA, Maraganore DM, O'Brien PC, Rocca WA. Medical services utilization and prognosis in Parkinson disease: a population-based study. *Mayo Clin Proc*. (2002) 77:918–25. doi: 10.4065/77.9.918
3. Suchowersky O, Reich S, Perlmutter J, Zesiewicz T, Gronseth G, Weiner WJ, et al. Practice parameter: diagnosis and prognosis of new onset Parkinson disease (an evidence-based review): report of the quality standards subcommittee of the American academy of neurology. *Neurology*. (2006) 66:968–75. doi: 10.1212/01.wnl.0000215437.80053.d0
4. Braak H, Del Tredici K, Rub U, de Vos RA, Jansen Steur EN, Braak E. Staging of brain pathology related to sporadic Parkinson's disease. *Neurobiol Aging*. (2003) 24:197–211. doi: 10.1016/S0197-4580(02)00065-9
5. Seeley WW, Crawford RK, Zhou J, Miller BL, Greicius MD. Neurodegenerative diseases target large-scale human brain networks. *Neuron*. (2009) 62:42–52. doi: 10.1016/j.neuron.2009.03.024
6. Forno LS. Neuropathology of Parkinson's disease. *J Neuropathol Exp Neurol*. (1996) 55:259–72. doi: 10.1097/00005072-199603000-00001
7. Kordower JH, Olanow CW, Dodiya HB, Chu Y, Beach TG, Adler CH, et al. Disease duration and the integrity of the nigrostriatal system in Parkinson's disease. *Brain*. (2013) 136(Pt 8):2419–31. doi: 10.1093/brain/awt192
8. Le W, Dong J, Li S, Korczyn AD. Can biomarkers help the early diagnosis of Parkinson's disease? *Neurosci Bull*. (2017) 33:535–42. doi: 10.1007/s12264-017-0174-6
9. Ashburner J, Friston KJ. Voxel-based morphometry–the methods. *Neuroimage*. (2000) 11(6 Pt 1):805–21. doi: 10.1006/nimg.2000.0582
10. Shao N, Yang J, Shang H. Voxelwise meta-analysis of gray matter anomalies in Parkinson variant of multiple system atrophy and Parkinson's disease using anatomic likelihood estimation. *Neurosci Lett*. (2015) 587:79–86. doi: 10.1016/j.neulet.2014.12.007
11. Vriend C, Boedhoe PS, Rutten S, Berendse HW, van der Werf YD, van den Heuvel OA. A smaller amygdala is associated with anxiety in Parkinson's disease: a combined freeSurfer-VBM study. *J Neurol Neurosurg Psychiatry*. (2016) 87:493–500. doi: 10.1136/jnnp-2015-310383
12. Buhmann C, Glauche V, Sturenburg HJ, Oechsner M, Weiller C, Buchel C. Pharmacologically modulated fMRI–cortical responsiveness to levodopa in drug-naive hemiparkinsonian patients. *Brain*. (2003) 126(Pt 2):451–61. doi: 10.1093/brain/awg033
13. Mohl B, Berman BD, Shelton E, Tanabe J. Levodopa response differs in Parkinson's motor subtypes: a task-based effective connectivity study. *J Comp Neurol*. (2017) 525:2192–201. doi: 10.1002/cne.24197
14. Spraker MB, Prodoehl J, Corcos DM, Comella CL, Vaillancourt DE. Basal ganglia hypoactivity during grip force in drug naive Parkinson's disease. *Hum Brain Mapp*. (2010) 31:1928–41. doi: 10.1002/hbm.20987
15. Biswal B, Yetkin FZ, Haughton VM, Hyde JS. Functional connectivity in the motor cortex of resting human brain using echo-planar MRI. *Magn Reson Med*. (1995) 34:537–41. doi: 10.1002/mrm.1910340409
16. Helmich RC, Derikx LC, Bakker M, Scheeringa R, Bloem BR, Toni I. Spatial remapping of cortico-striatal connectivity in Parkinson's disease. *Cereb Cortex*. (2010) 20:1175–86. doi: 10.1093/cercor/bhp178
17. Le Bihan D, Mangin JF, Poupon C, Clark CA, Pappata S, Molko N, et al. Diffusion tensor imaging: concepts and applications. *J Magn Reson Imaging*. (2001) 13:534–46. doi: 10.1002/jmri.1076
18. Basser PJ, Mattiello J, LeBihan D. MR diffusion tensor spectroscopy and imaging. *Biophys J*. (1994) 66:259–67. doi: 10.1016/S0006-3495(94)80775-1
19. Mori S, Zhang J. Principles of diffusion tensor imaging and its applications to basic neuroscience research. *Neuron*. (2006) 51:527–39. doi: 10.1016/j.neuron.2006.08.012
20. Hagmann P, Jonasson L, Maeder P, Thiran JP, Wedeen VJ, Meuli R. Understanding diffusion MR imaging techniques: from scalar diffusion-weighted imaging to diffusion tensor imaging and beyond. *Radiographics*. (2006) 26(Suppl. 1):S205–23. doi: 10.1148/rg.26si065510
21. Jellison BJ, Field AS, Medow J, Lazar M, Salamat MS, Alexander AL. Diffusion tensor imaging of cerebral white matter: a pictorial review of physics, fiber tract anatomy, and tumor imaging patterns. *AJNR Am J Neuroradiol*. (2004) 25:356–69.
22. Le Bihan D, Iima M. Diffusion magnetic resonance imaging: what water tells us about biological tissues. *PLoS Biol*. (2015) 13:e1002203. doi: 10.1371/journal.pbio.1002203
23. Soares JM, Marques P, Alves V, Sousa N. A hitchhiker's guide to diffusion tensor imaging. *Front Neurosci*. (2013) 7:31. doi: 10.3389/fnins.2013.00031
24. Atkinson-Clement C, Pinto S, Eusebio A, Coulon O. Diffusion tensor imaging in Parkinson's disease: review and meta-analysis. *Neuroimage Clin*. (2017) 16:98–110. doi: 10.1016/j.nicl.2017.07.011
25. Liberati A, Altman DG, Tetzlaff J, Mulrow C, Gotzsche PC, Ioannidis JP, et al. The PRISMA statement for reporting systematic reviews and meta-analyses of studies that evaluate health care interventions: explanation and elaboration. *J Clin Epidemiol*. (2009) 62:e1–34. doi: 10.1016/j.jclinepi.2009.06.006
26. Vriend C, van den Heuvel OA, Berendse HW, van der Werf YD, Douw L. Global and subnetwork changes of the structural connectome in *de novo* Parkinson's disease. *Neuroscience*. (2018) 386:295–308. doi: 10.1016/j.neuroscience.2018.06.050
27. Arrigo A, Calamuneri A, Milardi D, Mormina E, Rania L, Postorino E, et al. Visual system involvement in patients with newly diagnosed Parkinson disease. *Radiology*. (2017) 285:885–95. doi: 10.1148/radiol.2017161732
28. Tinaz S, Lauro PM, Ghosh P, Lungu C, Horovitz SG. Changes in functional organization and white matter integrity in the connectome in Parkinson's disease. *Neuroimage Clin*. (2017) 13:395–404. doi: 10.1016/j.nicl.2016.12.019
29. Pena-Nogales O, Ellmore TM, de Luis-Garcia R, Suescun J, Schiess MC, Giancardo L. Longitudinal connectomes as a candidate progression marker for prodromal Parkinson's disease. *Front Neurosci*. (2018) 12:967. doi: 10.3389/fnins.2018.00967
30. Nigro S, Riccelli R, Passamonti L, Arabia G, Morelli M, Nistico R, et al. Characterizing structural neural networks in *de novo* Parkinson disease

patients using diffusion tensor imaging. *Hum Brain Mapp.* (2016) 37:4500–10. doi: 10.1002/hbm.23324
31. Tessa C, Giannelli M, Della Nave R, Lucetti C, Berti C, Ginestroni A, et al. A whole-brain analysis in *de novo* Parkinson disease. *AJNR Am J Neuroradiol.* (2008) 29:674–80. doi: 10.3174/ajnr.A0900
32. Knossalla F, Kohl Z, Winkler J, Schwab S, Schenk T, Engelhorn T, et al. High-resolution diffusion tensor-imaging indicates asymmetric microstructural disorganization within substantia nigra in early Parkinson's disease. *J Clin Neurosci.* (2018) 50:199–202. doi: 10.1016/j.jocn.2018.01.023
33. Joshi N, Rolheiser TM, Fisk JD, McKelvey JR, Schoffer K, Phillips G, et al. Lateralized microstructural changes in early-stage Parkinson's disease in anterior olfactory structures, but not in substantia nigra. *J Neurol.* (2017) 264:1497–505. doi: 10.1007/s00415-017-8555-3
34. Wang J, Yang QX, Sun X, Vesek J, Mosher Z, Vasavada M, et al. MRI evaluation of asymmetry of nigrostriatal damage in the early stage of early-onset Parkinson's disease. *Parkinsonism Relat Disord.* (2015) 21:590–6. doi: 10.1016/j.parkreldis.2015.03.012
35. Aquino D, Contarino V, Albanese A, Minati L, Farina L, Grisoli M, et al. Substantia nigra in Parkinson's disease: a multimodal MRI comparison between early and advanced stages of the disease. *Neurol Sci.* (2014) 35:753–8. doi: 10.1007/s10072-013-1595-2
36. Vaillancourt DE, Spraker MB, Prodoehl J, Abraham I, Corcos DM, Zhou XJ, et al. High-resolution diffusion tensor imaging in the substantia nigra of *de novo* Parkinson disease. *Neurology.* (2009) 72:1378–84. doi: 10.1212/01.wnl.0000340982.01727.6e
37. Gattellaro G, Minati L, Grisoli M, Mariani C, Carella F, Osio M, et al. White matter involvement in idiopathic Parkinson disease: a diffusion tensor imaging study. *AJNR Am J Neuroradiol.* (2009) 30:1222–6. doi: 10.3174/ajnr.A1556
38. Du G, Lewis MM, Sen S, Wang J, Shaffer ML, Styner M, et al. Imaging nigral pathology and clinical progression in Parkinson's disease. *Mov Disord.* (2012) 27:1636–43. doi: 10.1002/mds.25182
39. Loane C, Politis M, Kefalopoulou Z, Valle-Guzman N, Paul G, Widner H, et al. Aberrant nigral diffusion in Parkinson's disease: a longitudinal diffusion tensor imaging study. *Mov Disord.* (2016) 31:1020–6. doi: 10.1002/mds.26606
40. Schuff N, Wu IW, Buckley S, Foster ED, Coffey CS, Gitelman DR, et al. Diffusion imaging of nigral alterations in early Parkinson's disease with dopaminergic deficits. *Mov Disord.* (2015) 30:1885–92. doi: 10.1002/mds.26325
41. Pelizzari L, Lagana MM, Di Tella S, Rossetto F, Bergsland N, Nemni R, et al. Combined assessment of diffusion parameters and cerebral blood flow within basal ganglia in early Parkinson's disease. *Front Aging Neurosci.* (2019) 11:134. doi: 10.3389/fnagi.2019.00134
42. Guan J, Ma X, Geng Y, Qi D, Shen Y, Shen Z, et al. Diffusion kurtosis imaging for detection of early brain changes in Parkinson's disease. *Front Neurol.* (2019) 10:1285. doi: 10.3389/fneur.2019.01285
43. Liu L, Chen Y, Fang Y, He Q, Yang Y, Du D, et al. DTI and ESWAN sequences are effective for the early diagnosis of Parkinson's disease. *Int J Clin Exp Med.* (2016) 9:19815–820. Available online at: https://www.ijcem.com/ISSN:1940-5901/IJCEM0030923
44. Mangia S, Svatkova A, Mascali D, Nissi MJ, Burton PC, Bednarik P, et al. Multi-modal brain MRI in subjects with PD and iRBD. *Front Neurosci.* (2017) 11:709. doi: 10.3389/fnins.2017.00709
45. Klein JC, Rolinski M, Griffanti L, Szewczyk-Krolikowski K, Baig F, Ruffmann C, et al. Cortical structural involvement and cognitive dysfunction in early Parkinson's disease. *NMR Biomed.* (2018) 31:e3900. doi: 10.1002/nbm.3900
46. Planetta PJ, Schulze ET, Geary EK, Corcos DM, Goldman JG, Little DM, et al. Thalamic projection fiber integrity in *de novo* Parkinson disease. *AJNR Am J Neuroradiol.* (2013) 34:74–9. doi: 10.3174/ajnr.A3178
47. Wei X, Yan R, Chen Z, Weng R, Liu X, Gao H, et al. Combined diffusion tensor imaging and arterial spin labeling as markers of early Parkinson's disease. *Sci Rep.* (2016) 6:33762. doi: 10.1038/srep33762
48. Li XR, Ren YD, Cao B, Huang XL. Analysis of white matter characteristics with tract-based spatial statistics according to diffusion tensor imaging in early Parkinson's disease. *Neurosci Lett.* (2018) 675:127–32. doi: 10.1016/j.neulet.2017.11.064
49. Rolheiser TM, Fulton HG, Good KP, Fisk JD, McKelvey JR, Scherfler C, et al. Diffusion tensor imaging and olfactory identification testing in early-stage Parkinson's disease. *J Neurol.* (2011) 258:1254–60. doi: 10.1007/s00415-011-5915-2
50. Ibarretxe-Bilbao N, Junque C, Marti MJ, Valldeoriola F, Vendrell P, Bargallo N, et al. Olfactory impairment in Parkinson's disease and white matter abnormalities in central olfactory areas: a voxel-based diffusion tensor imaging study. *Mov Disord.* (2010) 25:1888–94. doi: 10.1002/mds.23208
51. Minett T, Su L, Mak E, Williams G, Firbank M, Lawson RA, et al. Longitudinal diffusion tensor imaging changes in early Parkinson's disease: ICICLE-PD study. *J Neurol.* (2018) 265:1528–39. doi: 10.1007/s00415-018-8873-0
52. Duncan GW, Firbank MJ, Yarnall AJ, Khoo TK, Brooks DJ, Barker RA, et al. Gray and white matter imaging: A biomarker for cognitive impairment in early Parkinson's disease? *Mov Disord.* (2016) 31:103–10. doi: 10.1002/mds.26312
53. Lacey C, Ohlhauser L, Gawryluk JR. Microstructural white matter characteristics in Parkinson's disease with depression: a diffusion tensor imaging replication study. *Front Neurol.* (2019) 10:884. doi: 10.3389/fneur.2019.00884
54. Pozorski V, Oh JM, Adluru N, Merluzzi AP, Theisen F, Okonkwo O, et al. Longitudinal white matter microstructural change in Parkinson's disease. *Hum Brain Mapp.* (2018) 39:4150–61. doi: 10.1002/hbm.24239
55. Rektor I, Svatkova A, Vojtisek L, Zikmundova I, Vanicek J, Kiraly A, et al. White matter alterations in Parkinson's disease with normal cognition precede grey matter atrophy. *PLoS ONE.* (2018) 13:e0187939. doi: 10.1371/journal.pone.0187939
56. Pelizzari L, Di Tella S, Lagana MM, Bergsland N, Rossetto F, Nemni R, et al. White matter alterations in early Parkinson's disease: role of motor symptom lateralization. *Neurol Sci.* (2020) 41:357–64. doi: 10.1007/s10072-019-04084-y
57. Chen NK, Chou YH, Sundman M, Hickey P, Kasoff WS, Bernstein A, et al. Alteration of diffusion-tensor magnetic resonance imaging measures in brain regions involved in early stages of Parkinson's disease. *Brain Connect.* (2018) 8:343–49. doi: 10.1089/brain.2017.0558
58. Mishra VR, Sreenivasan KR, Zhuang X, Yang Z, Cordes D, Walsh RR. Influence of analytic techniques on comparing DTI-derived measurements in early stage Parkinson's disease. *Heliyon.* (2019) 5:e01481. doi: 10.1016/j.heliyon.2019.e01481
59. Gou L, Zhang W, Li C, Shi X, Zhou Z, Zhong W, et al. Structural brain network alteration and its correlation with structural impairments in patients with depression in *de novo* and drug-naive Parkinson's disease. *Front Neurol.* (2018) 9:608. doi: 10.3389/fneur.2018.00608
60. Meijer FJ, van Rumund A, Tuladhar AM, Aerts MB, Titulaer I, Esselink RA, et al. Conventional 3T brain MRI and diffusion tensor imaging in the diagnostic workup of early stage parkinsonism. *Neuroradiology.* (2015) 57:655–69. doi: 10.1007/s00234-015-1515-7
61. Guimaraes RP, Campos BM, de Rezende TJ, Piovesana L, Azevedo PC, Amato-Filho AC, et al. Is diffusion tensor imaging a good biomarker for early Parkinson's disease? *Front Neurol.* (2018) 9:626. doi: 10.3389/fneur.2018.00626
62. Prange S, Metereau E, Maillet A, Lhommee E, Klinger H, Pelissier P, et al. Early limbic microstructural alterations in apathy and depression in *de novo* Parkinson's disease. *Mov Disord.* (2019) 34:1644–54. doi: 10.1002/mds.27793
63. Ford AH, Duncan GW, Firbank MJ, Yarnall AJ, Khoo TK, Burn DJ, et al. Rapid eye movement sleep behavior disorder in Parkinson's disease: magnetic resonance imaging study. *Mov Disord.* (2013) 28:832–6. doi: 10.1002/mds.25367
64. Zhang Y, Wu IW, Buckley S, Coffey CS, Foster E, Mendick S, et al. *Diffusion tensor imaging of the nigrostriatal fibers in Parkinson's disease. Mov Disord.* (2015) 30:1229–36. doi: 10.1002/mds.26251
65. Lorio S, Sambataro F, Bertolino A, Draganski B, Dukart J. The combination of DAT-SPECT, structural and diffusion MRI predicts clinical progression in Parkinson's disease. *Front Aging Neurosci.* (2019) 11:57. doi: 10.3389/fnagi.2019.00057
66. Taylor KI, Sambataro F, Boess F, Bertolino A, Dukart J. Progressive decline in gray and white matter integrity in *de novo* Parkinson's disease: an analysis of longitudinal Parkinson progression markers

initiative diffusion tensor imaging data. *Front Aging Neurosci.* (2018) 10:318. doi: 10.3389/fnagi.2018.00318
67. Planetta PJ, Ofori E, Pasternak O, Burciu RG, Shukla P, DeSimone JC, et al. Free-water imaging in Parkinson's disease and atypical parkinsonism. *Brain.* (2016) 139(Pt 2):495–508. doi: 10.1093/brain/awv361
68. Rahmani F, Aarabi MH. Does apolipoprotein A1 predict microstructural changes in subgenual cingulum in early Parkinson? *J Neurol.* (2017) 264:684–93. doi: 10.1007/s00415-017-8403-5
69. Ghazi Sherbaf F, Rahmani F, Jooyandeh SM, Aarabi MH. Microstructural changes in patients with Parkinson disease and REM sleep behavior disorder: depressive symptoms versus non-depressed. *Acta Neurol Belg.* (2018) 118:415–21. doi: 10.1007/s13760-018-0896-x
70. Ansari M, Adib Moradi S, Ghazi Sherbaf F, Hedayatnia A, Aarabi MH. Comparison of structural connectivity in Parkinson's disease with depressive symptoms versus non-depressed: a diffusion MRI connectometry study. *Int Psychogeriatr.* (2019) 31:5–12. doi: 10.1017/S1041610218000170
71. Ansari M, Rahmani F, Dolatshahi M, Pooyan A, Aarabi MH. Brain pathway differences between Parkinson's disease patients with and without REM sleep behavior disorder. *Sleep Breath.* (2017) 21:155–61. doi: 10.1007/s11325-016-1435-8
72. Ghazi Sherbaf F, Rostam Abadi Y, Mojtahed Zadeh M, Ashraf-Ganjouei A, Sanjari Moghaddam H, Aarabi MH. Microstructural changes in patients with Parkinson's disease comorbid with REM sleep behaviour disorder and depressive symptoms. *Front Neurol.* (2018) 9:441. doi: 10.3389/fneur.2018.00441
73. Wen MC, Heng HSE, Hsu JL, Xu Z, Liew GM, Au WL, et al. Structural connectome alterations in prodromal and *de novo* Parkinson's disease patients. *Parkinsonism Relat Disord.* (2017) 45:21–7. doi: 10.1016/j.parkreldis.2017.09.019
74. Haghshomar M, Rahmani F, Hadi Aarabi M, Shahjouei S, Sobhani S, Rahmani M. White matter changes correlates of peripheral neuroinflammation in patients with Parkinson's disease. *Neuroscience.* (2019) 403:70–8. doi: 10.1016/j.neuroscience.2017.10.050
75. Ashraf-Ganjouei A, Majd A, Javinani A, Aarabi MH. Autonomic dysfunction and white matter microstructural changes in drug-naive patients with Parkinson's disease. *PeerJ.* (2018) 6:e5539. doi: 10.7717/peerj.5539
76. Sanjari Moghaddam H, Dolatshahi M, Salardini E, Aarabi MH. Association of olfaction dysfunction with brain microstructure in prodromal Parkinson disease. *Neurol Sci.* (2019) 40:283–91. doi: 10.1007/s10072-018-3629-2
77. Sobhani S, Rahmani F, Aarabi MH, Sadr AV. Exploring white matter microstructure and olfaction dysfunction in early parkinson disease: diffusion MRI reveals new insight. *Brain Imaging Behav.* (2019) 13:210–9. doi: 10.1007/s11682-017-9781-0
78. Ghazi Sherbaf F, Mohajer B, Ashraf-Ganjouei A, Mojtahed Zadeh M, Javinani A, Sanjari Moghaddam H, et al. Serum insulin-like growth factor-1 in Parkinson's disease; study of cerebrospinal fluid biomarkers and white matter microstructure. *Front Endocrinol (Lausanne).* (2018) 9:608. doi: 10.3389/fendo.2018.00608
79. Wen MC, Heng HS, Ng SY, Tan LC, Chan LL, Tan EK. White matter microstructural characteristics in newly diagnosed Parkinson's disease: an unbiased whole-brain study. *Sci Rep.* (2016) 6:35601. doi: 10.1038/srep35601
80. Wen MC, Heng HSE, Lu Z, Xu Z, Chan LL, Tan EK, et al. Differential white matter regional alterations in motor subtypes of early drug-naive Parkinson's disease patients. *Neurorehabil Neural Repair.* (2018) 32:129–41. doi: 10.1177/1545968317753075
81. Wen MC, Xu Z, Lu Z, Chan LL, Tan EK, Tan LCS. Microstructural network alterations of olfactory dysfunction in newly diagnosed Parkinson's disease. *Sci Rep.* (2017) 7:12559. doi: 10.1038/s41598-017-12947-7
82. Zhang G, Zhang C, Wang Y, Wang L, Zhang Y, Xie H, et al. Is hyperhomocysteinemia associated with the structural changes of the substantia nigra in Parkinson's disease? A two-year follow-up study. *Parkinsonism Relat Disord.* (2019) 60:46–50. doi: 10.1016/j.parkreldis.2018.10.008
83. Zhang G, Zhang Y, Zhang C, Wang Y, Ma G, Nie K, et al. Diffusion kurtosis imaging of substantia nigra is a sensitive method for early diagnosis and disease evaluation in Parkinson's disease. *Parkinsons Dis.* (2015) 2015:207624. doi: 10.1155/2015/207624
84. Zhang G, Zhang C, Zhang Y, Wang Y, Nie K, Zhang B, et al. The effects of striatal silent lacunar infarction on the substantia nigra and movement disorders in Parkinson's disease: a follow-up study. *Parkinsonism Relat Disord.* (2017) 43:33–7. doi: 10.1016/j.parkreldis.2017.06.020
85. Zhang G, Zhang Y, Zhang C, Wang Y, Ma G, Nie K, et al. Striatal silent lacunar infarction is associated with changes to the substantia nigra in patients with early-stage Parkinson's disease: a diffusion kurtosis imaging study. *J Clin Neurosci.* (2016) 33:138–141. doi: 10.1016/j.jocn.2016.03.032
86. Surova Y, Lampinen B, Nilsson M, Latt J, Hall S, Widner H, et al. Alterations of diffusion kurtosis and neurite density measures in deep grey matter and white matter in Parkinson's disease. *PLoS ONE.* (2016) 11:e0157755. doi: 10.1371/journal.pone.0157755
87. Andica C, Kamagata K, Hatano T, Okuzumi A, Saito A, Nakazawa M, et al. Neurite orientation dispersion and density imaging of the nigrostriatal pathway in Parkinson's disease: retrograde degeneration observed by tract-profile analysis. *Parkinsonism Relat Disord.* (2018) 51:55–60. doi: 10.1016/j.parkreldis.2018.02.046
88. Basser PJ, Pajevic S, Pierpaoli C, Duda J, Aldroubi A. *In vivo* fiber tractography using DT-MRI data. *Magn Reson Med.* (2000) 44:625–32. doi: 10.1002/1522-2594(200010)44:4<625::aid-mrm17>3.0.co;2-o
89. Mori S, Crain BJ, Chacko VP, van Zijl PC. Three-dimensional tracking of axonal projections in the brain by magnetic resonance imaging. *Ann Neurol.* (1999) 45:265–9. doi: 10.1002/1531-8249(199902)45:2<265::aid-ana21>3.0.co;2-3
90. Concha L. A macroscopic view of microstructure: using diffusion-weighted images to infer damage, repair, and plasticity of white matter. *Neuroscience.* (2014) 276:14–28. doi: 10.1016/j.neuroscience.2013.09.004
91. Song SK, Sun SW, Ramsbottom MJ, Chang C, Russell J, Cross AH. Dysmyelination revealed through MRI as increased radial (but unchanged axial) diffusion of water. *Neuroimage.* (2002) 17:1429–36. doi: 10.1006/nimg.2002.1267
92. Jones DK, Cercignani M. Twenty-five pitfalls in the analysis of diffusion MRI data. *NMR Biomed.* (2010) 23:803–20. doi: 10.1002/nbm.1543
93. Vos SB, Jones DK, Jeurissen B, Viergever MA, Leemans A. The influence of complex white matter architecture on the mean diffusivity in diffusion tensor MRI of the human brain. *Neuroimage.* (2012) 59:2208–16. doi: 10.1016/j.neuroimage.2011.09.086
94. Beaulieu C. What makes diffusion anisotropic in the nervous system? In: *Diffusion MRI: Theory, Methods, Applications*, ed D. K. Jones. New York, NY: Oxford University Press (2010). p. 92–109. doi: 10.1093/med/9780195369779.003.0007
95. Takahashi M, Hackney DB, Zhang G, Wehrli SL, Wright AC, O'Brien WT, et al. Magnetic resonance microimaging of intraaxonal water diffusion in live excised lamprey spinal cord. *Proc Natl Acad Sci USA.* (2002) 99:16192–6. doi: 10.1073/pnas.252249999
96. Alexander AL, Hasan K, Kindlmann G, Parker DL, Tsuruda JS. A geometric analysis of diffusion tensor measurements of the human brain. *Magn Reson Med.* (2000) 44:283–91. doi: 10.1002/1522-2594(200008)44:2<283::aid-mrm16>3.0.co;2-v
97. Armitage PA, Bastin ME. Selecting an appropriate anisotropy index for displaying diffusion tensor imaging data with improved contrast and sensitivity. *Magn Reson Med.* (2000) 44:117–21. doi: 10.1002/1522-2594(200007)44:1<117::aid-mrm17>3.0.co;2-d
98. Bammer R, Acar B, Moseley ME. *In vivo* MR tractography using diffusion imaging. *Eur J Radiol.* (2003) 45:223–34. doi: 10.1016/S0720-048X(02)00311-X
99. Jones DK. *Diffusion MRI: Theory, Methods, Applications*. (2010). New York, NY: Oxford University Press.
100. Smith SM, Jenkinson M, Johansen-Berg H, Rueckert D, Nichols TE, Mackay CE, et al. Tract-based spatial statistics: voxelwise analysis of multi-subject diffusion data. *Neuroimage.* (2006) 31:1487–505. doi: 10.1016/j.neuroimage.2006.02.024
101. Zalesky A. Moderating registration misalignment in voxelwise comparisons of DTI data: a performance evaluation of skeleton projection. *Magn Reson Imaging.* (2011). 29:111–25. doi: 10.1016/j.mri.2010.06.027

102. Schwarz CG, Reid RI, Gunter JL, Senjem ML, Przybelski SA, Zuk SM, et al. Improved DTI registration allows voxel-based analysis that outperforms tract-based spatial statistics. *Neuroimage.* (2014) 94:65–78. doi: 10.1016/j.neuroimage.2014.03.026
103. Yeh FC, Badre D, Verstynen T. Connectometry: a statistical approach harnessing the analytical potential of the local connectome. *Neuroimage.* (2016) 125:162–71. doi: 10.1016/j.neuroimage.2015.10.053
104. Doty RL. Olfactory dysfunction in Parkinson disease. *Nat Rev Neurol.* (2012). 8:329–39. doi: 10.1038/nrneurol.2012.80
105. Mishra VR, Sreenivasan KR, Yang Z, Zhuang X, Cordes D, Mari Z, et al. Unique white matter structural connectivity in early-stage drug-naive Parkinson disease. *Neurology.* (2020) 94:e774–84. doi: 10.1212/WNL.0000000000008867
106. Skorpil M, Soderlund V, Sundin A, Svenningsson P. MRI diffusion in Parkinson's disease: using the technique's inherent directional information to study the olfactory bulb and substantia nigra. *J Parkinsons Dis.* (2012) 2:171–80. doi: 10.3233/JPD-2012-12091
107. Kamagata K, Zalesky A, Hatano T, Ueda R, Di Biase MA, Okuzumi A, et al. Gray matter abnormalities in idiopathic Parkinson's disease: evaluation by diffusional kurtosis imaging and neurite orientation dispersion and density imaging. *Hum Brain Mapp.* (2017) 38:3704–22. doi: 10.1002/hbm.23628
108. Fuller PM, Saper CB, Lu J. The pontine REM switch: past and present. *J Physiol.* (2007) 584(Pt 3):735–41. doi: 10.1113/jphysiol.2007.140160
109. Wen MC, Chan LL, Tan LC, Tan EK. Depression, anxiety, and apathy in Parkinson's disease: insights from neuroimaging studies. *Eur J Neurol.* (2016) 23:1001–19. doi: 10.1111/ene.13002
110. Pierpaoli C, Jezzard P, Basser PJ, Barnett A, Di Chiro G. Diffusion tensor MR imaging of the human brain. *Radiology.* (1996) 201:637–48. doi: 10.1148/radiology.201.3.8939209
111. Latour LL, Warach S. Cerebral spinal fluid contamination of the measurement of the apparent diffusion coefficient of water in acute stroke. *Magn Reson Med.* (2002) 48:478–86. doi: 10.1002/mrm.10238
112. Chou MC, Lin YR, Huang TY, Wang CY, Chung HW, Juan CJ, et al. FLAIR diffusion-tensor MR tractography: comparison of fiber tracking with conventional imaging. *AJNR Am J Neuroradiol.* (2005) 26:591–7.
113. Pasternak O, Sochen N, Gur Y, Intrator N, Assaf Y. Free water elimination and mapping from diffusion MRI. *Magn Reson Med.* (2009) 62:717–30. doi: 10.1002/mrm.22055
114. Hoy AR, Koay CG, Kecskemeti SR, Alexander AL. Optimization of a free water elimination two-compartment model for diffusion tensor imaging. *Neuroimage.* (2014) 103:323–33. doi: 10.1016/j.neuroimage.2014.09.053
115. Mishra V, Guo X, Delgado MR, Huang H. Toward tract-specific fractional anisotropy (TSFA) at crossing-fiber regions with clinical diffusion MRI. *Magn Reson Med.* (2015) 74:1768–79. doi: 10.1002/mrm.25548
116. Jeurissen B, Leemans A, Tournier JD, Jones DK, Sijbers J. Investigating the prevalence of complex fiber configurations in white matter tissue with diffusion magnetic resonance imaging. *Hum Brain Mapp.* (2013) 34:2747–66. doi: 10.1002/hbm.22099
117. Jensen JH, Helpern JA, Ramani A, Lu H, Kaczynski K. Diffusional kurtosis imaging: the quantification of non-gaussian water diffusion by means of magnetic resonance imaging. *Magn Reson Med.* (2005) 53:1432–40. doi: 10.1002/mrm.20508
118. Poot DH, den Dekker AJ, Achten E, Verhoye M, Sijbers J. Optimal experimental design for diffusion kurtosis imaging. *IEEE Trans Med Imaging.* (2010) 29:819–29. doi: 10.1109/TMI.2009.2037915
119. Zhu J, Zhuo C, Qin W, Wang D, Ma X, Zhou Y, et al. Performances of diffusion kurtosis imaging and diffusion tensor imaging in detecting white matter abnormality in schizophrenia. *Neuroimage Clin.* (2015) 7:170–6. doi: 10.1016/j.nicl.2014.12.008
120. Zhang H, Schneider T, Wheeler-Kingshott CA, Alexander DC. NODDI: practical *in vivo* neurite orientation dispersion and density imaging of the human brain. *Neuroimage.* (2012) 61:1000–16. doi: 10.1016/j.neuroimage.2012.03.072
121. Le Bihan D. *Diffusion and Perfusion Magnetic Resonance Imaging: Applications to Functional MRI*. New York, NY: Raven Press (1995). doi: 10.1097/00004728-199509000-00032
122. Fukutomi H, Glasser MF, Murata K, Akasaka T, Fujimoto K, Yamamoto T, et al. Diffusion tensor model links to neurite orientation dispersion and density imaging at high b-value in cerebral cortical gray matter. *Sci Rep.* (2019) 9:12246. doi: 10.1038/s41598-019-48671-7
123. Tuch DS, Reese TG, Wiegell MR, Makris N, Belliveau JW, Wedeen VJ. High angular resolution diffusion imaging reveals intravoxel white matter fiber heterogeneity. *Magn Reson Med.* (2002) 48:577–82. doi: 10.1002/mrm.10268
124. Wiegell MR, Larsson HB, Wedeen VJ. Fiber crossing in human brain depicted with diffusion tensor MR imaging. *Radiology.* (2000) 217:897–903. doi: 10.1148/radiology.217.3.r00nv43897
125. Wedeen VJ, Hagmann P, Tseng WY, Reese TG, Weisskoff RM. Mapping complex tissue architecture with diffusion spectrum magnetic resonance imaging. *Magn Reson Med.* (2005) 54:1377–86. doi: 10.1002/mrm.20642
126. Yeh FC, Wedeen VJ, Tseng WY. Generalized q-sampling imaging. *IEEE Trans Med Imaging.* (2010) 29:1626–35. doi: 10.1109/TMI.2010.2045126
127. Yeh FC, Tseng WY. NTU-90: a high angular resolution brain atlas constructed by q-space diffeomorphic reconstruction. *Neuroimage.* (2011) 58:91–9. doi: 10.1016/j.neuroimage.2011.06.021
128. Yeh FC, Verstynen TD, Wang Y, Fernandez-Miranda JC, Tseng WY. Deterministic diffusion fiber tracking improved by quantitative anisotropy. *PLoS ONE.* (2013) 8:e80713. doi: 10.1371/journal.pone.0080713
129. Farrell JA, Landman BA, Jones CK, Smith SA, Prince JL, van Zijl PC, et al. Effects of signal-to-noise ratio on the accuracy and reproducibility of diffusion tensor imaging-derived fractional anisotropy, mean diffusivity, and principal eigenvector measurements at 1.5 T. *J Magn Reson Imaging.* (2007) 26:756–67. doi: 10.1002/jmri.21053
130. Jones DK. The effect of gradient sampling schemes on measures derived from diffusion tensor MRI: a monte carlo study. *Magn Reson Med.* (2004) 51:807–15. doi: 10.1002/mrm.20033
131. Bergamino M, Farmer M, Yeh HW, Paul E, Hamilton JP. Statistical differences in the white matter tracts in subjects with depression by using different skeletonized voxel-wise analysis approaches and DTI fitting procedures. *Brain Res.* (2017) 1669:131–40. doi: 10.1016/j.brainres.2017.06.013
132. Maximov II, Thonnessen H, Konrad K, Amort L, Neuner I, Shah NJ, et al. Statistical instability of TBSS analysis based on DTI fitting algorithm. *J Neuroimaging.* (2015) 25:883–91. doi: 10.1111/jon.12215
133. King MD, Houseman J, Roussel SA, van Bruggen N, Williams SR, Gadian DG. q-Space imaging of the brain. *Magn Reson Med.* (1994) 32:707–13. doi: 10.1002/mrm.1910320605
134. Yoshikawa K, Nakata Y, Yamada K, Nakagawa M. Early pathological changes in the parkinsonian brain demonstrated by diffusion tensor MRI. *J Neurol Neurosurg Psychiatry.* (2004) 75:481–4. doi: 10.1136/jnnp.2003.021873
135. Zhan W, Kang GA, Glass GA, Zhang Y, Shirley C, Millin R, et al. Regional alterations of brain microstructure in Parkinson's disease using diffusion tensor imaging. *Mov Disord.* (2012) 27:90–7. doi: 10.1002/mds.23917
136. Postuma RB, Aarsland D, Barone P, Burn DJ, Hawkes CH, Oertel W, et al. Identifying prodromal Parkinson's disease: pre-motor disorders in Parkinson's disease. *Mov Disord.* (2012) 27:617–26. doi: 10.1002/mds.24996
137. Chondrogiorgi M, Tzarouchi LC, Zikou AK, Astrakas LG, Kosta P, Argyropoulou MI, et al. Multimodal imaging evaluation of excessive daytime sleepiness in Parkinson's disease. *Int J Neurosci.* (2016) 126:422–8. doi: 10.3109/00207454.2015.1023437
138. Heller J, Brcina N, Dogan I, Holtbernd F, Romanzetti S, Schulz JB, et al. Brain imaging findings in idiopathic REM sleep behavior disorder (RBD) - a systematic review on potential biomarkers for neurodegeneration. *Sleep Med Rev.* (2017) 34:23–33. doi: 10.1016/j.smrv.2016.06.006

Conflict of Interest: The authors declare that the research was conducted in the absence of any commercial or financial relationships that could be construed as a potential conflict of interest.

Copyright © 2020 Bergamino, Keeling, Mishra, Stokes and Walsh. This is an open-access article distributed under the terms of the Creative Commons Attribution License (CC BY). The use, distribution or reproduction in other forums is permitted, provided the original author(s) and the copyright owner(s) are credited and that the original publication in this journal is cited, in accordance with accepted academic practice. No use, distribution or reproduction is permitted which does not comply with these terms.

frontiers in Neurology

SYSTEMATIC REVIEW
published: 28 May 2020
doi: 10.3389/fneur.2020.00366

Iron Imaging as a Diagnostic Tool for Parkinson's Disease: A Systematic Review and Meta-Analysis

Nadya Pyatigorskaya [1,2,3], Clara B. Sanz-Morère [1,2,3], Rahul Gaurav [1,2], Emma Biondetti [1,2], Romain Valabregue [1,2], Mathieu Santin [1,2], Lydia Yahia-Cherif [1,2] and Stéphane Lehéricy [1,2,3]*

[1] Institut du Cerveau et de la Moelle épinière (ICM), Centre de NeuroImagerie de Recherche (CENIR), ICM, Paris, France, [2] Sorbonne Université, UPMC Univ Paris 06, UMR S 1127, CNRS UMR 7225, ICM, Paris, France, [3] Assistance Publique Hôpitaux de Paris, Service de neuroradiologie, Hôpital Pitié-Salpêtrière, Paris, France

Background: Parkinson's disease (PD) is a progressive neurodegenerative disease whose main neuropathological feature is the loss of dopaminergic neurons of the substantia nigra (SN). There is also an increase in iron content in the SN in postmortem and imaging studies using iron-sensitive MRI techniques. However, MRI results are variable across studies.

Objectives: We performed a systematic meta-analysis of SN iron imaging studies in PD to better understand the role of iron-sensitive MRI quantification to distinguish patients from healthy controls. We also studied the factors that may influence iron quantification and analyzed the correlations between demographic and clinical data and iron load.

Methods: We searched PubMed and ScienceDirect databases (from January 1994 to December 2019) for studies that analyzed iron load in the SN of PD patients using T2*, R2*, susceptibility weighting imaging (SWI), or quantitative susceptibility mapping (QSM) and compared the values with healthy controls. Details for each study regarding participants, imaging methods, and results were extracted. The effect size and confidence interval (CI) of 95% were calculated for each study as well as the pooled weighted effect size for each marker over studies. Hence, the correlations between technical and clinical metrics with iron load were analyzed.

Results: Forty-six articles fulfilled the inclusion criteria including 27 for T2*/R2* measures, 10 for SWI, and 17 for QSM (3,135 patients and 1,675 controls). Eight of the articles analyzed both R2* and QSM. A notable effect size was found in the SN in PD for R2* increase (effect size: 0.84, 95% CI: 0.60 to 1.08), for SWI measurements (1.14, 95% CI: 0.54 to 1.73), and for QSM increase (1.13, 95% CI: 0.86 to 1.39). Correlations between imaging measures and Unified Parkinson's Disease Rating Scale (UPDRS) scores were mostly observed for QSM.

Conclusions: The consistent increase in MRI measures of iron content in PD across the literature using R2*, SWI, or QSM techniques confirmed that these measurements provided reliable markers of iron content in PD. Several of these measurements correlated with the severity of motor symptoms. Lastly, QSM appeared more robust and reproducible than R2* and more suited to multicenter studies.

Keywords: substantia nigra, iron, Parkinson's disease, QSM, SWI, R2*

OPEN ACCESS

Edited by:
Maria Carmela Tartaglia, University of Toronto, Canada

Reviewed by:
Peng Lei, Sichuan University, China
Juan Carlos Martinez Castrillo, Hospital Universitario Ramón y Cajal, Spain

****Correspondence:***
Nadya Pyatigorskaya
nadya.pyatigorskaya@gmail.com

Specialty section:
This article was submitted to Movement Disorders, a section of the journal Frontiers in Neurology

Received: *11 February 2020*
Accepted: *14 April 2020*
Published: *28 May 2020*

Citation:
Pyatigorskaya N, Sanz-Morère CB, Gaurav R, Biondetti E, Valabregue R, Santin M, Yahia-Cherif L and Lehéricy S (2020) Iron Imaging as a Diagnostic Tool for Parkinson's Disease: A Systematic Review and Meta-Analysis. Front. Neurol. 11:366. doi: 10.3389/fneur.2020.00366

INTRODUCTION

Parkinson's disease (PD) is a progressive neurodegenerative disease whose main neuropathological characteristic is the loss of dopaminergic neurons of the substantia nigra (SN) pars compacta (SNc) (1). Degeneration of dopaminergic neurons in the SN of PD patients is accompanied by an increase in iron content. Iron is necessary for body homeostasis, oxygen transport, or central nervous system development, but its capacity of producing reactive oxygen species that lead to stress oxidation can have a deleterious effect on the SN of PD patients. Iron also plays an important role in the neurodegenerative processes associated with PD (2–4).

Iron is a paramagnetic element that induces magnetic field inhomogeneities, that is, differences in the local magnetic field relative to the mainly diamagnetic surrounding brain tissues. Iron-induced local field inhomogeneities increase spin–spin interactions, thus accelerating the transverse relaxation of the MRI signal (5). This property can be exploited to estimate iron content using MRI based on a reduction in T2* relaxation time or an increase in R2* (1/T2*), phase changes in susceptibility-weighted imaging (SWI), or increased susceptibility values on quantitative susceptibility mapping (QSM). Based on these techniques, iron-sensitive MRI provides a noninvasive estimation of iron content as shown in primate and postmortem studies in humans (6, 7). Recent studies using iron-sensitive MRI in PD have investigated whether iron increase in basal ganglia, particularly in the SN, can be used as a biomarker in PD diagnosis and follow-up of iron content in the disease.

Studies using iron-sensitive MRI to quantify iron content in PD have reported variable results. Some have reported increased iron content over the global SN (8–11). Others have only reported increased iron contents in some SN subregions (12, 13) or have not reported any increase in iron levels (14). Moreover, the role of iron for monitoring disease progression in PD and its correlation with clinical symptoms is still under debate (15–17). Finally, to estimate iron content, a wide variety of techniques have been employed, and no systematic comparison of the results from these studies has yet been carried out. Thus, to elucidate the current role of iron-sensitive MRI in PD and its potential application as a biomarker of PD diagnosis, we carried out a systematic review of publications employing iron-sensitive MRI to study SN in PD. We sought to determine whether MRI of iron using R2*, SWI, or QSM measurements could successfully distinguish PD patients from healthy controls (HCs), showing the pathological increase in iron of the SN. We also investigated the factors that could influence iron quantification and analyzed the correlations between demographic and clinical data and iron load in the SN.

METHODS

Articles Review

The study was performed in accordance with the "Preferred Reporting Items for Systematic Reviews and Meta-analysis" (PRISMA) statement and checklist (**Supplementary Table 1**) (18).

To identify all the relevant literature on iron-sensitive MRI in the SN in PD, PubMed and ScienceDirect databases (from January 1994 to December 2019) were searched. A combination of the following search term was used: ("Parkinson" OR Parkinsonism OR substantia nigra) AND ("magnetic resonance imaging" OR MRI) AND (R2* OR SWI OR QSM OR susceptibility). All titles and abstracts from the retrieved articles were screened, and the full text of those that could be eligible was obtained. Reference lists of identified studies were also screened for additional studies. Two independent assessors (CSM and NP) performed this literature search, selected all relevant studies based on the Patient, Intervention, Comparison, Outcome, and Study type (PICOS) guidelines, and extracted all the information on iron estimation from the selected studies (18).

Criteria for study inclusion were publication as a full-text original article redacted in English, the use of iron-sensitive MRI as a diagnostic tool (T2*, R2*, SWI, or QSM), availability of iron level estimation in the SN, and the differentiation of participants with PD from HCs. For PD, a probable diagnosis based on standard diagnostic criteria was considered sufficient for inclusion (19). Articles using additional non-iron-sensitive MRI techniques, analyzing additional regions of interest other than the SN, or investigating additional pathologies other than PD were also included. In the case of multiple publications on the same population or overlapping populations, the study describing results in the largest number of subjects was included in the meta-analysis (20, 21). Studies in the same study populations were included when they reported results in different parts of the SN or the ipsilateral and contralateral hemispheres separately. For longitudinal trials, only the data from the first period were included. The articles were included if the measurements on the level of SN were available. We did not reject articles if other techniques along with R2*, other regions of interest, or other pathologies along with PD were studied. Criteria for study exclusion comprised unavailability of any iron-sensitive MRI analysis (R2*, QSM, or SWI) in the SN or of the numerical results or absence of a HC group.

For each study, when available, the following information on the subject population was extracted: mean age of PD and HC subjects, disease duration, severity of PD [Hoehn and Yahr (HY) stage and Unified Parkinson's Disease Rating Scale (UPDRS)], and medication dose. For iron imaging, the following information was extracted: magnetic field strength, scanner vendor, number of echoes for T2* measurements, type of measurements (R2* or T2*, SWI, or QSM), and region-of-interest (ROI) location. Mean and standard deviation (SD) of the different metrics were recorded (R2*, SWI, and QSM). One article only provided the ranges of the values (22). Four articles did not report values as mean ± SD but as median (range) (10, 16, 23, 24).

Statistical Meta-Analysis

Statistical parameter computation was performed using in-house software written in MATLAB R2016a software (the MathWorks, Inc., Natick, MA, USA). The meta-analysis was conducted in R version 3.5.1 (R Development Core Team, 2018) using the meta package (25). A random-effect model based on restricted

maximum likelihood estimator of the between-studies variance was used.

Data Extraction

The mean and SDs of R2*, SWI, and QSM measurements in the SN were extracted from the tables or the body of the manuscript when tables were unavailable. If values were only available as part of a diagram, the values were extracted using manual measurement on an image editing tool (GIMP, version 2.8) on three separate occasions (1 day apart) and averaged.

In the studies where only the median value and range of values were available, the mean and SD were estimated as previously described (26).

To combine T2* and R2* values from separate studies into a single analysis, all T2* values were converted to R2*, with the formula $R2^* = 1/T2^*$.

Effect Size

Effect size was computed as the standardized mean difference (Hedge's g) by subtracting the mean of the HC group from that of PD patients divided by the pooled standard deviation (25). Each g was weighted by the inverse of its variance and adjusted for small sample bias (27). The pooled effect size was calculated separately for R2*, SWI, and QSM. To allow comparability within the meta-analysis, when the SN was subdivided into several ROIs and R2*, SWI, or QSM values for the entire SN were not available, the mean value over the SN region was calculated (10, 17, 28–33). If the mean values were separately presented for PD patients with different severity levels, they were weighted and averaged. SWI articles used different techniques, and Hedge's g was assumed as the absolute value of the result. An effect size of $g > 0.70$ was considered as a large effect. Confidence interval (CI) of 95% was calculated using the standard error (SE). A fixed-effect or random-effect (restricted maximum likelihood) model was used based on the Q statistics.

Between-Study Heterogeneity

The across-study heterogeneity for all the articles included in the meta-analysis was analyzed by calculating Cochrane's Q and I^2 statistic. Values range from 0.0% (no heterogeneity) to 100% (high heterogeneity); values of 25%, 50%, and 75% have been suggested as benchmarks of low, moderate, and high heterogeneity, respectively (34).

Outliers

Effect sizes greater than three standard deviations from the mean were considered outliers. Results were reported with and without outliers (35).

Risk of Bias

The risk-of-bias analysis in individual studies was performed with a tool for the quality assessment of studies of diagnostic accuracy (QUADAS). The rating was performed by two independent raters (NP and CSM), and discordant ratings were resolved by consensus. The QUADAS questionnaire included 14 items covering the following issues: reference standard, covered patient spectrum, verification bias, disease progression bias, review bias, incorporation bias, clinical review bias, test execution, indeterminate results, and study withdrawals (**Supplementary Table 2**). Publication bias across studies for each outcome measure was examined by visually inspecting the funnel asymmetry plot and by applying the Egger regression intercept test.

Other Statistical Tests

Between-group differences; differences in R2*, SWI, and QSM values between SN subregions; the effect of magnetic field strength; the effect of MRI vendor; and the effect of ROI delineation methods were assessed using the nonparametric Wilcoxon, Mann–Whitney, and Kruskal–Wallis test.

Correlations

To assess the relationship between R2*, SWI, and QSM values with the clinical characteristics of patients [age, disease duration, UPDRS levels, H&Y stage, or technical parameters (number of echoes and voxel size)], a correlation analysis was performed. Correlation coefficients were computed between R2*, SWI, and QSM values and the clinical scores. To correct for multiple comparisons across several clinical scores, an approximate multivariate permutation test was conducted, and the sampling distribution was built to calculate the corrected p-value as the proportion of values that were larger than the observed correlation coefficient value (36).

RESULTS

The search of the database revealed 479 results in both PubMed and 1,425 ScienceDirect databases. After applying inclusion and exclusion criteria on the basis of titles and/or abstracts, 86 full-text articles were reviewed. Of these, 40 articles were excluded for the following reasons: the average R2*, QSM, or SWI results in the SN were not measured or not explicitly reported ($n = 28$), presence of duplicated data ($n = 4$), review articles ($n = 8$). Forty-six studies were included in the meta-analysis: 3 T2* based, 24 R2* based, 10 SWI, and 17 QSM-based (**Supplementary Figure 1**). Eight of these studies presented measurements for both R2* and QSM. We show the relevant publications, population characteristics, and technical details of the included studies in **Tables 1**, **2** for R2*, **Tables 4**, **5** for SWI, and **Tables 7**, **8** for QSM.

No significant publication bias was identified by a funnel plot and Egger regression intercept test. The funnel plots were symmetrical, and the Egger regression intercept test had no significant publication bias for the meta-analysis of R2*, SWI, and QSM changes ($p = 0.13$, $p = 0.58$, and $p = 0.45$, respectively, **Supplementary Figures 2–4**). The risk-of-bias analysis in individual studies is presented in **Supplementary Table 2**.

Regions of Interest in the SN

All included studies investigated differences in R2*/T2*, QSM, or SWI in the SN. Mean and SDs of R2* or T2*, SWI, and QSM were extracted for each ROI delineated in each study. In all the studies, SN ROIs were either manually drawn or calculated by using semiautomatic methods followed by manual

TABLE 1 | Demographic and clinical data of subjects of the articles included in the R2* meta-analysis.

References	Age PD	Disease duration PD	UPDRS level PD	H&Y PD	LEDD PD	Age HC
Ordidge et al. (22)	47–72	2–13	N/A	1.5-3	N/A	47–72
Graham et al. (9)	61.4 (7.3)	11.1 (4.5)	N/A	N/A	N/A	64.0 (6.6)
Martin et al. (28)	61.9 (9.0)	3.2 (1.7)	16.7 (7.1)	N/A	N/A	55.9 (7.3)
Baudrexel et al. (32)	62.2 (10.2)	4.0 (2.3)	18.3 (6.1)	1.7 (0.5)	N/A	62.3 (10.8)
Péran et al. (29)	61.9 (11.1)	4.5 (2.5)	12.0 (5.9)	1.7 (0.5)	886.8 (399.5)	57.4 (9.7)
Focke et al. (37)	66.3 (7.8)	N/A	N/A	N/A	N/A	67.6 (10.5)
Du et al. (20)	60.8 (8.2)	4.2 (4.7)	23.5 (15.1)	1.8 (0.6)	528.0 (401.0)	59.8 (7.0)
Bunzeck et al. (33)	66.3 (9.0)	6.3 (4.4)	34.6 (17.4)	N/A	393.8 (339.0)	66.0 (9.1)
Rossi et al. (23)	67.5 (12.9)	1.4 (1.0)	25 (11.8)	N/A	N/A	67.0 (6.5)
Ulla et al. (13)	60.2 (10.7)	5.7 (4.4)	12.1 (8.5)	1.9 (0.7)	614.0 (317.0)	57.0 (8.5)
Lewis et al. (38)	60.6 (8.0)	4.4 (4.7)	23.8 (15.4)	1.7 (0.6)	535.0 (400.0)	59.9 (7.0)
Barbosa et al. (39)	66.0 (8.0)	8.1 (4.1)	N/A	2.3 (0.6)	N/A	64.0 (7.0)
He et al. (31)	58.0 (8.8)	2.8 (1.6)	15.6 (6.22)	1.4 (0.5)	N/A	60.5 (6.5)
Murakami et al. (40)	72.0 (7.5)	2.7 (2.3)	N/A	2.0 (0.6)	N/A	69.7 (8.6)
Pyatigorskaya et al. (8)	54.3 (10.9)	5.2 (4.2)	18.6 (9.1)	1.6 (0.6)	N/A	55.8 (7.4)
Reimão et al. (26)	65.1 (9.2)	1-5	27.4 (12.8)	2.0 (0.0)	N/A	61.2 (7.3)
Wieler et al. (41)	59.8 (7.3)	1.8 (1.3)	14.3 (5.1)	N/A	N/A	56.0 (6.9)
Guan et al. (30)	55.4 (9.5)	4.7 (3.8)	27.1 (15.4)	2.2 (0.7)	N/A	56.6 (9.9)
Hopes et al. (10)	60.4 (3.2)	5.1 (0.6)	28.8 (2.6)	1.9 (0.2)	N/A	60.0 (2.4)
Isaias et al. (12)	62.8 (9.0)	7.5 (3.57)	14.5 (5.78)	2	502.0 (183.0)	60 (8.74)
Langkammer et al. (42)	64.7 (8.8)	3.4	31.3 (14.6)	2 (0.5)	182.5 (436.9)	65 59.3)
Du et al. (43)	66.3 (9.5)	4.5 (4.5)	21.5 (14.7)	1.7 (0.7)	669.0 (464.0)	66.2 (10.2)
	64.5 (9.2)	4.3 (4.1)	19.8 (5.9)	N/A	N/A	63 (9)
Langley et al. (13)	63.6 (7.0)	6.1 (4.6)	22.2 (12.4)	N/A	N/A	63.1 (7.2)
Pesch et al. (16)	59.5 (3.5)	4.9 (1.5)	34 (10.1)	N/A	N/A	65.5 (4.7)
Ghassaban et al. (44)	61.8 (6.4)	N/A	N/A	N/A	N/A	63.4 (8)
Arribarat et al. (11)	65.2 (6.6)	6.8 (4.7)	11.4 (4.9)	N/A	N/A	66 (4.9)
Li et al. (14)	68.2 (6.1)	N/A	27 (15.7)	N/A	N/A	64.8 (8)

Data are presented as mean (STD). N/A, not available.

correction. In all studies, one or two reviewers blinded to the subject characteristics analyzed the MRI images and drew the contours of the SN (or its different subregions) by hand. As for studies using R2* MRI, 16 studies drew the SN ROI on anatomical images [T2-weighted images (8, 9, 11, 20, 38, 43), T2*-weighted images (10, 12, 13, 17, 22, 28, 29, 41), or T1-weighted (16, 24)], and nine used quantitative maps [six used QSM maps (14, 30, 31, 39, 42, 44), one used an R2* map (40), one used a T2* map (23), one used a T1 map (32), two used magnetization transfer (MT) images, and one of them combined with an anatomical T1-weighted image (33, 37)]. The majority of studies assumed that the SN corresponded to the hypointense region on T2-weighted images between the red nucleus and the cerebral peduncle (8, 10, 20, 23, 38). For SWI (12, 23, 45–52) and QSM studies (14, 30, 31, 39, 40, 42–44, 53–61), all ROIs were manually segmented on the phase or QSM images.

Some studies placed ROIs in different subregions of the SN. In the R2*-based studies, some divided the SN into SNc and SN pars reticulata (SNr) (17, 28, 30, 39, 47, 51), defining the SNr as a hyperintense or hypointense region (depending on the image contrast) in the ventrolateral midbrain and the SNc as the region between the SNr and red nucleus (28, 30, 41). In three studies, rostral and caudal SNs were defined as the upper and lower parts of the SN (20, 32). Also, several articles studied the differences between the SN contralateral (opposite side) or ipsilateral (same side) to the most affected limb of the body (20, 31, 32, 49, 53). Three others analyzed the lateral, central, or medial of the SN separately. As for the SWI-based studies, two divided the SN into SNc and SNr (47, 51), two in ipsilateral and contralateral SNs (12, 49), and one divided the SNc into lateral and medial (23). As for the QSM-based studies, three measured the magnetic susceptibility in the ipsilateral and contralateral SNs (31, 53, 57), seven in SNc and SNr (30, 39, 43, 54, 56–58), and two in the anterior and posterior SNs (53, 55). The subregion segmentations were mostly performed on QSM images, while one study also used neuromelanin-sensitive imaging to help the SNc delineation (56).

Group Comparisons and Effect Sizes

R2* Meta-Analysis

Searching the database returned 27 R2*/T2*-based articles. The R2* meta-analysis included a population of 1,629 subjects with 879 PD patients and 750 HCs. Among all studies, the mean age of the patients (62.8 ± 3.7 years, range 54 to 72 years) did not

TABLE 2 | Technical characteristics of the studies included in the R2* meta-analysis.

References	Magnetic field	MRI machine	Method	ROIs drew in	No. echoes	Voxel size
Ordidge et al. (22)	3 T	Magnex Scientific Ltd.	T2*	T2* weighted	6	N/A
Graham et al. (9)	1.5 T	Marconi Medical Systems	R2*	T2 weighted	6	0.9 × 0.9 × 2.5
Martin et al. (28)	3 T	Magnex Scientific Ltd.	R2*	T2* weighted	6	2.3 × 2.3 × 5.0
Baudrexel et al. (32)	3 T	Siemens	T2*	T1 map	8	1.0 × 1.0 × 2.0
Péran et al. (29)	3 T	Siemens	R2*	T2* weighted	6	1.8 × 1.8 × 1.8
Focke et al. (37)	3 T	Siemens	R2*	T1 MPRAGE + MT	5	1.7 × 1.7 × 1.7
Du et al. (20)	3 T	Siemens	R2*	T2 weighted	6	1.0 × 1.0 × 1.0
Bunzeck et al. (33)	3 T	Siemens	R2*	MT	6	1.0 × 1.0 × 1.0
Rossi et al. (23)	3 T	Siemens	R2*	T2* map	5	0.6 × 0.6 × 4.0
Ulla et al. (13)	1.5 T	Siemens	R2*	T2* weighted	6	2.2 × 2.2 × 2.5
Lewis et al. (38)	3 T	Siemens	R2*	T2 weighted	6	1.0 × 1.0 × 1.0
Barbosa et al. (39)	3 T	Philips	R2*	QSM	4	0.5 × 0.5 × 2.0
He et al. (31)	3 T	GE	R2*	QSM	8	0.5 × 0.5 × 2.0
Murakami et al. (40)	3 T	GE	R2*	R2* map	11	1.5 × 2.5 × 1.5
Pyatigorskaya et al. (8)	3 T	Siemens	R2*	T2 weighted	6	2.0 × 2.0 × 2.0
Reimão et al. (26)	3 T	Philips	T2*	Spin-echo T1 neuromelanin sensitive	7	1.2 × 0.9 × 4.0
Wieler et al. (41)	3 T	Magnex Scientific Ltd.	R2*	T2* weighted	6	2.3 × 2.3 × 5.0
Guan et al. (30)	3 T	GE	R2*	QSM	8	0.8 × 0.8 × 2.8
Hopes et al. (10)	3 T	Philips	R2*	T2* weighted	15	2.0 × 2.0 × 2.0
Isaias et al. (12)	3 T	Philips	R2*	T2* weighted	2	1 × 1 × 1
Langkammer et al. (42)	3 T	Siemens	R2*	QSM	6	0.9 × 0.9 × 2.0
Du et al. (21)	3 T	Siemens	R2*	T2 weighted	8	0.9 × 0.9 × 2.0
Langley et al. (13)	3 T	Siemens	R2*	T2* weighted	6	0.5 × 0.5 × 1
Pesch et al. (16)	3 T	Philips	R2*	3D T1 weighted	N/A	1.5 × 1.5 × 1.5
Ghassaban et al. (44)	3 T	GE	R2*	QSM	N/A	0.86 × 0.86 × 1
Arribarat et al. (11)	3 T	Siemens	R2*	T2 weighted	6	1.8 × 1.8 × 1.8
Li et al. (14)	3 T	Siemens	R2*	QSM	8	0.63 × 0.63 × 2.0

differ from that of the HCs (61.0 ± 4.3 years, $p = 0.35$). Disease duration was 5.3 ± 2.2 (range 1.4 to 11.1 years). UPDRS scores were 21.9 ± 7.8 (range 12.0 to 34.6). HY score was 1.9 ± 0.3 (range 1.4 to 2.6). The levodopa-equivalent daily dose (LEDD) was specified in eight articles, with a mean of 539.4 ± 204.6 mg (**Table 1**). The between-study variation was $I^2 = 78\%$, which indicated a relatively high heterogeneity between studies. For R2* measurements, the standardized mean difference was 0.84 with a CI of 95% between 0.60 and 1.08 (range: 0.16 to 4.36, $p < 0.001$, **Table 3**, **Supplementary Figure 5**). R2* ranged from 23.70 to 54.02 s^{-1} (mean 36.88 ± 7.51 s^{-1}) for PD patients and from 21.20 to 45.78 s^{-1} (mean 33.28 ± 6.44 s^{-1}) for HCs ($p = 0.03$). One study was an outlier with effect sizes greater than three standard deviations (10). After the outlier was excluded, the heterogeneity was $I^2 = 36\%$, indicating that moderate heterogeneity and standardized mean difference was 0.70 with a CI of 95% between 0.56 and 0.84 (range: 0.16 and 2.72, $p = 0.04$, **Figure 1**). R2* ranged from 23.70 to 54.02 s^{-1} (mean 36.63 ± 7.44 s^{-1}) for PD patients and from 21.20 to 45.78 s^{-1} (mean 33.12 ± 6.52 s^{-1}) for HCs ($p = 0.04$). All studies have shown a relative increase in R2* values in PD. Differences existed in R2* values between studies that used anatomical images (T1 or T2 weighted) to draw the ROIs or QSM maps. Anatomical-based ROI had lower R2* values (mean 33.3 ± 8.9 s^{-1}) than QSM-based ROI (mean 38.1 ± 7.3 s^{-1}, $p = 0.33$) and higher Hedge's g (1.3 ± 1.2 vs. 0.6 ± 0.2, $p = 0.07$), but these differences were not significant. As for the SN subregions, increased iron contents were observed at the level of the SNc in PD, while there were no significant changes in iron content in the SNr ($p = 0.003$ vs. $p = 0.07$), with effect size significantly higher in the SNc compared to the SNr (1.78 vs. 1.23, respectively, $p = 0.09$). R2* was increased in the lateral compared to medial SNc ($p = 0.02$ and 0.06, respectively) with nonsignificantly higher effect size in lateral than in median SNc (0.86 vs. 0.52, respectively, $p = 0.11$) possibly due to the low number of articles reporting distinct measurements, while both ipsilateral and contralateral sides had the same effect size (0.95 vs. 0.93, $p = 0.89$) with no difference for R2* ($p = 0.31$) (**Figure 2**).

SWI Meta-Analysis

Searching the database returned 10 SWI-based articles. The SWI meta-analysis included a population of 655 subjects with 361 PD patients and 294 HCs (**Table 4**). Among all studies, the mean age of the patients (62.2 ± 3.6 years, range 56 to 67 years) did not differ from that of the HCs (59.9 ± 4.7 years, $p = 0.17$). Disease duration was 4.3 ± 2.3 (range 1.4 to 8.1 years). UPDRS scores were 20.2 ± 6.9 (range 14.8 to 31.5). HY score was 2.1 ± 0.4 (range 1.8 to 2.7). The LEDD was specified in two articles only, with a mean of 532.5 ± 43.13 mg. The between-study variation of

TABLE 3 | Meta-analysis results: SWI mean values of PD and HC were used to calculate the effect size value and confidence interval.

References	SN division	PD			HC			Hedge's *g*	SE	Confidence interval	
		N	Mean	SD	N	Mean	SD			Low	High
Ordidge et al. (22)	Global[NA]	7	45.68	2.69	7	37.59	2.87	2.72	0.77	1.22	4.23
Graham et al. (9)	Global*	20	23.70	3.50	13	21.20	2.60	0.76	0.37	0.05	1.48
Martin et al. (28)	SNc lateral**	22	26.90	2.80	11	22.80	2.80	1.43	0.41	0.62	2.23
	SNc medial*		29.00	7.20		25.90	7.30	0.42	0.37	−0.31	1.15
	SNr lateral		35.80	5.50		37.90	5.50	−0.37	0.37	−1.10	0.36
	SNr medial		38.40	5.80		39.90	5.90	−0.25	0.37	−0.98	0.48
Baudrexel et al. (32)	Rostral ipsilateral*	20	27.17	3.14	20	24.45	2.28	0.97	0.34	0.31	1.63
	Rostral contralateral*		28.01	3.86		25.32	2.64	0.80	0.34	0.15	1.44
	Caudal ipsilateral		19.60	10.40		21.65	10.10	−0.20	0.33	−0.82	0.43
	Caudal contralateral		20.04	10.60		20.75	7.90	−0.07	0.32	−0.69	0.55
Péran et al. (29)	Right***	30	33.34	4.72	22	29.89	2.08	0.90	0.30	0.31	1.46
	Left***		32.27	3.90		29.02	2.11	0.99	0.30	0.40	1.56
Focke et al. (37)	Right	12	32.42	5.58	13	31.31	5.15	0.20	0.40	−0.59	0.99
	Left		33.03	4.30		30.20	4.30	0.64	0.41	−0.17	1.44
Du et al. (20)	Global***	40	33.40	5.42	28	28.70	4.19	0.94	0.26	0.43	1.45
Ulla et al. (13)	SNc**	27	22.58	0.68	26	20.65	0.60	2.96	0.40	2.18	3.75
	SNr*		27.07	1.26		25.09	0.92	1.76	0.34	1.13	2.40
Rossi et al. (23)	Medial SNc***	37	51.00	10.00	21	43.00	7.00	0.87	0.29	0.31	1.43
	Lateral SNc***		50.00	10.00		42.00	6.00	0.90	0.29	0.34	1.46
Bunzeck et al. (33)	Left	20	30.00	8.00	20	26.00	3.00	0.65	0.33	0.01	1.29
	Right		31.00	8.00		28.00	3.00	0.49	0.32	−0.14	1.12
Lewis et al. (38)	Global**	38	31.00	5.00	23	27.00	4.00	0.85	0.28	0.31	1.39
Barbosa et al. (39)	SNc*	20	52.80	11.70	30	47.70	8.40	0.51	0.32	−0.06	1.09
	Global*		47.70	8.50		45.70	6.50	0, 27	0.29	−0.30	0.84
He et al. (31)	Contralateral*	44	38.90	5.91	35	34.90	4.41	0.75	0.24	0.29	1.21
	Ipsilateral		38.10	5.26		34.90	4.41	0.65	0.23	0.19	1.10
Reimão et al. (26)	Global	22	54.02	19.39	10	44.37	17.95	0.50	0.39	−0.26	1.25
	Lateral		46.60	19.28		35.45	7.58	0.65	0.39	−0.11	1.42
	Central		50.07	22.47		40.97	10.46	0.45	0.39	−0.30	1.21
	Medial		58.27	15.96		49.77	17.73	0.50	0.39	−0.26	1.26
Murakami et al. (40)	Global*	21	30.10	1.50	21	29.00	2.00	0.61	0.32	−0.01	1.23
Pyatigorskaya et al. (8)	Global*	20	27.80	1.50	20	25.10	2.10	1.45	0.36	0.75	2.15
Wieler et al. (41)	Lateral SNc*	19	26.23	3.08	13	22.82	5.13	0.83	0.38	0.09	1.56
Guan et al. (30)	SNc*	60	28.18	3.57	40	25.25	3.03	0.86	0.22	0.45	1.28
	SNr		43.79	5.28		40.94	5.71	0.52	0.21	0.11	0.93
Hopes et al. (10)	Left*	70	46.44	2.17	20	37.60	0.87	4.46	0.42	3.64	5.29
	Right*		46.22	2.31		36.90	1.16	4.37	0.42	3.56	5.18
Isaias et al. (12)	Ipsilateral	18	41.17	10.96	18	37.47	5.16	0.42	0.34	−0.24	1.08
	Contralateral		43.30	10.01		39.09	5.74	0.50	0.34	−0.16	1.17
Langkammer et al. (42)	Global*	66	41.10	8.70	58	37.60	5.80	0.46	0.18	0.11	0.82
Du et al. (43)	SNc***	72	28.00	0.40	62	25.90	0.40	5.22	0.37	4.51	5.93
	SNr**		41.50	1.00		37.30	1.10	3.98	0.30	3.40	4.58
Langley et al. (13)	SNc cohort 1***		32.50	5.60	32	27.50	4.30	0.98	0.26	0.48	1.48
	SNr cohort 1*		37.80	5.40	32	35.40	5.20	0.44	0.25	−0.03	0.93
	SNc cohort 2***	42	34.30	4.90	46	29.50	4.40	1.02	0.23	0.58	1.47
	SNr cohort 2		40.70	6.00		39.20	8.40	0.20	0.21	−0.22	0.62
Pesch et al. (16)	Global	35	49.35	6.46	35	45.78	2.98	0.71	0.25	0.22	1.18
Ghassaban et al. (44)	Right*	25	42.00	4.00	24	39.00	4.00	0.74	0.30	0.16	1.32
	Left*	25	43.00	4.00		39.00	4.00	0.98	0.31	0.39	1.58
Arribarat et al. (11)	Posterior	18	25.96	3.12	21	25.02	2, 14	0.35	0.33	−0.29	0.98
	Anterior**		31.05	3.61		27.26	2.97	1.13	0.35	0.45	1.81
	Global***		34.47	3.03		29.96	2.97	1.47	0.36	0.76	2.19
Li et al. (14)	Global	28	35.78	5.08	28	35.37	4.35	0.09	0.27	−0.44	0.61

*All SN subdivisions are included. *Significantly different from controls ($p < 0.05$). **Significantly different from controls ($p < 0.005$). ***Significantly different from controls ($p < 0.001$). NA, non available.*

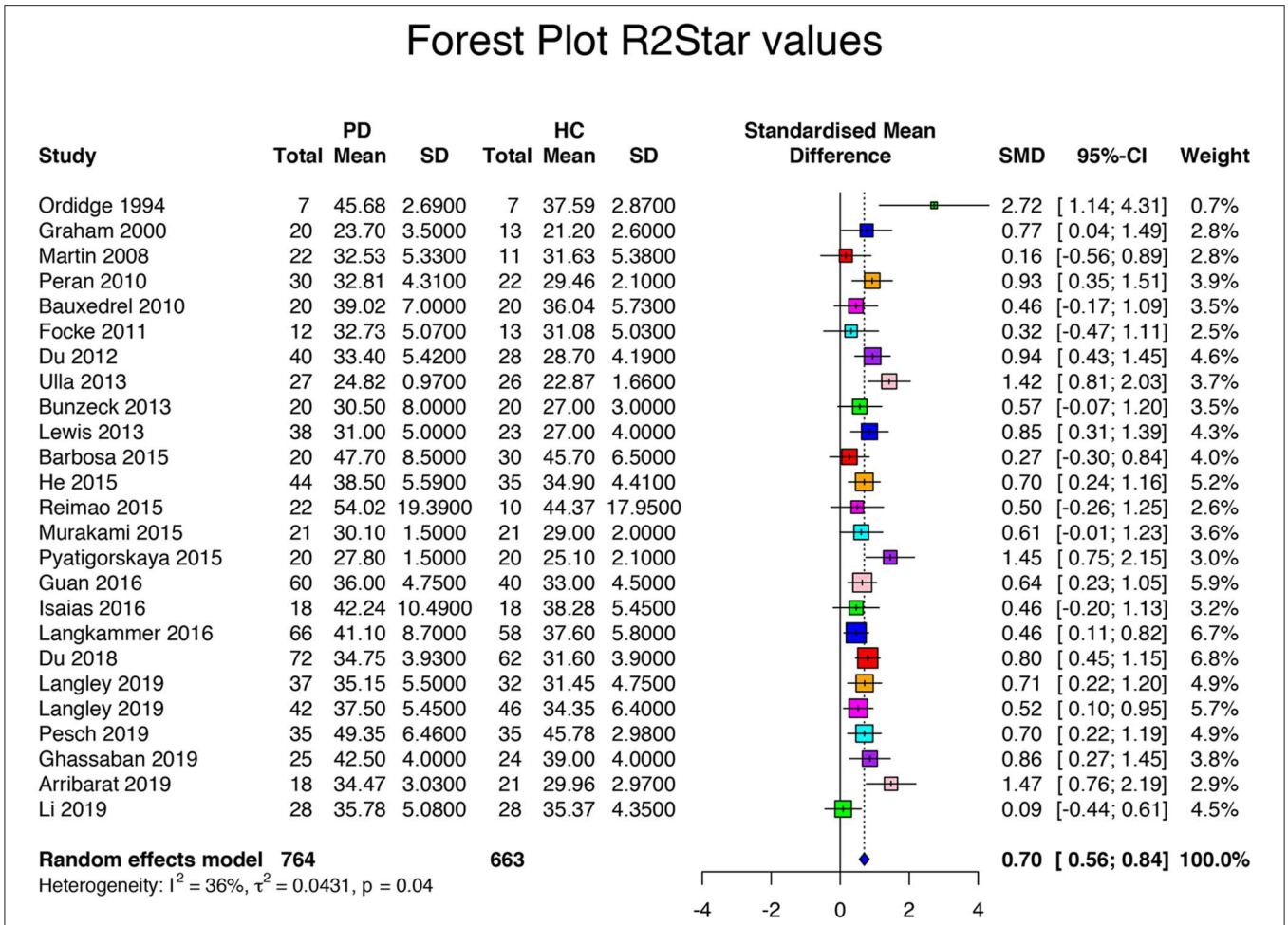


FIGURE 1 | Forest plot of significant R2* values of the 26 articles included in the meta-analysis. Forest plot of the computed disease effect sizes (Hedge's g, x-axis) of studies included into the meta-analysis on R2* measures of the substantia nigra when comparing PD patients and controls. Pooled SMD (95%) (0.7, [0.56, 0.84]) is denoted by a blue diamond.

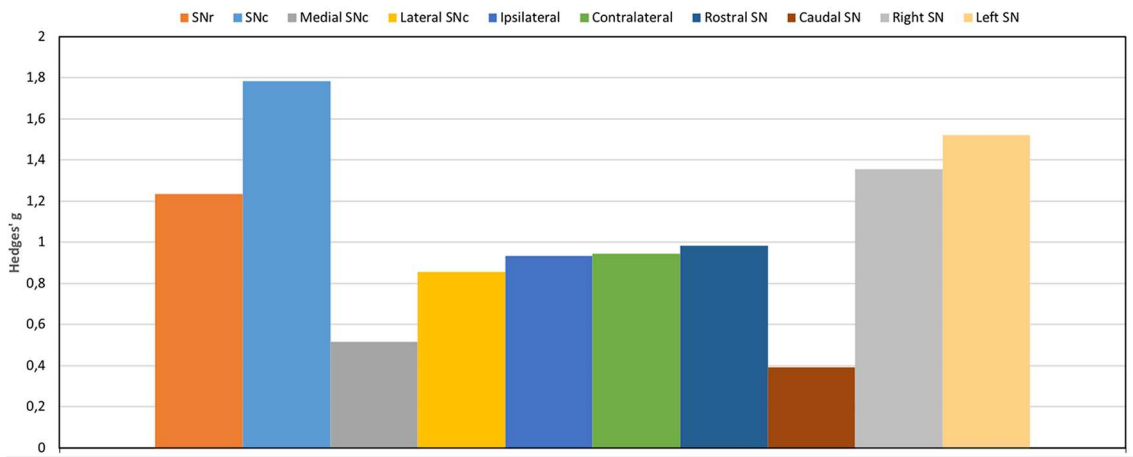


FIGURE 2 | Graphical representation of the different effect sizes in each division of the SN ROIs using R2*.

TABLE 4 | Demographic and clinical data of subjects of the articles included in the SWI meta-analysis.

References	PD					HC
	Age	Disease duration	UPDRS	H/Y	LEDD (mg)	Age
Gupta et al. (45)	61.5 (5.9)	8.1 (3.9)	21.4 (14.6)	N/A	N/A	54.9 (3.1)
Zhang et al. (49)	58.7 (12.8)	3.6 (2.9)	19.0 (7.8)	N/A	N/A	57.3 (11.6)
Jin et al. (50)	59.8 (11.1)	3.1 (3.0)	14.8 (9.2)	1.75 (0.8)	N/A	57.36 (13.4)
Lotfipour et al. (51)	64.7 (13.3)	N/A	N/A	1.8 (0.83)	N/A	59.2 (8.6)
Wang et al. (46)	63.3 (10.6)	2.5 (1.7)	N/A	N/A	N/A	59.4 (11.8)
Rossi et al. (23)	67.5 (12.9)	1.4 (1.0)	25 (11.8)	N/A	N/A	67.0 (6.5)
Wang et al. (47)	67.7 (9.3)	3.0 (2.7)	N/A	13 < 2.5 7 > 3	N/A	64.3 (12.7)
Wu et al. (48)	65.6 (5.8)	N/A	N/A	2.58 (1.29)	N/A	66.5 (6.0)
Isaias et al. (12)	62.8 (9.0)	7.5 (3.57)	14.5 (5.78)	2	502 (183)	60 (8.7)
Martin-Bastida et al. (52)	55.8 (7.2)	5.4 (2.5)	31.5 (11.6)	1.9 (0.5)	563 (344)	53.1 (11.7)

Data are presented as mean (STD). N/A, not available.

TABLE 5 | Technical characteristics of the studies included in the SWI meta-analysis.

References	Technical aspects				
	Magnetic field	Vendor	Method	ROIs drawn in	Voxel size (mm3)
Gupta et al. (45)	1.5 T	Siemens	Hypointensity scores	SWI	N/A
Zhang et al. (49)	3 T	Siemens	Phase shift	Phase images	0.5 × 0.5
Jin et al. (50)	3 T	GE	Phase values	Phase images	0.8 × 0.9 × 2
Lotfipour et al. (51)	7 T	Philips	Relative susceptibility	Modulus images and then applied to SWI	Protocol A: 0.7 × 0.7 × 0.7 Protocol B 0.4 × 0.4 × 0.5
Wang et al. (46)	1.5 T	Siemens	Phase shift	Phase images	0.5 × 1 × 2
Rossi et al. (23)	3 T	Siemens	SWI contrast	Phase images	0.9 × 0.9 × 1.5
Wang et al. (47)	3 T	GE	Phase values	Phase images	0.5 × 0.8 × 2
Wu et al. (48)	3 T	Philips	Phase values	Phase images	0.5 × 0.6 × 1.5
Isaias et al. (12)	3 T	Philips	Phase values	Phase images	1 × 1 × 1
Martin-Bastida et al. (52)	3 T	Siemens	Phase shift	Phase images	N/A

SWI values was $I^2 = 89\%$, which indicated a high heterogeneity between studies. Most SWI-based studies calculated the phase of images, but others used the relative susceptibility, the SWI contrast, or the SWI hypointensity (**Table 5**); consequently, Hedge's g was calculated as the absolute value. In the SWI-based studies, the standardized mean difference was 1.14 with a CI of 95% between 0.54 and 1.73 (range 0.36 to 3.47), confirming the difference in susceptibility values between HC and PD patients (**Table 6**, **Figure 3**). There were not enough SWI-based articles to access the quality of SWI-based discrimination of different SN subregions, contralateral or ipsilateral SN sides, or field strengths.

QSM Meta-Analysis

The database search returned 17 QSM-based articles. The QSM meta-analysis included a population of 1,154 subjects with 652 PD patients and 502 HC. Among all studies, the mean age of the patients (64.4 ± 5.5 years, range 50 to 72 years) did not differ from that of the HC (63.4 ± 4.3 years, $p = 0.55$). Disease duration was 4.2 ± 1.9 (range 1 to 8.1 years). UPDRS scores were 24.4 ± 10.1 (range 13.0 to 39.5). HY score was 2.1 ± 0.4 (range 1.4 to 2.8). The LEDD was specified in three articles, with a mean of 539.4 ± 204.6 mg (**Tables 7**, **8**). The between-study variation was $I^2 = 75\%$ which indicated a relatively high heterogeneity between studies. The standard mean difference was 1.13 with a CI of 95% between 0.86 and 1.39 (range = 0.34 to 3.83). The QSM values for PD patients ranged from 78.9 to 239.0 ppb (mean 138.8 ± 44.3 ppb) and for HC from 62.4 to 199.0 ppb (mean 112.9 ± 37.7 ppb, $p = 0.001$, **Table 9**, **Supplementary Figure 6**). One study was an outlier (61). After the outlier was excluded, the heterogeneity was $I^2 = 66\%$, indicating moderate heterogeneity and a standardized mean difference of 1.04 with a CI of 95% between 0.82 and 1.27 (range: 0.34 and 2.02, $p < 0.01$, **Figure 4**). The QSM values ranged from 78.9 to 224.0 ppb (mean 138.8 ± 44.3 ppb) for PD patients and from 62.39 to 199.0 ppb (mean 112.9 ± 37.7 ppb, $p = 0.001$) for HC. As for SN subregions, increased QSM values were observed at both levels of the SNc and the SNr in PD ($p = 0.006$ vs. $p = 0.04$, respectively). Hedge's g was not significantly higher in the SNc than in the SNr (1.24 vs. 0.94, respectively, $p = 0.23$). Also, there

TABLE 6 | Meta-analysis results: SWI mean values of PD and HC were used to calculate the effect size value and confidence interval.

References	SN division	Method	PD			HC			Hedge's *g*	SE	Confidence interval	
			N	Mean	SD	*N*	Mean	SD			Low	High
Gupta et al. (45)	Global	SWI hypointensity	11	0.36	0.81	11	0.64	0.67	0.36	0.43	−0.48	1.21
Zhang et al. (49)	Ipsilateral	Phase values	40	0.13	0.05	26	0.12	0.04	0.21	0.25	−0.28	0.71
	Contralateral***			0.16	0.05		0.12	0.04	0.85	0.26	0.34	1.37
Jin et al. (50)	Global***	Phase values	87	−0.18	0.03	50	−0.16	0.03	0.66	0.18	0.31	1.02
Lotfipour et al. (51)	SN	Relative susceptibility	9	0.05	0.01	11	0.04	0.01	0.96	0.48	0.02	1.89
	SNc*			0.06	0.01		0.04	0.01	1.92	0.55	0.84	2.99
Wang et al. (46)	Global*	Phase values	16	−0.23	0.05	44	−0.17	0.07	0.91	0.30	0.31	1.50
Rossi et al. (23)	Lateral SNc	SWI contrast	36	7.20	3.50	21	9.10	5.20	0.45	0.28	−0.10	0.99
	Medial SNc*			5.70	5.90		9.90	6.50	0.68	0.28	0.12	1.23
Wang et al. (47)	SNc**	Phase values	20	0.03	0.03	14	0.08	0.02	1.85	0.42	1.03	2.67
	SNr**			−0.55	0.18		−0.37	0.17	1.00	0.37	0.27	1.72
Wu et al. (48)	Global*	Phase values	54	−0.13	0.01	40	−0.10	0.02	1.97	0.25	1.48	2.47
Isaias et al. (12)	Ipsilateral	Phase values	18	0.16	0.05	18	0.13	0.03	0.71	0.34	0.04	1.39
	Contralateral			0.15	0.05		0.13	0.03	0.47	0.34	−0.19	1.14
Martin-Bastida et al. (52)	Global**	Phase values	70	0.11	0.02	20	0.04	0.02	3.47	0.36	2.76	4.18

*All SN subdivisions were included. ***Significantly different from controls ($p < 0.001$). **Significantly different from controls ($p < 0.01$). *Significantly different from controls ($p < 0.05$).*

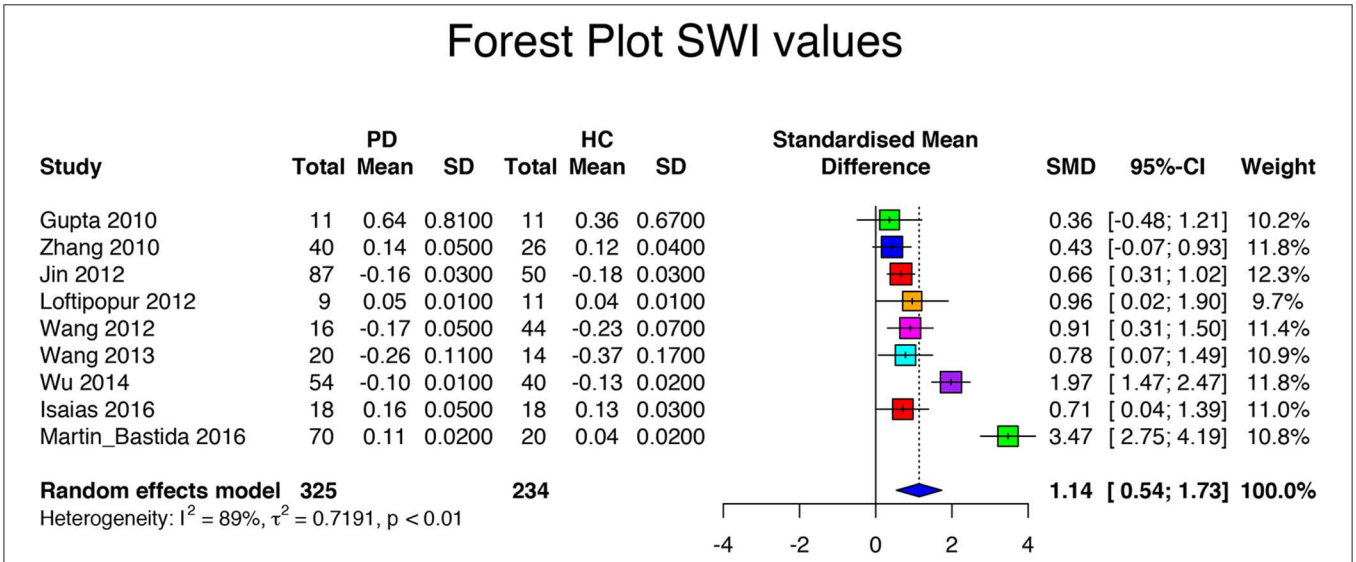


FIGURE 3 | Forest plot of significant SWI values of the 10 articles included in the meta-analysis. Forest plot of the computed disease effect sizes (Hedge's g, x-axis) of studies included into the meta-analysis on QSM measures of the substantia nigra when comparing PD patients and controls. Pooled SMD (95%) (1.14, [0.54, 1.73]) is denoted by a blue diamond.

was no significant difference in effect size between the ipsilateral and contralateral SNs to the most affected side (0.64 vs. 0.68, $p = 0.71$) and no significant difference in QSM values between the ipsilateral and contralateral SNs ($p = 0.22$).

Comparison Between R2* and QSM

In the eight articles that analyzed both R2* and QSM, Hedge's *g* was significantly higher for QSM than for R2* values (1.16 ± 0.45 vs. 0.55 ± 0.26, $p = 0.0006$).

Correlation Analyses

Both R2* values and Hedge's *g* did not correlate with either clinical characteristics (age, disease duration, UPDRS, and LEDD) or imaging parameters (voxel size and number of echoes).

For SWI, effect size correlated positively with UPDRS values ($r = 0.84$, $p = 0.04$) and voxel size ($r = 0.65$, $p = 0.04$).

There was a positive correlation between QSM values and age of PD patients ($r = 0.64$, $p = 0.0001$), UPDRS values ($r = 0.57$, p=0.0008) and voxel size ($r = 0.47$, $p = 0.04$).

TABLE 7 | Demographic and clinical data of subjects of the articles included in the QSM meta-analysis.

References	PD					HC
	Age	Disease duration	UPDRS level	H&Y stage	LEDD (mg)	Age
Barbosa et al. (39)	66 (8.0)	8.1 (4.1)	N/A	2.3 (0.6)	N/A	64.0 (7.0)
He et al. (31)	58 (8.8)	2.8 (1.6)	15.57 (66.22)	1.4 (0.5)	N/A	60.5 (6.5)
Murakami et al. (40)	72.0 (7.5)	2.7 (2.3)	N/A	2.0 (0.6)	N/A	69.7 (8.6)
Azuma et al. (53)	63.3 (11.0)	6.4 (3.6)	20.8 (11.6)	N/A	456.2 (265.2)	64.1 (10.0)
Guan et al. (30)	58.5 (7.5)	5.7 (4.2)	33.65 (12.4)	2.6 (2.5)	N/A	56.6 (9.9)
Langkammer et al. (42)	60.1 (6.2)	6.2 (4.2)	18.6 (7.6)	2 (1)	N/A	58.1 (8.7)
Xuan et al. (54)	67.3 (9.9)	4.1 (2.1)	13 (7.1)	2.1 (0.95)	N/A	66.9 (9.1)
Du et al. (21)	70.6 (9)	1.5 (8.5)	20.3 (10.7)	1.9 (0.7)	175 (215)	67.6 (5)
Kim et al. (60)	71.2 (6.9)	5.4 (2)	13.1 (7.2)	1.9 (0.4)	N/A	67.1 (4.7)
An et al. (59)	61.8 (6.4)	N/A	N/A	N/A	N/A	63.4 (8)
Takahashi et al. (56)	68.2 (6.1)	N/A	27 (15.7)	N/A	N/A	64.8 (8)
Shin et al. (25)	64.6 (11.2)	2.8 (2.4)	N/A	2.8 (2.4)	N/A	62.6 (10.6)
Bergsland et al. (55)	66.2 (8.5)	N/A	N/A	2.1 (0.5)	N/A	64.9 (9.2)
Shahmaei et al. (61)	60.1 (6.2)	6.2 (4.2)	18.6 (7.6)	2 (1)	N/A	58.1 (8.7)
Ghassaban et al. (44)	67.3 (9.9)	4.1 (2.1)	13 (7.1)	2.1 (0.95)	N/A	66.9 (9.1)
Li et al. (14)	71.2 (6.9)	5.4 (2)	13.1 (7.2)	1.9 (0.4)	N/A	67.1 (4.7)
Chen et al. (58)	70.6 (9)	1.5 (8.5)	20.3 (10.7)	1.9 (0.7)	175 (215)	67.6 (5)

Data are presented as mean (STD). N/A, not available.

TABLE 8 | Technical characteristics of the studies included in the QSM meta-analysis.

References	Magnetic field	Vendor	Values obtained	ROIs drawn in	Voxel size
Barbosa et al. (23)	3 T	Philips	Susceptibility	QSM	0.5 × 0.5 × 2.0
He et al. (31)	3 T	GE	Susceptibility	QSM	0.5 × 0.5 × 2.0
Murakami et al. (40)	3 T	GE	Susceptibility	QSM	1.5 × 2.5 × 1.5
Guan et al. (30)	3 T	GE	Susceptibility	QSM	0.8 × 0.8 × 2.8
Azuma et al. (53)	3 T	Siemens	Susceptibility	QSM	0.9 × 0.9 × 2.0
Langkammer et al. (42)	3 T	Siemens	Susceptibility	QSM	0.9 × 0.9 × 2.0
Xuan et al. (54)	3 T	GE	Susceptibility	QSM	0.6 × 0.6 × 2.8
Du et al. (21)	3 T	Siemens	Susceptibility	QSM	0.9 × 0.9 × 2.0
Kim et al. (60)	3 T	Siemens	Susceptibility	QSM	1 × 1 × 1
An et al. (59)	3 T	Siemens	Susceptibility	QSM	0.62 × 0.62 × 2
Takahashi et al. (56)	3 T	GE	Susceptibility	QSM	0.57 × 0.86 × 2.4
Shin et al. (25)	3 T	Philips	Susceptibility	QSM	0.4 × 0.4 × 2
Bergsland et al. (55)	3 T	GE	Susceptibility	QSM	0.5 × 1 × 2
Shahmaei et al. (61)	3 T	Siemens	Susceptibility	QSM	1 × 1 × 1.5
Ghassaban et al. (44)	3 T	GE	Susceptibility	QSM	0.86 × 0.86 × 1
Li et al. (14)	3 T	Siemens	Susceptibility	QSM	0.63 × 0.63 × 2.0
Chen et al. (58)	3 T	Philips	Susceptibility	QSM	0.5 × 0.5 × 2

Scanner Effects

As expected, R2* values in the SN were lower at 1.5 T (mean 24.45 s^{-1}) (9, 17) than at 3 T (mean 38.26 s^{-1}), due to the known increase of R2* with magnetic field strength. However, no statistical comparison could be performed due to the low number of data acquired at 1.5 T. In R2*, there was a statistical difference between the four vendors ($p = 0.0006$) with Philips providing higher R2* values (mean 50.25 s^{-1}) than the other vendors, that is, Siemens (mean 34.68 s^{-1}, $p = 0.0001$), Magnex Scientific (mean 34.99 s^{-1}, $p = 0.015$), and General Electrics (mean 37.77 s^{-1}, $p = 0.0008$) while there was no significant difference between Siemens and General Electrics ($p = 0.22$). There was no longer a statistical difference between the four manufacturers ($p = 0.93$) when R2* values were normalized using control values.

In SWI, there was no between-vendor significant difference in effect size or phase values ($p = 0.22$ and $p = 0.21$, respectively).

TABLE 9 | Meta-analysis results: QSM mean values of PD and HC are used to calculate the effect size value and confidence interval.

References	SN division	PD			HC			Hedge's *g*	SE	Confidence interval	
		N	Mean	SD	*N*	Mean	SD			Low	High
Barbosa et al. (23)	SN**	20	150.90	41.50	30	114.70	32.50	0.98	0.31	0.38	1.58
	SNc***		186.70	53.20		140.10	38.50	1.02	0.31	0.42	1.62
He et al. (31)	Ipsilateral***	44	100.00	16.50	35	83.70	15.60	1.00	0.24	0.53	1.47
	Contralateral***		100.00	18.30		83.70	15.60	0.94	0.24	0.47	1.41
Murakami et al. (40)	Global*	21	224.00	14.00	21	199.00	24.00	1.25	0.34	0.59	1.91
Azuma et al. (53)	Global**	24	148.15	45.75	24	104.70	31.00	1.09	0.31	0.49	1.70
	Contralateral aSN***		186.6	57.50		142.90	43.70	0.84	0.30	0.25	1.43
	Contralateral mSN***		166.6	53.20		104.60	28.70	1.43	0.32	0.79	2.06
	Contralateral pSN***		120.8	38.70		66.50	25.60	1.63	0.33	0.97	2.28
	Ipsilateral aSN		178.60	54.70		142.90	43.70	0.71	0.30	0.13	1.29
	Ipsilateral mSN*		141.40	51.10		104.60	28.70	0.87	0.30	0.28	1.47
	Ipsilateral pSN*		94.70	38.00		66.50	25.60	0.86	0.30	0.26	1.45
Guan et al. (30)	SNc**	60	47.00	15.00	40	20.00	15.00	1.79	0.24	1.31	2.26
	SNr		122.50	25.00		101.00	25.00	0.85	0.21	0.44	1.27
Langkammer et al. (42)	Global***	66	114.00	40.00	58	90.00	30.00	0.67	0.18	0.31	1.03
Xuan et al. (54)	SNc (young)**	35	37.00	25.00	24	25.00	15.00	0.55	0.27	0.02	1.08
	SNr (young)*		117.00	20.00		104.00	22.00	0.62	0.27	0.08	1.15
	SNc (old)**	33	45.00	18.00	22	28.00	20.00	0.89	0.29	0.33	1.46
	SNr (old)*		123.00	27.00		106.00	30.00	0.59	0.28	0.04	1.14
Du et al. (43)	SNc**	72	64.20	15.21	62	44.80	14.35	1.30	0.19	0.93	1.68
	SNr**		157.30	15.21		129.90	14.35	1.84	0.21	1.43	2.24
Kim et al. (60)	Global***	36	125.81	16.27	25	98.41	11.70	1.85	0.31	1.25	2.46
An et al. (59)	Global**	44	179.55	65.72	31	138.04	37.32	0.74	0.24	0.26	1.21
Takahashi et al. (56)	SNc*	18	87.67	24.48	18	67.78	24.48	0.79	0.35	0.11	1.47
	SNc dorsolateral*		85.78	28.45		52.19	23.01	1.27	0.37	0.55	1.99
Shin et al. (25)	SNc ipsilateral	29	123.00	39.00	19	121.00	32.00	0.05	0.30	−0.52	0.63
	SNc contralateral		132.00	39.00		121.00	32.00	0.30	0.30	−0.28	0.88
	SNr ipsilateral		125.00	39.00		115.00	39.00	0.25	0.30	−0.33	0.83
	SNr contralateral		130.00	40.00		115.00	39.00	0.37	0.30	−0.21	0.96
Bergsland et al. (55)	Ventral posterior***	32	113.10	36.20		62.10	29.10	1.51	0.39	0.74	2.27
	Ventral anterior*		160.70	40.40		124.00	38.40	0.91	0.36	0.20	1.62
	Dorsal posterior		78.00	35.00		66.90	23.50	0.36	0.35	−0.32	1.04
	Dorsal anterior		111.30	36.00		100.80	390.40	0.04	0.34	−0.64	0.71
Shahmaei et al. (61)	Global***	15	239.00	21.00	15	146.00	26.00	3.83	0.63	2.60	5.06
Ghassaban et al. (44)	Right*	24	139.80	10.40	24	115.40	11.60	2.18	0.37	1.46	2.90
	Left*		147.50	10.50		127.50	10.80	1.85	0.35	1.17	2.53
Li et al. (14)	Global*	28	166.03	43,00	28	137.63	34.99	0.71	0.28	0.17	1.26
Chen et al. (58)	SNc*	33	163.47	49.16	26	85.18	30.57	1.84	0.31	1.22	2.45
	SNr		153.16	30.57		134.90	41.02	0.51	0.27	−0.02	1.03

*All SN subdivisions are included. ***Significantly different from controls ($p < 0.001$). **Significantly different from controls ($p < 0.005$). *Significantly different from controls ($p < 0.05$).*

In QSM values and Hedge's *g*, there were no between-vendor significant differences ($p = 0.78$ and $p = 0.07$, respectively), and all the studies were similar in ROI definition.

DISCUSSION

Overall, studies reported in this meta-analysis systematically detected iron overload in the SN by iron-sensitive MRI compatible with PD patients compared to HCs even in the early stages of the disease. This result was in agreement with the abnormal iron metabolism in PD that is associated with the SN cell loss (62).

Studies differed in iron measurement techniques, the studied ROIs, methods of image acquisition and analysis, and patient population. The main measures used to quantify iron load were the R2*, the phase and relative phase of the images for SWI, and the susceptibility for QSM. In R2* and QSM, positive values of Hedge's *g* were related to an increase in iron in PD patients as

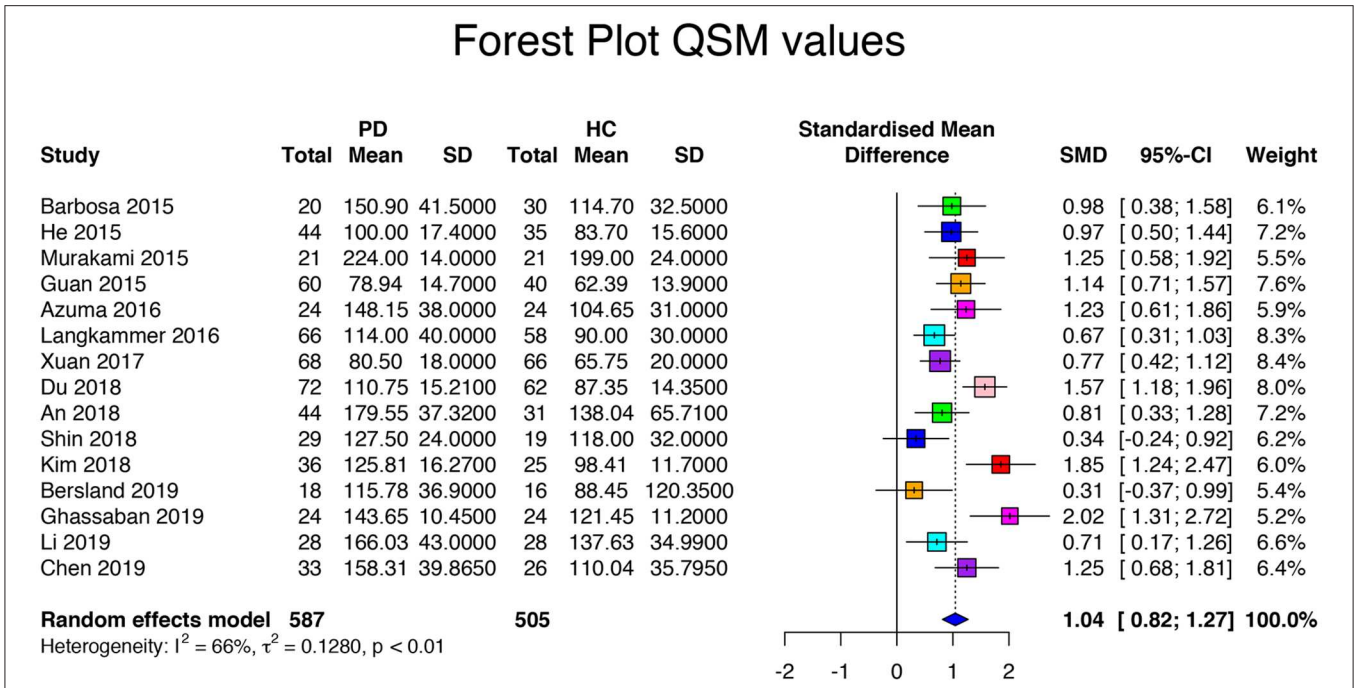


FIGURE 4 | Forest plot of significant QSM values of the 16 articles included in the meta-analysis. Forest plot of the computed disease effect sizes (Hedge's g, x-axis) of studies included into the meta-analysis on QSM measures of the substantia nigra when comparing PD patients and controls. Pooled SMD (95%) (1.04, [0.82, 1.27]) is denoted by a blue diamond.

compared to the HCs (6, 7). In SWI, studies used different image analysis techniques while we used Hedge's *g* as an absolute value of the result.

Regarding R2* values, there was a high variability between studies that was due to several factors. First, the age range of PD patients was wide (58 to 72 years). Second, we observed a dependence of the R2* value on the vendor, magnetic field strength, and ROI placement methods. Moreover, previous studies have shown that R2* depends not only on iron content but is also affected by the orientation of the head in the scanner, the surrounding iron distribution (blooming artifacts), the magnetic field strength, and imaging parameters such as the echo time or voxel size (53, 63, 64). Yet all studies demonstrated a significant increase in R2*, suggesting that R2* was a robust biomarker of SN changes in PD, especially when using a given protocol on a given scanner. Nevertheless, R2* values in PD became comparable across scanners after normalization by the HC values. Multicenter studies should consider the strong difference in R2* between vendors, especially for Philips, and consider normalizing data.

As for manual or semiautomated segmentation methods, the effect size was higher when the segmentation was performed using anatomical images such as 3D T2-weighted and T2*-weighted rather than using R2* or QSM maps, although the difference was not statistically significant. This difference may be related to the better resolution of the anatomical images. However, the constant improvements in resolution and contrast of parametric mapping, especially at ultra-high-field strength, especially in QSM, may modify this observation in future studies. There were no significant correlations for R2* values or for R2* effect size with clinical parameters. The lack of correlations may be due to the large variability of R2* results as well as to a high number of possible confounding factors. Finally, while most articles reported UPDRS values, a large proportion of them did not specify if the values were obtained using on or off medication. In PD, degeneration of dopaminergic neurons predominates in the lateral part of the SNc, particularly in nigrosome 1 (65); therefore, greater differences were expected in this region. The highest effect size was observed in this lateral part of the SN consistent with this hypothesis. Some authors have analyzed separately the SN contra and ipsilateral to the most affected side in the hypothesis that the contralateral SN would show greater nigral damage (12, 31, 32). However, we found no difference for both R2* values and effect sizes. This suggests that at PD onset, both SNc and SNr are already affected with increased iron overload.

SWI measurements were the most variable across studies. SWI is purely a qualitative method that some studies have however used to carry out local measurements (66). However, this is intrinsically incorrect, since these phase measurements do not reflect local modifications because the phase shift of the signal inside a voxel comes not only from sources of susceptibility inside this voxel but also from neighboring sources outside this voxel (67). This can be a reason for the high variability across studies (I^2 = 89%), even if the pooled effect

size was rather high. Additional reasons for the variability of SWI values in these studies can be the presence of blooming artifacts on phase and SWI images (similar to R2*) and the dependence of SWI on tissue geometry and orientation dependence relative to the direction of the main magnetic field. Limitations of SWI induced by the nonlocal, geometry-dependent, and orientation-dependent nature of the signal phase are overcome by QSM, which directly estimates the tissue susceptibility distribution based on the local perturbation of the magnetic field (64). Still, there was a positive correlation between the UPDRS scores and the effect size of phase measurements, suggesting a correlation between iron load and the severity of motor symptoms.

The effect size observed for QSM was higher than the one for R2* although the difference was not significant. Moreover, in studies that compared R2* and QSM values in the same patients, the effect size was significantly higher for QSM than for R2*, suggesting that QSM might be a more robust marker than R2*. In addition, there were no significant differences in QSM values between the vendors. The QSM values also correlated significantly with age and UPDRS. The variability of susceptibility measurements was lower than that for SWI; however, this variability was still high, suggesting that more work needs to be done to standardize QSM image processing pipelines between centers. There were no significant differences in QSM values between the different subdivisions of the SN or between the SN contra or ipsilateral to the most affected side. Overall, while we would expect more significant changes in the SNc than the SNr based on pathological studies, this difference was not found in a high proportion of studies. This lack of difference could be due to the segmentation techniques, since the SNc was not clearly visible on the R2 * or QSM images due to the relatively weak presence of iron in this region and its segmentation most often using a probabilistic method. A neuromelanin-based segmentation method could help better delineate the SNc (56).

Finally, the results of this meta-analysis suggest that QSM has some advantages over R2* because it provides a quantification of magnetic susceptibility, which might better reflect the underlying tissue iron content compared to R2*. Moreover, both QSM and R2* are preferable to SWI because they provide quantitative values unlike SWI.

In terms of implementation, however, all methods pose some issues. Firstly, QSM and SWI require acquiring images of the MRI signal phase, whereas R2* only requires acquiring images of the MRI signal magnitude. Although protocols for SWI are now available for most vendors, for QSM, the correct acquisition of the phase might pose a technical issue in a clinical setting, as not all vendors correctly combine the phase from multiple elements of a phased-array coil, and dedicated software is required in these cases (68). Secondly, SWI only requires a single-echo acquisition, whereas multi-echo acquisitions are required for R2* and are in general preferable for QSM too (69–71). This might pose a time issue in clinical practice. Therefore, when deciding which methods to use, one should consider the need for quantitative vs. qualitative imaging, the ease of implementation on clinical systems, and time constraints.

Our study has several limitations. First, despite the careful search across several databases, some studies could have been missed (72). Second, common with all literature searches and meta-analysis publication practices, usually publishing positive rather than negative studies might have biased the results. Consequently, the mean effect size could be somehow overestimated as unpublished negative data were probably underrepresented. Third, there was a large heterogeneity of R2* and SWI values, indicating a large variability of these measurements, that depended on blooming artifacts and the fact that, in contrast with QSM, neither R2* nor SWI directly quantifies the changes in magnetic susceptibility due to iron deposition in the SN. Moreover, the values varied with the scanner vendor and other technical parameters.

In summary, we have observed a consistent increase in MRI measures of iron content in PD across the literature using R2*, SWI, or QSM techniques, confirming that these measurements provide reliable markers of iron content in PD. Several of these measurements correlated with the severity of motor symptoms. Lastly, QSM appeared to be a more robust biomarker than R2*. However, image processing pipelines for QSM are not yet fully standardized, although efforts in this direction are being made (68, 73, 74). Therefore, QSM is a promising biomarker of disease-related iron accumulation in PD, but further work is needed to establish it as a robust biomarker in multicenter clinical studies and its usefulness as a longitudinal marker.

DATA AVAILABILITY STATEMENT

All datasets generated for this study are included in the article/**Supplementary Material**.

AUTHOR CONTRIBUTIONS

NP, CS-M, and SL contributed conception and design of the study. NP, RG, and CS-M organized the database. LY-C performed the statistical analysis. NP wrote the first draft of the manuscript. NP, CS-M, EB, MS, and SL wrote sections of the manuscript. All authors contributed to manuscript revision, read, and approved the submitted version.

SUPPLEMENTARY MATERIAL

The Supplementary Material for this article can be found online at: https://www.frontiersin.org/articles/10.3389/fneur.2020.00366/full#supplementary-material

Supplementary Figure 1 | Prisma 2009 flow diagram showing an overview of study selection.

Supplementary Figure 2 | Funnel plot of R2* values.

Supplementary Figure 3 | Funnel plot of SWI values.

Supplementary Figure 4 | Funnel plot of QSM values.

Supplementary Figure 5 | Forest plot of significant R2* values of the 27 articles included in the meta-analysis. Forest plot of the computed diseases effect sizes (Hedge's g, x-axis) of studies included into the meta-analysis on R2* measures of

the substantia nigra when comparing PD patients and controls. Pooled SMD (95%) *(0.84, [0. 60, 1.08])* is denoted by a blue diamond.

Supplementary Figure 6 | Forest plot of significant *QSM* values of the *16* articles included in the meta-analysis. Forest plot of the computed diseases effect sizes (Hedge's g, x-axis) of studies included into the meta-analysis on *QSM* measures of the substantia nigra when comparing PD patients and controls. Pooled SMD (95%) (*1.13*, [*0.86*, *1.39*]) is denoted by a blue diamond.

Supplementary Table 1 | PRISMA checklist.

Supplementary Table 2 | Quadas questionnaire.

REFERENCES

1. Fearnley JM, Lees AJ. Ageing and Parkinson's disease: substantia nigra regional selectivity. *Brain.* (1991) 114(Pt 5):2283–301. doi: 10.1093/brain/114.5.2283
2. Dexter DT, Wells FR, Lees AJ, Agid F, Agid Y, Jenner P, et al. Increased nigral iron content and alterations in other metal ions occurring in brain in Parkinson's disease. *J Neurochem.* (1989) 52:1830–6. doi: 10.1111/j.1471-4159.1989.tb07264.x
3. Sofic E, Paulus W, Jellinger K, Riederer P, Youdim MB. Selective increase of iron in substantia nigra zona compacta of parkinsonian brains. *J Neurochem.* (1991) 56:978–82. doi: 10.1111/j.1471-4159.1991.tb02017.x
4. Griffiths PD, Dobson BR, Jones GR, Clarke DT. Iron in the basal ganglia in Parkinson's disease. An *in vitro* study using extended X-ray absorption fine structure and cryo-electron microscopy. *Brain.* (1999) 122(Pt 4):667–73. doi: 10.1093/brain/122.4.667
5. Duyn JH, Schenck J. Contributions to magnetic susceptibility of brain tissue. *NMR Biomed.* (2017) 30:3546. doi: 10.1002/nbm.3546
6. Langkammer C, Krebs N, Goessler W, Scheurer E, Ebner F, Yen K, et al. Quantitative MR imaging of brain iron: a postmortem validation study. *Radiology.* (2010) 257:455–62. doi: 10.1148/radiol.10100495
7. Langkammer C, Schweser F, Krebs N, Deistung A, Goessler W, Scheurer E, et al. Quantitative susceptibility mapping (QSM) as a means to measure brain iron? A post mortem validation study. *Neuroimage.* (2012) 62:1593–9. doi: 10.1016/j.neuroimage.2012.05.049
8. Pyatigorskaya N, Sharman M, Corvol J-C, Valabregue R, Yahia-Cherif L, Poupon F, et al. High nigral iron deposition in LRRK2 and Parkin mutation carriers using R2* relaxometry. *Mov Disord.* (2015) 30:1077–84. doi: 10.1002/mds.26218
9. Graham JM, Paley MN, Grünewald RA, Hoggard N, Griffiths PD. Brain iron deposition in Parkinson's disease imaged using the PRIME magnetic resonance sequence. *Brain.* (2000) 123 Pt 12:2423–31. doi: 10.1093/brain/123.12.2423
10. Hopes L, Grolez G, Moreau C, Lopes R, Ryckewaert G, Carrière N, et al. Magnetic Resonance Imaging Features of the Nigrostriatal System: Biomarkers of Parkinson's Disease Stages? *PLoS ONE.* (2016) 11:e0147947. doi: 10.1371/journal.pone.0147947
11. Arribarat G, Pasternak O, De Barros A, Galitzky M, Rascol O, Péran P. Substantia nigra locations of iron-content, free-water and mean diffusivity abnormalities in moderate stage Parkinson's disease. *Parkinsonism Relat Disord.* (2019) 65:146–52. doi: 10.1016/j.parkreldis.2019.05.033
12. Isaias IU, Trujillo P, Summers P, Marotta G, Mainardi L, Pezzoli G, et al. Neuromelanin imaging and dopaminergic loss in Parkinson's disease. *Front Aging Neurosci.* (2016) 8:196. doi: 10.3389/fnagi.2016.00196
13. Langley J, He N, Huddleston DE, Chen S, Yan F, Crosson B, et al. Reproducible detection of nigral iron deposition in 2 Parkinson's disease cohorts. *Mov Disord.* (2019) 34:416–9. doi: 10.1002/mds.27608
14. Li G, Zhai G, Zhao X, An H, Spincemaille P, Gillen KM, et al. 3D texture analyses within the substantia nigra of Parkinson's disease patients on quantitative susceptibility maps and R2∗ maps. *Neuroimage.* (2019) 188:465–72. doi: 10.1016/j.neuroimage.2018.12.041
15. Saeed U, Compagnone J, Aviv RI, Strafella AP, Black SE, Lang AE, et al. Imaging biomarkers in Parkinson's disease and Parkinsonian syndromes: current and emerging concepts. *Transl Neurodegener.* (2017) 6:6. doi: 10.1186/s40035-017-0076-6
16. Pesch B, Casjens S, Woitalla D, Dharmadhikari S, Edmondson DA, Zella MAS, et al. Impairment of motor function correlates with neurometabolite and brain iron alterations in Parkinson's disease. *Cells.* (2019) 8:96. doi: 10.3390/cells8020096
17. Ulla M, Bonny JM, Ouchchane L, Rieu I, Claise B, Durif F. Is R2* a new MRI biomarker for the progression of Parkinson's disease? A longitudinal follow-up. *PLoS ONE.* (2013) 8:e57904. doi: 10.1371/journal.pone.0057904
18. Eriksen MB, Frandsen TF. The impact of patient, intervention, comparison, outcome (PICO) as a search strategy tool on literature search quality: a systematic review. *J Med Libr Assoc.* (2018) 106:420–31. doi: 10.5195/JMLA.2018.345
19. Postuma RB, Berg D, Stern M, Poewe W, Olanow CW, Oertel W, et al. MDS clinical diagnostic criteria for Parkinson's disease. *Mov Disord.* (2015) 30:1591–601. doi: 10.1002/mds.26424
20. Du G, Lewis MM, Sen S, Wang J, Shaffer ML, Styner M, et al. Imaging nigral pathology and clinical progression in Parkinson's disease. *Mov Disord.* (2012) 27:1636–43. doi: 10.1002/mds.25182
21. Du G, Lewis MM, Styner M, Shaffer ML, Sen S, Yang QX, et al. Combined R2* and diffusion tensor imaging changes in the substantia nigra in Parkinson's disease. *Mov Disord.* (2011) 26:1627–32. doi: 10.1002/mds.23643
22. Ordidge RJ, Gorell JM, Deniau JC, Knight RA, Helpern JA. Assessment of relative brain iron concentrations using T2-weighted and T2*-weighted MRI at 3 Tesla. *Magn Reson Med.* (1994) 32:335–41. doi: 10.1002/mrm.1910320309
23. Rossi M, Ruottinen H, Soimakallio S, Elovaara I, Dastidar P. Clinical MRI for iron detection in Parkinson's disease. *Clin Imaging.* (2013) 37:631–6. doi: 10.1016/j.clinimag.2013.02.001
24. Reimão S, Ferreira S, Nunes RG, Pita Lobo P, Neutel D, Abreu D, et al. Magnetic resonance correlation of iron content with neuromelanin in the substantia nigra of early-stage Parkinson's disease. *Eur J Neurol.* (2016) 23:368–74. doi: 10.1111/ene.12838
25. Balduzzi S, Rücker G, Schwarzer G. How to perform a meta-analysis with R: a practical tutorial. *Evid Based Ment Health.* (2019) 22:153–60. doi: 10.1136/ebmental-2019-300117
26. Hozo SP, Djulbegovic B, Hozo I. Estimating the mean and variance from the median, range, and the size of a sample. *BMC Med Res Methodol.* (2005) 5:13. doi: 10.1186/1471-2288-5-13
27. Hedges LV. Distribution theory for glass's estimator of effect size and related estimators. *J Educ Stat.* (2016) 6:107–28. doi: 10.1302/10769986006002107
28. Martin WRW, Wieler M, Gee M. Midbrain iron content in early Parkinson disease: a potential biomarker of disease status. *Neurology.* (2008) 70:1411–7. doi: 10.1212/01.wnl.0000286384.31050.b5
29. Péran P, Cherubini A, Assogna F, Piras F, Quattrocchi C, Peppe A, et al. Magnetic resonance imaging markers of Parkinson's disease nigrostriatal signature. *Brain.* (2010) 133:3423–33. doi: 10.1093/brain/awq212
30. Guan X, Xuan M, Gu Q, Xu X, Huang P, Wang N, et al. Influence of regional iron on the motor impairments of Parkinson's disease: A quantitative susceptibility mapping study. *J Magn Reson Imaging.* (2017) 45:1335–42. doi: 10.1002/jmri.25434
31. He N, Ling H, Ding B, Huang J, Zhang Y, Zhang Z, et al. Region-specific disturbed iron distribution in early idiopathic Parkinson's disease measured by quantitative susceptibility mapping. *Hum Brain Mapp.* (2015) 36:4407–20. doi: 10.1002/hbm.22928
32. Baudrexel S, Nürnberger L, Rüb U, Seifried C, Klein JC, Deller T, et al. Quantitative mapping of T1 and T2* discloses nigral and brainstem pathology in early Parkinson's disease. *Neuroimage.* (2010) 51:512–20. doi: 10.1016/j.neuroimage.2010.03.005
33. Bunzeck N, Singh-Curry V, Eckart C, Weiskopf N, Perry RJ, Bain PG, et al. Motor phenotype and magnetic resonance measures of basal ganglia iron levels in Parkinson's disease. *Parkinsonism Relat Disord.* (2013) 19:1136–42. doi: 10.1016/j.parkreldis.2013.08.011
34. Borenstein M, Hedges LV, Higgins JPT, Rothstein HR. *Introduction to Meta-Analysis*. Chichester: John Wiley & Sons. (2011).

35. Bender A, Hagan KE, Kingston N. The association of folate and depression: a meta-analysis. *J Psychiatr Res.* (2017) 95:9–18. doi: 10.1016/j.jpsychires.2017.07.019
36. Nichols TE, Holmes AP. Nonparametric permutation tests for functional neuroimaging: a primer with examples. *Hum Brain Mapp.* (2002) 15:1–25. doi: 10.1002/hbm.1058
37. Focke NK, Helms G, Pantel PM, Scheewe S, Knauth M, Bachmann CG, et al. Differentiation of typical and atypical Parkinson syndromes by quantitative MR imaging. *AJNR Am J Neuroradiol.* (2011) 32:2087–92. doi: 10.3174/ajnr.A2865
38. Lewis MM, Du G, Kidacki M, Patel N, Shaffer ML, Mailman RB, et al. Higher iron in the red nucleus marks Parkinson's dyskinesia. *Neurobiol Aging.* (2013) 34:1497–503. doi: 10.1016/j.neurobiolaging.2012.10.025
39. Barbosa JHO, Santos AC, Tumas V, Liu M, Zheng W, Haacke EM, et al. Quantifying brain iron deposition in patients with Parkinson's disease using quantitative susceptibility mapping, R2 and R2. *Magn Reson Imaging.* (2015) 33:559–65. doi: 10.1016/j.mri.2015.02.021
40. Murakami Y, Kakeda S, Watanabe K, Ueda I, Ogasawara A, Moriya J, et al. Usefulness of quantitative susceptibility mapping for the diagnosis of Parkinson disease. *AJNR Am J Neuroradiol.* (2015) 36:1102–8. doi: 10.3174/ajnr.A4260
41. Wieler M, Gee M, Martin WRW. Longitudinal midbrain changes in early Parkinson's disease: iron content estimated from R2*/MRI. *Parkinsonism Relat Disord.* (2015) 21:179–83. doi: 10.1016/j.parkreldis.2014.11.017
42. Langkammer C, Pirpamer L, Seiler S, Deistung A, Schweser F, Franthal S, et al. Quantitative susceptibility mapping in Parkinson's Disease. *PLoS ONE.* (2016) 11:e0162460. doi: 10.1371/journal.pone.0162460
43. Du G, Lewis MM, Sica C, He L, Connor JR, Kong L, et al. Distinct progression pattern of susceptibility MRI in the substantia nigra of Parkinson's patients. *Mov Disord.* (2018) 33:1423–31. doi: 10.1002/mds.27318
44. Ghassaban K, He N, Sethi SK, Huang P, Chen S, Yan F, et al. Regional high iron in the substantia nigra differentiates parkinson's disease patients from healthy controls. *Front Aging Neurosci.* (2019) 11:106. doi: 10.3389/fnagi.2019.00106
45. Gupta D, Saini J, Kesavadas C, Sarma PS, Kishore A. Utility of susceptibility-weighted MRI in differentiating Parkinson's disease and atypical parkinsonism. *Neuroradiology.* (2010) 52:1087–94. doi: 10.1007/s00234-010-0677-6
46. Wang Y, Butros SR, Shuai X, Dai Y, Chen C, Liu M, et al. Different iron-deposition patterns of multiple system atrophy with predominant parkinsonism and idiopathetic Parkinson diseases demonstrated by phase-corrected susceptibility-weighted imaging. *AJNR Am J Neuroradiol.* (2012) 33:266–73. doi: 10.3174/ajnr.A2765
47. Wang C, Fan G, Xu K, Wang S. Quantitative assessment of iron deposition in the midbrain using 3D-enhanced T2 star weighted angiography (ESWAN): a preliminary cross-sectional study of 20 Parkinson's disease patients. *Magn Reson Imaging.* (2013) 31:1068–73. doi: 10.1016/j.mri.2013.04.015
48. Wu S-F, Zhu Z-F, Kong Y, Zhang H-P, Zhou G-Q, Jiang Q-T, et al. Assessment of cerebral iron content in patients with Parkinson's disease by the susceptibility-weighted MRI. *Eur Rev Med Pharmacol Sci.* (2014) 18:2605–8.
49. Zhang J, Zhang Y, Wang J, Cai P, Luo C, Qian Z, et al. Characterizing iron deposition in Parkinson's disease using susceptibility-weighted imaging: an *in vivo* MR study. *Brain Res.* (2010) 1330:124–30. doi: 10.1016/j.brainres.2010.03.036
50. Jin L, Wang J, Jin H, Fei G, Zhang Y, Chen W, et al. Nigral iron deposition occurs across motor phenotypes of Parkinson's disease. *Eur J Neurol.* (2012) 19:969–76. doi: 10.1111/j.1468-1331.2011.03658.x
51. Lotfipour AK, Wharton S, Schwarz ST, Gontu V, Schäfer A, Peters AM, et al. High resolution magnetic susceptibility mapping of the substantia nigra in Parkinson's disease. *J Magn Reson Imaging.* (2012) 35:48–55. doi: 10.1002/jmri.22752
52. Martin-Bastida A, Lao-Kaim NP, Loane C, Politis M, Roussakis AA, Valle-Guzman N, et al. Motor associations of iron accumulation in deep grey matter nuclei in Parkinson's disease: a cross-sectional study of iron-related magnetic resonance imaging susceptibility. *Eur J Neurol.* (2017) 24:357–65. doi: 10.1111/ene.13208
53. Azuma M, Hirai T, Yamada K, Yamashita S, Ando Y, Tateishi M, et al. Lateral asymmetry and spatial difference of iron deposition in the substantia nigra of patients with Parkinson disease measured with quantitative susceptibility mapping. *AJNR Am J Neuroradiol.* (2016) 37:782–8. doi: 10.3174/ajnr.A4645
54. Xuan M, Guan X, Gu Q, Shen Z, Yu X, Qiu T, et al. Different iron deposition patterns in early- and middle-late-onset Parkinson's disease. *Parkinsonism Relat Disord.* (2017) 44:23–7. doi: 10.1016/j.parkreldis.2017.08.013
55. Bergsland N, Zivadinov R, Schweser F, Hagemeier J, Lichter D, Guttuso T. Ventral posterior substantia nigra iron increases over 3 years in Parkinson's disease. *Mov Disord.* (2019) 34:1006–13. doi: 10.1002/mds.27730
56. Takahashi H, Watanabe Y, Tanaka H, Mihara M, Mochizuki H, Liu T, et al. Quantifying changes in nigrosomes using quantitative susceptibility mapping and neuromelanin imaging for the diagnosis of early-stage Parkinson's disease. *Br J Radiol.* (2018) 91:20180037. doi: 10.1259/bjr.20180037
57. Shin C, Lee S, Lee JY, Rhim JH, Park SW. Non-motor symptom burdens are not associated with iron accumulation in early Parkinson's disease: a quantitative susceptibility mapping study. *J Korean Med Sci.* (2018) 33:e96. doi: 10.3346/jkms.2018.33.e96
58. Chen Q, Chen Y, Zhang Y, Wang F, Yu H, Zhang C, et al. Iron deposition in Parkinson's disease by quantitative susceptibility mapping. *BMC Neurosci.* (2019) 20:23. doi: 10.1186/s12868-019-0505-9
59. An H, Zeng X, Niu T, Li G, Yang J, Zheng L, et al. Quantifying iron deposition within the substantia nigra of Parkinson's disease by quantitative susceptibility mapping. *J Neurol Sci.* (2018) 386:46–52. doi: 10.1016/j.jns.2018.01.008
60. Kim EY, Sung YH, Shin HG, Noh Y, Nam Y, Lee J. Diagnosis of early-stage idiopathic parkinson's disease using high-resolution quantitative susceptibility mapping combined with histogram analysis in the substantia nigra at 3 T. *J Clin Neurol.* (2018) 14:90–7. doi: 10.3988/jcn.2018.14.1.90
61. Shahmaei V, Faeghi F, Mohammdbeigi A, Hashemi H, Ashrafi F. Evaluation of iron deposition in brain basal ganglia of patients with Parkinson's disease using quantitative susceptibility mapping. *Eur J Radiol Open.* (2019) 6:169–74. doi: 10.1016/j.ejro.2019.04.005
62. Hirsch EC. Altered regulation of iron transport and storage in Parkinson's disease. *J Neural Transm Suppl.* (2006) 71:201–4. doi: 10.1007/978-3-211-33328-0_21
63. Yablonskiy DA, Haacke EM. Theory of NMR signal behavior in magnetically inhomogeneous tissues: the static dephasing regime. *Magn Reson Med.* (1994) 32:749–63. doi: 10.1002/mrm.1910320610
64. Li J, Chang S, Liu T, Wang Q, Cui D, Chen X, et al. Reducing the object orientation dependence of susceptibility effects in gradient echo MRI through quantitative susceptibility mapping. *Magn Reson Med.* (2012) 68:1563–9. doi: 10.1002/mrm.24135
65. Damier P, Hirsch EC, Agid Y, Graybiel AM. The substantia nigra of the human brain. II. Patterns of loss of dopamine-containing neurons in Parkinson's disease. *Brain.* (1999) 122(Pt 8):1437–48. doi: 10.1093/brain/122.8.1437
66. Park MJ, Kim HS, Jahng G-H, Ryu C-W, Park SM, Kim SY. Semiquantitative assessment of intratumoral susceptibility signals using non-contrast-enhanced high-field high-resolution susceptibility-weighted imaging in patients with gliomas: comparison with MR perfusion imaging. *Am J Neuroradiol.* (2009) 30:1402–8. doi: 10.3174/ajnr.A1593
67. Schäfer A, Wharton S, Gowland P, Bowtell R. Using magnetic field simulation to study susceptibility-related phase contrast in gradient echo MRI. *Neuroimage.* (2009) 48:126–37. doi: 10.1016/j.neuroimage.2009.05.093
68. Robinson SD, Bredies K, Khabipova D, Dymerska B, Marques JP, Schweser F. An illustrated comparison of processing methods for MR phase imaging and QSM: combining array coil signals and phase unwrapping. *NMR Biomed.* (2017) 30:e3601. doi: 10.1002/nbm.3601
69. Haacke EM, Liu S, Buch S, Zheng W, Wu D, Ye Y. Quantitative susceptibility mapping: current status and future directions. *Mag Reson Imag.* (2015) 33:1–25. doi: 10.1016/j.mri.2014.09.004
70. Wu B, Li W, Avram AV, Gho S-M, Liu C. Fast and tissue-optimized mapping of magnetic susceptibility and T2* with multi-echo and multi-shot spirals. *NeuroImage.* (2012) 59:297–305. doi: 10.1016/j.neuroimage.2011.07.019
71. Liu T, Surapaneni K, Lou M, Cheng L, Spincemaille P, Wang Y. Cerebral microbleeds: burden assessment by using quantitative susceptibility mapping. *Radiology.* (2012) 262:269–78. doi: 10.1148/radiol.11110251
72. Moher D, Liberati A, Tetzlaff J, Altman DG, PRISMA Group. Preferred reporting items for systematic reviews and meta-analyses: the PRISMA

statement. J Clin Epidemiol (2009) 62:1006-1012. doi: 10.1016/j.jclinepi.2009.06.005

73. Schweser F, Robinson SD, Rochefort L de, Li W, Bredies K. An illustrated comparison of processing methods for phase MRI and QSM: removal of background field contributions from sources outside the region of interest. *NMR in Biomedicine.* (2017) 30:e3604. doi: 10.1002/nbm.3604
74. Langkammer C, Schweser F, Shmueli K, Kames C, Li X, Guo L, et al. Quantitative susceptibility mapping: Report from the 2016 reconstruction challenge. *Magn Reson Med.* (2018) 79:1661–1673. doi: 10.1002/mrm.26830

Conflict of Interest: The authors declare that the research was conducted in the absence of any commercial or financial relationships that could be construed as a potential conflict of interest.

Copyright © 2020 Pyatigorskaya, Sanz-Morère, Gaurav, Biondetti, Valabregue, Santin, Yahia-Cherif and Lehéricy. This is an open-access article distributed under the terms of the Creative Commons Attribution License (CC BY). The use, distribution or reproduction in other forums is permitted, provided the original author(s) and the copyright owner(s) are credited and that the original publication in this journal is cited, in accordance with accepted academic practice. No use, distribution or reproduction is permitted which does not comply with these terms.

frontiers in Neurology

ORIGINAL RESEARCH
published: 10 July 2020
doi: 10.3389/fneur.2020.00574

PET Tau Imaging and Motor Impairments Differ Between Corticobasal Syndrome and Progressive Supranuclear Palsy With and Without Alzheimer's Disease Biomarkers

*Anna Vasilevskaya[1,2], Foad Taghdiri[2], Namita Multani[2,3], Cassandra Anor[2,3], Karen Misquitta[2,3], Sylvain Houle[4], Charles Burke[5], David Tang-Wai[3], Anthony E. Lang[6], Susan Fox[6], Elizabeth Slow[6], Pablo Rusjan[4] and Maria C. Tartaglia[2,3]**

[1] Institute of Medical Science, University of Toronto, Toronto, ON, Canada, [2] Tanz Centre for Research in Neurodegenerative Diseases, University of Toronto, Toronto, ON, Canada, [3] Division of Neurology, Toronto Western Hospital, University Health Network, Toronto, ON, Canada, [4] PET Centre, Centre for Addiction and Mental Health, Toronto, ON, Canada, [5] School of Medicine and Dentistry, Western University, Windsor, ON, Canada, [6] Edmond J. Safra Program for Parkinson Disease and the Morton and Gloria Shulman Movement Disorders Clinic, Toronto Western Hospital, University Health Network, Toronto, ON, Canada

OPEN ACCESS

Edited by:
Antonio Pisani,
University of Rome Tor Vergata, Italy

Reviewed by:
Agostino Chiaravalloti,
University of Rome Tor Vergata, Italy
Pedro Chana-Cuevas,
University of Santiago, Chile

***Correspondence:**
Maria C. Tartaglia
carmela.tartaglia@uhn.ca

Specialty section:
This article was submitted to Movement Disorders, a section of the journal Frontiers in Neurology

Received: 13 March 2020
Accepted: 19 May 2020
Published: 10 July 2020

Citation:
Vasilevskaya A, Taghdiri F, Multani N, Anor C, Misquitta K, Houle S, Burke C, Tang-Wai D, Lang AE, Fox S, Slow E, Rusjan P and Tartaglia MC (2020) PET Tau Imaging and Motor Impairments Differ Between Corticobasal Syndrome and Progressive Supranuclear Palsy With and Without Alzheimer's Disease Biomarkers. Front. Neurol. 11:574. doi: 10.3389/fneur.2020.00574

Introduction: Frontotemporal lobar degeneration (FTLD)-related syndrome includes progressive supranuclear palsy (PSP) and corticobasal syndrome (CBS). PSP is usually caused by a tauopathy but can have associated Alzheimer's disease (AD) while CBS can be caused by tauopathy, transactive response DNA binding protein 43 kDa, or AD pathology. Our aim was to compare the parkinsonian syndromes presenting without AD biomarkers (CBS/PSP-non-AD) to parkinsonian syndromes with AD biomarkers (CBS/PSP-AD).

Materials and Methods: Twenty-four patients [11 males, 13 females; age (68.46 ± 7.23)] were recruited for this study. The whole cohort was divided into parkinsonian syndromes without AD biomarkers [$N = 17$; diagnoses (6 CBS, 11 PSP)] and parkinsonian syndromes with AD biomarkers [$N = 7$; diagnoses (6 CBS-AD, 1 PSP-AD)]. Anatomical MRI and PET imaging with tau ligand [18F]-AV1451 tracer was completed. Cerebrospinal fluid analysis or [18F]-AV1451 PET imaging was used to assess for the presence of AD biomarkers. Progressive supranuclear palsy rating scale (PSPRS) and unified Parkinson's disease rating scale (UPDRS) motor exam were implemented to assess for motor disturbances. Language and cognitive testing were completed.

Results: The CBS/PSP-non-AD group [age (70.18 ± 6.65)] was significantly older ($p = 0.028$) than the CBS/PSP-AD group [age (64.29 ± 7.32)]. There were no differences between the groups in terms of gender, education, years of disease duration, and disease severity as measured with the Clinical Dementia Rating scale. The CBS/PSP-non-AD group had significantly lower PET Tau Standard Volume Uptake Ratio (SUVR) values compared to the CBS/PSP-AD group in multiple frontal and temporal areas,

and inferior parietal (all $p < 0.03$). The CBS/PSP-non-AD group had significantly higher scores compared to the CBS/PSP-AD group on PSPRS ($p = 0.004$) and UPDRS motor exam ($p = 0.045$). The CBS/PSP-non-AD group had higher volumes of inferior parietal, precuneus, and hippocampus (all $p < 0.02$), but lower volume of midbrain ($p = 0.02$), compared to the CBS/PSP-AD group.

Discussion: The CBS/PSP-non-AD group had higher motor disturbances compared to the CBS/PSP-AD group; however, both groups performed similarly on neuropsychological measures. The AD biomarker group had increased global uptake of PET Tau SUVR and lower volumes in AD-specific areas. These results show that the presenting phenotype of CBS and PSP syndromes and the distribution of injury are strongly affected by the presence of AD biomarkers.

Keywords: corticobasal syndrome, progressive supranuclear palsy, Alzheimer's disease, positron emission tomography, motor symptoms, PSPRS, UPDRS

INTRODUCTION

Frontotemporal lobar degeneration (FTLD) is an umbrella term used to describe neurodegenerative diseases with an underlying pathology preferentially involving frontal and temporal lobes (1). Two syndromes that fall under the FTLD umbrella are corticobasal syndrome (CBS) and progressive supranuclear palsy (PSP). CBS and PSP are syndromes with motor and cognitive deficits with high overlap in clinical presentation and underlying pathology, but with their own distinct features (2, 3). CBS presents with subcortical motor features of akinetic rigidity, dystonia, and progressive asymmetric bradykinesia, as well as cortical deficits of ideomotor limb apraxia, myoclonus, and alien limb phenomenon (4–6). Cognitive features that are prominent in CBS include language disfunction (i.e., non-fluency, word finding difficulty, and sentence repetition problems), visuospatial, and social cognition abnormalities. Executive function and memory impairments may present in some CBS cases, but are non-specific and cannot distinguish CBS from other neurodegenerative diseases like PSP or Alzheimer's disease (AD) (3). Initially, the pathology underlying CBS was thought to be exclusively corticobasal degeneration (CBD)—a 4-repeat tauopathy. With the emergence of multiple post-mortem case studies, CBS is now known to have heterogeneous neuropathological underpinnings including AD, Pick's disease, FTLD with transactivation response DNA binding protein 43 kDa (TDP-43) inclusions, and FTLD with ubiquitin-immunoreactive inclusions negative for TDP-43 (3, 7–9) as well as cerebrovascular pathology (3, 9, 10). The most common neuropathological cause of CBS is due to CBD; however, it accounts for <50% of all CBS cases. The second and third most common causes of CBS are PSP and AD pathology, respectively (11).

PSP is the other motor-predominant FTLD syndrome and is associated with early postural instability, falls, and abnormal eye movements (12, 13). This describes the classic Richardson's syndrome; it is now known that PSP can present with language, cognitive, or behavioral deficits (14). The underlying pathology of PSP (a 4-repeat tauopathy, like CBD) is confirmed in ∼90% of all cases of the Richardson syndrome and consists of 4-repeat tau immunoreactive inclusions in brainstem and basal ganglia (12).

AD is a neurodegenerative disease associated with abnormal deposits of amyloid β-peptide (Aβ) plaques and neurofibrillary tangles of hyperphosphorylated tau protein and is a mixed 3-repeat and 4-repeat tauopathy with tau in the form of paired helical filaments. It is now known that AD can present with a variety of phenotypes so that aside from the classic amnestic variant, there can be presentations with language, visual processing, executive, and behavioral symptoms (15). There is also the increased recognition that co-pathology exists and is a common feature of neurogenerative diseases (9, 16, 17). It is unclear how the presence of AD biomarkers as a surrogate of AD pathology affects the clinical presentation of FTLD-motor syndromes. The aim of the current study is to compare the parkinsonian syndromes presenting without AD biomarkers to parkinsonian syndromes with AD biomarkers on measures of motor scales, cognition, and neuroimaging outcomes.

MATERIALS AND METHODS

Participants

Twenty-four participants with current diagnoses of PSP or CBS were included in this study. Participants were included if they were 18–90 years old, able to read, understand, and speak English for neuropsychological testing. Participants must have had a reliable study partner who could provide independent evaluation of functioning. Exclusion criteria were history of traumatic brain injury, brain tumors, stroke, or other neurological or psychiatric disorders that could explain symptoms. The diagnosis of PSP was made based on the National Institute of Neurological Disorders and Stroke Society of Progressive Supranuclear Palsy (NINDS-SPSP), and further refined in the multicenter on Neuroprotection and Natural History in Parkinson Plus Syndromes (NNIPPS) study (12, 18, 19). The diagnosis of CBS was made based on the current criteria for CBS (20). Nineteen of twenty-four participants underwent a lumbar puncture procedure to collect and analyze cerebrospinal fluid (CSF) for the presence of AD pathology. For the five participants who refused lumbar

punctures, PET tau imaging was examined by a cognitive neurologist (MCT) for evidence of a pattern typical of AD. Participants were divided into two groups: (1) participants with diagnoses of PSP and CBS negative for AD biomarkers (FTLD-non-AD) and (2) participants with diagnoses of PSP and CBS positive for AD biomarkers (FTLD-AD). Written consent was obtained from all study participants and caregivers. The study was approved by the University Health Network and Center for Addiction and Mental Health Research Ethics Boards.

Motor and Neuropsychological Testing

All participants were assessed by a cognitive neurologist (MCT), and Progressive Supranuclear Palsy Rating Scale (PSPRS) (21) and Unified Parkinson's Disease Rating Scale (UPDRS) (22) motor part were completed. The global level of functioning was measured using clinical dementia rating scale (CDR) (23) through interviews of caregivers by trained research assistants. CDR global score and sum of boxes were calculated. Participants underwent comprehensive neuropsychological testing across the following domains: language, executive function, memory, and visuospatial function. Language assessments included Multilingual Naming Test (MiNT) (24), Pyramids and Palm Trees (25), sentence repetition, and semantic and lexical fluency (26). Executive function assessments included trail making test part B (TMT B) (27, 28) and Digit Symbol coding test (29). Memory assessments included California Verbal Learning Test learning score, delayed 10-min recall scores, and Benson figure recall score. Attention and working memory are assessed using digit span forward and digit span backward, respectively (26, 29). Assessment of visuospatial function was completed using the Visual Object and Space Perception battery (VOSP) (30). Higher score for TMT part B signified worse function, while for the rest of the assessments, the higher score signified better cognitive functioning.

Cerebrospinal Fluid

Lumbar puncture procedure to collect CSF was performed following the AD Neuroimaging Initiative (ADNI) protocol (31). CSF was collected into polypropylene tubes, and a sandwich ELISA technique was implemented to measure levels of Aβ42, phosphorylated tau (p-tau), and total tau (t-tau) (32, 33). AD pathology was deemed present if p-tau $>$ 68 pg/ml and Aβ42 to t-tau index $<$ 0.8 (34, 35).

MRI Acquisition

All structural and DTI scans were obtained using a 3-T MRI Scanner (GE Signa HDx, Milwaukee, WI, USA) with 8-channel head coil. T1-weighted structural MRI scans were acquired using inversion recovery spoiled gradient echo (IR-SPGR) in the sagittal plane using the following scan parameters: TE = 2.8 ms, TR = 7 ms, flip angle = 11°; 176 slices, slice thickness = 1.2 mm, 256 × 256 matrix, FOV = 26 cm. One DWI scan was obtained with the diffusion gradient applied across 60 spatial directions (b = 1,000 s/mm^2) and 10 non-diffusion-weighted Bo scans. The DWI was acquired with the following parameters: 2.4-mm-thick axial slices, TR = 17,000 ms, FOV = 23 cm, 2.4 × 2.4 mm in-plane resolution.

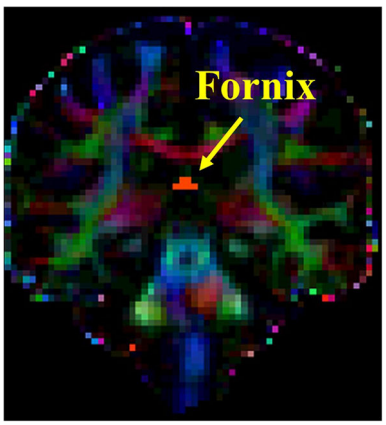


FIGURE 1 | Seed placement for tractography of fornix.

Structural MRI Analysis

T1-weighted structural 3D MRI images analysis was performed with the FreeSurfer v.6 image analysis suite, which is freely available online with documentations (http://surfer.nmr.mgh.harvard.edu/). Structural MRI was preprocessed using the standardized "recon-all" FreeSurfer pipeline, which is described elsewhere (36). Volumes of interest for the following brain regions were extracted: posterior cingulate, inferior parietal, precuneus, lateral orbitofrontal, caudal middle frontal, hippocampus, caudate, and thalamus. Brainstem subfields FreeSurfer pipeline was implemented to extract midbrain volumes (37). To account for individual differences in head size, each volume of interest was corrected for total intracranial volume (ICV) by dividing each structure's volume by ICV (volume-to-ICV ratio) (38).

DTI Analysis

The DTI analysis was conducted using the FMRIB Software Library (FSL) tools (http://www.fmrib.ox.ac.uk/fsl/fdt/index.html). The region of interest (ROI) analysis was performed for the following tracks: right and left superior longitudinal fasciculus (SLF) and fornix. Multiple DTI metrics representing different aspects of white matter integrity were extracted including the following: (a) fractional anisotropy (FA), (b) medial diffusivity (MD), (c) axial diffusivity (AxD), and (d) radial diffusivity (RD). The processing steps of the DTI data, ROI definition, and fiber tracking steps for SLF were completed as previously described (39, 40). The ROI for the fornix was placed on the coronal slice at the point where the posterior pillars of the fornix join together to form the body of fornix (see **Figure 1**). Prior to conducting DTI analysis, subjects' FLAIR images were reviewed by a neurologist (MCT) for presence of no or minimal amount of white matter hyperintensity to ensure accurate tractography results.

PET Acquisition and Analysis

All participants underwent PET imaging with 5 mCi of [F-18]AV1451 ([F-18]T807; Flortaucipir, AVID

Radiopharmaceuticals) tau-specific tracer. Twenty-one participants were scanned using a Biograph HiRez XVI PET/CT scanner (Siemens Molecular Imaging, Knoxville, TN, USA), while three participants were scanned using High-Resolution Research Tomograph (HRRT) (CPS/Siemens, Knoxville, TN, USA) PET scanner.

Emission PET data were acquired in list mode for 75 min starting 45 min after a bolus injection of [F-18]AV1451. The emission list mode data were re-binned into eight 3D sinograms (1×5 min, 7×10 min). For the HRRT acquisitions, a transmission scan was acquired using a single photon point source, ^{137}Cs ($T_{½} = 30.2$ years, $E_{\gamma} = 662$ keV), immediately after the emission acquisition, which was then used to correct the emission data for photon attenuation. Similarly, for the PET/CT acquisitions, a low-dose CT scan was acquired immediately prior to the emission acquisition for the attenuation correction of the emission data. The 3D sinograms were gap-filled, for the HRRT, normalized and scatter corrected, prior to Fourier rebinning of the 3D sinograms into 2D sinograms. The images were reconstructed from the 2D sinograms using a 2D filtered-back projection algorithm, with a HANN filter (HRRT) or ramp filter (PET/CT) at Nyquist cutoff frequency. During image reconstruction, the images were dead-time-corrected and decay-corrected to the start of acquisition. For the HRRT, the reconstructed image had $256 \times 256 \times 207$ 1.22-mm isotropic voxels with a reconstructed resolution of *ca.* 4.5 mm., full width at half maximum (FWHM) in-plane and axially. For the PET/CT, the image had $256 \times 256 \times 81$ voxels each of $2 \times 2 \times 2.07$ mm and an in-plane and axial resolution of 5 and 5.5 mm FWHM, respectively. A thermoplastic mask was made for each participant and used in conjunction with a head fixation system for the duration of both the transmission/CT acquisition and PET acquisition to constrain the subject's head movement. In-house ROMI software was implemented for ROI analysis of the PET data (41). Briefly, ROMI uses a T1-MRI of each subject and a template of ROIs based on the MNI template to individualize the ROIs to each subject's MRI. ROMI uses the segmentation from Statistical Parametric Mapping version 8 (SPM8; https://www.fil.ion.ucl.ac.uk/spm/software/spm8/) and Matlab 8.5.0 (Math Works, Natick, MA) to find the non-linear transformation and later uses the probability of each voxel to be gray matter and some morphological operations to refine the delineation. After realignment of the PET frames to correct for potential motion, a summed PET image was produced for each subject. Normalized mutual information implemented in Statistical Parametric Mapping version 2 (SPM2; https://www.fil.ion.ucl.ac.uk/spm/software/spm2/) was used to co-register the PET and MRI images. The rigid-body transformation was applied to the individualized ROIs to map them into the PET image. The PET images were corrected for partial volume effect (42). ROIs in the PET space were used to mask the PET images and extract the time activity curves for each ROI. For each ROI (i.e., dorsal caudate, insula, thalamus, midbrain, lateral temporal, prefrontal cortex, dorsolateral prefrontal cortex, ventrolateral prefrontal cortex, orbitofrontal cortex, hippocampus, inferior parietal, and cortical gray matter) and time frame, standard uptake volume ratios (SUVRs) were calculated using cerebellar gray matter as the reference region. SUVR of each time frame was averaged for the frames between 50 and 80 min post-injection time.

Voxel-Based PET Analysis

Voxel-based analysis on the PET images was completed using the Statistical Parametric Mapping version 12 (SPM12; https://www.fil.ion.ucl.ac.uk/spm/software/spm12/) and Matlab 8.5.0 (Math Works, Natick, MA). PET frames were realigned to correct for motion, and voxel intensity in each PET frame was normalized to the average signal from the inferior cerebellar gray matter, which was extracted using a native atlas from the automated in-house ROMI software (41). Parametric maps were then averaged between 50 and 80 post-injection time and spatially normalized into the Montreal Neurological Institute (MNI) template to control for variability between subjects. Images were smoothed with a FWHM 8-mm Gaussian kernel in order to increase signal-to-noise ratio. The whole-brain exploratory between-group analysis was completed using the two-sample *t*-test from SPM12 in order to compare the FTLD-non-AD and FTLD-AD groups. Both uncorrected ($p < 0.001$; extent threshold, $k = 50$) and multiple comparison corrected results are presented (FWE corrected at $p < 0.05$; extent threshold, $k = 50$).

Statistical Analysis

Statistical analysis was completed using IBM SPSS Statistics version 24 (IBM Corp., Armonk, NY, USA). All between-group demographics, neuropsychological testing and neuroimaging comparisons were completed using Mann-Whitney *U*-test, with the type of scanner and sex comparisons completed using Fisher's exact test. Pearson partial correlations with age as a covariate were used to analyze associations between PSPRS/UPDRS motor exam scores in relation to volumes of [18-F]AV1451 PET tau areas of interest. Pearson partial correlations with age as a covariate were used to analyze the following relationships: CSF measures with cortical gray matter PET tau; right SLF white matter integrity measures with visuospatial assessments; left SLF white matter integrity measures in relation to language assessments; fornix white matter integrity measures with memory assessments; language assessments and [18-F]AV1451 PET tau SUVR in left lateral temporal and insula areas; executive function assessments and [18-F]AV1451 PET tau SUVR in the dorsolateral prefrontal cortex; learning score and delayed recall with [18-F]AV1451 PET tau SUVR in the prefrontal cortex and left hippocampus; the Benson recall and [18-F]AV1451 PET tau SUVR in the prefrontal cortex and the right hippocampus; digit forward and digit backward with [18-F]AV1451 PET tau SUVR in the prefrontal cortex and the whole hippocampus; and the visuospatial assessments with the [18-F]AV1451 PET tau SUVR in the inferior parietal area. False discovery rate (FDR) correction with Benjamini–Hochberg procedure has been applied for all multiple comparisons and both adjusted and non-adjusted *p*-values are reported with a significance level set at $p < 0.05$.

TABLE 1 | Demographics of the FTLD-non-AD and FTLD-AD groups (mean ± standard deviation).

	FTLD-non-AD	FTLD-AD	*p*-value
N	**17**	**7**	
Demographics			
Age (years)	70.18 ± 6.65	64.29 ± 7.32	0.028
Age of onset (years)	63.82 ± 8.10	60.43 ± 7.68	0.19
Education (years)	14.71 ± 3.41	15.57 ± 4.39	0.58
Sex	8 Males:9 Females	3 Males:4 Females	1.00
Disease duration	6.35 ± 5.23	3.86 ± 2.85	0.28
Diagnosis	11 PSP, 6 CBS	1 PSP-AD, 6 CBS-AD	N.A.
PET scanner	15 PET/CT, 2 HRRT	6 PET/CT, 1 HRRT	1.00
PSPRS	40.76 ± 18.61	18.29 ± 6.65	0.004
UPDRS motor scale	36.06 ± 21.49	15.71 ± 8.34	0.045
CDR global score	1.09 ± 0.83	0.79 ± 0.64	0.43
CDR sum of boxes	6.88 ± 5.28	4.79 ± 3.87	0.36

Fisher's exact test and Mann–Whitney U comparison; unadjusted significance level set at $p < 0.05$ (two-sided).

TABLE 2 | Neuropsychological assessments comparison of FTLD-non-AD and FTLD-AD groups (mean ± standard deviation).

	FTLD-non-AD	FTLD-AD	Unadjusted *p*	Adjusted *p*
N	**17**	**7**		
Neuropsychological assessments				
Language				
Naming	11.47 ± 3.09	8.29 ± 4.99	0.10	N.S.
Pyramids and palm trees	40.44 ± 13.79[a]	39.60 ± 22.20[b]	0.41	N.S.
Sentence repetition	4.13 ± 1.46[b]	2.43 ± 1.90	0.031	N.S.
Semantic fluency	8.06 ± 6.13	7.57 ± 4.69	0.98	N.S.
Lexical fluency	5.76 ± 4.70	7.00 ± 4.90	0.48	N.S.
Executive function				
TMT B total seconds	217.14 ± 100.94[c]	267.14 ± 86.93	0.15	N.S.
Total digit symbol	21.71 ± 20.00[c]	17.43 ± 17.46	0.65	N.S.
Memory				
Learning score	13.12 ± 6.27	8.86 ± 7.86	0.27	N.S.
Delayed recall (10 min)	3.47 ± 2.70	2.14 ± 2.27	0.26	N.S.
Benson recall	7.43 ± 5.96[c]	3.00 ± 2.24	0.10	N.S.
Digit forward	5.47 ± 2.07	3.86 ± 1.77	0.06	N.S.
Digit backward	3.53 ± 2.32	2.43 ± 1.99	0.30	N.S.
Visuospatial function				
VOSP position discrimination	15.94 ± 5.76	15.67 ± 8.04[a]	0.49	N.S.
VOSP number location	4.88 ± 3.59	6.00 ± 3.58[a]	0.55	N.S.

Mann–Whitney U comparisons; unadjusted significance level set at $p < 0.05$ (two-sided). FDR Benjamini–Hochberg adjusted p-value; significant at $p < 0.05$.
N.S., not significant after multiple comparisons.
[a] One participant refused the assessment.
[b] Two participants refused the assessment.
[c] Three participants did not complete the assessment because could not move their hands.

RESULTS

Participant Demographics and Neuropsychological Assessments

Twenty-four participants were included in this study (age, 68.46 ± 7.23 years; disease duration, 5.63 ± 4.74 years; 11 males and 13 females). Among the cohort were 12 CBS cases with 6 CBS positive for AD biomarkers and 12 PSP cases with 1 PSP case positive for AD biomarkers. The between-group demographics on FTLD-non-AD and FTLD-AD groups are presented in **Table 1**. The FTLD-non-AD group was significantly older than FTLD-AD group ($p = 0.028$). There were no significant differences between groups on age of disease onset, years of education, sex, disease duration, or the PET scanner used (all $p > 0.19$). The FTLD-non-AD group had significantly higher scores on both the PSPRS ($p = 0.004$) and UPDRS motor scales ($p = 0.045$) compared to the FTLD-AD group. Finally, there was no significant difference between FTLD-non-AD and FTLD-AD groups on CDR global and CDR sum of boxes scores (all $p > 0.3$). The FTLD-non-AD and FTLD-AD groups did not differ on measures of language, executive function, memory, or visuospatial function (see **Table 2**). There was a trend in the FTLD-non-AD group to have higher scores in sentence repetition (unadjusted $p = 0.031$) and digit span forward (unadjusted $p = 0.06$) assessments compared to the FTLD-AD group; however, this did not survive multiple comparisons.

[18-F]AV1451 PET Tau and CSF Measures Comparison

The associations between cortical gray matter [18-F]AV1451 PET and CSF measures were completed across the entire cohort ($N = 19$). The Aβ42 measure was not successful for one participant. Significant relationships were found between cortical PET tau SUVR values and the following CSF measures corrected for age: t-tau (pg/ml; $N = 19$; unadjusted $r = 0.639$, $p < 0.005$), Aβ42 (pg/ml; $N = 18$; unadjusted $r = -0.557$, $p = 0.020$), and ATI ($N = 18$; unadjusted $r = -0.629$, $p < 0.01$). The comparisons between cortical gray matter PET tau SUVR and t-tau, Aβ42, and ATI remained significant after controlling for multiple comparisons using FDR significant at $p < 0.05$. For visual representations of these comparisons, see **Figure 2**. There was no significant relationship between cortical gray matter PET tau SUVR values and p-tau (pg/ml) values ($N = 19$; unadjusted $r = 0.388$, $p > 0.1$), corrected for age.

Neuroimaging Comparisons

Neuroimaging comparisons between FTLD-non-AD and FTLD-AD groups are summarized in **Table 3**. The FTLD-non-AD had significantly higher volumes compared to the FTLD-AD group in the following areas: inferior parietal ($p = 0.018$), precuneus ($p = 0.018$), and hippocampus ($p = 0.020$). The FTLD-non-AD group had significantly lower midbrain volume ($p = 0.020$), compared to the FTLD-AD group. The FTLD-non-AD and FTLD-AD groups did not significantly differ in the following volumes of interest: posterior cingulate, lateral orbitofrontal, caudal middle frontal, caudate, and thalamus. There were no

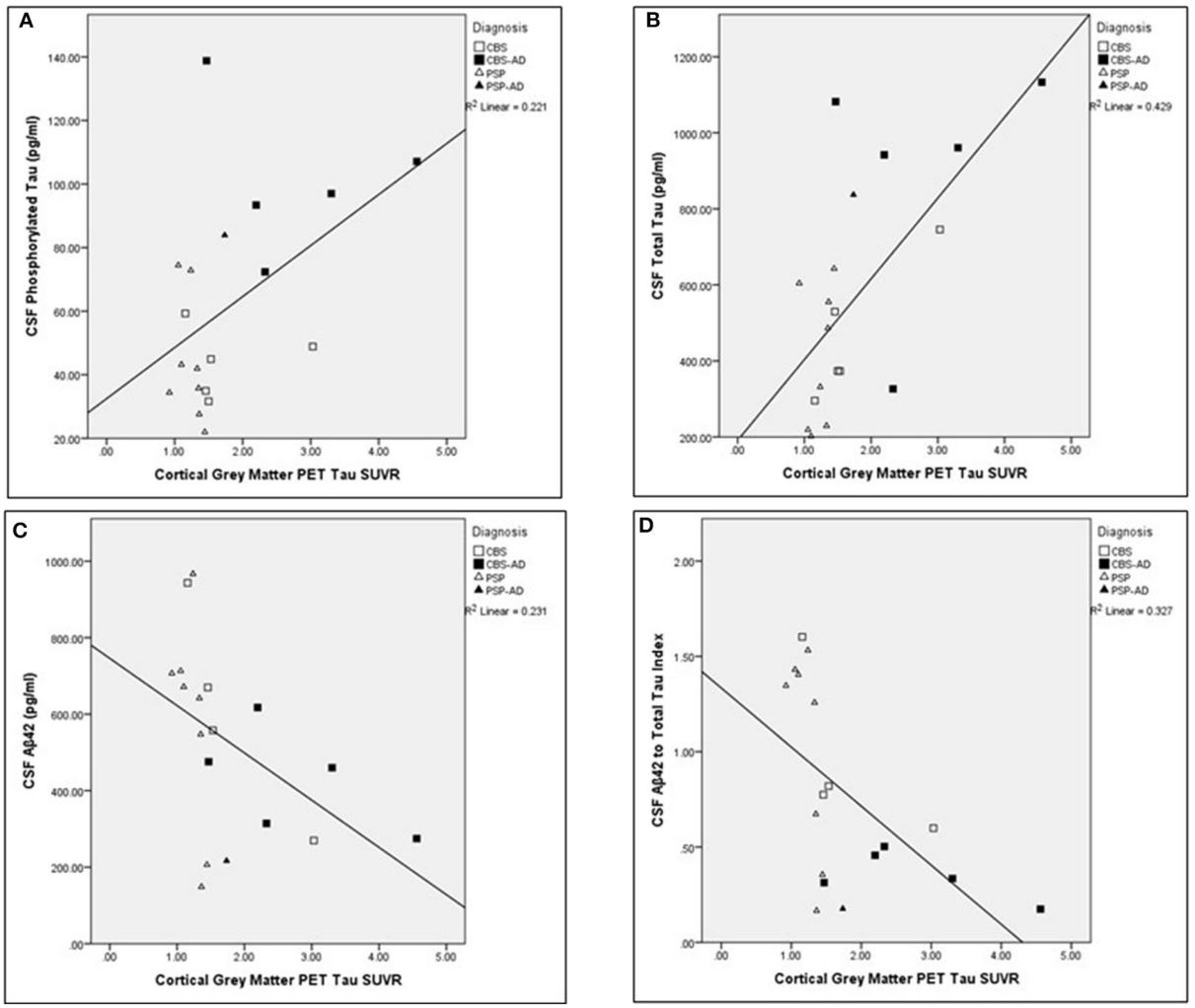


FIGURE 2 | Associations between cortical gray matter PET tau SUVR values and cerebrospinal fluid analysis measures across the whole cohort. Scatter plots presenting associations between cortical gray matter PET tau SUVR and the following cerebrospinal fluid (CSF) measures: **(A)** phosphorylated tau (pg/ml; adjusted $p > 0.1$), **(B)** total tau (pg/ml; adjusted $p < 0.05$), **(C)** Aβ42 (pg/ml; adjusted $p < 0.05$), and **(D)** Aβ42 to t-tau index (adjusted $p < 0.05$). Pearson partial correlations with age as a covariate. FDR Benjamini–Hochberg adjusted p-values, significant at $p < 0.05$.

significant differences between FTLD-non-AD and FTLD-AD groups in measures of white matter integrity in right and left SLF, and fornix. The FTLD-non-AD compared to the FTLD-AD group had significantly lower PET tau SUVR values in the following brain regions: lateral temporal ($p = 0.005$), dorsolateral prefrontal cortex ($p = 0.009$), ventrolateral prefrontal cortex ($p = 0.026$), orbitofrontal cortex ($p = 0.009$), hippocampus ($p = 0.006$), and inferior parietal ($p = 0.005$). There were no significant differences between FTLD-non-AD and FTLD-AD in measures of PET tau in the areas of dorsal caudate, thalamus, and midbrain.

Voxel-Based PET Analysis

Figure 3 shows visual comparison of brain regions with higher [18-F]AV1451 PET tau signal among the FTLD-AD, compared to the FTLD-non-AD group (unadjusted $p < 0.001$; extent threshold, $k = 50$). The increased uptake in the FTLD-AD group is extensive among posterior and middle temporal regions; however, these clusters did not all survive multiple comparisons. **Figure 4** shows the two clusters in the bilateral hippocampi that survived the multiple comparisons (FWE $p < 0.05$; corrected $T = 6.02$; extent threshold, $k = 50$). The bilateral hippocampi showed significantly increased uptake of [18-F]AV1451 PET tau in the FTLD-AD group in comparison to the FTLD-non-AD group.

Relationship Between [18-F]AV1451 PET Tau and Neuropsychological Assessments

The ROI analysis exploring the associations between [18-F]AV1451 PET tau and neuropsychological assessments was completed across the entire cohort ($N = 24$). Out of the language assessments, a significant relationship was found between naming and left lateral temporal PET tau SUVR values ($N = 24$; unadjusted $r = -0.469$, $p = 0.024$), controlled for

TABLE 3 | Summary of neuroimaging comparisons between FTLD-non-AD and FTLD-AD groups (mean ± standard deviation).

	FTLD-non-AD	FTLD-AD	Unadjusted *p*	Adjusted *p*
N	**17**	**7**		
Volumetric Analysis (Volume-to-ICV ratio × 10^{-3})				
Posterior cingulate	3.60 ± 0.48[a]	3.70 ± 0.60	0.42	N.S.
Inferior parietal	16.10 ± 1.80[a]	13.10 ± 1.81	0.004	***0.018***
Precuneus	12.00 ± 1.04[a]	9.70 ± 1.44	0.003	***0.018***
Lateral orbitofrontal	9.20 ± 1.46[a]	10.00 ± 0.83	0.23	N.S.
Caudal middle frontal	6.40 ± 1.47[a]	6.20 ± 0.56	0.84	N.S.
Hippocampus	5.20 ± 0.44[a]	4.60 ± 0.36	0.009	***0.020***
Caudate	4.58 ± 0.62[a]	4.45 ± 0.65	0.74	N.S.
Thalamus	7.68 ± 0.77[a]	7.81 ± 0.48	0.35	N.S.
Midbrain	3.50 ± 0.44[a]	4.00 ± 0.27	0.009	***0.020***
DTI (mm^2/s)				
Right SLF				
FA	0.35 ± 0.03[b]	0.34 ± 0.03	0.50	N.S.
MD ($\times 10^{-3}$)	0.88 ± 0.04[b]	0.90 ± 0.05	0.46	N.S.
AxD ($\times 10^{-3}$)	1.21 ± 0.04[b]	1.23 ± 0.04	0.17	N.S.
RD ($\times 10^{-3}$)	0.72 ± 0.05[b]	0.74 ± 0.06	0.39	N.S.
Left SLF				
FA	0.34 ± 0.03[b]	0.34 ± 0.02	0.71	N.S.
MD ($\times 10^{-3}$)	0.89 ± 0.07[b]	0.92 ± 0.04	0.13	N.S.
AxD ($\times 10^{-3}$)	1.22 ± 0.06[b]	1.25 ± 0.05	0.12	N.S.
RD ($\times 10^{-3}$)	0.73 ± 0.08[b]	0.75 ± 0.04	0.23	N.S.
Fornix				
FA	0.20 ± 0.03[b]	0.20 ± 0.02	0.71	N.S.
MD ($\times 10^{-3}$)	2.16 ± 0.22[b]	2.15 ± 0.22	0.82	N.S.
AxD ($\times 10^{-3}$)	2.60 ± 0.23[b]	2.58 ± 0.26	1.00	N.S.
RD ($\times 10^{-3}$)	1.94 ± 0.22[b]	1.93 ± 0.20	0.82	N.S.
PET (SUVR)				
Dorsal caudate	1.52 ± 0.38	1.90 ± 0.43	0.06	N.S.
Thalamus	1.43 ± 0.24	1.64 ± 0.37	0.17	N.S.
Midbrain	1.45 ± 0.30	1.42 ± 0.26	0.87	N.S.
Lateral temporal	1.33 ± 0.43	3.12 ± 1.35	0.001	***0.005***
Dorsolateral prefrontal cortex	1.62 ± 0.57	3.22 ± 1.76	0.005	***0.009***
Ventrolateral prefrontal cortex	1.53 ± 0.46	2.77 ± 1.45	0.017	***0.026***
Orbitofrontal cortex	1.52 ± 0.39	2.53 ± 1.23	0.004	***0.009***
Hippocampus	1.20 ± 0.28	1.80 ± 0.39	0.002	***0.006***
Inferior parietal	1.49 ± 0.56	3.26 ± 1.53	0.001	***0.005***

Mann–Whitney U comparisons; unadjusted significance level set at $p < 0.05$ (two-sided). FDR Benjamini–Hochberg adjusted p-values presented in bold italics; significant at $p < 0.05$.

N.S., not significant after multiple comparisons.

DTI, diffuse tensor imaging; SLF, superior longitudinal fasciculus; PET, positron emission tomography; SUVR, standard uptake volume ratio; FA, fractional anisotropy; MD, mean diffusivity; AxD, axial diffusivity; RD, radial diffusivity.

[a]*Data for one participant are missing because of FreeSurfer preprocessing failure.*

[b]*Data for three participants are missing because of movement during DTI acquisition.*

age. Three participants refused to undergo the Pyramids and Palm Trees assessment and significant relationships were found between the Pyramids and Palm Trees scores and the following areas of interest: left lateral temporal PET tau SUVR ($N = 21$; unadjusted $r = -0.599$, $p = 0.005$), controlled for age. Two participants refused the sentence repetition assessment, and there were trends between the sentence repetition scores and the following areas of interest: left lateral temporal PET tau SUVR ($N = 22$; unadjusted $r = -0.430$, $p = 0.052$), adjusted for age. The relationships between Pyramids and Palm Trees scores and left lateral temporal PET tau SUVR values remained significant after controlling for multiple comparisons using FDR significant at $p < 0.05$. There were no significant relationships between the executive function assessments and the dorsolateral prefrontal cortex PET tau SUVR, controlled for age. Out of the memory assessments, a significant relationship was found between the learning score and the left hippocampus PET tau SUVR ($N = 24$; unadjusted $r = -0.640$, $p = 0.001$), controlled for age. The delayed recall was significantly associated with the left hippocampus PET tau SUVR ($N = 24$; unadjusted $r = -0.520$, $p = 0.011$), controlled for age. Three participants could not complete the Benson figure visual recall, and there were significant relationships between the Benson recall scores and the right hippocampus PET tau SUVR ($N = 21$; unadjusted $r = -0.630$, $p = 0.003$), controlled for age. The digit forward scores had a significant association with prefrontal cortex PET tau SUVR ($N = 24$; unadjusted $r = -0.601$, $p = 0.002$), controlled for age. The digit backward scores had significant associations with the following areas of interest: prefrontal cortex PET tau SUVR ($N = 24$; unadjusted $r = -0.608$, $p = 0.002$) and hippocampus PET tau SUVR ($N = 24$; unadjusted $r = -0.623$, $p = 0.001$), controlled for age. All of the memory comparisons with PET tau SUVR remained significant after controlling for multiple comparisons using FDR significant at $p < 0.05$. Out of the visuospatial assessments, a significant relationship was found between the position discrimination and the inferior parietal PET tau SUVR ($N = 24$; unadjusted $r = -0.569$, $p = 0.006$), controlled for age. This relationship remained significant after controlling for multiple comparisons using FDR significant at $p < 0.05$. The relationships between the neuropsychological assessments and the PET tau burden could not be assessed separately in the FTLD-non-AD and FTLD-AD groups due to small sample size.

Relationship Between [18-F]AV1451 PET Tau and PSPRS/UPDRS Scores

The ROI analysis exploring the associations between [18-F]AV1451 PET tau in relation to PSPRS and UPDRS scores was completed across the whole cohort ($N = 24$). Neither the PSPRS nor the UPDRS scores were found to be significantly associated with any of the PET tau areas of interest, controlled for age.

Relationship Between PSPRS Scores and Volumes

For summary of associations between PSPRS scores in relation to lateral orbitofrontal, caudal middle frontal, caudate, thalamus, and midbrain volume, controlled for age, see **Table 4**. There were no significant relationships between PSPRS scores and volumes of lateral orbitofrontal, caudal

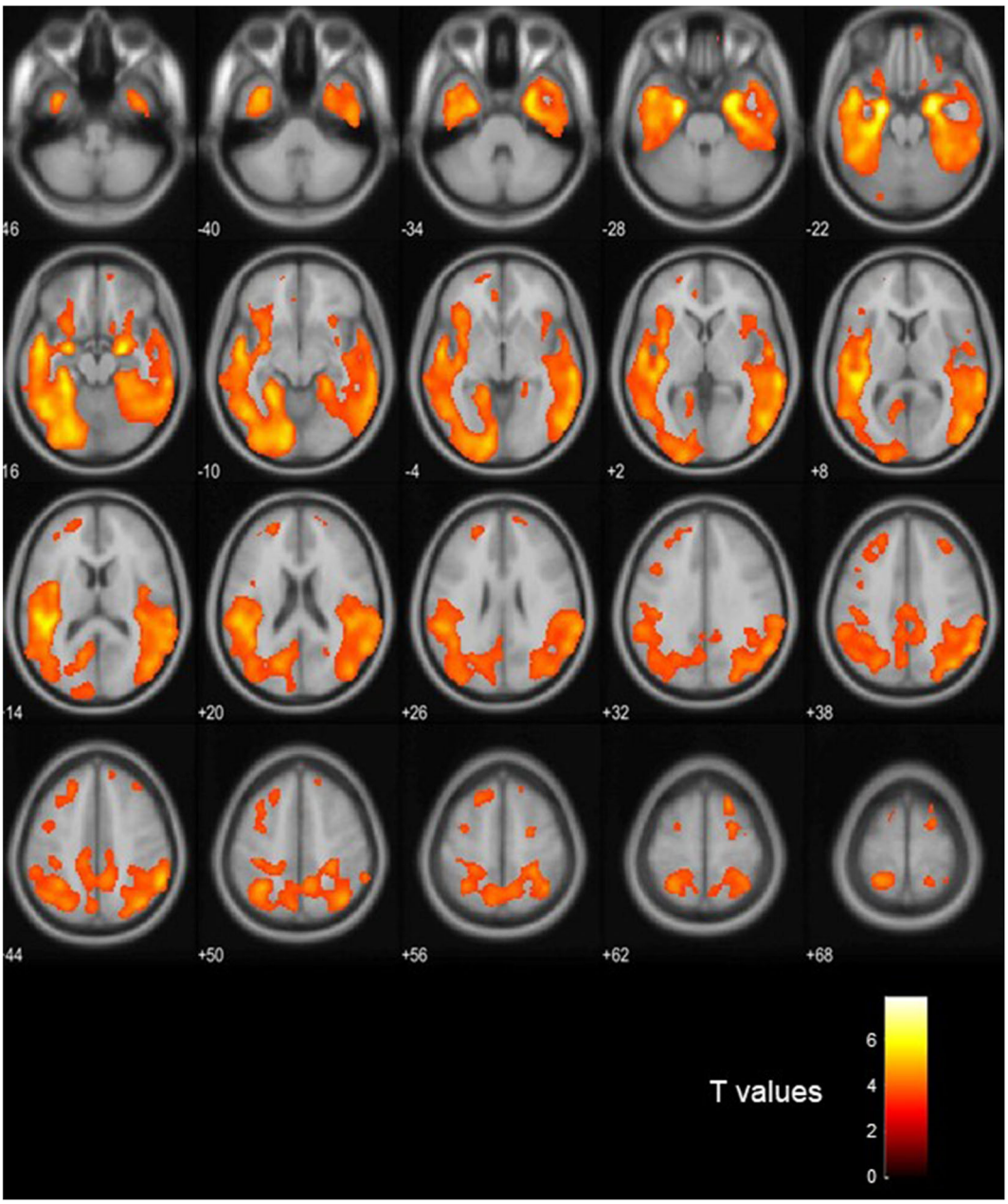


FIGURE 3 | Visualization of the voxel-based [18-F]AV1451 PET tau analysis. The colors signify the regions with increased [18-F]AV1451 signal in the FTLD-AD group, compared to the FTLD-non-AD group (uncorrected $p < 0.001$; extent threshold, $k = 50$).

middle frontal, caudate, thalamus, and midbrain in the FTLD-non-AD group, controlled for age. There was a trend in the FTLD-non-AD group between PSPRS scores and lateral orbitofrontal (unadjusted $r = -0.555$, $p = 0.032$), caudal middle frontal (unadjusted $r = -0.632$, $p = 0.011$), caudate (unadjusted $r = -0.526$, $p = 0.044$), and thalami (unadjusted $r = -0.505$, $p = 0.055$) volumes, adjusted for age, but the associations did not survive multiple comparisons. There were no significant relationships between PSPRS scores and lateral orbitofrontal, caudal middle frontal, caudate, thalamus, and midbrain volumes in the FTLD-AD group, controlled for age.

Relationship Between UPDRS Scores and Volumes

For summary of associations between UPDRS motor scale scores in relation to caudate, thalamus, and midbrain, controlled for age, see **Table 5**. There was a significant negative correlation in the FTLD-non-AD group between UPDRS motor scale scores

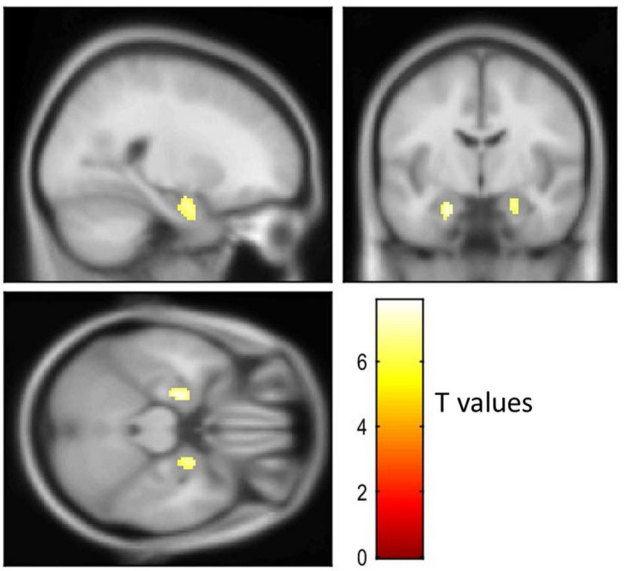


FIGURE 4 | Visualization of the voxel-based [18-F]AV1451 PET tau analysis. The cluster with increased [18-F]AV1451 signal in the FTLD-AD group, compared to the FTLD-non-AD group after controlling for multiple comparisons (FEW-corrected $p < 0.05$; extent threshold, $k = 50$).

TABLE 4 | Associations between PSPRS scores and volumes in FTLD-non-AD and FTLD-AD groups (mean ± standard deviation).

	FTLD-non-AD	FTLD-AD
N	**17**	**7**
Volumetric analysis (volume-to-ICV ratio)		
Lateral Orbitofrontal	$r = -0.555$, $p = 0.032$[a] *N.S.*	$r = 0.019$, $p = 0.98$ *N.S.*
Caudal Middle Frontal	$r = -0.632$, $p = 0.011$[a] *N.S.*	$r = 0.829$, $p = 0.041$ *N.S.*
Caudate	$r = -0.526$, $p = 0.044$[a] *N.S.*	$r = 0.380$, $p = 0.46$ *N.S.*
Thalamus	$r = -0.505$, $p = 0.055$[a] *N.S.*	$r = -0.505$, $p = 0.31$ *N.S.*
Midbrain	$r = -0.322$, $p = 0.24$[a] *N.S.*	$r = 0.175$, $p = 0.41$ *N.S.*

Pearson partial correlations with age as a covariate; unadjusted significance level set at $p < 0.05$.
FDR Benjamini–Hochberg adjusted p-values presented in italics; significant at $p < 0.05$.
N.S., not significant after multiple comparisons.
[a]*Data for one participant are missing because of FreeSurfer preprocessing failure.*

in relation to caudate ($r = -0.891$, $p < 0.003$), controlled for age. There were no significant associations in the FTLD-non-AD group between UPDRS motor scale scores and thalami and midbrain volumes, controlled for age. There were no significant association in the FTLD-AD group between UPDRS motor scale scores and any volumes of interest (i.e., caudate, thalamus, midbrain), controlled for age.

TABLE 5 | Associations between UPDRS motor scale scores and volumes in FTLD-non-AD and FTLD-AD groups (mean ± standard deviation).

	FTLD-non-AD	FTLD-AD
N	**17**	**7**
Volumetric analysis (volume-to-ICV ratio)		
Caudate	$r = -0.891$, $p < 0.001$[a] ***p < 0.003***	$r = 0.899$ $p = 0.015$ *N.S.*
Thalamus	$r = -0.340$, $p = 0.215$[a] *N.S.*	$r = -0.016$, $p = 0.98$ *N.S.*
Midbrain	$r = 0.014$, $p = 0.96$[a] *N.S.*	$r = 0.360$, $p = 0.48$ *N.S.*

Pearson partial correlations with age as a covariate; unadjusted significance level set at $p < 0.05$.
FDR Benjamini–Hochberg adjusted p-values presented in bold italics; significant at $p < 0.05$.
N.S., not significant after multiple comparisons.
[a]*Data for one participant is missing because of FreeSurfer preprocessing failure.*

Relationship Between Left SLF and Language

For a summary of associations between left SLF white matter integrity measures in relation to language assessments across the whole cohort, controlled for age, see **Table 6**. The following associations between left SLF white matter integrity measures and language assessments were completed across the entire cohort. There was a significant negative correlation between naming score and the following left SLF white matter integrity measures: MD ($r = -0.633$, $p = 0.008$), AxD ($r = -0.732$, $p < 0.007$), and RD ($r = -0.563$, $p = 0.022$), controlled for age. There was a significant negative correlation between Pyramids and Palm Trees score and the following left SLF white matter integrity measures: MD ($r = -0.792$, $p < 0.007$), AxD ($r = -0.910$, $p < 0.007$), and RD ($r = -0.707$, $p = 0.008$), controlled for age. There was a significant negative correlation between semantic fluency score and the following left SLF white matter integrity measures: MD ($r = -0.655$, $p = 0.008$), AxD ($r = -0.632$, $p = 0.008$), and RD ($r = -0.635$, $p = 0.008$); controlled for age. There was a significant negative correlation between lexical fluency score and the following left SLF white matter integrity measures: MD ($r = -0.507$, $p = 0.04$) and RD ($r = -0.512$, $p = 0.04$), controlled for age. There was no significant correlation between sentence repetition scores and left SLF white matter integrity measures, controlled for age. There were no significant correlations between left SLF FA measures and any of the language assessments, controlled for age. Finally, there was no significant correlation between left SLF AxD values and lexical fluency scores, controlled for age. For visual representation of associations between left SLF MD and language assessments (see **Figure 5**).

Relationship Between Right SLF and Visuospatial Assessments

There were no significant correlations between any white matter integrity measures (FA, MD, AxD, and RD) of right SLF and VOSP position discrimination and number location assessments

TABLE 6 | Associations between left SLF and language assessments across the whole cohort (mean ± standard deviation).

	Left SLF measures (mm^2/s); N = 24[a]			
	FA	**MD**	**AxD**	**RD**
Language assessments				
Naming	$r = 0.285$, $p = 0.22$ *N.S.*	$r = -0.633$, $p = 0.003$ ***p = 0.008***	$r = -0.732$, $p < 0.001$ ***p < 0.007***	$r = -0.563$, $p = 0.010$ ***p = 0.022***
Pyramids and Palm Trees[b]	$r = 0.409$, $p = 0.10$ *N.S.*	$r = -0.792$, $p < 0.001$ ***p < 0.007***	$r = -0.910$, $p < 0.001$ ***p < 0.007***	$r = -0.707$, $p = 0.002$ ***p = 0.008***
Sentence Repetition[c]	$r = -0.003$, $p = 0.99$ *N.S.*	$r = -0.279$, $p = 0.26$ *N.S.*	$r = -0.363$, $p = 0.14$ *N.S.*	$r = -0.229$, $p = 0.36$ *N.S.*
Semantic Fluency	$r = 0.434$, $p = 0.056$ *N.S.*	$r = -0.655$, $p = 0.002$ ***p = 0.008***	$r = -0.632$, $p = 0.003$ ***p = 0.008***	$r = -0.635$, $p = 0.003$ ***p = 0.008***
Lexical Fluency	$r = 0.390$, $p = 0.09$ *N.S.*	$r = -0.507$, $p = 0.022$ ***p = 0.04***	$r = -0.442$, $p = 0.051$ *N.S.*	$r = -0.512$, $p = 0.021$ ***p = 0.040***

Pearson partial correlations with age as a covariate; unadjusted significance level set at $p < 0.05$.
FDR Benjamini–Hochberg adjusted p-values presented in bold italics; significant at $p < 0.05$.
N.S., not significant after multiple comparisons.
SLF, superior longitudinal fasciculus; FA, fractional anisotropy; MD, mean diffusivity; AxD, axial diffusivity; RD, radial diffusivity.
[a] *Data for three participants are missing because of movement during DTI acquisition.*
[b] *Three participants refused the assessment.*
[c] *Two participants refused the assessment.*

(all unadjusted $p > 0.29$) across the entire cohort, controlled for age.

Relationship Between Fornix and Memory Assessments

There were no significant correlations between any white matter integrity measures (FA, MD, AxD, RD) of fornix and memory assessments (all unadjusted $p > 0.34$) across the entire cohort, controlled for age.

DISCUSSION

To our knowledge, this is the first study comparing parkinsonian syndromes (PSP and CBS) with and without AD biomarkers on measures of cognition, motor symptom burden, and neuroimaging findings of PET tau, white matter integrity, and volumes. Even though the FTLD-non-AD group was significantly older than the FTLD-AD group, there were no differences between groups on disease duration, severity of cognitive deficits as measured by CDR, and age of onset. The results about disease duration and age of onset might be inconclusive given high variability within each group and small sample size. Both groups had similar functioning on measures of language, executive function, memory, and visuospatial function. There were trends in FTLD-non-AD group for better functioning on the sentence repetition and digit forward assessments compared to the FTLD-AD group; however, these differences did not survive multiple comparisons. The results of this study showed significantly worse motor and parkinsonian symptom burden in the FTLD-non-AD group, compared to FTLD-AD. The higher motor disturbances and parkinsonian symptom burden were associated with smaller volumes in the basal ganglia and midbrain specifically across the FTLD-non-AD group; no such relationships were observed in the FTLD-AD group. The FTLD-AD group, in turn, had higher PET tau SUVR values on the ROI analysis across multiple frontal and temporal regions, and inferior parietal, compared to the FTLD-non-AD group. The FTLD-AD group had smaller volumes in AD-specific areas compared to the FTLD-non-AD group: inferior parietal, precuneus, and hippocampus. In turn, the FTLD-non-AD group had smaller midbrain volume compared to the FTLD-AD group. These results show that the presence of underlying AD pathology was associated with differences in phenotype of CBS and PSP syndromes with the AD biomarker positive group having less motor deficits and a trend that repetition is better in the non-AD group. Presumably, AD pathology as evidenced by AD biomarkers has a predilection for specific areas such as the inferior parietal, precuneus, and hippocampus while four repeat tau pathology has a predilection for the midbrain. Relative volumetric differences may be a potential biomarker to discriminate FTLD-non-AD from FTLD-AD. PET tau signal was increased globally across the brain regions in the FTLD-AD group, which was not specific to AD-related areas only.

The [18-F]AV1451 PET was significantly associated with measures of language, memory, and visuospatial function across the entire study cohort. The association between cognitive measures and [18-F]AV1451 PET tau is widely established in AD studies (43–45); however, the relationship between cognition and [18-F]AV1451 PET tau among the PSP and CBS cases is usually described as poor (45, 46). In this study, although the AD biomarker positive group was small, there was a significant relationship across the whole group between PET Tau SUVR in neuroanatomically relevant areas and cognitive function. This suggests that the ligand is detecting some abnormality even if it is not specific to the straight filaments seen in 4-repeat tau of PSP and CBD.

The voxel-based analysis of [18-F]AV1451 PET tau showed extensive areas of posterior and middle temporal signal increase

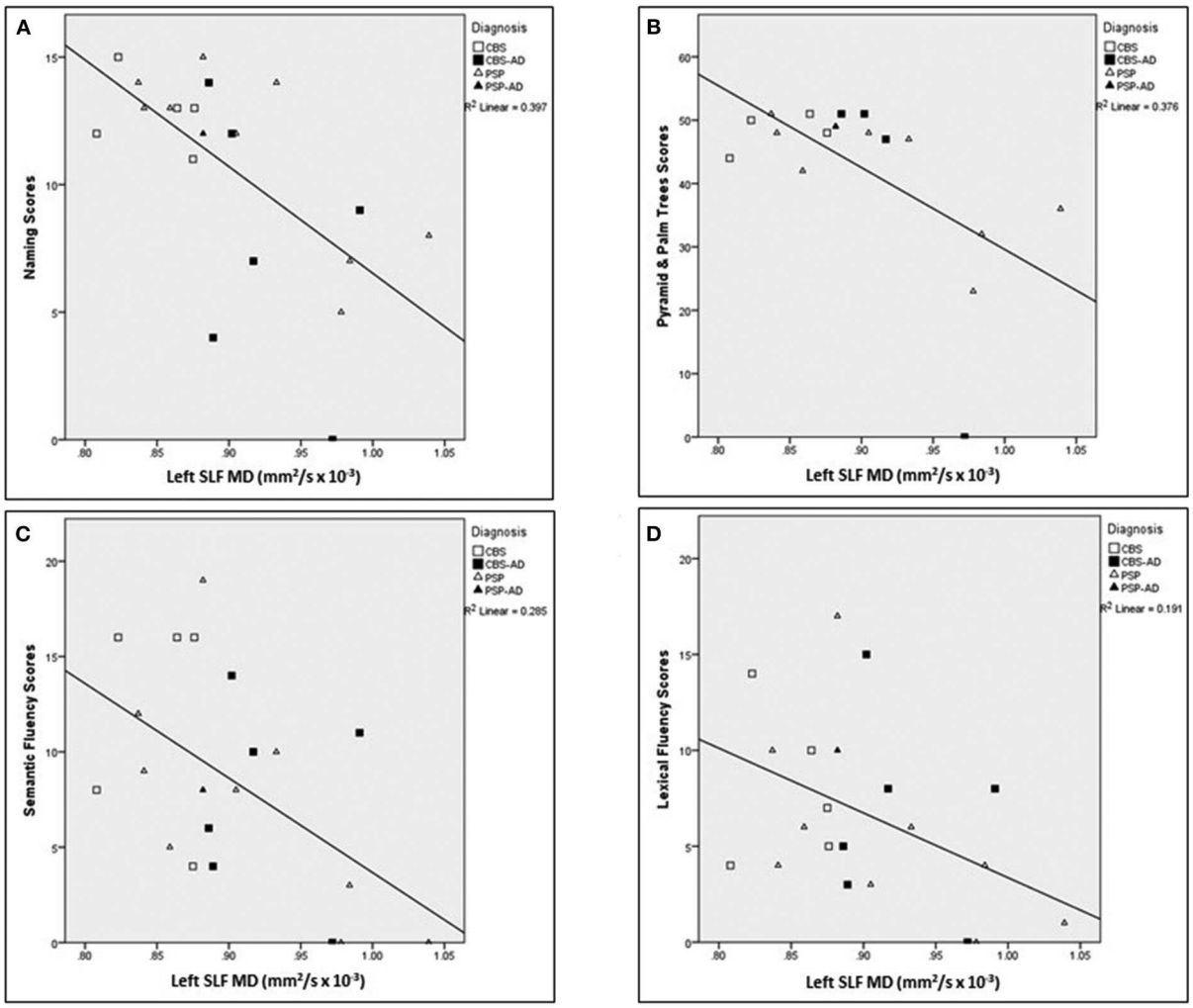


FIGURE 5 | Associations between left SLF MD and language assessments across the whole cohort. Scatter plots presenting associations between left SLF MD ($mm^2/s \times 10^{-3}$) and the following language assessments: **(A)** naming scores, **(B)** Pyramids and Palm Trees scores, **(C)** semantic fluency scores, and **(D)** lexical fluency scores. SLF, Superior longitudinal fasciculus; MD, Mean diffusivity.

in the FTLD-AD group, in comparison with FTLD-non-AD group and this pattern of uptake is consistent with previously published literature on distribution of [18-F]AV1451 ligand in AD (47). Aside from the cluster involving bilateral hippocampi, the rest of the clusters did not survive multiple comparisons. The reason could be that our study is underpowered due to the small sample size. Because of the small sample size, the comparisons between [18-F]AV1451 PET tau and CSF measures were completed across the entire cohort. Cortical gray matter was chosen as a global measure of PET tau signal, and it was significantly associated with CSF measures of t-tau, Aβ42, and ATI; however, there was no significant relationship with p-tau. Our results confirm previous reports stating a good correlation between CSF t-tau and [18-F]AV1451 PET (48, 49), but we found less robust relationship between p-tau and [18-F]AV1451 compared to others. Even though there is high concordance between CSF and [18-F]AV1451 measures, CSF p-tau abnormality seems to precede [18-F]AV1451 PET tau positivity and marks the early stages of underlying AD pathology (49). However, at the later stages of disease where cognitive decline has become apparent, [18-F]AV1451 PET tau has proven to be a significantly better diagnostic tool of AD than CSF measures, hippocampal atrophy, or temporal cortices thickness (50).

The literature on biomarkers to detect the differences between FTLD-non-AD and FTLD-AD is quite limited and mostly comes from pure cohorts of either CBS or PSP cases (not heterogeneous cohorts as implemented in this study) or from single case studies. PET with [18-F]AV1451 tracer has been established as a biomarker of tau accumulation in the form of AD's paired helical filament and showed good correlation with Braak stages of AD and post-mortem assessments (51). The PET [18-F]AV1451 tracer has not been reported suitable to detect the straight filament tau of CBD and PSP, and showed poor correlation to post-mortem studies in these cohorts (52–54). From previous reports, increased PET tau tracer retention in

CBS cases without underlying AD pathology was noted in the motor cortex, corticospinal tract, and basal ganglia contralateral to the affected body side, while the tracer retention pattern in AD is concentrated mostly in temporal and parietal cortices (55). Studies using the same PET tau tracer in PSP cases reported increased retention in basal ganglia, but not cortical regions (52). Our study shows similar findings of increased tracer uptake in dorsal caudate, thalamus, and brainstem (the regions affected by pathology in parkinsonian syndromes), and these findings were similar in both FTLD-non-AD and FTLD-AD groups and did not differentiate one group from another. The increased PET tau SUVR values in the FTLD-AD group were seen across multiple frontal and temporal regions, as well as inferior parietal, and the signal was not restricted to AD-specific regions. This goes in hand with previous literature stating that PET [18-F]AV1451 tracer is better suited for detecting tau in AD. The [18-F]AV1451 PET tau tracer is a biomarker that can discriminate parkinsonian syndromes with and without underlying AD pathology, but does not tell us about the extent of AD pathology in the FTLD-AD group.

The decreased focal volumes in the FTLD-AD group of our study support previous findings in cohorts with clinical presentation of CBS with evidence of AD pathology having a higher degree of volume loss in the temporoparietal regions, compared to CBS due to non-AD pathologies (5). Even though our FTLD-non-AD cohort has PSP cases in addition to CBS, cortical and sub-cortical volume loss was not reported to be different across parkinsonian syndromes (56), and therefore it is unlikely that our results were affected by the heterogeneity of our cohort. Midbrain atrophy was previously reported to be a hallmark of clinical PSP, but not the pathological diagnosis of PSP without the clinical PSP presentation (57). Also, clinically diagnosed CBS and PSP cohorts had similar levels of midbrain atrophy upon comparison (58). Our study also included clinically diagnosed CBS and PSP cases, and the FTLD-non-AD group had a higher degree of midbrain atrophy compared to the FTLD-AD group. These results imply that AD and 4-repeat pathology have a predilection for different areas.

One study comparing CBS-non-AD and CBS-AD across neuropsychological tests concluded similar levels of memory impairment and attention deficits in both groups (59). When comparing CBS-AD cases to AD patients with typical amnestic syndrome (AD-AS), it was reported that language problems were more frequent in the CBS-AD group, while memory impairment was the hallmark of the AD-AS group. As expected and in contrast to AD-AS, CBS-AD had prominent motor deficits (60). Since language impairments are an early and persistent problem in CBS and PSP (61), our results support previous literature as in our study too, the FTLD-non-AD and the FTLD-AD groups had similar language and cognitive functioning; however, motor impairments were worse in the FTLD-non-AD group. Due to similar levels of language impairment across FTLD-non-AD and FTLD-AD groups, the two groups were combined, and as expected, decreased white matter integrity in the left SLF tract (implicated in language) corresponded to a higher degree of impairment on language assessments (**Figure 2**). This suggests similar degrees of underlying pathological changes in white matter integrity across both groups, and these white matter changes are at least partially contributing to the widespread language impairments in CBS and PSP.

There are a number of limitations in the current study, including the small cohort size, which decreases the power of our analyses. The participants' head movement can always introduce artifacts into the PET data affecting the results, despite completing the PET frame realignment in order to correct for motion. Participants with CBS and PSP diagnoses are not equally represented in both groups, which could have affected the results. Due to the absence of post-mortem assessment results, there is no way of knowing the dominant or exclusive underlying pathological diagnoses, and the diagnoses were made based on the clinical presentation and progression of the symptoms. Patients lacking markers for AD probably had predominant 4R tau pathology, although CBS patients could have had other non-tau non-AD pathology. Patients with AD markers may have had only AD pathology or a combination of AD plus other pathologies, especially 4R tauopathy. In addition, the absence of a reliable control group did not allow us to draw any conclusions about the degree of pathological changes that either one of our study groups had in comparison to healthy aging. Finally, we could not assess the relationship between the neuropsychological measures, CSF markers, and [18-F]AV1451 PET tau in FTLD-non-AD and FTLD-AD groups separately due to small sample size.

Overall, our results showed that PET with [18-F]AV1451 tau-specific tracer can discriminate FTLD-non-AD and FTLD-AD cohort by its high specificity to paired-helical filaments seen in AD, and is associated with a higher global PET signal in the FTLD-AD group. Volumetric analysis seems to provide evidence of pathological vulnerability. There is decreased volume in areas implicated in classic AD in the CBS-AD and PSP-AD groups (hippocampus and precuneus), which implies that there are AD pathology vulnerable areas, as this group was younger than the non-AD group so less atrophy might have been expected. The presence of underlying AD pathology in parkinsonian syndromes is associated with a different phenotype of the presenting illness, with increased motor disturbances in the FTLD-non-AD group, while the level of cognitive functioning is the same irrespective of the presence of AD pathology.

DATA AVAILABILITY STATEMENT

The datasets generated for this study are available on request to the corresponding author.

ETHICS STATEMENT

The studies involving human participants were reviewed and approved by University Health Network and Center for Addiction and Mental Health. The patients/participants provided their written informed consent to participate in this study.

AUTHOR CONTRIBUTIONS

AV acquired the data, analyzed the data, interpreted the data, and drafted the manuscript for intellectual content.

FT analyzed and interpreted the data. NM, CA, and KM had major roles in data acquisition. SH interpreted the data and revised the manuscript for intellectual content. CB analyzed and interpreted the data. DT-W, AL, SF, and ES had major roles in data acquisition. PR interpreted the data and revised the manuscript for intellectual content. MT had a major role in acquisition of data, interpreted the data, and drafted and revised the manuscript for intellectual content. All authors contributed to the article and approved the submitted version.

FUNDING

This work was supported by CIHR.

ACKNOWLEDGMENTS

We would like to thank all participants for generous donation of their time to participate in this research program. We thank E. Hlasny, K. Ta, B. Li, and Dr. A. Crawley for their support in image acquisition, and Peter M. Bloomfield for physics support.

REFERENCES

1. Cairns NJ, Bigio EH, Mackenzie IR, Neumann M, Lee VMY, Hatanpaa KJ, et al. Neuropathologic diagnostic and nosologic criteria for frontotemporal lobar degeneration: consensus of the consortium for frontotemporal lobar degeneration. *Acta Neuropathol*. (2007) 114:5–22. doi: 10.1007/s00401-007-0237-2
2. Boeve BF. Links between frontotemporal lobar degeneration, corticobasal degeneration, progressive supranuclear palsy, and amyotrophic lateral sclerosis. *Alzheimer Dis Assoc Disord*. (2007) 21:S31–8. doi: 10.1097/WAD.0b013e31815bf454
3. Burrell JR, Hodges JR, Rowe JB. Cognition in corticobasal syndrome and progressive supranuclear palsy: a review. *Mov Disord*. (2014) 29:684–93. doi: 10.1002/mds.25872
4. Boeve BF, Lang AE, Litvan I. Corticobasal degeneration and its relationship to progressive supranuclear palsy and frontotemporal dementia. *Ann Neurol*. (2003) 54:S15–9. doi: 10.1002/ana.10570
5. Whitwell JL, Jack C, Boeve BF, Parisi JE, Ahlskog J, Drubach D, et al. Imaging correlates of pathology in corticobasal syndrome. *Neurology*. (2010) 75:1879–87. doi: 10.1212/WNL.0b013e3181feb2e8
6. Lewis-Smith DJ, Wolpe N, Ghosh BC, Rowe JB. Alien limb in the corticobasal syndrome: phenomenological characteristics and relationship to apraxia. *J. Neurol*. (2020) 267:1147–57. doi: 10.1007/s00415-019-09672-8
7. Yokota O, Tsuchiya K, Terada S, Ishizu H, Uchikado H, Ikeda M, et al. Basophilic inclusion body disease and neuronal intermediate filament inclusion disease: a comparative clinicopathological study. *Acta Neuropathol*. (2008) 115:561–75. doi: 10.1007/s00401-007-0329-z
8. Tartaglia MC, Sidhu M, Laluz V, Racine C, Rabinovici GD, Creighton K, et al. Sporadic corticobasal syndrome due to FTLD-TDP. *Acta Neuropathol*. (2010) 119:365–74. doi: 10.1007/s00401-009-0605-1
9. Lee SE, Rabinovici GD, Mayo MC, Wilson SM, Seeley WW, DeArmond SJ, et al. Clinicopathological correlations in corticobasal degeneration. *Ann Neurol*. (2011) 70:327–40. doi: 10.1002/ana.22424
10. Koga S, Roemer SF, Kasanuki K, Dickson DW. Cerebrovascular pathology presenting as corticobasal syndrome: an autopsy case series of "vascular CBS". *Parkinsonism Relat. Disord*. (2019) 68:79–84. doi: 10.1016/j.parkreldis.2019.09.001
11. Saranza GM, Whitwell JL, Kovacs GG, Lang AE. Corticobasal degeneration. *Int Rev Neurobiol*. (2019) 149:87–136. doi: 10.1016/bs.irn.2019.10.014
12. Litvan I, Agid Y, Calne D, Campbell G, Dubois B, Duvoisin R, et al. Clinical research criteria for the diagnosis of progressive supranuclear palsy (steele-Richardson-Olszewski syndrome): report of the NINDS-SPSP international workshop. *Neurology*. (1996) 47:1–9. doi: 10.1212/WNL.47.1.1
13. Respondek G, Höglinger G. The phenotypic spectrum of progressive supranuclear palsy. *Parkinsonism Relat Disord*. (2016) 22:S34–6. doi: 10.1016/j.parkreldis.2015.09.041
14. Höglinger GU, Respondek G, Stamelou M, Kurz C, Josephs KA, Lang AE, et al. Clinical diagnosis of progressive supranuclear palsy: the movement disorder society criteria. *Mov Disord*. (2017) 32:853–64. doi: 10.1002/mds.26987
15. McKhann GM, Knopman DS, Chertkow H, Hyman BT, Jack CR Jr, Kawas CH, et al. The diagnosis of dementia due to Alzheimer's disease: recommendations from the national institute on aging-alzheimer's association workgroups on diagnostic guidelines for Alzheimer's disease. *Alzheimer's Dement*. (2011) 7:263–9. doi: 10.1016/j.jalz.2011.03.005
16. Robinson JL, Lee EB, Xie SX, Rennert L, Suh E, Bredenberg C, et al. Neurodegenerative disease concomitant proteinopathies are prevalent, age-related and APOE4-associated. *Brain*. (2018) 141:2181–93. doi: 10.1093/brain/awy146
17. Leon JD, Mandelli ML, Nolan A, Miller ZA, Mead C, Watson C, et al. Atypical clinical features associated with mixed pathology in a case of non-fluent variant primary progressive aphasia. *Neurocase*. (2019) 25:39–47. doi: 10.1080/13554794.2019.1609522
18. Litvan I, Grimes D, Lang A, Jankovic J, McKee A, Verny M, et al. Clinical features differentiating patients with postmortem confirmed progressive supranuclear palsy and corticobasal degeneration. *J Neurol*. (1999) 246:II1–5. doi: 10.1007/BF03161075
19. Bensimon G, Ludolph A, Agid Y, Vidailhet M, Payan C, Leigh PN, et al. Riluzole treatment, survival and diagnostic criteria in Parkinson plus disorders: the NNIPPS study. *Brain*. (2009) 132:156–71. doi: 10.1093/brain/awn291
20. Armstrong MJ, Litvan I, Lang AE, Bak TH, Bhatia KP, Borroni B, et al. Criteria for the diagnosis of corticobasal degeneration. *Neurology*. (2013) 80:496–503. doi: 10.1212/WNL.0b013e31827f0fd1
21. Golbe LI, Ohman-Strickland PA. A clinical rating scale for progressive supranuclear palsy. *Brain*. (2007) 130:1552–65. doi: 10.1093/brain/awm032
22. Martínez Martín P, Gil-Nagel A, Gracia LM, Gómez JB, Martinez-Sarries J, Bermejo F, et al. Unified Parkinson's disease rating scale characteristics and structure. *Mov Disord*. (1994) 9:76–83. doi: 10.1002/mds.870090112
23. O'Bryant SE, Waring SC, Cullum CM, Hall J, Lacritz L, Massman PJ, et al. Staging dementia using clinical dementia rating scale sum of boxes scores: a texas Alzheimer's research consortium study. *Arch Neurol*. (2008) 65:1091–5. doi: 10.1001/archneur.65.8.1091
24. Gollan TH, Weissberger GH, Runnqvist E, Montoya RI, Cera CM. Self-ratings of spoken language dominance: a multilingual naming test (MINT) and preliminary norms for young and aging Spanish–English bilinguals. *Biling*. (2012) 15:594–615. doi: 10.1017/S1366728911000332
25. Howard D, Patterson K. *The Pyramids and Palm Trees Test: A Test of Semantic Access From Words and Pictures*. Cambridge: Thames Valley Test Co. (1992).
26. Weintraub S, Besser L, Dodge HH, Teylan M, Ferris S, Goldstein FC, et al. Version 3 of the alzheimer Disease centers' neuropsychological test battery in the uniform data set (UDS). *Alzheimer Dis Assoc Disord*. (2018) 32:10–7. doi: 10.1097/WAD.0000000000000223
27. Kortte KB, Horner MD, Windham WK. The trail making test, part B: cognitive flexibility or ability to maintain set? *Appl Neuropsychol*. (2002) 9:106–9. doi: 10.1207/S15324826AN0902_5
28. Strauss E, Sherman EM, Spreen O. *A Compendium of Neuropsychological Tests: Administration, Norms, and Commentary*. Oxford, UK: Oxford University Press. (2006).
29. Wechsler D. *WAIS-III: Administration and scoring manual: Wechsler adult intelligence scale: Psychological corporation*. San Antonio, TX (1997).
30. Quental NBM, Brucki SMD, Bueno OFA. Visuospatial function in early Alzheimer's disease—the use of the visual object and space perception (VOSP) battery. *PLoS ONE*. (2013) 8:e68398. doi: 10.1371/journal.pone.0068398

31. Jack CR Jr, Bernstein MA, Fox NC, Thompson P, Alexander G, Harvey D, et al. The Alzheimer's disease neuroimaging initiative (ADNI): MRI methods. *J Magn Reson Imaging*. (2008) 27:685–91. doi: 10.1002/jmri.21049
32. Hulstaert F, Blennow K, Ivanoiu A, Schoonderwaldt H, Riemenschneider M, De Deyn P, et al. Improved discrimination of AD patients using β-amyloid (1-42) and tau levels in CSF. *Neurology*. (1999) 52:1555. doi: 10.1212/WNL.52.8.1555
33. Maddalena A, Papassotiropoulos A, Müller-Tillmanns B, Jung HH, Hegi T, Nitsch RM, et al. Biochemical diagnosis of Alzheimer disease by measuring the cerebrospinal fluid ratio of phosphorylated tau protein to β-amyloid peptide42. *Arch Neurol*. (2003) 60:1202–6. doi: 10.1001/archneur.60.9.1202
34. Blennow K. Cerebrospinal fluid protein biomarkers for Alzheimer's disease. *NeuroRx*. (2004) 1:213–25. doi: 10.1602/neurorx.1.2.213
35. Blennow K, Dubois B, Fagan AM, Lewczuk P, de Leon MJ, Hampel H. Clinical utility of cerebrospinal fluid biomarkers in the diagnosis of early Alzheimer's disease. *Alzheimer's Dement*. (2015) 11:58–69. doi: 10.1016/j.jalz.2014.02.004
36. Fischl B, Salat DH, Busa E, Albert M, Dieterich M, Haselgrove C, et al. Whole brain segmentation: automated labeling of neuroanatomical structures in the human brain. *Neuron*. (2002) 33:341–55. doi: 10.1016/S0896-6273(02)00569-X
37. Iglesias JE, Van Leemput K, Bhatt P, Casillas C, Dutt S, Schuff N, et al. Bayesian segmentation of brainstem structures in MRI. *Neuroimage*. (2015) 113:184–95. doi: 10.1016/j.neuroimage.2015.02.065
38. Buckner RL, Head D, Parker J, Fotenos AF, Marcus D, Morris JC, et al. A unified approach for morphometric and functional data analysis in young, old, and demented adults using automated atlas-based head size normalization: reliability and validation against manual measurement of total intracranial volume. *Neuroimage*. (2004) 23:724–38. doi: 10.1016/j.neuroimage.2004.06.018
39. Galantucci S, Tartaglia MC, Wilson SM, Henry ML, Filippi M, Agosta F, et al. White matter damage in primary progressive aphasias: a diffusion tensor tractography study. *Brain*. (2011) 134:3011–29. doi: 10.1093/brain/awr099
40. Taghdiri F, Chung J, Irwin S, Multani N, Tarazi A, Ebraheem A, et al. Decreased number of self-paced saccades in post-concussion syndrome associated with higher symptom burden and reduced white matter integrity. *J Neurotrauma*. (2018) 35:719–29. doi: 10.1089/neu.2017.5274
41. Rusjan P, Mamo D, Ginovart N, Hussey D, Vitcu I, Yasuno F, et al. An automated method for the extraction of regional data from PET images. *Psychiatry Res*. (2006) 147:79–89. doi: 10.1016/j.pscychresns.2006.01.011
42. Müller-Gärtner HW, Links JM, Prince JL, Bryan RN, McVeigh E, Leal JP, et al. Measurement of radiotracer concentration in brain gray matter using positron emission tomography: MRI-based correction for partial volume effects. *J Cereb Blood Flow Metab*. (1992) 12:571–83. doi: 10.1038/jcbfm.1992.81
43. Brier MR, Gordon B, Friedrichsen K, McCarthy J, Stern A, Christensen J, et al. Tau and Aβ imaging, CSF measures, and cognition in Alzheimer's disease. *Sci Transl Med*. (2016) 8:338ra66. doi: 10.1126/scitranslmed.aaf2362
44. Aschenbrenner AJ, Gordon BA, Benzinger TLS, Morris JC, Hassenstab JJ. Influence of tau PET, amyloid PET, and hippocampal volume on cognition in Alzheimer disease. *Neurology*. (2018) 91:e859–66. doi: 10.1212/WNL.0000000000006075
45. Leuzy A, Chiotis K, Lemoine L, Gillberg P-G, Almkvist O, Rodriguez-Vieitez E, et al. Tau PET imaging in neurodegenerative tauopathies—still a challenge. *Mol Psychiatry*. (2019) 24:1112–34. doi: 10.1038/s41380-018-0342-8
46. Hall B, Mak E, Cervenka S, Aigbirhio FI, Rowe JB, O'Brien JT. *In vivo* tau PET imaging in dementia: pathophysiology, radiotracer quantification, and a systematic review of clinical findings. *Ageing Res Rev*. (2017) 36:50–63. doi: 10.1016/j.arr.2017.03.002
47. Xia C, Makaretz SJ, Caso C, McGinnis S, Gomperts SN, Sepulcre J, et al. Association of *in vivo* [18F]AV-1451 tau PET imaging results with cortical atrophy and symptoms in typical and atypical Alzheimer disease. *JAMA Neurol*. (2017) 74:427–36. doi: 10.1001/jamaneurol.2016.5755
48. La Joie R, Bejanin A, Fagan AM, Ayakta N, Baker SL, Bourakova V, et al. Associations between [18F] AV1451 tau PET and CSF measures of tau pathology in a clinical sample. *Neurology*. (2018) 90:e282–90. doi: 10.1212/WNL.0000000000004860
49. Meyer P-F, Binette AP, Gonneaud J, Breitner JCS, Villeneuve S. Characterization of Alzheimer disease biomarker discrepancies using cerebrospinal fluid phosphorylated tau and AV1451 positron emission tomography. *JAMA Neurol*. (2020) 77:508–16. doi: 10.1001/jamaneurol.2019.4749
50. Mattsson N, Smith R, Strandberg O, Palmqvist S, Schöll M, Insel PS, et al. Comparing 18F-AV-1451 with CSF t-tau and p-tau for diagnosis of Alzheimer disease. *Neurology*. (2018) 90:e388–95. doi: 10.1212/WNL.0000000000004887
51. Marquié M, Normandin MD, Vanderburg CR, Costantino IM, Bien EA, Rycyna LG, et al. Validating novel tau positron emission tomography tracer [F-18]-AV-1451 (T807) on postmortem brain tissue. *Ann Neurol*. (2015) 78:787–800. doi: 10.1002/ana.24517
52. Smith R, Schöll M, Honer M, Nilsson CF, Englund E, Hansson O. Tau neuropathology correlates with FDG-PET, but not AV-1451-PET, in progressive supranuclear palsy. *Acta Neuropathol*. (2017) 133:149–51. doi: 10.1007/s00401-016-1650-1
53. Coakeley S, Cho SS, Koshimori Y, Rusjan P, Ghadery C, Kim J, et al. [18F]AV-1451 binding to neuromelanin in the substantia nigra in PD and PSP. *Brain Struct Funct*. (2018) 223:589–95. doi: 10.1007/s00429-017-1507-y
54. Svenningsson P. Corticobasal degeneration: advances in clinicopathology and biomarkers. *Curr Opin Neurol*. (2019) 32:597–603. doi: 10.1097/WCO.0000000000000707
55. Smith R, Schöll M, Widner H, van Westen D, Svenningsson P, Hägerström D, et al. In vivo retention of ^{18} F-AV-1451 in corticobasal syndrome. *Neurology*. (2017) 89:845–53. doi: 10.1212/WNL.0000000000004264
56. Upadhyay N, Suppa A, Piattella MC, Bologna M, Di Stasio F, Formica A, et al. MRI gray and white matter measures in progressive supranuclear palsy and corticobasal syndrome. *J Neurol*. (2016) 263:2022–31. doi: 10.1007/s00415-016-8224-y
57. Whitwell JL, Jack CR, Parisi JE, Gunter JL, Weigand SD, Boeve BF, et al. Midbrain atrophy is not a biomarker of progressive supranuclear palsy pathology. *Eur J Neurol*. (2013) 20:1417–22. doi: 10.1111/ene.12212
58. Dutt S, Binney RJ, Heuer HW, Luong P, Attygalle S, Bhatt P, et al. Progression of brain atrophy in PSP and CBS over 6 months and 1 year. *Neurology*. (2016) 87:2016–25. doi: 10.1212/WNL.0000000000003305
59. Hu WT, Rippon GW, Boeve BF, Knopman DS, Petersen RC, Parisi JE, et al. Alzheimer's disease and corticobasal degeneration presenting as corticobasal syndrome. *Mov Disord*. (2009) 24:1375–9. doi: 10.1002/mds.22574
60. Sakae N, Josephs KA, Litvan I, Murray ME, Duara R, Uitti RJ, et al. Clinicopathologic subtype of Alzheimer's disease presenting as corticobasal syndrome. *Alzheimer's Dement*. (2019) 15:1218–28. doi: 10.1016/j.jalz.2019.04.011
61. Peterson K, Patterson K, Rowe J. Language impairment in progressive supranuclear palsy and corticobasal syndrome. *J Neurol*. (2019) 1–14. doi: 10.1007/s00415-019-09463-1

Conflict of Interest: The authors declare that the research was conducted in the absence of any commercial or financial relationships that could be construed as a potential conflict of interest.

Copyright © 2020 Vasilevskaya, Taghdiri, Multani, Anor, Misquitta, Houle, Burke, Tang-Wai, Lang, Fox, Slow, Rusjan and Tartaglia. This is an open-access article distributed under the terms of the Creative Commons Attribution License (CC BY). The use, distribution or reproduction in other forums is permitted, provided the original author(s) and the copyright owner(s) are credited and that the original publication in this journal is cited, in accordance with accepted academic practice. No use, distribution or reproduction is permitted which does not comply with these terms.

frontiers in Neurology

REVIEW
published: 17 July 2020
doi: 10.3389/fneur.2020.00665

The Role of Magnetic Resonance Imaging for the Diagnosis of Atypical Parkinsonism

Lydia Chougar[1,2,3,4]*, *Nadya Pyatigorskaya*[1,2,3,4], *Bertrand Degos*[5,6], *David Grabli*[7] and *Stéphane Lehéricy*[1,2,3,4]

[1] Institut du Cerveau et de la Moelle épinière–ICM, INSERM U 1127, CNRS UMR 7225, Sorbonne Université, UPMC Univ Paris 06, UMRS 1127, CNRS UMR 7225, Paris, France, [2] ICM, "Movement Investigations and Therapeutics" Team (MOV'IT), Paris, France, [3] ICM, Centre de NeuroImagerie de Recherche–CENIR, Paris, France, [4] Service de Neuroradiologie, Hôpital Pitié-Salpêtrière, APHP, Paris, France, [5] Dynamics and Pathophysiology of Neuronal Networks Team, Center for Interdisciplinary Research in Biology, Collège de France, CNRS UMR7241/INSERM U1050, MemoLife Labex, Paris, France, [6] Department of Neurology, Avicenne University Hospital, Sorbonne Paris Nord University, Bobigny, France, [7] Département des Maladies du Système Nerveux, Hôpital Pitié-Salpêtrière, APHP, Paris, France

The diagnosis of Parkinson's disease and atypical Parkinsonism remains clinically difficult, especially at the early stage of the disease, since there is a significant overlap of symptoms. Multimodal MRI has significantly improved diagnostic accuracy and understanding of the pathophysiology of Parkinsonian disorders. Structural and quantitative MRI sequences provide biomarkers sensitive to different tissue properties that detect abnormalities specific to each disease and contribute to the diagnosis. Machine learning techniques using these MRI biomarkers can effectively differentiate atypical Parkinsonian syndromes. Such approaches could be implemented in a clinical environment and improve the management of Parkinsonian patients. This review presents different structural and quantitative MRI techniques, their contribution to the differential diagnosis of atypical Parkinsonian disorders and their interest for individual-level diagnosis.

Keywords: parkinson's disease, progressive supranuclear palsy, multiple system atrophy, multimodal magnetic resonance imaging, diagnosis, machine learning

OPEN ACCESS

Edited by:
Yu Zhang,
VA Palo Alto Health Care System,
United States

Reviewed by:
Nikolaus R. McFarland,
University of Florida, United States
Hong Li,
Medical University of South Carolina,
United States
Mechelle M. Lewis,
Pennsylvania State University (PSU),
United States

***Correspondence:**
Lydia Chougar
chougar.lydia@gmail.com

Specialty section:
This article was submitted to Movement Disorders, a section of the journal Frontiers in Neurology

Received: *01 March 2020*
Accepted: *03 June 2020*
Published: *17 July 2020*

Citation:
Chougar L, Pyatigorskaya N, Degos B, Grabli D and Lehéricy S (2020) The Role of Magnetic Resonance Imaging for the Diagnosis of Atypical Parkinsonism. Front. Neurol. 11:665. doi: 10.3389/fneur.2020.00665

INTRODUCTION

Parkinsonism is defined by the presence of resting tremor, rigidity, bradykinesia, and postural instability. Parkinson's disease (PD) is the most common neurodegenerative cause of Parkinsonism. Atypical Parkinsonism refers to other neurodegenerative disorders that commonly include progressive supranuclear palsy (PSP), corticobasal degeneration, multiple system atrophy (MSA), with its cerebellar (MSA-C) and Parkinsonian (MSA-P) variants, and dementia with Lewy body (1–6). Degeneration of the substantia nigra (SN) is the pathological hallmark of neurodegenerative Parkinsonian disorders (1, 3–7). Neuroimaging plays a major role in the diagnosis of Parkinsonian disorders and the differentiation of PD from atypical Parkinsonism. Magnetic resonance imaging (MRI) improves diagnostic accuracy, reduces the rate of misdiagnosis, facilitates early diagnosis, and may be useful for the follow-up of disease progression (8–11). Usually, the diagnosis of sporadic PD does not require an MRI examination when the clinical presentation is typical. In contrast, MRI is needed when the clinical presentation is atypical, that is, in the presence of symptoms called "red flags," such as rapid progression of

gait impairment, early and recurrent falls and impaired balance, early bulbar or inspiratory respiratory dysfunction, and early and severe autonomic dysfunction (12). In this case, MRI shows a number of features that can help the clinician to distinguish PD from atypical Parkinsonism. This review details the main MRI characteristics of PD and the two main causes of atypical Parkinsonism, PSP and MSA, focusing on the features that can be used in clinical practice.

MRI TECHNIQUES AND BIOMARKERS

MRI provides *in vivo* biomarkers that inform about the underlying neurodegenerative processes. Regional brain atrophy is detected using T1-weighted three-dimensional (3D) sequences and reflects neuronal loss. Diffusion anomalies reflect the presence of microstructural alterations in the tissues, while iron-sensitive imaging detects the presence of iron deposits. Multimodal MRI is defined as the combination of information provided by these different sequences. Brain abnormalities can be assessed in several ways: (i) qualitatively, by visual inspection of regional brain atrophy and signal changes using conventional structural MRI, or (ii) quantitatively, by measurements of changes in volumes, diffusion metrics and iron-related signals (8–10, 13, 14). The main MRI techniques and their respective contributions are summarized in **Table 1**. The usefulness of neuroimaging biomarkers can be assessed by a five-level scale, as recently proposed for PSP (9). Level 1 defines biomarkers useful at the group level when comparing a specific disease with healthy subjects or other clinically overlapping diseases. Level 2 defines a biomarker useful at the individual level because it reaches a sensitivity and specificity >80% for the clinical diagnosis of a given patient. Level 3 indicates that the biomarker is effective for early clinical diagnosis, when patients present with mild or non-specific symptoms but do not yet meet the clinical criteria for the disease. Level 4 biomarkers are strongly correlated with pathology and could be used as surrogate criteria for pathological diagnosis. Level 5 biomarkers provide a direct measure of the underlying neuropathological changes (9). Here, we detail the different biomarkers in the three diseases in light of this scale.

IMAGING FINDINGS IN PARKINSONIAN DISORDERS

Parkinson's Disease

Parkinson's disease is an alpha-synucleinopathy, the main neuropathological characteristic of which is the neurodegeneration of the dopaminergic neurons of the substantia nigra *pars compacta* (SNpc) (1–3, 15, 16). In addition to SN degeneration, several other nuclei in the brainstem, basal forebrain and cortex are affected in PD in later stages, which helps to explain the presence of non-motor symptoms (15, 16). However, conventional MRI most often does not reveal specific abnormalities in PD outside the SN, and the basal ganglia are normal or only show subtle changes in terms of volume, diffusion measurements or iron deposition (8, 17–19). Lesions of the small brainstem nuclei, basal forebrain and cortex are mostly detected using specific quantitative approaches that are not used in clinical practice except for the locus coeruleus (18).

Conventional and Structural Imaging

Substantia nigra

In clinical practice, degeneration of the SNpc can be detected by visual inspection of the images using neuromelanin-sensitive and iron-sensitive imaging. These nigral changes differentiate neurodegenerative Parkinsonism from essential tremor and other non-degenerative Parkinsonian syndromes (20). Neuromelanin-sensitive imaging relies on the T1 shortening effect of neuromelanin, a pigment contained in the SNpc, that has paramagnetic properties when it is bound to iron (17, 21, 22). A direct correlation between the signal intensity of post-mortem samples of SNpc on neuromelanin-sensitive sequences and the density of neuromelanin-containing neurons has been demonstrated (23). Using neuromelanin-sensitive imaging, the SNpc appears as an area of high signal intensity in healthy subjects. Patients with degenerative Parkinsonian syndromes show a reduction in the size and signal intensity of the SNpc, reflecting the loss of dopaminergic neurons (11, 24, 25) (**Figure 1**). The sensitivity and specificity of this technique are above 80%, and the performances between the visual assessment of trained radiologists and the quantification of volume and signal intensity are similar (26). In line with neuropathological findings (7), greater involvement of the posterolateral part of the SNpc with relative preservation of the medial part has been shown in patients with PD (27). A neuromelanin signal decrease has also been observed in patients with idiopathic rapid eye movement sleep behavior disorder (RBD) (28). RBD is a frequent non-motor feature of PD characterized by abnormal behavior and increased muscle tone during rapid eye movement sleep (29, 30). Patients with RBD have a high risk of developing Parkinsonism, including PD, dementia with Lewy bodies and, more rarely, MSA, with a rate of conversion of 33.5% within 5 years and 82.4% at 10 years, as reported by a recent meta-analysis (31). Idiopathic RBD is therefore considered a prodromal phase of Parkinsonism and PD, with an estimated period of 10–15 years of progressive neuronal loss before the onset of the main motor symptoms (31–33).

Using susceptibility-weighted imaging (SWI), healthy subjects show an area of normal high signal intensity located at the dorsolateral part of the SNpc, a feature also known as the "swallow tail sign" or the "dorsolateral nigral hyperintensity" (DNH) sign (34). Histopathological correlations have shown that the DNH corresponds to nigrosome 1, a region where dopaminergic neurons are affected early and severely (35) (**Figure 2**). The loss of this hyperintensity in Parkinsonian subjects is probably due to the presence of iron deposits in Parkinsonian subjects (17, 22). The absence of DNH was shown to be predictive for ipsilateral dopamine transporter (DAT) deficiency on radiotracer imaging, with high sensitivity and specificity (87.5 and 83.6%), supporting its potential as a marker of SN pathology (36). This DNH sign has a sensitivity between 79 and 100% and a specificity between 85 and 100% for the differentiation of degenerative Parkinsonian syndromes from

TABLE 1 | Magnetic resonance imaging techniques.

Techniques	Measures	Information
CONVENTIONAL MRI		
T1-w,	Shape, volume	Atrophy
T2-w, FLAIR, PD-w	Signal changes	Signal abnormalities (gliosis and demyelination of white matter)
T2*-w, SWI	Iron load	Iron deposition Nigral dorsolateral hyperintensity
Neuromelanin-sensitive sequence	Signal and volume	Content of catecholaminergic neurons in the SNpc and the locus coeruleus
ASSESSMENT OF REGIONAL ATROPHY		
3D gradient echo T1-weighted	Anteroposterior midbrain diameter	Midbrain atrophy
	Midbrain to pons midsagittal surface ratio	Ratio of midbrain vs. pons atrophy
	MRPI [(P/M)*(MCP/SCP)][a] MRPI 2.0 [MRPI * (V3/VL)] [b]	Brainstem and cerebellar peduncle atrophy
	Automated segmentation	
IRON-SENSITIVE IMAGING		
T2*-weighted multiecho Magnitude image	Relaxation times R2* = 1/T2*	Iron load
Magnitude and phase images	Quantitative susceptibility mapping	Iron load
DIFFUSION IMAGING		
Diffusion-weighted imaging (DWI)	Apparent diffusion coefficient (ADC), Trace (D)	Magnitude of water diffusion
Diffusion tensor imaging (DTI)	Mean Diffusivity (MD)	Mean magnitude of water diffusion
	Axial Diffusivity (AD) Radial diffusivity (RD)	Magnitude of water diffusion along the main direction Magnitude of water diffusion along the perpendicular direction
	Fractional Anisotropy (FA)	Directionality of water diffusion
Bitensor model	Free water	Magnitude of free water diffusion
Neurite Orientation Dispersion and Density Imaging (NODDI)	Intracellular volume fraction Orientation dispersion index Isotropic volume fraction	Neurite density and dendritic structure
Tractotraphy	Number of tracks, probability of connection	Damage in specific fiber tracts
MAGNETIZATION TRANSFER (MT)		
Images with (M_T) and without (M_0) MT pulse	MT ratio (MTR) (MTR = (M_0 – M_T)/M_0)	Degree of myelination, axonal density
MAGNETIC RESONANCE SPECTROSCOPY		
^{1}H	N-acetyl-aspartate (NAA) Creatine (Cr) Choline (Cho) Myo-Inositol (mIns) Glutamate/Glutamine, GABA	Neuronal number and health Used as reference concentration Demyelination and cell proliferation Osmotic stress or astrogliosis Neurotransmitters
^{31}P	ADP/ATP/PCr	Energy metabolism
RESTING-STATE FUNCTIONAL MRI		
Blood oxygen level dependent (BOLD) contrast	Temporal correlation of BOLD signal fluctuations	Functional connectivity within brain networks
ARTERIAL SPIN LABELING (ASL)		
ASL perfusion imaging	Cerebral blood flow	Brain perfusion

[a] *The Magnetic Resonance Parkinsonism Index (MRPI) is defined by the product of the pons to midbrain area ratio (P/M) by the middle to superior cerebellar peduncles width ratio (MCP/SCP).*

[b] *The MRPI 2.0 is defined by the product of the MRPI by the third ventricle width/frontal horns width ratio (V3/VL).*

healthy subjects (34, 36, 37). The DNH sign is also an early marker observed in two-thirds of idiopathic RBD patients (38).

Locus coeruleus/subcoeruleus complex

The locus coeruleus/subcoeruleus complex is composed of catecholaminergic neurons containing neuromelanin and is affected in approximately two-thirds of PD patients (39, 40). Using neuromelanin-sensitive imaging, the signal is decreased within the coeruleus/subcoeruleus complex of these patients. The involvement of this nucleus has been associated with the presence of RBD in PD patients and with idiopathic RBD (40, 41). The relationship between RBD and signal changes in this complex

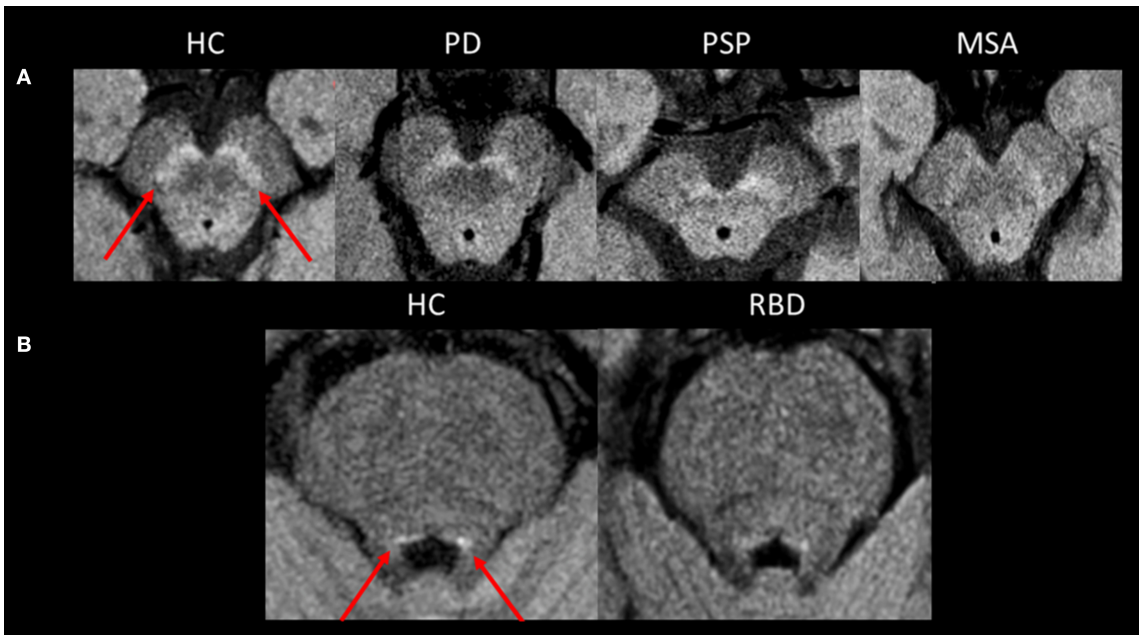


FIGURE 1 | Neuromelanin imaging. **(A)** Axial neuromelanin-sensitive images at 3 Tesla passing through the midbrain at the level of the substantia nigra *pars compacta* in a healthy control and patients with PD, PSP, and MSA. The substantia nigra *pars compacta* is seen as an area of high signal in a healthy control (arrows). Its size and signal are decreased in neurodegenerative Parkinsonian syndromes. **(B)** Axial neuromelanin-sensitive images at 3 Tesla passing through the midbrain at the level of the coeruleus/subcoeruleus complex. The signal within the coeruleus/subcoeruleus complex is decreased in the patient with RBD compared to the healthy control. HC, healthy control; MSA, multiple system atrophy; PD, Parkinson's disease; PSP, progressive supranuclear palsy; RBD, rapid-eye movement sleep behavior disorder.

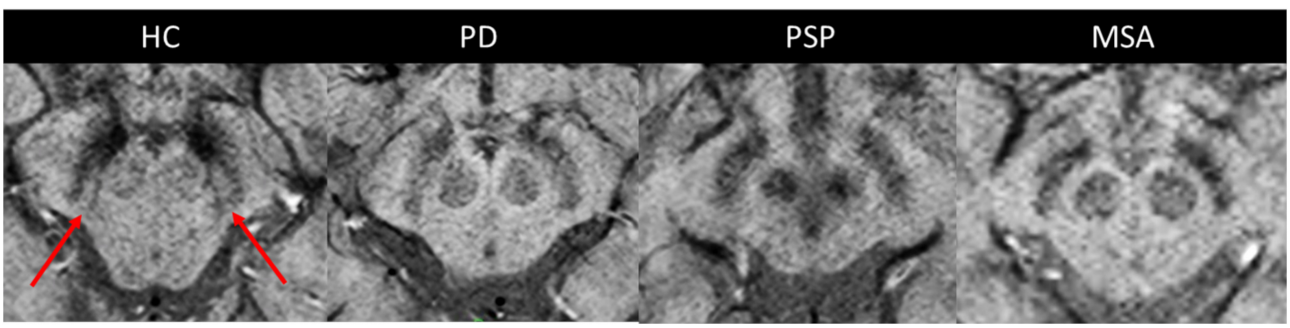


FIGURE 2 | The dorsolateral nigral hyperintensity. Axial susceptibility-weighted images at 3 Tesla passing through the midbrain at the level of the substantia nigra *pars compacta* in a healthy control and patients with PD, PSP, and MSA. The dorsolateral nigral hyperintensity is well-depicted at the dorsolateral part of the substantia nigra *pars compacta* in a healthy control (arrows). It is lost in neurodegenerative parkinsonian syndromes. HC, healthy control; MSA, multiple system atrophy; PD, Parkinson's disease; PSP, progressive supranuclear palsy.

suggests that RBD in PD may be related to damage of the subcoeruleus part of the complex that is involved in the control of movement during REM sleep (29, 30, 40).

Brainstem

Structural brain imaging using conventional MRI with visual assessment of T2- and T1-weighted sequences is usually normal in patients with PD. Its main role is to detect or exclude secondary causes of Parkinsonism (such as vascular encephalopathy, demyelinating lesions, tumors or normal pressure hydrocephalus) and to look for signs of atypical Parkinsonism (10, 13, 19, 42). Manual morphometric measurements of the brainstem, including the anteroposterior midbrain diameter (43, 44), the midsagittal midbrain area, the midbrain to pons area ratio (43, 45) and the magnetic resonance Parkinsonism index (MRPI), are normal in PD (45, 46). Atrophy rates of the brainstem are not different from those of healthy subjects (47).

Other areas

Overall, except for the SN, the basal ganglia are mostly spared in PD patients (48, 49). In the cortex, no or mild changes

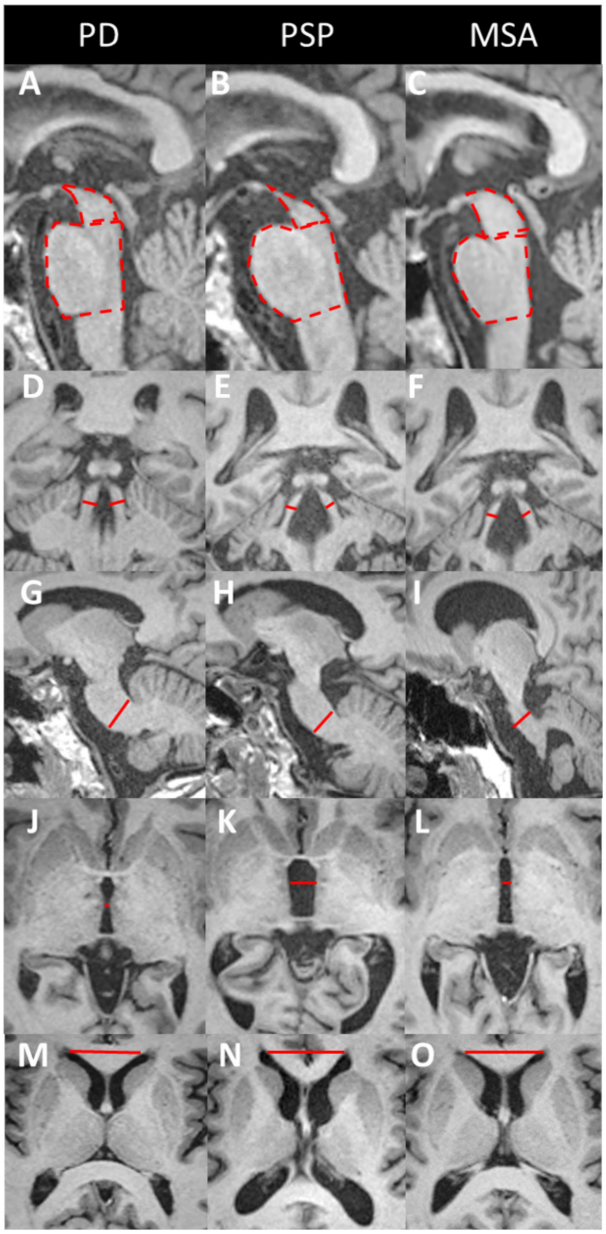


FIGURE 3 | Midbrain to pons area ratio, Magnetic resonance Parkinsonism index (MRPI) and MRPI 2.0. Three-dimensional T1-weighted images in patients with PD (left), PSP (middle), and MSA (right). The MRPI combines measurements of the midsagittal surfaces of the midbrain (dashed line) and pons (dashed line) **(A–C)** and widths of the superior (red lines, **D–F**) and middle (red line, **G–I**) cerebellar peduncles [MRPI = (pons/midbrain) × (middle cerebellar peduncle/superior cerebellar peduncle)]. The limit between the midbrain and pons is defined by the line passing through the inferior border of the inferior colliculus and the pontomesencephalic sulcus. The inferior border of the pons is parallel to the previous one. The widths of the superior **(D–F)** and middle cerebellar peduncles **(G–I)** are measured in the parasagittal and coronal planes that best show the peduncles, respectively.
The MRPI 2.0 is the product of the MRPI by the ratio of the width of the third ventricle (red line, **J–L**) to the largest left-to right width of the frontal horns of the lateral ventricles (red line, **M–O**) on axial views. For further details about the measurement technique [please refer to Quattrone et al. (46, 85)]. PSP patients show atrophy of the midbrain **(B)** and superior cerebellar peduncles *(Continued)*

FIGURE 3 | (E) and enlargement of the third ventricle **(K)**. In MSA patients, the atrophy is greater in the pons **(C)** and middle cerebellar peduncles (l), with an enlarged fourth ventricle. PD patients do not show any significant brainstem atrophy or MRPI changes. MSA, multiple system atrophy; PD, Parkinson's disease; PSP, progressive supranuclear palsy.

have been reported in early PD (50). Conversely, impaired cognition and dementia in PD have been associated with marked cortical atrophy in many brain regions, including the frontal, parietal, and temporal areas, and the substantia innominata (50–52). Cortical atrophy accelerates with disease progression and worsening of cognitive decline (50). Longitudinal MRI studies have reported a higher rate of cortical thinning in PD patients with mild cognitive impairment than in PD patients with normal cognition and healthy subjects, which is correlated with cognitive decline (50, 51).

Diffusion Imaging

In the SN, changes in diffusion metrics have been reported at the group level. Using diffusion tensor imaging (DTI), reduced fractional anisotropy (FA) (26, 53) and increased diffusivity (26) values were evidenced in the SN in PD patients. However, there is a large variability of results across studies, and these measures do not appear useful at the individual level (54). Using DTI, two meta-analyses reported either frontal predominance of extranigral FA changes (55) or more widespread FA and mean diffusivity (MD) changes involving the corpus callosum and cingulate and temporal cortices in PD patients (56). Most studies did not detect any significant changes using global region-of-interest analyses in the putamen (57–61), midbrain (62, 63), pons (57–61, 64) and cerebellum (65). Free water is a more advanced diffusion metric derived from a bi-tensor diffusion model that shows better sensitivity and reliability for the discrimination of PD from healthy subjects. Increased free water values have only been observed in the SN in PD (66, 67), while no changes were found in other brain regions (66). In contrast, using region-of-interest measurements, diffusivity changes were measured in specific regions that are affected in PD, including the pedunculopontine nucleus in relation to gait disorders (68), the locus coeruleus for RBD (40), the medulla oblongata for autonomic dysfunction (69), and basal forebrain for cognitive decline (70).

Iron Imaging

Using R2* relaxometry (71, 72) or quantitative susceptibility mapping (QSM) (71, 73, 74), an increase in iron deposition was detected in the SN, with QSM showing greater accuracy than R2* relaxometry (71, 75, 76). Outside the SN, R2*, and susceptibility values were mostly normal in the putamen (61, 73, 74, 77). However, an increase in susceptibility values was reported in the red nucleus and globus pallidus of patients with late-stage PD (73).

Summary

The neuromelanin signal decrease within the SNpc is an early marker of Parkinsonism, useful at the individual level, meeting

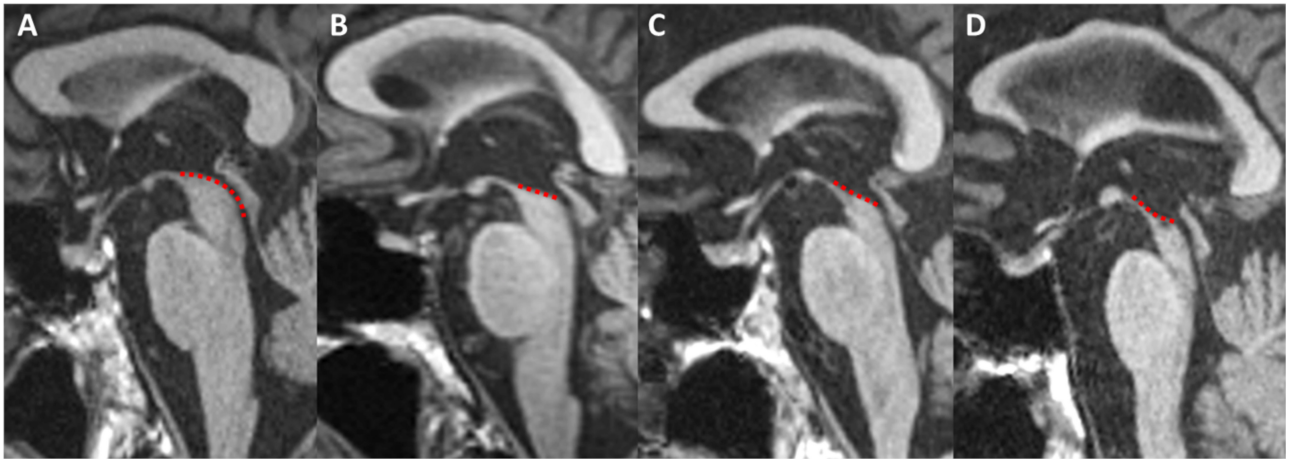


FIGURE 4 | Midbrain atrophy in PSP patients. Midsagittal T1-weighted images in a healthy control **(A)** and PSP patients with increasing midbrain atrophy **(B–D)**. Healthy subjects and PD patients show a normal convex profile of the midbrain superior surface. PSP patients present a flat (mild) or concave (moderate to severe) aspect (dashed line). This shape is known as the "penguin" or "hummingbird" sign. HC, healthy control; PD, Parkinson's disease; PSP, progressive supranuclear palsy.

the criteria for a level 3 biomarker. Neuromelanin signal also correlates with the reduction of dopaminergic neurons in the SN and may be a surrogate marker of dopaminergic neuron degeneration (level 4). The DNH sign is also a level 3 biomarker and may hold potential for being a level 4 biomarker, although a direct correlation with the SN degeneration has not yet been evidenced. Neuromelanin signal decrease within the coeruleus/subcoeruleus complex may also be used as an early biomarker of Parkinsonism at the individual level (level 3). Free water changes appear useful at the individual level (level 2) although their correlation with neurodegenerative changes remains to be determined. Their use in clinical practice would require normative values that are currently not available in Radiology departments. Other findings were mostly shown at the group-level (level 1), with no demonstrable clinical relevance to date.

Progressive Supranuclear Palsy

Progressive supranuclear palsy (PSP) is a tauopathy characterized by the presence of intracerebral depositions of Tau protein and neurodegeneration predominant in the brainstem, basal ganglia and cerebellar nuclei (3, 5, 6, 78, 79). PSP has a heterogeneous clinical expression. The most common clinical presentation of PSP is Richardson's syndrome (PSP-RS), which is characterized by early axial rigidity, postural instability, falls and vertical supranuclear gaze palsy (5, 79, 80). There are a number of other clinical phenotypes of PSP, including PSP with predominant Parkinsonism (PSP-P), progressive gait freezing (PSP-PGF), postural instability (PSP-PI), frontal presentation (PSP-F), speech/language disorder (PSP-SL), ocular motor dysfunction and corticobasal syndrome (PSP-CBS) (5, 79, 80). Imaging patterns in PSP variants are not clearly understood since most studies have focused on PSP-RS and/or did not differentiate PSP variants.

Conventional and Structural Imaging

Substantia nigra

As in PD, PSP patients also show a reduction in the neuromelanin signal and volume of the SNpc (27, 81, 82) and a loss of the DNH sign (37). Neuropathological studies have reported a different pattern of nigral degeneration from PD without predilection for the lateral part (7). Only one study using neuromelanin-sensitive imaging reported a difference between signal changes in PD and PSP (27), but this requires further investigation.

Locus coeruleus/subcoeruleus complex

The coeruleus/subcoeruleus complex is also involved in PSP (3, 5, 6). In line with histological studies, decreased neuromelanin signal of the coeruleus/subcoeruleus complex has been reported in PSP (18), but other studies did not find such changes (27).

Brainstem

Patients with PSP-RS typically exhibit marked midbrain atrophy. The "hummingbird" sign (83), less frequently called the "penguin" sign (84), describes the flat or concave aspect of the midbrain tegmentum visible on midline T1-weighted sagittal sections (**Figures 3**, **4**). The "morning glory" sign corresponds to the concave aspect of the lateral margin of the midbrain tegmentum on axial slices, which is also observed in PSP-RS (86). Although these features are suggestive of PSP-RS with a specificity of 99.5% for the "hummingbird sign" and 97.7% for the "morning glory sign," they show low sensitivity (51.6 and 36.8%, respectively) (87) (**Table 2**).

Several manual morphometric indexes have been proposed as clinical biomarkers usable in individual patients. The anteroposterior midbrain diameter has limited discriminating power with a significant overlap of individual values (9, 44). The midbrain midsagittal area discriminate PSP-RS from healthy subjects and PD patients (<122 mm^2) with sensitivity and specificity above 80% and from MSA patients (<114 mm^2)

TABLE 2 | Magnetic resonance findings in progressive supranuclear palsy.

Imaging biomarker	Findings	Performance (sensitivity/specificity, AUC)	References
MIDBRAIN			
Hummingbird/penguin sign	Flat or concave superior profile in sagittal images	51.6/88.8% 68/88.8%	Mueller et al. (87) Righini et al. (44)
Morning glory sign	Concavity of the lateral margin of the midbrain on axial images	36.8/97.7%	Mueller et al. (87)
Anteroposterior diameter	<8.9 vs. PD and MSA <12 mm vs. PD	90/90%, AUC 0.94	Mangesius et al. (43) Righini et al. (44)
Sagittal area	<122 mm^2 vs. PD <117 mm^2 vs. MSA-P <114 mm^2 vs. MSA-C	83/84% 76/82% 74/81%	Moller et al. (45)
Midbrain/pons ratio	<0.18 vs. PD and MSA <0.215 vs. PD and MSA-P <0.275 vs. MSA-C	81/87% 76.4/80% 96.2/81%	Mangesius et al. (43) Moller et al. (45) Moller et al. (45)
MRPI	>13.6 vs. PD and HC >12.9 vs. MSA-P	100/100% 100/100%	Quattrone et al. (46) Quattrone et al. (46)
MRPI 2.0	>2.5 vs. PD and HC	100/100%	Quattrone et al. (85)
FLAIR signal	Increased vs. PD	28/100%	Righini et al. (44)
Diffusivity	Increased vs. PD and MSA-P	81/81%, AUC: 0.90	Surova et al. (62) Tsukamoto et al. (63)
SUPERIOR CEREBELLAR PEDUNCLES			
Volume	Reduced vs. PD and MSA	74/94%	Paviour et al. (88) Quattrone et al. (46)
FLAIR signal	Increased	19.6/100%	Kataoka et al. (89)
Diffusivity	Increased • vs. PD • vs. MSA-P	 100/100% 96.4/93.3%	 Nicoletti et al. (90)
PUTAMEN			
Volume	Reduced vs. PD	AUC: 0.93	Pyatigorskaya et al. (18) Messina et al. (48)
Diffusivity	Increased vs. PD	75/100% 90/100%	Nicoletti et al. (58) Schocke et al. (91)
Susceptibility, R2*	Increased vs. PD	AUC: 0.83	Sjöstrom et al. (74) Lee et al. (77)
THALAMUS			
Volume	Decreased vs. PD and MSA-P	AUC: 0.86	Pyatigorskaya et al. (18) Messina et al. (48) Surova et al. (62)
Diffusivity	Increased vs. PD and MSA-P	81/77%, AUC: 0.81	Surova et al. (62)
GLOBUS PALLIDUS			
Volume	Decreased vs. PD and MSA-P	AUC: 0.86	Lee et al. (77) Messina et al. (48) Surova et al. (62)
Diffusivity	Increased	——	Nicoletti et al. (58) Seppi et al. (92) Schocke et al. (91)
Susceptibility	Increased • vs. PD • vs. MSA	 AUC: 0.75 AUC: 0.73	Sjöstrom et al. (74)
RED NUCLEUS			
Susceptibility	Increased • vs. PD • vs. MSA	 AUC: 0.97 AUC: 0.75	Sjöstrom et al. (74)
CORTICAL REGIONS			
Frontal cortex	Atrophic	——	Worker et al. (93) Huppertz et al. (94)

The table provides optimal cut-off points with the corresponding sensitivity and specificity, as proposed by the studies. AUC values were reported when available. These values depend on which disease groups are compared. They were not validated and may vary from one study to another. The patient characteristics for each reference are listed in the ***Supplementary Table****.*

AUC, area under the ROC curve; DP, proton density-weighted; HC, healthy controls; MRPI, Magnetic Resonance Parkinsonism Index; MSA, multiple system atrophy; MSA-C, cerebellar variant of MSA; MSA-P, Parkinsonian variant of MSA; PD, Parkinson's disease; PSP-RS, progressive supranuclear palsy with Richardson syndrome; SWI, susceptibility-weighted imaging.

with a lower sensitivity (45). The midbrain to pons midsagittal surface ratio (<0.18) has a sensitivity and specificity >90% in differentiating PSP-RS from healthy subjects, PD and MSA-P patients (43, 46), although some studies have found lower accuracies (45).

The superior cerebellar peduncles (SCPs) are atrophic in PSP, while the middle cerebellar peduncles (MCPs) are relatively spared, resulting in an increase in the MRPI in PSP. Compared to the midbrain to pons ratio, the MRPI showed better performance for the differentiation of PSP-RS from PD (when > 13.6) and from MSA-P (when > 12.9), with very good (43) to excellent sensitivity and specificity (46, 95, 96) (**Figure 3**, **Table 2**). Manual and automated approaches have shown similar performance for measuring the MRPI (96). A recent study has validated the use of a web platform providing an automated calculation of the MRPI, suggesting that the approach could be applicable in clinical practice (97). Automated MRPI values showed high performance in differentiating PSP-RS and PSP-P patients from non-PSP participants (93.6 and 86.5% accuracy, respectively). Differentiation was also good at the early stage of the disease (90.1 and 85.9%, respectively) (97). More recently, the MRPI 2.0 has been introduced to improve the discrimination of PSP-P from PD over that of the MRPI (sensitivity: 100% for the MRPI 2.0 vs. 73.5% for the MRPI) (85). Abnormal MRPI and MRPI 2.0 values also appeared to be early features of PSP-P (98) (**Figure 3**, **Table 2**).

In line with studies based on morphometric measurements, group-level studies using voxel-by-voxel analyses (49, 94, 99) or automated segmentation software, such as Freesurfer (48, 100) have reported volume reductions in the brainstem, including the midbrain and superior cerebellar peduncles, in PSP-RS.

Longitudinal studies have shown that the rates of midbrain atrophy in PSP (2.2 ± 1.5% per year) were seven times greater than those in healthy subjects (47). Furthermore, motor deficit severity correlates with midbrain atrophy (47). Similarly, the rate of progression of brainstem atrophy measured by the MRPI and MRPI 2.0 over 1- and 2-years intervals was higher in PSP patients than in PD patients (101). The progression rate was greater in PSP-RS patients than in PSP-P patients (101).

There is evidence that midbrain atrophy is a marker of PSP-RS phenotype rather than PSP pathology, as suggested by the absence of midbrain atrophy in patients with autopsy-proven PSP without clinical presentation of PSP-RS (9, 102). Other studies have also found midbrain atrophy in PSP variants, including PSP-P (9, 46, 98, 103), PSP-SL (102, 104, 105), and PSP-F (9, 102, 106), although it is typically less severe in these variants than in PSP-RS (9, 103, 107).

Other regions

In PSP-RS, among the basal ganglia, the volumes of the putamen and globus pallidus are smaller than those in PD, and the volume of the thalamus is smaller than that in MSA-P (8, 9, 48, 62). The usefulness of these findings at the individual level remains to be determined (9). Cortical atrophy with preferential frontal involvement has been demonstrated in PSP-RS patients but not in healthy subjects, PD and MSA patients at the group level (18, 93, 94). Frontal atrophy also occurs in PSP variants, particularly in PSP-F (9, 106), PSP-SL (9, 108), and PSP-CBS (9, 109), and to a greater extent than that of PSP-RS, probably reflecting different pathological loads between the brainstem and the cortex (9). The rate of frontal atrophy in PSP was shown to be three times that of healthy subjects and twice that of PD (47). Executive dysfunction correlated with increased rates of frontal atrophy in PSP (47).

Diffusion Imaging

In the SN, decreased FA (18) and increased free water (66) have been reported at the group level in PSP. Diffusion-weighted imaging (DWI) studies using manual measurements of apparent diffusion coefficient (ADC) and DTI studies in PSP-RS patients have demonstrated increased diffusivity values in the putamen, the caudate nucleus and the globus pallidus compared with those in PD patients and healthy subjects (58, 63, 92, 110, 111), as well as in the thalamus (58), the midbrain (18, 63, 110), the SCP (90, 110, 112), and the precentral and prefrontal white matter (58, 110) compared with those in PD, MSA and healthy subjects (58, 110, 111). In the SCP, ADC values were higher in PSP-RS than in healthy subjects and PD patients with a sensitivity of 90–100% and a specificity of 85–100% (90, 111) and in MSA-P patients with a sensitivity of 96.4% and a specificity of 93.3% (90), supporting the use of this measurement as a level 2 biomarker (9). Putamen diffusivity values were higher in PSP than in PD but overlapped between PSP and MSA-P (57, 90, 92, 113). Diffusivity in the thalamus was greater in PSP patients than in MSA patients (62) (**Table 2**). Reduced FA has been reported in the midbrain, pons, SCP, thalamus, cerebellar white and gray matter, dentate nucleus, corpus callosum, the precentral, superior frontal and parieto-occipital gray matter and the precentral white matter of PSP patients compared to healthy subjects and PD patients (18). In line with these results, free-water measurements were increased in the basal ganglia, midbrain, thalamus, dentate nucleus, cerebellar peduncles, cerebellar vermis and lobules V and VI, and corpus callosum in PSP patients compared with those in PD patients and healthy subjects (66). Free water-corrected fractional anisotropy values were increased in the putamen, caudate, thalamus, and vermis and decreased in the superior cerebellar peduncle and corpus callosum (66).

Tractography studies have shown more specific involvement of the SCP, corpus callosum and superior longitudinal fasciculus in PSP than in PD and MSA-P (9).

Iron-Sensitive Imaging

PSP patients show increased iron deposition in many regions. R2* relaxation rates were increased in the putamen, caudate nucleus and globus pallidus compared to those in PD patients and healthy subjects (77, 114). R2* and QSM values in the putamen overlapped between PSP and MSA (74, 113). Using QSM, PSP patients had higher susceptibilities in the basal ganglia and thalamus than healthy subjects and early-stage PD patients (115) and in the red nucleus than in MSA patients (74) (**Table 2**).

Other Biomarkers

Other techniques have been investigated in a research setting, with differences only being observed at the group level. Compared to that in healthy subjects, the magnetization transfer ratio in PSP patients was reduced in the globus pallidus,

putamen, caudate nucleus, SN, and white matter, possibly reflecting changes in the degree of myelination or axonal density in the affected structures (116). Using spectroscopy, metabolic changes were observed in the basal ganglia and the frontal areas. Reduced N-acetylcholine (NAA)/creatine (Cr) or NAA/choline (Cho) ratios were reported in the lentiform nucleus (117–121), and a reduced NAA/Cr ratio was reported in the frontal cortex (117). Using resting-state fMRI, PSP patients have shown connectivity disruptions between the dorsal midbrain tegmentum and subcortical and cortical networks, including those involving the cerebellar, diencephalic, basal ganglia, and cortical regions (122), and between the thalamus and the striatum, supplementary motor area and cerebellum (123). These findings help to understand the pathophysiology of Parkinsonism but are of little use in discriminating diseases.

Summary

Measurements of midbrain atrophy including the midbrain to pons ratio, the MRPI and the MRPI 2.0 are the most robust biomarkers for clinical diagnosis of PSP-RS at the individual level (level 2). Frontal atrophy in addition to midbrain atrophy has also been reported as a level 2 biomarker although the degree of evidence appears lower. Further, the midbrain to pons ratio, the MRPI and the MRPI 2.0 have proven to be useful for the early diagnosis of PSP-RS (level 3), but their relevance at the prodromal stage of the disease remains unclear. Increased MRPI and the MRPI 2.0 also appear to be early features in PSP-P (98). Relevant biomarkers have not yet been validated for other PSP variants. Diffusivity in the SCP has shown accuracies above 90% for the differentiation of PSP-RS from PD and MSA, suggesting its clinical utility as a level 2 biomarker. However, normative values in healthy subjects and cut-off values still need to be defined.

Multiple System Atrophy

Multiple system atrophy (MSA) is a synucleinopathy characterized by the accumulation of alpha-synuclein within glial cytoplasmic inclusions (3, 4, 78). MSA patients typically present with autonomic dysfunction with a variable degree of Parkinsonism, more predominantly in the Parkinsonian variant (MSA-P), and with cerebellar signs, more predominantly in the cerebellar variant (MSA-C). MSA-P is mainly associated with changes in the putamen, whereas MSA-C shows prominent involvement of the cerebellum, pons and MCP (3, 4, 8, 78). Striatonigral degeneration and olivopontocerebellar atrophy often overlap in MSA patients (3, 4), and a clinical and brain imaging continuum exists between both variants as the disease evolves (3, 4, 78, 124).

Conventional and Structural Imaging

Substantia nigra

Nigral abnormalities can be depicted using neuromelanin-sensitive imaging (27, 81, 82) and SWI (37). Neuropathological descriptions and neuromelanin-based imaging studies have shown a similar pattern of nigral degeneration between MSA-P and PD, with a greater involvement of the lateral part of the SNpc (7, 27).

Locus coeruleus/subcoeruleus complex

The locus coeruleus/subcoeruleus complex may be involved in MSA (3), resulting in signal loss on neuromelanin-sensitive imaging (27) that is less severe than that in PD patients (3, 27).

Basal ganglia, brainstem and cerebellum

In MSA-P, the putamen is atrophic, with a characteristic flattening of its lateral border, hypointense on T1-weighted gradient echo images, and hypointense in SWI due to the presence of iron deposits (125) (**Figure 5**). This hypointensity is surrounded by a rim of hyperintensity at its dorsolateral margin on proton density- and T2-weighted images (126) (**Figure 5**). In line with the underlying neuropathology (3), these signal changes are typically more prominent on the posterior part of the putamen (125). A hyperintense putaminal rim may occasionally be seen in PD patients and healthy subjects (3, 87, 95, 97). Signal abnormalities are influenced by the sequence parameters and the magnetic field strength of the MRI scanner (112). Hypointensity in the putamen have been shown to be greater using SWI than T2*- and T2-weighted images and increased with field strength (127). Therefore, overall sensitivity values are extremely variable across studies, ranging from 38 to 100% for T2 hypointensity in the putamen and from 56 to 90% for the hyperintense dorsolateral rim, whereas specificity values varied between 87 and 100% in distinguishing MSA-P patients from PD or healthy subjects (125) (**Table 3**).

In MSA-C, the pons is atrophic, showing areas of increased signal intensity on proton density-weighted images affecting the transverse pontine fibers with the shape of a cross, well-known as the "hot cross bun" sign (126) (**Figure 6**). This sign has limited specificity, as it can be encountered in other pathologies, such as spinocerebellar ataxia (128). The MCPs present with atrophy and T2 hyperintensity, and the cerebellum is atrophic (8) (**Table 3**).

Regional brain atrophy can be quantified. While PSP patients have greater midbrain and SCP atrophy, MSA-C patients have predominant atrophy in the pons and MCPs, resulting in increased midbrain to pons ratio and decreased MRPI, with sensitivity and specificity equal to 95% and 100% for the categorization of MSA-P and PSP patients, respectively (46). Therefore, the midbrain to pons ratio and the MRPI could be suggested as level 2 biomarkers.

In MSA-P, atrophy rates have been shown to be greatest in the pons, equal to 4.5 $\pm$ 3.2% per year, over 20 times that in healthy subjects and three times the rate of pontine atrophy in PSP. Atrophy rates in the cerebellum (3.2 $\pm$ 1.9% per year) were more than ten times higher than those of healthy subjects and twice that of PSP (47). The severity of motor deficit correlated with ponto-cerebellar atrophy in MSA-P (47).

Diffusion

In MSA-P, diffusivity of the posterior putamen is increased, which is visible by simple inspection of ADC maps and can also be quantified (**Figure 5**). DWI studies have consistently reported an increase in ADC and Trace(D) values in the putamen in MSA-P compared to healthy subjects and PD patients (57–61, 90, 92, 129, 130), with an overall sensitivity of 90% and

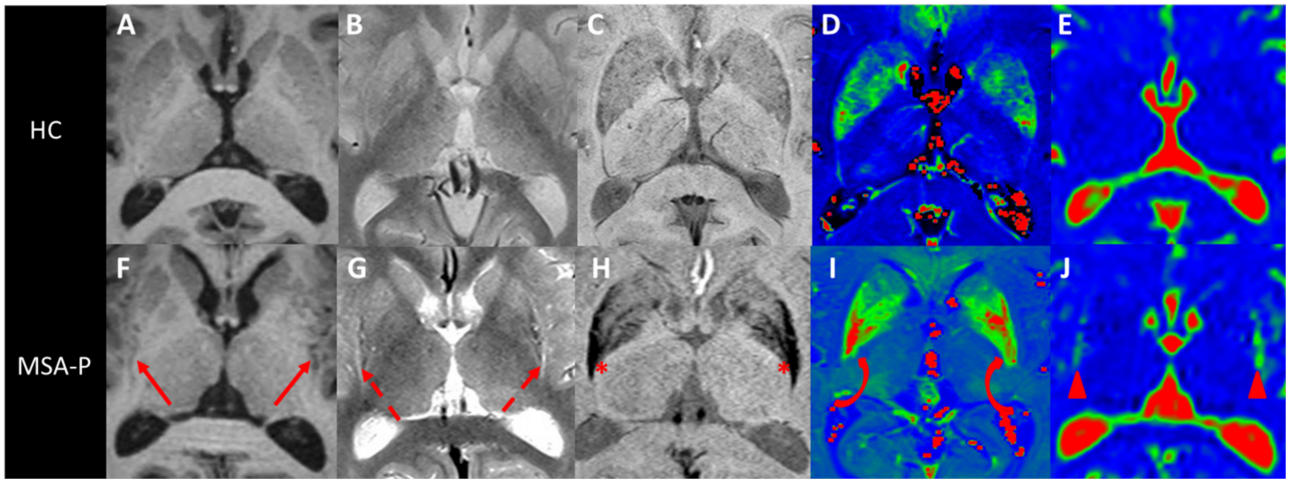


FIGURE 5 | Putaminal abnormalities in MSA-P. Axial T1 **(A,F)**, proton density **(B,G)**, and susceptibility **(C,H)** weighted images and R2* **(D,I)** and ADC **(E,J)** maps passing through the putamen in a healthy control (upper row) and a patient with MSA-P (lower row). The posterior putamen are atrophic (**F**, arrows), showing a lateral hyperintense rim (**G**, dashed arrows), a hypointensity on susceptibility-weighted images (**H**, *) associated with increased R2* values (**I**, curved arrows), reflecting elevated iron depositions, and increased ADC values (**J**, arrowheads). ADC, apparent diffusion coefficient; HC, healthy control; MSA-P, Parkinsonian variant of multiple system atrophy; R2*, T2* relaxation rate.

specificity of 93% in discriminating MSA-P from PD patients in a recent meta-analysis (57). These diffusion abnormalities were greater in the posterior putamen (59, 63, 129). UPDRS motor scores correlated positively with Trace(D) values in both the entire and posterior putamen in MSA-P patients (60). However, the ability of diffusivity measurements in the putamen to distinguish MSA and PSP is debated. Some studies have reported reliably higher ADC values in MSA-P than PSP (58, 111), while others have described a significant overlap of values, which would limit the interest for discriminating individual patients (57, 58, 129).

Other diffusion abnormalities in MSA-P involve the MCPs, the pons and the cerebellum (58–61, 64, 90–92, 130), reflecting a certain degree of olivopontocerebellar changes in addition to striatonigral degeneration (58). Increased ADC values in the MCPs allow complete differentiation of MSA-P from PD and PSP patients with 100% sensitivity and specificity (58). FA values are decreased in the MCP and pons (64). Diffusivity in the putamen and the MCP could therefore improve the categorization between MSA-P and MP on an individual basis. Increased diffusivity was also observed in the thalamus of MSA-P patients (58–61, 90–92) but to a lesser extent compared to PSP patients (62) (**Table 3**).

In MSA-C, the MCPs and cerebellum are more affected and the putamen is less affected than in MSA-P (8, 131, 132). Mean diffusivity in the cerebellum seems to be a robust discriminating marker, allowing the differentiation of MSA-P and MSA-C from PD and PSP-RS patients with a 100% positive predictive value (65) (**Table 3**).

Increased disease duration correlated with increased Trace(D) values in the pons of MSA-P patients and in the cerebellum and MCPs of MSA-C patients (64, 91).

Iron-Sensitive Imaging

MSA patients have greater iron deposits in the putamen than healthy subjects and PD patients (115), with greater involvement of the posterolateral part of the putamen (115, 133) (**Figure 5**). Increased R2* values in the putamen showed 78% sensitivity and 100% specificity for the discrimination of MSA-P patients from healthy subjects and PD patients (61, 77, 113). R2* values correlated positively with atrophy of the putamen (77). Similar differences are observed between MSA-C and PD (61). Using QSM, susceptibility values were also shown to be increased in MSA compared to PD (74). The combination of mean diffusivity and R2* measurements in the putamen improved the distinction between MSA-P and PD patients, resulting in an accuracy of 96% (61). Although the signal decrease due to the presence of iron deposits observed using SWI in the putamen is visually greater in MSA-P than PSP, there is a significant overlap of R2* and susceptibility values in the putamen between the two diseases (74, 113) (**Table 3**).

Other Biomarkers

The magnetization transfer ratio was reduced in the putamen of MSA patients (116). Using spectroscopy, decreased NAA/Cr and Cho/Cr ratios were reported in the lenticular nucleus in MSA-P compared to those in healthy subjects. The NAA/Cr ratio in the lenticular nucleus (118) and NAA/Cr in the cerebellum were decreased in MSA-C (134). The NAA/Cr ratio was decreased in the pons in both MSA types (135). Resting-state fMRI studies have shown connectivity abnormalities in the primary sensorimotor and premotor cortex and prefrontal, inferior parietal and occipital areas in MSA-C and MSA-P patients. Unlike in

TABLE 3 | Magnetic resonance findings in multiple system atrophy.

Imaging biomarker	Findings	Performance (sensitivity/specificity, AUC)	References
PONS			
Sagittal area	MSA-P vs. PD <553 mm^2	61.7/75.0%	Moller et al. (45)
	MSA-C vs. PD <538 mm^2	81.0/82.8%	
Midbrain/pons ratio	MSA-P vs. PSP >0.215	76/80%	Moller et al. (45)
	MSA-C vs. PSP >0.275	96.0/81.2%	
	MSA-C vs. PD >0.290	81.0/79.9%	
MRPI	MSA-P vs. PSP <12.9	100/100%	Quattrone et al. (46)
Signal on PD-w images	Hot cross bun sign	—–	Way et al. (128)
Diffusivity	Increased	—–	Nicoletti et al. (58, 90)
			Pellecchia et al. (94, 99)
			Schocke et al. (91)
			Seppi et al. (92)
			Seppi et al. (129, 130)
			Barbagallo et al. (61)
			Chen et al. (64)
MIDDLE CEREBELLAR PEDUNCLE			
Volume	Decreased	—–	Quattrone et al. (46)
Signal on T2-w images	High signal	—–	Heim et al. (3)
Diffusivity	Increased	100/100%	Nicoletti et al. (58)
	MSA-P vs. PD and PSP		
PUTAMEN			
Volume	Reduced	—–	Seppi et al. (129, 130)
			Messina et al. (48)
			Scherfler et al. (100)
			Huppertz et al. (94)
Signal on SWI	Hypointensity	—–	Seppi et al. (129, 130)
Signal on T2/PD-w images	Hyperintense dorsolateral rim	—–	Seppi et al. (129, 130)
			Watanabe et al. (126)
Diffusivity	Increased		
	• vs. PD	90–100/93–100%	Bajaj et al. (72)
	• vs. PSP	100/81.2%	Nicoletti et al. (58)
			Pellecchia et al. (94, 99)
			Schocke et al. (91)
			Seppi et al. (92)
			Seppi et al. (129, 130)
			Barbagallo et al. (61)
R2*	Increased	77.8/100%	Focke et al. (113)
			Barbagallo et al. (61)
			Lee et al. (77)
Susceptibility	Increased vs. PD	AUC: 0.77	Sjöstrom et al. (74)
CEREBELLUM			
Volume	Decreased	—–	Scherfler et al. (100)
			Huppertz et al. (94)
Diffusion	Increased vs. PD and PSP	100/100%	Nicoletti et al. (65)

AUC values were reported when available.

AUC, area under the ROC curve; DP, proton density-weighted; HC, healthy controls; MRPI, Magnetic Resonance Parkinsonism Index; MSA, multiple system atrophy; MSA-C, cerebellar variant of MSA; MSA-P, Parkinsonian variant of MSA; PD, Parkinson's disease; PSP-RS, progressive supranuclear palsy with Richardson syndrome; SWI, susceptibility-weighted imaging.

patients with PD, decreased or increased connectivity in different regions of the visual associative cortices and decreased connectivity in the right cerebellum were observed in MSA patients (136).

Summary

Although morphometric measurements, such as the midbrain to pons ratio and the MRPI were initially designed for PSP, these indices also allow differentiation MSA from PSP and PD.

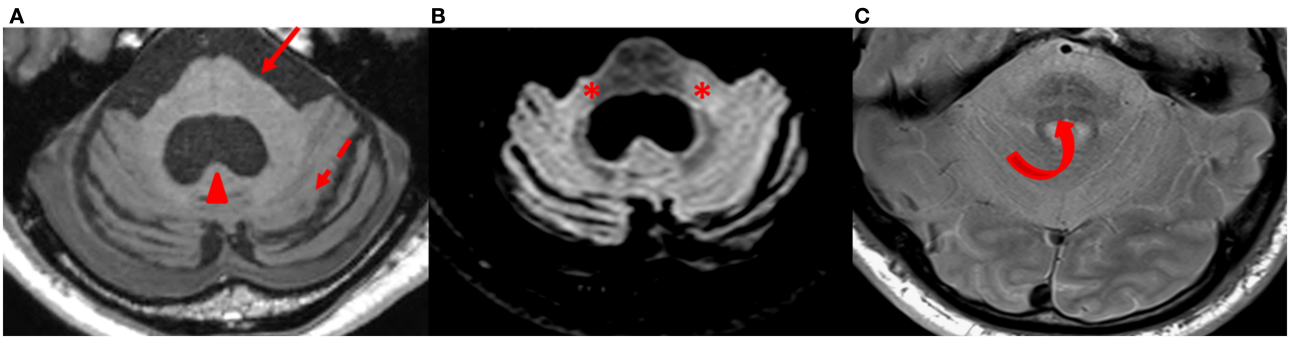


FIGURE 6 | Findings in MSA-C patients. Axial T1-weighted **(A)**, FLAIR **(B)**, and proton density-weighted **(C)** images at the level of the pons and cerebellum in a patient with MSA-C. The pons (arrow) and the cerebellum (dashed arrow) are atrophic with an enlarged fourth ventricle (arrowhead) **(A)**. Middle cerebellar peduncles are hyperintense on FLAIR images (*) **(B)**. A "hot cross bun sign" is well visible in the pons (curved arrow) **(C)**. MSA-C, cerebellar variant of multiple system atrophy.

Thus, they could be used as clinical biomarkers for MSA (level 2). Other level 2 biomarkers include the characteristic shape of the putamen, T2* and SWI signal decrease and ADC increase in the posterior putamen in MSA-P, and atrophy of the pons, cerebellar peduncles and cerebellum with the cross-bun sign in MSA-C. The potential utility of these measurements for the early diagnosis has to be investigated. Putamen abnormalities assessed by quantitative MRI techniques contribute to the diagnosis of MSA-P as level 2 biomarkers, although there is a significant overlap of diffusivity and R2* values between PSP and MSA-P. Other potential clinical biomarkers include diffusivity in the MCP and the cerebellum.

MACHINE-LEARNING-BASED DIFFERENTIATION OF PARKINSONIAN DISORDERS

Very promising results have been obtained by combining fully automated quantitative MRI analysis with machine learning approaches to discriminate between Parkinsonian syndromes (94, 100, 137). Machine learning algorithms first learn to classify individual patients into different diagnostic categories using training data sets and then are applied to a new test data set. The algorithm then classifies each new subject in one of the groups of patients (138). Diagnostic precision is usually assessed with accuracy or balanced accuracy, which takes into account the differences in the number of subjects between the groups (94). A large multicenter study ($n = 464$) including healthy subjects ($n = 73$) and patients with PD (204), PSP-RS (109), MSA-P (20), and MSA-C (59) using a support vector machine (SVM) trained with MRI morphometric data reported balanced accuracies above 80% for between-group classification (94). The volumes of the midbrain, basal ganglia, and cerebellar peduncles had the largest contribution to group differentiation (94). Another volumetric study including 110 Parkinsonian patients in the early to moderate stages of the disease (40 PD, 40 MSA, 30 PSP) using measurements in 22 subcortical regions showed an accuracy of 97.4% for the discrimination of PD from to MSA and PSP (100). In contrast, the diagnostic accuracy using validated clinical consensus criteria obtained at the time of MRI acquisition was only 62.9%. The midbrain, putamen and cerebellar gray matter volumes were the most significant brain regions involved in this classification (100).

Combining volumetric measures with diffusion or iron measures could improve categorization. In one study, the combination of volumetry and DTI metrics allowed 100% accuracy in the discrimination of PD and PSP patients using SVM (99). Adding R2* values to volumetry and DTI metrics resulted in 95% accuracy for the classification of PD, MSA-C and MSA-P patients in another study (139). Machine learning approaches appeared also applicable to data from different clinical departments and MRI scanners. A recent multicenter study used free water and free water-corrected fractional anisotropy measurements as input for a linear SVM algorithm to differentiate between Parkinsonian syndromes (140). This automated pipeline was referred to as automated imaging differentiation in Parkinsonism (AID-P). The study included the largest cohort of subjects to date ($n = 1{,}002$) collected from 17 international sites using MRI scanners from different vendors. Three models were tested, which included diffusion imaging measurements from several brain regions, scores from the Movement Disorders Society Unified Parkinson's Disease Rating Scale part III (MDS-UPDRS III), and both diffusion imaging and MDS-UPDRS III. In the differentiation of PD from atypical Parkinsonism, diffusion imaging plus MDS-UPDRS III showed a significantly higher AUC (0.962) than the MDS-UPDRS III score alone (0.775), similar to that of diffusion imaging alone (0.955). Similarly, diffusion imaging plus MDS-UPDRS III (AUC 0·897) and diffusion imaging alone (AUC 0.926) significantly outperformed MDS-UPDRS III alone (AUC 0.582) in the differentiation of MSA from PSP. Harmonization of diffusion imaging data did not significantly improve the performance of machine learning models. These fully automated approaches promise to be highly generalizable (140). Further studies including PSP variants are needed, however. In addition, validation as part

of the diagnostic assessment of clinical populations would make it possible to implement machine learning approaches in clinical practice.

CONCLUSION

Research using multimodal MRI in Parkinsonian syndromes has enabled the development of several *in vivo* biomarkers, some of which have demonstrated individual-level diagnostic utility. SNpc neurodegeneration in Parkinsonism is evidenced by a reduction in neuromelanin-sensitive signal and a loss of DNH in SWI. Similarly, the decrease in neuromelanin-sensitive signal in the coeruleus/subcoeruleus complex, which is associated with RBD, is an early marker of PD and MSA, and may be considered a surrogate biomarker for the degeneration of catecholaminergic neurons in this complex. However, to date, there is no definitive MRI biomarker of Parkinsonism. Overall, apart from SN changes and from the quantitative changes in specific regions of interest reported in group studies, conventional MRI used in clinical practice is generally normal in early PD patients. The midbrain to pons ratio and the MRPI are robust clinical biomarkers of PSP-RS, while abnormalities in the putamen (atrophy, flattening of the lateral border, T2, T2* and SWI signal changes, and increased diffusivity) and in the pons and cerebellum (atrophy and signal changes) strongly suggest the diagnosis of MSA-P and MSA-C, respectively. Diffusion imaging and R2* relaxometry allow accurate differentiation of groups, but the lack of normative and cut-off values, which vary with scanners, still hampers their use in clinical routine. New consensus criteria for the diagnosis of Parkinsonian syndromes incorporating MRI biomarkers should be considered in the future. Diagnostic accuracy could also benefit from machine learning approaches at a time when artificial intelligence promises to play a growing role in medicine.

AUTHOR CONTRIBUTIONS

LC drafted the manuscript. NP, BD, and DG revised the manuscript. SL drafted and revised the manuscript.

SUPPLEMENTARY MATERIAL

The Supplementary Material for this article can be found online at: https://www.frontiersin.org/articles/10.3389/fneur.2020.00665/full#supplementary-material

REFERENCES

1. Dickson DW. Neuropathology of Parkinson disease. *Parkinsonism Relat Disord.* (2018) 46:S30–3. doi: 10.1016/j.parkreldis.2017.07.033
2. Kalia LV, Lang AE. Parkinson's disease. *Lancet.* (2015) 386:896–912. doi: 10.1016/S0140-6736(14)61393-3
3. Dickson DW. Parkinson's disease and Parkinsonism: neuropathology. *Cold Spring Harb Perspect Med.* (2012) 2:a009258. doi: 10.1101/cshperspect.a009258
4. Castellani R. Multiple system atrophy. *Am J Pathol.* (1998) 153:671–6. doi: 10.1016/S0002-9440(10)65608-8
5. Steele JC, Richardson JC, Olszewski J. Progressive supranuclear palsy: a heterogeneous degeneration involving the brain stem, Basal Ganglia and cerebellum with vertical gaze and pseudobulbar palsy, nuchal dystonia and dementia. *Semin Neurol.* (2014) 34:129–50. doi: 10.1055/s-0034-1377058
6. Dickson DW, Rademakers R, Hutton ML. Progressive supranuclear palsy: pathology and genetics. *Brain Pathol.* (2007) 17:74–82. doi: 10.1111/j.1750-3639.2007.00054.x
7. Fearnley JM, Lees AJ. Ageing and Parkinson's disease: substantia nigra regional selectivity. *Brain.* (1991) 114 (Pt 5):2283–301. doi: 10.1093/brain/114.5.2283
8. Heim B, Krismer F, Seppi K. Structural imaging in Atypical Parkinsonism. *Int Rev Neurobiol.* (2018) 142:67–148. doi: 10.1016/bs.irn.2018.08.010
9. Whitwell JL, Höglinger GU, Antonini A, Bordelon Y, Boxer AL, Colosimo C, et al. Radiological biomarkers for diagnosis in PSP: where are we and where do we need to be? *Mov Disord.* (2017) 32:955–71. doi: 10.1002/mds.27038
10. Kassubek J. MRI-based neuroimaging: atypical Parkinsonisms and other movement disorders. *Curr Opin Neurol.* (2018) 31:425–30. doi: 10.1097/WCO.0000000000000578
11. Lehericy S, Vaillancourt DE, Seppi K, Monchi O, Rektorova I, Antonini A, et al. The role of high-field magnetic resonance imaging in Parkinsonian disorders: pushing the boundaries forward. *Mov Disord.* (2017) 32:510–25. doi: 10.1002/mds.26968
12. Postuma RB, Berg D, Stern M, Poewe W, Olanow CW, Oertel W, et al. MDS clinical diagnostic criteria for Parkinson's disease. *Mov Disord.* (2015) 30:1591–601. doi: 10.1002/mds.26424
13. Rizzo G, Zanigni S, De Blasi R, Grasso D, Martino D, Savica R, et al. Brain MR contribution to the differential diagnosis of Parkinsonian syndromes: an update. *Parkinsons Dis.* (2016) 2016:2983638. doi: 10.1155/2016/2983638
14. Saeed U, Compagnone J, Aviv RI, Strafella AP, Black SE, Lang AE, et al. Imaging biomarkers in Parkinson's disease and Parkinsonian syndromes: current and emerging concepts. *Transl Neurodegener.* (2017) 6:8. doi: 10.1186/s40035-017-0076-6
15. Braak H, Del Tredici K, Rüb U, de Vos RAI, Jansen Steur ENH, Braak E. Staging of brain pathology related to sporadic Parkinson's disease. *Neurobiol Aging.* (2003) 24:197–11. doi: 10.1016/S0197-4580(02)00065-9
16. Del Tredici K, Braak H. Review: sporadic Parkinson's disease: development and distribution of α-synuclein pathology. *Neuropathol Appl Neurobiol.* (2016) 42:33–50. doi: 10.1111/nan.12298
17. Lehéricy S, Bardinet E, Poupon C, Vidailhet M, François C. 7 Tesla magnetic resonance imaging: a closer look at substantia nigra anatomy in Parkinson's disease. *Mov Disord.* (2014) 29:1574–81. doi: 10.1002/mds.26043
18. Pyatigorskaya N, Yahia-Cherif L, Gaurav R, Ewenczyk C, Gallea C, Valabregue R, et al. Multimodal magnetic resonance imaging quantification of brain changes in progressive Supranuclear palsy. *Mov Disord.* (2020) 35:161–70. doi: 10.1002/mds.27877
19. Heim B, Krismer F, de Marzi R, Seppi K. Magnetic resonance imaging for the diagnosis of Parkinson's disease. *J Neural Transm (Vienna).* (2017) 124:915–64. doi: 10.1007/s00702-017-1717-8
20. Reimão S, Pita Lobo P, Neutel D, Guedes LC, Coelho M, Rosa MM, et al. Substantia nigra neuromelanin-MR imaging differentiates essential tremor from Parkinson's disease. *Mov Disord.* (2015) 30:953–9. doi: 10.1002/mds.26182
21. Cassidy CM, Zucca FA, Girgis RR, Baker SC, Weinstein JJ, Sharp ME, et al. Neuromelanin-sensitive MRI as a noninvasive proxy measure of dopamine function in the human brain. *Proc Natl Acad Sci USA.* (2019) 116:5108–17. doi: 10.1073/pnas.1807983116
22. Lehéricy S, Sharman MA, Dos Santos CL, Paquin R, Gallea C. Magnetic resonance imaging of the substantia nigra in Parkinson's disease. *Mov Disord.* (2012) 27:822–30. doi: 10.1002/mds.25015
23. Kitao S, Matsusue E, Fujii S, Miyoshi F, Kaminou T, Kato S, et al. Correlation between pathology and neuromelanin MR imaging in Parkinson's disease and dementia with Lewy bodies. *Neuroradiology.* (2013) 55:947–53. doi: 10.1007/s00234-013-1199-9
24. Sulzer D, Cassidy C, Horga G, Kang UJ, Fahn S, Casella L, et al. Neuromelanin detection by magnetic resonance imaging (MRI) and its promise as a biomarker for Parkinson's disease. *NPJ Parkinson's Dis.* (2018) 4:11. doi: 10.1038/s41531-018-0047-3

25. Sasaki M, Shibata E, Tohyama K, Takahashi J, Otsuka K, Tsuchiya K, et al. Neuromelanin magnetic resonance imaging of locus ceruleus and substantia nigra in Parkinson's disease. *Neuroreport.* (2006) 17:1215–8. doi: 10.1097/01.wnr.0000227984.84927.a7
26. Pyatigorskaya N, Magnin B, Mongin M, Yahia-Cherif L, Valabregue R, Arnaldi D, et al. comparative study of MRI biomarkers in the substantia nigra to discriminate idiopathic Parkinson disease. *Am J Neuroradiol.* (2018) 39:1460–7. doi: 10.3174/ajnr.A5702
27. Ohtsuka C, Sasaki M, Konno K, Kato K, Takahashi J, Yamashita F, et al. Differentiation of early-stage Parkinsonisms using neuromelanin-sensitive magnetic resonance imaging. *Parkinsonism Relat Disord.* (2014) 20:755–60. doi: 10.1016/j.parkreldis.2014.04.005
28. Pyatigorskaya N, Gaurav R, Arnaldi D, Leu-Semenescu S, Yahia-Cherif L, Valabregue R, et al. Magnetic resonance imaging biomarkers to assess substantia nigra damage in idiopathic rapid eye movement sleep behavior disorder. *Sleep.* (2017) 4**0**: doi: 10.1093/sleep/zsx149
29. Arnulf I, Neutel D, Herlin B, Golmard J-L, Leu-Semenescu S, Cochen de Cock V, et al. Sleepiness in idiopathic REM sleep behavior disorder and Parkinson disease. *Sleep.* (2015) 38:1529–35. doi: 10.5665/sleep.5040
30. Boeve BF, Silber MH, Saper CB, Ferman TJ, Dickson DW, Parisi JE, et al. Pathophysiology of REM sleep behaviour disorder and relevance to neurodegenerative disease. *Brain.* (2007) 130:2770–88. doi: 10.1093/brain/awm056
31. Galbiati A, Verga L, Giora E, Zucconi M, Ferini-Strambi L. The risk of neurodegeneration in REM sleep behavior disorder: a systematic review and meta-analysis of longitudinal studies. *Sleep Med Rev.* (2019) 43:37–46. doi: 10.1016/j.smrv.2018.09.008
32. Postuma RB, Gagnon JF, Vendette M, Fantini ML, Massicotte-Marquez J, Montplaisir J. Quantifying the risk of neurodegenerative disease in idiopathic REM sleep behavior disorder. *Neurology.* (2009) 72:1296–300. doi: 10.1212/01.wnl.0000340980.19702.6e
33. Iranzo A, Tolosa E, Gelpi E, Molinuevo JL, Valldeoriola F, Serradell M, et al. Neurodegenerative disease status and post-mortem pathology in idiopathic rapid-eye-movement sleep behaviour disorder: an observational cohort study. *Lancet Neurol.* (2013) 12:443–53. doi: 10.1016/S1474-4422(13)70056-5
34. Schwarz ST, Afzal M, Morgan PS, Bajaj N, Gowland PA, Auer DP. The "swallow tail" appearance of the healthy nigrosome–a new accurate test of Parkinson's disease: a case-control and retrospective cross-sectional MRI study at 3T. *PLoS ONE.* (2014) 9:e93814. doi: 10.1371/journal.pone.0093814
35. Damier P, Hirsch EC, Agid Y, Graybiel AM. The substantia nigra of the human brain. I. Nigrosomes and the nigral matrix, a compartmental organization based on calbindin D(28K) immunohistochemistry. *Brain.* (1999) 122 (Pt 8):1421–36. doi: 10.1093/brain/122.8.1421
36. Mahlknecht P, Krismer F, Poewe W, Seppi K. Meta-analysis of dorsolateral nigral hyperintensity on magnetic resonance imaging as a marker for Parkinson's disease. *Mov Disord.* (2017) 32:619–23. doi: 10.1002/mds.26932
37. Reiter E, Mueller C, Pinter B, Krismer F, Scherfler C, Esterhammer R, et al. Dorsolateral nigral hyperintensity on 3.0T susceptibility-weighted imaging in neurodegenerative Parkinsonism. *Mov Disord.* (2015) 30:1068–76. doi: 10.1002/mds.26171
38. De Marzi R, Seppi K, Högl B, Müller C, Scherfler C, Stefani A, et al. Loss of dorsolateral nigral hyperintensity on 3.0 tesla susceptibility-weighted imaging in idiopathic rapid eye movement sleep behavior disorder. *Ann Neurol.* (2016) 79:1026–30. doi: 10.1002/ana.24646
39. Ehrminger M, Latimier A, Pyatigorskaya N, Garcia-Lorenzo D, Leu-Semenescu S, Vidailhet M, et al. The coeruleus/subcoeruleus complex in idiopathic rapid eye movement sleep behaviour disorder. *Brain.* (2016) 139:1180–8. doi: 10.1093/brain/aww006
40. García-Lorenzo D, Longo-Dos Santos C, Ewenczyk C, Leu-Semenescu S, Gallea C, Quattrocchi G, et al. The coeruleus/subcoeruleus complex in rapid eye movement sleep behaviour disorders in Parkinson's disease. *Brain.* (2013) 136:2120–9. doi: 10.1093/brain/awt152
41. Knudsen K, Fedorova TD, Hansen AK, Sommerauer M, Otto M, Svendsen KB, et al. *In-vivo* staging of pathology in REM sleep behaviour disorder: a multimodality imaging case-control study. *Lancet Neurol.* (2018) 17:618–28. doi: 10.1016/S1474-4422(18)30162-5
42. Rizzo G, Copetti M, Arcuti S, Martino D, Fontana A, Logroscino G. Accuracy of clinical diagnosis of Parkinson disease: a systematic review and meta-analysis. *Neurology.* (2016) 86:566–76. doi: 10.1212/WNL.0000000000002350
43. Mangesius S, Hussl A, Krismer F, Mahlknecht P, Reiter E, Tagwercher S, et al. MR planimetry in neurodegenerative Parkinsonism yields high diagnostic accuracy for PSP. *Parkinsonism Relat Disord.* (2018) 46:47–55. doi: 10.1016/j.parkreldis.2017.10.020
44. Righini A, Antonini A, De Notaris R, Bianchini E, Meucci N, Sacilotto G, et al. MR imaging of the superior profile of the midbrain: differential diagnosis between progressive supranuclear palsy and Parkinson disease. *AJNR Am J Neuroradiol.* (2004) 25:927–32.
45. Möller L, Kassubek J, Südmeyer M, Hilker R, Hattingen E, Egger K, et al. Manual MRI morphometry in Parkinsonian syndromes. *Mov Disord.* (2017) 32:778–82. doi: 10.1002/mds.26921
46. Quattrone A, Nicoletti G, Messina D, Fera F, Condino F, Pugliese P, et al. MR imaging index for differentiation of progressive supranuclear palsy from Parkinson disease and the Parkinson variant of multiple system atrophy. *Radiology.* (2008) 246:214–21. doi: 10.1148/radiol.2453061703
47. Paviour DC, Price SL, Jahanshahi M, Lees AJ, Fox NC. Longitudinal MRI in progressive supranuclear palsy and multiple system atrophy: rates and regions of atrophy. *Brain.* (2006) 129:1040–9. doi: 10.1093/brain/awl021
48. Messina D, Cerasa A, Condino F, Arabia G, Novellino F, Nicoletti G, et al. Patterns of brain atrophy in Parkinson's disease, progressive supranuclear palsy and multiple system atrophy. *Parkinsonism Relat Disord.* (2011) 17:172–6. doi: 10.1016/j.parkreldis.2010.12.010
49. Yu F, Barron DS, Tantiwongkosi B, Fox P. Patterns of gray matter atrophy in atypical Parkinsonism syndromes: a VBM meta-analysis. *Brain Behav.* (2015) 5:e00329. doi: 10.1002/brb3.329
50. Compta Y, Pereira JB, Ríos J, Ibarretxe-Bilbao N, Junqué C, Bargalló N, et al. Combined dementia-risk biomarkers in Parkinson's disease: a prospective longitudinal study. *Parkinsonism Relat Disord.* (2013) 19:717–24. doi: 10.1016/j.parkreldis.2013.03.009
51. Delgado-Alvarado M, Gago B, Navalpotro-Gomez I, Jiménez-Urbieta H, Rodriguez-Oroz MC. Biomarkers for dementia and mild cognitive impairment in Parkinson's disease. *Mov Disord.* (2016) 31:861–81. doi: 10.1002/mds.26662
52. Gratwicke J, Jahanshahi M, Foltynie T. Parkinson's disease dementia: a neural networks perspective. *Brain.* (2015) 138:1454–76. doi: 10.1093/brain/awv104
53. Vaillancourt DE, Spraker MB, Prodoehl J, Abraham I, Corcos DM, Zhou XJ, et al. High-resolution diffusion tensor imaging in the substantia nigra of *de novo* Parkinson disease. *Neurology.* (2009) 72:1378–84. doi: 10.1212/01.wnl.0000340982.01727.6e
54. Schwarz ST, Abaei M, Gontu V, Morgan PS, Bajaj N, Auer DP. Diffusion tensor imaging of nigral degeneration in Parkinson's disease: a region-of-interest and voxel-based study at 3 T and systematic review with meta-analysis. *Neuroimage Clin.* (2013) 3:481–8. doi: 10.1016/j.nicl.2013.10.006
55. Cochrane CJ, Ebmeier KP. Diffusion tensor imaging in Parkinsonian syndromes: a systematic review and meta-analysis. *Neurology.* (2013) 80:857–64. doi: 10.1212/WNL.0b013e318284070c
56. Atkinson-Clement C, Pinto S, Eusebio A, Coulon O. Diffusion tensor imaging in Parkinson's disease: review and meta-analysis. *Neuroimage Clin.* (2017) 16:98–110. doi: 10.1016/j.nicl.2017.07.011
57. Bajaj S, Krismer F, Palma J-A, Wenning GK, Kaufmann H, Poewe W, et al. Diffusion-weighted MRI distinguishes Parkinson disease from the Parkinsonian variant of multiple system atrophy: a systematic review and meta-analysis. *PLoS ONE.* (2017) 12:e0189897. doi: 10.1371/journal.pone.0189897
58. Nicoletti G, Lodi R, Condino F, Tonon C, Fera F, Malucelli E, et al. Apparent diffusion coefficient measurements of the middle cerebellar peduncle differentiate the Parkinson variant of MSA from Parkinson's disease and progressive supranuclear palsy. *Brain.* (2006) 129:2679–87. doi: 10.1093/brain/awl166
59. Pellecchia MT, Barone P, Mollica C, Salvatore E, Ianniciello M, Longo K, et al. Diffusion-weighted imaging in multiple system atrophy: a comparison between clinical subtypes. *Mov Disord.* (2009) 24:689–96. doi: 10.1002/mds.22440
60. Pellecchia MT, Barone P, Vicidomini C, Mollica C, Salvatore E, Ianniciello M, et al. Progression of striatal and extrastriatal degeneration in multiple system atrophy: a longitudinal diffusion-weighted MR study. *Mov Disord.* (2011) 26:1303–9. doi: 10.1002/mds.23601

61. Barbagallo G, Sierra-Peña M, Nemmi F, Traon AP-L, Meissner WG, Rascol O, et al. Multimodal MRI assessment of nigro-striatal pathway in multiple system atrophy and Parkinson disease. *Mov Disord.* (2016) 31:325–34. doi: 10.1002/mds.26471
62. Surova Y, Nilsson M, Lätt J, Lampinen B, Lindberg O, Hall S, et al. Disease-specific structural changes in thalamus and dentatorubrothalamic tract in progressive supranuclear palsy. *Neuroradiology.* (2015) 57:1079–91. doi: 10.1007/s00234-015-1563-z
63. Tsukamoto K, Matsusue E, Kanasaki Y, Kakite S, Fujii S, Kaminou T, et al. Significance of apparent diffusion coefficient measurement for the differential diagnosis of multiple system atrophy, progressive supranuclear palsy, and Parkinson's disease: evaluation by 3.0-T MR imaging. *Neuroradiology.* (2012) 54:947–55. doi: 10.1007/s00234-012-1009-9
64. Chen B, Fan G, Sun W, Shang X, Shi S, Wang S, et al. Usefulness of diffusion-tensor MRI in the diagnosis of Parkinson variant of multiple system atrophy and Parkinson's disease: a valuable tool to differentiate between them? *Clin Radiol.* (2017) 72:610.e9–15. doi: 10.1016/j.crad.2017.02.005
65. Nicoletti G, Rizzo G, Barbagallo G, Tonon C, Condino F, Manners D, et al. Diffusivity of cerebellar hemispheres enables discrimination of cerebellar or Parkinsonian multiple system atrophy from progressive supranuclear palsy-Richardson syndrome and Parkinson disease. *Radiology.* (2013) 267:843–50. doi: 10.1148/radiol.12120364
66. Planetta PJ, Ofori E, Pasternak O, Burciu RG, Shukla P, DeSimone JC, et al. Free-water imaging in Parkinson's disease and atypical Parkinsonism. *Brain.* (2016) 139:495–508. doi: 10.1093/brain/awv361
67. Ofori E, Pasternak O, Planetta PJ, Li H, Burciu RG, Snyder AF, et al. Longitudinal changes in free-water within the substantia nigra of Parkinson's disease. *Brain.* (2015) 138:2322–31. doi: 10.1093/brain/awv136
68. Gallea C, Ewenczyk C, Degos B, Welter M-L, Grabli D, Leu-Semenescu S, et al. Pedunculopontine network dysfunction in Parkinson's disease with postural control and sleep disorders. *Mov Disord.* (2017) 32:693–704. doi: 10.1002/mds.26923
69. Pyatigorskaya N, Mongin M, Valabregue R, Yahia-Cherif L, Ewenczyk C, Poupon C, et al. Medulla oblongata damage and cardiac autonomic dysfunction in Parkinson disease. *Neurology.* (2016) 87:2540–5. doi: 10.1212/WNL.0000000000003426
70. Schulz J, Pagano G, Fernández Bonfante JA, Wilson H, Politis M. Nucleus basalis of Meynert degeneration precedes and predicts cognitive impairment in Parkinson's disease. *Brain.* (2018) 141:1501–16. doi: 10.1093/brain/awy072
71. Barbosa JHO, Santos AC, Tumas V, Liu M, Zheng W, Haacke EM, et al. Quantifying brain iron deposition in patients with Parkinson's disease using quantitative susceptibility mapping, R2 and R2. *Magn Reson Imaging.* (2015) 33:559–65. doi: 10.1016/j.mri.2015.02.021
72. Du G, Lewis MM, Kanekar S, Sterling NW, He L, Kong L, et al. Combined diffusion tensor imaging and apparent transverse relaxation rate differentiate Parkinson disease and Atypical Parkinsonism. *AJNR Am J Neuroradiol.* (2017) 38:966–72. doi: 10.3174/ajnr.A5136
73. Guan X, Xuan M, Gu Q, Huang P, Liu C, Wang N, et al. Regionally progressive accumulation of iron in Parkinson's disease as measured by quantitative susceptibility mapping. *NMR Biomed.* (2017) 30:3489. doi: 10.1002/nbm.3489
74. Sjöström H, Granberg T, Westman E, Svenningsson P. Quantitative susceptibility mapping differentiates between Parkinsonian disorders. *Parkinsonism Relat Disord.* (2017) 44:51–7. doi: 10.1016/j.parkreldis.2017.08.029
75. Deistung A, Schäfer A, Schweser F, Biedermann U, Turner R, Reichenbach JR. Toward *in vivo* histology: a comparison of quantitative susceptibility mapping (QSM) with magnitude-, phase-, and R2*-imaging at ultra-high magnetic field strength. *Neuroimage.* (2013) 65:299–314. doi: 10.1016/j.neuroimage.2012.09.055
76. Deistung A, Schweser F, Reichenbach JR. Overview of quantitative susceptibility mapping. *NMR Biomed.* (2017) 30:3569. doi: 10.1002/nbm.3569
77. Lee J-H, Han Y-H, Kang B-M, Mun C-W, Lee S-J, Baik S-K. Quantitative assessment of subcortical atrophy and iron content in progressive supranuclear palsy and Parkinsonian variant of multiple system atrophy. *J Neurol.* (2013) 260:2094–101. doi: 10.1007/s00415-013-6951-x
78. Levin J, Kurz A, Arzberger T, Giese A, Höglinger GU. The differential diagnosis and treatment of Atypical Parkinsonism. *Dtsch Arztebl Int.* (2016) 113:61–9. doi: 10.3238/arztebl.2016.0061
79. Höglinger GU, Respondek G, Stamelou M, Kurz C, Josephs KA, Lang AE, et al. Clinical diagnosis of progressive supranuclear palsy: the movement disorder society criteria. *Mov Disord.* (2017) 32:853–64. doi: 10.1002/mds.26987.
80. Litvan I, Agid Y, Calne D, Campbell G, Dubois B, Duvoisin RC, et al. Clinical research criteria for the diagnosis of progressive supranuclear palsy (Steele-Richardson-Olszewski syndrome): report of the NINDS-SPSP international workshop. *Neurology.* (1996) 47:1–9. doi: 10.1212/WNL.47.1.1
81. Kashihara K, Shinya T, Higaki F. Reduction of neuromelanin-positive nigral volume in patients with MSA, PSP and CBD. *Intern Med.* (2011) 50:1683–7. doi: 10.2169/internalmedicine.50.5101
82. Martin-Bastida A, Pietracupa S, Piccini P. Neuromelanin in Parkinsonian disorders: an update. *Int J Neurosci.* (2017) 127:1116–23. doi: 10.1080/00207454.2017.1325883
83. Oba H, Yagishita A, Terada H, Barkovich AJ, Kutomi K, Yamauchi T, et al. New and reliable MRI diagnosis for progressive supranuclear palsy. *Neurology.* (2005) 64:2050–5. doi: 10.1212/01.WNL.0000165960.04422.D0
84. Kato N, Arai K, Hattori T. Study of the rostral midbrain atrophy in progressive supranuclear palsy. *J Neurol Sci.* (2003) 210:57–60. doi: 10.1016/S0022-510X(03)00014-5
85. Quattrone A, Morelli M, Nigro S, Quattrone A, Vescio B, Arabia G, et al. A new MR imaging index for differentiation of progressive supranuclear palsy-Parkinsonism from Parkinson's disease. *Parkinsonism Relat Disord.* (2018) 54:3–8. doi: 10.1016/j.parkreldis.2018.07.016
86. Adachi M, Kawanami T, Ohshima H, Sugai Y, Hosoya T. Morning glory sign: a particular MR finding in progressive supranuclear palsy. *Magn Reson Med Sci.* (2004) 3:125–32. doi: 10.2463/mrms.3.125
87. Mueller C, Hussl A, Krismer F, Heim B, Mahlknecht P, Nocker M, et al. The diagnostic accuracy of the hummingbird and morning glory sign in patients with neurodegenerative Parkinsonism. *Parkinsonism Relat Disord.* (2018) 54:90–4. doi: 10.1016/j.parkreldis.2018.04.005
88. Paviour DC, Price SL, Stevens JM, Lees AJ, Fox NC. Quantitative MRI measurement of superior cerebellar peduncle in progressive supranuclear palsy. *Neurology.* (2005) 64:675–9. doi: 10.1212/01.WNL.0000151854.85743.C7
89. Kataoka H, Nishimori Y, Kiriyama T, Nanaura H, Izumi T, Eura N, et al. Increased signal in the superior cerebellar peduncle of patients with progressive Supranuclear Palsy. *J Mov Disord.* (2019) 12:166–71. doi: 10.14802/jmd.19002
90. Nicoletti G, Tonon C, Lodi R, Condino F, Manners D, Malucelli E, et al. Apparent diffusion coefficient of the superior cerebellar peduncle differentiates progressive supranuclear palsy from Parkinson's disease. *Mov Disord.* (2008) 23:2370–6. doi: 10.1002/mds.22279
91. Schocke MFH, Seppi K, Esterhammer R, Kremser C, Mair KJ, Czermak BV, et al. Trace of diffusion tensor differentiates the Parkinson variant of multiple system atrophy and Parkinson's disease. *Neuroimage.* (2004) 21:1443–51. doi: 10.1016/j.neuroimage.2003.12.005
92. Seppi K, Schocke MFH, Esterhammer R, Kremser C, Brenneis C, Mueller J, et al. Diffusion-weighted imaging discriminates progressive supranuclear palsy from PD, but not from the Parkinson variant of multiple system atrophy. *Neurology.* (2003) 60:922–7. doi: 10.1212/01.WNL.0000049911.91657.9D
93. Worker A, Blain C, Jarosz J, Chaudhuri KR, Barker GJ, Williams SCR, et al. Cortical thickness, surface area and volume measures in Parkinson's disease, multiple system atrophy and progressive supranuclear palsy. *PLoS ONE.* (2014) 9:e114167. doi: 10.1371/journal.pone.0114167
94. Huppertz H-J, Möller L, Südmeyer M, Hilker R, Hattingen E, Egger K, et al. Differentiation of neurodegenerative Parkinsonian syndromes by volumetric magnetic resonance imaging analysis and support vector machine classification. *Mov Disord.* (2016) 31:1506–17. doi: 10.1002/mds.26715
95. Morelli M, Arabia G, Novellino F, Salsone M, Giofrè L, Condino F, et al. MRI measurements predict PSP in unclassifiable Parkinsonisms: a cohort study. *Neurology.* (2011) 77:1042–7. doi: 10.1212/WNL.0b013e31822e55d0

96. Nigro S, Arabia G, Antonini A, Weis L, Marcante A, Tessitore A, et al. Magnetic resonance Parkinsonism index: diagnostic accuracy of a fully automated algorithm in comparison with the manual measurement in a large Italian multicentre study in patients with progressive supranuclear palsy. *Eur Radiol.* (2017) 27:2665–75. doi: 10.1007/s00330-016-4622-x
97. Nigro S, Antonini A, Vaillancourt DE, Seppi K, Ceravolo R, Strafella AP, et al. Automated MRI classification in progressive Supranuclear palsy: a large International Cohort study. *Mov Disord.* (2020) 35:976–83. doi: 10.1002/mds.28007
98. Quattrone A, Morelli M, Williams DR, Vescio B, Arabia G, Nigro S, et al. MR Parkinsonism index predicts vertical supranuclear gaze palsy in patients with PSP-Parkinsonism. *Neurology.* (2016) 87:1266–73. doi: 10.1212/WNL.0000000000003125
99. Cherubini A, Morelli M, Nisticó R, Salsone M, Arabia G, Vasta R, et al. Magnetic resonance support vector machine discriminates between Parkinson disease and progressive supranuclear palsy. *Mov Disord.* (2014) 29:266–9. doi: 10.1002/mds.25737
100. Scherfler C, Göbel G, Müller C, Nocker M, Wenning GK, Schocke M, et al. Diagnostic potential of automated subcortical volume segmentation in atypical Parkinsonism. *Neurology.* (2016) 86:1242–9. doi: 10.1212/WNL.0000000000002518
101. Quattrone A, Morelli M, Quattrone A, Vescio B, Nigro S, Arabia G, et al. Magnetic resonance Parkinsonism index for evaluating disease progression rate in progressive supranuclear palsy: a longitudinal 2-year study. *Parkinsonism Relat Disord.* (2020) 72:1–6. doi: 10.1016/j.parkreldis.2020.01.019
102. Whitwell JL, Jack CR, Parisi JE, Gunter JL, Weigand SD, Boeve BF, et al. Midbrain atrophy is not a biomarker of progressive supranuclear palsy pathology. *Eur J Neurol.* (2013) 20:1417–22. doi: 10.1111/ene.12212
103. Agosta F, Kostić VS, Galantucci S, Mesaros S, Svetel M, Pagani E, et al. The *in vivo* distribution of brain tissue loss in Richardson's syndrome and PSP-Parkinsonism: a VBM-DARTEL study. *Eur J Neurosci.* (2010) 32:640–7. doi: 10.1111/j.1460-9568.2010.07304.x
104. Whitwell JL, Duffy JR, Strand EA, Machulda MM, Senjem ML, Gunter JL, et al. Neuroimaging comparison of primary progressive apraxia of speech and progressive supranuclear palsy. *Eur J Neurol.* (2013) 20:629–37. doi: 10.1111/ene.12004
105. Josephs KA, Duffy JR, Strand EA, Machulda MM, Senjem ML, Master AV, et al. Characterizing a neurodegenerative syndrome: primary progressive apraxia of speech. *Brain.* (2012) 135:1522–36. doi: 10.1093/brain/aws032
106. Hassan A, Parisi JE, Josephs KA. Autopsy-proven progressive supranuclear palsy presenting as behavioral variant frontotemporal dementia. *Neurocase.* (2012) 18:478–88. doi: 10.1080/13554794.2011.627345
107. Longoni G, Agosta F, Kostić VS, Stojković T, Pagani E, Stošić-Opinćal T, et al. MRI measurements of brainstem structures in patients with Richardson's syndrome, progressive supranuclear palsy-Parkinsonism, and Parkinson's disease. *Mov Disord.* (2011) 26:247–55. doi: 10.1002/mds.23293
108. Santos-Santos MA, Mandelli ML, Binney RJ, Ogar J, Wilson SM, Henry ML, et al. Features of patients with Nonfluent/Agrammatic primary progressive aphasia with underlying progressive supranuclear palsy pathology or corticobasal degeneration. *JAMA Neurol.* (2016) 73:733–42. doi: 10.1001/jamaneurol.2016.0412
109. Whitwell JL, Jack CR, Boeve BF, Parisi JE, Ahlskog JE, Drubach DA, et al. Imaging correlates of pathology in corticobasal syndrome. *Neurology.* (2010) 75:1879–87. doi: 10.1212/WNL.0b013e3181feb2e8
110. Lehéricy S, Hartmann A, Lannuzel A, Galanaud D, Delmaire C, Bienaimée M-J, et al. Magnetic resonance imaging lesion pattern in Guadeloupean Parkinsonism is distinct from progressive supranuclear palsy. *Brain.* (2010) 133:2410–25. doi: 10.1093/brain/awq162
111. Rizzo G, Martinelli P, Manners D, Scaglione C, Tonon C, Cortelli P, et al. Diffusion-weighted brain imaging study of patients with clinical diagnosis of corticobasal degeneration, progressive supranuclear palsy and Parkinson's disease. *Brain.* (2008) 131:2690–700. doi: 10.1093/brain/awn195
112. Mahlknecht P, Hotter A, Hussl A, Esterhammer R, Schocke M, Seppi K. Significance of MRI in diagnosis and differential diagnosis of Parkinson's disease. *Neurodegener Dis.* (2010) 7:300–18. doi: 10.1159/000314495
113. Focke NK, Helms G, Pantel PM, Scheewe S, Knauth M, Bachmann CG, et al. Differentiation of typical and atypical Parkinson syndromes by quantitative MR imaging. *Am J Neuroradiol.* (2011) 32:2087–92. doi: 10.3174/ajnr.A2865
114. Boelmans K, Holst B, Hackius M, Finsterbusch J, Gerloff C, Fiehler J, et al. Brain iron deposition fingerprints in Parkinson's disease and progressive supranuclear palsy. *Mov Disord.* (2012) 27:421–7. doi: 10.1002/mds.24926
115. Han Y-H, Lee J-H, Kang B-M, Mun C-W, Baik S-K, Shin Y-I, et al. Topographical differences of brain iron deposition between progressive supranuclear palsy and Parkinsonian variant multiple system atrophy. *J Neurol Sci.* (2013) 325:29–35. doi: 10.1016/j.jns.2012.11.009
116. Eckert T, Sailer M, Kaufmann J, Schrader C, Peschel T, Bodammer N, et al. Differentiation of idiopathic Parkinson's disease, multiple system atrophy, progressive supranuclear palsy, and healthy controls using magnetization transfer imaging. *Neuroimage.* (2004) 21:229–35. doi: 10.1016/j.neuroimage.2003.08.028
117. Abe K, Terakawa H, Takanashi M, Watanabe Y, Tanaka H, Fujita N, et al. Proton magnetic resonance spectroscopy of patients with Parkinsonism. *Brain Res Bull.* (2000) 52:589–95. doi: 10.1016/S0361-9230(00)00321-X
118. Davie CA, Barker GJ, Machado C, Miller DH, Lees AJ. Proton magnetic resonance spectroscopy in Steele-Richardson-Olszewski syndrome. *Mov Disord.* (1997) 12:767–71. doi: 10.1002/mds.870120525
119. Federico F, Simone IL, Lucivero V, de Mari M, Giannini P, Iliceto G, et al. Proton magnetic resonance spectroscopy in Parkinson's disease and progressive supranuclear palsy. *J Neurol Neurosurg Psychiatry.* (1997) 62:239–42. doi: 10.1136/jnnp.62.3.239
120. Guevara CA, Blain CR, Stahl D, Lythgoe DJ, Leigh PN, Barker GJ. Quantitative magnetic resonance spectroscopic imaging in Parkinson's disease, progressive supranuclear palsy and multiple system atrophy. *Eur J Neurol.* (2010) 17:1193–202. doi: 10.1111/j.1468-1331.2010.03010.x
121. Tedeschi G, Litvan I, Bonavita S, Bertolino A, Lundbom N, Patronas NJ, et al. Proton magnetic resonance spectroscopic imaging in progressive supranuclear palsy, Parkinson's disease and corticobasal degeneration. *Brain.* (1997) 120 (Pt 9):1541–52. doi: 10.1093/brain/120.9.1541
122. Gardner RC, Boxer AL, Trujillo A, Mirsky JB, Guo CC, Gennatas ED, et al. Intrinsic connectivity network disruption in progressive supranuclear palsy. *Ann Neurol.* (2013) 73:603–16. doi: 10.1002/ana.23844
123. Whitwell JL, Avula R, Master A, Vemuri P, Senjem ML, Jones DT, et al. Disrupted thalamocortical connectivity in PSP: a resting-state fMRI, DTI, and VBM study. *Parkinsonism Relat Disord.* (2011) 17:599–605. doi: 10.1016/j.parkreldis.2011.05.013
124. Bhattacharya K, Saadia D, Eisenkraft B, Yahr M, Olanow W, Drayer B, et al. Brain magnetic resonance imaging in multiple-system atrophy and Parkinson disease: a diagnostic algorithm. *Arch Neurol.* (2002) 59:835–42. doi: 10.1001/archneur.59.5.835
125. Lehericy S, Bensimon G, Vidailhet M. Parkinsonian syndromes. In: Toga AW editor. *Brain Mapping* (Waltham: Academic Press), 769–85. doi: 10.1016/B978-0-12-397025-1.00088-9
126. Watanabe H, Saito Y, Terao S, Ando T, Kachi T, Mukai E, et al. Progression and prognosis in multiple system atrophy: an analysis of 230 Japanese patients. *Brain.* (2002) 125:1070–83. doi: 10.1093/brain/awf117
127. Watanabe H, Ito M, Fukatsu H, Senda J, Atsuta N, Kaga T, et al. Putaminal magnetic resonance imaging features at various magnetic field strengths in multiple system atrophy. *Mov Disord.* (2010) 25:1916–23. doi: 10.1002/mds.23196
128. Way C, Pettersson D, Hiller A. The "hot cross bun" sign is not always multiple system Atrophy: etiologies of 11 cases. *J Mov Disord.* (2019) 12:27–30. doi: 10.14802/jmd.18
129. Seppi K, Schocke MFH, Prennschuetz-Schuetzenau K, Mair KJ, Esterhammer R, Kremser C, et al. Topography of putaminal degeneration in multiple system atrophy: a diffusion magnetic resonance study. *Mov Disord.* (2006) 21:847–52. doi: 10.1002/mds.20843
130. Seppi K, Schocke MFH, Mair KJ, Esterhammer R, Scherfler C, Geser F, et al. Progression of putaminal degeneration in multiple system atrophy: a serial diffusion MR study. *Neuroimage.* (2006) 31:240–5. doi: 10.1016/j.neuroimage.2005.12.006
131. Prakash N, Hageman N, Hua X, Toga AW, Perlman SL, Salamon N. Patterns of fractional anisotropy changes in white matter of cerebellar peduncles distinguish spinocerebellar ataxia-1 from multiple

system atrophy and other ataxia syndromes. *Neuroimage.* (2009) 47:T72–81. doi: 10.1016/j.neuroimage.2009.05.013
132. Oishi K, Konishi J, Mori S, Ishihara H, Kawamitsu H, Fujii M, et al. Reduced fractional anisotropy in early-stage cerebellar variant of multiple system atrophy. *J Neuroimaging.* (2009) 19:127–31. doi: 10.1111/j.1552-6569.2008.00262.x
133. Yoon RG, Kim SJ, Kim HS, Choi CG, Kim JS, Oh J, et al. The utility of susceptibility-weighted imaging for differentiating Parkinsonism-predominant multiple system atrophy from Parkinson's disease: correlation with 18F-flurodeoxyglucose positron-emission tomography. *Neurosci Lett.* (2015) 584:296–301. doi: 10.1016/j.neulet.2014.10.046
134. Zanigni S, Evangelisti S, Testa C, Manners DN, Calandra-Buonaura G, Guarino M, et al. White matter and cortical changes in atypical Parkinsonisms: a multimodal quantitative MR study. *Parkinsonism Relat Disord.* (2017) 39:44–51. doi: 10.1016/j.parkreldis.2017.03.001
135. Watanabe H, Fukatsu H, Katsuno M, Sugiura M, Hamada K, Okada Y, et al. Multiple regional 1H-MR spectroscopy in multiple system atrophy: NAA/Cr reduction in pontine base as a valuable diagnostic marker. *J Neurol Neurosurg Psychiatry.* (2004) 75:103–9.
136. Agosta F, Sarasso E, Filippi M. Functional MRI in Atypical Parkinsonisms. *Int Rev Neurobiol.* (2018) 142:149–73. doi: 10.1016/bs.irn.2018.09.002
137. Salvatore C, Cerasa A, Castiglioni I, Gallivanone F, Augimeri A, Lopez M, et al. Machine learning on brain MRI data for differential diagnosis of Parkinson's disease and progressive Supranuclear palsy. *J Neurosci Methods.* (2014) 222:230–7. doi: 10.1016/j.jneumeth.2013.11.016
138. Orrù G, Pettersson-Yeo W, Marquand AF, Sartori G, Mechelli A. Using support vector machine to identify imaging biomarkers of neurological and psychiatric disease: a critical review. *Neurosci Biobehav Rev.* (2012) 36:1140–52. doi: 10.1016/j.neubiorev.2012.01.004
139. Péran P, Barbagallo G, Nemmi F, Sierra M, Galitzky M, Traon AP-L, et al. MRI supervised and unsupervised classification of Parkinson's disease and multiple system atrophy. *Mov Disord.* (2018) 33:600–8. doi: 10.1002/mds.27307
140. Archer DB, Bricker JT, Chu WT, Burciu RG, McCracken JL. *Development and Validation of the Automated Imaging Differentiation in Parkinsonism (AID-P): A Multicentre Machine Learning Study–The Lancet Digital Health.* Available online at: https://www.thelancet.com/journals/landig/article/PIIS2589-7500(19)30105-0/fulltext (accessed December 13, 2019).

Conflict of Interest: BD received research support grants from Fondation de France, Inserm, ANR; speech honoraria from Ipsen, Merz Pharma, Orkyn; and received travel funding from Merz Pharma, Elivie, Orkyn. SL received grants from Investissements d'avenir [grant numbers ANR-10-IAIHU-06 and ANR-11-INBS-0006] and Biogen Inc.

The remaining authors declare that the research was conducted in the absence of any commercial or financial relationships that could be construed as a potential conflict of interest.

Copyright © 2020 Chougar, Pyatigorskaya, Degos, Grabli and Lehéricy. This is an open-access article distributed under the terms of the Creative Commons Attribution License (CC BY). The use, distribution or reproduction in other forums is permitted, provided the original author(s) and the copyright owner(s) are credited and that the original publication in this journal is cited, in accordance with accepted academic practice. No use, distribution or reproduction is permitted which does not comply with these terms.

frontiers in Neurology

ORIGINAL RESEARCH
published: 28 July 2020
doi: 10.3389/fneur.2020.00727

Abnormal Spontaneous Brain Activity in Left-Onset Parkinson Disease: A Resting-State Functional MRI Study

Kai Li[1†], Wen Su[1,2†], Min Chen[3], Chun-Mei Li[3], Xin-Xin Ma[1], Rui Wang[3], Bao-Hui Lou[3], Hong Zhao[1], Hai-Bo Chen[1] and Chuan-Zhu Yan[2*]*

[1] Department of Neurology, National Center of Gerontology, Beijing Hospital, Beijing, China, [2] Department of Neurology, Research Institute of Neuromuscular and Neurodegenerative Disease, Qilu Hospital of Shandong University, Jinan, China, [3] Department of Radiology, National Center of Gerontology, Beijing Hospital, Beijing, China

Objective: Motor asymmetry is characteristic in Parkinson disease (PD). This phenomenon is originated from uneven degeneration of bilateral substantia nigra. However, this asymmetry may not restrict to substantia nigra or striatum. We aimed to determine the effect of asymmetry on spontaneous brain activity across the whole brain.

Methods: We consecutively recruited 71 patients with PD, as well as 35 healthy controls, and collected relevant demographic, clinical, and neuropsychological information. The PD patients were divided into two groups according to the side of motor symptom onset. All the participants underwent resting-state functional magnetic resonance imaging, and spontaneous brain activity was assessed using amplitude of low-frequency fluctuation (ALFF). The associations between areas showing significant group differences and various clinical and neuropsychological measures were analyzed.

Results: Finally, the data of 30 PD patients with left-onset (LPD), 27 PD patients with right-onset (RPD), and 32 healthy controls were obtained. The three groups had similar age and gender ratios. Our results demonstrated that LPD patients had increased ALFF in the left inferior temporal gyrus and decreased ALFF in bilateral thalamus and cerebellum anterior lobes than the control group. The value of ALFF of the left inferior temporal gyrus was correlated with motor function, and ALFF value of the thalamus was associated with cognition. Comparisons between LPD and RPD patients and between RPD patients and the controls did not yield significant difference.

Conclusions: The present study provides new insights into the distinct characteristics of spontaneous brain activity in LPD, which may be associated with motor and cognitive function.

Keywords: Parkinson's disease, resting-state functional MRI (rs-fMRI), amplitude of low frequency fluctuation (ALFF), asymmetry, spontaneous brain activity

OPEN ACCESS

Edited by:
Wang Zhan,
University of Maryland, College Park, United States

Reviewed by:
Pedro Ribeiro,
Federal University of Rio de Janeiro, Brazil
Silmar Teixeira,
Federal University of Piauí, Brazil

***Correspondence:**
Hai-Bo Chen
chenhb_bjh@hotmail.com;
chenhbneuro@263.net
Chuan-Zhu Yan
chuanzhuyan@163.com

[†]These authors have contributed equally to this work

Specialty section:
This article was submitted to Movement Disorders, a section of the journal Frontiers in Neurology

Received: *13 January 2020*
Accepted: *15 June 2020*
Published: *28 July 2020*

Citation:
Li K, Su W, Chen M, Li C-M, Ma X-X, Wang R, Lou B-H, Zhao H, Chen H-B and Yan C-Z (2020) Abnormal Spontaneous Brain Activity in Left-Onset Parkinson Disease: A Resting-State Functional MRI Study. Front. Neurol. 11:727. doi: 10.3389/fneur.2020.00727

INTRODUCTION

Parkinson disease (PD) is a common neurodegenerative disorder and manifests as motor symptoms including bradykinesia, resting tremor, and rigidity, as well as a series of non-motor symptoms (1). One enigmatic characteristic of PD is the asymmetry of motor symptoms, which presents since disease onset and persists along with disease progression (2, 3). This asymmetry of motor symptoms is unique among various neurodegenerative disorders with parkinsonian syndromes and can serve as a clue for differential diagnosis (4). The mechanism underlying motor symptoms

asymmetry is the unequal degeneration of dopaminergic neurons in the midbrain and consistently revealed through autopsy, positron emission tomography, and single-photon emission tomography examinations (5–7).

Furthermore, motor asymmetry also affects non-motor profiles, such as cognitive impairment, psychiatric symptoms, pain, sleep disorders, and olfactory function (8–12). Regarding cognitive function, patients with right-sided PD (RPD) typically have language-related impairments, whereas patients with left-sided PD (LPD) mainly have visuospatial-associated dysfunction (8). The mechanism how lateralization influences non-motor symptoms is still elusive. Unequal impairments of bilateral dopaminergic circuits might partially underlie this phenomenon; more widespread destructions involving multiple brain areas may also account for the impact of lateralization on various non-motor symptoms (8, 13).

A variety of magnetic resonance imaging (MRI) techniques contributes to our improved understanding on structural and functional asymmetric impairment of the brain in PD. A longitudinal study demonstrated that the lateral ventricular volume contralateral to motor symptom onset increased faster than that ipsilateral to motor symptoms onset (14). Magnetic resonance imaging using voxel-based morphometry has revealed that LPD patients had gray matter volume loss primarily in the right hemisphere (15). Diffusion tensor imaging has shown that the substantial nigra contralateral to the side with more severe symptoms had a larger decrease in fractional anisotropy than the opposite side (16). Functional MRI (fMRI) is a valuable tool for the revelation of brain activity and has been used in the exploration of functional substrate of asymmetrical impairment in PD.

Functional MRI can be classified into task-based fMRI and resting-state fMRI (rs-fMRI). The former requires the subject to perform a specific task; the latter needs almost no effort from the patient (17). To date, there have been only few studies employing rs-fMRI in the topic of asymmetry of PD. Tang et al. (18) used whole-brain functional connectivity in mild–moderate PD patients and found that RPD patients had more functional connectivity abnormalities, especially in the brain regions of the left hemisphere belonging to the somatosensory and motor networks, as well as the default mode network. Another study using rs-fMRI analyzed the associations between brain functional connectivity and PD symptoms. They found that Movement Disorder Society (MDS)–Unified PD Rating Scale (UPDRS) part I score was correlated with functional connectivity centered in the inferior orbitofrontal area ipsilateral to the side of more severe motor symptoms, and MDS-UPDRS part III score was correlated with functional connectivity of inferior parietal contralateral to the side of more severe motor symptoms (19). Huang et al. (20) assessed regional homogeneity (ReHo) in the striatum as a measure of brain activity and tested the PD patients' feedback-based associative learning. In their study, LPD patients performed worse than did RPD patients and controls, and this cognitive impairment was associated with ReHo in the right dorsal rostral putamen (20). Amplitude of low-frequency fluctuations (ALFF) is a widely used measure that conveniently reflects regional spontaneous activities of the whole human brain (21). Previous studies on PD using ALFF have indicated that the changes in brain function did not restrict to basal ganglia, but also involved various cerebral areas (22, 23). However, these studies combined LPD and RPD patients as a single group and thus could not reveal differences between spontaneous brain activities of these two subgroups. Therefore, the present study aimed to assess the influence of motor asymmetry on brain activities in PD with the help ALFF.

METHODS

Participants

From 2012 to 2014, we consecutively enrolled 71 patients with idiopathic PD, and 35 age-, sex-, and general cognitive status–matched controls with no history of neurological or psychiatric disorders. All the patients were diagnosed according to the United Kingdom Parkinson's Disease Society brain bank diagnostic criteria (4).

Demographic and clinical information was collected from all the participants. Side of motor symptom onset was determined by medical history and confirmed by neurological examinations. The patients whose side of onset could not be ascertained would be excluded. Patients with dementia, moderate to severe head tremor, head trauma, deep brain stimulation, alcohol or drug abuse, or with other neurological or psychiatric disorders were excluded. Participants who were left-handed were also excluded from this study.

All the PD patients underwent MRI examination and motor and non-motor function evaluations in a practically defined "off" state, after withdrawing all the antiparkinsonian medications for ∼12 h. UPDRS, Hoehn-Yahr staging, Mini-Mental State Examination (MMSE), Hamilton Depression Rating Scale (HAMD), Hamilton Anxiety Rating Scale (HAMA), and Non-Motor Symptoms Questionnaire (NMSQ) were assessed in all the PD patients. The control subjects were evaluated by MMSE.

The study was in accordance with relevant guidelines and regulations and approved by the ethics committee of Beijing Hospital. This study was carried out according to the Declaration of Helsinki. All the subjects gave written informed consent prior to participation.

MRI Data Acquisition

All the MRI scans were performed on a 3.0-T scanner (Achieva TX; Philips Medical Systems, Best, the Netherlands) at Beijing Hospital. Foam padding and headphones were used to minimize head motion and reduce scanning noise. Participants were asked to lie still, relax, keep their eyes closed, and remain awake through the entire scan. High-resolution T1-weighted images (three-dimensional turbo field echo) were acquired with the following parameters: repetition time (TR) = 7.4 ms, echo time (TE) = 3.0 ms, flip angle = 8°, field of view (FOV) = 240 × 240 mm, matrix size = 256 × 256, voxel dimensions = 0.94 × 0.94 × 1.20 mm, slice thickness = 1.2 mm, 140 slices. Functional images were obtained using axial echo-planar imaging with the following parameters: TR = 3,000 ms, TE = 35 ms, flip angle = 90°, FOV = 240 × 240 mm, matrix size = 64 × 64, voxel dimensions 3.75

× 3.75 × 4.00 mm, slice thickness = 4 mm, slices = 33, time points = 210.

rs-fMRI Data Preprocessing

Resting-state fMRI data preprocessing and ALFF computation were carried out using RESTplus V 1.2 (24), which is a toolkit based on SPM 12 (http://www.fil.ion.ucl.ac.uk/spm). Generally, the preprocessing pipeline included (1) the first 10 volumes were discarded for participants' acclimatization and signal equilibrium. (2) The remaining 200 time points were corrected for slice-timing. (3) Realignment to account for head motion. Subjects were excluded if their head motion exceeded 2 mm in displacement or 2° in rotation. (4) Functional images were coregistered to the structural T1 images and were normalized to the Montreal Neurological Institute (MNI) template using the coregistered T1 images (by DARTEL) (25). Then they were resliced to a resolution of $3 \times 3 \times 3$ mm^3. (5) Smoothing using a Gaussian kernel (6-mm full-width-half-maximum, FWHM). (6) Detrending was employed to reduce the systematic shift. (7) Nuisance covariates regression, which regressed out Friston-24 head motion parameters (26), white matter and cerebrospinal fluid signals.

ALFF Calculations

Amplitude of low-frequency fluctuation was calculated using RESTplus V 1.2, and the algorithms have been published previously (21). Briefly, the time series of all the voxels were converted to the frequency domain using fast Fourier transform. Then the power spectrum was obtained across the frequency of 0.01–0.1 Hz. Afterward, the ALFF value of each voxel was divided by the global mean ALFF value for the standardization across participants. After the ALFF computation, band-pass filtering ($0.01 < f < 0.1$ Hz) was performed to remove the influences of low-frequency drift and high-frequency physiological noise.

Statistical Analysis

Demographic and clinical variables were analyzed using SPSS (version 23.0; IBM Corp, Armonk, NY, USA). Data are presented as mean ± standard deviation unless stated otherwise. The Kolmogorov–Smirnov test was applied to assess data normality. The one-way analysis of variance or Kruskal–Wallis test was employed to test differences of numerical variables between the LPD, RPD, and control groups. χ^2 or Fisher exact test was used to compare categorical variables between groups. Differences were considered statistically significant when $p < 0.05$.

Statistical analysis of ALFF was performed using DPABI [Data Processing and Analysis for (Resting-State) Brain Imaging] V4.2 (27). Comparisons between the LPD, RPD, and control groups were conducted using the analysis of covariance model. We used a gray matter mask and set age and gray matter density as covariates to control for the effects of age and structural differences. *Post-hoc* pairwise analyses were corrected by the least significant difference method. Multiple-comparisons corrections were performed based on Gaussian random field theory (voxel-level $P < 0.001$; cluster-level $P < 0.05$; two-tailed) (28, 29). Effect sizes were evaluated using Cohen f^2, which was given by DPABI. We also calculated the statistical power for the clusters having significant between group differences using G*Power 3.1.9.7 (30). The ALFF values of clusters showing significant between group differences were extracted, and the relationship between the ALFF values of these positive clusters and clinical and neuropsychological variables was explored via Spearman correlation.

TABLE 1 | Demographic and clinical characteristics of the PD patients and controls.

	LPD	RPD	Controls	*p*-value
No. of subjects	30	27	32	
Age	62.63 ± 8.88	65.85 ± 6.982	62.41 ± 7.07	0.056
Gender (male/female)	14/16	14/13	16/16	0.924
Disease duration	6.80 ± 3.62	6.15 ± 3.59		0.499
Hoehn-Yahr staging	2.13 ± 0.71	2.28 ± 0.67		0.416
UPDRS	49.90 ± 18.82	48.85 ± 12.83		0.809
MMSE	28.50 ± 1.50	27.56 ± 2.28	27.78 ± 2.25	0.203
HAMD	9.07 ± 5.27	9.56 ± 5.09		0.724
HAMA	9.93 ± 5.04	10.52 ± 6.03		0.691
NMSQ	11.07 ± 5.77	11.56 ± 4.86		0.732

RESULTS

Demographic and Clinical Information

Finally, we included 57 patients with PD and 32 controls. Four of the PD patients and two of the controls were excluded because of left-handedness. Five PD patients and one control were excluded because of excessive head motion. One PD patient was excluded because of poor image quality. Four PD patients were excluded because of bilateral motor symptom onset.

Demographic and clinical characteristics are shown in **Table 1**. There were 30, 27, and 32 subjects in the LPD, RPD, and controls groups, respectively. There was no significant difference in age, sex, or MMSE across the three groups. Disease duration was comparable in PD patients with left- and right-side onset. UPDRS, Hoehn-Yahr staging, HAMD, HAMA, and NMSQ scores were similar between the LPD and RPD groups.

Group Differences in ALFF

Analysis of covariance and the followed *post-hoc* pairwise analyses only identified different brain activities between the LPD and control groups, whereas there was no significant difference between the LPD and RPD groups, or between the RPD and control groups.

Left-sided PD patients exhibited increased ALFF in the left inferior temporal gyrus (**Figure 1**), as well as deceased ALFF in bilateral thalamus (**Figure 2**) and cerebellum anterior lobes (**Figure 3**), compared with the controls. The results are illustrated in **Table 2**.

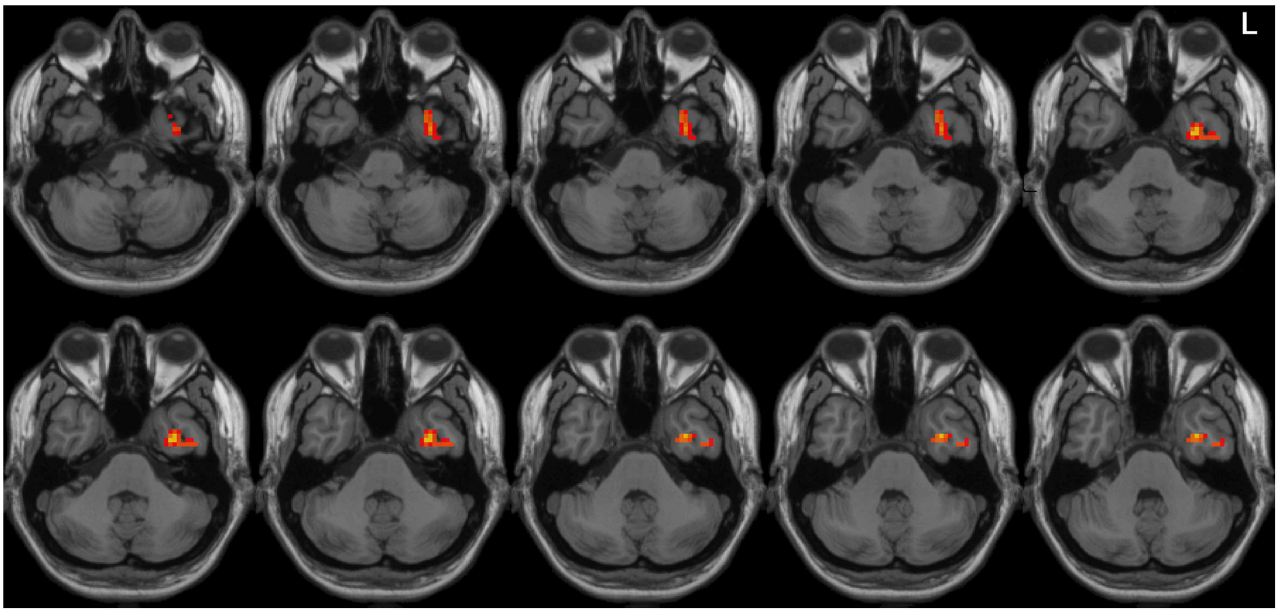


FIGURE 1 | Increased ALFF in the left inferior temporal gyrus in the LPD patients compared with the controls. L indicates the left side.

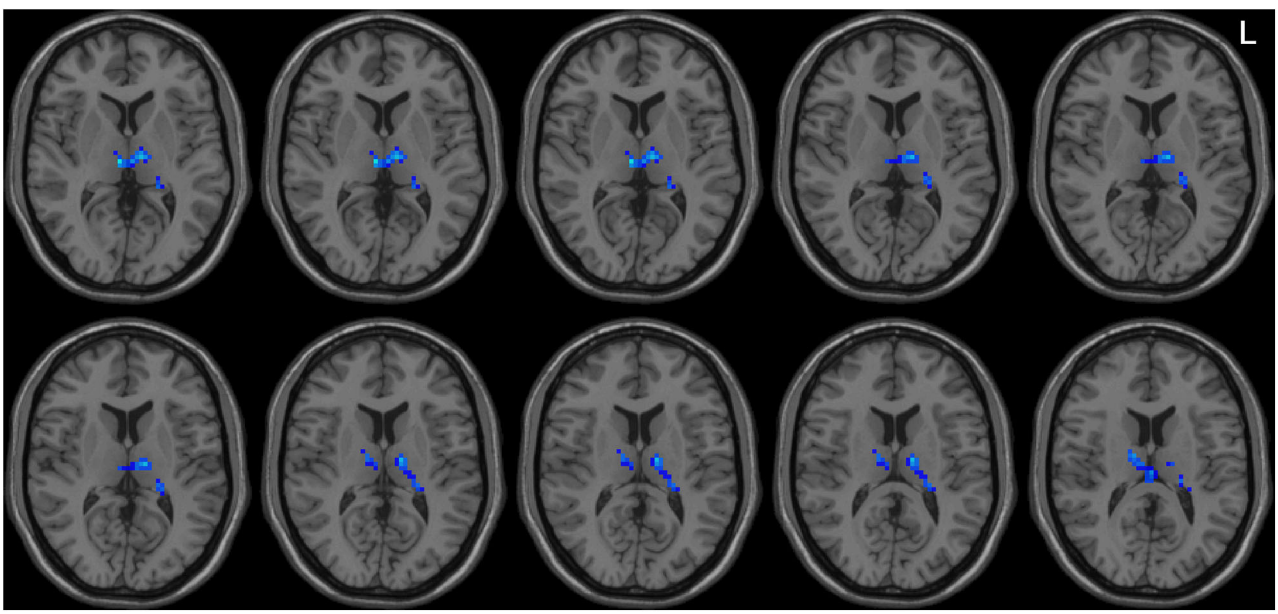


FIGURE 2 | Decreased ALFF in bilateral thalamus in the LPD patients compared with the controls. L indicates the left side.

Correlation Analysis

We performed Spearman correlation analyses between ALFF values of the above three positive clusters and Hoehn-Yahr staging; UPDRS parts I, II, III, and IV; MMSE; HAMD; HAMA; and NMSQ scores in LPD patients. There were three significant correlations: ALFF value of the inferior temporal gyrus was significantly correlated with scores of UPDRS parts II and III ($r = 0.371$, and 0.363; $p = 0.044$ and 0.049, respectively); ALFF value of the thalamus was significantly associated with MMSE score ($r = 0.496$, $p = 0.005$). The degree of freedom of the correlation analysis was 28.

DISCUSSION

This is the first study to investigate the pattern of spontaneous whole-brain activities in PD patients with left and right onset

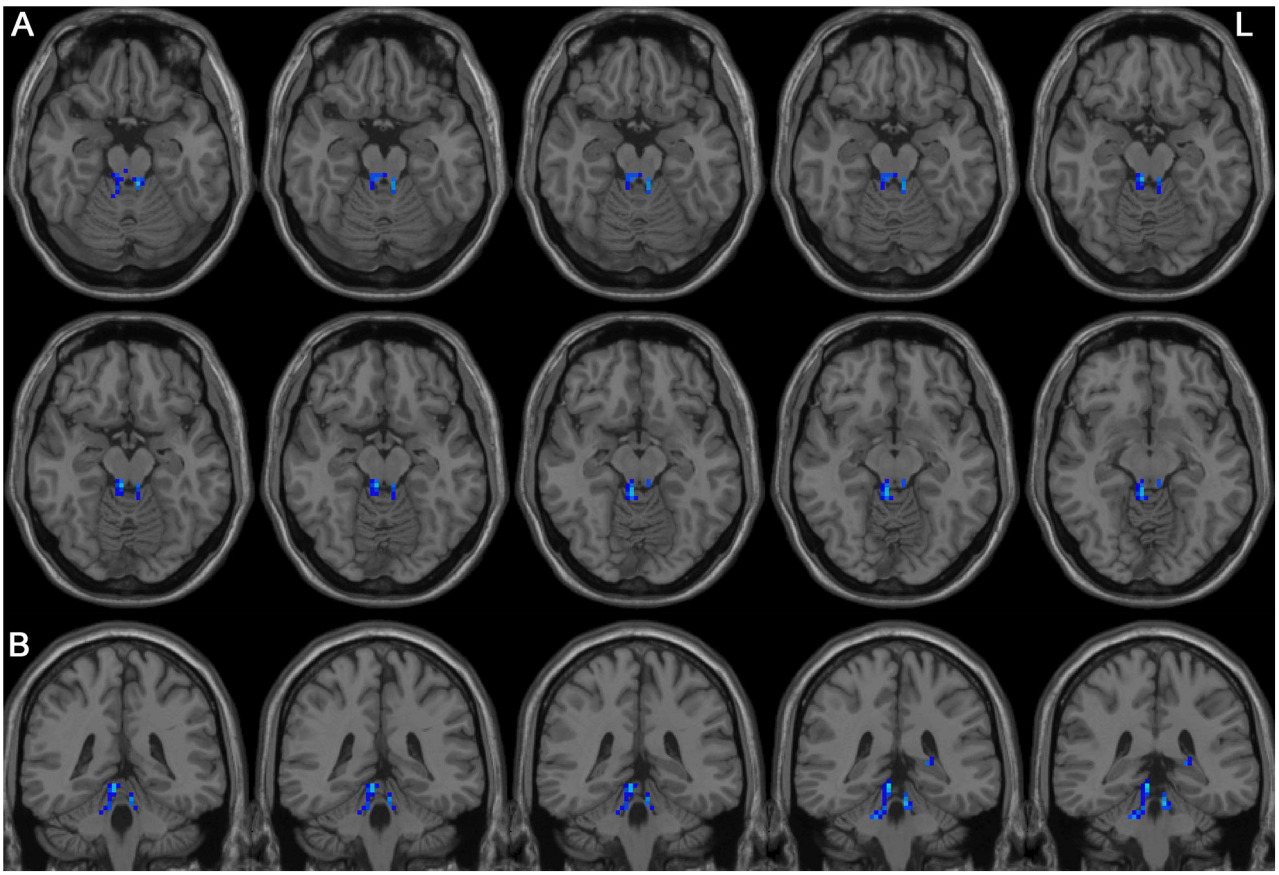


FIGURE 3 | Decreased ALFF in bilateral cerebellum anterior lobes in the LPD patients compared with the controls. **(A)** and **(B)** indicate axial and sagittal views, respectively. L indicates the left side.

TABLE 2 | Brain regions with significant differences in ALFF values between LPD and control subjects.

Brain regions	Side	Peak MNI coordinates			No. of voxels	*T*-value	Effect sizes, Cohen f^2	Statistical power
		x	*y*	*z*				
Inferior temporal gyrus	L	−33	−3	−39	59	4.354	0.243	0.9998
Cerebellum anterior lobe	Bilat	6	−36	−9	78	−4.367	0.212	0.9982
Thalamus	Bilat	6	−18	6	155	−4.431	0.207	0.9986

separately. Although directly comparing LPD and RPD patients did not identify significant different regional brain activities, only LPD patients had several areas with abnormal ALFF compared with healthy controls. LPD patients showed increased ALFF in the left inferior temporal lobe, as well as decreased ALFF in bilateral thalamus and cerebellum anterior lobes. Moreover, ALFF value of the left inferior temporal gyrus was associated with scores of activities of daily living and motor parts of UPDRS, and bilateral thalamus ALFF value was associated with cognitive function in the LPD group.

Comparing ALFF values with healthy controls obtained different results for LPD and RPD patients. This difference indicates that the pathological and compensatory mechanisms may be different in LPD and RPD patients. Some studies suggested that LPD and RPD might have different disease severity and speed of progression, and RPD patients had better neural reserve and/or greater neural plasticity than LPD patients (31, 32). In addition, Kim et al. (33) and Lee et al. (15) also found that LPD patients had more areas of atrophy than RPD patients, when the two PD subgroups were compared with control subjects (15, 33). These findings are in concordance with ours that the brains of RPD patients were less impaired than those of LPD patients. It is interesting to follow up the patients, to explore whether widespread aberrant brain activates in the LPD patients would translate to faster progression. The present study underscores the importance of dividing PD patients according to side of onset in future studies, to confirm their distinct brain activity characteristics.

Nevertheless, the direct comparison between LPD and RPD patients did not show significant difference. Moreover, the studies by Kim et al. (33) and Lee et al. (15) also failed to identify areas with significant different cortical thickness or gray matter volume in the direct comparison between LPD and RPD patients, although these two groups showed different patterns of abnormalities compared with the controls (15, 33). We have to be cautious to assert that LPD and RPD have different profiles of brain activity. The mean disease duration was longer than 6 years, and the mean Hoehn-Yahr stage was higher than 2 in both PD groups in the present study. Therefore, most of the PD patients recruited already had bilateral brain impairments. The disparity between the two PD subgroups might be masked by prominent similarities. Although still in controversy, some studies demonstrated that the degree of asymmetry decreased during disease progression (3, 34). Our findings should be considered preliminary results, and further studies including a larger sample and particularly patients with only unilateral symptoms may better reveal the influence of lateralization on cerebral activities in PD.

There were three regions with aberrant ALFF in the comparison between LPD patients and the controls. The Cohen f^2-values indicated medium effect sizes ($0.15 < f^2 < 0.35$) (35), and correlation analysis showed that the altered brain activity in these areas might play a role in motor and non-motor symptoms.

Left-sided PD patients had increased ALFF in the left inferior temporal lobe, and this abnormality was associated motor symptoms and daily activities. Increased ALFF in the left inferior temporal lobe has been reported by several studies (36–39). In the studies by Mi et al. (37), Hu et al. (38), and Chen et al. (39), increased ALFF in this area was associated with motor functions such as posture instability and gait disturbances. It is well-known that the left inferior temporal lobe is critical for semantic integration and visual processing (40, 41). Lahr et al. (42) have demonstrated that PD patients relied on visual input to maintain upright postural control. Integration of visual sensory information is essential for appropriate movement initiation and execution. Inferior temporal lobe dysfunction may influence motor function and daily activities through impaired processing of visual information (37, 42). How does aberrant brain activity of this zone affect motor function in LPD patients needs further investigation.

We found that ALFF of bilateral thalamus was lower in LPD patients than the controls, and ALFF value of thalamus was positively correlated with cognitive function. This positive correlation suggested that the lower the ALFF, the worse the cognitive function. Thus, this abnormality may be a pathological rather than a compensatory change. Thalamus is not only a vital relay of sensory pathways, but also a key component in corticobasal ganglia–thalamic circuits, which modulates motor and cognitive function (43). Decreased thalamic ALFF in PD has been reported in a number of studies (36, 37, 44, 45) and might be associated with depression and gait disturbance (36, 37). Our findings suggest that impaired thalamic activity may be associated with cognitive function in PD. This brain activity change may be mediated through disrupted corticobasal ganglia–thalamic circuit (46), as supported by an rs-fMRI study using functional connectivity (47). Additionally, there is histopathological evidence of thalamic damage and its correlation with cognitive dysfunction in PD (48, 49). Overall, our study confirmed thalamus dysfunction in LPD and suggested its association with cognitive impairment in PD.

The present study revealed lower ALFF in bilateral cerebellum anterior lobes. Cerebellar regulates motor and cognitive function through the cerebellothalamocortical circuit, which has several overlapping structures with the corticobasal ganglia–thalamic loop (40). Mi et al. (37) also revealed decreased ALFF in the cerebellum anterior lobe in PD patients. Wu and Hallett (50) assessed brain activity during automatic movements using fMRI and found increased cerebellar activity of bilateral cerebellum anterior lobes during automatic movements. They suggested that cerebellum might play a compensatory role in automatic movements. We did not find associations between the ALFF value of this area and motor or cognitive function. Maybe a more thorough evaluation especially including automatic movement performance would confirm its role in motor function.

It is noteworthy that there are some limitations of the study. First, the sample size is not very large. We obtained different results in comparisons between the two PD groups and the controls, but directly comparison between LPD and RPD patients did not show any significant difference. This may be due to the small difference between the two PD groups, and a larger sample size may have enough power to detect discrepancies between PD patients with left and right onset. Second, all the patients underwent dopaminergic medications; although we performed rs-fMRI examination in a practically defined off-state, the influence of antiparkinsonism medications cannot be completely ruled out. However, this practically defined off-state is quite commonly used in rs-fMRI studies in PD and would facilitate comparisons with other studies in this topic.

In conclusion, the present study showed that LPD had abnormalities in spontaneous brain activities in the left temporal lobe, bilateral thalamus, and cerebellum anterior lobes, and some of these changes were related to motor and cognitive function. However, RPD and healthy controls did not have significant difference in brain activities measured by ALFF. This finding indicates that LPD and RPD might have different neural mechanisms during neurodegeneration. Furthermore, this study highlights the necessity of dividing PD patients according to side of onset, to detect the characteristic pathophysiology of these two subgroups of PD.

DATA AVAILABILITY STATEMENT

The datasets generated for this study are available on request to the corresponding author.

ETHICS STATEMENT

The studies involving human participants were reviewed and approved by the Ethics Committee of Beijing Hospital. The patients/participants provided their written informed consent to participate in this study.

AUTHOR CONTRIBUTIONS

WS, H-BC, and C-ZY conceived and designed the experiments. KL analyzed the fMRI data. MC, C-ML, RW, and B-HL were responsible for the fMRI scans and helped fMRI data analyses. WS and H-BC recruited the subjects. X-XM, HZ, and KL collected the demographic, clinical, and neuropsychological information of the subjects. KL and WS wrote the manuscript. All the authors have read and approved the final manuscript.

FUNDING

This work was supported by the grant from the National Key R&D Program of China (2017YFC1310200), the grant of the 12th 5-year Plan for National Science & Technology Supporting Program (2012BAI10B03 and 2012BAI10B04). This work was also supported by the project National Major Multidisciplinary Cooperative Diagnosis and Treatment Capacity Building Project from National Health Commission of the People's Republic of China.

ACKNOWLEDGMENTS

We are grateful to Professor Yu-Feng Zang and his colleague Mr. Xi-Ze Jia from Hangzhou Normal University, Professor Chao-Gan Yan and his colleagues Dr. Xiao Chen, Mr. Bin Lu from the Institute of Psychology, Chinese Academy of Sciences (IPCAS), for their support in fMRI data analysis.

REFERENCES

1. Postuma RB, Berg D, Stern M, Poewe W, Olanow CW, Oertel W, et al. MDS clinical diagnostic criteria for Parkinson's disease. *Mov Disord.* (2015) 30:1591–601. doi: 10.1002/mds.26424
2. Hoehn MM, Yahr MD. Parkinsonism: onset, progression and mortality. *Neurology.* (1967) 17:427–42. doi: 10.1212/WNL.17.5.427
3. Miller-Patterson C, Buesa R, McLaughlin N, Jones R, Akbar U, Friedman JH. Motor asymmetry over time in Parkinson's disease. *J Neurol Sci.* (2018) 393:14–7. doi: 10.1016/j.jns.2018.08.001
4. Hughes AJ, Daniel SE, Kilford L, Lees AJ. Accuracy of clinical diagnosis of idiopathic Parkinson's disease: a clinico-pathological study of 100 cases. *J Neurol Neurosurg Psychiatry.* (1992) 55:181–4. doi: 10.1136/jnnp.55.3.181
5. Kempster PA, Gibb WR, Stern GM, Lees AJ. Asymmetry of substantia nigra neuronal loss in Parkinson's disease and its relevance to the mechanism of levodopa related motor fluctuations. *J Neurol Neurosurg Psychiatry.* (1989) 52:72–6. doi: 10.1136/jnnp.52.1.72
6. Leenders KL, Salmon EP, Tyrrell P, Perani D, Brooks DJ, Sager H, et al. The nigrostriatal dopaminergic system assessed *in vivo* by positron emission tomography in healthy volunteer subjects and patients with Parkinson's disease. *Arch Neurol.* (1990) 47:1290–8. doi: 10.1001/archneur.1990.00530120034007
7. Booth TC, Nathan M, Waldman AD, Quigley AM, Schapira AH, Buscombe J. The role of functional dopamine-transporter SPECT imaging in parkinsonian syndromes, part 2. *AJNR Am J Neuroradiol.* (2015) 36:236–44. doi: 10.3174/ajnr.A3971
8. Verreyt N, Nys GM, Santens P, Vingerhoets G. Cognitive differences between patients with left-sided and right-sided Parkinson's disease. *A review. Neuropsychol Rev.* (2011) 21:405–24. doi: 10.1007/s11065-011-9182-x
9. Modestino EJ, Amenechi C, Reinhofer A, O'Toole P. Side-of-onset of Parkinson's disease in relation to neuropsychological measures. *Brain Behav.* (2017) 7:e00590. doi: 10.1002/brb3.590
10. Djaldetti R, Shifrin A, Rogowski Z, Sprecher E, Melamed E, Yarnitsky D. Quantitative measurement of pain sensation in patients with parkinson disease. *Neurology.* (2004) 62:2171–5. doi: 10.1212/01.WNL.0000130455.38550.9D
11. Baumann CR, Held U, Valko PO, Wienecke M, Waldvogel D. Body side and predominant motor features at the onset of Parkinson's disease are linked to motor and nonmotor progression. *Mov Disord.* (2014) 29:207–13. doi: 10.1002/mds.25650
12. Zucco GM, Rovatti F, Stevenson RJ. Olfactory asymmetric dysfunction in early parkinson patients affected by unilateral disorder. *Front Psychol.* (2015) 6:1020. doi: 10.3389/fpsyg.2015.01020
13. Riederer P, Jellinger KA, Kolber P, Hipp G, Sian-Hulsmann J, Kruger R. Lateralisation in parkinson disease. *Cell Tissue Res.* (2018) 373:297–312. doi: 10.1007/s00441-018-2832-z
14. Lewis MM, Smith AB, Styner M, Gu H, Poole R, Zhu H, et al. Asymmetrical lateral ventricular enlargement in Parkinson's disease. *Eur J Neurol.* (2009) 16:475–81. doi: 10.1111/j.1468-1331.2008.02430.x
15. Lee EY, Sen S, Eslinger PJ, Wagner D, Kong L, Lewis MM, et al. Side of motor onset is associated with hemisphere-specific memory decline and lateralized gray matter loss in Parkinson's disease. *Parkinsonism Relat Disord.* (2015) 21:465–70. doi: 10.1016/j.parkreldis.2015.02.008
16. Langley J, Huddleston DE, Merritt M, Chen X, McMurray R, Silver M, et al. Diffusion tensor imaging of the substantia nigra in Parkinson's disease revisited. *Hum Brain Mapp.* (2016) 37:2547–56. doi: 10.1002/hbm.23192
17. Azeez AK, Biswal BB. A review of resting-state analysis methods. *Neuroimaging Clin N Am.* (2017) 27:581–92. doi: 10.1016/j.nic.2017.06.001
18. Tang Y, Liu B, Yang Y, Wang CM, Meng L, Tang BS, et al. Identifying mild-moderate Parkinson's disease using whole-brain functional connectivity. *Clin Neurophysiol.* (2018) 129:2507–16. doi: 10.1016/j.clinph.2018.09.006
19. Yoo K, Chung SJ, Kim HS, Choung OH, Lee YB, Kim MJ, et al. Neural substrates of motor and non-motor symptoms in Parkinson's disease: a resting FMRI study. *PLoS ONE.* (2015) 10:e0125455. doi: 10.1371/journal.pone.0125455
20. Huang P, Tan YY, Liu DQ, Herzallah MM, Lapidow E, Wang Y, et al. Motor-symptom laterality affects acquisition in Parkinson's disease: a cognitive and functional magnetic resonance imaging study. *Mov Disord.* (2017) 32:1047–55. doi: 10.1002/mds.27000
21. Zang YF, He Y, Zhu CZ, Cao QJ, Sui MQ, Liang M, et al. Altered baseline brain activity in children with ADHD revealed by resting-state functional MRI. *Brain Dev.* (2007) 29:83–91. doi: 10.1016/j.braindev.2006.07.002
22. Pan P, Zhang Y, Liu Y, Zhang H, Guan D, Xu Y. Abnormalities of regional brain function in Parkinson's disease: a meta-analysis of resting state functional magnetic resonance imaging studies. *Sci Rep.* (2017) 7:40469. doi: 10.1038/srep40469
23. Wang J, Zhang JR, Zang YF, Wu T. Consistent decreased activity in the putamen in Parkinson's disease: a meta-analysis and an independent validation of resting-state fMRI. *Gigascience.* (2018) 7:giy071. doi: 10.1093/gigascience/giy071
24. Jia X-Z, Wang J, Sun H-Y, Zhang H, Liao W, Wang Z, et al. RESTplus: an improved toolkit for resting-state functional magnetic resonance imaging data processing. *Sci Bull.* (2019) 64:953–4. doi: 10.1016/j.scib.2019.05.008
25. Ashburner J. A fast diffeomorphic image registration algorithm. *Neuroimage.* (2007) 38:95–113. doi: 10.1016/j.neuroimage.2007.07.007
26. Friston KJ, Williams S, Howard R, Frackowiak RS, Turner R. Movement-related effects in fMRI time-series. *Magn Reson Med.* (1996) 35:346–55. doi: 10.1002/mrm.1910350312
27. Yan CG, Wang XD, Zuo XN, Zang YF. DPABI: data processing & analysis for (resting-state) brain imaging. *Neuroinformatics.* (2016) 14:339–51. doi: 10.1007/s12021-016-9299-4
28. Nichols T, Hayasaka S. Controlling the familywise error rate in functional neuroimaging: a comparative review. *Stat Methods Med Res.* (2003) 12:419–46. doi: 10.1191/0962280203sm341ra

29. Chen X, Lu B, Yan CG. Reproducibility of R-fMRI metrics on the impact of different strategies for multiple comparison correction and sample sizes. *Hum Brain Mapp.* (2018) 39:300–18. doi: 10.1002/hbm.23843
30. Faul F, Erdfelder E, Lang AG, Buchner A. G*Power 3: a flexible statistical power analysis program for the social, behavioral, and biomedical sciences. *Behav Res Methods.* (2007) 39:175–91. doi: 10.3758/BF03193146
31. Ham JH, Lee JJ, Kim JS, Lee PH, Sohn YH. Is dominant-side onset associated with a better motor compensation in Parkinson's disease? *Mov Disord.* (2015) 30:1921–5. doi: 10.1002/mds.26418
32. Chung SJ, Yoo HS, Lee HS, Lee PH, Sohn YH. Does the side onset of Parkinson's disease influence the time to develop levodopa-induced dyskinesia? *J Parkinsons Dis.* (2019) 9:241–7. doi: 10.3233/JPD-181512
33. Kim JS, Yang JJ, Lee JM, Youn J, Kim JM, Cho JW. Topographic pattern of cortical thinning with consideration of motor laterality in parkinson disease. *Parkinsonism Relat Disord.* (2014) 20:1186–90. doi: 10.1016/j.parkreldis.2014.08.021
34. Marinus J, van Hilten JJ. The significance of motor (a)symmetry in Parkinson's disease. *Mov Disord.* (2015) 30:379–85. doi: 10.1002/mds.26107
35. Selya AS, Rose JS, Dierker LC, Hedeker D, Mermelstein RJ. A practical guide to calculating cohen's f(2), a measure of local effect size, from PROC MIXED. *Front Psychol.* (2012) 3:111. doi: 10.3389/fpsyg.2012.00111
36. Wen X, Wu X, Liu J, Li K, Yao L. Abnormal baseline brain activity in non-depressed Parkinson's disease and depressed Parkinson's disease: a resting-state functional magnetic resonance imaging study. *PLoS ONE.* (2013) 8:e63691. doi: 10.1371/journal.pone.0063691
37. Mi TM, Mei SS, Liang PP, Gao LL, Li KC, Wu T, et al. Altered resting-state brain activity in Parkinson's Parkinson's disease patients with freezing of gait. *Sci Rep.* (2017) 7:16711. doi: 10.1038/s41598-017-16922-0
38. Hu H, Chen J, Huang H, Zhou C, Zhang S, Liu X, et al. Common and specific altered amplitude of low-frequency fluctuations in Parkinson's disease patients with and without freezing of gait in different frequency bands. *Brain Imaging Behav.* (2019) 857–68. doi: 10.1007/s11682-018-0031-x
39. Chen HM, Wang ZJ, Fang JP, Gao LY, Ma LY, Wu T, et al. Different patterns of spontaneous brain activity between tremor-dominant and postural instability/gait difficulty subtypes of Parkinson's disease: a resting-state fMRI study. *CNS Neurosci Ther.* (2015) 21:855–66. doi: 10.1111/cns.12464
40. Jung-Beeman M. Bilateral brain processes for comprehending natural language. *Trends Cogn Sci.* (2005) 9:512–8. doi: 10.1016/j.tics.2005.09.009
41. Goodale MA, Milner AD. Separate visual pathways for perception and action. *Trends Neurosci.* (1992) 15:20–5. doi: 10.1016/0166-2236(92)90344-8
42. Lahr J, Pereira MP, Pelicioni PH, De Morais LC, Gobbi LT. Parkinson's disease patients with dominant hemibody affected by the disease rely more on vision to maintain upright postural control. *Percept Mot Skills.* (2015) 121:923–34. doi: 10.2466/15.PMS.121c26x0
43. Herrero MT, Barcia C, Navarro JM. Functional anatomy of thalamus and basal ganglia. *Childs Nerv Syst.* (2002) 18:386–404. doi: 10.1007/s00381-002-0604-1
44. Xiang J, Jia X, Li H, Qin J, Liang P, Li K. Altered spontaneous brain activity in cortical and subcortical regions in Parkinson's disease. *Parkinsons Dis.* (2016) 2016:5246021. doi: 10.1155/2016/5246021
45. Zhang J, Wei L, Hu X, Zhang Y, Zhou D, Li C, et al. Specific frequency band of amplitude low-frequency fluctuation predicts Parkinson's disease. *Behav Brain Res.* (2013) 252:18–23. doi: 10.1016/j.bbr.2013.05.039
46. McGregor MM, Nelson AB. Circuit mechanisms of Parkinson's disease. *Neuron.* (2019) 101:1042–56. doi: 10.1016/j.neuron.2019.03.004
47. Gorges M, Muller HP, Lule D, Consortium L, Pinkhardt EH, Ludolph AC, et al. To rise and to fall: functional connectivity in cognitively normal and cognitively impaired patients with Parkinson's disease. *Neurobiol Aging.* (2015) 36:1727–35. doi: 10.1016/j.neurobiolaging.2014.12.026
48. Halliday GM. Thalamic changes in Parkinson's disease. *Parkinsonism Relat Disord.* (2009) 15(Suppl 3):S152–5. doi: 10.1016/S1353-8020(09)70804-1
49. Brooks D, Halliday GM. Intralaminar nuclei of the thalamus in lewy body diseases. *Brain Res Bull.* (2009) 78:97–104. doi: 10.1016/j.brainresbull.2008.08.014
50. Wu T, Hallett M. A functional MRI study of automatic movements in patients with Parkinson's disease. *Brain.* (2005) 128:2250–9. doi: 10.1093/brain/awh56

Conflict of Interest: The authors declare that the research was conducted in the absence of any commercial or financial relationships that could be construed as a potential conflict of interest.

Copyright © 2020 Li, Su, Chen, Li, Ma, Wang, Lou, Zhao, Chen and Yan. This is an open-access article distributed under the terms of the Creative Commons Attribution License (CC BY). The use, distribution or reproduction in other forums is permitted, provided the original author(s) and the copyright owner(s) are credited and that the original publication in this journal is cited, in accordance with accepted academic practice. No use, distribution or reproduction is permitted which does not comply with these terms.

frontiers in Neurology

MINI REVIEW
published: 04 August 2020
doi: 10.3389/fneur.2020.00791

Modern Brainstem MRI Techniques for the Diagnosis of Parkinson's Disease and Parkinsonisms

Germain Arribarat[1,2], *Amaury De Barros*[1,3] *and Patrice Péran*[1]*

[1] *ToNIC, Toulouse NeuroImaging Center, Université de Toulouse, Inserm, UPS, Toulouse, France,* [2] *Centre de Recherche Cerveau et Cognition (CNRS, Cerco, UMR5549), UPS, Toulouse, France,* [3] *Department of Anatomy, Toulouse Faculty of Medicine, Toulouse, France*

The brainstem is the earliest vulnerable structure in many neurodegenerative diseases like in Multiple System Atrophy (MSA) or Parkinson's disease (PD). Up-to-now, MRI studies have mainly focused on whole-brain data acquisition. Due to its spatial localization, size, and tissue characteristics, brainstem poses particular challenges for MRI. We provide a brief overview on recent advances in brainstem-related MRI markers in Parkinson's disease and Parkinsonism's. Several MRI techniques investigating brainstem, mainly the midbrain, showed to be able to discriminate PD patients from controls or to discriminate PD patients from atypical parkinsonism patients: iron-sensitive MRI, nigrosome imaging, neuromelanin-sensitive MRI, diffusion tensor imaging and advanced diffusion imaging. A standardized multimodal brainstem-dedicated MRI approach at high resolution able to quantify microstructural modification in brainstem nuclei would be a promising tool to detect early changes in parkinsonian syndromes.

Keywords: iron, neuromelanin (NM), multiple system atrophy (MSA), NODDI, diffusion kurtosis imaging (DKI), nigrosome

OPEN ACCESS

Edited by:
Yu Zhang,
VA Palo Alto Health Care System,
United States

Reviewed by:
Matteo Bologna,
Sapienza University of Rome, Italy
Maria A. Pastor,
University of Navarra, Spain

***Correspondence:**
Patrice Péran
patrice.peran@inserm.fr

Specialty section:
This article was submitted to Movement Disorders, a section of the journal Frontiers in Neurology

Received: *06 March 2020*
Accepted: *25 June 2020*
Published: *04 August 2020*

Citation:
Arribarat G, De Barros A and Péran P (2020) Modern Brainstem MRI Techniques for the Diagnosis of Parkinson's Disease and Parkinsonisms. Front. Neurol. 11:791. doi: 10.3389/fneur.2020.00791

INTRODUCTION

In Parkinson's disease (PD), the first central neuropathological events occur in the brainstem and olfactory bulb. The dorsal motor nucleus of the vagal nerve in the medulla oblongata, which receives inputs from the neurenteric system, is classically considered to be the first nucleus involved before the ascending diffusion through other brainstem structures such as the serotoninergic raphe nuclei and noradrenergic coeruleus nuclei of the pons (1). Neurodegeneration then reaches the midbrain, and more particularly the dopaminergic substantia nigra pars compacta (SNc) and cholinergic pedunculopontine nuclei (PPN). The SNc plays a pivotal role, with classic PD motor symptoms occurring when 30% or more of its dopaminergic neurons have disappeared (2).

Before the appearance of these motor symptoms, the spread of alpha-synuclein across the brainstem following the Braak stages is responsible for many non-motor symptoms, such as cardiac autonomic dysfunction, rapid eye movement behavior disorder, apathy, asthenia, depression and dysexecutive syndrome, arising from alteration of the different nuclei and white-matter bundles of the brainstem (3, 4). The ensuing SNc degeneration caused by disruption of serotoninergic, extranigral dopaminergic, cholinergic, and noradrenergic pathways leads to the limbic and cognitive network dysfunction that has been amply described in numerous molecular imaging studies (5, 6). Recent advances in structural MRI techniques, such as water molecular diffusion based techniques and neuromelanin (NM) or iron-sensitive sequences, are resulting in the ever more precise characterization of brainstem damage in PD and atypical parkinsonism, including

a more precise comprehension of brainstem networks involved in non-motor symptoms. When extrapyramidal motor symptoms are present, the challenge is to differentiate true PD from atypical parkinsonian syndromes, the most challenging of these being progressive supranuclear paralysis (PSP), Parkinsonian or cerebellar variant of multiple system atrophy (MSAp, MSAc), and dementia with Lewy bodies (DLB). *Red flags* for these syndromes in otherwise normal routine MRI sequences for PD often take the form of anatomical structure atrophy, reflecting the massive neuronal loss and gliosis that generally characterize the more advanced stages (for a review of classic MRI signs for differential diagnosis, see (7).

As these red flags are already familiar to clinicians, the present review focuses on modern structural MRI techniques for PD diagnosis and the differential diagnosis of atypical parkinsonism, considering structures involved in motor networks, but also those involved in non-motor networks.

NIGROSOME IMAGING

Located in the midbrain, the susbtantia nigra (SN) is functionally and structurally divided into two parts: the SNc and the pars reticulata (SNr). The rostroventral GABAergic SNr projects toward the thalamus, and the dopaminergic SNc toward the striatum. Calbindin immunohistochemistry has allowed a labeled nigral matrix and five unlabeled clusters or nigrosomes to be identified within the SNc. These are compartments of dopaminergic neurons where degeneration is particularly marked in PD (8–10). Five nigrosomes measuring up to several millimeters long have been described (11), the largest of which (Nigrosome-1) is found in the dorsal region of the SNc.

The structure of Nigrosome-1 has been successfully delineated on 7T MRI using high-resolution susceptibility weighted imaging (SWI) (12, 13). On SWI, this nigrosome has a hypersignal in the axial section, in either linear or comma form. It is bordered anteriorly, laterally and medially by a low-intensity signal, giving it a *swallow tail* appearance. The absence of this sign is viewed as a reliable diagnostic criterion for PD (12, 14). Nigrosome-1 visualization at 7T has high diagnostic accuracy: sensitivity (100%), specificity (87–100%), positive predictive value (91–100%), and negative predictive value (100%) (15).

This structure has also been observed on SWI at 3T with reduced contrast (14, 16). The phase information, used here as a weighting mask, improves the visualization of the nigrosome's (16–18). This improvement stems from the difference in susceptibility between Nigrosome-1 and the surrounding nigral matrix in healthy individuals. As nigrosomes have a low iron concentration, they are visualized as a T2* hypersignal, contrasting with the nigral matrix. Recently, a meta-analysis reporting different nigrosome imaging techniques confirmed that visual assessment of dorsolateral nigral hyperintensity provides excellent diagnostic accuracy for PD vs. controls (19).

The two purported mechanisms behind the disappearance of the swallow tail sign are an increase in iron and a decrease in NM. A decrease in NM can cause a decrease in iron retention capacity, and therefore an increase in the amount of free iron. In both cases, the presence of iron induces paramagnetic properties of the signal (20).

IRON-SENSITIVE IMAGING

During the last decade, many works, using different iron-sensitive MRI methods, confirmed the importance of nigral iron increase in PD patients compared to controls (21). Iron-sensitive MRI has several applications, especially in neurodegenerative disorders (22). Technically, iron content can be estimated in specific regions by measuring T2 and T2* relaxation rates, using either magnitude (R2*) (23–25) or phase (quantitative susceptibility mapping, QSM) imaging (26). QSM method demonstrated to be the most sensitive quantitative technique for detecting a significant increase of iron for PD (27). QSM is able to detect nigral iron increase even in prodromal stage of PD such as idiopathic rapid eye movement sleep behavior disorder (28). It is important to note that iron-content in the substantia nigra do not differ between PD and multiple system atrophy (MSA) patients (i.e., patient with atypical parkinsonism), and between MSA variants (29). Accordingly, studies have shown that QSM more closely reflects levodopa dosage and disease severity (30, 31).

Concerning the differential diagnosis between PD and atypical parkinsonism's, QSM techniques allow for more sensitive measures in the nigral and extranigral regions. Mazzucchi et al. (32) found that the greatest diagnostic accuracy for PSP was for increased χ values in the RN, subthalamic nucleus (STN), and medial part of the SN, whereas for MSA, it was a significantly higher level of iron deposition in the putamen, reflecting the different patterns of pathological involvement that characterize these diseases (32).

NEUROMELANIN-SENSITIVE IMAGING

NM is a dark pigment composed of melanin, proteins, lipids and metal ions (33, 34). NM-containing neurons are particularly concentrated in the SNc and locus coeruleus (LC). This pigment is found in both the nigral matrix and the nigrosomes. The MR signal in NM-containing neurons is paramagnetic and therefore allows easy MR imaging where it is sensitive to this type of signal (35–37). T1-weighted NM-sensitive MRI (NM-MRI) produces hyperintense signals in regions containing NM. Indeed, the primary mechanism underlying contrast in NM-MRI appears to be the T1 reduction associated with melanin–iron complexes (38).

Studies have confirmed that patients with PD have a significantly reduced NM signal in the SN and LC (20, 37, 37, 39–41). These signal changes have been found to be correlated with the absorption values of the nigrostriatal dopamine transporter (42). In this same study, volumetric analysis of the NM-related signal also revealed a significant degree of atrophy. Measurement of NM-sensitive images has high diagnostic accuracy for PD. Several teams have recently evaluated a multimodal methodological approach, combining diffusion and NM-sensitive MRI. Pyatigorskaya et al. (43) concluded that

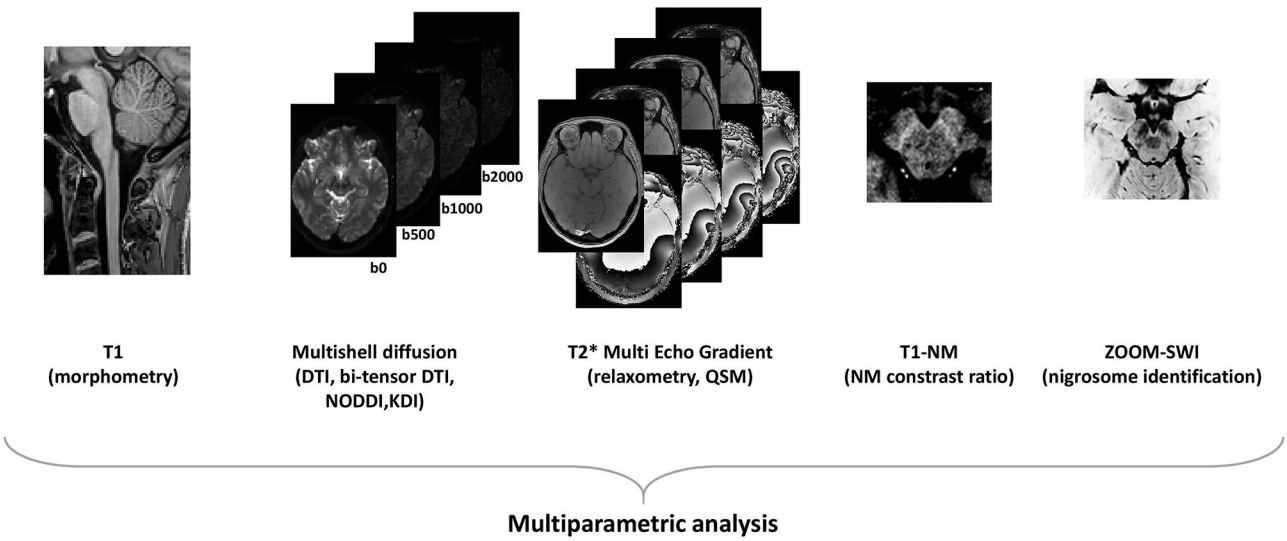


FIGURE 1 | Modern MRI acquisitions to asses brainstem.

volume delineation by the NM signal, combined with fractional anisotropy, has excellent diagnostic accuracy for PD. More specifically, NM signal intensities can potentially be located in the SNc (43). Another study found a lower NM signal in PD and MSAp groups than in an PSP group, with lower intensities in the LC in patients with PD. Sensitivity and specificity were 60 and 90% for PD vs. MSAp, 63–88% and 77–92% for PD vs. PSP, and 80 and 85% for MSAp vs. PSP (44).

DIFFUSION WEIGHTED IMAGING

Diffusion Tensor Imaging (DTI)

There are conflicting findings concerning the usefulness of SN DTI metrics in PD diagnosis, according to recent meta-analyses (45–47) and recent voxelwise analysis-based studies concerning the whole SN (48–50). Fractional Anisotropy (FA) in the posterior part seems to be the most discriminant feature (51, 52). With the ADC for the whole SN, Zhong et al. (53) found accuracy of 0.72, which is not sufficient in routine diagnosis. Interestingly, DTI metrics have also been used in a longitudinal approach, providing precious information on structural changes in the SN over the years (53–56).

In a longitudinal study applying a voxelwise approach, Pozorski et al. (50) found that patients with PD and controls differed on all DTI metrics in different brainstem regions (midbrain and pontine tegmentum, pontine crossing tract, periaqueductal gray matter). Furthermore, Mean diffusivity (MD) in the brainstem were negatively associated with disease duration. Pyatigorskaya et al. (57) correlated DTI metrics in the medulla oblongata with cardiac and respiratory variability in patients with PD compared with controls, reflecting their autonomic dysfunction (Stage 1) (57). Prange et al. (58) correlated apathy and depression with DTI measures and serotoninergic molecular imaging in the limbic system, and with the mode of anisotropy (sensitive to the orientation of crossing fibers) in the caudal midbrain, or more specifically the serotoninergic raphe nuclei (Stage 2) (58). Rapid eye movement behavior disorder has also been linked to DTI changes in the pons, SN and LC (59–61). Freezing of gait has been correlated with an FA decrease and MD increase in the PPN (62).

Diffusivity in the striatum, brainstem and cerebellum has been extensively studied (7, 63), but with rather mediocre results for the differential diagnosis of PD. FA or MD in the brainstem can be included in a multimodal approach with relatively good accuracy (49, 64). For example, the area under the curve (AUC) was above 0.95 for the diagnosis of PD vs. MSA in Péran et al. (49). Combining FA and MD in multiple ROIs including brainstem structures, Du et al. (51) were able to discriminate parkinsonian syndromes. With R2*, the AUC rose to 0.98–0.99. Pyatigorskaya et al. (43) recently found substantial differences in FA between patients with PSP and patients with PD or controls in the SN, LC, midbrain tegmentum, and pons. The highest AUC for PD vs. PSP was in the LC (0.94). In the same vein, Talai et al. (65) found AUCs of 0.95 and 0.97 based on DTI metrics in the midbrain for PD vs. PSP. DTI abnormalities in the midbrain of patients with PSP reflect microstructural changes that precede the macrostructural changes revealed by midbrain atrophy (65).

Advanced Diffusion Approaches

Despite unique insights yielded by DTI metrics acquired in a single shell, microstructural changes are considered non-specific.

Recently, bi-tensor model have been used on diffusion imaging is to differentiate free water (FW) (cerebrospinal fluid or extracellular vasogenic edema) from other compartments,

and either eliminate it from DTI measures or directly map it. Although it was initially developed with a single shell (66), double-shell acquisition could offer greater accuracy and stability (67). The most striking feature is the FW increase in the posterior part of the SN in early PD (68), MSA and PSP (69), as confirmed by (70). Findings of longitudinal FW changes over 4 years in the posterior SN of patients with early PD (71), followed by an FW increase over 3 years in the anterior SN of patients with advanced PD (72), emphasize the usefulness of FW imaging for PD diagnosis and follow-up. This posterior-anterior gradient of extracellular space expansion could reflect the neuroinflammation and cell loss revealed by histopathology. Increased FW in the posterior SN has been correlated with striatal dopaminergic denervation and reflects both motor and cognitive deficits (73). Planetta et al. (74) found an FW increase in the SN, as well as in the STN, red nucleus, PPN, cerebellum and basal ganglia, in patients with PSP and MSA, compared with patients with PD and controls. FW in the PPN and STN was discriminant for the diagnosis of MSA versus PSP (AUC = 0.97) (74).

Estimating kurtosis provides a better means of assessing diffusion heterogeneity in tissues. Diffusion kurtosis imaging (DKI) requires diffusion acquisition in two shells (often b = 1,000 and 2,000 s/mm2) (75). Elevated mean kurtosis in the SN has been found to be more sensitive than FA reduction in patients with PD versus controls (AUC > 0.95) and is correlated with motor scores (76).

White-matter tissue has been simplified in a model with intra-axonal, extra-axonal, and cerebrospinal fluid compartments. Neurite orientation dispersion and density imaging (NODDI) takes all three compartments into account. Three new metrics can be extracted from NODDI: isotropic volume fraction (Viso), reflecting extracellular space like FW; intracellular volume fraction (Vic); and orientation dispersion index (ODI), reflecting neurite integrity. An ODI increase in white matter reflects axonal loss or disorganization, while ODI and Vic decreases in gray-matter structures reflect dendritic thinning and density (77). Kamagata et al. (78) found that Vic in the contralateral SNc is useful for diagnosing patients with PD vs. controls (AUC = 0.91) and correlates with disease severity (78). NODDI was recently compared with FW for diagnosing PD, PSP and MSAp. For PD and MSAp, Viso in the posterior SN was increased (FW accumulation). In PSP, all three NODDI metrics were disturbed in the whole SN, STN, RN and PPN. Interestingly, the authors considered the NODDI metrics to be inferior to FW for PD vs. MSAp/PSP diagnosis, and found that FW based on a single shell was just as accurate and actually faster than multishell FW (79).

Restriction spectrum imaging (RSI) (80, 81) is a new diffusion model based on high angular resolution diffusion imaging (HARDI), acquired in multiple directions at different high b values. RSI highlights hindered and restricted diffusion in extracellular and intracellular compartments. With the development of several new metrics, RSI can now provide information about neurite density and orientation. Hope et al. (81) were the first to compare RSI with DTI in patients with PD. They defined a cellularity index and a neurite density index. In an ROI comprising the whole brainstem, they found significant differences in the cellularity index between patients with PD and controls (AUC = 0.69). RSI is a promising new, but time-consuming, method for vulnerable patients. Further research with more precise anatomical ROIs is needed.

DWI offers the possibility of visualizing white-matter tracts with a multitude of tractography techniques. HARDI-based tractography allows complex fiber tracts such as the nigrostriatal pathways (NSPs) to be reconstructed (82, 83). An FA decrease and an AD/RD increase have been found in the NSPs of patients with PD using deterministic tractography (84). Based on NODDI, Andica et al. (85) found that the contralateral distal (relative to the striatum) Vic of NSPs was significantly decreased in patients with PD compared with controls, reflecting the *dying back* of dopaminergic neurons (85). From our point of view, the deterministic tractography of NSPs described in these studies does not render the exact structural connectivity between the striatum, pallidum and SN revealed by a probabilistic approach (82) or by susceptibility imaging (86). The tract-based approach to PD diagnosis is promising but needs further clarification of mesencephalon/diencephalon structural connectivity.

The dentatorubrothalamic tract (DRTT) connects the cerebellum with the thalamus via the superior cerebellar peduncle and tegmental midbrain. An FA decrease and an MD increase have been found in the DRTT of patients with PSP, compared with controls and patients with PD or MSAp (64, 87). In patients with MSAc, an FA decrease and an MD increase in the pontine crossing tract and middle cerebellar peduncles have been found before the appearance of the *hot cross bun* sign (88, 89). Using diffusion kurtosis imaging, Ito et al. (90, 91) described a ratio of midbrain tegmentum diffusion to pontine crossing tract diffusion to distinguish between patients with PSP, MSA or PD and controls (90, 91). Interestingly, Juttukonda et al. (92) also found an FA decrease in the pontine crossing tract in patients with essential tremor vs. PD (92).

CONCLUSION

An important consideration is that MRI quantitative markers with good performances for diagnosis are not necessarily the best suited to monitor disease progression. More efforts need to be done in order to increase reliably and sensitivity of progression MRI markers of PD (93). A standardized multimodal brainstem-dedicated MRI approach at high spatial resolution (**Figure 1**) able to quantify microstructural modification in brainstem nuclei would be a promising tool to detect early changes in PD and parkinsonism and to follow disease progression.

AUTHOR CONTRIBUTIONS

AD, GA, and PP contributed conception and design of the review. AD and GA wrote the first draft of the manuscript. PP reviewed the first draft. All authors contributed to manuscript revision, read, and approved the submitted version.

REFERENCES

1. Braak H, Ghebremedhin E, Rüb U, Bratzke H, Tredici K. Stages in the development of {Parkinson}'s disease-related pathology. *Cell Tissue Res.* (2004) 318:121–34. doi: 10.1007/s00441-004-0956-9
2. Cheng H-C, Ulane CM, Burke RE. Clinical progression in Parkinson disease and the neurobiology of axons. *Ann Neurol.* (2010) 67:715–25. doi: 10.1002/ana.21995
3. Grinberg LT, Rueb U, Alho AT, di L, Heinsen H. Brainstem pathology and non-motor symptoms in PD. *J Neurol Sci.* (2010) 289:81–8. doi: 10.1016/j.jns.2009.08.021
4. Seidel K, Mahlke J, Siswanto S, Krüger R, Heinsen H, Auburger G, et al. The brainstem pathologies of parkinson's disease and dementia with lewy bodies. *Brain Pathol.* (2015) 25:121–35. doi: 10.1111/bpa.12168
5. Strafella AP, Bohnen NI, Perlmutter JS, Eidelberg D, Pavese N, Van Eimeren T, et al. Molecular imaging to track Parkinson's disease and atypical parkinsonisms: new imaging frontiers. *Mov Disord.* (2017) 32:181–92. doi: 10.1002/mds.26907
6. Strafella AP, Bohnen NI, Pavese N, Vaillancourt DE, Eimeren T, Politis M, et al. Imaging markers of progression in parkinson's disease. *Mov Disord Clin Pract.* (2018) 5:586–96. doi: 10.1002/mdc3.12673
7. Heim B, Krismer F, De Marzi R, Seppi K. Magnetic resonance imaging for the diagnosis of Parkinson's disease. *J Neural Transm.* (2017) 124:915–64. doi: 10.1007/s00702-017-1717-8
8. Hirsch E, Graybiel AM, Agid YA. Melanized dopaminergic neurons are differentially susceptible to degeneration in Parkinson's disease. *Nature.* (1988) 334:345–8. doi: 10.1038/334345a0
9. Damier P, Hirsch EC, Agid Y, Graybiel AM. The substantia nigra of the human brain. I. Nigrosomes and the nigral matrix, a compartmental organization based on calbindin D(28K) immunohistochemistry. *Brain.* (1999) 122(Pt 8):1421–36. doi: 10.1093/brain/122.8.1421
10. Damier P, Hirsch EC, Agid Y, Graybiel AM.. The substantia nigra of the human brain. II. Patterns of loss of dopamine-containing neurons in Parkinson's disease. *Brain.* (1999) 122(Pt 8):1437–48. doi: 10.1093/brain/122.8.1437
11. Schwarz ST, Mougin O, Xing Y, Blazejewska A, Bajaj N, Auer DP, et al. Parkinson's disease related signal change in the nigrosomes 1–5 and the substantia nigra using T2* weighted 7T MRI. *NeuroImage Clin.* (2018) 19:683–9. doi: 10.1016/j.nicl.2018.05.027
12. Blazejewska AI, Schwarz ST, Pitiot A, Stephenson MC, Lowe J, Bajaj N, et al. Visualization of nigrosome 1 and its loss in PD: Pathoanatomical correlation and *in vivo* 7 T MRI. *Neurology.* (2013) 81:534–40. doi: 10.1212/WNL.0b013e31829e6fd2
13. Lehéricy S, Bardinet E, Poupon C, Vidailhet M, François C. 7 tesla magnetic resonance imaging: a closer look at substantia nigra anatomy in Parkinson's disease. *Mov Disord.* (2014) 29:1574–81. doi: 10.1002/mds.26043
14. Schwarz ST, Afzal M, Morgan PS, Bajaj N, Gowland PA, Auer DP. The "swallow tail" appearance of the healthy nigrosome - a new accurate test of Parkinson's disease: a case-control and retrospective cross-sectional MRI study at 3T. *PLoS ONE.* (2014) 9:93814. doi: 10.1371/journal.pone.0093814
15. Cosottini M, Frosini D, Pesaresi I, Costagli M, Biagi L, Ceravolo R, et al. MR imaging of the substantia nigra at 7 T enables diagnosis of parkinson disease. *Radiology.* (2014) 271:831–8. doi: 10.1148/radiol.14131448
16. Gao P, Zhou PY, Li G, Zhang GB, Wang PQ, Liu JZ, et al. Visualization of nigrosomes-1 in 3T MR susceptibility weighted imaging and its absence in diagnosing Parkinson's disease. *Eur Rev Med Pharmacol Sci.* (2015) 19:4603–9.
17. Nam Y, Gho SM, Kim DH, Kim EY, Lee J. Imaging of nigrosome 1 in substantia nigra at 3T using multiecho susceptibility map-weighted imaging (SMWI). *J Magn Reson Imaging.* (2017) 46:528–36. doi: 10.1002/jmri.25553
18. Jo M, Oh S. A preliminary attempt to visualize nigrosome 1 in the subtantia nigra for parkinson's disease at 3T: an efficient susceptibility map-weighted imaging (SMWI) with quantitative susceptibility mapping using deep neural network (QSMnet). *Med Phys.* (2019) 47, 604–613. doi: 10.1002/mp.13999
19. Mahlknecht P, Krismer F, Poewe W, Seppi K. Meta-analysis of dorsolateral nigral hyperintensity on magnetic resonance imaging as a marker for Parkinson's disease. *Mov Disord.* (2017) 32:619–23. doi: 10.1002/mds.26932
20. Takahashi H, Watanabe Y, Tanaka H, Mihara M, Mochizuki H, Liu T, et al. Quantifying changes in nigrosomes using quantitative susceptibility mapping and neuromelanin imaging for the diagnosis of early-stage Parkinson's disease. *Br J Radiol.* (2018) 91:20180037. doi: 10.1259/bjr.20180037
21. Guan X, Xu X, Zhang M. Region-specific iron measured by MRI as a biomarker for parkinson's disease. *Neurosci Bull.* (2017) 33:561–7. doi: 10.1007/s12264-017-0138-x
22. De Barros A, Arribarat G, Combis J, Chaynes P, Péran P. Matching *ex vivo* MRI with Iron histology: pearls and pitfalls. *Front Neuroanat.* (2019) 13:68. doi: 10.3389/fnana.2019.00068
23. Péran P, Hagberg G, Luccichenti G, Cherubini A, Brainovich V, Celsis P, et al. Voxel-based analysis of R2* maps in the healthy human brain. *J Magn Reson Imaging.* (2007) 26:1413–20. doi: 10.1002/jmri.21204
24. Péran P, Cherubini A, Luccichenti G, Hagberg G, Démonet J-F, Rascol O, et al. Volume and iron content in basal ganglia and thalamus. *Hum Brain Mapp.* (2009) 30:2667–75. doi: 10.1002/hbm.20698
25. Cherubini A, Péran P, Caltagirone C, Sabatini U, Spalletta G. Aging of subcortical nuclei: microstructural, mineralization and atrophy modifications measured *in vivo* using MRI. *Neuroimage.* (2009) 48:29–36. doi: 10.1016/j.neuroimage.2009.06.035
26. De Rochefort L, Liu T, Kressler B, Liu J, Spincemaille P, Lebon V, et al. Quantitative susceptibility map reconstruction from MR phase data using bayesian regularization: validation and application to brain imaging. *Magn Reson Med.* (2010) 63:194–206. doi: 10.1002/mrm.22187
27. Barbosa JHO, Santos AC, Tumas V, Liu M, Zheng W, Haacke EM, et al. Quantifying brain iron deposition in patients with Parkinson's disease using quantitative susceptibility mapping, R2 and R2*. *Magn Reson Imaging.* (2015) 33:559–65. doi: 10.1016/j.mri.2015.02.021
28. Sun J, Lai Z, Ma J, Gao L, Chen M, Chen J, et al. Quantitative evaluation of iron content in idiopathic rapid eye movement sleep behavior disorder. *Mov Disord.* (2019) 35:478–85. doi: 10.1002/mds.27929
29. Barbagallo G, Sierra-Peña M, Nemmi F, Traon AP, Meissner L, Rascol WG, et al. Multimodal MRI assessment of nigro-striatal pathway in multiple system atrophy and Parkinson disease. *Mov Disord.* (2016) 31:325–34. doi: 10.1002/mds.26471
30. Langkammer C, Pirpamer L, Seiler S, Deistung A, Schweser F, Franthal S, et al. Quantitative susceptibility mapping in parkinson's disease. *PLoS ONE.* (2016) 11:e0162460. doi: 10.1371/journal.pone.0162460
31. Ropele S, Langkammer C. Iron quantification with susceptibility. *NMR Biomed.* (2017) 30:e3534. doi: 10.1002/nbm.3534
32. Mazzucchi S, Frosini D, Costagli M, Del Prete E, Donatelli G, Cecchi P, et al. Quantitative susceptibility mapping in atypical Parkinsonisms. *NeuroImage Clin.* (2019) 24:101999. doi: 10.1016/j.nicl.2019.101999
33. Zecca L, Shima T, Stroppolo A, Goj C, Battiston GA, Gerbasi R, et al. Interaction of neuromelanin and iron in substantia nigra and other areas of human brain. *Neuroscience.* (1996) 73:407–15. doi: 10.1016/0306-4522(96)00047-4
34. Zecca L, Bellei C, Costi P, Albertini A, Monzani E, Casella L, et al. New melanic pigments in the human brain that accumulate in aging and block environmental toxic metals. *Proc Natl Acad Sci USA.* (2008) 105:17567–72. doi: 10.1073/pnas.0808768105
35. Sasaki M, Shibata E, Tohyama K, Takahashi J, Otsuka K, Tsuchiya K, et al. Neuromelanin magnetic resonance imaging of locus ceruleus and substantia nigra in Parkinson's disease. *Neuroreport.* (2006) 17:1215–8. doi: 10.1097/01.wnr.0000227984.84927.a7
36. Sasaki M, Shibata E, Kudo K, Tohyama K. Neuromelanin-{Sensitive} {MRI}. *Clin Neuroradiol.* (2008) 18:147–53. doi: 10.1007/s00062-008-8018-4
37. Sulzer D, Cassidy C, Horga G, Kang UJ, Fahn S, Casella L, et al. Neuromelanin detection by magnetic resonance imaging (MRI) and its promise as a biomarker for Parkinson's disease. *NPJ Park Dis.* (2018) 4:11. doi: 10.1038/s41531-018-0047-3
38. Trujillo P, Summers PE, Ferrari E, Zucca FA, Sturini M, Mainardi LT, et al. Contrast mechanisms associated with neuromelanin-MRI. *Magn Reson Med.* (2017) 78:1790–800. doi: 10.1002/mrm.26584
39. Ogisu K, Kudo K, Sasaki M, Sakushima K, Yabe I, Sasaki H, et al. 3D neuromelanin-sensitive magnetic resonance imaging with semi-automated volume measurement of the substantia nigra pars compacta

for diagnosis of Parkinson's disease. *Neuroradiology.* (2013) 55:719–24. doi: 10.1007/s00234-013-1171-8
40. Castellanos G, Fernández-Seara MA, Lorenzo-Betancor O, Ortega-Cubero S, Puigvert M, Uranga J, et al. Automated neuromelanin imaging as a diagnostic biomarker for parkinson's disease. *Mov Disord.* (2015) 30:945–52. doi: 10.1002/mds.26201
41. Pavese N, Tai YF. Nigrosome imaging and neuromelanin sensitive MRI in diagnostic evaluation of parkinsonism. *Mov Disord Clin Pract.* (2018) 5:131–40. doi: 10.1002/mdc3.12590
42. Kuya K, Ogawa T, Shinohara Y, Ishibashi M, Fujii S, Mukuda N, et al. Evaluation of Parkinson's disease by neuromelanin-sensitive magnetic resonance imaging and 123I-FP-CIT SPECT. *Acta Radiol.* (2018) 59:593–8. doi: 10.1177/0284185117722812
43. Pyatigorskaya N, Magnin B, Mongin M, Yahia-Cherif L, Valabregue R, Arnaldi D, et al. Comparative study of MRI biomarkers in the substantia nigra to discriminate idiopathic Parkinson disease. *Am J Neuroradiol.* (2018) 39:1460–7. doi: 10.3174/ajnr.A5702
44. Ohtsuka C, Sasaki M, Konno K, Kato K, Takahashi J, Yamashita F, et al. Differentiation of early-stage parkinsonisms using neuromelanin-sensitive magnetic resonance imaging. *Park Relat Disord.* (2014) 20:755–60. doi: 10.1016/j.parkreldis.2014.04.005
45. Atkinson-Clement C, Pinto S, Eusebio A, Coulon O. Diffusion tensor imaging in Parkinson's disease: review and meta-analysis. *NeuroImage Clin.* (2017) 16:98–110. doi: 10.1016/j.nicl.2017.07.011
46. Hirata FCC, Sato JR, Vieira G, Lucato LT, Leite CC, Bor-Seng-Shu E, et al. Substantia nigra fractional anisotropy is not a diagnostic biomarker of Parkinson's disease: a diagnostic performance study and meta-analysis. *Eur Radiol.* (2017) 27:2640–8. doi: 10.1007/s00330-016-4611-0
47. Deng X-Y, Wang L, Yang T-T, Li R, Yu G. A meta-analysis of diffusion tensor imaging of substantia nigra in patients with Parkinson's disease. *Sci Rep.* (2018) 8:2941. doi: 10.1038/s41598-018-20076-y
48. Haehner A, Schöpf V, Loureiro A, Linn J, Reichmann H, Hummel T, et al. Substantia nigra fractional anisotropy changes confirm the PD at-risk status of patients with idiopathic smell loss. *Park Relat Disord.* (2018) 50:113–6. doi: 10.1016/j.parkreldis.2018.02.026
49. Péran P, Barbagallo G, Nemmi F, Sierra M, Galitzky M, Traon AP-L, et al. MRI supervised and unsupervised classification of Parkinson's disease and multiple system atrophy. *Mov Disord.* (2018) 33:600–8. doi: 10.1002/mds.27307
50. Pozorski V, Oh JM, Adluru N, Merluzzi AP, Theisen F, Okonkwo O, et al. Longitudinal white matter microstructural change in Parkinson's disease. *Hum Brain Mapp.* (2018) 39:4150–61. doi: 10.1002/hbm.24239
51. Du G, Lewis MM, Kanekar S, Sterling NW, He L, Kong L, et al. Combined diffusion tensor imaging and apparent transverse relaxation rate differentiate Parkinson disease and atypical parkinsonism. *Am J Neuroradiol.* (2017) 38:966–72. doi: 10.3174/ajnr.A5136
52. Knossalla F, Kohl Z, Winkler J, Schwab S, Schenk T, Engelhorn T, et al. High-resolution diffusion tensor-imaging indicates asymmetric microstructural disorganization within substantia nigra in early Parkinson's disease. *J Clin Neurosci.* (2018) 50:199–202. doi: 10.1016/j.jocn.2018.01.023
53. Zhong Z, Merkitch D, Karaman MM, Zhang J, Sui Y, Goldman JG, et al. High-spatial-resolution diffusion MRI in parkinson disease: lateral asymmetry of the substantia nigra. *Radiology.* (2019) 291:149–57. doi: 10.1148/radiol.2019181042
54. Zhang Y, Wu IW, Tosun D, Foster E, Schuff N. Progression of regional microstructural degeneration in Parkinson's disease: a multicenter diffusion tensor imaging study. *PLoS ONE.* (2016) 11:e0165540. doi: 10.1371/journal.pone.0165540
55. Lenfeldt N, Eriksson J, Åström B, Forsgren L, Mo SJ. Fractional anisotropy and mean diffusion as measures of dopaminergic function in parkinson's disease: challenging results. *J Parkinsons Dis.* (2017) 7:129–42. doi: 10.3233/JPD-161011
56. Taylor KI, Sambataro F, Boess F, Bertolino A, Dukart J. Progressive decline in gray and white matter integrity in *de novo* Parkinson's disease: an analysis of longitudinal Parkinson progression markers initiative diffusion tensor imaging data. *Front Aging Neurosci.* (2018) 10:318. doi: 10.3389/fnagi.2018.00318
57. Pyatigorskaya N, Mongin M, Valabregue R, Yahia-Cherif L, Ewenczyk C, Poupon C, et al. Medulla oblongata damage and cardiac autonomic dysfunction in Parkinson disease. *Neurology.* (2016) 87:2540–5. doi: 10.1212/WNL.0000000000003426
58. Prange S, Metereau E, Maillet A, Lhommée E, Klinger H, Pelissier P, et al. Early limbic microstructural alterations in apathy and depression in *de novo* Parkinson's disease. *Mov Disord.* (2019) 34:1644–54. doi: 10.1002/mds.27793
59. Unger MM, Belke M, Menzler K, Heverhagen JT, Keil B, Stiasny-Kolster K, et al. Diffusion tensor imaging in idiopathic REM sleep behavior disorder reveals microstructural changes in the brainstem, substantia nigra, olfactory region, and other brain regions. *Sleep.* (2010) 33:767–73. doi: 10.1093/sleep/33.6.767
60. García-Lorenzo D, Longo-Dos Santos C, Ewenczyk C, Leu-Semenescu S, Gallea C, Quattrocchi G, et al. The coeruleus/subcoeruleus complex in rapid eye movement sleep behaviour disorders in Parkinson's disease. *Brain.* (2013) 136:2120–9. doi: 10.1093/brain/awt152
61. Pyatigorskaya N, Gaurav R, Arnaldi D, Leu-Semenescu S, Yahia-Cherif L, Valabregue R, et al. Magnetic resonance imaging biomarkers to assess substantia nigra damage in idiopathic rapid eye movement sleep behavior disorder. *Sleep.* (2017) 40. doi: 10.1093/sleep/zsx149
62. Youn J, Lee JM, Kwon H, Kim JS, Son TO, Cho JW. Alterations of mean diffusivity of pedunculopontine nucleus pathway in Parkinson's disease patients with freezing of gait. *Park Relat Disord.* (2015) 21:12–7. doi: 10.1016/j.parkreldis.2014.10.003
63. Heim B, Krismer F, Seppi K. Structural imaging in atypical parkinsonism. *Int Rev Neurobiol.* (2018)142:67–148. doi: 10.1016/bs.irn.2018.08.010
64. Seki M, Seppi K, Mueller C, Potrusil T, Goebel G, Reiter E, et al. Diagnostic potential of multimodal MRI markers in atypical parkinsonian disorders. *J Parkinsons Dis.* (2019) 9:681–91. doi: 10.3233/JPD-181568
65. Talai AS, Sedlacik J, Boelmans K, Forkert ND. Widespread diffusion changes differentiate Parkinson's disease and progressive supranuclear palsy. *NeuroImage Clin.* (2018) 20:1037–43. doi: 10.1016/j.nicl.2018.09.028
66. Pasternak O, Sochen N, Gur Y, Intrator N, Assaf Y. Free water elimination and mapping from diffusion MRI. *Magn Reson Med.* (2009) 62:717–30. doi: 10.1002/mrm.22055
67. Pasternak O, Westin C-F, Bouix S, Seidman LJ, Goldstein JM, Woo T-UW, et al. Excessive extracellular volume reveals a neurodegenerative pattern in schizophrenia onset. *J Neurosci.* (2012) 32:17365–72. doi: 10.1523/JNEUROSCI.2904-12.2012
68. Ofori E, Pasternak O, Planetta PJ, Li H, Burciu RG, Snyder AF, et al. Longitudinal changes in free-water within the substantia nigra of Parkinson's disease. *Brain.* (2015) 138:2322–31. doi: 10.1093/brain/awv136
69. Ofori E, Krismer F, Burciu RG, Pasternak O, McCracken JL, Lewis MM, et al. Free water improves detection of changes in the substantia nigra in parkinsonism: a multisite study. *Mov Disord.* (2017) 32:1457–64. doi: 10.1002/mds.27100
70. Arribarat G, Pasternak O, De Barros A, Galitzky M, Rascol O, Péran P. Substantia nigra locations of iron-content, free-water and mean diffusivity abnormalities in moderate stage Parkinson's disease. *Parkinsonism Relat Disord.* (2019) 65:146–152. doi: 10.1016/j.parkreldis.2019.05.033
71. Burciu RG, Ofori E, Archer DB, Wu SS, Pasternak O, McFarland NR, et al. Progression marker of Parkinson's disease: a 4-year multi-site imaging study. *Brain.* (2017) 140:2183–92. doi: 10.1093/brain/awx146
72. Guttuso T, Bergsland N, Hagemeier J, Lichter DG, Pasternak O, Zivadinov R. Substantia nigra free water increases longitudinally in parkinson disease. *Am J Neuroradiol.* (2018) 39:479–84. doi: 10.3174/ajnr.A5545
73. Yang J, Archer DB, Burciu RG, Müller MLTM, Roy A, Ofori E, et al. Multimodal dopaminergic and free-water imaging in Parkinson's disease. *Park Relat Disord.* (2019) 62:10–5. doi: 10.1016/j.parkreldis.2019.01.007
74. Planetta PJ, Ofori E, Pasternak O, Burciu RG, Shukla P, DeSimone JC, et al. Free-water imaging in Parkinson's disease and atypical parkinsonism. *Brain.* (2016) 139(Pt 2):495–508. doi: 10.1093/brain/awv361
75. Jelescu IO, Budde MD. Design and validation of diffusion MRI models of white matter. *Front Phys.* (2017) 5:61. doi: 10.3389/fphy.2017.00061
76. Wang JJ, Lin WY, Lu CS, Weng YH, Ng SH, Wang CH, et al. Parkinson disease: diagnostic utility of diffusion kurtosis imaging. *Radiology.* (2011) 261:210–7. doi: 10.1148/radiol.11102277
77. Zhang H, Schneider T, Wheeler-Kingshott CA, Alexander DC. NODDI: practical *in vivo* neurite orientation dispersion and density

imaging of the human brain. *Neuroimage.* (2012) 61:1000–16. doi: 10.1016/j.neuroimage.2012.03.072
78. Kamagata K, Hatano T, Okuzumi A, Motoi Y, Abe O, Shimoji K, et al. Neurite orientation dispersion and density imaging in the substantia nigra in idiopathic Parkinson disease. *Eur Radiol.* (2016) 26:2567–77. doi: 10.1007/s00330-015-4066-8
79. Mitchell T, Archer DB, Chu WT, Coombes SA, Lai S, Wilkes BJ, et al. Neurite orientation dispersion and density imaging (NODDI) and free-water imaging in Parkinsonism. *Hum Brain Mapp.* (2019) 40:5094–107. doi: 10.1002/hbm.24760
80. White NS, Leergaard TB, D'Arceuil H, Bjaalie JG, Dale AM. Probing tissue microstructure with restriction spectrum imaging: histological and theoretical validation. *Hum Brain Mapp.* (2013) 34:327–46. doi: 10.1002/hbm.21454
81. Hope TR, Selnes P, Rektorová I, Anderkova L, Nemcova-Elfmarkova N, BaláŽová Z, et al. Diffusion tensor and restriction spectrum imaging reflect different aspects of neurodegeneration in Parkinson's disease. *PLoS ONE.* (2019) 14:e0217922. doi: 10.1371/journal.pone.0217922
82. Lenglet C, Abosch A, Yacoub E, De Martino F, Sapiro G, Harel N. Comprehensive *in vivo* mapping of the human basal ganglia and thalamic connectome in individuals using 7T MRI. *PLoS ONE.* (2012) 7:e29153. doi: 10.1371/journal.pone.0029153
83. Plantinga BR, Roebroeck A, Kemper VG, Uludag K, Melse M, Mai J, et al. Ultra-high field MRI post mortem structural connectivity of the human subthalamic nucleus, Substantia nigra, and globus pallidus. *Front Neuroanat.* (2016) 10:66. doi: 10.3389/fnana.2016.00066
84. Abulaiti A, Kamagata K, Motoi Y, Hori M, Hattori N, Aoki S. Nigrostriatal degeneration in parkinson disease: evaluation by diffusion tensor tract-specific analysis. *Open J Radiol.* (2015) 05:199–204. doi: 10.4236/ojrad.2015.54027
85. Andica C, Kamagata K, Hatano T, Okuzumi A, Saito A, Nakazawa M, et al. Neurite orientation dispersion and density imaging of the nigrostriatal pathway in Parkinson's disease: Retrograde degeneration observed by tract-profile analysis. *Park Relat Disord.* (2018) 51:55–60. doi: 10.1016/j.parkreldis.2018.02.046
86. Schneider TM, Deistung A, Biedermann U, Matthies C, Ernestus RI, Volkmann J, et al. Susceptibility sensitive magnetic resonance imaging displays pallidofugal and striatonigral fiber tracts. *Oper Neurosurg.* (2016) 12:330–8. doi: 10.1227/NEU.0000000000001256
87. Surova Y, Nilsson M, Lätt J, Lampinen B, Lindberg O, Hall S, et al. Disease-specific structural changes in thalamus and dentatorubrothalamic tract in progressive supranuclear palsy. *Neuroradiology.* (2015) 57:1079–91. doi: 10.1007/s00234-015-1563-z
88. Nilsson C, Markenroth Bloch K, Brockstedt S, Lätt J, Widner H, Larsson EM. Tracking the neurodegeneration of parkinsonian disorders - a pilot study. *Neuroradiology.* (2007) 49:111–9. doi: 10.1007/s00234-006-0165-1
89. Yang H, Wang X, Liao W, Zhou G, Li L, Ouyang L. Application of diffusion tensor imaging in multiple system atrophy: the involvement of pontine transverse and longitudinal fibers. *Int J Neurosci.* (2015) 125:18–24. doi: 10.3109/00207454.2014.896914
90. Ito K, Sasaki M, Ohtsuka C, Yokosawa S, Harada T, Uwano I, et al. Differentiation among parkinsonisms using quantitative diffusion kurtosis imaging. *Neuroreport.* (2015) 26:267–72. doi: 10.1097/WNR.0000000000000341
91. Ito K, Ohtsuka C, Yoshioka K, Kameda H, Yokosawa S, Sato R, et al. Differential diagnosis of parkinsonism by a combined use of diffusion kurtosis imaging and quantitative susceptibility mapping. *Neuroradiology.* (2017) 59:759–69. doi: 10.1007/s00234-017-1870-7
92. Juttukonda MR, Franco G, Englot DJ, Lin YC, Petersen KJ, Trujillo P, et al. White matter differences between essential tremor and Parkinson disease. *Neurology.* (2019) 92:E30–9. doi: 10.1212/WNL.0000000000006694
93. Yang J, Burciu RG, Vaillancourt DE. Longitudinal progression markers of parkinson's disease: current view on structural imaging. *Curr Neurol Neurosci Rep.* (2018) 18:1–11. doi: 10.1007/s11910-018-0894-7

Conflict of Interest: The authors declare that the research was conducted in the absence of any commercial or financial relationships that could be construed as a potential conflict of interest.

Copyright © 2020 Arribarat, De Barros and Péran. This is an open-access article distributed under the terms of the Creative Commons Attribution License (CC BY). The use, distribution or reproduction in other forums is permitted, provided the original author(s) and the copyright owner(s) are credited and that the original publication in this journal is cited, in accordance with accepted academic practice. No use, distribution or reproduction is permitted which does not comply with these terms.

frontiers in Neurology

ORIGINAL RESEARCH
published: 21 August 2020
doi: 10.3389/fneur.2020.00754

Usefulness of PET With [^{18}F]LBT-999 for the Evaluation of Presynaptic Dopaminergic Neuronal Loss in a Clinical Environment

Maria-Joao Ribeiro[1,2,3]*, *Johnny Vercouillie*[1,2,3], *Nicolas Arlicot*[1,2,3], *Clovis Tauber*[1], *Valérie Gissot*[2,3], *Karl Mondon*[2], *Laurent Barantin*[1,2], *Jean-Philippe Cottier*[1,2], *Serge Maia*[2], *Jean-Bernard Deloye*[4], *Patrick Emond*[1,2] and *Denis Guilloteau*[1,2,3]

[1] UMR 1253, iBrain, Université de Tours, Tours, France, [2] CHRU, Tours, France, [3] Inserm CIC 1415, CHRU, Tours, France, [4] Zionexa, Saint-Beauzire, France

Purpose: The density of the neuronal dopamine transporter (DAT) is directly correlated with the presynaptic dopaminergic system injury. In a first study, we evaluated the brain distribution and kinetics of [^{18}F]LBT-999, a DAT PET radioligand, in a group of eight healthy subjects. Taking into account the results obtained in healthy volunteers, we wanted to evaluate whether the loss of presynaptic striatal dopaminergic fibers could be estimated, under routine clinical conditions, using [^{18}F]LBT-999 and a short PET acquisition.

Materials and methods: Six patients with Parkinson's disease (PD) were compared with eight controls. Eighty-nine minutes of dynamic PET following an intravenous injection of [^{18}F]LBT-999 were acquired. Using regions of interest for striatal nuclei, substantia nigra (SN), cerebellum, and occipital cortex, defined over each T1 3D MRI, time–activity curves (TACs) were obtained. From TACs, binding potential (BP_{ND}) using the simplified reference tissue model and distribution volume ratios (DVRs) using Logan graphical analysis were calculated. Ratios obtained for a 10-min image, acquired between 30 and 40 min post-injection, were also calculated. Cerebellum activity was used as non-specific reference region.

Results: In PD patients and as expected, striatal uptake was lower than in controls which is confirmed by BP_{ND}, DVR, and ratios calculated for both striatal nuclei and SN, significantly inferior in PD patients compared with controls ($p < 0.001$).

Conclusions: PET with [^{18}F]LBT-999 could be an alternative to assess dopaminergic presynaptic injury in a clinical environment using a single 10 min acquisition.

Keywords: Parkinson's disease, dopamine, DAT, PET, radiopharmaceutical

OPEN ACCESS

Edited by:
Yu Zhang,
VA Palo Alto Health Care System, United States

Reviewed by:
Jungsu S. Oh,
Asan Medical Center, College of Medicine, University of Ulsan, South Korea
Doris Doudet,
University of British Columbia, Canada

***Correspondence:**
Maria-Joao Ribeiro
maria.ribeiro@univ-tours.fr

Specialty section:
This article was submitted to Movement Disorders, a section of the journal Frontiers in Neurology

Received: *21 January 2020*
Accepted: *18 June 2020*
Published: *21 August 2020*

Citation:
Ribeiro M-J, Vercouillie J, Arlicot N, Tauber C, Gissot V, Mondon K, Barantin L, Cottier J-P, Maia S, Deloye J-B, Emond P and Guilloteau D (2020) Usefulness of PET With [^{18}F]LBT-999 for the Evaluation of Presynaptic Dopaminergic Neuronal Loss in a Clinical Environment. Front. Neurol. 11:754. doi: 10.3389/fneur.2020.00754

INTRODUCTION

The core symptoms of parkinsonian syndrome (akinetic rigid syndrome, tremor syndrome, etc.) may not always be present in a single patient (1). Although Parkinson-like symptoms are often observed in many diseases, the positive diagnosis of Parkinson's disease (PD), despite consensus disease criteria, remains inaccurate. For example, the accuracy of clinical diagnosis of PD varies

between 74% (diagnostic performed by non-experts) and 84% (diagnosis performed by movement disorders experts), and it has not significantly improved in the last 25 years (2).

It has been known for many years that the dopaminergic neurotransmitter system plays a major role in movement disorders, and particularly in PD, as well as in dementia with Lewy body (DLB) (3–7).

The dopamine neuronal transporter (DAT) is responsible for the re-uptake of dopamine from the synaptic cleft to the pre-synaptic neuron and could be used to evaluate the integrity of pre-synaptic dopaminergic fibers (8–13). In this field, molecular imaging exploration of the DAT is a marker of pre-synaptic neuronal integrity and could be very useful for the early diagnosis and follow-up of PD (14) and DLB (6). Currently, in our nuclear medicine department, as in many others, the evaluation of the pre-synaptic dopaminergic neuron's degeneration is explored in clinical routine with a SPECT DAT ligand, the FP-CIT labeled with iodine-123 (15, 16).

However, using a tracer labeled with iodine-123, the protection of the thyroid gland is required beforehand. This protection can be performed with potassium perchlorate 20 min before injection or potassium iodine 1 h before [^{123}I] FP-CIT injection. Then, between the administration of the radiotracer and the SPECT acquisition, a minimum period of 3 h is necessary. Finally, the typical total scan time is around 30 and 45 min depending on the imaging gamma camera used (16).

Thus, the ability to evaluate the integrity of the pre-synaptic dopaminergic system with a radiotracer that does not require a protection of the thyroid—with a relatively short delay between injection and imaging procedure, as well as a fast acquisition—becomes a priority.

For PET imaging, several DAT radioligands labeled with carbon-11 have been proposed for many years. However, since [^{18}F] can be more largely used for clinical purposes than [^{11}C] owing to its longer physical period (110 vs. 20 min), there is an increasing need to produce high-performance radioligands labeled with fluorine-18.

Cocaine derivatives have high affinity for DAT and, among these ligands, the [^{18}F] (2S,3S)-methyl-8-((E)-4-fluorobut-2-en-1-yl)-3-(p-tolyl)-8-azabicyclo[3.2.1]octane-2-carboxylate, or [^{18}F]LBT-999, has been developed for DAT brain imaging. *In vitro* studies have demonstrated that LBT-999 has high affinity for DAT ($K_d = 9$ nM, $B_{max} = 17$ pmol/mg protein) and very high selectivity for DAT vs. serotonin and noradrenaline transporters (17, 18).

In vivo kinetic PET studies using this radioligand in baboons have showed a fast and very high uptake of the tracer in the striatum, with a plateau at 30 min post-injection and a maximal putamen/cerebellum ratio of 30 (19).

In a previous study, our group demonstrated that the cerebral distribution of [^{18}F]LBT-999 on healthy controls was consistent with DAT density and in good agreement with other PET DAT radioligands in the human brain (20).

The use of a PET semi-quantitative index is very interesting to compare populations or to analyze the evolution of the disease or the effectiveness of a treatment. The validated methods for DAT quantification based on a simplified reference tissue model (SRTM) or a Logan analysis rely on PET a dynamic acquisition, which consistently limits their use in clinical settings where dynamic acquisitions are not always feasible. Thus, we not only evaluated whether [^{18}F]LBT-999 would be useful in estimating presynaptic dopaminergic injury but also if this could be done using a 10-min PET acquisition.

MATERIALS AND METHODS

Radiosynthesis

No-carrier-added [^{18}F]LBT-999 was prepared according to Dollé et al. (17) and Sérrière et al. (21). [^{18}F]LBT-999 was produced with a 35 ± 8% radiochemical yield, radiochemical purity higher than 98%, and a mean molar activity of 143 ± 123 GBq/μmol.

Subjects

PET studies with [^{18}F]LBT-999 were performed in a group of six PD patients (age: 69 ± 7 years, Hoehn and Yahr: stages I–II without atypical signs) and compared with our group of eight healthy controls (HC) (age: 69 ± 9 years) initially studied with this same radioligand (20).

In order to meet French regulations and laws on biomedical research, the study was approved by the regional Ethic Committee and the French Agency for Safety and Security for Medical Devices. All the subjects were affiliated to the French social security system and gave their written informed consent after the nature of the procedure had been fully explained.

PET and MRI Acquisitions

An 89 min list mode PET acquisition was acquired followed an intravenous injection of [^{18}F]LBT-999 (3.6 MBq/kg; mean specific activity of 63.4 GBq/μmol at the moment of injection) using an Ingenuity Philips tomograph (Ingenuity TF64; Philips Medical Systems). The acquisition started just before the bolus injection to get the vascular peak. Acquired data were processed with the standard package delivered with the system (PET view software; Philips Medical Systems). For cerebral studies, a low-dose CT helical scan was performed at 80 keV and 40 mAs, delivering an irradiation dose of about 40 mGy × cm. PET sinograms were corrected for tissue attenuation, decay, scatter, and random radiation, and then they were reconstructed using a 3D iterative RAMLA algorithm in voxels of 2 × 2 × 2 mm^3.

Brain MRIs were obtained for all subjects using a 3-T imager (Siemens Verio). T2-weighted images from each subject were used to reveal eventually brain lesions and signal abnormalities in the basal ganglia. In addition, a T1-weighted SPGR acquisition with inversion-recovery was performed to allow a 3D reconstruction of MRI images.

PET Analysis

The time frames collected between 0 and 59 min after injection were summed to create an integrated image, which is used to perform the PET-MRI co-registration. To obtain time–activity curves (TACs) from 0 to 89 min post-injection, volumes of interest for caudate (Cd) and putamen (Pu) nuclei, substantia nigra (SN), occipital cortex, and cerebellum

were defined over each T1 3D MRI, and after the PET-MRI co-registration displaced over PET images, using Pmod (version 3.4) software.

Using TACs (0–89 min) and Pmod software, binding potential (BP_{ND}) using the SRTM and distribution volume ratio (DVR) obtained from Logan graphical analysis were calculated for striatal nuclei and SN. Ratios obtained for a 10-min image (acquired between 30 and 40 min post-injection) were obtained for the same regions. For all the calculations, the cerebellum activity was used as non-specific reference region.

Statistical Analysis

All data are presented as mean ± SD. Mann–Whitney non-parametric *U*-test was used for comparison of tracers binding between PD patients and healthy controls. Statistics were performed using the XLStat software. All tests were two sided, with a significance set at $p < 0.05$.

RESULTS

Figure 1 shows examples of axial PET/MRI fusion images obtained between 30 and 40 min post-injection in a healthy control (HC) and in a parkinsonian patient. A quite homogeneous and symmetrical striatal uptake for healthy controls was observed. In PD patients, the uptake is clearly reduced, especially on the putamen, and as expected, asymmetrical according to the clinically more affected side.

Figure 2 shows examples of TACs obtained for a HC and a PD patient. For the control, we present mean TACs corresponding to caudate nucleus, putamen, and SN. For the patient, the TACs are presented taking into account the more and less affected side of each structure. In the patient, the maximum striatal uptake is lower than that observed in the control. This is especially marked for the more affected putamen that shows a slow radioactive concentration decrease from 20 min post-injection until the end of the acquisition. For the less affected putamen and the more affected caudate nucleus after a plateau between 20 and 60 min post-injection, the radioactive concentration decreases progressively. The less affected caudate presents an uptake distribution quite similar to that of the striatal structures of the controls. For SN, the evolution of radioactivity distribution in controls and PD is very similar with a peak at 10 min and a progressive decrease until the end of the acquisition. The TACs corresponding to the occipital cortex and cerebellum are overlapping for control and patient.

Regarding the cerebral kinetics results obtained in the controls, with stability of the [18F]LBT-999 striatal uptake from 20 min post-injection to the end of the study, and the evidence of an acceptable *in vivo* metabolism, ratios between the striatum and the cerebellum were calculated using a 10-min image acquired between 30 and 40 min post-injection (20).

On **Table 1**, mean ± SD for BP_{ND}, DVR, and ratio values obtained for caudate and putamen nuclei and SN in controls and PD patients are shown. In PD patients, for striatal structures, BP_{ND}, DVR, and ratios were significantly decreased compared with the control group ($p < 0.001$). This decrease is, as expected, more pronounced for the putamen ($p < 0.001$ and 0.01 for putamen and caudate, respectively) and especially for the most affected putamen. This decrease is obviously asymmetrical taking into account the more affected striatal side. However, for SN no significant asymmetry between the two sides is evidenced. No significant differences between BP_{ND} and DVR-1 are found ($p > 0.5$).

DISCUSSION

The results of the present study are not surprising and show, as expected, a decrease of the [18F]LBT-999 striatal uptake in parkinsonian patients. An asymmetrical striatal uptake according to the most affected clinical side was also observed. This is, as expected, more pronounced for the putamen. Concerning SN, we observed a quite symmetric uptake decrease. We should note that the partial volume effect has not been corrected, probably influencing the values calculated for SN

The activity of the occipital cortex is more often used as a non-specific reference region. In this study, we used the cerebellum based on the similarity of the cerebellar and occipital distribution of [18F]LBT-999 evidenced by the TACs. This suggests that these two regions may reflect the non-specific binding of the radioligand. Using three methods of estimation of DAT density, one of which is a simplified method using ratios and a 10-min image, a significant loss of dopaminergic pre-synaptic neurons PD was confirmed. Even using the ratios, and despite an underestimation of the neuronal loss, it is possible to distinguish patients with dopamine striatal damage from normal subjects.

One of the features that could influence the accuracy of the use of ratios is the time peak equilibrium. Unfortunately, for healthy controls, the peak of specific uptake reached at about 80–90 min post-injection, the duration of our acquisition (20). A longer acquisition could probably suggest a more appropriate PET acquisition time window. In any case, very long acquisitions (e.g., 3 h, even with a break) are difficult to accept by PD patients.

However, on the other hand, the metabolic results indicated that the unmetabolized plasmatic fraction of [18F]LBT-999 is predominant up to 45 min post-injection, leading us to propose as a compromise a simple image of 10 min acquired between 30 and 40 min post-injection, certainly well tolerated by the majority of the patients (20).

Another major limitation is that we were unable to take arterial samples that would allow us to validate the quantification methods used. In the validation of any new radioligand, this step is undoubtedly fundamental. We have assumed that either the cerebellum or the occipital cortex can be used as non-specific reference based on studies with other DAT radioligands. We also did not perform tests/retest PET, which could have contributed to the validation of the methods used.

Another important limitation of this study is that we did not compare [18F]LBT-999 with other DAT PET radioligands in the same subjects. In fact, other fluorine-18-labeled

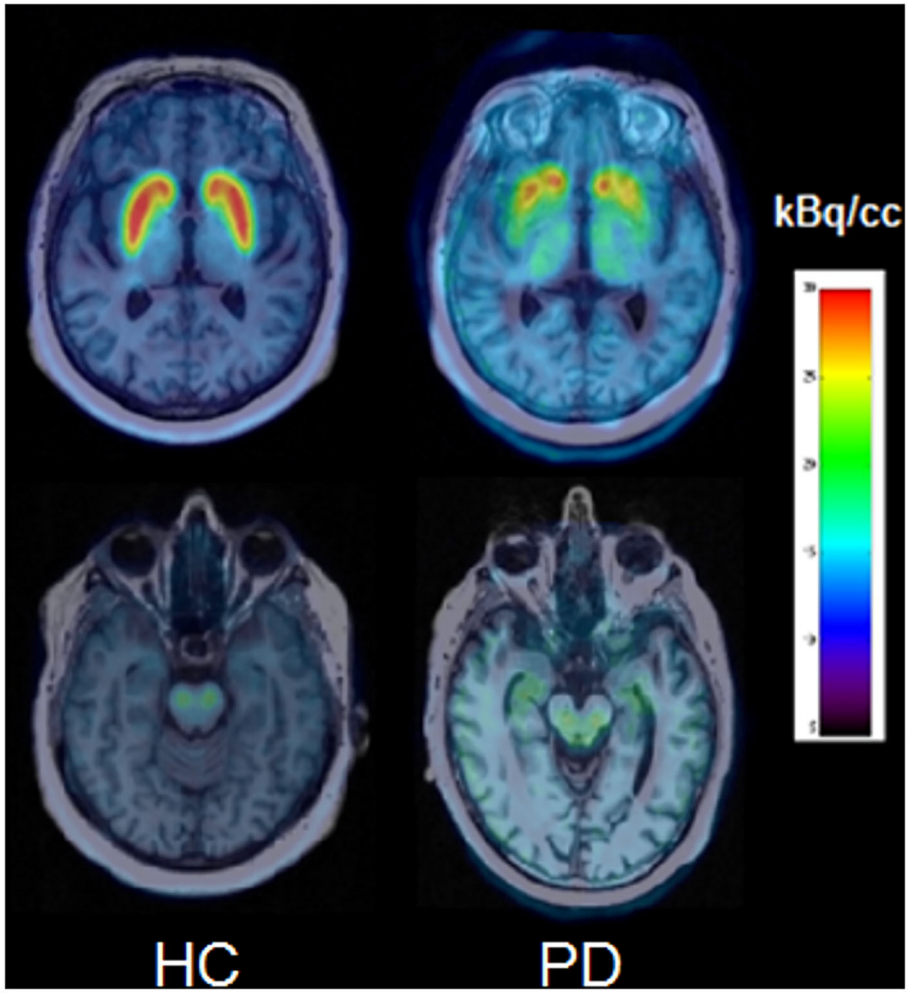


FIGURE 1 | PET/MRI axial slices obtained between 30 and 40 min post-injection for a healthy control (HC) and a PD patient at the level of striatal nuclei **(top)** and midbrain **(bottom)**.

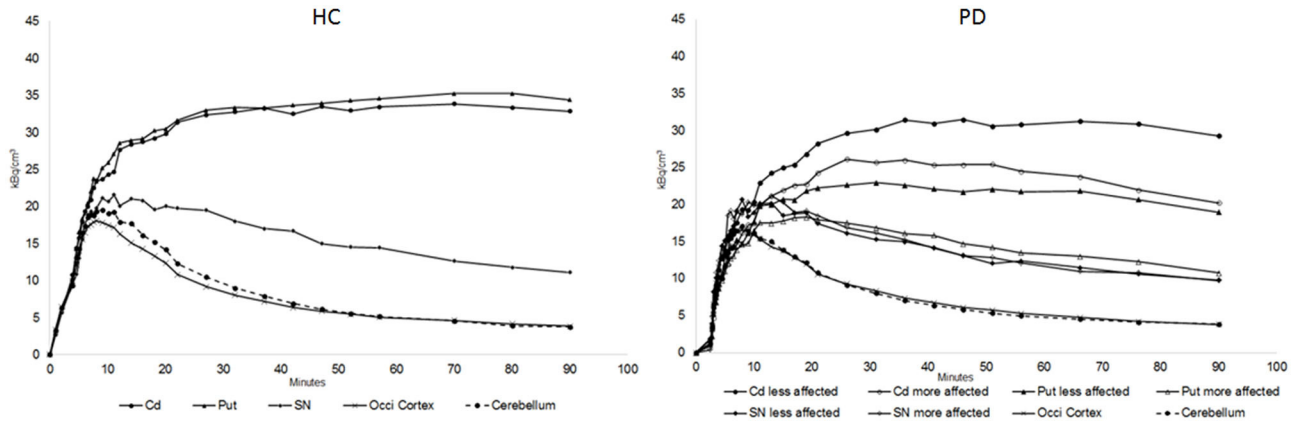


FIGURE 2 | Average TAC of [18F]LBT-999 for caudate (Cd) and putamen (Put) nuclei, substantia nigra (SN), occipital cortex, and cerebellum for a healthy control (HC). For PD patients, TACs are presented for the more and less affected side for the same specific regions.

TABLE 1 | BP_{ND} and DVR (using the dynamic 89 min acquisition) and ratios (calculated from the image acquired between 30 and 40 min post-injection).

		Dynamic acquisition		30–40 min
		BP_{ND}	DVR-1	Ratio
HC	Caudate	6.3 ± 1.2	5.2 ± 0.9	5.0 ± 0.7
	Putamen	6.8 ± 1.2	5.6 ± 1.0	5.4 ± 0.7
	SN	1.3 ± 0.5	1.2 ± 0.5	2.1 ± 0.5
PD	Caudate more affected	3.5 ± 1.5	3.0 ± 0.8	3.5 ± 0.8
	Caudate less affected	4.1 ± 1.4	3.8 ± 1.0	4.0 ± 0.9
	Putamen more affected	2.1 ± 1.4	1.9 ± 0.9	2.8 ± 0.7
	Putamen less affected	3.0 ± 1.8	2.8 ± 1.2	3.4 ± 0.9
	SN more affected	0.6 ± 0.3	0.5 ± 0.3	1.5 ± 0.3
	SN less affected	0.7 ± 0.3	0.6 ± 0.2	1.5 ± 0.3

For patients with Parkinson's disease, we present the values for the more and the less decreased uptake sides.
More affected and less affected sides correspond to the hemispheres contralateral and ipsilateral, respectively, to the less and more clinically affected hemibodies.
Values are mean ± SD.

DAT radioligands have been developed. Among them are [18F]FP-CIT and [18F]FECNT. However, although the former has a concomitant affinity for dopamine and serotonin transporters, the latter presents radiolabeled metabolites that cross the blood–brain barrier with cerebellar accumulation (22, 23).

In the desire to get a tracer targeting the dopamine transporter, our laboratory was involved in the design and the synthesis of new molecules. Among the first compounds developed, PE2I has a very high affinity for the DAT associated with a very good selectivity regarding other monoaminergic transporters (24). This molecule, either radiolabeled with iodine-123 or carbon-11, has been used in many studies in both animals and humans (25, 26). The main limitation of PE2I in PET imaging is that it can only be used by hospitals equipped with a cyclotron owing to the half-life of carbon-11.

In the perspective of having a tracer that can be used more broadly, we invested in the development of analogous of PE2I radiolabeled with fluorine-18. Two molecules have been prepared: LBT-999, the radioligand used in this work, and FE-PE2I. These two tracers, both cocaine derivatives with similar DAT affinity, share the aforementioned structural elements that are decisive to be very potent and selective DAT tracers (9 nM for LBT-999 and 12 nM for FE-PE2I) (18, 27). However, the strategy for obtaining the two radioligands is quite different leading to production times of about 90 min for the [18F]FE-PE2I (28) compared with 30 min for [18F]LBT-999 which is more compatible with a production on an industrial scale (17).

Because FE-PE2I and LBT-999 share similar chemical structures, their *in vitro* and *in vivo* metabolisms are similar (29–31). However, compared with [18F]FE-PE2I, whose metabolism produces five radiometabolites, [18F]LBT-999 produces only three radiometabolites that can potentially interfere with image quality. However, the large number of studies in humans using [18F]FE-PE2I show that, despite this metabolism, fast DAT imaging is possible without observable interference as observed in the present work using [18F]LBT-999 (32).

We also did not compare [18F]LBT-999 to the reference radioligand used in clinical routine in the majority of nuclear medicine centers. Nevertheless, because it is an iodine-123-labeled tracer ([123I]FP-CIT), we must consider the intrinsic characteristics of both nuclear imaging systems. The intrinsic performance of PET compared with SPECT, in terms of spatial resolution and sensitivity, led the exploration of extrapyramidal syndromes with a DAT PET radioligand to become more comfortable for patients: a significantly shorter time of study, with an interval of about 30 min between injection and PET acquisition, and an image acquisition during only 10 min. In fact, for many patients with extrapyramidal syndrome, an acquisition of 35–40 min (as it is necessary in SPECT using the only radiopharmaceutical with the mandatory permissions to clinical use) is often hard to be tolerated. Finally, using non-iodine-labeled DAT ligands, pre-medication to prevent thyroid uptake is not necessary.

Even an important number of limitations, the results of this proof-of-concept study show that [18F]LBT-999 could be used as an alternative to other DAT radiotracers to evaluate the integrity of pre-synaptic striatal dopaminergic fibers with a short image acquired only during 10 min.

Studies including a greater number of patients, with other pathologies with dopaminergic system impairment and if possibly comparing this radioligand with other DAT radioligands are still necessary before validation of [18F]LBT-999 for clinical routine use.

DATA AVAILABILITY STATEMENT

The database of this study has been saved by the clinical research department of the CHU of Tours, which cannot be modified but remains available if requested.

ETHICS STATEMENT

The studies involving human participants were reviewed and approved by Regional Ethic Committee and the French Agency for Safety and Security for Medical Devices. The patients/participants provided their written informed consent to participate in this study.

AUTHOR CONTRIBUTIONS

M-JR, DG, and J-BD contributed for conception and design of the study. JV, SM, and NA contributed for radiopharmaceutical production and controls. M-JR, LB, J-PC, VG, and KM were responsible for acquisition of data. M-JR, J-PC, CT, and PE performed analysis of imaging data. M-JR, JV, KM, CT, PE, and DG wrote sections of the manuscript. M-JR wrote first draft and final version of the manuscript. M-JR, JV, DG, and PE were responsible for critical revision of the manuscript for

important intellectual content. J-BD and DG obtained funding. M-JR and DG were responsible for study supervision. All authors contributed to the article and approved the submitted version.

FUNDING

This study was supported by the French National Agency for Research (INSERM) CVT Aviesan/DVS Agents d'imagerie and Investissements d'Avenir No. ANR-11-LABX-0018-01(IRON) No. EudraCT/ID RCB: 2014-004229-42.

ACKNOWLEDGMENTS

We thank the technical and nursing staffs of CERRP, the Service de Médecine Nucléaire, CIC, and CHRU Tours for their collaboration and assistance.

REFERENCES

1. Zaidel A, Arkadir D, Israel Z, Bergman H. Akineto-rigid vs. tremor syndromes in Parkinsonism. *Curr Opin Neurol.* (2009) 22:387–93. doi: 10.1097/WCO.0b013e32832d9d67
2. Rizzo G, Copetti M, Arcuti S, Martino D, Fontana A, Logroscino G. Accuracy of clinical diagnosis of Parkinson disease: a systematic review and meta-analysis. *Neurology.* (2016) 86:566–76. doi: 10.1212/WNL.0000000000002350
3. Brooks DJ, Salmon EP, Mathias CJ, Quinn N, Leenders KL, Bannister R, et al. The relationship between locomotor disability, autonomic dysfunction, and the integrity of the striatal dopaminergic system in patients with multiple system atrophy, pure autonomic failure, and Parkinson's disease, studied with PET. *Brain.* (1990) 113:1539–52. doi: 10.1093/brain/113.5.1539
4. Leenders KL, Salmon EP, Tyrrell P, Perani D, Brooks DJ, Sager H, et al. The nigrostriatal dopaminergic system assessed *in vivo* by positron emission tomography in healthy volunteer subjects and patients with Parkinson's disease. *Arch Neurol.* (1990) 47:1290–8. doi: 10.1001/archneur.1990.00530120034007
5. Allard PO, Rinne J, Marcusson JO. Dopamine uptake sites in Parkinson's disease and in dementia of the Alzheimer type. *Brain Res.* (1994) 637:262–6. doi: 10.1016/0006-8993(94)91242-4
6. McKeith I, O'Brien J, Walker Z, Tatsch K, Booij J, Darcourt J, et al. Sensitivity and specificity of dopamine transporter imaging with 123I-FP-CIT SPECT in dementia with Lewy bodies: a phase III, multicentre study. *Lancet Neurol.* (2007) 6:305–1. doi: 10.1016/S1474-4422(07)70057-1
7. McCleery J, Morgan S, Bradley KM, Noel-Storr AH, Ansorge O, Hyde C. Dopamine transporter imaging for the diagnosis of dementia with Lewy bodies. *Cochrane Database Syst Rev.* (2015) 1:CD010633. doi: 10.1002/14651858.CD010633.pub2
8. Fischman AJ, Bonab AA, Babich JW, Palmer EP, Alpert NM, Elmaleh DR, et al. Rapid detection of Parkinson's disease by SPECT with altropane: a selective ligand for dopamine transporters. *Synapse.* (1998) 29:128–41. doi: 10.1002/(SICI)1098-2396(199806)29:2<128::AID-SYN4>3.0.CO;2-9
9. Huang WS, Chiang YH, Lin JC, Chou YH, Cheng CY, Liu RS. Crossover study of (99m)Tc-TRODAT-1 SPECT and (18)F-FDOPA PET in Parkinson's disease patients. *J Nucl Med.* (2003) 44:999–5.
10. Varrone A, Halldin C. Molecular imaging of the dopamine transporter. *J Nucl Med.* (2010) 51:1331–4. doi: 10.2967/jnumed.109.065656
11. Ribeiro MJ, Vidailhet M, Loc'h C, Dupel C, Nguyen JP, Ponchant M, et al. Dopaminergic function and dopamine transporter binding assessed with positron emission tomography in Parkinson disease. *Arch Neurol.* (2002) 59:580–6. doi: 10.1001/archneur.59.4.580
12. Bohnen NI, Albin RL, Koeppe RA, Wernette KA, Kilbourn MR, Minoshima S, et al. Positron emission tomography of monoaminergic vesicular binding in aging and Parkinson disease. *J Cereb Blood Flow Metab.* (2006) 26:1198–212. doi: 10.1038/sj.jcbfm.9600276
13. Ba F, Martin WR. Dopamine transporter imaging as a diagnostic tool for parkinsonism and related disorders in clinical practice. *Parkinsonism Relat Disord.* (2015) 21:87–94. doi: 10.1016/j.parkreldis.2014.11.007
14. Catafau AM, Tolosa E. Impact of dopamine transporter SPECT using 123I-Ioflupane on diagnosis and management of patients with clinically uncertain Parkinsonian syndromes. *Mov Disord.* (2004) 19:1175–82. doi: 10.1002/mds.20112
15. Grosset DG, Tatsch K, Oertel WH, Tolosa E, Bajaj N, Kupsch A, et al. Safety analysis of 10 clinical trials and for 13 years after first approval of ioflupane 123I injection (DaTscan). *J Nucl Med.* (2014) 55:1281–7. doi: 10.2967/jnumed.114.138032
16. Isaacson SH, Fisher S, Gupta F, Hermanowicz N, Kremens DE, Lew MF, et al. Clinical utility of DaTscan^{TM} imaging in the evaluation of patients with parkinsonism: a US perspective. *Expert Rev Neurother.* (2017) 17:219–25. doi: 10.1080/14737175.2017.1256205
17. Dollé F, Emond P, Mavel S, Demphel S, Hinnen F, Mincheva Z, et al. Synthesis, radiosynthesis and *in vivo* preliminary evaluation of [11C]LBT-999, a selective radioligand for the visualisation of the dopamine transporter with PET. *Bioorg Med Chem.* (2006) 14:1115–25. doi: 10.1016/j.bmc.2005.09.035
18. Chalon S, Hall H, Saba W, Garreau L, Dollé F, Halldin C, et al. Pharmacological characterization of (E)-N-(4-fluorobut-2-enyl)-2β-carbomethoxy-3β-(4′-tolyl)nortropane (LBT-999) as a highly promising fluorinated ligand for the dopamine transporter. *J Pharmacol Exp Ther.* (2006) 317:147–52. doi: 10.1124/jpet.105.096792
19. Varrone A, Stepanov V, Nakao R, Tóth M, Gulyás B, Emond P, et al. Imaging of the striatal and extrastriatal dopamine transporter with (18)F-LBT-999: quantification, biodistribution, and radiation dosimetry in nonhuman primates. *J Nucl Med.* (2011) 52:1313–21. doi: 10.2967/jnumed.111.089953
20. Arlicot N, Vercouillie J, Malherbe C, Bidault R, Gissot V, Maia S, et al. PET imaging of dopamine transporter with [18F]LBT-999: initial evaluation in healthy volunteers. *Q J Nucl Med Mol Imaging.* (2019). doi: 10.23736/S1824-4785.19.03175-3. [Epub ahead of print].
21. Sérrière S, Tauber C, Vercouillie J, Guilloteau D, Deloye JB, Garreau L, et al. *In vivo* PET quantification of the dopamine transporter in rat brain with [^{1}8F]LBT-999. *Nucl Med Biol.* (2014) 41:106–13 doi: 10.1016/j.nucmedbio.2013.09.007
22. Seo M, Oh M, Cho M, Chung SJ, Lee CS, Kim JS. The effect of SSRIs on the binding of (18)F-FP-CIT in Parkinson patients: a retrospective case control Study. *Nucl Med Mol Imaging.* (2014) 48:287–94. doi: 10.1007/s13139-014-0286-0
23. Zoghbi SS, Shetty HU, Ichise M, Fujita M, Imaizumi M, Liow JS, et al. PET imaging of the dopamine transporter with 18F-FECNT: a polar radiometabolite confounds brain radioligand measurements. *J Nucl Med.* (2006) 47:520–7.
24. Emond P, Guilloteau D, Chalon S. PE2I: a radiopharmaceutical for *in vivo* exploration of the dopamine transporter. *CNS Neurosci Ther.* (2008) 14:47–64. doi: 10.1111/j.1755-5949.2007.00033.x
25. Pinborg LH, Videbaek C, Svarer C, Yndgaard S, Paulson OB, Knudsen GM. Quantification of [(123)I]PE2I binding to dopamine transporters with SPET. *Eur J Nucl Med Mol Imaging.* (2002) 29:623–31. doi: 10.1007/s00259-001-0742-9
26. Ribeiro MJ, Thobois S, Lohmann E, du Montcel ST, Lesage S, Pelissolo A, et al. A multitracer dopaminergic PET study of young-onset parkinsonian patients with and without parkin gene mutations. *J Nucl Med.* (2009) 50:1244–50. doi: 10.2967/jnumed.109.063529
27. Varrone A, Steiger C, Schou M, Takano A, Finnema SJ, Guilloteau D, et al. *In vitro* autoradiography and *in vivo* evaluation in cynomolgus monkey of [18F]FE-PE2I, a new dopamine transporter PET radioligand. *Synapse.* (2009) 63:871–80. doi: 10.1002/syn.20670
28. Schou M, Steiger C, Varrone A, Guilloteau D, Halldin C. Synthesis, radiolabeling and preliminary *in vivo* evaluation of [18F]FE-PE2I, a new probe for the dopamine transporter. *Bioorg Med Chem Lett.* (2009) 19:4843–45. doi: 10.1016/j.bmcl.2009.06.032

29. Amini N, Nakao R, Schou M, Halldin C. Identification of PET radiometabolites by cytochrome P450, UHPLC/Q-ToF-MS and fast radio-LC [11C] Flumazenil, [18F] FE-PE21, and [11C] PBR28. *Anal Bioanal Chem.* (2013) 405:1303–10. doi: 10.1007/s00216-012-6541-2
30. Saba W, Peyronneau MA, Dolle F, Goutal S, Bottlaender M, Valette H. Difficulties in dopamine transport radioligand PET analysis: the example of LBT-999 using [18F] and [11C] labeling Part I: PET studies. *Nucl Med Biol.* (2012) 39:227–33 doi: 10.1016/j.nucmedbio.2011.08.003
31. Peyronneau MA, Saba W, Dollé F, Goutal S, Coulon C, Bottlaender M, et al. Difficulties in dopamine transport radioligand PET analysis: the example of LBT-999 using [18F] and [11C] labeling: part II: metabolism studies. *Nucl Med Biol.* (2012) 39:347–59. doi: 10.1016/j.nucmedbio.2011.09.006
32. Sonni I, Fazio P, Schain M, Christer Halldin C, Per Svenningsson P, Farde L, et al. Optimal acquisition time window and simplified quantification of dopamine transporter availability using 18F-FE-PE2I in healthy controls and Parkinson disease patients. *J Nucl Med.* (2016) 57:1529–34. doi: 10.2967/jnumed.115.171231

Conflict of Interest: J-BD works for Zionexa (formerly Laboratoires Cyclopharma).

The remaining authors declare that the research was conducted in the absence of any commercial or financial relationships that could be construed as a potential conflict of interest.

Copyright © 2020 Ribeiro, Vercouillie, Arlicot, Tauber, Gissot, Mondon, Barantin, Cottier, Maia, Deloye, Emond and Guilloteau. This is an open-access article distributed under the terms of the Creative Commons Attribution License (CC BY). The use, distribution or reproduction in other forums is permitted, provided the original author(s) and the copyright owner(s) are credited and that the original publication in this journal is cited, in accordance with accepted academic practice. No use, distribution or reproduction is permitted which does not comply with these terms.

frontiers in Neurology

BRIEF RESEARCH REPORT
published: 11 September 2020
doi: 10.3389/fneur.2020.540291

Efficacy of Olfactory and Pareidolia Tests Compared With That of Indicative Biomarkers in Diagnosis of Dementia With Lewy Bodies

Yuta Inagawa, Hidekazu Kanetaka, Akito Tsugawa, Shu Sakurai, Shuntaro Serisawa, Soichiro Shimizu, Hirofumi Sakurai and Haruo Hanyu*

Department of Geriatric Medicine, Tokyo Medical University, Tokyo, Japan

Purpose: Although olfactory decline and visual hallucinations are useful in distinguishing dementia with Lewy bodies (DLB) from Alzheimer's disease (AD) in a clinical setting, neither is easy to evaluate objectively. The pareidolia test is used to assess susceptibility to visual hallucinations, while in Japan, the Odor Stick Identification Test for the Japanese (OSIT-J) is used to objectively quantify olfactory decline. The present study investigated the efficacy of these olfactory and pareidolia tests in differentiating AD from DLB. Their usefulness was then compared with that of the indicative biomarkers in neuroimaging for a clinical diagnosis of DLB listed in the Fourth Consensus Report of the Dementia with Lewy Bodies Consortium.

Methods: A total of 24 probable DLB and 22 probable AD patients were enrolled. All underwent 4 diagnostic procedures: uptake of dopamine transporter in single photon emission computed tomography (DaT-SPECT) and meta-iodobenzylguanidine (MIBG) in myocardial scintigraphy, the pareidolia test, and OSIT-J. The sensitivity, specificity, and accuracy of these methods in differentiating DLB from AD were compared.

Results: Sensitivity and specificity in differentiating DLB from AD were 86 and 100% by the heart-to-mediastinum ratio of MIBG uptake; 82 and 96% by the specific binding ratio on DaT-SPECT; 77 and 67% by the combination of OSIT-J and pareidolia test scores; 73 and 62% by the pareidolia test scores; and 77 and 58% by the OSIT-J scores, respectively.

Conclusions: The present results suggest that the pareidolia and OSIT-J tests may be considered before resorting to nuclear neuroimaging in the diagnosis of DLB.

Keywords: MIBG cardiac scintigraphy, DAT (dopamine transporter), pareidolia test, OSIT-J, AD, DLB, dementia with Lewy bodies

OPEN ACCESS

Edited by:
Yu Zhang,
VA Palo Alto Health Care System, United States

Reviewed by:
Fransje Reesink,
University Medical Center Groningen, Netherlands
Emilia J. Sitek,
Medical University of Gdansk, Poland

****Correspondence:***
Yuta Inagawa
yutainagawa0813@yahoo.co.jp

Specialty section:
This article was submitted to Movement Disorders, a section of the journal Frontiers in Neurology

Received: *25 March 2020*
Accepted: *14 August 2020*
Published: *11 September 2020*

Citation:
Inagawa Y, Kanetaka H, Tsugawa A, Sakurai S, Serisawa S, Shimizu S, Sakurai H and Hanyu H (2020) Efficacy of Olfactory and Pareidolia Tests Compared With That of Indicative Biomarkers in Diagnosis of Dementia With Lewy Bodies. Front. Neurol. 11:540291. doi: 10.3389/fneur.2020.540291

INTRODUCTION

Dementia with Lewy bodies (DLB) is recognized as the second most common cause of degenerative dementia in older people after Alzheimer's disease (AD). The Fourth Consensus Report of the Dementia with Lewy Bodies Consortium, published in 2017 (1), lists two indicative biomarkers of DLB in neuroimaging: uptake of dopamine transporter in single photon

emission computed tomography (DaT-SPECT) and that of meta-iodobenzylguanidine (MIBG) in myocardial scintigraphy.

These same diagnostic criteria also include visual hallucinations as a core clinical feature of DLB, along with olfactory decline as a supportive clinical feature that is often also present in such cases. This latter, however, has yet to be proven diagnostically specific. Although these two symptoms are useful in distinguishing DLB from AD in a clinical setting, however, neither is easy to evaluate quantitively.

Pareidolia is similar to visual hallucinations and may be an alternative indicator of hallucinations. The pareidolia test was developed as a tool for evaluating pareidolia (2). The Odor Stick Identification Test for the Japanese (OSIT-J) was developed as a tool for objectively assessing olfactory decline in Japanese people. It is easy to perform and involves the use of odorants and cards (3). The purpose of the present study was to determine the efficacy of olfactory and pareidolia tests in differentiating between AD and DLB. Their usefulness was then compared with that of the indicative biomarkers in neuroimaging for a clinical diagnosis of DLB listed in the 2017 report described above. To our knowledge, this is the first study to compare the diagnostic value of the pareidolia test, OSIT-J, DaT-SPECT, and MIBG myocardial scintigraphy in differentiating DLB from AD in a patient group that underwent all 4 procedures.

METHODS

Patients

A total of 24 probable DLB and 22 probable AD patients who underwent 4 diagnostic procedures (DaT-SPECT, MIBG, the pareidolia test, and OSIT-J®) on their first visit to our establishment were enrolled from the Memory Disorder Clinic at the Department of Geriatric Medicine, Tokyo Medical University. The diagnosis of probable DLB was based solely on the core clinical features of DLB listed in the 2017 report discussed above (1). The diagnosis of probable AD was based on the criteria established by the National Institute on Aging-Alzheimer's Association in 2011 (4). All the AD patients enrolled in this study were of the typical amnestic subtype, and all presented with the complaint of impaired memory. All patients falling under other clinical subtypes of AD (those with posterior cortical atrophy, of the aphasia subtype, or with the frontal variant, for example) were deemed ineligible for inclusion.

The severity of dementia was classified as 0.5 (questionable) to 2 (moderate) in both groups of patients based on Clinical Dementia Rating (5). The Mini-Mental State Examination (6) scores were between 12 and 29.

None of the patients had a history of cerebrovascular disease, degenerative disease, infarction in the region of the basal ganglia or intracranial lesions on brain MRI, thyroid disease, diabetes mellitus, or previous relevant cardiac disease; none were taking any medications or substances known to interact with the striatal binding of ^{123}I-2β-Carbomethoxy-3β-(4-iodophenyl)-N-(3-fluoropropyl) nortropane (^{123}I-FP-CIT) (e.g., cocaine, amphetamines, bupropion, selective serotonin reuptake inhibitors) (7, 8) or that might affect accumulation of MIBG (9). The exclusion criteria comprised a history of nasal disease and current smokers and extremely poor visual acuity, as these may have compromised the reliability of the results of the OSIT- J and pareidolia tests.

The protocol of this study was approved by the Ethics Committee of Tokyo Medical University. Informed consent was obtained from all the study participants (either the patients themselves or their closest relative) before entry, following a detailed explanation of the aim of the study.

Dopamine Transporter Uptake in Single Photon Emission Computed Tomography

Three hours after injecting approximately 185 MBq of ^{123}I-FP-CIT, projection data were acquired on a 128 × 128 matrix by a Siemens Symbia T16 equipped with a low-to-medium energy general purpose collimator. The specific binding ratio (SBR) was calculated semi-quantitatively using DAT VIEW software (AZE, Tokyo, Japan) based on the Tossici-Bolt method described previously (10). In the present study, the left-right average of the SBR was used for the analysis.

Meta-Iodobenzylguanidine Myocardial Scintigraphy

A total of 123 MBq of ^{123}I-MIBG was administered intravenously. Early and delayed SPECT were performed at 20 min and at 4 h after injection, respectively. Planar scanning and SPECT were performed with a gamma camera (PRISM 2000VP, Picker). After scatter correction, relative organ uptake was determined by setting the anterior region of interest (ROI) (11). The heart-to-mediastinum ratio (H/M) was calculated by dividing the left ventricular ROI count density by the mediastinal ROI count density according to the standard method (12). Delayed phase image data were used for the analysis.

Pareidolia Test

The pareidolia test was used to determine the presence of hallucinations, a core clinical feature of DLB. The face version of the noise pareidolia test developed by Yokoi et al. (Tohoku University, Japan) was adopted (13). A total of 40 black and white images (16 × 16 cm^2) with a spatial frequency of 1/f^3 are used in this test, in 8 of which a face is included. All the patients were allowed to undergo training in this test prior to the recording of the results. They were instructed to state whether they observed a face or not on presentation of each image. When the participants observed a face, they were requested to point to it.

The pareidolic illusion rate is defined as the ratio of the total number of images (40) to the number of images that are mistakenly recognized as containing the image of a face (13).

Odor Stick Identification Test (OSIT-J)

Decline in olfactory function was determined with the OSIT-J (Daiichi Yakuhin, Co., Tokyo, Japan). This test comprises the following 12 kinds of odorant: rose, condensed milk, Japanese orange, curry, roasted garlic, fermented beans, sweaty socks, cooking gas, menthol, India ink, wood, and Japanese cypress (*hinoki*), all of which are familiar to Japanese people (14).

Each odorant is encapsulated in a melamine resin microcapsule, which resembles a stick of lip gloss. The examiner

uses each one to paint a 2-cm circle on a piece of paper. They then crush the microcapsule by folding the piece of paper and handing it to the patient. After sampling each odor, the patient is presented with a card showing the names of the 4 odors and asked to make selection. The total number of correct answers for the 12 odorants presented is the OSIT-J score, and the range of the OSIT-J score is 0–12 (15). The cut-off value for decreased olfaction in elderly people over the age of 60 yr is 4–6 points (16).

Statistical Analysis

The Mann-Whitney test, $\chi 2$ test, and Student's *t*-test were used for the analysis. All the values obtained are expressed as the mean ± SD or median, min-max. These data were statistically analyzed using IBM SPSS Statistics version 25 software (Chicago, IL).

The sensitivity and specificity of the respective diagnostic index (H/M ratios of MIBG uptake in the delayed phase); the left-right average of the SBR on DaT-SPECT; the pareidolic illusion rate; the OSIT-J® score; and the combined pareidolic illusion rate and OSIT-J® score to differentiate between DLB and AD were assessed using receiver-operating characteristic (ROC) analysis.

The method of DeLong was used to analyze differences in the area under the curve (AUC) for each result. These data were statistically analyzed using MedCalc version 19 software (Belgium).

A $p < 0.05$ was considered to indicate a statistically significant difference between the two groups.

For the combined use of the pareidolia test and OSIT-J® score, we have developed the "OSIT-J*Pareidolia Test" index, which is defined as the OSIT-J® score* (1-pareidolic illusion rate).

RESULTS

Table 1 shows the characteristics of the patients. The mean age of the patients in the DLB group was 82.4 ± 5.0 yr, while that in the AD group was 80.0 ± 5.6 yr. No significant difference was observed between the two groups (*p*-value, 0.071).

The H/M ratios of MIBG uptake in the delayed phase were 1.3 ± 0.3 and 2.9 ± 0.7 ($p < 0.001$); the left-right average of the SBR on DaT-SPECT 2.2 ± 1.2 and 4.7 ± 1.2 ($p < 0.001$); the OSIT-J* Pareidolia Test scores 2.3 ± 1.9 and 4.2 ± 2.6 ($p < 0.003$); the pareidolia test scores 10.6 ± 11.7 and 3.7 ± 6.6 ($p < 0.011$); and the OSIT-J scores 2.5 ± 2.0 and 4.4 ± 2.6 ($p < 0.004$) in the DLB and AD patients, respectively. The results of all the tests administered (MIBG myocardial scintigraphy, DaT-SPECT, OSIT-J* Pareidolia combination test, pareidolia test, and OSIT-J) all showed a significant difference between the AD and DLB groups.

Figure 1 and **Table 2** show the results of the ROC curve analysis of discrimination between DLB and AD in each test. With MIBG myocardial scintigraphy, the AUC was 0.96, the cut-off score 2.54, sensitivity 86%, specificity 100%, positive predictive value (PPV) 100%, and negative predictive value (NPV) 67%; DaT-SPECT showed an AUC of 0.93, cut-off score of 3.93, sensitivity of 82%, specificity of 96%, PPV of 85%, and NPV of 95%; the OSIT-J* Pareidolia Test showed an AUC of 0.75, a cut-off score of 2.93, sensitivity of 77%, specificity of 67%, PPV of 73%, and NPV of 67%; the pareidolia test showed an AUC of 0.73, cut-off score of 2.50, sensitivity of 73%, specificity of 62%, PPV of 70%, and NPV of 74%; and the OSIT-J showed an AUC of 0.72, cut-off score of 3, sensitivity of 77%, specificity of 58%, PPV of 74%, and NPV 63%. Here, a reduction in the OSIT-J® score was defined as 3 points or fewer, and pareidolia-positive was defined as having a pareidolic illusion rate of >2.5%.

Table 3 shows the results of the comparison of the two ROC curves. The *p*-value for DaT-SPECT vs. MIBG myocardial scintigraphy was 0.54; DaT-SPECT vs. OSIT-J, 0.001; DaT-SPECT vs. the pareidolia test, 0.02; DaT-SPECT vs. the OSIT-J* Pareidolia Test, 0.02; MIBG myocardial scintigraphy vs. OSIT-J, 0.001; MIBG myocardial scintigraphy vs. the pareidolia test, 0.005; MIBG myocardial scintigraphy vs. the OSIT-J* Pareidolia Test, 0.002; OSIT-J vs. the pareidolia test, 0.94; OSIT-J vs. the OSIT-J* Pareidolia Test, 0.75; and the pareidolia test vs. the OSIT-J* Pareidolia Test, 0.9.

TABLE 1 | Patient characteristics.

	DLB group	AD group	*p*-value
Number of patients	24	22	–
Age (year) (median, min–max.)	82.4 (73–91)	80.5 (61–88)	0.071[a]
Male/Female	14/10	11/11	0.5716
Educational history(year) (mean, SD)	13.1 ± 2.8	12.1 ± 2.8	0.227[c]
MMSE score (median, min–max.)	22.9 ± 3.4	20.4 ± 4.8	0.046[a]
OSIT—J score (median, min—max.)	2.0 (0–8)	4.0 (0–11)	0.004[a]
The pareidolic illusion rate (%) (mean, SD)	10.6 + 11.7	3.7 ± 6.6	0.011[c]
OSIT—J*Pareidolia test (median, min–max.)	1.8 (0.0–6.8)	3.9 (0.0–11.0)	0.003[a]
DaT—SPECT SBR(average) (median, min–max.)	2.2 (0.1–4.2)	4.5 (2.7–7.4)	<0.001[a]
MIBG H/M ratio (delay phase) (median, min–max.)	1.2 (0.9–2.2)	3.0 (1.2–4.1)	<0.001[a]

[a]*Mann-Whitney U-test.* [b]X^2 *test.* [c]*Student's t-test.*

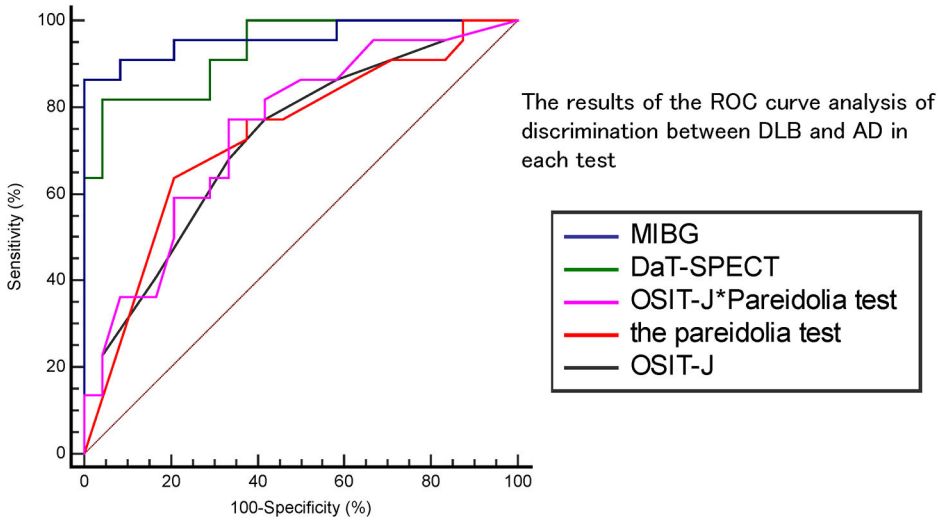


FIGURE 1 | The results of the ROC curve analysis of discrimination between DLB and AD in each test.

TABLE 2 | The results of the ROC curve analysis of discrimination between DLB and AD in each test.

	Sensitivity (%)	Specificity (%)	PPV (%)	NPV (%)	Cut-off score	AUC
MIBG	86	100	100	67	2.54	0.96
DaT-SPECT	82	96	85	95	3.93	0.93
OSIT-J*Pareidolia test	77	67	73	67	2.93	0.75
The pareidolia test	73	62	70	74	2..50	0.73
OSIT-J	77	58	74	63	3	0.72

PPV, Positive Predictive Value; NPV, Negative Predictive Value; AUC, Area under the curve.

TABLE 3 | The results of the comparison of the two ROC curves.

	Difference between areas	Standard Error	Z statistic	*p*-value
MIBG vs. DaT-SPECT	0.028	0.046	0.613	0.540
MIBG vs. OSIT-J	0.237	0.072	3.294	0.001
MIBG vs. the pareidolia test	0.228	0.081	2.832	0.005
MIBG vs. OSIT-J*Pareidolia test	0.214	0.070	3.073	0.002
DaT-SPECT vs. OSIT-J	0.208	0.083	2.520	0.011
DaT-SPECT vs. the pareidolia test	0.200	0.087	2.304	0.021
DaT-SPECT vs. OSIT-J*Pareidolia test	0.186	0.083	2.247	0.024
OSIT-J vs. the pareidolia test	0.008	0.109	0.078	0.938
OSIT-J vs. OSIT-J*Pareidolia test	0.023	0.013	1.703	0.089
the pareidolia test vs. OSIT-J*Pareidolia test	0.014	0.101	0.140	0.089

DISCUSSION

Although both DaT-SPECT and MIBG myocardial scintigraphy are neuroimaging techniques that have high power in diagnosing DLB, they have the disadvantage of being expensive, and can be performed only at hospitals with the necessary equipment. Therefore, there is a growing need for biomarkers that can be tested more easily and cheaply. Typical subjective symptoms related to the diagnosis of DLB include visual hallucinations and decreased olfaction. Assessment of visual hallucinations and decreased olfaction is difficult, however, especially when the patient's own awareness of these symptoms is poor, or

when the caregiver is unable to grasp the true situation as the patient is living alone. The question also remains as to whether subjective reporting of symptoms is truly reliable. Therefore, we hypothesized that if we could objectively assess visual hallucinations and decreased olfaction, it might be useful as a biomarker for DLB diagnosis. The OSIT-J and pareidolia tests are covered by the initial cost of consultation, relieving the patient of a significant financial burden. Moreover, they can be performed in clinics or other small facilities, as no special equipment or space is required.

The results of the present study revealed that patients in the DLB group had a significantly higher pareidolic illusion rate and lower OSIT-J score than those in the AD group. These findings indicate that pareidolia tests, which assess susceptibility to visual hallucinations, and the OSIT-J, which allows quantitative assessment of olfactory decline, are useful in differentiating DLB from AD.

Although the pareidolia test did not show such high sensitivity and specificity in present study, one previous study reported a sensitivity of 100% and specificity of 88% in differentiating DLB from AD (2). This previous study showed no significant difference in visual acuity between the DLB and AD groups. The fact that the current study did not perform an accurate visual acuity test and only excluded patients who were noted to have obvious vision loss during the neuropsychological examination may have affected the accuracy of the pareidolia test.

It has been reported that hyposmia was not only pre-symptomatic of DLB, but also more frequent than the core clinical features normally associated with DLB (17). Therefore, sense of smell is widely considered a major factor in the diagnosis of DLB, making its objective evaluation by means of the OSIT-J® all the more important. In the present study, the OSIT-J® cut-off score for distinguishing DLB from AD was 3 points. One earlier study suggested that the cut-off value for decreased olfaction in elderly people over the age of 60 years is 4–6 points (16). In brief, the cut-off value for discriminating DLB from AD with OSIT-J® was lower than that in screening for hyposmia in the elderly. One study noted that the sense of smell was reduced in not only DLB, but also AD patients (18). Therefore, we believe that the cut-off value in discriminating AD from DLB to be lower than that for olfactory decline.

The diagnostic utility of the tests applied in the present study was not as high as that of DaT-SPECT or MIBG myocardial scintigraphy, both of which have been recommended as useful in detecting indicative biomarkers of DLB in recent diagnostic criteria. Nonetheless, we believe that they do have some utility as they are cheaper and simpler than these standard alternatives. This suggests that the pareidolia and OSIT-J tests may be useful in determining whether to perform further nuclear imaging, or may aid in the diagnosis in areas where nuclear imaging is not available. The present results also revealed that the discriminatory power of the combination of the olfactory and pareidolia tests was not significantly greater than that with either alone.

Therefore, while it is desirable to perform both tests, only one of them may be useful in some cases. In other words, in obtaining diagnostic clues, only olfactory tests may be suitable for patients with visual impairment and pareidolia tests for those with olfactory disorders.

This study had several critical limitations. Firstly, determination of visual hallucinations was based solely on patient-reported symptoms or third-party reporting (caregiver). Further study should use the scale for visual hallucinations as recommended in the "DIAMOND Lewy study (19)." Secondly, it was carried out at a single memory disorder clinic; therefore, the number of patients enrolled in each group was relatively small. Thirdly, the OSIT-J* Pareidolia Test index is an original index devised by our group for this study. Therefore, statistical weighting was not taken into account when setting this index. Further study is necessary to determine the validity of the OSIT-J* Pareidolia Index. Another potential limitation of the present study was the lack of autopsy confirmation in all cases. Rigorous standardized sets of diagnostic criteria were applied, however, all of which have been shown to have a positive predictive value of >80% when judged by postmortem diagnosis (20, 21). Further, large-scale, multicenter studies taking the results of pathological examination into consideration are required to confirm the present results.

In conclusion, the results of the present study suggest that the pareidolia and OSIT-J® tests may be considered before resorting to nuclear neuroimaging in the diagnosis of DLB.

DATA AVAILABILITY STATEMENT

The original contributions presented in the study are included in the article/supplementary material, further inquiries can be directed to the corresponding author/s.

ETHICS STATEMENT

The studies involving human participants were reviewed and approved by the Ethics Committee of Tokyo Medical University. The patients/participants provided their written informed consent to participate in this study.

AUTHOR CONTRIBUTIONS

YI and HK: conception and design of the study. SSa, SSe, HK, and SSh: acquisition and analysis of data. HS and HH: drafting a significant portion of the manuscript or figures. All authors contributed to the article and approved the submitted version.

ACKNOWLEDGMENTS

We would like to thank Professor Jeremy Williams of the Department of International Medical Communications at Tokyo Medical University for reviewing this manuscript.

REFERENCES

1. McKeith IG, Boeve BF, Dickson DW, Halliday G, Taylor JP, Weintraub D, et al. Diagnosis and management of dementia with Lewy bodies: fourth consensus report of the DLB consortium. *Neurology.* (2017) 89:88–100. doi: 10.1212/WNL.0000000000004058
2. Uchiyama M, Nishio Y, Yokoi K, Hirayama K, Imamura T, Shimomura T, et al. Pareidolias: complex visual illusions in dementia with Lewy bodies. *Brain.* (2012) 135:2458–69. doi: 10.1093/brain/aws126
3. Saito S, Ayabe-Kanamura S, Takashima Y, Gotow N, Naito N, Nozawa T, et al. Development of a smell identification test using a novel stick-type odor presentation kit: *Chem Senses*. (2006) 31:379–91. doi: 10.1093/chemse/bjj042
4. McKhann GM, Knopman DS, Chertkow H, Hyman BT, Jack CR Jr, Kawas CH, et al. The diagnosis of dementia due to Alzheimer's disease: Recommendations from the National Institute on Aging Alzheimer's Association workgroups on diagnostic guidelines for Alzheimer's disease. *Alzheimers Dement.* (2011) 7:263-—9. doi: 10.1016/j.jalz.2011.03.005
5. Hughes CP, Berg L, Danziger WL, Coben LA, Martin RL. A new clinical scale for the staging of dementia. *Br J Psychiatry.* (1982) 140:566-—72. doi: 10.1192/bjp.140.6.566
6. Folstein MF, Folstein SE, McHugh PR. "MINI-MENTAL STATE" a practical method for grading the cognitive state of patients for the clinician. *J Gsychiaf Res.* (1975) 12:189–98. doi: 10.1016/0022-3956(75)90026-6
7. Booij J, Kemp P. Dopamine transporter imaging with 123I-FP-CIT SPECT: potential effects of drugs. *Eur J Nucl Med Mol Imaging.* (2008) 35:424–38. doi: 10.1007/s00259-007-0621-0
8. Djang DS, Janssen MJ, Bohnen N, Booij J, Henderson TA, Herholz K, et al. SNM practice guideline for dopamine transporter imaging with 123I-ioflupane SPECT 1.0. *J Nucl Med.* (2012) 53:154–63. doi: 10.2967/jnumed.111.100784
9. Solanki KK, Bomanji J, Moyes J, Mather SJ, Trainer PJ, Britton KE. A pharmacological guide to medicines which interfere with the biodistribution of radiolabelled Meta-Iodobenzylguanidine (MIBG). *Nucl Med Commun.* (1992) 13:513–21. doi: 10.1097/00006231-199207000-00006
10. Tossici-Bolt L, Hoffmann SM, Kemp PM, Mehta RL, Fleming JS. Quantification of [123I]FP-CIT SPECT brain images: an accurate technique for measurement of the specific binding ratio. *Eur J Nucl Med Mol Imaging.* (2006) 33:1491–9. doi: 10.1007/s00259-006-0155-x
11. Kobayashi H, Momose M, Kanaya S, Kondo C, Kusakabe K, Mitsuhashi N. Scatter correction by two-window method standardizes cardiac I-123 MIBG uptake in various gamma camera systems. *Ann Nucl Med.* (2003) 17:309–13. doi: 10.1007/BF02988527
12. Yoshita M, Taki J, Yamada M. A clinical role for [(123)I]MIBG myocardial scintigraphy in the distinction between dementia of the Alzheimer's-type and dementia with Lewy bodies. *J Neurol Neurosurg Psychiatry.* (2001) 71:583–8. doi: 10.1136/jnnp.71.5.583
13. Yokoi K, Nishio Y, Uchiyama M, Shimomura T, Iizuka O, Mori E. Hallucinators find meaning in noises: pareidolic illusions in dementia with Lewy bodies. *Neuropsychologia.* (2014) 56:245–54. doi: 10.1016/j.neuropsychologia.2014.01.017
14. Kobayashi M, Saito S, Kobayakawa T, Deguchi Y, Costanzo RM. Cross-cultural comparison of data using the odor stick identification test for Japanese (OSIT-J). *Chem Senses.* (2006) 31:335–42. doi: 10.1093/chemse/bjj037
15. Iijima M, Kobayakawa T, Saito S, Osawa M, Tsutsumi Y, Hashimoto S, et al. Smell identification in Japanese Parkinson's disease patients: using the odor stick identification test for Japanese subjects. *Intern Med.* (2008) 47:1887–92. doi: 10.2169/internalmedicine.47.1345
16. Shino M, Furuta A, Uchida J, Ooki S, Suzaki H. Odor stick identification test for Japanese patients with olfactory disturbances. *J Otolaryngol Japan.* (2006) 109:689–95. doi: 10.3950/jibiinkoka.109.689
17. Utsumi K, Hatakeyama S, Horano A, Iwamoto T, Takenami M, Himeno D, et al. The incidences of initial symptoms and relevant symptoms of dementia with Lewy bodies, and sex difference, and the relation of prodromal stage: relationship of these symptoms and SPECT, MIBG, DaT. *Japan J Geriatr Psychiatry.* (2017) 28:173–86. Available online at: https://ndlonline.ndl.go.jp/#!/detail/R300000002-I028009031-00
18. Peters JM, Hummel T, Kratzsch T, Lötsch J, Skarke C, Frölich L. Olfactory function in mild cognitive impairment and Alzheimer's disease. *Am J Psychiatry.* (2003) 160:1995–2002. doi: 10.1176/appi.ajp.160.11.1995
19. Thomas AJ, Taylor JP, McKeith I, Bamford C, Burn D, Allan L, et al. Revision of assessment toolkits for improving the diagnosis of Lewy body dementia: the DIAMOND Lewy study. *Int J Geriatr Psychiatry.* (2018) 33:1293–304. doi: 10.1002/gps.4948
20. Knopman DS, DeKosky ST, Cummings JL, Chui H, Corey-Bloom J, Relkin N, et al. Practice parameter: diagnosis of dementia (an evidence-based review). Report of the quality standards subcommittee of the American Academy of Neurology. *Neurology.* (2001) 56:1143–53. doi: 10.1212/WNL.56.9.1143
21. McKeith IG, Ballard CG, Perry RH, Ince PG, O'Brien JT, Neill D, et al. Prospective validation of consensus criteria for the diagnosis of dementia with Lewy bodies. *Neurology.* (2000) 54:1050–8. doi: 10.1212/WNL.54.5.1050

Conflict of Interest: The authors declare that the research was conducted in the absence of any commercial or financial relationships that could be construed as a potential conflict of interest.

Copyright © 2020 Inagawa, Kanetaka, Tsugawa, Sakurai, Serisawa, Shimizu, Sakurai and Hanyu. This is an open-access article distributed under the terms of the Creative Commons Attribution License (CC BY). The use, distribution or reproduction in other forums is permitted, provided the original author(s) and the copyright owner(s) are credited and that the original publication in this journal is cited, in accordance with accepted academic practice. No use, distribution or reproduction is permitted which does not comply with these terms.

frontiers in Neurology

REVIEW
published: 25 September 2020
doi: 10.3389/fneur.2020.531993

Diffusion Tensor Imaging in Parkinson's Disease and Parkinsonian Syndrome: A Systematic Review

Yu Zhang[1]* *and Marc A. Burock*[2]

[1] Department of Psychiatry, War Related Illness and Injury Study Center, Veterans Affairs Palo Alto Health Care System, Palo Alto, CA, United States, [2] Department of Psychiatry, Mainline Health, Bryn Mawr Hospital, Bryn Mawr, PA, United States

Diffusion tensor imaging (DTI) allows measuring fractional anisotropy and similar microstructural indices of the brain white matter. Lower than normal fractional anisotropy as well as higher than normal diffusivity is associated with loss of microstructural integrity and neurodegeneration. Previous DTI studies in Parkinson's disease (PD) have demonstrated abnormal fractional anisotropy in multiple white matter regions, particularly in the dopaminergic nuclei and dopaminergic pathways. However, DTI is not considered a diagnostic marker for the earliest Parkinson's disease since anisotropic alterations present a temporally divergent pattern during the earliest Parkinson's course. This article reviews a majority of clinically employed DTI studies in PD, and it aims to prove the utilities of DTI as a marker of diagnosing PD, correlating clinical symptomatology, tracking disease progression, and treatment effects. To address the challenge of DTI being a diagnostic marker for early PD, this article also provides a comparison of the results from a longitudinal, early stage, multicenter clinical cohort of Parkinson's research with previous publications. This review provides evidences of DTI as a promising marker for monitoring PD progression and classifying atypical PD types, and it also interprets the possible pathophysiologic processes under the complex pattern of fractional anisotropic changes in the first few years of PD. Recent technical advantages, limitations, and further research strategies of clinical DTI in PD are additionally discussed.

Keywords: diffusion tensor imaging (DTI), fractional anisotropy (FA), Parkinson's progression marker initiative (PPMI), diffusion tensor tractography (DTT), dopaminergic pathway, substantia nigra (SN), Parkinsion's disease (PD)

OPEN ACCESS

Edited by:
Emily Keshner,
Temple University, United States

Reviewed by:
Fred Sampedro,
Sant Pau Institute for Biomedical Research, Spain
Shantanu Ghosh,
Akal University, India

***Correspondence:**
Yu Zhang
yuzhangucsfedu@gmail.com;
Yu.Zhang@va.gov

Specialty section:
This article was submitted to Movement Disorders, a section of the journal Frontiers in Neurology

Received: *20 April 2020*
Accepted: *18 August 2020*
Published: *25 September 2020*

Citation:
Zhang Y and Burock MA (2020) Diffusion Tensor Imaging in Parkinson's Disease and Parkinsonian Syndrome: A Systematic Review. Front. Neurol. 11:531993. doi: 10.3389/fneur.2020.531993

INTRODUCTION

Parkinson's disease (PD) is the second most common neurodegenerative disorder after Alzheimer disease. PD generally begins with motor symptoms, including bradykinesia, rigidity, resting tremor, and postural instability. PD also includes numerous non-motor symptoms (such as cognitive impairment, depression, sleep behavioral problems, and olfactory dysfunction) (1). The classical neuropathologic hallmark of PD involves the loss of dopaminergic neurons in the substantia nigra (SN), resulting in a decreased dopaminergic output through the cortico-basal ganglia-thalamocortical motor circuit, which causes dysregulation of motor functions (2). Another neuropathologic characteristic of PD is the presence of Lewy bodies (3) and neurites in both neuron bodies and axons, including aggregates of the α-synuclein protein (4). When

PD begins, the complex features of motor and non-motor symptoms reflect the progression of underlying pathologies, including α-synuclein immunoreactive inclusions in Lewy bodies; loss of dopaminergic, cholinergic, serotonergic, and noradrenergic projections from the brainstem to the midbrain and basal forebrain; and, finally, to the neocortex (5). Over the course of PD, patients commonly experienced comorbid neuropsychiatric disturbances, including depression, behavioral and cognitive deficits, and dementia, which need to be differentiated from other neurodegenerative causes such as dementia with Lewy bodies (DLB) and Alzheimer's disease. On the other hand, the term "parkinsonism" refers to motor syndromes that also present in PD, including bradykinesia, cogwheel rigidity, resting tremor, a slow shuffling gait, and imbalance. The atypical causes of parkinsonism that mimic idiopathic PD include multiple system atrophy (MSA), progressive supranuclear palsy (PSP), or corticobasal syndrome (CBS), as well as drug-induced parkinsonism and others. The most common motor and non-motor syndromes of PD, and other causes of parkinsonism that are involved in PD differential diagnosis, are listed in **Table 1**.

In PD, the loss of dopaminergic neurons and the accumulation of Lewy bodies are typically accompanied by damage of neuroglial cells and demyelination of axons with increasing microglia concentration in extracellular spaces. It is therefore plausible that the detection of extracellular microstructural abnormalities in brain regions with dopaminergic neurons and along dopaminergic pathways might be a biomarker of incipient PD.

TABLE 1 | Motor and non-motor syndromes of PD and other causes of Parkinsonism.

Idiopathic PD motor syndromes	Diseases showing similar motor dysfunctions	Idiopathic PD non-motor syndromes	Diseases showing similar non-motor dysfunctions
- Resting tremor - Bradykinesia - Rigidity - Postural instability - Freezing of gait - Micrographia - Decreased facial movements - Unwanted rapid movements - Other: dystonia, speech problem, Difficulty swallowing, Sexual Dysfunction, Cramping	- Multiple system atrophy (MSA) - Progressive supranuclear palsy (PSP) - Corticobasal syndrome (CBS) - Other: Essential Tremor (ET), drug-induced parkinsonism, normal -pressure hydrocephalus	- Neurodegeneration: Mild cognitive impairment, executive dysfunction, Dementia - Mood and emotion: depression, anxiety, apathy - Smell: hyposmia - Sleep: REM behavioral disorder, Insomnia, Excessive daytime sleepiness - Hallucinations, delusions - Other: fatigue, Autonomic, Pain, Skin problems, Impulsive behaviors due to the side effects of medication	- Dementia with Lewy bodies (DLB) - Demented PD (PDD) vs. Alzheimer's disease - PD with depression

Diffusion Tensor Imaging (DTI), one of the magnetic resonance imaging (MRI) sequences, has been employed to measure white matter microstructural integrity in neurodegenerative diseases, as well as to visualize brain fiber connections via tractography (6). Many quantitative DTI indices (as summarized in **Table 2**) could be derived from a clinical DTI sequence. Fractional anisotropy (FA), radial (RD), axial (AD), and mean diffusivity (MD) have been most commonly used to describe the degree of random motion of water molecules on a microscopic scale. Specifically, FA, which measures the directionality of random water motion, has been used to probe nerve fiber arrangements, axonal integrity, and the degree of axonal myelination (64). FA is clinically feasible to deduce the microstructural integrity of brain tissues, especially preferred to oriented tissues, such as white matter and fiber-tract architectures. MD measures the magnitude of water diffusion. A high MD is thought to indicate broad cellular damages including edema and necrosis. MD is used clinically to capture these microstructural alterations in both gray and white matter tissues (65). AD measures the magnitude of diffusion along the main axis, and RD measures the magnitude of transverse diffusion. In animal studies, increased RD appears to describe myelin pathology-induced myelin thinning (66), while decreased AD indicates acute axonal injury but does not correlate with chronic axonal damage (67). However, the clinical utilities of these DTI metrics have to consider several limitations: (1) All these DTI metrics lack validations with specific neuropathology in postmortem brain. (2) The interpretation of RD/AD might be difficult in voxels containing isotropic structure. Wheeler-Kingshott and Cercignani (68) reported that fictitious changes between RD and AD could occur in areas of low anisotropy, severe pathology, partial volume, and crossing-fibers. They advised that interpretations of RD/AD should be strongly discouraged under such circumstances. (3) There is no appropriate neurobiological implication for AD increases. Linking the increased AD to axonal recovery (as a reverse response of axonal injury) remains questioned, because many studies found AD increase is associated with neurodegenerative disorders such as dementia (69). Despite these limitations, the decreased FA and increased MD have been found correlated with neuronal degeneration (70) and degeneration caused by dopamine loss (71). Further, previous studies (72, 73) reported that abnormal FA values are detected in PD prior to atrophy, suggesting the usefulness of DTI measures as a biomarker of PD in clinical studies.

This study aims to review a majority of clinically employed DTI studies in investigations of PD, together with a comparison of the results from a longitudinal, early stage, multicenter clinical cohort. It is sought to prove the utilities of DTI as a biomarker of diagnosing PD, correlating clinical symptomatology, and tracking disease progression and treatment effects on PD. Advantages and challenges of clinical application of DTI in PD will be discussed further.

TABLE 2 | Summary 1of common microstructural and connectivity indices derived from DTI, as well as their utilities, interpretations, and clinical correlations in PD.

Measures	Modality	Analysis	Interpretation of abnormal indicates	Clinical correlation in PD
Microstructural indices				
Fractional anisotropy (FA)	Diffusion tensor imaging	All analytic types	Low FA: reduced integrity, axonal loss, demyelination, etc. High FA: improved axonal alignment, re-myelination, crossing-fiber, etc.	- Low FA of the SN (7–12), NST (13), thalamic tract (anterior nucleus) (14) correlated with motor dysfunction (UPDRS-III). - Low FA of the basal ganglia regions correlated with non-motor dysfunction (UPDRS except part III) (15). - Low FA of the CC body correlated with the high risk of falls (16). - Low FA of the PPN correlated with severe degree of FOG (17). - Low FA of the entrance to the EC, lateral to the anterior horn of the ventricle, and four ROIs in PFC correlated with severe PIGD symptoms (18). - Low FA correlated of the thalamus with a poor motor speed and balance (19). - Low FA of primarily the frontal and parietal regions correlated with executive, visuospatial dysfunctions (20–24). - Low FA of the parietal regions, CG, UF, ILF SLF, Fornix tracts, correlated with low aggregate cognition, and memory (25, 26). - Low FA of the thalamus (27), left deep temporal cortex (28) correlated with the severe depression. - Low FA of the frontal regions, IFOF correlated with severe sadness (29). - Low FA of the multiple brain tracts, IFL, SFL, cerebellum, IFOF correlated with severe neuroinflammation (30, 31). - Low FA of the Fornix correlated with excessive daytime sleepiness (32). - Low FA of the brainstem correlated with autonomic dysfunction during REM sleep (33). - Low FA of the gyrus rectus correlated with smell loss (34). - Low anisotropy of the CC, Fornix correlated with severe olfactory dysfunction (35). - Low FA of the rostral SN correlated with low DAT-SBR of the putamen (7).
Mean diffusivity (MD)	Diffusion tensor imaging	All analytic types	High MD: atrophy, damaged cellularity, edema, necrosis, etc. less specific to tissue type	- High MD of the SN (36), contralateral Put (37), GP (38), Genu, EC, SCR, ACR (39) corrected with motor dysfunction (UPDRS-III). - High MD of the basal ganglia regions correlated with non-motor dysfunction (UPDRS except part III) (15). - High MD of the CC body correlated with the higher risk of falls (16). - High MD of the PPN (17), PLIC (40) correlated with severe degree of FOG. - High MD of the entrance to the EC, lateral to the anterior horn of the ventricle, and four ROIs in PFC correlated with severe PIGD symptoms (18). - High MD of the brainstem, thalamus, IC and SCR (41), the tracts projecting to the right pre- and primary motor cortices correlated with high tremor scores (42). - High MD of the thalamus, SLF correlated with a worse motor speed and balance (19). - High MD of the frontal, parietal, temporal regions correlated with executive dysfunction (21, 24, 43, 44). - High MD of extensive regions, UF, ILF SLF tracts, correlated with low global cognition dysfunction (26, 45, 46). - High MD of the medial temporal region, Hippocampus, ILF, CG correlated with memory dysfunction (47, 48). - High MD of the IFL, SFL, cerebellum, IFOF correlated with high inflammatory parameters (30). - High MD of the temporal region, ILF, CG, Fornix correlated with language dysfunction (47). - High MD of the brainstem correlated with autonomic dysfunction during REM sleep (33). - High MD of the SN correlated with smell loss (49).

(Continued)

TABLE 2 | Continued

Measures	Modality	Analysis	Interpretation of abnormal indicates	Clinical correlation in PD
Radial and axial diffusivity (RD, AD)	Diffusion tensor imaging	All analytic types	High RD: de- or dys-myelination, changes in the axonal diameters or density. Low AD: axonal injury. High AD: unclear	- High RD/AD of the SN (7), NST (13), EC, SCR, ACR, IFOF, PTR (39), CST, CG, CC (50) correlated with motor dysfunction (UPDRS-III). - High RD/AD of the basal ganglia regions correlated with non-motor dysfunction (UPDRS except part III) (15). - High RD of the entrance to the EC, lateral to the anterior horn of the ventricle, and four ROIs in PFC correlated with severe PIGD symptoms (18). - High RD of the prefrontal cortex region correlated with executive and visuospatial dysfunction (51). - High RD/AD of the CG associated with global cognitive decline (50). - High RD of the basal forebrain Cholinergic regions correlated with memory and executive dysfunctions (52). - High RD of the IFL, SFL, cerebellum, IFOF correlated with high inflammatory parameters (30). - High RD/AD of the SN correlated with smell loss (49).
Mean kurtosis (MK)	Diffusion kurtosis imaging using multiple *b* values	ROI and whole brain	High MK: more hindered and restricted diffusion environment. Low MK: more tissue complexity	- High MK of the SN correlated with motor dysfunction (H&Y, and UPDRS-III) (53). - High MK of the frontal, temporal, basal ganglia, limbic, and paralimbic regions correlated with motor deficits (UPDRS-III) (54).
Free water (FW)	Reconstructed from DTI, using bi-tensor model	ROIs, local tracts	High FW: increased extra-cellular space can be attributed to atrophy	- High FW of the SN correlated with motor dysfunction (UPDRS-III, H&Y) in overall PD and control groups (55, 56). - High FW of the SN correlated with low cognition (MoCA) in PD and control groups (55, 56). - High FW of the posterior SN correlated with low DAT-SBR of the putamen (55).
Connectivity indices:				
Streamline/fiber numbers, density or volume	Diffusion tensor tractography, tensor density imaging (TDI)	Local or whole brain tracts	Low streamline profiles: lost axons, disrupted neuropathway, artifact or crossing-fiber	- Low connectivity matrix of the pallidum–putamen connection correlated with motor dysfunction (UPDRS-III) (57). High connectivity matrix of sensorimotor cortex–putamen correlated with motor dysfunction (UPDRS-III) (57). - Low connectivity metrics between bilateral SMAs correlated with smell loss and motor dysfunction (UPDRS-III) (58). - Low fiber count of the NST correlated with motor dysfunction (UPDRS-III) (59). - Low fiber density of the basal ganglia local connections correlated with motor dysfunction (UPDRS-III) (60).
Intracellular volume fraction (Vic), Orientation dispersion index (OD)	Multiple *b* values fitted to the neurite orientation dispersion and density imaging (NODDI) model	Local tracts	Likely to explain neurite density Low Vic and OD: neuronal loss or loss of neuronal fibers	- Low Vic and OD of the putamen and SNc correlated with increased PD duration and UPDRS-III (61).
Connectome	Graph theory and network measures	Whole brain inter-Connectivity	Likely to explain structural connectivity according to global efficiency, clustering coefficient, path length, etc.	- Low local efficiency between putamen and local regions correlated with motor dysfunction (UPDRS-III) (62). - Low global efficiency and clustering coefficient correlated with decreased CSF levels of a-synuclein, and $A\beta_{42}$ – abnormal aggregation (63).

SN, substantia nigra; NST, nigrostriatal tract; CC, corpus callosum; PPN, pedunculopontine nucleus; PLIC, posterior limb of the internal capsule; FOG, freezing of gait; PFC, prefrontal cortex; PIGD, postural imbalance and gait difficulty; CG, cingulum, or cingulate tract; UF, uncinate fasciculus; ILF, inferior longitudinal fasciculus; SLF, superior longitudinal fasciculus; IFOF, inferior fronto-occipital fasciculus; Put, putamen; GP, globus pallidum; EC, external capsule; IC, internal capsule; SCR, superior corona radiata; ACR, anterior corona radiata; PTR, posterior thalamic radiation; CST, corticospinal tract; SMA, supplementary motor areas; DAT-SBR, striatal binding ratios on dopamine transporter single photon emission tomography; REM sleep, rapid eye movement sleep.

DTI ASSESSMENT OF PD DIAGNOSIS

Non-hypothesis Driven, Voxel-Wise DTI Analyses in PD

The voxel-based whole brain analysis is a computational approach to identify to what extent in brain anatomy there are significant group differences in DTI indices, via a voxel-by-voxel comparison throughout the entire brain. This analysis automatically registers individual DTI maps to a template, which reduces the significant differences in brain anatomy between people. Registration algorithms can be intensity-based, for example, voxel-based analyses (VBA) (74), or tract-based, for example, tract-based spatial statistics (TBSS) (75). The advantages of the whole brain analyses are fully automatic, unbiased, unsupervised, without the need of prior hypotheses. However, the disadvantages of the whole brain approaches could be sensitive to various artifacts and technical issues, which include mis-registration of brain tissues, mis-classification of tissue types, etc. All these matters may confound the statistical analysis and either decrease the sensitivity to true DTI effects or increase the chance of false positives. Multiple studies have utilized non-hypothesis driven DTI analyses (**Table 3**) in comparing PD with healthy controls (HC). By analyzing datasets with a large variety of sample ages, disease severity, medication status, and non-motor symptoms, these studies reported a heterogeneous, multifocal pattern of abnormal DTI changes. The complex distribution of abnormal DTI changes is consistent with the notion that PD is a multisystem disorder involving several neurotransmitters beyond the loss of only dopamine. A recent review (102) summarized the various anatomical regions where abnormal DTI values correlated with a variety of PD symptomatology, including motor and motor phenotypes as well as non-motor features such as cognitive, mood, olfactory dysfunction, hallucinations/psychosis, and sleep disturbance, such as rapid eye movement sleep behavior disorder (RBD). It is therefore conceivable that the inconsistent findings of DTI abnormality across previous studies reflect the clinical heterogeneity of the study population. In this context, it will be indeed necessary to replicate these findings in a large population, detect imaging-clinical correlations under unique types of dysfunction, and track how these findings may alter during the early course of PD.

The Parkinson's Progression Markers Initiative (PPMI) Findings

Previous studies have highlighted a very complex picture of DTI as a PD-specific biomarker. For example, some studies reported that PD exhibits significantly lower FA, but some others showed PD has higher FA than HC subjects. To address if an FA increase or decrease is a characteristic feature of PD, we investigated the temporal changes of FA along the early disease course, by analyzing data from a multicenter, longitudinal PPMI (103) cohort (from now on termed "this study"). The methodological details of data selection, MRI acquisition, image processing, and analyses of this study are described in the **Supplementary Material S1–S3**. Overall, the PPMI data is characterized as early diagnosed cases (diagnosed within 2 years), drug-naïve (*de-novo*) including 22% patients with onset at young adulthood (i.e., age $\leq$ 50 years). Figures below depict the findings resulted from this study, as a comparison with the numerous results published previously.

Figure 1 shows statistical T-maps of FA differences between PD groups within year-1 (Y0) or more than 3 years (Y3), and demographically matched HC groups. Considering the impact of age at PD onset, the figure illustrated results of group differences separately for young-onset group (YPD, age of onset $\leq$ 50 years) and typical-onset group (OPD, age of onset $>$ 50 years). In comparison between YPD(Y0) and YHC, significantly higher FA was observed in patients in multiple brain regions, including the bilateral corticospinal tract (CST), internal capsule, striatum (the putamen, pallidum, and caudate nuclei), anterior and posterior and superior corona radiata, as well as in white matter areas that lie next to the motor and supplementary motor cortices. Further, a comparison between YPD(Y3) and YHC showed that higher FA in patients remained significant in the internal capsule, striatum, corona radiata, and motor and supplementary motor white matter areas, but with a lesser extent of distribution. In the comparison between YPD and YHC groups, no region was found with lower-than-normal FA. On the other hand, the comparison between OPD(Y0) and OHC showed significantly higher FA in patients only in the bilateral CST. The comparison between OPD(Y3) and OHC showed prominently lower FA in patients in the SN, midbrain, thalamus, and multifocal non-motor areas of the white matter across all major lobes, while no area was found with higher-than-normal FA.

Figure 2 depicts temporal pattern of FA changes during the early course of PD (from 0 to 79 months after the clinical diagnosis was made) in the SN and CST. For comparison, FA of the HC subjects at baseline are presented. The scatter plots are separately illustrated for the YPD vs. YHC groups and OPD vs. OHC groups. In CST, FA was significantly increased from the first year through the third year for both YPD and OPD, and later decreased to a normal level after the third year of clinical PD. In the SN, FA reduced steadily for OPD throughout the PD course.

Despite a multifocal regional pattern of FA reduction, which has been consistent with those commonly reported in literature, this study presented a robust FA increase in extensive motor areas in a large sample of the earliest and young-onset PD. The FA increase in the CST and other motor areas is not surprising because it has been also reported in previous studies using PPMI data (89, 97, 98) or other pilot data (80, 85, 92). Reduced FA is often found in neurodegenerative conditions, such as aging, Alzheimer's disease, and Parkinsonism, and is believed to be attributed to demyelination, loss of axons, and interrupted connection. It is unlikely that an FA increase is interpreted as its opposite physiological meaning (e.g., axonal regeneration, remyelination, redundant white matter networks) in neurodegenerative disorders. A meta-analysis (104) revealed that previous studies usually considered the FA increase to be due to methodological confounding factors. For example, different MRI scanners, field strength, and the number of diffusion directions could result in variability of the FA measurement and make group comparisons very difficult based on a multi-center population. Another issue is that voxels composed of

TABLE 3 | An overview of the non-hypothesis driven DTI studies in Parkinson's disease.

Author, year	Group	Age	Duration (years)	UPDRS-III	H&Y	Medication	Non-motor syndromes	Region of FA decrease/MD increase	Region of FA increase/MD decrease
Zhang et al. (76)	25 HC 25 PD	58.4 (9.8) 58.4 (9.3)	5 (2–29)	48.0 (14.0)	1–3	Medicated	w/o factory dysfunction; normal cognition	[FA] bilateral cerebellar hemispheres, right rectus gyrus [MD] bilateral orbitofrontal cortices, bilateral inferior temporal gyri	[FA] *n.s.* [MD] bilateral parietal lobes and left MC
Rae et al. (21)	15 HC 14 PD	64 (50–75) 65 (51–78)	10 (4–20)	20 (14–32)	2.1 (1.5–3)	Medicated (ON/OFF)		[FA] prefrontal and parietal WM, the CC, and the superior CST [MD] prefrontal WM and the CC	
Zhan et al. (11)	20 HC 12 PD	67.4 (8) 67.2 (8)		26.3 (12.2)		Medicatd (OFF)		[FA] superior and inferior MC, superior postcentral gyrus, posterior striatum, frontal WM, and along projections to the SMA, IC, EC, in the proximity of the Put, thalamus, and SN	
Gallagher et al. (22)	15 HC 15 PD	60.3 (10) 62.7 (6.5)	5.6 (5)	10 (12)	1.63	Medicated	w/ executive dysfunction	[FA] ALIC, ACR, body of CC, SS, UF, and deep cerebellar WM [MD] similar and more extensive than distribution of FA	
Kim et al. (77)	64 HC 64 PD	63.0 (8.9) 62.9 (9)	5.3 (5.4)		2 (1-4)	Medicated (OFF)	Normal cognition	[FA] *n.s.* [MD] corticofugal tract, CG, UF, FXST, CC, EC, SLF, PTR, and tracts adjacent to the precuneus and supramarginal gyrus	
Theilmann et al. (23)	26 HC 25 PD	65.9 (8.4) 68.0 (8.9)	7.2 (4.8)	25.4 (8.9)	2.4 (0.3)	Medicated (ON)	w/ impaired cognition	[FA] widespread, bilateral frontal tracts, left parietal and occipital tracts [MD] widespread, bilateral frontal tracts, parietal and occipital tracts	
Auning et al. (51)	19 HC 18 PD	64.6 (6.5) 66.7 (5.1)	2.2 (1.1)	12.3 (6.8)	1.7 (0.6)	Medicated	Slightly depressed	[FA] frontoparietal regions, CC and the posterior CG	
Diez-Cirarda et al. (78)	15 HC 37 PD	65.1 (7.0) 68.0 (6.2)	6.96 (5.6)	21.7 (10.3)	1.9 (0.5)	Medicated (ON)	w/impaired cognition	[FA] right UF [MD] *n.s.*	
Jiang et al. (79)	34 HC 31 PD	69.3 (8) 69.4 (8)	∼4 (2)	∼20 (9)	∼3 (1)	Partly medicated	w/ depression, impaired cognition and self-care ability	[FA] CC, SLF, ILF, CG, optic radiation, left IC and subcortical arcuate fibers	
Koshimori et al. (43)	14 HC 16 PD	67.1 (5.1) 70.5 (5.6)	6.7 (4.2)	25.3 (15.3)		Medicated (ON)	w/ impaired cognition	[FA] *n.s.* [MD] larger area of bilateral frontal and temporal regions and smaller areas of the left parietal and occipital regions	
Skidmore et al. (80)	22 HC 20 PD	64 (9) 61 (13)	5–12	34 (14)	3 (1.5–5)	Medicated (OFF)	w/ impaired cognition, depression		[FA] Rectal gyrus, middle CG, bilateral Put, left thalamus
Vercruysse et al. (81)	15 HC 15 PD	68.1 (6.5) 67.6 (5.6)	7.6 (5.3)	32.5 (9.1)	2.5 (2–2.5)	Medicated	w/o freezing of gait		[FA] body of CC [MD] body of CC, CST, pre-central WM, Anterior cerebellum

(Continued)

TABLE 3 | Continued

Author, year	Group	Age	Duration (years)	UPDRS-III	H&Y	Medication	Non-motor syndromes	Region of FA decrease/MD increase	Region of FA increase/MD decrease
Yoo et al. (82)	18 HC 9 PD	54.4 (6.5) 59.6 (8.6)	10.6 (3.9)	14.4 (8.0)	2.2 (0.4)	Medicated (ON)	w/o impulse control disorder	[FA] bilateral orbitofrontal, medial prefrontal, anterior cingulate areas [MD] *n.s.*	
Youn et al. (17)	33 HC 42 PD	69.6 (5.8) 69.1 (6.4)	9.2 (4.0)	20.1 (10.6)	2.3 (0.3)	Medicated (ON)	w/ and w/o freezing of gait	[FA] left thalamus, bilateral orbitofrontal area, bilateral SN [MD] bilateral inferior temporal cortex, orbitofrontal cortex, insula and left frontal area	
Duncan et al. (44)	50 HC 125 PD	65.8 (8.0) 66.0 (10.5)	0.51 (0.4)	26.8 (11)[b]	2 (1–3)	Medicated (ON)	w/ impaired cognition	[FA] *n.s.* [MD] forceps minor, CG, SLF, ILF, IFOF, CST, CC and IC	
Price et al. (83)	40 HC 40 PD	68.2 (4.6) 67.8 (5.4)	7.5 (5.1)	2.8 (3.4) 17.6 (10.7)	1.6 (0.8)	Medicated (ON)	w/ some impaired cognition	[FA] genu and body of CC, forceps minor, ATR, IFOF and UF	
Lim et al. (84)	25 HC 14 PD	68.5 (6.6) 69.7 (7.2)	4.4 (3.7)	22.4 (10.6)	1.6 (0.5)	Medicated (OFF)	w/o rapid eye movement sleep behavior disorder	[FA] mainly in both frontal Areas [MD] widespread	
Mole et al. (85)	26 HC 24 PD	64.9 (8.1) 63.4 (10.8)		25 (11)	1.8 (0.4)	Medicated (OFF)		[FA] right UF	[FA] CST, right Put-SMA, bilateral Thalamus-MC
Wang et al. (86)	16 HC 16 PD	68.6 (2.6) 68.9 (6.0)	3.7 (2.9)	20.9 (10.6)		Not mentioned	w/o freezing of gait	[FA] genu and body of CC, left SCR [MD] CC (genu, body, splenium), right SCR, right IC and EC, bilateral PTR, SLF, and corona radiata	
Wen et al. (39)[a]	60 HC 54 HY1PD 87 HY2PD	60.3 (10.8) 60.2 (9.6) 62.0 (9.3)	0.5 (0.5) 0.6 (0.6)	14.7 (5.7)[b] 25.1 (8.6) [b]	1 2	*de-novo*			[FA] CC, forceps minor, the thalamic radiation, ACR, SCR, and PLIC, EC, SLF, ILF, IFOF and CG [MD] aforementioned WM tracts
Canu et al. (87)	28 HC 28 PD	61.9 (8.3) 63.6 (6.5)	9.7 (5.4)	47.3 (8.2)	2.6 (0.5)	Medicated (ON)	w/o impulsive-compulsive behaviors, with depression	[FA] *n.s.* [MD] left pedunculopontine tract and splenium of CC	
Chen et al. (88)	24 HC 18 PD	62.9 (3.7) 62.3 (4.6)	3.1 (2.8)	17.4 (8.7)		Medicated (OFF)		[FA] body of CC, fornix, left hippocampus, and left IFOF	
Chen et al. (24)	33 HC 24 PD	48.6 (7.8) 48.4 (6.5)	3.2 (3.0)	19.1 (13.6)	1.7 (1.0)	Not mentioned	w/ abnormal executive and visuospatial function	[FA] right SLF, right temporal WM, left inferior and superior parietal WM, bilateral ATR, bilateral occipital WM, left IFOF, left CST, left Put [MD] left inferior parietal WM, bilateral occipital WM, right parietal WM, and right posterior SLF	

(Continued)

TABLE 3 | Continued

Author, year	Group	Age	Duration (years)	UPDRS-III	H&Y	Medication	Non-motor syndromes	Region of FA decrease/MD increase	Region of FA increase/MD decrease
Chiang et al. (30)	67 HC 66 PD	56.8 (9.8) 58.1 (8.7)	9.4 (4.5)	22.7 (16.8)	2.0 (1.1)	Medicated	w/ inflammation	[FA] left parietal and right occipital ILF, left postcentral and right parietal SLF, left cerebellum, and left IFOF. [MD] left ILF, right SLF, left cerebellum, and left IFOF	
Cousineau et al. (89)[a]	179 HC 412 PD		<2		1–2	*de-novo*			[FA] CC, CST, nigro-subthalamo-putaminal-thalamocortical connections
Georgiopoulos et al. (90)	13 HC 22 PD	68 (65–70) 68 (67–70)	7 (2)	20 (16–27)	2 (1.5–3)	Medicated (ON)	w/ olfactory dysfunction		[FA] *n.s.* [MD] left CST, bilateral PLIC, neural tracts adjacent to left SN
Kamagata et al. (54)	28 HC 30 PD	66.5 (10.8) 67.6 (9.8)	6.4 (3.7)	16.1 (8.8)	2.1 (0.9)	Medicated		[FA] left temporal, left limbic, and paralimbic areas [MD] left frontal, left temporal, left limbic, and paralimbic areas	
Lee et al. (91)	30 HC 21 PD	68.6 (6.0) 66.2 (6.8)	7.0 (4.2)	16.4 (5.1)	1.8 (0.5)	medicated	w/o visual hallucination	[FA] the bilateral fronto-temporo-parietal areas, midbrain and pons [MD] *n.s.*	
Luo et al. (41)	26 HC 30 PD-TD	53.4 (10) 54.5 (8)	2.0 (1.7)	25.4 (12)	1.6 (0.5)	Partly medicated (OFF)		[FA] *n.s.* [MD] MCP, SCP, cerebral peduncles, thalamus, IC, and SCR, fornix, ILF, and IFOF	
Chen et al. (92)	30 HC 30 PD	58.0 (9.3) 64.3 (10.3)	5.2 (3.6)	17.9 (9.3)	1.8 (0.9)	Medicated (ON)	No psychiatric, neurological disorder	[FA] olfactory tract, hippocampal CG, SLF (temporal part)	[FA] Corticospinal tract
Guimaraes et al. (50)	137 HC 132 PD	57.8 (9.4) 60.9 (9.8)	7.8 (6.4)	16 (8.2)	2.8 (1.3)	Medicated (ON)		[FA] genu, body, and splenium of CC, IC and EC, corona radiata, PTR, SS, CG and SLF	
Li et al. (93)	22 HC 31 PD	59.7 (8.6) 60.5 (9.3)		26.4 (10.1)	1.6 (0.5)	Not mentioned	w/ depression, memory, olfactory dysfunction	[FA] bilateral ALIC, bilateral EC, right ACR, genu, body and pad of CC, left sagittal layer.	
Minett et al. (94)	48 HC 93 PD	66.0 (7.9) 64.3 (10.8)	0.5 (0.0)	25.9 (1.1)	1.9 (0.1)	Medicated (ON)	Normal cognition	[FA] n.s. [MD] bilateral corona radiata, IC and EC, CC, IFOF, SFOF, forceps minor, CG, SLD, ILF	
Pietracupa et al. (95)	19 HC 16 PD	66.7 (7.7) 69.7 (11)	9.5 (6.2)	29.8 (17)	2.5 (1.1)	Medicated (ON/OFF)	w/o freezing of gait	[FA] *n.s.* [MD] right cingulum (angular bundle)	
Rektor et al. (96)	21 HC 20 PD	57.9 (7.2) 61.9 (7.6)	<5		1–.5	Medicated (ON)	normal cognition	[FA] *n.s.* [MD] left SCR, SLF, EC, IC, temporal, and prefrontal WM	

(Continued)

TABLE 3 | Continued

Author, year	Group	Age	Duration (years)	UPDRS-III	H&Y	Medication	Non-motor syndromes	Region of FA decrease/MD increase	Region of FA increase/MD decrease
Taylor et al. (97)[a]	45 HC 71 PD	59.6 (11) 61.3 (9)	<2	0.7 (1.6)[b] 21.3 (8.9) [b]		Medicated (OFF)	Normal cognition		[FA] Midbrain, CST, pontine and cerebellar WM, anterior CC, right ACR, Left ILF, IFOF, ACR
Wen et al. (98)[a]	61 HC 52 PD-TD	60.2 (10.8) 60.5 (9.6)	0.63(0.7)	0.6 (1.4)[b] 19.8 (9.5) [b]	1–2	*de-novo*	Normal cognition		[FA] Left ATR, IFOF, bilateral ILF, SLF, SS, right CST [MD] *n.s.*
Guan et al. (99)	46 HC 65 PD	57.8 (9.4) 55.5 (9.5)	4.7 (3.9)	27.1 (14.4)	2.3 (0.7)	Medicated (OFF)		[FA] right UF [MD] right EC and forceps minor, left CG	
This study[a]	15 YHC 25 YPD(Y0) 19 YPD(Y3) 60 OHC 104 OPD(Y0) 72 OPD(Y3)	42.3 (6) 46.1 (4) 50.6 (4) 63.4 (8) 63.8 (7) 67.2 (7)	0.3 (0.2) 4.4 (0.8) 0.4 (0.2) 4.3 (0.7)	0.2 (0.4)[b] 18.0 (7.8[b] 25.2 (12)[b] 0.7 (1.5)[b] 20.5 (8.6)[b] 29.1 (12)[b]	1.6(0.5) 1.8 (0.4) 1.6 (0.5) 1.9 (0.6)	Medicated (OFF) Partly Medicated (OFF)	w/o cognitive impairment Mildly impaired cognition	[FA of YPD] *n.s.* [FA of OPD(Y>3)] genu, body and splenium of CC, CG, SN, midbrain, geniculate nuclei of the thalamus, fronto- parieto-occipito- temporal multifocal non-motor areas	[FA of YPD] CST, ALIC, PLIC, striatum (Put, pallidum, caudate), PTR, SCR, white matter adjacent to SMA, MC and postcentral cortex [FA of OPD(Y0-1)] CST

[a]*Studies using PPMI data. Other studies in the list were using independent data source.* [b]*Measured by MDS-UPDRS version. UPDRS-III = motor exams (part-III) of the Unified Parkinson's Disease Rating scale (100); MDS-UPDRS-III = motor exams (part-III) of the Movement Disorder Society – sponsored revision of the Unified Parkinson's Disease Rating scale (101). n.s., not significant; WM, white matter; CC, corpus callosum; CST, corticospinal tract; Put, putamen; SN, substantia nigra; MC, motor cortex or precentral gyrus; SMA, supplementary motor areas; IC, internal capsule; EC, external capsule; ALIC, anterior limb of internal capsule; ACR, anterior corona radiata; SS, sagittal stratum; UF, uncinate fasciculus; CG, cingulum, or cingulate tract; FXST, crus of fornix or stria terminalis; SLF, superior longitudinal fasciculus; PTR, posterior thalamic radiation; ILF, inferior longitudinal fasciculus; IFOF, inferior fronto-occipital fasciculus; ATR, anterior thalamic radiation; SCR, superior corona radiata; PLIC, posterior limb of internal capsule; GM, gray matter; SFOF, superior fronto-occipital fasciculus; MCP, middle cerebral peduncle; SCP, superior cerebral peduncle; PD-TD, tremor dominant PD; YPD and OPD, PD onset age ≤ 50 years and > 50 years; YHC and OHC, healthy controls age ≤ 50 years and > 50 years.*

fiber populations with different spatial orientations (so called "crossing-fibers") may result in an average increase in FA. There are about 90% white matter voxels containing crossing-fibers (105). Crossing-fibers may affect an anisotropy analysis and might lead to difficulties in interpreting FA increases (106). In addition, a concomitant FA increase may also be due to the variability in ROI sizes, with less or more inclusion of voxels containing surrounding isotropic neurons with low FA. However, the coexistence of FA increase and FA reduction in this study is consistent with the previous meta-analysis (107), which by accounting for heterogeneities of 39 published articles revealed FA increase in the CST and caudate nuclei, and FA decrease in the SN, corpus callosum, cingulate, and temporal areas. With an increasing number of consistent findings, an elevated FA in early PD cannot merely be attributed to methodological confounding factors but could instead indicate some pathophysiological correspondences of the disease. Possible interpretations of the FA increase include compensatory responses or excitatory reactions, which have been proposed by many fMRI (108), perfusion (109), and glucose metabolic (110) studies as a PD-related anatomical pattern of motor dysfunction (PDRD). Compensatory increased structural connectivity could be parallel to hyper-functional activation in similar motor areas (111) and are particularly activated in young aged PD (112). A previous study (98), also using PPMI data, found an FA increase in the tremor dominant (TD) phenotype, but not in the postural instability and gait difficulty (PIGD) phenotype of PD, suggesting that the compensatory white matter reorganization is more specific to the TD type in early PD. Moreover, an earlier study (73) using pilot data reported a whole-brain FA increase only in the akinetic-rigid (AR) phenotype of PD. It is therefore highly encouraged to have more investigations to validate whether the pattern of FA increase is selectively associated with a specific phenotype of motor dysfunction (i.e., TD vs. PIGD or AR subtypes), in addition to several existing pilot cohorts showing conflicting results (18, 19, 41, 113). Although there is a lack of research to date, the pattern of coexisting FA divergency in early PD is likely also explained by the pathophysiology of inhibition (reduced white matter integrity) through direct pathways and disinhibition (increased

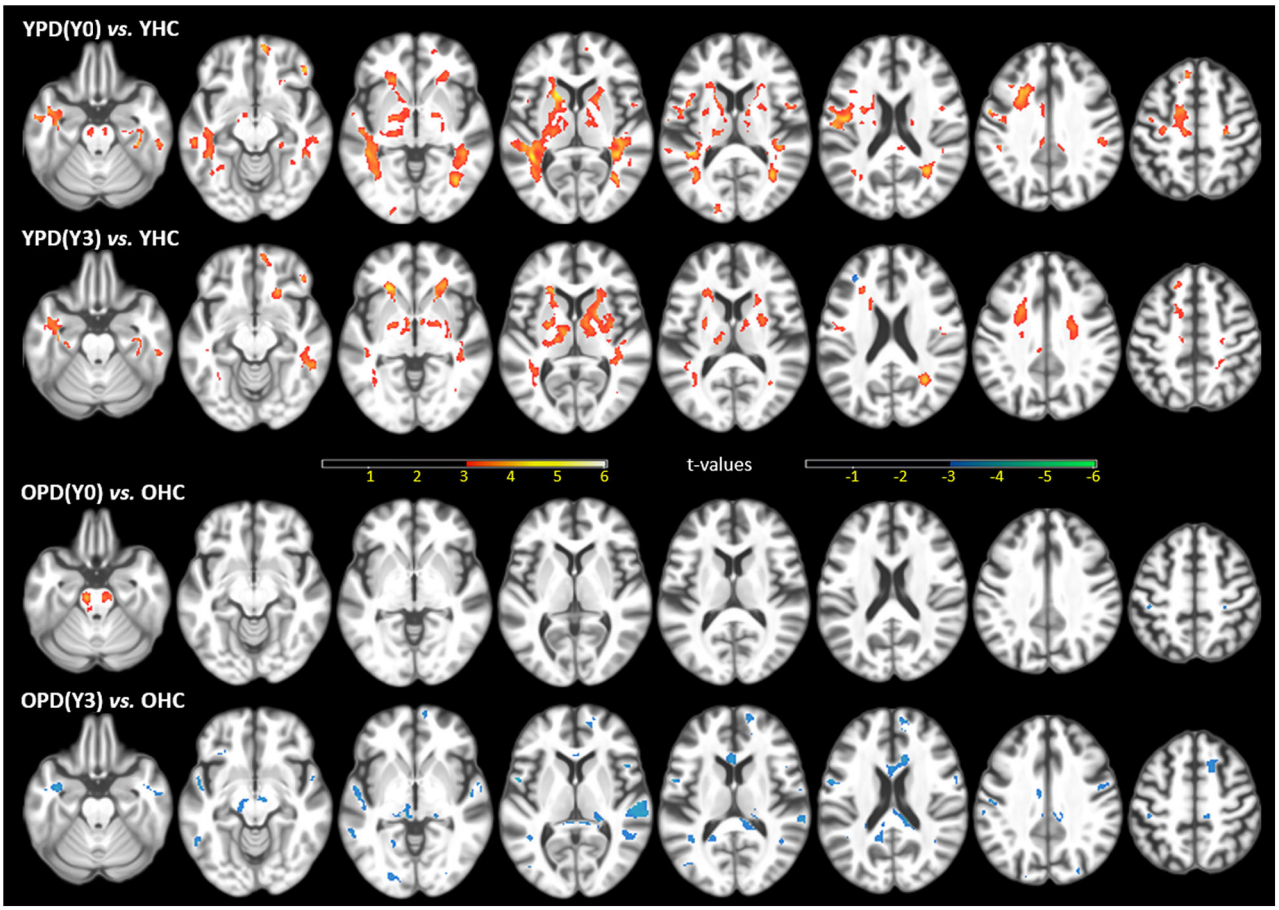


FIGURE 1 | Statistical t-maps of fractional anisotropy (FA) maps, superimposed on a T1WI, of the significant differences between the first-year PD(Y0) or after the 3rd-year PD(Y3) patients and demographically matched HC (ANCOVA $p \leq 0.001$, uncorrected for multiple comparison), separated for young onset (YPD) and old onset (OPD) groups, and demographically matched young (YHC) and old (OHC) controls. Clusters in warm colors indicate regions of higher FA values in PD than HC; clusters in cool colors indicate the opposite. This figure is illustrative and is created by the author.

white matter integrity) through indirect pathways in the basal ganglia (114).

Hypothesis Driven DTI Analyses in PD

DTI Changes in SN and SN Subdivisions

In contrast to the voxel-based whole-brain analysis, the hypothesis-driven region-of-interest (ROI) analysis is often used to identify DTI abnormalities in patients with PD in regions that are known to be specific to the characteristic PD pathologies. SN is one of the main sites of selective loss of dopaminergic neurons in PD, because there is already a loss of 60–80% dopaminergic neurons in the SN before PD motor symptoms emerge (115, 116). **Table 4** lists 32 independent studies that analyzed DTI in the total SN area and SN sub-regions in order to identify substantial DTI alterations in patients with PD. These studies were included in four previous meta-analyses and reviews (104, 131, 135, 136). Except for two studies that reported elevated FA values in the SN of PD, 11 studies found no FA abnormalities. The other 19 studies reported significantly reduced FA values in the entire SN. Aside from FA, only a few studies found an MD increase in the SN, while most others found no significant MD abnormalities, suggesting FA is a better contributive index in identifying nigral abnormalities in PD. However, it remains unclear whether or not FA alterations in the entire SN (Type A ROI subdivision as illustrated in **Table 4**) is sensitive to capture the dopamine loss in PD.

Molecular and neuropathological studies (137) of PD have highlighted that progressive loss of dopaminergic neurons is primarily involved in the pars compacta (SNc), which contains rich pigment neuromelanin formed by dopaminergic neurons, and lies in the inferior and posterior part of the SN, in contrast to the pars reticulata (SNr), which lies lateral to the SNc. Therefore, focusing the microstructural alterations on SN subregions, such as the SNc, would appear to be ideal and vital in identifying dopamine loss-related abnormality. In general practice, it is challenging to delineate the SNc on DTI image because there are no well-defined borders of this substructure. An earlier study (129) reported that reduced FA in the caudal and lateral sub-regions of the SN could completely separate patients with PD from HC with 100% diagnostic accuracy. The authors

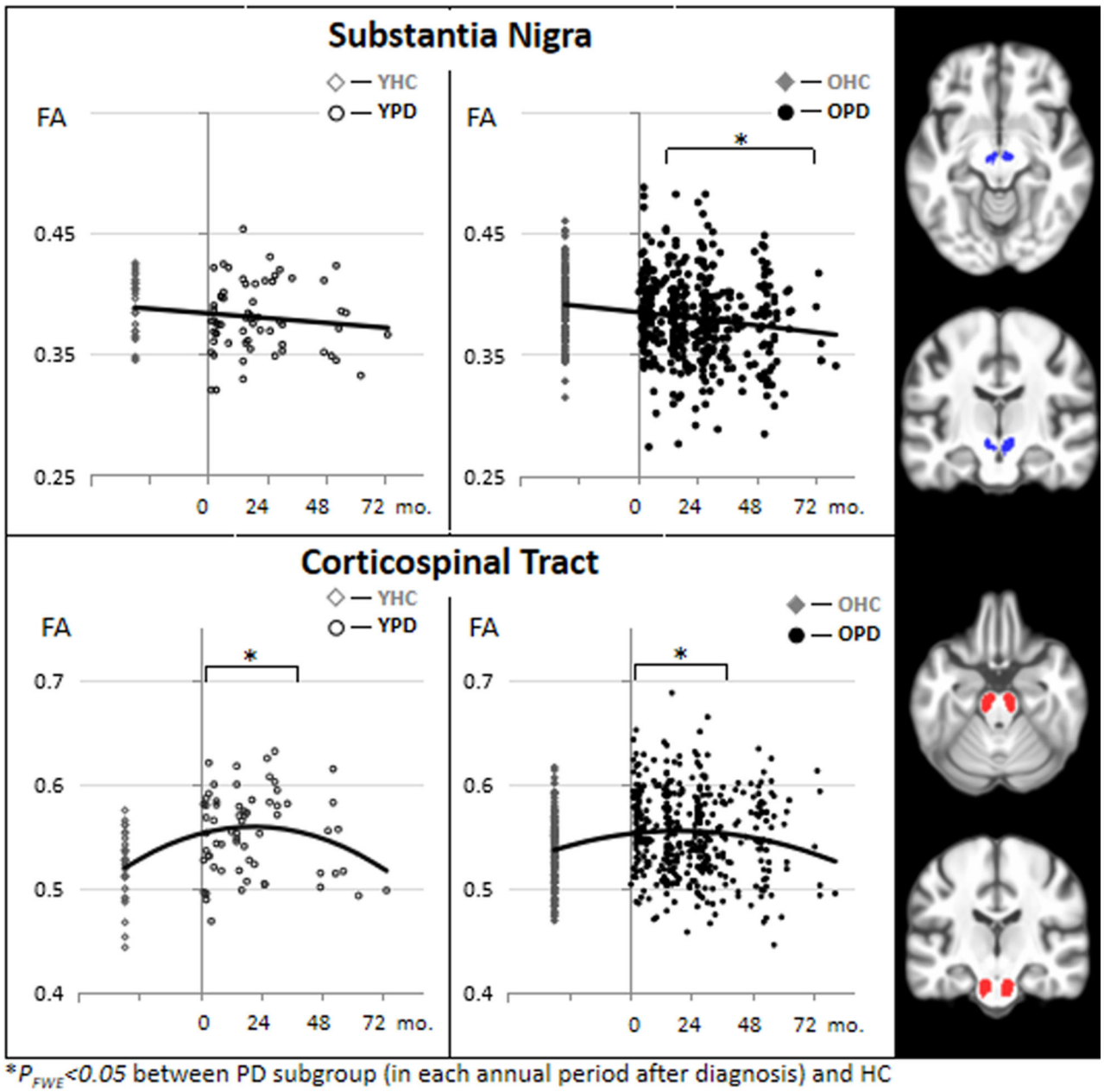


FIGURE 2 | Scatter plots and binominal trend lines of FA changes during the course of PD (from 0 to 72 months after PD diagnosis) in the substantia nigra and the corticospinal tract, separated for young onset (YPD) and old onset (OPD) groups. FA values of the HC subjects are also separated into demographically comparable groups (OHC and YHC). This figure is illustrative and is created by the author.

proposed that FA measurements in the caudal and lateral sub-regions of the SN, presumably coinciding with the histological described SNc location (ROI subdivision Type B1), have the best diagnostic value for PD. However, eight subsequent studies with the same SN subdivision (subdivision Type B) reported discrepant findings: two studies (13, 132) likely replicated the findings of FA reduction in the dorsal lateral sub-region of the SN in PD; five other studies (7, 8, 55, 104, 131) found no significant FA differences between PD and HC in any SN sub-region; and one (130) reported elevated FA in all the SN sub-regions in PD. Technical difficulties outlining the sub-regions may explain these discrepant findings. To combat these issues, several studies (9, 36, 133) have divided the SN into two or three segments from the anterior top position through the posterior bottom position (ROI subdivision Type C). All these studies reported significantly decreased FA in the caudal (or inferior) segment of SN in patients with PD as compared with HC. Among these studies, Langley 2016 (9) used a mask of caudal zone in the

SN that was previously established in a brain atlas based on magnetization transfer MRI that is sensitive to neuromelanin. This mask (i.e., the inferior portion of SN) supposedly coincides with the neuromelanin accumulation site. Another study (134) localized SN subfields using DTI tractography to segment the SN into an internal and an external part (ROI subdivision Type D), claiming that each part represents the SNc (the internal SN) and SNr (the external SN), respectively. However, no significant differences in FA or MD values between patients with PD and HC were identified in any of these subdivisions. It is likely that differences in delineating and partitioning the SN sub-regions across DTI studies are largely responsible for the inconsistent findings. Further methodological improvements are needed to ultimately demonstrate that microstructural alterations in SNc are a sensitive marker for diagnosing PD.

DTI Changes in Dopaminergic Tracts

The classical pathophysiological model of PD and recent updates have been established based on experimental and clinical studies (138–141), which consists of functional disabilities of two main pathways: an "indirect circuit," which interconnects neocortex-putamen-external pallidum/subthalamic nucleus-SN, and a "direct circuit," which interconnects neocortex-putamen-internal pallidum-SN-thalamus-neocortex. Under the conditions of PD, the reduced dopamine (results from neuronal loss in the SN) inhibits the indirect pathway, resulting in slow movement, and excites the direct pathway that may lead to unwanted movement such as resting tremor. **Figure 3** (left panel) illustrates an example of these basial ganglia pathways on DTI imaging. Neuroanatomically, the dopaminergic pathway, meaning the structural connection between SN and putamen, has been assumed to contain dual effects of activities onto the indirect and direct pathways. Detecting white matter damage to these neuromodulator pathways could add to the understanding of PD pathophysiology.

Diffusion tensor tractography, as an alternative DTI-based approach, offers a possibility to detect the disrupted connections of the dopaminergic pathway and may aid the early diagnosis of PD. White matter tracts that connect the SN and striatum, namely the nigrostriatal tract (NST), are considered one of the major dopaminergic pathways, and have been shown clinically applicable in viewing anatomy of the healthy human brain (142), as well as targeting deep brain stimulation (DBS) (143, 144). Although diffusion tensor tractography could not reach much detailed pathophysiologic meanings due to the limited resolution and directional information, it might still indirectly reflect a functional dysregulation of the dopaminergic circuits on a neuroanatomical basis. **Figure 3** (right panel) shows an example of the nigrostriatal tractography in a healthy PPMI subject. An early DTI study (120) measured DTI indices in 11 oval ROIs that were arrayed along a line between the SN and caudate/putamen complex, and reported significantly lower than normal FA values in patients with parkinsonism at all disease stages. With the advances of DTI tractography, recent studies (13, 59, 89, 145, 146) have assessed the FA and tract connectivity profiles of the NST in identifying differences of nigrostriatal connection between patients with PD and healthy subjects. Most of these studies reported either an FA decrease (along with an increase in RD) (13, 59) in PD or reduced tract connectivity (59, 145, 146). Some studies (13, 59, 60) also found that reductions in FA or tract profiles are associated with the severity of motor dysfunctions in PD patients. These consistent findings provide a possible explanation of PD pathophysiological mechanism, that is, the main motor manifestations of PD are related to the diminished connectivity of this dopaminergic circuit. Although based on a small sample, Menke et al. (147) demonstrated that the combination of volumes of the SN and the NST could achieve 100% sensitivity and 80% specificity for PD classification. Taken together, these studies suggest that DTI tractography is a promising, complementary marker of PD diagnosis. On the other hand, a tractographic analysis of the NST also benefits new PD treatment strategies that target the nigrostriatal pathway, such as deep brain stimulation, dopamine graft implantation, and infusion of glial-cell-line–derived neurotrophic factor.

Other white matter circuits that may be involved in PD pathology are of research interests. Braak et al. (3) suggested that Lewy bodies are mainly confined to the medulla oblongata/pontine tegmentum and olfactory bulb/anterior olfactory nucleus in the earliest stages of PD. Using voxel-based analysis, two studies (90, 148) found PD is associated with abnormal diffusivity in white matter tracts adjacent to the olfactory sulcus. Although tractography of the olfactory tract is practically difficult in this area, using ROI drawing, some studies (92, 119, 122) reported low FA of the olfactory tract in PD. Another interesting approach is the tractographic analysis in corticothalamic connections of PD. The reduction of dopamine in SN results in abnormal activation of connections between the thalamus and the motor cortices. This may subsequently lead to inhibition of basal ganglia output and dysfunction in the cortical-subcortical circuits. Several studies have focused on the DTI connection of the corticothalamic tracts (14, 60, 85). However, diverse FA changes were reported in these studies.

DTI ASSESSMENT OF CLINICAL SYMPTOMATOLOGY AND DOPAMINE TRANSPORTER

PD is characterized as a wide variety of motor and non-motor symptoms, while the neuropathological processes underlying these heterogeneous symptoms are not fully understood. Assessing imaging-clinical correlations in PD has been considered useful for adding further insights into neuropathological underpinnings of PD symptomatology. **Table 2** summarizes the findings of correlations between available DTI metrics and clinical assessments.

DTI Correlates of Motor Dysfunction

A previous article (102) provided a thorough review of the correlations between diffusivity abnormalities and PD motor symptoms, but it lacked information about FA. Many studies, including the analyses with PPMI data, have reported significant correlations between decreased FA in the SN and increased severity of the motor symptoms, which are assessed by the motor

TABLE 4 | Overview of studies in comparison of FA/MD differences in the SN and SN subregions between PD and HC.

First Author, Year	No. of PD/HC	Age of PD	Duration (years)	UPDRS-III	H&Y	ROI sub-division	FA decrease	MD increase
Peran et al. (117)	30/22	61.9 (11.1)	4.5 (± 2.5)	12 (± 6)	1.6	Type A1	SN	*n.s.*
Du et al. (118)	16/16		4.8 (3.0)	23.1 (12.3)		Type A1	SN (contra-lateral)	*n.s.*
Zhan et al. (11)	12/20	67.4 (8.0)		26.3 (12.2)		Type A1	SN	*n.s.*
Nagae et al. (113)	21/20	61.1 (7.7)	5.5 (3.4)	31.4 (10)[b]	2.2	Type A1	SN (contra-, ipsi-lateral)	SN (ipsi-, contra-lateral)
Johsi et al. (119)	24/26	61.9 (4.9)	2.9 (2.9)	22.2 (11)	1.6	Type A1	*n.s.*	Not tested
Chen et al. (92)	30/30	64.3 (10.3)	5.2 (3.6)	17.9 (9)	1.8	Type A1	*n.s.*	*n.s.*
This study[a]	482/146[a]	61.5 (9.4)	1.9 (1.4)	23.4 (11)[b]	1.7	Type A1	SN	*n.s.*
Yoshikawa et al. (120)	12/8	71.3 (7.7)			1–3	Type A2	SN	Not tested
Chan et al. (121)	73/78	63.6 (9.8)	5.0 (± 4.1)		2.4	Type A2	SN	*n.s.*
Rolheiser et al. (122)	14/14	56.0 (4.8)	2.5 (1.5)		1.3	Type A2	SN	*n.s.*
Wang et al. (123)	30/30	64.5 (3.4)	5.2 (2.0)	33.6 (14.1)	2	Type A2	SN[c]	*n.s.*
Skorpil et al. (124)	14/15	64 (43–73)		32.1 (6)	1.75	Type A2	SN	*n.s.*
Perea et al. (125)	12/13	67.5 (4.0)		19.6 (7.1)		Type A2	*n.s.*	*n.s.*
Li et al. (126)	23/23	65.6 (46–77)				Type A2	SN	*n.s.*
Kamagata et al. (61)	58/36	68.8 (7.5)	7.4 (4.4)	18.0 (8.5)	2.5	Type A2	SN (contra-lateral)	SN (contra-, ipsi-, bi-lateral)
Loane et al. (127)	18/14	56.8 (6.8)	3.9 (2.2)	26.2 (9.2)		Type A2	*n.s.*	*n.s.*
Wei et al. (12)	22/22	61.4 (9.7)			<2	Type A2	SN	Not tested
Gattellaro et al. (128)	10/10	63.8 (15.7)				Type A3	not tested	SN
Chan et al. (16)	21/19	72.0 (4.8)			2.2	Type A3	*n.s.*	SN
Jiang et al. (79)	31/34	69.4 (8.0)	4.4	20.4	2.6	Type A3	SN	*n.s.*
Vaillancourt et al. (129)	14/14	57.2 (9.6)	1.3 (± 0.9)	18 (± 8.1)	1.7	Type B1	SN (posterior> middle>anterior)	Not tested
Prakash et al. (8)	11/12	60.4 (9.3)	5.7 (4.2)	23.5 (9.5)	2.1	Type B1	*n.s.*(asymmetric)	*n.s.* (asymmetric)
Schwarz et al. (104)	32/27	64.8 (11.8)	6.4 (± 4.2)	26.1 (13.9)	1.7	Type B1	*n.s.*	SN (all ROIs)
Lenfeldt et al. (130)	122/34	70.3 (9.7)	2.1 (± 2.0)	26.1 (10.6)		Type B1	SN (all ROIs)[c]	*n.s.*
Schuff et al. (7)[a]	153/67[a]	61.0 (10)	<2	22 (9)[b]	1.6	Type B1	*n.s.*	*n.s.*
Zhang et al. (53)	72/72	66.8 (5.4)	1.1 (± 0.6)	14.9 (3.9)	1.67	Type B1	SN (averaged ROIs)	Not tested
Hirata et al. (131)	72/42	62.6 (11.8)	5.7 (± 5.5)	28.7 (14)		Type B1	*n.s.*	Not tested
Knossalla et al. (132)	10/10	57.9 (10.6)		12.9 (11)	1.4	Type B1	SNc (posterior)	Not tested
Ofori et al. (55)[a]	28/20	64.7 (8.2)	3.4 (± 1.7)	29.8 (9)[b]		Type B2	*n.s.*	Not tested
	78/56[a]	61.6 (9.2)	0.7 (± 0.7)	22.9 (9)[b]		Type B2	*n.s.*	Not tested
Du et al. (133)	40/28	60.8 (8.2)	4.2 (± 4.7)	23.5 (15)	1.7	Type C1	SN (inferior)	*n.s.*
Langley et al. (9)	20/17	60.3 (8.4)		23.2 (9)		Type C1	NM SN (inferior)	NM SN (inferior)
Scherfler et al. (36)	16/14	68.1 (6.1)	3.7 (± 3.7)	20 (10.3)	2.3	Type C2	SN (inferior-medial)	SN (middle, inferior-medial)
Menke et al. (134)	10/10	63.7 6.7)	6.1 (± 4.4)		2.3	Type D	*n.s.*	*n.s.*

ROI subdivision. Type A1: volume-of-interest of whole SN was auto-transformed from standard atlas; Type A2: manually ROI drawn in a middle slice (or a few slices) of SN; Type A3: one ball/cubical/ellipsoid ROI manually I drawn in a middle slice on each side of SN; Type B1: Middle segment of bilateral SN: three (anterior-medial, middle and posterior-lateral), or Type B2: two (anterior-medial and posterior-lateral) ball/cubical ROIs of SN on each side; Type C1: the whole volume of SN was divided into superior (SNr) and inferior (SNc) segments; Type C2: the whole volume of SN was divided into superior, middle and inferior segment; Type D = SN was divided into lateral SNr (lateral part) and SNc (medial part) based on connectivity profiles. n.s., not significant; SN, substantia nigra; NM SN, neuromelanin-portion of SN; SNr, substantia nigra pars reticula; SNc, substantia nigra pars compacta. [a]*Studies using PPMI data.* [b]*Measured by MDS-UPDRS version.* [c]*PD has significantly increased FA than HC.*

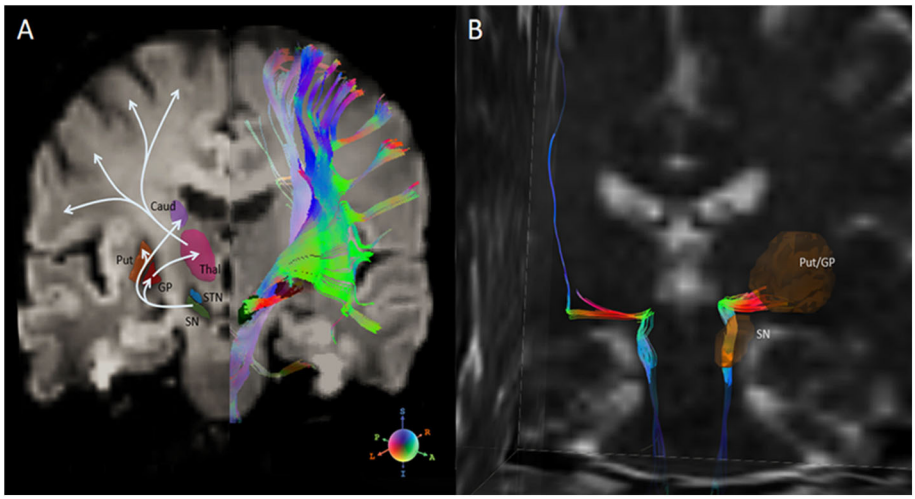


FIGURE 3 | (A) Left half-panel: basal ganglia nuclei and connections of the direct and indirect pathways for movement. Right half-panel: diffusion tensor tractography of all fiber streamlines that path through the SN. **(B)** Isolation of the nigrostriatal tract (NST) between SN and inferior Put/GP in a healthy subject. Diffusion tensor tractographic streamlines on the right hemisphere shows the nigrostriatal tract anatomically connects through brainstem, SN and Put/GP. A part of the streamlines further connects through the Thal, and finally projects into the premotor cortex. Fiber orientation is R-G-B coded. Note, DTI tractography does not separate the afferent and efferent directions. SN, substantia nigra; Put, putamen; GP, globus pallidus; Caud, caudate nucleus; Thal, thalamus; STN, subthalamic nuclei. This figure is illustrative and is created by the author.

exams (part-III) of the Unified Parkinson's Disease Rating Scale (UPDRS) (7–12, 61, 92) or H&Y scales (113, 121). However, some other studies failed to observe significant correlations. One reason for the discrepant reports of previous studies is the variation of "on-medication" or "off-medication" conditions in real-time examination of the PD patients. Dopaminergic treatments have substantial effects on the clinical measurement of motor symptoms such as UPDRS, whereas they have less effects on structural imaging such as DTI. Another complication is that, unlike quantitative imaging measurement, UPDRS is a subject measurement and depends on observers' experiences (149). Nevertheless, the consistent correlation findings from many previous studies imply that nigral FA values could offer an objective assessment of severity of the PD motor dysfunction, when clinical motor measurement is not affected by real-time treatment effects.

Investigations of the correlations between DTI and subtypes of motor dysfunctions remain rudimentary. A few studies revealed significant correlations between DTI changes and severities in terms of freezing of gait (17, 40), risk of falling (16), severity of postural instability and gait disturbance (PIGD) symptoms (18), motor speed and balance (19), and the degree of tremor (41, 42). Some studies, using DTI for classifying PD motor subtypes (73, 95), have found differentiable group effects only, but no substantial clinical correlations were observed in patients. The abnormal DTI changes in specific regions are considered useful biomarkers that characterize PD symptomology or differentiate PD phenotypes, and thus may provide an enormous potential for managing treatment directions of PD. However, it should be cautioned that the diversity of the subtype definition and the substantial instability in motor scoring might hamper the actual imaging-clinical correlations and interpretations. More reliable, objective measures of motor subtypes are necessary to validate these subtype-associated DTI changes conclusively.

DTI Correlates of Non-motor Dysfunction

Cognitive impairment is one of the major non-motor syndromes in PD. In patients with non-demented PD, the relationships between white matter integrity and global cognition, functions of various cognitive domains have been investigated in multiple studies (as illustrated in **Table 2**). For example, global cognitive function measured by Mini-Mental State Examination (MMSE) or Montreal Cognitive Assessment (MoCA) has been found to be associated with abnormal DTI variables in the bilateral frontal, parietal, and temporal regions, long association tracts connecting these cortices, and the hippocampus (25, 26, 43, 45, 95). Executive dysfunctions are associated with abnormal DTI variables widely distributed in the parietal and frontal regions (20–23, 43–45, 51). Declined verbal and semantic fluency and visuospatial memory are associated with abnormal diffusion variables in the parietal and frontal regions (23, 24, 44, 51). Worsened performance of language and attention is associated with abnormal diffusivities in frontal and temporal regions and the fornix (46, 47). Memory impairments are correlated with the frontal and hippocampal diffusivity abnormalities (45, 48, 52). Overall, the characteristic white matter abnormalities associated with cognitive impairment in PD can be summarized as follows: multiple regions are involved with a heterogeneous pattern; abnormal diffusion

variables are widely distributed in white matter adjacent to cortices and limbic subcortices; the diffusion abnormalities are predominantly shown as the diffusivity changes but not the FA.

DTI correlates with other non-motor manifestations in PD have been comprehensively reviewed in a previous article (102). Briefly, DTI alterations in the thalamus (27), damaged long association tracts connecting to the frontal cortices, are associated with depression (28) and sadness (29). Diffusion changes of the hippocampus are found to be related to the impaired visuospatial memory, leading to visual hallucinations (150) in the advanced stages of PD. Diffusivity changes in the brainstem, midbrain, and pons are associated with autonomic dysfunction during a rapid eye movement (REM) sleep (33), and diffusion alterations of the limbic fornix are associated with excessive daytime sleepiness (32). However, most of these studies have been limited to small sample sizes, resulting in a low statistical power, and conflictions in terms of findings and interpretations. Further replication studies are needed to elucidate these abnormalities in more details and to truly aid the unique insights into PD symptomology.

DTI Correlates of Striatal DAT-SPECT

Dopamine transporter single photon emission tomography (DAT-SPECT) provides a meaningful measurement of striatal dopaminergic deafferentation. The best quantitative assessment on DAT-SPECT is to measure the striatal dopamine transporters binding ratio (SBR) in the left and right putamen and caudate nucleus. Studies have demonstrated substantial SBR signal loss in early PD patient relative to controls (151, 152). Recent machine learning techniques (such as using the support vector machine, SVM) have shown that the SBR measures achieve high accuracies (97–100%) in predicting early PD (153, 154). Additionally, the SBR has been shown strongly correlated with the number of dopaminergic neurons in substantia nigra (155). Pathological data also confirmed that quantitative measures of SBR enhance the accuracy of detecting dopaminergic neuron loss in PD (156), suggesting that SBR might be a reliable diagnostic biomarker of PD. Therefore, identifying a significant relationship between abnormal DTI and diminished SBR would support the idea that DTI alteration in the dopaminergic area is a potential marker of PD pathology. Recent findings showed a strong relationship between abnormal DTI [including decreased free water (FW) (7, 55) and increased FW (157) of the SN] and decreased putaminal SBR in PD patients. Furthermore, the progressive reduction of nigral FA has been shown correlated with the rate of SBR reduction over the first year of the PPMI patients (158). Aside from a few studies (159, 160) that reported controversial findings, the strong inter-modality correlations suggest that the abnormal DTI changes in the SN are, at least indirectly, associated with the loss of dopaminergic neurons in PD. Thus, this supports the usefulness of nigral DTI measures in linking neurodegeneration to the characterized dopaminergic deficiency in PD.

DTI ASSESSMENT OF PD PROGRESSION AND TREATMENT EFFECT

Although it remains a question using the DTI as a diagnostic marker of early PD, many previous studies have reported stable, region-specific, cross-sectional correlations between DTI alterations in the dopaminergic regions and motor symptom severities, suggesting the usefulness of longitudinal DTI as a reliable biomarker for monitoring PD progression. A recent longitudinal DTI study (127) has found increased rate of DTI abnormalities (i.e., FA decrease and MD increase) in the SN of PD patients over a 19.3-month follow-up. Ofori et al. (161) reported significant FW increases in the posterior SN at 1-year follow-up of PD. Further, the same authors' group (162) confirmed these longitudinal FW increases using PPMI data (103 PD at baseline, the 1st, 2nd, and 4th year) in comparison with unchanged FW in the control group (49 HC at baseline, the 1st year). Another longitudinal study (158) measuring FA and diffusivity variables of the PPMI data (122 PD vs. 50 age matched HC at baseline and 1-year follow-up) reported that PD has the highest annual rate of 3.6 $\pm$ 1.4% FA reduction in the SN, followed with a moderate rate of FA reduction in the basal ganglia, in comparison with the non-significant DTI changes in HC. Several longitudinal DTI studies identified other vulnerable regions over the PD progression: a recent study (163) found PD had a greater decrease in FA and increase in MD in the rostral brainstem, compared to controls; a 2-years longitudinal DTI study (164) reported a decrease in FA in the putamen of PD patients; another cohort (94) with 18-month follow-up of PD patients with cognitive impairment revealed greater MD increases in frontal white matter than those patients with normal cognition. These studies have presented a similar topology (mainly in the SN, also involved in the midbrain, thalamus, and to some extent to the frontal white matter) of FA decrease/MD increase over the PD course. This anatomical pattern of longitudinal DTI changes is consistent with the regional spread of Lewy body and the accumulation of Lewy neurites during PD progression (5). According to the generally consistent findings, longitudinal DTI shows a promising PD progression marker and could be valuable for monitoring and evaluating treatment effects.

Outcome measures that are most commonly used for tracking the PD treatment effects are the standard UPDRS scores (165, 166) and, sometimes, the dopamine transporter imaging (167). A PPMI study (168) followed 423 patients from treatment beginning to year-5 and found that dopaminergic therapy provides significant improvements in the Movement Disorder Society revised UPDRS (MDS-UPDRS) scores and the SBR calculated from DAT-SPECT. However, these functional outcome measures may appear significantly different depending on whether they are evaluated at ON or OFF medication status. Tracking the long-term treatment effects using DTI measures could be promising as DTI is used to identify chronic responses of the brain microstructure, and thus is considered to be less affected by the ON or OFF medication status at the imaging time. **Figure 4** depicts individual trajectories of

nigral FA values extracted from the PPMI data (134 patients and 75 healthy subjects) over a maximum of 36 months (data information is provided in **Supplementary Material S1**–**S3**). It shows that the untreated PD patients exhibit on average a steeper decline in FA than HC subjects, while the treated PD patients maintain their respective FA levels to a decline that begins in the 3rd year of medication. This finding supports the fact that early PD is generally responsive to medications. Taken together with recent PPMI findings that nigral FA is associated with disease duration and motor rating scales (97, 169), we suggest that disease modifying effects of levodopa treatment can be measured by longitudinal changes of nigral FA, at least in the first few years of treatment. Further DTI studies of PD clinical trials are needed to validate whether this is indeed true.

DTI ASSESSMENT OF DIFFERENTIAL DIAGNOSIS

Differentiation Between PD and Atypical PD

It is important to diagnostically differentiate between idiopathic PD and atypical parkinsonism (aPD), including the three most common sporadic neurodegenerative syndromes: multiple system atrophy (MSA), progressive supranuclear palsy (PSP), and corticobasal syndrome (CBS), because interventional management and prognosis could be different and difficult for aPDs. DTI shows a substantial value in such differentiation.

Compared to idiopathic PD, various DTI studies have demonstrated reduced FA and/or increased MD in the pons, cerebellum, middle cerebellar peduncles (MCP), and putamen in patients with a Parkinsonian type of MSA (MSA-P) (88, 126, 170–174). Several cross-validation studies (173, 175–178) reported that diffusion measurement has 73–94% sensitivity and 89–94% specificity, and 89–100% area under curve (AUC) in discriminating MSA-P from idiopathic PD.

PSP and CBS are neurodegenerative disorders characterized by abnormal tau pathology in the form of globose neurofibrillary tangles, tufted astrocytes, coiled bodies, and threads, with a predominance of 4-repeat (4R) tau isoforms (179). Both diseases provoke symptoms characteristic of PD. A recent review (180) suggests that quantitative measures and visual assessments of atrophy in the superior cerebellar peduncles (SCP) are substantial for differentiating PSP from PD, suggesting microstructural analysis of this key anatomy may provide supportive information. DTI studies (174, 181–183) showed that patients with PSP present strikingly decreased FA and increased MD in the SCP in comparison to patients with idiopathic PD. Studies (174, 184) examining FA of the SCP yielded 86–94% sensitivity and 88–94% specificity for differentiating PSP from PD. Although there are few related investigations in literature, a previous study reported significantly decreased FA and increased MD in the posterior callosal truncus in CBS patients in comparison to PD. Measuring MD of the truncus yielded a 78% AUC in discriminating between CBS and PD.

In summary, PD and aPD are differentiable according to their unique anatomical distributions of microstructural abnormalities detected by reduced FA and increased MD. For example, abnormal DTI in the cerebellum and MCP may be primarily involved in MSA-P; DTI of the SCP is mostly vulnerable in PSP; and abnormal DTI in the supratentorial white matter regions is primarily involved in CBS. Additional evidence that supports these regionally specific changes in PSP and CBS are the high progressive rate of DTI abnormalities (185) and the progressive atrophy (186, 187) in respective key regions of PSP and CBS observed in previous longitudinal imaging studies. For idiopathic PD, the predominant DTI changes are characterized in the SN and the basal ganglia.

Differentiation Between PD and Associated Cognitive Impairment and Dementia

Cognitive impairment, one of the non-motor symptoms, is particularly problematic in PD. Mild cognitive impairment (MCI) occurs in approximately 30% of PD patients (188). Up to 80% of late-staged PD patients eventually develop an associated dementia (PDD) (189, 190). In general, subtle cognitive deficits occur in early-staged PD patients, and dementia typically occurs in elderly patients or patients in advanced stages. With matched stages and ages, PD patients with MCI (PD-MCI) show a decreased FA and increased MD compared to cognitively normal PD (PD-CN) predominantly in the frontal and interhemispheric white matter (i.e., genu and body of the corpus callosum) (45, 191–193). The PDD group, when compared to the non-demented PD group, showed FA decrease and/or MD increase in the bilateral cingulate tract (194–196), hippocampus (26), prefrontal white matter, and the genu of the corpus callosum (196, 197). In addition, cognitive status, measured by MMSE or MoCA, was associated with abnormal DTI changes in the corpus callosum, anterior cingulate, and several frontal white matter areas (26, 195, 196, 198). Moreover, Shchuz's study (199) suggested that degeneration of the nucleus basalis of Meynert measured by DTI predicts the onset of cognitive impairment, whereas a PPMI study (200) could not confirm DTI as a predictor for further cognitive decline.

The neuropathological basis of dementia in PD is not yet clear. Detectable DTI alterations in the white matter connecting to the neocortex and limbic cortex, including the frontal white matter, the corpus callosum, cingulum, and hippocampus may provide meaningful information in identifying dementia from PD. Consistent with Braak's stages V-VI (3), when α-synuclein spreads to neocortex particularly to the frontal, temporal, and limbic cortices, the abnormal DTI changes in these neuronal fibers play an important role in manifesting dementia processing in PD. On the other hand, the primary mechanisms of cognitive impairment in PD have been manifested by atrophy and reduced glucose hypometabolism in the cerebral cortices (e.g., the temporoparietal cortices) and limbic cortices (e.g., the posterior cingulate gyrus and the hippocampus) (201). White matter burden might occur secondarily or indirectly after the gray matter pathologies such as cortical accumulations of amyloid beta and tau. Further, a study (202) reported that PD with early

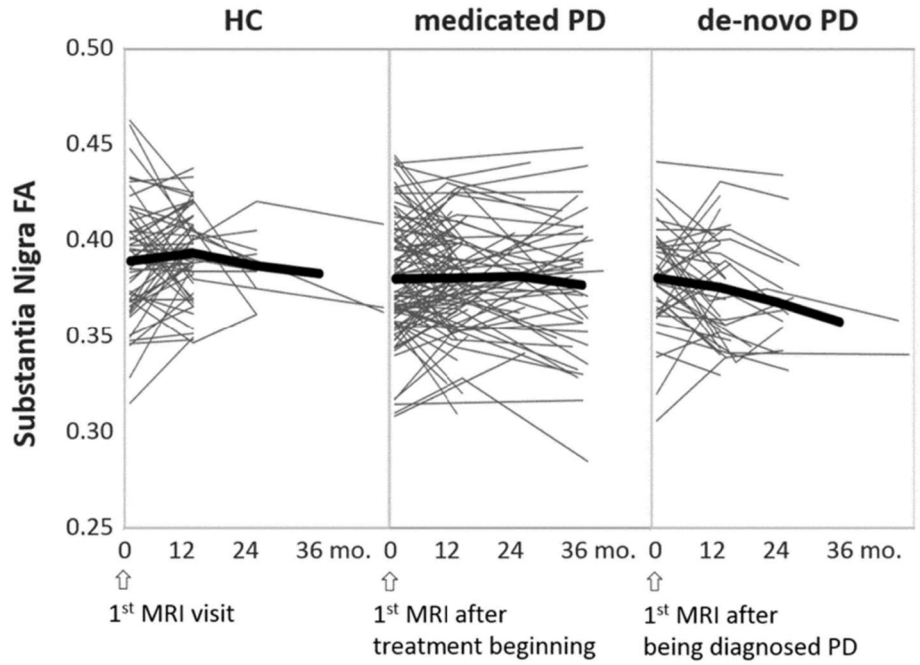


FIGURE 4 | Individual trajectories of the nigral FA changes over time, separately illustrated for HC, treated (medicated), and untreated (*de-novo*) PD groups. The thick black lines indicate the mean trajectory of FA changes over time at each group level. Time is represented as the MRI intervals, starting from the baseline MRI through the latest follow-up MRI. This figure is illustrative and is created by the author.

onset of MCI (onset at PD $<$ 1 year) exhibited lower FA and higher diffusivities in the frontal white matter than PD with late onset of MCI (onset at PD $\geq$1 year). In this context, whether the cognitive decline and dementia are manifested by age or dopamine deficiency needs further investigations.

A few studies (25, 203) using DTI in differentiation between PDD and Lewy body dementia (LBD) found generally similar regions of reduced FA in both disorders. A few other studies (51, 125) comparing PDD with Alzheimer's disease suggested that PDD may exhibit greater white matter abnormalities than Alzheimer's disease, whereas Novellin et al. (204) suggested the controversial findings. Due to the limited number investigations and the conflicting results, whether DTI can reliably differentiate PDD from LBD or Alzheimer's disease remains unknown.

DEVELOPMENTS IN DTI TECHNIQUES

Advanced Diffusion Imaging Technology

Table 5 lists a comparison of imaging parameters in conventional DTI, PPMI, and advanced diffusion imaging techniques. To date, DTI is not broadly applied in clinically standard MRI examinations. In clinical practice, the conventional DTI sequence, especially for scanning patients, has to be performed within 10 min or so. The limited scan time results in problems such as low resolution, noise, artifacts, distortion and crossing-fibers, and reduces qualities of the DTI image and its quantitative measures. Technical developments and limitations of DTI studies in clinical PD have been well-documented in recent review papers (107, 205). New developments of diffusion imaging techniques, such as high angular resolution diffusion imaging (HARDI) (206) and diffusion spectrum imaging (DSI) (207), have shown improvements including increased signal sensitivity and resolution, gaining details of intravoxel directions and allowing a better differentiation of the crossing fibers or the joining fibers. These novel techniques are primarily used for mapping human brain connectome and brain fiber atlas building. Optimization of these sequences to be a clinically tolerable acquisition will be necessary for their clinical application.

Variables Beyond Traditional DTI Indices

Beyond the commonly employed DTI metrics including FA and diffusivities, other quantitative indices that derived from special diffusion sequence or post-image modeling provide additional information on PD biomarker research. FW is an index generated from bi-tensor diffusion model (208) and estimates fractional volume of free water within a voxel without bias from directional dependence and cellular environmental restrictions. FW expresses atrophy-based microstructural degenerations and is also used to correct partial volume effects on FA and MD measures. FW has been found more sensitive than FA in identifying abnormalities in the SN (55), significantly correlated with UPDRS (157), and persistently increased in 1, 2, and 4 years of PD (161, 209). Diffusion kurtosis (210) is an index modeled from multiple *b*-values. Mean kurtosis (MK) estimates non-gaussian forms of diffusion and indicates microstructural complexity such as water leakage through cell membranes and

TABLE 5 | Comparison of DTI scan parameters in conventional DTI, PPMI study, and advanced diffusion imaging techniques.

Scan parameters	Conventional DTI (employed in clinical PD studies)	PPMI	Sophisticated techniques (e.g., HARDI, DSI)
Magnetic fields	1.5–3 Tesla	3 Tesla	3,7 Tesla or greater
Number of $b = 0$ (s/mm^2)	Usually one (can be multiple)	One	One or multiple
Maximum b value (s/mm^2)	800, 1,000, or 2,000	1,000	1,000, 2,000 or more
Spatial resolution	$1 \times 1 \times 2.5$–$2 \times 2 \times 2$ mm^3 (or larger)	$2 \times 2 \times 2$ mm^3	$3 \times 3 \times 2$ mm^3 (or larger)
Number of directions	12–80	64	256 and more
Approximate scan time	4–10 min (or longer)	8 min	20–50 min (or longer)
Tractography	Yes (quality depends on direction number)	Yes	Yes, with improved quality
Clinical feasibility	Yes	Yes	Not yet

myelin breakdown. It resolves the adverse effects of crossing-fibers, which may influence the accuracy the FA assessment, and thus provide better efficiency in diagnosing early PD (53, 211). More recently, there are increasing interests in the use of structural connectome measures to identify abnormal structural connectivity in PD or in PD motor-subtypes through network-based statistical analysis (57, 63, 212–217). The commonly used indices derived from DTI, together with their biological interpretations and clinical correlations in PD, are summarized in **Table 2**. Notably, none of the aforementioned variables are specific to PD neuropathology. Postmortem studies are compulsory to confirm these imaging-pathological correlations.

DTI in Gray Matter

Voxel-based whole brain analyses provide fully automated processing and become popular in DTI studies in PD. However, these analyses have been predominantly focused on white matter structures, because the approaches highly depend on reliable co-registration and spatial normalization methods, while most image registration algorisms used for DTI analyses are established based on white matter skeleton (such as TBSS) or FA intensity, and accompany a use of FA mask (usually sets at absolute FA > 0.2) to constrain DTI analyses within the white matter. These techniques provide substantial improvements of white matter registration, but the accuracy of gray matter registration is sacrificed. Although the motor dysfunctions in PD could be examined through white matter in the pyramidal and extrapyramidal motor pathways, the non-motor symptoms are primarily driven by abnormalities in the cortical and limbic subcortical gray matter (218). Specifically, cortical deficits can be presented in early PD with mild cognitive impairments (219). Therefore, identifying PD-related gray matter microstructural abnormality would be crucial, because it can alert treatment strategies and potentially prevent patients from developing to dementia. Recent technical advantages in DTI processing, including cortical surface-based (220) registration, such as using FreeSurfer (https://surfer.nmr.mgh.harvard.edu/), as well as gray matter skeleton-based registration, such as using Gray matter-based Spatial Statistics (GBSS) (221, 222), permit highly reliable DTI analyses of the gray matter. On the other hand, diffusivity variables are considered having a better sensitivity than FA in capturing neurodegenerative abnormalities in gray matter (223). Using a FreeSurfer registration, and intracortical MD measures of the PPMI data, two recent studies (224, 225) with cross-sectional and longitudinal (within 1-year follow up) analyses have found that compared to controls, PD patients had significantly increased MD in the frontal and occipital cortices; among PD patients these cortical MD changes correlated with worsened cognitive performance; furthermore, the posterior-cortical (i.e., medial temporal and temporo-occipital) MD significantly correlated with the increases of serum neurofilament light chain. These DTI studies in gray matter benefits the understanding of neuropathologic mechanisms underlying PD, especially those accompanied with cognitive impairments.

CONCLUSION

This review outlines the clinical utilities of the low-cost, non-invasive diffusion tensor MRI for biomarker of diagnosing PD, correlating PD symptomatology, assessing PD progression, and differentiating atypical types of parkinsonism. The robustness of the findings provides compelling evidences that DTI may be a promising marker for monitoring PD progressing and classifying atypical PD types. Therefore, it provides outcome measures to clinical trials and helps clinicians find better patient management. But the utility of DTI for diagnosing early PD is still challenging. Another merit is that, together with the findings on PPMI data, this review presented a divergent pattern of temporal FA changes in the earliest stage of PD. In particular, FA increase is pronounced in the young onset PD and in the earliest years of PD. These observations help to improve understanding of the pathophysiologic basis (e.g., the compensatory mechanisms, excitations of the inhibitory circuits) during the earliest stages of PD.

Limitations of clinical utilities of DTI shall be mentioned: (1) Because alterations of all DTI variables generally explain the non-specific biological features, they only permit indirect interpretations of the pathogenesis underlying PD. More investigations of imaging-pathological correlations are needed to corroborate a direct implication. Clinical DTI scans are subjected to low resolution, crossing-fibers, noise, and distortions. These factors affect a precise delineation of the key substructures [e.g., SNc, olfactory bulbs and tracts, locus coeruleus, nucleus accumbens, and small fiber connections in the brainstem (226)] that might be specific to PD pathology. Advanced diffusion techniques, such as high-resolution, high filed MRI, improved distortion-corrections, as well as solutions of fiber crossings, will lead

to better qualities of DTI analyses, but it is rather important to develop clinically feasible parameters upon these novel techniques. (3) DTI variables are highly dependent on scan parameters, such as MRI field strength, number of encoding directions, and maximum b values. To finally benefit the individual definition and interventions of PD, DTI measures across different MRI centers need to be harmonized, and standardized cutoff points for these DTI measures need to be established.

Further research studies are required to address (1) whether anatomically specific DTI changes are related to the core motor symptom domains (e.g., tremor, rigidity, bradykinesia, gait or postural problems) of PD and how DTI could be able to distinguish these motor subtypes; (2) how DTI change is associated with PD-risks (e.g., prodromal syndromes, risk genes) and whether this DTI change could predict further conversions to PD; (3) whether combining DTI analyses with other imaging modalities (e.g., MRI volumetric and thickness analyses, task-based and resting-state functional MRI, DAT-SPECT and neuroimaging of dopamine or alpha-synuclein, etc.), and clinical evaluations (227) could improve precisions in diagnosing early PD; (4) whether the advanced DTI analyses help the understanding of the brainstem reticular circuits and their roles in the brainstem neurotransmitter systems and how they impact the PD non-motor features (e.g., autonomic syndromes, sleep difficult and sleep behavior problems, pain, fatigue, etc.); and (5) lastly, further validation studies need to take into account of the age of PD onset, disease duration, and whether the non-motor features (especially cognitive deficits) present at the same time as the motor features, whether the PD patients are examined with MRI under an ON or OFF medication status, as well as the history and dosage of medication.

AUTHOR CONTRIBUTIONS

YZ: conception and research design, literature review, imaging data processing and analyses, results interpretation, and drafting the first manuscript. MB: conception and research design, results interpretation, language-editing, review, and critical revision of the manuscript. All authors contributed to the article and approved the submitted version.

ACKNOWLEDGMENTS

Data used in the preparation of this article were obtained from the Parkinson's Progression Markers Initiative (PPMI) database (www.ppmi-info.org/data). For up-to-date information on the study, visit www.ppmi-info.org. PPMI—a public-private partnership—is funded by the Michael J. Fox Foundation for Parkinson's Research and funding partners, including AbbVie, Avid Radiopharmaceuticals, Biogen, Bristol-Myers Squibb, Covance, GE Healthcare, Genentech, GlaxoSmithKline (GSK), Eli Lilly and Company, Lundbeck, Merck, Meso Scale Discovery (MSD), Pfizer, Piramal Imaging, Roche, Sanofi Genzyme, Servier, Teva, and UCB (www.ppmi-info.org/fundingpartners). We want to thank all patients, volunteers, and clinical staffs who participated the PPMI study. We thank Dr. Norbert Schuff for his previous leadership of the PPMI diffusion tensor imaging core. We thank Ms. I-Wei Wu for her previous work on collecting and coordinating the PPMI data.

SUPPLEMENTARY MATERIAL

The Supplementary Material for this article can be found online at: https://www.frontiersin.org/articles/10.3389/fneur.2020.531993/full#supplementary-material

REFERENCES

1. de Lau LM, Breteler MM. Epidemiology of Parkinson's disease. *Lancet Neurol.* (2006) 5:525–35. doi: 10.1016/S1474-4422(06)70471-9
2. DeLong MR. Primate models of movement disorders of basal ganglia origin. *Trends Neurosci.* (1990) 13:281–5. doi: 10.1016/0166-2236(90)90110-V
3. Braak H, Ghebremedhin E, Rub U, Bratzke H, Del Tredici K. Stages in the development of Parkinson's disease-related pathology. *Cell Tissue Res.* (2004) 318:121–34. doi: 10.1007/s00441-004-0956-9
4. Saha AR, Hill J, Utton MA, Asuni AA, Ackerley S, Grierson AJ, et al. Parkinson's disease alpha-synuclein mutations exhibit defective axonal transport in cultured neurons. *J Cell Sci.* (2004) 117:1017–24. doi: 10.1242/jcs.00967
5. Braak H, Del Tredici K, Rub U, de Vos RA, Jansen Steur EN, Braak E. Staging of brain pathology related to sporadic Parkinson's disease. *Neurobiol Aging.* (2003) 24:197–211. doi: 10.1016/S0197-4580(02)00065-9
6. Moseley ME, Kucharczyk J, Asgari HS, Norman D. Anisotropy in diffusion-weighted MRI. *Magn Reson Med.* (1991) 19:321–6. doi: 10.1002/mrm.1910190222
7. Schuff N, Wu IW, Buckley S, Foster ED, Coffey CS, Gitelman DR, et al. Diffusion imaging of nigral alterations in early Parkinson's disease with dopaminergic deficits. *Mov Disord.* (2015) 30:1885–92. doi: 10.1002/mds.26325
8. Prakash BD, Sitoh YY, Tan LC, Au WL. Asymmetrical diffusion tensor imaging indices of the rostral substantia nigra in Parkinson's disease. *Parkinsonism Relat Disord.* (2012) 18:1029–33. doi: 10.1016/j.parkreldis.2012.05.021
9. Langley J, Huddleston DE, Merritt M, Chen X, McMurray R, Silver M, et al. Diffusion tensor imaging of the substantia nigra in Parkinson's disease revisited. *Hum Brain Mapp.* (2016) 37:2547–56. doi: 10.1002/hbm.23192
10. Modrego PJ, Fayed N, Artal J, Olmos S. Correlation of findings in advanced MRI techniques with global severity scales in patients with Parkinson disease. *Acad Radiol.* (2011) 18:235–41. doi: 10.1016/j.acra.2010.09.022
11. Zhan W, Kang GA, Glass GA, Zhang Y, Shirley C, Millin R, et al., et al. Regional alterations of brain microstructure in Parkinson's disease using diffusion tensor imaging. *Mov Disord.* (2012) 27:90–7. doi: 10.1002/mds.23917
12. Wei X, Yan R, Chen Z, Weng R, Liu X, Gao H, et al. Combined diffusion tensor imaging and arterial spin labeling as markers of early parkinson's disease. *Sci Rep.* (2016) 6:33762. doi: 10.1038/srep33762
13. Zhang Y, Wu IW, Buckley S, Coffey CS, Foster E, Mendick S, et al. Diffusion tensor imaging of the nigrostriatal fibers in Parkinson's disease. *Mov Disord.* (2015) 30:1229–36. doi: 10.1002/mds.26251
14. Planetta PJ, Schulze ET, Geary EK, Corcos DM, Goldman JG, Little DM, et al. Thalamic projection fiber integrity in *de novo* Parkinson disease. *AJNR Am J Neuroradiol.* (2013) 34:74–9. doi: 10.3174/ajnr.A3178
15. Lenfeldt N, Hansson W, Larsson A, Nyberg L, Birgander R, Forsgren L. Diffusion tensor imaging and correlations to Parkinson rating scales. *J Neurol.* (2013) 260:2823–30. doi: 10.1007/s00415-013-7080-2

16. Chan LL, Ng KM, Rumpel H, Fook-Chong S, Li HH, Tan EK. Transcallosal diffusion tensor abnormalities in predominant gait disorder parkinsonism. *Parkinsonism Relat Disord.* (2014) 20:53–9. doi: 10.1016/j.parkreldis.2013.09.017
17. Youn J, Lee JM, Kwon H, Kim JS, Son TO, Cho JW. Alterations of mean diffusivity of pedunculopontine nucleus pathway in Parkinson's disease patients with freezing of gait. *Parkinsonism Relat Disord.* (2015) 21:12–7. doi: 10.1016/j.parkreldis.2014.10.003
18. Lenfeldt N, Holmlund H, Larsson A, Birgander R, Forsgren L. Frontal white matter injuries predestine gait difficulties in Parkinson's disease. *Acta Neurol Scand.* (2016) 134:210–8. doi: 10.1111/ane.12532
19. Surova Y, Lampinen B, Nilsson M, Latt J, Hall S, Widner H, et al. Alterations of diffusion kurtosis and neurite density measures in deep grey matter and white matter in parkinson's disease. *PLoS ONE.* (2016) 11:e0157755. doi: 10.1371/journal.pone.0157755
20. Matsui H, Nishinaka K, Oda M, Niikawa H, Komatsu K, Kubori T, et al. Wisconsin card sorting test in Parkinson's disease: diffusion tensor imaging. *Acta Neurol Scand.* (2007) 116:108–12. doi: 10.1111/j.1600-0404.2006.00795.x
21. Rae CL, Correia MM, Altena E, Hughes LE, Barker RA, Rowe JB. White matter pathology in Parkinson's disease: the effect of imaging protocol differences and relevance to executive function. *Neuroimage.* (2012) 62:1675–84. doi: 10.1016/j.neuroimage.2012.06.012
22. Gallagher C, Bell B, Bendlin B, Palotti M, Okonkwo O, Sodhi A, et al. White matter microstructural integrity and executive function in Parkinson's disease. *J Int Neuropsychol Soc.* (2013) 19:349–54. doi: 10.1017/S1355617712001373
23. Theilmann RJ, Reed JD, Song DD, Huang MX, Lee RR, Litvan I, et al. White-matter changes correlate with cognitive functioning in Parkinson's disease. *Front Neurol.* (2013) 4:37. doi: 10.3389/fneur.2013.00037
24. Chen YS, Chen MH, Lu CH, Chen PC, Chen HL, Yang IH, et al. Associations among cognitive functions, plasma DNA, and white matter integrity in patients with early-onset Parkinson's disease. *Front Neurosci.* (2017) 11:9. doi: 10.3389/fnins.2017.00009
25. Hattori T, Orimo S, Aoki S, Ito K, Abe O, Amano A, et al. Cognitive status correlates with white matter alteration in Parkinson's disease. *Hum Brain Mapp.* (2012) 33:727–39. doi: 10.1002/hbm.21245
26. Chen B, Fan GG, Liu H, Wang S. Changes in anatomical and functional connectivity of Parkinson's disease patients according to cognitive status. *Eur J Radiol.* (2015) 84:1318–24. doi: 10.1016/j.ejrad.2015.04.014
27. Li W, Liu J, Skidmore F, Liu Y, Tian J, Li K. White matter microstructure changes in the thalamus in Parkinson disease with depression: a diffusion tensor MR imaging study. *AJNR Am J Neuroradiol.* (2010) 31:1861–6. doi: 10.3174/ajnr.A2195
28. Huang P, Xu X, Gu Q, Xuan M, Yu X, Luo W, et al. Disrupted white matter integrity in depressed versus non-depressed Parkinson's disease patients: a tract-based spatial statistics study. *J Neurol Sci.* (2014) 346:145–8. doi: 10.1016/j.jns.2014.08.011
29. Baggio HC, Segura B, Ibarretxe-Bilbao N, Valldeoriola F, Marti MJ, Compta Y, et al. Structural correlates of facial emotion recognition deficits in Parkinson's disease patients. *Neuropsychologia.* (2012) 50:2121–8. doi: 10.1016/j.neuropsychologia.2012.05.020
30. Chiang PL, Chen HL, Lu CH, Chen PC, Chen MH, Yang IH, et al. White matter damage and systemic inflammation in Parkinson's disease. *BMC Neurosci.* (2017) 18:48. doi: 10.1186/s12868-017-0367-y
31. Haghshomar M, Rahmani F, Hadi Aarabi M, Shahjouei S, Sobhani S, Rahmani M. White matter changes correlates of peripheral neuroinflammation in patients with Parkinson's disease. *Neuroscience.* (2019) 403:70–8. doi: 10.1016/j.neuroscience.2017.10.050
32. Matsui H, Nishinaka K, Oda M, Niikawa H, Komatsu K, Kubori T, et al. Disruptions of the fornix fiber in Parkinsonian patients with excessive daytime sleepiness. *Parkinsonism Relat Disord.* (2006) 12:319–22. doi: 10.1016/j.parkreldis.2006.01.007
33. Pyatigorskaya N, Mongin M, Valabregue R, Yahia-Cherif L, Ewenczyk C, Poupon C, et al. Medulla oblongata damage and cardiac autonomic dysfunction in Parkinson disease. *Neurology.* (2016) 87:2540–5. doi: 10.1212/WNL.0000000000003426
34. Ibarretxe-Bilbao N, Junque C, Marti MJ, Valldeoriola F, Vendrell P, Bargallo N, et al. Olfactory impairment in Parkinson's disease and white matter abnormalities in central olfactory areas: a voxel-based diffusion tensor imaging study. *Mov Disord.* (2010) 25:1888–94. doi: 10.1002/mds.23208
35. Sobhani S, Rahmani F, Aarabi MH, Sadr AV. Exploring white matter microstructure and olfaction dysfunction in early parkinson disease: diffusion MRI reveals new insight. *Brain Imaging Behav.* (2019) 13:210–9. doi: 10.1007/s11682-017-9781-0
36. Scherfler C, Esterhammer R, Nocker M, Mahlknecht P, Stockner H, Warwitz B, et al. Correlation of dopaminergic terminal dysfunction and microstructural abnormalities of the basal ganglia and the olfactory tract in Parkinson's disease. *Brain.* (2013) 136:3028–37. doi: 10.1093/brain/awt234
37. Wang J, Yang QX, Sun X, Vesek J, Mosher Z, Vasavada M, et al. MRI evaluation of asymmetry of nigrostriatal damage in the early stage of early-onset Parkinson's disease. *Parkinsonism Relat Disord.* (2015) 21:590–6. doi: 10.1016/j.parkreldis.2015.03.012
38. Esterhammer R, Seppi K, Reiter E, Pinter B, Mueller C, Kremser C, et al. Potential of diffusion tensor imaging and relaxometry for the detection of specific pathological alterations in Parkinson's Disease (PD). *PLoS ONE.* (2015) 10:e0145493. doi: 10.1371/journal.pone.0145493
39. Wen MC, Heng HS, Ng SY, Tan LC, Chan LL, Tan EK. White matter microstructural characteristics in newly diagnosed Parkinson's disease: an unbiased whole-brain study. *Sci Rep.* (2016) 6:35601. doi: 10.1038/srep35601
40. Iseki K, Fukuyama H, Oishi N, Tomimoto H, Otsuka Y, Nankaku M, et al. Freezing of gait and white matter changes: a tract-based spatial statistics study. *J Clin Mov Disord.* (2015) 2:1. doi: 10.1186/s40734-014-0011-2
41. Luo C, Song W, Chen Q, Yang J, Gong Q, Shang HF. White matter microstructure damage in tremor-dominant Parkinson's disease patients. *Neuroradiology.* (2017) 59:691–8. doi: 10.1007/s00234-017-1846-7
42. Vervoort G, Leunissen I, Firbank M, Heremans E, Nackaerts E, Vandenberghe W, et al. Structural brain alterations in motor subtypes of Parkinson's disease: evidence from probabilistic tractography and shape analysis. *PLoS ONE.* (2016) 11:e0157743. doi: 10.1371/journal.pone.0157743
43. Koshimori Y, Segura B, Christopher L, Lobaugh N, Duff-Canning S, Mizrahi R, et al. Imaging changes associated with cognitive abnormalities in Parkinson's disease. *Brain Struct Funct.* (2015) 220:2249–61. doi: 10.1007/s00429-014-0785-x
44. Duncan GW, Firbank MJ, Yarnall AJ, Khoo TK, Brooks DJ, Barker RA, et al. Gray and white matter imaging: a biomarker for cognitive impairment in early Parkinson's disease? *Mov Disord.* (2016) 31:103–110. doi: 10.1002/mds.26312
45. Melzer TR, Watts R, MacAskill MR, Pitcher TL, Livingston L, Keenan RJ, et al. White matter microstructure deteriorates across cognitive stages in Parkinson disease. *Neurology.* (2013) 80:1841–9. doi: 10.1212/WNL.0b013e3182929f62
46. Zheng Z, Shemmassian S, Wijekoon C, Kim W, Bookheimer SY, Pouratian N. DTI correlates of distinct cognitive impairments in Parkinson's disease. *Hum Brain Mapp.* (2014) 35:1325–33. doi: 10.1002/hbm.22256
47. Kantarci K, Senjem ML, Avula R, Zhang B, Samikoglu AR, Weigand SD, et al. Diffusion tensor imaging and cognitive function in older adults with no dementia. *Neurology.* (2011) 77:26–34. doi: 10.1212/WNL.0b013e31822313dc
48. Carlesimo GA, Piras F, Assogna F, Pontieri FE, Caltagirone C, Spalletta G. Hippocampal abnormalities and memory deficits in Parkinson disease: a multimodal imaging study. *Neurology.* (2012) 78:1939–45. doi: 10.1212/WNL.0b013e318259e1c5
49. Haehner A, Schopf V, Loureiro A, Linn J, Reichmann H, Hummel T, et al. Substantia nigra fractional anisotropy changes confirm the PD at-risk status of patients with idiopathic smell loss. *Parkinsonism Relat Disord.* (2018) 50:113–6. doi: 10.1016/j.parkreldis.2018.02.026
50. Guimaraes RP, Campos BM, de Rezende TJ, Piovesana L, Azevedo PC, Amato-Filho AC, et al. Is diffusion tensor imaging a good biomarker for early Parkinson's disease? *Front Neurol.* (2018) 9:626. doi: 10.3389/fneur.2018.00626
51. Auning E, Kjaervik VK, Selnes P, Aarsland D, Haram A, Bjornerud A, et al. White matter integrity and cognition in Parkinson's disease: a cross-sectional study. *BMJ Open.* (2014) 4:e003976. doi: 10.1136/bmjopen-2013-003976

52. Gargouri F, Gallea C, Mongin M, Pyatigorskaya N, Valabregue R, Ewenczyk C, et al. Multimodal magnetic resonance imaging investigation of basal forebrain damage and cognitive deficits in Parkinson's disease. *Mov Disord.* (2019) 34:516–25. doi: 10.1002/mds.27561
53. Zhang G, Zhang Y, Zhang C, Wang Y, Ma G, Nie K, et al. Diffusion kurtosis imaging of substantia nigra is a sensitive method for early diagnosis and disease evaluation in Parkinson's disease. *Parkinsons Dis.* (2015) 2015:207624. doi: 10.1155/2015/207624
54. Kamagata K, Zalesky A, Hatano T, Ueda R, Di Biase MA, Okuzumi A, et al. Gray matter abnormalities in idiopathic Parkinson's disease: evaluation by diffusional kurtosis imaging and neurite orientation dispersion and density imaging. *Hum Brain Mapp.* (2017) 38:3704–22. doi: 10.1002/hbm.23628
55. Ofori E, Pasternak O, Planetta PJ, Burciu R, Snyder A, Febo M, et al. Increased free water in the substantia nigra of Parkinson's disease: a single-site and multi-site study. *Neurobiol Aging.* (2015) 36:1097–104. doi: 10.1016/j.neurobiolaging.2014.10.029
56. Planetta PJ, Ofori E, Pasternak O, Burciu RG, Shukla P, DeSimone JC, et al. Free-water imaging in Parkinson's disease and atypical parkinsonism. *Brain.* (2016) 139:495–508. doi: 10.1093/brain/awv361
57. Kim M, Park H. Structural connectivity profile of scans without evidence of dopaminergic deficit (SWEDD) patients compared to normal controls and Parkinson's disease patients. *Springerplus.* (2016) 5:1421. doi: 10.1186/s40064-016-3110-8
58. Wen MC, Xu Z, Lu Z, Chan LL, Tan EK, Tan LCS. Microstructural network alterations of olfactory dysfunction in newly diagnosed Parkinson's disease. *Sci Rep.* (2017) 7:12559. doi: 10.1038/s41598-017-12947-7
59. Tan WQ, Yeoh CS, Rumpel H, Nadkarni N, Lye WK, Tan EK, et al. Deterministic tractography of the nigrostriatal-nigropallidal pathway in parkinson's disease. *Sci Rep.* (2015) 5:17283. doi: 10.1038/srep17283
60. Son SJ, Kim M, Park H. Imaging analysis of Parkinson's disease patients using SPECT and tractography. *Sci Rep.* (2016) 6:38070. doi: 10.1038/srep38070
61. Kamagata K, Hatano T, Okuzumi A, Motoi Y, Abe O, Shimoji K, et al. Neurite orientation dispersion and density imaging in the substantia nigra in idiopathic Parkinson disease. *Eur Radiol.* (2016) 26:2567–77. doi: 10.1007/s00330-015-4066-8
62. Kamagata K, Zalesky A, Hatano T, Di Biase MA, El Samad O, Saiki S, et al. Connectome analysis with diffusion MRI in idiopathic Parkinson's disease: evaluation using multi-shell, multi-tissue, constrained spherical deconvolution. *Neuroimage Clin.* (2018) 17:518–29. doi: 10.1016/j.nicl.2017.11.007
63. Abbasi N, Mohajer B, Abbasi S, Hasanabadi P, Abdolalizadeh A, Rajimehr R. Relationship between cerebrospinal fluid biomarkers and structural brain network properties in Parkinson's disease. *Mov Disord.* (2018) 33:431–9. doi: 10.1002/mds.27284
64. Basser PJ, Jones DK. Diffusion-tensor MRI. Theory, experimental design and data analysis - a technical review. *NMR Biomed.* (2002) 15:456–67. doi: 10.1002/nbm.783
65. Pierpaoli C, Jezzard P, Basser PJ, Barnett A, Di Chiro G. Diffusion tensor MR imaging of the human brain. *Radiology.* (1996) 201:637–48. doi: 10.1148/radiology.201.3.8939209
66. Song SK, Sun SW, Ramsbottom MJ, Chang C, Russell J, Cross AH. Dysmyelination revealed through MRI as increased radial (but unchanged axial) diffusion of water. *Neuroimage.* (2002) 17:1429–36. doi: 10.1006/nimg.2002.1267
67. Kim JH, Budde MD, Liang HF, Klein RS, Russell JH, Cross AH, et al. Detecting axon damage in spinal cord from a mouse model of multiple sclerosis. *Neurobiol Dis.* (2006) 21:626–32. doi: 10.1016/j.nbd.2005.09.009
68. Wheeler-Kingshott CA, Cercignani M. About "axial" and "radial" diffusivities. *Magn Reson Med.* (2009) 61:1255–60. doi: 10.1002/mrm.21965
69. Acosta-Cabronero J, Williams GB, Pengas G, Nestor PJ. Absolute diffusivities define the landscape of white matter degeneration in Alzheimer's disease. *Brain.* (2010) 133:529–39. doi: 10.1093/brain/awp257
70. Thomalla G, Glauche V, Koch MA, Beaulieu C, Weiller C, Rother J. Diffusion tensor imaging detects early Wallerian degeneration of the pyramidal tract after ischemic stroke. *Neuroimage.* (2004) 22:1767–74. doi: 10.1016/j.neuroimage.2004.03.041
71. Boska MD, Hasan KM, Kibuule D, Banerjee R, McIntyre E, Nelson JA, et al. Quantitative diffusion tensor imaging detects dopaminergic neuronal degeneration in a murine model of Parkinson's disease. *Neurobiol Dis.* (2007) 26:590–6. doi: 10.1016/j.nbd.2007.02.010
72. Karagulle Kendi AT, Lehericy S, Luciana M, Ugurbil K, Tuite P. Altered diffusion in the frontal lobe in Parkinson disease. *AJNR Am J Neuroradiol.* (2008) 29:501–5. doi: 10.3174/ajnr.A0850
73. Tessa C, Giannelli M, Della Nave R, Lucetti C, Berti C, Ginestroni A, et al. A whole-brain analysis in *de novo* Parkinson disease. *AJNR Am J Neuroradiol.* (2008) 29:674–80. doi: 10.3174/ajnr.A0900
74. Soares JM, Marques P, Alves V, Sousa N. A hitchhiker's guide to diffusion tensor imaging. *Front Neurosci.* (2013) 7:31. doi: 10.3389/fnins.2013.00031
75. Smith SM, Jenkinson M, Johansen-Berg H, Rueckert D, Nichols TE, Mackay CE, et al. Tract-based spatial statistics: voxelwise analysis of multi-subject diffusion data. *Neuroimage.* (2006) 31:1487–505. doi: 10.1016/j.neuroimage.2006.02.024
76. Zhang K, Yu C, Zhang Y, Wu X, Zhu C, Chan P, et al. Voxel-based analysis of diffusion tensor indices in the brain in patients with Parkinson's disease. *Eur J Radiol.* (2011) 77:269–73. doi: 10.1016/j.ejrad.2009.07.032
77. Kim HJ, Kim SJ, Kim HS, Choi CG, Kim N, Han S, et al. Alterations of mean diffusivity in brain white matter and deep gray matter in Parkinson's disease. *Neurosci Lett.* (2013) 550:64–8. doi: 10.1016/j.neulet.2013.06.050
78. Diez-Cirarda M, Ojeda N, Pena J, Cabrera-Zubizarreta A, Gomez-Beldarrain MA, Gomez-Esteban JC, et al. Neuroanatomical correlates of theory of mind deficit in Parkinson's disease: a multimodal imaging study. *PLoS ONE.* (2015) 10:e0142234. doi: 10.1371/journal.pone.0142234
79. Jiang MF, Shi F, Niu GM, Xie SH, Yu SY. A novel method for evaluating brain function and microstructural changes in Parkinson's disease. *Neural Regen Res.* (2015) 10:2025–2032. doi: 10.4103/1673-5374.172322
80. Skidmore FM, Spetsieris PG, Anthony T, Cutter GR, von Deneen KM, Liu Y, et al. A full-brain, bootstrapped analysis of diffusion tensor imaging robustly differentiates Parkinson disease from healthy controls. *Neuroinformatics.* (2015) 13:7–18. doi: 10.1007/s12021-014-9222-9
81. Vercruysse S, Leunissen I, Vervoort G, Vandenberghe W, Swinnen S, Nieuwboer A. Microstructural changes in white matter associated with freezing of gait in Parkinson's disease. *Mov Disord.* (2015) 30:567–76. doi: 10.1002/mds.26130
82. Yoo HB, Lee JY, Lee JS, Kang H, Kim YK, Song IC, et al. Whole-brain diffusion-tensor changes in parkinsonian patients with impulse control disorders. *J Clin Neurol.* (2015) 11:42–7. doi: 10.3988/jcn.2015.11.1.42
83. Price CC, Tanner J, Nguyen PT, Schwab NA, Mitchell S, Slonena E, et al. Gray and white matter contributions to cognitive frontostriatal deficits in non-demented Parkinson's disease. *PLoS ONE.* (2016) 11:e0147332. doi: 10.1371/journal.pone.0147332
84. Lim JS, Shin SA, Lee JY, Nam H, Lee JY, Kim YK. Neural substrates of rapid eye movement sleep behavior disorder in Parkinson's disease. *Parkinsonism Relat Disord.* (2016) 23:31–36. doi: 10.1016/j.parkreldis.2015.11.027
85. Mole JP, Subramanian L, Bracht T, Morris H, Metzler-Baddeley C, Linden DE. Increased fractional anisotropy in the motor tracts of Parkinson's disease suggests compensatory neuroplasticity or selective neurodegeneration. *Eur Radiol.* (2016) 26:3327–35. doi: 10.1007/s00330-015-4178-1
86. Wang M, Jiang S, Yuan Y, Zhang L, Ding J, Wang J, et al. Alterations of functional and structural connectivity of freezing of gait in Parkinson's disease. *J Neurol.* (2016) 263:1583–92. doi: 10.1007/s00415-016-8174-4
87. Canu E, Agosta F, Markovic V, Petrovic I, Stankovic I, Imperiale F, et al. White matter tract alterations in Parkinson's disease patients with punding. *Parkinsonism Relat Disord.* (2017) 43:85–91. doi: 10.1016/j.parkreldis.2017.07.025
88. Chen B, Fan G, Sun W, Shang X, Shi S, Wang S, et al. Usefulness of diffusion-tensor MRI in the diagnosis of Parkinson variant of multiple system atrophy and Parkinson's disease: a valuable tool to differentiate between them? *Clin Radiol.* (2017) 72:610 e619–e15. doi: 10.1016/j.crad.2017.02.005
89. Cousineau M, Jodoin PM, Morency FC, Rozanski V, Grand'Maison M, Bedell BJ, et al. A test-retest study on Parkinson's PPMI dataset yields statistically significant white matter fascicles. *Neuroimage Clin.* (2017) 16:222–33. doi: 10.1016/j.nicl.2017.07.020
90. Georgiopoulos C, Warntjes M, Dizdar N, Zachrisson H, Engstrom M, Haller S, et al. Olfactory impairment in parkinson's disease studied with diffusion tensor and magnetization transfer imaging. *J Parkinsons Dis.* (2017) 7:301–11. doi: 10.3233/JPD-161060

91. Lee WW, Yoon EJ, Lee JY, Park SW, Kim YK. Visual hallucination and pattern of brain degeneration in Parkinson's disease. *Neurodegener Dis.* (2017) 17:63–72. doi: 10.1159/000448517
92. Chen NK, Chou YH, Sundman M, Hickey P, Kasoff WS, Bernstein A, et al. Alteration of diffusion-tensor magnetic resonance imaging measures in brain regions involved in early stages of Parkinson's disease. *Brain Connect.* (2018) 8:343–9. doi: 10.1089/brain.2017.0558
93. Li XR, Ren YD, Cao B, Huang XL. Analysis of white matter characteristics with tract-based spatial statistics according to diffusion tensor imaging in early Parkinson's disease. *Neurosci Lett.* (2018) 675:127–32. doi: 10.1016/j.neulet.2017.11.064
94. Minett T, Su L, Mak E, Williams G, Firbank M, Lawson RA, et al. Longitudinal diffusion tensor imaging changes in early Parkinson's disease: ICICLE-PD study. *J Neurol.* (2018) 265:1528–39. doi: 10.1007/s00415-018-8873-0
95. Pietracupa S, Suppa A, Upadhyay N, Gianni C, Grillea G, Leodori G, et al. Freezing of gait in Parkinson's disease: gray and white matter abnormalities. *J Neurol.* (2018) 265:52–62. doi: 10.1007/s00415-017-8654-1
96. Rektor I, Svatkova A, Vojtisek L, Zikmundova I, Vanicek J, Kiraly A, et al. White matter alterations in Parkinson's disease with normal cognition precede grey matter atrophy. *PLoS ONE.* (2018) 13:e0187939. doi: 10.1371/journal.pone.0187939
97. Taylor KI, Sambataro F, Boess F, Bertolino A, Dukart J. Progressive decline in gray and white matter integrity in *de novo* parkinson's disease: an analysis of longitudinal parkinson progression markers initiative diffusion tensor imaging data. *Front Aging Neurosci.* (2018) 10:318. doi: 10.3389/fnagi.2018.00318
98. Wen MC, Heng HSE, Lu Z, Xu Z, Chan LL, Tan EK, et al. Differential white matter regional alterations in motor subtypes of early drug-naive parkinson's disease patients. *Neurorehabil Neural Repair.* (2018) 32:129–41. doi: 10.1177/1545968317753075
99. Guan X, Huang P, Zeng Q, Liu C, Wei H, Xuan M, et al. Quantitative susceptibility mapping as a biomarker for evaluating white matter alterations in Parkinson's disease. *Brain Imaging Behav.* (2019) 13:220–31. doi: 10.1007/s11682-018-9842-z
100. Movement Disorder Society Task Force on Rating Scales for Parkinson's D. The Unified Parkinson's Disease Rating Scale (UPDRS): status and recommendations. *Mov Disord.* (2003) 18:738–50. doi: 10.1002/mds.10473
101. Goetz CG, Fahn S, Martinez-Martin P, Poewe W, Sampaio C, Stebbins GT, et al. Movement Disorder Society-sponsored revision of the Unified Parkinson's Disease Rating Scale (MDS-UPDRS): Process, format, and clinimetric testing plan. *Mov Disord.* (2007) 22:41–7. doi: 10.1002/mds.21198
102. Hall JM, Ehgoetz Martens KA, Walton CC, O'Callaghan C, Keller PE, Lewis SJ, et al. Diffusion alterations associated with Parkinson's disease symptomatology: a review of the literature. *Parkinsonism Relat Disord.* (2016) 33:12–26. doi: 10.1016/j.parkreldis.2016.09.026
103. Marek K. The Parkinson Progression Marker Initiative (PPMI). *Prog Neurobiol.* (2011) 95:629–35. doi: 10.1016/j.pneurobio.2011.09.005
104. Schwarz ST, Abaei M, Gontu V, Morgan PS, Bajaj N, Auer DP. Diffusion tensor imaging of nigral degeneration in Parkinson's disease: a region-of-interest and voxel-based study at 3 T and systematic review with meta-analysis. *Neuroimage Clin.* (2013) 3:481–8. doi: 10.1016/j.nicl.2013.10.006
105. Jeurissen B, Leemans A, Tournier JD, Jones DK, Sijbers J. Investigating the prevalence of complex fiber configurations in white matter tissue with diffusion magnetic resonance imaging. *Hum Brain Mapp.* (2013) 34:2747–66. doi: 10.1002/hbm.22099
106. Mori S. *Introduction to Diffusion Tensor Imaging. 1st Ed*n. Elsevier Science (2007). doi: 10.1016/b978-0-444-52828-5.x5014-5
107. Atkinson-Clement C, Pinto S, Eusebio A, Coulon O. Diffusion tensor imaging in Parkinson's disease: review and meta-analysis. *Neuroimage Clin.* (2017) 16:98–110. doi: 10.1016/j.nicl.2017.07.011
108. Baudrexel S, Witte T, Seifried C, von Wegner F, Beissner F, Klein JC, et al. Resting state fMRI reveals increased subthalamic nucleus-motor cortex connectivity in Parkinson's disease. *Neuroimage.* (2011) 55:1728–38. doi: 10.1016/j.neuroimage.2011.01.017
109. Melzer TR, Watts R, MacAskill MR, Pearson JF, Rueger S, Pitcher TL, et al. Arterial spin labelling reveals an abnormal cerebral perfusion pattern in Parkinson's disease. *Brain.* (2011) 134:845–55. doi: 10.1093/brain/awq377
110. Ma Y, Tang C, Spetsieris PG, Dhawan V, Eidelberg D. Abnormal metabolic network activity in Parkinson's disease: test-retest reproducibility. *J Cereb Blood Flow Metab.* (2007) 27:597–605. doi: 10.1038/sj.jcbfm.9600358
111. Collier TJ, Lipton J, Daley BF, Palfi S, Chu Y, Sortwell C, et al. Aging-related changes in the nigrostriatal dopamine system and the response to MPTP in nonhuman primates: diminished compensatory mechanisms as a prelude to parkinsonism. *Neurobiol Dis.* (2007) 26:56–65. doi: 10.1016/j.nbd.2006.11.013
112. Hindle JV. Ageing, neurodegeneration and Parkinson's disease. *Age Ageing.* (2010) 39:156–61. doi: 10.1093/ageing/afp223
113. Nagae LM, Honce JM, Tanabe J, Shelton E, Sillau SH, Berman BD. Microstructural changes within the basal ganglia differ between Parkinson disease subtypes. *Front Neuroanat.* (2016) 10:17. doi: 10.3389/fnana.2016.00017
114. Alexander GE. Biology of Parkinson's disease: pathogenesis and pathophysiology of a multisystem neurodegenerative disorder. *Dialogues Clin Neurosci.* (2004) 6:259–80.
115. Marsden CD. Parkinson's disease. *Lancet.* (1990) 335:948–52. doi: 10.1016/0140-6736(90)91006-V
116. Cheng HC, Ulane CM, Burke RE. Clinical progression in Parkinson disease and the neurobiology of axons. *Ann Neurol.* (2010) 67:715–25. doi: 10.1002/ana.21995
117. Peran P, Cherubini A, Assogna F, Piras F, Quattrocchi C, Peppe A, et al. Magnetic resonance imaging markers of Parkinson's disease nigrostriatal signature. *Brain.* (2010) 133:3423–33. doi: 10.1093/brain/awq212
118. Du G, Lewis MM, Styner M, Shaffer ML, Sen S, Yang QX, et al. Combined R2* and diffusion tensor imaging changes in the substantia nigra in Parkinson's disease. *Mov Disord.* (2011) 26:1627–32. doi: 10.1002/mds.23643
119. Joshi N, Rolheiser TM, Fisk JD, McKelvey JR, Schoffer K, Phillips G, et al. Lateralized microstructural changes in early-stage Parkinson's disease in anterior olfactory structures, but not in substantia nigra. *J Neurol.* (2017) 264:1497–505. doi: 10.1007/s00415-017-8555-3
120. Yoshikawa K, Nakata Y, Yamada K, Nakagawa M. Early pathological changes in the parkinsonian brain demonstrated by diffusion tensor MRI. *J Neurol Neurosurg Psychiatr.* (2004) 75:481–4. doi: 10.1136/jnnp.2003.021873
121. Chan LL, Rumpel H, Yap K, Lee E, Loo HV, Ho GL, et al. Case control study of diffusion tensor imaging in Parkinson's disease. *J Neurol Neurosurg Psychiatr.* (2007) 78:1383–6. doi: 10.1136/jnnp.2007.121525
122. Rolheiser TM, Fulton HG, Good KP, Fisk JD, McKelvey JR, Scherfler C, et al. Diffusion tensor imaging and olfactory identification testing in early-stage Parkinson's disease. *J Neurol.* (2011) 258:1254–60. doi: 10.1007/s00415-011-5915-2
123. Wang JJ, Lin WY, Lu CS, Weng YH, Ng SH, Wang CH, et al. Parkinson disease: diagnostic utility of diffusion kurtosis imaging. *Radiology.* (2011) 261:210–7. doi: 10.1148/radiol.11102277
124. Skorpil M, Soderlund V, Sundin A, Svenningsson P. MRI diffusion in Parkinson's disease: using the technique's inherent directional information to study the olfactory bulb and substantia nigra. *J Parkinsons Dis.* (2012) 2:171–80. doi: 10.3233/JPD-2012-12091
125. Perea RD, Rada RC, Wilson J, Vidoni ED, Morris JK, Lyons KE, et al. A comparative white matter study with Parkinson's disease, Parkinson's disease with dementia and Alzheimer's disease. *J Alzheimers Dis Parkinsonism.* (2013) 3:123. doi: 10.4172/2161-0460.1000123
126. Ji L, Wang Y, Zhu D, Liu W, Shi J. White matter differences between multiple system atrophy (parkinsonian type) and Parkinson's disease: a diffusion tensor image study. *Neuroscience.* (2015) 305:109–16. doi: 10.1016/j.neuroscience.2015.07.060
127. Loane C, Politis M, Kefalopoulou Z, Valle-Guzman N, Paul G, Widner H, et al. Aberrant nigral diffusion in Parkinson's disease: a longitudinal diffusion tensor imaging study. *Mov Disord.* (2016) 31:1020–6. doi: 10.1002/mds.26606
128. Gattellaro G, Minati L, Grisoli M, Mariani C, Carella F, Osio M, et al. White matter involvement in idiopathic Parkinson disease: a diffusion tensor imaging study. *AJNR Am J Neuroradiol.* (2009) 30:1222–6. doi: 10.3174/ajnr.A1556
129. Vaillancourt DE, Spraker MB, Prodoehl J, Abraham I, Corcos DM, Zhou XJ, et al. High-resolution diffusion tensor imaging in the

substantia nigra of *de novo* Parkinson disease. *Neurology.* (2009) 72:1378–84. doi: 10.1212/01.wnl.0000340982.01727.6e
130. Lenfeldt N, Larsson A, Nyberg L, Birgander R, Forsgren L. Fractional anisotropy in the substantia nigra in Parkinson's disease: a complex picture. *Eur J Neurol.* (2015) 22:1408–14. doi: 10.1111/ene.12760
131. Hirata FCC, Sato JR, Vieira G, Lucato LT, Leite CC, Bor-Seng-Shu E, et al. Substantia nigra fractional anisotropy is not a diagnostic biomarker of Parkinson's disease: a diagnostic performance study and meta-analysis. *Eur Radiol.* (2017) 27:2640–8. doi: 10.1007/s00330-016-4611-0
132. Knossalla F, Kohl Z, Winkler J, Schwab S, Schenk T, Engelhorn T, et al. High-resolution diffusion tensor-imaging indicates asymmetric microstructural disorganization within substantia nigra in early Parkinson's disease. *J Clin Neurosci.* (2018) 50:199–202. doi: 10.1016/j.jocn.2018.01.023
133. Du G, Lewis MM, Sen S, Wang J, Shaffer ML, Styner M, et al. Imaging nigral pathology and clinical progression in Parkinson's disease. *Mov Disord.* (2012) 27:1636–43. doi: 10.1002/mds.25182
134. Menke RA, Jbabdi S, Miller KL, Matthews PM, Zarei M. Connectivity-based segmentation of the substantia nigra in human and its implications in Parkinson's disease. *Neuroimage.* (2010) 52:1175–80. doi: 10.1016/j.neuroimage.2010.05.086
135. Deng XY, Wang L, Yang TT, Li R, Yu G. A meta-analysis of diffusion tensor imaging of substantia nigra in patients with Parkinson's disease. *Sci Rep.* (2018) 8:2941. doi: 10.1038/s41598-018-20076-y
136. Cochrane CJ, Ebmeier KP. Diffusion tensor imaging in parkinsonian syndromes: a systematic review and meta-analysis. *Neurology.* (2013) 80:857–64. doi: 10.1212/WNL.0b013e318284070c
137. Fearnley JM, Lees AJ. Ageing and Parkinson's disease: substantia nigra regional selectivity. *Brain.* (1991) 114:2283–301. doi: 10.1093/brain/114.5.2283
138. Rodriguez-Oroz MC, Jahanshahi M, Krack P, Litvan I, Macias R, Bezard E, et al. Initial clinical manifestations of Parkinson's disease: features and pathophysiological mechanisms. *Lancet Neurol.* (2009) 8:1128–39. doi: 10.1016/S1474-4422(09)70293-5
139. Lau A, So RWL, Lau HHC, Sang JC, Ruiz-Riquelme A, Fleck SC, et al. alpha-Synuclein strains target distinct brain regions and cell types. *Nat Neurosci.* (2020) 23:21–31. doi: 10.1038/s41593-019-0541-x
140. McColgan P, Joubert J, Tabrizi SJ, Rees G. The human motor cortex microcircuit: insights for neurodegenerative disease. *Nat Rev Neurosci.* (2020) 21:401–5. doi: 10.1038/s41583-020-0315-1
141. Westbrook A, van den Bosch R, Maatta JI, Hofmans L, Papadopetraki D, Cools R, et al. Dopamine promotes cognitive effort by biasing the benefits versus costs of cognitive work. *Science.* (2020) 367:1362–6. doi: 10.1126/science.aaz5891
142. Lehericy S, Ducros M, Van de Moortele PF, Francois C, Thivard L, Poupon C, et al. Diffusion tensor fiber tracking shows distinct corticostriatal circuits in humans. *Ann Neurol.* (2004) 55:522–9. doi: 10.1002/ana.20030
143. Sedrak M, Gorgulho A, Bari A, Behnke E, Frew A, Gevorkyan I, et al. Diffusion tensor imaging (DTI) and colored fractional anisotropy (FA) mapping of the subthalamic nucleus (STN) and the globus pallidus interna (GPi). *Acta Neurochir.* (2010) 152:2079–84. doi: 10.1007/s00701-010-0813-4
144. Hauptman JS, DeSalles AA, Espinoza R, Sedrak M, Ishida W. Potential surgical targets for deep brain stimulation in treatment-resistant depression. *Neurosurg Focus.* (2008) 25:E3. doi: 10.3171/FOC/2008/25/7/E3
145. Andica C, Kamagata K, Hatano T, Okuzumi A, Saito A, Nakazawa M, et al. Neurite orientation dispersion and density imaging of the nigrostriatal pathway in Parkinson's disease: retrograde degeneration observed by tract-profile analysis. *Parkinsonism Relat Disord.* (2018) 51:55–60. doi: 10.1016/j.parkreldis.2018.02.046
146. Theisen F, Leda R, Pozorski V, Oh JM, Adluru N, Wong R, et al. Evaluation of striatonigral connectivity using probabilistic tractography in Parkinson's disease. *Neuroimage Clin.* (2017) 16:557–63. doi: 10.1016/j.nicl.2017.09.009
147. Menke RA, Scholz J, Miller KL, Deoni S, Jbabdi S, Matthews PM, et al. MRI characteristics of the substantia nigra in Parkinson's disease: a combined quantitative T1 and DTI study. *Neuroimage.* (2009) 47:435–41. doi: 10.1016/j.neuroimage.2009.05.017
148. Scherfler C, Schocke MF, Seppi K, Esterhammer R, Brenneis C, Jaschke W, et al. Voxel-wise analysis of diffusion weighted imaging reveals disruption of the olfactory tract in Parkinson's disease. *Brain.* (2006) 129:538–42. doi: 10.1093/brain/awh674
149. Mentzel TQ, Lieverse R, Levens A, Mentzel CL, Tenback DE, Bakker PR, et al. Reliability and validity of an instrument for the assessment of bradykinesia. *Psychiatr Res.* (2016) 238:189–95. doi: 10.1016/j.psychres.2016.02.011
150. Yao N, Cheung C, Pang S, Shek-kwan Chang R, Lau KK, Suckling J, et al. Multimodal MRI of the hippocampus in Parkinson's disease with visual hallucinations. *Brain Struct Funct.* (2016) 221:287–300. doi: 10.1007/s00429-014-0907-5
151. Buchert R, Lange C, Spehl TS, Apostolova I, Frings L, Jonsson C, et al. Diagnostic performance of the specific uptake size index for semi-quantitative analysis of I-123-FP-CIT SPECT. Harmonized multi-center research setting versus typical clinical single-camera setting. *EJNMMI Res.* (2019) 9:37. doi: 10.1186/s13550-019-0506-9
152. Jakobson Mo S, Axelsson J, Jonasson L, Larsson A, Ogren MJ, Ogren M, et al. Dopamine transporter imaging with [(18)F]FE-PE2I PET and [(123)I]FP-CIT SPECT-a clinical comparison. *EJNMMI Res.* (2018) 8:100. doi: 10.1186/s13550-018-0450-0
153. Prashanth R, Roy SD, Mandal PK, Ghosh S. High-accuracy classification of Parkinson's disease through shape analysis and surface fitting in 123I-Ioflupane SPECT imaging. *IEEE J Biomed Health Inform.* (2017) 21:794–802. doi: 10.1109/JBHI.2016.2547901
154. Augimeri A, Cherubini A, Cascini GL, Galea D, Caligiuri ME, Barbagallo G, et al. CADA-computer-aided DaTSCAN analysis. *EJNMMI Phys.* (2016) 3:4. doi: 10.1186/s40658-016-0140-9
155. Kraemmer J, Kovacs GG, Perju-Dumbrava L, Pirker S, Traub-Weidinger T, Pirker W. Correlation of striatal dopamine transporter imaging with post mortem substantia nigra cell counts. *Mov Disord.* (2014) 29:1767–73. doi: 10.1002/mds.25975
156. Walker Z, Jaros E, Walker RW, Lee L, Costa DC, Livingston G, et al. Dementia with Lewy bodies: a comparison of clinical diagnosis, FP-CIT single photon emission computed tomography imaging and autopsy. *J Neurol Neurosurg Psychiatr.* (2007) 78:1176–81. doi: 10.1136/jnnp.2006.110122
157. Yang J, Archer DB, Burciu RG, Muller M, Roy A, Ofori E, et al. Multimodal dopaminergic and free-water imaging in Parkinson's disease. *Parkinsonism Relat Disord.* (2019) 62:10–5. doi: 10.1016/j.parkreldis.2019.01.007
158. Zhang Y, Wu IW, Tosun D, Foster E, Schuff N, Parkinson's Progression Markers I. Progression of regional microstructural degeneration in Parkinson's disease: a multicenter diffusion tensor imaging study. *PLoS ONE.* (2016) 11:e0165540. doi: 10.1371/journal.pone.0165540
159. Lenfeldt N, Eriksson J, Astrom B, Forsgren L, Mo SJ. Fractional anisotropy and mean diffusion as measures of dopaminergic function in parkinson's disease: challenging results. *J Parkinsons Dis.* (2017) 7:129–42. doi: 10.3233/JPD-161011
160. Lorio S, Sambataro F, Bertolino A, Draganski B, Dukart J. The combination of DAT-SPECT, structural and diffusion MRI predicts clinical progression in Parkinson's disease. *Front Aging Neurosci.* (2019) 11:57. doi: 10.3389/fnagi.2019.00057
161. Ofori E, Pasternak O, Planetta PJ, Li H, Burciu RG, Snyder AF, et al. Longitudinal changes in free-water within the substantia nigra of Parkinson's disease. *Brain.* (2015) 138:2322–31. doi: 10.1093/brain/awv136
162. Burciu RG, Ofori E, Archer DB, Wu SS, Pasternak O, McFarland NR, et al. Progression marker of Parkinson's disease: a 4-year multi-site imaging study. *Brain.* (2017) 140:2183–92. doi: 10.1093/brain/awx146
163. Pozorski V, Oh JM, Adluru N, Merluzzi AP, Theisen F, Okonkwo O, et al. Longitudinal white matter microstructural change in Parkinson's disease. *Hum Brain Mapp.* (2018) 39:4150–61. doi: 10.1002/hbm.24239
164. Surova Y, Nilsson M, Lampinen B, Latt J, Hall S, Widner H, et al. Alteration of putaminal fractional anisotropy in Parkinson's disease: a longitudinal diffusion kurtosis imaging study. *Neuroradiology.* (2018) 60:247–54. doi: 10.1007/s00234-017-1971-3
165. Miyasaki JM, Martin W, Suchowersky O, Weiner WJ, Lang AE. Practice parameter: initiation of treatment for Parkinson's disease: an evidence-based review: report of the quality standards subcommittee of the American academy of neurology. *Neurology.* (2002) 58:11–7. doi: 10.1212/WNL.58.1.11

166. Elm JJ, Goetz CG, Ravina B, Shannon K, Wooten GF, Tanner CM, et al. A responsive outcome for Parkinson's disease neuroprotection futility studies. *Ann Neurol.* (2005) 57:197–203. doi: 10.1002/ana.20361
167. Ravina B, Marek K, Eberly S, Oakes D, Kurlan R, Ascherio A, et al. Dopamine transporter imaging is associated with long-term outcomes in Parkinson's disease. *Mov Disord.* (2012) 27:1392–7. doi: 10.1002/mds.25157
168. Simuni T, Siderowf A, Lasch S, Coffey CS, Caspell-Garcia C, Jennings D, et al. longitudinal change of clinical and biological measures in early Parkinson's disease: Parkinson's progression markers initiative cohort. *Mov Disord.* (2018) 33:771–82. doi: 10.1002/mds.27361
169. Mishra VR, Sreenivasan KR, Zhuang X, Yang Z, Cordes D, Walsh RR. Influence of analytic techniques on comparing DTI-derived measurements in early stage Parkinson's disease. *Heliyon.* (2019) 5:e01481. doi: 10.1016/j.heliyon.2019.e01481
170. Ito M, Watanabe H, Kawai Y, Atsuta N, Tanaka F, Naganawa S, et al. Usefulness of combined fractional anisotropy and apparent diffusion coefficient values for detection of involvement in multiple system atrophy. *J Neurol Neurosurg Psychiatr.* (2007) 78:722–8. doi: 10.1136/jnnp.2006.104075
171. Wang PS, Wu HM, Lin CP, Soong BW. Use of diffusion tensor imaging to identify similarities and differences between cerebellar and Parkinsonism forms of multiple system atrophy. *Neuroradiology.* (2011) 53:471–81. doi: 10.1007/s00234-010-0757-7
172. Ota M, Nakata Y, Ito K, Kamiya K, Ogawa M, Murata M, et al. Differential diagnosis tool for parkinsonian syndrome using multiple structural brain measures. *Comput Math Methods Med.* (2013) 2013:571289. doi: 10.1155/2013/571289
173. Peran P, Barbagallo G, Nemmi F, Sierra M, Galitzky M, Traon AP, et al. MRI supervised and unsupervised classification of Parkinson's disease and multiple system atrophy. *Mov Disord.* (2018) 33:600–8. doi: 10.1002/mds.27307
174. Du G, Lewis MM, Kanekar S, Sterling NW, He L, Kong L, et al. Combined diffusion tensor imaging and apparent transverse relaxation rate differentiate Parkinson disease and atypical Parkinsonism. *AJNR Am J Neuroradiol.* (2017) 38:966–72. doi: 10.3174/ajnr.A5136
175. Umemura A, Oeda T, Hayashi R, Tomita S, Kohsaka M, Yamamoto K, et al. Diagnostic accuracy of apparent diffusion coefficient and 123I-metaiodobenzylguanidine for differentiation of multiple system atrophy and Parkinson's disease. *PLoS ONE.* (2013) 8:e61066. doi: 10.1371/journal.pone.0061066
176. Prodoehl J, Li H, Planetta PJ, Goetz CG, Shannon KM, Tangonan R, et al. Diffusion tensor imaging of Parkinson's disease, atypical parkinsonism, and essential tremor. *Mov Disord.* (2013) 28:1816–22. doi: 10.1002/mds.25491
177. Baudrexel S, Seifried C, Penndorf B, Klein JC, Middendorp M, Steinmetz H, et al. The value of putaminal diffusion imaging versus 18-fluorodeoxyglucose positron emission tomography for the differential diagnosis of the Parkinson variant of multiple system atrophy. *Mov Disord.* (2014) 29:380–7. doi: 10.1002/mds.25749
178. Sako W, Abe T, Murakami N, Miyazaki Y, Izumi Y, Harada M, et al. Imaging-based differential diagnosis between multiple system atrophy and Parkinson's disease. *J Neurol Sci.* (2016) 368:104–8. doi: 10.1016/j.jns.2016.06.061
179. Dickson DW, Hauw JJ, Agid Y, Litvan I. *Progressive Supranuclear Palsy and Corticobasal Degeneration. 2nd ed*. Chichester: Wiley-Blackwell. (2011). doi: 10.1002/9781444341256.ch15
180. Whitwell JL, Hoglinger GU, Antonini A, Bordelon Y, Boxer AL, Colosimo C, et al. Radiological biomarkers for diagnosis in PSP. Where are we and where do we need to be? *Mov Disord.* (2017) 32:955–71. doi: 10.1002/mds.27038
181. Blain CR, Barker GJ, Jarosz JM, Coyle NA, Landau S, Brown RG, et al. Measuring brain stem and cerebellar damage in parkinsonian syndromes using diffusion tensor MRI. *Neurology*. (2006) 67:2199–205. doi: 10.1212/01.wnl.0000249307.59950.f8
182. Worker A, Blain C, Jarosz J, Chaudhuri KR, Barker GJ, Williams SC, et al. Diffusion tensor imaging of Parkinson's disease, multiple system atrophy and progressive supranuclear palsy: a tract-based spatial statistics study. *PLoS ONE.* (2014) 9:e112638. doi: 10.1371/journal.pone.0112638
183. Seki M, Seppi K, Mueller C, Potrusil T, Goebel G, Reiter E, et al. Diagnostic potential of dentatorubrothalamic tract analysis in progressive supranuclear palsy. *Parkins Relat Disord.* (2018) 49:81–7. doi: 10.1016/j.parkreldis.2018.02.004
184. Cherubini A, Morelli M, Nistico R, Salsone M, Arabia G, Vasta R, et al. Magnetic resonance support vector machine discriminates between Parkinson disease and progressive supranuclear palsy. *Mov Disord.* (2014) 29:266–9. doi: 10.1002/mds.25737
185. Zhang Y, Walter R, Ng P, Luong PN, Dutt S, Heuer H, et al. Progression of microstructural degeneration in progressive supranuclear palsy and corticobasal syndrome: a longitudinal diffusion tensor imaging study. *PLoS ONE.* (2016) 11:e0157218. doi: 10.1371/journal.pone.0157218
186. Paviour DC, Price SL, Jahanshahi M, Lees AJ, Fox NC. Longitudinal MRI in progressive supranuclear palsy and multiple system atrophy: rates and regions of atrophy. *Brain.* (2006) 129(Pt 4):1040–9. doi: 10.1093/brain/awl021
187. Dutt S, Binney RJ, Heuer HW, Luong P, Attygalle S, Bhatt P, et al. Progression of brain atrophy in PSP and CBS over 6 months and 1 year. *Neurology.* (2016) 87:2016–25. doi: 10.1212/WNL.0000000000003305
188. Litvan I, Goldman JG, Troster AI, Schmand BA, Weintraub D, Petersen RC, et al. Diagnostic criteria for mild cognitive impairment in Parkinson's disease: movement disorder society task force guidelines. *Mov Disord.* (2012) 27:349–56. doi: 10.1002/mds.24893
189. Aarsland D, Andersen K, Larsen JP, Lolk A, Kragh-Sorensen P. Prevalence and characteristics of dementia in Parkinson disease: an 8-year prospective study. *Arch Neurol.* (2003) 60:387–92. doi: 10.1001/archneur.60.3.387
190. Hely MA, Reid WG, Adena MA, Halliday GM, Morris JG. The sydney multicenter study of Parkinson's disease: the inevitability of dementia at 20 years. *Mov Disord.* (2008) 23:837–44. doi: 10.1002/mds.21956
191. Bertrand JA, Bedetti C, Postuma RB, Monchi O, Genier Marchand D, Jubault T, et al. Color discrimination deficits in Parkinson's disease are related to cognitive impairment and white-matter alterations. *Mov Disord.* (2012) 27:1781–8. doi: 10.1002/mds.25272
192. Deng B, Zhang Y, Wang L, Peng K, Han L, Nie K, et al. Diffusion tensor imaging reveals white matter changes associated with cognitive status in patients with Parkinson's disease. *Am J Alzheimers Dis Other Demen.* (2013) 28:154–64. doi: 10.1177/1533317512470207
193. Agosta F, Canu E, Stefanova E, Sarro L, Tomic A, Spica V, et al. Mild cognitive impairment in Parkinson's disease is associated with a distributed pattern of brain white matter damage. *Hum Brain Mapp.* (2014) 35:1921–9. doi: 10.1002/hbm.22302
194. Matsui H, Nishinaka K, Oda M, Niikawa H, Kubori T, Udaka F. Dementia in Parkinson's disease: diffusion tensor imaging. *Acta Neurol Scand.* (2007) 116:177–81. doi: 10.1111/j.1600-0404.2007.00838.x
195. Kamagata K, Motoi Y, Abe O, Shimoji K, Hori M, Nakanishi A, et al. White matter alteration of the cingulum in Parkinson disease with and without dementia: evaluation by diffusion tensor tract-specific analysis. *AJNR Am J Neuroradiol.* (2012) 33:890–5. doi: 10.3174/ajnr.A2860
196. Chondrogiorgi M, Astrakas LG, Zikou AK, Weis L, Xydis VG, Antonini A, et al. Multifocal alterations of white matter accompany the transition from normal cognition to dementia in Parkinson's disease patients. *Brain Imaging Behav.* (2019) 13:232–40. doi: 10.1007/s11682-018-9863-7
197. Kamagata K, Motoi Y, Tomiyama H, Abe O, Ito K, Shimoji K, et al. Relationship between cognitive impairment and white-matter alteration in Parkinson's disease with dementia: tract-based spatial statistics and tract-specific analysis. *Eur Radiol.* (2013) 23:1946–55. doi: 10.1007/s00330-013-2775-4
198. Wiltshire K, Concha L, Gee M, Bouchard T, Beaulieu C, Camicioli R. Corpus callosum and cingulum tractography in Parkinson's disease. *Can J Neurol Sci.* (2010) 37:595–600. doi: 10.1017/S0317167100010751
199. Schulz J, Pagano G, Fernandez Bonfante JA, Wilson H, Politis M. Nucleus basalis of Meynert degeneration precedes and predicts cognitive impairment in Parkinson's disease. *Brain.* (2018) 141:1501–16. doi: 10.1093/brain/awy072
200. Caspell-Garcia C, Simuni T, Tosun-Turgut D, Wu IW, Zhang Y, Nalls M, et al. Multiple modality biomarker prediction of cognitive impairment in prospectively followed *de novo* Parkinson disease. *PLoS ONE.* (2017) 12:e0175674. doi: 10.1371/journal.pone.0175674
201. Silbert LC, Kaye J. Neuroimaging and cognition in Parkinson's disease dementia. *Brain Pathol.* (2010) 20:646–53. doi: 10.1111/j.1750-3639.2009.00368.x

202. Shin NY, Shin YS, Lee PH, Yoon U, Han S, Kim DJ, et al. Different functional and microstructural changes depending on duration of mild cognitive impairment in Parkinson disease. *AJNR Am J Neuroradiol.* (2016) 37:897–903. doi: 10.3174/ajnr.A4626
203. Lee JE, Park HJ, Park B, Song SK, Sohn YH, Lee JD, et al. A comparative analysis of cognitive profiles and white-matter alterations using voxel-based diffusion tensor imaging between patients with Parkinson's disease dementia and dementia with Lewy bodies. *J Neurol Neurosurg Psychiatr.* (2010) 81:320–6. doi: 10.1136/jnnp.2009.184747
204. Novellino F, Vasta R, Sarica A, Chiriaco C, Salsone M, Morelli M, et al. Relationship between hippocampal subfields and category cued recall in AD and PDD. A multimodal MRI study. *Neuroscience.* (2018) 371:506–17. doi: 10.1016/j.neuroscience.2017.12.028
205. Bergamino M, Keeling EG, Mishra VR, Stokes AM, Walsh RR. Assessing white matter pathology in early-stage Parkinson disease using diffusion MRI. A systematic review. *Front Neurol.* (2020) 11:314. doi: 10.3389/fneur.2020.00314
206. Tuch DS, Reese TG, Wiegell MR, Makris N, Belliveau JW, Wedeen VJ. High angular resolution diffusion imaging reveals intravoxel white matter fiber heterogeneity. *Magn Reson Med.* (2002) 48:577–82. doi: 10.1002/mrm.10268
207. Wedeen VJ, Wang RP, Schmahmann JD, Benner T, Tseng WY, Dai G, et al. Diffusion spectrum magnetic resonance imaging (DSI) tractography of crossing fibers. *Neuroimage.* (2008) 41:1267–77. doi: 10.1016/j.neuroimage.2008.03.036
208. Pasternak O, Sochen N, Gur Y, Intrator N, Assaf Y. Free water elimination mapping from diffusion MRI. *Magn Reson Med.* (2009) 62:717–30. doi: 10.1002/mrm.22055
209. Guttuso T, Jr., Bergsland N, Hagemeier J, Lichter DG, Pasternak O, et al. Substantia nigra free water increases longitudinally in Parkinson disease. *AJNR Am J Neuroradiol.* (2018) 39:479–84. doi: 10.3174/ajnr.A5545
210. Jensen JH, Helpern JA, Ramani A, Lu H, Kaczynski K. Diffusional kurtosis imaging: the quantification of non-gaussian water diffusion by means of magnetic resonance imaging. *Magn Reson Med.* (2005) 53:1432–40. doi: 10.1002/mrm.20508
211. Kamagata K, Tomiyama H, Hatano T, Motoi Y, Abe O, Shimoji K, et al. A preliminary diffusional kurtosis imaging study of Parkinson disease: comparison with conventional diffusion tensor imaging. *Neuroradiology.* (2014) 56:251–8. doi: 10.1007/s00234-014-1327-1
212. Vriend C, van den Heuvel OA, Berendse HW, van der Werf YD, Douw L. Global and subnetwork changes of the structural connectome in *de novo* Parkinson's disease. *Neuroscience.* (2018) 386:295–308. doi: 10.1016/j.neuroscience.2018.06.050
213. Hall JM, Shine JM, Ehgoetz Martens KA, Gilat M, Broadhouse KM, Szeto JYY, et al. Alterations in white matter network topology contribute to freezing of gait in Parkinson's disease. *J Neurol.* (2018) 265:1353–64. doi: 10.1007/s00415-018-8846-3
214. Tinaz S, Lauro PM, Ghosh P, Lungu C, Horovitz SG. Changes in functional organization and white matter integrity in the connectome in Parkinson's disease. *Neuroimage Clin.* (2017) 13:395–404. doi: 10.1016/j.nicl.2016.12.019
215. Galantucci S, Agosta F, Stefanova E, Basaia S, van den Heuvel MP, Stojkovic T, et al. Structural brain connectome and cognitive impairment in Parkinson disease. *Radiology.* (2017) 283:515–25. doi: 10.1148/radiol.2016160274
216. Nigro S, Riccelli R, Passamonti L, Arabia G, Morelli M, Nistico R, et al. Characterizing structural neural networks in *de novo* Parkinson disease patients using diffusion tensor imaging. *Hum Brain Mapp.* (2016) 37:4500–10. doi: 10.1002/hbm.23324
217. Sharman M, Valabregue R, Perlbarg V, Marrakchi-Kacem L, Vidailhet M, Benali H, et al. Parkinson's disease patients show reduced cortical-subcortical sensorimotor connectivity. *Mov Disord.* (2013) 28:447–54. doi: 10.1002/mds.25255
218. Sterling NW, Du G, Lewis MM, Swavely S, Kong L, Styner M, et al. Cortical gray and subcortical white matter associations in Parkinson's disease. *Neurobiol Aging.* (2017) 49:100–8. doi: 10.1016/j.neurobiolaging.2016.09.015
219. Pagonabarraga J, Kulisevsky J. Cognitive impairment and dementia in Parkinson's disease. *Neurobiol Dis.* (2012) 46:590–6. doi: 10.1016/j.nbd.2012.03.029
220. Illan-Gala I, Montal V, Borrego-Ecija S, Vilaplana E, Pegueroles J, Alcolea D, et al. Cortical microstructure in the behavioural variant of frontotemporal dementia: looking beyond atrophy. *Brain.* (2019) 142:1121–33. doi: 10.1093/brain/awz031
221. Ball G, Srinivasan L, Aljabar P, Counsell SJ, Durighel G, Hajnal JV, et al. Development of cortical microstructure in the preterm human brain. *Proc Natl Acad Sci USA.* (2013) 110:9541–6. doi: 10.1073/pnas.1301652110
222. Andica C, Kamagata K, Hatano T, Saito A, Uchida W, Ogawa T, et al. Free-water imaging in white and gray matter in Parkinson's disease. *Cells.* (2019) 8:839. doi: 10.3390/cells8080839
223. Weston PS, Simpson IJ, Ryan NS, Ourselin S, Fox NC. Diffusion imaging changes in grey matter in Alzheimer's disease: a potential marker of early neurodegeneration. *Alzheimers Res Ther.* (2015) 7:47. doi: 10.1186/s13195-015-0132-3
224. Sampedro F, Perez-Gonzalez R, Martinez-Horta S, Marin-Lahoz J, Pagonabarraga J, Kulisevsky J. Serum neurofilament light chain levels reflect cortical neurodegeneration in *de novo* Parkinson's disease. *Parkinsonism Relat Disord.* (2020) 74:43–9. doi: 10.1016/j.parkreldis.2020.04.009
225. Sampedro F, Martinez-Horta S, Marin-Lahoz J, Pagonabarraga J, Kulisevsky J. Longitudinal intracortical diffusivity changes in de-novo Parkinson's disease: a promising imaging biomarker. *Parkinsonism Relat Disord.* (2019) 68:22–5. doi: 10.1016/j.parkreldis.2019.09.031
226. Zhang Y, Vakhtin AV, Jennings JS, Massaband P, Wintermark M, Craig PL, et al. Diffusion tensor tractography of brainstem fibers and its application in pain. *PLoS ONE.* (2019) 15:e0213952. doi: 10.1371/journal.pone.0213952
227. Tolosa E, Wenning G, Poewe W. The diagnosis of Parkinson's disease. *Lancet Neurol.* (2006) 5:75–86. doi: 10.1016/S1474-4422(05)70285-4

Conflict of Interest: The authors declare that the research was conducted in the absence of any commercial or financial relationships that could be construed as a potential conflict of interest.

Copyright © 2020 Zhang and Burock. This is an open-access article distributed under the terms of the Creative Commons Attribution License (CC BY). The use, distribution or reproduction in other forums is permitted, provided the original author(s) and the copyright owner(s) are credited and that the original publication in this journal is cited, in accordance with accepted academic practice. No use, distribution or reproduction is permitted which does not comply with these terms.

frontiers in Neurology

CORRECTION
published: 29 October 2020
doi: 10.3389/fneur.2020.612069

Corrigendum: Diffusion Tensor Imaging in Parkinson's Disease and Parkinsonian Syndrome: A Systematic Review

Yu Zhang[1]* *and Marc A. Burock*[2]

[1] Department of Psychiatry, War Related Illness and Injury Study Center, Veterans Affairs Palo Alto Health Care System, Palo Alto, CA, United States, [2] Department of Psychiatry, Mainline Health, Bryn Mawr Hospital, Bryn Mawr, PA, United States

OPEN ACCESS

Approved by:
Frontiers Editorial Office, Frontiers Media SA, Switzerland

***Correspondence:**
Yu Zhang
yuzhangucsfedu@gmail.com;
Yu.Zhang@va.gov

Specialty section:
This article was submitted to Movement Disorders, a section of the journal Frontiers in Neurology

Received: 30 September 2020
Accepted: 01 October 2020
Published: 29 October 2020

Citation:
Zhang Y and Burock MA (2020) Corrigendum: Diffusion Tensor Imaging in Parkinson's Disease and Parkinsonian Syndrome: A Systematic Review. Front. Neurol. 11:612069. doi: 10.3389/fneur.2020.612069

Keywords: diffusion tensor imaging (DTI), fractional anisotropy (FA), Parkinson's progression marker initiative (PPMI), diffusion tensor tractography (DTT), dopaminergic pathway, substantia nigra (SN), Parkinson's disease (PD)

A Corrigendum on

Diffusion Tensor Imaging in Parkinson's Disease and Parkinsonian Syndrome: A Systematic Review

by Zhang, Y., and Burock, M. A. (2020). Front. Neurol. 11:531993. doi: 10.3389/fneur.2020.531993

In the original article, reference 31 was incorrectly written as Haghshomar M, Rahmani F. Cognitive challenge to choose healthier food is reflected in heart rate variability. *Front Neurosci.* (2017) 11:353. doi: 10.3389/fnins.2017.00353 It should be Haghshomar M, Rahmani F, Hadi Aarabi M, Shahjouei S, Sobhani S, Rahmani M. White matter changes correlates of peripheral neuroinflammation in patients with Parkinson's disease. *Neuroscience.* (2019) 403:70–8. doi: 10.1016/j.neuroscience.2017.10.050.

The authors apologize for this error and state that this does not change the scientific conclusions of the article in any way. The original article has been updated.

Copyright © 2020 Zhang and Burock. This is an open-access article distributed under the terms of the Creative Commons Attribution License (CC BY). The use, distribution or reproduction in other forums is permitted, provided the original author(s) and the copyright owner(s) are credited and that the original publication in this journal is cited, in accordance with accepted academic practice. No use, distribution or reproduction is permitted which does not comply with these terms.

frontiers in Neurology

REVIEW
published: 15 October 2020
doi: 10.3389/fneur.2020.572976

Neuroimaging Advances in Parkinson's Disease and Atypical Parkinsonian Syndromes

Usman Saeed[1], *Anthony E. Lang*[2,3] *and Mario Masellis*[1,2,4,5]*

[1] Hurvitz Brain Sciences Program, Sunnybrook Research Institute, Toronto, ON, Canada, [2] Division of Neurology, Department of Medicine, University of Toronto, Toronto, ON, Canada, [3] Edmond J Safra Program in Parkinson's Disease and the Morton and Gloria Shulman Movement Disorders Clinic, Toronto Western Hospital, University Health Network, Toronto, ON, Canada, [4] L.C. Campbell Cognitive Neurology Research Unit, Sunnybrook Health Sciences Center, Toronto, ON, Canada, [5] Cognitive and Movement Disorders Clinic, Sunnybrook Health Sciences Center, Toronto, ON, Canada

Parkinson's disease (PD) and atypical Parkinsonian syndromes are progressive heterogeneous neurodegenerative diseases that share clinical characteristic of parkinsonism as a common feature, but are considered distinct clinicopathological disorders. Based on the predominant protein aggregates observed within the brain, these disorders are categorized as, (1) α-synucleinopathies, which include PD and other Lewy body spectrum disorders as well as multiple system atrophy, and (2) tauopathies, which comprise progressive supranuclear palsy and corticobasal degeneration. Although, great strides have been made in neurodegenerative disease research since the first medical description of PD in 1817 by James Parkinson, these disorders remain a major diagnostic and treatment challenge. A valid diagnosis at early disease stages is of paramount importance, as it can help accommodate differential prognostic and disease management approaches, enable the elucidation of reliable clinicopathological relationships ideally at prodromal stages, as well as facilitate the evaluation of novel therapeutics in clinical trials. However, the pursuit for early diagnosis in PD and atypical Parkinsonian syndromes is hindered by substantial clinical and pathological heterogeneity, which can influence disease presentation and progression. Therefore, reliable neuroimaging biomarkers are required in order to enhance diagnostic certainty and ensure more informed diagnostic decisions. In this article, an updated presentation of well-established and emerging neuroimaging biomarkers are reviewed from the following modalities: (1) structural magnetic resonance imaging (MRI), (2) diffusion-weighted and diffusion tensor MRI, (3) resting-state and task-based functional MRI, (4) proton magnetic resonance spectroscopy, (5) transcranial B-mode sonography for measuring substantia nigra and lentiform nucleus echogenicity, (6) single photon emission computed tomography for assessing the dopaminergic system and cerebral perfusion, and (7) positron emission tomography for quantifying nigrostriatal functions, glucose metabolism, amyloid, tau and α-synuclein molecular imaging, as well as neuroinflammation. Multiple biomarkers obtained from different neuroimaging modalities can provide distinct yet corroborative information on the underlying neurodegenerative processes. This integrative "multimodal approach" may prove superior to single modality-based

OPEN ACCESS

Edited by:
Yu Zhang,
VA Palo Alto Health Care System, United States

Reviewed by:
Andrzej Friedman, Medical University of Warsaw, Poland
Juan Carlos Martinez Castrillo, Ramón y Cajal University Hospital, Spain
José Luiz Pedroso, Federal University of São Paul, Brazil

***Correspondence:**
Mario Masellis
mario.masellis@sunnybrook.ca

Specialty section:
This article was submitted to Movement Disorders, a section of the journal Frontiers in Neurology

Received: *15 June 2020*
Accepted: *02 September 2020*
Published: *15 October 2020*

Citation:
Saeed U, Lang AE and Masellis M (2020) Neuroimaging Advances in Parkinson's Disease and Atypical Parkinsonian Syndromes. Front. Neurol. 11:572976. doi: 10.3389/fneur.2020.572976

methods. Indeed, owing to the international, multi-centered, collaborative research initiatives as well as refinements in neuroimaging technology that are currently underway, the upcoming decades will mark a pivotal and exciting era of further advancements in this field of neuroscience.

Keywords: biomarkers, Parkinson's disease (PD), atypical Parkinsonian syndromes, magnetic resonance imaging (MRI), single photon emission computed tomography (SPECT), diffusion-weighted imaging (DWI), transcranial sonography (TCS), positron emission tomography (PET)

BACKGROUND

Parkinsonism defined by the presence of cardinal clinical motor features of rigidity, bradykinesia and tremor impacts the functioning of affected patients and can result in a significant loss of quality of life. Parkinson's disease (PD) is the most prevalent cause of neurodegenerative parkinsonism affecting more than 10 million individuals globally and bears a huge socioeconomic burden (1). The motor symptoms of PD, especially as seen in the early stages of the disease, are largely due to the loss of dopamine-producing neurons within the substantia nigra pars compacta (SNpc), whereas non-motor features that include olfactory and autonomic dysfunction, sleep disorders, psychiatric symptoms, depression, pain, fatigue, and cognitive impairment result from a more widespread neurodegeneration involving other neurotransmitter systems (2). On the basis of dopaminergic denervation, PD patients typically show a good response to levodopa. Conversely, the atypical Parkinsonian syndromes (PS) are a group of heterogenous neurodegenerative diseases that also present with parkinsonism, although they generally do not respond well to levodopa treatment and are considered distinct clinicopathological disorders.

Neurodegenerative diseases causing parkinsonism are categorized based on the predominant protein aggregates found within the brain, which are believed to be intimately involved in the underlying pathogenic mechanisms. Lewy body spectrum disorders (LBSD), including PD with and without cognitive impairment, Parkinson's disease dementia (PDD) and dementia with Lewy bodies (DLB) as well as multiple system atrophy (MSA) are classified as α-synucleinopathies due to the presence of misfolded α-synuclein aggregates. Progressive supranuclear palsy (PSP) and corticobasal degeneration (CBD) are categorized as tauopathies due to the preponderance of aggregated tau inclusions within the brain. With better understanding of these syndromes, the presence of "mixed" pathologies is increasingly being recognized. Indeed, concomitant aggregation of amyloid, tau, and α-synuclein proteins within the brain contribute to substantial heterogeneity in disease presentation and progression. The core neuropathological and clinical characterization of tauopathies and α-synucleinopathies are detailed in **Table 1**.

Our understanding of PD and atypical PS has been significantly enhanced by methodological and analytical improvements in *in vivo* neuroimaging techniques. Neuroimaging can be used to: (1) identify disease-specific structural and functional biomarkers, some of which have been incorporated into the diagnostic criteria and may serve to enhance diagnostic confidence, (2) rule out unrelated abnormalities (e.g., neoplasms, strokes, extensive cerebrovascular pathology) as primary or contributory cause of the symptoms, (3) validate promising prodromal biomarkers for diagnostic purposes, which may also assist in patient recruitment or sample enrichment for therapeutic trials, (4) quantify whole-brain or regional burden of misfolded neuropathological molecules (e.g., amyloid, tau, or α-synuclein and their co-aggregation) as well as other physiological processes (e.g., neuroinflammation), and (5) study disease progression over time or in response to therapeutic interventions via the evaluation of neuroimaging-based secondary outcome measures. Several neuroimaging modalities have been developed and applied to Parkinsonian disorders, each providing distinct information on the underlying brain disorders. An overview of the common neuroimaging techniques is summarized in **Table 2**.

In this review, a comprehensive presentation of the current and emerging biomarkers from multiple neuroimaging modalities in PD and atypical PS will be undertaken with emphasis on some of the distinguishing characteristics.

SEARCH STRATEGY

The literature search was performed on the PubMed database using the following disease-specific keywords: "Parkinson*,"

Abbreviations: AADC, Aromatic amino acid decarboxylase; AD, Alzheimer's disease; ADC, Apparent diffusion coefficient; APOE-ε4, Apolipoprotein E ε4-allele; CBD, Corticobasal degeneration; CBS, Corticobasal syndrome; Cr, Creatine; *D*, Mean diffusivity; DAT, Dopamine transporter; DLB, Dementia with Lewy bodies; DTI, Diffusion tensor imaging; FA, Fractional anisotropy; GM, Gray matter; LBSD, Lewy body spectrum disorders; LN, Lentiform nucleus; MAO, Monoamine oxidase; MCP, Middle cerebellar peduncle; MRI, Magnetic resonance imaging; MSA, Multiple system atrophy; MSA-C, Multiple system atrophy-cerebellar type; MSA-P, Multiple system atrophy-parkinsonian type; NAA, N-acetyl aspartate; NPV, Negative predictive value; PD, Parkinson's disease; PDD, Parkinson's disease dementia; PD-MCI, Parkinson's disease-mild cognitive impairment; PDRP, Parkinson's disease-related motor pattern; PDCP, Parkinson's disease-related cognitive pattern; PET, Positron emission tomography; PPV, Positive predictive value; PS, Parkinsonian syndrome; PSP, Progressive supranuclear palsy; PSP-RS, Progressive supranuclear palsy-Richardson's syndrome; RBD, Rapid eye movement sleep behavior disorder; SCP, Superior cerebellar peduncle; SN, Substantia nigra; SNpc, Substantia nigra pars compacta; SPECT, Single photon emission computed tomography; TDP-43, Transactive response DNA binding protein-43 kDa; TSPO, Translocator protein-18 kDa; VBM, Voxel-based morphometry; VMAT2, Vesicular monoamine transporter type 2; WM, White matter.

TABLE 1 | Neuropathological and clinical characteristics of α-synucleinopathies and tauopathies.

Neuropathological classifications	**α-Synucleinopathies**		**Tauopathies**	
Neurodegenerative disorders	Lewy body spectrum disorders	Multiple system atrophy (MSA)	Progressive supranuclear palsy (PSP)	Corticobasal degeneration/syndrome (CBD/CBS)
Clinical subtypes	• Parkinson's disease (PD) • Parkinson's disease-mild cognitive impairment (PD-MCI) • Parkinson's disease dementia (PDD) • Dementia with Lewy bodies (DLB)	• MSA-parkinsonian (MSA-P) • MSA-cerebellar (MSA-C) • MSA with varying degrees of both parkinsonian and cerebellar features	• PSP-Richardson's syndrome (PSP-RS) • PSP-ocular motor • PSP-postural instability • PSP-parkinsonism (PSP-P) • PSP-frontal • PSP-progressive gait freezing • PSP-corticobasal syndrome • PSP-speech/language disorder • PSP-primary lateral sclerosis[a] • PSP-cerebellar ataxia (PSP-C)[a] (3, 4)	• CBS is clinically defined and is the most common manifestation of underlying CBD neuropathology, but it is not specific. Besides CBS, other presentations associated with CBD include progressive non-fluent aphasia, speech apraxia, posterior cortical atrophy, behavior variant frontotemporal lobal degeneration, PSP-like syndrome, among others (5, 6)
Core neuropathological features	• Intraneuronal fibrillar inclusions composed predominantly of misfolded α-synuclein protein within the cell body (Lewy bodies) and neuronal processes (Lewy neurites) (2) • Lewy pathology in Lewy body spectrum disorders may spread in a prion-like fashion beginning in the peripheral (e.g., enteric) nervous system and spreading to the lower brainstem (dorsal motor nucleus of the cranial nerve IX/X), followed by spread to the pons, midbrain, and subcortical regions (affecting dopaminergic neurons in the substantia nigra pars compacta, as in PD), eventually reaching the neocortex (as in DLB and PDD) (7). Whether this sequential spread is followed in all cases with Lewy body disorders is unclear • Based on autopsy, four Lewy-related disease subtypes have been identified: olfactory bulb only, amygdala predominant, brainstem, limbic (transitional), and diffuse neocortical (8) • Lewy pathology affecting the brainstem, limbic and neocortical regions is typically observed in DLB and PDD, whereas, brainstem Lewy pathology is predominant in PD (2, 8, 9) • Mixed AD pathology (amyloid and tau aggregates) is more frequently observed in DLB and PDD, which may lead to heterogeneity in the disease presentation (2, 10)	• Fibrillar cytoplasmic inclusions composed of misfolded α-synuclein protein within the oligodendrocytes (Papp-Lantos bodies) (11) • Loss of myelin, gliosis, axonal degeneration, and neuronal loss is observed in the olivopontocerebellar and striatonigral regions, hypothalamus, brainstem nuclei, as well as in the intermediolateral cell columns of the spinal cord (11, 12) • Pathogenesis of MSA may involve the interaction between p25α (a stabilizer of myelin integrity) and α-synuclein within the oligodendrocytes. This may initiate a cascade of events leading to neuroinflammation, loss of neurotrophic support, and neuronal dysfunction, eventually causing neurodegeneration in the striatonigral and olivopontocerebellar regions, as well as in the central autonomic pathways (11)	• Neurofibrillary tangles composed of hyperphosphorylated 4-repeat tau protein, neuropil threads, star-shaped tufted astrocytes, oligodendroglial coiled bodies, and gliosis are present, primarily in the basal ganglia, brainstem and diencephalon (4, 13, 14)	• Hyperphosphorylated 4-repeat tau protein within the cell bodies in the form of swollen, achromatic (ballooned) neurons, and in glial cells as astrocytic plaques. Gross neuronal loss is seen in an asymmetric fashion in the frontoparietal lobe (15) • The diagnosis of CBS is clinical in the absence of histopathological confirmation, and may include other pathologies in addition to the histopathologically-confirmed CBD, such as those of AD, PSP, Lewy bodies, and other tau-positive and tau-negative (primarily TDP-43 positive) forms of frontotemporal lobar degeneration (6)

(Continued)

TABLE 1 | Continued

Neuropathological classifications	α-Synucleinopathies		Tauopathies	
Predominant clinical features	• Cardinal motor manifestations of PD consist of bradykinesia, rigidity, resting tremor, and postural and gait disturbances • Non-motor manifestations of PD may involve olfactory and autonomic dysfunction, sleep disorders, psychiatric symptoms, pain, depression, fatigue and cognitive impairment (2, 16) • Core clinical features of DLB include dementia together with cognitive and alertness fluctuations, recurrent visual hallucinations, features of parkinsonism, and/or rapid eye movement sleep behavior disorder. Other features, including repeated falls, dysautonomia (syncope, constipation, orthostatic hypotension, urinary incontinence), other psychiatric manifestations (delusion, apathy, depression), and hypersensitivity to neuroleptic medications may also be present in DLB and PDD (8, 12) • Distinction between PDD and DLB is based on the arbitrary "1 year" rule: dementia onset within 12 months of or contemporarily with motor symptoms qualifies as DLB, whereas parkinsonism must precede dementia by at minimum 1 year for PDD diagnosis. The MDS's diagnostic criteria for PD (17) do not apply this 1 year rule; patients can receive a diagnosis of PD even if they develop dementia before or within 1 year of parkinsonism • It is currently debatable whether PDD and DLB are distinct disorders with overlapping features or are the same disease with variability in clinical presentation (18)	• Non-motor features may precede the motor abnormalities, however, MSA is diagnosed and classified based on the predominant motor symptomology, as follows (19): 1) MSA-P, with parkinsonism as the predominant feature, which typically responds poorly to levodopa treatment, and is associated with marked striatonigral degeneration 2) MSA-C, with cerebellar syndrome and is associated with marked olivopontocerebellar atrophy 3) MSA patients showing varying degrees of both cerebellar and parkinsonian symptomology • Early dysautonomia is a non-motor characteristic of MSA, which includes orthostatic hypotension, erectile dysfunction, constipation, urinary incontinence/retention, respiratory stridor, and sweat gland dysfunction, where the latter may lead to thermoregulatory failure (11, 12, 19)	• Clinical manifestations are classified into four functional domains that include ocular motor dysfunction, postural instability, akinesia, and cognitive dysfunction (see below). Each of these domains contains features with varying degrees of certainty for the clinical diagnosis of PSP. Other supportive clinical and imaging features have also been incorporated in the new diagnostic criteria (3) • Ocular motor dysfunction includes features of vertical supranuclear gaze palsy, slow velocity of vertical saccades, and frequent macro square wave jerks or "eyelid opening apraxia" (3) • Postural instability includes symptoms of repeated unprovoked falls, tendency to fall on the pull test, and taking greater than two steps backward on the pull test, all within 3 years of symptom onset (3) • Akinesia includes the following features (with diminishing specificity for the diagnosis): (1) progressive gait freezing within 3 years, (2) parkinsonism that is akinetic-rigid, predominantly axial and levodopa resistant, and/or (3) parkinsonism accompanied by tremor and/or presence of asymmetry and/or levodopa responsiveness (3) • Cognitive dysfunction includes speech/language disorder, frontal cognitive or behavioral presentations, or corticobasal syndrome (3) • Unlike the classic syndrome PSP-RS, identified only in 24% of cases (20), the PSP-P variant presents with more prominent limb rigidity with bradykinesia and/or tremor with moderate response to levodopa in some patients, without early ocular or postural dysfunction (14)	• Classical syndrome associated with CBD includes basal ganglionic features, such as asymmetric limb rigidity, bradykinesia and dystonia, as well as cortical features, such as limb apraxia, aphasia, alien limb phenomenon and stimulus-sensitive myoclonus. Cognitive and behavioral changes may be seen early in the course of the disease (5, 10, 15) • Clinical findings are usually asymmetric, although this may not always be the case (15) • A large proportion of CBD cases initially present with behavioral or cognitive problems, whereas less than half initially present with motor involvement (15) • Clinicopathologic heterogeneity challenges the development of specific diagnostic criteria, as the pathology of CBD is predicted antemortem in only 25–56% of cases (15, 21)

AD, Alzheimer's disease; CBD, corticobasal degeneration; CBS, corticobasal syndrome; DLB, dementia with Lewy bodies; MDS, Movement Disorder Society; MSA, multiple system atrophy; MSA-C, MSA-cerebellar type; MSA-P, MSA-parkinsonian type; PD, Parkinson's disease; PD-MCI, Parkinson's disease-mild cognitive impairment; PDD, Parkinson's disease dementia; PSP, progressive supranuclear palsy; PSP-C, PSP-cerebellar ataxia type; PSP-P, PSP-parkinsonism type; PSP-RS, PSP-Richardson's syndrome; TDP-43, transactive response DNA binding protein-43 kDa; a = these phenotypes are not included in the new diagnostic criteria due to low specificity for PSP (3, 4).

TABLE 2 | An overview of the common neuroimaging modalities discussed in this article.

Neuroimaging modality	Measures	Description
1) MRI		
• Structural MRI	Atrophy pattern, volume, cortical thickness, ventricular enlargement, white matter hyperintensities, magnetic inhomogeneity effects	Visualization and quantification of brain's structural changes using regions-of-interest or whole-brain approaches. The following MRI sequences are commonly used: T1, T2, T2*, R2* (R2* = 1/T2*)-weighted, susceptibility-weighted, proton-density-weighted, fluid-attenuated inversion recovery, and neuromelanin-sensitive sequences
• Diffusion-weighted and diffusion tensor MRI	Mean diffusivity (*D*), radial diffusivity, axial diffusivity, fractional anisotropy (FA)	Measures brain's microstructural integrity by assessing the movement of water molecules. Damage to white matter tracts restricts the directional movement of water molecules resulting in increased *D* and decreased FA
• Functional MRI	Functional connectivity, change or correlation in blood-oxygen-level-dependent signal	Evaluates neuronal activity in the brain by measuring the transient variations in the blood flow and whether this variation correlates in functionally-connected regions. Functional MRI can be utilized under a variety of experimental paradigms (e.g., task-based vs. control conditions) or under resting-state conditions
2) Proton magnetic resonance spectroscopy	Abundance of metabolites	Estimates the relative concentrations of proton-containing metabolites in the brain. In neurodegenerative disorders, the following metabolites are commonly assessed: N-acetyl aspartate, choline-containing compounds (including free choline, phosphorylcholine and glycerophosphorylcholine), myo-inositol, and creatine
3) Transcranial B-mode sonography	Echogenicity	Uses an ultrasound machine to measure the echogenicity of brain tissues or structures (e.g., substantia nigra, lentiform nucleus, basal ganglia) through the intact cranium. Limitations include the lack of sufficient bone window rendering this technique infeasible in some subjects, and the need for trained examiners for reliable detection and measurement of the imaged features
4) SPECT		
• Striatal presynaptic dopaminergic system	Dopamine transporter (DAT) density	Evaluates nigrostriatal integrity by measuring the density of DATs—sodium-coupled transmembrane protein located at the presynaptic nigrostriatal terminals that mediate the reuptake of dopamine from the synaptic cleft. The most widely used radioligand for measuring DAT density has been ^{123}I-FP-CIT
• Striatal postsynaptic dopaminergic system	Dopamine D2 receptor density	Evaluates nigrostriatal integrity by measuring the density of striatal postsynaptic dopamine D2 receptors (G-protein-coupled) using radioligands, such as ^{123}I-IBZM and ^{123}I-IBF
• Cerebral perfusion	Metabolic activity (by measuring changes in the cerebral blood flow)	Provides a measure of the perfusion and metabolic status of the brain tissues, which can be imaged using lipophilic radiotracers, such as ^{99m}Tc-ECD, ^{99m}Tc-HMPAO and ^{123}I-IMP
5) PET		
• Striatal presynaptic dopaminergic system	Aromatic amino acid decarboxylase (AADC) activity, vesicular monoamine transporter type 2 (VMAT2) density	Density of presynaptic nigrostriatal axons can be assessed using ^{18}F-dopa radiotracer for PET. Specifically, the activity of AADC protein is evaluated, which converts ^{18}F-dopa into ^{18}F-dopamine, providing an approximation of dopaminergic storage pool. Presynaptic monoaminergic system can be assessed using ^{11}C-DTBZ or ^{18}F-labeled analogs (e.g., ^{18}F-AV133), which binds to VMAT2—a presynaptic transmembrane protein essential for packaging and storing monoamines (which include dopamine) into synaptic vesicles
• Striatal postsynaptic dopaminergic system	Dopamine D2 receptor density	Density of postsynaptic dopamine D2 receptors can be examined using ^{11}C-raclopride radiotracer for PET
• Cholinergic system	Acetylcholine esterase activity	Integrity of cholinergic neurons (e.g., in the nucleus basalis of Meynert) can be assessed using PET tracers, ^{11}C-NMP4A or ^{11}C-PMP, which measure the activity of acetylcholine esterase
• Serotonergic system	Serotonin transporter, 5-HT1A receptor sites on serotonergic neurons	Serotonergic function can be evaluated by targeting, (1) 5-HT1A autoreceptors found on serotonergic cell bodies in the median raphe and on pyramidal cells in the limbic cortex using ^{11}C-WAY100635 or ^{18}F-MPPF PET, or (2) serotonin transporters found in the brainstem and cortex using ^{11}C-DASB PET as well as other SPECT tracers
• Noradrenaline system	Noradrenaline transporter	Noradrenaline neurotransmitter dysfunction may be quantified using ^{11}C-RTI-32 ligand, which binds to both dopamine and noradrenaline transporters
• Glucose metabolism	Metabolic activity (by measuring changes in the glucose consumption)	Cerebral glucose metabolism can be measured using ^{18}F-labeled fluorodeoxyglucose (^{18}F-FDG) radiotracer. Decreased ^{18}F-FDG uptake on PET is indicative of lower regional tissue metabolism of glucose
• Amyloid	Amyloid pathology	Cerebral amyloidopathy has commonly been evaluated on PET using Pittsburgh compound B (^{11}C-PIB)—a ^{11}C-labeled thioflavin analog with a half-life of 20 min—as well as using other ^{18}F-labeled radioligands that have a relatively longer half-life (~110 min), such as ^{18}F-florbetapir, ^{18}F-florbetaben, and ^{18}F-flutemetamol
• Tau	Tau pathology	Cerebral tauopathy can be visualized using PET radiotracers including ^{18}F-AV-1451 (known as ^{18}F-flortaucipir or ^{18}F-T807), ^{18}F-FDDNP, ^{18}F-THK523, ^{18}F-THK5351, ^{18}F-THK5105, and ^{11}C-PBB3

(Continued)

TABLE 2 | Continued

Neuroimaging modality	Measures	Description
• α-Synuclein	α-Synuclein pathology	Several PET radiolabeled probes for imaging cerebral α-synucleinopathy have been explored (phenothiazine, indolinone, indolinone-diene and chalcone analogs); however, none have been approved for use in clinical and research settings
• Neuroinflammation	Microglia-mediated inflammatory processes	Neuroinflammation can be assessed using PET radiotracers including ^{11}C-PK11195, ^{11}C-PBR28 and ^{18}F-FEPPA, which detect the upregulation of TSPO protein located on the outer mitochondrial membrane of microglia

AADC, aromatic amino acid decarboxylase; D, mean diffusivity; DAT, dopamine transporter; FA, fractional anisotropy; MRI, magnetic resonance imaging; PET, positron emission tomography; SPECT, single photon emission computed tomography; TSPO, translocator protein-18 kDa; VMAT2, vesicular monoamine transporter type 2.

"Lewy*," "multiple system atrophy," "corticobasal degeneration," "progressive supranuclear palsy" —together with one of the modality-specific keywords: "magnetic resonance imaging," "positron emission tomography," "single-photon emission computed tomography," "diffusion tensor," "diffusion-weighted," "proton spectroscopy," and "transcranial sonography." Acronyms, e.g., "PET" for "positron emission tomography," were entered as appropriate. The literature search was restricted to articles written in English, and published between January 1, 1995 and December 31, 2019. All abstracts were screened for relevance. The most pertinent articles were then read and discussed.

STRUCTURAL NEUROIMAGING IN PARKINSONIAN DISORDERS

Parkinson's Disease (PD)

Structural Magnetic Resonance Imaging in PD

Structural changes on conventional magnetic resonance imaging (MRI) are minimal and less apparent, especially in early stages of PD (10). A six-stage model depicting the sequential progression of α-synuclein pathology in PD has been proposed by Braak et al. (7) (**Figure 1**). As per this "gut to brain" transmission model, neuroimaging studies may predominantly observe brainstem and subcortical involvement in early PD stages with greater cortical involvement in late stage PD as well as in PD-MCI, PDD and DLB cases. Compared to normal controls, voxel-based morphometry (VBM) studies in PD may identify atrophy in the basal ganglia (22) (as consistent with nigrostriatal degeneration and consequential dysfunction in the basal ganglia thalamocortical circuit), frontal lobe (23), and non-specifically in the right hippocampus, left anterior cingulate and superior temporal gyri (24). Although inconsistently shown, cortical thinning in the orbitofrontal, ventrolateral prefrontal, and occipitoparietal cortical regions has been identified in PD, along with volumetric reductions in the caudate and putamen (25, 26). Some studies do not observe appreciable differences on conventional MRI compared to controls (27, 28). In PD patients with olfactory disturbances, reduced volume in the olfactory bulb and tract was evident vs. MSA and controls (29). In PD patients with respiratory dysfunction, gray matter (GM) atrophy was reported in the left parahippocampal formation, right fusiform gyrus, right cerebellum crus, and left postcentral gyri compared to PD with normal pulmonary functions (30). Freezing of gait symptomatology in PD was associated with posterior GM atrophy (specifically, left cuneus, precuneus, lingual gyrus, and posterior cingulate cortex) (27). In advanced PD, atrophy in the subcortical GM structures was found to be more pronounced vs. those in early PD stages (31) (**Figure 2**).

Changes within the SN may emerge as promising early diagnostic biomarkers of PD (10). Within the SNpc, calbindin-negative pockets termed "nigrosomes" are observed (34). The greatest loss in neuromelanin containing neurons takes place in the nigrosome-1, which is located in the caudal and mediolateral portion of SNpc (35). Nigrosome-1 shows a significant loss of hyperintensity on T2* and neuromelanin-sensitive MRI in PD, probably caused by decreased neuromelanin, increased iron content, or loss of paramagnetic neuromelanin–iron complexes (36–38). On susceptibility-weighted imaging (modality of choice), healthy nigrosome-1 and the surrounding neuroanatomy of the dorsolateral SN may appear as the tail of a swallow bird ("swallow-tail" sign). Loss of this feature in PD vs. controls may assist in the differential diagnosis (sensitivity 80%, specificity 89%) (39, 40) (**Figure 3**). Finally, neuromelanin-sensitive MRI has shown promise in the differentiation of PD from essential tremor and normal controls (37, 41), and this technique may prove invaluable as a marker of disease progression in PD.

In PD patients with polysomnography-confirmed rapid eye movement sleep behavior disorder (RBD), cortical thinning was reported in the right perisylvian and inferior temporal cortices together with shape changes in the putamen compared to PD without RBD (42). Likewise, decreased volume in the right putamen correlating with RBD symptom severity was identified in PD with RBD vs. those without (43). On susceptibility-weighted imaging, loss of dorsal nigral hyperintensity (corresponding to nigrosome-1) was observed in ∼25% of patients with idiopathic RBD, which associated with lower putaminal dopamine transporter (DAT) binding on single-photon emission computed tomography (SPECT) (44). This may suggest nigrosome-1 degeneration in some of the RBD cases, likely those at risk of progression to PD (44). These studies propose a link between PD, the presence of RBD, and greater neurodegeneration especially in subcortical structures.

Volumetric changes in the SN have been inconsistently reported in PD vs. controls (45–48). A high resolution

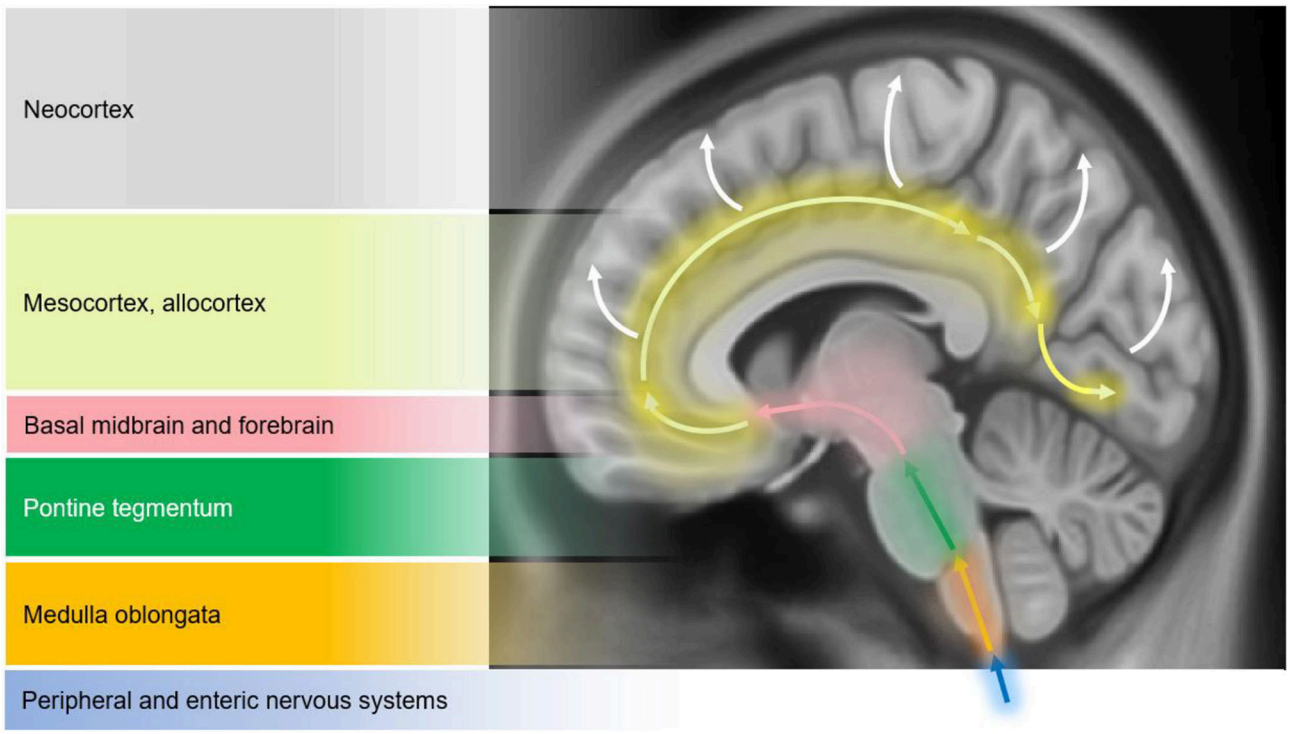


FIGURE 1 | Schematic diagram illustrating the progression of α-synuclein pathology (Lewy bodies and Lewy neurites) in Parkinson's disease (PD), as proposed by Braak et al. (7). According to the Braak model, α-synuclein pathology in the brain spreads caudo-rostrally in a characteristic pattern starting in stage I and II in the lower brainstem regions of medulla oblongata and pons (dorsal motor nucleus of the cranial nerve IX/X, raphe nuclei, gigantocellular reticular nucleus, and coeruleus-subcoeruleus complex). In stages III and IV, α-synucleinopathy spreads further to the susceptible regions of the midbrain (e.g., dopaminergic neurons in the substantia nigra pars compacta), forebrain (e.g., hypothalamus, thalamus, and limbic system), as well as involving some of the cortical regions in the temporal mesocortex (transentorhinal region) and allocortex. In the last two stages (V and VI), α-synuclein pathology reaches the neocortex contributing to cognitive dysfunction (as seen in dementia with Lewy bodies and PD dementia). It is hypothesized that the initiation site of α-synuclein pathology may be outside the central nervous system (CNS), probably beginning in the peripheral (enteric) nervous system and gaining access to the CNS through retrograde transport mechanisms in a prion-like fashion. Whether this sequential spread of α-synuclein pathology as proposed by the Braak model is followed in all cases in Lewy body spectrum disorders is less clear. Figure adapted from Visanji et al. (32), under the Creative Commons Attribution License (https://creativecommons.org/licenses/by/2.0/).

examination of structural alterations in the SN is possible using ultra-high-field MRI (49). For example, susceptibility-weighted imaging at 7T permitted the visualization of the anatomical layers of the SN, allowing excellent discrimination between PD and controls (sensitivity 100%, specificity 96.2%) (50). Correlations between motor symptoms and increased R2* (apparent transverse relaxation rate, R2* =1/T2*) values in the SN have also been reported in PD (46, 51–53), which may reflect ferritin-induced magnetic field inhomogeneities. A recent study applied quantitative susceptibility mapping in PD to evaluate the magnetostatic alterations caused by changes in the iron distribution across the whole brain (54). The apparent magnetic susceptibility was found to be elevated in the dorsal and ventral SN, rostral pontine regions, and the cortex (primarily in the temporal paralimbic, prefrontal, and occipitoparietal regions) (54). Conversely, reduced magnetic susceptibility was detected in the normally iron-rich cerebellar region of the dentate nucleus suggesting decreased iron content (54). Interestingly, the striatum as well as the primary motor and somatosensory fields were spared (54). Future research will highlight whether iron accumulation is the consequence or cause of neurodegenerative changes associated with PD.

Diffusion-Weighted and Diffusion Tensor Imaging in PD

Reduced fractional anisotropy (FA) in the SN is commonly observed in PD (55, 56). Increased mean diffusivity (*D*) in the olfactory tracts and decreased FA in the anterior olfactory structures have been reported (57, 58), as consistent with neuronal loss observed in these regions (29). Significant differences in *D* or FA may not be evident in early PD due to milder neurodegeneration (59, 60). Combined analysis of diffusion parameters and apparent transverse relaxation rates was found to be superior in differentiating PD vs. MSA-P (sensitivity 97%, specificity 100%, positive predictive value [PPV] 100%, negative predictive value [NPV] 93%), and PD vs. MSA-P/PSP group (sensitivity 86%, specificity 87%, PPV 88%, NPV 84%) (61). In SNpc (delineated using a probabilistic atlas based on neuromelanin sensitive imaging), asymmetric alterations predominantly in the diffusion metrices rather than anisotropy were observed (62).

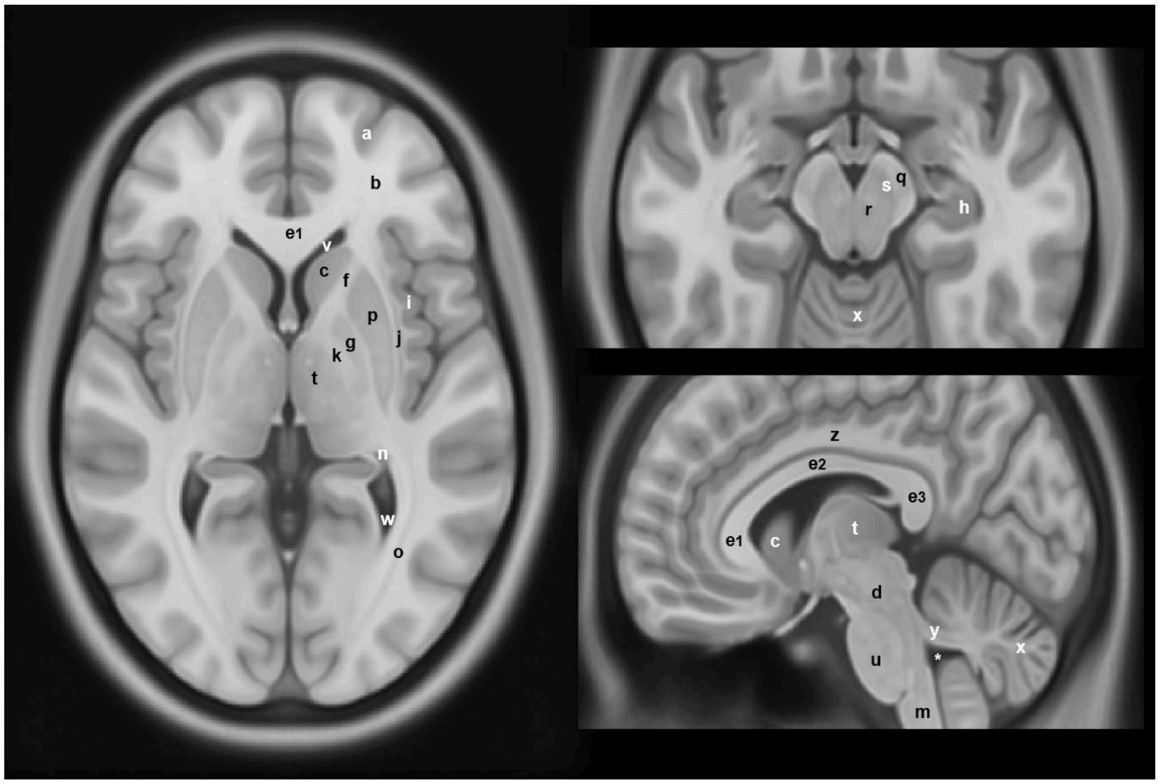


FIGURE 2 | Anatomical locations of some of the structures and regions important in Parkinson's disease and atypical Parkinsonian syndromes, highlighted on a standard averaged T1-weighted MNI template for normal population. Labeling: a = cerebral gray matter (frontal lobe), b = cerebral white matter (frontal lobe), c = head of caudate nucleus, d = midbrain, e1 = genu of corpus callosum, e2 = body of corpus callosum, e3 = splenium of corpus callosum, f = anterior limb of internal capsule, g = globus pallidus, h = hippocampus, i = insular cortex, j = claustrum, k = posterior limb of internal capsule, m = medulla oblongata, n = tail of caudate nucleus, o = optic radiation, p = putamen, q = crus cerebri (anterior portion of cerebral peduncle), r = red nucleus, s = substantia nigra, t = thalamus, u = pons, v = anterior horn of lateral ventricle, w = posterior horn of lateral ventricle, x = cerebellum, y = superior cerebellar peduncle, z = cingulate gyrus, * = fourth ventricle. Note: p and g together constitute the lentiform nucleus; c and p together constitute the dorsal striatum. The template was obtained from McConnell Brain Imaging Center, Montreal Neurological Institute, McGill University Copyright 1993–2004 Fonov et al. (33).

PD-MCI cases showed increased *D* as well as lower GM volume in the nucleus basalis of Meynert vs. cognitively normal PD (60). The degeneration of this cholinergic structure may identify patients at risk of more significant cognitive decline and dementia (60). Another study delineated the cortical projections of five corpus callosum segments and highlighted the role of callosal white matter (WM) abnormalities in cognitive dysfunction, which can occur via disruption of interhemispheric information transfer along callosal-cortical projections (63). In PD, increased axial diffusivity was identified in the three anterior callosal segments (projecting to prefrontal, premotor, motor, and supplementary motor cortices) vs. controls (63). Cognitive performance strongly related to diffusion tensor imaging (DTI) metrics in the most anterior (projecting to prefrontal cortex) and most posterior callosal sections (projecting to parietal, temporal, and occipital cortex), which may contribute to "fronto-striatal" and "posterior cortical" types of cognitive deficits seen in PD, respectively (63).

Free water was elevated in PD in posterior SN vs. controls (52, 64, 65). Increase in free water in posterior SN over time was observed in *de novo* PD patients, which was associated with motor severity and putaminal DAT SPECT binding (64). Given the posterior-to-anterior pattern of degenerative changes reported in SN, elevated free-water may also be observed in the anterior SN (66), especially in late-stage idiopathic PD (67). In contrast, free-water-corrected FA values were found to be unchanged in PD vs. controls, as assessed using the bi-tensor diffusion model (66, 68). Free-water and free-water-corrected FA values beyond SN and from multiple brain regions may help distinguish PD, MSA, and PSP cases from each other (66).

Proton Magnetic Resonance Spectroscopy in PD

Reduced N-acetyl aspartate/creatine (NAA/Cr) ratios in the SN have been observed in PD vs. controls, which were shown to correlate with disease severity (69, 70). Lowered NAA or NAA/Cr values have also been detected in other regions, including the lentiform nucleus (LN) (comprises of putamen and globus pallidus; basic anatomy presented in **Figure 2**), temporoparietal and posterior cingulate cortex, and pre-supplementary motor area vs. controls (71–74). However, the correlation between NAA/Cr ratios in these regions with disease severity or duration is inconsistently reported (72, 73). Another study compared

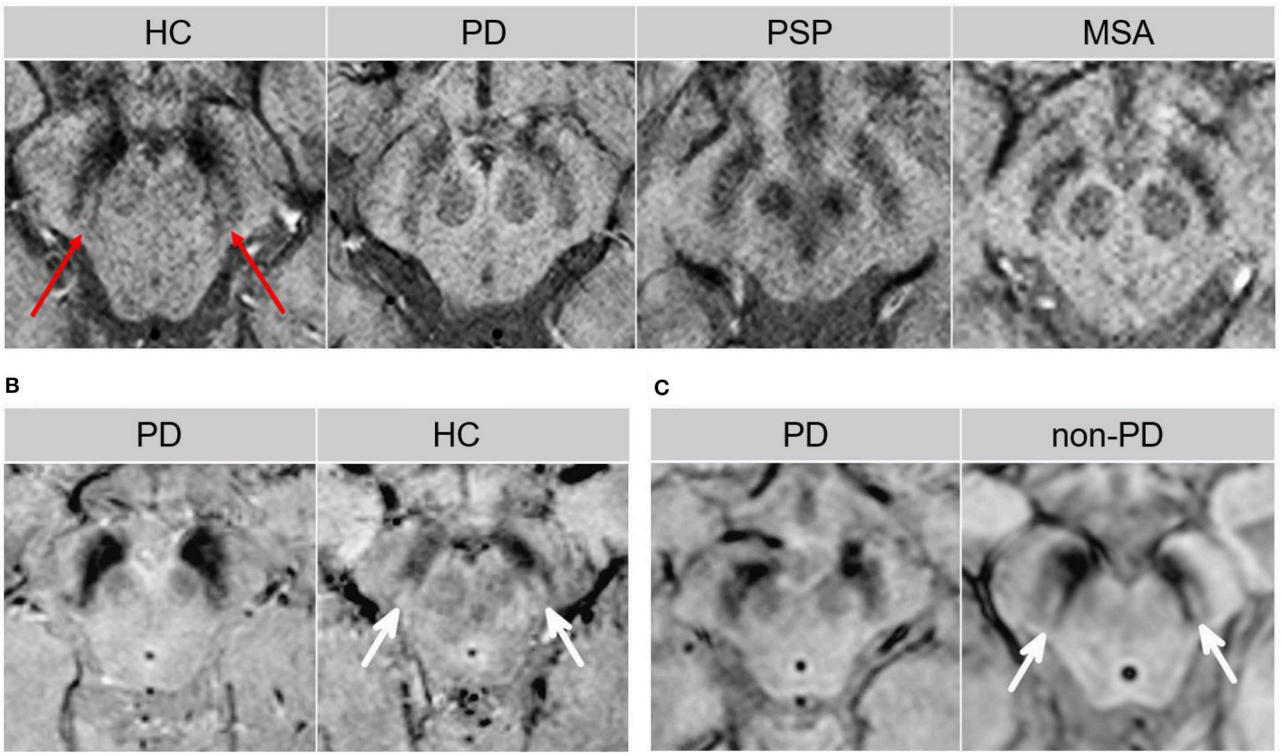


FIGURE 3 | The "swallow tail" sign. All MRI presented above are taken at the level of substantia nigra in the midbrain. **(A)** Susceptibility-weighted MRI depicting dorsolateral nigral hyperintensity (the "swallow tail" sign, red arrows) in a healthy control. Loss of dorsolateral nigral hyperintensity can be seen in PD and may even be seen in some PSP and MSA cases on susceptibility-weighted MRI. **(B)** High resolution susceptibility-weighted MRI (gradient echo-echo planar imaging sequence, magnitude image) is shown for a PD patient and a control. **(C)** High resolution T2*/susceptibility-weighted MRI (multi-shot fast field echo-echo planar imaging sequence) is shown for a PD patient and a non-PD case who was diagnosed with aneurysmal subarachnoid hemorrhage. In both **(B,C)**, loss of dorsolateral nigral hyperintensity (white arrows) corresponding to nigrosome-1 can be seen in PD as compared to control and a non-PD subject. **(A)** was adapted from Chougar et al. (40), and **(B,C)** were adapted from Schwarz et al. (39), under the Creative Commons Attribution License (https://creativecommons.org/licenses/by/4.0/). HC, healthy control; MSA, multiple system atrophy; PD, Parkinson's disease; PSP, progressive supranuclear palsy.

the NAA/Cr ratios in the rostral and caudal SN, and found lower values in the rostral region in PD, whereas this pattern was inverted in the atypical PS group and controls (75). In tremor-dominant PD, reduced NAA/Cr and Choline/Cr values were detected in the thalamus vs. patients with essential tremor presenting with resting tremor (76). Cerebellar NAA/Cr and NAA/myo-inositol ratios were smaller in the atypical PS group compared to PD and controls (77). One study has also suggested the utility of proton magnetic resonance spectroscopy for the evaluation of treatment efficacy in PD (78). Specifically, the putaminal levels of myo-inositol, total Cr, and total NAA metabolites were reduced in the drug-off condition in PD vs. healthy controls. The administration of levodopa resulted in the restoration of total Cr and total NAA levels suggesting therapeutic responsiveness (78).

Lewy Body Spectrum Disorders (LBSD)

Structural Magnetic Resonance Imaging in LBSD

In DLB and PDD, conventional MRI typically shows variable changes. Compared to controls, VBM studies in PDD have identified a diffuse pattern of cortical atrophy involving the occipital, temporal, right frontal, and left parietal lobe (23), as well as atrophy involving the putamen, hippocampus, parahippocampal region, anterior cingulate gyrus, nucleus accumbens and the thalamic nuclei (24). Although inconsistently reported (23), a greater cortical loss in the temporal, occipital, and parietal lobes was noted in DLB vs. PDD (79). Indeed, pathological heterogeneity evident in these two closely related α-synucleinopathies is in part responsible for variable findings. Compared to PD, atrophy in the occipital lobe and entorhinal cortex may help differentiate PDD (23, 80).

The relative preservation of total hippocampus compared to AD is a supportive diagnostic feature of DLB (8). Within the hippocampus, the CA1 subfield shows preservation (81), which aligns with the histopathological evidence showing Lewy body aggregates and neuronal loss largely localized to the CA2/3 subfields in DLB cases (81, 82). Conversely, atrophy in the CA1 subfield is indicative of neurofibrillary tangle pathology as evident in AD. Hippocampal atrophy is in fact observed in LBSD, controls and AD in a characteristic pattern [controls <

PD < PDD/DLB < AD (9, 83)] and the extent of atrophy aligns with the underlying concomitant AD-type pathology (9). Smaller caudate and putaminal volumes have also been reported in PD and DLB vs. AD and controls, albeit inconsistently (26, 84). WM hyperintensities are more prevalent in PDD and DLB vs. PD and controls (85).

PD-MCI patients may show greater cortical thinning in temporoparietal, occipital, and supplementary motor area vs. cognitively-normal PD (86). A recent meta-analysis evaluating VBM studies identified pronounced GM atrophy in the left anterior insula in PD-MCI vs. cognitively-normal PD cases (87). Longitudinal cognitive decline in PD was associated with an AD-like pattern of cerebral atrophy at baseline, underscoring the contribution of the hippocampus and temporoparietal cortex in the cognitive sequelae of PD (88).

The ε4-allele of the apolipoprotein E gene (*APOE*-ε4) is a shared risk factor for AD, PDD, and DLB disorders (89). Therefore, the identification of neuroimaging and cognitive endophenotypes of *APOE*-ε4 irrespective of the clinical diagnosis has been pursued (9). Recent investigations indicate that *APOE*-ε4 is related to hippocampal atrophy along with learning and memory performance in DLB as well as across the AD/DLB spectrum, implicating *APOE*-ε4-associated shared neurodegenerative mechanisms across these disorders (9). Similarly, MRI-derived WM hyperintensity burden was inversely related to learning/memory, attention/executive and language performances in *APOE*-ε4 carriers across the AD/DLB spectrum (90). In addition to the *APOE*-ε4's influence on amyloidopathy, these results are consistent with the emerging evidence indicating an independent role of *APOE*-ε4 in modulating α-synucleinopathy in the brain (91).

Diffusion-Weighted and Diffusion Tensor Imaging in LBSD

In DLB vs. controls, diffusion imaging studies reveal *D* and FA abnormalities in the corpus callosum, pericallosal regions, caudate nucleus (suggestive of nigrostriatal involvement), amygdala, inferior longitudinal fasciculus, precuneus, as well as in the frontal, parietal, and occipital WM with milder involvement of the temporal lobe early in the disease (92–94). In DLB, elevated *D* in the amygdala (a region preferentially affected by Lewy pathology) was observed in the absence of significant GM density changes, probably suggesting microvacuolation or spongiosis as one of the possible mechanisms (93). Increased *D* in the longitudinal fasciculus was identified in DLB patients with hallucinations vs. those without (93). In PDD, reduced FA in the bilateral posterior cingulate bundle was reported vs. PD (95). Compared to AD, decreased FA was noted in the pons and left thalamus in DLB (96). However, given the significant pathological overlap between AD and DLB, diffusion imaging studies may not reveal consistent findings, particularly in subjects at advanced disease stages (94).

Proton Magnetic Resonance Spectroscopy in LBSD

In DLB, lower NAA/Cr ratios in the bilateral hippocampus were evident relative to controls (97), albeit milder than typically seen in AD. Lower NAA/Cr ratios were observed in the posterior cingulate gyrus in PDD vs. cognitively normal PD patients (98).

Multiple System Atrophy (MSA)

Magnetic Resonance Imaging in MSA

Several visible features that may be identifiable on conventional MRI have been reported. On T2-weighted images, these include the presence of bilateral hyperintense rim lining the dorsolateral borders of the putamen ("putaminal rim" sign) and putaminal hypointensity in MSA-parkinsonian subtype (MSA-P) cases (11, 99). In addition, atrophy of the putamen, cerebellum, middle cerebellar peduncles (MCP), or pons may be noticed. In MSA-cerebellar subtype (MSA-C), visible features on T2-weighted and fluid-attenuated inversion recovery images may include cruciform pontine hyperintensity ("hot cross bun" sign; specificity 100%, sensitivity 58%; **Figure 4a**) and hyperintensity in the MCP (MCP sign; specificity 100%, sensitivity 50%; **Figure 4b**) (11, 99). Atrophy of the putamen, pons, cerebellum or MCP may be evident on T1-weighted images (**Figure 4c**). Notably, these signs have low sensitivity values and the appearance of these MRI markers can be influenced by image acquisition factors. For example, the "hot cross bun" sign was suggested to be more conspicuous on T2*-weighted vs. T2-weighted images (100), probably due to the presence of increased iron (100, 101).

The volume of the putamen was found to be significantly reduced in MSA vs. PD cases (102). While putaminal atrophy has been shown to differentiate MSA/MSA-P from PD with high specificity (∼92%), a rather low sensitivity (∼44%) was noted (99, 103). When putaminal changes are present and are asymmetric, they reliably correlate with the asymmetry of clinical features in patients with MSA-P. Several studies suggest that the analysis of multiple biomarkers may improve differentiation. For example, combined analysis of putaminal hypointensity visualized on gradient echo sequence along with putaminal atrophy improved the overall diagnostic accuracy of MSA-P cases vs. PD and PSP (104). Likewise, analyzing DTI and R2* relaxation rate together enabled the identification of abnormal patterns unique to PD, PSP, and MSA disorders (61). On the other hand, a multimodal study (incorporating R2*, R1, and R2 mapping, magnetization transfer and DTI) found elevated putaminal R2* values to be superior in the differentiation of MSA-P from PD, likely representing iron accumulation in the putamen (105).

In MSA vs. controls, volumetric and VBM studies commonly show striatonigral and olivopontocerebellar atrophy (11). Reduced volumes in the striatum and brainstem areas were observed in MSA vs. PD (28, 106), although with extensive overlap with PSP cases (28). In MSA-P, VBM studies also show atrophy in the primary motor and supplementary motor cortex indicating sensorimotor cortical degeneration (106, 107), as well as in the prefrontal and insular cortices compared to PD (106). Likewise, VBM analysis in MSA-P vs. PD revealed atrophy in the superior cerebellar peduncle (SCP), MCP, cerebellum, pons, midbrain, and putamen, but not in the globus pallidus (71). Cerebellar atrophy was evident in both MSA-P and MSA-C subtypes to varying degrees (28, 108). In an analysis of cerebellar neuroanatomical differences in MSA subtypes, a relatively

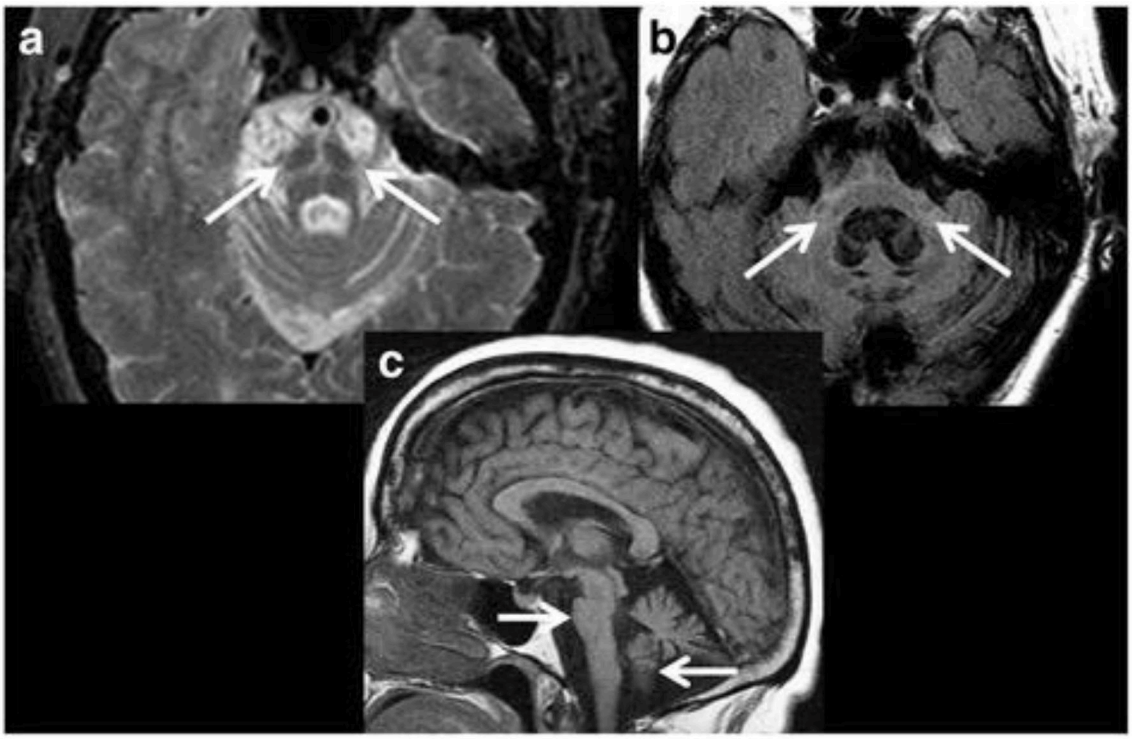


FIGURE 4 | Magnetic resonance imaging of a patient clinically-diagnosed with multiple system atrophy (cerebellar type). **(a)** Axial proton density weighted sequence is presented at the level of pons, which shows cruciform pontine T2 hyperintensity as consistent with the "hot cross bun" sign, resulting from selective susceptibility of the pontocerebellar tract in multiple system atrophy (cerebellar type). In addition, disproportionate atrophy of the pons and partially visible cerebellar hemispheres are also apparent. **(b)** Axial fluid-attenuated inversion recovery (FLAIR) sequence is presented with cruciform T2 hyperintensity within the pons and middle cerebellar peduncles (i.e., "middle cerebellar peduncle" sign) along with marked atrophy. In addition, cerebellar hemispheric and vermian atrophy is evident with *ex vacuo* dilatation of the fourth ventricle. **(c)** Sagittal T1-weighted sequence is presented showing disproportionate atrophy of the brainstem and cerebellar vermis. Figure reproduced from Saeed et al. (10), under the Creative Commons Attribution License 4.0 (https://creativecommons.org/licenses/by/4.0/).

greater GM atrophy was observed in MSA-C cases (vs. MSA-P) in the right Crus II—a cerebellar region involved in executive motor control (108). Both MSA-P and MSA-C patients may exhibit putaminal and infratentorial atrophy with considerable overlap, however, putaminal/supratentorial atrophy was more predominant in MSA-P subtype, whereas infratentorial atrophy was more prominent in MSA-C subtype (109, 110).

MSA patients with cognitive impairment showed volumetric reduction in the left dorsolateral prefrontal cortex vs. cognitively-normal MSA cases (111). The authors suggested that cortical pathology contributes minimally to cognitive deficits in MSA, whereas frontostriatal degeneration may be the primary driver of cognitive dysfunction (as per the concept of "subcortical cognitive impairment") (111). Another study identified cortical thinning in the parahippocampal and lingual cortices in MSA with dementia vs. cognitively-normal MSA patients (112).

Diffusion-Weighted and Diffusion Tensor Imaging in MSA

In MSA-P, higher *D* was identified in the putamen compared to subjects with PD, MSA-C and controls (113). Similarly, reduced FA and elevated apparent diffusion coefficient (ADC) values were observed in MSA-P in the putamen, cerebellum and pons vs. PD and controls (114). Combined analysis of elevated T2* relaxation rate and putaminal *D* allowed discrimination of PD from MSA-P with high accuracy (113). Likewise, a multiregional evaluation of diffusivity changes in the pons, putamen and cerebellum was found to be more useful than single-region analysis (114). Compared to PSP, increased *D* was observed in MCP and pons in MSA cases, which correlated with cerebellar ataxia in these regions (115). In a comparison between MSA-P and MSA-C subtypes, elevated ADC values were observed in the putamen and pons in MSA-P cases vs. MSA-C, and in the cerebellum and MCP in MSA-C cases vs. MSA-P, highlighting distinct microstructural damage in these subtypes (116). Microstructural changes in the WM may be more pronounced early in the disease in MSA-C than in MSA-P (110). In MSA patients with cognitive impairment, a greater involvement of the cerebrum (specifically, reduced FA in the anterior corpus callosum) was identified compared to cognitively-normal MSA patients (117).

Using the bi-tensor diffusion analysis model, free-water was found to be elevated in the posterior SN in PSP, MSA, and PD vs. controls, however, this increase was significantly greater in PSP than in PD/MSA patients (118). In addition, depending upon the disease severity, free-water may be elevated in both the anterior and posterior SN in PD, MSA and PSP vs. controls (66).

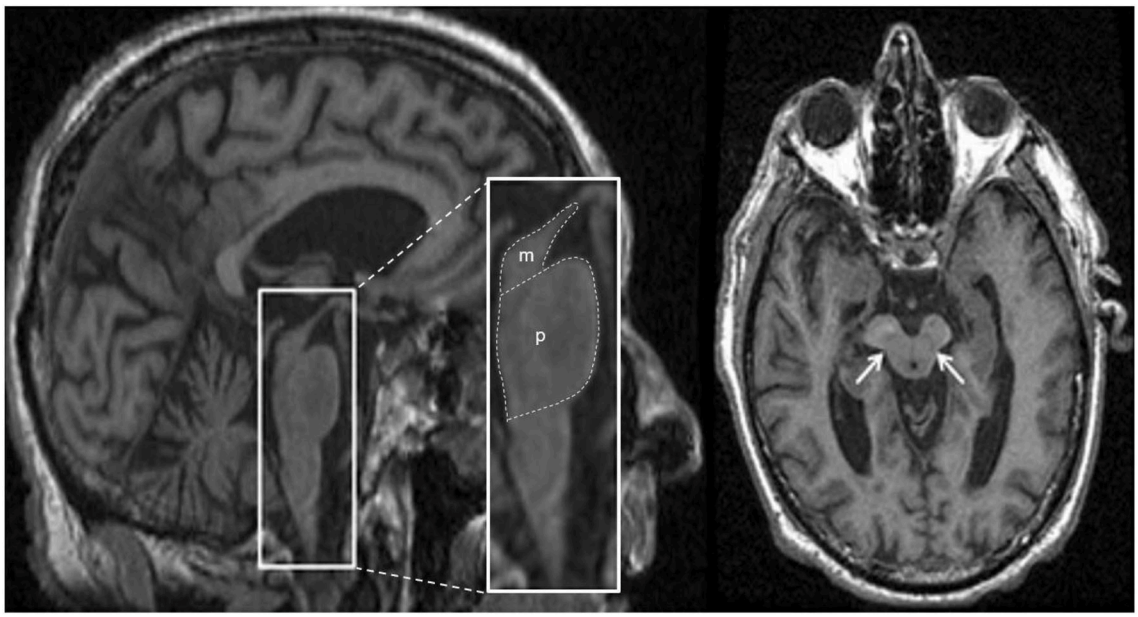


FIGURE 5 | Magnetic resonance imaging of a patient clinically-diagnosed with progressive supranuclear palsy. The left image is a sagittal T1-weighted sequence showing the "hummingbird" sign (smaller box), while the right image is an axial T1-weighted sequence showing the "morning glory" sign (arrows); both features are seen in progressive supranuclear palsy. The pons (p) and midbrain (m) areas are also shown (larger box), and their ratios have been used to calculate an index to assist in the diagnosis (128). Figure adapted from Saeed et al. (10), under the Creative Commons Attribution License 4.0 (https://creativecommons.org/licenses/by/4.0/).

Free-water-corrected FA was elevated in MSA in the putamen and caudate vs. controls; whereas, it was decreased in the thalamus and increased in the SCP in MSA vs. PSP (66). Using a machine learning algorithm, combined analysis of free-water and free-water-corrected FA derived from selective regions-of-interest achieved excellent separation among PD, MSA, and PSP cases (66). Unsupervised machine learning-based classification of PD, MSA-P and MSA-C patients using multimodal neuroimaging measures (GM density, T2* relaxation rate, and DTI) have also been pursued with favorable results (119). Free-water imaging using advanced diffusion models may become an effective tool in the differential diagnosis of parkinsonian disorders in the future.

Proton Magnetic Resonance Spectroscopy in MSA

Compared to controls, NAA/Cr ratios were smaller in the putamen in MSA-P, and in the pontine base in both MSA-P and MSA-C cases (120). Lower NAA/Cr ratios in the putamen and pontine base best discriminated MSA-P cases from PD (120). In another study, no significant differences were observed in the metabolites examined between MSA-P and PD, suggesting similar metabolic alterations in the two disorders (71). Likewise, cerebellar NAA/Cr and NAA/myo-inositol levels in MSA-P subjects were similar to those seen in PD (77). In MSA-C patients, cerebellar NAA/Cr and NAA/myo-inositol ratios were significantly reduced compared to PD, MSA-P, PSP-Richardson's syndrome (PSP-RS), and controls, whereas cerebellar myo-inositol/Cr ratios were elevated in MSA-C compared to controls (77).

Progressive Supranuclear Palsy (PSP)

Magnetic Resonance Imaging in PSP

Structural MRI typically shows atrophy of the midbrain and SCP in PSP compared to PD, MSA-P, CBD/CBS and controls (121–124). Several morphological markers suggestive of PSP on MRI have been reported, including midbrain atrophy compared to pons ("hummingbird" sign; specificity ∼99.5%, sensitivity ∼51%; **Figure 5**), atrophy of the midbrain tegmentum ("morning glory" sign, specificity ∼97%, sensitivity ∼37%; visualized as concavity of the lateral margins of the midbrain tegmentum on axial images; **Figure 5**) (125–127), midbrain T2 hyperintensity, as well as atrophy of the midbrain tegmentum with relative preservation of the midbrain tectum and cerebral peduncles ("mickey mouse" sign, visualized as rounded rather than rectangular midbrain peduncles on axial images) (99, 125). Importantly, the "hummingbird" and "morning glory" signs had high specificity but low sensitivity (99). Furthermore, image acquisition parameters may influence the appearance of these morphological features (4).

In PSP vs. controls, reduced volumes were reported in the brainstem, midbrain, and frontal GM (129), however, only the midbrain volume showed minimal overlap with the normal range on a case by case basis (129). In PSP-RS, atrophy of the midbrain was the predominant feature (4, 130). In a pathology-proven sample, atrophy of the midbrain and SCP was associated with PSP, whereas frontoparietal and pallidum degeneration in the absence of significant brainstem atrophy was suggestive of CBD (123). The premotor cortices and supplementary motor area were involved in both PSP and CBD cases (123). Besides midbrain

atrophy, VBM studies also show degeneration in the subcortical structures including pons, thalamus and striatum, as well as widespread cortical atrophy in the frontal, prefrontal, insular, premotor and supplementary motor areas vs. controls (121, 131, 132). Moreover, WM degeneration was reported in the pulvinar, dorsomedial and anterior nuclei of the thalamus, superior and inferior colliculi, as well as in the mesencephalic, and frontotemporal regions (131, 132). Pontine atrophy rates were significantly slower in PSP vs. MSA-P, and rates in the frontal lobe and midbrain in PSP were associated with executive and motor impairment, respectively (133). The midbrain atrophy rate may serve as an effective outcome measure in PSP clinical trials (134). In addition, the support vector machine classification method yielded accuracy rates >80% for predicting PSP diagnosis using disease-specific regions-of-interest (pallidum, putamen, caudate nucleus, thalamus, midbrain and insula) compared to the whole-brain approach (135).

Predominant midbrain atrophy has been incorporated as a supportive imaging feature in the Movement Disorders Society's PSP diagnostic criteria (3). The ratios of the pons to midbrain area (P/M) (as shown in **Figure 5**) and MCP to SCP widths (MCP/SCP) were found to be larger in PSP compared to PD, MSA-P and controls (specificity and sensitivity, 100%) (128, 136). Using these ratios, an index was calculated as [(P/M) x (MCP/SCP)], termed the "magnetic resonance parkinsonism index," which proved to be highly sensitive and specific for distinguishing PSP from PD, MSA-P and controls (128). A revised version incorporating the width of the third ventricle has been proposed ["magnetic resonance parkinsonism index" × (third ventricle width)/(frontal horns width)], which showed superior sensitivity (100%) and specificity (94.3%) in differentiating PSP-parkinsonism patients with slowness of vertical saccades from PD (137). It is important to recognize that midbrain atrophy may not be evident in all PSP subtypes and thus, atrophy patterns from other brain regions (such as the globus pallidus, frontal lobe, and cerebral peduncle) may provide additional information (138). It is unknown whether the above quantitative measures can distinguish PSP patients at early disease stages, or whether PSP subtypes with less pronounced midbrain atrophy can be distinguished, which provides impetus for further research.

Diffusion-Weighted and Diffusion Tensor Imaging in PSP

Compared to controls, diffusion imaging studies in PSP show variable findings and may reveal the following: increased *D* or decreased FA in the decussation of SCP, orbitofrontal WM, thalamus, cingulum, motor and supplementary motor area, as well as in the inferior fronto-occipital fasciculus, superior longitudinal fasciculus, anterior corpus callosum, arcuate fasciculus, posterior thalamic radiations, and internal capsule (115, 132, 139, 140). Elevated ADC values were observed in the putamen in PSP vs. controls over a 2 year period (141). Increased *D* in the decussation of SCP may discriminate PSP from MSA and PD (115), whereas increased ADC values in the putamen, globus pallidus and caudate nucleus may help distinguish PSP cases from PD (142). Another study calculated the FA score per subject for regions hypothesized to be involved in PSP (i.e., the SCP and frontal WM region), and reported >85% sensitivity and specificity for differentiating PSP from PD/DLB cases (143).

A multimodal study integrated volumetric MRI, DTI and neuromelanin-sensitive imaging, and identified several predictors for separating PSP-RS from controls (144). The best predictor was the neuromelanin-based SN volume followed by FA in the midbrain (144). The separation of PSP-RS cases from PD was achieved using neuromelanin-based SN volume, pons FA values, midbrain and globus pallidus volumes, and basal forebrain FA values (144). Another study identified greater atrophy, decreased FA, and increased *D* in the SCPs bilaterally in PSP-RS patients as compared to PD and controls (145). More advanced neuroimaging techniques have identified changes in the free water in the posterior SN (118). Specifically, free-water values derived from the bi-tensor diffusion model were significantly elevated in PSP in the posterior SN vs. MSA, PD and controls, and were observed in a characteristic pattern: PSP > MSA/PD > HC (118). In addition, free-water-corrected FA was elevated in PSP in the caudate, putamen, thalamus and vermis with accompanying decreases seen in the SCP and corpus callosum compared to controls (66).

Other studies have compared diffusion imaging parameters in PSP subtypes. Lower FA values were exclusively detected in the SCP in PSP-RS vs. PSP-parkinsonism patients, implicating SCP's involvement in postural instability (146). PSP patients with vertical supranuclear gaze palsy exhibited lower FA values in the midbrain vs. those with slowness of vertical saccades, highlighting the role of midbrain atrophy in vertical ocular dysfunction (146). PSP-RS patients also showed more severe and widespread diffusion abnormalities vs. PD, which reflects greater microstructural damage as consistent with greater overall brain atrophy often found in PSP-RS than in PD cases (147). Moreover, damage to the SCPs may be detected in both PSP-RS and PSP-parkinsonism subtypes (130, 145). When the two subtypes were directly compared, PSP-RS patients showed decreased FA and increased *D* in the left SCP vs. PSP-parkinsonism patients (145). Computer-aided diagnosis of PSP and its subtypes may be possible using diffusion-weighted/DTI measures (145, 147).

Proton Magnetic Resonance Spectroscopy in PSP

In PSP, reductions in the NAA/Cr ratios in the LN, brainstem, centrum semiovale, frontal, and precentral cortex, as well as reductions in the NAA/choline values in the LN are observed relative to controls (148, 149). A more prominent decline in NAA/Cr ratio was noted in the putamen vs. PD and MSA (150). PSP-RS patients had reduced cerebellar NAA/Cr and NAA/myo-inositol ratios vs. controls, and reduced cerebellar NAA/Cr ratio vs. PD patients (77). Compared to controls, PSP patients also showed a decrease in scyllo-inositol concentration (a stereoisomer of inositol) and scyllo-inositol/Cr ratio in the supplementary motor area, and both of these metabolic measures were directly related to attention and working memory functions (151). The pathological significance of scyllo-inositol reduction in PSP is currently uncertain (151).

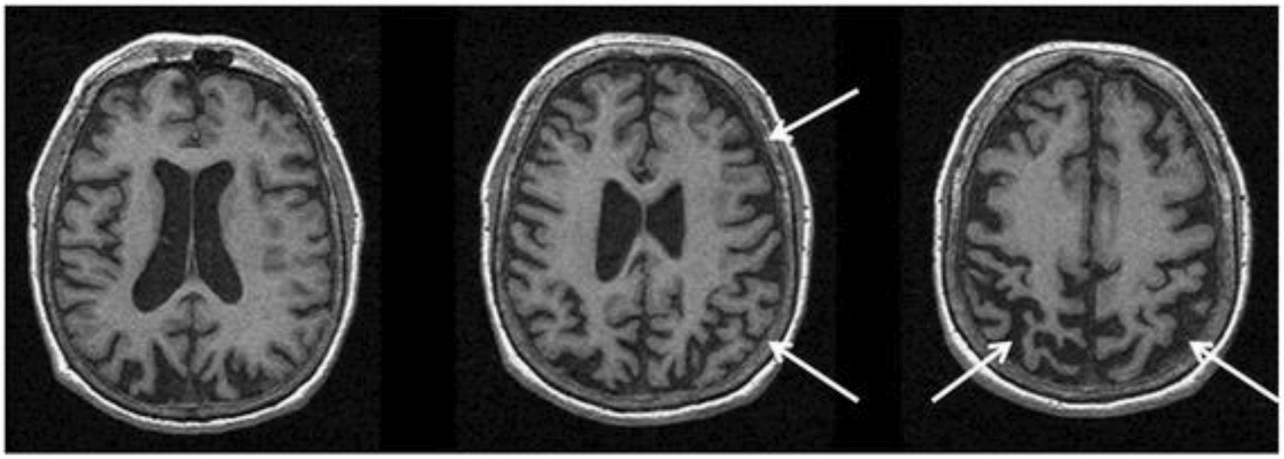


FIGURE 6 | Magnetic resonance imaging of a patient with a pathology-proven diagnosis of corticobasal degeneration. Serial axial T1-weighted sequences are presented showing right greater than left parietofrontal atrophy commonly seen in corticobasal syndrome. Figure reproduced from Saeed et al. (10), under the Creative Commons Attribution License 4.0 (https://creativecommons.org/licenses/by/4.0/).

Corticobasal Degeneration/Syndrome (CBD/CBS)

Magnetic Resonance Imaging in CBD/CBS

In CBS/CBD, asymmetrical cortical atrophy in the frontoparietal lobe is commonly observed (**Figure 6**), contralateral to the clinically more affected side of the body (however, laterality may not be present in all cases). In CBS vs. controls, an asymmetric pattern of atrophy in the bilateral premotor cortex, superior parietal lobules, and striatum was identified (121). Compared to PSP, greater atrophy was observed in the dorsofrontal and parietal cortices in CBS (121, 129), whereas midbrain atrophy was more pronounced in PSP vs. CBS (121). Likewise, greater asymmetric GM degeneration in the inferior frontal and premotor cortex, parietal operculum, superior temporal gyrus, and hippocampus was detected, along with decline in FA primarily in the frontoparietal region vs. controls (152). In a meta-analysis of VBM studies, although a significant overlap was detected among PSP, MSA-P, and CBS cases, more prominent atrophy in the superior parietal lobe was observed in CBS (153). Importantly, CBS can be associated with significant pathological heterogeneity difficult to predict based on clinical presentation in life (15, 154). Thus, neuroimaging patterns using pathology-proven samples can improve diagnostic accuracy.

On MRI, the pattern of atrophy in CBS aligns with the "true" underlying pathology. Although, GM atrophy in a clinically-diagnosed CBS group was observed in the premotor cortices, supplemental motor area and insula, the pattern of atrophy aligned more closely with neuropathological diagnosis (155). For example, frontotemporal atrophy in CBS was associated with frontotemporal lobar degeneration with transactive response DNA binding protein-43 kDa (TDP-43) pathology, whereas temporoparietal atrophy was related to AD pathology (155). In contrast, focal atrophy predominantly involving the premotor cortex and supplementary motor area was observed in those pathologically diagnosed with CBD and PSP, although more severe changes in these regions suggested CBD over PSP (155). The degree of gross global atrophy is typically more severe in CBD vs. PSP (156). Another pathology-confirmed study observed GM degeneration in the dorsal prefrontal and perirolandic cortex, striatum, and brainstem in CBD vs. controls (6). Furthermore, in CBS due to frontotemporal lobar degeneration (tau or TDP-43), atrophy pattern progressed into the prefrontal cortex, striatum and brainstem, while in CBS due to AD, atrophy stretched into the temporoparietal cortex and precuneus regions (6). The predominant clinical syndrome in CBS (extrapyramidal vs. cognitive) was associated closely to the regional atrophy patterns (123). On fluid-attenuated inversion recovery images, subcortical WM hyperintensities with ventricular dilation (greater in the more affected lobe) were reported (157), however, these changes are not specific to CBS/CBD.

Diffusion-Weighted and Diffusion Tensor Imaging in CBD/CBS

Elevated *D* and reduced FA were detected in the posterior truncus of the corpus callosum in CBS compared to PD and controls suggesting transcallosal fiber degeneration (59). In addition to the corpus callosum (59, 152, 158), decreased FA in CBS was observed in the long frontoparietal connecting tracts, intraparietal associative fibers, and sensorimotor cortical projections (152). Similarly, reduced FA and increased *D* were noted in the WM of premotor, prefrontal and motor cortices, as well as in the middle cingulate bundle vs. controls—changes that were more pronounced contralateral to the more affected side (158). Compared to PSP, a more asymmetric, supratentorial and posterior pattern of WM tract degeneration was reported in CBS with greater involvement of the splenium of the corpus callosum, WM of the motor and premotor cortices, as well as the parietal lobes (158).

Proton Magnetic Resonance Spectroscopy in CBD/CBS

NAA/Choline and NAA/Cr levels were reduced in CBS patients in the frontoparietal cortex, LN and centrum semiovale vs. controls (149, 159). Lower NAA/Choline levels in the frontoparietal lobe may help differentiate CBS cases from PSP (149). In the parietal cortex of CBS patients, the NAA/Choline values were reduced contralateral to the clinically more affected side (159). A more pronounced reduction in NAA/Cr values was observed in the frontal cortex and putamen vs. PD, MSA and vascular parkinsonism, with prominent asymmetry in NAA/Cr ratios in the putamen (150). Lower putaminal NAA levels have been reported across the PD, MSA, PSP and CBS patients to varying degrees. Thus, laterality of metabolite ratios observed in the putamen in CBS may be helpful in differentiation in some cases.

FUNCTIONAL MAGNETIC RESONANCE IMAGING IN PARKINSONIAN DISORDERS

Using resting-state and task-based functional MRI, several large-scale networks involved in motor, cognitive, and affective processes have been identified (**Table 3**). Impairments in these networks as well as in specific circuits (e.g., basal ganglia thalamocortical circuit and cortical-subcortical sensorimotor circuit) have been associated with motor and non-motor symptoms in PD and atypical PS. Reduced resting-state functional connectivity between the striatum and the thalamus, midbrain, pons and cerebellum was observed in PD, highlighting connectivity alterations within the brainstem (160). Within the striatum, a greater change in connectivity was evident in the posterior putamen, followed by the anterior putamen and caudate (160) as consistent with the patterns of striatal dopaminergic dysfunction in PD (161–163). Connectivity changes between the striatum and sensorimotor and visual cortical areas as well as the supramarginal gyrus were also evident (160) probably highlighting dysfunction of the cortical-subcortical sensorimotor circuit in PD (164). Furthermore, reduced resting-state functional connectivity within the basal ganglia network allowed differentiation of PD cases in the drug-off state from controls (sensitivity 100%, specificity 89.5%) (165). Conversely, increased functional connectivity was detected in associative and limbic connections in PD likely indicating compensatory changes due to dopaminergic deficits and the ensuing alterations in related circuits (164).

In tremor-dominant PD, the globus pallidus internus and putamen exhibited elevated functional connectivity with the cerebellothalamic circuit that modulates tremor amplitude. It was suggested that basal ganglia degeneration (and the resulting dopamine deficiency) can cause tremors by disrupting cerebellothalamic circuit signaling (166). PD patients with freezing of gait showed abnormal functional connectivity in the pedunculopontine nucleus, which primarily affected the corticopontine-cerebellar pathways and visual temporal areas involved in visual processing (167). These findings are consistent with observations seen in DTI structural connectivity studies (168). Furthermore, PD patients with sleep disturbance showed changes in cortical functional connectivity within the default mode network, central executive network, and dorsal attention network vs. PD patients without sleep disturbance (169). Hallucinations in PD were found to be associated with functional connectivity changes within the default mode network and visual processing areas implicating networks involved in perceptual and attentional processing (170).

Compared to PD, patients with MSA displayed reduced cerebellar connectivity within multiple brain networks as well as the striatum (171). Overlap in functional connectivity was noted in PD and PSP patients within the thalamus, striatum, and prefrontal cortex, however, not surprisingly, the PSP group showed more extensive functional connectivity disruptions throughout the brain (particularly in the midbrain, precentral gyrus, parietal cortex, basal ganglia, and cerebellum) (172). Another study identified deficits in the resting-state functional connectivity in PSP cases in the rostral midbrain tegmentum network (173). In CBS, decreased functional connectivity was reported in the right central operculum, middle temporal gyrus, and posterior insula, whereas an increase in connectivity was identified in the anterior cingulum, medial superior frontal gyrus, and bilateral caudate nuclei (174). Thalamic functional connectivity was decreased in both PSP and CBS groups in multiple cortical, subcortical, and cerebellar regions (175). In contrast, whole brain functional connectivity of the dentate nucleus differed between PSP and CBS: it was reduced in the subcortical and prefrontal cortical areas in PSP, whereas it increased asymmetrically in the frontal cortex in CBS (175).

In a longitudinal task-based functional MRI study that incorporated a motor control paradigm, a decline in activity within the putamen and primary motor cortex was identified over 1 year in PD patients vs. controls (176). Conversely, a more widespread and unique pattern of functional changes were observed in MSA and PSP patients compared to PD. In MSA, changes were exclusively extrastriatal (i.e., the primary motor cortex, supplementary motor area and superior cerebellum) (176). In PSP, all regions-of-interest were less active at 1 year compared to baseline, including the contralateral putamen, ipsilateral putamen, contralateral primary motor cortex, contralateral supplementary motor area, and ipsilateral superior cerebellum (176).

Changes in functional connectivity after symptomatic treatment interventions have also been observed. For example, increase in functional connectivity was identified in the supplementary motor area (part of the sensorimotor resting-state network) after levodopa administration in drug-naïve PD patients (177). The sensorimotor system was suggested to be one of the targets of acute levodopa treatment (177). Likewise, the administration of dopaminergic medication resulted in enhanced connectivity within the basal ganglia network (165). Finally, repetitive transcranial magnetic stimulation can improve motor symptomatology by influencing functional hubs connecting to motor-related networks, including the default mode, cerebellar, and limbic networks (178).

TABLE 3 | An overview of 4 core brain networks.

Networks[‡]	Description	Common network-associated regions
Default mode network	Involved in endogenously mediated activities at rest including self-referential and social cognitive processes, and it is inactive during external goal-oriented processes	Posterior cingulate cortex, medial prefrontal cortex, precuneus, and inferior parietal and medial temporal cortices
Salience network	Involved in the bottom-up detection of salient stimuli that require dynamic switching between the central executive and default-mode networks, in order to keep cognitive resources focused on task-relevant goals	Anterior cingulate and anterior insular cortices, as well as amygdala, thalamus, hypothalamus, ventral striatum, and substantia nigra
Central executive network	Involved in external goal-oriented and cognitively demanding processes including working memory, planning, and decision making	Dorsolateral prefrontal cortex and posterior parietal cortex
Sensorimotor network	Involved in the execution of voluntary motor activities	Primary motor cortex, supplementary motor area, primary and secondary sensory cortices

[†] *Several other networks, including frontoparietal network, dorsal and ventral attentional networks, and visual network (among others) have also been postulated.*

TRANSCRANIAL B-MODE SONOGRAPHIC IMAGING IN PARKINSONIAN DISORDERS

Echogenicity in Substantia Nigra

In PD, increased echogenicity of the SN is commonly observed, which can be visualized at the mesencephalic plane as an enlarged, lighter (i.e., mildly echogenic) region within the darker mesencephalon (179–182) (**Figure 7**). Similar to idiopathic PD, increased SN echogenicity is seen in PD patients carrying *LRRK2* and *GBA* mutations (183). Although, the precise etiology of SN hyperechogenicity is under research, it is likely due to the known nigral pathology and associated accumulation of free (unbound) iron within the SN.

SN hyperechogenicity may be present in preclinical stages as detected in those with increased risk of PD, e.g., individuals with a family history of PD (184). The area of SN hyperechogenicity remained stable in PD over a 5 year period (185) suggesting that this feature may be considered an early "trait" marker of vulnerability, as opposed to a marker of progression in PD. Indeed, studies have not consistently shown a correlation between SN hyperechogenicity and disease severity or duration (181, 186–188). Likewise, no correlation has been observed between SN hyperechogenicity and the degree of presynaptic DAT loss in PD (189). SN hyperechogenicity may not differ based on PD laterality and has been observed in both hemispheres, irrespective of the clinically affected side (187).

It is also important to note that ∼10% of healthy controls, as well as ∼16% of patients with essential tremor may show elevated echogenicity in the SN (190), thus limiting the utility of this "echofeature" as a standalone biomarker of PD. For example, in a 3 year longitudinal study, baseline SN hyperechogenicity was evident not only in PD, but also in patients with essential tremor, who subsequently developed parkinsonian symptoms during the follow-up period (191).

Increased echogenicity of the SN, particularly when marked, has been reported to differentiate PD cases from atypical PS (PSP and MSA as a group) with good sensitivity (∼91%) and specificity (∼82–96%) (179, 192). When experienced examiners are available, this technique can be resourceful in differentiating PD from atypical PS. However, patients with DLB and PDD also present with hyperechogenic SN in frequencies similar to those in PD. For example, ∼80% of DLB cases showed hyperechogenic SN bilaterally, and thus the differential diagnosis in PDD/DLB relies upon other clinical features and diagnostic biomarkers (193). Nevertheless, it is suggested that the discrimination between DLB and PDD using transcranial sonography may be made by combining SN echogenic sizes, asymmetry indices, and onset age (sensitivity 96%, specificity 80%) (193). Hyperechogenic SN can also be seen in CBS (∼60–80%) and PSP disorders [∼10–20%, especially in PSP-parkinsonism subtype (194)]; however, studies in CBS and PSP are limited by small sample sizes and lack of neuropathological confirmation (195–197).

Echogenicity of the Lentiform Nucleus

Increased echogenicity of the LN is a feature noted in some atypical PS and may be of diagnostic utility when examined together with SN echogenicity. In healthy individuals, the LN is visualized as an isoechogenic structure, located between the caudate nucleus and thalamus. Hyperechogenic LN may support a diagnosis of atypical PS when seen together with normoechogenic SN (188). Specifically, this echogenic profile was observed in MSA-P and PSP patients with good sensitivity (100%), albeit with a low specificity (∼59%). Normal echogenicity of the SN alone aligned with a diagnosis of MSA-P (sensitivity 90%, specificity 98%), while increased echogenicity of the LN alone was unhelpful in the differential diagnosis of parkinsonian syndromes since PD and PSP patients may show this feature to some degree (197). Enlargement of the third ventricle can also be examined using transcranial sonography. Ventricular enlargement >10 mm together with LN hyperechogenicity may indicate PSP (197), whereas normal LN echogenicity was observed in CBS patients (195). Given the considerable heterogeneity evident in atypical PS, more studies are needed to develop reliable sonographic profiles of these disorders.

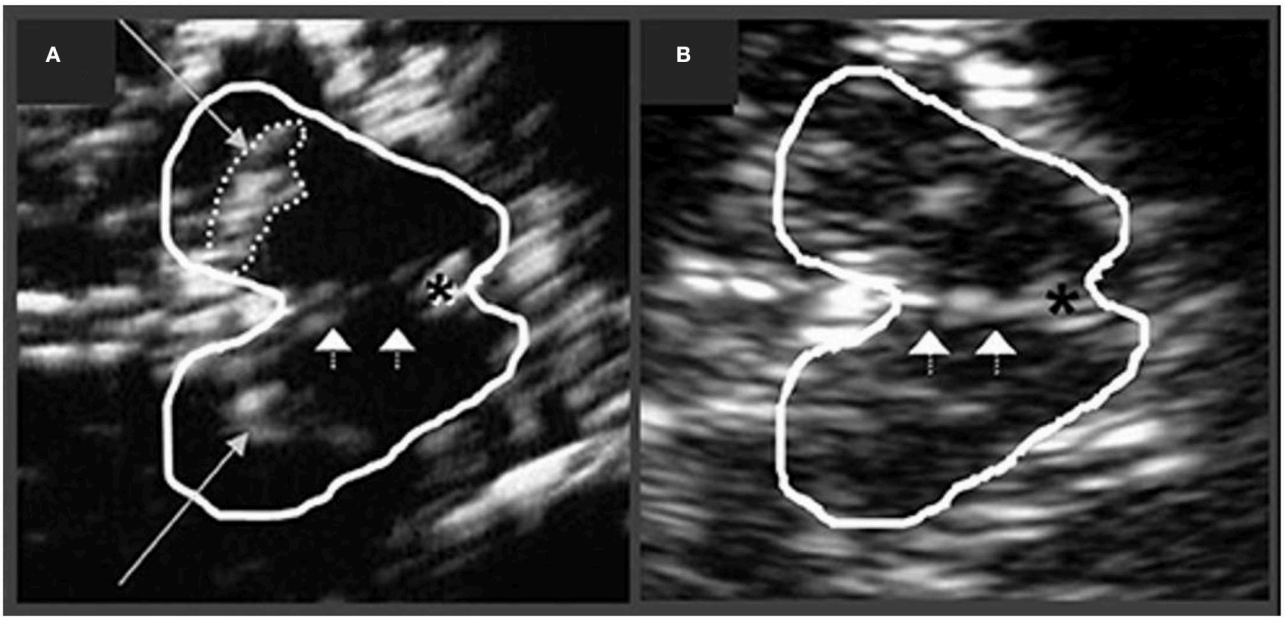


FIGURE 7 | Transcranial sonographic image outlining the butterfly-shaped midbrain at the mesencephalic plane. In **(A)**, enlarged area of echogenicity at the anatomical site of substantia nigra (long arrows) is depicted, as may be seen in Parkinson's disease patients. In addition, interrupted echogenic line of the raphe can be observed (short arrows). In **(B)**, normal midbrain echogenicity is shown. The aqueduct is indicated by an asterisk. Figure adapted from Richter et al. (182), under the Creative Commons Attribution License (https://creativecommons.org/licenses/by/4.0/).

SPECT AND PET IMAGING OF THE DOPAMINERGIC SYSTEM IN PARKINSONIAN DISORDERS

Presynaptic Dopamine Transporter (DAT)

Normal DAT binding on ^{123}I-FP-CIT SPECT can be visualized as two bright symmetric "comma-shaped" regions, signifying intense activity in the striatum (striatum includes caudate nucleus and putamen; **Figure 2**). Any change in this activity on ^{123}I-FP-CIT SPECT may indicate presynaptic nigrostriatal injury (198, 199). Overall, DAT SPECT shows normal presynaptic nigrostriatal activity in normal individuals, essential tremor cases, and in drug-induced or psychogenic/functional parkinsonism (200–202).

Conversely, reduced DAT binding on SPECT has been observed in PD, DLB/PDD, MSA, and PSP patients to varying degrees suggesting nigrostriatal degeneration (200, 203–205). The utility of DAT SPECT in differentiating PD in early stages from normal subjects and cases with essential tremor and vascular parkinsonism with high accuracy has been suggested (206). In PD, the posterior putamen exhibits earlier and more severe reduction in activity compared to the anterior putamen or caudate nucleus (161). The decline in DAT signal is often more pronounced in the hemisphere contralateral to parkinsonian symptomatology, whereas binding may appear symmetric in cases with symmetric motor deficits (161). Striatal DAT SPECT binding has been shown to correlate with PD severity and motor impairment (202, 207–209). Reduced DAT binding can differentiate patients with PD and DLB from AD (210, 211). In a recent population-based study, striatal DAT deficits (particularly in the caudate nucleus) were associated with shorter survival in PD patients (212).

Similar to SPECT, ^{18}F-dopa PET studies evaluating the presynaptic nigrostriatal dopaminergic system have found reduced radiotracer uptake in PD, MSA-P, PSP and DLB groups vs. controls, whereas normal uptake was observed in cases with essential tremor (205, 213). Specifically, ^{18}F-dopa PET measures the activity of aromatic amino acid decarboxylase (AADC) enzyme, which converts ^{18}F-dopa into ^{18}F-dopamine, providing an approximation of dopaminergic storage levels. In PD, decreased ^{18}F-dopa uptake was first evident in the posterior putamen, followed by anterior putamen and caudate nucleus, contralateral to the clinically affected side (162, 163). Striatal and putaminal ^{18}F-dopa uptake have been shown to associate with PD progression and motor severity, respectively (163). Other PET radiotracers, such as ^{11}C-DTBZ, can be used to evaluate the presynaptic monoaminergic system by labeling the vesicular monoamine transporter type 2 (VMAT2)—a presynaptic transmembrane protein essential for packaging and storing monoamines (including dopamine) in synaptic vesicles. Reduced VMAT2 binding in the striatum was detected in PD on ^{11}C-DTBZ PET (214). As identified in ^{18}F-dopa PET, the greatest regional decrease in VMAT2 binding in PD (using ^{18}F-AV-133) was observed in the posterior putamen, followed by the anterior putamen and caudate nucleus (215). Notably, due to ongoing compensatory changes in response to neurodegeneration (AADC upregulation, presynaptic DAT down-regulation), the nigrostriatal presynaptic

dopaminergic injury may be underestimated using PET and SPECT imaging (214). Furthermore, an approximated 10–20% of clinically diagnosed PD cases that were enrolled in neuroprotective trials of PD and underwent DAT imaging presented with "scans without evidence of dopaminergic deficit" (216). Studies have shown this group of cases to be quite heterogeneous and [among other reasons (10)] represent a clinical misdiagnosis of PD in most cases (10, 216). Reduced DAT binding using ^{11}C-methylphenidate PET has also been identified in clinically-unaffected mutation carriers of *LRRK2* gene associated with dominant inheritance of PD (217). Elevated dopamine turnover in the putamen was suggested to be an even more sensitive subclinical indicator of PD in *LRRK2* mutation carriers compared with reduced dopaminergic terminal integrity as assessed by VMAT2 and DAT binding (218).

DAT SPECT imaging can be invaluable in differentiating DLB from other forms of dementia (219). For example, an abnormal DAT scan can enhance the diagnostic certainty of DLB from "possible" to "probable" (220), and assist in differentiating DLB without clinically significant parkinsonism from AD (221–223). The development of parkinsonism over 6 months was associated with abnormal baseline ^{123}I-FP-CIT SPECT scan in possible DLB patients (224). Although, an abnormal DAT scan supports the diagnosis of DLB, a normal scan does not exclude DLB altogether, including those cases that present with minimal brainstem involvement (223).

In MSA-P, signal loss on DAT SPECT was greater over time in the caudate and anterior putamen vs. PD, as consistent with a relatively faster rate of disease progression in MSA-P (225). Patients with CBS may show striatal DAT SPECT reduction with greater hemispheric asymmetry vs. PD (226, 227). Furthermore, patients with CBS/CBD may show normal nigrostriatal DAT SPECT scans, especially early in the course of the disease, suggesting that nigrostriatal degeneration may be a late pathological feature of CBD (228). Patients with PSP tend to exhibit more pronounced but fairly uniform DAT loss in the striatum (204). In contrast to PD, a relatively uniform involvement of presynaptic striatal dopaminergic neurons was observed in PSP, as evidenced by lower striatal-to-occipital but higher putamen-to-caudate DAT binding ratios (229, 230). Likewise, a more symmetric pattern of DAT loss was detected in PSP vs. PD and MSA-P (202, 229, 230), with the index of asymmetry significantly greater in PD relative to PSP (230). A recent meta-analysis further confirmed reduced DAT activity in the caudate nucleus and putamen in PSP vs. PD and MSA-P, and in MSA-P vs. MSA-C (231). Investigations using ^{18}F-dopa PET mirror these SPECT-based findings as follows: putaminal uptake was significantly lower in atypical PS and PD vs. controls (232–234). However, a more severe decline was noted in the caudate head in atypical PS vs. PD (234). As compared to PD, putamen and caudate regions were equally abnormal in PSP (232). Despite these findings, the presynaptic striatal binding patterns using PET and SPECT are currently unreliable in differentiating parkinsonian disorders on a case-by-case basis. Finally, using ^{99m}Tc-TRODAT-1 SPECT, lower putaminal DAT uptake was associated with shorter time of conversion from idiopathic RBD diagnosis to an α-synucleinopathy vs. those with higher putaminal DAT uptake (235). This may suggest a predictive role of nigrostriatal damage in idiopathic RBD in terms of conversion to an α-synucleinopathy (235). However, an abnormal DAT scan was found to be less sensitive than motor features in predicting phenoconversion from idiopathic RBD to overt neurodegenerative syndrome (of PD, LBSD, and MSA) (236).

Postsynaptic Dopamine D2 Receptor

In drug-naïve PD patients compared to controls, binding potential for the G-protein-coupled dopamine D2 receptors measured using ^{11}C-raclopride PET may appear normal or upregulated contralateral to the clinically affected side (237–239). Similarly, striatal dopamine D2 receptor upregulation was observed in drug-naïve PD patients using SPECT ligands (^{123}I-IBZM and ^{123}I-IBF) probably suggesting compensatory changes secondary to nigrostriatal denervation, with higher upregulation detected in the posterior putamen (161, 240). In medicated PD cases, postsynaptic D2 receptor binding was reduced or within the normal range compared to controls in PET and SPECT studies (161, 200, 237, 241). Normal D2 binding potential was also observed in patients with DLB and essential tremor (161, 200), while reductions were reported in atypical PS cases (239).

In PSP vs. controls, reduced D2 receptor binding was detected in PET and SPECT studies (200, 239, 242). Likewise, D2 binding reductions were noted in MSA patients compared to PD (233, 241) and controls (200, 233, 241, 242) correlating with striatal glucose hypometabolism (241). In CBS, studies typically show preservation of postsynaptic D2 receptors, although inconsistently, which is not surprising given the pathologic heterogeneity evident in this disorder (200, 203, 243).

The posterior putamen to caudate binding ratios were >1 in almost all drug-naïve and medicated PD and PSP cases (161). In contrast, this ratio was <1 in most MSA cases indicating greater loss of D2 receptors in the posterior putamen in MSA (161). This finding is consistent with a ^{11}C-raclopride PET study, whereby elevated caudate-to-putamen and anterior-to-posterior putamen D2 receptor binding ratios were observed in MSA-P vs. PD suggesting greater D2 receptor loss in the posterior putamen in MSA-P cases (244).

Combining SPECT-based presynaptic DAT and postsynaptic D2 receptor imaging may improve diagnostic capacity (245). For example, a study suggested increased accuracy in differentiating PD from atypical PS using a multidimensional combination of striatal presynaptic DAT imaging, postsynaptic D2 receptor imaging, and myocardial scintigraphy [evaluates cardiac postganglionic sympathetic fiber function, which is significantly impaired in early PD and LBSD, as reviewed in (10)] (246). Further studies

with pathology proven samples are needed to improve the utility of postsynaptic D2 receptor imaging in differentiating parkinsonian disorders.

SPECT IMAGING OF CEREBRAL PERFUSION IN PARKINSONIAN DISORDERS

Cerebral perfusion SPECT evaluates the metabolic status of brain tissue by quantifying changes in the regional cerebral blood flow using various radiotracers (**Table 2**). Occipital hypoperfusion is frequently observed in DLB, however, it may not be present in all cases on an individual basis. When present, it should raise the possibility of DLB as the underlying cause of the disease. Using ^{99m}Tc-HMPAO as a radiotracer, temporoparietal hypoperfusion was detected in both AD and DLB cases to varying degrees vs. controls, whereas occipital hypoperfusion was the differentiating feature in DLB vs. AD (247). Occipital hypoperfusion has also been detected using other SPECT radiotracers (e.g., ^{123}I-IMP and ^{99m}Tc-ECD). Perfusion SPECT was unable to differentiate PDD cases from DLB, revealing similar perfusion profiles in some studies (248, 249). In addition, hypoperfusion in the left occipital region along with worse episodic memory performance was found to distinguish DLB patients without visual hallucinations from CBS at earlier disease stages (250).

Patients with CBS tend to show asymmetric perfusion profiles (251, 252), however, asymmetry may not be observed in all cases. Compared to PSP (using ^{123}I-IMP tracer), asymmetrically reduced perfusion was noted in CBS in the inferior prefrontal, sensorimotor, and posterior parietal cortices, with overlap in the medial frontal region (252). Perfusion asymmetry may serve as a supportive feature when differentiating CBS from other atypical PS patients. The differentiation of LBSD from atypical PS may be feasible using an automated image-based classification system, which incorporates striatal DAT uptake and regional perfusion patterns (253).

Hypoperfusion in the occipital cortex using SPECT has also been seen in PD vs. controls (249, 254), whereas frontal lobe hypoperfusion was present in both PD and MSA-P patients (254). Hypoperfusion in the frontal lobe was observed in a 1 year longitudinal study in PD (255). In MSA-P cases, hypoperfusion in the putamen was noted compared to that in PD (256), whereas hypoperfusion together with local cerebral atrophy was found in the cerebellum and pons in MSA-C patients vs. controls (257). The current literature on perfusion SPECT is limited by lack of pathology-confirmed investigations, small sample sizes, and a handful of studies in MSA, PSP, and CBS. Moreover, given the overlap in perfusion profiles, other techniques (e.g., ^{123}I-metaiodobenzylguanidine myocardial scintigraphy or DAT imaging) may perform superior to perfusion SPECT in some cases (258). Multimodal imaging can provide valuable diagnostic information in uncertain cases (10).

PET IMAGING OF GLUCOSE METABOLISM IN PARKINSONIAN DISORDERS

Metabolic Patterns Using Regional and Voxel-Based Analyses

Cerebral glucose metabolism can be evaluated using ^{18}F-labeled fluorodeoxyglucose [^{18}F-FDG] where reduced tracer uptake is indicative of lower glucose utilization by the tissue. Normal metabolism or hypermetabolism involving the LN (which includes putamen and globus pallidus) and possibly the thalamus, motor cortex, and cerebellum may be observed in PD on ^{18}F-FDG-PET, whereas hypometabolism may be seen in parieto-occipital association areas and in the dorsolateral prefrontal cortex (259, 260). Preserved glucose metabolism in the basal ganglia may differentiate PD from MSA and PSP, where a corresponding glucose hypometabolism is typically seen in the latter (259). A meta-analysis found decreased glucose metabolism in the bilateral inferior parietal cortex and left caudate nucleus in PD, which was linked to cognitive deficits and motor symptoms, respectively (261). In MSA, glucose hypometabolism may be observed in the putamen and brainstem, with or without hypometabolism in the cerebellum compared to PD and controls (259, 262). Glucose hypometabolism may be more predominant in the bilateral putamen in MSA-P and bilateral cerebellum in MSA-C (263), based on the most affected regions in these disorders. In addition, microstructural damage as assessed using DTI was found to be associated with glucose hypometabolism in the posterior putamen in MSA-P patients (264).

In PSP, glucose hypometabolism was evident in the caudate/basal ganglia, midbrain, thalamus, as well as anterior cingulate, frontal and primary motor cortices vs. controls (259, 263, 265). Midbrain hypometabolism visualized as an oval or round region on ^{18}F-FDG-PET was identified in PSP as compared to MSA and CBS patients (specificity 100%, sensitivity 29%), and may reflect midbrain atrophy (266). Compared to PD, MSA, and controls, glucose hypometabolism in PSP was reported in the caudate nucleus, thalamus, midbrain, and cingulate gyrus (262). In CBS, an asymmetric glucose hypometabolism in the basal ganglia and frontoparietal cortices may be apparent, contralateral to the clinically more affected side (263, 267). Hypometabolism in the parietal lobe may help discriminate CBS patients from PSP (268).

Patients with PDD and DLB often show a similar pattern of bilateral glucose hypometabolism vs. controls in the posterior cortical areas, including lateral frontal, temporoparietal, and occipital regions (269, 270). A more prominent hypometabolism in the anterior cingulate cortex may distinguish DLB from PDD (270). Occipital hypometabolism combined with less prominent metabolic decline in the medial temporal lobe (particularly the hippocampus) may be useful in differentiating DLB/PDD from AD (269). When differentiating DLB from AD, hypometabolism in the lateral occipital cortex achieved the highest sensitivity (88%), while relatively preserved metabolism in the posterior cingulate cortex ("cingulate island" sign) attained the highest sensitivity (100%) (271). It is suggested

that ^{18}F-FDG-PET may perform superior to ^{123}I-IBZM-SPECT for discriminating Lewy body disorders from atypical PS (272). Moreover, computer-assisted interpretation of FDG-PET data may be used for objective evaluation in parkinsonian disorders, which can provide accuracy equivalent to visual reading especially in places where skilled readers are not available (260).

Metabolic Patterns Based on Spatial Covariance Analysis

The spatial covariance analysis on resting-state ^{18}F-FDG-PET data has enabled the identification of disease-related metabolic patterns in PD and atypical PS. In PD, a specific and relatively stable PD-related motor pattern (PDRP) and PD-related cognitive pattern (PDCP) have been identified. The PDRP is characterized by elevated pallidothalamic and pontine metabolic activity associated with reduction in the supplementary motor area, premotor cortex, and parietal association areas (273). The expression level of PDRP correlated with the loss of presynaptic nigrostriatal dopaminergic integrity and motor dysfunction (274, 275), and was also elevated in patients with idiopathic RBD (276). Likewise, the PDCP pattern was characterized by metabolic reduction in the medial frontal and parietal association regions, and metabolic increase in cerebellar cortex and dentate nuclei (273). The PDCP expression was elevated and increased over time in PD (274) and was higher in those was dementia (277). The level of PDCP expression correlated with memory and executive performance in PD (273) and, unlike PDRP, appeared relatively unaffected by treatments with intravenous levodopa or deep brain stimulation (278), which supports its utility as a reproducible imaging biomarker of cognitive dysfunction in PD.

Specific disease-related metabolic patterns based on ^{18}F-FDG-PET data have also been reported for MSA, PSP (279), and CBS (267) disorders. The MSA-related pattern was elucidated as a metabolic reduction in the putamen and cerebellum, whereas PSP-related pattern showed decreased metabolism in the brainstem and medial frontal cortex compared to normal subjects (273, 279). The CBS-related pattern was characterized by asymmetric, bilateral hypometabolism involving the frontal and parietal cortex, thalamus, and caudate nucleus, where greater abnormalities were found contralateral to the clinically more affected side (267). Although, metabolic asymmetry scores for the CBS-related pattern may help in the differentiation, significant overlap with PSP patients on a case-by-case basis is often observed (267). Furthermore, the CBS-related pattern highly correlates with the features of the clinical syndrome (i.e., where) but does not provide information on the underlying causative pathology (i.e., what). In conjunction with other imaging modalities, these disease-related covariance patterns can be useful for the assessment of metabolic changes due to the underlying pathology as well as in response to disease-modifying therapies (**Table 4**).

PET IMAGING OF NEUROPATHOLOGY IN PARKINSONIAN DISORDERS

Amyloid

Cerebral amyloid deposition can be assessed on PET using ^{11}C-PIB (Pittsburgh compound B) as well as using other ^{18}F-labeled radiotracers (**Table 2**). Uptake on ^{11}C-PIB PET accurately reflects amyloid deposition antemortem as validated against postmortem neuropathologic findings (280). The apparent gradient of increasing amyloidopathy as visualized on PET can be conceptualized as PD < PD-MCI < PDD < DLB, which has been supported by pathology-proven investigations (281, 282). However, inconsistencies in results may be observed in part due to the substantial pathological heterogeneity evident in these disorders.

An elevated ^{11}C-PIB binding is typically observed in more than 50% of DLB cases, which can be of diagnostic relevance. Compared to controls, studies in DLB have reported elevated amyloid deposition in cortical association areas, frontal and temporoparietal cortices, cingulum and striatum, whereas non-significant differences in ^{11}C-PIB binding were observed in the majority of PDD and all PD cases (283). Amyloid positivity on PET may be more frequent in PDD vs. PD cases, however, such differences were reported inconsistently (284). Compared to DLB, although most studies have found infrequent and modest uptakes in PDD cases (283), others have reported non-significant differences in binding between these two disorders (285). Similarly, a greater ^{11}C-PIB retention was noted in DLB compared to PD, PD-MCI, PDD and controls—where the latter four groups showed no significant differences in the tracer retention (286). Furthermore, the *APOE-ε4* allele has been associated with greater ^{11}C-PIB binding in DLB, PDD and PD-MCI cases (286).

Elevated amyloid pathology on PET is most consistently associated with worse global cognition in LBSD, while its relationship with the timing of dementia onset, motor functions, and dementia progression is mixed (285–287). A recent 1 year study in DLB cases reported greater decline in the mini-mental state examination scores and daily functioning in those with amyloid-positive PET scan (288). In PD, the presence of striatal combined with cortical amyloidopathy was associated with greater cognitive dysfunction vs. cortical amyloidopathy alone, which underscores the cumulative and detrimental influence of amyloid deposition on cognition (289).

Greater ^{11}C-PIB binding has also been associated with lower cerebrospinal fluid levels of amyloid beta-42 peptide in LBSD (290, 291). Lower medial temporal lobe perfusion was identified in amyloid-positive DLB cases (292). Glucose hypometabolism was found to align with regions of amyloid presence (293). On the other hand, ^{11}C-PIB retention was virtually absent in MSA patients (293). Amyloid deposition in the brain quantified using ^{11}C-PIB PET may be seen in PSP, MSA, and CBD/CBS disorders, although it may be attributable to age-related changes (294). Importantly, however, significant tracer retention on amyloid PET combined with cerebrospinal fluid findings (reduced amyloid beta-42 and elevated total tau/phospho-tau) may point

toward primary Alzheimer's disease (AD) pathology, which is exclusionary to CBD/CBS and PSP diagnoses (3, 15). Thus, amyloid imaging plays a critical role in this regard and any future trials of putative tau-based disease modifying therapies that enroll patients with CBS and PSP would need to exclude AD using these methods.

Tau

Several PET radiotracers have been developed to image tauopathy in the brain (**Table 2**) (295). These first-generation radiotracers initially developed for AD have generated considerable interest for their potential to quantify the topological distribution of tau, which can be valuable in monitoring disease progression and improving clinical diagnosis of PSP and CBS. However, several challenges have emerged: 1) lack of specificity and variable affinities to the multiple conformations of tau fibrils (e.g., 4R straight chain filaments in PSP vs. 3/4R paired helical filaments in AD), 2) non-negligible off-target binding to neuromelanin and monoamine oxidase A/B, and 3) the role of primary age-related tauopathy, which is not considered pathogenic and may require careful interpretation of PET data. The first-generation tau PET tracers are under study to evaluate their usefulness, and second-generation tracers with improved binding selectivity and pharmacokinetics are being developed (296).

Overall, tau PET studies reveal distinct patterns of tracer retention in tauopathies. Compared to controls, elevated ^{18}F-AV-1451 uptake in PSP cases was observed in the putamen, pallidum, thalamus, midbrain, and cerebellar dentate nucleus (297–300). Likewise, increased ^{18}F-AV-1451 retention in PSP was detected in the basal ganglia, although with extensive overlap and age-dependent increase in both the PSP and control groups (301). Another study included ^{11}C-PIB-negative PSP patients and observed elevated ^{11}C-PBB3 retention in regions similar to those seen using ^{18}F-AV-1451 tracer (302). The midbrain atrophy rate, however, was identified to be a superior progression biomarker for PSP than the change in ^{18}F-AV-1451 tracer retention (299). In PSP vs. PD, increased uptake in the globus pallidus, midbrain, and subthalamus was detected (303, 304). Most studies did not observe a correlation between clinical severity and ^{18}F-AV-1451 uptake in PSP (299, 304), although results are mixed (300). Midbrain ^{18}F-THK5351 uptake was found to correlate with clinical severity in PSP cases (305).

In CBS vs. controls, asymmetrically elevated ^{18}F-AV-1451 binding contralateral to the clinically affected side was evident in the putamen, globus pallidus, and thalamus, as well as in the motor-related GM and WM subcortical structures, including the midbrain (306). Similarly, ^{18}F-AV-1451 retention was observed in the motor cortex, corticospinal tract, and basal ganglia contralateral to the clinically more affected side in CBS, allowing differentiation from AD and PSP (307). However, cortical atrophy on MRI and ^{18}F-FDG-PET reductions were found to be more widespread compared to the ^{18}F-AV-1451 retention, making this technique a less sensitive indicator of neuronal loss (307). This observation may in part be due to the lack of ^{18}F-AV-1451's specificity for 4-repeat tauopathies. Indeed, post-mortem studies have shown significant binding of ^{18}F-AV-1451 to the AD-related paired helical tau filaments. Conversely, ^{18}F-AV-1451 does not bind appreciably to straight tau filaments associated with 4-repeat tauopathies including PSP and CBS (297, 308). Finally, elevated ^{18}F-AV-1451 binding in DLB was reported in the primary sensorimotor and visual cortices with less involvement of the temporal cortex (vs. AD), suggesting a pattern distinct from AD (309).

The ^{18}F-AV-1451 tracer exhibits an off-target binding to neuromelanin neurons in the midbrain (308, 310). Compared to controls, a visually apparent decline in the midbrain ^{18}F-AV-1451 signal has been reported in PD and PSP patients (310, 311), however, no correlation with disease duration or motor dysfunction was observed (298, 310). The utility of this off-target binding in differentiating PD from PSP requires further research (311). The ^{18}F-AV-1451 tracer also shows an off-target binding to monoamine oxidase (MAO) A and B (312). Furthermore, recent investigations have demonstrated the binding of ^{18}F-THK5351 to MAO-B—a marker for astrogliosis (313). Thus, ^{18}F-THK5351 signal may suggest reactive astrocytes expressing MAO-B protein (314) and the utility of this tracer in monitoring the progression of astrogliosis in CBS has been proposed (315). Overall, an off-target binding to MAO (and other targets) can confound PET data, especially given the abundance of these proteins across the entire brain, which can fluctuate during the course of the disease and with treatment interventions.

Recently, it is suggested that ^{11}C-PBB3 and ^{18}F-AV-1451 radioligands may show differential selectivity for the different tau isoforms, with ^{18}F-AV-1451 binding predominantly to AD-type tau deposits, whereas ^{11}C-PBB3 and the THK family of tracers exhibiting a higher affinity for non-AD tau aggregates (i.e., 4R as seen in CBD/PSP) (316, 317). Moreover, besides binding tau aggregates in PSP, the ^{11}C-PBB3 tracer also showed binding in patients expected to have α-synuclein pathology (318). It was suggested that ^{11}C-PBB3 may exhibit off-target binding to α-synuclein or other associated proteins (318), although further studies are required for confirmation. Indeed, given the conformational diversity of tau fibrils, validating ligands specific to different tau strains would be promising in the differential diagnosis of tauopathies, which can be challenging to diagnose at early stages.

Alpha-Synuclein

Successful imaging of α-synuclein pathology using PET radiotracers is expected to be transformative in clinical and research settings. Several radiolabeled probes for imaging α-synucleinopathy in the brain have been explored, including the phenothiazine, indolinone, indolinone-diene and chalcone analogs, and structural congeners (319). However, no radiotracer has currently been approved for use in humans for diagnostic or research purposes. A consortium of researchers has been convened by the Michael J. Fox Foundation to develop α-synuclein PET radiotracers. When developed, these tracers may allow, (1) the identification of patients at prodromal or early stages of an α-synucleinopathy, (2) evaluation of the degree, location, and progression of the disease, as well as therapeutic effectiveness, (3) differentiation of α-synucleinopathies (LBSD and MSA) from tauopathies (PSP and CBD) and AD, and (4) insights into the contribution of α-synuclein pathology for

TABLE 4 | Summary of neuroimaging findings in α-synucleinopathies.

Disorder, neuroimaging modality	Brief summary of findings[a]	References
Parkinson's disease		
• Structural MRI	MRI signs: loss of dorsolateral nigral hyperintensity (swallow tail sign) ↓ in frontal lobe, basal ganglia (pronounced in advanced PD), hippocampus, anterior cingulate and superior temporal gyri, olfactory bulb and tract volume vs. NC ↓ in orbitofrontal, ventrolateral prefrontal, and occipitoparietal cortex vs. NC ↓ in olfactory bulb and tract volume in PD with olfactory disturbances vs. NC ↓ in left cuneus, precuneus, lingual gyrus and posterior cingulate cortex in PD with freezing of gait vs. PD without ↓ in right perisylvian and inferior temporal cortex along with putaminal shape changes in PD with RBD vs. PD without	(22–27, 29, 31, 39, 40, 42)
• Functional MRI	Resting-state connectivity changes in several networks (default mode, salience, central executive, sensorimotor) and in specific circuits (basal ganglia thalamocortical, cortical-subcortical sensorimotor, cerebellothalamic)	(160, 164–170)
• DWI/DTI MRI	↓ FA in SN and anterior olfactory structures and ↑ *D* in olfactory tract vs. NC ↑ free water in posterior SN over time vs. NC	(52, 55–60, 64, 65)
• Proton MRS	↓ NAA/Cr ratio in SN, LN, temporoparietal and posterior cingulate cortex, and pre-SMA vs. NC	(71–74)
• PET and SPECT [b]	*Dopaminergic system:* [b] ↓ striatal presynaptic DAT binding contralateral to parkinsonian symptomatology with greater reduction in posterior putamen than in anterior putamen or caudate nucleus; normal or ↑ dopamine D2 receptor binding in drug-naïve PD vs. NC	(161, 202, 205, 206, 213, 237–240)
	Glucose metabolism: PD-related spatial covariance pattern may involve ↑ pallidothalamic and pontine activity associated with ↓ metabolism in SMA, premotor cortex, and parietal association areas	(273)
	Neuroinflammation: ↑ microglial activity in pons, basal ganglia, frontal and temporal cortex and midbrain vs. NC	(324, 325)
• Transcranial S [b]	↑ SN echogenicity vs. HC	(179, 192)
Lewy body spectrum disorders		
• Structural MRI	↓ in temporoparietal and occipital cortex and in SMA in PD-MCI vs. cognitively normal PD. Diffuse atrophy in occipital, temporal, right frontal and left parietal lobe; and in putamen, hippocampus, parahippocampal region, anterior cingulate gyrus, nucleus accumbens and thalamic nuclei in PDD vs. NC. Atrophy in occipital lobe and entorhinal cortex in PDD vs. PD; in temporoparietal and occipital cortex in DLB vs. PDD. Preserved hippocampal volume (mainly cornu ammonis-1 subfield) in DLB vs. AD. *APOE*-ε4 may influence hippocampal atrophy in PDD/DLB	(8, 9, 23, 24, 79, 81, 86)
• DWI/DTI MRI	↑ *D* in nucleus basalis of Meynert in PD-MCI vs. cognitively normal PD ↑ *D* and ↓ FA in corpus callosum, pericallosal regions, caudate nucleus, amygdala, inferior longitudinal fasciculus, precuneus, and frontal, parietal, and occipital white matter with milder mediotemporal involvement in DLB vs. NC ↓ FA in bilateral posterior cingulate bundle in PDD vs. PD	(9, 60, 92–95)
• Proton MRS	↓ NAA/Cr ratio in hippocampus in DLB vs. NC, albeit to a lesser degree vs. AD ↓ NAA/Cr ratio in posterior cingulate gyrus in PDD vs. PD	(97, 98)
• PET and SPECT [b]	*Perfusion:* occipital hypoperfusion in DLB vs. NC	(247)
	Glucose metabolism: occipital hypometabolism with moderate mediotemporal hypometabolism in DLB vs. AD and HC. Hypometabolism in anterior cingulate cortex may distinguish DLB from PDD PD-related cognitive spatial covariance pattern may involve metabolic ↓ in medial frontal and parietal association regions, and metabolic ↑ in cerebellar cortex and dentate nuclei	(269, 270, 273)
	Dopaminergic system: [b] ↓ striatal presynaptic DAT binding in PDD/DLB vs. NC	(220–223)
	Amyloid: the gradient of increasing amyloidopathy on PET may be conceptualized as PD < PD-MCI < PDD < DLB	(281–287, 290, 291)
	Tau: ↑ binding in primary sensorimotor and visual cortices with less mediotemporal involvement in DLB vs. AD	(309)
	Neuroinflammation: ↑ microglial activity in frontal and temporal lobe, striatum, precuneus, and dorsolateral prefrontal cortex in PD-MCI vs. NC; ↑ microglial activity in anterior and posterior cingulate, striatum, and in frontal, temporal, parietal and occipital cortices with ↑ parieto-occipital binding in PDD vs. NC; the spatial extent of microglial involvement was ↑ in PDD vs. PD	(327, 330)
• Transcranial S [b]	↑ SN echogenicity in DLB and PDD vs. HC	(193)
Multiple system atrophy		
• Structural MRI	MRI signs: putaminal rim sign, hot cross bun sign, middle cerebellar peduncles (MCP) sign Striatonigral and olivopontocerebellar atrophy is observed in MSA vs. NC ↓ in putamen, MCP, cerebellum, and pons in MSA-P vs. PD Supratentorial atrophy (putamen) in MSA-P, whereas infratentorial atrophy in MSA-C may be more predominant	(11, 28, 71, 99, 102, 103, 106–110)

(Continued)

TABLE 4 | Continued

Disorder, neuroimaging modality	Brief summary of findings[a]	References
Multiple system atrophy		
• DWI/DTI MRI	↑ *D* in putamen in MSA-P vs. PD, MSA-C, and NC. ↓ FA and ↑ ADC in putamen, cerebellum, and pons in MSA-P vs. PD and NC ↑ *D* in MCP and pons in MSA vs. PSP ↑ ADC in putamen and pons in MSA-P vs. MSA-C; cerebellum and MCP in MSA-C vs. MSA-P ↑ free water-corrected FA in putamen and caudate nucleus in MSA vs. NC	(66, 113–116)
• Proton MRS	↓ NAA/Cr ratio in putamen in MSA-P, and in pontine base in both MSA-P and MSA-C vs. NC ↓ NAA/Cr ratio in putamen and pontine base may discriminate MSA-P from PD	(120)
• PET and SPECT [b]	*Glucose metabolism:* MSA-related spatial covariance pattern may involve metabolic ↓ in putamen and cerebellum	(273, 279)
	Dopaminergic system: [b] ↓ striatal presynaptic DAT binding and ↓ dopamine D2 receptor binding vs. NC	(225, 241, 242)
	Neuroinflammation: ↑ microglial activity in dorsolateral prefrontal cortex, putamen, pallidum, pons, and SN vs. NC	(332)
• Transcranial S [b]	↑ LN echogenicity along with normal or ↑ SN echogenicity may be seen	(188, 197)

AD, Alzheimer's disease; ADC, apparent diffusion coefficient; D, mean diffusivity; DAT, dopamine transporter; DLB, dementia with Lewy bodies; DWI/DTI, diffusion-weighted and diffusion tensor imaging; FA, fractional anisotropy; LN, lentiform nucleus; MCP, middle cerebellar peduncle; MRI, magnetic resonance imaging; MRS, magnetic resonance spectroscopy; MSA, multiple system atrophy; MSA-C, MSA-cerebellar type; MSA-P, MSA-parkinsonian type; NAA, N-acetyl aspartate; NC, normal controls; PD, Parkinson's disease; PDD, Parkinson's disease dementia; PD-MCI, Parkinson's disease-mild cognitive impairment; PET, positron emission tomography; PSP, progressive supranuclear palsy; RBD, rapid eye movement sleep behavior disorder; SMA, supplementary motor area; SN, substantia nigra; SPECT, single photon emission computed tomography; transcranial S, transcranial sonography. a = not all findings discussed in the review are presented; please refer to relevant sections of the review for full details. b = readers are referred to Table 3 in Saeed et al. (10) for further comparisons of SPECT, PET, and transcranial sonography findings in Parkinson's disease and atypical Parkinsonian syndromes.

clinical outcomes (320). Some of the developmental challenges [see reference (321)], although similar to those of tau PET radiotracers, include the intracellular nature of most α-synuclein aggregates requiring ideal lipophilicity and molecular size, multiple α-synuclein strains that may interact differently with some tracers, colocalization of α-synuclein with other protein aggregates, relatively less abundance of α-synuclein over amyloid and tau aggregates requiring higher tracer selectivity, as well as the potential for off-target binding which may necessitate further validation.

PET IMAGING OF NEUROINFLAMMATION IN PARKINSONIAN DISORDERS

Microglia are the primary macrophages involved in the innate immune response of the central nervous system. It is suggested that microglia-mediated inflammatory processes can aggravate injury, leading to events that may result in neurodegeneration (322). A widely used PET ligand for imaging neuroinflammation has been ^{11}C-PK11195, which binds to the 18 kDa translocator protein (TSPO), located on the outer mitochondrial membrane in microglia. Upregulation of TSPO is suggestive of microglial activation in the central nervous system. However, there are several limitations of ^{11}C-PK11195 (e.g., non-specific binding, low brain penetration, high plasma protein binding), which has prompted the development of improved second-generation radiotracers, including ^{11}C-PBR28 and ^{18}F-FEPPA (323).

Compared to controls, increased ^{11}C-PK11195 binding in PD was observed in the pons, basal ganglia, frontal and temporal cortices (324), as well as in the midbrain contralateral to the clinically affected side (325). The correlation of ^{11}C-PK11195 binding with clinical severity or with putaminal presynaptic dopaminergic integrity is inconsistently reported (324, 325). Recently, considerable interindividual variability in the binding affinity of second-generation radiotracers (e.g., ^{18}F-FEPPA) to the TSPO protein has been observed, which is attributed to a single nucleotide polymorphism located at exon 4 of the *TSPO* gene (rs6971) (323, 326). Three patterns of binding affinities based on this genetic polymorphism have been identified: low, high, and mixed affinity binders. This finding suggests a possible interaction between the rs6791 polymorphism and neuroinflammation resulting in interindividual variability in the outcome measures. Further studies are warranted to study this interaction. Increased ^{18}F-FEPPA binding was also reported in PD-MCI in the frontal and temporal lobe, striatum, precuneus, and dorsolateral prefrontal cortex in association with amyloid deposition in these regions (327), suggesting a link between amyloidopathy and neuroinflammation.

RBD is a significant risk factor for the development of α-synucleinopathies (236). In polysomnography-confirmed cases with idiopathic RBD, elevated ^{11}C-PK11195 binding was reported in the occipital lobe (probably highlighting those at increased risk of developing DLB) (328), as well as in the left SN, although no significant differences in ^{11}C-PK11195 binding were noted in the putamen or caudate (despite lower putaminal ^{18}F-dopa uptake) (329). Longitudinal studies are needed to identify biomarkers for those likely to convert earlier vs. later into an overt symptomatic synucleinopathy (i.e., dementia or parkinsonism) when presenting with RBD.

PDD patients exhibited widespread microglial activation vs. controls in the anterior and posterior cingulate, striatum, as well as in the frontal, temporal, parietal, and occipital cortices, with pronounced parieto-occipital binding (330). Compared to PD,

however, the spatial extent of microglial cortical involvement was greater in PDD (330). Additionally, an inverse correlation between microglial activation and glucose metabolism in the temporoparietal cortex has been reported in PDD (331). As consistent with the known neuropathological burden, augmented ^{11}C-PK11195 binding compared to controls was evident in the dorsolateral prefrontal cortex, putamen, pallidum, pons, and SN in MSA cases (332), and in the basal ganglia,

TABLE 5 | Summary of neuroimaging findings in tauopathies.

Disorder, neuroimaging modality	Brief summary of findings[a]	References
Progressive supranuclear palsy		
• Structural MRI	MRI signs: hummingbird sign, morning glory sign ↓ in midbrain and SCP vs. PD, MSA-P, CBD/CBS, and NC ↓ in brainstem and gray matter of frontal lobe vs. NC Magnetic resonance parkinsonism index: ratios of pons-to-midbrain area and MCP-to-SCP widths were ↑ in PSP vs. PD, MSA-P and NC. The revised version of index incorporates third ventricle width and frontal horns width	(121–129, 131, 132, 136)
• DWI/DTI MRI	↑ *D* and ↓ FA in multiple regions including midbrain, SCP, orbitofrontal white matter, thalamus, motor and SMA vs. NC ↑ *D* in the decussation of SCP vs. MSA and PD ↑ ADC in putamen, globus pallidus, and caudate nucleus vs. PD ↓ FA in SCP in PSP-RS vs. PSP-parkinsonism ↑ free water in posterior SN vs. MSA, PD and NC; ↑ free water-corrected FA in caudate nucleus, putamen, thalamus and vermis and ↓ in SCP and corpus callosum vs. NC	(66, 115, 118, 132, 139–142, 145–147)
• Proton MRS	↓ NAA/Cr ratio in LN, brainstem, centrum semiovale, frontal, and precentral cortex vs. NC ↓ NAA/choline ratio in LN vs. NC; ↓ NAA/Cr ratio in putamen vs. PD and MSA ↓ cerebellar NAA/Cr and NAA/myo-inositol ratios in PSP-RS vs. NC, and ↓ cerebellar NAA/Cr ratio in PSP-RS vs. PD	(77, 148–150)
• PET and SPECT [b]	*Dopaminergic system:* [b] ↓ striatal presynaptic DAT binding, with ↑ but fairly uniform DAT loss in striatum vs. PD ↓ dopamine D2 receptor binding vs. NC	(200, 204, 229, 230, 239, 242)
	Glucose metabolism: PSP-related spatial covariance pattern may show hypometabolism in brainstem and mediofrontal cortex	(273, 279)
	Tau: ↑ binding in putamen, pallidum, thalamus, midbrain, cerebellar dentate nucleus, and basal ganglia vs. NC ↑ binding in globus pallidus, midbrain, and subthalamus in PSP vs. PD	(297–301, 303, 304)
	Neuroinflammation: ↑ microglial activity in basal ganglia, midbrain, frontal lobe, and cerebellum vs. NC	(324)
Corticobasal degeneration/syndrome		
• Structural MRI	Atrophy patterns align with the "true" underlying pathology The predominant clinical syndrome in CBS relates closely to regional atrophy patterns In general, asymmetric cortical atrophy in frontoparietal lobe contralateral to more affected side in CBD/CBS vs. NC ↓ in bilateral premotor cortex, superior parietal lobules, and striatum in CBS vs. NC ↓ in dorsofrontal and parietal cortex and ↑ global brain atrophy in CBS vs. PSP; ↓ in midbrain in PSP vs. CBS	(6, 121, 123, 129, 152, 153, 155, 156)
• DWI/DTI MRI	↑ *D* and ↓ FA in posterior truncus of corpus callosum in CBS vs. PD and NC ↓ FA in long frontoparietal connecting tracts, intraparietal associative fibers, corpus callosum, and sensorimotor cortical projections in CBS vs. NC	(59, 152, 158)
• Proton MRS	↓ NAA/Choline and NAA/Cr ratios in contralateral frontoparietal cortex, LN and centrum semiovale in CBS vs. NC ↓ NAA/Cr ratio in frontal cortex and asymmetrically in putamen in CBS vs. PD, MSA and vascular parkinsonism	(149, 150, 159)
• PET and SPECT [b]	*Glucose metabolism:* CBS-related spatial covariance pattern may show asymmetric, bilateral hypometabolism involving frontal and parietal cortex, thalamus, and caudate nucleus, with ↑ abnormalities contralaterally	(267)
	Dopaminergic system: [b] ↓ striatal presynaptic DAT binding with hemispheric asymmetry vs. PD.	(226, 227)
	Tau: ↑ asymmetric binding contralateral to the clinically affected side in putamen, globus pallidus, thalamus, and midbrain vs. NC, and in motor cortex, corticospinal tract, and basal ganglia vs. AD and PSP	(306, 307)
	Neuroinflammation: ↑ microglial activity in caudate nucleus, putamen, SN, pons, pre- and post-central gyrus and frontal lobe vs. NC	(334)

AD, Alzheimer's disease; ADC, apparent diffusion coefficient; APOE-ε4, apolipoprotein E ε4-allele; CBD, corticobasal degeneration; CBS, corticobasal syndrome; NC, normal controls; Cr, creatine; D, mean diffusivity; DAT, dopamine transporter; DWI/DTI, diffusion-weighted and diffusion tensor imaging; FA, fractional anisotropy; LN, lentiform nucleus; MCP, middle cerebellar peduncle; MRI, magnetic resonance imaging; MRS, magnetic resonance spectroscopy; MSA, multiple system atrophy; MSA-P, MSA-parkinsonian type; NAA, N-acetyl aspartate; PD, Parkinson's disease; PET, positron emission tomography; PSP, progressive supranuclear palsy; PSP-RS, PSP-Richardson's syndrome; SCP, superior cerebellar peduncle; SMA, supplementary motor area; SN, substantia nigra; SPECT, single photon emission computed tomography. a = not all findings discussed in the review are presented; please refer to relevant sections of the review for full details. b = readers are referred to Table 3 in Saeed et al. (10) for further comparisons of SPECT, PET, and transcranial sonography findings in Parkinson's disease vs. atypical Parkinsonian syndromes.

midbrain, frontal lobe, and cerebellum in PSP cases (324). Microglial activity in PSP-RS was identified in the thalamus, putamen, and pallidum (333). Finally, CBS patients typically show ^{11}C-PK11195 uptake in the caudate nucleus, putamen, SN, pons, pre- and post-central gyrus and the frontal lobe (334). Although, the overall patterns of microglial activity align with neuropathological findings, these patterns may not allow differentiation in a clinical setting, and may be more appropriate as biomarkers of prodromal changes or therapeutic effectiveness in clinical trials.

Summary of neuroimaging findings in α-synucleinopathies and tauopathies are presented (**Tables 4**, **5**).

CONCLUSIONS

Research using multimodal neuroimaging has facilitated a better understanding of the disease processes in PD and atypical PS—neurodegenerative disorders that often present with substantial clinical and pathological heterogeneity. As per the "multimodal approach," multiple biomarkers obtained from different neuroimaging modalities can provide distinct yet corroborative data on the underlying neurodegenerative processes, and this integrative approach may prove superior to single-modality-based methods. Future efforts are needed to validate biomarkers in well-characterized cohorts. Some of these biomarkers may help improve the current consensus diagnostic guidelines and allow clinicians to ascertain an optimal approach for diagnostic purposes in combination with their experience and professional training.

AUTHOR CONTRIBUTIONS

US reviewed the literature, wrote the manuscript, and prepared tables and figures. MM supervised the writing of this review paper. MM and AL reviewed and critiqued the manuscript for intellectual content. All authors read and approved the final manuscript.

ACKNOWLEDGMENTS

The authors would like to acknowledge support from New Investigator Award from Parkinson Society Canada and Early Researcher Award to MM from the Ministry of Research, Innovation, and Science (MRIS; Ontario). The authors also acknowledge support from the Ontario Brain Institute, an independent non-profit corporation, funded partially by the Ontario government. The opinions, results and conclusions are those of the authors and no endorsement by the Ontario Brain Institute is intended or should be inferred. Matching funds were provided by participating hospital and research institute foundations, including the Baycrest Foundation, Bruyère Research Institute, Center for Addiction and Mental Health Foundation, London Health Sciences Foundation, McMaster University Faculty of Health Sciences, Ottawa Brain and Mind Research Institute, Queen's University Faculty of Health Sciences, Providence Care (Kingston), St. Michael's Hospital, Sunnybrook Health Sciences Foundation, the Thunder Bay Regional Health Sciences Center, the University of Ottawa Faculty of Medicine, and the Windsor/Essex County ALS Association.

REFERENCES

1. Parkinson's Disease Foundation. *Statistics*. Available online at: https://www.parkinson.org/Understanding-Parkinsons/Statistics (accessed April 14, 2020).
2. Kalia LV, Lang AE. Parkinson's disease. *Lancet*. (2015) 386:896–912. doi: 10.1016/S0140-6736(14)61393-3
3. Höglinger GU, Respondek G, Stamelou M, Kurz C, Josephs KA, Lang AE, et al. Clinical diagnosis of progressive supranuclear palsy: the movement disorder society criteria. *Mov Disord*. (2017) 32:853–64. doi: 10.1002/mds.26987
4. Armstrong MJ. Progressive supranuclear palsy: an update. *Curr Neurol Neurosci Rep*. (2018) 18:12. doi: 10.1007/s11910-018-0819-5
5. Wadia PM, Lang AE. The many faces of corticobasal degeneration. *Parkinsonism Relat Disord*. (2007) 13(Suppl. 3):S336–40. doi: 10.1016/S1353-8020(08)70027-0
6. Lee SE, Rabinovici GD, Mayo MC, Wilson SM, Seeley WW, Dearmond SJ, et al. Clinicopathological correlations in corticobasal degeneration. *Ann Neurol*. (2011) 70:327–40. doi: 10.1002/ana.22424
7. Braak H, Del Tredici K, Rüb U, De Vos RAI, Jansen Steur ENH, Braak E. Staging of brain pathology related to sporadic Parkinson's disease. *Neurobiol Aging*. (2003) 24:197–211. doi: 10.1016/S0197-4580(02)00065-9
8. McKeith IG, Boeve BF, Dickson DW, Halliday G, Taylor J-P, Weintraub D, et al. Diagnosis and management of dementia with lewy bodies: fourth consensus report of the DLB consortium. *Neurology*. (2017) 89:88–100. doi: 10.1212/WNL.0000000000004058
9. Saeed U, Mirza SS, MacIntosh BJ, Herrmann N, Keith J, Ramirez J, et al. APOE-ε4 associates with hippocampal volume, learning, and memory across the spectrum of alzheimer's disease and dementia with lewy bodies. *Alzheimer's Dement*. (2018) 14:1137–47. doi: 10.1016/j.jalz.2018.04.005
10. Saeed U, Compagnone J, Aviv RI, Strafella AP, Black SE, Lang AE, et al. Imaging biomarkers in Parkinson's disease and parkinsonian syndromes: current and emerging concepts. *Transl Neurodegen*. (2017) 6:8. doi: 10.1186/s40035-017-0076-6
11. Fanciulli A, Wenning GK. Multiple-system atrophy. *N Engl J Med*. (2015) 372:249–63. doi: 10.1056/NEJMra1311488
12. Erkkinen MG, Kim MO, Geschwind MD. Clinical neurology and epidemiology of the major neurodegenerative diseases. *Cold Spring Harb Perspect Biol*. (2018) 10:a033118. doi: 10.1101/cshperspect.a033118
13. Dickson DW, Rademakers R, Hutton ML. Progressive supranuclear palsy: pathology and genetics. *Brain Pathol*. (2007) 17:74–82. doi: 10.1111/j.1750-3639.2007.00054.x
14. Williams DR, Lees AJ. Progressive supranuclear palsy: clinicopathological concepts and diagnostic challenges. *Lancet Neurol*. (2009) 8:270–79. doi: 10.1016/S1474-4422(09)70042-0
15. Armstrong MJ, Litvan I, Lang AE, Bak TH, Bhatia KP, Borroni B, et al. Criteria for the diagnosis of corticobasal degeneration. *Neurology*. (2013) 80:496–503. doi: 10.1212/WNL.0b013e31827f0fd1
16. Rana AQ, Saeed U, Masroor MS, Yousuf MS, Siddiqui I. A cross-sectional study investigating clinical predictors and physical experiences of pain in Parkinson's disease. *Funct Neurol*. (2013) 28:297–304.
17. Postuma RB, Berg D, Stern M, Poewe W, Olanow CW, Oertel W, et al. MDS clinical diagnostic criteria for Parkinson's disease. *Mov Disord*. (2015) 30:1591–601. doi: 10.1002/mds.26424
18. Jellinger KA, Korczyn AD. Are dementia with lewy bodies and Parkinson's disease dementia the same disease? *BMC Med*. (2018) 16:34. doi: 10.1186/s12916-018-1016-8

19. Gilman S, Wenning GK, Low PA, Brooks DJ, Mathias CJ, Trojanowski JQ, et al. Second consensus statement on the diagnosis of multiple system atrophy. *Neurology*. (2008) 71:670–6. doi: 10.1212/01.wnl.0000324625.00404.15
20. Respondek G, Stamelou M, Kurz C, Ferguson LW, Rajput A, Chiu WZ, et al. The phenotypic spectrum of progressive supranuclear palsy: a retrospective multicenter study of 100 definite cases. *Mov Disord*. (2014) 29:1758–66. doi: 10.1002/mds.26054
21. Litvan I, Agid Y, Goetz C, Jankovic J, Wenning GK, Brandel JP, et al. Accuracy of the clinical diagnosis of corticobasal degeneration: a clinicopathologic study. *Neurology*. (1997) 48:119–25. doi: 10.1212/WNL.48.1.119
22. Xu X, Han Q, lin J, Wang L, Wu F, Shang H. Grey matter abnormalities in Parkinson's disease: a voxel-wise meta-analysis. *Eur J Neurol*. (2019) 27:653–9. doi: 10.1111/ene.14132
23. Burton EJ, McKeith IG, Burn DJ, Williams ED, O'Brien JT. Cerebral atrophy in Parkinson's disease with and without dementia: a comparison with Alzheimer's disease, dementia with Lewy bodies and controls. *Brain*. (2004) 127:791–800. doi: 10.1093/brain/awh088
24. Summerfield C, Junqué C, Tolosa E, Salgado-Pineda P, Gómez-Ansón B, Martí MJ, et al. Structural brain changes in Parkinson disease with dementia: a voxel-based morphometry study. *Arch Neurol*. (2005) 62:281–5. doi: 10.1001/archneur.62.2.281
25. Tinaz S, Courtney MG, Stern CE. Focal cortical and subcortical atrophy in early Parkinson's disease. *Mov Disord*. (2011) 26:436–41. doi: 10.1002/mds.23453
26. Pitcher TL, Melzer TR, MacAskill MR, Graham CF, Livingston L, Keenan RJ, et al. Reduced striatal volumes in Parkinson's disease: a magnetic resonance imaging study. *Transl Neurodegener*. (2012) 1:17 doi: 10.1186/2047-9158-1-17
27. Tessitore A, Amboni M, Cirillo G, Corbo D, Picillo M, Russo A, et al. Regional gray matter atrophy in patients with Parkinson disease and freezing of gait. *AJNR Am J Neuroradiol*. (2012) 33:1804–9. doi: 10.3174/ajnr.A3066
28. Schulz JB, Skalej M, Wedekind D, Luft AR, Abele M, Voigt K, et al. Magnetic resonance imaging-based volumetry differentiates idiopathic Parkinson's syndrome from multiple system atrophy and progressive supranuclear palsy. *Ann Neurol*. (1999) 45:65–74.
29. Chen S, Tan H-Y, Wu Z-H, Sun C-P, He J-X, Li X-C, et al. Imaging of olfactory bulb and gray matter volumes in brain areas associated with olfactory function in patients with Parkinson's disease and multiple system atrophy. *Eur J Radiol*. (2013) 83:564–70. doi: 10.1016/j.ejrad.2013.11.024
30. Lee SY, Chen MH, Chiang PL, Chen HL, Chou KH, Chen YC, et al. Reduced gray matter volume and respiratory dysfunction in Parkinson's disease: a voxel-based morphometry study. *BMC Neurol*. (2018) 18:73. doi: 10.1186/s12883-018-1074-8
31. Blair JC, Barrett MJ, Patrie J, Flanigan JL, Sperling SA, Elias WJ, et al. Brain MRI reveals ascending atrophy in Parkinson's disease across severity. *Front Neurol*. (2019) 10:1329. doi: 10.3389/fneur.2019.01329
32. Visanji NP, Brooks PL, Hazrati L-N, Lang AE. The prion hypothesis in Parkinson's disease: braak to the future. *Acta Neuropathol Commun*. (2013) 1:2. doi: 10.1186/2051-5960-1-2
33. Fonov V, Evans AC, Botteron K, Almli CR, McKinstry RC, Collins DL. Unbiased average age-appropriate atlases for pediatric studies. *Neuroimage*. (2011) 54:313–27. doi: 10.1016/j.neuroimage.2010.07.033
34. Damier P, Hirsch EC, Agid Y, Graybiel AM. The substantia nigra of the human brain: I. Nigrosomes and the nigral matrix, a compartmental organization based on calbindin D(28K) immunohistochemistry. *Brain*. (1999) 122:1421–36. doi: 10.1093/brain/122.8.1421
35. Damier P, Hirsch EC, Agid Y, Graybiel AM. The substantia nigra of the human brain: II. Patterns of loss of dopamine-containing neurons in Parkinson's disease. *Brain*. (1999) 122:1437–48. doi: 10.1093/brain/122.8.1437
36. Blazejewska AI, Schwarz ST, Pitiot A, Stephenson MC, Lowe J, Bajaj N, et al. Visualization of nigrosome 1 and its loss in PD: pathoanatomical correlation and *in vivo* 7 T MRI. *Neurology*. (2013) 81:534–40. doi: 10.1212/WNL.0b013e31829e6fd2
37. Castellanos G, Fernández-Seara MA, Lorenzo-Betancor O, Ortega-Cubero S, Puigvert M, Uranga J, et al. Automated neuromelanin imaging as a diagnostic biomarker for Parkinson's disease. *Mov Disord*. (2015) 30:945–52. doi: 10.1002/mds.26201
38. Lehéricy S, Bardinet E, Poupon C, Vidailhet M, François C. 7 Tesla magnetic resonance imaging: a closer look at substantia nigra anatomy in Parkinson's disease. *Mov Disord*. (2014) 29:1574–81. doi: 10.1002/mds.26043
39. Schwarz ST, Afzal M, Morgan PS, Bajaj N, Gowland PA, Auer DP. The "swallow tail" appearance of the healthy nigrosome - a new accurate test of Parkinson's disease: a case-control and retrospective cross-sectional MRI study at 3T. *PLoS ONE*. (2014) 9:e93814. doi: 10.1371/journal.pone.0093814
40. Chougar L, Pyatigorskaya N, Degos B, Grabli D, Lehéricy S. The role of magnetic resonance imaging for the diagnosis of atypical parkinsonism. *Front Neurol*. (2020) 11:665. doi: 10.3389/fneur.2020.00665
41. Reimão S, Pita Lobo P, Neutel D, Guedes LC, Coelho M, Rosa MM, et al. Substantia nigra neuromelanin-MR imaging differentiates essential tremor from Parkinson's disease. *Mov Disord*. (2015) 30:953–9. doi: 10.1002/mds.26182
42. Rahayel S, Gaubert M, Postuma RB, Montplaisir J, Carrier J, Monchi O, et al. Brain atrophy in Parkinson's disease with polysomnographyconfirmed REM sleep behavior disorder. *Sleep*. (2019) 42:zsz062. doi: 10.1093/sleep/zsz062
43. Kamps S, van den Heuvel OA, van der Werf YD, Berendse HW, Weintraub D, Vriend C. Smaller subcortical volume in Parkinson patients with rapid eye movement sleep behavior disorder. *Brain Imaging Behav*. (2019) 13:1352–60. doi: 10.1007/s11682-018-9939-4
44. Barber TR, Griffanti L, Bradley KM, McGowan DR, Lo C, Mackay CE, et al. Nigrosome 1 imaging in REM sleep behavior disorder and its association with dopaminergic decline. *Ann Clin Transl Neurol*. (2020) 7:26–35. doi: 10.1002/acn3.50962
45. Oikawa H, Sasaki M, Tamakawa Y, Ehara S, Tohyama K. The substantia nigra in Parkinson disease: proton density-weighted spin-echo and fast short inversion time inversion-recovery MR findings. *Am J Neuroradiol*. (2002) 23:1747–56.
46. Péran P, Cherubini A, Assogna F, Piras F, Quattrocchi C, Peppe A, et al. Magnetic resonance imaging markers of Parkinson's disease nigrostriatal signature. *Brain*. (2010) 133:3423–33. doi: 10.1093/brain/awq212
47. Minati L, Grisoli M, Carella F, De Simone T, Bruzzone MG, Savoiardo M. Imaging degeneration of the substantia Nigra in Parkinson disease with inversion-recovery MR imaging. *Am J Neuroradiol*. (2007) 28:309–13.
48. Kwon D-H, Kim J-M, Oh S-H, Jeong H-J, Park S-Y, Oh E-S, et al. Seven-Tesla magnetic resonance images of the substantia nigra in Parkinson disease. *Ann Neurol*. (2012) 71:267–77. doi: 10.1002/ana.22592
49. Cho Z-H, Oh S-H, Kim J-M, Park S-Y, Kwon D-H, Jeong H-J, et al. Direct visualization of Parkinson's disease by *in vivo* human brain imaging using 7.0T magnetic resonance imaging. *Mov Disord*. (2011) 26:713–8. doi: 10.1002/mds.23465
50. Cosottini M, Frosini D, Pesaresi I, Costagli M, Biagi L, Ceravolo R, et al. MR imaging of the substantia nigra at 7 T enables diagnosis of Parkinson disease. *Radiology*. (2014) 271:831–8. doi: 10.1148/radiol.14131448
51. Ulla M, Bonny JM, Ouchchane L, Rieu I, Claise B, Durif F. Is R_2^* a new MRI biomarker for the progression of Parkinson's disease? A longitudinal follow-up. *PLoS ONE*. (2013) 8:e57904. doi: 10.1371/journal.pone.0057904
52. Arribarat G, Pasternak O, De Barros A, Galitzky M, Rascol O, Péran P. Substantia nigra locations of iron-content, free-water and mean diffusivity abnormalities in moderate stage Parkinson's disease. *Parkinsonism Relat Disord*. (2019) 65:146–52. doi: 10.1016/j.parkreldis.2019.05.033
53. Wieler M, Gee M, Camicioli R, Martin WRW. Freezing of gait in early Parkinson's disease: nigral iron content estimated from magnetic resonance imaging. *J Neurol Sci*. (2016) 361:87–91. doi: 10.1016/j.jns.2015.12.008
54. Acosta-Cabronero J, Cardenas-Blanco A, Betts MJ, Butryn M, Valdes-Herrera JP, Galazky I, et al. The whole-brain pattern of magnetic susceptibility perturbations in Parkinson's disease. *Brain*. (2017) 140:118–31. doi: 10.1093/brain/aww278
55. Cochrane CJ, Ebmeier KP. Diffusion tensor imaging in parkinsonian syndromes: a systematic review and meta-analysis. *Neurology*. (2013) 80:857–64. doi: 10.1212/WNL.0b013e318284070c
56. Vaillancourt DE, Prodoehl J, Abraham I, Corcos DM, Zhou XJ, Cornelia CL, et al. High-resolution diffusion tensor imaging in the substantia nigra of *de novo* Parkinson disease. *Neurology*. (2009) 72:1378–84. doi: 10.1212/01.wnl.0000340982.01727.6e

57. Scherfler C, Schocke MF, Seppi K, Esterhammer R, Brenneis C, Jaschke W, et al. Voxel-wise analysis of diffusion weighted imaging reveals disruption of the olfactory tract in Parkinson's disease. *Brain.* (2006) 129:538–42. doi: 10.1093/brain/awh674
58. Rolheiser TM, Fulton HG, Good KP, Fisk JD, McKelvey JR, Scherfler C, et al. Diffusion tensor imaging and olfactory identification testing in early-stage Parkinson's disease. *J Neurol.* (2011) 258:1254–60. doi: 10.1007/s00415-011-5915-2
59. Boelmans K, Bodammer NC, Suchorska B, Kaufmann J, Ebersbach G, Heinze HJ, et al. Diffusion tensor imaging of the corpus callosum differentiates corticobasal syndrome from Parkinson's disease. *Parkinsonism Relat Disord.* (2010) 16:498–502. doi: 10.1016/j.parkreldis.2010.05.006
60. Schulz J, Pagano G, Fernández Bonfante JA, Wilson H, Politis M. Nucleus basalis of meynert degeneration precedes and predicts cognitive impairment in Parkinson's disease. *Brain*. (2018) 141:1501–16. doi: 10.1093/brain/awy072
61. Du G, Lewis MM, Kanekar S, Sterling NW, He L, Kong L, et al. Combined diffusion tensor imaging and apparent transverse relaxation rate differentiate Parkinson disease and atypical parkinsonism. *Am J Neuroradiol.* (2017) 38:966–72. doi: 10.3174/ajnr.A5136
62. Safai A, Prasad S, Chougule T, Saini J, Pal PK, Ingalhalikar M. Microstructural abnormalities of substantia nigra in Parkinson's disease: a neuromelanin sensitive MRI atlas based study. *Hum Brain Map*. (2019) 41:1323–33. doi: 10.1101/686154
63. Bledsoe IO, Stebbins GT, Merkitch D, Goldman JG. White matter abnormalities in the corpus callosum with cognitive impairment in Parkinson disease. *Neurology*. (2018) 91:e2244–55. doi: 10.1212/WNL.0000000000006646
64. Burciu RG, Ofori E, Archer DB, Wu SS, Pasternak O, McFarland NR, et al. Progression marker of Parkinson's disease: a 4-year multi-site imaging study. *Brain*. (2017) 140:2183–92. doi: 10.1093/brain/awx146
65. Ofori E, Pasternak O, Planetta PJ, Li H, Burciu RG, Snyder AF, et al. Longitudinal changes in free-water within the substantia nigra of Parkinson's disease. *Brain*. (2015) 138:2322–31. doi: 10.1093/brain/awv136
66. Planetta PJ, Ofori E, Pasternak O, Burciu RG, Shukla P, Desimone JC, et al. Free-water imaging in Parkinson's disease and atypical parkinsonism. *Brain*. (2016) 139:495–508. doi: 10.1093/brain/awv361
67. Guttuso T, Bergsland N, Hagemeier J, Lichter DG, Pasternak O, Zivadinov R. Substantia nigra free water increases longitudinally in Parkinson disease. *Am J Neuroradiol*. (2018) 39:479–84. doi: 10.3174/ajnr.A5545
68. Ofori E, Pasternak O, Planetta PJ, Burciu R, Snyder A, Febo M, et al. Increased free water in the substantia nigra of Parkinson's disease: a single-site and multi-site study. *Neurobiol Aging*. (2015) 36:1097–104. doi: 10.1016/j.neurobiolaging.2014.10.029
69. Guan J, Rong Y, Wen Y, Wu H, Qin H, Zhang Q, et al. Detection and application of neurochemical profile by multiple regional 1H-MRS in Parkinson's disease. *Brain Behav*. (2017) 7:e00792. doi: 10.1002/brb3.792
70. Cao H, Shi J, Cao B, Kang B, Zhang M, Qu Q. Evaluation of the braak staging of brain pathology with 1H-MRS in patients with Parkinson's disease. *Neurosci Lett*. (2017) 660:57–62. doi: 10.1016/j.neulet.2017.08.050
71. Tsuda M, Asano S, Kato Y, Murai K, Miyazaki M. Differential diagnosis of multiple system atrophy with predominant parkinsonism and Parkinson's disease using neural networks. *J Neurol Sci*. (2019) 401:19–26. doi: 10.1016/j.jns.2019.04.014
72. Taylor-Robinson SD, Turjanski N, Bhattacharya S, Seery JP, Sargentoni J, Brooks DJ, et al. A proton magnetic resonance spectroscopy study of the striatum and cerebral cortex in Parkinson's disease. *Metab Brain Dis.* (1999) 14:45–55. doi: 10.1023/A:1020609530444
73. Camicioli RM, Hanstock CC, Bouchard TP, Gee M, Fisher NJ, Martin WRW. Magnetic resonance spectroscopic evidence for presupplementary motor area neuronal dysfunction in Parkinson's disease. *Mov Disord.* (2007) 22:382–6. doi: 10.1002/mds.21288
74. Firbank MJ, Harrison RM, O'Brien JT. A comprehensive review of proton magnetic resonance spectroscopy studies in dementia and Parkinson's disease. *Dement Geriatr Cogn Disord.* (2002) 14:64–76. doi: 10.1159/000064927
75. Gröger A, Bender B, Wurster I, Chadzynski GL, Klose U, Berg D. Differentiation between idiopathic and atypical parkinsonian syndromes using three-dimensional magnetic resonance spectroscopic imaging. *J Neurol Neurosurg Psychiatry*. (2013) 84:644–9. doi: 10.1136/jnnp-2012-302699
76. Barbagallo G, Arabia G, Morelli M, Nisticò R, Novellino F, Salsone M, et al. Thalamic neurometabolic alterations in tremulous Parkinson's disease: a preliminary proton MR spectroscopy study. *Parkinsonism Relat Disord*. (2017) 43:78–84. doi: 10.1016/j.parkreldis.2017.07.028
77. Zanigni S, Testa C, Calandra-Buonaura G, Sambati L, Guarino M, Gabellini A, et al. The contribution of cerebellar proton magnetic resonance spectroscopy in the differential diagnosis among parkinsonian syndromes. *Parkinsonism Relat Disord*. (2015) 21:929–37. doi: 10.1016/j.parkreldis.2015.05.025
78. Mazuel L, Chassain C, Jean B, Pereira B, Cladiere A, Speziale C, et al. Proton MR spectroscopy for diagnosis and evaluation of treatment efficacy in parkinson disease. *Radiology*. (2015) 278:142764. doi: 10.1148/radiol.2015142764
79. Beyer MK, Larsen JP, Aarsland D. Gray matter atrophy in Parkinson disease with dementia and dementia with lewy bodies. *Neurology*. (2007) 69:747–54. doi: 10.1212/01.wnl.0000269666.62598.1c
80. Goldman JG, Stebbins GT, Bernard B, Stoub TR, Goetz CG, deToledo-Morrell L. Entorhinal cortex atrophy differentiates Parkinson's disease patients with and without dementia. *Mov Disord.* (2012) 27:727–34. doi: 10.1002/mds.24938
81. Mak E, Gabel S, Su L, Williams GB, Arnold R, Passamonti L, et al. Multi-modal MRI investigation of volumetric and microstructural changes in the hippocampus and its subfields in mild cognitive impairment, Alzheimer's disease, and dementia with lewy bodies. *Int Psychogeriatr.* (2017) 29:545–55. doi: 10.1017/S1041610216002143
82. Adamowicz DH, Roy S, Salmon DP, Galasko DR, Hansen LA, Masliah E, et al. Hippocampal α-synuclein in dementia with lewy bodies contributes to memory impairment and is consistent with spread of pathology. *J Neurosci.* (2017) 37:1675–84. doi: 10.1523/JNEUROSCI.3047-16.2016
83. Camicioli R, Moore MM, Kinney A, Corbridge E, Glassberg K, Kaye JA. Parkinson's disease is associated with hippocampal atrophy. *Mov Disord.* (2003) 18:784–90. doi: 10.1002/mds.10444
84. Cousins DA, Burton EJ, Burn D, Gholkar a, McKeith IG, O'Brien JT. Atrophy of the putamen in dementia with lewy bodies but not Alzheimer's disease: an MRI study. *Neurology*. (2003) 61:1191–5. doi: 10.1212/01.WNL.0000091889.20347.30
85. Joki H, Higashiyama Y, Nakae Y, Kugimoto C, Doi H, Kimura K, et al. White matter hyperintensities on MRI in dementia with Lewy bodies, Parkinson's disease with dementia, and Alzheimer's disease. *J Neurol Sci*. (2018) 385:99–104. doi: 10.1016/j.jns.2017.12.018
86. Hanganu A, Bedetti C, Degroot C, Mejia-Constain B, Lafontaine AL, Soland V, et al. Mild cognitive impairment is linked with faster rate of cortical thinning in patients with Parkinson's disease longitudinally. *Brain.* (2014) 137:1120–9. doi: 10.1093/brain/awu036
87. Zheng D, Chen C, Song WC, Yi ZQ, Zhao PW, Zhong JG, et al. Regional gray matter reductions associated with mild cognitive impairment in Parkinson's disease: a meta-analysis of voxel-based morphometry studies. *Behav Brain Res.* (2019) 371:111973. doi: 10.1016/j.bbr.2019.111973
88. Weintraub D, Dietz N, Duda JE, Wolk DA, Doshi J, Xie SX, et al. Alzheimer's disease pattern of brain atrophy predicts cognitive decline in Parkinson's disease. *Brain.* (2012) 135:170–80. doi: 10.1093/brain/awr277
89. Guerreiro R, Ross OA, Kun-Rodrigues C, Hernandez DG, Orme T, Eicher JD, et al. Investigating the genetic architecture of dementia with lewy bodies: a two-stage genome-wide association study. *Lancet Neurol.* (2018) 17:64–74. doi: 10.1016/S1474-4422(17)30400-3
90. Mirza SS, Saeed U, Knight J, Ramirez J, Stuss DT, Keith J, et al. APOE *ε4*, white matter hyperintensities, and cognition in Alzheimer and lewy body dementia. *Neurology*. (2019) 93:e1807–19. doi: 10.1212/WNL.0000000000008377
91. Dickson DW, Heckman MG, Murray ME, Soto AI, Walton RL, Diehl NN, et al. APOE ε4 is associated with severity of lewy body pathology independent of Alzheimer pathology. *Neurology*. (2018) 91:e1182–95. doi: 10.1212/WNL.0000000000006212
92. Bozzali M, Falini A, Cercignani M, Baglio F, Farina E, Alberoni M, et al. Brain tissue damage in dementia with lewy bodies: an *in vivo* diffusion tensor MRI study. *Brain.* (2005) 128:1595–604. doi: 10.1093/brain/awh493

93. Kantarci K, Avula R, Senjem ML, Samikoglu AR, Zhang B, Weigand SD, et al. Dementia with lewy bodies and Alzheimer disease: neurodegenerative patterns characterized by DTI. *Neurology*. (2010) 74:1814–21. doi: 10.1212/WNL.0b013e3181e0f7cf
94. Firbank MJ, Blamire AM, Krishnan MS, Teodorczuk A, English P, Gholkar A, et al. Diffusion tensor imaging in dementia with lewy bodies and Alzheimer's disease. *Psychiatry Res.* (2007) 155:135–45. doi: 10.1016/j.pscychresns.2007.01.001
95. Matsui H, Nishinaka K, Oda M, Niikawa H, Kubori T, Udaka F. Dementia in Parkinson's disease: diffusion tensor imaging. *Acta Neurol Scand.* (2007) 116:177–81. doi: 10.1111/j.1600-0404.2007.00838.x
96. Watson R, Blamire AM, Colloby SJ, Wood JS, Barber R, He J, et al. Characterizing dementia with lewy bodies by means of diffusion tensor imaging. *Neurology*. (2012) 79:906–14. doi: 10.1212/WNL.0b013e318266fc51
97. Xuan X, Ding M, Gong X. Proton magnetic resonance spectroscopy detects a relative decrease of N-acetylaspartate in the hippocampus of patients with dementia with lewy bodies. *J Neuroimag.* (2008) 18:137–41. doi: 10.1111/j.1552-6569.2007.00203.x
98. Griffith HR, den Hollander JA, Okonkwo OC, O'Brien T, Watts RL, Marson DC. Brain N-acetylaspartate is reduced in Parkinson disease with dementia. *Alzheimer Dis Assoc Disord.* (2008) 22:54–60. doi: 10.1097/WAD.0b013e3181611011
99. Massey L a, Micallef C, Paviour DC, O'Sullivan SS, Ling H, Williams DR, et al. Conventional magnetic resonance imaging in confirmed progressive supranuclear palsy and multiple system atrophy. *Mov Disord.* (2012) 27:1754–62. doi: 10.1002/mds.24968
100. Deguchi K, Ikeda K, Kume K, Takata T, Kokudo Y, Kamada M, et al. Significance of the hot-cross bun sign on T2*-weighted MRI for the diagnosis of multiple system atrophy. *J Neurol.* (2015) 262:1433–9. doi: 10.1007/s00415-015-7728-1
101. Wang Y, Butros SR, Shuai X, Dai Y, Chen C, Liu M, et al. Different iron-deposition patterns of multiple system atrophy with predominant parkinsonism and idiopathetic Parkinson diseases demonstrated by phase-corrected susceptibility-weighted imaging. *Am J Neuroradiol.* (2012) 33:266–73. doi: 10.3174/ajnr.A2765
102. Sako W, Murakami N, Izumi Y, Kaji R. The difference in putamen volume between {MSA} and PD: evidence from a meta-analysis. *Parkinsonism Relat Disord.* (2014) 20:873–7. doi: 10.1016/j.parkreldis.2014.04.028
103. Feng J, Huang B, Yang W, Zhang Y, Wang L, Wang L, et al. The putaminal abnormalities on 3.0T magnetic resonance imaging: can they separate parkinsonism-predominant multiple system atrophy from Parkinson's disease? *Acta Radiol.* (2014) 56:322–8. doi: 10.1177/0284185114524090
104. Wadia PM, Howard P, Ribeirro MQ, Robblee J, Asante A, Mikulis DJ, et al. The value of GRE, ADC and routine MRI in distinguishing parkinsonian disorders. *Can J Neurol Sci.* (2013) 40:389–402. doi: 10.1017/S0317167100014360
105. Focke NK, Helms G, Pantel PM, Scheewe S, Knauth M, Bachmann CG, et al. Differentiation of typical and atypical Parkinson syndromes by quantitative MR imaging. *Am J Neuroradiol.* (2011) 32:2087–92. doi: 10.3174/ajnr.A2865
106. Brenneis C, Seppi K, Schocke MF, Müller J, Luginger E, Bösch S, et al. Voxel-based morphometry detects cortical atrophy in the Parkinson variant of multiple system atrophy. *Mov Disord.* (2003) 18:1132–8. doi: 10.1002/mds.10502
107. Tir M, Delmaire C, le Thuc V, Duhamel A, Destée A, Pruvo JP, et al. Motor-related circuit dysfunction in MSA-P: usefulness of combined whole-brain imaging analysis. *Mov Disord.* (2009) 24:863–70. doi: 10.1002/mds.22463
108. Yang HG, Wang N, Luo XG, Lv H, Liu H, Li YM, et al. Cerebellar atrophy and its contribution to motor and cognitive performance in multiple system atrophy. *NeuroImage Clin*. (2019) 23:101891. doi: 10.1016/j.nicl.2019.101891
109. Krismer F, Seppi K, Göbel G, Steiger R, Zucal I, Boesch S, et al. Morphometric MRI profiles of multiple system atrophy variants and implications for differential diagnosis. *Mov Disord.* (2019) 34:1041–8. doi: 10.1002/mds.27669
110. Dash SK, Stezin A, Takalkar T, George L, Kamble NL, Netravathi M, et al. Abnormalities of white and grey matter in early multiple system atrophy: comparison of parkinsonian and cerebellar variants. *Eur Radiol.* (2019) 29:716–24. doi: 10.1007/s00330-018-5594-9
111. Fiorenzato E, Weis L, Seppi K, Onofrj M, Cortelli P, Zanigni S, et al. Brain structural profile of multiple system atrophy patients with cognitive impairment. *J Neural Transm.* (2017) 124:293–302. doi: 10.1007/s00702-016-1636-0
112. Kim H-J, Jeon BS, Kim YE, Kim J-Y, Kim YK, Sohn C-H, et al. Clinical and imaging characteristics of dementia in multiple system atrophy. *Parkinsonism Relat Disord.* (2013) 19:617–21. doi: 10.1016/j.parkreldis.2013.02.012
113. Barbagallo G, Sierra-Peña M, Nemmi F, Traon AP Le, Meissner WG, Rascol O, et al. Multimodal MRI assessment of nigro-striatal pathway in multiple system atrophy and Parkinson disease. *Mov Disord.* (2016) 31:325–34. doi: 10.1002/mds.26471
114. Ito M, Watanabe H, Kawai Y, Atsuta N, Tanaka F, Naganawa S, et al. Usefulness of combined fractional anisotropy and apparent diffusion coefficient values for detection of involvement in multiple system atrophy. *J Neurol Neurosurg Psychiatry.* (2007) 78:722–8. doi: 10.1136/jnnp.2006.104075
115. Blain CR V, Barker GJ, Jarosz JM, Coyle NA, Landau S, Brown RG, et al. Measuring brain stem and cerebellar damage in parkinsonian syndromes using diffusion tensor MRI. *Neurology.* (2006) 67:2199–205. doi: 10.1212/01.wnl.0000249307.59950.f8
116. Pellecchia MT, Barone P, Mollica C, Salvatore E, Ianniciello M, Longo K, et al. Diffusion-weighted imaging in multiple system atrophy: a comparison between clinical subtypes. *Mov Disord.* (2009) 24:689–96. doi: 10.1002/mds.22440
117. Hara K, Watanabe H, Bagarinao E, Kawabata K, Yoneyama N, Ohdake R, et al. Corpus callosal involvement is correlated with cognitive impairment in multiple system atrophy. *J Neurol.* (2018) 265:2079–87. doi: 10.1007/s00415-018-8923-7
118. Ofori E, Krismer F, Burciu RG, Pasternak O, McCracken JL, Lewis MM, et al. Free water improves detection of changes in the substantia nigra in parkinsonism: A multisite study. *Mov Disord.* (2017) 32:1457–64. doi: 10.1002/mds.27100
119. Péran P, Barbagallo G, Nemmi F, Sierra M, Galitzky M, Traon AP Le, et al. MRI supervised and unsupervised classification of Parkinson's disease and multiple system atrophy. *Mov Disord.* (2018) 33:600–8. doi: 10.1002/mds.27307
120. Watanabe H, Fukatsu H, Katsuno M, Sugiura M, Hamada K, Okada Y, et al. Multiple regional 1H-MR spectroscopy in multiple system atrophy: NAA/Cr reduction in pontine base as a valuable diagnostic marker. *J Neurol Neurosurg Psychiatry.* (2004) 75:103–9.
121. Boxer AL, Geschwind MD, Belfor N, Gorno-Tempini ML, Schauer GF, Miller BL, et al. Patterns of brain atrophy that differentiate corticobasal degeneration syndrome from progressive supranuclear palsy. *Arch Neurol.* (2006) 63:81–6. doi: 10.1001/archneur.63.1.81
122. Kurata T, Kametaka S, Ohta Y, Morimoto N, Deguchi S, Deguchi K, et al. PSP as distinguished from CBD, MSA-P and PD by clinical and imaging differences at an early stage. *Intern Med.* (2011) 50:2775–81. doi: 10.2169/internalmedicine.50.5954
123. Josephs KA, Whitwell JL, Dickson DW, Boeve BF, Knopman DS, Petersen RC, et al. Voxel-based morphometry in autopsy proven PSP and CBD. *Neurobiol Aging.* (2008) 29:280–9. doi: 10.1016/j.neurobiolaging.2006.09.019
124. Price S, Paviour D, Scahill R, Stevens J, Rossor M, Lees A, et al. Voxel-based morphometry detects patterns of atrophy that help differentiate progressive supranuclear palsy and Parkinson's disease. *NeuroImage.* (2004) 23:663–9. doi: 10.1016/j.neuroimage.2004.06.013
125. Whitwell JL, Höglinger GU, Antonini A, Bordelon Y, Boxer AL, Colosimo C, et al. Radiological biomarkers for diagnosis in PSP: where are we and where do we need to be? *MovDisord*. (2017) 32:955–71. doi: 10.1002/mds.27038
126. Adachi M, Kawanami T, Ohshima H, Sugai Y, Hosoya T. Morning glory sign: a particular MR finding in progressive supranuclear palsy. *Mag Reson Med Sci*. (2004) 3:125–32. doi: 10.2463/mrms.3.125
127. Mueller C, Hussl A, Krismer F, Heim B, Mahlknecht P, Nocker M, et al. The diagnostic accuracy of the hummingbird and morning glory sign in patients with neurodegenerative parkinsonism. *Parkinsonism Relat Disord*. (2018) 54:90–4. doi: 10.1016/j.parkreldis.2018.04.005
128. Quattrone A, Nicoletti G, Messina D, Fera F, Condino F, Pugliese P, et al. MR imaging index for differentiation of progressive supranuclear palsy from

Parkinson disease and the Parkinson variant of multiple system atrophy. *Radiology*. (2008) 246:214–21. doi: 10.1148/radiol.2453061703
129. Gröschel K, Hauser TK, Luft A, Patronas N, Dichgans J, Litvan I, et al. Magnetic resonance imaging-based volumetry differentiates progressive supranuclear palsy from corticobasal degeneration. *NeuroImage.* (2004) 21:714–24. doi: 10.1016/j.neuroimage.2003.09.070
130. Zanigni S, Evangelisti S, Testa C, Manners DN, Calandra-Buonaura G, Guarino M, et al. White matter and cortical changes in atypical parkinsonisms: a multimodal quantitative MR study. *Parkinsonism Relat Disord*. (2017) 39:44–51. doi: 10.1016/j.parkreldis.2017.03.001
131. Brenneis C, Seppi K, Schocke M, Benke T, Wenning GK, Poewe W. Voxel based morphometry reveals a distinct pattern of frontal atrophy in progressive supranuclear palsy. *J Neurol Neurosurg Psychiatry.* (2004) 75:246–9.
132. Padovani A, Borroni B, Brambati SM, Agosti C, Broli M, Alonso R, et al. Diffusion tensor imaging and voxel based morphometry study in early progressive supranuclear palsy. *J Neurol Neurosurg Psychiatry.* (2006) 77:457–63. doi: 10.1136/jnnp.2005.075713
133. Paviour DC, Price SL, Jahanshahi M, Lees AJ, Fox NC. Longitudinal MRI in progressive supranuclear palsy and multiple system atrophy: rates and regions of atrophy. *Brain.* (2006) 129:1040–9. doi: 10.1093/brain/awl021
134. Whitwell JL, Xu J, Mandrekar JN, Gunter JL, Jack CR, Josephs KA. Rates of brain atrophy and clinical decline over 6 and 12-month intervals in PSP: determining sample size for treatment trials. *Parkinsonism Relat Disord.* (2012) 18:252–6. doi: 10.1016/j.parkreldis.2011.10.013
135. Mueller K, Jech R, Bonnet C, Tintera J, Hanuška J, Möller HE, et al. Disease-specific regions outperform whole-brain approaches in identifying progressive supranuclear palsy: a multicentric MRI study. *Front Neurosci.* (2017) 11:100. doi: 10.3389/fnins.2017.00100
136. Kaasinen V, Kangassalo N, Gardberg M, Isotalo J, Karhu J, Parkkola R, et al. Midbrain-to-pons ratio in autopsy-confirmed progressive supranuclear palsy: replication in an independent cohort. *Neurol Sci.* (2015) 36:1251–3. doi: 10.1007/s10072-015-2184-3
137. Quattrone A, Morelli M, Nigro S, Quattrone A, Vescio B, Arabia G, et al. A new MR imaging index for differentiation of progressive supranuclear palsy-parkinsonism from Parkinson's disease. *Parkinsonism Relat Disord*. (2018) 54:3–8. doi: 10.1016/j.parkreldis.2018.07.016
138. Sakurai K, Tokumaru AM, Shimoji K, Murayama S, Kanemaru K, Morimoto S, et al. Beyond the midbrain atrophy: wide spectrum of structural MRI finding in cases of pathologically proven progressive supranuclear palsy. *Neuroradiology*. (2017) 59:431–43. doi: 10.1007/s00234-017-1812-4
139. Erbetta A, Mandelli ML, Savoiardo M, Grisoli M, Bizzi A, Soliveri P, et al. Diffusion tensor imaging shows different topographic involvement of the thalamus in progressive supranuclear palsy and corticobasal degeneration. *Am J Neuroradiol.* (2009) 30:1482–7. doi: 10.3174/ajnr.A1615
140. Kvickström P, Eriksson B, van Westen D, Lätt J, Elfgren C, Nilsson C. Selective frontal neurodegeneration of the inferior fronto-occipital fasciculus in progressive supranuclear palsy (PSP) demonstrated by diffusion tensor tractography. *BMC Neurol.* (2011) 11:13. doi: 10.1186/1471-2377-11-13
141. Reginold W, Lang AE, Marras C, Heyn C, Alharbi M, Mikulis DJ. Longitudinal quantitative MRI in multiple system atrophy and progressive supranuclear palsy. *Parkinsonism Relat Disord.* (2014) 20:222–5. doi: 10.1016/j.parkreldis.2013.10.002
142. Seppi K, Schocke MFH, Esterhammer R, Kremser C, Brenneis C, Mueller J, et al. Diffusion-weighted imaging discriminates progressive supranuclear palsy from PD, but not from the parkinson variant of multiple system atrophy. *Neurology.* (2003) 60:922–7. doi: 10.1212/01.WNL.0000049911.91657.9D
143. Spotorno N, Hall S, Irwin DJ, Rumetshofer T, Acosta-Cabronero J, Deik AF, et al. Diffusion tensor MRI to distinguish progressive supranuclear palsy from a-synucleinopathies. *Radiology*. (2019) 293:646–53. doi: 10.1148/radiol.2019190406
144. Pyatigorskaya N, Yahia-Cherif L, Gaurav R, Ewenczyk C, Gallea C, Valabregue R, et al. Multimodal magnetic resonance imaging quantification of brain changes in progressive supranuclear palsy. *Mov Disord.* (2019) 35:161–70.doi: 10.1002/mds.27877
145. Nicoletti G, Caligiuri ME, Cherubini A, Morelli M, Novellino F, Arabia G, et al. A fully automated, atlas-based approach for superior cerebellar peduncle evaluation in progressive supranuclear palsy phenotypes. *Am J Neuroradiol*. (2017) 38:523–30. doi: 10.3174/ajnr.A5048
146. Quattrone A, Caligiuri ME, Morelli M, Nigro S, Vescio B, Arabia G, et al. Imaging counterpart of postural instability and vertical ocular dysfunction in patients with PSP: a multimodal MRI study. *Parkinsonism Relat Disord.* (2019) 63:124–30. doi: 10.1016/j.parkreldis.2019.02.022
147. Talai AS, Sedlacik J, Boelmans K, Forkert ND. Widespread diffusion changes differentiate Parkinson's disease and progressive supranuclear palsy. *Neuroimage Clin*. (2018) 20:1037–43. doi: 10.1016/j.nicl.2018.09.028
148. Federico F, Simone IL, Lucivero V, De Mari M, Giannini P, Iliceto G, et al. Proton magnetic resonance spectroscopy in Parkinson's disease and progressive supranuclear palsy. *J Neurol Neurosurg Psychiatry.* (1997) 62:239–42. doi: 10.1136/jnnp.62.3.239
149. Negoro K, Tada Y, Ogasawara J, Kawai M, Morimatsu M, Hashida M, et al. Proton magnetic resonance spectroscopy in corticobasal degeneration and progressive supranuclear palsy. *Geriatr Gerontol Int.* (2004) 4:84–92. doi: 10.1111/j.1447-0594.2004.00124.x
150. Abe K, Terakawa H, Takanashi M, Watanabe Y, Tanaka H, Fujita N, et al. Proton magnetic resonance spectroscopy of patients with parkinsonism. *Brain Res Bull.* (2000) 52:589–95. doi: 10.1016/S0361-9230(00)00321-X
151. Barbagallo G, Morelli M, Quattrone A, Chiriaco C, Vaccaro MG, Gullà D, et al. *In vivo* evidence for decreased scyllo-inositol levels in the supplementary motor area of patients with progressive supranuclear palsy: a proton MR spectroscopy study. *Parkinsonism Relat Disord*. (2019) 62:185–91. doi: 10.1016/j.parkreldis.2018.12.008
152. Borroni B, Garibotto V, Agosti C, Brambati SM, Bellelli G, Gasparotti R, et al. White matter changes in corticobasal degeneration syndrome and correlation with limb apraxia. *Arch Neurol.* (2008) 65:796–801. doi: 10.1001/archneur.65.6.796
153. Yu F, Barron DS, Tantiwongkosi B, Fox P. Patterns of gray matter atrophy in atypical parkinsonism syndromes: a VBM meta-analysis. *Brain Behav*. (2015) 5:e00329. doi: 10.1002/brb3.329
154. Josephs K a, Tang-Wai DF, Edland SD, Knopman DS, Dickson DW, Parisi JE, et al. Correlation between antemortem magnetic resonance imaging findings and pathologically confirmed corticobasal degeneration. *Arch Neurol.* (2004) 61:1881–4. doi: 10.1001/archneur.61.12.1881
155. Whitwell JL, Jack CR, Boeve BF, Parisi JE, Ahlskog JE, Drubach DA, et al. Imaging correlates of pathology in corticobasal syndrome. *Neurology.* (2010) 75:1879–87. doi: 10.1212/WNL.0b013e3181feb2e8
156. Schofield EC, Caine D, Kril JJ, Cordato NJ, Halliday GM. Staging disease severity in movement disorder tauopathies: brain atrophy separates progressive supranuclear palsy from corticobasal degeneration. *Mov Disord.* (2005) 20:34–9. doi: 10.1002/mds.20286
157. Arakawa A, Saito Y, Seki T, Mitsutake A, Sato T, Katsumata J, et al. Corticobasal degeneration with deep white matter lesion diagnosed by brain biopsy. *Neuropathology*. (2020) 40:287–94. doi: 10.1111/neup.12638
158. Whitwell JL, Schwarz CG, Reid RI, Kantarci K, Jack CR, Josephs KA. Diffusion tensor imaging comparison of progressive supranuclear palsy and corticobasal syndromes. *Parkinsonism Relat Disord*. (2014) 20:493–8. doi: 10.1016/j.parkreldis.2014.01.023
159. Tedeschi G, Litvan I, Bonavita S, Bertolino A, Lundbom N, Patronas NJ, et al. Proton magnetic resonance spectroscopic imaging in progressive supranuclear palsy, Parkinson's disease and corticobasal degeneration. *Brain.* (1997) 120:1541–52. doi: 10.1093/brain/120.9.1541
160. Hacker CD, Perlmutter JS, Criswell SR, Ances BM, Snyder AZ. Resting state functional connectivity of the striatum in Parkinson's disease. *Brain*. (2012) 135:3699–711. doi: 10.1093/brain/aws281
161. Kim YJ, Ichise M, Ballinger JR, Vines D, Erami SS, Tatschida T, et al. Combination of dopamine transporter and D2 receptor SPECT in the diagnostic evaluation of PD, MSA, and PSP. *Mov Disord.* (2002) 17:303–12. doi: 10.1002/mds.10042
162. Nurmi E, Ruottinen HM, Bergman J, Haaparanta M, Solin O, Sonninen P, et al. Rate of progression in Parkinson's disease: A 6-[18F]fluoro-L-dopa PET study. *Mov Disord.* (2001) 16:608–15. doi: 10.1002/mds.1139
163. Broussolle E, Dentresangle C, Landais P, Garcia-Larrea L, Pollak P, Croisile B, et al. The relation of putamen and caudate nucleus 18F-Dopa uptake to motor and cognitive performances in Parkinson's disease. *J Neurol Sci.* (1999) 166:141–51. doi: 10.1016/S0022-510X(99)00127-6

164. Sharman M, Valabregue R, Perlbarg V, Marrakchi-Kacem L, Vidailhet M, Benali H, et al. Parkinson's disease patients show reduced cortical-subcortical sensorimotor connectivity. *Mov Disord*. (2013) 28:447–54. doi: 10.1002/mds.25255
165. Szewczyk-Krolikowski K, Menke RAL, Rolinski M, Duff E, Salimi-Khorshidi G, Filippini N, et al. Functional connectivity in the basal ganglia network differentiates PD patients from controls. *Neurology*. (2014) 83:208–14. doi: 10.1212/WNL.0000000000000592
166. Helmich RC, Janssen MJR, Oyen WJG, Bloem BR, Toni I. Pallidal dysfunction drives a cerebellothalamic circuit into Parkinson tremor. *Ann Neurol*. (2011) 69:269–81. doi: 10.1002/ana.22361
167. Wang M, Jiang S, Yuan Y, Zhang L, Ding J, Wang J, et al. Alterations of functional and structural connectivity of freezing of gait in Parkinson's disease. *J Neurol*. (2016) 263:1583–92. doi: 10.1007/s00415-016-8174-4
168. Fling BW, Cohen RG, Mancini M, Nutt JG, Fair DA, Horak FB. Asymmetric pedunculopontine network connectivity in parkinsonian patients with freezing of gait. *Brain*. (2013) 136:2405–18. doi: 10.1093/brain/awt172
169. Chung SJ, Choi YH, Kwon H, Park YH, Yun HJ, Yoo HS, et al. Sleep disturbance may alter white matter and resting state functional connectivities in Parkinson's disease. *Sleep*. (2017) 40. doi: 10.1093/sleep/zsx009
170. Bejr-kasem H, Pagonabarraga J, Martínez-Horta S, Sampedro F, Marín-Lahoz J, Horta-Barba A, et al. Disruption of the default mode network and its intrinsic functional connectivity underlies minor hallucinations in Parkinson's disease. *Mov Disord*. (2019) 34:78–86. doi: 10.1002/mds.27557
171. Baggio HC, Abos A, Segura B, Campabadal A, Uribe C, Giraldo DM, et al. Cerebellar resting-state functional connectivity in Parkinson's disease and multiple system atrophy: characterization of abnormalities and potential for differential diagnosis at the single-patient level. *Neuroimage Clin*. (2019) 22:101720. doi: 10.1016/j.nicl.2019.101720
172. Yu F, Barron DS, Tantiwongkosi B, Fox M, Fox P. Characterisation of meta-analytical functional connectivity in progressive supranuclear palsy. *Clin Radiol*. (2018) 73:415.e1-7. doi: 10.1016/j.crad.2017.11.007
173. Brown JA, Hua AY, Trujllo A, Attygalle S, Binney RJ, Spina S, et al. Advancing functional dysconnectivity and atrophy in progressive supranuclear palsy. *Neuroimage Clin*. (2017) 16:564–74. doi: 10.1016/j.nicl.2017.09.008
174. Ballarini T, Albrecht F, Mueller K, Jech R, Diehl-Schmid J, Fliessbach K, et al. Disentangling brain functional network remodeling in corticobasal syndrome – a multimodal MRI study. *Neuroimage Clin*. (2020) 25:102112. doi: 10.1016/j.nicl.2019.102112
175. Upadhyay N, Suppa A, Piattella MC, Giannì C, Bologna M, Di Stasio F, et al. Functional disconnection of thalamic and cerebellar dentate nucleus networks in progressive supranuclear palsy and corticobasal syndrome. *Parkinsonism Relat Disord*. (2017) 39:52–57. doi: 10.1016/j.parkreldis.2017.03.008
176. Burciu RG, Chung JW, Shukla P, Ofori E, Li H, McFarland NR, et al. Functional MRI of disease progression in Parkinson disease and atypical parkinsonian syndromes. *Neurology*. (2016) 87:709–17. doi: 10.1212/WNL.0000000000002985
177. Esposito F, Tessitore A, Giordano A, De Micco R, Paccone A, Conforti R, et al. Rhythm-specific modulation of the sensorimotor network in drug-naïve patients with Parkinson's disease by levodopa. *Brain*. (2013) 136:710–25. doi: 10.1093/brain/awt007
178. Chou YH, You H, Wang H, Zhao YP, Hou B, Chen NK, et al. Effect of repetitive transcranial magnetic stimulation on fMRI resting-state connectivity in multiple system atrophy. *Brain Connect*. (2015) 5:451–9. doi: 10.1089/brain.2014.0325
179. Gaenslen A, Unmuth B, Godau J, Liepelt I, Di Santo A, Schweitzer KJ, et al. The specificity and sensitivity of transcranial ultrasound in the differential diagnosis of Parkinson's disease: a prospective blinded study. *Lancet Neurol*. (2008) 7:417–24. doi: 10.1016/S1474-4422(08)70067-X
180. Li DH, He YC, Liu J, Chen SD. Diagnostic accuracy of transcranial sonography of the substantia nigra in Parkinson's disease: a systematic review and meta-analysis. *Sci Rep*. (2016) 6:20863. doi: 10.1038/srep20863
181. Berg D, Siefker C, Becker G. Echogenicity of the substantia nigra in Parkinson's disease and its relation to clinical findings. *J Neurol*. (2001) 248:684–9. doi: 10.1007/s004150170114
182. Richter D, Woitalla D, Muhlack S, Gold R, Tönges L, Krogias C. Brainstem raphe alterations in TCS: a biomarker for depression and apathy in Parkinson's disease patients. *Front Neurol*. (2018) 9:645. doi: 10.3389/fneur.2018.00645
183. Barrett MJ, Hagenah J, Dhawan V, Peng S, Stanley K, Raymond D, et al. Transcranial sonography and functional imaging in glucocerebrosidase mutation Parkinson disease. *Parkinsonism Relat Disord*. (2013) 19:186–91. doi: 10.1016/j.parkreldis.2012.09.007
184. Schweitzer KJ, Behnke S, Liepelt I, Wolf B, Grosser C, Godau J, et al. Cross-sectional study discloses a positive family history for Parkinson's disease and male gender as epidemiological risk factors for substantia nigra hyperechogenicity. *J Neural Transm*. (2007) 114:1167–71. doi: 10.1007/s00702-007-0725-5
185. Berg D, Merz B, Reiners K, Naumann M, Becker G. Five-year follow-up study of hyperechogenicity of the substantia nigra in Parkinson's disease. *Mov Disord*. (2005) 20:383–5. doi: 10.1002/mds.20311
186. Becker G, Seufert J, Bogdahn U, Reichmann H, Reiners K. Degeneration of substantia nigra in chronic Parkinson's disease visualized by transcranial color-coded real-time sonography. *Neurology*. (1995) 45:182–4. doi: 10.1212/WNL.45.1.182
187. Prati P, Bignamini A, Coppo L, Naldi A, Comi C, Cantello R, et al. The measuring of substantia nigra hyperechogenicity in an Italian cohort of Parkinson disease patients: a case/control study (NOBIS Study). *J Neural Transm*. (2017) 124:869–9. doi: 10.1007/s00702-017-1724-9
188. Behnke S, Berg D, Naumann M, Becker G. Differentiation of Parkinson's disease and atypical parkinsonian syndromes by transcranial ultrasound. *J Neurol Neurosurg Psychiatry*. (2005) 76:423–5. doi: 10.1136/jnnp.2004.049221
189. Spiegel J, Hellwig D, Möllers MO, Behnke S, Jost W, Fassbender K, et al. Transcranial sonography and [123I]FP-CIT SPECT disclose complementary aspects of Parkinson's disease. *Brain*. (2006) 129:1188–93. doi: 10.1093/brain/awl042
190. Berg D, Becker G, Zeiler B, Tucha O, Hofmann E, Preier M, et al. Vulnerability of the nigrostriatal system as detected by transcranial ultrasound. *Neurology*. (1999) 53:1026–31. doi: 10.1212/WNL.53.5.1026
191. Cardaioli G, Ripandelli F, Paolini Paoletti F, Nigro P, Simoni S, Brahimi E, et al. Substantia nigra hyperechogenicity in essential tremor and Parkinson's disease: a longitudinal study. *Eur J Neurol*. (2019) 26:1370–6. doi: 10.1111/ene.13988
192. Walter U, Niehaus L, Probst T, Benecke R, Meyer BU, Dressler D. Brain parenchyma sonography discriminates Parkinson's disease and atypical parkinsonian syndromes. *Neurology*. (2003) 60:74–7. doi: 10.1212/WNL.60.1.74
193. Walter U, Dressler D, Wolters A, Wittstock M, Greim B, Benecke R. Sonographic discrimination of dementia with Lewy bodies and Parkinson's disease with dementia. *J Neurol*. (2006) 253:448–54. doi: 10.1007/s00415-005-0023-9
194. Ebentheuer J, Canelo M, Trautmann E, Trenkwalder C. Substantia nigra echogenicity in progressive supranuclear palsy. *Mov Disord*. (2010) 25:773–7. doi: 10.1002/mds.22981
195. Sadowski K, Serafin-Król M, Szlachta K, Friedman A. Basal ganglia echogenicity in tauopathies. *J Neural Transm*. (2014) 122:863–5. doi: 10.1007/s00702-014-1310-3
196. Walter U, Dressler D, Wolters A, Probst T, Grossmann A, Benecke R. Sonographic discrimination of corticobasal degeneration vs progressive supranuclear palsy. *Neurology*. (2004) 63:504–9. doi: 10.1212/01.WNL.0000133006.17909.32
197. Walter U, Dressler D, Probst T, Wolters A, Abu-Mugheisib M, Wittstock M, et al. Transcranial brain sonography findings in discriminating between parkinsonism and idiopathic parkinson disease. *Arch Neurol*. (2007) 64:1635–40. doi: 10.1001/archneur.64.11.1635
198. Djang DSW, Janssen MJR, Bohnen N, Booij J, Henderson TA, Herholz K, et al. SNM practice guideline for dopamine transporter imaging with 123I-Ioflupane SPECT 1.0. *J Nuclear Med*. (2012) 53:154–63. doi: 10.2967/jnumed.111.100784
199. Catafau AM, Tolosa E, Laloux P, Vander Borght T, Van Zandijcke M, De Geeter F, et al. Impact of dopamine transporter SPECT using 123I-Ioflupane on diagnosis and management of patients with clinically uncertain parkinsonian syndromes. *Mov Disord*. (2004) 19:1175–82. doi: 10.1002/mds.20112

200. Plotkin M, Amthauer H, Klaffke S, Kühn A, Lüdemann L, Arnold G, et al. Combined 123I-FP-CIT and 123I-IBZM SPECT for the diagnosis of parkinsonian syndromes: study on 72 patients *. *J Neural Transm.* (2005) 112:677–92. doi: 10.1007/s00702-004-0208-x
201. Politis M. Neuroimaging in Parkinson disease: from research setting to clinical practice. *Nat Rev Neurol.* (2014) 10:708–22. doi: 10.1038/nrneurol.2014.205
202. Brücke T, Asenbaum S, Pirker W, Djamshidian S, Wenger S, Wöber C, et al. Measurement of the dopaminergic degeneration in Parkinson's disease with [123I] beta-CIT and SPECT. Correlation with clinical findings and comparison with multiple system atrophy and progressive supranuclear palsy. *J Neural Transm Suppl.* (1997) 50:9–24. doi: 10.1007/978-3-7091-6842-4_2
203. Klaffke S, Kuhn A a, Plotkin M, Amthauer H, Harnack D, Felix R, et al. Dopamine transporters, D2 receptors, and glucose metabolism in corticobasal degeneration. *Mov Disord.* (2006) 21:1724–7. doi: 10.1002/mds.21004
204. Im J-H, Chung SJ, Kim J-S, Lee MC. Differential patterns of dopamine transporter loss in the basal ganglia of progressive supranuclear palsy and Parkinson's disease: analysis with [(123)I]IPT single photon emission computed tomography. *J Neurol Sci.* (2006) 244:103–9. doi: 10.1016/j.jns.2006.01.006
205. Fazio P, Svenningsson P, Forsberg A, Jönsson EG, Amini N, Nakao R, et al. Quantitative analysis of 18F-(E)-N-(3-iodoprop-2-enyl)-2β-carbofluoroethoxy-3β-(4'-methyl-phenyl) nortropane binding to the dopamine transporter in Parkinson disease. *J Nuclear Med.* (2015) 56:714–20. doi: 10.2967/jnumed.114.152421
206. Vlaar AMM, van Kroonenburgh MJPG, Kessels AGH, Weber WEJ. Meta-analysis of the literature on diagnostic accuracy of SPECT in parkinsonian syndromes. *BMC Neurol.* (2007) 7:27. doi: 10.1186/1471-2377-7-27
207. Del Sole A, Perini G, Lecchi M, Mariani C, Lucignani G, Clerici F. Correlation between 123I-FP-CIT brain SPECT and parkinsonism in dementia with lewy bodies: caveat for clinical use. *Clin Nuclear Med.* (2015) 40:32–5. doi: 10.1097/RLU.0000000000000602
208. Spiegel J, Möllers MO, Jost WH, Fuss G, Samnick S, Dillmann U, et al. FP-CIT and MIBG scintigraphy in early Parkinson's disease. *Mov Disord.* (2005) 20:552–61. doi: 10.1002/mds.20369
209. Benamer HTS, Patterson J, Wyper DJ, Hadley DM, Macphee GJA, Grosset DG. Correlation of Parkinson's disease severity and duration with 123I-FP-CIT SPECT striatal uptake. *Mov Disord.* (2000) 15:692–8. doi: 10.1002/1531-8257(200007)15:4&<;692::AID-MDS1014&>;3.0.CO;2-V
210. O'Brien JT, Colloby S, Fenwick J, Williams ED, Firbank M, Burn D, et al. Dopamine transporter loss visualized with FP-CIT SPECT in the differential diagnosis of dementia with lewy bodies. *Arch Neurol.* (2004) 61:919–25. doi: 10.1001/archneur.61.6.919
211. Walker Z, Costa DC, Walker RWH, Shaw K, Gacinovic S, Stevens T, et al. Differentiation of dementia with lewy bodies from Alzheimer's disease using a dopaminergic presynaptic ligand. *J Neurol Neurosurg Psychiatry.* (2002) 73:134–40. doi: 10.1136/jnnp.73.2.134
212. Bäckström D, Granåsen G, Domellöf ME, Linder J, Mo SJ, Riklund K, et al. Early predictors of mortality in parkinsonism and Parkinson disease a population-based study. *Neurology.* (2018) 91:e2045–56. doi: 10.1212/WNL.0000000000006576
213. Jin S, Oh M, Oh SJ, Oh JS, Lee SJ, Chung SJ, et al. Differential diagnosis of parkinsonism using dual-phase F-18 FP-CIT PET imaging. *Nuclear Med Mol Imaging.* (2013) 47:44–51. doi: 10.1007/s13139-012-0182-4
214. Lee CS, Samii A, Sossi V, Ruth TJ, Schulzer M, Holden JE, et al. *In vivo* positron emission tomographic evidence for compensatory changes in presynaptic dopaminergic nerve terminals in Parkinson's disease. *Ann Neurol.* (2000) 47:493–503. doi: 10.1002/1531-8249(200004)47:4&<;493::AID-ANA13&>;3.0.CO;2-4
215. Okamura N, Villemagne VL, Drago J, Pejoska S, Dhamija RK, Mulligan RS, et al. *In vivo* measurement of vesicular monoamine transporter type 2 density in Parkinson disease with (18)F-AV-133. *J Nucl Med.* (2010) 51:223–8. doi: 10.2967/jnumed.109.070094
216. Erro R, Schneider S a, Quinn NP, Bhatia KP. What do patients with scans without evidence of dopaminergic deficit (SWEDD) have? New evidence and continuing controversies. *J Neurol Neurosurg Psychiatry.* (2015) 87:1–5. doi: 10.1136/jnnp-2014-310256
217. Nandhagopal R, Mak E, Schulzer M, McKenzie J, McCormick S, Sossi V, et al. Progression of dopaminergic dysfunction in a LRRK2 kindred: a multitracer PET study. *Neurology.* (2008) 71:1790–5. doi: 10.1212/01.wnl.0000335973.66333.58
218. Sossi V, De La Fuente-Fernández R, Nandhagopal R, Schulzer M, McKenzie J, Ruth TJ, et al. Dopamine turnover increases in asymptomatic LRRK2 mutations carriers. *Mov Disord.* (2010) 25:2717–23. doi: 10.1002/mds.23356
219. Papathanasiou ND, Boutsiadis A, Dickson J, Bomanji JB. Diagnostic accuracy of ^{123}I-FP-CIT (DaTSCAN) in dementia with lewy bodies: a meta-analysis of published studies. *Parkinsonism Relat Disord.* (2012) 18:225–9. doi: 10.1016/j.parkreldis.2011.09.015
220. O'Brien JT, McKeith IG, Walker Z, Tatsch K, Booij J, Darcourt J, et al. Diagnostic accuracy of 123I-FP-CIT SPECT in possible dementia with lewy bodies. *Br J Psychiatry.* (2009) 194:34–39. doi: 10.1192/bjp.bp.108.052050
221. Walker Z, Jaros E, Walker RWH, Lee L, Costa DC, Livingston G, et al. Dementia with lewy bodies: a comparison of clinical diagnosis, FP-CIT single photon emission computed tomography imaging and autopsy. *J Neurol Neurosurg Psychiatry.* (2007) 78:1176–81. doi: 10.1136/jnnp.2006.110122
222. Brigo F, Turri G, Tinazzi M. 123I-FP-CIT SPECT in the differential diagnosis between dementia with lewy bodies and other dementias. *J Neurol Sci.* (2015) 359:161–71. doi: 10.1016/j.jns.2015.11.004
223. Thomas AJ, Attems J, Colloby SJ, O'Brien JT, Mckeith I, Walker R, et al. Autopsy validation of 123 I-FP-CIT dopaminergic neuroimaging for the diagnosis of DLB. *Neurology.* (2017) 88:276–83. doi: 10.1212/WNL.0000000000004254
224. Walker Z, Moreno E, Thomas A, Inglis F, Tabet N, Stevens T, et al. Evolution of clinical features in possible DLB depending on FP-CIT SPECT result. *Neurology.* (2016) 87:1045–51. doi: 10.1212/WNL.0000000000003076
225. Nocker M, Seppi K, Donnemiller E, Virgolini I, Wenning GK, Poewe W, et al. Progression of dopamine transporter decline in patients with the Parkinson variant of multiple system atrophy: a voxel-based analysis of [123I]β-CIT SPECT. *Eur J Nuclear Med Mol Imaging.* (2012) 39:1012–20. doi: 10.1007/s00259-012-2100-5
226. Cilia R, Rossi C, Frosini D, Volterrani D, Siri C, Pagni C, et al. Dopamine transporter spect imaging in corticobasal syndrome. *PLoS ONE.* (2011) 6:e18301. doi: 10.1371/journal.pone.0018301
227. Pirker S, Perju-Dumbrava L, Kovacs GG, Traub-Weidinger T, Pirker W. Progressive dopamine transporter binding loss in autopsy-confirmed corticobasal degeneration. *J Parkinson's Dis.* (2015) 5:907–12. doi: 10.3233/JPD-150625
228. Ling H, Kovacs GG, Vonsattel JPG, Davey K, Mok KY, Hardy J, et al. Astrogliopathy predominates the earliest stage of corticobasal degeneration pathology. *Brain.* (2016) 139:3237–52. doi: 10.1093/brain/aww256
229. Antonini A, Benti R, De Notaris R, Tesei S, Zecchinelli A, Sacilotto G, et al. 123I-Ioflupane/SPECT binding to striatal dopamine transporter (DAT) uptake in patients with Parkinson's disease, multiple system atrophy, and progressive supranuclear palsy. *Neurol Sci.* (2003) 24:149–50. doi: 10.1007/s10072-003-0103-5
230. Filippi L, Manni C, Pierantozzi M, Brusa L, Danieli R, Stanzione P, et al. 123I-FP-CIT in progressive supranuclear palsy and in Parkinson's disease: a SPECT semiquantitative study. *Nuclear Med Commun.* (2006) 27:381–6. doi: 10.1097/01.mnm.0000202858.45522.df
231. Kaasinen V, Kankare T, Joutsa J, Vahlberg T. Presynaptic striatal dopaminergic function in atypical parkinsonism: a metaanalysis of imaging studies. *J Nucl Med.* (2019) 60:1757–63. doi: 10.2967/jnumed.119.227140
232. Brooks DJ, Ibanez V, Sawle G V, Quinn N, Lees AJ, Mathias CJ, et al. Differing patterns of striatal 18F-dopa uptake in Parkinson's disease, multiple system atrophy, and progressive supranuclear palsy. *Ann Neurol.* (1990) 28:547–55. doi: 10.1002/ana.410280412
233. Ghaemi M, Hilker R, Rudolf J, Sobesky J, Heiss WD. Differentiating multiple system atrophy from Parkinson's disease: contribution of striatal and midbrain MRI volumetry and multi-tracer PET imaging. *J Neurol Neurosurg Psychiatry.* (2002) 73:517–23. doi: 10.1136/jnnp.73.5.517

234. Otsuka M, Ichiya Y, Hosokawa S, Kuwabara Y, Tahara T, Fukumura T, et al. Striatal blood flow, glucose metabolism and 18F-dopa uptake: difference in Parkinson's disease and atypical parkinsonism. *J Neurol Neurosurg Psychiatry*. (1991) 54:898–904. doi: 10.1136/jnnp.54.10.898
235. Li Y, Kang W, Yang Q, Zhang L, Zhang L, Dong F, et al. Predictive markers for early conversion of iRBD to neurodegenerative synucleinopathy diseases. *Neurology*. (2017) 88:1493–100. doi: 10.1212/WNL.0000000000003838
236. Postuma RB, Iranzo A, Hu M, Högl B, Boeve BF, Manni R, et al. Risk and predictors of dementia and parkinsonism in idiopathic REM sleep behaviour disorder: a multicentre study. *Brain*. (2019) 142:744–59. doi: 10.1093/brain/awz030
237. Antonini A, Schwarz J, Oertel WH, Beer HF, Madeja UD, Leenders KL. [11C]raclopride and positron emission tomography in previously untreated patients with Parkinson's disease: influence of L-dopa and lisuride therapy on striatal dopamine D2-receptors. *Neurology*. (1994) 44:1325–9. doi: 10.1212/WNL.44.7.1325
238. Rinne UK, Laihinen A, Rinne JO, Nagren K, Bergman J, Ruotsalainen U. Positron emission tomography demonstrates dopamine D2 receptor supersensitivity in the striatum of patients with early Parkinson's disease. *Mov Disord.* (1990) 5:55–59. doi: 10.1002/mds.870050114
239. Brooks DJ, Ibanez V, Sawle G V, Playford ED, Quinn N, Mathias CJ, et al. Striatal D2 receptor status in patients with Parkinson's disease, striatonigral degeneration, and progressive supranuclear palsy, measured with 11C-raclopride and positron emission tomography. *Ann Neurol.* (1992) 31:184–92. doi: 10.1002/ana.410310209
240. Ichise M, Kim YJ, Ballinger JR, Vines D, Erami SS, Tanaka F, et al. SPECT imaging of pre- and postsynaptic dopaminergic alterations in L-dopa-untreated PD. *Neurology*. (1999) 52:1206–14.
241. Antonini a, Leenders KL, Vontobel P, Maguire RP, Missimer J, Psylla M, et al. Complementary PET studies of striatal neuronal function in the differential diagnosis between multiple system atrophy and Parkinson's disease. *Brain*. (1997) 120 (Pt. 1):2187–95. doi: 10.1093/brain/120.12.2187
242. van Royen E, Verhoeff NF, Speelman JD, Wolters EC, Kuiper MA, Janssen AG. Multiple system atrophy and progressive supranuclear palsy. Diminished striatal D2 dopamine receptor activity demonstrated by 123I-IBZM single photon emission computed tomography. *Arch Neurol.* (1993) 50:513–16. doi: 10.1001/archneur.1993.00540050063017
243. Pirker S, Perju-Dumbrava L, Kovacs GG, Traub-Weidinger T, Asenbaum S, Pirker W. Dopamine D2 receptor SPECT in corticobasal syndrome and autopsy-confirmed corticobasal degeneration. *Parkinsonism Relat Disord.* (2013) 19:222–6. doi: 10.1016/j.parkreldis.2012.10.010
244. Van Laere K, Clerinx K, D'Hondt E, de Groot T, Vandenberghe W. Combined striatal binding and cerebral influx analysis of dynamic 11C-raclopride PET improves early differentiation between multiple-system atrophy and parkinson disease. *J Nucl Med.* (2010) 51:588–95. doi: 10.2967/jnumed.109.070144
245. Koch W, Hamann C, Radau PE, Tatsch K. Does combined imaging of the pre- and postsynaptic dopaminergic system increase the diagnostic accuracy in the differential diagnosis of parkinsonism? *Eur J Nucl Med Mol Imag.* (2007) 34:1265–73. doi: 10.1007/s00259-007-0375-8
246. Südmeyer M, Antke C, Zizek T, Beu M, Nikolaus S, Wojtecki L, et al. Diagnostic accuracy of combined FP-CIT, IBZM, and MIBG scintigraphy in the differential diagnosis of degenerative parkinsonism: a multidimensional statistical approach. *J Nucl Med.* (2011) 52:733–40. doi: 10.2967/jnumed.110.086959
247. Lobotesis K, Fenwick JD, Phipps a, Ryman a, Swann a, Ballard C, et al. Occipital hypoperfusion on SPECT in dementia with lewy bodies but not AD. *Neurology*. (2001) 56:643–9. doi: 10.1212/WNL.56.5.643
248. Rossi C, Volterrani D, Nicoletti V, Manca G, Frosini D, Kiferle L, et al. "Parkinson-dementia" diseases: a comparison by double tracer SPECT studies. *Parkinsonism Relat Disord.* (2009) 15:762–6. doi: 10.1016/j.parkreldis.2009.05.012
249. Antonini A, De Notaris R, Benti R, De Gaspari D, Pezzoli G. Perfusion ECD/SPECT in the characterization of cognitive deficits in Parkinson's disease. *Neurol Sci.* (2001) 22:45–6. doi: 10.1007/s100720170039
250. Misch MR, Mitchell S, Francis PL, Sherborn K, Meradje K, McNeely A a, et al. Differentiating between visual hallucination-free dementia with lewy bodies and corticobasal syndrome on the basis of neuropsychology and perfusion single-photon emission computed tomography. *Alzheimer's Res Ther.* (2014) 6:71. doi: 10.1186/s13195-014-0071-4
251. Zhang L, Murata Y, Ishida R, Saitoh Y, Mizusawa H, Shibuya H. Differentiating between progressive supranuclear palsy and corticobasal degeneration by brain perfusion spet. *Nucl Med Commun*. (2001) 22:767–72. doi: 10.1097/00006231-200107000-00007
252. Okuda B, Tachibana H, Kawabata K, Takeda M, Sugita M. Cerebral blood flow in corticobasal degeneration and progressive supranuclear palsy. *Alzheimer Dis Assoc Disorders*. (2000) 14:46–52. doi: 10.1097/00002093-200001000-00006
253. Takaya S, Sawamoto N, Okada T, Okubo G, Nishida S, Togashi K, et al. Differential diagnosis of parkinsonian syndromes using dopamine transporter and perfusion SPECT. *Parkinsonism Relat Disord*. (2018) 47:15–21. doi: 10.1016/j.parkreldis.2017.11.333
254. Song I-U, Yoo I, Chung Y-A, Jeong J. The value of brain perfusion SPECT for differentiation between mildly symptomatic idiopathic Parkinson's disease and the Parkinson variant of multiple system atrophy. *Nucl Med Commun.* (2015) 36:1049–54. doi: 10.1097/MNM.0000000000000354
255. Firbank MJ, Molloy S, McKeith IG, Burn DJ, O'Brien JT. Longitudinal change in 99mTcHMPAO cerebral perfusion SPECT in Parkinson's disease over one year. *J Neurol Neurosurg Psychiatry*. (2005) 76:1448–51. doi: 10.1136/jnnp.2004.058685
256. Matsui H, Udaka F, Miyoshi T, Hara N, Tamura A, Oda M, et al. Brain perfusion differences between Parkinson's disease and multiple system atrophy with predominant parkinsonian features. *Parkinsonism Relat Disord.* (2005) 11:227–32. doi: 10.1016/j.parkreldis.2005.01.001
257. Matsuda H, Imabayashi E, Kuji I, Seto A, Ito K, Kikuta D, et al. Evaluation of both perfusion and atrophy in multiple system atrophy of the cerebellar type using brain SPECT alone. *BMC Med Imag.* (2010) 10:17. doi: 10.1186/1471-2342-10-17
258. Sakamoto F, Shiraishi S, Tsuda N, Hashimoto M, Tomiguchi S, Ikeda M, et al. Diagnosis of dementia with lewy bodies: Can 123I-IMP and 123I-MIBG scintigraphy yield new core features? *Br J Radiol*. (2017) 90:20160156. doi: 10.1259/bjr.20160156
259. Eckert T, Barnes A, Dhawan V, Frucht S, Gordon MF, Feigin AS, et al. FDG PET in the differential diagnosis of parkinsonian disorders. *Neuroimage*. (2005) 26:912–21. doi: 10.1016/j.neuroimage.2005.03.012
260. Tripathi M, Dhawan V, Peng S, Kushwaha S, Batla A, Jaimini A, et al. Differential diagnosis of parkinsonian syndromes using F-18 fluorodeoxyglucose positron emission tomography. *Neuroradiology*. (2013) 55:483–92. doi: 10.1007/s00234-012-1132-7
261. Albrecht F, Ballarini T, Neumann J, Schroeter ML. FDG-PET hypometabolism is more sensitive than MRI atrophy in Parkinson's disease: a whole-brain multimodal imaging meta-analysis. *Neuroimage Clin*. (2019) 21:101594. doi: 10.1016/j.nicl.2018.11.004
262. Juh R, Kim J, Moon D, Choe B, Suh T. Different metabolic patterns analysis of parkinsonism on the 18F-FDG PET. *Eur J Radiol.* (2004) 51:223–33. doi: 10.1016/S0720-048X(03)00214-6
263. Zhao P, Zhang B, Gao S. 18F-FDG PET study on the idiopathic Parkinson's disease from several parkinsonian-plus syndromes. *Parkinsonism Relat Disord.* (2012) 18(Suppl. 1):S60–2. doi: 10.1016/S1353-8020(11)70020-7
264. Baudrexel S, Seifried C, Penndorf B, Klein JC, Middendorp M, Steinmetz H, et al. The value of putaminal diffusion imaging versus 18-fluorodeoxyglucose positron emission tomography for the differential diagnosis of the parkinson variant of multiple system atrophy. *Mov Disord.* (2014) 29:380–7. doi: 10.1002/mds.25749
265. Zalewski N, Botha H, Whitwell JL, Lowe V, Dickson DW, Josephs KA. FDG-PET in pathologically confirmed spontaneous 4R-tauopathy variants. *J Neurol*. (2014) 261:710–6. doi: 10.1007/s00415-014-7256-4
266. Botha H, Whitwell JL, Madhaven A, Senjem ML, Lowe V, Josephs KA. The pimple sign of progressive supranuclear palsy syndrome. *Parkinsonism Relat Disord.* (2014) 20:180–85. doi: 10.1016/j.parkreldis.2013.10.023
267. Niethammer M, Tang CC, Feigin A, Allen PJ, Heinen L, Hellwig S, et al. A disease-specific metabolic brain network associated with corticobasal degeneration. *Brain.* (2014) 137:3036–46. doi: 10.1093/brain/awu256
268. Hosaka K, Ishii K, Sakamoto S, Mori T, Sasaki M, Hirono N, et al. Voxel-based comparison of regional cerebral glucose metabolism

between PSP and corticobasal degeneration. *J Neurol Sci.* (2002) 199:67–71. doi: 10.1016/S0022-510X(02)00102-8
269. Mosconi L, Tsui WH, Herholz K, Pupi A, Drzezga A, Lucignani G, et al. Multicenter standardized 18F-FDG PET diagnosis of mild cognitive impairment, Alzheimer's disease, and other dementias. *J Nucl Med.* (2008) 49:390–8. doi: 10.2967/jnumed.107.045385
270. Yong SW, Yoon JK, An YS, Lee PH. A comparison of cerebral glucose metabolism in Parkinson's disease, Parkinson's disease dementia and dementia with lewy bodies. *Eur J Neurol.* (2007) 14:1357–62. doi: 10.1111/j.1468-1331.2007.01977.x
271. Lim SM, Katsifis A, Villemagne VL, Best R, Jones G, Saling M, et al. The 18F-FDG PET cingulate island sign and comparison to 123I-beta-CIT SPECT for diagnosis of dementia with lewy bodies. *J Nucl Med.* (2009) 50:1638–45. doi: 10.2967/jnumed.109.065870
272. Hellwig S, Amtage F, Kreft A, Buchert R, Winz OH, Vach W, et al. [18F]FDG-PET is superior to [123I]IBZM-SPECT for the differential diagnosis of parkinsonism. *Neurology*. (2012) 79:1314–22. doi: 10.1212/WNL.0b013e31826c1b0a
273. Eidelberg D. Metabolic brain networks in neurodegenerative disorders: a functional imaging approach. *Trends Neurosci.* (2009) 32:548–7. doi: 10.1016/j.tins.2009.06.003
274. Huang C, Tang C, Feigin A, Lesser M, Ma Y, Pourfar M, et al. Changes in network activity with the progression of Parkinson's disease. *Brain.* (2007) 130:1834–46. doi: 10.1093/brain/awm086
275. Holtbernd F, Ma Y, Peng S, Schwartz F, Timmermann L, Kracht L, et al. Dopaminergic correlates of metabolic network activity in Parkinson's disease. *Hum Brain Mapp*. (2015) 36:3575–85. doi: 10.1002/hbm.22863
276. Wu P, Yu H, Peng S, Dauvilliers Y, Wang J, Ge J, et al. Consistent abnormalities in metabolic network activity in idiopathic rapid eye movement sleep behaviour disorder. *Brain*. (2014) 137:3122–8. doi: 10.1093/brain/awu290
277. Niethammer M, Eidelberg D. Metabolic brain networks in translational neurology: Concepts and applications. *Ann Neurol*. (2012) 72:635–47. doi: 10.1002/ana.23631
278. Huang C, Mattis P, Tang C, Perrine K, Carbon M, Eidelberg D. Metabolic brain networks associated with cognitive function in Parkinson's disease. *Neuroimage.* (2007) 34:714–23. doi: 10.1016/j.neuroimage.2006.09.003
279. Eckert T, Tang C, Ma Y, Brown N, Lin T, Frucht S, et al. Abnormal metabolic networks in atypical parkinsonism. *Mov Disord.* (2008) 23:727–33. doi: 10.1002/mds.21933
280. Shirvan J, Clement N, Ye R, Katz S, Schultz A, Johnson KA, et al. Neuropathologic correlates of amyloid and dopamine transporter imaging in lewy body disease. *Neurology*. (2019) 93:e476–84. doi: 10.1212/WNL.0000000000007855
281. Harding AJ, Halliday GM. Cortical lewy body pathology in the diagnosis of dementia. *Acta Neuropathol.* (2001) 102:355–63. doi: 10.1007/s004010100390
282. Irwin DJ, White MT, Toledo JB, Xie SX, Robinson JL, Van Deerlin V, et al. Neuropathologic substrates of Parkinson disease dementia. *Ann Neurol.* (2012) 72:587–98. doi: 10.1002/ana.23659
283. Edison P, Rowe CC, Rinne JO, Ng S, Ahmed I, Kemppainen N, et al. Amyloid load in Parkinson's disease dementia and lewy body dementia measured with [11C]PIB positron emission tomography. *J Neurol Neurosurg Psychiatry.* (2008) 79:1331–8. doi: 10.1136/jnnp.2007.127878
284. Donaghy P, Thomas AJ, O'Brien JT. Amyloid PET imaging in lewy body disorders. *Am J Geriatr Psychiatry.* (2015) 23:23–37. doi: 10.1016/j.jagp.2013.03.001
285. Foster ER, Campbell MC, Burack MA, Hartlein J, Flores HP, Cairns NJ, et al. Amyloid imaging of Lewy body-associated disorders. *Mov Disord.* (2010) 25:2516–23. doi: 10.1002/mds.23393
286. Gomperts SN, Locascio JJ, Marquie M, Santarlasci AL, Rentz DM, Maye J, et al. Brain amyloid and cognition in lewy body diseases. *Mov Disord.* (2012) 27:965–73. doi: 10.1002/mds.25048
287. Petrou M, Bohnen NI, Müller MLTM, Koeppe RA, Albin RL, Frey KA. Aβ-Amyloid deposition in patients with parkinson disease at risk for development of dementia. *Neurology*. (2012) 79:1161–7. doi: 10.1212/WNL.0b013e3182698d4a
288. Donaghy PC, Firbank MJ, Thomas AJ, Lloyd J, Petrides G, Barnett N, et al. Amyloid imaging and longitudinal clinical progression in dementia with lewy bodies. *Am J Geriatr Psychiatry*. (2020) 28:573–77. doi: 10.1016/j.jagp.2019.12.009
289. Shah N, Frey KA, Müller MLTM, Petrou M, Kotagal V, Koeppe RA, et al. Striatal and cortical β-amyloidopathy and cognition in Parkinson's disease. *Mov Disord*. (2016) 31:111–7. doi: 10.1002/mds.26369
290. Fagan AM, Mintun MA, Mach RH, Lee SY, Dence CS, Shah AR, et al. Inverse relation between *in vivo* amyloid imaging load and cerebrospinal fluid Abeta42 in humans. *Ann Neurol*. (2006) 59:512–9. doi: 10.1002/ana.20730
291. Maetzler W, Liepelt I, Reimold M, Reischl G, Solbach C, Becker C, et al. Cortical PIB binding in Lewy body disease is associated with Alzheimer-like characteristics. *Neurobiol Dis.* (2009) 34:107–12. doi: 10.1016/j.nbd.2008.12.008
292. Donaghy PC, Firbank MJ, Thomas AJ, Lloyd J, Petrides G, Barnett N, et al. Clinical and imaging correlates of amyloid deposition in dementia with lewy bodies. *Mov Disord*. (2018) 33:1130–8. doi: 10.1002/mds.27403
293. Claassen DO, Lowe VJ, Peller PJ, Petersen RC, Josephs KA. Amyloid and glucose imaging in dementia with lewy bodies and multiple systems atrophy. *Parkinsonism Relat Disord.* (2011) 17:160–5. doi: 10.1016/j.parkreldis.2010.12.006
294. Whitwell JL, Ahlskog JE, Tosakulwong N, Senjem ML, Spychalla AJ, Petersen RC, et al. Pittsburgh compound B and AV-1451 positron emission tomography assessment of molecular pathologies of Alzheimer's disease in progressive supranuclear palsy. *Parkinsonism Relat Disord*. (2018) 48:3–9. doi: 10.1016/j.parkreldis.2017.12.016
295. Villemagne VL, Fodero-Tavoletti MT, Masters CL, Rowe CC. Tau imaging: early progress and future directions. *Lancet Neurol.* (2015) 14:114–24. doi: 10.1016/S1474-4422(14)70252-2
296. Okamura N, Harada R, Ishiki A, Kikuchi A, Nakamura T, Kudo Y. The development and validation of tau PET tracers: current status and future directions. *Clin Transl Imag.* (2018) 6:305–16. doi: 10.1007/s40336-018-0290-y
297. Passamonti L, Rodríguez PV, Hong YT, Allinson KSJ, Williamson D, Borchert RJ, et al. 18F-AV-1451 positron emission tomography in Alzheimer's disease and progressive supranuclear palsy. *Brain.* (2017) 140:781–91. doi: 10.1093/brain/aww340
298. Cho H, Choi JY, Hwang MS, Lee SH, Ryu YH, Lee MS, et al. Subcortical (18) F-AV-1451 binding patterns in progressive supranuclear palsy. *Mov Disord*. (2016) 32:134–40. doi: 10.1002/mds.26844
299. Whitwell JL, Tosakulwong N, Schwarz CG, Botha H, Senjem ML, Spychalla AJ, et al. MRI outperforms [18F]AV-1451 PET as a longitudinal biomarker in progressive supranuclear palsy. *Mov Disord.* (2019) 34:105–13. doi: 10.1002/mds.27546
300. Whitwell JL, Lowe VJ, Tosakulwong N, Weigand SD, Senjem ML, Schwarz CG, et al. [18F]AV-1451 tau positron emission tomography in progressive supranuclear palsy. *Mov Disord*. (2017) 32:124–33. doi: 10.1002/mds.26834
301. Smith R, Schain M, Nilsson C, Strandberg O, Olsson T, Hägerström D, et al. Increased basal ganglia binding of (18) F-AV-1451 in patients with progressive supranuclear palsy. *Mov Disord*. (2016) 32:108–14. doi: 10.1002/mds.26813
302. Endo H, Shimada H, Sahara N, Ono M, Koga S, Kitamura S, et al. *In vivo* binding of a tau imaging probe, [(11) C]PBB3, in patients with progressive supranuclear palsy. *Mov Disord.* (2019) 34:744–54. doi: 10.1002/mds.27643
303. Kepe V, Bordelon Y, Boxer A, Huang SC, Liu J, Thiede FC, et al. PET imaging of neuropathology in tauopathies: progressive supranuclear palsy. *J Alzheimer's Dis.* (2013) 36:145–53. doi: 10.3233/JAD-130032
304. Schonhaut DR, McMillan CT, Spina S, Dickerson BC, Siderowf A, Devous MD, et al. 18F-flortaucipir tau positron emission tomography distinguishes established progressive supranuclear palsy from controls and parkinson disease: a multicenter study. *Ann Neurol.* (2017) 82:622–34. doi: 10.1002/ana.25060
305. Brendel M, Schönecker S, Höglinger G, Lindner S, Havla J, Blautzik J, et al. [18F]-THK5351 PET correlates with topology and symptom severity in progressive supranuclear palsy. *Front Aging Neurosci.* (2018) 9:440. doi: 10.3389/fnagi.2017.00440

306. Cho H, Baek MS, Choi JY, Lee SH, Kim JS, Ryu YH, 18F-AV-1451 binds to motor-related subcortical gray and white matter in corticobasal syndrome. *Neurology*. (2017) 89:1170–8. doi: 10.1212/WNL.0000000000004364
307. Smith R, Schöll M, Widner H, Van Westen D, Svenningsson P, Hägerström D, et al. *In vivo* retention of 18 F-AV-1451 in corticobasal syndrome. *Neurology*. (2017) 89:845–53. doi: 10.1212/WNL.0000000000004264
308. Marquié M, Normandin MD, Vanderburg CR, Costantino IM, Bien EA, Rycyna LG, et al. Validating novel tau positron emission tomography tracer [F-18]-AV-1451 (T807) on postmortem brain tissue. *Ann Neurol.* (2015) 78:787–800. doi: 10.1002/ana.24517
309. Lee SH, Cho H, Choi JY, Lee JH, Ryu YH, Lee MS, et al. Distinct patterns of amyloid-dependent tau accumulation in Lewy body diseases. *Mov Disord*. (2018) 33:262–72. doi: 10.1002/mds.27252
310. Hansen AK, Knudsen K, Lillethorup TP, Landau AM, Parbo P, Fedorova T, et al. *In vivo* imaging of neuromelanin in Parkinson's disease using 18F-AV-1451 PET. *Brain.* (2016) 139:2039–49. doi: 10.1093/brain/aww098
311. Coakeley S, Cho SS, Koshimori Y, Rusjan P, Ghadery C, Kim J, et al. [18F]AV-1451 binding to neuromelanin in the substantia nigra in PD and PSP. *Brain Struct Funct*. (2018) 223:589–95. doi: 10.1007/s00429-017-1507-y
312. Vermeiren C, Motte P, Viot D, Mairet-Coello G, Courade JP, Citron M, et al. The tau positron-emission tomography tracer AV-1451 binds with similar affinities to tau fibrils and monoamine oxidases. *Mov Disord*. (2018) 33:273–81. doi: 10.1002/mds.27271
313. Ng KP, Pascoal TA, Mathotaarachchi S, Therriault J, Kang MS, Shin M, et al. Monoamine oxidase B inhibitor, selegiline, reduces 18F-THK5351 uptake in the human brain. *Alzheimer's Res Ther*. (2017) 9:25. doi: 10.1186/s13195-017-0253-y
314. Ishiki A, Harada R, Kai H, Sato N, Totsune T, Tomita N, et al. Neuroimaging-pathological correlations of [(18)F]THK5351 PET in progressive supranuclear palsy. *Acta Neuropathol Commun*. (2018) 6:53. doi: 10.1186/s40478-018-0556-7
315. Ezura M, Kikuchi A, Ishiki A, Okamura N, Hasegawa T, Harada R, et al. Longitudinal changes in 18F-THK5351 positron emission tomography in corticobasal syndrome. *Eur J Neurol*. (2019) 26:1205–11. doi: 10.1111/ene.13966
316. Ono M, Sahara N, Kumata K, Ji B, Ni R, Koga S, et al. Distinct binding of PET ligands PBB3 and AV-1451 to tau fibril strains in neurodegenerative tauopathies. *Brain*. (2017) 140:764–80. doi: 10.1093/brain/aww339
317. Leuzy A, Chiotis K, Lemoine L, Gillberg PG, Almkvist O, Rodriguez-Vieitez E, et al. Tau PET imaging in neurodegenerative tauopathies—still a challenge. *Mol Psychiatry*. (2019) 24:1112–34. doi: 10.1038/s41380-018-0342-8
318. Perez-Soriano A, Arena JE, Dinelle K, Miao Q, McKenzie J, Neilson N, et al. PBB3 imaging in Parkinsonian disorders: evidence for binding to tau and other proteins. *Mov Disord*. (2017) 32:1016–24. doi: 10.1002/mds.27029
319. Eberling JL, Dave KD, Frasier MA. α-synuclein imaging: a critical need for Parkinson's disease research. *J Parkinson's Dis.* (2013) 3:565–7. doi: 10.3233/JPD-130247
320. Kotzbauer PT, Tu Z, Mach RH. Current status of the development of PET radiotracers for imaging alpha synuclein aggregates in Lewy bodies and Lewy neurites. *Clin Transl Imag*. (2017) 5:3–14. doi: 10.1007/s40336-016-0217-4
321. Shah M, Seibyl J, Cartier A, Bhatt R, Catafau AM. Molecular imaging insights into neurodegeneration: focus on α-synuclein radiotracers. *J Nucl Med*. (2014) 55:1397–400. doi: 10.2967/jnumed.113.136515
322. Hirsch EC, Hunot S. Neuroinflammation in Parkinson's disease: a target for neuroprotection? *Lancet Neurol.* (2009) 8:382–97. doi: 10.1016/S1474-4422(09)70062-6
323. Mizrahi R, Rusjan PM, Kennedy J, Pollock B, Mulsant B, Suridjan I, et al. Translocator protein (18 kDa) polymorphism (rs6971) explains *in-vivo* brain binding affinity of the PET radioligand [18F]-FEPPA. *J Cereb Blood Flow Metab*. (2012) 32:968–72. doi: 10.1038/jcbfm.2012.46
324. Gerhard A, Trender-Gerhard I, Turkheimer F, Quinn NP, Bhatia KP and Brooks DJ. *In vivo* imaging of microglial activation with [11C](R)?PK11195 PET in progressive supranuclear palsy. *Mov. Disord.* (2006) 21:89–93. doi: 10.1002/mds.20668
325. Ouchi Y, Yoshikawa E, Sekine Y, Futatsubashi M, Kanno T, Ogusu T, et al. Microglial activation and dopamine terminal loss in early Parkinson's disease. *Ann Neurol.* (2005) 57:168–75. doi: 10.1002/ana.20338
326. Ghadery C, Koshimori Y, Coakeley S, Harris M, Rusjan P, Kim J, et al. Microglial activation in Parkinson's disease using [18F]-FEPPA. *J Neuroinflammation*. (2017) 14:8. doi: 10.1186/s12974-016-0778-1
327. Ghadery C, Koshimori Y, Christopher L, Kim J, Rusjan P, Lang AE, et al. The interaction between neuroinflammation and β-amyloid in cognitive decline in Parkinson's disease. *Mol Neurobiol.* (2020) 57:492–501. doi: 10.1007/s12035-019-01714-6
328. Stokholm MG, Iranzo A, Østergaard K, Serradell M, Otto M, Bacher Svendsen K, Garrido A, et al. Extrastriatal monoaminergic dysfunction and enhanced microglial activation in idiopathic rapid eye movement sleep behaviour disorder. *Neurobiol Dis*. (2018) 115:9–16. doi: 10.1016/j.nbd.2018.02.017
329. Stokholm MG, Iranzo A, Østergaard K, Serradell M, Otto M, Svendsen KB, Garrido A, et al. Assessment of neuroinflammation in patients with idiopathic rapid-eye-movement sleep behaviour disorder: a case-control study. *Lancet Neurol*. (2017) 16:789–96. doi: 10.1016/S1474-4422(17)30173-4
330. Edison P, Ahmed I, Fan Z, Hinz R, Gelosa G, Ray Chaudhuri K, et al. Microglia, amyloid, and glucose metabolism in Parkinson's disease with and without dementia. *Neuropsychopharmacology.* (2013) 38:938–49. doi: 10.1038/npp.2012.255
331. Fan Z, Aman Y, Ahmed I, Chetelat G, Landeau B, Ray Chaudhuri K, et al. Influence of microglial activation on neuronal function in Alzheimer's and Parkinson's disease dementia. *Alzheimer's Dement*. (2015) 11:608–621.e7. doi: 10.1016/j.jalz.2014.06.016
332. Gerhard A, Banati RB, Goerres GB, Cagnin A, Myers R, Gunn RN, et al. [11C](R)-PK11195 PET imaging of microglial activation in multiple system atrophy. *Neurology*. (2003) 61:686–9. doi: 10.1212/01.WNL.0000078192.95645.E6
333. Passamonti L, Rodríguez PV, Hong YT, Allinson KSJ, Bevan-Jones WR, Williamson D, et al. PK11195 binding in Alzheimer disease and progressive supranuclear palsy. *Neurology*. (2018) 90:e1989–96. doi: 10.1212/WNL.0000000000005610
334. Gerhard A, Watts J, Trender-Gerhard I, Turkheimer F, Banati RB, Bhatia K, et al. *In vivo* imaging of microglial activation with [11C](R)-PK11195 PET in corticobasal degeneration. *Mov Disord.* (2004) 19:1221–6. doi: 10.1002/mds.20162

Conflict of Interest: The authors declare that the research was conducted in the absence of any commercial or financial relationships that could be construed as a potential conflict of interest.

Copyright © 2020 Saeed, Lang and Masellis. This is an open-access article distributed under the terms of the Creative Commons Attribution License (CC BY). The use, distribution or reproduction in other forums is permitted, provided the original author(s) and the copyright owner(s) are credited and that the original publication in this journal is cited, in accordance with accepted academic practice. No use, distribution or reproduction is permitted which does not comply with these terms.

frontiers in Neurology

ORIGINAL RESEARCH
published: 12 November 2020
doi: 10.3389/fneur.2020.603161

Association of MRI Measures With Disease Severity and Progression in Progressive Supranuclear Palsy

Marina Picillo[1], Filomena Abate[1], Sara Ponticorvo[2], Maria Francesca Tepedino[1], Roberto Erro[1], Daniela Frosini[3], Eleonora Del Prete[3], Paolo Cecchi[4], Mirco Cosottini[4], Roberto Ceravolo[3], Gianfranco Di Salle[5], Francesco Di Salle[2], Fabrizio Esposito[2,6], Maria Teresa Pellecchia[1], Renzo Manara[7] and Paolo Barone[1]*

[1] Center for Neurodegenerative Diseases (CEMAND), Department of Medicine, Surgery and Dentistry, Neuroscience Section, University of Salerno, Fisciano, Italy, [2] Department of Medicine, Surgery & Dentistry, Scuola Medica Salernitana, University of Salerno, Baronissi, Italy, [3] Dipartimento di Medicina Clinica e Sperimentale Università di Pisa, Pisa, Italy, [4] Dipartimento di Ricerca Traslazionale e delle Nuove Tecnologie in Medicina e Chirurgia, Università di Pisa, Pisa, Italy, [5] Scuola Superiore Sant'Anna, Pisa, Italy, [6] Department of Diagnostic Imaging, University Hospital A.O.U. OO.RR. San Giovanni di Dio e Ruggi D'Aragona, Scuola Medica Salernitana, Salerno, Italy, [7] Department of Neurosciences, University of Padua, Padua, Italy

OPEN ACCESS

Edited by:
Maria Carmela Tartaglia, University of Toronto, Canada

Reviewed by:
Günter Höglinger, Technical University of Munich, Germany
Marian L. Dale, Oregon Health and Science University, United States

***Correspondence:**
Renzo Manara
renzo.manara@unipd.it

Specialty section:
This article was submitted to Movement Disorders, a section of the journal Frontiers in Neurology

Received: *05 September 2020*
Accepted: *13 October 2020*
Published: *12 November 2020*

Citation:
Picillo M, Abate F, Ponticorvo S, Tepedino MF, Erro R, Frosini D, Del Prete E, Cecchi P, Cosottini M, Ceravolo R, Salle GD, Salle FD, Esposito F, Pellecchia MT, Manara R and Barone P (2020) Association of MRI Measures With Disease Severity and Progression in Progressive Supranuclear Palsy. Front. Neurol. 11:603161. doi: 10.3389/fneur.2020.603161

Objective: To verify the association of midbrain-based MRI measures as well as cortical volumes with disease core features and progression in patients with Progressive Supranuclear Palsy (PSP).

Methods: Sixty-seven patients (52.2% with Richardson's syndrome) were included in the present analysis. Available midbrain-based MRI morphometric assessments as well as cortical lobar volumes were computed. Ocular, gait and postural involvement at the time of MRI was evaluated with the PSP rating scale. Specific milestones or death were used to estimate disease progression up to 72 months follow up. Hierarchical regression models and survival analysis were used for analyzing cross-sectional and longitudinal data, respectively.

Results: Multivariate models showed vertical supranuclear gaze palsy was associated with smaller midbrain area (OR: 0.02, 95% CI 0.00–0.175, $p = 0.006$). Cox regression adjusted for age, disease duration, and phenotype demonstrated that lower midbrain area (HR: 0.122, 95% CI 0.030–0.493, $p = 0.003$) and diameter (HR: 0.313, 95% CI 0.112–0.878, $p = 0.027$), higher MR Parkinsonism Index (HR: 6.162, 95% CI 1.790–21.209, $p = 0.004$) and larger third ventricle width (HR: 2.755, 95% CI 1.068–7.108, $p = 0.036$) were associated with higher risk of dependency on wheelchair.

Conclusions: Irrespective of disease features and other MRI parameters, reduced midbrain size is significantly associated with greater ocular motor dysfunction at the time of MRI and more rapid disease progression over follow up. This is the first comprehensive study to systematically assess the association of available midbrain-based MRI measures and cortical volumes with disease severity and progression in a large cohort of patients with PSP in a real-world setting.

Keywords: progressive supranuclear palsy, imaging, disease severity, disease progression, milestones

INTRODUCTION

Progressive Supranuclear Palsy (PSP) is a rare, rapidly progressive, neurodegenerative disease characterized by dysfunction in four core domains including ocular motor function, postural instability, akinesia, and cognition represented by a number of clinical features (1). The diverse combination of core clinical features is relevant for the attribution of the degree of diagnostic certainty as well as the clinical phenotype of disease (1). While PSP Richardson's syndrome (PSP-RS) is the most common clinical phenotype, other distinct variants, each featured by a specific predominant symptom, have been described (vPSP) (1). Irrespective of the phenotype, the presence of either slowing velocity of vertical saccades or vertical supranuclear gaze palsy (VSGP) is mandatory for the diagnosis of probable PSP (1).

To date, research studies on magnetic resonance imaging (MRI) measures in PSP have focused on supporting the clinical diagnosis of disease. Given the key role of midbrain in PSP-related pathological process, a number of midbrain-based MRI morphometric measures have shown adequate diagnostic accuracy in differentiating PSP-RS from healthy subjects and other parkinsonian disorders (2–7).

Conversely, few studies focused on the association between MRI measures and disease severity and progression in PSP. Evidence showed the MR Parkinsonism Index (MRPI) anticipated the development of VSGP in 11 out of 21 patients with PSP with predominant parkinsonism after a mean follow up of 28.5 months and a decreased midbrain-to-pons area ratio predicted shorter survival and earlier institutionalization in 51 patients fulfilling criteria for probable and possible PSP (8, 9). However, a comprehensive screening of the association of available midbrain-based MRI measures with disease severity and progression is lacking.

Demonstrating a relationship between MRI imaging markers and disease severity and progression in a real-world setting is pivotal to identify surrogate markers of disease to be used in the context of clinical trials evaluating disease-modifying treatments (10). Aim of the present study is to verify the association of midbrain-based MRI measures with disease core features and progression in patients with PSP. As most novel measures include a surrogate evaluation of other brain regions involved in the pathological process (e.g., frontal cortical atrophy in MRPI 2.0), we also analyzed the impact of cortical lobar atrophy on disease features and progression. In the cross-sectional phase of the study, MRI correlates of VSGP, severe postural instability and gait impairment were investigated. In the longitudinal phase, relationship between baseline MRI parameters and disease-specific milestones and survival was explored.

Abbreviations: CI, confidence interval; HR, hazard ratio; MCP/SCP, middle cerebellar peduncles to superior cerebellar peduncles ratio; MDS, movement disorder society; MRI, magnetic resonance imaging; MRPI, MR Parkinsonism index; MRPI 2.0, MR Parkinsonism index 2.0 version; OR, odds ratio; P/M, pons-to-midbrain area ratio; P/M 2.0, pons-to-midbrain area ratio 2.0 version; PSP, progressive supranuclear palsy; PSP-RS, PSP Richardson's syndrome; vPSP, other variant syndromes of PSP; VSGP, vertical supranuclear gaze palsy.

METHODS

Patients and Clinical Evaluation

Sixty-seven patients with probable or possible PSP according to the Movement Disorder Society (MDS) criteria were included in the present analysis. Detailed information on enrollment and application of the PSP diagnostic criteria to determine disease phenotype is available elsewhere (7, 11, 12). Briefly, 78 PSP outpatients were enrolled from the Movement Disorders Centers of the University of Salerno and the University of Pisa between November 2015 and December 2018. Eleven patients were excluded because already presented one of the milestones at baseline (i.e., dementia) (see below). All had diagnosis of probable PSP but those with corticobasal predominant phenotype which—by definition—qualifies for possible PSP (1).

In a preliminary exploratory analysis, PSP rating scale considered as total score did not show any significant relationship with any MRI measure (data not shown). Thus, for the cross-sectional phase, severity of disease was evaluated according to specific items from the PSP rating scale scoring core features of the disease (13). As for ocular dysfunction, patients presenting a score >2 on both items 14 and 15 (i.e., saccadic amplitude reduced by more than 50% on the vertical plane) were considered affected by VSGP. As for postural instability, patients presenting a score >2 on item 27 (i.e., must be caught by the examiner on backward pull or requiring assistance to stand still) were deemed affected by severe postural instability. As for gait impairment, patients presenting a score >2 on item 26 (i.e., need for assistance all or almost all time or inability to walk) were considered affected by severe gait disturbance.

For the longitudinal phase, PSP rating scale was available only for a subset of patients (42) and no relationship was evident between change in PSP rating scale and baseline MRI measure in an exploratory analysis. Thus, the following milestones were selected to define disease progression: (1) dependence on wheelchair; (2) unintelligible speech; (3) dementia (i.e., cognitive impairment severe enough to significantly affect activities of daily living). These milestones have been selected because they are clinically relevant and represent the different domains of impairment of functioning in PSP (14, 15). All enrolled patients but 5 were re-evaluated after a mean (standard deviation) of 16.36 (11.51) months. Eleven patients (including 8 deceased) were not available for in-hospital follow up and a telephone assessment with caregiver was proposed. Thus, milestones were retrieved from medical records and/or with a semi-structured interview administered to the caregiver by telephone. Time to development of each milestone and death were calculated since baseline MRI (range: 1–72 months).

MRI Imaging Protocol

Brain MRI was performed at the time of baseline evaluation. Eighty-two percent (55/67) of patients underwent 3T brain MRI with the same scanner (Skyra, Siemens, Erlangen, Germany); the remaining patients had MRI with different scanners (1.5 and 3T). On the 3T MRI scanner a volumetric 3D T1-weighted magnetization prepared rapid gradient echo (MPRAGE) sequence was acquired with the following parameters: repetition

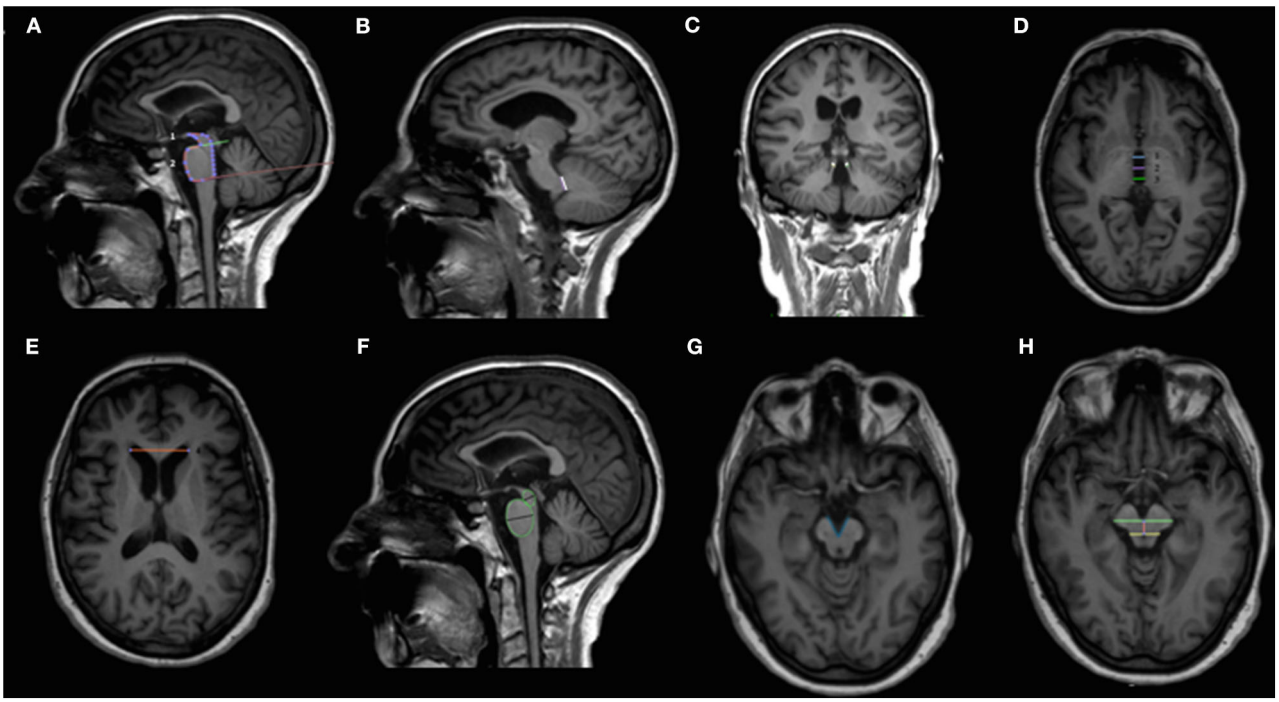


FIGURE 1 | Overview of the midbrain-based measures computed. Sagittal **(A,B,F)**, coronal **(C)** and axial **(D,E,G,H)** T1-weighted volumetric MR images. Midsagittal midbrain area (1) and midsagittal pons area (2) used for calculating the pons-to-midbrain area ratio (P/M) are shown in **(A)**. Middle and superior cerebellar peduncles used to compute middle cerebellar peduncles to superior cerebellar peduncles ratio (MCP/SCP) are shown in **(B)** and **(C)**, respectively. Third ventricle measurements at the level of anterior and posterior commissures [third ventricle width derives from the mean of the anterior (1), medium (2), and posterior lines (3)] and frontal horns width are shown in **(D)** and **(E)**, respectively. MRPI is calculated with the following formula: (P/M) × (MCP/SCP); MRPI 2.0 is calculated with the following formula: MRPI × (third ventricle width/frontal horns width); P/M 2.0 is calculated with the following formula: (P/M) × (third ventricle width/frontal horns width). Midbrain and pons diameters obtained from midsagittal elliptical regions of interests are shown in **(F)**. Minor axes were used to calculate the pons-to-midbrain diameter ratio. The interpeduncular angle, calculated on a plane parallel to anterior commissure-posterior commissure line and right below the mammillary bodies, is shown in **(G)**. The length of midbrain tegmentum, measured as the distance between the interpeduncular fossa and the center of the aqueduct at the level of mammillary bodies, on a plane parallel to the anterior commissure-posterior commissure line is shown in **(H)**. MCP/SCP, middle cerebellar peduncles to superior cerebellar peduncles ratio; MR, magnetic resonance; MRPI, MR Parkinsonism index; MRPI 2.0, MR Parkinsonism index 2.0 version; P/M, pons-to-midbrain area ratio; P/M 2.0, pons-to-midbrain area ratio 2.0 version.

time = 2,400 ms, echo time = 2.25 ms, resolution = 1 × 1 × 1 mm^3, matrix size = 256 × 256, 192 sagittal slices, anterior–posterior phase-encoding direction, generalized autocalibrating partially parallel acquisition (GRAPPA) factor of 2 in phase-encoding direction.

Sagittal partitions were obtained and multiplanar reconstructions were obtained in the conventional transverse and coronal planes.

Morphometric Measurements

Midbrain-based measures were retrospectively calculated for all included patients and included midsagittal midbrain area, length of midbrain tegmentum, midbrain diameter, pons-to-midbrain diameter ratio, cerebral interpeduncolar angle, middle cerebellar peduncles to superior cerebellar peduncles ratio (MCP/SCP), pons-to midbrain area ratio (P/M), and MRPI as well as P/M 2.0 and MRPI 2.0 (MRPI and P/M multiplied by third ventricle width/frontal horns width ratio) (**Figure 1**) (3, 4, 7, 16–18). Given its relevance in PSP, both the latter include a surrogate measure of the frontal lobe volume (4, 10).

All midbrain measures were manually computed according to published methods by the same neuroradiologist (R.M.) with more than 15 years of experience in neurodegenerative diseases (7). Acceptable inter-rater agreement for manually computed measures between two different neuroradiologists as well as excellent agreement between manual and computerized MRPI have been already demonstrated elsewhere for the data considered in the present analysis (7).

Cortical volume was evaluated for a subset of 49 patients (73%). MPRAGE images were processed using FreeSurfer version 6.0 (https://surfer.nmr.mgh.harvard.edu/) using the standard structural image preprocessing and surface reconstruction pipeline via the "recon-all" command (for a detailed description of this procedure please see https://surfer.nmr.mgh.harvard.edu/fswiki/ReconAllTableStableV5.3) (19–25). Preprocessed data were visually inspected to assure the quality of each reconstruction. Cortical volume was extracted for each region of

the Desikan-Killiany cortical atlas and then regions were merged (and volumes were summed) to obtain one regional value for each cerebral lobe (frontal, parietal, occipital, temporal, and cingulate) (26).

Standard Protocol Approvals, Registrations, and Patient Consent

The project was approved by the local Ethics Committees and each subject was included after signing the informed consent form.

Statistical Analysis

Differences in variables between groups were computed with χ^2 or Mann-Whitney test, as appropriate.

In line with the principles of multilevel modeling, hierarchical regression has been used for the present analysis (27). For the cross-sectional phase, multivariate logistic regression was implemented to explore imaging correlates of VSGP (non-VSGP = 0 vs. VSGP = 1), severe postural instability (non-severe postural instability = 0 vs. severe postural instability = 1) and severe gait impairment (non-severe gait impairment = 0 vs. sever gait impairment = 1). After adjusting for age and disease duration, the univariate relationship between each clinical outcome and each imaging parameter was examined. Any variables that had univariate associations with p values <0.10 were included in a multivariate model, also adjusting for disease phenotype (PSP-RS vs. vPSP). A backward selection approach was used to choose the best model. Variables were removed one at

TABLE 1 | Demographic, clinical, imaging features, and time to reach disease milestones and death for the whole cohort and according to disease phenotype.

	Whole cohort (67)	PSP-RS (35)	vPSP (32)	*p*
Demographics				
Age, years	70.5 (52–85)	71 (52–79)	70 (56–85)	0.772
Gender (men/women), *n* (%)	32/35 (47.8–52.2)	16/19 (45.71/54.28)	16/16 (50–50)	0.726
Clinical features				
Age at onset, years	66 (47–82)	67 (52–79)	65 (47–76)	0.627
Disease duration, years	4 (1–11)	3 (1–11)	5 (1–8)	0.142
PSP rating scale	43 (10–86)	46 (16–86)	42 (10–82)	0.292
MRI measures				
Midbrain area, mm^2	0.74 (0.51–1.31)	0.9 (0.5–1.84)	1.1 (0.63–1.84)	**0.037**
Length of midbrain tegmentum, mm	8.34 (5.07–12.13)	8.01 (5.07–10.63)	9.25 (6.52–12.13)	**0.006**
P_d/M_d	2.06 (1.44–2.92)	2.23 (1.45–2.92)	1.94 (1.44–2.67)	**0.006**
Cerebral peduncle angle, degree	68 (52–94)	69 (58–94)	66.5 (52–84)	0.218
MCP/SCP	2.67 (1.27–4.1)	2.67 (1.27–4,1)	2.67 (1.54–3.74)	0.87
P_a/M_a	5.68 (2.26–8.96)	6 (2.29–8.96)	5.39 (2.26–8.42)	0.223
MRPI	15.15 (4.2–36.63)	15.82 (4.53–36.63)	13.99 (4.2–31.49)	0.459
P_a/M_a 2.0	1.41 (0.34–2.91)	1.56 (0.57–2,91)	1.28 (0.34–2.63)	0.259
MRPI 2.0	3.74 (0.79–11.89)	4.45 (1.11–11.89)	3.53 (0.79–8.64)	0.393
Frontal volume*	134.51 (78.8–161.58)	134.51 (78.8–153.06)	134.22 (107.79–161.58)	0.920
Parietal volume*	93.10 (54.26–113.68)	94.14 (54.26–113.68)	91.08 (74.29–107.52)	0.342
Temporal volume*	92.26 (35.56–110.49)	93.44 (35.56–110.49)	90.01 (68.75–109.6)	0.585
Occipital volume*	43.73 (30.33–54.14)	43.73 (30.33–54.15)	43.55 (36.35–53.45)	0.467
Cingulate volume*	16.28 (5.28–20.8)	16.28 (5.28–19.5)	16.39 (13.47–20.8)	0.936
Disease milestones				
Time to wheelchair, months	*N* = 30 (44.7%)	*N* = 18 (58.1%)	*N* = 12 (40%)	0.204
	16 (1–42)	16 (1–42)	16 (5–41)	0.871
Time to unintelligible speech, months	*N* = 32 (47.7%)	*N* = 18 (58.1%)	*N* = 14 (48.3%)	0.605
	19 (1–48)	21 (1–48)	18 (5–39)	0.633
Time to dementia, months	*N* = 40 (59.7%)	*N* = 20 (71.4%)	*N* = 20 (69%)	1.000
	16 (1–72)	14 (1–72)	18 (5–38)	0.517
Time to death, months	*N* = 9 (13.4%)	*N* = 7 (24.1%)	*N* = 2 (6.9%)	0.144
	19 (1–72)	21 (1–72)	18 (5–41)	0.641

Data are expressed in median (range), unless otherwise specified.
vPSP included 13 with predominant parkinsonism, 6 with progressive gait freezing, 9 with predominant corticobasal syndrome and 4 with predominant frontal presentation.
**Data available for 49 subjects (21 PSP-RS and 28 vPSP).*
MCP/SCP, middle cerebellar peduncles to superior cerebellar peduncles ratio; MRPI, MR Parkinsonism index; MRPI 2.0, MR Parkinsonism index 2.0 version; P_a/M_a, pons-to midbrain area ratio; P_a/M_a 2.0, pons-to midbrain area ratio 2.0 version; P_d/M_d, pons-to-midbrain diameter ratio; PSP-RS, progressive supranuclear palsy with richardson's syndrome; vPSP, the other variant syndromes of Progressive Supranuclear Palsy.
Significant differences are highlighted in bold.

a time until all variables remaining in the model were significant at the 0.05 level. To avoid collinearity issues between individual MRI measures and midbrain ratios, if any individual measures were significant, they were considered in the multivariate model. The midbrain ratios were only considered in the multivariate model if neither of the individual components was significant. All odds ratio (OR, CI 95%) and *p*-values are from the backwards selection models.

For the longitudinal phase, patients were divided into two subgroups (i.e., less atrophy vs. more atrophy) using the median value of each imaging parameter at baseline. Kaplan-Meier curves and log-rank (Mantel-Cox) test were computed to assess the association of baseline imaging variable with the risk of developing each disease milestone and the risk of death over the follow up. For variables significant at the 0.05 level, univariate Cox proportional hazards regression models were computed and HRs and 95% CIs were estimated adjusting for age, disease duration, and phenotype. Statistical significance was set at $p \leq 0.05$. Data analysis was conducted with SPSS (version 23.0).

RESULTS

Demographics, Clinical, and Imaging Features

Demographic, clinical, imaging features, and time to reach disease milestones and death of the 67 PSP patients (52.2% PSP-RS) included in the analysis are shown in **Table 1**. Irrespective of similar demographics and clinical features, PSP-RS had lower midbrain area and length of midbrain tegmentum and higher pons-to-midbrain diameter ratio compared to vPSP. Clinical phenotypes did not differ in time to reach disease milestones or death.

Association of Imaging Parameters With Disease Severity at Baseline

Imaging correlates of VSGP, severe postural instability and gait impairment are shown in **Table 2** and **Supplementary Table 1**.

After adjusting for age and disease duration in the univariate model, VSGP was associated with PSP-RS phenotype, midbrain area, midbrain diameter, pons diameter, length of midbrain tegmentum, MCP, SCP, MRPI, P/M, pons-to-midbrain diameter ratio, occipital volume (all $p < 0.1$). Only association with smaller midbrain area was confirmed in the multivariate model (**Table 2**).

After adjusting for age and disease duration in the univariate model, severe postural instability was associated with PSP-RS phenotype, midbrain area, midbrain diameter, pons-to-midbrain diameter ratio, M/P, M/P 2.0, MRPI, MRPI 2.0, length of midbrain tegmentum, MCP/SCP, third ventricle and frontal horns width and cingulate volume (all $p < 0.1$). In the multivariate model, all became non-significant (**Supplementary Table 1**).

After adjusting for age and disease duration in the univariate model, severe gait impairment was associated with PSP-RS phenotype, midbrain area, midbrain diameter, SCP, pons diameter and M/P (all $p < 0.1$). In the multivariate model, all became non-significant (**Supplementary Table 1**).

TABLE 2 | Imaging correlates of vertical supranuclear gaze palsy.

Variables	Univariate *p* value	Multivariate OR (CI 95%)	Multivariate *p* value
Vertical supranuclear gaze palsy			
Clinical phenotype (PSP-RS vs. vPSP)	0.012	-	NS
Midbrain area	0.003	0.02 (0.00–0.175)	0.006
Pons area	0.120	-	-
P_a/M_a	0.022	-	Not included
MCP	0.085	-	NS
SCP	0.091	-	NS
MCP/SCP	0.462	-	-
MRPI	0.076	-	Not included
Third ventricle width	0.772	-	-
Frontal horns width	0.965	-	-
P_a/M_a 2.0	0.125	-	-
MRPI 2.0	0.175	-	-
Interpeduncolar angle	0.117	-	-
Pons diameter	0.012	-	NS
Midbrain diameter	0.012	-	NS
P_d/M_d	0.016	-	Not included
Lenght of midbrain tegmentum	0.004	-	NS
Frontal volume	0.140	-	-
Parietal volume	0.960	-	-
Temporal volume	0.662	-	-
Occipital volume	0.065	-	NS
Cingulate volume	0.252	-	-

Each univariate as well as multivariate models were adjusted for age and disease duration. The midbrain ratios were only considered in the multivariate model if neither of the individual components was significant.

M_d, Midbrain diameter; MCP/SCP, middle cerebellar peduncles to superior cerebellar peduncles ratio; MRPI, MR Parkinsonism index; MRPI 2.0, MR Parkinsonism index 2.0 version; NS, not significant; OR, odds ratio; P_a/M_a, pons-to midbrain area ratio; P_a/M_a 2.0, pons-to midbrain area ratio 2.0 version; P_d/M_d, pons-to-midbrain diameter ratio; PSP-RS, progressive supranuclear palsy with Richardson's syndrome; vPSP, the other variant syndromes of progressive supranuclear palsy.

Association of Imaging Parameters at Baseline With Disease Progression

Kaplan Meier curves showed lower midbrain area ($p = 0.006$), midbrain diameter ($p = 0.013$), length of midbrain tegmentum ($p = 0.044$), higher MRPI ($p = 0.008$) and larger third ventricle width ($p = 0.029$) were associated with higher risk of dependency on wheelchair (**Figure 2**). In addition, lower MCP ($p = 0.044$) and larger third ventricle width ($p = 0.050$) were associated with higher risk of death (**Figure 3**).

Cox regression analysis adjusted for age, disease duration and phenotype demonstrated that lower midbrain area (HR: 0.122, 95% CI 0.030–0.493, $p = 0.003$), midbrain diameter (HR: 0.313, 95% CI 0.112–0.878, $p = 0.027$), higher MRPI (HR: 6.162, 95% CI 1.790–21.209, $p = 0.004$) and larger third ventricle width (HR: 2.755, 95% CI 1.068–7.108, $p = 0.036$) but not length of midbrain tegmentum (HR: 0.431, 95% CI 0.176–1.056, $p = 0.066$)

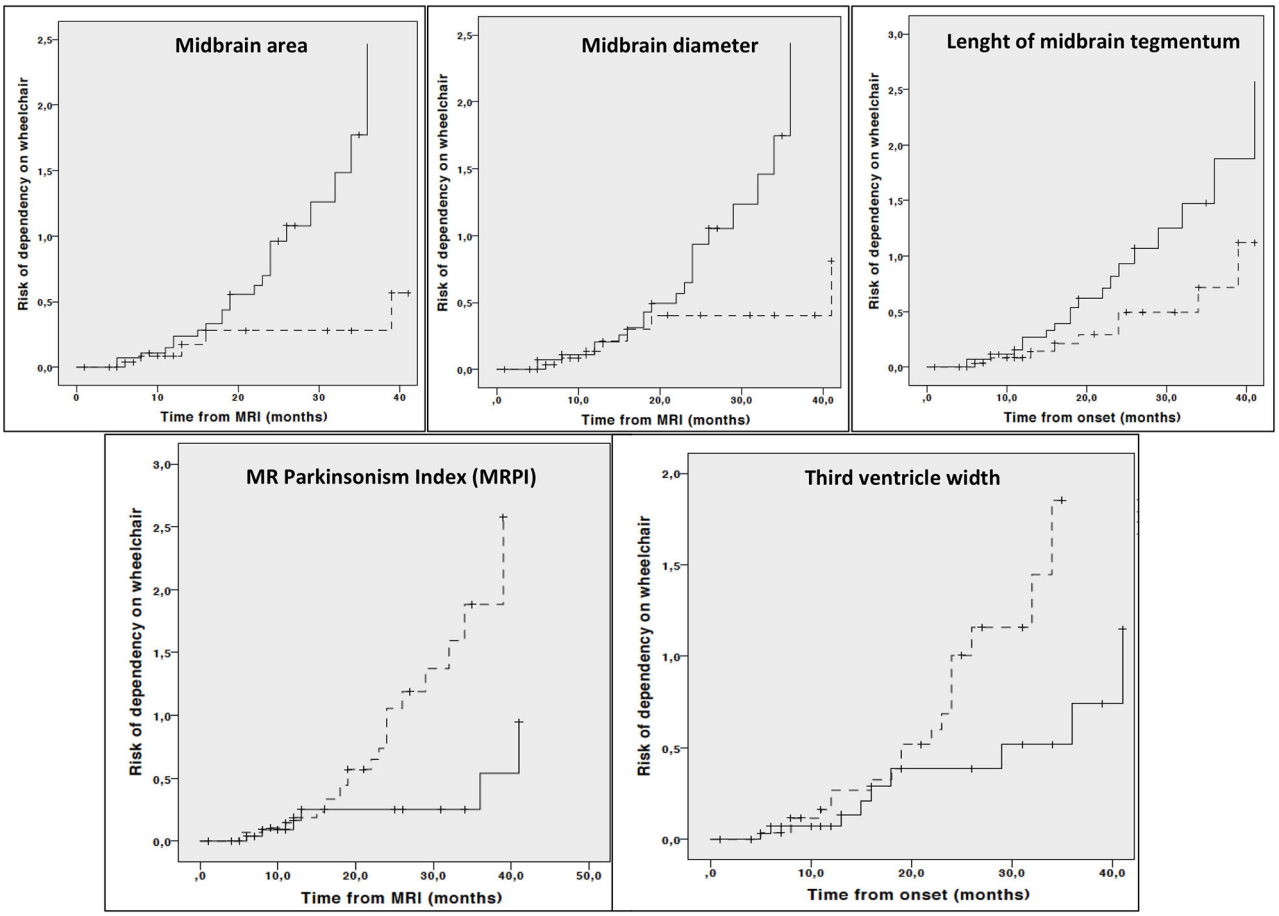


FIGURE 2 | Cumulative risk of dependency on wheelchair by each MRI parameter (less atrophy vs. more atrophy). Only curves with significant log-rank test at 0.05 level are reported. Dotted line: values above median; Continuous line: values below median.

were associated with a significant higher risk of dependency on wheelchair. On the contrary, neither third ventricle width (HR: 3.328 95% CI 0.358–30.997, $p = 0.291$) or MCP (HR: 0.263, 95% CI 0.047–1.467, $p = 0.128$) were associated with higher risk of death when considering age, disease duration and phenotype as covariate.

DISCUSSION

Although previous studies have shown association of regional brain atrophy with disease features in PSP (8, 9, 28, 29), this is the first comprehensive study to systematically assess the association of available midbrain-based MRI measures and cortical volumes with disease severity and progression in a large cohort of patients with PSP in a real-world setting. Our findings showed that, irrespective to other disease and imaging features, reduced midbrain area is significantly associated with greater ocular motor dysfunction at the time of MRI and more rapid disease progression on follow up.

In the cross-sectional part of our study, we demonstrated a direct association between VSGP and midbrain area. This finding was not surprising as a large body of evidence confirms that vertical saccades are triggered by the rostral interstitial nucleus of the medial longitudinal fasciculus located in the midbrain (30). As such, vertical saccades as assessed with video-oculography have been linked with midbrain size as well as midbrain network dysfunction in PSP (28, 29). Our data are also in line with previous evidence of reduced midbrain area in patients with VSGP (O1 domain from MDS criteria) compared to those with slowing of vertical saccades (O2 domain) (31).

Given our methodological approach, we were able to show that ocular motor dysfunction is specifically linked to the midbrain, that is, a brain region crucially involved in the underlying PSP-related pathological process (2, 32). Several methodological considerations strengthen our data. First, the statistical approach provided direct evidence of such relationship irrespective of age, disease duration, and phenotype as well as other MRI parameters (28, 29). Second, clinical evaluation of ocular movements was rated with specific items from the PSP rating scale, the most used tool in the context of disease-modifying clinical trials, with no need to use more sophisticated and time-consuming assessments (13). Finally, our

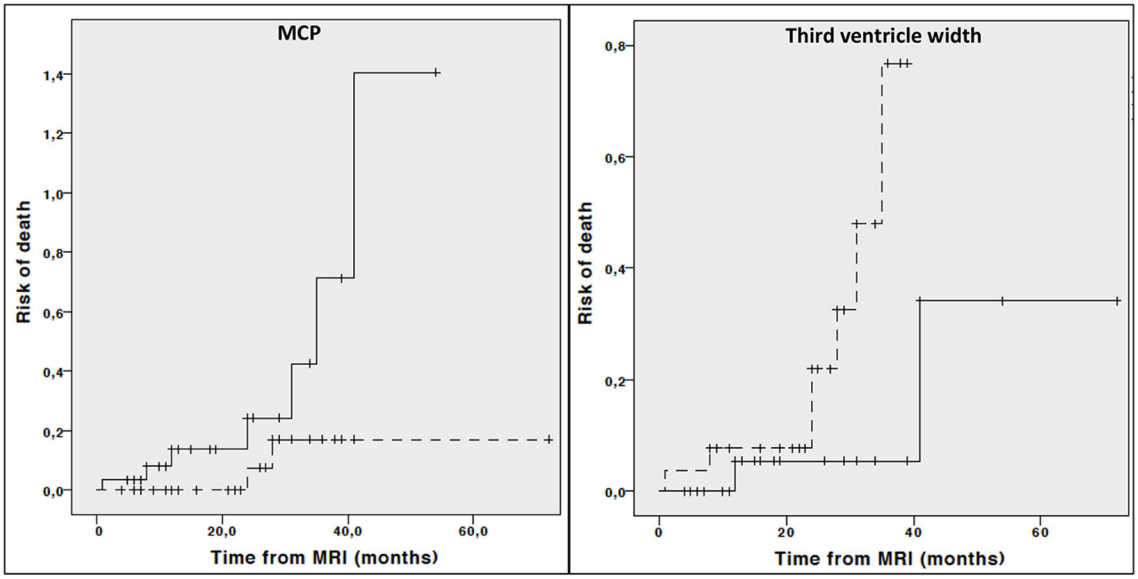


FIGURE 3 | Cumulative risk of death by each MRI parameter (less atrophy vs. more atrophy). Only curves with significant log-rank test at 0.05 level are reported. Dotted line: values above median; Continous line: values below median.

patients were diagnosed and phenotyped with the most up-to-date set of available criteria (1).

On the other hand, relationship between gait impairment and postural instability with multiple midbrain parameters (area, diameter, length of tegmentum) was demonstrated in the univariate analysis only and not confirmed when accounting for age, disease duration and phenotype as well as other MRI parameters. Taken together such findings suggest that a broader disruption of the complex interplay between different networks and structures likely underpins the severity of gait and postural issues in PSP (29).

In the longitudinal part of our study, the relationship between multiple baseline midbrain-based parameters as well as cortical lobe volumes and disease-specific milestones was investigated. Again, irrespective of age, disease duration, and phenotype, different direct and indirect midbrain parameters (i.e, midbrain area, midbrain diameter, third ventricle width and MRPI) predicted higher risk of dependency on wheelchair. On the other hand, relationship between risk of death with MCP and third ventricle width was demonstrated in the univariate analysis only and not confirmed when accounting for age, disease duration and phenotype. Finally, none of baseline MRI measures were able to predict either dementia or unintelligible speech or survival.

In line with previous data (8), our findings suggest midbrain area—the simplest imaging parameter to measure—is able to predict disease progression. This adds to data from a previous study showing a relationship between midbrain tau-PET signal and severity of disease as assessed with PSP rating scale (33). From a practical point of view, midbrain area measurement is much easier to perform by neuroradiologists and general radiologists not specifically working with movement disorders (it requires only the mid-sagittal image without further specific reconstructed planes or repetitive and less reproducible measurements on the superior and middle cerebellar peduncles) and, thus, might be more appropriate than other measures in a real-world setting.

Strikingly, we failed to find any relationship between cortical lobe volumes and development of dementia. A note of caution on such conclusion, however, is that cortical lobe volumes were available only for a limited number of subjects (i.e., 49/67). Also, dementia was evaluated according to clinician-based opinion instead of using a formal cognitive battery. Similarly, lack of any association with risk of death may be related to the lower percentage of deceased in our cohort (13.4%) over the follow up. Finally, we acknowledge we used a simplistic approach considering cortical lobe volumes and, as such, we can not exclude specific cortical regions would be associated with impairment in specific functional domains. However, this was out of the scope of the present analysis.

Our study has limitations. First, we recognize the lack of pathological confirmation of both diagnosis and phenotypic categorization, still the gold standard for PSP diagnosis. Although our data are based only on clinical judgment, both the MDS diagnostic flow chart and phenotypic attribution have been applied independently by two experts in movement disorders as detailed elsewhere (7). In addition, evaluation of clinical features was conducted by movement disorders specialists with more than 10 years of experience in movement disorders (MP, RC and DF).

As a second drawback, we acknowledge that merging PSP with predominant parkinsonism, PSP with progressive gait freezing, PSP with predominant corticobasal syndrome and PSP with predominant frontal presentation into a single group (i.e., vPSP) to increase the statistical power of our analysis may limit the interpretation of the results for PSP subtype comparisons. Indeed, further studies enrolling a larger number of phenotypes other than PSP-RS are needed to better characterize

the relationship between radiological biomarkers and disease severity and progression according to phenotype. Also we failed to report on other important clinical milestones as dysphagia.

From a technical standpoint, we recognize the lack of longitudinal MRIs from a healthy control group prevent us from quantifying atrophy rate in PSP compared to age-matched healthy subjects. However, previous data already shown midbrain area had diagnostic value in differentiating PSP vs. healthy controls and prognostic value as marker of disease progression in PSP (10, 34, 35). Furthermore, we recognize MRI imaging was not standardized across the two sites. However, 82% of the cohort was enrolled at Salerno center and underwent MRI with the same facility. Also, midbrain-based morphometric assessments were computed by the same examiner (RM) who received the whole set of images and personally performed sagittal partitions and multiplanar reconstructions. Finally, cortical volumes were available for a subset of 49 patients, all from the center of Salerno.

In conclusion, our study demonstrates that, irrespective of disease features and other MRI parameters, reduced midbrain size is significantly associated with greater ocular motor dysfunction at the time of MRI and more rapid disease progression on follow up. Longitudinal imaging studies are required to validate midbrain area as a marker of disease progression in different phenotypes and accounting for other disease and imaging features.

This is the first comprehensive study to systematically assess the association of available midbrain-based MRI measures and cortical lobe volumes with disease severity and progression in a large cohort of patients with PSP diagnosed according with MDS criteria in a real-world setting.

DATA AVAILABILITY STATEMENT

The deidentified dataset used to generate the results in the current study is available from the corresponding author on request.

ETHICS STATEMENT

The studies involving human participants were reviewed and approved by Ethic Committee Campania Tre Sud. The patients/participants provided their written informed consent to participate in this study.

AUTHOR CONTRIBUTIONS

MP: conception, organization, and execution of the research project, design and execution of statistical analysis, and writing the first draft of the manuscript. FA, SP, and MT: organization and execution of the research project, review and critique of statistical analysis, and review and critique of the manuscript. RE, ED, PC, MC, RC, GS, FS, FE, MTP, RM, and PB: execution of the research project, review and critique of statistical analysis, and review and critique of the manuscript. All authors contributed to the article and approved the submitted version.

FUNDING

MP was supported by the Michael J Fox Foundation for Parkinson's research; PB received consultancies as a member of the advisory board for Zambon, Lundbeck, UCB, Chiesi, Abbvie, and Acorda; Dr. RE received consultancies from Zambon and honoraria from TEVA.

SUPPLEMENTARY MATERIAL

The Supplementary Material for this article can be found online at: https://www.frontiersin.org/articles/10.3389/fneur.2020.603161/full#supplementary-material

REFERENCES

1. Hoglinger GH, Respondek G, Stamelou M, Kurz C, Josephs KA, Lang AE, et al. Clinical diagnosis of progressive supranuclear palsy: the movement disorder society criteria. *Mov. Disord.* (2017) 32:853–64. doi: 10.1002/mds.26987
2. Kovacs GG. Neuropathology of tauopathies: principles and practice. *Neuropathol. Appl. Neurobiol.* (2015) 41:3–23. doi: 10.1111/nan.12208
3. Whitwell JL, Hoglinger GU, Antonini A, Bordelon Y, Boxer AL, Colosimo C, et al. Radiological biomarkers for diagnosis in PSP: where are we and where do we need to be. *Mov. Disord.* (2017) 32:955–71. doi: 10.1002/mds.27038
4. Quattrone A, Morelli M, Nigro S, Quattrone A, Vescio B, Arabia G, et al. A new MR imaging index for differentiation of progressive supranuclear palsy-parkinsonism from Parkinson's disease. *Parkinsonism Relat. Disord.* (2018) 54:3–8. doi: 10.1016/j.parkreldis.2018.07.016
5. Quattrone A, Morelli M, Vescio B, Nigro S, Le Piane E, Sabatini U, et al. Refining initial diagnosis of Parkinson's disease after follow-up: a 4-year prospective clinical and magnetic resonance imaging study. *Mov. Disord.* (2019) 34:487–95. doi: 10.1002/mds.27621
6. Nigro S, Antonini A, Vaillancourt DE, Seppi K, Ceravolo R, Strafella AP, et al. Automated MRI classification in progressive supranuclear palsy: a large international cohort study. *Mov. Disord.* (2020) 35:976–83. doi: 10.1002/mds.28007
7. Picillo M, Tepedino MF, Abate F, Erro R, Ponticorvo S, Tartaglione S, et al. Midbrain MRI assessments in progressive supranuclear palsy subtypes. *J. Neurol. Neurosurg. Psychiatr.* (2020) 91:98–103. doi: 10.1136/jnnp-2019-321354
8. Quattrone A, Morelli M, Williams DR, Vescio B, Arabia G, Nigro S, et al. MR parkinsonism index predicts vertical supranuclear gaze palsy in patients with PSP-parkinsonism. *Neurology.* (2016) 87:1266–73. doi: 10.1212/WNL.0000000000003125
9. Cui SS, Ling HW, Du JJ, Lin YQ, Pan J, Zhou HY, et al. Midbrain/pons area ratio and clinical features predict the prognosis of progressive supranuclear palsy. *BMC Neurol.* (2020) 20:114. doi: 10.1186/s12883-020-01692-6
10. Höglinger GU, Schöpe J, Stamelou M, Kassubek J, Del Ser T, Boxer AL, et al. Movement disorder society-endorsed psp study group. longitudinal magnetic resonance imaging in progressive supranuclear palsy: a new combined score for clinical trials. *Mov. Disord.* (2017) 32:842–52. doi: 10.1002/mds.26973
11. Picillo M, Erro R, Cuoco S, Tepedino MF, Manara R, Pellecchia MT, et al. MDS PSP criteria in real-life clinical setting: motor and cognitive characterization of subtypes. *Mov. Disord.* (2018) 33:1361–5. doi: 10.1002/mds.27408

12. Picillo M, Cuoco S, Tepedino MF, Cappiello A, Volpe G, Erro R, et al. Motor, cognitive and behavioral differences in MDS PSP phenotypes. *J. Neurol.* (2019) 266:1727–35. doi: 10.1007/s00415-019-09324-x
13. Golbe LI, Ohman-Strickland PA. A clinical rating scale for progressive supranuclear palsy. *Brain*. (2007) 130:1552–65. doi: 10.1093/brain/awm032
14. O'Sullivan SS, Massey LA, Williams DR, Silveira-Moriyama L, Kempster PA, Holton JL, et al. Clinical outcomes of progressive supranuclear palsy and multiple system atrophy. *Brain.* (2008) 131:1362–72. doi: 10.1093/brain/awn065
15. Oliveira MCB, Ling H, Lees AJ, Holton JL, De Pablo-Fernandez E, Warner TT. Association of autonomic symptoms with disease progression and survival in progressive supranuclear palsy. *J. Neurol. Neurosurg. Psychiatr*. (2019) 90:555–61. doi: 10.1136/jnnp-2018-319374
16. Fatterpekar GM, Dietrich A, Pantano P, Saba L, Knopp EA, Piattella MC, et al. Cerebral peduncle angle: an objective criterion for assessing progressive supranuclear palsy Richardson syndrome. *AJR Am. J. Roentgenol.* (2015) 205:386–91. doi: 10.2214/AJR.14.12724
17. Eraslan C, Acarer A, Guneyli S, Akyuz E, Aydin E, Colakoglu Z, et al. MRI evaluation of progressive supranuclear palsy: differentiation from Parkinson's disease and multiple system atrophy. *Neurol. Res*. (2019) 41:110–7. doi: 10.1080/01616412.2018.1541115
18. Mangesius S, Hussl A, Krismer F, Mahlknecht P, Reiter E, Tagwercher S, et al. MR planimetry in neurodegenerative parkinsonism yields high diagnostic accuracy for PSP. *Parkinsonism Relat. Disord.* (2018) 46:47–55. doi: 10.1016/j.parkreldis.2017.10.020
19. Dale AM, Sereno MI. Improved localization of cortical activity by combining EEG and MEG with MRI cortical surface reconstruction: a linear approach. *J. Cogn. Neurosci.* (1993) 5:162–76. doi: 10.1162/jocn.1993.5.2.162
20. Dale AM, Fischl B, Sereno MI. Cortical surface-based analysis. I. Segmentation and surface reconstruction. *Neuroimage*. (1999) 9:179–94. doi: 10.1006/nimg.1998.0395
21. Fischl B, Dale AM. Measuring the thickness of the human cerebral cortex from magnetic resonance images. *Proc. Natl. Acad. Sci. U.S.A*. (2000) 97:11050–5. doi: 10.1073/pnas.200033797
22. Fischl B, Liu A, Dale AM. Automated manifold surgery: constructing geometrically accurate and topologically correct models of the human cerebral cortex. *IEEE Trans. Med. Imaging*. (2001) 20:70–80. doi: 10.1109/42.906426
23. Fischl B, Salat DH, Busa E, Albert M, Dieterich M, Haselgrove C, et al. Whole brain segmentation: neurotechnique automated labeling of neuroanatomical structures in the human brain. *Neuron*. (2002) 33:241–355. doi: 10.1016/S0896-6273(02)00569-X
24. Ségonne F, Dale AM. Busa E, Glessner M, Salat D, Hahn HK, et al. A hybrid approach to the skull stripping problem in MRI. *Neuroimage*. (2004) 22:1060–75. doi: 10.1016/j.neuroimage.2004.03.032
25. Salat DH, Buckner RL, Snyder AZ, Greve DN, Desikan RSR, Busa E, et al. Thinning of the cerebral cortex in aging. *Cereb. Cortex*. (2004) 14:721–30. doi: 10.1093/cercor/bhh032
26. Desikan RS, Ségonne F, Fischl B, Quinn BT, Dickerson BC, Blacker D, et al. An automated labeling system for subdividing the human cerebral cortex on MRI scans into gyral based regions of interest. *Neuroimage*. (2006) 31:968–80. doi: 10.1016/j.neuroimage.2006.01.021
27. Greenland S. Principles of multilevel modelling. *Int. J. Epidemiol.* (2000) 29:158–67. doi: 10.1093/ije/29.1.158
28. Vintonyak O, Gorges M, Muller HP, Pinkhardt EH, Ludolph AC, Huppertz HJ, et al. Patterns of eye movement impairment correlate with regional brain atrophy in neurodegenerative parkinsonism. *Neurodegener. Dis*. (2017) 17:117–26. doi: 10.1159/000454880
29. Rosskopf J, Gorges M, Muller HP, Lulè D, Uttner I, Ludolph AC, et al. Intrinsic functional connectivity alterations in progressive supranuclear palsy: differential effects in frontal cortex, motor and midbrain networks. *Mov. Disord.* (2017) 32:1006–15. doi: 10.1002/mds.27039
30. Zee DS. Brain stem and cerebellar deficits in eye movement control. *Trans. Ophthalmol. Soc.* (1986) 105(Pt 5):599–605.
31. Quattrone A, Caligiuri MA, Morelli M, Nigro S, Vescio B, Arabia G, et al. Imaging counterpart of postural instability and vertical ocular dysfunction in patients with PSP: a multimodal MRI study. *Parkinsonism Relat. Disord.* (2019) 63:124–30. doi: 10.1016/j.parkreldis.2019.02.022
32. Ludolph AC, Kassubek J, Landwehrmeyer BG, Menelkow E, Mandelkow EM, Brun DJ, et al. Tauopathies with parkinsonism: clinical spectrum, neuropathologic basis, biological markers and treatment options. *Eur. J. Neurol.* (2009) 16:297–309. doi: 10.1111/j.1468-1331.2008.02513.x
33. Whitwell JL, Lowe VJ, Tosakulwong N, Weigand SD, Senjem ML, Schwarz CG, et al. [^{18}F]AV-1451 tau positron emission tomography in progressive supranuclear palsy. *Mov. Disord.* (2017) 32:124–33. doi: 10.1002/mds.26834
34. Moller L, Kassubek J, Sudmeyer M, Hiker R, Hattingen E, Egger K, et al. Manual MRI morphometry in parkinsonian syndromes. *Mov. Disord*. (2017) 32:778–82. doi: 10.1002/mds.26921
35. Huppertz HJ, Moller L, Sudmeyer M, Hilker R, Hattingen E, Egger K, et al. Differentiation of neurodegenerative parkinsonian syndromes by volumetric magnetic resonance imaging analysis and support vector machine classification. *Mov. Disord*. (2016) 31:1506–17. doi: 10.1002/mds.26715

Conflict of Interest: The authors declare that the research was conducted in the absence of any commercial or financial relationships that could be construed as a potential conflict of interest.

Copyright © 2020 Picillo, Abate, Ponticorvo, Tepedino, Erro, Frosini, Del Prete, Cecchi, Cosottini, Ceravolo, Salle, Salle, Esposito, Pellecchia, Manara and Barone. This is an open-access article distributed under the terms of the Creative Commons Attribution License (CC BY). The use, distribution or reproduction in other forums is permitted, provided the original author(s) and the copyright owner(s) are credited and that the original publication in this journal is cited, in accordance with accepted academic practice. No use, distribution or reproduction is permitted which does not comply with these terms.

frontiers in Neurology

BRIEF RESEARCH REPORT
published: 19 November 2020
doi: 10.3389/fneur.2020.568438

Differentiating Mild Cognitive Impairment, Alzheimer's Disease, and Dementia With Lewy Bodies Using Cingulate Island Sign on Perfusion IMP-SPECT

Hidekazu Kanetaka, Soichiro Shimizu, Yuta Inagawa, Daisuke Hirose, Naoto Takenoshita, Hirofumi Sakurai and Haruo Hanyu*

Department of Geriatric Medicine, Tokyo Medical University, Tokyo, Japan

The cingulate island sign (CIS) on fludeoxyglucose (FDG)-positron emission tomography (PET) is a supporting biomarker of dementia with Lewy bodies (DLB). Its diagnostic accuracy has only been investigated in FDG-PET, however. The present prospective study compared the CIS on I-iodoamphetamine-single photon emission computed tomography (SPECT) among patients with mild cognitive impairment (MCI), AD, or DLB. Fifty-eight patients with MCI, 42 with probable AD, and 58 with probable DLB were enrolled. The "CIScore" used to evaluate the CIS was defined as the ratio of volume of interest (VOI)-1 (indicating posterior cingulate gyrus [PCG]) to VOI-2 (area of significantly reduced regional cerebral blood perfusion [rCBF] in DLB patients compared with in healthy controls). It was calculated using eZIS software. The CIScore for MCI, DLB, and AD was 0.22, 0.23, and 0.28, respectively. The CIScore in the AD group was significantly higher than that in the DLB or MCI groups (AD vs. DLB: $p < 0.001$, AD vs. MCI: $p < 0.005$). This suggests that the CIScore can discriminate DLB from AD, if the decrease in rCBF in the PCG is similar between them. We believe that it is difficult to identify MCI based on the CIScore, as the decrease in rCBF in the PCG is not severe. The diagnostic accuracy of the CIScore may be low as it often shows an increase in elderly DLB patients, in whom the pathologically common form is most prevalent (1). Further study should include assessment of multiple components such as symptom classification and age.

Keywords: cingulate island sign, IMP-SPECT, CIS, Alzheimer's disease, dementia with Lewy bodies (DLB)

OPEN ACCESS

Edited by:
Yu Zhang,
VA Palo Alto Health Care System, United States

Reviewed by:
Daichi Sone,
University College London, United Kingdom
Nicolas Nicastro,
Geneva University Hospitals (HUG), Switzerland

****Correspondence:***
Hidekazu Kanetaka
hidekazu@xg7.so-net.ne.jp

Specialty section:
This article was submitted to Applied Neuroimaging, a section of the journal Frontiers in Neurology

Received: *01 June 2020*
Accepted: *21 October 2020*
Published: *19 November 2020*

Citation:
Kanetaka H, Shimizu S, Inagawa Y, Hirose D, Takenoshita N, Sakurai H and Hanyu H (2020) Differentiating Mild Cognitive Impairment, Alzheimer's Disease, and Dementia With Lewy Bodies Using Cingulate Island Sign on Perfusion IMP-SPECT. Front. Neurol. 11:568438. doi: 10.3389/fneur.2020.568438

INTRODUCTION

It is clinically important to distinguish dementia with Lewy bodies (DLB) from Alzheimer's disease (AD) as the type of treatment required for each differs. There are a number of characteristics particular to patients with DLB. These include occipital hypoperfusion, and greater preservation of metabolism in the posterior cingulate gyrus (PCG) than in the precunei, the latter being known as the cingulate island sign (CIS).

The CIS on FDG-PET is recognized as a supporting biomarker of DLB according to the International DLB Diagnostic Criteria published in 2017 (2, 3). Although the diagnostic accuracy of the CIS has been investigated in FDG-PET (4, 5), to our knowledge, it has yet to be determined in brain perfusion SPECT.

One previous study (6) investigated the diagnostic accuracy of the CIS on technetium-99m ethyl cysteinate dimer (ECD)-SPECT in a cohort of 13 patients with DLB and 13 with AD. The results revealed DLB-specific VOIs in areas showing a significant decrease in brain perfusion in the DLB group. As numerators of these ratios, early Alzheimer's disease-specific VOIs were used after subtracting DLB-specific VOIs. The DLB-specific VOIs were used as the denominator. The CIScore was generated from the SPECT Z-scores using the Z-score imaging system (eZIS). The results indicated that DLB could be differentiated from AD by this method with an accuracy, sensitivity, and specificity of 84.6, 92.3, and 76.9%, respectively, with a threshold value of 0.281 (CIScore).

One study reported that ^{123}-I-iodoamphetamine (IMP)-SPECT faithfully reflected cerebral blood flow, even in areas where it was high, whereas ECD showed a weaker correlation (7). This suggests that IMP is more likely to capture mild change in blood flow.

It should also be noted that IMP is the more suitable option in observation of the cerebral cortex, as cerebellar accumulation is less than that in the cerebral cortex. This modality offers the best linearity with true cerebral blood flow among the three formulations of SPECT available. Therefore, we believe that IMP offers the best means of capturing mild change in cerebral blood flow.

The purpose of this study was to compare the CIS on IMP-SPECT among patients with mild cognitive impairment (MCI), AD, or DLB.

METHODS

Ethics

Written informed consent was obtained from the patients or their next of kin/legal guardian if they were a minor for the publication of any potentially identifiable images or data included in this article.

The study protocol was approved by the Ethics Committee of Tokyo Medical University (Approval no: 3304).

Patients

The participants in this prospective study comprised patients with MCI, AD, or DLB attending the Memory Clinic at our hospital. All MCI patients were categorized as the amnestic type. The exclusion criteria were any medication such as benzodiazepine, antidepressants, or antipsychotics.

A total of 58 patients with MCI, 42 with probable AD, and 58 with probable DLB were enrolled (**Table 1**).

The diagnosis of MCI or AD was based on the National Institute on Aging and Alzheimer's Association criteria for a diagnosis of MCI or probable AD (8). The diagnosis of DLB was based on the updated diagnostic criteria published in 2017 by the International DLB Consortium.

None of the patients with MCI or probable AD showed fluctuating cognition, visual hallucinations, parkinsonism, or REM sleep behavior disorder (RBD) as determined by geriatric neurologists.

TABLE 1 | Patient characteristics.

	MCI	AD	DLB
Total: 158	58	42	58
Age (average)	54–97 (77.5)	52–91 (78.8)	70–94 (81.5)#†
MMSE	26.6 ± 1.9	20.9 ± 2.9**	20.5 ± 5.0**
MoCA-J	20.1 ± 3.0	17.5 ± 4.3	14.3 ± 4.6*
ADAS-Jcog	8.8 ± 3.5	16.4 ± 4.8*	16.5 ± 7.3*
WMS-R (logical memory I)	11.5 ± 6.4	5.9 ± 3.4**	7.3 ± 4.8
	6.6 ± 6.1	4.0 ± 3.7	3.1 ± 4.4

*#p < 0.05, *p < 0.01, **p < 0.001, vs. MCI† p < 0.01, vs. AD.*
MMSE, Mini-Mental State Examination; MoCA-J, Japanese version of Montreal Cognitive Assessment; ADAS-Jcog, Alzheimer's Disease Assessment Scale-cognitive component-Japanese version; WMS-R, Wechsler Memory Scale-Revised.

Some of the patients with probable DLB showed fluctuating cognition (22%), visual hallucinations (53%), parkinsonism (45%); Hoehn & Yahr stage 2.3 ± 1.3, or RBD (40%). None of the patients were taking any medication such as benzodiazepine, antidepressants, or antipsychotics.

The mean ages of the patients in the MCI, AD, and DLB groups were 77.5 ± 8.8, 78.8 ± 7.1, and 81.5 ± 5.5 years, respectively. Although no significant difference was observed in age between the MCI and AD groups, it was significantly higher in the DLB group. All the patients underwent a general physical examination. They were also required to undergo the following neurological and neurocognitive tests: Mini-Mental State Examination, MMSE (9); the Japanese version of the Montreal Cognitive Assessment, MoCA-J; the Japanese version of the Alzheimer's Disease Assessment Scale-cognitive component, ADAS-Jcog (10); and the Wechsler Memory Scale-Revised logical memory 1, WMS-R (11). All the patients were also required to undergo IMP-SPECT.

SPECT imaging was performed using a triple-head rotating gamma camera (PRISM 3000 XP, Picker). Imaging was commenced at 15 min following intravenous administration of 222 MBq of N-isopropyl-p-[123I] iodoamphetamine. The slice thickness was 4.3 mm (128 × 128 matrix).

Regarding the Z-Score, eZIS System, and CIScore

The details of the eZIS have been described previously (12, 13). Briefly, voxel-by-voxel Z-score analysis was performed after voxel normalization to global mean or cerebellar values. The Z-score was derived according to the following formula: ([healthy control mean]—[individual patient value])/(healthy control SD).

A database of values obtained from healthy controls was then constructed by Matsuda et al. (12) at the National Center of Neurology and Psychiatry, which included data on 40 cognitively healthy individuals aged between 70 and 87 years.

The eZIS is considered to be very useful in diagnosing dementia in routine studies, because the degree of expertise of the observer does not influence the result, and a common database is available for converting site-specific SPECT data to core data.

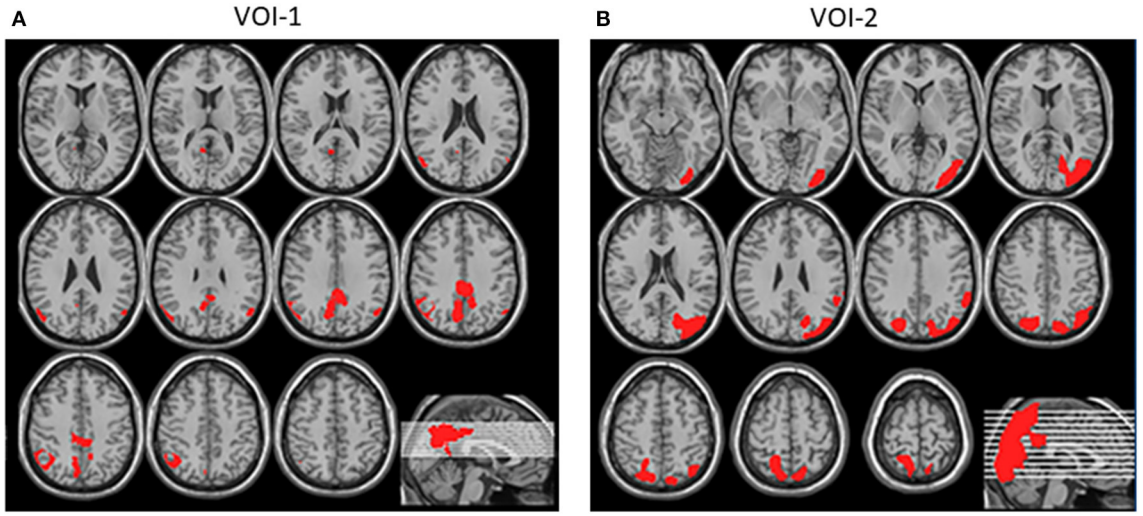


FIGURE 1 | (A) VOI-1, shown in red, was defined as indicating PCG, an area characteristically involved in AD. **(B)** VOI-2, shown in red, was defined as area indicating significant reduction in cerebral perfusion in DLB patients compared with in healthy controls (Quotes from reference 5).

This program also allows statistical parametric mapping results to be incorporated into an automated analysis of the Z-score values in the volume of interest (VOI). The new version of the eZIS program has the following two types of VOI: VOI-1, which indicates the PCG, an area characteristically involved in AD; and VOI-2, an area defined as indicating a significant reduction in cerebral perfusion in DLB patients compared with in healthy controls (**Figure 1**). The CIScore is defined as the ratio of the VOI-2 to the VOI-1 Z-score, and is automatically calculated by the eZIS software, as is the Z-score for each VOI. The CIS is only a visual assessment, while the CIScore is a quantitative parameter.

Statistical Analysis

Values are expressed as the mean ± SD. Comparisons among the three groups were performed with a one-way analysis of variance (ANOVA); a *post-hoc* Tukey-Kramer test was used to analyze changes in the multidimensional rating scales in each group.

A p-value of < 0.05 was considered to indicate a statistically significant difference between two groups. All the analyses were performed with "IBM SPSS Statistics (Chicago, IL)."

The discrimination rate of the CIScore between AD and DLB was determined using ROC analysis. The cutoff value was defined by the Youden index.

RESULTS

The results of the neurological and neurocognitive tests were as follows: the MMSE scores in the MCI, AD, and DLB groups were 26.6 ± 1.9, 20.9 ± 2.9, and 20.5 ± 5.0; the MoCA-J scores 20.1 ± 3.0, 17.5 ± 4.3, and 14.3 ± 4.6; the ADAS-Jcog scores 8.8 ± 3.5, 16.4 ± 4.8, and 16.5 ± 7.3; and the WMS-R scores 6.6 ± 6.1, 4.0 ± 3.7, and 3.1 ± 4.4, respectively.

The ANOVA revealed a significant difference in the CIScore among the three groups ($p < 0.001$). The CIScore in the MCI, AD, and DLB groups was 0.22 ± 0.07, 0.28 ± 0.11, and 0.23 ± 0.06, respectively (**Figure 2A**). The CIScore in the AD group was significantly higher than that in the DLB or MCI groups (AD vs. DLB: $p < 0.001$, AD vs. MCI: $p < 0.005$). Receiver operating characteristic analysis revealed a significant difference in the CIScore between the AD and DLB groups. The cut-off value of the CIScore was determined to 0.23 according to the ROC analysis (Youden index). The area under the curve was 0.620 ($p < 0.05$); and sensitivity and specificity were 0.50 and 0.73, respectively. No significant difference was observed between the MCI and DLB groups, however.

The Z-scores in the MCI, AD, and DLB groups were 2.1 ± 0.5, 2.7 ± 0.7, and 3.0 ± 0.9, respectively (**Figure 2B**). A significant difference was observed in the Z-scores for VOI-1 (which demonstrated a decrease in blood perfusion flow in the PCG) between the MCI group and each other group ($p < 0.001$ by ANOVA). The scores in the AD and DLB groups were significantly higher than that in the MCI group (AD vs. MCI: $p < 0.005$, DLB vs. MCI: $p < 0.001$). No significant difference was observed between the scores in the AD and DLB groups, however.

DISCUSSION

The present results suggest that the CIScore can be used to differentiate DLB from AD when patients show similar levels of decrease in regional cerebral blood flow (rCBF) in the PCG. In Japan, SPECT is widely used in the diagnosis of dementia. Although a diagnosis may be possible by gross examination in some typical cases (**Figure 3**), a qualitative diagnosis offers the potential of improved efficiency in this respect. Analysis of the CIScore may increase the value and usefulness of IMP-SPECT as

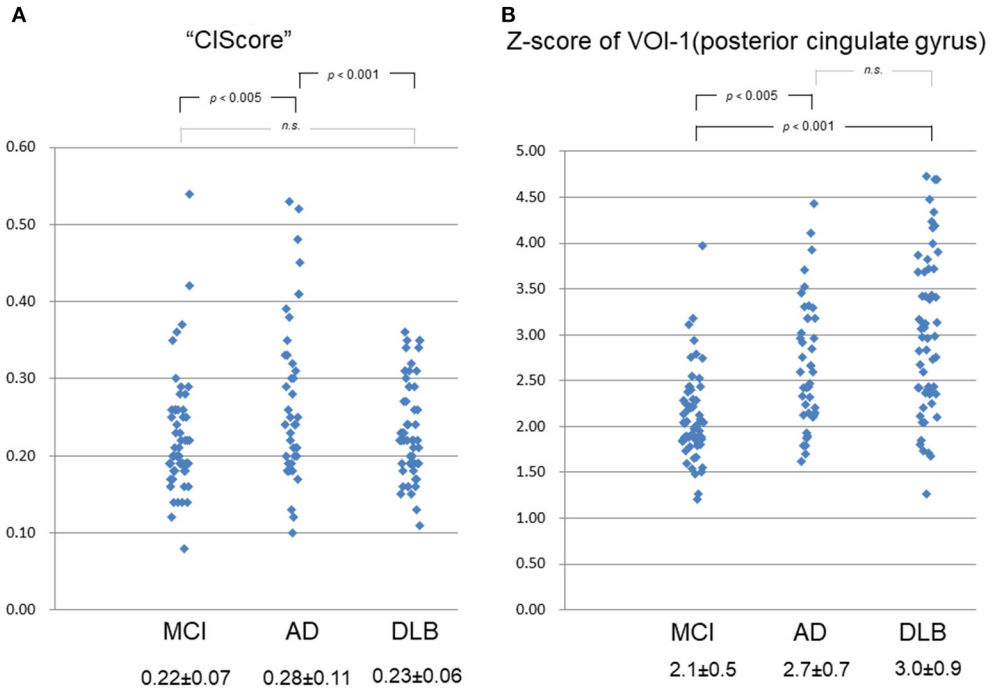


FIGURE 2 | (A) CIScore in MCI, AD, and DLB groups was 0.22 ± 0.07, 0.28 ± 0.11, and 0.23 ± 0.06, respectively. CIScore in AD group was significantly higher than that in DLB or MCI group (AD vs. DLB: $p < 0.001$, AD vs. MCI: $p < 0.005$). No significant difference was observed between MCI and DLB groups, however. **(B)** Z-scores of VOI-1 in MCI, AD, and DLB groups were 2.1 ± 0.5, 2.7 ± 0.7, and 3.0 ± 0.9, respectively. Scores in AD and DLB groups were significantly higher than that in MCI group (AD vs. MCI: $p < 0.005$, DLB vs. MCI: $p < 0.001$). No significant difference was observed between scores in AD and DLB groups, however.

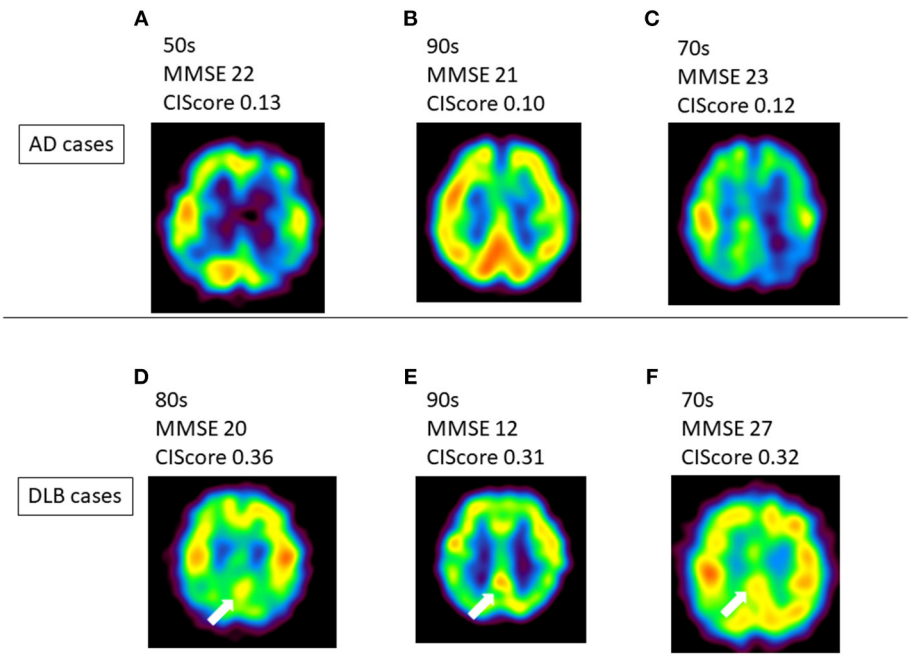


FIGURE 3 | (A–C) Several Alzheimer's disease (AD) patients showed no CIS. **(D–F)** Typical dementia with Lewy bodies (DLB) cases showed CIS on IMP-SPECT. CIS is indicated by white arrow in these images. There were some cases that it is hard to detect CIS like case-(f). CIS, Cingulate Island sign; MMSE, Mini-Mental State Examination.

an inexpensive and simple method of differentiating DLB from AD (14, 15).

In the present study, the CIScore in the MCI patients was low, making it difficult to detect. This was because the decrease in rCBF in the PCG was not severe. However, as DLB patients may be affected by the coexistence of AD pathologies, there is a significant difference in the PCG between MCI and DLB.

As rCBF in VOI-1 (PCG) in the MCI patients was maintained, no significant difference was observed in the CIScore. This suggests that it is difficult to detect DLB when it is at the MCI stage. Therefore, observing the progress of dementia may be required to avoid misdiagnosis. In addition, the diagnostic accuracy of the CIScore may be low. The diagnostic accuracy of the CIScore may be low as it often shows an increase in elderly DLB patients, in whom the pathologically common form is most prevalent (1). Further study should include assessment of multiple components such as symptom classification and age.

The ability to cross-reference different databases using the eZIS system may greatly enhance the diagnostic value of brain SPECT imaging, however. It is possible that defining an IMP-SPECT-specific VOI would improve the identification rate between MCI, AD, and DLB, although further study is required to confirm this.

Future studies assessing multiple components (such as symptom classification, age, etc.) are required to determine the accuracy of the present method. The presence or absence of hallucinations, in particular, may be affected by occipital lobe blood flow. Determining the clinical characteristics in DLB patients with low CIScores may lead to greater accuracy in diagnosis.

This study had several crucial limitations. Firstly, the diagnostic utility of the CIScore in discriminating DLB from AD may not be high due to the coexistence of DLB and AD pathologies. Here, the diagnosis of AD or DLB was based on diagnostic criteria (those of the National Institute of Neurological and Communicative Disorders and Stroke and Alzheimer's Disease and Related Disorders Association, and the DLB International Workshop), and complications could not be completely ruled out. The DLB International Workshop criteria revealed the coexistence of DLB and AD pathologies. Most patients with DLB also demonstrate AD pathology, including cortical amyloid plaques and neurofibrillary tangles. Therefore, we hypothesized that the absence of the CIS in DLB patients would suggest the coexistence of DLB and AD pathologies, whereas its presence would indicate DLB alone. Our next step in future study, therefore, will be to investigate the CIScore in patients in whom DLB is confirmed pathologically.

Secondly, the absence of healthy controls in the present study is not a trivial limitation. However, fundamental ethical problems associated with the use of imaging techniques in healthy controls in the field of nuclear medicine make this problematic.

Thirdly, this study was carried out at a single memory disorder clinic; therefore, the number of patients enrolled was relatively small, and the age of the patients in the DLB group was significantly higher than that in the AD or MCI groups.

Fourthly, only clinical interviews were used to assess the DLB patients. Further study should also incorporate objective measurements such as the Cognitive Fluctuation Inventory and the Unified Parkinson's Disease Rating Scale.

Further study should also include additional amyloid PET. Such studies should also be multi-center and include larger patient cohorts, including a healthy control group. The results of pathological examination will also be required to confirm the validity of the results.

In conclusion, the present results showed a significant difference among the three groups using IMP. This suggests that the diagnostic power of IMP is not inferior to that of ECD. They also suggest that the CIScore in brain perfusion IMP-SPECT is useful in clinically differentiating DLB from AD.

DATA AVAILABILITY STATEMENT

The original contributions presented in the study are included in the article/supplementary materials, further inquiries can be directed to the corresponding author/s.

ETHICS STATEMENT

The studies involving human participants were reviewed and approved by MAMORY SUZUKI, Ethics Committee of Tokyo Medical University (Approval no: 3304). The patients/participants provided their written informed consent to participate in this study. Written informed consent was obtained from the patients or their next of kin/legal guardian if they were a minor for the publication of any potentially identifiable images or data included in this article.

AUTHOR CONTRIBUTIONS

SS, HS, and HH: patients recruitment. YI, DH, and NT: data assessment. All authors contributed to the article and approved the submitted version.

FUNDING

This work was supported by a JSPS KAKENHI Grant (Number 18K07479).

ACKNOWLEDGMENTS

The authors would like to thank Professor Jeremy Williams of the Department of International Medical Communications at Tokyo Medical University for editing and reviewing the English of this manuscript.

REFERENCES

1. Kosaka K. Diffuse Lewy body disease in Japan. *J Neurol*. (1990) 237:197–204. doi: 10.1007/BF00314594
2. McKeith IG, Boeve BF, Dickson DW, Halliday G, Taylor JP, Weintraub D, et al. Diagnosis and management of dementia with Lewy bodies: fourth consensus report of the DLB Consortium. *Neurology*. (2017) 89:88–100. doi: 10.1212/WNL.0000000000004058
3. Graff-Radford J, Murray ME, Lowe VJ, Boeve BF, Ferman TJ, Przybelski SA, et al. Dementia with Lewy bodies: basis of cingulate island sign. *Neurology*. (2014) 83:801–9. doi: 10.1212/WNL.0000000000000734
4. Lim SM, Katsifis A, Villemagne VL, Best R, Jones G, Saling M, et al. The 18F-FDG PET cingulate island sign and comparison to 123I-beta-CIT SPECT for diagnosis of dementia with Lewy bodies. *J Nucl Med*. (2009) 50:1638–45. doi: 10.2967/jnumed.109.065870
5. Iizuka T, Kameyama M. Cingulate island sign on FDG-PET is associated with medial temporal lobe atrophy in dementia with Lewy bodies. *Ann Nucl Med*. (2016) 30:421–9. doi: 10.1007/s12149-016-1076-9
6. Imabayashi E, Soma T, Sone D, Tsukamoto T, Kimura Y, Sato N, et al. Validation of the cingulate island sign with optimized ratios for discriminating dementia with Lewy bodies from Alzheimer's disease using brain perfusion SPECT. *Ann Nucl Med*. (2017) 31:536–43. doi: 10.1007/s12149-017-1181-4
7. Iida H, Akutsu T, Endo K, Fukuda H, Inoue T, Ito H, et al. A multicenter validation of regional cerebral blood flow quantitation using e23I]iodoamphetamine and single photon emission computed tomography. *J Cereb Blood Flow Metab*. (1996) 16:781–93. doi: 10.1097/00004647-199609000-00003
8. Hyman BT, Phelps CH, Beach TG, Bigio EH, Cairns NJ, Carrillo MC, et al. National Institute on Aging-Alzheimer's Association guidelines for the neuropathologic assessment of Alzheimer's disease. *Alzheimers Dement*. (2012) 8:1–13. doi: 10.1016/j.jalz.2011.10.007
9. Folstein MF, Folstein SE, McHugh PR. 'Mini-Mental State'. A practical method for grading the cognitive state of patients for the clinician. *J Psychiatr Res*. (1975) 12:189–98. doi: 10.1016/0022-3956(75)90026-6
10. Rosen WG, Mohs RC, Davis KL. A new rating scale for Alzheimer's disease. *Am J Psychiatry*. (1984) 141:1356–64. doi: 10.1176/ajp.141.11.1356
11. Wechsler D. *WMS-R: Wechsler Memory Scale-Revised Manual*. NewYork, NY:The Psychological Corporation; Harcourt BraceJovanovich (1987).
12. Matsuda H, Mizumura S, Nagao T, Ota T, Iizuka T, Nemoto K, et al. An easy Z-score imaging system for discrimination between very early Alzheimer's disease and controls using brain perfusion SPECT in a multicentre study. *Nucl Med Commun*. (2007) 28:199–205. doi: 10.1097/MNM.0b013e328013eb8b
13. Matsuda H. Neurological diseases and SPECT–analysis using easy Z-score imaging system (eZIS). *Brain Nerve*. (2007) 59:487–93.
14. Hirose D, Shimizu S, Hirao K, Ogawa Y, Sato T, Kaneko Y, et al. Neuroimaging characteristics of frailty status in patients with alzheimer's disease. *J Alzheimers Dis*. (2019) 67:1201–8. doi: 10.3233/JAD-180701
15. Chiba Y, Fujishiro H, Iseki E, Kasanuki K, Sato K. The cingulate island sign in patients with dementia with Lewy bodies or Alzheimer's disease: a direct comparison between 18F-FDG PET and 123I-IMP SPECT. *Neurosci Lett*. (2018) 683:168–73. doi: 10.1016/j.neulet.2018.07.040

Conflict of Interest: The authors declare that the research was conducted in the absence of any commercial or financial relationships that could be construed as a potential conflict of interest.

Copyright © 2020 Kanetaka, Shimizu, Inagawa, Hirose, Takenoshita, Sakurai and Hanyu. This is an open-access article distributed under the terms of the Creative Commons Attribution License (CC BY). The use, distribution or reproduction in other forums is permitted, provided the original author(s) and the copyright owner(s) are credited and that the original publication in this journal is cited, in accordance with accepted academic practice. No use, distribution or reproduction is permitted which does not comply with these terms.

frontiers in Neurology

ORIGINAL RESEARCH
published: 10 December 2020
doi: 10.3389/fneur.2020.601686

Changes in Prefrontal Cortical Activity During Walking and Cognitive Functions Among Patients With Parkinson's Disease

Maud Ranchet[1], Isabelle Hoang[1], Maxime Cheminon[2], Romain Derollepot[1], Hannes Devos[3], Stephane Perrey[4], Jacques Luauté[2,5,6], Teodor Danaila[7] and Laurence Paire-Ficout[1]*

[1] TS2-LESCOT, Univ Gustave Eiffel, IFSTTAR, Univ Lyon, Lyon, France, [2] Service de Médecine Physique et de Réadaptation Neurologique, Hôpital Henry-Gabrielle, Hospices Civils de Lyon, Lyon, France, [3] Department of Physical Therapy and Rehabilitation Science, School of Health Professions, The University of Kansas Medical Center, Kansas City, KS, United States, [4] EuroMov Digital Health in Motion, Univ Montpellier, IMT Mînes Ales, Montpellier, France, [5] Inserm UMR-S 1028, CNRS UMR 529, ImpAct, Center de Recherche en Neurosciences de Lyon, Université Lyon-1, Bron, France, [6] Université de Lyon, Université Claude Bernard Lyon 1, Lyon, France, [7] Center de Neurosciences Cognitives, Service de Neurologie C, Hôpital Neurologique Pierre Wertheimer, Hospices Civils de Lyon, Université Claude Bernard Lyon I, Lyon, France

OPEN ACCESS

Edited by:
Edward Ofori,
Arizona State University, United States

Reviewed by:
Rodrigo Vitório,
Oregon Health & Science University, United States
Ji Hyun Ko,
University of Manitoba, Canada

***Correspondence:**
Maud Ranchet
maud.ranchet@univ-eiffel.fr

Specialty section:
This article was submitted to Movement Disorders, a section of the journal Frontiers in Neurology

Received: 23 September 2020
Accepted: 16 November 2020
Published: 10 December 2020

Citation:
Ranchet M, Hoang I, Cheminon M, Derollepot R, Devos H, Perrey S, Luauté J, Danaila T and Paire-Ficout L (2020) Changes in Prefrontal Cortical Activity During Walking and Cognitive Functions Among Patients With Parkinson's Disease. Front. Neurol. 11:601686. doi: 10.3389/fneur.2020.601686

Background: Walking becomes more and more degraded as Parkinson's Disease (PD) progresses. Previous research examined factors contributing to this deterioration. Among them, changes in brain cortical activity during walking have been less studied in this clinical population.

Objectives: This study aimed to: (1) investigate changes in dorsolateral prefrontal cortex (DLPFC) activation during usual walking and dual-task walking conditions in patients with PD; (2) examine the association between cortical activity and behavioral/cognitive outcomes; and (3) explore which factors best predict increased activation of the DLPFC during usual walking.

Methods: Eighteen patients with early stage PD and 18 controls performed 4 conditions: (1) standing while subtracting, (2) usual walking, (3) walking while counting forward, and (4) walking while subtracting. Cortical activity in DLPFC, assessed by changes in oxy-hemoglobin (ΔHbO_2) and deoxy-hemoglobin (ΔHbR), was measured using functional near infrared spectroscopy (fNIRS). Gait performance was recorded using wearables sensors. Cognition was also assessed using neuropsychological tests, including the Trail Making Test (TMT).

Results: DLPFC activity was higher in patients compared to controls during both usual walking and walking while subtracting conditions. Patients had impaired walking performance compared to controls only during walking while subtracting task. Moderate-to-strong correlations between ΔHbO_2 and coefficients of variation of all gait parameters were found for usual walking and during walking while counting forward conditions. Part-B of TMT predicted 21% of the variance of ΔHbO_2 during usual walking after adjustment for group status.

Conclusions: The increased DLPFC activity in patients during usual walking suggests a potential compensation for executive deficits. Understanding changes in DLPFC activity during walking may have implications for rehabilitation of gait in patients with PD.

Keywords: Parkinson's disease, fNIRS, walking, cognition, dual-task walking, gait

INTRODUCTION

Walking in everyday life may be a complex task for individuals with Parkinson's Disease (PD). Patients with PD have gait problems, such as reduced gait speed and step length (1), that worsen as the disease progresses. These gait problems may be exacerbated during dual-task (DT) walking combining both motor and cognitive activities. This may lead to a higher risk of falls (2), reduced mobility and quality of life (3).

Previous studies have investigated behavioral (e.g., cognitive, motor) and neurophysiological measures [e.g., functional magnetic resonance imagery (fMRI), electroencephalography (EEG)] that could predict impaired walking or falls risk in patients with PD (2, 4–6). Among neurophysiological measures, changes in brain cortical activity during walking have been less studied in patients with PD (7). Different neurophysiological techniques have been proposed to better examine changes in brain activation during walking in PD.

Evidence from functional magnetic resonance imagery (fMRI) suggest that patients with PD had higher activation in frontal, parietal, temporal, and occipital lobes than healthy older adults during imagined usual walking (6). The increased cortical activation in patients with PD may reflect a compensatory mechanism to overcome inefficient neural activation. Although fMRI has adequate spatial resolution, changes in brain activation during real walking conditions in patients with PD are unfeasible to capture in such neuroimaging studies. Portable electroencephalography (EEG) or functional near-infrared spectroscopy (fNIRS) techniques have allowed investigation of cortical activity during real-time walking (8). Using EEG, specific changes in electrical brain activity during DT walking were found in patients with PD (9). Patients with PD showed reduced P300 amplitude during DT walking compared to standing. This reduced P300 amplitude reflects unsynchronized activation of various resources (lower timing and coordination between different brain regions), suggesting less neural recruitment during DT walking. EEG has a good temporal resolution compared to other neuroimaging techniques. However, the spatial resolution of EEG is relatively low compared to fNIRS and neck muscles as well as artifacts such as eye movements can affect the quality of the recordings. With recent advances in technology, fNIRS allows an indirect evaluation of brain activation by measuring changes in brain blood oxygen levels. The fNIRS technique emits light with different wavelengths that is partly absorbed by the chromophores such as oxygenated and deoxygenated hemoglobin (HbO_2 and HbR, respectively). Increased brain activation induces an intensified blood flow in the active brain regions leading to an increase in HbO_2 and decrease of HbR (10).

To date, few studies have explored cortical activity during walking in patients with PD, using fNIRS (6, 11–18). Some studies reported both HbO_2 and HbR (12) and only one study used reference channels to correct for superficial hemodynamic interferences (15). Furthermore, the associations between neurophysiological and behavioral outcomes during usual and DT walking tasks were poorly understood (19) in patients with PD (20, 21). Under challenging tasks [e.g., obstacle negotiation (20) or DT walking while subtracting (12, 14)], patients showed an increased activation of prefrontal cortex (PFC) that may affect walking performance. An explanation to this increased activation in the PFC could be that basal ganglia dysfunction leads to reduced movement automaticity, which increases reliance on executive resources to control movements. The PFC, specifically the DLPFC plays a major role in executive functions, essential for the management of cognitive functions including planning, working memory and cognitive flexibility (22). Compared to healthy older adults, patients with PD showed a higher activation in the PFC compared to controls, even during usual walking (12, 20). This may reduce the functional reserve needed during more demanding tasks which may contribute to high prevalence of falls and DT difficulties among patients with PD (6). The role of DLPFC activity during usual walking should therefore better be explored in individuals with PD.

The objectives of this study were (1) to investigate changes in DLPFC activation during usual walking and DT walking conditions in patients with PD compared to controls, (2) to examine the association between cortical activity and behavioral/cognitive outcomes, and (3) to explore which factors best predict increased activation of the DLPFC during usual walking.

MATERIALS AND METHODS

Participants

Patients were recruited from the Henry-Gabrielle Hospital, Lyon and healthy older adults (controls) were recruited through advertisements between September 1, 2018 to December 17, 2019.

General inclusion criteria were: 50 years old and above and able to walk unassisted for at least 20 mins. All participants had normal-to-corrected vision. All participants had no other visual, neurological (other than PD for the PD group), internal or psychiatric conditions that may interfere with walking. Patients with PD were excluded if they had Montreal Cognitive Assessment (MOCA) scores $\leq$ 15, other parkinsonian syndromes, severe dyskinesia, deep brain stimulation,

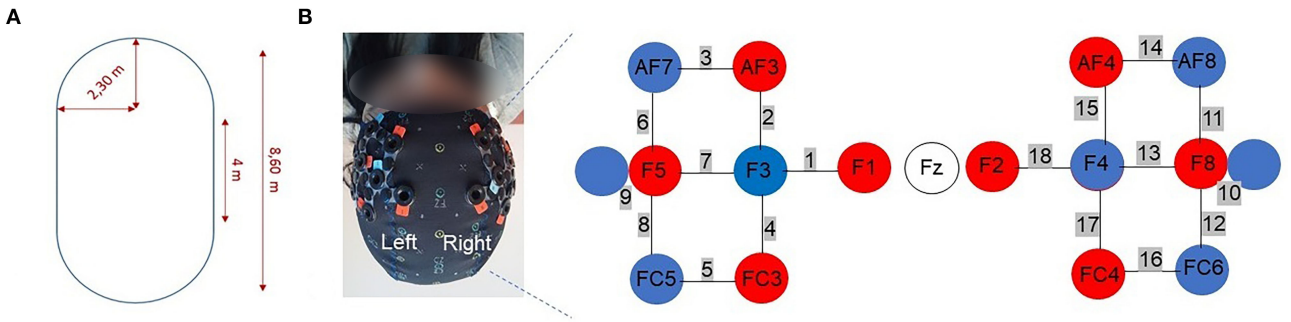


FIGURE 1 | (A) Walking path configuration. **(B)** Optodes configuration. The right panels show the optodes with respect to the Fz locations of the international 10-10 system. Red circles represent the sources and blue circles represent the detectors. The numbers in gray represent the channels. Channels 9 and 10 represent the short separation channels.

unpredictable motor fluctuations, or ocular diseases causing significant visual impairment.

Fear of falling was assessed by the Falls Efficacy Scale International (FES-I) and symptoms of depression were measured by the Beck Depression Inventory scale. Total daily levodopa-equivalent dose was calculated for each PD patient (23). All patients were medicated and tested in the "on" medication state. The "on" state was defined by a doctor (MC or TD) during the medical examination that preceded the experiment. Patients were tested between 1 and 3 h after taking their medication.

The study was approved by the French biomedical ethics committee on March, 9 2018 (Comité de Protection des Personnes Nord Ouest III Réf. CPP: 2018-01 N° ID RCB: 2017-A03187-46). Informed written consent was obtained from all participants.

Protocol

Participants performed in a single session 4 conditions: (1) standing while subtracting, (2) usual walking, (3) walking while counting forward, and (4) walking while subtracting. In the standing while subtracting condition, participants were required to stand still while subtracting 7 to a 3-digit number out loud. In the usual walking condition, participants were asked to walk at their "normal pace." In the walking condition while counting forward, they were instructed to walk while counting forward out loud from a random 3-digit number. In the walking condition while subtracting, they were asked to subtract 7 from a random 3-digit number out loud. No instructions about priorization were given for the DT walking conditions. Each condition included 5 trials of 30 s. The duration of rest periods between trials ranged from 25 to 35 s in order to avoid anticipation of block onset. During rest periods, participants were instructed to stand still quietly. During the standing while subtracting and the two DT walking conditions, cognitive performance was measured and defined as the number of correct operations. The order of each condition was randomized between participants. Each condition started with 45 s of standing quietly (resting state period), with the instruction to refrain from talking and moving the head. The walking path configuration was an oval shape whose dimensions are displayed in **Figure 1A**. In order to assist participants to walk on the path, there were markings on the floor. Participants were allowed to take breaks between conditions. Furthermore, all experiments took place in the morning, the fatigue being less pronounced than in the afternoon.

Gait was assessed using two wearable sensors placed on the shoes (Physiolog®5, Gait Up, Switzerland). Walking performance parameters included mean gait speed (m/s), cadence (step/min), stride length (m), gait cycle time (s), and their coefficient of variation (CV) calculated as (standard deviation/mean)*100. For each condition, gait outcome measures were averaged over the 5 trials.

Relative concentration changes of HbO_2 and HbR (ΔHbO_2 and ΔHbR in μmol/L, respectively) in the DLPFC were measured using a wireless continuous waves fNIRS device (NIRSport, NIRx Medical Technologies) with 16 optodes (8 sources and 8 detectors).

Functional Near Infrared Spectroscopy

An increase of ΔHbO_2 associated with a slight decrease of ΔHbR reflects a functional activation for the task (24). Fourteen optodes, corresponding to the 8 sources and 6 detectors separated by ∼30 mm, were placed on the DLPFC according to the modified international EEG 10-10 system. Two short separation channels (channels 9 and 10, see **Figure 1B**) with an interoptode distance of 15 mm were used in order to account for peripheral tissue signals. The near infrared light was emitted by sources with wavelengths of 760 and 850 nm at a sampling rate of 7.81 Hz. Textile EEG caps in 3 different sizes (i.e., circumference of 54, 56, 58 cm) were used in order to fix the sources and detectors on the participant's head. An overcap was used to prevent ambient-light contamination. Raw intensities were recorded using the software provided by the manufacturer (NIRStar, version 15.1 and 15.2).

Data Processing

The data were analyzed using the open-access software Homer 2 within MATLAB (R2019b, Mathworks). The first processing step was to convert raw data into optical density. Then, a low pass filter with a cut-off of 0.1 Hz was applied to attenuate respiration and cardiac activity and high frequency noise (25). The next

step was a motion artifact correction using wavelet-based filters (iqr = 1.5) (26, 27). After motion correction, optical density was converted into relative concentration changes of HbO_2 and HbR using the modified Beer-Lambert law with constant differential path length factors (DPF) values of 6 (28). Finally, contribution of short separation channels was removed from the signal using a Kalman filter dynamic estimator (29). Using the block average method, mean amplitude difference of ΔHbO_2 and ΔHbR for each channel was obtained using the last 5 s of the resting state before each trial and 30 s after the "start" instruction. Signal quality of each channel was visually checked to ensure divergence between the HbO_2 and HbR traces (15) and extreme values were detected using the box-plot method. When the number of extreme values were inferior or equal to 3 ($\leq$10%) for a channel, values were replaced by mean values of the group in the specific condition. Otherwise, the channel was removed for all participants. For the subtraction task, C5 and C12 were therefore removed for all participants. Signals from channels were averaged over the PFC (channels 1–8; 11–18), in line with previous research (21). Recommendations and good practices were followed according to a recent consensus paper (30).

Neuropsychological Tasks

Participants completed a series of tests assessing global cognition (MOCA) (31), inhibition (Stroop test; inhibition cost) (32), psychomotor speed, working memory, and attentional shift [Trail Making Test (TMT) part A and B, TMT (B-A)] (33), attention and processing speed [Digit Symbol Substitution Test (DSST)] (34), mental flexibility (Plus Minus Task; shift cost) (35) and visuospatial abilities (Bells Test) (36). The order of neuropsychological tasks was randomized between participants. They were administered before or after the walking task.

Statistical Analyses

Kolmogorov-Smirnov tests were used to determine the normality of variables. For demographic, clinical, and neuropsychological variables, between-group differences were examined using Fisher's Exact tests, independent student *t*-tests or Wilcoxon rank-sum tests, as appropriate. For neuropsychological tests, *p*-values were corrected for multiple comparisons using Bonferroni adjustment. A score is significant only if the corresponding *p*-value is $\leq$0.05/5 ($p \leq 0.01$).

Repeated measures univariate analyses of variance (ANOVA) with group (patients vs. controls) as between subject factor and condition (standing while subtracting, usual walking and the two DT walking) as within subject factor, and group by condition as interaction effect, were applied on fNIRS data, as recommended in a previous study (37). Dependent variables were ΔHbO_2 and ΔHbR.

Repeated measures multivariate ANOVA with group as a between subject factor and condition as within subject factor, and group by condition, were applied on gait parameters (gait speed, cadence, stride length and gait cycle time). Dependent variables were mean gait parameters and CV of gait parameters, respectively.

For each ANOVA, effect sizes (η^2) were reported and were interpreted as small (0.02), medium (0.13), and large (0.26) (38). Bonferroni correction for multiple comparisons was applied during the *post-hoc* analyses.

In all participants, Pearson or Spearman rank correlations were analyzed to investigate associations between cortical activity (ΔHbO_2) and behavioral performance (gait and neuropsychological outcomes) within condition. Pearson correlations (r) were used when data was distributed normally whereas Spearman rank correlations (ρ) were used when data was not distributed normally. Correlations (ρ or r) were considered weak below 0.10, moderate between 0.10 and 0.49 and strong between 0.50 and 1.00 (39). To determine which factors (age, gender, years of education, BDI, FES-I or/and neuropsychological factors) were the best predictors of HbO_2 levels during usual walking, stepwise linear regression model was employed with group as a covariate. Only variables that significantly correlated with ΔHbO_2 during usual walking and did not show strong intercorrelations ($r < 0.80$) were selected for entry in the model. $P < 0.05$ were considered significant. All statistical analyses were conducted using SPSS, version 26.0.

TABLE 1 | Demographic and clinical characteristics for all participants.

Variables	PD patients $N = 18$	Controls $N = 18$	*P*-value
Age, years	68 ± 8	66 ± 7	0.48
Gender (M/F)	11/7	11/7	1.00
Education, years	14.5 ± 3	14.5 ± 2	0.85
MOCA score (0–30)	27.5 (26–29)	27 (26–29)	0.82
BDI score 21 items	6 ± 4	2 ± 2	**0.001**
FES-I score (maximum score, 64)	25 ± 8	19 ± 3	**0.02**
Disease duration, years	5 (2–8)	NA	
Hoehn and Yahr stage (on)	(2–2)	NA	
UPDRS motor (on)	17 (12–26)	NA	
LED, mg/day	604 (310–898)	NA	

Values are expressed as mean ± SD or median (Q1–Q3). Values in bold are significant. BDI, Beck Depression Inventory; LED, L-Dopa Equivalent Dosage; M, Male; F, Female; FES-I, Falls Efficacy Scale International; MOCA, Montreal Cognitive Assessment; NA, not applicable; UPDRS, Unified Parkinson Disease Rating Scale.

RESULTS

Participants

Eighteen patients with early stage PD and 18 controls matched for age, sex and education level were included (**Table 1**). Patients were categorized into 3 clinical subtypes: 3 patients were classified as postural instability and gait difficulty-predominant disease, 8 patients were classified as tremor-dominant disease, and 7 patients were rigidity-dominant disease. Scores on BDI and FES-I scale were significantly higher in patients with PD, compared to controls. Patients were in early stages of the disease, based on disease duration, the Hoehn and Yahr scale and the motor section of the Unified Parkinson's Disease Rating Scale (UPDRS). Three patients had a Hoehn and Yahr rating at stage 1, 13 were at stage 2, and 2 were at stage 3.

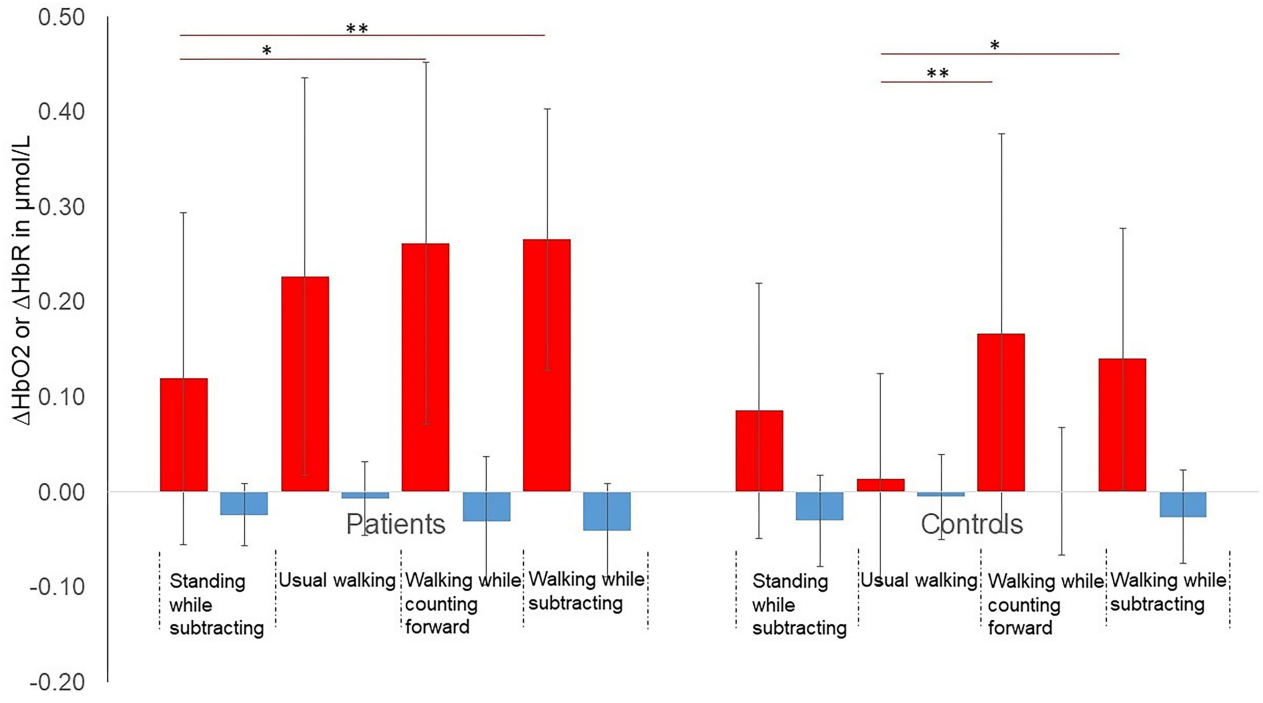


FIGURE 2 | Mean (SD) changes (Δ) in HbO_2 and HbR during the 4 conditions in both groups. *$p < 0.05$, **$p < 0.01$. *P*-values adjusted for Bonferroni correction. Red bars represent ΔHbO_2 and blue bars represent ΔHbR. Red lines represent significant within-group differences in ΔHbO_2 between 2 conditions.

Changes in Dorsolateral Prefrontal Cortex Activation

ΔHbO_2 and ΔHbR

Group Effect

Patients had higher ΔHbO_2 than controls [$F_{(1, 34)} = 7.11$, $p = 0.01$, $\eta^2 = 0.17$]. No between-group differences were found for ΔHbR [$F_{(1, 34)} = 0.54$, $p = 0.47$, $\eta^2 = 0.02$].

Condition Effect

Furthermore, significant differences in ΔHbO_2 and in ΔHbR between conditions [$F_{(3, 102)} = 7.71$, $p < 0.001$, $\eta^2 = 0.19$; $F_{(3, 102)} = 8.91$, $p < 0.001$, $\eta^2 = 0.21$, respectively] were found. ΔHbO_2 significantly increased during walking while counting forward compared to usual walking ($p = 0.02$). ΔHbO_2 tended to increase during walking while subtracting condition compared to usual walking ($p = 0.06$). ΔHbO_2 also increased during both DT walking conditions compared to standing while subtracting condition ($p < 0.01$). ΔHbR significantly decreased during walking while subtracting compared to usual walking ($p < 0.001$) and walking while counting ($p < 0.001$) (**Figure 2**).

Group Condition Interaction*

In addition, the interaction between condition and group on ΔHbO_2 was significant [$F_{(3, 102)} = 3.34$, $p = 0.02$, $\eta^2 = 0.09$]. Patients had higher ΔHbO_2 than controls during usual walking ($p = 0.001$) and in DT-walking while subtracting ($p = 0.02$) (**Figure 2**). In controls, ΔHbO_2 increased during both DT walking conditions compared to usual walking, which was not the case for the patients ($p = 1.00$). Only in patients, ΔHbO_2 was significantly higher during the 2 DT walking conditions compared to the standing while subtracting condition. No significant interaction between condition and group was found on ΔHbR [$F_{(3, 102)} = 1.65$, $p = 0.18$, $\eta^2 = 0.05$]. The **Figure 3** shows the averaged time courses of HbO_2 and HbR in the DLPFC for the 4 conditions in both groups. For all conditions, the average relative concentration changes of HbO_2 increased after starting the task. The average relative concentration changes of HbR showed slight reductions or remained relatively stable during the task.

Behavioral Performance

Gait Performance

Group Effect

Patients had reduced stride length compared to controls ($p < 0.05$) (**Table 2**).

Condition Effect

Speed, cadence, stride length, as well as gait cycle time were altered as the walking task difficulty increased (see **Table 2**). CV of cadence, speed and gait cycle time were greater during the 2 DT walking conditions than during the usual walking (CV of cadence, speed, and gait cycle time, $p \leq 0.001$). CV of stride length was greater during walking while subtracting condition than during walking while counting ($p = 0.04$) or during usual walking ($p < 0.001$).

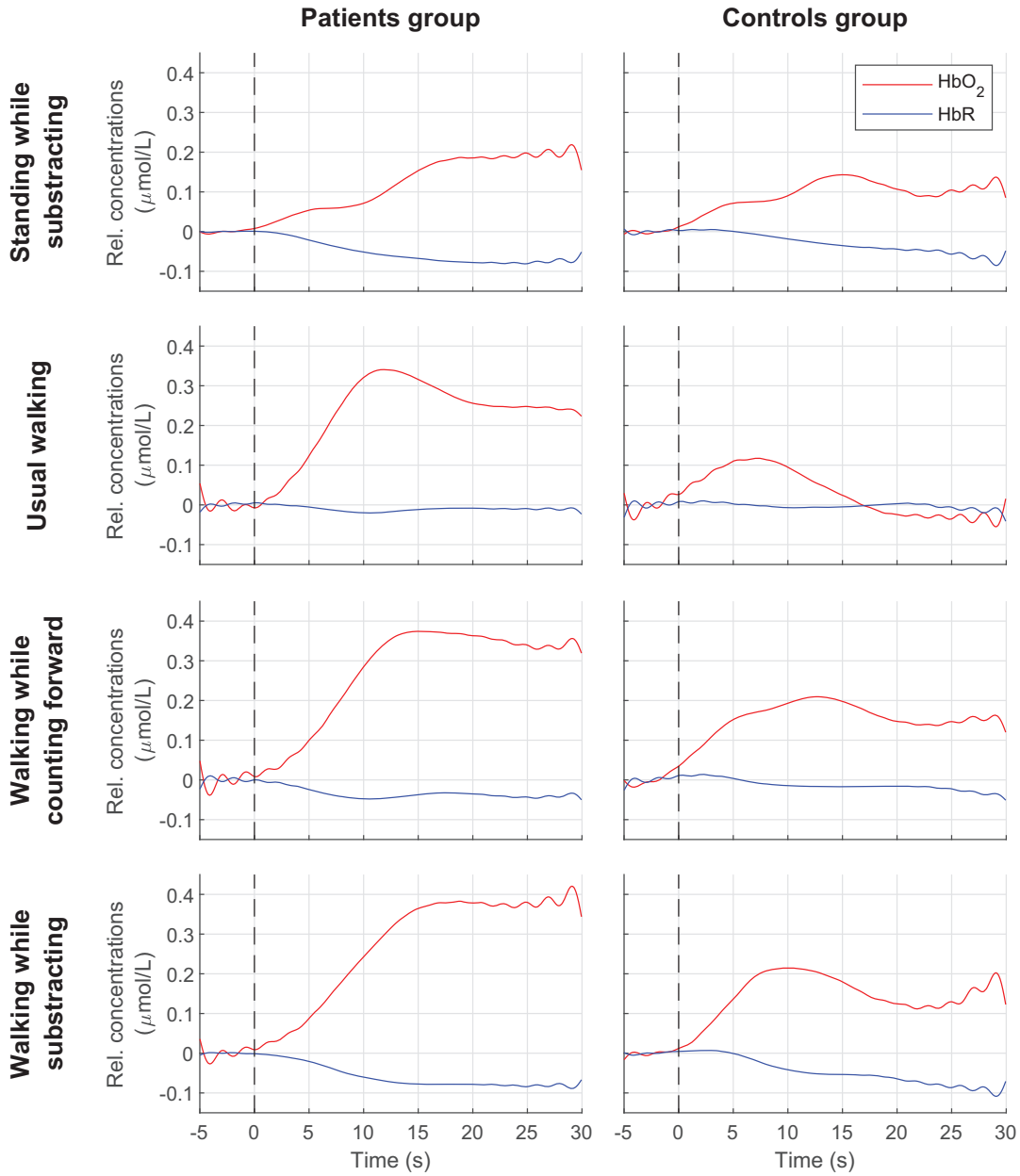


FIGURE 3 | Averaged time courses of HbO_2 and HbR in the DLPFC for each condition in both groups. Vertical dashed lines indicate start of the task. Rel. concentrations, Relative concentrations.

*Group*Condition Interaction*

No interaction between group and condition was found in any of the mean gait parameters ($p > 0.12$) (**Table 2**). However, two interactions between group and condition on CV of speed ($p = 0.04$) and CV of gait cycle time ($p = 0.007$) were significant. In patients, CV of speed increased during both DT walking conditions compared to usual walking whereas no pairwise comparisons for the CV of speed were found for the controls. Furthermore, patients had greater CV of speed than controls during the walking while subtracting condition ($p = 0.02$) (**Figure 4**). In patients, CV of gait cycle time increased as walking task difficulty increased whereas in controls, CV of gait cycle time increased during DT walking while counting forward compared to usual walking ($p = 0.03$). Patients also had a greater CV of gait cycle time than controls during the DT walking while subtracting ($p = 0.04$).

Cognitive Performance

No significant between-group differences in cognitive performance were found during the standing while subtracting

TABLE 2 | Repeated analyses of variance for gait parameters.

Gait parameters		Condition	Group	Condition*Group Pairwise comparisons 1–2; 1–3; 2-3[a] *p*-value[b]
Speed	Mean	**$F_{(2,68)} = 50.08$, $p < 0.001$, $\eta^2 = 0.60$**	$F_{(1,34)} = 3.51$, $p = 0.07$, $\eta^2 = 0.09$	$F_{(2,68)} = 1.98$, $p = 0.15$, $\eta^2 = 0.06$
	CV	**$F_{(2,68)} = 15.74$, $p < 0.001$, $\eta^2 = 0.32$**	**$F_{(1,34)} = 4.28$, $p = 0.046$, $\eta^2 = 0.11$**	**$F_{(2,68)} = 3.32$, $p = 0.04$, $\eta^2 = 0.09$** For patients: **0.002; <0.001**; NS For controls: NS; NS; NS
Cadence	Mean	**$F_{(2,68)} = 45.18$, $p < 0.001$, $\eta^2 = 0.57$**	$F_{(1,34)} = 0.83$, $p = 0.37$, $\eta^2 = 0.02$	$F_{(2,68)} = 1.43$, $p = 0.25$, $\eta^2 = 0.04$
	CV	**$F_{(2,68)} = 20.84$, $p < 0.001$, $\eta^2 = 0.38$**	$F_{(1,34)} = 1.06$, $p = 0.31$, $\eta^2 = 0.03$	$F_{(2,68)} = 2.87$, $p = 0.06$, $\eta^2 = 0.08$
Stride length	Mean	**$F_{(2,68)} = 29.27$, $p < 0.001$, $\eta^2 = 0.46$**	**$F_{(1,34)} = 4.35$, $p = 0.045$, $\eta^2 = 0.11$**	$F_{(2,68)} = 2.20$, $p = 0.12$, $\eta^2 = 0.06$
	CV	**$F_{(2,68)} = 12.25$, $p < 0.001$, $\eta^2 = 0.27$**	$F_{(1,34)} = 2.00$, $p = 0.17$, $\eta^2 = 0.06$	$F_{(2,68)} = 2.35$, $p = 0.10$, $\eta^2 = 0.07$
Gait cycle time	Mean	**$F_{(2,68)} = 36.31$, $p < 0.001$, $\eta^2 = 0.52$**	$F_{(1,34)} = 1.06$, $p = 0.31$, $\eta^2 = 0.03$	$F_{(2,68)} = 1.72$, $p = 0.19$, $\eta^2 = 0.048$
	CV	**$F_{(2,68)} = 16.93$, $p < 0.001$, $\eta^2 = 0.33$**	$F_{(1,34)} = 1.20$, $p = 0.28$, $\eta^2 = 0.03$	**$F_{(2,68)} = 5.38$, $p = 0.007$, $\eta^2 = 0.14$** For patients: **0.001; <0.001; 0.001** For controls: **0.03;** NS; NS

Values in bold are significant. [a]*(1) Usual walking; (2) Walking while counting forward; (3) Walking while subtracting.* [b]*Adjusted for multiple comparisons using Bonferroni correction. NS, Not Significant; CV, Coefficient of variation.*

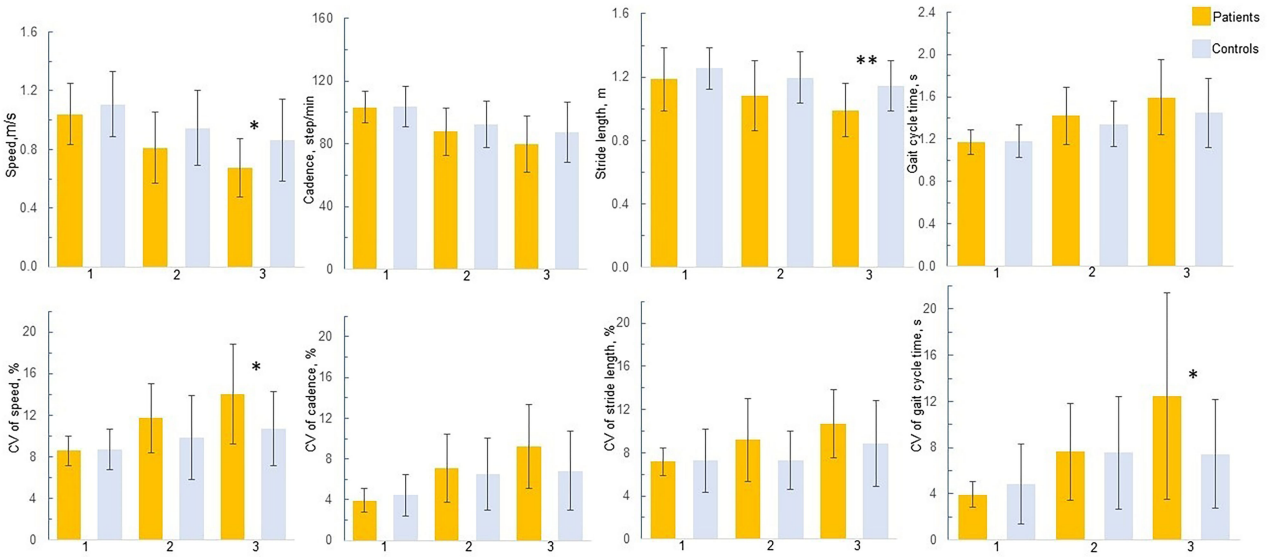


FIGURE 4 | Gait performance in patients and controls. 1 = Usual walking; 2 = Walking while counting forward; 3 = Walking while subtracting. $^*p < 0.05$, $^{**}p < 0.01$; *P*-values adjusted for Bonferroni correction. Only significant between-group differences are presented in the figure.

and walking while subtracting conditions (standing while subtracting: Controls: 5.61 ± 3.19; patients: 5.91 ± 3.22, $p = 0.83$; walking while subtracting: Controls: 4.85 ± 2.74; patients: 5.28 ± 3.11, $p = 0.67$). Patients were significantly better than controls in the walking while counting forward condition (27.31 ± 5.60 vs. 22.42 ± 7.17, $p = 0.02$).

Patients were significantly slower than controls to perform the Stroop test (word reading conditions), the TMT (part A and B), and the PMT (the addition list) (see **Table 3**). They performed worse than controls on the DSST.

Correlations Between ΔHbO_2 and Behavioral Measures

Strong correlations between ΔHbO_2 during usual walking and CV of cadence, stride length and gait cycle time were found (**Table 4**). Moderate correlations were also found between ΔHbO_2 during walking while counting forward and CV of all gait parameters. No significant correlations between ΔHbO_2 during walking while subtracting condition and gait outcomes were found. A higher number of significant correlations between ΔHbO_2 and cognitive performance was found for the usual walking condition than for the other conditions. Increased

ΔHbO_2 during usual walking was negatively correlated with worse performance on TMT, DSST, and Stroop test (color and word conditions). Note that no significant correlations between ΔHbO_2 and behavioral measures were found when conducting correlation analyses in each group (data available upon request).

TABLE 3 | Comparison of performance on neuropsychological tests between PD patients and controls.

	PD patients $N = 18$	Controls $N = 18$	P-value[b]
Stroop color, s (1)	68.00 (62.00–75.00)	58.50 (54.00–72.00)	0.03
Stroop word, s	48.00 (45.00–53.00)	42.00 (38.00–46.00)	**0.002**
Stroop C/W, s (2)	132.50 (108.00–140.00)	102.50 (89.00–135.00)	0.06
Inhibition cost, s (2)–(1)	55.50 (47.00–74.00)	45.00 (33.00–58.00)	0.24
TMT A, s (3)	53.50 (44.00–72.00)	40.50 (35.00–45.00)	**0.009**
TMT B, s (4)	119.00 (94.00–157.00)	67.50 (60.00–88.00)	**0.002**
TMT (B-A), s (4)–(3)	67.50 (50.00–83.00)	29.50 (25.00–44.00)	**0.004**
DSST, score	50.11 ± 14.00	66.78 ± 16.32	**0.002**
PMT—addition list, s (5)	68.00 (54.00–78.00)	50.50 (43.00–58.00)	**0.006**
PMT—subtraction list, s (6)	102.50 (74.00–117.00)	74.00 (54.00–100.00)	0.04
PMT—alternance list, s (7)	109.50 (87.00–133.00)	78.00 (72.00–101.00)	0.05
PMT—shift cost, s[a]	18.25 (9.00–28.50)	18.75 (10.50–29.00)	0.85
Bells, score	34.00 (33.00–35.00)	34.00 (33.00–35.00)	0.48
Bells, time	153.13 ± 38.11	137.89 ± 51.52	0.31

Values are expressed in mean ± SD or median (Q1–Q3). Values in bold are significant. [a] (7) – [(6) +(5)]/2 [b] adjusted for Bonferroni correction.
DSST, Digit Symbol Substitution Test; PMT, Plus-Minus Task; Stroop C/W, Color-Word condition of the Stroop Test; TMT, Trail Making Test.

Linear Regression Analysis

Among demographic variables, age and years of education were also significantly correlated with ΔHbO_2 during usual walking (age: $r = 0.37$, $p = 0.03$; level of education: $r = -0.39$, $p = 0.02$).

Age, years of education, time to complete the color condition of the Stroop test, times to complete part A and B of the TMT, CV of cadence, CV of stride length were included in the model, with the group as a covariate. Stepwise linear regression revealed that part B of TMT was the most significant predictor of ΔHbO_2 during usual walking. This test explained 21% of the variance. Years of education was then introduced in addition to part B of TMT, explaining an additional 6% of the variance (**Table 5**). Note that part B of TMT was the most significant predictor, explaining 27% of the variance when the stepwise linear regression was performed in PD patients only.

DISCUSSION

In this study, we aimed to investigate changes in cortical activity of the DLPFC during usual walking and DT walking conditions in patients with PD in comparison with controls.

TABLE 4 | Associations between ΔHbO_2 and behavioral performance.

		HbO_2			
		Standing while subtracting	**Usual walking**	**Walking while counting forward**	**Walking while subtracting**
Speed	Mean	NA	−0.23	−0.04	−0.09
	CV (%)		−0.008	**0.45*** **	0.25
Cadence	Mean		−0.05	−0.01	0.006
	CV (%)		***−0.12***	**−0.39***	0.11
Stride length	Mean		−0.28	−0.05	−0.14
	CV (%)		***0.18***	**−0.50****	0.14
Gait cycle time	Mean		0.06	0.08	0.06
	CV (%)		***−0.11***	**0.42****	0.18
MOCA score		−0.01	−0.17	0.04	−0.04
Stroop color		0.26	**0.40***	0.27	0.33
Stroop word		**0.36***	**0.35***	0.24	0.33
Stroop C/W		0.22	0.24	0.12	0.16
Inhibition cost		*0.09*	*−0.18*	*−0.06*	*0.08*
TMT A		*0.31*	***0.55*****	***0.33****	***0.46*****
TMT B		*0.11*	***0.64*****	*0.29*	***0.39****
TMT (B-A)		*−0.08*	***0.62*****	*0.25*	*0.33*
DSST		−0.04	**−0.40***	−0.11	**−0.33***
PMT—addition list		0.11	0.16	0.07	0.17
PMT—subtraction list		0.19	0.10	0.24	0.03
PMT—alternance		0.21	0.20	0.07	0.22
PMT—shift cost		0.14	0.18	0.06	0.09
Bells score		*−0.15*	*−0.10*	*−0.08*	*−0.27*
Bells time		0.30	0.30	0.12	0.18

*The values correspond to Pearson correlations except for the ones in italics which represent Spearman correlations. Values in bold are significant. *$p < 0.05$; **$p < 0.01$; ***$p < 0.001$.*
DSST, Digit Symbol Substitution Test; NA, Not Applicable; PMT, Plus-Minus Task; TMT, Trail Making Test.

TABLE 5 | Predictors of ΔHbO_2 during usual walking.

Independent variables included in the model	R^2	R^2 *change*	*B*	*t*	*P*-value
Step 1					
Group[a]	0.29	0.29	0.21	3.66	**<0.001**
Step 2					
Group	0.49	0.21	0.13	2.29	**0.03**
TMT-B			0.001	3.60	**0.001**
Step 3					
Group	0.56	0.06	0.14	2.67	**0.01**
TMT- B			0.001	2.91	**0.007**
Years of education			−0.02	−2.08	**0.04**

ΔHbO2 was the dependent variable. Values in bold are significant. [a]Included in the model as a covariate.

Associations between cortical activity in the DLPFC during usual and DT walking and behavioral/cognitive outcomes were also examined. A third objective was to determine the best predictors of an increased activation in the DLPFC during usual walking. The novelty of this research is that we further explored the determinants of an increased cortical activity during usual walking. This may help to better understand falls risk or gait deficits before they emerge.

Increased Brain Activity in DLPFC in Patients With PD During Walking

Usual Walking

Moderate to strong associations were found during usual walking between increased cortical activity and poorer performance in neuropsychological tests assessing executive functions, speed of processing and psychomotor speed (i.e., TMT, DSST, and color and word conditions of the Stroop test). These findings suggest that normal walking is already a complex process that requires input from executive functions (40), that is carried out by DLPFC with other projections to various cortical and subcortical regions (41). As expected, patients had executive deficits and processing speed slowness compared to controls.

Patients with PD had also higher levels of DLPFC activation in comparison with controls, even during usual walking, which is consistent with previous studies (6, 11, 13, 21, 42, 43). However, patients did not show decreased walking performance compared to controls during usual walking. These results are not consistent with previous studies reporting decreased walking performance in patients already during the usual walking condition (20, 44). An explanation could be due to clinical and demographic characteristics of our group of patients. Our patients were at the earliest stages of PD, based on disease duration and motor score of UPDRS. They were also younger than those recruited in previous studies (20, 44). Furthermore, they were all volunteers to participate in this study and physically active. As in most research, there is a recruitment bias: it is often the fittest patients who agree to participate. It is therefore not excluded that these patients represent a special category, not quite representative of PD patients' population. It is also possible that our path configuration with markings on the floor helped patients to walk. Other measures, such as measures of arm swing while walking could be used in future studies, to better discriminate patients with PD from controls. Indeed, this measure has been shown as a new prodomal marker of PD (45).

Finally, this increased cortical activity in the DLPFC in absence of gait impairments during usual walking may reflect a compensatory mechanism to overcome executive deficits, processing speed slowness and deficits in movement automaticity in early stage PD (46).

DT Walking

No significant increase of DLPFC activity in patients was found from usual walking to DT walking conditions whereas in controls, significant increase appeared from usual walking to DT walking conditions. Findings on patients are consistent with previous studies that used the same type of DT walking (20). These results suggest that patients are unable to further increase DLPFC activity, due to a reduction of their cognitive resources and their limited cognitive capacity. Results in controls are consistent with previous studies reporting a significant increase in PFC, as a compensatory mechanism in healthy older adults during DT walking (e.g., walking while serially subtracting 3s) (47–50). This is also in line with the cognitive resource theories of aging which postulated that brain activity will be more pronounced with increasing task demands in older adults (51). Increased prefrontal activity in older adults may also be due to the fact that most of healthy older adults in the present study were younger than 70s. A recent study suggested that healthy older adults in the 70s were unable to further increase prefrontal cortex activity, leading to a decrease of walking performance (52).

During walking while counting forward, no significant between-group differences were observed for DLPFC activity and gait measures. Furthermore, patients performed better in the counting forward condition while walking than controls. It is possible that patients prioritize the counting task at the expense of the walking task. Patients are globally slower, with a reduced cadence and shorter stride length than controls during this condition although no significant between-group differences in gait performance were found. Another explanation could be that patients had sufficient cognitive resources to perform both the counting forward condition and the walking task. Association between cortical activity in the DLPFC and cognitive measures revealed that increased DLPFC activity during walking while counting forward condition is rather associated with psychomotor slowness than executive functions. This result also highlights the major role of this cortical area on psychomotor functioning (53). The lack of significant differences between groups in cortical activity and gait measures may also be due to a high heterogeneity in the performance.

Patients with PD had higher levels of DLPFC activation than controls during walking while subtracting condition. As expected, increased DLPFC activity during walking while subtracting condition was found to be associated with executive deficits and psychomotor slowness. Furthermore, patients performed as well as controls the subtraction task while walking. However, they walked slower and had shorter stride length than

controls. Patients were also more irregular than controls, as reflected by a greater variability of speed and gait cycle time. Based on the concept that attentional capacity is limited, it is possible that patients allocated their available cognitive resources to the subtraction task at the expense of the walking task. Increased DLPFC activation in patients during this complex DT condition is therefore insufficient to compensate for motor and executive deficits and may lead to decreased walking performance (12).

Associations Between Cortical Activity and Gait Parameters

Associations between increased activation in the DLPFC and higher gait variability in all participants were already found during usual walking. Similar findings were found in previous studies in older adults during obstacle negotiation (48). These authors discussed the fact that increased activation in the DLPFC may reflect a compensatory attempt to overcome inefficient neural activation in the face of demanding tasks. The inefficiency was unable to cope with the motor needs. During the walking while counting forward condition, increased cortical activity was associated with lower variability of their cadence and stride length as well as a greater variability of speed and gait cycle time. A possible explanation of the lower variability of cadence and stride length is that counting forward may induce a rhythm on which participants paced their walking. However, higher variability in their speed and gait cycle time seems to be moderately associated with increased cortical activity in the DLPFC during walking while counting forward. The lack of significant correlations between HbO_2 and gait parameters in the DT walking while subtracting condition could be explained by the fact that patients with PD are unable to further increase their cortical activity in the DLPFC.

In the literature, measures of gait variability were found to be closely related to instability and fall risk (54). Strong relationships between high gait variability and increased cortical activity during usual walking supports the notion that subtle variations in the gait during usual walking, particularly in older individuals with PD, may precede disturbances in DT walking, leading to a higher risk of falls. To our knowledge, few studies explored associations between cortical activity and behavioral measures in walking tasks in older individuals with or without PD (52, 55). Further studies with larger sample size are needed to better understand the relationships between cortical activity and gait parameters in this population.

Best Predictors of Increased Cortical Activity During Usual Walking

Poorer performances on part B of TMT, and a low level of education significantly contributed to explain increased cortical activity in the DLPFC during usual walking. Particularly, the TMT-B explained 21% of the variance after adjusting for group status. These findings highlight the major role of TMT-B in predicting cortical activity of the DLPFC during usual walking. This complex test requires executive functions (updating information in working memory, shifting attention between letters and number as well as inhibit non-relevant information), which is affected by PD. This test in clinic may prove useful to determine difficulties in activities of daily living in patients with PD, as previously reported in a driving context (56). Yet, caution with the interpretation is warranted as the sample of the study was relatively small. Finally, a lower level of education also contributed to increased cortical activity in the DLPFC which is in accordance with the evidence that better executive functions are related to an increased number of education years (57). Further studies should therefore consider the level of education of patients with PD when exploring changes in brain activity in the DLPFC.

Methodological Considerations

Methodological considerations of this study included the use of short-separation reference channels (1.5 cm apart) to remove for peripheral hemodynamic response (i.e., artifact caused by breathing, cardiac cycle or other error related to movement) which has been used only once in patients with PD (15). Furthermore, both Hb species were reported. ΔHbO_2 was found to be the most sensitive indicator of regional cerebral blood flow in NIRS measurements (58) whereas ΔHbR better reflects the match between oxygen supply and demand (59). In this study, fNIRS processing was the same for patients with PD and healthy older individuals. Although a recent study showed few effects of different processing methods on fNIRS signals assessed during active walking tasks in older adults (60), future studies applying specific fNIRS processing (e.g., age-dependent DPF values) are warranted. Furthermore, it would have been interesting to include a standing while counting forward condition in order to determine different patterns of task prioritization between groups (61). However, as the duration of the experiment was already long, we preferred to limit the number of conditions. The small sample size including volunteers with well-preserved cognitive abilities among PD participants limits the generalizability of the results. One limitation of the present study is that only the activity of DLPFC cortex is recorded. Further studies should assess multiple cognitive regions while walking to provide a greater understanding of the contribution of brain areas to walking and dual tasking (62). Finally, except the fear-of-falling inventory, no direct measures on the number of falls in patients with PD was reported in this study. Further studies should include a detailed questionnaire reporting the number of falls.

Clinical Implications

These findings may have important clinical implications for training program: it is possible that cognitive intervention decreases DLPFC activity and therefore improve the ability to walk in usual and complex situations. However, the increased cortical activity in the DLPFC is also due to deficits in automaticity (46). Multimodal intervention that targets both motor and cognitive aspects should therefore be developed to improve cognition and movement automaticity and promote mobility in individuals with PD. As a consequence, a reduction in the DLPFC activity while walking after the intervention should be expected. Further studies investigating the effect of training programs on cortical activity in DLPFC in patients with PD are therefore warranted.

CONCLUSIONS

This present study shows that patients with early stage PD increased their DLPFC activity, already during usual walking to compensate for subcortical dysfunction and executive deficits. Furthermore, strong relationships between cortical activity in the DLPFC during usual walking and behavioral measures were found in all participants. Finally, longer times to complete part B of TMT, and lower number of education years were found to be the best predictors of an increased of ΔHbO_2 during usual walking.

DATA AVAILABILITY STATEMENT

The raw data supporting the conclusions of this article will be made available by the authors, without undue reservation.

ETHICS STATEMENT

The studies involving human participants were reviewed and approved by Comité de Protection des Personnes Nord Ouest III Réf. CPP: 2018-01 No. ID RCB: 2017-A03187-46. All participants provided their written informed consent to participate in this study.

AUTHOR CONTRIBUTIONS

MR, IH, MC, JL, TD, and LP-F conceived and designed the study. MR, IH, MC, RD, TD, and LP-F contributed to data collection. MR, IH, RD, and LP-F contributed to data analysis and interpretation. IH, MC, RD, HD, SP, JL, TD, and LP-F contributed to the critical revision for important intellectual content. MR wrote the first draft. All authors contributed to the article and approved the submitted version.

FUNDING

This work is part of the PARACHUTE project that was supported by the National Research Agency under the Future Investment Programme (ref. ANR-16-IDEX-0003), managed by the French government.

ACKNOWLEDGMENTS

Many thanks to M. F. Boyer for the inclusion of healthy older adults. We also would like to thank all the participants for their willingness to volunteer for this study. We are grateful to Biomechanics and Impact Mechanics Laboratory for the material provided.

REFERENCES

1. Mirelman A, Bonato P, Camicioli R, Ellis TD, Giladi N, Hamilton JL, et al. Gait impairments in Parkinson's disease. *Lancet Neurol.* (2019) 18:697–708. doi: 10.1016/S1474-4422(19)30044-4
2. Fasano A, Canning CG, Hausdorff JM, Lord S, Rochester L. Falls in Parkinson's disease: a complex and evolving picture. *Mov Disord.* (2017) 32:1524–36. doi: 10.1002/mds.27195
3. Montero-Odasso M, Bherer L, Studenski S, Gopaul K, Oteng-Amoako A, Woolmore-Goodwin S, et al. Mobility and cognition in seniors. Report from the 2008 institute of aging (CIHR) mobility and cognition workshop. *Can Geriatr J.* (2015) 18:159–67. doi: 10.5770/cgj.18.188
4. Mak MK, Wong A, Pang MY. Impaired executive function can predict recurrent falls in Parkinson's disease. *Arch Phys Med Rehabil.* (2014) 95:2390–5. doi: 10.1016/j.apmr.2014.08.006
5. Canning CG, Paul SS, Nieuwboer A. Prevention of falls in Parkinson's disease: a review of fall risk factors and the role of physical interventions. *Neurodegener Dis Manag.* (2014) 4:203–21. doi: 10.2217/nmt.14.22
6. Maidan I, Rosenberg-Katz K, Jacob Y, Giladi N, Deutsch JE, Hausdorff JM, et al. Altered brain activation in complex walking conditions in patients with Parkinson's disease. *Parkinsonism Relat Disord.* (2016) 25:91–6. doi: 10.1016/j.parkreldis.2016.01.025
7. Kahya M, Moon S, Lyons KE, Pahwa R, Akinwuntan AE, Devos H. Pupillary response to cognitive demand in Parkinson's disease: a pilot study. *Front Aging Neurosci.* (2018) 10:90. doi: 10.3389/fnagi.2018.00090
8. Perrey S. Possibilities for examining the neural control of gait in humans with fNIRS. *Front Physiol.* (2014) 5:204. doi: 10.3389/fphys.2014.00204
9. Maidan I, Fahoum F, Shustak S, Gazit E, Patashov D, Tchertov D, et al. Changes in event-related potentials during dual task walking in aging and Parkinson's disease. *Clin Neurophysiol.* (2019) 130:224–30. doi: 10.1016/j.clinph.2018.11.019
10. Villringer A, Planck J, Hock C, Schleinkofer L, Dirnagl U. Near infrared spectroscopy (NIRS): a new tool to study hemodynamic changes during activation of brain function in human adults. *Neurosci Lett.* (1993) 154:101–4. doi: 10.1016/0304-3940(93)90181-J
11. Maidan I, Bernad-Elazari H, Gazit E, Mirelman A, Hausdorff J, Giladi N. Increased activation of the frontal lobe is associated with freezing of gait in patients with parkinson's disease: an fNIRS study (P6.074). *Neurology.* (2015) 84.
12. Al-Yahya E, Mahmoud W, Meester D, Esser P, Dawes H. Neural substrates of cognitive motor interference during walking; peripheral and central mechanisms. *Front Hum Neurosci.* (2019) 12:536. doi: 10.3389/fnhum.2018.00536
13. Maidan I, Bernad-Elazari H, Giladi N, Hausdorff JM, Mirelman A. When is higher level cognitive control needed for locomotor tasks among patients with Parkinson's disease? *Brain Topogr.* (2017) 30:531–8. doi: 10.1007/s10548-017-0564-0
14. Nieuwhof F, Reelick MF, Maidan I, Mirelman A, Hausdorff JM, Olde Rikkert MGM, et al. Measuring prefrontal cortical activity during dual task walking in patients with Parkinson's disease: feasibility of using a new portable fNIRS device. *Pilot Feasibil Stud.* (2016) 2:59. doi: 10.1186/s40814-016-0099-2
15. Stuart S, Belluscio V, Quinn JF, Mancini M. Pre-frontal cortical activity during walking and turning is reliable and differentiates across young, older adults and people with Parkinson's disease. *Front Neurol.* (2019) 10:536. doi: 10.3389/fneur.2019.00536
16. Orcioli-Silva D, Vitório R, Nóbrega-Sousa P, da Conceição NR, Beretta VS, Lirani-Silva E, et al. Levodopa facilitates prefrontal cortex activation during dual task walking in Parkinson disease. *Neurorehabil Neural Repair.* (2020) 34:589–9. doi: 10.1177/1545968320924430
17. Orcioli-Silva D, Vitório R, Beretta VS, da Conceição NR, Nóbrega-Sousa P, Oliveira A de SC, et al. Is cortical activation during walking different between Parkinson's disease motor subtypes? *J Gerontol A Biol Sci Med Sci.* (2020) 16:glaa174. doi: 10.1093/gerona/glaa174
18. Stuart S, Morris R, Giritharan A, Quinn J, Nutt JG, Mancini M. Prefrontal cortex activity and gait in Parkinson's disease with cholinergic and dopaminergic therapy. *Mov Disord.* (2020). doi: 10.1002/mds.28214
19. Doi T, Makizako H, Shimada H, Park H, Tsutsumimoto K, Uemura K, et al. Brain activation during dual-task walking and executive function among older adults with mild cognitive impairment: a fNIRS study. *Aging Clin Exp Res.* (2013) 25:539–44. doi: 10.1007/s40520-013-0119-5

20. Maidan I, Nieuwhof F, Bernad-Elazari H, Reelick MF, Bloem BR, Giladi N, et al. The role of the frontal lobe in complex walking among patients with Parkinson's disease and healthy older adults: an fnirs study. *Neurorehabil Neural Repair.* (2016) 30:963–71. doi: 10.1177/1545968316650426
21. Stuart S, Vitorio R, Morris R, Martini DN, Fino PC, Mancini M. Cortical activity during walking and balance tasks in older adults and in people with Parkinson's disease: a structured review. *Maturitas.* (2018) 113:53–72. doi: 10.1016/j.maturitas.2018.04.011
22. Panikratova YR, Vlasova RM, Akhutina TV, Korneev AA, Sinitsyn VE, Pechenkova EV. Functional connectivity of the dorsolateral prefrontal cortex contributes to different components of executive functions. *Int J Psychophysiol.* (2020) 151:70–9. doi: 10.1016/j.ijpsycho.2020.02.013
23. Tomlinson CL, Stowe R, Patel S, Rick C, Gray R, Clarke CE. Systematic review of levodopa dose equivalency reporting in Parkinson's disease. *Mov Disord.* (2010) 25:2649–53. doi: 10.1002/mds.23429
24. Villringer A. Non-invasive optical spectroscopy and imaging of human brain function. *Trends Neurosci.* (1997) 20:435–42. doi: 10.1016/S0166-2236(97)01132-6
25. Huppert TJ. Commentary on the statistical properties of noise and its implication on general linear models in functional near-infrared spectroscopy. *Neurophotonics.* (2016) 3:010401. doi: 10.1117/1.NPh.3.1.010401
26. Cooper R, Selb J, Gagnon L, Phillip D, Schytz HW, Iversen HK, et al. A systematic comparison of motion artifact correction techniques for functional near-infrared spectroscopy. *Front Neurosci.* (2012) 6:147. doi: 10.3389/fnins.2012.00147
27. Molavi B, Dumont GA. Wavelet-based motion artifact removal for functional near-infrared spectroscopy. *Physiol Meas.* (2012) 33:259–70. doi: 10.1088/0967-3334/33/2/259
28. Herold F, Wiegel P, Scholkmann F, Thiers A, Hamacher D, Schega L. Functional near-infrared spectroscopy in movement science: a systematic review on cortical activity in postural and walking tasks. *Neurophotonics.* (2017) 4:041403. doi: 10.1117/1.NPh.4.4.041403
29. Gagnon L, Perdue K, Greve DN, Goldenholz D, Kaskhedikar G, Boas DA. Improved recovery of the hemodynamic response in diffuse optical imaging using short optode separations and state-space modeling. *NeuroImage.* (2011) 56:1362–71. doi: 10.1016/j.neuroimage.2011.03.001
30. Menant JC, Maidan I, Alcock L, Al-Yahya E, Cerasa A, Clark DJ, et al. A consensus guide to using functional near-infrared spectroscopy in posture and gait research. *Gait Posture.* (2020) 82:254–65. doi: 10.1016/j.gaitpost.2020.09.012
31. Hoops S, Nazem S, Siderowf AD, Duda JE, Xie SX, Stern MB, et al. Validity of the MoCA and MMSE in the detection of MCI and dementia in Parkinson disease. *Neurology.* (2009) 73:1738–45. doi: 10.1212/WNL.0b013e3181c34b47
32. Azouvi P, Didic-Hamel C, Fluchaire I, Godefroy O, Hoclet E, Le Gall D, et al. L'évaluation des fonctions exécutives en pratique clinique. *Revue Neuropsychol.* (2001) 11:383–433.
33. Reitan RM. Validity of the trail making test as an indicator of organic brain damage. *Percept Motor Skills.* (1958) 8:271–6. doi: 10.2466/pms.1958.8.3.271
34. Lafont S, Marin-Lamellet C, Paire-Ficout L, Thomas-Anterion C, Laurent B, Fabrigoule C. The Wechsler digit symbol substitution test as the best indicator of the risk of impaired driving in Alzheimer disease and normal aging. *Dement Geriatr Cogn Disord.* (2010) 29:154–63. doi: 10.1159/000264631
35. Miyake A, Friedman NP, Emerson MJ, Witzki AH, Howerter A, Wager TD. The unity and diversity of executive functions and their contributions to complex "Frontal Lobe" tasks: a latent variable analysis. *Cogn Psychol.* (2000) 41:49–100. doi: 10.1006/cogp.1999.0734
36. Gauthier L, Dehaut F, Joanette Y. The bells test: a quantitative and qualitative test for visual neglect. *Int J Clin Neuropsychol.* (1989) 11:49–54. doi: 10.1037/t28075-000
37. Sato T, Ito M, Suto T, Kameyama M, Suda M, Yamagishi Y, et al. Time courses of brain activation and their implications for function: a multichannel near-infrared spectroscopy study during finger tapping. *Neurosci Res.* (2007) 58:297–304. doi: 10.1016/j.neures.2007.03.014
38. Bakeman R. Recommended effect size statistics for repeated measures designs. *Behav Res Methods.* (2005) 37:379–84. doi: 10.3758/BF03192707
39. Cohen J. A power primer. *Psychol Bull.* (1992) 112:155–9. doi: 10.1037/0033-2909.112.1.155
40. Holtzer R, Verghese J, Xue X, Lipton RB. Cognitive processes related to gait velocity: results from the Einstein aging study. *Neuropsychology.* (2006) 20:215–23. doi: 10.1037/0894-4105.20.2.215
41. Leh SE, Petrides M, Strafella AP. The neural circuitry of executive functions in healthy subjects and Parkinson's disease. *Neuropsychopharmacology.* (2010) 35:70–85. doi: 10.1038/npp.2009.88
42. Vitorio R, Stuart S, Rochester L, Alcock L, Pantall A. fNIRS response during walking — artefact or cortical activity? A systematic review. *Neurosci Biobehav Rev.* (2017) 83:160–72. doi: 10.1016/j.neubiorev.2017.10.002
43. Maidan I, Bernad-Elazari H, Gazit E, Giladi N, Hausdorff JM, Mirelman A. Changes in oxygenated hemoglobin link freezing of gait to frontal activation in patients with Parkinson disease: an fNIRS study of transient motor-cognitive failures. *J Neurol.* (2015) 262:899–908. doi: 10.1007/s00415-015-7650-6
44. Yamada P de A, Amaral-Felipe KM, Spinoso DH, Abreu DCC de, Stroppa-Marques AEZ, Faganello-Navega FR. Everyday tasks impair spatiotemporal variables of gait in older adults with Parkinson's disease. *Hum Mov Sci.* (2020) 70:102591. doi: 10.1016/j.humov.2020.102591
45. Mirelman A, Bernad-Elazari H, Thaler A, Giladi-Yacobi E, Gurevich T, Gana-Weisz M, et al. Arm swing as a potential new prodromal marker of Parkinson's disease. *Mov Disord.* (2016) 31:1527–34. doi: 10.1002/mds.26720
46. Vandenbossche J, Deroost N, Soetens E, Coomans D, Spildooren J, Vercruysse S, et al. Freezing of gait in Parkinson's disease: disturbances in automaticity and control. *Front Hum Neurosci.* (2012) 6:356. doi: 10.3389/fnhum.2012.00356
47. Beurskens R, Helmich I, Rein R, Bock O. Age-related changes in prefrontal activity during walking in dual-task situations: a fNIRS study. *Int J Psychophysiol.* (2014) 92:122–8. doi: 10.1016/j.ijpsycho.2014.03.005
48. Mirelman A, Maidan I, Bernad-Elazari H, Shustack S, Giladi N, Hausdorff JM. Effects of aging on prefrontal brain activation during challenging walking conditions. *Brain Cogn.* (2017) 115:41–6. doi: 10.1016/j.bandc.2017.04.002
49. Holtzer R, Mahoney JR, Izzetoglu M, Izzetoglu K, Onaral B, Verghese J. fnirs study of walking and walking while talking in young and old individuals. *J Gerontol A Biol Sci Med Sci.* (2011) 66A:879–87. doi: 10.1093/gerona/glr068
50. Mirelman A, Maidan I, Bernad-Elazari H, Nieuwhof F, Reelick M, Giladi N, et al. Increased frontal brain activation during walking while dual tasking: an fNIRS study in healthy young adults. *J Neuroeng Rehabil.* (2014) 11:85. doi: 10.1186/1743-0003-11-85
51. Steffener J, Stern Y. Exploring the neural basis of cognitive reserve in aging. *Biochim Biophys Acta.* (2012) 1822:467–73. doi: 10.1016/j.bbadis.2011.09.012
52. Nóbrega-Sousa P, Gobbi LTB, Orcioli-Silva D, Conceição NR da, Beretta VS, Vitório R. Prefrontal cortex activity during walking: effects of aging and associations with gait and executive function. *Neurorehabil Neural Repair.* (2020) 34:915–24. doi: 10.1177/1545968320953824
53. Schrijvers D, Hulstijn W, Sabbe BGC. Psychomotor symptoms in depression: a diagnostic, pathophysiological and therapeutic tool. *J Affect Disord.* (2008) 109:1–20. doi: 10.1016/j.jad.2007.10.019
54. Hausdorff JM. Gait variability: methods, modeling and meaning. *J Neuroeng Rehabil.* (2005) 2:19. doi: 10.1186/1743-0003-2-19
55. Stuart S, Mancini M. Prefrontal cortical activation with open and closed-loop tactile cueing when walking and turning in parkinson disease: a pilot study. *J Neurol Phys Ther.* (2020) 44:121–31. doi: 10.1097/NPT.0000000000000286
56. Ranchet M, Paire-Ficout L, Marin-Lamellet C, Laurent B, Broussolle E. Impaired updating ability in drivers with Parkinson's disease. *J Neurol Neurosurg Psychiatr.* (2011) 82:218–23. doi: 10.1136/jnnp.2009.203166
57. Grasset L, Jacqmin-Gadda H, Proust-Lima C, Pérès K, Amieva H, Dartigues J-F, et al. Temporal trends in the level and decline of cognition and disability in an elderly population: the PAQUID study. *Am J Epidemiol.* (2018) 187:2168–76. doi: 10.1093/aje/kwy118
58. Hoshi Y, Kobayashi N, Tamura M. Interpretation of near-infrared spectroscopy signals: a study with a newly developed perfused rat brain model. *J Appl Physiol.* (2001) 90:1657–62. doi: 10.1152/jappl.2001.90.5.1657
59. Elwell CE, Cope M, Edwards AD, Wyatt JS, Delpy DT, Reynolds EO. Quantification of adult cerebral hemodynamics by near-infrared spectroscopy. *J Appl Physiol.* (1994) 77:2753–60. doi: 10.1152/jappl.1994.77.6.2753

60. Izzetoglu M, Holtzer R. Effects of processing methods on fnirs signals assessed during active walking tasks in older adults. *IEEE Trans Neural Syst Rehabil Eng.* (2020) 28:699–709. doi: 10.1109/TNSRE.2020.2970407
61. Plummer P, Eskes G. Measuring treatment effects on dual-task performance: a framework for research and clinical practice. *Front Hum Neurosci.* (2015) 9:225. doi: 10.3389/fnhum.2015.00225
62. Stuart S, Alcock L, Rochester L, Vitorio R, Pantall A. Monitoring multiple cortical regions during walking in young and older adults: dual-task response and comparison challenges. *Int J Psychophysiol.* (2019) 135:63–72. doi: 10.1016/j.ijpsycho.2018.11.006

Conflict of Interest: The authors declare that the research was conducted in the absence of any commercial or financial relationships that could be construed as a potential conflict of interest.

Copyright © 2020 Ranchet, Hoang, Cheminon, Derollepot, Devos, Perrey, Luauté, Danaila and Paire-Ficout. This is an open-access article distributed under the terms of the Creative Commons Attribution License (CC BY). The use, distribution or reproduction in other forums is permitted, provided the original author(s) and the copyright owner(s) are credited and that the original publication in this journal is cited, in accordance with accepted academic practice. No use, distribution or reproduction is permitted which does not comply with these terms.

frontiers in Neurology

ORIGINAL RESEARCH
published: 14 April 2021
doi: 10.3389/fneur.2021.648548

Utility of Multi-Modal MRI for Differentiating of Parkinson's Disease and Progressive Supranuclear Palsy Using Machine Learning

*Aron S. Talai[1], Jan Sedlacik[2], Kai Boelmans[3,4] and Nils D. Forkert[1]**

[1] Department of Radiology, University of Calgary, Calgary, AB, Canada, [2] Department of Diagnostic and Interventional Neuroradiology, University Medical Center Hamburg-Eppendorf, Hamburg, Germany, [3] Department of Neurology, University Hospital Würzburg, Würzburg, Germany, [4] Department of Neurology, Klinikum Bremerhaven-Reinkenheide, Bremerhaven, Germany

Background: Patients with Parkinson's disease (PD) and progressive supranuclear palsy Richardson's syndrome (PSP-RS) often show overlapping clinical features, leading to misdiagnoses. The objective of this study was to investigate the feasibility and utility of using multi-modal MRI datasets for an automatic differentiation of PD patients, PSP-RS patients, and healthy control (HC) subjects.

Material and Methods: T1-weighted, T2-weighted, and diffusion-tensor (DTI) MRI datasets from 45 PD patients, 20 PSP-RS patients, and 38 HC subjects were available for this study. Using an atlas-based approach, regional values of brain morphology (T1-weighted), brain iron metabolism (T2-weighted), and microstructural integrity (DTI) were measured and employed for feature selection and subsequent classification using combinations of various established machine learning methods.

Results: The optimal machine learning model using regional morphology features only achieved a classification accuracy of 65% (67/103 correct classifications) differentiating PD patients, PSP-RS patients, and HC subjects. The optimal machine learning model using only quantitative T2 values performed slightly better and achieved an accuracy of 75.7% (78/103). The optimal classifier using DTI features alone performed considerably better with 95.1% accuracy (98/103). The optimal multi-modal classifier using all features also achieved an accuracy of 95.1% but required more features and achieved a slightly lower F1-score compared to the optimal model using DTI features alone.

Conclusion: Machine learning models using multi-modal MRI perform significantly better than uni-modal machine learning models using morphological parameters based on T1-weighted MRI datasets alone or brain iron metabolism markers based on T2-weighted MRI datasets alone. However, machine learnig models using regional brain microstructural integrity metrics computed from DTI datasets perform similar to the optimal multi-modal machine learning model. Thus, given the results from this study cohort, it appears that morphology and brain iron metabolism markers may not provide additional value for classification compared to using DTI metrics alone.

Keywords: machine learning, magnetic resonance imaging, computer-assisted image analysis, Parkinson's disease, progressive supranuclear palsy

OPEN ACCESS

Edited by:
Maria Carmela Tartaglia, University of Toronto, Canada

Reviewed by:
Matteo Bologna, Sapienza University of Rome, Italy
Alexandru Hanganu, Centre de Recherche de l'Institut Universitaire de Gériatrie de Montréal (CRIUGM), Canada

***Correspondence:**
Nils D. Forkert
nils.forkert@ucalgary.ca

Specialty section:
This article was submitted to Movement Disorders, a section of the journal Frontiers in Neurology

Received: *31 December 2020*
Accepted: *22 March 2021*
Published: *14 April 2021*

Citation:
Talai AS, Sedlacik J, Boelmans K and Forkert ND (2021) Utility of Multi-Modal MRI for Differentiating of Parkinson's Disease and Progressive Supranuclear Palsy Using Machine Learning. Front. Neurol. 12:648548. doi: 10.3389/fneur.2021.648548

INTRODUCTION

The early differential diagnosis of classical Parkinson's disease (PD) and progressive supranuclear palsy (PSP)—in particular the Richardson's syndrome (PSP-RS)—is often limited by overlapping symptom profiles, which are not effectively captured by existing clinical scores or established diagnostic methods. Within this context, failure rates of up to 24% have been reported, even by movement disorders specialists (1). In clinical practice, diagnosis of PD and PSP-RS is mostly based on clinical examination including key features, response to levodopa, and established scores such as the Unified PD Rating Scale (UPDRS) (2). However, due to significant overlap of clinical symptoms and inadequate accuracy of bedside tests, differential diagnosis is often challenging, particularly in the early disease course. The relevance of an accurate early diagnosis is closely related to better disease management via appropriate drug administration, patient care protocols, and might improve disease prognosis considerably. Furthermore, the identification of early disease manifestations may lead to better targeted pharmaceutical therapies and enable advancements in developing more effective drug therapies in this domain.

In this context, group-wise studies using various magnetic resonance imaging (MRI) modalities such as T1-weighted (3, 4), T2-weighted (5, 6), and diffusion-tensor MRI (DTI) (7, 8) have shown significant differences between PD and PSP-RS patients and healthy control (HC) subjects. These differences indicate alterations in regional brain volume, brain iron metabolism, and microstructural brain tissue degradation, all off which are closely related to the neurodegenerative profiles of PD and PSP-RS compared to HC subjects (9–11). Supervised machine learning techniques are capable of identifying complex patterns in high-dimensional data, whereas the identified patterns can then be used to make patient-specific predictions on new unseen cases (12). Machine learning has been used successfully for various precision medicine problems (13) and multiple studies have attempted to utilize features obtained from the aforementioned group-wise studies to classify individual PD and PSP-RS patients [e.g., (14–16)].

However, only a few scientific studies have truly tried to harness the power of multi-modal imaging features to improve differential classification of patients with PD and PSP-RS so far [e.g., (17, 18)]. Moreover, the true benefit of using multi-modal imaging over single modality imaging information has not been explored in detail yet. Therefore, this study aims to present a comprehensive end-to-end framework to classify patients with PD, patients with PSP-RS, and HC subjects using T1-weighted, T2-weighted, and DTI datasets and evaluate the accuracy of optimal machine learning models trained using individual single modality features as well as multi-modality features.

MATERIALS AND METHODS

Patients and Imaging

The study cohort used for this work has been previously described in detail by Boelmans et al. (16). Briefly described, 45 PD, 20 PSP-RS, and 38 HC subjects presenting to the movement disorder outpatient clinic of the Neurology Department of the University Medical Center Hamburg-Eppendorf between July 2009 and September 2010 were used for this secondary, retrospective study. No sample size estimates were computed or required for the primary observational study. The clinical diagnosis of PD and PSP-RS was conducted according to the UK Brain Bank criteria (19) and the National Institute of Neurological Disorders and Stroke and Society for PSP (NINDS-SPSP) (20), respectively. The inclusion criteria for the PSP-RS group were probable PSP-RS subjects presenting as classical Richardson's syndrome with vertical palsy, axial rigidity, and balance instability with early falls. PSP-RS patients who exhibited prominent freezing phenomena, asymmetric clinical features, and a clinically relevant levodopa response were excluded from the study. The clinical characteristics of the study participants are summarized in **Table 1**. The study was approved by the local ethics committee and informed consent was attained from all subjects.

All participants were scanned at the University Medical Center Hamburg-Eppendorf, Germany, using a 3T Siemens Skyra MR scanner (**Figure 1**). Among others, T1-weighted MPRAGE, DTI, and triple-echo T2- and T2*-weighted MRI datasets were acquired for each patient. The high-resolution T1-weighted MPRAGE dataset was acquired using TR = 1,900 ms, TE = 2.46 ms, flip angle = 90°, TI = 900 ms, image in-plane resolution of 0.94 × 0.94 mm², and 0.94 mm slice thickness.

T2-weighted and T2*-weighted image sequences were acquired for this study for R2, R2*, and R2′ mapping. In detail, for R2 mapping, a spin-echo sequence with 15 echoes per shot was employed to record images using echo times of 12, 85, and 158 ms. A total of 24 slices with a thickness of 5 mm with a field-of-view of 240 mm were acquired using a repetition time of 4,590 ms and a flip angle of 150°. The T2*-weighted images were acquired with the same settings except for using a single shot echo-planar sequence with TEs of 21, 52, and 88 ms.

TABLE 1 | Demographic and clinical characteristics of study participants.

	Parkinson's disease	Progressive supranuclear palsy	Healthy controls
Number of patients	45	20	38
Sex, M/F	33/12	9/11	24/14
Age at examination, y, mean ± SD (range)	66.1 ± 7.2 (45–77)	71.2 ± 5.7 (59–79)	61.9 ± 11.3 (41–80)
Disease duration, y, mean ± SD (range)	13.7 ± 6.6 (2–30)	6.1 ± 3.4 (1–12)	-
Hoehn&Yahr, mean ± SD (range)	2.6 ± 0.8 (1–4)	2.6 ± 0.8 (1–4)	-
UPDRS motor score (OFF condition), mean ± SD (range)	37.4 ± 13.1 (14–63)	32.8 ± 12.0 (9–52)	-
UPDRS motor score (ON condition), mean ± SD (range)	20.0 ± 10.7 (5–52)	28.9 ± 10.8 (6–48)	-
MMSE, mean ± SD (range)	28.1 ± 1.4 (23–30)	25.1 ± 2.8 (19–29)	-

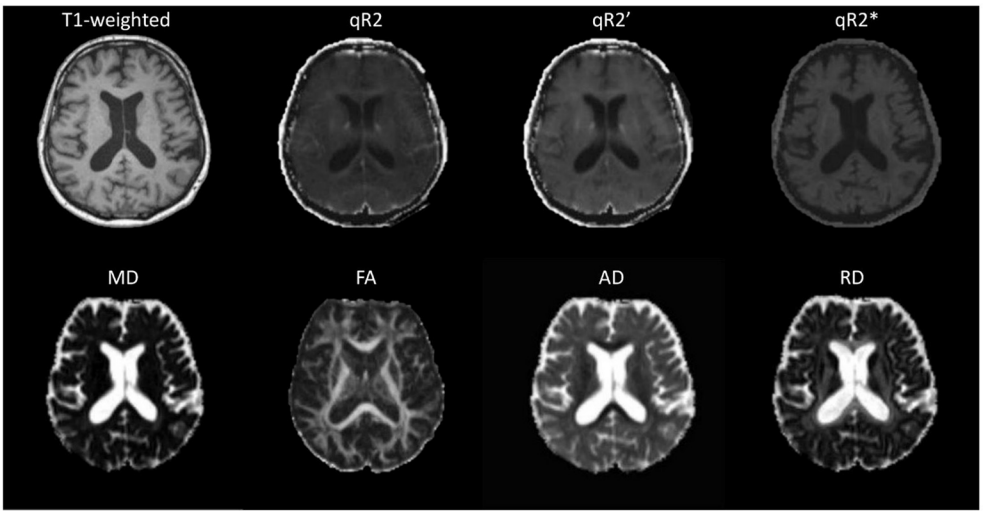


FIGURE 1 | Selected slice from a multi-modal MRI dataset of a patient with Parkinson's disease.

The R2 map was calculated by fitting the exponential function $SI(t) = SI_0 \exp(-t/\mathrm{T2})$ to the signal intensity decay curve $SI(t)$ given by the three TE images for each voxel of the T2-weighted sequence, whereas R2 is defined by R2 = 1/T2. The R2* map was calculated in the same fashion using the three TE images of the T2*-weighted sequence. Finally, the R2′ map was calculated using the formula: $1/\mathrm{T2}' = 1/\mathrm{qT2}^* - 1/\mathrm{qT2}$, whereas R2′ is defined by $\mathrm{R2}' = 1/\mathrm{T2}'$. All computations required for R2/T2 mapping were performed using the in-house developed software tool Antonia (21).

The DTI sequence was acquired using a single-shot balanced echo-planar imaging sequence with TR = 4,500 ms, TE = 83 ms, and flip angle = 90°. A total of 27 slices with a thickness of 5 mm with an image in-plane resolution of 1.875 × 1.875 mm^2 were acquired without diffusion gradients (b = 0 s/mm^2) and with diffusion gradients (b = 1,000 s/mm^2) applied along 20 non-collinear directions, averaged over two acquisitions. The DTI preprocess tool (22) was used for DTI processing to generate the diffusion parameter maps (mean diffusivity [MD], fractional anisotropy [FA], radial diffusivity [RD], and axial diffusivity [AD]).

Image Registration

The automatic segmentation of anatomical brain regions was performed by registration of the Montreal Neurological Institute (MNI 152) brain atlas to each T1-weighted MPRAGE image using NiftyReg (23), which allows transforming atlas brain regions defined in the MNI space to each individual dataset for volumetric analysis. More precisely, the MNI brain atlas was registered to each T1-weighted MRI dataset using a rigid transformation followed by an affine transformation. The resulting affine transformation was then used for initialization of a non-linear registration using a cubic B-Spline parametrisation (free-form deformation). After this, the Harvard-Oxford cortical, Harvard-Oxford subcortical, MNI, and the Johns Hopkins University (JHU) white matter tractography atlas brain regions were transformed to each T1-weighted MRI dataset using the corresponding non-linear transformation and a nearest-neighbor interpolation. In addition to the parcellated atlas brain regions, the non-linear deformation field was also used for transforming a binary segmentation of the total intracranial volume to the T1-weighted dataset of each patient.

After this, the T2-weighted and diffusion-weighted datasets were non-linearly registered to the corresponding T1-weighted MRI dataset from the same patients using ANTs (24) to enable a combined analysis. More precisely, the average (b = 1,000 s/mm^2) DTI image was used as the reference for this due to improved anatomical details and higher similarity to the T1-weighted dataset. This registration also consisted of a rigid followed by an affine transformation used for initialization of the non-linear registration, which was performed using a symmetric diffeomorphic image registration method, to allow correcting for distortion artifacts. The resulting transformation was then used to transform the DTI-derived parameter maps (MD, FA, RD, AD) to the corresponding T1-weighted MRI dataset from the same patient. The same approach was used for registration of the T2-weighted datasets to the T1-weighted MRI dataset whereas the dataset from the triple-echo T2-weighted sequence acquired with the longest echo time was used as the reference in this case. The resulting transformation was then used to transform the T2 parameter maps (R2, R2*, R2′) to the corresponding T1-weighted MRI dataset. All registration results were visually checked to ensure optimal registration quality, so that no missing values or significant outliers were present in the extracted features.

Feature Extraction

An overview of the extracted features using the different brain atlas regions is presented in **Table 2**. In detail, the Harvard-Oxford subcortical atlas defined in the MNI reference space

TABLE 2 | Overview of atlases and number of features extracted for regional analysis of morphology, brain iron accumulation/deposition, and microstructural integrity.

Modality	Type of feature	Atlases used	Total number of extracted features
T1-weighted MRI	**Morphology:** Regional Volume (V) Regional Brain Surface (SA) Regional Surface area to Volume Ratio (SA:V)	Harvard-Oxford Cortical Harvard-Oxford Sub Cortical MNI brain regions	234
T2-weighted MRI	**Brain iron content:** R2, R2*, R2′	Harvard-Oxford Cortical Harvard-Oxford Sub Cortical Johns Hopkins University White Matter Tractography	396
Diffusion-tensor MRI	**Microstructural integrity:** Mean diffusivity (MD) Fractional anisotropy (FA) Radial diffusivity (RD) Axial diffusivity (AD)	Harvard-Oxford Cortical Harvard-Oxford Sub Cortical Johns Hopkins University White Matter Tractography	520

consists of 21 brain regions such as the thalamus, caudate, hippocampus, and brainstem. The Harvard-Oxford cortical atlas consists of 48 brain regions such as the insular cortex, precentral gyrus, and temporal pole. The MNI brain regions (not to be confused with the MNI 152 atlas used for registration) include nine well-known large structures such as the cerebellum, frontal lobe, temporal lobe, and others. Finally, the JHU atlas includes 20 structural white matter tracts such as anterior thalamic radiation, forceps major/minor, superior longitudinal fasciculus and others, which have been widely used in DTI-based studies.

In a first step, the registered Harvard-Oxford cortical, Harvard-Oxford sub-cortical, and MNI brain regions were used to quantify the volumes of the corresponding brain regions. To account for different global head sizes, the extracted volumes were normalized using the full intracranial volumes as described previously (25). Apart from the volume, the surface area as well as the surface-area-to-volume ratio (SA:V) was also determined for each brain region in the Harvard-Oxford cortical, Harvard-Oxford sub-cortical, and MNI brain atlas. For calculation of the SA:V, the raw regional volumes instead of the volumes corrected for the full intracranial volume were used since the SA:V metric is intrinsically normalized by dividing the surface area by the corresponding volume and would be skewed otherwise. Since the morphological parameters are of reduced interest for white matter tract analysis, the JHU atlas regions were not considered for morphological analysis. It should be noted that the regions used from the MNI brain atlas for the morphological analysis include the large lobes and cerebellum, which are composed of many of the smaller structures defined in the other atlases. These larger structures were included for the morphological analysis to quantify more global atrophy effects that might be missed when analyzing the small structures only. As each lobe contains a large number of the smaller structures defined in the other atlases, the measured morphological parameters for the large lobes are not likely to show high redundancy despite the overlap.

After this, the registered Harvard-Oxford cortical, Harvard-Oxford sub-cortical, and JHU atlas brain regions were used to quantify the corresponding median DTI parameters (MD, FA, RD, AD) and T2 parameters (R2, R2*, R2′) in the corresponding atlas brain regions. Median instead of average values were used to account for potential non-normal value distribution and partial volume effects at the border of brain structures. The MNI brain regions were not used for analysis of the DTI and T2-weighted datasets because the corresponding brain regions are rather large, so that localized microstructural and iron deposition differences would not be captured. Using this approach, a total of 1,150 features describing the regional morphology, iron accumulation/deposition, and microstructural integrity were extracted and used for training and testing of machine learning models described below.

Machine Learning Pipeline

The machine learning framework implemented for this study consists of a feature ranking/selection and classification stage. In detail, features are initially ranked based on their relevance for the classification task using each of the following feature selection algorithms: correlation attribute evaluator, gain ratio/information gain evaluator, principle component analysis, RELIEFF, and support vector machine attribute evaluator. After this, the 100 highest ranked features for each ranking method were selected for initial inclusion for classification. This number was selected to decrease computational processing times associated with higher number of features but also to ensure that more observations than features are available to solve the classification problems. Each set of ranked features was then used to train each of the following classification models: simple decision tree, random forest, logistic model tree, k-nearest neighbors, naive Bayes, support vector machine (SVM), and multi-layer perceptron. All models were trained using the models implemented in Weka (26) with standard hyper-parameter values to reduce the risk of overfitting.

A leave-one-out cross validation routine was employed for classifier performance evaluation. To prevent double dipping, the leave-one-out cross validation also included the feature ranking. The optimal number of highest ranked features used for training

TABLE 3 | Confusion matrix following a gain ratio + SVM classification combination using morphological features only.

Morphology Features (Surface area, Volume, and Surface-Area-to-Volume Ratio Features)											
Class	**TP Rate**	**FP Rate**	**Precision**	**Recall**	**F-Measure**	**MCC**	**ROC Area**	**Confusion Matrix**			**Accuracy**
								HC	**PD**	**PSP-RS**	
HC	0.605	0.185	0.657	0.605	0.630	0.429	0.710	23	12	3	65.0%
PD	0.622	0.241	0.667	0.622	0.644	0.384	0.690	10	28	7	
PSP-RS	0.800	0.120	0.615	0.800	0.696	0.619	0.840	2	2	16	

TP, True Positive; FP, False Positive; MCC, Matthews Correlation Coefficient; ROC AUC, Area under the receiver operating characteristic curve; HC, Healthy Controls; PD, Parkinson's disease; PSP-RS, Progressive supranuclear palsy Richardson's syndrome.

TABLE 4 | Confusion matrix following a PCA + LMT classification combination using brain iron content measures only.

T2-weighted Image Features (based on quantitative R2, R2′, and R2* Features)											
Class	**TP Rate**	**FP Rate**	**Precision**	**Recall**	**F-Measure**	**MCC**	**ROC Area**	**Confusion Matrix**			**Accuracy**
								HC	**PD**	**PSP-RS**	
HC	0.763	0.108	0.806	0.763	0.784	0.663	0.875	29	7	2	75.7%
PD	0.756	0.207	0.739	0.756	0.747	0.547	0.845	7	34	4	
PSP-RS	0.750	0.072	0.714	0.750	0.732	0.665	0.948	0	5	15	

TP, True Positive; FP, False Positive; MCC, Matthews Correlation Coefficient; ROC AUC, Area under the receiver operating characteristic curve; HC, Healthy Controls; PD, Parkinson's disease; PSP-RS, Progressive supranuclear palsy Richardson's syndrome.

and testing of the classifier was systematically optimized by iteratively removing the lowest ranked feature from the training and testing sets. This recursive feature elimination approach was performed by continuously removing the features from the initial 100 highest ranked features until only a single feature was left in the training and testing sets.

In order to identify the optimal combination of feature selection and classification method, the overall 3-level classification accuracy was used as the main evaluation metric. In case of equal classification performance, the feature selection and classification method combination requiring the lowest number of features is reported following the Occam's razor principle (27).

The pipeline described above was applied four times: (1) using the morphological features only, (2) using the R2 features only, (3) using the diffusion features only, and (4) using all features together.

RESULTS

In the following, the results of the best performing feature selection and classification combination using the single modality features and the combined multi-modal features, as well as the corresponding selected features are described.

T1-Weighted MRI

Regional brain volume, surface area, and surface area to volume ratio features derived from structural T1-weighted MRI datasets resulted in a top overall accuracy of 65% differentiating PD, PSP-RS, and HC subjects, respectively. The confusion matrix and additional evaluation metrics for the optimal machine learning model are presented in **Table 3**. This accuracy was achieved when the top 40 features were selected using a combination of the gain ratio feature ranking and linear kernel SVM classification approach. In detail, the differentiation of HC subjects and patients with PD or PSP-RS was rather poor, with a total of 15 out of 38 misclassified HC subjects. Furthermore, classification of PD was also sub-optimal, resulting in 10 and seven PD patients wrongly classified as HC and PSP-RS, respectively. The top ranked features consisted mainly of sub-cortical structures such as brainstem, pallidum, putamen, thalamus, and cortical structures, including the occipital pole, frontal and temporal gyrus, and opercular gyrus. In addition, volume, surface area, and SA:V features were equally present in the ranking, indicating the importance of including various multi-aspect (not multi-modal) T1-weighted features and not only the simple volumes.

T2-Weighted MRI

The classification results using the regional R2, R2*, and R2′ features are described in **Table 4**. In this case, the highest classification accuracy of 75.7% was obtained using the top 30 features selected by the principle component feature selection method in combination with a logistic model tree (LMT) classification model. In detail, nine HC subjects were misclassified as patients (7 PD and 2 PSP-RS), seven PD patients were wrongly classified as HC, and two PD patients wrongly classified as PSP-RS. In addition, five patients with PSP-RS were wrongly classified as PD. Overall, weighted combinations of brain iron metabolism measures in the cerebral cortex, left accumbens, left amygdala, and left hippocampus were present in the highest ranked principle component features.

TABLE 5 | Confusion matrix following an information gain + LMT classification combination using DTI maps only.

Diffusion Tensor Imaging Features (MD, FA, RD, AD Features)											
Class	**TP Rate**	**FP Rate**	**Precision**	**Recall**	**F-Measure**	**MCC**	**ROC Area**	**Confusion Matrix**			**Accuracy**
								HC	**PD**	**PSP-RS**	
HC	1.000	0.000	1.000	1.000	1.000	1.000	1.000	38	0	0	95.1%
PD	0.933	0.034	0.955	0.933	0.944	0.901	0.975	0	42	3	
PSP-RS	0.900	0.036	0.857	0.900	0.878	0.848	0.968	0	2	18	

TP, True Positive; FP, False Positive; MCC, Matthews Correlation Coefficient; ROC AUC, Area under the receiver operating characteristic curve; HC, Healthy Controls; PD, Parkinson's disease; PSP-RS, Progressive supranuclear palsy Richardson's syndrome; MD, Mean diffusivity; FA, Fractional anisotropy; RD, Radial diffusivity; AD, Axial diffusivity.

Diffusion-Tensor Imaging (DTI)

The classification results based on the DTI measurements alone (MD, FA, RD, AD maps) are shown in **Table 5**. The highest classification accuracy was obtained when the top 69 features were used. In detail, the information gain-based feature ranking method in combination with a logistic model tree (LMT) classification resulted in a classification accuracy of 95.1%. Overall, a total of five subjects were misclassified (three PD and two PSP-RS patients), whereas no HC subjects were misclassified. The highest-ranking diffusion features included mostly cortical regions such as the parahipocampal gyrus, cingulum, cingulate gyrus, opercular cortex as well as sub-cortical structures such as the thalamus, brainstem, and pallidum.

Combining Multiple Modalities

The classification results based on the complete multi-modal feature set utilizing features from T1-weighted MRI (brain surface area, brain volume, SA:V), T2-weighted MRI (R2, R2*, and R2′), as well as DTI (MD, FA, RD, AD maps) are shown in **Table 6**. The highest classification accuracy in this multi-modal model was obtained when the top 79 features were used. In detail, the support vector machine feature ranking method in combination with a multi layer perceptron (MLP) classification resulted in the highest performance of 95%. Overall, a total of five subjects were misclassified including one PD and four PSP-RS patients, whereas none of the HC subjects were misclassified.

The selected features included features from all three MRI sequences (see **Table 7**). In detail, eleven features from the total set of 79 were morphological features, including deep gray matter regions such as the left pallidum, left and right thalamus, left caudate, and brainstem. Several cortical structures such as precentral and supramarginal gyrus, angular gyrus, temporal fusiform cortex, and planum polare were also among the top ranked features. Moreover, most of the morphological features selected for this classification problem included volume values rather than brain surface area or the SA:V. In terms of brain iron metabolism markers, a total of 12 features were present in the optimal feature set. Brain iron metabolism markers in areas such as the temporal fusiform, parahippocampal gyrus, frontal gyrus, and others were ranked highly according to the SVM-based feature selector with R2′ features being selected more than twice as often as R2 and R2* features. All remaining top ranked features ($n = 56$) were diffusion features. Diffusion attributes in regions such as parahippocampal gyrus, insular cortex, pallidum, thalamus, brainstem, putamen, and others were ranked as the most discriminative features. Similar numbers of all diffusion parameters were selected.

DISCUSSION

Low accuracies of differential diagnosis between classical PD and PSP-RS based on established criteria, even when combined with standard anatomical MRI, have promoted the development of sophisticated machine learning frameworks for assisting with clinical diagnosis. Neuro-imaging data obtained from various MRI modalities have been widely employed for this purpose, whereas T1-, T2-, and diffusion-tensor MRI have been used most frequently. The main contribution of this work is that, for the first time, the benefit of a multi-parametric machine learning approach compared to uni-modal machine learning models was systematically investigated, whereas the results indicate that brain morphology and brain iron metabolism markers do not lead to quantitative benefits compared to using DTI features alone for an automatic classification of PD patients, PSP-RS patients, and HC subjects.

Overall, the results of this study are generally well in line with previous research as discussed in the following. However, it should be noted that it is not possible to directly compare the individual classification results of this study with others due to different patient samples, different evaluation schemes, and specific aims.

T1-Weighted MRI

Most previously described classification models are based on morphological parameters determined using T1-weighted MRI datasets. While several other individual level classification studies using volumetric features have reported accuracies differentiating Parkinsonian syndromes ranging from <50% up to 86% [e.g., (14, 28)], previously described volumetric-based studies mostly report low accuracies differentiating patients with PD from HC subjects using volume-based features. The optimal morphology-based classifier in this study performed poorly classifying PD patients and HC subjects resulting in a ∼26% error rate. Thus, the results obtained in this study for classifying PD patients and HC subjects using morphology features are consistent with previous studies. One potential reason for the poor ability of morphology

TABLE 6 | Confusion matrix following an SVM based feature selection + MLP classification combination using features from multiple MRI modalities.

Combination of All Imaging Features (Morphology, Brain Iron Content Marker, Diffusion)											
Class	**TP Rate**	**FP Rate**	**Precision**	**Recall**	**F-Measure**	**MCC**	**ROC AUC**	**Confusion Matrix**			**Accuracy**
								HC	**PD**	**PSP-RS**	
HC	1.000	0.000	1.000	1.000	1.000	1.000	1.000	38	0	0	95.1%
PD	0.978	0.069	0.917	0.978	0.946	0.904	0.986	0	44	1	
PSP-RS	0.800	0.012	0.941	0.800	0.865	0.840	0.983	0	4	16	

TP, True Positive; FP, False Positive; MCC, Matthews Correlation Coefficient; ROC AUC, Area under the receiver operating characteristic curve; HC Healthy Controls; PD, Parkinson's disease; PSP-RS, Progressive supranuclear palsy Richardson's syndrome.

TABLE 7 | Feature composition of the SVM based feature selection + MLP classification combination using features from multiple MRI modalities.

Modality	**V**	**SA**	**SA:V**	**R2**	**R2***	**R2′**	**FA**	**MD**	**AD**	**RD**	**Total**
T1-weighted	6	2	3	–	–	–	–	–	–	–	11
T2-weighted	–	–	–	2	3	7	–	–	–	–	12
DTI	–	–	–	–	–	–	15	12	13	16	56

V, Volume; SA, Surface Area; SA:V, Surface-Area-to-Volume ratio; FA, Fractional Anisotropy; MD, Mean Diffusivity; AD, Axial Diffusivity; RD, Radial Diffusivity.

metrics to differentiate PD patients and HC subjects could be related to less pronounced structural differences in these groups (29). Consequently, macro-structural features (i.e., morphology) do not seem sensitive enough to differentiate PD patients from HC subjects. In terms of PD vs. PSP classification, individual level classification methods using morphology features as, for example, previously described by Scherfler et al. (30), Sarica et al. (31), and Focke et al. (32) all reported comparably high classification accuracies. Unlike the PD vs. HC classification, it appears that features derived from high-resolution T1-weighted images are indeed valuable for differentiation of these two entities. Similarly, the optimal machine learning model in this work performed relatively well, only misclassifying 13% of the patients. Finally, studies focusing on PSP vs. HC classification have resulted in even higher accuracies of up to 94%. In detail, the highest accuracy for classification of PSP vs. HC with 93.98% was previously reported by Sarica et al. (31) by using volumetric features in a naive Bayes classifier validated by a 10-fold cross validation in a relatively large cohort of 46 HC, 65 PD, and 32 PSP. These results are to be expected considering the significant structural and functional differences in PSP patients compared to HC subjects. In the present study, a classification accuracy of 89% was achieved for the PSP-RS vs. HC classification in a three-level classification routine, also including HC subjects. Due to the clear potential for differentiating PSP-RS patients from PD patients and HC subjects, incorporation of morphological features within a computer-aided diagnosis framework appears still valuable and can add predictive value to such tools.

The main findings of this research project with implications to future developments of classification methods for PD vs. PSP-RS vs. HC differentiation using morphology features are 2-fold. First, the inclusion of the surface area and SA:V values provide complimentary information compared to using volumetric features only as the top features for this classification task consist (almost evenly) of a wide variety of all three morphological metrics, which is in line with findings from another recent study (25). Second, adding the morphological profiles of cortical structures for classification does not seem to improve the classification accuracy as most selected features belong to sub-cortical rather than cortical regions, which is in line with previous findings (25).

T2-Weighted MRI

In a similar study, Boelmans et al. utilized brain iron metabolism markers in a logistic discriminant analysis approach to classify 24 HC, 30 PD, and 12 PSP subjects (16). Subsequently, the classification resulted in an overall accuracy of 74.2%. Using a similar classification pipeline, Eckert et al. achieved a total accuracy of 75.4% based on a sample of 20 HC, 15 PD, 10 PSP, and 12 multiple system atrophy (MSA) subjects (33). However, the two studies mentioned did not utilize a feature section method but employed a manual selection of a few brain regions. In this study, a similar accuracy of 75.7% was obtained using a sample size of 45 PD, 20 PSP-RS, and 38 HC subjects following an automatic PCA feature selection and LMT classification method. While the accuracies obtained are similar, there are three significant differences between the other two studies and ours. First, the patient sample used in this study is considerably larger. Second, the previous studies did not perform cross validation, whereas leave-one-out-cross-validation was used in this study. Third, the features used for classification in the two previous studies were handpicked and not automatically identified as done in this work, which could introduce a selection bias.

In terms of PD vs. HC classification, the optimal machine learning model identified in this study performs rather poorly with seven PD wrongly classified as HC subjects and vice versa. The misclassification in this category was also the main contributor for downgrading the overall classification performance. A potential explanation for this result could

be that iron metabolism markers do not differ considerably between HC subjects and PD patients, therefore resulting in sub-optimal classification performance. Similar to morphological information, brain iron metabolism markers, seem to be inadequate features to differentiate between PD patients and HC subjects. Likewise, the differentiation of PSP-RS vs. PD patients was rather modest with four PD and five PSP-RS patients wrongly classified as PSP-RS and PD, respectively. While the optimal classifier using morphological features also resulted in a total of nine misclassified instances differentiating PD vs. PSP-RS, the difference is that misclassified patients using brain iron metabolism features were rather balanced between the two diseases, whereas morphological features exhibited a weaker PSP-RS classification ability. In addition, the differentiation of HC subjects vs. PSP-RS patients was far better resulting in only two PSP-RS subjects misclassified as HC. Thus, regional iron metabolism markers seem to differ considerably between PSP-RS patients and HC subjects, which is consistent with current literature (34).

Overall, brain iron metabolism markers do not seem to be good predictors for the differentiation of HC subjects from PD patients and PSP-RS from PD patients. Finally, it should be mentioned that the optimal feature selection method used for this classification task (PCA: principle component analysis) composes new features from a linear combination of the original features, which makes it more complicated to investigate how individual features from the initial feature set contribute to the overall classification. Generally, more research needs to be focused on investigating the association of the regional brain atrophy (i.e., morphological cell loss) and tissue iron accumulation.

Diffusion-Tensor MRI

Various previous studies have shown that diffusion-based features can be used for a classification of PD patients and HC subjects. For example, Scherfler et al. (35), Salamanca et al. (36), and Banerjee et al. (37) used diffusion metrics such as MD (synonym: apparent diffusion coefficient [ADC]) and FA parameter maps for classification and obtained accuracies of up to 98%. This is generally in line with the findings of this work, with a top accuracy of 100% achieved for the classification of PD patients and HC subjects using an information gain feature ranking and LMT classification approach with a sample size of 45 PD patients and 38 HC subjects. Thus, it may be concluded that the differentiation potential of DTI measurements is much higher than the previously discussed regional brain morphological and iron metabolism features. One potential explanation for this finding is that micro-structural changes are assumed to occur earlier than macro-structural changes or measurable tissue iron accumulation (38).

With respect to differentiating PD and PSP-RS syndromes, two PSP-RS and three PD patients were wrongly classified as PD and PSP-RS, respectively. The obtained sub-syndrome classification accuracy is among the top results reported in literature thus far. However, it should be noted that this is not the first work to employ DTI measurements for classification of PD and PSP-RS subjects although previous research on this is rather scarce. For example, Haller et al. presented an approach to classify PD subjects ($n = 17$) and subjects with atypical forms ($n = 23$) of Parkinsonism using the RELIEFF feature selection method and a support vector machine classifier, and voxel-wise FA values as features (15). A correct classification between PD patients vs. patients with atypical forms was achieved in up to $97.5 \pm 7.5\%$. However, it should be noted that the group of 23 subjects with atypical forms of Parkinsonism included only one patient with PSP while the other subjects in this group were, for example, diagnosed with MSA, dementia with Lewy bodies, vascular Parkinsonism, and even traumatic brain injury. Thus, the results are not really comparable to those described in this work.

Several interesting conclusions can be made by investigating the results of the optimal classification model and selected features in more detail. First, it appears that diffusion changes are a global effect since cortical as well as sub-cortical structures brain regions can be found among the highest ranked features selected for the classification. The 69 selected features used for classification included brain regions that are well-known to be affected in by PD such as the brainstem, and deep gray matter structures including the thalamus, putamen, and pallidum. Additionally, brain regions that are part of the frontal cortex, namely the superior frontal gyrus and frontal medial cortex are among the selected regions, which are part of the prefrontal dopaminergic system. Additionally, it appears useful to investigate all four diffusion parameters as similar numbers of the four DTI features were selected for the optimal machine learning model. Within this context, it should be noted that most previous studies have only used FA and MD values for classification or group-wise studies. Similar to the different morphological features, the incorporation of multi-facet DTI features seems to have the potential to improve machine learning models by elucidating several aspects of PD syndromes.

Multi-Modal Features

Several studies have been performed in the past aiming to classify patients with PD and HC patients by combining multi-modal image features. For example, Long et al. utilized structural and functional MRI information to classify PD patients and HC subjects (17). The results reported show that the combination of features leads to an improved classification accuracy of 86.9%. In a study similar to this work, Peran et al. combined T1-weighted, T2-weighted, and diffusion-weighted MRI features and reported a PD vs. HC classification accuracy of 95% for the corresponding machine learning model (18). In line with these findings, the optimal PD vs. HC classification model developed in this work using the multi-modal MRI data achieved a slightly better accuracy of 100% for differentiating PD patients and HC subjects. However, unlike the aforementioned studies that performed binary classifications, the differentiation task in this study was inherently more complex as three classes (PD, PSP-RS, HC) were considered. While the differentiation of PD vs. HC using the full multi-modal feature set outperformed single modality machine learning models using morphological and iron content markers alone, it was not superior compared to the

machine learning model using only DTI features. In line with this finding, most of the features selected for the final model were DTI parameters.

Similarly, multiple studies have also attempted to develop and evaluate multi-modal machine learning models for classification of PD vs. PSP. For example, Morisi et al. combined volumetric, diffusion, and proton spectroscopy measures within a linear kernel SVM model and obtained an accuracy of 98% (39). Cherubini et al. used volumetric and diffusion features from a large sample of 57 PD and 21 PSP patients and achieved an accuracy of 100% using only white matter features (40). In the present study, a PSP vs. PD differentiation of 93% was achieved using multi-modal MRI features, which is in the range of the previously described results of binary classification problems. While the multi-modal machine learning model clearly outperforms the corresponding machine learning models using morphology or brain iron accumulation features alone, the accuracy is on par with the machine learning model using DTI parameters only. However, the multi-modal model was more precise correctly classifying PD patients, but less precise correctly classifying PSP patients compared to the machine learning model using DTI metrics only.

Classification Model

A large number of feature selection methods such as information gain, principal component analysis, linear-kernel SVM based feature selection, RELIEFF, Fisher vector algorithm, evolutionary based techniques, fuzzy based data transformation, graph theory methods, and others have been employed in previous studies. At the same time, many previous studies did not incorporate any feature selection algorithm and simply employed pre-selected sub-syndrome specific features from a limited number of regions-of-interest instead. Within this context, the use of feature selection methods allows identifying important regions in a data-driven way, while manually selecting brain regions for a machine learning model might miss important regions.

Similar to the feature selection methods, a wide range of classification techniques such as support vector machines, different types of decision trees, linear and logistic regression, multi-layer perceptron models, and others have been used in previous machine learning models.

The fact that different setups of feature selection methods and machine learning models were found to be optimal for the different classification tasks in this work shows that it is important to test and evaluate different setups to identify the optimal setup for a given classification task. Within this context, it is important to ensure that the developed models do not overfit the training data. For this reason, the machine learning models were trained and tested only using the standard hyper parameters in this work. Additionally, the results of all machine learning models were carefully checked and none of the models reported outperformed the next best machine learning model by far. Thus, further classification improvements might be possible by further fine-tuning of the hyper-parameters. Nevertheless, we are confident that the main findings of this research study will still hold true.

Limitations

This study has some limitations that should be discussed. First, the study cohort used in this work, while relatively large compared to similar studies, is still not large enough to fully expand on the generalizability of the proposed model. This limitation is further perpetuated by the lower incidences for PSP-RS compared to PD. Furthermore, an independent validation dataset, preferably acquired in different imaging centers, would be a more rigorous approach of model verification. However, this separate dataset was not available for this present study to further test the proposed model. We opted not to separate the current dataset into completely separate training and validation sub-groups as the training cohort would not have been sufficiently large enough to train a generalized classifier, potentially resulting in an over-fitted model. It is worth noting that studies employing separate validation datasets are rather scarce in this context, so that cross validation methods are used most frequently for classifier validation. Second, the ground truth classifications were determined by an expert clinician according to established consensus criteria without neuropathological proofs. Thus, there may be still a minor level of uncertainty left regarding the ground truth classification used for training and evaluation of the classifier. It should also be mentioned that due to the retrospective design of this study, the ground truth diagnoses were not based on the most recent guidelines for PD and PSP-RS diagnosis (41–43). However, all patients and participants included in this study were seen by two movement disorder specialists at least two times ensuring highly probable ground truth classifications. Third, the patient groups differed considerably regarding the age and sex distribution, which might bias the results obtained in this research project towards higher accuracies. Ideally, datasets from subjects with similar age and sex distributions should be used for training and testing to obtain more accurate and generalizable classification models. However, this is not an easy task as obtaining data with such strict specifications is time-consuming and expensive and is an undertaking that was not feasible for this research project due to the retrospective data analysis. Finally, it should be mentioned that only conventional machine learning techniques were used in this study instead of sophisticated deep learning models, which have recently shown good achievements for PD classification (44). However, the machine learning models used in this work require less data compared to novel deep learning models and, thus, allowed investigating different imaging setups in detail given the sample size available. We believe that the main findings of this study also hold true for novel deep learning methods with a deep learning model using DTI parameter maps performing on par or outperforming deep learning models based on T1-weighted datasets or T2-weighted datasets alone or a combination of all of these images. Nevertheless, this needs to be investigated in future studies with larger sample sizes as deep learning models are assumed to be more "data-hungry" compared to traditional machine learning techniques.

CONCLUSION

The results of this study suggest that machine learning models using regional brain microstructural integrity metrics computed from DTI datasets perform similar to multi-modal machine learning models incorporating additional imaging metrics such as brain morphology and iron metabolism to differentiate PD, PSP-RS, and HC subjects.

DATA AVAILABILITY STATEMENT

The data analyzed in this study is subject to the following licenses/restrictions: The datasets generated during and/or analyzed during the current study are not publicly available due to containing information that could compromise the privacy of research participants but are available upon reasonable request with approval of the local ethics board. Requests to access these datasets should be directed to nils.forkert@ucalgary.ca.

AUTHOR CONTRIBUTIONS

AT: study design, image processing, data analysis, and drafting the manuscript and revising it critically. JS: data acquisition and critical revision of the manuscript. KB: study design, data acquisition, and critical revision of the manuscript. NF: study design, image processing, data analysis, and drafting the manuscript and revising it critically. All authors contributed to the article and approved the submitted version.

FUNDING

This work was supported by Parkinson Alberta, the Canada Research Chairs program, and the River Fund at Calgary Foundation. These funding sources had no role in the design of this study and no role during its execution, analyses, interpretation of the data, or decision to submit results.

REFERENCES

1. Hughes AJ, Daniel SE, Kilford L, Lees AJ. Accuracy of clinical diagnosis of idiopathic Parkinson's disease: a clinico-pathological study of 100 cases. *J Neurol Neurosurg Psychiatry.* (1992) 55:181–4. doi: 10.1136/jnnp.55.3.181
2. Ramaker C, Marinus J, Stiggelbout AM, Van Hilten BJ. Systematic evaluation of rating scales for impairment and disability in Parkinson's disease. *Mov Disord.* (2002) 17:867–76. doi: 10.1002/mds.10248
3. Messina D, Cerasa A, Condino F, Arabia G, Novellino F, Nicoletti G, et al. Patterns of brain atrophy in Parkinson's disease, progressive supranuclear palsy and multiple system atrophy. *Parkinsonism Relat Disord.* (2011) 17:172–6. doi: 10.1016/j.parkreldis.2010.12.010
4. Duchesne S, Rolland Y, Vérin M. Automated computer differential classification in Parkinsonian Syndromes via pattern analysis on MRI. *Acad Radiol.* (2009) 16:61–70. doi: 10.1016/j.acra.2008.05.024
5. Lee JH, Han YH, Kang BM, Mun CW, Lee SJ, Baik SK. Quantitative assessment of subcortical atrophy and iron content in progressive supranuclear palsy and parkinsonian variant of multiple system atrophy. *J Neurol.* (2013) 260:2094–101. doi: 10.1007/s00415-013-6951-x
6. Forkert ND, Schmidt-Richberg A, Treszl A, Hilgetag C, Fiehler J, Münchau A, et al. Automated volumes-of-interest identification for classical and atypical Parkinsonian syndrome differentiation using T2′ MR imaging. *Methods Inf Med.* (2013) 52:128–36. doi: 10.3414/ME12-01-0044
7. Rizzo G, Martinelli P, Manners D, Scaglione C, Tonon C, Cortelli P, et al. Diffusion-weighted brain imaging study of patients with clinical diagnosis of corticobasal degeneration, progressive supranuclear palsy and Parkinson's disease. *Brain.* (2008) 131:2690–700. doi: 10.1093/brain/awn195
8. Seppi K, Schocke MF, Esterhammer R, Kremser C, Brenneis C, Mueller J, et al. Diffusion-weighted imaging discriminates progressive supranuclear palsy from PD, but not from the parkinson variant of multiple system atrophy. *Neurology.* (2003) 60:922–7. doi: 10.1212/01.WNL.0000049911.91657.9D
9. Lee JH, Lee MS. Brain iron accumulation in atypical Parkinsonian syndromes: *in vivo* MRI Evidences for distinctive patterns. *Front Neurol.* (2019) 10:74. doi: 10.3389/fneur.2019.00074
10. Maiti P, Manna J, Dunbar GL. Current understanding of the molecular mechanisms in Parkinson's disease: Targets for potential treatments. *Translational Neurodegeneration.* (2017) 6:28. doi: 10.1186/s40035-017-0099-z
11. Zhang Y, Burock MA. Diffusion tensor imaging in Parkinson's disease and Parkinsonian syndrome: a systematic review. *Fronti Neurol.* (2020) 11:531993. doi: 10.3389/fneur.2020.612069
12. Lo Vercio L, Amador K, Bannister JJ, Crites S, Gutierrez A, MacDonald ME, et al. Supervised machine learning tools: a tutorial for clinicians. *J Neural Eng.* (2020) 17:062001. doi: 10.1088/1741-2552/abbff2
13. MacEachern SJ, Forkert ND. Machine learning for precision medicine. *Genome*. (2020) doi: 10.1139/gen-2020-0131. [Epub ahead of print].
14. Salvatore C, Cerasa A, Castiglioni I, Gallivanone F, Augimeri A, Lopez M, et al. Machine learning on brain MRI data for differential diagnosis of Parkinson's disease and Progressive Supranuclear Palsy. *J Neurosci Methods.* (2014) 222:230–7. doi: 10.1016/j.jneumeth.2013.11.016
15. Haller S, Badoud S, Nguyen D, Garibotto V, Lovblad KO, Burkhard PR. Individual detection of patients with Parkinson disease using support vector machine analysis of diffusion tensor imaging data: initial results. *AJNR Am J Neuroradiol.* (2012) 33:2123–8. doi: 10.3174/ajnr.A3126
16. Boelmans K, Holst B, Hackius M, Finsterbusch J, Gerloff C, Fiehler J, et al. Brain iron deposition fingerprints in Parkinson's disease and progressive supranuclear palsy. *Mov Disord.* (2012) 27:421–7. doi: 10.1002/mds.24926
17. Long D, Wang J, Xuan M, Gu Q, Xu X, Kong D, et al. Automatic classification of early Parkinson's disease with multi-modal MR imaging. *PLoS ONE.* (2012) 7:e47714. doi: 10.1371/journal.pone.0047714
18. Péran P, Cherubini A, Assogna F, Piras F, Quattrocchi C, Peppe A, et al. Magnetic resonance imaging markers of Parkinson's disease nigrostriatal signature. *Brain.* (2010) 133:3423–33. doi: 10.1093/brain/awq212
19. Tolosa E, Wenning G, Poewe W. The diagnosis of Parkinson's disease. *Lancet Neurol.* (2006) 5:75–86. doi: 10.1016/S1474-4422(05)70285-4
20. Litvan I, Agid Y, Calne D, Campbell G, Dubois B, Duvoisin RC, et al. Clinical research criteria for the diagnosis of progressive supranuclear palsy (Steele-Richardson-Olszewski syndrome): report of the NINDS-SPSP international workshop. *Neurology.* (1996) 47:1–9. doi: 10.1212/WNL.47.1.1
21. Forkert ND, Cheng B, Kemmling A, Thomalla G, Fiehler J. ANTONIA perfusion and stroke. A software tool for the multi-purpose analysis of MR perfusion-weighted datasets and quantitative ischemic stroke assessment. *Methods Inf Med.* (2014) 53:469–81. doi: 10.3414/ME14-01-0007
22. Jenkinson M, Fast, automated, N-dimensional phase-unwrapping algorithm. *Magn Reson Med*. (2003) 49:193–7. doi: 10.1002/mrm.10354
23. Modat M, Cash DM, Daga P, Winston GP, Duncan JS, Ourselin S. Global image registration using a symmetric block-matching approach. *J Med Imaging (Bellingham).* (2014) 1:024003. doi: 10.1117/1.JMI.1.2.024003
24. Avants BB, Epstein CL, Grossman M, Gee JC. Symmetric diffeomorphic image registration with cross-correlation: evaluating automated labeling of elderly and neurodegenerative brain. *Med Image Anal.* (2008) 12:26–41. doi: 10.1016/j.media.2007.06.004
25. Talai AS, Ismail Z, Sedlacik J, Boelmans K, Forkert ND. Improved automatic morphology-based classification of Parkinson's disease and progressive supranuclear palsy. *Clin Neuroradiol.* (2019) 29:605–14. doi: 10.1007/s00062-018-0727-8

26. Hall M, Frank E, Holmes G, Pfahringer B, Reutemann P, Witten IH. The WEKA data mining software: an update. *SIGKDD Explor Newsl.* (2009) 11:10–8. doi: 10.1145/1656274.1656278
27. Wardrop D. Ockham's razor:sharpen or re-sheathe? *J R Soc Med.* (2008) 101:50–1. doi: 10.1258/jrsm.2007.070416
28. Lin WC, Chou KH, Lee PL, Tsai NW, Chen HL, Hsu AL, et al. Parkinson's disease: diagnostic utility of volumetric imaging. *Neuroradiology.* (2017) 59:367–77. doi: 10.1007/s00234-017-1808-0
29. Guevara C, Bulatova K, Barker GJ, Gonzalez G, Crossley N, Kempton MJ. Whole-brain atrophy rate in idiopathic Parkinson's disease, multiple system atrophy, and progressive supranuclear palsy. *Parkinson's Disease.* (2016) 2016:9631041. doi: 10.1155/2016/9631041
30. Scherfler C, Göbel G, Müller C, Nocker M, Wenning GK, Schocke M, et al. Diagnostic potential of automated subcortical volume segmentation in atypical parkinsonism. *Neurology.* (2016) 86:1242–9. doi: 10.1212/WNL.0000000000002518
31. Sarica A, Critelli C, Guzzi PH, Cerasa A, Quattrone A, Cannataro M. Application of different classification techniques on brain morphological data. *Proceedings of the 26th IEEE International Symposium on Computer-Based Medical Systems*. (2013). p. 425–8. doi: 10.1109/CBMS.2013.6627832
32. Focke NK, Helms G, Scheewe S, Pantel PM, Bachmann CG, Dechent P, et al. Individual voxel-based subtype prediction can differentiate progressive supranuclear palsy from idiopathic Parkinson syndrome and healthy controls. *Hum Brain Mapp.* (2011) 32:1905–15. doi: 10.1002/hbm.21161
33. Eckert T, Sailer M, Kaufmann J, Schrader C, Peschel T, Bodammer N, et al. Differentiation of idiopathic Parkinson's disease, multiple system atrophy, progressive supranuclear palsy, and healthy controls using magnetization transfer imaging. *Neuroimage.* (2004) 21:229–35. doi: 10.1016/j.neuroimage.2003.08.028
34. Schenck JF, Zimmerman EA. High-field magnetic resonance imaging of brain iron:birth of a biomarker? *NMR Biomed.* (2004) 17:433–45. doi: 10.1002/nbm.922
35. Scherfler C, Schocke MF, Seppi K, Esterhammer R, Brenneis C, Jaschke W, et al. Voxel-wise analysis of diffusion weighted imaging reveals disruption of the olfactory tract in Parkinson's disease. *Brain.* (2006) 129:538–42. doi: 10.1093/brain/awh674
36. Salamanca L, Vlassis N, Diederich N, Bernard F, Skupin A. *Improved Parkinson's Disease Classification From Diffusion MRI Data by Fisher Vector Descriptors*. Cham: Springer International Publishing (2015). p. 119–26. doi: 10.1007/978-3-319-24571-3_15
37. Banerjee M, Okun MS, Vaillancourt DE, Vemuri BC. A method for automated classification of Parkinson's disease diagnosis using an ensemble average propagator template brain map estimated from diffusion MRI. *PLoS ONE.* (2016) 11:e0155764. doi: 10.1371/journal.pone.0155764
38. Talai AS, Sedlacik J, Boelmans K, Forkert ND. Widespread diffusion changes differentiate Parkinson's disease and progressive supranuclear palsy. *Neuroimage Clin.* (2018) 20:1037–43. doi: 10.1016/j.nicl.2018.09.028
39. Morisi R, Gnecco G, Lanconelli N, Zanigni S, Manners DN, Testa C, et al. *Binary and multi-class Parkinsonian Disorders Classification Using Support Vector Machines*. Cham: Springer International Publishing (2015). p. 379–86. doi: 10.1007/978-3-319-19390-8_43
40. Cherubini A, Morelli M, Nisticó R, Salsone M, Arabia G, Vasta R, et al. Magnetic resonance support vector machine discriminates between Parkinson disease and progressive supranuclear palsy. *Mov Disord.* (2014) 29:266–9. doi: 10.1002/mds.25737
41. Höglinger GU, Respondek G, Stamelou M, Kurz C, Josephs KA, Lang AE, et al. Clinical diagnosis of progressive supranuclear palsy: the movement disorder society criteria. *Movement Disorders.* (2017) 32:853–64. doi: 10.1002/mds.26987
42. Boxer AL, Yu J-T, Golbe LI, Litvan I, Lang AE, Höglinger GU. Advances in progressive supranuclear palsy: new diagnostic criteria, biomarkers, therapeutic approaches. *Lancet Neurol.* (2017) 16:552–63. doi: 10.1016/S1474-4422(17)30157-6
43. Postuma RB, Berg D, Stern M, Poewe W, Olanow CW, Oertel W, et al. MDS clinical diagnostic criteria for Parkinson's disease. *Movement Disord.* (2015) 30:1591–601. doi: 10.1002/mds.26424
44. Sivaranjini S, Sujatha CM. Deep learning based diagnosis of Parkinson's disease using convolutional neural network. *Multimedia Tools Appl.* (2020) 79:15467–79. doi: 10.1007/s11042-019-7469-8

Conflict of Interest: NF owns equity in Eppdata GmbH.

The remaining authors declare that the research was conducted in the absence of any commercial or financial relationships that could be construed as a potential conflict of interest.

Copyright © 2021 Talai, Sedlacik, Boelmans and Forkert. This is an open-access article distributed under the terms of the Creative Commons Attribution License (CC BY). The use, distribution or reproduction in other forums is permitted, provided the original author(s) and the copyright owner(s) are credited and that the original publication in this journal is cited, in accordance with accepted academic practice. No use, distribution or reproduction is permitted which does not comply with these terms.

frontiers in Neurology

ORIGINAL RESEARCH
published: 15 April 2021
doi: 10.3389/fneur.2021.609866

Integrating Structural and Functional Interhemispheric Brain Connectivity of Gait Freezing in Parkinson's Disease

Chaoyang Jin[1], *Shouliang Qi*[1,2]*, *Yueyang Teng*[1], *Chen Li*[1], *Yudong Yao*[3], *Xiuhang Ruan*[4] *and Xinhua Wei*[4]*

[1] College of Medicine and Biological Information Engineering, Northeastern University, Shenyang, China, [2] Key Laboratory of Intelligent Computing in Medical Image, Ministry of Education, Northeastern University, Shenyang, China, [3] Department of Electrical and Computer Engineering, Stevens Institute of Technology, Hoboken, NJ, United States, [4] Department of Radiology, Guangzhou First People's Hospital, School of Medicine, South China University of Technology, Guangzhou, China

Freezing of gait (FOG) has devastating consequences for patients with Parkinson's disease (PD), but the underlying pathophysiological mechanism is unclear. This was investigated in the present study by integrated structural and functional connectivity analyses of PD patients with or without FOG (PD FOG+ and PD FOG–, respectively) and healthy control (HC) subjects. We performed resting-state functional magnetic resonance imaging (fMRI) and diffusion tensor imaging of 24 PD FOG+ patients, 37 PD FOG– patients, and 24 HCs. Tract-based spatial statistics was applied to identify white matter (WM) abnormalities across the whole brain. Fractional anisotropy (FA) and mean diffusivity (MD) of abnormal WM areas were compared among groups, and correlations between these parameters and clinical severity as determined by FOG Questionnaire (FOGQ) score were analyzed. Voxel-mirrored homotopic connectivity (VMHC) was calculated to identify brain regions with abnormal interhemispheric connectivity. Structural and functional measures were integrated by calculating correlations between VMHC and FOGQ score and between FA, MD, and VMHC. The results showed that PD FOG+ and PD FOG– patients had decreased FA in the corpus callosum (CC), cingulum (hippocampus), and superior longitudinal fasciculus and increased MD in the CC, internal capsule, corona radiata, superior longitudinal fasciculus, and thalamus. PD FOG+ patients had more WM abnormalities than PD FOG– patients. FA and MD differed significantly among the splenium, body, and genu of the CC in all three groups ($P < 0.05$). The decreased FA in the CC was positively correlated with FOGQ score. PD FOG+ patients showed decreased VMHC in the post-central gyrus (PCG), pre-central gyrus, and parietal inferior margin. In PD FOG+ patients, VMHC in the PCG was negatively correlated with FOGQ score but positively correlated with FA in CC. Thus, FOG is associated with impaired interhemispheric brain connectivity measured by FA, MD, and VMHC, which are related to clinical FOG severity. These results demonstrate that integrating structural and functional MRI data can provide new insight into the pathophysiological mechanism of FOG in PD.

Keywords: Parkinson's disease, freezing of gait, diffusion tensor imaging, resting state fMRI, voxel-mirrored homotopic connectivity

OPEN ACCESS

Edited by:
Wang Zhan,
University of Maryland, United States

Reviewed by:
Bruno J. Weder,
University of Bern, Switzerland
Amgad Droby,
Tel Aviv University, Israel

***Correspondence:**
Shouliang Qi
qisl@bmie.neu.edu.cn
Xinhua Wei
eyxinhuawei@scut.edu.cn

Specialty section:
This article was submitted to Applied Neuroimaging, a section of the journal Frontiers in Neurology

Received: *24 September 2020*
Accepted: *04 March 2021*
Published: *15 April 2021*

Citation:
Jin C, Qi S, Teng Y, Li C, Yao Y, Ruan X and Wei X (2021) Integrating Structural and Functional Interhemispheric Brain Connectivity of Gait Freezing in Parkinson's Disease. Front. Neurol. 12:609866. doi: 10.3389/fneur.2021.609866

INTRODUCTION

Freezing of gait (FOG), which is among the most serious symptoms of Parkinson's disease (PD) (1), is defined as the inability to achieve an effective gait when walking (2). PD with FOG (PD FOG+) is characterized by severe and sudden gait disorder, with patients describing a feeling that their feet are glued to the floor. The duration of FOG is usually a few seconds but occasionally lasts for dozens of seconds or more. Unlike other cardinal symptoms, FOG is difficult to manage with dopaminergic drugs or deep brain stimulation (3).

FOG is considered a mysterious clinical phenomenon, and the underlying pathophysiological mechanism is unclear (1, 2, 4). One explanation that has been proposed is that the difficulty of performing movements autonomously results in an increased reliance on attention to execute movements (5). It has also been suggested that executive dysfunction prevents PD patients from performing an action when it is required (6). Impaired control of rhythmicity, bilateral coordination, and gait asymmetry are also important aspects of freezing (7).

Brain white matter (WM) abnormalities in PD FOG+ rarely overlap. Altered WM connectivity has been observed in the bilateral pedunculopontine nucleus and superior premotor cortex and left supplementary motor area (8). One study found no difference in the tract projecting from the supplementary motor region to subcortical regions between PD FOG+ and PD without FOG (PD FOG–) (9). However, damage to multiple cortical areas involved in high-level gait control along with WM disruption in motor, cognitive, and limbic structures may constitute the anatomic correlates of FOG (10).

Voxel-mirrored homotopic connectivity (VMHC) analysis based on resting-state functional magnetic resonance imaging (fMRI) data has been proposed as a means of measuring the synchronization of spontaneous neural activity [functional connectivity (FC)] between interhemispheric regions (11). Specifically, Pearson's correlation coefficient between the time series of the low-frequency (0.01–0.08 Hz) blood oxygen level-dependent signal of each voxel and that of its spatially symmetric counterpart in the contralateral hemisphere is calculated, and the VMHC value is calculated by Fisher's Z transformation and weighting by voxel-wise gray matter probability. Further group-level analysis is performed to identify clusters or brain regions with significantly different VMHC (12, 13). A decreased VMHC has been reported in PD in brain regions related to information processing, sensory integration, and motor coordination (11) including the putamen and cortex (14). Moreover, PD FOG+ patients were shown to have lower VMHC in the inferior parietal lobe than PD FOG– patients (15).

Few studies have investigated the etiology of FOG in PD by integrating structural and functional brain connectivity data because of the difficulty of data acquisition. Tract-based spatial statistics (TBSS) and independent component analysis have been used to investigate abnormalities in structural connectivity and FC, respectively (16). However, no WM differences have been observed between PD FOG+ and PD FOG– patients (17). In another study, no structural abnormalities were found in PD FOG+ patients by TBSS and FC analysis (2).

In the present study, we used TBSS to examine structural defects in the brain of PD patients with or without FOG. Fractional anisotropy (FA) and mean diffusivity (MD) in the splenium, body, and genu of the corpus callosum (CC) were compared between PD FOG+ and PD FOG– patients and healthy control (HC) subjects, and the correlations between these parameters and clinical severity as reflected by FOG Questionnaire (FOGQ) score (18) were analyzed. We also used VMHC to identify regions with abnormal interhemispheric FC. After evaluating the correlation between VMHC and FOGQ score, correlations between VMHC, FA, and MD were determined to integrate structural and functional indices.

METHODS

Participants

A total of 61 right-handed PD patients were recruited for this study. All patients met the Parkinson's diagnostic criteria of the UK Brain Bank. The exclusion criteria were as follows: (1) previous history of cerebrovascular disease, brain injury, or other neurodegenerative disease; (2) PD co-occurring with diseases that seriously affect gait such as eye disease, osteoarthritis, and neuromuscular disease; (3) severe cognitive impairment or dementia [Mini-mental State Examination (MMSE) score <24]; and (4) major diseases or contraindications for MRI.

Patients who scored >1 point on the third item of the FOGQ or who were determined to have FOG by more than two experienced neurologists in a series of motion tests were considered as PD FOG+. Of the 61 PD patients, 24 were PD FOG+ and 37 were PD FOG–. Additionally, 24 right-handed HCs who were matched to the patients in terms of age, sex, and education level were recruited. The study was approved by the ethics committee of Guangzhou First People's Hospital and was carried out in accordance with the 1964 Helsinki Declaration and its later amendments or comparable ethical standards. All subjects were informed of and understood the study protocol and signed the informed consent form prior to participation in the study.

Clinical Assessment

All patients were assessed in terms of motor, visuospatial, cognitive, executive, and attention functions. The Unified Parkinson's Disease Rating Scale (UPDRS-III) (19) and Hoehn and Yahr (H&Y) scale were used to assess the severity of motor symptoms (20). The Timed Up and Go (TUG) test was

Abbreviations: CC, corpus callosum; CSF, cerebrospinal fluid; DTI, diffusion tensor imaging; EPI, echo planar imaging; FA, fractional anisotropy; FAB, Frontal Assessment Battery; FC, functional connectivity; FDR, false discovery rate; fMRI, functional magnetic resonance imaging; FOG, freezing of gait; FOGQ, freezing of gait questionnaire; FOV, field of view; HARS, Hamilton Anxiety Rating Scale; HC, healthy control; HDRS, Hamilton Depression Rating Scale; H&Y, Hoehn and Yahr; MD, mean diffusivity; MMSE, Mini-mental State Examination; MoCA, Montreal Cognitive Assessment; MRI, magnetic resonance imaging; PCG, post-central gyrus; PD, Parkinson's disease; PD FOG+, Parkinson's disease with freezing of gait; PD FOG–, Parkinson's disease without freezing of gait; PRG, pre-central gyrus; TBSS, tract-based spatial statistics; TE, echo time; TR, repetition time; TUG, timed up and go; UPDRS, Unified Parkinson's Disease Resting Scale; VMHC, voxel-mirrored homotopic connectivity; WM, white matter.

used to evaluate patients' mobility (21). The FOGQ was used to assess the severity of freezing. MMSE, Montreal Cognitive Assessment (MoCA), and Frontal Assessment Battery (FAB) (22) were used to evaluate cognitive function; and the mental state of the participants was assessed with the Hamilton Depression Rating Scale (HDRS) and Hamilton Anxiety Rating Scale (HARS).

Age and education level were compared among the three groups by one-way analysis of variance, and the chi-squared test was used to compare sex ratios. The two-sample *t*-test was used for comparisons of disease duration and scores for UPDRS-III, H&Y scale, FOGQ, MMSE, MOCA, FAB, TUG, HDRS, and HARS.

MRI Data Acquisition

MRI images of PD patients were collected in the "off" state (i.e., patients had stopped taking anti-Parkinson drugs for at least 12 h) to eliminate the effects of drugs on neural activity. MRI scans were performed with a 3.0-T MAGNETOM Verio whole-body MRI system (Siemens, Munich, Germany) equipped with eight-channel phase-array head coils. Tight foam padding was used to minimize head movement, and earplugs were used to reduce noise. Subjects were instructed to remain motionless, close their eyes and remain awake, and avoid thinking about anything.

Three-dimensional (3D) T1-weighted images were acquired with a 3D magnetization-prepared rapid gradient echo sequence [repetition time (TR) = 1,900 ms, echo time (TE) = 102 ms, flip angle = 9°, thickness = 1.0 mm, slices = 160, field of view (FOV) = 250 × 250 mm^2, matrix = 256 × 256, and voxel size = 1.0 × 1.0 × 1.0 mm^3]. Resting-state fMRI images are collected with an echo-planar imaging (EPI) sequence (TR = 2,000 ms, TE = 21 ms, flip angle = 78°, FOV = 256 × 256 mm^2, matrix = 64 × 64, slices = 220, thickness = 4.0 mm, and voxel size = 3.5 × 3.5 × 4.0 mm^3). Diffusion tensor imaging (DTI) was performed with a spin EPI sequence (TR = 8,700 ms, TE = 102 ms, FOV = 230 × 230 mm^2, voxel size = 2.5 × 2.5 × 2.5 mm^3, matrix = 92 × 92, thickness = 2.5 mm, and slice gap = 0 mm). Diffusion gradients were applied in 30 non-collinear directions with a b factor of 2,000 s/mm^2 after acquisition with b = 0 s/mm^2.

Overview of the Study Protocol

The study consisted of the following six steps (**Figure 1**): (1) Image processing was carried out for resting-state fMRI and DTI data; (2) TBSS were used to identify WM abnormalities throughout the whole brain; (3) the two-sample *t*-test was used to evaluate differences in FA and MD in the splenium, corpus, and genu of the CC across the three groups; (4) a correlation analysis was performed between FA, MD, and FOGQ scores in the CC; (5) a VMHC analysis was performed to explore homotopic connectivity; and (6) correlations between FA, MD, and VMHC were analyzed.

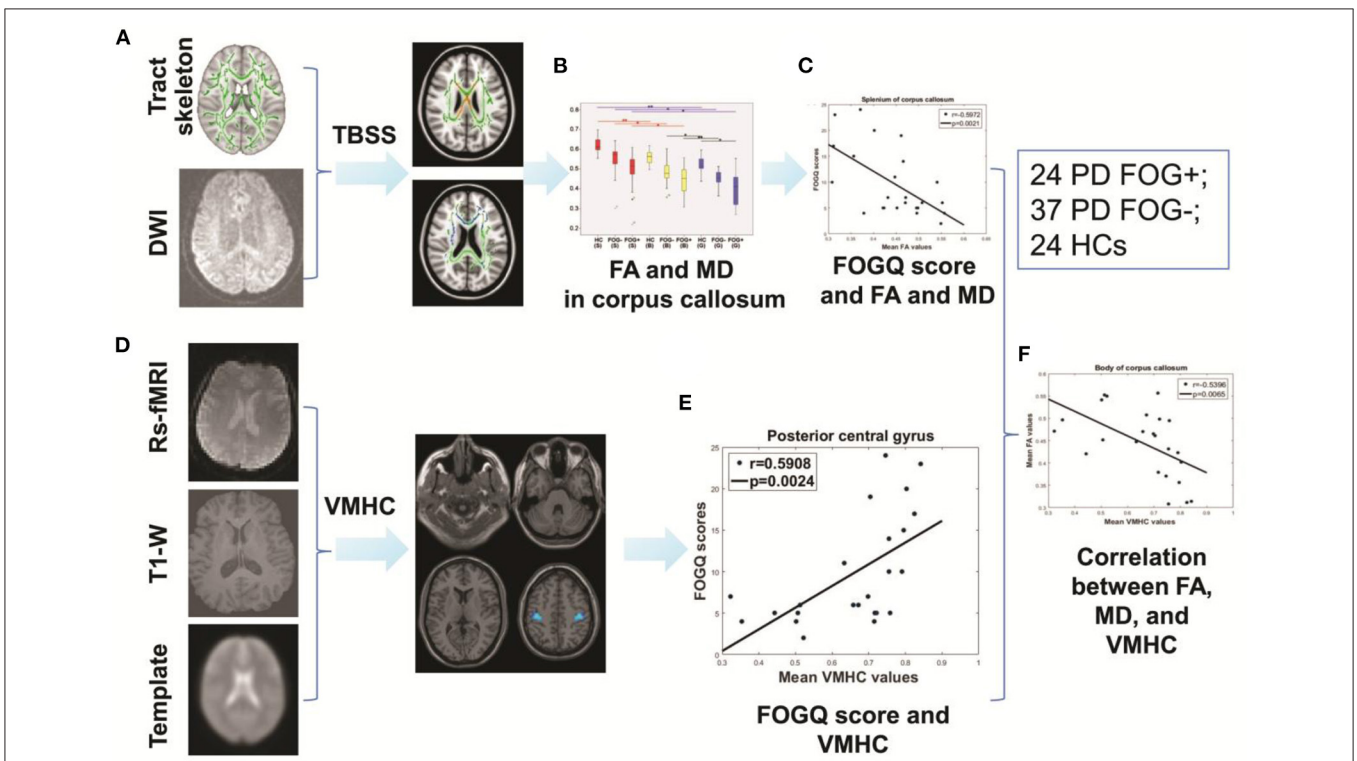


FIGURE 1 | Study protocol. **(A)** TBSS. **(B)** Intergroup comparisons of FA and MD in the CC. **(C)** Correlation between FA, MD, and FOGQ scores. **(D)** Analysis of VMHC. **(E)** Correlation between FOGQ scores and VMHC. **(F)** Correlation between FA, MD, and VMHC.

TBSS and Analysis of FA, MD, and FOGQ Score

DTI data were preprocessed and analyzed using the Pipeline for Analyzing Brain Diffusion Images toolkit (http://www.nitrc.org/projects/panda). FA and MD maps were obtained after standard preprocessing including eddy current correction and brain extraction (23).

The TBSS procedure consisted of four steps: (1) The nonlinear registration method was used to register each FA image to the target template; (2) all registered FA images were used to generate the average FA template, extract its skeleton, and remove smaller edge fiber bundles according to a threshold value of 0.2; (3) FA in each standard space was mapped to the FA skeleton map; and (4) the Tbss-no_FA tool was for TBSS analysis of MD images. Family-wise error correction was applied to the statistical results of TBSS. The threshold-free cluster enhancement correction method was used for the correction of multiple comparisons. The number of permutations was set to 5,000, and differences with $P < 0.05$ were considered statistically significant.

The Johns Hopkins University ICBM-DTI-81 WM atlas was used to identify areas of WM impairment. FA and MD in these areas were compared among groups with the two-sample *t*-test, and their correlations with FOGQ score were analyzed. False discovery rate (FDR) correction was applied to multiple comparisons of FA and MD.

Preprocessing of fMRI Data

Data processing assistant for resting-state fMRI was used to preprocess the fMRI data (24). The first 10 time points were removed. The head movement standard was set to 2 mm (translation) or 2° (rotation). The brain was segmented into gray matter, WM, and cerebrospinal fluid (CSF). After head movement correction, the images were standardized and resampled to $3 \times 3 \times 3$ mm^3. Linear regression was used to remove the influence of six head movement parameters and WM and CSF signals (25). A Gaussian kernel with 6-mm full width at half maximum was used for spatial smoothing. The data were detrended and filtered at low frequency (0.01–0.08 Hz).

VMHC and FOGQ Score and Integration of FA, MD, and VMHC

VMHC was calculated using Resting-State fMRI Data Analysis Toolkit plus software package [(26); http://www.restfmri.net]. After obtaining the time series of each voxel, homotopic FC was calculated as the Pearson correlation coefficient between each voxel and the contralateral mirror voxel. The coefficients were then converted into T values with Fisher's Z transformation for normalization; these values represented VMHC (27).

In the VMHC map, the mean value was standardized to reduce differences between subjects. Analysis of covariance was carried out to identify brain regions with significant differences among the three groups. Using the resultant regions as masks, the two-sample *t*-test and multiple comparison correction of the Gaussian random field (voxel $P < 0.001$, cluster $P < 0.05$) were performed to evaluate differences in VMHC between groups.

TABLE 1 | Demographic and clinical characteristics of participants.

Parameter	HC ($n = 24$)	PD FOG+ ($n = 24$)	PD FOG– ($n = 37$)	*P*-value
Age, years	62.5 ± 3.8	65.5 ± 6.1	64.1 ± 8.2	0.298[a]
Education, years	10.98 ± 2.34	9.35 ± 3.42	10.65 ± 4.25	0.36[a]
Sex, female/male	15/9	11/13	18/19	0.452[b]
Disease duration, years	NA	6.00 ± 5.25	3.01 ± 3.21	0.062[c]
UPDRS-III	NA	22.4 ± 6.72	21.34 ± 10.30	0.19[c]
H&Y scale	NA	2.49 ± 0.51	2.07 ± 0.49	0.16[c]
FOGQ	NA	9.25 ± 5.87	1.54 ± 1.67	<0.001[c*]
MMSE	NA	25.27 ± 4.01	25.71 ± 4.25	0.46[c]
MoCA	NA	21.08 ± 4.77	21.89 ± 5.66	0.353[c]
FAB	NA	13.8 ± 2.6	15.7 ± 1.5	<0.001[c*]
TUG	NA	12.5 ± 1.6	1.9 ± 0.7	<0.001[c*]
HDRS	NA	7.82 ± 6.35	9.67 ± 6.23	0.34[c]
HARS	NA	11.32 ± 6.74	10.56 ± 7.56	0.76[c]

Data are shown as mean ± standard deviation.

**P < 0.05.*

[a] One-way analysis of variance.

[b] Chi-squared test.

[c] Two-sample t-test.

FAB, Frontal Assessment Battery; FOGQ, Freezing of Gait Questionnaire; H&Y, Hoehn and Yahr; HARS, Hamilton Anxiety Rating Scale; HDRS, Hamilton Depression Rating Scale; HC, healthy control; MMSE, Mini-mental State Examination; MoCA, Montreal Cognitive Assessment; NA, not applicable; PD FOG+, Parkinson's disease with freezing of gait; PD FOG–, Parkinson's disease without freezing of gait; TUG, Timed Up and Go; UPDRS, Unified Parkinson's Disease Rating Scale.

To clarify the relationship between interhemispheric connectivity and FOG severity, the correlation between VMHC in regions with WM abnormalities and FOGQ score was analyzed. To explore the relationship between CC abnormalities and interhemispheric connectivity of the post-central gyrus (PCG), correlations between MD and FA of the CC and VMHC of the PCG were determined.

RESULTS

Demographic and Clinical Characteristics of the Study Population

Demographic and clinical characteristics of the participants are shown in **Table 1**. There were no significant differences between PD FOG+ and PD FOG– groups in terms of age ($P = 0.298$), education level ($P = 0.36$), sex ratio ($P = 0.452$), disease duration ($P = 0.062$), UPDRS-III score ($P = 0.19$), and H&Y scale score ($P = 0.16$). As expected, FOGQ, FAB, and TUG scores differed between PD FOG+ and PD FOG– patients ($P < 0.001$), but there were no differences in MMSE ($P = 0.46$), MoCA ($P = 0.353$), HDRS ($P = 0.34$), or HARS ($P = 0.76$) scores between the two groups.

WM Abnormalities Identified by TBSS

Compared to HCs, FA in the CC was reduced while MD was increased in the PD FOG+ group (**Figure 2A**). The same trends were observed in the PD FOG– group—i.e., FA was lower and

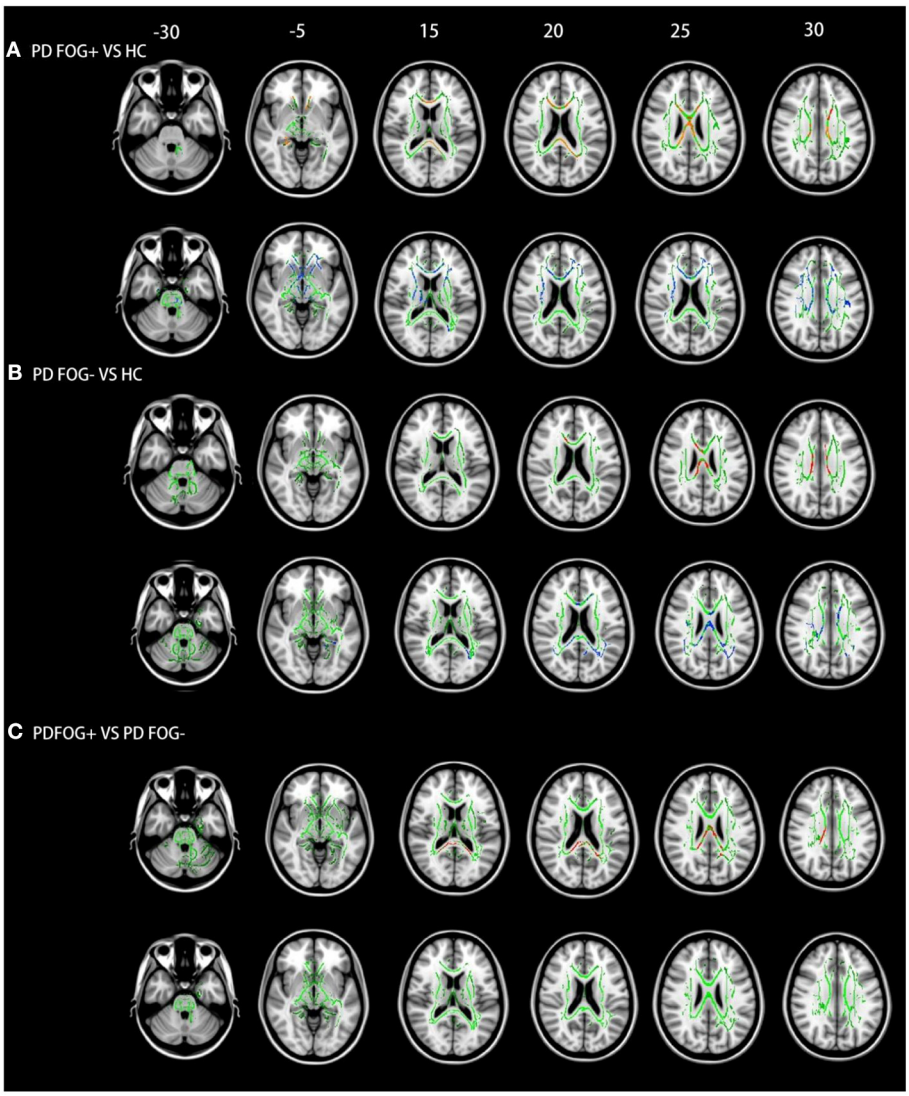


FIGURE 2 | TBSS results in the three groups. **(A)** PD FOG+ vs. HC. **(B)** PD FOG– vs. HC. **(C)** PD FOG+ vs. PD FOG–. Red and blue represent regions with reduced FA and increased MD, respectively. The WM skeleton is shown in green. Results are shown at $P < 0.05$ (family-wise error-corrected).

MD was higher in the CC and corona radiata compared to HCs (**Figure 2B**). PD FOG+ patients had more WM abnormalities than PD FOG– patients. Notably, FA in the CC was lower in PD FOG+ patients than in PD FOG– patients (**Figure 2C**), but there was no difference in MD between the two groups.

WM abnormalities were also observed in brain areas outside the CC in PD FOG+ patients: compared to HCs, FA was decreased in the cingulum (hippocampus) and superior longitudinal fasciculus, while MD was increased in the internal capsule, corona radiata, superior longitudinal fasciculus, and thalamus (**Figure 2A**). In PD FOG– patients, there were no decreases in FA in any WM areas outside the CC; however, increased MD was observed in the cingulum (hippocampus), superior longitudinal fasciculus, thalamus, and external capsule (**Figure 2B**). Widespread WM changes were observed in the PD FOG+ group compared to the PD FOG– group, including in FA in the cingulum (hippocampus) and superior longitudinal fasciculus and in MD in the internal capsule, corona radiata, superior longitudinal fasciculus, and thalamus (**Figure 2C**).

FA and MD in the Splenium, Body, and Genu of the CC

FA and MD differed significantly among the splenium, body, and genu of the CC in the three groups; the rank order of FA values was splenium > body > genu ($P < 0.05$, FDR corrected; **Figure 3**). PD FOG+ patients had the lowest FA in all three parts of the CC, while PD FOG– patients had lower FA values than HCs ($P < 0.05$, FDR corrected). The median FA values in the splenium were 0.612 for HCs, 0.574 for PD FOG– patients, and 0.515 for PD FOG+ patients; compared to

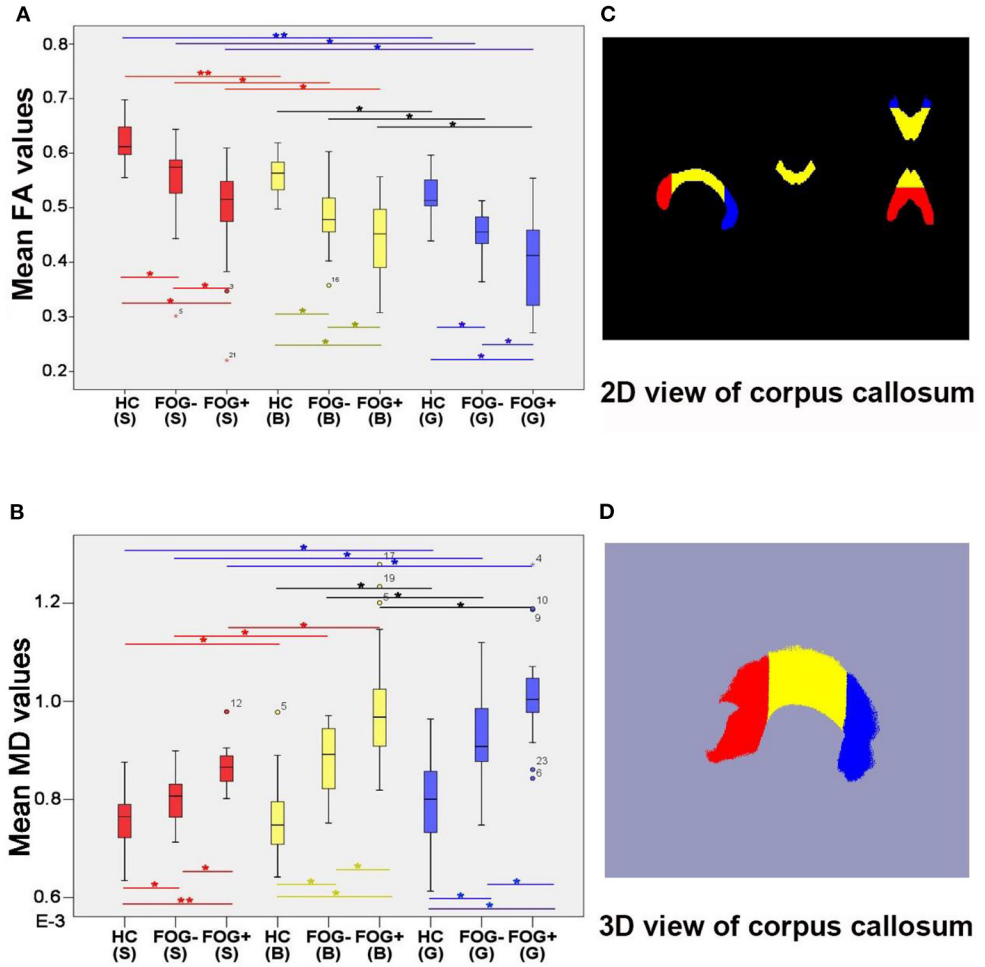


FIGURE 3 | Comparison of FA and MD values of CC splenium, body, and genu. **(A)** Comparison of FA values. **(B)** Comparison of MD values. **(C)** 2D view of CC. **(D)** 3D view of CC. $^{*}P < 0.05$, $^{**}P < 0.01$ (two-sample *t*-test; FDR correction was applied to multiple comparisons). B, body; G, genu; S, splenium.

HCs, the values for the PD FOG– and PD FOG+ groups were 6.13 and 15.73% lower, respectively. In the body, the median FA values for PD FOG– patients (0.478) and PD FOG+ patients (0.452) were 15.09 and 19.75% lower, respectively, than that in HCs (0.563). For the genu, the median FA values were 0.455 for PD FOG– patients and 0.412 for PD FOG+ patients, which were 11.30 and 19.67% lower, respectively, than that in HCs (0.513). Thus, the greatest difference in FA between PD patients and HCs was in the body of the CC. The rank order of MD value was body > splenium > genu. The PD FOG+ group had the highest MD in all three parts of the CC, PD FOG– group had lower MD values, and HCs had the lowest values ($P < 0.05$, FDR corrected).

Correlations Between FA, MD, and FOGQ Score

There was a significantly negative correlation between FA values in the CC and FOGQ scores (splenium: $P = 0.0021$, $r = -0.5972$; body: $P = 0.0001$, $r = -0.7038$; genu: $P = 0.0086$, $r = -0.5237$; **Figure 4**). This suggests that the integrity of the WM declined with the severity of FOG. MD values in the CC were positively correlated with FOGQ score (splenium: $P = 0.0006$, $r = 0.6491$; body: $P = 0.0039$, $r = 0.5665$; genu: $P = 0.0059$, $r = 0.5448$), indicating that more severe hematogenous edema of the CC was associated with increased FOG severity.

Correlation Between VMHC and FOGQ Score

Compared to HCs, VMHC in the PCG, pre-central gyrus (PRG), and angular gyrus of the parietal inferior margin was reduced in PD FOG+ and PD FOG– patients (**Figure 5**). Lower VMHC in the PCG, PRG, and parietal inferior margin was observed in PD FOG+ patients compared to PD FOG– patients. In the comparison between PD FOG+ and PD FOG–, the local maxima of the cluster with a significant difference in VMHC was located at $x = \pm 48$, $y = -18$, and $z = 48$; the *T*-value was −1.351, and the number of voxels in the PCG, PRG, and parietal inferior margin was 130, 51, and 6, respectively (**Table 2**).

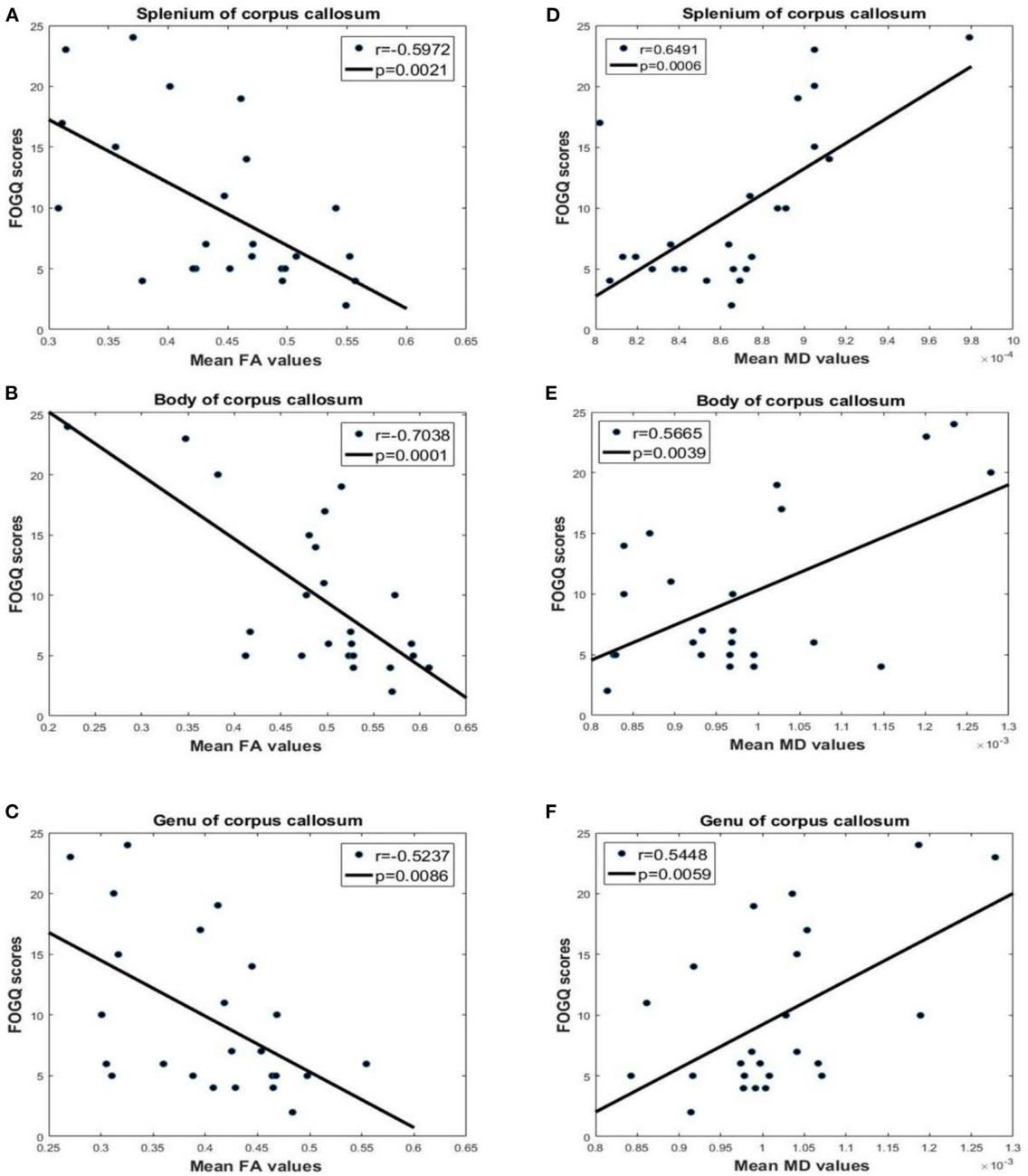


FIGURE 4 | Correlation analysis of FA, MD, and FOGQ scores for the splenium, body, and genu of the CC. FOGQ scores and FA values of the **(A)** splenium, **(B)** body, and **(C)** genu. FOGQ scores and MD values of the **(D)** splenium, **(E)** body, and **(F)** genu.

The T values for PD FOG+ vs. HC and PD FOG– vs. HC were −5.354 and −4.479, respectively; thus, the difference between PD FOG+ patients and HCs was more significant than that between PD FOG– patients and HCs. FOGQ score was negatively correlated with VMHC in the PCG ($P = 0.0007$, $r = -0.6443$), suggesting that PD patients with more severe FOG have lower PCG functioning.

Integration of FA, MD, and VMHC

FA of the CC was positively correlated with VMHC in the PCG (splenium: $P = 0.0002$, $r = 0.6825$; body: $P = 0.0046$, $r = 0.5585$; genu: $P = 0.0060$, $r = 0.5438$; **Figure 6**). On the other hand, there was a negative correlation between MD in the CC and VMHC in the PCG (splenium: $P = 0.0223$, $r = -0.4643$; body: $P = 0.0001$, $r = -0.7206$; genu: $P = 0.0003$, $r = -0.6741$). This suggests that

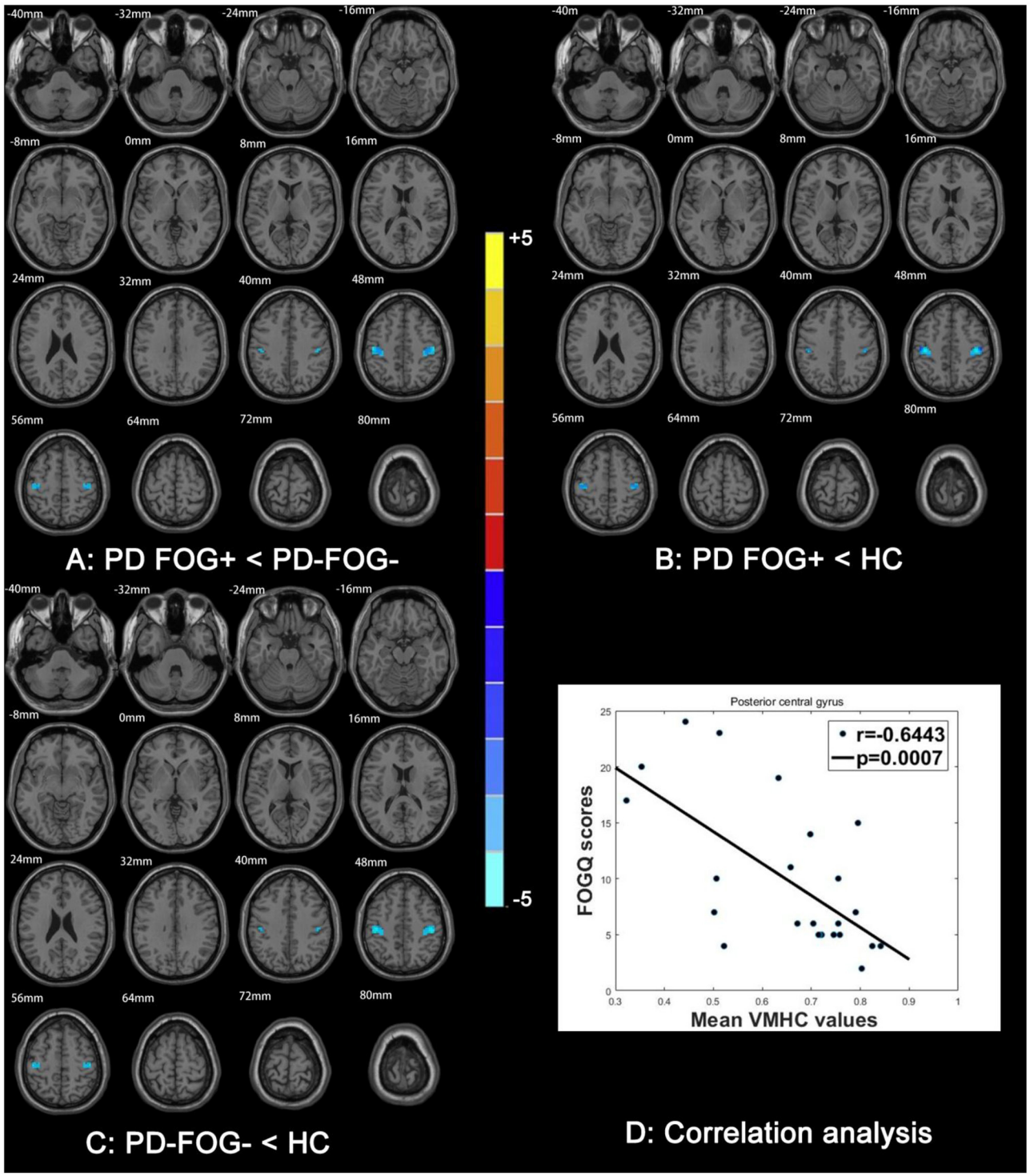


FIGURE 5 | Comparison of VMHC among PD FOG+, PD FOG–, and HC groups. VMHC between **(A)** PD FOG+ and PD FOG–, **(B)** PD FOG+ and HC, and **(C)** PD FOG– and HC. **(D)** Correlation analysis between FOGQ scores and VMHC of PCG.

TABLE 2 | VMHC differences among PD FOG+ and PD FOG–patients and HCs.

Anatomic region (AAL)	Number of voxels	MNI coordinates of local maxima			*T*-value
		x	*y*	*z*	
PD FOG+ vs. PD FOG–		±48	−18	48	−1.351
PCG	130				
PRG	51				
Parietal_Inf	6				
PD FOG+ vs. HC		±39	−21	51	−4.479
PCG	118				
PCG	60				
Parietal_Inf	8				
PD FOG– vs. HC		±45	−24	48	−5.354
PCG	120				
PCG	58				
Parietal_Inf	12				

AAL, Automated Anatomical Labeling; HC, healthy control; Parietal_Inf, parietal inferior margin; PD FOG+, MNI, Montreal Neurological Institute; Parkinson's disease with freezing of gait; PD FOG–, Parkinson's disease without freezing of gait; PCG, post-central gyrus; PRG, pre-central gyrus; VMHC, voxel-mirrored homotopic connectivity.

the abnormalities in the CC of PD FOG+ patients are related to a decrease in VMHC in the PCG.

DISCUSSION

The present study investigated changes in brain structure and FC in patients with PD with or without FOG. WM impairment was identified by TBSS, and FA and MD in the CC were compared among groups, and their correlations with FOGQ score were analyzed. VMHC analysis can reveal brain regions with abnormal interhemispheric FC. There were four major findings from our study: (1) structural connectivity was decreased in all three parts of the CC in patients with PD; (2) widespread impairment in the frontal lobe WM was present in PD patients; (3) PD FOG+ patients showed decreased VMHC in the PCG, PRG, and angular gyrus of the parietal inferior margin; and (4) FA, MD, VMHC, and FOGQ score were correlated.

Decreased Interhemispheric Structural Connectivity in the CC

The TBSS analysis revealed decreased FA and increased MD values in the CC of PD FOG+ patients compared to PD FOG– patients and HCs, indicating that WM microstructure in the CC was abnormal. The CC is the largest connecting tract between the left and right brain hemispheres (28); lesions in the CC result in decreased interhemispheric structural connectivity, which can disrupt brain functions requiring interhemispheric coordination such as cognition, executive functions, and attention. All of these resources are required for gait, especially in unfamiliar environments (25, 29, 30). Thus, our findings suggest that limited cognition/attention/execution resources resulting from CC impairment underlie FOG in PD.

Fiber tracts for leg motor control are located in the CC; a DTI study revealed callosal leg motor fibers passing through the isthmus of the CC (31), which has been confirmed using Klingler's fiber dissection technique (32). Therefore, the impairment in CC (especially splenium) might be associated with FOG in PD patients.

Widespread Impairment of Frontal Lobe WM

We observed widespread impairment in frontal WM beyond the CC in PD FOG+ patients. This is in line with a previous study in which PD patients with postural imbalance and gait difficulty were found to have a lower FA in the prefrontal cortex than tremor-dominant patients (33). A loss of integrity of WM tracts including superior and inferior longitudinal fasciculus, pedunculopontine nucleus, and corticospinal tract has also been observed in PD patients with FOG (34). Frontal areas are important for higher-order motor control (35); thus, frontal WM disease is another possible cause of PD FOG+ and gait disorder. It should be noted that prefrontal and premotor fibers pass through the anterior part and body of the CC, respectively (31), which are associated with higher-order motor control in the frontal lobe. The lower FAB score in the PD FOG+ group was also indicative of frontal lobe defects.

Impaired Interhemispheric Functional Coordination in Sensorimotor and Visuospatial Regions

In PD FOG+ patients, VMHC was decreased in the PCG and PRG, which are critical for sensory and motor functions, respectively. This is consistent with several previous fMRI studies reporting a decreased FC between the sensorimotor network and other brain regions (36, 37). A decreased VMHC was also observed in the angular gyrus of the parietal inferior margin in the PD FOG+ group. This is an important component of the frontoparietal network for visuospatial function, and its impairment can lead to left–right disorientation (38, 39). Our results indicate that PD FOG+ patients have visuospatial dysfunction resulting from structural or functional alterations in the frontoparietal network (40).

Gait is neither a sensorimotor skill (e.g., like daily hand motor skill) nor an automatized motor action. A growing body of evidence indicates that gait has the multidimensionality and relies on high cognitive aspects including attention, executive control, and sensorimotor integration, which are all especially impaired in FOG (41–45). It will be interrupted by freezing of gait in PD, representing a pathological condition that can be resolved by a sensory cue. The impaired interhemispheric functional coordination in sensorimotor and visual–spatial regions might be associated with the pathological condition in PD FOG+.

FA, MD, and VMHC as Potential Biomarkers of FOG Severity

FA and MD in the CC and VMHC in the PCG, PRG, and parietal inferior margin were significantly correlated with the

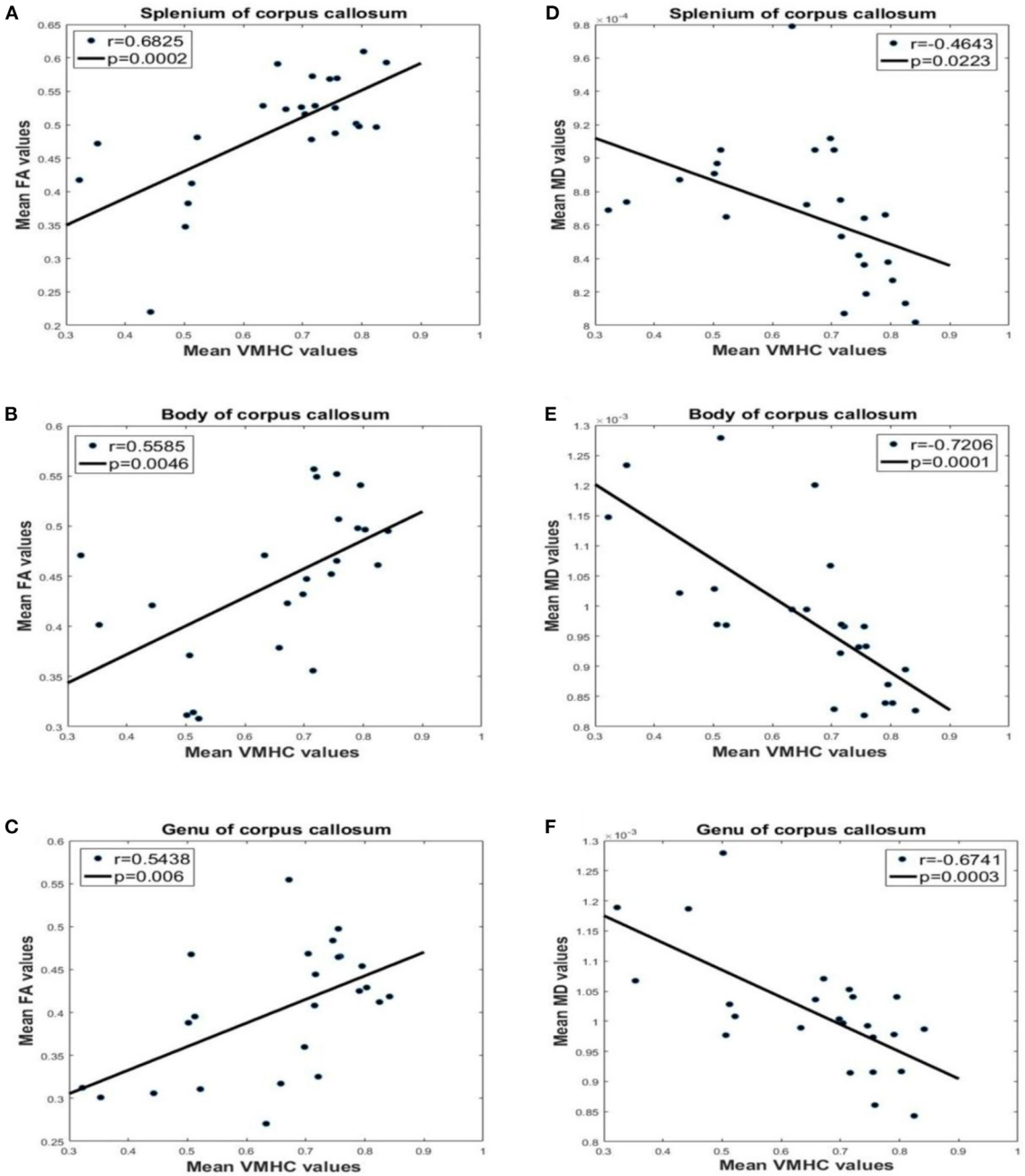


FIGURE 6 | Correlation analysis between FA, MD, and VMHC values for different parts of the CC. VMHC and FA in the **(A)** splenium, **(B)** body, and **(C)** genu. VMHC and MD in the **(D)** splenium, **(E)** body, and **(F)** genu.

FOGQ score. Other indices such as FC in the sensorimotor network were reported to be correlated with the severity of motor impairment (46). VMHC in the inferior parietal lobe was shown to be negatively correlated with FOGQ score (15). This implies that FA, MD, and VMHC are potential quantitative biomarkers of FOG severity that can be used in conjunction with FOGQ score—which has large interobserver variability—to reduce the risk of misdiagnosing FOG.

Integrating Structural Connectivity and FC

This is the first study to establish correlations between FA, MD, and VMHC from the same PD FOG+ dataset. FA and MD measure the structural connectivity (i.e., in WM), while VMHC reflects functional homotopic FC. The structural and functional data were concordant and indicated that interhemispheric brain connectivity is impaired in PD FOG+. Thus, integrative analysis of structural connectivity and FC

can provide detailed insight into the mechanisms of FOG in PD.

It should be noted that the interhemispheric fibers subserving the three areas with decreased VMHC (PCG, PRG, and parietal inferior margin) likely intersect in the body of the CC. A recent study reported that transection of the CC decreased VMHC, with a greater reduction in the frontal and parietal lobes than in sensorimotor and visual areas (47). The areas of decreased VMHC found in our study were less affected than would be expected following complete and partial callosotomy. Nonetheless, the impairment of the CC in our PD FOG+ patients presumably decreased interhemispheric coordination, leading to visuospatial and sensorimotor dysfunction and loss of the leg motor control.

There were limitations to our study. First, the sample size was relatively small, which may have reduced the statistical power. Second, the asymmetry of cortical structures could affect VMHC, although asymmetric template in fMRI data processing was used to reduce this effect. Third, as our study was cross-sectional, changes in related regions and indices in the progression of FOG– to FOG+ could not be examined. In future work, we will investigate the structural and functional brain networks of PD constructed from multimodal MRI data (34, 48–50) and identify potential network biomarkers of PD FOG+ using machine learning algorithms (51, 52).

CONCLUSION

PD FOG+ was found to be associated with abnormal interhemispheric brain connectivity as measured by FA, MD, and VMHC, which were correlated with clinical FOG severity. Our results suggest that decreased FA in the CC impairs all advanced brain functions requiring interhemispheric coordination, and decreased VMHC in three brain regions (PCG, PRG, and parietal inferior margin) underlies defects in visuospatial and sensorimotor functions in FOG. Additionally, our data indicate that FA, MD, and VMHC are potential biomarkers of FOG severity in PD patients and demonstrate that integrating structural and functional MRI measures can provide novel insight into the pathophysiological mechanisms of FOG.

DATA AVAILABILITY STATEMENT

The original contributions presented in the study are included in the article/supplementary material, further inquiries can be directed to the corresponding author/s.

ETHICS STATEMENT

The studies involving human participants were reviewed and approved by the ethics committee of Guangzhou First People's Hospital. The patients/participants provided their written informed consent to participate in this study.

AUTHOR CONTRIBUTIONS

CJ performed experiments and analyzed the data along with SQ. SQ, YY, and XW conceived the study, presented the results, and wrote the manuscript along with CJ. XR collected and analyzed the data. YT and CL supervised the algorithm development and analyzed the data. All authors read and approved the final manuscript.

FUNDING

This work was partly supported by the National Natural Science Foundation of China (Grant Nos. 81671773, 61672146, and 81871846), Fundamental Research Funds for the Central Universities (Grant Nos. N181904003, N172008008, and N2024005-2), and Science and Technology Planning Project of Guangzhou (Grant No. 201804010032).

REFERENCES

1. Nutt JG, Bloem BR, Giladi N, Hallett M, Horak FB, Nieuwboer A. Freezing of gait: moving forward on a mysterious clinical phenomenon. *Lancet Neurol.* (2011) 10:734–44. doi: 10.1016/S1474-4422(11)70143-0
2. Wang M, Jiang S, Yuan Y, Zhang L, Ding J, Wang J, et al. Alterations of functional and structural connectivity of freezing of gait in Parkinson's disease. *J Neurol.* (2016) 263:1583–92. doi: 10.1007/s00415-016-8174-4
3. Bensimon G, Ludolph A, Agid Y, Vidailhet M, Payan C, Leigh PN, et al. Riluzole treatment, survival and diagnostic criteria in Parkinson plus disorders: the NNIPPS study. *Brain.* (2009) 132:156–71. doi: 10.1093/brain/awn291
4. Shine JM, Naismith SL, Lewis SJ. The pathophysiological mechanisms underlying freezing of gait in Parkinson's Disease. *J Clin Neurosci.* (2011) 18:1154–7. doi: 10.1016/j.jocn.2011.02.007
5. Litvan I, Agid Y, Calne D, Campbell G, Dubois B, Duvoisin RC, et al. Clinical research criteria for the diagnosis of progressive supranuclear palsy (Steele-Richardson-Olszewski syndrome): report of the NINDS-SPSP International Workshop. *Neurology.* (1996) 47:1–9. doi: 10.1212/wnl.47.1.1
6. Nieuwboer A, Giladi N. Characterizing freezing of gait in Parkinson's disease: models of an episodic phenomenon. *Mov Disord.* (2013) 28:1509–19. doi: 10.1002/mds.25683
7. Bächlin M, Plotnik M, Roggen D, Maidan I, Hausdorff JM, Giladi N, et al. Wearable assistant for Parkinson's disease patients with the freezing of gait symptom. *IEEE Trans Inf Technol Biomed.* (2010) 14:436–46. doi: 10.1109/TITB.2009.2036165
8. Youn J, Cho JW, Lee WY, Kim GM, Kim ST, Kim HT. Diffusion tensor imaging of freezing of gait in patients with white matter changes. *Mov Disord.* (2012) 277:760–4. doi: 10.1002/mds.24034
9. Fling BW, Cohen RG, Mancini M, Carpenter SD, Fair DA, Nutt JG, et al. Functional reorganization of the locomotor network in Parkinson patients with freezing of gait. *PLoS ONE.* (2014) 9:e100291.doi: 10.1371/journal.pone.0100291
10. Pietracupa S, Suppa A, Upadhyay N, Giannì C, Grillea G, Leodori G, et al. Freezing of gait in Parkinson's disease: gray and white matter abnormalities. *J Neurol.* (2018) 26:552–62. doi: 10.1007/s00415-017-8654-1
11. Stark DE, Margulies DS, Shehzad ZE, Reiss P, Kelly AM, Uddin LQ, et al. Regional variation in interhemispheric coordination of intrinsic hemodynamic fluctuations. *J Neurosci.* (2008) 28:13754. doi: 10.1523/JNEUROSCI.4544-08.2008

12. Fox MD, Raichle ME. Spontaneous fluctuations in brain activity observed with functional magnetic resonance imaging. *Nat Rev Neurosci*. (2007) 8:700–11. doi: 10.1038/nrn2201
13. Zuo XN, Kelly C, Di Martino A, Mennes M, Margulies DS, Bangaru S, et al. Growing together and growing apart: regional and sex differences in the lifespan developmental trajectories of functional homotopy. *J Neurosci*. (2010) 30:15034–43. doi: 10.1523/JNEUROSCI.2612-10.2010
14. Luo C, Guo X, Song W, Zhao B, Cao B, Yang J, et al. Decreased resting-state interhemispheric functional connectivity in Parkinson's disease. *Biomed Res Int*. (2015) 2015:692684. doi: 10.1155/2015/692684
15. Li J, Yuan Y, Wang M, Zhang J, Zhang L, Jiang S, et al. Decreased interhemispheric homotopic connectivity in Parkinson's disease patients with freezing of gait: a resting state fMRI study. *Parkinsonism Relat Disord*. (2018) 52:30–6. doi: 10.1016/j.parkreldis.2018.03.015
16. Canu E, Agosta F, Sarasso E, Volontè MA, Basaia S, Stojkovic T, et al. Brain structural and functional connectivity in Parkinson's disease with freezing of gait. *Hum Brain Mapp*. (2015) 36:5064–78. doi: 10.1002/hbm.22994
17. Chung SJ, Lee YH, Yoo HS, Oh JS, Kim JS, Ye BS, et al. White matter hyperintensities as a predictor of freezing of gait in Parkinson's disease. *Parkinsonism Relat Disord*. (2019) 66:105–9. doi: 10.1016/j.parkreldis.2019.07.019
18. Giladi N, Shabtai H, Simon ES, Biran S, Tal J, Korczyn AD. Construction of freezing of gait questionnaire for patients with Parkinsonism. *Parkinsonism Relat Disord*. (2000) 6:165–70. doi: 10.1016/s1353-8020(99)00062-0
19. Movement Disorder Society Task Force on Rating Scales for Parkinson's Disease. The Unified Parkinson's Disease Rating Scale (UPDRS): status and recommendations. *Mov Disord*. (2003) 18:738–50. doi: 10.1002/mds.10473
20. Diedrichsen J, Maderwald S, Küper M, Thürling M, Rabe K, Gizewski ER, et al. Imaging the deep cerebellar nuclei: a probabilistic atlas and normalization procedure. *NeuroImage*. (2011) 54:1786–94. doi: 10.1016/j.neuroimage.2010.10.035
21. Kleiner A, Pacifici I, Vagnini A, Camerota F, Celletti C, Stocchi F, et al. Timed Up and Go evaluation with wearable devices: validation in Parkinson's disease. *J Bodyw Mov Ther*. (2018) 22:390–5. doi: 10.1016/j.jbmt.2017.07.006
22. Datta AK, Das D, Bhattacharyya KB, Bose P, Mishra AK, Das SK. Frontal assessment battery in Parkinson's disease: a study on 170 patients. *Neurol India*. (2019) 67:433–8. doi: 10.4103/0028-3886.258052
23. Smith SM, Jenkinson M, Johansen-Berg H, Rueckert D, Nichols TE, Mackay CE, et al. Tract-based spatial statistics: voxelwise analysis of multi-subject diffusion data. *NeuroImage*. (2006) 31:1487–505. doi: 10.1016/j.neuroimage.2006.02.024
24. Chao-Gan Y, Yu-Feng Z. DPARSF: a MATLAB toolbox for "pipeline" data analysis of resting-state fMRI. *Front Syst Neurosci*. (2010) 4:13. doi: 10.3389/fnsys.2010.00013
25. Bharti K, Suppa A, Tommasin S, Zampogna A, Pietracupa S, Berardelli A, et al. Neuroimaging advances in Parkinson's disease with freezing of gait: a systematic review. *Neuroimage Clin*. (2019) 24:102059. doi: 10.1016/j.nicl.2019.102059
26. Jia X-Z, Wang J, Sun H-Y, Zhang H, Liao W, Wang Z, et al. RESTplus: an improved toolkit for resting-state functional magnetic resonance imaging data processing. *Sci Bull*. (2019) 64:953–4. doi: 10.1016/j.scib.2019.05.008
27. Fan H, Yang X, Zhang J, Chen Y, Li T, Ma X. Analysis of voxel-mirrored homotopic connectivity in medication-free, current major depressive disorder. *J Affect Disord*. (2018) 240:171–6. doi: 10.1016/j.jad.2018.07.037
28. Xue C, Shi L, Hui S, Wang D, Lam TP, Ip CB, et al. Altered white matter microstructure in the corpus callosum and its cerebral interhemispheric tracts in adolescent idiopathic scoliosis: diffusion tensor imaging analysis. *Am J Neuroradiol*. (2018) 39:1177–84. doi: 10.3174/ajnr.A5634
29. Hall JM, Ehgoetz Martens KA, Walton CC, O'Callaghan C, Keller PE, Lewis SJ, et al. Diffusion alterations associated with Parkinson's disease symptomatology: a review of the literature. *Parkinsonism Relat Disord*. (2016) 33:12–26. doi: 10.1016/j.parkreldis.2016.09.026
30. Hall JM, Shine JM, Ehgoetz Martens KA, Gilat M, Broadhouse KM, Szeto J, et al. Alterations in white matter network topology contribute to freezing of gait in Parkinson's disease. *J Neurol*. (2018) 265:1353–64. doi: 10.1007/s00415-018-8846-3
31. Wahl M, Lauterbach-Soon B, Hattingen E, Jung P, Singer O, Volz S, et al. Human motor corpuscallosum: topography, somatotopy, and link between microstructure and function. *J Neurosci*. (2007) 27:12132–8. doi: 10.1523/JNEUROSCI.2320-07.2007
32. Naets W, Van Loon J, Paglioli E, Van Paesschen W, Palmini A, Theys T. Callosotopy: leg motor connections illustrated by fiber dissection. *Brain Struct Funct*. (2017) 222:661–7. doi: 10.1007/s00429-015-1167-8
33. Lenfeldt N, Holmlund H, Larsson A, Birgander R, Forsgren L. Frontal white matter injuries predestine gait difficulties in Parkinson'sdisease. *Acta Neurol Scand*. (2016) 134:210–8. doi: 10.1111/ane.12532
34. Allali G, Blumen HM, Devanne H, Pirondini E, Delval A, Van De Ville D. Brain imaging of locomotion in neurological conditions. *Neurophysiol Clin*. (2018) 48:337–59. doi: 10.1016/j.neucli.2018.10.004
35. Bohnen NI, Jahn K. Imaging: What can it tell us about parkinsonian gait? *Mov Disord*. (2013) 28:1492–500. doi: 10.1002/mds.25534
36. Lenka A, Naduthota RM, Jha M, Panda R, Prajapati A, Jhunjhunwala K, et al. Freezing of gait in Parkinson's disease is associated with altered functional brain connectivity. *Parkinsonism Relat Disord*. (2016) 24:100–6. doi: 10.1016/j.parkreldis.2015.12.016
37. Myers PS, McNeely ME, Pickett KA, Duncan RP, Earhart GM. Effects of exercise on gait and motor imagery in people with Parkinson disease and freezing of gait. *Parkinsonism Relat Disord*. (2018) 53:89–95. doi: 10.1016/j.parkreldis.2018.05.006
38. Barthel C, Nonnekes J, van Helvert M, Haan R, Janssen A, Delval A, et al. The laser shoes: a new ambulatory device to alleviate freezing of gait in Parkinson disease. *Neurology*. (2018) 90:e164–71. doi: 10.1212/WNL.0000000000004795
39. Seghier ML. The angular gyrus: multiple functions and multiple subdivisions. *Neuroscientist*. (2013) 19:43–61. doi: 10.1177/1073858412440596
40. Bharti K, Suppa A, Pietracupa S, Upadhyay N, Giannì C, Leodori G, et al. Abnormal cerebellar connectivity patterns in patients with Parkinson's disease and freezing of gait. *Cerebellum*. (2019) 18:298–308. doi: 10.1007/s12311-018-0988-4
41. Verghese A. Physicians and addiction. *N Engl J Med*. (2002) 346:1510–1. doi: 10.1056/NEJM200205163462002
42. Lewis SJ, Shine JM. The next step: a common neural mechanism for freezing of gait. *Neuroscientist*. (2014) 22:72–82. doi: 10.1177/1073858414559101
43. Gilat M, Martens KAE, Miranda-Domínguez O, Arpan I, Shine JM, Mancini M, et al. Dysfunctional limbic circuitry underlying freezing of gait in Parkinson's disease. *Neuroscience*. (2018) 374:119–32. doi: 10.1016/j.neuroscience.2018.01.044
44. Maidan I, Jacob Y, Giladi N, Hausdorff JM, Mirelman A. Altered organization of the dorsal attention network is associated with freezing of gait in Parkinson's disease. *Parkinsonism Relat Disord*. (2019) 63:77–82. doi: 10.1016/j.parkreldis.2019.02.036
45. Li KZH, Bherer L, Mirelman A, Maidan I, Hausdorff JM. Cognitive involvement in balance, gait and dual-tasking in aging: a focused review from a neuroscience of aging perspective. *Front Neurol*. (2018) 9:913. doi: 10.3389/fneur.2018.00913
46. Yoo HS, Bak Y, Chung SJ, Lee Y, Ye BS, Sohn YH, et al. Impaired functional connectivity of sensorimotor network predicts recovery in drug-induced parkinsonism. *Parkinsonism Relat Disord*. (2020) 74:16–21. doi: 10.1016/j.parkreldis.2020.03.031
47. Roland JL, Snyder AZ, Hacker CD, Mitra A, Shimony JS, Limbrick DD, et al. On the role of the corpus callosum in interhemispheric functional connectivity in humans. *Proc Natl Acad Sci USA*. (2017) 114:13278–83. doi: 10.1073/pnas.1707050114
48. Qi S, Meesters S, Nicolay K, Romeny BM, Ossenblok P. The influence of construction methodology on structural brain network measures: a review. *J Neurosci Methods*. (2015) 253:170–82. doi: 10.1016/j.jneumeth.2015.06.016

49. Qi S, Meesters S, Nicolay K, Romeny BM, Ossenblok P. Structural brain network: what is the effect of LiFE optimization of whole brain tractography? *Front Comput Neurosci*. (2016) 10:12. doi: 10.3389/fncom.2016.00012
50. Qi S, Gao Q, Shen J, Teng Y, Xie X, Sun Y, et al. Multiple frequency bands analysis of large scale intrinsic brain networks and its application in schizotypal personality disorder. *Front Comput Neurosci*. (2018) 12:64. doi: 10.3389/fncom.2018.00064
51. Qian H, Qin D, Qi S, Teng Y, Li C, Yao Y, et al. Less is better: Single-digit brain functional connections predict T2DM and T2DM-induced cognitive impairment. *Front Neurosci*. (2021) 14:588684. doi: 10.3389/fnins.2020.588684
52. Zhu Y, Qi S, Zhang B, He D, Teng Y, Hu J, et al. Connectome-based biomarkers predict subclinical depression and identify abnormal brain connections with the lateral habenula and thalamus. *Front Psychiatry*. (2019) 10:371. doi: 10.3389/fpsyt.2019.00371

Conflict of Interest: The authors declare that the research was conducted in the absence of any commercial or financial relationships that could be construed as a potential conflict of interest.

Copyright © 2021 Jin, Qi, Teng, Li, Yao, Ruan and Wei. This is an open-access article distributed under the terms of the Creative Commons Attribution License (CC BY). The use, distribution or reproduction in other forums is permitted, provided the original author(s) and the copyright owner(s) are credited and that the original publication in this journal is cited, in accordance with accepted academic practice. No use, distribution or reproduction is permitted which does not comply with these terms.

frontiers in Neurology

ORIGINAL RESEARCH
published: 30 April 2021
doi: 10.3389/fneur.2021.583593

A Multimodal Imaging Approach Demonstrates Reduced Midbrain Functional Network Connectivity Is Associated With Freezing of Gait in Parkinson's Disease

Amgad Droby[1†], Elisa Pelosin[2,3†], Martina Putzolu[2], Giulia Bommarito[2], Roberta Marchese[3], Luca Mazzella[4], Laura Avanzino[3,5‡] and Matilde Inglese[1,2,3‡]*

[1] Department of Neurology, Icahn School of Medicine at Mount Sinai, New York, NY, United States, [2] Department of Neuroscience, Rehabilitation, Ophthalmology, Genetics and Maternal Child Health, University of Genoa, Genoa, Italy, [3] Ospedale Policlinico San Martino, Istituti di Ricovero e Cura a Carattere Scientifico (IRCCS), Genoa, Italy, [4] Asl3, Genovese Centri per i Disturbi Cognitivi e le Demenze (CDCD) Ponente, Genoa, Italy, [5] Department of Experimental Medicine, Section of Human Physiology, University of Genoa, Genoa, Italy

OPEN ACCESS

Edited by:
Yu Zhang,
VA Palo Alto Health Care System,
United States

Reviewed by:
Mario Treviño,
University of Guadalajara, Mexico
Daniele Corbo,
University of Brescia, Italy

***Correspondence:**
Matilde Inglese
m.inglese@unige.it

[†] These authors share first authorship

[‡] These authors share last authorship

Specialty section:
This article was submitted to Movement Disorders, a section of the journal Frontiers in Neurology

Received: *15 July 2020*
Accepted: *23 March 2021*
Published: *30 April 2021*

Citation:
Droby A, Pelosin E, Putzolu M, Bommarito G, Marchese R, Mazzella L, Avanzino L and Inglese M (2021) A Multimodal Imaging Approach Demonstrates Reduced Midbrain Functional Network Connectivity Is Associated With Freezing of Gait in Parkinson's Disease. Front. Neurol. 12:583593. doi: 10.3389/fneur.2021.583593

Background: The pathophysiological mechanisms underlying freezing of gait (FOG) are poorly defined. MRI studies in FOG showed a distinct pattern of cortical atrophy and decreased functional connectivity (FC) within motor and cognitive networks. Furthermore, reduced rs-FC within midbrain, frontal, and temporal areas has been also described. This study investigated the patterns of whole-brain FC alterations within midbrain inter-connected regions in PD-FOG patients, and whether these patterns are linked to midbrain structural damage using a multi-modal imaging approach, combing structural and functional imaging techniques.

Methods: Thirty three PD patients (16 PD-FOG, 17 PD noFOG), and 21 sex- and age-matched healthy controls (HCs) were prospectively enrolled. All subjects underwent MRI scan at 1.5T, whereas only PD patients underwent clinical and cognitive assessment. Grey matter (GM) integrity was measured using voxel-based morphometry (VBM). VBM findings served as basis to localize midbrain damage, and were further used as a seed region for investigating whole-brain FC alterations using rs-fMRI.

Results: In rs-fMRI, patients with PD and FOG demonstrated significant decrease of midbrain-cortical FC levels in the R PCG, right postcentral, and supramarginal gyri compared to controls and the middle cingulate compared to noFOG group. Based on the regression analysis, MOCA, UPDRS-III total score, and FOG severity scores were associated with FC levels in several frontal, parietal and temporal regions.

Discussion: The present results suggest that midbrain structural damage as well as decreased FC within the brainstem functional network might contribute to FOG occurrence in PD patients.

Keywords: freezing of gait, functional connectivity, resting-state fMRI, Parkinson's disease, gait analysis

INTRODUCTION

Freezing of gait (FOG), defined as a "brief, episodic absence or marked reduction of forward progression of the feet despite the intention to walk" (1), is a debilitating feature in Parkinson's disease (PD) (2) which have a dramatic impact on quality of life. FOG can be triggered or exacerbated by specific situations (e.g., turning, narrow passages) or can occur in response to increased motor (e.g., obstacle crossing), cognitive (dual task) and limbic (e.g., emotions) load. Indeed, besides motor symptoms, FOG can be associated with executive functions deficits, as well as mood disorders (e.g., anxiety) (1). The underlying pathophysiological mechanisms of FOG remain poorly understood. However, evidence suggests that (i) FOG does not originate from a single isolated brain region, but results from impaired communication within the corti co-subcortical-cortical circuitry and, (ii) the mesencephalic loco motor region (MLR) plays a role in this impaired communication. Among the different proposed models regarding FOG pathophysiology, the interference model by Nieuwboer and Giladi (3) suggests that FOG is a net result of top-down processing impairment, where breakdown of communication between motor, associative, and limbic pathways at a subcortical level leads to interruption of gait (4–6). Based on this, the interaction between these multiple failing neural circuits may underlie the heterogeneity of FOG features (7).

Structural MRI imaging studies have demonstrated patterns of gray matter (GM) atrophy including the left cuneus, precuneus, lingual gyrus, and posterior cingulate cortex in PD patients with FOG compared with PD patients without FOG and healthy individuals, and this GM decrease was correlated with performance in executive functioning (8). In white matter (WM), PD patients with FOG demonstrated reduced connectivity in the MLR involving mainly fibers connecting the peduncolopontine nucleus (PPN) with the medial frontal cortices and cerebellum (9–11).

Resting-state functional MRI (rs-fMRI) allows the investigation of the underlying pathophysiology in FOG on whole-brain functional network level (12, 13). Several rs-fMRI studies have reported reduced functional connectivity (FC) within several brain resting-state networks (RSNs) (14) including the sensorimotor network (SMN), the default mode network (DMN) (15) and the executive control network in PD patients with FOG (15–17). A study by Tessitore et al., reported altered FC within regions of the executive network and the visual functional network in PD with FOG, that was also associated with executive and visuo spatial performance (16). Furthermore, reduced rs-FC of the MLR and the cerebellum loco motor region with the supplementary motor area has been also described in PD patients with FOG, possibly reflecting a less automatic control of movement (17). Finally, rs-FC of the PPN, a major nucleus of the MLR, was also assessed, reporting an altered FC with visual temporal areas, as well as within the cortico-pontine-cerebellar pathways (18).

On these premises, we sought to investigate the patterns of whole-brain FC alterations within midbrain inter-connected regions in PD-FOG patients, and whether these patterns are linked to midbrain structural damage using a multi-modal imaging approach.

METHODS

Participants

Fifty-four subjects (33 patients and 21 healthy controls) were prospectively enrolled in the study Patients with PD were classified as having FOG or not based on the score of the new FOG Questionnaire (FOG-Q) (19). Sixteen out of 33 patients who experienced FOG at least once a month (minimum score of 1 on item 2), for at least 2 sec (minimum score of 2 on item 4) were included in the PD-FOG group (5 female, mean age 72.43 $\pm$ 3.94 years), and 17 PD subjects (7 females, mean age 69.00 $\pm$ 5.43 years) were included in the PD-noFOG group. Twenty-one healthy subjects (HCs) (12 females, mean age 69 $\pm$ 13.5 years) served as a control group.

The inclusion criteria for patients with PD were: (a) age $\geq$ 18 years, (b) idiopathic PD according to the United Kingdom Parkinson's Disease Society Brain Bank criteria (20); (c) Hoehn and Yahr (H&Y) stage score $\leq$ 3, (d) stable PD pharmacological treatment for at least 1 month prior to the study; (e) ability to walk without any assistance for 2 min. Exclusion criteria for all participants were: (a) pre-existing history of neurological disorders other than PD, (b) psychiatric co-morbidity and history of psychiatric pharmacological treatments, (c) contraindications to Magnetic Resonance Imaging (MRI), (d) excessive head motion during MRI scan (>3mm average frame-wise displacement).

In PD patients, motor impairment was assessed with the Unified Parkinson's disease rating scale part III (MDS UPDRS-III) (20). PD participants were tested in the ON phase of their medication cycle (about 45 min after having taking anti-parkinsonian medications) both during MRI exam and during the clinical evaluation. Furthermore, in all participants global cognitive function was tested by using the Montreal Cognitive Assessment (MOCA) (21). All participants provided written informed consent prior to starting any procedures and after receiving an extensive explanation of the experimental protocol. This study was approved by the Ethics committee of the University of Genoa and each participant provided written informed consent prior to starting any procedures.

MRI Data Acquisition

MR data were acquired for all patients using a 1.5 T Signa Excite (Signa Excite General Electric Healthcare, WI, USA) MR scanner with 8-channels phased-array head coil. The MRI protocol included: (a) high resolution Fast Spoiled Gradient Echo (FSPGR) 3-D T1-weighted sequence (TR/TE/TI = 11.56/5.048/500ms; FA = 8°, voxel size = 1 × 1 × 1 mm^3), (b) axial T2-weighted (TR/TE1/TE2 = 2340/102/38.25ms; FA = 90°; voxel size = 0.94 × 0.94 × 4 mm^3), and (c) 180 volumes resting-state fMRI datasets using single-shot echo-planar imaging (EPI) sequence (TR/TE = 3,000/60ms; FA = 90°, slice spacing = 1 mm, voxel size = 3.75 × 3.75 × 4 mm^3).

TABLE 1 | Demographic, and clinical characteristics of the study groups.

	FOG	noFOG	HC	
Gender (F/M)	5/11	5/10	11/9	$p = 0.27$
Age	72 ± 3	68.2 ± 5	64 ± 13.5	$p = 0.056$
H&Y stage	2.46 (2,3)	1.75 (1,2)	–	$p < 0.001$
Total UPDRS score	56.17 ± 24.33	32.93 ± 14	–	$p < 0.001$
UPDRS-III score	27.91 ± 16.27	18.87 ± 9.41		$P < 0.001$
UPDRS-III gait sub-score (item 3.10)	1.81 ± 1.10	1 ± 0.73		$p = 0.02$
FOG-Q	16.44 ± 8.9	–	–	–
MOCA-Total	23.4 ± 3.01	25.81 ± 2.79	–	$p = 0.001$
MOCA-Visuospatial	3.5 ± 1.9	4.4 ± 0.9	–	$p = 0.001$
MOCA-Attention	4.7 ± 1.2	5.7 ± 0.5	–	$p = 0.001$

Values are reported as mean ± SD; H&Y data are expressed as median and range. H&Y, Hoehn & Yahr; UPDRS, unified Parkinson's disease rating scale; FOG-Q, freezing of gait questionnaire; MOCA, Montreal cognitive assessment.

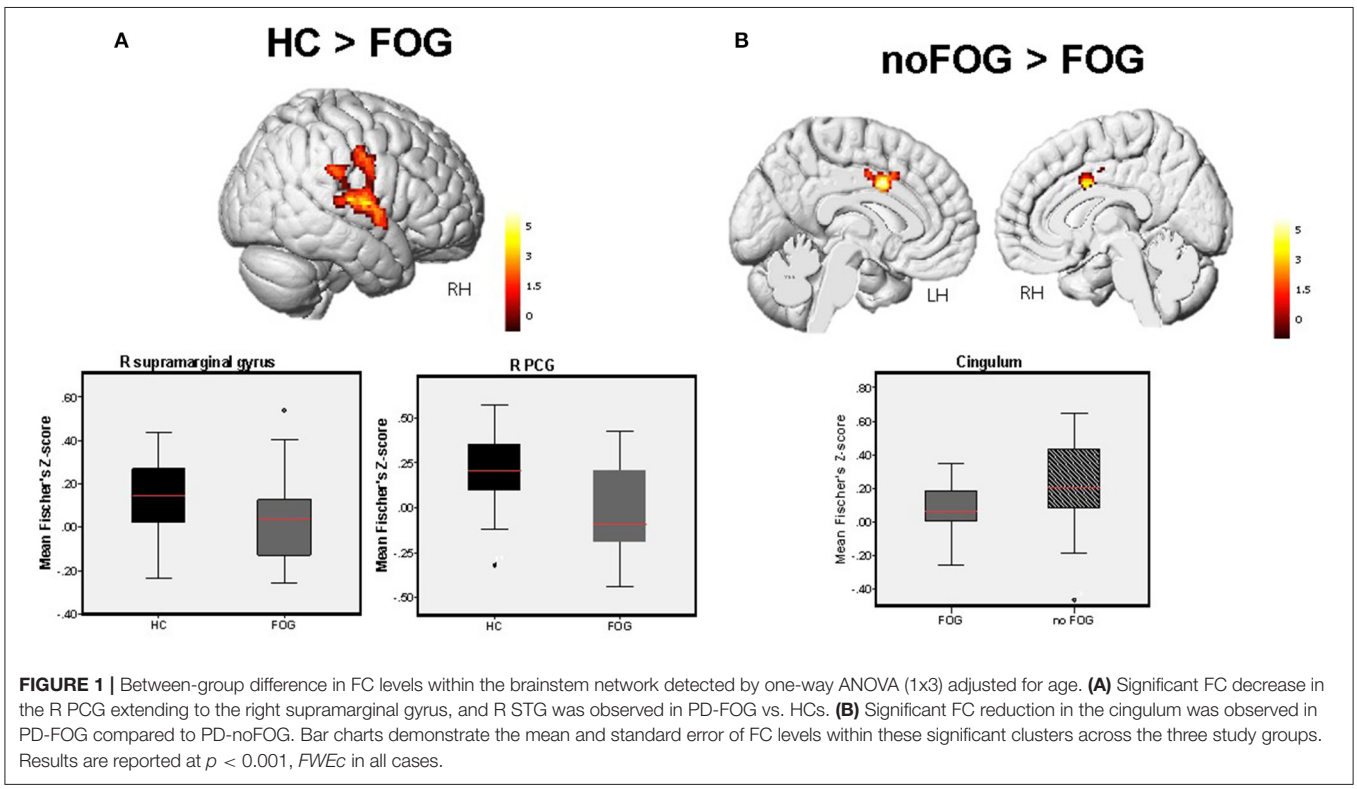


FIGURE 1 | Between-group difference in FC levels within the brainstem network detected by one-way ANOVA (1x3) adjusted for age. **(A)** Significant FC decrease in the R PCG extending to the right supramarginal gyrus, and R STG was observed in PD-FOG vs. HCs. **(B)** Significant FC reduction in the cingulum was observed in PD-FOG compared to PD-noFOG. Bar charts demonstrate the mean and standard error of FC levels within these significant clusters across the three study groups. Results are reported at $p < 0.001$, *FWEc* in all cases.

MRI Data Processing

Using a multi-modal imaging approach, we first investigated atrophy patterns of midbrain and cortex in PD-FOG relative to PD patients without FOG and HCs using voxel-based morphometry [(VBM); see **Supplementary Material** for further details]. VBM findings served as basis to localize midbrain damage, and further used as a seed region for investigating whole-brain FC alterations using rs-fMRI.

rs-fMRI datasets were pre-processed using SPM12 (https://www.fil.ion.ucl.ac.uk/spm/), where following steps were applied: slice time correction, re-alignment to the first volume image in order to correct for head movement, normalization to MNI using the parameters obtained from the segmentation procedure, and smoothing using an 8 mm full width at half maximum (FWHM) kernel. The de-noising and filtering of pre-processed rs-fMRI data sets were performed using the CONN (v.17) toolbox (McGovern Institute for Brain Research, Massachusetts Institute of Technology, Cambridge; https://web.conn-toolbox.org/), where, linear de-trending, temporal de-spiking, band-pass filtering (0.08 Hz – 0.1 Hz) were carried out after regression. The subjects' six head motion parameters, average WM, and CSF time course were entered as covariates of no interest in the regression model. Here, for each subject, functional connectivity (FC) maps of the brainstem network were calculated following

TABLE 2 | Brain regions showing between-group significant differences in FC within the brainstem network.

Comparison	Brain region	MNI coordinates *x y z*	Cluster size (# of voxels)	*Z*-value	*T*-value	*p*-value
HC > FOG	R PCG	64 −10 10	1,034	4.51	5.09	< 0.001**
	R supramarginal gyrus	64 −30 30				
	R STG	52 0 4				
noFOG > FOG	Middle cingulate	−6 4 36	261	4.61	5.23	0.025*

*RS, resting-state; FC, functional connectivity; MNI, montreal neurological institute; HC, healthy control; PD, Parkison's disease; FOG, freezing of gait; R, right; L, left; PCG, post- central gyrus; STG, superior temporal gyrus. *$p < 0.001$; FWE_C cluster size > 450, **$p < 0.001$; FWE_C cluster size > 200 voxels.*

seed-based approach, where a midbrain anatomical seed was applied based on the Harvard-Oxford Atlas available in CONN (see **Supplementary Figure 1**). Finally, the spatial accuracy of the constructed midbrain FC maps was visually inspected at both group–as well as individual level (22, 23).

Statistical Analysis

All statistical analyses were performed using Statistical Package for Social Science (SPSS® v.23, IBM). Gender differences among the groups (PD-FOG, PD-noFOG and HC) were assessed by Chi-square test. Groups' difference at baseline for age and MOCA scores were assessed by the non-parametric Kruskal-Wallis test because data were not normally distributed. Two-sample *t*-test was used to detect differences between PD-FOG and PD-noFOG group for Hoehn and Yahr (H&Y) stage, for MDS-UPDRS part III total score and its gait sub-score (item 3.10). *P*-values < 0.05 were considered as a threshold for statistical significance.

Second level analysis of the MRI data was performed using SPM. 1 × 3 ANOVA was also conducted to assess between groups differences in FC within the brainstem functional network. The following contrasts were of interest: HC > FOG, noFOG > FOG, and HC > noFOG. Age, gender, and H&Y stage were entered as covariates in the design metrics of all the performed second-level analyses. Significance threshold for all between-groups statistical comparisons of interest was set to $p < 0.001$, family-wise error corrected for cluster size *(FWEc)* based on multiple-comparisons corrected using the Monte Carlo simulation (as implemented in Alphasim, AFNI).

Finally, a voxel-wise multiple regression was performed to explore the association between FC levels of brain regions within the midbrain network, disease severity (UPDRS III total score), gait performance (UPDRS III gait sub-score, item 3.10), cognitive performance (total MOCA score) in both patients' subgroups, and FOG severity (FOG-Q score) in PD-FOG only. Age, gender, and H&Y stage were included as covariates into the regression model. Significance threshold for all contrasts of interest was set to $p < 0.01$ and $FWEc > 200$ voxels.

Peak voxels β-weights within the detected clusters from the VBM, rs-fMRI, and regression analyses were extracted for further correlation analyses with clinical and performance scores.

RESULTS

Participants' Characteristics

Of the total 54 participants enrolled to the study, 1 HC and 2 PD-noFOG were excluded due to motion artifacts, image artifacts, or low-quality images.

Detailed characteristics of the included participants can be viewed in **Table 1**. Briefly, no differences were observed in age and gender among the three groups (PD-FOG, PD-noFOG and HCs). As expected, patients with FOG had more severe motor impairments ($p < 0.001$ for UPDRS III and total score), higher H&Y score ($p < 0.001$) and worse cognitive performance compared with no freezers ($p = 0.001$).

Resting-State fMRI-Brainstem Network Functional Connectivity

Based on the calculated FC maps, frontal, parietal, and limbic brain regions were found to be functionally interconnected within the midbrain functional network (see **Supplementary Figure 1**). Based on the between-group comparisons of the calculated FC maps, PD-FOG patients showed significant FC decrease in the parieto-temporal cortex (right post central gyrus, right supra marginal gyrus, right superior temporal gyrus) compared to HCs (**Figure 1A**). Additionally, compared with PD-noFOG, PD-FOG patients exhibited decreased functional connectivity in the mid-cingulate ($p_{FWEc} < 0.001$) (**Figure 1B**). No significant differences were identified between PD noFOG patients and HCs. Results for functional connectivity within the brainstem network in the three groups are reported in **Table 2**.

Voxel-Wise Multiple Regression Analysis

Disease Severity and Gait Performance

Regression analysis showed significant correlations between disease severity, gait performance and functional connectivity levels at threshold $p_{FWEc} < 0.01$ in both PD groups. The scatter plots in **Figure 2** illustrate the association between the measured FC levels in these detected clusters, UPDRS-III total score and UPDRS-III gait sub-score (3.10).

UPDRS-III total scores were found to be significantly associated with FC levels in the left medial orbital gyrus (L MOFG), and the right anterior cingulate (ACC) in PD-FOG group (**Table 3** and **Figure 2A**). In the PD-noFOG group, higher UPDRS-III total score was associated with increased FC levels in mid-cingulate cortex (MCC), the right fusiform gyrus, and left and right ACC (**Table 3** and **Figure 2A**).

In the PD-FOG group, worse gait performance (i.e., higher gait sub-score in the UPDRS-III) correlated negatively with FC levels in the left cerebellar culmen (**Table 3** and **Figure 2B**). UPDRS-III gait sub-scores were positively associated with FC in the right superior temporal gyrus (R STG), right cuneus, and

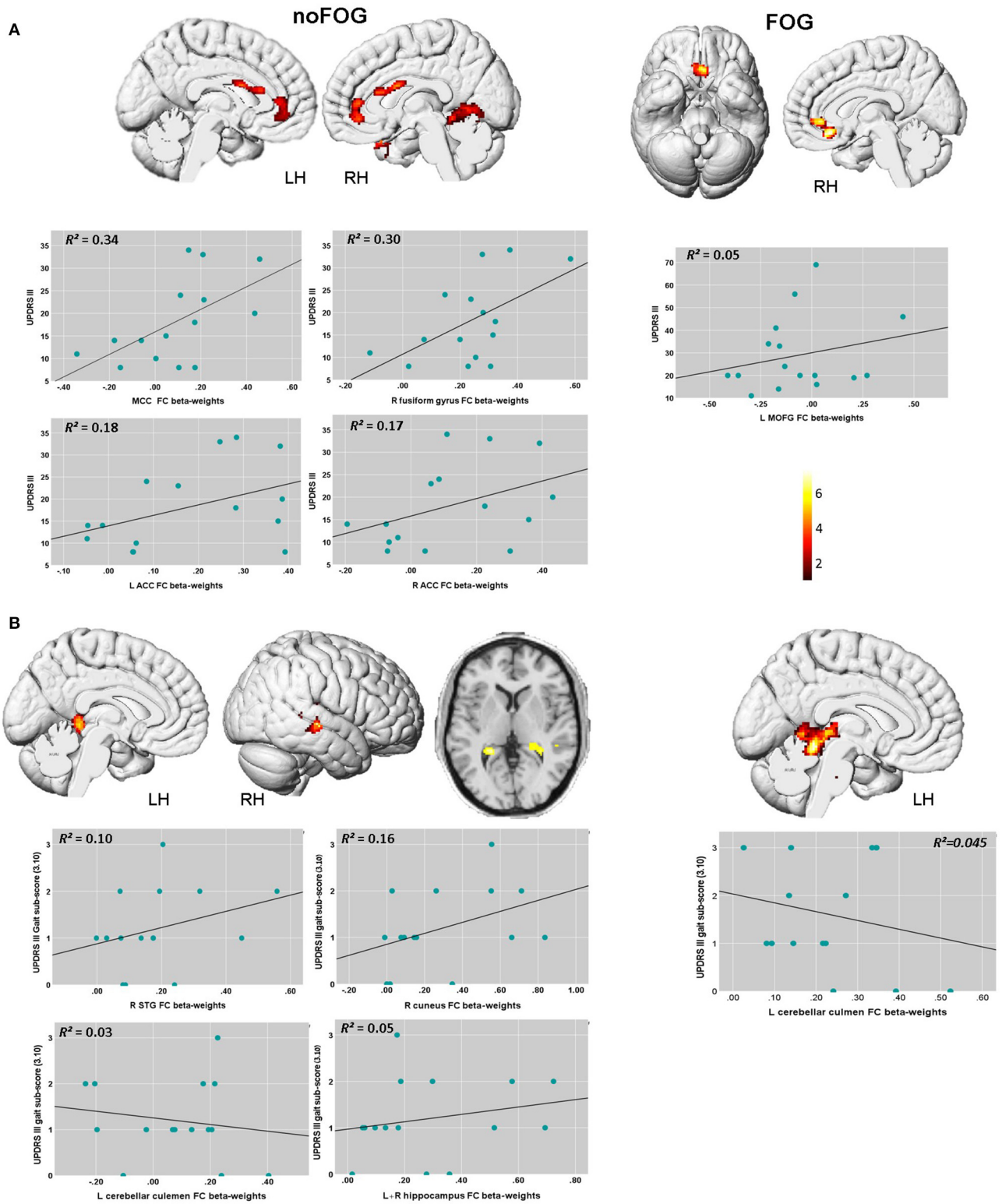


FIGURE 2 | Brain regions within the brainstem network showing significant associations between FC levels, UPDRS III total score, and UPDRS-III gait sub-score (item 3.10) based on the voxel-wise regression analysis. **(A)** In the PD-NOFOG group, positive association between UPDRS III total score and FC levels were detected, with higher UPDRS III score associated with higher FC levels in the MCC, the right fusiform gyrus, and bilateral ACC. In PD-FOG group, UPDRS III total score correlated positively with FC levels in theL MOFG, and the right ACC. **(B)** In the PD-NOFOG group, association between gait sub-score in the UPDRS-III and FC levels were

(Continued)

FIGURE 2 | detected, with higher UPDRS III gait sub-score associated with increased FC levels in R STG, R cuneus, L hippocampus and lower FC levels in L cerebellar culmen. In the PD-FOG group, higher UPDRS III gait sub-score was associated with lower FC levels in L cerebellar culmen. Results are reported at threshold $p < 0.01$- FWEc, scatter plots depict the association between UPDRS-3 scores and FC β-weights in these clusters.

left hippocampus, and negatively in the left cerebellar culmen (**Table 3** and **Figure 2B**)

Finally, in PD-FOG, severity of freezing (i.e., FOG-Q score) correlated negatively with FC levels within the right post central gyrus (R PCG) (**Table 4** and **Figure 3**).

MOCA

Based on the correlation analysis between MOCA scores and the extracted FC β-weights from the detected clusters in the regression analysis at threshold $p_{FWEc} < 0.01$, significant correlations between FC levels and total MOCA scores were obtained in the L ACC ($r^2 = 0.39$), the right cerebellar crus II ($r^2 = 0.05$), and SMA ($r^2 = 0.11$) (**Table 4** and **Figure 3**). No significant clusters were found to be associated with the MOCA scores in the noFOG group.

DISCUSSION

Here we applied a multimodal neuroimaging approach combing structural and functional imaging techniques for the study of whole-brain neural correlates of midbrain damage in age-and-gender matched PD-FOG and PD-noFOG patients. In a multi-step approach, we first identified GM atrophy using VBM, midbrain regions showing a significant GM decrease in PD with FOG compared to PD without FOG and healthy controls from the VBM analysis were used as seed region for midbrain FC calculation.

As a first result, patients with PD and FOG exhibited a greater GM atrophy in midbrain structures, as well as in parietal regions (including the bilateral precuneus and cuneal regions), thalamus and putamen compared to PD-FOG.

The observed patterns of cortical GM atrophy are in accordance with those reported by previous studies, in which significant difference in frontal and parietal GM volumes in FOG patients with respect to healthy and PD-no FOG participants (8, 24), where this pattern of GM atrophy was found to associated with FOG severity. Compared with PD-noFOG group, PD-FOG patients showed significant GM decrease in midbrain structures, thalamus, and putamen suggesting that damage in these subcortical regions might be linked to the development of FOG. GM decrease in the mesencephalic motor regions (MLR) and thalamus in freezers compared with non-freezers (22) was previously described, where thalamic atrophy in PD-FOG patients was found to be associated with visual recognition performance (25). These findings further highlight the role of these sub-cortical structures in the multi-sensory integration process where they play a key role in sustaining gait (7, 26). This is further supported by our obtained rs-fMRI results.

Based on the rs-fMRI analysis, here we found that patients with PD and FOG demonstrated significant decrease of midbrain-cortical FC levels in the R PCG, R supra marginal gyrus, and R STG compared to controls; and the middle cingulate compared to no-FOG group. Such patterns of FC alterations in FOG patients involving associative frontal, parietal, and limbic brain areas implies that higher cognitive networks that are involved in attention and visuo motor integration also give rise to gait disturbances in FOG (6, 27–29). Furthermore, the regression analysis with the UPDRS III total score, and UPDRS III gait performance sub-score showed that FC in a complex network involving the anterior and middle cingulate cortex, the fusiform gyrus and the superior temporal gyrus was associated with disease severity and worse gait performance in PD-noFO group, but not in PD patients with FOG. Differently, in both PD-FOG and PD-noFOG groups, FC connectivity of L cerebellar culmen was associated with better gait performance (lower scores at UPDRS III gait performance sub-score).

A possible explanation is that recruitment of compensatory areas that are involved in higher order functions, such as connecting emotion to motor control (30), multisensory integration (31), and integration for both egocentric and object-centered reference systems (32) might not be sufficient anymore for improving motor performance deficits in PD-noFOG group (maladaptive compensation), whereas the additional recruitment of cerebellum leads to better gait performance (adaptive compensation). In PD patients with FOG, we detected only adaptive compensatory activity of L cerebellar culmen in counteracting gait disturbances, possibly reflecting lower neural reserve.

Our rs-fMRI findings are all related to midbrain-cortical FC patterns. The pendunculopontine nucleus (PPN) is a major nucleus of the MLR, and has been implied in gait control and FOG pathophysiology [for a review see (33)]. Experimental data on neurophysiology of the PPN strongly support that PPN participates in higher functions of the brain. A considerable number of PPN cholinergic fibers innervate the centro median-para fascicular (CM-Pf) complex of the thalamus, which in turn innervates the cerebral cortex (34–36). Thus, the CM-Pf nucleus allows the PPN to gain access to different cortical functions and to several high-order functions of the brain, including attention, action selection, learning, memory, spatial perception, control of impulsivity and decision-making. PPN neurons may also participate in these functions through their axons ending in the striatum, where they synapse onto medium spiny neurons and cholinergic interneurons (37). In line with this, local field potentials recordings from PPN- implanted electrodes for deep brain stimulation in PD patients have demonstrated peaks in both alpha and beta bands, coherent with the cortex (38–41). Whilst beta band activity recorded from the basal ganglia and cortex has been linked to motor function, increasing evidence indicate that alpha oscillatory activity has an important role in attention and the allocation of processing resources (42).

TABLE 3 | Brain regions within the brainstem network showing significant correlations between UPDRS III total score and UPDRS III gait sub-score (item 3.10) and RS-FC levels based on voxel-wise multiple regression.

		Brain region	MNI coordinates X Y Z	Cluster size (# of voxels)	*Z*-value	*T*-value	*p*-value*
UPDRS III	*noFOG*	MCC	2 4 22	210	4.34	7.01	0.055
		R Fusiform gyrus	36 −64 −12	557	3.44	4.63	0.004
		L ACC	−4 40 6	293	3.13	4	0.027
		R ACC cingulate	6 42 6				
	FOG	L MOFG	−4 28 −14	298	3.39	4.42	0.024
		R anterior cingulate	6 38 −2				
UPDRS III gait sub-score (3.10)	*noFOG*	R STG	48 −22 −4	214	3.98	6.19	0.05
		R cuneus	22 −36 −2	452	3.39	4.66	0.007
		L hippocampus	−28 −38 −6	252	3.37	4.61	0.036
		L cerebellar culmen	−16 42 −16	232	3.11	4.07	0.043
	FOG	L cerebellar culmen	−28 −30 −34	1,373	4.54	7.7	0.001

*RS, resting-state; FC, functional connectivity; MNI, Montreal neurological institute; FOG, freezing of gait, R, right; L, left; MCC, mid-cingulate cortex; ACC, anterior cingulate cortex; MOFG, medial orbitofrontal gyrus; STG, superior temporal gyru; *FWEc>200 voxels.*

TABLE 4 | Brain regions within the brainstem network showing significant correlations between performance in MOCA, FOG severity, and RS-FC levels based on voxel-wise multiple regression.

		Brain region	MNI coordinates X Y Z	Cluster size (# of voxels)	*Z*-value	*T*-value	*p*-value
MOCA-Total							
	FOG	L Anterior cingulate	−16 30 22	4,115	4.68	8.71	<0.001*
		L MFG	−30 30 32		4.58	8.28	
		SMA	2 8 72	1,870	4.58	8.28	<0.001*
		L PCG	−20 −46 36				
		R cerebellum (Crus II)	24 −87 −50	702	3.85	5.82	0.001*
FOG severity							
	FOG	R PCG	56 −6 48	218	3.48	4.86	0.032

*RS, resting-state; FC, functional connectivity; MNI, Montreal neurological institute; MOCA, Montreal cognitive assessment battery for dementia; PD, Parkison's disease; FOG, freezing of gait; R, right; L, left; MFG, middle frontal gyrus; SMA, supplementary motor area; PCG, post central gyrus; *FWEc>200 voxels.*

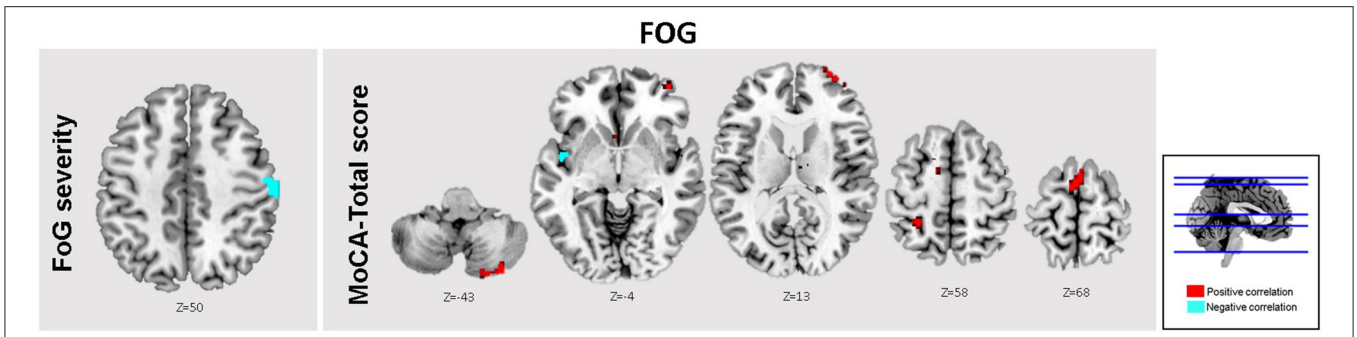


FIGURE 3 | Brain regions within the brainstem network showing significant associations between FC levels, and clinical scores. In the FOG group, the total MOCA scores were significantly associated with FC levels in the A ACC, SMA, L MFG, and bilateral cerebellar crus II (Red). Moreover, significant inverse associations between FOG severity scores and FC levels within the R PCG (Cyan). Results are reported at threshold $p < 0.01$-*FWEc*.

A magneto encephalography (MEG) study reported that these two PPN oscillatory bands show distinct connectivity patterns – with the beta band network coherent with the supplementary motor area (SMA), as well as the alpha network including the posterior mid-cingulate that is involved in integrating sensorimotor feedback during movement (43, 44). Our current findings further corroborate these reports, demonstrating that FOG, worse gait, as well as cognitive performance are associated with reduced midbrain-cortex FC in a large network including parieto-temporal cortex, and mid-cingulate.

Nonetheless, the limitations of the study deserve to be discussed. Firstly, our multimodal investigation was at 1.5T MR field strength, allowing a sub-optimal delineation of the PPN and other neighboring midbrain anatomical structures. Secondly, the relatively small sample size is also a limitation. However, it is worth pointing out that both PD groups were well-matched in terms of age and gender, but differed significantly in UPDRS and MOCA scores, which is expected as FOG is more commonly observed in the later stages of the disease (1). Moreover, PD patients enrolled to this were in a mid-stage of the disease, thus future studies should also include patients in an earlier and more advanced stage of the disease in order to better investigate the relationship between disease severity and local GM reduction in FOG.

In conclusion, using a multimodal approach, the present study offers novel information on the role of midbrain in FOG pathophysiology. Based on our results, we postulate that in the advanced stages of PD, structural integrity loss of the midbrain and the accompanying FC reductions between these structures and brains' higher cortical regions contribute to the occurrence and severity of FOG.

DATA AVAILABILITY STATEMENT

The raw data supporting the conclusions of this article will be made available by the authors, without undue reservation.

ETHICS STATEMENT

The studies involving human participants were reviewed and approved by the ethics committee of the University of Genoa, Italy. The patients/participants provided their written informed consent to participate in this study.

AUTHOR CONTRIBUTIONS

AD and MI: data analysis, writing, and finalizing manuscript. EP and LA: data collection, writing, and finalizing manuscript. MP and GB: data collection and revising manuscript. RM and LM: revising manuscript. All authors contributed to the article and approved the submitted version.

FUNDING

This study was partially funded by the Italian Ministry of Health (Grant No. GR-2011-0234976).

SUPPLEMENTARY MATERIAL

The Supplementary Material for this article can be found online at: https://www.frontiersin.org/articles/10.3389/fneur.2021.583593/full#supplementary-material

REFERENCES

1. Nutt JG, Bloem BR, Giladi N, Hallet M, Horak FB, Nieuwboer A. Freezing of gait: moving forward on a mysterious clinical phenomenon. *Lancet Neurol.* (2011) 10:734–44. doi: 10.1016/S1474-4422(11)70143-0
2. Giladi N, Treves TA, Simon ES, Shabtai H, Orlov Y, Kandinov B, et al. Freezing of gait in patients with advanced Parkinson's disease. *J Neural Transm.* (2011) 108:53–61. doi: 10.1007/s007020170096
3. Nieuwboer A, Giladi N. Characterizing freezing of gait in Parkinson's disease: models of an episodic phenomenon. *Mov Disord.* (2013) 28:1509–19. doi: 10.1002/mds.25683
4. Lewis SJG, Barker RA. A pathophysiological model of freezing of gait in Parkinson's disease. *Parkinsonism Relat Disord.* (2009) 15:333–8. doi: 10.1016/j.parkreldis.2008.08.006
5. Magrinelli F, Picelli A, Tocco P, Federico A, Roncari L, Smania N, et al. Pathophysiology of Motor Dysfunction in Parkinson's disease as the Rationale for Drug Treatment and Rehabilitation. *Parkinson's Dis.* (2016) 2016:9832839. doi: 10.1155/2016/9832839
6. Gilat M, Ehgoetz Martens KA, Miranda-Dominguez O, Arpan I, Shine JM, Mancini M, et al. Dysfunctional limbic circuitry underlying freezing of gait in Parkinson's disease. *Neuroscience.* (2018) 374:119–32. doi: 10.1016/j.neuroscience.2018.01.044
7. Lewis SJG, Shine M. The next step: a common neural mechanism for freezing of gait. *Neuroscientist.* (2016) 22:72–82. doi: 10.1177/1073858414559101
8. Tessitore A, Amboni M, Cirillo G, Corbo D, Picillo M, Russo A, et al. Regional gray matter atrophy in patients with Parkinson disease and freezing of gait. *AJNR.* (2012) 33:1804–9. doi: 10.3174/ajnr.A3066
9. Fling BW, Cohen RG, Mancini M, Nutt JG, Fair DA, Horak FB. Asymmetric pedunculopontine network connectivity in parkinsonian patients with freezing of gait. *Brain.* (2013) 136(Pt. 8):2405–18. doi: 10.1093/brain/awt172
10. Schweder PM, Hansen PC, Green AL, Quaghebeur G, Stein J, Aziz TA. Connectivity of the pedunculupontine nucleus in Parkinsonian freezing of gait. *Neuroreport.* (2010) 21:914–6. doi: 10.1097/WNR.0b013e32833ce5f1
11. Vercruysse S, Leunissen I, Vervoort G, Vandenberghe W, Swinnen S, Nieuwboer A. Microstructural changes in white matter associated with freezing of gait in Parkinson's disease. *Mov Disord.* (2015) 30:567–76. doi: 10.1002/mds.26130
12. Snyder AZ, Raichle ME. A brief history of the resting state: the Washington University perspective. *Neuroimage.* (2012) 62:902–10. doi: 10.1016/j.neuroimage.2012.01.044
13. Filippini N, MacIntosh BJ, Hough MG, Goodwin GM, Frisoni GB, Smith SM, et al. Distinct patterns of brain activity in young carriers of the APOE-ε4 allele. *Proc Natl Acad Sci USA.* (2009) 106:7209–14. doi: 10.1073/pnas.0811879106
14. Lenka A, Naduthota RM, Jha M, Panda R, Prajapati A, Jhunjhuwala K, et al. Freezing of gait in Parkinson's disease is associated with altered functional brain connectivity. *Parkinsonism Relat Disord.* (2016) 24:100–6. doi: 10.1016/j.parkreldis.2015.12.016
15. Canu E, Agosta F, Sarasso E, Volonte MA, Basaia S, Stojkovic T, et al. Brain structural and functional connectivity in Parkinson's disease with freezing of gait. *Hum Brain Mapp.* (2015) 36:5064–78. doi: 10.1002/hbm.22994
16. Tessitore A, Amboni M, Esposito F, Russo A, Picillo M, Marcuccio L, et al. Resting-state brain connectivity in patients with Parkinson's disease and freezing of gait. *Parkinsonism Relat Disord.* (2012) 18:781–7. doi: 10.1016/j.parkreldis.2012.03.018
17. Fling BW, Cohen RG, Mancicni M, Carpenter SD, Fair DA, Nutt JG, et al. Functional reorganization of the locomotor network in Parkinson patients with freezing of gait. *PLoS ONE.* (2014) 9:e100291. doi: 10.1371/journal.pone.0100291
18. Wang M, Jiang S, Yuan Y, Zhang L, Ding J, Wang J, et al. Alterations of functional and structural connectivity of freezing of gait in Parkinson's disease. *J Neurol.* (2016) 263:1583–92. doi: 10.1007/s00415-016-8174-4
19. Nieuwboer A, Rochester L, Herman T, et al. Reliability of the new freezing of gait questionnaire: agreement between patients with Parkinson's disease and their carers. *Gait Posture.* (2009) 30:459–63. doi: 10.1016/j.gaitpost.2009.07.108

20. Angelo Antonini, GA. Validation of the Italian version of the movement disorder society-unified Parkinson's disease rating scale. *Neurol Sci.* (2013) 34:683–7. doi: 10.1007/s10072-012-1112-z
21. Nasreddine ZS, Phillips N, Bedirian V, Charbonneau S, Whitehead V, Collin I, et al. The montreal cognitive assessment, MoCA: a brief screening tool for mild cognitive impairment. *J Am Geriatr Soc.* (2005) 53:695–9. doi: 10.1111/j.1532-5415.2005.53221.x
22. Snijders AH, Leunissen I, Bakker M, Overeem S, Helmich RC, Bloem BR, et al. Gait-related cerebral alterations in patients with Parkinson's disease with freezing of gait. *Brain.* (2011) 134(Pt. 1):59–72. doi: 10.1093/brain/awq324
23. Baer KJ, de la Cruz, Schumann A, Koehler S, Sauer H, Critchley H, et al. Functional connectivity and network analysis of midbrain and brainstem nuclei. *NeuroImage.* (2016) 134:53–63. doi: 10.1016/j.neuroimage.2016.03.071
24. Kostic V, Agosta F, Pievani M, Stefanova E, Jecmenica-Lukic M, Scarale A, et al. Pattern of brain tissue loss associated with freezing of gait in Parkinson disease. *Neurology.* (2012) 78:409–16. doi: 10.1212/WNL.0b013e318245d23c
25. Sunwoo MK, Choo KH, Hong JY, Lee JE, Sohn YH, Lee PH. Thalamic volume and related visual recognition are associated with freezing of gait in non-demented patients with Parkinson's disease. *Parkinsonism Relat Disord.* (2013) 19:1106–9. doi: 10.1016/j.parkreldis.2013.07.023
26. Keijsers NLW.Admiraal MA, Cools AR, Bloem BR, Gielen CCAM. Differential progression of proprioceptive and visual information processing deficits in Parkinson's disease. *Eur J Neurosci.* (2005) 21:239–48. doi: 10.1111/j.1460-9568.2004.03840.x
27. Okuma Y, Yanagisawa N. The clinical spectrum of freezing of gait in Parkinson's disease. *Mov Disord.* (2008) 23(Suppl. 2):S426–30. doi: 10.1002/mds.21934
28. Vercruysse S, Devos H, Munks L, Spidooren J, Vandenbossche J, Vandenberghe W, et al. Explaining freezing of gait in Parkinson's disease: motor and cognitive determinants. *Mov Disord.* (2012) 27:1644–51. doi: 10.1002/mds.25183
29. Weiss D, Schoellmann A, Fox MD, Bohnnen N, Factor SA, et al. Freezing of gait: understanding the complexity of an enigmatic phenomenon. *Brain.* (2020) 143:14–30. doi: 10.1093/brain/awz314
30. Shackman AJ, Salomons TV, Slagter HA, Fox AS, Winter JJ, Davidson RJ. The integration of negative affect, pain, and cognitive control in the cingulate cortex. *Nat Rev Neurosci.* (2011) 12:154–67. doi: 10.1038/nrn2994
31. McDonald JJ, Teder-Sälejärvi WA, Ward LM. Multisensory integration and crossmodal attention effects in the human brain. *Science.* (2001) 292:1791. doi: 10.1126/science.292.5523.1791a
32. Karnath HO. New insights into the functions of the superior temporal cortex. *Nat Rev Neurosci.* (2001) 2:568–76. doi: 10.1038/35086057
33. Thevathasan W, Moro E. What is the therapeutic mechanism of pedunculopontine nucleus stimulation in Parkinson's disease? *Neurobiol Dis.* (2019) 128:67–74. doi: 10.1016/j.nbd.2018.06.014
34. Kobayashi S, Nakamura Y. Synaptic organization of the rat parafascicular nu- cleus, with special reference to its afferents from the superior colliculus and the pedunculopontine tegmental nucleus. *Brain Res.* (2003) 980:80–91. doi: 10.1016/S0006-8993(03)02921-4
35. Saper CB, Loewy AD. Projections of the pedunculopontine tegmental nucleus in the rat: evidence for additional extrapyramidal circuitry. *Brain Res.* (1982) 252:367–72. doi: 10.1016/0006-8993(82)90404-8
36. Sugimoto T, Hattori T. Organization and efferent projections of nucleus tegmenti pedunculopontinus pars compacta with special reference to its cholinergic aspects. *Neuroscience.* (1984) 11:931–46. doi: 10.1016/0306-4522(84)90204-5
37. Lapper SR, Bolam JP. Input from the frontal cortex and the parafascicular nucleus to cholinergic interneurons in the dorsal striatum of the rat. *Neuroscience.* (1992) 51:533–45. doi: 10.1016/0306-4522(92)90293-B
38. Androulidakis AG, Khan S, Litvak V, Pleydell-Pearce C, Brown P, Gill SS. Local field potential recordings from the pedunculopontine nucleus in a parkinsonian patient. *Neuroreport.* (2008) 19:59–62. doi: 10.1097/WNR.0b013e3282f2e2d1
39. AndroulidakisAG, Mazzone P, Litvak V, Penny W, Dilone M, Doyle Gaynor LMF, et al. Oscillatory activity in the pedunculopontine area of patients with Parkinson's disease. *Exp Neurol.* (2008) 211:59–66. doi: 10.1016/j.expneurol.2008.01.002
40. Lau B, Welter ML, Belaid H, Vidal SF, Bardinet E, Grabli D, et al. The integrative role of the pedunculopontine nucleus in human gait. *Brain.* (2015) 138(Pt. 5):1284–96. doi: 10.1093/brain/awv047
41. Thevathasan W, Pogosyan A, Hyam JA, Jenjinson N, Foltynie T, Limousin P, et al. Alpha oscillations in the pedunculopontine nucleus correlate with gait performance in parkinsonism. *Brain.* (2012) 135(Pt. 1):148–60. doi: 10.1093/brain/awr315
42. Eusebio A, Brown P. Synchronisation in the beta frequency-band—the bad boy ofparkinsonism or an innocent bystander? *Exp Neurol.* (2009) 217:1–3. doi: 10.1016/j.expneurol.2009.02.003
43. Jha A, Litval V, Taulu S, Thevathsan W, Hyam JA, Foltynie T, et al. Functional connectivity of the pedunculopontine nucleus and surrounding region in Parkinson's disease. *Cereb Cortex.* (2017) 27:54–67. doi: 10.1093/cercor/bhw340
44. Vogt BA. Pain and emotion interactions in sub regions of the cingulate gyrus. *Nat Rev Neurosci.* (2005) 6:533–44. doi: 10.1038/nrn1704

Conflict of Interest: EP: received research grants from Italian Ministry of Health and the Michael J. Fox foundation. LA: received research grants from Italian Ministry of Health and Gossweiler Foundation. MI: received research grants from NIH, DOD, NMSS, FISM, and Teva Neuroscience; received fees for participating in advisory boards from Roche, Biogen, Merck and Genzyme.

The remaining authors declare that the research was conducted in the absence of any commercial or financial relationships that could be construed as a potential conflict of interest.

Copyright © 2021 Droby, Pelosin, Putzolu, Bommarito, Marchese, Mazzella, Avanzino and Inglese. This is an open-access article distributed under the terms of the Creative Commons Attribution License (CC BY). The use, distribution or reproduction in other forums is permitted, provided the original author(s) and the copyright owner(s) are credited and that the original publication in this journal is cited, in accordance with accepted academic practice. No use, distribution or reproduction is permitted which does not comply with these terms.

frontiers in Neurology

ORIGINAL RESEARCH
published: 28 February 2022
doi: 10.3389/fneur.2022.594711

Proton Magnetic Resonance Spectroscopy for Diagnosis of Non-Motor Symptoms in Parkinson's Disease

Ji-tian Guan[1†], Xin Zheng[2†], Lingfeng Lai[1†], Shuyi Sun[1†], Yiqun Geng[3], Xiaolei Zhang[1], Teng Zhou[4], Huan-ze Wu[5], Jia-qing Chen[5], Zhong-xian Yang[1], Xiao-hong zheng[5], Jia-xu Wang[5], Wei Chen[5] and You-qiao Zhang[5*]*

[1] Department of Radiology, Second Affiliated Hospital of Shantou University Medical College, Shantou, China, [2] Cell Therapy Center, Beijing Institute of Geriatrics, Xuanwu Hospital Capital Medical University, National Clinical Research Center for Geriatric Diseases and Key Laboratory of Neurodegenerative Diseases, Ministry of Education, Beijing, China, [3] Laboratory of Molecular Pathology, Shantou University Medical College, Shantou, China, [4] Department of Computer Science, Shantou University, Shantou, China, [5] Department of Neurology, Second Affiliated Hospital of Shantou University Medical College, Shantou, China

OPEN ACCESS

Edited by:
Wang Zhan,
University of Maryland, United States

Reviewed by:
Joseph O'Neill,
University of California, Los Angeles, United States
Reza Daneshvar,
Kashan University of Medical Science, Iran
Gina Ferrazzano,
Sapienza University of Rome, Italy

***Correspondence:**
Wei Chen
chw7203@126.com
You-qiao Zhang
youqiaozhang@163.com

[†] These authors share first authorship

Specialty section:
This article was submitted to Applied Neuroimaging, a section of the journal Frontiers in Neurology

Received: 14 August 2020
Accepted: 04 January 2022
Published: 28 February 2022

Citation:
Guan J-t, Zheng X, Lai L, Sun S, Geng Y, Zhang X, Zhou T, Wu H-z, Chen J-q, Yang Z-x, zheng X-h, Wang J-x, Chen W and Zhang Y-q (2022) Proton Magnetic Resonance Spectroscopy for Diagnosis of Non-Motor Symptoms in Parkinson's Disease. Front. Neurol. 13:594711. doi: 10.3389/fneur.2022.594711

Background: The current diagnosis of Parkinson's disease (PD) is mainly based on the typical clinical manifestations. However, 60% dopaminergic neurons have died when the typical clinical manifestations occur. Predictive neurobiomarkers may help identify those PD patients having non-motor disorders or in different stage and achieving the aim of early diagnosis. Up to date, few if any neuroimaging techniques have been described useful for non-movement disorders diagnosis in PD patients. Here, we investigated the alteration of metabolites in PD patients in different stage of PD and non-motor symptoms including sleep, gastrointestinal and cognitive dysfunction, by using the 1H-MRS.

Methods: A total of 48 subjects were included between 2017 and 2019: 37 PD (15 men, age 47–82 years) and 11 healthy people (8 men, age 49–74 years). All participants underwent MRI and multi-voxel ^{1}H-MRS examination within 3 days in admission. Six kinds of metabolites, such as creatine (Cr), N-acetyl aspartate/creatine (NAA/Cr), N-acetyl aspartate/choline (NAA/Cho), choline/creatine (Cho/Cr), lipid/creatine (LL/Cr), and myo-Inositol/creatine ratio (ml/Cr) were tested among the PD group and the control groups. Statistical analyses and correlation analyses were performed by using SPSS. The $p < 0.05$ was considered statistically significant.

Results: Compared late PD group with a control group or early group, higher Cr ratio and lower NAA/Cr ratio were observed in the late PD group ($p < 0.05$). The ml/Cr in the late PD group was also lower than that in the early PD group ($p < 0.05$). Regarding the relationship between metabolites and NMS, Cho/Cr was higher in the sleep disorder group, whereas ml/Cr was lower in the gastrointestinal dysfunction group in comparison with the non-symptom groups. Moreover, Cr, Cho/Cr, ml/Cr, and LL/Cr were identified to have higher concentrations in the cognitive group in thalamus.

Conclusions: Proton magnetic resonance spectroscopy is an advanced tool to quantify the metabolic changes in PD. Three biomarkers (Cr, NAA/Cr, and mI/Cr) were detected in the late stage of PD, suggesting that these markers might be potential to imply the progression of PD. In addition, subgroups analysis showed that MRS of thalamus is a sensitive region for the detection of cognitive decline in PD, and the alteration of neurochemicals (involving Cr, Cho, mI, and LL) may be promising biomarkers to predict cognitive decline in PD.

Keywords: early diagnosis, biomarker, Parkinson's disease, proton magnetic resonance spectroscopy, MRI

INTRODUCTION

With an estimated prevalence of 1–2 case per 1,000 persons above 60 years, Parkinson's disease (PD) is the second common neurodegenerative disease after Alzheimer's disease (AD) (1). Clinical symptoms of PD include motor disorders (such as, quiescent tremor, motor retardation, muscular rigidity, and postural gait abnormalities) (2) and non-motor disorders (sleep disturbances, cognitive disorders, emotional disorders, olfactory impairment, gastrointestinal dysfunction, bladder dysfunction, etc.) (3). The most important pathological change is the degeneration of dopamine (DA) neurons in the substantia nigra where it has been identified to have an accumulation of intracytoplasmic inclusions called Lewy bodies containing α-synuclein (4). Aggregates of α-synuclein have been found to spread from peripheral regions (olfactory bulb and gastrointestinal tract) to the lower brainstem, resulting in early emergence of premotor and non-motor symptoms (NMS) (5). A total of 60% dopaminergic neurons have died when the typical clinical manifestations occur (6). The Hoehn and Yahr scale (H&Y) is commonly used to assess the disease progression (Stage I–II for the early stage of PD, and Stage III–IV for the progressive PD) (7). The Movement Disorder Society–Unified Parkinson's Disease Rating Scale (MDS–UPDRS) and the NMS Scale (NMSS) are, respectively, used to evaluate the clinical severity of motor symptoms (8) and NMS for PD (9). The score of "Recall/Memory" in Mini-Mental State Examination (MMSE) is used to identify the cognitive state in patients with PD (10). However, a lack of objective data may result in decreased diagnostic accuracy of clinical NMS. In addition, early diagnosis before the onset of motor symptoms remains challenging since lack of distinguishable clinical and laboratory markers in premotor PD. Given the background, finding sensitive biomarkers in NMS and early stage PD *via* neuroimaging may not only help understand PD pathogenesis and progression, but also provide better early diagnosis and therapies for patients with PD (11).

Magnetic resonance spectroscopy (MRS) is a MRI technique that allows for direct quantifying microstructural, biochemical, and functional changes in human brain (12). Proton MRS (^{1}H-MRS) has been utilized to detect a wide range of endogenous neurochemicals in PD, such as N-acetylaspartate (NAA) as a marker reflecting the density of healthy neurons and the activity of neuronal function, Creatine (Cr) as a marker of energy metabolism, Choline (Cho) as a marker of both membrane catabolism and anabolism, and myo-Inositol (mI) as a marker of glial reaction. Besides, some magnetic resonance peaks overlap between lipid (Lip) and lactic acid (Lac), so the term "LL" is used in this study to qualify the sum of these two substances and to subsequently indicate the ischemia and the hypoxia in the neurodegenerative regions. Whole-brain MRS imaging was performed and the regions associated with NMS were selected for the spectral analysis, such as substantia nigra, pallidum, thalamus, prefrontal cortex, hippocampus, and parahippocampal gyrus (13).

In the previous study, we demonstrated that ^{1}H-MRS is a sensitive tool that is able to detect the alterations of neural-related metabolites in multiple cerebral regions, such as lower ratios of NAA/Cr and NAA/Cho in substantia nigra, globus pallidus, prefrontal lobe, hippocampus, cuneus gyrus, and dorsal thalamus (14). In addition, the reduced NAA/Cr and NAA/Cho were positively correlated with the unilateral disorder and cognitive impairment, while negatively correlated with UPDRS score. In the present study, we recollected data and mainly focused on assessing the cerebellar biochemical profile in different stages of patients with PD, especially patients with NMS, by using the ^{1}H-MRS. Correlation analysis will subsequently be conducted to investigate the relationship between metabolism levels and the H&Y stage, UPDRS scale, NMSS scale, MMSE score, or clinical factors in patients with PD.

MATERIALS AND METHODS

Subjects

This study was approved by the Ethics Committee of the Second Affiliated Hospital of Shantou University Medical College and was performed according to the Declaration of Helsinki. Written informed consent was obtained from all participants. A total of 48 subjects were included in our hospital between 2017 and 2019: 37 PD (15 mens, age 47–82 years) and 11 health people (8 mens, age 49–74 years). All subjects complied with the diagnostic criteria (2) and diagnosed by a neurologist. Exclusion criteria include (1) history of brain disease (cerebral infarction or cerebral hemorrhage), (2) presence of mental illness or metabolic syndrome, (3) severe heart, lung, liver, kidney, and other organ dysfunction, and (4) inability to provide consent. Patients were evaluated by the modified Hoehn-Yahr stage, UPDRS, NMSS, and MMSE scales. The Hoehn-Yahr stage included stages 1–5,

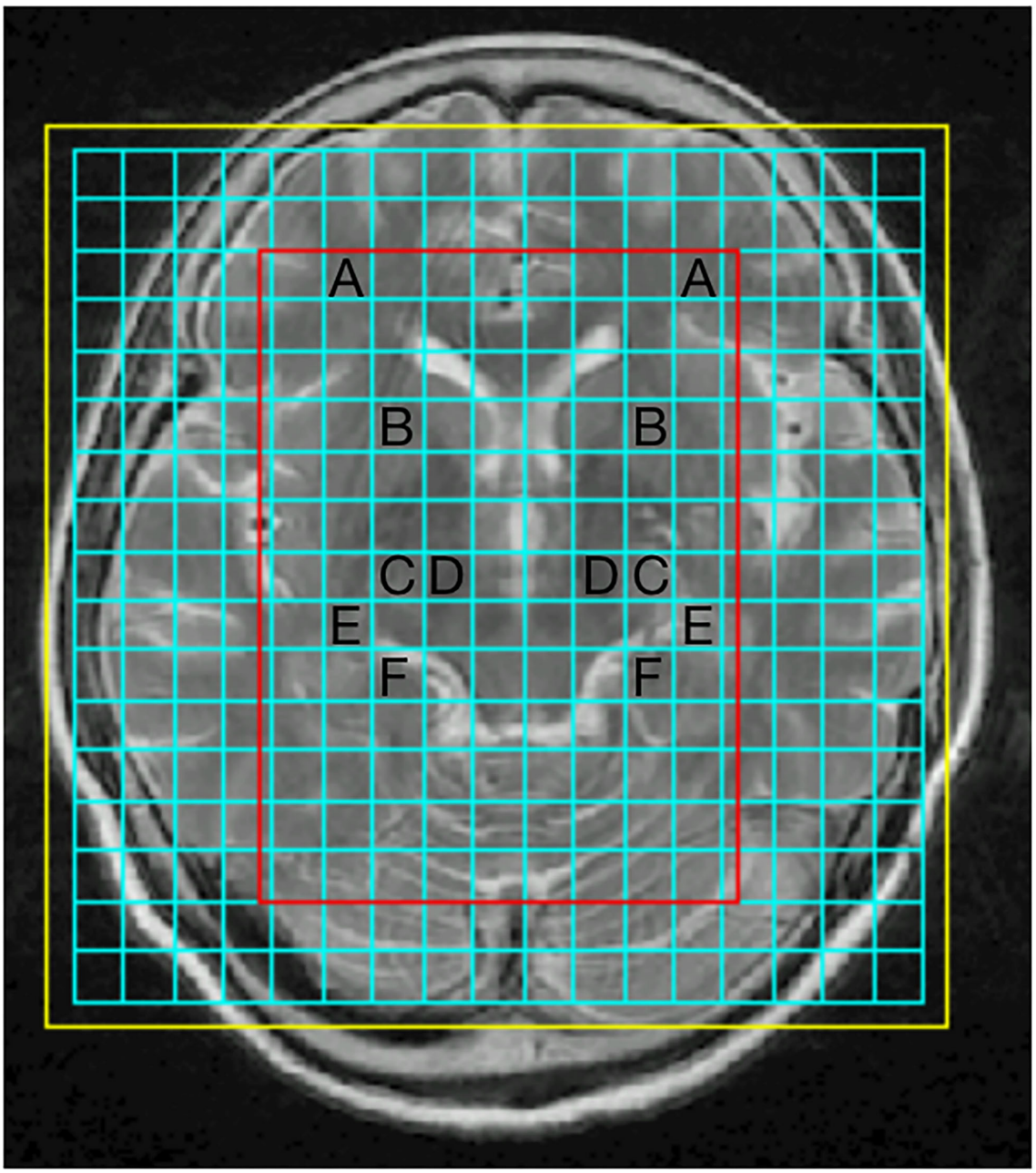


FIGURE 1 | Representative proton magnetic resonance spectroscopy (^{1}H-MRS) spectra for four brain regions: prefrontal cortex **(A)**, pallidum **(B)**, thalamus **(C)**, substantia nigra **(D)**, hippocampus **(E)**, parahippocampal gyrus **(F)**.

≤1.5 defined as the early stage of PD, while ≥1.5 defined as late-stage PD. All participants underwent MRI and multi-voxel ^{1}H-MRS examination within 3 days of admission.

MR Imaging and ^{1}H-MRS

The 3-T MRI system was used for conventional MRI and ^{1}H-MRS (GE signa excite 3T HD Ecospeed) with a standard 8-channel head coil, MR ADW 4.3 workstation Functool software. The axial scanning direction was parallel to the anterior cranial fossa, with a thickness of 5 mm, an interval of 1.5 mm, and a field of vision (FOV) of 24 cm. A total of 20 MRI images were obtained by scanning downward from the cranial top. Scanning parameters of each sequence are as follows: (1) T1WI: Using T1-weighted flux-Attenuated Inversion recovery imaging (T1-FLAIR), repetition time (TR) 2,000 ms, echo time (TE) 24 ms, number of excitations (NEX) = 2, FOV 24 × 18 cm, Matrix 320 × 224, slice thickness 5 mm and interlayer thickness 1.5 mm. (2) T2WI: Using T2-Weighted fast Recovery

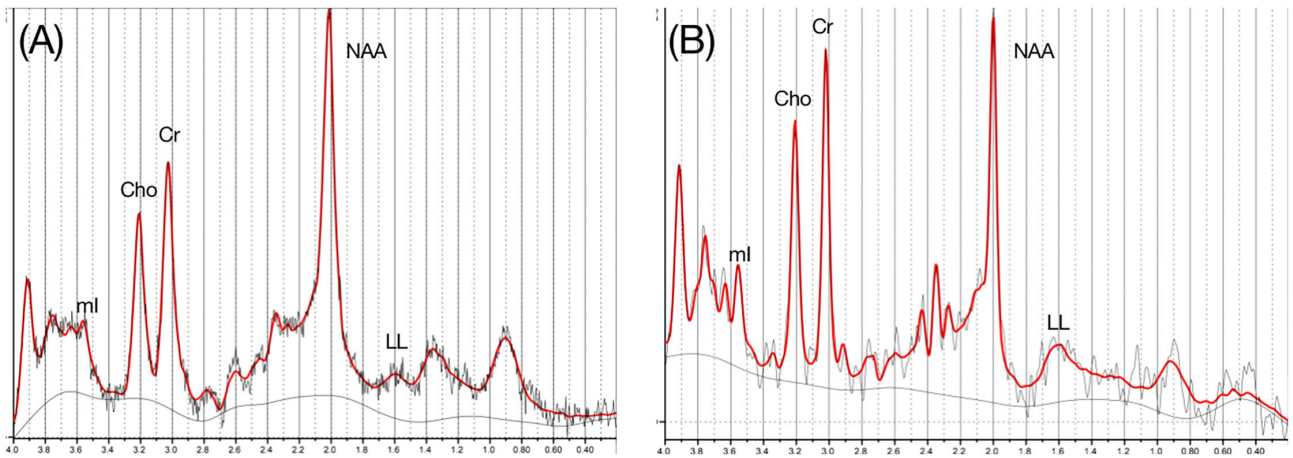


FIGURE 2 | ^{1}H-MRS spectra obtained from a control subject **(A)** and a patient with PD **(B)**.

fast spin-echo imaging (T2-FRfSE), TR 4,600 ms, TE 106 ms, NEX 1.5, FOV 24 × 24 cm, Matrix 384 × 384, slice thickness 5 mm and interlayer thickness 1.5 mm. Multi-voxel ^{1}H-MRS was performed using a 2D point resolved spectroscopy (2D PROBE-CSI PRESS) with the following parameters: TR, 1,500 ms; TE, 35 ms; phase × frequency = 18 × 18, volume of interest, 8 × 10 × 1 cm; FOV, 240 × 240 mm and NEX, 1. Voxel regions of interest (ROI) is located in the substantia nigra, pallidum, thalamus, prefrontal cortex, hippocampus, and parahippocampal gyrus. Typical ROI were chosen from the examined brain regions (**Figure 1**).

The spectral data obtained by GE MR imaging system were analyzed by using Cr as internal reference to calculate the neurometabolites ratio. Original data were sent to ADW4.3 workstation (GE Mediacel System Advantage Window 4.3), and the Functool software was used to process the ^{1}H-MRS image. Six kinds of metabolites, such as creatine (Cr), N-acetyl aspartate-to-creatine (NAA/Cr), N-acetylaspartate-to-choline (NAA/Cho), choline-to-creatine (Cho/Cr), lipid-to-creatine (LL/Cr), and myo-Inositol-to-creatine (mI/Cr) ratios were tested among PD group and the control groups. Examples of spectra are presented in **Figure 2**.

Statistical Analysis

The cerebral metabolites (Cr, NAA/Cr, NAA/Cho, Cho/Cr, LL/Cr, and mI/Cr ratios) of the early PD group, the progressive PD group and the control group were tested by using SPSS26.0 statistical analysis software. According to the homogeneity of variance, two independent sample *t*-test or approximate *t*-test (*t*-test) were used to compare the cerebral metabolites among the NMS subgroups in the case group. Spearman's correlation analysis was used to analyze the correlation of cerebral metabolites with gender, age, H&Y stage, MDS-UPDRS, NMSS, MMSE scales, hypertension, and diabetes in patients with PD. The $p < 0.05$ was considered statistically significant.

TABLE 1 | Demographics and clinical characteristics of the PD patients.

	Control group ($n = 11$)	Early PD group ($n = 24$)	Late PD group ($n = 13$)	*p1*	*p2*	*p3*
Age	57.45 ± 10.09	64.50 ± 10.54	65.84 ± 7.53	0.072	0.029	0.687
H-Y Score	0 ± 0	1.29 ± 0.46	3.15 ± 0.38	0.000	0.000	0.000
MDS-UPDR Score	0 ± 0	28.29 ± 12.82	51.46 ± 18.94	0.000	0.000	0.000
NMSS score	0 ± 0	63.83 ± 14.65	80.23 ± 16.59	0.000	0.000	0.004

p1 represents the p-value of the control group and the early stage group, p2 represents the p-value of the control group and the progressive group, and p3 represents the p-value of the early stage group and the progressive group.

RESULTS

Compare Age and Score of H&Y, MDS-UPDRS, NMSS Between Control Group, Early PD Group, and Late PD Group

The 24 cases (H&Y: 1.29 ± 0.46) showed premotor symptoms and 13 cases (H&Y: 3.15 ± 0.38) showed progressive symptoms. Three groups had statistical difference in Age, H&Y score, MDS-UPDRS score, and NMSS score (all $p < 0.05$). The baseline characteristics of the cases are showed in **Table 1**.

Compare Metabolic Status in Multiple Cerebral Regions Between Control Group, Early PD Group, and Late PD Group

There were statistically significant differences between two compared group (late PD group and control group; late PD group and early PD group) in metabolite ratios, while no statistically differences between early PD group and control group ($p > 0.05$). Due to the limit on the scope of this article, we predominantly presented the positive MRS results in **Table 2**.

TABLE 2 | Summary of the positive MRS results shown in left/right cerebral hemisphere in the early, late PD group and the control group.

		Early PD group/control group	Late PD group/control group	Late PD group/early PD group
Substantia Nigra	Left	–	NAA/Cr ↓	–
	Right	–	NAA/Cr ↓	–
Pallidum	Left	–	–	Cr ↑
	Right	–	–	–
Thalamus	Left	–	–	Cr ↑; mI/Cr ↓
	Right	–	–	–
Prefrontal Cortex	Left	–	–	–
	Right	–	Cr ↑	–
Parahippocampal Gyrus	Left	–	–	–
	Right	–	–	NAA/Cr ↓

Detail metabolic information of MRS results will be summarized in the **Supplementary Table 1**.

Compared late PD group with the control group, Cr in the right prefrontal cortex in the late PD group was higher than that in the control group ($p < 0.05$). NAA/Cr ratio in the bilateral substantia nigra in the late PD group was lower than that in the control group ($p < 0.05$). Compare late PD group with early group, Cr in the left pallium and the left thalamic in the late PD group was higher than that in the early PD group ($p < 0.05$). NAA/Cr in the right parahippocampal gyrus in the late PD group was lower than that in the early PD group ($p < 0.05$). The mI/Cr in the left thalamic in the late PD group was lower than that in the early PD group ($p < 0.05$). Cho/Cr and NAA/Cho were almost no statistically differences between the early PD group, the late PD group, and the control group ($p > 0.05$). Error bars of mean and standard deviation values of Cr, NAA/Cr were shown in **Figure 3**.

The Number and Ratio of NMS in PD Group

Overall, 37 patients (24 for early stage PD, 13 for progressive PD) and 11 controls were recruited in the study. For the cases, 70% patients suffering with sleep disorders, nearly 67% patients have gastrointestinal and/or bladder dysfunction, 35% for memory decline (shown in **Table 3**). The NMS gradually increase and worsen as PD disease progresses.

Comparison of Metabolites Between NMS Subgroups

Non-motor symptoms were categorized into three subgroups according to sleep condition, bowel condition, and cognitive state (as shown in **Table 4**). Cho/Cr in the right hippocampus in sleep disorder group was higher than that in the non-sleep disorder group ($t = 2.184$, $p < 0.005$). The mI/Cr in the right parahippocampal gyrus in gastrointestinal dysfunction group was lower than that in the non-gastrointestinal dysfunction group ($t = -2.210$, $p < 0.005$).

Comparing the cognitive group with non-cognitive group, four metabolites in twelve brain sites showed statistically difference (Cr, Cho/Cr, LL/Cr, mI/Cr, bilateral substantia nigra, bilateral globus pallidus, bilateral thalami, left prefrontal cortex, and right hippocampus), shown in **Figure 4**: (1) Cr in cognitive decline group was higher than non-cognitive declined group in bilateral substantia nigra (left: $t = 2.575$, $p < 0.05$, right: $t = 4.701$, $p < 0.01$), in the right pallidum ($t = 2.245$, $p < 0.05$), and in the left thalamus ($t = 2.442$, $p < 0.05$). (2) Cho/Cr in cognitive decline group was higher than non-cognitive declined group in the left thalamus ($t = 2.467$, $p < 0.05$) and the left prefrontal cortex ($t = -2.142$, $p < 0.05$). (3) LL/Cr in cognitive decline group was higher than non-cognitive declined group in left substantia nigra ($t = 2.766$, $p < 0.05$) and bilateral thalamus ($t = 2.746$ for left, 3.561 for right, $p < 0.05$). (4) mI/Cr in cognitive decline group was higher than non-cognitive declined group in bilateral thalamus ($t = 2.184$ for left, 2.096 for right, $p < 0.05$) and in right parahippocampal gyrus ($t = 3.147$, $p < 0.05$). Notably, other metabolites such as NAA/Cr and NAA/Cho had almost no statistical difference in all brain region in NMS subgroups ($p > 0.05$). Moreover, there was no statistically significant difference in Age and Score of H&Y, MDS-UPDRS, NMSS among the three subgroups. For more detail please see the **Supplementary Table 2**.

Correlation Analysis Between Cerebral Metabolites and Clinical Factors of PD

Spearman's correlation analysis was used to learn the relationship between cerebral metabolites and clinical factors such as age, gender, disease duration, H&Y scale, UPDRS score, NMSS score, hypertension, and diabetes in patients with PD (as shown in **Table 5**). Regarding to the correlation of age and metabolites in patients with PD, positive correlation between age and Cr was observed in bilateral substantia nigra ($r = 0.413$ for left, 0.420 for right, $p < 0.05$), in bilateral pallidum ($r = 0.356$ for left side, 0.360 for right, $p < 0.05$), in left prefrontal cortex ($r = 0.337$, $p < 0.05$), in right hippocampus ($r = 0.387$, $p < 0.05$), and in left parahippocampal gyrus ($r = 0.338$, $p < 0.05$). For the correlation of gender and MRS in PD, NAA/Cr in the right substantia nigra or thalamus, NAA/Cho in the right parahippocampal gyrus were found to be positively correlated with men.

In terms of the correlation of UPDRS score and metabolites in patients with PD, LL/Cr were positively correlated with MDS-UPDRS in bilateral pallidum ($r = 0.374$ for both side, $p < 0.05$), in left thalamus ($r = 0.338$, $p < 0.05$) and right hippocampus ($r = 0.380$, $p < 0.05$). Cho/Cr was positively correlated in the right substantia nigra ($r = 0.405$, $p < 0.05$) and the left thalamus ($r = 0.639$, $p < 0.05$). NAA/Cr was statistically significant negative correlation in the right prefrontal gyrus ($r = -0.338$, $p < 0.05$). For the correlation of MMSS and metabolites in PD, there was statistically significant positive correlation between Cho/Cr in the left thalamus ($r = 0.506$), whereas negative correlation in the substantia nigra. Of note, there was no statistically correlation between metabolites and disease duration or H&Y scale ($p > 0.05$).

When analyzing the correlation between MRS and common chronic diseases (such as hypertension and diabetes) in patients with PD, positive correlations in hypertension were observed in Cr in bilateral substantia nigra ($r = 0.356$ for left, 0.353

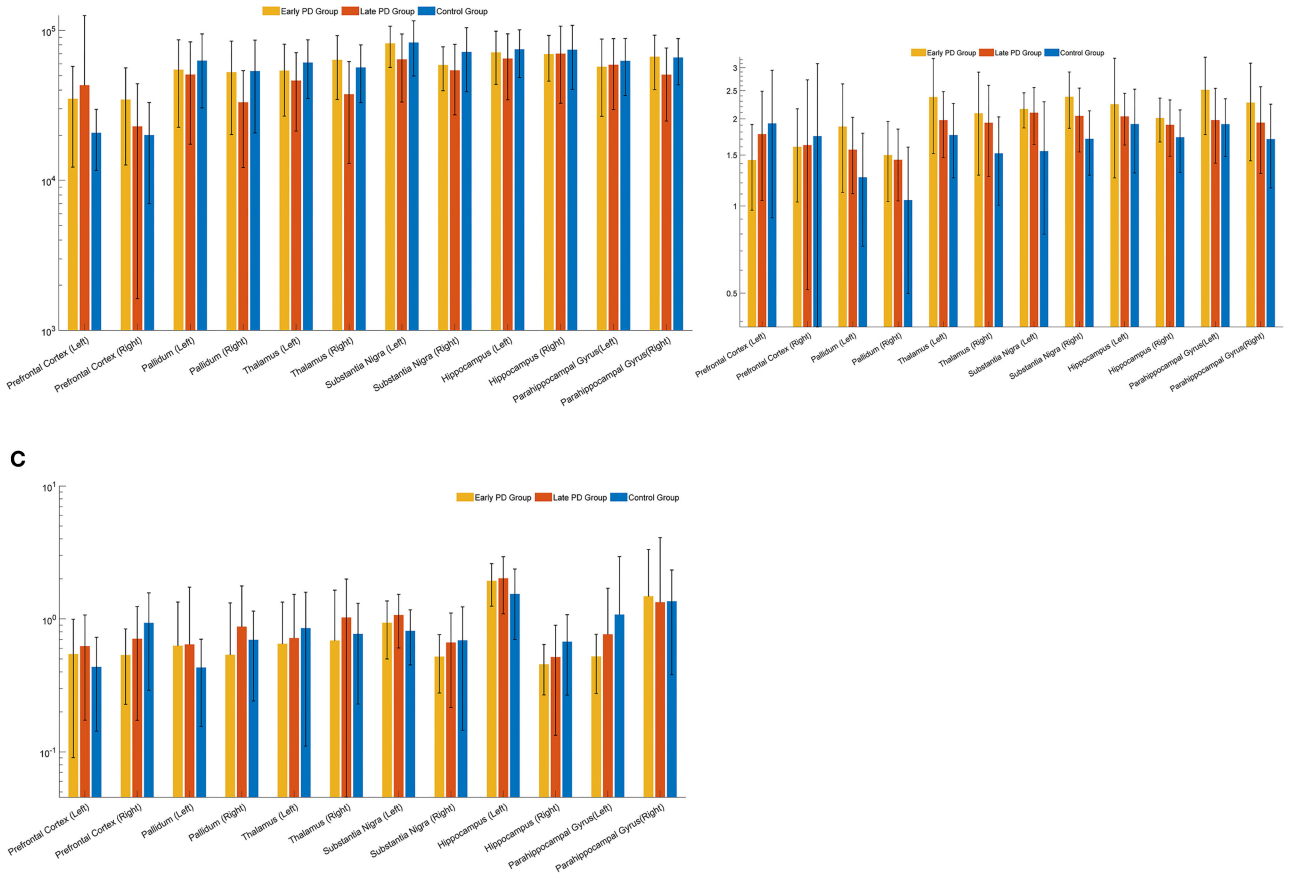


FIGURE 3 | Error bars of mean and standard deviation values of creatine (Cr) **(A)**, N-acetyl aspartate-to-creatine (NAA/Cr) **(B)**, and myo-Inositol-to-creatine (mI/Cr) **(C)**, at different sites in the early, late PD group, and the control group.

for right) and in the right pallidum ($r = 0.427$), and identified in NAA/Cr in the right parahippocampal gyrus ($r = 0.351$). Similarly, positive correlations in diabetes were observed in NAA/Cr in the right parahippocampal gyrus and hippocampus ($r = 0.330$, 0.242, respectively). By contrast, negative correlation was found between hypertension and MRS in mI/Cr in the left hippocampus ($r = -0.376$), and between diabetes and MRS in LL/Cr in the left pallidum and hippocampus ($r = -0.408$ to -0.342, respectively).

DISCUSSION

We enrolled 48 participants (37 patients and 11 controls) and conducted the statistical difference between control group, the early stage of PD, and the late stage of PD in age, clinical characteristics. A total of 24 cases (H&Y: 1.29 ± 0.46) showed premotor symptoms and 13 cases (H&Y: 3.15 ± 0.38) showed progressive symptoms. Statistical difference was observed in Age, H&Y score, MDS-UPDRS score, and NMSS score among different groups (all $p < 0.05$). MRS was then performed in the specific cerebral regions, such as substantia nigra, pallidum, thalamus, prefrontal cortex, hippocampus, and parahippocampal gyrus, to investigate the change of neurometabolic in different stage of PD. There were no statistical differences between the early PD group and the control group with regard to the metabolites ($p > 0.05$), suggesting that no metabolic abnormalities were detectable in early stage patients with PD in our study, which is consistent with another study by Nora Weiduschat et al., who also used MRS but did not detect any effects of PD on the concentrations of NAA, Cho, and Cr in striatal and gray matter in early stage patients with PD (15). Of note, the olfactory center and the dorsal nucleus of the vagus oblongata, which were mainly affected by the lesions in the early stage of Braak's study (13), were not selected in the present and Nora's study. The failure to detect changes in early biomarkers may be related to the inadequate coverage of ROIs. However, some studies had pointed out that the neurodegenerative process can affect different brain regions in the early PD stage, not just affect local areas by dopaminergic denervation. Martin Klietz et al. utilized the MRS technique to estimate the changes

TABLE 3 | Number and rate of non-motor symptoms (according to the results of MDS-UPDRS and NMSS scale).

	Symptoms	PD group overall case (ratio %)	Early PD group overall case (ratio %)	Late PD group overall case (ratio %)
	Overall case (ratio %)	37	24 (64.9)	13 (35.1)
1	Depression	31 (83.8)	20 (83.3)	11 (84.6)
2	Fatigue	28 (75.7)	18 (75.0)	10 (76.9)
3	Sleep disturbance	26 (70.2)	16 (66.7)	10 (76.9)
4	Anxiety	26 (70.2)	17 (70.8)	9 (69.2)
5	Gastrointestinal dysfunction	25 (67.6)	15 (62.5)	10 (76.9)
6	Bladder dysfunction	25 (67.6)	14 (58.3)	11 (84.6)
7	Apathy	19 (51.3)	11 (45.8)	8 (61.5)
8	Pain	17 (45.9)	8 (33.3)	9 (69.2)
9	Cognitive decline	13 (35.1)	7 (29.1)	6 (46.1)
10	Hallucination	2 (5.4)	2 (8.3)	0 (0.0)

TABLE 4 | The results of MRS in left/right cerebral hemisphere among the three subgroups of NMS-PD.

		Sleep disorder group/non sleep disorder	Gastrointestinal dysfunction/non gastrointestinal dysfunction	Cognitive decline/non cognitive decline
Substantia nigra	Left			Cr ↑; LL/Cr ↑
	Right			Cr ↑
Pallidum	Left			
	Right			Cr ↑
Thalamus	Left			Cr ↑; Cho/Cr ↑; LL/Cr ↑; mI/Cr↑
	Right			LL/Cr ↑; mI/Cr↑
Prefrontal cortex	Left			Cho/Cr ↑
	Right			
Hippocampus	Left			
	Right	Cho/Cr ↑		
Parahippocampal gyrus	Left			
	Right		mI/Cr ↓	mI/Cr ↑

in neurometabolic characteristics of early patients with PD in subcortical basal ganglia structures of bilateral frontal lobes, temporal lobes, parietal lobes, occipital lobes, and the cerebellum (16). Decreased NAA, Cho, and Cr were calculated in temporal-parietal, frontal, and occipital lobe. To put it in a nutshell, the alteration of pathology and neurometabolites in the present study may not spread to the substantia nigra, thalamus, hippocampus, and prefrontal lobes. Future studies should engage more ROIs for spectral analysis to identify more metabolic alterations and regions involved in the early pathological changes.

Compared late PD group with a control group or early group, higher Cr ratio and lower NAA/Cr ratio were observed in the late PD group ($p < 0.05$), which reflects the occurrence of neural cells apoptosis and compensatory for the neuronal energy consumption in certain regions. In addition, mI/Cr in the left thalamus in the late PD group was lower and suggested the activation and proliferation of glial cells in thalamic nuclei. In comparison to the early stage of PD, the disease has progressed and lesion-related metabolites were detected in the globus pallidus, thalamus, and hippocampus, which are consistent with the expansion of clinical symptom dimensions such as fatigue, abnormalities of sensation, and motor disorders. Notably, Cho/Cr and NAA/Cho had almost no statistically difference between the early PD group, the late PD group, and the control group ($p > 0.05$). The results in comparison with the late PD group and control group or early group suggested that higher Cr ratio, lower NAA/Cr, and lower mI/Cr might be potential biomarkers to imply the progression of PD.

Different severity and progression of neuropathology are determinants of Parkinson's symptoms (5). Pathology of the inclusion body was limited to the medulla oblongata/pontine tegmentum and olfactory bulb/anterior olfactory nucleus during pre-symptomatic stages 1–2, resulting in the obvious appearance of NMS, whereas relatively slight damage of motor symptoms, neural cells and glial cell disorder. In stages 3–4, the lesions gradually spread upward to the midbrain substantia nigra

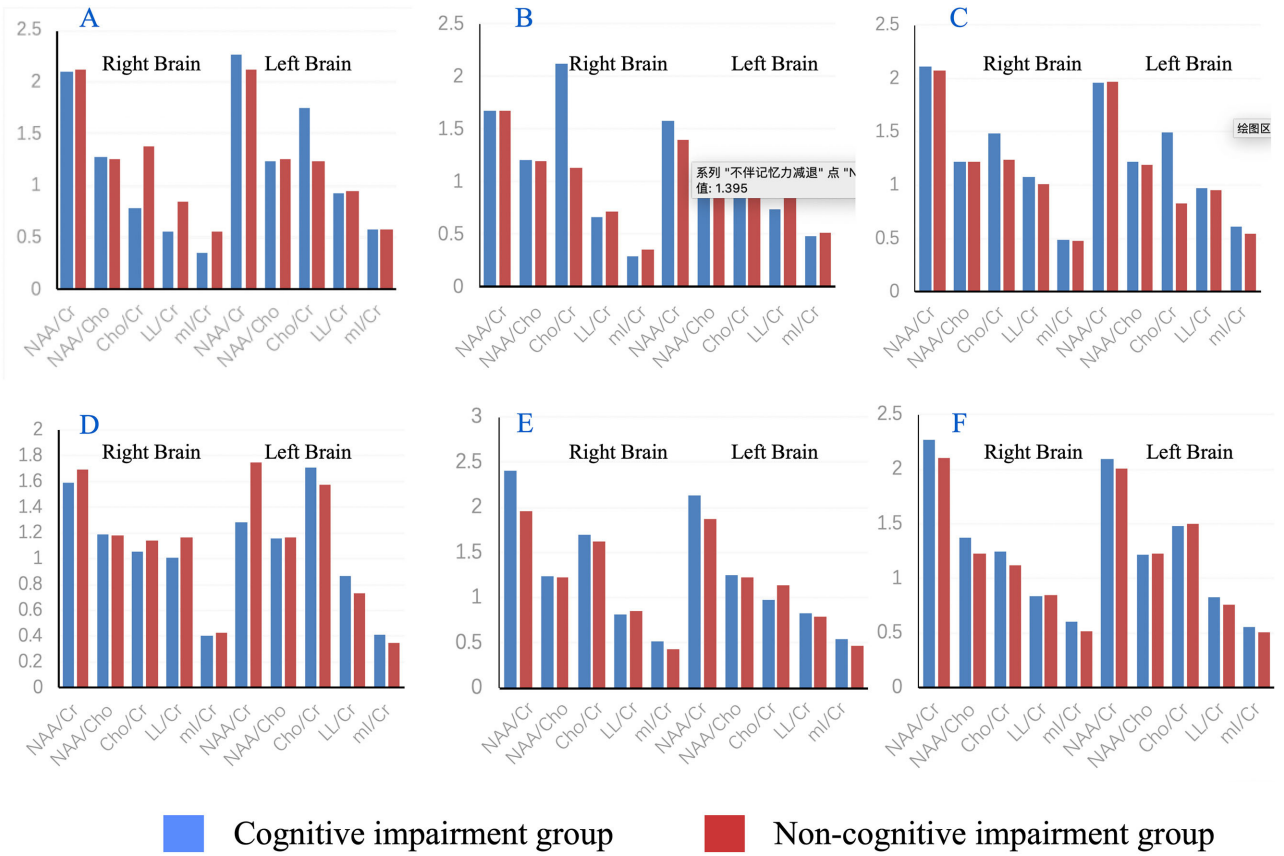


FIGURE 4 | Histogram of mean metabolite results in substantia nigra **(A)**, pallidum **(B)**, thalamus **(C)**, prefrontal cortex **(D)**, hippocampus **(E)** and parahippocampal gyrus **(F)** with comparison between the cognitive impairment group and non-memory impairment group.

and nuclear grays, causing the gradual reduction of dopamine transmitters in caudate and putamen regions. Motor symptoms emerged at this point. In the end-stages 5–6, pathologies enter to the cerebral cortex and limbic system, which give rise to the manifestation of cerebral cortex dysfunction such as cognitive impairment and emotional disorders.

To find out the specific neurometabolites in NMS patients, we first counted the number of NMS in our included sample. More than 10 kinds of NMS occur in the early stage of patients with PD, mainly depression, anxiety, fatigue, and sleep disorders, and it gradually increases and worse as PD disease progresses. Specific markers presented in different cerebral regions were identified *via* comparing the alteration of neurochemicals between certain symptoms. The results of this study suggested that Cho/Cr in the right hippocampus in sleep disorder group was higher than that in the non-sleep disorder group ($t = 2.184$, $p < 0.005$). The increased level of Cho/Cr reflects the enhanced of membrane catabolism in the damaged site of hippocampus, which is consistent with a study showed the reduced of hippocampal volume in patients with insomnia (17). Of note, the underlying neuropathology of rapid eye movement (REM) sleep behavior disorder (RBD) is the degeneration of cholinergic neurons and neurons in brain stem and limbic system caused by aggregation of α-synuclein (18). Considering the high incidence of RBD (up to 65% of patients with PD), we speculated that sleep disturbances in patients may be related to RBD. Future study about the relationship between MRS metabolic results and RBD should be carried out.

A previously study conducted in patients with mild cognitive impairment or dementia, indicated a significant reductions of NAA in occipital region (19), dorsolateral prefrontal cortex and hippocampus (20), and a dramatically decreased NAA/Cr in temporoparietal cortex (21), occipital lobe (22), and posterior cingulate cortex (23). In contrast, the Cho/Cr ratio increased in the posterior cingulate in patient with mild cognitive impairment (22, 23). However, these statistical differences became no significant after adjusting for age, gender, and MDS-UPDRS, suggesting that MRS of posterior cingulate is not a useful biomarker for revealing the cognitive impairment in PD (23). In the present study, multiple metabolites in cognitive group were higher than that in non-cognitive group, such as Cr in bilateral substantia nigra, right pallidum, and left thalamus, Cho/Cr in the left thalamus and left prefrontal cortex, mI/Cr in bilateral thalamus and right parahippocampal gyrus, LL/Cr in left substantia nigra and bilateral thalamus. Together, pathologies associated with cognitive impairment

TABLE 5 | Relationship between cerebral metabolites and clinical factors including age, gender, disease duration, H&Y scale, UPDRS score, NMSS score, hypertension and diabetes in PD patients was shown by using spearman correlation analysis.

Position	Metabolites	Gender		Age		Disease duration	
		r	*p*	*r*	*p*	*r*	*p*
Left substantia nigra	Cr	0.036	0.832	0.413*	0.011	−0.175	0.301
	NAA/Cr	0.250	0.135	0.069	0.685	0.176	0.296
	NAA/Cho	0.106	0.533	−0.018	0.917	0.092	0.589
	Cho/Cr	0.168	0.321	0.227	0.177	0.164	0.333
	LL/Cr	0.072	0.671	0.078	0.646	0.106	0.534
	ml/Cr	−0.013	0.940	−0.021	0.903	−0.343*	0.037
Right substantia nigra	Cr	0.129	0.447	0.420**	0.010	−0.073	0.669
	NAA/Cr	0.570**	0.000	0.248	0.139	−0.051	0.766
	NAA/Cho	0.279	0.095	0.260	0.121	−0.131	0.440
	Cho/Cr	0.121	0.475	−0.064	0.707	0.087	0.607
	LL/Cr	0.013	0.940	−0.194	0.251	0.317	0.056
	ml/Cr	−0.129	0.447	0.053	0.757	−0.188	0.265
Left pallidum	Cr	0.124	0.466	0.356*	0.030	0.074	0.664
	NAA/Cr	−0.155	0.360	0.171	0.312	0.154	0.364
	NAA/Cho	−0.008	0.964	0.171	0.311	0.141	0.406
	Cho/Cr	0.175	0.299	0.059	0.731	−0.014	0.936
	LL/Cr	0.000	1.000	−0.122	0.470	−0.062	0.715
	ml/Cr	0.052	0.762	0.040	0.816	0.002	0.990
Right pallidum	Cr	−0.077	0.649	0.360*	0.029	−0.132	0.437
	NAA/Cr	−0.139	0.411	0.024	0.890	−0.089	0.602
	NAA/Cho	−0.067	0.693	0.180	0.286	0.004	0.982
	Cho/Cr	0.309	0.062	−0.097	0.568	0.264	0.115
	LL/Cr	−0.026	0.880	−0.067	0.692	0.216	0.199
	ml/Cr	0.057	0.739	−0.311	0.061	−0.056	0.741
Left thalamus	Cr	0.222	0.187	0.285	0.087	0.106	0.533
	NAA/Cr	0.119	0.484	−0.005	0.977	−0.092	0.590
	NAA/Cho	−0.021	0.904	0.179	0.289	−0.031	0.854
	Cho/Cr	0.142	0.402	−0.129	0.445	0.088	0.605
	LL/Cr	−0.005	0.976	−0.043	0.802	0.245	0.144
	ml/Cr	0.015	0.928	0.137	0.418	−0.011	0.947
Right thalamus	Cr	0.031	0.856	0.221	0.188	−0.111	0.514
	NAA/Cr	0.389*	0.017	−0.047	0.780	0.095	0.576
	NAA/Cho	0.170	0.314	0.128	0.449	0.008	0.964
	Cho/Cr	−0.059	0.727	−0.015	0.930	0.203	0.229
	LL/Cr	0.224	0.182	0.128	0.451	0.092	0.589
	ml/Cr	−0.026	0.880	−0.020	0.908	0.037	0.828
Left prefrontal cortex	Cr	0.180	0.285	0.337*	0.041	0.096	0.570
	NAA/Cr	0.206	0.221	−0.260	0.120	0.222	0.186
	NAA/Cho	0.201	0.233	−0.080	0.637	0.103	0.545
	Cho/Cr	−0.134	0.429	0.140	0.410	−0.373*	0.023
	LL/Cr	0.075	0.660	0.012	0.946	−0.130	0.442
	ml/Cr	0.227	0.177	0.207	0.219	0.169	0.318
Right prefrontal cortex	Cr	−0.052	0.762	0.139	0.411	0.011	0.951
	NAA/Cr	0.013	0.940	0.044	0.794	−0.304	0.067
	NAA/Cho	0.070	0.682	0.012	0.945	−0.083	0.627
	Cho/Cr	−0.018	0.916	−0.079	0.643	0.224	0.183
	LL/Cr	−0.108	0.524	0.053	0.755	−0.097	0.567
	ml/Cr	0.077	0.649	−0.103	0.546	−0.029	0.864

(Continued)

TABLE 5 | Continued

Position	Metabolites	Gender		Age		Disease duration	
		r	*p*	*r*	*p*	*r*	*p*
Left hippocampus	Cr	−0.010	0.952	0.157	0.354	0.095	0.576
	NAA/Cr	−0.124	0.466	0.048	0.777	−0.223	0.185
	NAA/Cho	0.083	0.627	−0.080	0.637	0.057	0.740
	Cho/Cr	0.124	0.465	−0.322	0.052	−0.168	0.320
	LL/Cr	0.232	0.167	−0.051	0.765	0.140	0.408
	ml/Cr	−0.113	0.504	−0.148	0.381	−0.063	0.711
Right hippocampus	Cr	0.067	0.693	0.387*	0.018	−0.123	0.469
	NAA/Cr	−0.139	0.411	−0.032	0.849	0.011	0.949
	NAA/Cho	−0.183	0.278	−0.235	0.162	0.248	0.139
	Cho/Cr	0.085	0.617	0.027	0.876	0.152	0.368
	LL/Cr	−0.064	0.705	−0.314	0.058	0.172	0.309
	ml/Cr	−0.031	0.856	−0.122	0.472	−0.247	0.140
Left parahippocampal gyrus	Cr	0.005	0.976	0.338*	0.041	0.160	0.344
	NAA/Cr	−0.170	0.314	0.101	0.553	0.229	0.173
	NAA/Cho	−0.021	0.904	0.158	0.350	−0.128	0.450
	Cho/Cr	−0.286	0.086	0.216	0.198	0.224	0.183
	LL/Cr	0.103	0.544	0.013	0.941	0.077	0.649
	ml/Cr	−0.005	0.976	0.194	0.249	−0.154	0.362
Left parahippocampal gyrus	Cr	−0.113	0.504	0.056	0.741	−0.095	0.575
	NAA/Cr	−0.183	0.278	0.182	0.280	0.290	0.082
	NAA/Cho	0.387*	0.018	−0.178	0.292	0.287	0.085
	Cho/Cr	−0.508**	0.001	−0.099	0.561	0.020	0.906
	LL/Cr	−0.021	0.904	−0.069	0.685	0.089	0.600
	ml/Cr	0.103	0.544	−0.153	0.367	−0.136	0.423
Position	**Metabolites**	**H-Y classification**		**MDS-UPDRS scale score**		**NMSS scale score**	
		r	*p*	*r*	*p*	*r*	*p*
Left substantia nigra	Cr	0.089	0.602	0.208	0.217	0.081	0.634
	NAA/Cr	0.177	0.294	0.233	0.164	0.225	0.181
	NAA/Cho	−0.145	0.393	−0.131	0.439	0.028	0.870
	Cho/Cr	0.079	0.641	0.197	0.242	0.140	0.409
	LL/Cr	0.171	0.312	0.219	0.193	0.212	0.207
	ml/Cr	−0.236	0.160	−0.034	0.841	−0.192	0.256
Right substantia nigra	Cr	0.240	0.152	0.281	0.092	0.208	0.216
	NAA/Cr	−0.142	0.403	−0.083	0.624	0.067	0.694
	NAA/Cho	−0.059	0.728	0.144	0.395	0.197	0.243
	Cho/Cr	−0.193	0.25	0.405*	0.013	−0.339	0.051
	LL/Cr	−0.184	0.275	0.013	0.937	−0.201	0.234
	ml/Cr	−0.257	0.125	−0.044	0.796	−0.161	0.343
Left pallidum	Cr	0.041	0.81	0.106	0.534	−0.028	0.869
	NAA/Cr	0.110	0.517	0.073	0.666	0.080	0.637
	NAA/Cho	0.045	0.791	0.174	0.304	0.132	0.437
	Cho/Cr	0.165	0.328	−0.160	0.345	−0.215	0.200
	LL/Cr	0.011	0.947	0.374*	0.023	0.246	0.142
	ml/Cr	0.019	0.913	0.242	0.150	−0.056	0.743
Right pallidum	Cr	0.041	0.810	0.106	0.534	−0.028	0.869
	NAA/Cr	0.110	0.517	0.073	0.666	0.080	0.637

(Continued)

TABLE 5 | Continued

Position	Metabolites	Gender		Age		Disease duration	
		r	*p*	*r*	*p*	*r*	*p*
	NAA/Cho	0.045	0.791	0.174	0.304	0.132	0.437
	Cho/Cr	0.165	0.328	−0.160	0.345	−0.215	0.200
	LL/Cr	0.011	0.947	0.374*	0.023	0.246	0.142
	ml/Cr	0.019	0.913	0.242	0.150	−0.056	0.743
Left thalamu	Cr	−0.058	0.735	0.122	0.472	−0.021	0.904
	NAA/Cr	−0.036	0.830	0.115	0.496	0.116	0.495
	NAA/Cho	0.286	0.086	0.223	0.184	0.206	0.222
	Cho/Cr	0.213	0.207	0.639**	0.000	0.506**	0.001
	LL/Cr	0.163	0.334	0.338*	0.041	0.206	0.221
	ml/Cr	−0.233	0.164	0.075	0.660	−0.090	0.597
Right thalamus	Cr	−0.136	0.421	−0.011	0.947	0.007	0.968
	NAA/Cr	0.168	0.321	0.246	0.142	0.060	0.723
	NAA/Cho	0.106	0.531	0.138	0.416	0.022	0.897
	Cho/Cr	0.162	0.337	0.258	0.124	0.205	0.223
	LL/Cr	−0.024	0.887	0.123	0.470	0.108	0.525
	ml/Cr	0.049	0.772	0.133	0.433	−0.017	0.921
Left prefrontal cortex	Cr	0.146	0.389	0.253	0.130	0.119	0.484
	NAA/Cr	0.046	0.786	−0.009	0.956	0.052	0.762
	NAA/Cho	0.168	0.319	−0.021	0.903	0.165	0.329
	Cho/Cr	−0.309	0.063	−0.130	0.444	−0.280	0.093
	LL/Cr	0.077	0.651	0.139	0.411	0.081	0.635
	ml/Cr	−0.077	0.652	0.127	0.453	0.034	0.841
Right prefrontal cortex	Cr	0.107	0.529	0.160	0.345	0.097	0.569
	NAA/Cr	−0.265	0.113	−0.338*	0.041	−0.249	0.138
	NAA/Cho	−0.112	0.510	0.013	0.940	−0.072	0.672
	Cho/Cr	0.092	0.590	0.130	0.442	0.243	0.147
	LL/Cr	0.078	0.646	−0.033	0.847	−0.007	0.968
	ml/Cr	0.035	0.838	0.101	0.552	−0.007	0.968
Left hippocampus	Cr	−0.176	0.299	−0.049	0.774	–.354*	0.031
	NAA/Cr	0.145	0.391	0.135	0.426	0.296	0.075
	NAA/Cho	0.000	0.999	0.159	0.348	0.059	0.729
	Cho/Cr	−0.260	0.120	0.047	0.783	0.010	0.951
	LL/Cr	−0.164	0.332	−0.052	0.758	−0.085	0.615
	ml/Cr	−0.031	0.854	0.251	0.135	0.170	0.314
Right hippocampus	Cr	0.073	0.667	0.05	0.77	−0.083	0.627
	NAA/Cr	0.123	0.467	0.276	0.098	0.350*	0.034
	NAA/Cho	0.119	0.482	0.150	0.374	0.196	0.246
	Cho/Cr	−0.004	0.983	0.180	0.286	0.161	0.341
	LL/Cr	0.308	0.063	0.380*	0.020	0.121	0.477
	ml/Cr	−0.026	0.881	0.219	0.193	0.002	0.988
Left parahippocampal gyrus	Cr	0.068	0.689	0.160	0.345	−0.049	0.773
	NAA/Cr	0.270	0.106	−0.009	0.956	0.084	0.619
	NAA/Cho	0.179	0.288	0.024	0.886	0.119	0.483
	Cho/Cr	0.011	0.948	0.170	0.316	0.187	0.267
	LL/Cr	−0.133	0.432	0.091	0.592	−0.008	0.961
	ml/Cr	−0.064	0.705	0.072	0.670	0.075	0.657
Right parahippocampal gyrus	Cr	−0.029	0.865	0.305	0.067	0.128	0.451
	NAA/Cr	0.334*	0.043	0.237	0.158	0.163	0.335

(Continued)

TABLE 5 | Continued

Position	Metabolites	Gender		Age		Disease duration	
		r	*p*	*r*	*p*	*r*	*p*
	NAA/Cho	0.073	0.667	0.024	0.890	0.046	0.788
	Cho/Cr	−0.080	0.636	0.071	0.675	−0.110	0.517
	LL/Cr	0.123	0.470	0.297	0.075	0.142	0.402
	ml/Cr	−0.277	0.097	−0.017	0.922	−0.096	0.572

Position	Metabolites	Hypertension		Diabetes mellitus	
		r	*p*	*r*	*p*
Left substantia nigra	Cr	0.356*	0.030	0.236	0.159
	NAA/Cr	0.234	0.163	0.175	0.299
	NAA/Cho	0.154	0.362	0.094	0.580
	Cho/Cr	0.279	0.094	0.163	0.335
	LL/Cr	−0.160	0.345	−0.236	0.159
	ml/Cr	−0.066	0.700	−0.114	0.501
Right substantia nigra	Cr	0.353*	0.032	0.204	0.226
	NAA/Cr	0.228	0.175	0.041	0.811
	NAA/Cho	0.165	0.328	0.126	0.456
	Cho/Cr	−0.239	0.153	−0.143	0.400
	LL/Cr	−0.137	0.419	−0.245	0.145
	ml/Cr	−0.091	0.591	−0.073	0.666
Left pallidum	Cr	0.228	0.175	0.024	0.886
	NAA/Cr	0.091	0.591	0.237	0.159
	NAA/Cho	0.157	0.354	0.045	0.792
	Cho/Cr	0.046	0.789	0.024	0.886
	LL/Cr	−0.311	0.061	−0.408*	0.012
	ml/Cr	−0.188	0.265	−0.261	0.119
Right pallidum	Cr	0.427**	0.008	0.318	0.055
	NAA/Cr	−0.097	0.568	0.139	0.413
	NAA/Cho	0.131	0.439	0.143	0.400
	Cho/Cr	0.057	0.738	−0.273	0.102
	LL/Cr	−0.285	0.087	−0.098	0.565
	ml/Cr	−0.217	0.198	−0.293	0.078
Left thalamus	Cr	0.299	0.072	0.041	0.811
	NAA/Cr	−0.017	0.920	−0.139	0.413
	NAA/Cho	0.111	0.512	0.057	0.737
	Cho/Cr	0.148	0.381	0.049	0.774
	LL/Cr	−0.063	0.712	0.065	0.701
	ml/Cr	−0.074	0.663	−0.090	0.598
Right thalamus	Cr	0.302	0.069	0.041	0.811
	NAA/Cr	0.257	0.125	0.065	0.701
	NAA/Cho	0.259	0.121	0.122	0.471
	Cho/Cr	0.074	0.663	0.041	0.811
	LL/Cr	0.040	0.815	−0.147	0.386
	ml/Cr	−0.040	0.815	−0.057	0.737
Left prefrontal cortex	Cr	0.228	0.175	−0.033	0.848
	NAA/Cr	0.048	0.776	0.139	0.413
	NAA/Cho	0.051	0.763	0.045	0.792
	Cho/Cr	0.037	0.828	−0.033	0.848
	LL/Cr	0.020	0.907	0.041	0.811
	ml/Cr	−0.051	0.763	−0.179	0.288

(Continued)

TABLE 5 | Continued

Position	Metabolites	Hypertension		Diabetes mellitus	
		r	*p*	*r*	*p*
Right prefrontal cortex	Cr	0.239	0.154	0.049	0.774
	NAA/Cr	−0.023	0.893	−0.041	0.811
	NAA/Cho	0.160	0.345	−0.020	0.905
	Cho/Cr	−0.011	0.947	0.037	0.829
	LL/Cr	−0.040	0.815	−0.098	0.565
	mI/Cr	−0.057	0.738	−0.041	0.811
Left hippocampus	Cr	0.063	0.712	−0.057	0.737
	NAA/Cr	−0.023	0.893	0.273	0.102
	NAA/Cho	−0.063	0.712	−0.016	0.924
	Cho/Cr	−0.168	0.320	−0.196	0.246
	LL/Cr	−0.217	0.198	−0.342*	0.038
	mI/Cr	−0.376*	0.022	−0.041	0.811
Right hippocampus	Cr	0.171	0.312	0.139	0.413
	NAA/Cr	0.251	0.134	0.342*	0.038
	NAA/Cho	−0.126	0.459	0.188	0.266
	Cho/Cr	0.182	0.280	−0.155	0.360
	LL/Cr	−0.185	0.272	−0.110	0.517
	mI/Cr	−0.251	0.134	−0.073	0.666
Left parahippocampal gyrus	Cr	0.217	0.198	0.147	0.386
	NAA/Cr	0.194	0.250	0.192	0.256
	NAA/Cho	0.143	0.400	0.130	0.441
	Cho/Cr	0.040	0.815	0.122	0.471
	LL/Cr	−0.131	0.439	−0.187	0.266
	mI/Cr	−0.251	0.134	−0.130	0.442
Right parahippocampal gyrus	Cr	0.114	0.502	0.033	0.848
	NAA/Cr	0.351*	0.033	0.330*	0.046
	NAA/Cho	−0.011	0.947	−0.082	0.631
	Cho/Cr	−0.091	0.591	−0.053	0.755
	LL/Cr	0.017	0.920	0.049	0.774
	mI/Cr	−0.120	0.480	−0.196	0.246

*The relationship between metabolites and sex, age and disease cours. *means P ≤0.05; n represents the number of cases. The metabolites were correlated with H-Y classification, MDS-UPDRS scale score and NMSS scale score. *means P ≤ 0.05; n represents the number of cases. Association of metabolites with hypertension and diabetes mellitus. *means P ≤ 0.05; n represents the number of cases.*

were identified to gradually spread from midbrain to cerebral cortex. Cr, Cho/Cr, mI/Cr, and LL/Cr were all relatively high in the thalamus, suggesting that MRS of thalamus is sensitive for the detection of cognitive decline in PD. In addition, the alteration of neurochemicals in specific regions (such as Cr, Cho, MI, and LL) may be promising biomarkers to predict or identify cognitive decline in PD. Notably, other metabolites such as NAA/Cr and NAA/Cho had almost no statistical difference in the brain region in NMS subgroups ($p > 0.05$). There were no statistically differences between three NMS subgroups in Age, Score of H&Y, MDS-UPDRS, and NMSS.

Spearman's correlation analysis was used to study the connection between cerebral metabolites and clinical factors such as age, gender, disease duration, H&Y scale, UPDRS score, NMSS score, hypertension, and diabetes in patients with PD. Ratio of four metabolites, Cr, NAA/Cr, Cho/Cr, LL/Cr, mI/Cr, and NAA/Cho in twelve brain sites were obtained. Cr showed positive correlation with age. Normally, the decreased NAA was mainly associated with decreased gray matter volume and healthy neurons, while the increased Cho, Cr, and mI were related to the increased of white matter (24). The increased level of Cr is consistent with the reduced ratio of gray to white matter and the increased of energy metabolism requirements in the brain. On the other hand, for the relationship between metabolites and clinical symptoms, both Cho/Cr and LL/Cr had positive correlation with motor symptoms, while only Cho/Cr was positively correlated with the NMS. Choline is a component of cerebral myelin and cell membrane (16). The level of Cho might

be a helpful hint to imply pathological changes in patients with PD.

LIMITATION AND PERSPECTIVE

In the present study, it is difficult to acquire an accurate metabolic profile in the early stage of PD since some cerebral structures, which are too subtle to be detected and this neuroimaging technique may not be capable to avoid the partial volume effect of the adjacent structures. In addition, the metabolite concentrations of glutamate and GABA, as well as the region of the dorsal nucleus of the vagus oblongata and the olfactory center, were not measured due to a lack of appropriate processing software or equipment. Moreover, the sample size and the study time are not enough. The difference in the incidence of NMS between patients with PD and healthy individuals was not statistically analyzed. Further study could expand the sample size, extend the observation time, conduct more subgroups analysis, and engage more regions of interest (ROIs) for spectral analysis to identify more metabolic alteration. Currently, imaging techniques in the diagnosis of PD are still no clear. With the rapid development of MRS parameters, sequences, software and other technologies, the accuracy of MRS will continuously improve. Further study should be focused on the finding techniques which can directly reflect the changes of cell metabolites in different damaged sites so as to find out more objective markers that can be used to evaluate the site and severity of brain damage. Interestingly, the three-dimensional (3D) midbrain organoids, which are able to recapitulate features of the midbrain and simulate disease progression, can be combined with advanced neuroimaging techniques to investigate the complex pathological development.

CONCLUSION

Proton magnetic resonance spectroscopy is an advanced tool to quantify neuronal integrity deficits and metabolic changes in PD. Although no symbolic biomarkers were detected in early patients with PD in our study, three biomarkers (Cr, NAA/Cr, and mI/Cr) experienced statistically significant differences, with an increased level of Cr, whereas reduced ratio of NAA/Cr and mI/Cr. In addition, NMS were classified into several subgroups (such as sleep disorder group, gastrointestinal dysfunction group, and cognitive impairment group). Cho/Cr might be a useful marker to identify sleep disorder, while decreased mI/Cr ratio might imply gastrointestinal dysfunction. MRS of thalamus is sensitive for the detection of cognitive decline in PD. The alteration of neurochemicals in specific regions (such as Cr, Cho, mI, and LL) may be promising biomarkers to predict or identify cognitive decline in PD. Furthermore, patients in the late stage of PD, or with cognitive impairment, have relatively extensive and severe brain lesions.

DATA AVAILABILITY STATEMENT

The raw data supporting the conclusions of this article will be made available by the authors, without undue reservation.

ETHICS STATEMENT

The studies involving human participants were reviewed and approved by the Ethics Committee of the Second Affiliated Hospital of Shantou University Medical College and was performed according to the Declaration of Helsinki. The participants provided their written informed consent to participate in the study.

AUTHOR CONTRIBUTIONS

J-tG, XZ, L-fL, and S-yS contributed equally to study design and manuscript writing. Y-qG, Xl-Z, TZ, H-zW, J-qC, and Z-xY reviewed literature and analyzed data. X-hZ and T-xW conducted the neuroimaging. CW and Y-qZ assessed and treated the patients. All authors contributed to the article and approved the submitted version.

FUNDING

This study was supported by the clinical research promotion project of Shantou University Medical College (201409), Guangdong Science and Technology Special Foundation (2021)88-27, and 2020 Li Ka Shing Foundation Cross-Disciplinary Research Grant (No. 2020LKSFG05D).

SUPPLEMENTARY MATERIAL

The Supplementary Material for this article can be found online at: https://www.frontiersin.org/articles/10.3389/fneur.2022.594711/full#supplementary-material

REFERENCES

1. Tysnes OB, Storstein A. Epidemiology of Parkinson's disease. *J Neural Transm.* (2017) 124:901–5. doi: 10.1007/s00702-017-1686-y
2. Postuma RB, Berg D, Stern M, Poewe W, Olanow CW, Oertel W, et al. MDS clinical diagnostic criteria for Parkinson's disease. *Mov Disord.* (2015) 30:1591–601. doi: 10.1002/mds.26424
3. Schapira AHV, Chaudhuri KR, Jenner P. Non-motor features of Parkinson disease. *Nat Rev Neurosci.* (2017) 18:435–50. doi: 10.1038/nrn.2017.62
4. Poewe W, Seppi K, Tanner CM, Halliday GM, Brundin P, Volkmann J, et al. Parkinson disease. *Nat Rev Dis Primers.* (2017) 3:17013. doi: 10.1038/nrdp.2017.13
5. Braak H, Del Tredici. K. Neuropathological staging of brain pathology in sporadic parkinson's disease: separating the wheat from the Chaff. *J Parkinsons Dis.* (2017) 7:S71–85. doi: 10.3233/jpd-179001

6. Kordower JH, Olanow CW, Dodiya HB, Chu Y, Beach TG, Adler CH, et al. Disease duration and the integrity of the nigrostriatal system in Parkinson's disease. *Brain.* (2013) 136:2419–31. doi: 10.1093/brain/awt192
7. Hoehn MM, Yahr MD. Parkinsonism: onset, progression and mortality. *Neurology.* (1967) 17:427–42. doi: 10.1212/wnl.17.5.427
8. Goetz CG, Tilley BC, Shaftman SR, Stebbins GT, Fahn S, Martinez-Martin P, et al. Movement disorder society-sponsored revision of the Unified Parkinson's disease rating scale (MDS-UPDRS): scale presentation and clinimetric testing results. *Mov Disord.* (2008) 23:2129–70. doi: 10.1002/mds.22340
9. Chaudhuri KR, Martinez-Martin P, Brown RG, Sethi K, Stocchi F, Odin P, et al. The metric properties of a novel non-motor symptoms scale for Parkinson's disease: results from an international pilot study. *Mov Disord.* (2007) 22:1901–11. doi: 10.1002/mds.21596
10. Folstein MF, Folstein SE, McHugh PR. Mini-mental state. A practical method for grading the cognitive state of patients for the clinician. *J Psychiatr Res.* (1975) 12:189–98. doi: 10.1016/0022-3956(75)90026-6
11. Le W, Dong J, Li S, Korczyn AD. Can biomarkers help the early diagnosis of Parkinson's disease? *Neurosci Bull.* (2017) 33:535–42. doi: 10.1007/s12264-017-0174-6
12. Posse S, Otazo R, Dager SR, Alger J. MR spectroscopic imaging: principles and recent advances. *J Magn Reson Imag.* (2013) 37:1301–25. doi: 10.1002/jmri.23945
13. Braak H, Ghebremedhin E, Rüb U, Bratzke H, Del Tredici. K. Stages in the development of Parkinson's disease-related pathology. *Cell Tissue Res.* (2004) 318:121–34. doi: 10.1007/s00441-004-0956-9
14. Guan J, Rong Y, Wen Y, Wu H, Qin H, Zhang Q, et al. Detection and application of neurochemical profile by multiple regional (1)H-MRS in Parkinson's disease. *Brain Behav.* (2017) 7:e00792. doi: 10.1002/brb3.792
15. Weiduschat N, Mao X, Beal MF, Nirenberg MJ, Shungu DC, Henchcliffe C. Usefulness of proton and phosphorus MR spectroscopic imaging for early diagnosis of Parkinson's disease. *J Neuroimaging.* (2015) 25:105–10. doi: 10.1111/jon.12074
16. Klietz M, Bronzlik P, Nösel P, Wegner F, Dressler DW, Dadak M, et al. Altered neurometabolic profile in early parkinson's disease: a study with short echo-time whole brain MR spectroscopic imaging. *Front Neurol.* (2019) 10:777. doi: 10.3389/fneur.2019.00777
17. Winkelman JW, Benson KL, Buxton OM, Lyoo IK, Yoon S, O'Connor S, et al. Lack of hippocampal volume differences in primary insomnia and good sleeper controls: an MRI volumetric study at 3 Tesla. *Sleep Med.* (2010) 11:576–82. doi: 10.1016/j.sleep.2010.03.009
18. Adler CH, Beach TG. Neuropathological basis of nonmotor manifestations of Parkinson's disease. *Mov Disord.* (2016) 31:1114–9. doi: 10.1002/mds.26605
19. Summerfield C, Gómez-Ansón B, Tolosa E, Mercader JM, Martí MJ, Pastor P, et al. Dementia in Parkinson disease: a proton magnetic resonance spectroscopy study. *Arch Neurol.* (2002) 59:1415–20. doi: 10.1001/archneur.59.9.1415
20. Pagonabarraga J, Gómez-Ansón B, Rotger R, Llebaria G, García-Sánchez C, Pascual-Sedano B, et al. Spectroscopic changes associated with mild cognitive impairment and dementia in Parkinson's disease. *Dement Geriatr Cogn Disord.* (2012) 34:312–8. doi: 10.1159/000345537
21. Hu MT, Taylor-Robinson SD, Chaudhuri KR, Bell JD, Morris RG, Clough C, et al. Evidence for cortical dysfunction in clinically non-demented patients with Parkinson's disease: a proton MR spectroscopy study. *J Neurol Neurosurg Psychiatry.* (1999) 67:20–6. doi: 10.1136/jnnp.67.1.20
22. Nie K, Zhang Y, Huang B, Wang L, Zhao J, Huang Z, et al. Marked N-acetylaspartate and choline metabolite changes in Parkinson's disease patients with mild cognitive impairment. *Parkinsonism Relat Disord.* (2013) 19:329–34. doi: 10.1016/j.parkreldis.2012.11.012
23. Almuqbel M, Melzer TR, Myall DJ, MacAskill MR, Pitcher TL, Livingston L, et al. Metabolite ratios in the posterior cingulate cortex do not track cognitive decline in Parkinson's disease in a clinical setting. *Parkinsonism Relat Disord.* (2016) 22:54–61. doi: 10.1016/j.parkreldis.2015.11.008
24. Ding XQ, Maudsley AA, Sabati M, Sheriff S, Schmitz B, Schütze M, et al. Physiological neuronal decline in healthy aging human brain - an *in vivo* study with MRI and short echo-time whole-brain (1)H MR spectroscopic imaging. *Neuroimage.* (2016) 137:45–51. doi: 10.1016/j.neuroimage.2016.05.014

Conflict of Interest: The authors declare that the research was conducted in the absence of any commercial or financial relationships that could be construed as a potential conflict of interest.

Publisher's Note: All claims expressed in this article are solely those of the authors and do not necessarily represent those of their affiliated organizations, or those of the publisher, the editors and the reviewers. Any product that may be evaluated in this article, or claim that may be made by its manufacturer, is not guaranteed or endorsed by the publisher.

Copyright © 2022 Guan, Zheng, Lai, Sun, Geng, Zhang, Zhou, Wu, Chen, Yang, zheng, Wang, Chen and Zhang. This is an open-access article distributed under the terms of the Creative Commons Attribution License (CC BY). The use, distribution or reproduction in other forums is permitted, provided the original author(s) and the copyright owner(s) are credited and that the original publication in this journal is cited, in accordance with accepted academic practice. No use, distribution or reproduction is permitted which does not comply with these terms.

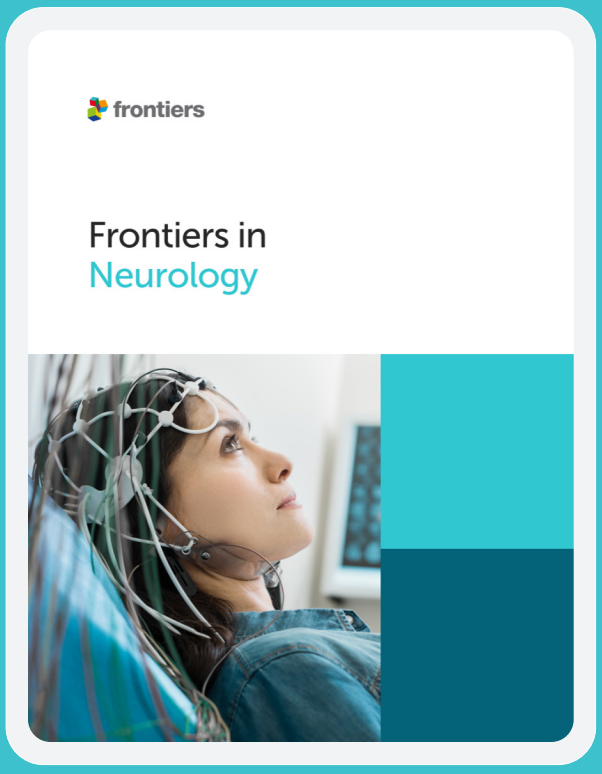
Frontiers in Neurology

Explores neurological illness to improve patient care

The third most-cited clinical neurology journal explores the diagnosis, causes, treatment, and public health aspects of neurological illnesses. Its ultimate aim is to inform improvements in patient care.

Discover the latest Research Topics

See more →



Frontiers

Avenue du Tribunal-Fédéral 34
1005 Lausanne, Switzerland
frontiersin.org

Contact us

+41 (0)21 510 17 00
frontiersin.org/about/contact